NASA/CR-97-206242/PT1

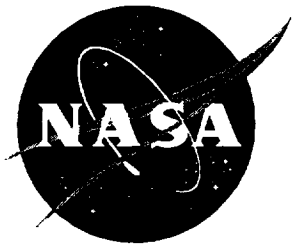

Magnetohydrodynamics Accelerator Research Into Advanced Hypersonics (MARIAH)

Final Report

Jack A. Baughman, David A. Micheletti, Gordon L. Nelson, and Gloyd A. Simmons
MSE Technology Applications, Inc., Butte, Montana

National Aeronautics and
Space Administration

Langley Research Center
Hampton, Virginia 23681-2199

Prepared for the National Aeronautics and Space Administration under Purchase Order A45416D and for the U.S. Department of Energy under Contract DE-AC22-96EW96405

October 1997

Acknowledgments

MSE Technology Applications, Inc., wishes to acknowledge the contributions to the MARIAH Project made by the following organizations:

University of Texas at Arlington
Ohio State University
Princeton University
NASA Ames Research Center
Bluesky Research, Inc.
Pulsatron
Russian Central Aerohydrodynamic Institute
ENGO

Available from the following:

NASA Center for AeroSpace Information (CASI)
800 Elkridge Landing Road
Linthicum Heights, MD 21090-2934
(301) 621-0390

National Technical Information Service (NTIS)
5285 Port Royal Road
Springfield, VA 22161-2171
(703) 487-4650

TABLE OF CONTENTS
Part I

TABLE OF CONTENTS (Cont'd)

TABLE OF CONTENTS
*** Part II (Included Under Separate Cover)**

FIGURES

TABLE OF CONTENTS (Cont'd)

TABLE OF CONTENTS (Cont'd)

TABLE OF CONTENTS (Cont'd)

TABLES

TABLE OF CONTENTS (Cont'd)

ACRONYMS

1-D	one-dimensional
2-D	two-dimensional
3-D	three-dimensional
ACCEL	MSE 1-D MHD Accelerator Code
ADI	alternating direction implicit
AEDC	Arnold Engineering Development Center
AEDC-VKF	AEDC von Karman Facility
AERL	Avco Everett Research Laboratory
AIAA	American Institute of Aeronautics and Astronautics
CEA	Chemical equilibrium with applications computer code (NASA, 1994)
CET89	Chemical equilibrium computer code (NASA, 1989)
CDIF	Component Development and Integration Facility
CFD	computational fluid dynamics
CPU	central processing unit
dc	direct current
DOE	U.S. Department of Energy
DOE-FETC	DOE Federal Energy Technology Center
e^-	electrons
e-beam	electron beam
EEDF	electron energy distribution function
ENGO	a private Russian consortium comprised of researchers from a number of Russian scientific, academic, and technical agencies (also known as ENERGYGO)
ERDA	U.S. Energy Research and Development Administration
FHO	forced harmonic oscillator
GASL	General Applied Sciences Laboratory
GE	General Electric Company
HiRho	high density MHD accelerator test program at AEDC
HPDE	High Performance Demonstration Experiment
HST	Chemical equilibrium computer code (Outokumpu Research, Finland)

ACRONYMS (Cont'd)

IMACON™	image converter camera
LANL	Los Alamos National Laboratory
LBI	linearized block implicit
LINACCS	linear accelerators
LoRho	low density MHD accelerator test program at AEDC
LSODE	ordinary differential equation system solver
LTE	local thermodynamic equilibrium
MARIAH	Magnetohydrodynamics Accelerator Research Into Advanced Hypersonics
MHD	magnetohydrodynamics
MIT	Massachusetts Institute of Technology
MSE	MSE Technology Applications, Inc.
NASA	National Aeronautics and Space Administration
NASA Ames	NASA Ames Research Center
NASA Ames EAST	NASA Ames Electric Arc-Driven Shock Tube
NASA-LaRC	NASA Langley Research Center
NASA-MSFC	NASA Marshall Space Flight Center
NSSK	North-South Station Keeping
ODE	ordinary differential equations
OSU	Ohio State University
PAC91	computer program for calculating and fitting thermodynamic functions (NASA, 1991)
PDE	pulse detonation engine
PGU	piston gasdynamic unit
PI	Principal Investigator
PM/SIC	pre-mixed, shock-induced combustor
POC	proof of concept
R&D	research and development
RCC	reinforced carbon-carbon
RDHWT	Radiatively Driven Hypersonic Wind Tunnel
rf	radio frequency

ACRONYMS (Cont'd)

RIME	rocket-induced MHD ejector
SAB	Scientific Advisory Board (USAF)
SOW	statement of work
SSTO	single-stage-to-orbit
T&E	testing and evaluation
TAV	transatmospheric vehicle
TEOS	Tetraethyl-Ortho Silicate
TPS	thermal protection systems
TsAGI	The Russian Central Aerohydrodynamic Institute
UHP	ultrahigh pressure
USAF	United States Air Force
UTA	University of Texas at Arlington
UTSI	University of Tennessee Space Institute
UV	ultraviolet
V-T	vibrational-translational
V-V	vibration-vibration

1. EXECUTIVE SUMMARY

1. EXECUTIVE SUMMARY

MSE Technology Applications, Inc. (MSE) initiated the Magnetohydrodynamics Accelerator Research Into Advanced Hypersonics (MARIAH) Project in April 1995 for the U.S. Department of Energy (DOE) and the National Aeronautics and Space Administration (NASA). The overall objective of the MARIAH Project was to investigate the feasibility of augmenting hypervelocity wind tunnels with magnetohydrodynamics (MHD) technology. The research was performed under the direction of the DOE Federal Energy Technology Center (DOE-FETC) and NASA Langley Research Center (NASA-LaRC).

Due to the increasing interest in the development of very high-speed air-breathing flight vehicles for flexible space access, global reach, and long-range missile defense/cruise missiles, there has been a growing awareness of the need for improved ground facilities capable of simulating the flight regimes in which such systems must operate. Hypersonic flow is fundamentally different than subsonic and low supersonic flow in that the stagnation (plenum) temperature is so high the air chemically reacts and cannot be contained with known materials. The present testing infrastructure assets in the United States are quite limited in this flight regime. For example, in testing scenarios that require continuous (long-duration) test runs (such as the testing and evaluation (T&E) of advanced air-breathing engines), the maximum velocity that can be achieved is approximately Mach 7. Other types of facilities, generally referred to as impulse facilities, can extend the Mach number up to and beyond orbital access velocities; however, the facilities suffer from having very short run times (approximately 1 to 4 milliseconds) and therefore are unsuited for T&E developmental experimentation. The U.S. Air Force (USAF) Scientific Advisory Board (SAB) has stated that improved ground test facilities will be essential to developing the next generation of hypervelocity air-breathing engines (Ref. 1). Indeed, the United States has never developed man-rated air-breathing flight vehicles without wind tunnel developmental propulsion testing. Consequently, there is a demonstrable need for improved hypervelocity ground test facilities capable of providing Mach 10-16, long-duration, true chemistry air flow, and because the limitations of conventional facilities are fundamental in nature, the development of new breakthrough technologies is required.

During the 1960s, both NASA and the USAF investigated the applicability of MHD accelerators for hypervelocity wind tunnel augmentation. These studies produced very promising results and provided evidence that MHD technology has the potential of providing the conditions required for testing hypervelocity systems. Tests utilized air as the working fluid but added an alkali metal seed to achieve the required ionization in the MHD accelerator. However, this seed material is a contaminant for propulsion testing and is a major concern in these types of accelerators since it can cause corrosion/contamination of test components and equipment, can possibly affect combustion and ignition reaction rates, and can distort instrumentation readings.

During the 1970s, the General Electric Company (GE) conducted unseeded MHD experiments. Due to the absence of seed contamination, these experiments duplicated typical flight environments more realistically but suffered from air dissociation at high temperature. These unseeded experiments utilized a shock tunnel driver, and the high temperature behind a reflected shock wave provided the required ionization and achieved the necessary electrical conductivity.

Unfortunately, achieving ionization by thermal means requires high gas temperature and is practical only for the short durations of shock tunnel experiments. Significant dissociation of oxygen (O_2) and nitrogen (N_2) also occurs from the high temperatures, resulting in a working fluid that may not be representative of true air.

Recent technology advances in aerospace materials, electronic controls, computers, superconductivity, and computational fluid dynamics (CFD) have the potential to significantly advance hypervelocity technology. Additionally, the development of lasers and electron beam (e-beam) devices, along with improvements in microwave technology, all have the potential to enhance the performance of MHD accelerators for hypervelocity testing.

The problem of duplicating the high enthalpy, dynamic pressure, and Mach numbers characteristic of hypervelocity flight continues to be a fundamental challenge to hypersonic researchers. A hypervelocity ground test facility must be capable of adding sufficient enthalpy in the facility flow to accurately simulate the total enthalpy of in-flight aircraft. Additionally, the flow through the test section must accurately duplicate true air chemistry. The facility must be large enough to reproduce the mixing and reaction processes occurring in a near full-scale engine, and test times must be long enough to allow heat transfer and flow processes to reach steady-state conditions.

The critical issues were identified as high-pressure MHD performance, MHD accelerator materials, and propulsion test air chemistry. High-pressure MHD performance was given the highest priority since this is critical to achieving the necessary test and evaluation performance levels. As a result, most of the MARIAH Project activities focused upon MHD accelerator performance at true hypervelocity dynamic pressures. This effort included analytical studies to evaluate the performance of MHD accelerators at high operating pressures, experimental studies to assess the electrical properties of high-pressure air, and system studies to assess the availability and performance of various seed materials and external ionization sources. The effect of seed material upon combustion processes and systems thermal management issues was also addressed.

The basic requirements of the MARIAH Project were established by conducting a review of the literature of hypersonic ground test facilities, as well as through extensive discussions between MSE, NASA-LaRC, and other members of the hypersonic community. The Project's basic requirements were as follows:

1. The facility should be a "T&E" facility capable of test durations on the order of tens of seconds to minutes.
2. The facility should be capable of testing near full-scale advanced air-breathing engine modules. An 80-square-foot (ft^2) test section was selected as the target.

3. The facility should be capable of simulating true total enthalpy and thermodynamic conditions, implying that post-bowshock Mach numbers, total enthalpies, and entropies must be duplicated. Specifically, the facility must be capable of matching post-bowshock conditions corresponding to a 2,000-pounds force per square foot (lbf/ft^2) free-stream dynamic pressure with a 5° deflection angle shock up to a free-stream Mach number of 16.

4. The facility should be capable of providing an airstream chemistry corresponding to the post-bowshock regime of hypervelocity aircraft (i.e., minimal dissociation, vibrational nonequilibrium, and contaminants).

5. The facility should be a true "T&E" facility, implying high testing throughput, high reliability/lifetimes for critical components, and MHD accelerator versatility across a wide range of pressures and Mach numbers.

MSE investigated three separate approaches to satisfying these requirements including: a) classical high temperature, arc heater-driven MHD accelerators utilizing alkali metal seed; b) unseeded arc heater-driven MHD accelerators with beamed energy addition; and c) a novel MHD/Radiatively Driven hybrid concept referred to hereafter as the MARIAH II concept. Each has the common feature of MHD acceleration of air but differs in the type of upstream driver utilized, the operational pressure/temperature regime, and the mechanism for the initiation and maintenance of accelerator electrical conductivity. The report documents the study's conclusions and addresses the open technology issues for each concept. Additionally, MSE conducted a cursory investigation of the major facility engineering issues associated with the three approaches.

Classical high temperature, arc heater-driven MHD accelerators utilizing alkali metal seed material was the MARIAH Project's most extensively evaluated approach. Several analytical, parametric, and optimization studies of this approach were performed assuming advanced arc heater, high field strength magnet, and relatively conventional linear, segmented Faraday MHD channel technology. Experiments were also conducted at both the NASA Ames Research Center (NASA Ames) and the University of Texas at Arlington (UTA). Seeded, arc heater-driven MHD accelerators were unable to achieve the targeted NASA requirements but were able to produce simulated flight conditions currently unattainable with conventional technologies. The high operating pressures required by NASA resulted in significant difficulties for these types of MHD accelerators. Additionally, system power requirements are considered to be a major obstacle to the development and construction of this type of ground test facility.

MSE also evaluated two separate approaches to the unseeded arc heater-driven MHD accelerator. Both involved elevated, nonequilibrium electron temperatures that produce nonequilibrium ionization through molecular collisions by utilizing external energy sources such as lasers, microwaves, and e-beams. This type of MHD accelerator was the subject of a previous MSE study and was believed to be potentially viable; however, the concept was also unable to produce the test conditions required by the MARIAH Project. Ohio State University (OSU) also studied the unseeded nonequilibrium concept analytically and came to essentially the same conclusion. It should be noted there is a relatively high degree of uncertainty in the analyses

performed for this approach due to the simplistic approach to the nonequilibrium ionization and high Hall parameter corrections used. However, the analysis does provide a technical basis for further considering the concept if the need for clean-air testing in the combustor entrance regime arises.

Finally, MSE performed a preliminary study of the MARIAH II concept. This concept takes advantage of the following features:

1. An ultrahigh-pressure (UHP) driver with heat energy addition via lasers, e-beams, or microwaves in the supersonic expansion zone, which reduces the reservoir entropy when compared to typical arc-heater entropy values.
2. Joule heating is minimized by utilizing a downstream (final segment) MHD accelerator.
3. The possibility of much lower core temperatures and reduced entropy generation through the flow train compared to either arc-heater or conventional MHD technology.
4. The natural synergy between the UHP driver and the MHD accelerator.
5. The potential to cover a much wider range of the total enthalpy vs. entropy diagram of interest to the hypersonic community.

MSE considered two possible approaches for the MARIAH II concept: a) the guided arc mode; and b) low-pressure, low temperature MHD acceleration with beamed energy addition.

Based upon the MARIAH Project's investigation of the three approaches for applying MHD technology for the augmentation of hypervelocity wind tunnels, MSE believes the MARIAH II concept to be the most promising. MSE's preliminary analyses of this concept indicate it can potentially satisfy all of NASA's target requirements and represents the lowest risk approach to the problem. Therefore, MSE recommends an R&D program based upon the MARIAH II concept be undertaken so the remaining technology issues of this promising concept can be addressed, and the nation's quest for air-breathing hypervelocitiy propulsion systems can be realized.

2. MHD ACCELERATOR TECHNOLOGY BACKGROUND

2. MHD ACCELERATOR TECHNOLOGY BACKGROUND

Since 1959, substantial effort has been devoted to exploring the conditions under which a conducting fluid (specifically a gaseous plasma or liquid metal) moving through a magnetic field might generate useful electric power, or inversely, might convert electrical energy into thrust for rocket propulsion in space or kinetic energy for a wind tunnel. The latter case has been explored in the MARIAH Project study for the purpose of producing hypervelocity flight conditions in a ground test facility for propulsion testing applications.

The development of a single-stage-to-orbit (SSTO) air-breathing propulsion system is deemed to be dependent upon the prior development of a wind tunnel test facility in which the many unknowns of the propulsion system can be investigated in a controlled manner. The alternative to this type of ground T&E facility would be to rely solely on flight testing, which is time and resource intensive.

MHD has been identified as a technology possessing the potential to produce true enthalpy test conditions for hypersonic research in the Mach 8 and above flight regime (Refs. 2, 3, 4). MHD has a distinct advantage in that kinetic energy is added directly to the working gas through electromagnetic body forces, thereby allowing the production of high Mach number, true velocity, test section conditions without prohibitive reservoir stagnation conditions required by other concepts. Furthermore, MHD accelerators can be operated in a continuous flow mode with run time limited only by available power supply, or they can be pulsed where augmentation of a shock tunnel is desired.

The study and experimental effort that has previously been expended (as reflected in the available literature) provides a record of the events that have taken place over the years to bring MHD technology to its present state. The leading organizations performing these studies and experiments have been the USAF Arnold Engineering Development Center (AEDC), NASA-LaRC, as well as MSE and Avco Everett Research Laboratory (AERL) under the sponsorship of the DOE. Other organizations that have participated in this effort are GE, the Aerospace Corporation, the University of Tennessee Space Institute (UTSI), General Applied Sciences Laboratory (GASL) and UTA. The literature generated as a result of the research performed by these contributors is compiled in Table 2-1.

This body of experimental work has been very important to the MARIAH Project as it has tended to focus the project and define the large issues confronting MHD accelerator technology. These issues include electrode lifetime; other materials issues (i.e., insulators, sidewalls, etc.); and the chemistry issues relating to achieving "true air" simulation (i.e., alkali metal seeding, creation of nitric oxide (NO) in arc heaters and accelerators, dissociation of diatomic species ($O_2 \rightarrow 2O$), vibrationally excited species, and electron attachment). Performance and efficiency questions need to be considered because an MHD accelerator is a device that converts electrical power to flow work plus heat. The arc heater functions similarly to an MHD accelerator, except it converts all the input power to Joule heating. Therefore, a key question is, "What is the advantage of MHD over the much simpler arc-heater technology?" The answer lies within the concept of conversion efficiency. To justify the use of MHD over heat addition technology, one must show the MHD accelerator can operate at high conversion efficiency.

Table 2- 1. MHD historical research data guide.				
Referenced Research	***Objective***	***Source***	***Refs. No. In Sect. 6***	***Sect. 2 Paragraph***
LoRho Program	Produce hypersonic flow simulation by augmenting arc-heater energy with an MHD accelerator.	AEDC	2, 3	2.1.1
HiRho Program	Development of a large test facility with velocities of 10,000 ft/s to orbital and altitudes of 50,000 to 250,000 feet.	AEDC	2, 4	2.1.2
Faraday Plasma Accelerator	Development of a high-speed facility for aerodynamic testing.	NASA-LaRC	5, 6	2.1.3
Unseeded MHD-Augmented Shock Tunnel Experiment	Feasibility study to provide MHD-augmented shock tunnel data using unseeded air flows to eliminate effects of seeded air on combustion.	GE	7	2.1.4
Pulsed MHD Accelerator	Accelerate a gas from 15,500 to 24,000 ft/s at constant enthalpy and at atmospheric pressure.	Aerospace Corp.	9	2.1.5
Russian MHD Hypervelocity Test Facilities	Report on 30 years of investigations with MHD accelerators, electrode studies, and wind tunnels.	Various		2.1.6, App. E
DOE National MHD Energy Program	Develop design basis for scaling to larger MHD power generation systems.	MSE	10, 11, 12	2.2.1
High Performance Demonstration Ezperiment (HPDE)	Demonstration of high enthalpy extraction in a clean gas to produce high power levels.	AEDC	13	2.2.2
Unseeded Nonequilibrium MHD Accelerator Study	Proposed concept to support air-breathing, hypervelocity propulsion testing where high quality air chemistry is desired.	MSE	14	2.3.1
MHD Accelerators for Hypersonic Applications	Comprehensive investigation to revisit the concept of hypersonic flow simulation through MHD acceleration.	UTSI/AEDC	15	2.3.2
Single-Stage-to-Orbit Propulsion Concept	Rocket-induced MHD ejector (RIME) engine investigation to support SSTO vehicle design.	NASA-MSFC	16	2.3.3
Other Analytical Studies	Various studies pertaining to the use of MHD acceleration to increase kinetic energy.	MSE, NASA GASL	17, 18, 19, 20, 21	2.3.4

The subsections of this background section provide a chronicle of the development of MHD technology as it has been applied to accelerator devices that could serve as drivers for hypervelocity ground testing facilities. The intent here is to open a window on the wealth of existing information relevant to the analysis and design of advanced ground test facilities. This discussion centers around the duration-type facility (i.e., MHD) rather than the impulse-type facility because only the former is suitable for use in hypervelocity vehicle ground T&E (developmental) testing.

This background information is presented in three segments: accelerator experimental data, generator experimental data, and accelerator studies.

2.1 MHD ACCELERATOR EXPERIMENTS

Experimental programs concentrating on the use of MHD devices as gas accelerators have been carried out at AEDC in both the low- and high-density modes (Refs. 2, 3, 4), at NASA-LaRC with linear cross-field plasma accelerators (Refs. 5, 6), and at the Russian Central Aerohydrodynamic Institute (TsAGI) (as described in Appendix E). The Aerospace Corporation undertook a pulsed MHD accelerator experiment (Ref. 9). In wind tunnel applications, GE tested an unseeded MHD-augmented shock tunnel concept, which closely simulated real flight conditions and eliminated seed contamination (Ref. 7) (see Table 2-1).

The AEDC LoRho (low density) and other experiments, with the exception of the TsAGI and the AEDC HiRho (high density), were demonstrations in which there were no aerodynamic test sections for collecting data. The TsAGI and HiRho experiments did include the ability to collect aerodynamic test data.

2.1.1 Low-Density (LoRho) MHD Experiments

In the early 1960s, the objective of the AEDC LoRho Program (Refs. 2, 3) was to extend the velocity and altitude capabilities of gas dynamic testing facilities using MHD accelerators. The program's goal was to produce hypersonic flow simulation by augmenting the energy of an arc heater with an MHD accelerator. The LoRho effort was envisioned as a three-phase program, beginning with a small-scale proof-of-concept (POC) experiment that would lead to a pilot facility and ultimately to a full-scale test facility. The latter was to be a large-scale, steady flow, hypersonic test facility providing true velocity test conditions over a wide range of low-density, hypersonic flight conditions. The POC experiments were performed, and some of the pilot-scale hardware was developed; however, the accelerator pilot facility was never operated, and the full-scale facility was never constructed.

Three configurations of the LoRho small-scale accelerators were tested with encouraging results. Nitrogen, seeded with 1% potassium (K) and heated by a 1.2-megawatt (MW) arc heater, was used as the working fluid. A 20-electrode pair accelerator (termed Accelerator A) demonstrated a centerline velocity increase of approximately 50% to 3,000 meters per second (m/s)

(9,800 ft/s). Two configurations of a 117 electrode pair accelerator (referred to as Accelerators B and B_1) resulted in approximately doubling the centerline plasma velocity from entrance to exit, achieving a maximum velocity of 3,900 m/s (12,800 ft/s). Further information on the theoretical and experimental results of the LoRho POC experiments can be obtained in Reference 3. These are discussed in more detail in the following paragraphs. Performance data from the LoRho Accelerator B was used in the MARIAH Project to validate the MSE Accelerator One-Dimensional (1-D) MHD Code (ACCEL). This is discussed further in Appendix Section B.1 and is summarized in Section 4.1.1 of this document.

2.1.1.1 Facility Description

Accelerator B entrance dimensions were 2.54 centimeters (cm) between the magnetic-field walls and 2.98 cm between the electrode walls. At the exit, the distance between the magnetic field was the same as at the entrance; however, the distance between the electrode walls increased to 6.22 cm. The accelerator length was 77 cm. The LoRho electrodes were liquid-cooled copper pieces that were sprayed with beryllium oxide (BeO) for electrical insulation. The plasma-exposed areas of the electrodes were uncoated to allow electrical discharge. An array of 1,700, 12-volt (V) automotive batteries provided electrical power that was applied to the 60 center electrode pairs during operation. Unpowered electrode pairs were used to determine the gas velocity along the channel by measuring induced voltage.

An arc heater was used as a plasma generator. A direct current (dc) power input of approximately 1.2 MW was used to heat N_2 at a flow rate of 0.095 kilograms per second (kg/s) and produce the plasma.

A magnetic field was produced for the LoRho experiments using an iron-core electromagnet with rectangular pole faces measuring 7.6×38.1 cm. This magnet was designed for a maximum field strength of 2 Tesla (T) with a coil current of 875 A but was limited to approximately 1.5 T for the LoRho experiments.

Several seeding arrangements were used for these investigations; however, in all cases the seed was injected into the stilling chamber where the temperature was high and the velocity of the plasma was low. Powdered potassium carbonates (K_2CO_3), as well as a eutectic solution of sodium and potassium (NaK), were injected into the plasma. Seeding with NaK was attempted because it has a low ionization potential and requires no carrier fluid. NaK has a high condensation temperature, which caused it to condense on the accelerator walls and electrodes resulting in axial shorting of the electrodes. When powdered K_2CO_3 was used, the condensate on the walls was a light film that did not form an electrical bridge to any great extent. A limited number of accelerator data points was obtained with powdered calcium oxide (CaO) as the seed material. CaO has possibilities since it is not hygroscopic; however, because of its higher ionization potential, a lower conductivity will result as compared to K.

2.1.1.2 Demonstrated Performance

During the accelerator test program, the plasma generator was operated at a nominal mass flow rate of 0.095 kg/s, total enthalpy levels of 1,500 to 1,600 kilocalorie per kilogram (kcal/kg), and total pressure levels from 2.2 to 3.3 atmospheres (atm). The LoRho accelerators were operated with power levels from zero to over 400 kilowatts (kW). The maximum average velocity at the accelerator exit achieved in the LoRho program was 2,800 m/s. This velocity was attained in Accelerator B operating at a power level of 371 kW and represented a velocity ratio (powered to unpowered) of 1.48. Centerline velocity for this test condition was 4,000 m/s for a centerline velocity ratio (powered to unpowered) of 2.1. Other exit properties for this test condition included total enthalpy of 8,400 kilojoules per kilogram (kJ/kg) [3,600 British thermal units per pounds per minute (Btu/lbm)], static pressure of approximately 0.25 atm, and average static temperature of 3,650 K. At the maximum power input (400 kW), the plasma exit-to-entrance velocity ratio was 2.06 on the centerline, and the average plasma velocity ratio was 1.62. The electrical power density was 1,000 MW/cubic meter (m^3).

The LoRho program demonstrated (as reported in Ref. 3, pp. 58-59) that the 1-D MHD channel flow equations can be used to predict the average plasma acceleration provided the current density, electric field, magnetic field, and plasma entrance conditions are specified. However, when equilibrium conductivity based on the average plasma temperature was used in the calculations, the 1-D equations predicted a higher acceleration than was measured experimentally because the plasma conductivity was reduced significantly as a result of the temperature variation across the accelerator wall boundary layers. Equilibrium conductivity calculations appeared valid when adjusted for the boundary layer variation.

Significant losses in total pressure through the accelerator were incurred when operated with no MHD electrical power input, thus a considerable power investment is required to attain the initial total pressure level at the exit. This result indicated that friction and heat-transfer effects could not be omitted from the 1-D equation when predictions are required for large length-to-diameter ratio accelerators.

Acceleration of the plasma was not uniform across the accelerator, with the maximum acceleration occurring in the center of the channel. This phenomenon has been shown to be a result of temperature variation across the accelerator, and the gas dynamic profiles were adequately predicted with a simple theoretical expression, which accounted for the temperature gradients.

The accelerator heat-transfer rate at zero power level was shown to correlate with a modification of McAdams' convection heat-transfer equation. Moreover, the equation was found to produce good agreement with the experimental data when the accelerator was powered, provided terms were added to account for the increased electrode heat-transfer rate resulting from the electrical discharge.

A number of materials were investigated for use as electrode and magnetic-field wall insulators. The most satisfactory of these appeared to be plasma-sprayed BeO, flame-plated alumina, and plasma-sprayed alumina.

The feasibility of accelerating a seeded plasma at near-atmospheric pressure with an MHD accelerator operated in the Faraday mode was demonstrated in the LoRho program. Effective acceleration was demonstrated, producing significant velocity increase at the exit. 1-D MHD channel flow models successfully predicted the accelerator performance when friction and heat transfer effects were included and electrical conductivity was adjusted to account for its variation in the wall boundary layers.

2.1.2 High-Density (HiRho) MHD Experiments

The HiRho Program was initiated at AEDC (Refs. 2, 4) with the objective of developing a large facility for aerodynamic testing in the velocity range from 10,000 ft/s (3,048 m/s) to orbital velocities [approximately 27,000 ft/s (8,000 m/s)] with test section densities corresponding to altitudes between 50,000 ft (15,240 m) and 250,000 ft (76,200 m). Prior theoretical and experimental studies had indicated a high performance shock tunnel augmented with an MHD accelerator offered reasonable potential for obtaining the desired conditions.

Originally, the HiRho Program was to be developed in three phases. The first phase was a research effort to demonstrate the feasibility of the MHD-augmented shock tunnel concept and to generate experimental data for the design of a pilot facility. The fabrication and operation of a pilot facility was to be the second phase followed by a final phase in which the construction and calibration of a full-scale facility would be completed. However, the HiRho Program was terminated during the research phase in 1971, thus the pilot and full-scale phases were never initiated.

2.1.2.1 Facility Description

The Tunnel J (Ref. 2) at the AEDC Von Karman Facility (AEDC-VKF) was used to investigate the MHD-augmented shock tube concept. The research phase concentrated on improving the basic performance of Tunnel J and developing an MHD nozzle accelerator to augment its performance. Tunnel J consisted of a 3.5-inch –diameter [88.9 millimeters (mm)] by 15-ft-long driver (457.2 cm). The driver gas was heated to temperatures up to 550 K. Routine operation was conducted over a driver pressure range of 5,000 pounds per square inch (psi) (239,400 Pa) to a maximum of 15,000 psi (718,200 Pa) using a stainless-steel single-diaphragm system.

The first-stage nozzle (as described in Ref. 4, pp. 291, Sect. 2.2) had a square cross section and a 1°26′ divergence angle from the throat to the nozzle exit. An accelerator section, 18 inches (45.72 cm) long with the inlet 16 inches (40.64 cm) from the throat, consisted of 11 pairs of beryllium-copper electrodes separated by 0.357-inch-thick (9.07 mm) nylon insulators. Accelerator sidewalls were fabricated from Lexan®. The accelerator was contained in a fiberglass shell and encased in a nonmagnetic steel alloy (Inconel®) pressure vessel. The second-stage nozzle was conical with a 20° half angle, a 2-inch (5.08 cm) inlet diameter, and a 12-inch (30.48 cm) exit diameter.

A capacitive energy supply providing 0.25 megajoules (MJ) and consisting of 190, 28-microfarad (μF) capacitors supplied an electric field for the MHD accelerator operation. Each electrode pair was connected to a capacitive power supply through a simulated transmission line consisting of capacitors and inductors that provided a constant voltage and current (± 5%) during the 1-millisecond (ms) test period. A magnetic field was generated using a copper-wound air-core magnet excited by four homopolar generators that developed a field strength of 7.5 T for the HiRho tests.

Measurements indicated the duration of gas conductivity was approximately 3 ms, sufficient for the 1-ms discharge time of the MHD accelerator. Conductivity levels and duration were measured using the induced voltage generated by the conducting gas as it passes through the magnetic field and with a broadside microwave technique.

A seeder system was located 5 inches (12.7 cm) from the downstream end wall of the reflected shock tube configuration. Calibration of the anhydrous K_2CO_3 seed mass ratio injected into the gas and gas electrical resistance experiments established that 1 gram (g) of seed (mass fraction of approximately 1.3% K) provided sufficient gas conductivity for MHD operation.

2.1.2.2 Demonstrated Performance

The MHD operating conditions obtained using the standard driver, which provided velocity increases of approximately 40 and 80% and limiting velocities of approximately 17,000 fps (5,182 m/s) and 22,000 fps (6,706 m/s), have been calibrated and used in aerodynamic tests. These two conditions were the result of two power levels tested (4 and 5 T). The data for the two power levels tested reveals that 85 to 90% of the power transmitted to the electrodes is converted into kinetic energy. The results of these experiments are reported in Reference 4, page 297, in Section 8, and are restated below.

Experimental data obtained in Tunnel J verified the validity and applicability of a shock tunnel employing an MHD nozzle accelerator for providing large increases in flow velocity. A maximum increase in test section flow velocity from 12,000 fps (3,658 m/s) to 21,000 fps (6,400 m/s) at a Mach number of 10 was demonstrated. Good agreement was obtained between experimental data and 1-D MHD models. Extensive operational experience, detailed calibration data, and basic aerodynamic measurements (model surface pressures) were successfully obtained using the MHD nozzle accelerator.

2.1.3 NASA Langley Research Center

During the late 1960s, NASA-LaRC had a continuing research program on linear crossed-field (Faraday) plasma accelerators with the principal objective being the development of a high-speed facility for aerodynamic testing (Refs. 5, 6). Evidence of steady-state acceleration of a high-density plasma was reported in Reference 7 (pp. 21, 66-180). The accelerator had a channel of only 1-cm-square cross section and was 8 cm long. Diagnostics and determination of the

operating characteristics were very difficult because of the small channel size. This led to the development of a larger accelerator that could perform the pilot-scale testing and flow diagnostics needed for a full-scale model capable of accommodating reentry velocities. This accelerator was 30-cm long with a 2.54-cm-square cross section. The channel had no external cooling, and therefore, could operate as a heat sink for approximately 3 seconds.

2.1.3.1 Facility Description

Plasma input was provided by a NASA-designed arc heater, which had been modified for this facility. The electrical energy supplied to the arc heater was derived from a set of motor generators delivering 4,000 V dc at 600 A.

The accelerator electrodes were axially symmetric, the outer edge being the cathode and the inner edge being the anode. The electrodes were liquid cooled. To improve mixing, seeding was done through the inner electrode

The cathodes were fabricated from 1/16-inch-thick (1.588 mm) thoriated tungsten. The accelerator anodes were of the same dimensions and constructed of pure tungsten. Both the anodes and cathodes were backed by graphite, and the insulators between electrodes and the sidewalls were constructed from boron nitride.

2.1.3.2 Demonstrated Performance

The conditions at the exit of the supersonic nozzle were determined by a lengthy series of experiments with the accelerator removed from the test section. Table 2- 2 (data taken from Ref. 5, pp. 8, 9) shows representative values for the state of the gas.

Table 2- 2. State of gas values in NASA 1-inch-square accelerator.

Parameter	Value	Parameter	Value
Mass Flow Rate (kg/s)	6.68×10^{-3}	Speed of Sound (m/s)	1.24×10^{3}
Total Enthalpy (J/kg)	8.2×10^{6}	Mass Density (Pa)	5.2×10^{-3}
Static Enthalpy (J/kg)	6.2×10^{6}	γ	1.16
Velocity (m/s)	2.0×10^{3}	Pressure (Pa)	6.9×10^{3}
Temperature (K)	4.4×10^{3}	Mach Number	1.6

Useful information for the design of MHD accelerators was obtained in the investigations with the NASA-LaRC 1-inch-square plasma accelerator. This information (reported in Ref. 6 and restated here) includes these items:

1. For a given applied voltage, maximum current and maximum pitot pressure were obtained with the cathodes shifted between zero and one electrode downstream. The Hall potential difference developed in the accelerator was smaller at the unshifted position than at the downstream position, and operation in this position may be preferable if breakdown between electrodes is a problem.

2. The velocity distribution at the accelerator exit was measured and found to be reasonably uniform over 80% of the channel width and height.

3. The best of several methods of channel sidewall construction was determined to be boron nitride sheets backed by water-cooled copper coated with BeO insulation.

Good agreement was obtained between measured and calculated exit velocity.

2.1.4 Unseeded MHD-Augmented Shock Tunnel Experiment

The results of a feasibility study conducted by GE are of particular interest in that they provide MHD-augmented shock tunnel data obtained utilizing unseeded airflow (Ref. 8). This type of operation eliminates concerns regarding flow-seeding effects on model heat transfer and flow chemistry, as well as possible particle damage to models being tested, as it more closely simulates real flight conditions. This study was conducted using a high-performance, electrically driven, reflected shock tunnel. The unique performance capability of this type of shock driving technique permitted the generation of high-pressure, high temperature shock tunnel reservoir conditions yielding highly ionized unseeded airflow in the accelerator and nozzle with moderate values of chemical dissociation.

2.1.4.1 Facility Description

The MHD accelerator channel was 12.25 inches (31.12 cm) long and had 38 segmented copper electrode pairs with a 0.5-inch-square (1.27-cm) cross section and an area ratio of 2. An average air electrical conductivity of 110 mho/m was obtained in high temperature unseeded air. A nominal magnetic field strength of 5.2 T was used in these experiments, and it was experimentally determined the flow duration was on the order of 300 microseconds (μs). The electrically arc-heated helium (He) driver generated a strong shock wave (M_s = 13.6 at P = 150 torr), which brought the air initially in the driven tube to the stagnation conditions. This highly ionized air was then expanded in a nozzle to the MHD accelerator entrance.

2.1.4.2 Demonstrated Performance

These experiments demonstrated that the analytically predicted increases in flow velocity were indeed achievable. MHD augmentation resulted in velocity increases from 19,600 fps (5,974 m/s) to 24,000 fps (7,315 m/s). The demonstrated accelerator efficiency was 75%.

2.1.5 Pulsed MHD Accelerator Experiment

The operation of a pulsed MHD accelerator for an MHD wind tunnel application was investigated by the Aerospace Corporation (Ref. 9). The accelerator was designed to accelerate a gas from a velocity of 15,500-fps (4,724 m/s) to 24,000 fps (7,315 m/s) at constant enthalpy and approximately atmospheric pressure. A hotshot driver produced the high temperature, high-pressure plasma that was expanded in a nozzle to provide the desired MHD channel entrance properties. After tunnel startup, a 3-ms constant power pulse was switched on to the electrodes; consequently, current flow was approximately perpendicular to a quasi-steady 4-T magnetic field. The power-on to power-off velocity ratio at the accelerator exit was determined by changes in the stagnation pressure and open-circuit induced potential. The corresponding enthalpy ratio was determined from the static pressure change and velocity ratio.

The magnetic field is produced by a 12-turn, 5-ft-long (1.524 m) coil powered by a 0.05-farad capacitor bank delivering 42,000 A when charged to 3,300 V. The capacitor bank used to power the hot shot was rated at 130 kJ at 20 kV and was sufficient to heat the initial 500-psi (3.447 MPa) charge of N_2 to the desired stagnation conditions. The segmented-electrode MHD accelerator channel was approximately 2.5-feet (76.2 cm) long, 0.5-inch (1.27 cm) square at the entrance, 0.78-inch (1.98 cm) square at the exit, and contained 94 pairs of copper electrodes insulated by boron nitride.

The hot shot produced a 9,000 K, 1,400-atm (142-MPa), K-seeded N_2 source gas that was expanded to 5.5 atm (557 kPa) and 4,000 K at the accelerator entrance, where a crossed magnetic field of 4 T was established. After steady flow was established in the accelerator, the power was switched on for a 3-ms quasi-steady test period. Results indicated that: a) the centerline velocity increased from 16 kft/s (4,877 m/s) to approximately 24 kft/s (7,315 m/s); b) the centerline enthalpy was a constant 0.5 ms after switch on; c) the centerline velocity increased further to 27 kft/s (8,230 m/s), and enthalpy increased approximately 20% prior to switch off as a result of constant power input at decreasing mass flow; and d) The ratio of axial-to-accelerating current was $0.05 \leq J_x/J \leq 0.25$. In general, the facility performed well relative to the 1-D design.

2.1.6 Russian MHD Hypersonic Ground Test Facilities

Over the past 30 years, a large body of research in MHD technology has been conducted by the Central Aerohydrodynamics Institute (TsAGI), a Russian governmental research organization. Both TsAGI and a private consortium called ENGO were subcontracted by MSE to conduct studies on MHD accelerators and facilities. The Principal Investigator for both of these efforts

was Dr. Vadim Alfyorov, a well-known MHD research scientist. Dr. Alfyorov and his colleagues developed an MHD accelerator facility with a small aerodynamic test section that can accommodate scale models up to approximately 15 cm in length. Until the inception of the MARIAH Project, a complete record of the TsAGI MHD capabilities and testing activities had not been documented. This was primarily due to the restrictive nature of the former Soviet Union regarding the disclosure of scientific data.

These two Russian organizations were subcontracted by MSE to assemble and record the information gathered over many years. The TsAGI subcontract had several objectives:

1. Summarize and document all of the operating characteristics and capabilities of the TsAGI MHD test facility and describe recent operating experience. This included an explanation of the significant facility limitations such as electrode lifetimes, power requirements and magnet limitations.

2. Provide descriptions and cost estimates of new equipment required to upgrade the facility. The specific envisioned facility upgrades included: 1) improved seed injection system, 2) special MHD accelerators for diagnostics on electrode walls, and 3) a 7.5-T superconducting magnet.

3. Investigate the electrode phenomena in the TsAGI MHD channel. This was understood to include a description of the basic modes of conduction within the sheath layers and electrode wall boundary layers along with experimental investigations to characterize the mode of conduction in the near-wall region (i.e., whether arc mode or diffuse mode). No new experiments were conducted for this phase of the research. Instead, data from past Russian papers and reports as well as data taken from previous electrode tests were reviewed and assembled into an comprehensive report.

The purpose of the ENGO subcontract was to investigate the potential of MHD technology to provide hypersonic test conditions adequate for advanced engine testing.

The results of the Russian research are contained in Appendix E of this document. A summary of this research may be found in Sections 2.1.6.1 through 2.1.6.3 below as well as in Section 4.1.6. A more detailed description of the Russian research may be found in Appendix E.

It has been reported that additional MHD accelerator research was conducted in recent years at the Russian TSNIIMASH facility. MSE has made several attempts to locate reports or publications on this research; however, these efforts have been unsuccessful. Reports from Russian MSE employees who have recently immigrated to the United States indicate that, until very recently, all or most of the research at TSNIIMASH has been of a military nature and has been classified. Some recent American Institute of Aeronautics and Astronautics (AIAA) papers describing experiments at TSNIIMASH have been published, but these address testing of a Piston Gasdynamic Unit (PGU) and are unrelated to MHD accelerator research. The PGU testing was done under a contractual arrangement between GASL and TSNIIMASH. These papers represent the only recent TSNIIMASH reports MSE has been able to locate.

2.1.6.1 TsAGI MHD Facility Capabilities

Subsections 1 and 2 of the TsAGI facilities report (Appendix E.1) give a reasonably detailed description of the test capabilities and operating conditions of the existing facility.

Table 2- 3. Summary of the TsAGI MHD Facility Operating Parameters	
ARC HEATER	
Power Input	200 - 260 kw
Stilling Chamber Temperature	3,700 K
Stilling Chamber Pressure	20 – 30 atm
Mass Flow Rate	7.0 to 22.5 g/s
ACCELERATOR	
Inlet Dimensions	1.5 x 1.0 or 1.5 x 1.5 cm^2
Channel Length	Variable, 14.5 to 72.5 cm
Inlet Flow Velocity	1,800 m/s
Inlet Mach Number	1.9 (variable, depending on choice of nozzle)
Magnetic Field	2.4 T
Gas Conductivity in Stilling Chamber	150 mho/m
Electrode Pitch (longitudinal)	8.0 mm
Electrode Width (in longitudinal direction)	4.5 mm
Number of Active Electrode Pairs	45
Maximum Current per Electrode Pair	55 A
Applied Voltage per Electrode Pair	200 - 400 V
Total Input Electric Power	0.5 - 1.0 MW
Heat Flux	10 - 50 MW/m^2
Powered Run Times	1 - 2 s
TEST SECTION	
Dimensions (cross section)	50 cm x 50 cm
Maximum Flow Velocity	7.5 km/s
Densities	10^{-4} - 10^{-2} kg/m^3
Mach Number	15 (for a sec. nozzle exit area of 20 x 20 cm^2)

Table 2- 3 is a duplicate of Table E.1 -1 in Appendix E. The table summarizes the present capabilities of the TsAGI MHD facility. Information in the table was derived from the TsAGI reports as well as from first hand observations of the facility made by MSE personnel during a site visit in September of 1995. As of that time, the facility was fully operational. For further information concerning testing and other experimental activities at the TsAGI facility, refer to Appendix E.

2.1.6.2 MHD Electrode Study

Current flow through an MHD accelerator is a complex process for many reasons. First, even in the ideal case where the pressure, temperature, velocity, and magnetic field are uniform, the current density and electric field vectors will not be parallel to each other due to the tensorial character of the generalized Ohm's Law relationship. Nonuniformities in temperature and velocity further complicate the current flow patterns. The TsAGI report addresses these issues in the context of three distinct zones within the flow stream in which the current flow and current nonuniformities are dominated by different mechanisms.

There are several other types of nonuniformities that can lead to either high current concentration or high local electric fields in an MHD channel. One is the thermal instability due to the interaction of Joule heating, electrical conductivity, and local heat transfer. A transient, localized temperature increase will cause an increase in electrical conductivity resulting in a local increase in the current density.

Another type of nonuniformity is a result of thermal overshoot within the boundary layer. This occurs only in high Mach number flows where the wall recovery temperatures may be substantially higher than the core flow static temperatures. In a high-speed flow, the temperature of an adiabatic wall can be estimated knowing the core flow properties (i.e., static temperature in the core flow, Mach number in the core flow, and the recovery factor depending on the Prandtl number, which is generally close to but less than 1). For a high Mach number, the adiabatic wall temperature may be significantly higher than the core flow temperature. In a real accelerator, the actual wall temperature will be lower than the adiabatic wall temperature. However, this results in thermal overshoots of 2,000 to 3,000 K in high Mach number flows due to the conversion of kinetic energy to thermal energy through the mechanism of viscous dissipation. The term "thermal overshoot" simply means that a local maximum occurs in the static temperature profile somewhere within the boundary layer. The TsAGI study on MHD electrodes examines the effects of these types of nonuniformities on electrode lifetime and performance. The results of a series of tests on segmented electrodes are reported in the study.

2.1.6.3 The Reproduction of Flight Conditions in Hypersonic Wind Tunnels

A major technical issue for MHD accelerators and other gas acceleration technologies is the problem of adding sufficient enthalpy to the flow while maintaining the entropy within the bounds of the targeted flight envelope. Since most MHD accelerators (such as the one at TsAGI) operate close to local thermodynamic equilibrium (LTE), they must rely on thermal ionization of an alkali metal seed material to achieve the requisite electrical conductivities. This generally implies the accelerator must operate at temperatures above 2,500 K. A major deficiency of the present TsAGI facility is the arc heater operates at a maximum stilling pressure of 20 atm and a temperature of about 3,800 K. The ENGO report has examined the H-S relationship for the TsAGI facility and has found the estimated conditions in the test section reflect a total enthalpy that is too low and an entropy that is too high. This implies that either the test section Mach numbers or the test section pressures will be lower than the corresponding post-bowshock. Since entropy scales inversely with the logarithm of pressure, the most direct way to improve this

situation is to either increase the operating pressure of the arc heater while maintaining a fixed temperature, thereby reducing the starting entropy, or increase the magnetic field, which will have the effect of increasing the slope of the H-S curves. Both strategies are considered in the ENGO report.

2.2 MHD GENERATOR EXPERIMENTS

Several experiments have been performed with the intent of better defining the use of MHD technology for the generation of electrical power. This is the inverse application of MHD to that described in Section 2.1, where the intent is to convert electrical energy to kinetic energy. Although the primary objective of the MARIAH Project was for the latter purpose, i.e., producing kinetic energy for wind tunnel applications, many of the performance characteristics, materials evaluation, and operating techniques are similar or exactly the same for both cases. Therefore, data on these power-generating experiments is highly useful. The major power-generating program to be discussed in this report is the DOE National MHD Energy Program. Another notable power generation experiment was the High Performance Demonstration Experiment (HPDE) performed by AEDC.

2.2.1 MSE Experiments in the DOE National MHD Energy Program

The DOE Component Development and Integration Facility (CDIF) located in Butte, Montana, and operated by MSE was responsible for obtaining MHD test data to provide the design basis for scaling to larger MHD power generation systems. The DOE MHD Program consisted of both topping cycle and bottoming cycle component research. This is depicted in Figure 2- 1 and documented in a summary report (Ref. 10). The topping cycle is the portion that contains the MHD generator, which is the topic of this section.

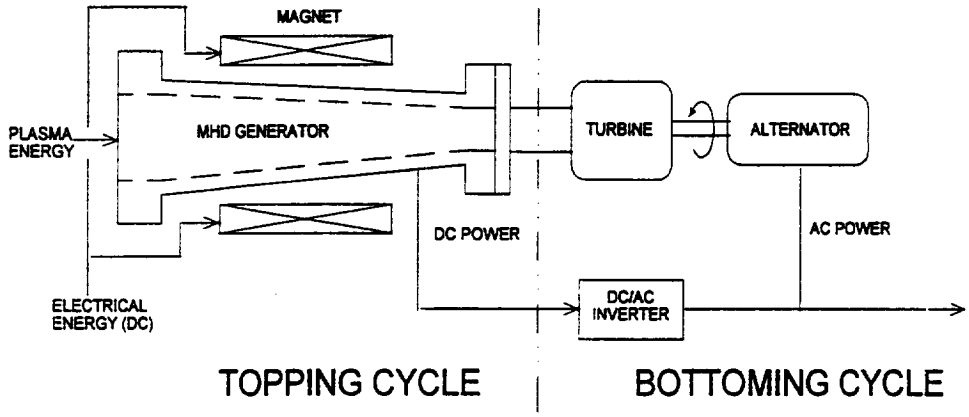

Figure 2- 1. DOE National MHD Energy Program configuration.

The CDIF was an engineering-scale development test facility at which MHD topping cycle components were integrated and tested. The facility was also used to demonstrate that advanced MHD power-generating cycles could be successfully integrated with typical power plant facility systems. Various MHD topping cycle components were integrated into an MHD power generation system and tested, demonstrated, and evaluated. Components tested at the CDIF

The CDIF was an engineering-scale development test facility at which MHD topping cycle components were integrated and tested. The facility was also used to demonstrate that advanced MHD power-generating cycles could be successfully integrated with typical power plant facility systems. Various MHD topping cycle components were integrated into an MHD power generation system and tested, demonstrated, and evaluated. Components tested at the CDIF included both oil-fired and coal-fired combustors, MHD generator channels, and power conditioning equipment.

During an 18-year period, the MHD generator system progressed through various configurations to arrive at the POC configuration, which demonstrated the ability to produce 1.5 megawatt electric (MW_e) while operating at stress levels deemed typical of future MHD baseload generators (Refs. 11, 12). At the conclusion of the POC testing in September of 1993, the POC MHD generator accumulated 525 hours of total operating time and 300 MW hours with an average peak power level of 1.2 MW_e.

2.2.2 High Performance Demonstration Experiment (HPDE)

AEDC entered into a contract with the Energy Research and Development Administration (ERDA) in December 1973 to modify existing equipment, install new hardware, and conduct an MHD HPDE (Ref. 13). One of the primary objectives of the HPDE was to demonstrate high enthalpy extraction in a clean combustion gas. Initial experimental results were obtained with the channel configured in the Faraday mode. The resistive loading was selected to give low supersonic velocities over the entire channel length. Tests were conducted at magnetic fields up to 4.1 T, and up to 23.5 MW of power was produced (50% of design) for an enthalpy extraction of approximately 9%.

The HPDE facility consisted of a fuel burner, an electromagnet, a generator channel, a diffuser and exhaust system, and all supporting equipment necessary to the various facility components. The generator channel was configured in the segmented Faraday mode, and a magnetic field of 6 T was designed to produce a nominal peak power of 50 MW at a plasma mass flow rate of 50 to 60 kg/s. System operation was limited to a nominal 15-s period for each test because of cooling constraints. The HPDE facility was successfully operated in the power-producing mode with a magnetic field of 3.48 T and produced electrical power at levels up to 23.5 MW with 9% enthalpy extraction.

Depending on the magnetic field strength, the Mach number at the first loaded electrode was approximately 1.35 (1,200 m/s) and between 1.5 and 2.0 at the channel exit. Mass flow rate for these tests ranged between 45 and 50 kg/s, with O_2-to-fuel ratios and seed percentage chosen to give a nominal electrical conductivity of 8 to 10 mho/m at the channel inlet. The power output was increased gradually by initially testing at a magnetic field strength of 1.6 T and later increasing the field strength in deliberate steps to 3.9 T to evaluate the influence of selected parameters on Faraday performance and hardware. The estimated conductivity is given for several powered tests in Table 4- 4, which was taken from Reference 13, pp. 86. These results confirm the required inlet conductivity levels were achieved at selected times during the powered

runs. The predicted value given in the table is based on a thermochemical calculation of plasma properties for the actual fuel, oxidizer, and seed flow rates for each test. The agreement between the experimental conductivity and that based on thermochemical calculations is very good for all cases.

Table 2- 4. Summary of HPDE power production runs.

Test	Total Flow, kg/s	N/O	Seed, %	Measured Cont'd., mho/m	Predicted Cont'd., mho/m	Peak Field, T	Duration, s	Power, MW
6-006	44.5	1.0	~1	~8.5	5.2	1.59	10	1.5
008	50	.976	0.8	~9	8.6	2.36	12	5.3*
010	50.5	.91	0.9	~15	9.4	2.70	7	17.6
013	49	.955	0.9	~9.6	8.0	2.78	10	12
014	49	.929	0.9	~11.6	9.1	3.20	8	22
015	50.5	.909	0.9	~7.7	7.7	3.48	10	23

*Grounded diffuser support

2.3 MHD ACCELERATOR STUDIES

This section reports on a number of MHD accelerator studies in which there was no notable direct experimentation involved with MHD hardware. Among these are studies relating to an unseeded accelerator for hypervelocity ground testing application prepared by MSE and a study for hypersonic facility development jointly prepared by AEDC and NASA-LaRC.

With the exception of the MHD research being conducted in Russia, the MARIAH Project could not identify any other foreign MHD accelerator research efforts.

2.3.1 Unseeded Nonequilibrium MHD Accelerator Concept

A unique, nonequilibrium ionization MHD accelerator that was conceived and reported by MSE in 1992 (Ref. 14) may have the potential to provide true air chemistry, true temperature, and hypervelocity test conditions in transatmospheric vehicle (TAV) flight regimes that cannot be simulated by any other ground test technologies. This accelerator concept was intended to support air-breathing, hypervelocity propulsion testing where a high-quality air chemistry is desirable with the correct temperature and pressure to properly simulate atmospheric flight conditions.

In its simplest form, the accelerator creates and maintains nonequilibrium ionization by imposing a strong electric field across the MHD channel. Free electrons are accelerated in the field resulting in a substantial increase in the temperature of the electron gas relative to the heavy molecules that make up the bulk of the flow. Collisions of these higher energy electrons with neutral atoms and molecules result in ionization of those with the lowest ionization potential. While the bulk gas temperature remains low, the elevated electron temperature produces a nonequilibrium ionization condition where the ionization level is determined by the electron temperature rather than by the heavy particle or bulk gas temperature.

The recommended concept, illustrated in Figure 2- 2, consists of an arc heater, resistance heater, or other preheater device, followed by an optional ionization duct in which the plasma is "preionized" by an external energy source before entering the MHD accelerator. The accelerator may be followed by an expansion nozzle to create the desired test section conditions or used in a direct connect configuration for air vehicle engine testing. A number of techniques have been identified for achieving the nonequilibrium preionization, including the use of microwaves, lasers, or e-beams. These devices may also be considered for supplementing the ionization within the MHD accelerator, if necessary, to reach more difficult test conditions.

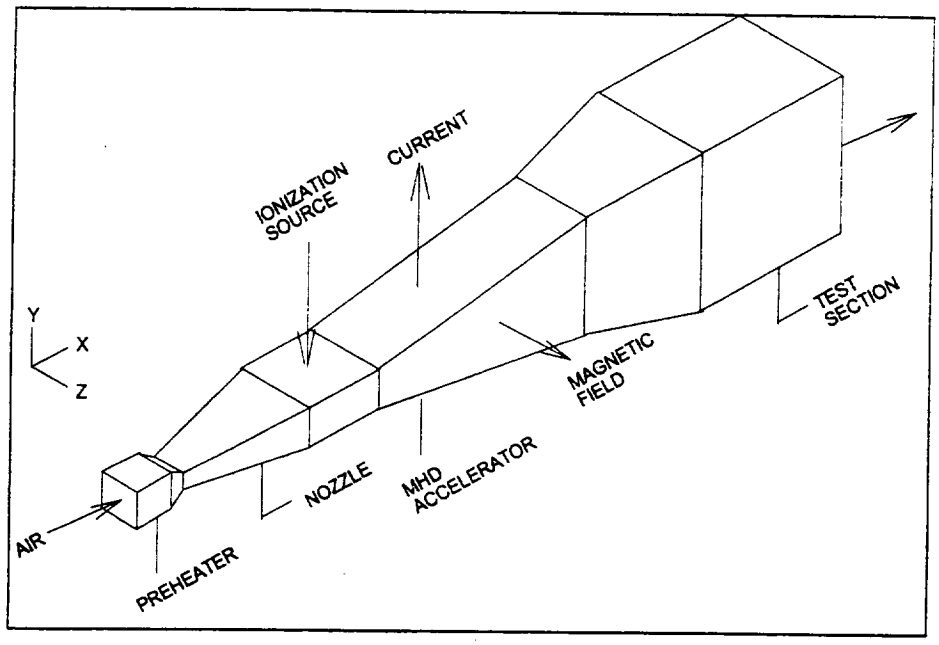

Figure 2- 2. Unseeded, nonequilibrium MHD accelerator concept.

The unseeded, nonequilibrium ionization MHD accelerator appears feasible for producing high enthalpy, true air, hypervelocity test conditions beyond the capabilities of proposed advanced arc heaters and with air chemistry that will likely be of significantly higher quality than arc heaters can produce. Test conditions were shown to approach combustor inlet conditions for free-stream Mach numbers of approximately 12 to 20. With the magnitude of the electric field at a maximum of 100 kV/m, the elevated electron temperature was sufficient to ionize the equilibrium NO and produce electrical conductivities that allowed reasonable MHD accelerator

performance. A major issue confronting the unseeded concept is the question of how the elevated electron temperature can be maintained, particularly at pressures greater than atmospheric. Based on research done to date, it is clear the accelerator must operate at low heavy particle number densities and high electric fields, i.e., the ratio E/N must be substantially larger than for equilibrium type accelerators. Details of this analysis may be found in Reference 15.

High Hall parameter values, due to low densities in the aft end of the channel, raise concern about ionizational instabilities. The Hall parameter was limited when it exceeded a critical value of five, and the electrical conductivities were reduced accordingly. Further investigation into the effects of the ionizational instabilities under the plasma dynamic conditions in the aft of these accelerators is essential in any future research. The Hall channel configuration should also be evaluated in future studies. Results from this study provide useful information on the performance of nonequilibrium MHD accelerators operated without seed.

2.3.2 MHD Accelerators for Hypersonic Applications

UTSI conducted a comprehensive investigation for AEDC, which revisited the concept of hypersonic flow simulation through MHD acceleration (Ref. 15). This study reviewed previous MHD accelerator work, conducted a theoretical analysis of performance potential, and identified critical technology issues. The primary goal of this investigation was to identify, by theoretical analysis, the performance potential of MHD accelerators and hot gas combinations for which satisfactory and credible design, construction, and operating characteristics could be predicted. This performance goal was to extend the hypersonic flight simulation limits from current arc-driven gas generator capability into the Mach 10 to 25 range. A secondary goal was the identification of critical technology issues, which require additional research prior to the development of an MHD-driven test facility.

This investigation reconfirmed the potential of the MHD accelerator for hypervelocity flow simulation. This study identified a number of critical technology areas, which should be addressed and resolved to ensure the successful development of an MHD-augmented hypervelocity test facility. These areas include the following:

1. Selecting and refining a hot gas generator. The candidates are the electric arc heater, a combustion heater, and the reflected shock tunnel.

2. A seeding concept is proposed where vaporized elemental K is injected into the stagnation region. This is considered a critical technology task.

3. Two transition nozzles are important to performance and flow quality. The critical issue is the development of a 3-D aerothermodynamic code with complete gas chemistry and viscous/thermal boundary layer effects.

4. The MHD channel electrode is a critical component, and the following elements need to be addressed: a) viscous, MHD code analysis, and modeling; b) electrode and channel current density limits; c) finite electrode 3-D effects; d) improved wall friction and heat transfer modeling; and e) channel flow quality.

5. Development of a magnet system that will produce the maximum field strength possible at an affordable cost.

6. Development of a dc power supply to operate at 1,000 to 5,000 V with currents up to 5,000 A.

Results of a parametric analysis of seeded MHD performance is presented in Appendix Section B.1. This study provides valuable analysis data on the potential performance of seeded MHD and a good discussion of technology development issues.

2.3.3 Single-Stage-to-Orbit Advanced Propulsion Concept

A rocket-induced MHD ejector (RIME) engine has been investigated by NASA Marshall Space Flight Center (NASA-MSFC) for an SSTO vehicle design (Ref. 16). The underlying principle consists of transferring energy from the rocket exhaust to the secondary flow (bypass air) using MHD technology. An MHD generator is used to extract electrical energy from the hot rocket exhaust, and this electrical energy is then used to accelerate the seeded, ionized bypass air flow in an MHD accelerator. This energy transfer, despite the conversion losses, may be more efficient than for conventional ejector concepts that rely on viscous forces in the mixing region between the primary and secondary streams, and therefore, is significantly dissipative. NASA-MSFC officials believe this concept shows promise, and it is presently being investigated. MSE is currently developing an engine performance computer code that will model the MHD ejector concept for NASA-MSFC.

2.3.4 Other Analytical Studies

There are various studies represented in the literature that pertain to the use of MHD acceleration to increase the kinetic energy flow in both space vehicle and ground test facility applications. These four studies are cited as examples, but in no way should these be considered exhaustive.

1. Nonequilibrium, chemically reacting, ionized gas flow modeling is being utilized to study the feasibility and efficiency of MHD acceleration of air flows for energy addition in wind tunnels by the MARIAH Project (Ref. 17).

2. UTA is supporting MSE in a NASA-LaRC sponsored program to develop MHD-augmented ground test facility concepts for achieving real-gas hypervelocity conditions (Ref. 18). The referenced paper reports on an effort in the theoretical and experimental determination of electrical conductivity, which is aimed at understanding the conductivity of air plasmas at high pressures.

3. A national study for hypersonic facility development has been documented by a joint effort between AEDC and NASA-LaRC (Ref. 19). To have beneficial access to the hypersonic flight regime in the post-2,000 era, a hypersonic technology infrastructure will be required. As was the case for both subsonic and supersonic technology development, hypersonic ground test facilities will be critical for success. This paper summarizes the results of two related studies on national hypersonic facilities needs and points out that 10 - 20 years will be required to develop and acquire these facilities.

4. Reference 21 documents results of a study conducted jointly by NASA-LaRC and GASL on the subject of facility needs and options for hypersonic air-breathing propulsion testing. As the authors emphasize, the requirements for advanced air-breathing engine testing are more severe in terms of facility scale, test duration, dynamic pressure, and air chemistry than for most other types of testing. The authors concluded the most promising concepts for producing the required clean air, high-dynamic-pressure environment were the free piston expansion tunnel, the Piston Gasdynamic Unit (PGU), and a Radiatively Driven Hypersonic Wind Tunnel (RDHWT) with an MHD accelerator as a second-stage driver. The last option is referred to as the MARIAH II concept in this report. A preliminary study of the MARIAH II concept has been completed by MSE and is described in Appendix F.

5. A design of an MHD accelerator for an arc-heated, MHD-augmented hypervelocity wind tunnel (Ref. 20). In this design, air would be initially preheated, seeded, and ionized by a conventional arc heater and passed through a low Mach number supersonic nozzle into the MHD accelerating channel where the electrical energy would be added to the plasma in the form of both directed kinetic energy and thermal energy. A secondary expansion nozzle would be placed at the accelerator exit to further expand the flow to a hypervelocity Mach number. The flow then passes through the test section into a diffuser for partial recovery prior to entering a vacuum tank. The primary advantages of this concept are the reduced initial pressure and temperature levels that must be achieved in the arc heater to subsequently expand the flow to high velocities, as well as the possibility of achieving equilibrium flow conditions in the test section.

3. STATEMENT OF THE PROBLEM AND APPROACH

3. STATEMENT OF THE PROBLEM AND APPROACH

The problem of duplicating, in a ground test facility, the high enthalpy, high dynamic pressure, high Mach number regime which is characteristic of hypervelocity flight, has been a challenge to airframe and engine designers for the past 40 years. The fundamental problem is to add sufficient enthalpy in the facility flow to match the total enthalpy of the in-flight aircraft. The problem is further constrained by the requirement that the flow through the test section must closely match the chemistry (i.e., species composition) of true air since this is what a real vehicle will experience. Other important requirements are that, for propulsion testing, the facility must be of sufficient scale and pressure to faithfully reproduce the mixing and reaction processes occurring in an actual engine and the test times must be sufficiently long to permit the heat transfer, material thermal soak, and flow processes to come to steady-state conditions. In the following sections the need for such hypervelocity test facilities is described, and the requirements of a hypothetical propulsion T&E facility are given. These requirements are based on a review of the recent literature as well as guidance received from the technical community generally and from NASA-LaRC in particular. The requirements given in Section 3.3 served as a basis for all of the technical evaluation of driver concepts that was performed as part of the MARIAH Project. It is noted below that current ground test facilities are unable to meet these requirements. Hence, in Section 3.4, some advanced driver concepts are described, which have the potential for dramatically improving the performance of hypervelocity test facilities.

3.1 FACILITY NEEDS

Figure 3- 1, taken from Reference 21, shows the current U.S. hypersonic test capabilities. Note that, with the exception of conventional wind tunnels and the arc tunnels, all of the facilities shown can be characterized as impulse test facilities, i.e., as facilities that have test times of a few ms or less. As noted in Reference 21, impulse facilities are inadequate for propulsion testing and evaluation (developmental) purposes due to short test times. These short run times associated with impulse facilities imply that steady-state heat conduction processes in the various engine structures cannot be reproduced.

Another shortcoming of existing propulsion test facilities is air chemistry. Virtually all ground test facilities compromise the chemistry of the flow stream in some way, either by the dissociation of O_2, the use of combustion processes (vitiated heaters) that introduce combustion products into the flow, contamination due to ablation of the walls and structures, or (in the case of MHD), the introduction of the alkali metal seed materials that are needed to achieve adequate electrical conductivity in the MHD accelerator channel. The chemistry issue becomes particularly acute for propulsion testing since incorrect simulation of the air ingested into the engine inlet may confound the chemistry of the high-speed combustion process. For this reason, there is a requirement that the flow in the test section must be close to true air.

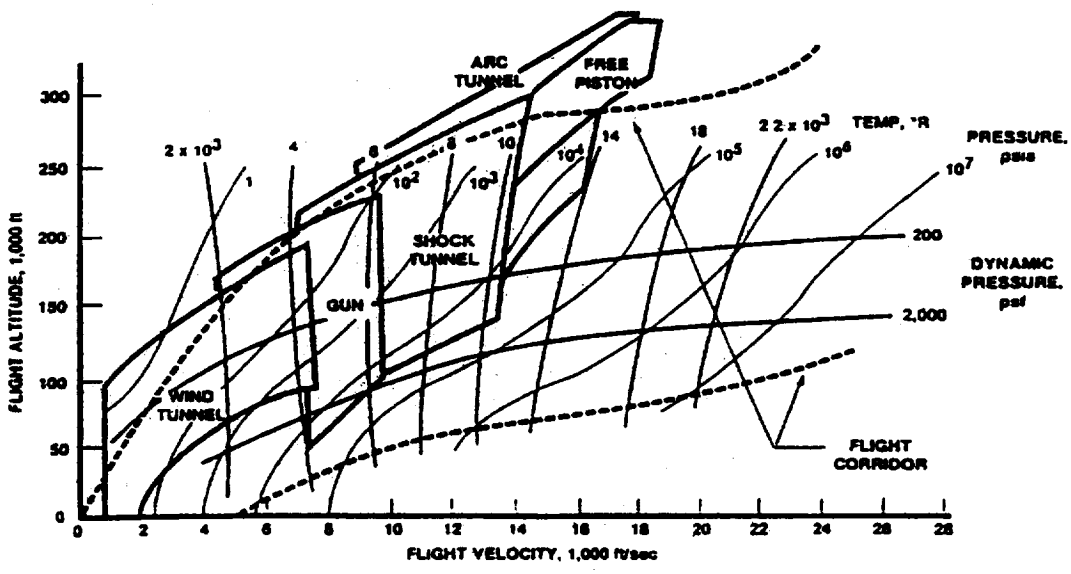

Figure 3- 1. Performance map of U.S. hypersonic test facilities.

Finally, a major inadequacy in present continuous flow facilities is their inability to provide true enthalpy air temperature and pressure. Arc heaters, for example, rely on Joule dissipation to increase the total enthalpy of the airstream. One consequence of the inherent limitations in arc heater design is the total enthalpy in the test section is below the targeted trajectory, and the test section entropy is higher to the right on the Mollier diagram than the targeted test point, resulting in test section pressures or Mach numbers that are lower than the targeted test condition. This point is addressed in greater detail in Section 3.3 and in Appendix F.

The above discussion has shown that present air-breathing test facilities are inadequate for a number of reasons, which include air chemistry, insufficient run times, facility scale, and the inability to provide sufficient enthalpy increase to the flow stream. These same conclusions were reached in the Hypersonic Test Investment Plan (HTIP) report of Reference 22. Thus, there is a demonstrated need for advanced propulsion test facilities, which can overcome all or most of these inadequacies. If present facilities are inadequate, then the question arises as to what constitutes a "good" propulsion system T&E facility. In Section 3.2, a provisional set of facility requirements, based primarily on the above discussion, are developed. These test requirements have been used to define the testing scenarios and the performance objectives of the MARIAH Project as well as to provide a basis for conducting various analytical studies on advanced MHD driver technologies.

3.2 FACILITY REQUIREMENTS

Facility requirements were addressed early in the MARIAH Project through consultation with the NASA technical community and by conducting a review of the literature on high-speed

ground test facilities. From the beginning, the Project was conceived as a facilities research effort aimed at developing a ground test facility capable of conducting "hot" propulsion tests on advanced integrated hypervelocity air-breathing engines. The basic requirements of such a facility were established through extensive discussions between MSE and the technical staff at NASA-LaRC as well as through a review of the literature on hypersonic test facilities.

The test requirements are summarized below:

1. The test facility should be a "T&E" facility capable of test durations of the order of tens of seconds to minutes.
2. The facility should be capable of testing advanced air-breathing engine modules at near full scale. An area cross-section for the test section of 80 ft^2 has been adopted as a working number.
3. The facility should be capable of simulating true total enthalpy and thermodynamic conditions. For engine testing, this implies that the Mach numbers, total enthalpies, and entropies should match those seen behind the bowshock of the hypervelocity aircraft. The facility should be capable of matching post-bowshock conditions corresponding to a 2,000-lbf/ft^2 free-stream dynamic pressure with a 5° deflection angle shock and a free-stream Mach number of 16.
4. The facility should provide an airstream chemistry corresponding approximately to the post-bowshock regime of the aircraft, i.e., having minimal dissociation, vibrational nonequilibrium, and contaminants.
5. The facility should be a true "T&E" facility implying high testing throughput, high reliability and lifetimes for critical components, and versatility of the MHD accelerator across a wide range of pressures and Mach numbers.

3.3 LIMITATIONS OF PRESENT DRIVER TECHNOLOGIES

For continuous flow testing (i.e., simulations that last for several seconds or more), the primary means of generating hypervelocity flows has been the arc heater. These devices have several fundamental limitations that are discussed below. Figure 3- 2, taken from Appendix F of this document, shows total enthalpy vs. entropy corresponding to the post-bowshock conditions experienced by a hypervelocity aircraft at selected dynamic pressures.

Figure 3- 2 indicates that to duplicate such conditions in a ground test facility will require the total enthalpy of the gas to be increased from ambient levels to tens of millions of joules per kg. Also shown in the diagram is the limiting envelope for arc heater operation taken from Reference 2. These devices operate at relatively low plenum pressures (below 150 atm) and high temperatures. They suffer from the limitation that all of the energy addition occurs by way of Joule dissipation resulting in entropy generation. This fact, coupled with a reasonably well-defined hypervelocity flight envelope, imposes second law limitations on the amount by which

the total enthalpy can be increased without crossing the targeted flight envelope. While the total enthalpy is limited only by the amount of electrical power added, the thermodynamic end point

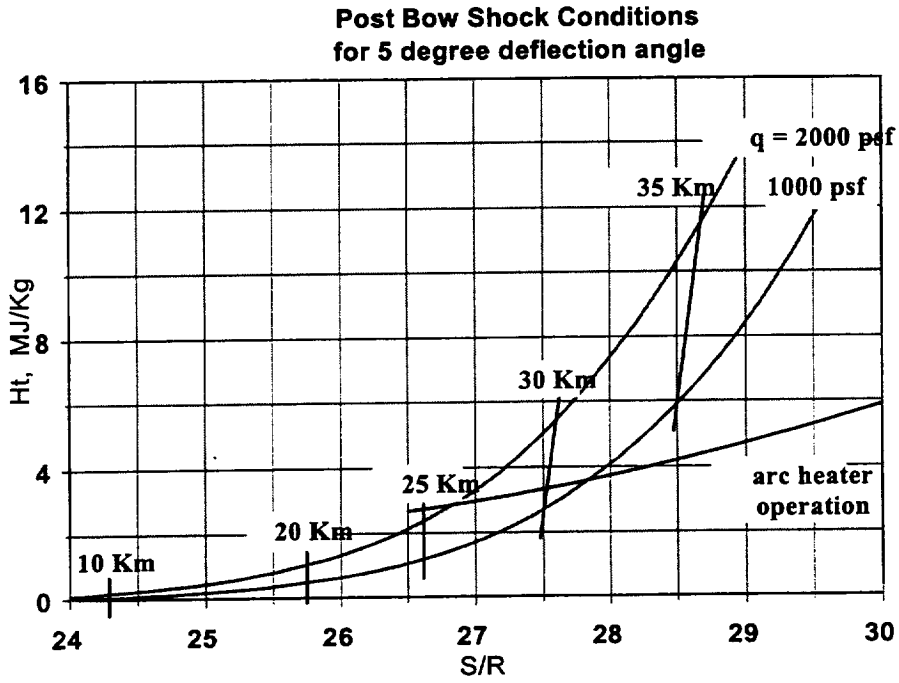

Figure 3- 2. Total enthalpy vs. entropy for selected dynamic pressures.

for arc heater operation is typically too far to the right on the Mollier diagram, as can be seen from the figure. Arc heaters can only provide true enthalpy air for simulations corresponding to altitudes below approximately 22 km at a dynamic pressure of 2,000 lbf/ft^2. At the higher altitudes, the enthalpy increment added to the flow is insufficient, and the entropy levels will be too high to match the required dynamic pressures. This implies that the test section pressures or Mach numbers will be consistently below the targeted values. A more detailed and quantitative discussion of the problem may be found in Appendix F.

As noted above, the fundamental limits on arc heater technology are associated with entropy production. There are two general strategies for improving the performance of continuous ground test facilities.

1. Improve the conversion efficiency by adding some fraction of the input power as work rather than Joule dissipation. This will have the effect of increasing the amount of enthalpy added per unit increase in the entropy. This is the essential argument for MHD. As noted in Appendix F, MHD is the only mature technology that has the capability to directly add work to the flow, thereby circumventing the Joule dissipation problem to some degree.
2. Start the energy addition process at much lower entropy levels. This will permit a greater amount of Joule dissipation to occur before the limiting trajectory is crossed. Note that, for a specified reservoir temperature, lowering of the entropy implies

increasing the reservoir pressure. The entropy consideration is the fundamental reason that arc heater development in the United States has focused on steadily increasing the operating pressures in the reservoir.

Each of the above strategies has a driver technology associated with it. For the first strategy, the driver technology is MHD with an unspecified heater or energy addition device upstream. For the second strategy, the driver technology is the UHP gas piston technology first developed in Russia. In recent years the UHP concept has been broadened and refined by the suggestion that beamed energy, in the form of laser, microwave, or e-beam, could be added in the supersonic expansion region downstream of the throat (Ref. 23). In this form, the concept has been called a RDHWT. The concept is described more fully in Appendix F.

3.4 STUDY APPROACH

Research to investigate the feasibility of using high-performance MHD accelerators for hypervelocity, air-breathing propulsion ground testing was initiated under the NASA MARIAH Project. Analytical, experimental, and systems studies were pursued to obtain the necessary information for assessment of this technology. Previous MHD accelerator research in the United States and Russia has focused on low-pressure, arc-heated systems that can generate test conditions for only the low-pressure flight testing applications. These accelerators produced high Mach number test conditions that were equivalent to flight at high altitude and low dynamic pressure; however high-pressure systems were never tested.

Renewed interest in TAVs and SSTO transportation during the 1980s highlighted the need for clean-air, true-temperature, hypervelocity ground test facilities for the development of air-breathing propulsion systems and propulsion integration. The USAF SAB and others identified a need for ground test facilities capable of producing conditions far beyond those available from conventional facilities and identified MHD as one of the few technologies potentially capable of producing these test conditions. However, to address the needs of this generation of hypervelocity research, MHD would need to operate in a much more harsh environment and produce cleaner air test conditions than previously attempted, thereby presenting many new challenges. Thus, the MARIAH Project was initiated to identify and address the issues that must be resolved for MHD to satisfy the needs for future hypervelocity vehicle test and evaluation.

The critical issues for this application were primarily the MHD performance issues for operation in the high-pressure environment, materials issues, and air-chemistry issues for propulsion testing. The first was judged to be the highest priority since the others would be irrelevant if MHD could not achieve the necessary performance levels to support the required testing. Thus, most of the effort in the MARIAH Project was directed toward the determination of MHD accelerator performance for the high-pressure testing application. This effort included analytical studies to evaluate the performance of MHD accelerators operating at high pressure, experimental studies to assess the electrical properties of high-pressure air, as well as system studies to assess the availability and performance of various seed materials and external ionization sources. In addition to the performance studies, preliminary investigations were conducted to address the most critical air-chemistry issue, the effect of the seed materials on

combustion, as well as thermal management issues, including the availability of high temperature materials.

1-D analytical studies were conducted to map the performance of MHD accelerators relative to the high Mach number, high flight dynamic pressure conditions identified by NASA as critical to the development of hypervelocity air-breathing vehicles. Parametric and optimization studies identified the regimes in which seeded and unseeded MHD accelerators can operate.

Preliminary studies indicated that electrical conductivity would be very low in the high-pressure air required for these test conditions. Since electrical conductivity is one of the most important MHD accelerator performance parameters, various means for enhancing the conductivity were explored. These included the evaluation of novel seed materials such as fullerenes, novel acceleration methods such as the Pulsatron ionization enhancement concepts, and external source ionization through the use of e-beams or microwave. Potassium has traditionally been used for seeding in MHD accelerators and generators since it has a low ionizational potential and is readily available. However, other alkali metals including cesium (Cs) and rubidium (Rb) have lower ionizational potentials and could provide better MHD performance; however, their availability for use in large quantity for this application was unknown. Therefore, a study of the availability, cost, and properties of these materials was accomplished to provide the data necessary for assessing the feasibility of their use.

A 1-D analysis with chemical and ionizational kinetics, including a Boltzmann solver for electron energy analysis, was necessary to address the nonequilibrium issues in both the seeded and unseeded MHD accelerator concepts. These studies addressed the use of nonequilibrium ionization created by strong electric fields and/or external e-beams to enhance the MHD performance. A 2-D MHD accelerator analysis code was also developed to investigate the multidimensional phenomena in these devices. This code was primarily used for evaluation of test data from NASA Ames experiments.

A critical deficiency that was identified early in the MARIAH Project was the lack of any experimental data on the electrical properties of high-pressure, high temperature air. Previous MHD accelerator experiments had been conducted at low pressure, providing a considerable amount of information on the properties and performance characteristics of both K-seeded and unseeded air in this regime. Furthermore, the electrical properties of atmospheric air have been extensively studied by researchers in various electrical products industries as well as in meteorology. However, very little research had previously been conducted in the high temperature, high-pressure regime needed for MHD accelerators, and absolutely no research had been conducted with seeded air for these conditions.

MSE addressed these deficiencies by conducting experimental studies at UTA and at NASA Ames. High-pressure, seeded air and N_2 studies were conducted at UTA to evaluate the electrical conductivity under typical high performance, MHD accelerator operating conditions. These studies provided data to verify chemical equilibrium electrical conductivity models, examine nonequilibrium issues, and confirm predictions of electron attachment to O_2 species in high-pressure air. Additional experiments at NASA Ames were designed to investigate electrical

discharge phenomena in high-pressure air. Specifically, these were needed to investigate the conditions under which diffuse discharge can be achieved as well as the phenomena involved in the breakdown and transition to strong arcs in the high-pressure air.

A review of previous MHD accelerator experiments in the United States and Russia was conducted to characterize the established performance capabilities of these devices and identify the deficits as a basis for the future research needs. A study of the Russian TsAGI MHD accelerator facility, which has been operating for over 30 years, was also performed through a subcontract to TsAGI. These studies focused on the performance of these small-scale devices as well as channel wall and electrode materials. Performance data from previous U.S. experiments, such as the AEDC LoRho experiment, was also used for validation of MHD accelerator codes.

Table 3- 1 provides a list of the various analytical, experimental, and systems studies that were conducted by the MARIAH Project. This table also indicates the appendix section in which each of the studies is discussed and identifies the applicability of each study to the three concepts evaluated by the MARIAH Project.

3.4.1 Classical High Temperature, Arc Heater-Driven MHD

The defining characteristics of this type of MHD acceleration system are: a) the use of an arc heater upstream of the MHD accelerator and b) the use of an alkali metal seed. This mode of MHD acceleration has been studied the most extensively, both experimentally and theoretically; therefore, one would assume it has the least technical risk.

In Appendices B.1 and B.2 of this document, we report on two separate analyses of MHD accelerators, which were conducted as a part of the MARIAH Project, for the purpose of investigating the performance limits of arc heater-driven MHD accelerators. Appendix Section B.1 contains a study conducted to examine the limits of conventional MHD accelerators. It was assumed the arc heater could operate at a maximum operating pressure of 200 atm and that the seed material was Cs. A rather detailed parametric study (presented in Appendix Section B.1) was conducted to attempt a first-order optimization.

The analysis in Appendix Section B.2 is based on a 1-D simulation of the entire flow train, starting at the plenum, passing through the nozzle and MHD accelerator, and continuing through the secondary expansion duct up to the inlet of the test section. Several issues have been investigated using this model, such as: a) the question of pressures needed in the heater or plenum region; b) whether e-beam addition can be utilized to enhance the unseeded flow conductivity in the MHD duct; c) the question of seeded vs. unseeded flows; and d) issues relating to basic thermodynamic limits of such drivers. These issues are discussed and reported in some depth in the Appendices.

Table 3- 1. MARIAH study topics vs. applicability.

ANALYTICAL STUDIES				
DESCRIPTION	**Section**	**A**	**B**	**C**
MSE ACCELERATOR STUDIES	B.1	X		
OSU FLOW TRAIN ANALYSIS	B.2	X	X	X
ENGO MHD ACCELERATOR STUDY	E.3	X		
OSU 2-D ANALYSIS	B.3	X	X	
PULSATRON MHD ACCELERATION METHODS	D.3	X	X	
MSE/PRINCETON MARIAH II CONCEPT STUDY	F			X
EXPERIMENTAL STUDIES				
DESCRIPTION	**Section**	**A**	**B**	**C**
UTA CONDUCTIVITY EXPERIMENTS	A.1	X		
NASA AMES CONDUCTIVITY EXPERIMENTS	A.2	X	X	
EVALUATION OF NASA AMES EXPERIMENTS	B.3.4	X	X	
TsAGI MHD ELECTRODES STUDY	E.2	X		
SYSTEMS AND SEED STUDIES				
DESCRIPTION	**Section**	**A**	**B**	**C**
FULLERENES AS SEED MATERIALS STUDY	C.1	X	X	X
Cs, Rb, and K AS SEED MATERIALS STUDY	C.2	X	X	X
EFFECTS OF SEEDING ON COMBUSTION	C.3	X	X	X
OXYGEN ATTACHMENT IN AIR STUDY	C.4	X	X	X
THERMAL MANAGEMENT OF MHD ACCELERATORS STUDY	D.1	X	X	X
IONIZATION TECHNOLOGIES FOR MHD STUDY	D.2		X	X
TsAGI FACILITY CAPABILITIES STUDY	E.1	X	X	X

Topics vs. Applicability

Concept A Seeded, Arc Heater-Driven MHD
Concept B Nonequilibrium, Arc Heater-Driven MHD
Concept C MARIAH II

3.4.2 Arc Heater-Driven MHD with Beamed Energy Addition

In this configuration, an arc heater or another plasma-generating technology could drive the unseeded MHD accelerator. The distinguishing characteristic of this scheme is the use of beamed energy addition in the form of e-beam, microwave, or laser to sustain the required electrical conductivities.

Recombination of free electrons is a major issue in this configuration. At pressures above 1 atm, recombination is very fast, and the length over which substantial numbers of free electrons can be sustained will be of the order of a centimeter or less. To minimize recombination rates, it will be necessary to work at subatmospheric pressures in the MHD channel. To stay within the entropy limits, the low-pressure requirement will dictate high Mach number operation in the channel that will result in low temperature as well. Some of the issues associated with the use of beamed energy for purposes of increasing the electrical conductivity are discussed in Appendix Section D.2.

3.4.3 The MARIAH II Concept

This mode of MHD acceleration relies on a UHP driver to confine the gas in a reservoir at pressures of up to 20,000 atm or higher, resulting in very low initial entropies. The gas would pass through a throat and into a supersonic expansion region where beamed energy would be added. An MHD accelerator acting as a second-stage driver would be located downstream of the expansion region. The advantage of this scheme is that it combines both strategies 1) and 2) discussed in Section 3.3 to maximize the performance of the device. The high-pressure driver permits the process to start at very low entropy levels, while the second-stage driver takes advantage of the higher conversion efficiencies that can be realized from MHD. A major issue here, as for the MHD with beamed energy concept, is recombination of the free electrons. Appendix F presents an initial feasibility study of the MARIAH II concept in much greater detail.

3.5 FACILITIES ISSUES

The single most challenging facilities issue is the huge amount of power required to drive a hypervelocity facility that would meet the requirements defined in Section 3.2. The large test section specified implies very high flow rates, which in turn implies very high total power requirements. For example, to reach an altitude of 35 km on the $q = 2{,}000$ lbf/ft^2 trajectory, the total enthalpy must be increased by about 12 MJ/kg above ambient conditions. At that point, the post-shock mass density and velocity are 0.0232 kg/m^3 and 4,790 m/s, respectively. A ground test facility must be capable of identically simulating these post-bowshock conditions in the test section. An area cross section of 80 ft^2 was specified as part of the facility requirements in Section 3.2. Since the mass flow is just the product of these last three numbers, we obtain a mass flow rate of approximately 820 kg/s. If one assumes that all the enthalpy increase is added by way of electric power (either in an arc heater or in an MHD accelerator), then the power

requirement is just the product of the total enthalpy increase and the mass flow rate, or about 9.8 gigawatt electric (GW_e). This huge power requirement represents a serious facilities issue but does not by itself constitute a fundamental barrier to the realization of the post-bowshock, hypervelocity flight regime. It should be noted that the 35-km, 2,000-lbf/ft^2 point represents the extreme target test point for the testing of air-breathing engines. The free-stream Mach number at this point is approximately 16. At free-stream Mach numbers close to 16, the engine will in all probability transition to rocket-mode operation. Points that are further down on the q = 2,000 lbf/ft^2 trajectory, as well as points that lie on lower dynamic pressure trajectories, will generally have more benign power requirements.

Other facility issues include those associated with downstream gas handling and the problems associated with slowing down a very high-speed flow while managing the associated temperature rise. The removal or handling of air contaminated with a seed material is yet another facility issue. Since the basic objective of the MARIAH Project was to examine the issues of technical feasibility of MHD accelerators, no specific approaches to these problems were studied in any detail. It was assumed that associated facility engineering issues would be the subject of separate study.

4. MARIAH PROJECT RESEARCH SUMMARY

4. MARIAH PROJECT RESEARCH SUMMARY

The research activity undertaken in the MARIAH Project includes computational studies in which various MHD codes have been examined and modified to support predictions of MHD system performance. Experimental studies were also performed to investigate specific MHD performance parameters to gain an insight into their characteristics under specific conditions. Additionally, certain issues concerning systematic elements of MHD accelerators, as well as other various general issues have been researched.

4.1 COMPUTATIONAL STUDIES

Three computational studies were performed by the MARIAH Project. MSE modified a previously developed 1-D MHD equilibrium code to predict MHD accelerator performance in both the equilibrium and nonequilibrium modes. This code was validated against the LoRho experimental data taken at AEDC. Two computational studies were also performed under a subcontract with OSU. Both 1-D and 2-D codes were used to analyze MHD accelerator performance. The detailed data on these codes appears in Appendix B of this report.

4.1.1 MSE MHD Accelerator Analysis

4.1.1.1 Overview

Parametric and optimization analyses were performed using the MSE ACCEL 1-D MHD code to evaluate the potential of MHD accelerators in high Mach number, high dynamic pressure, propulsion testing applications. Performance results from these analyses were compared to the stated test requirements specified by NASA for the MARIAH Project (discussed in Section 3). Generally stated, the NASA target test requirements for the MARIAH Project are the post-bowshock conditions for a 5° deflection angle shock at a flight Mach number of 16 and 2,000-lbf/ft^2 flight dynamic pressure. Results of the parametric and optimization analyses are summarized in Section 4.1.1.2 and 4.1.1.3 respectively and are fully documented in Appendix Section B.1.

All analyses discussed in this section were performed using the equilibrium, seeded model in the MSE ACCEL code. This computer program models segmented Faraday, MHD accelerator channel performance with a choice of four design models for studying different design constraints. This code models seeded and unseeded plasma accelerators using equilibrium chemistry and either equilibrium or two-temperature nonequilibrium ionization. The model includes approximations for electrode voltage drops, boundary layer voltage drops, finite segmentation effects, and critical Hall parameter limitations.

Verification and validation of the ACCEL code was completed prior to using the code for the MARIAH Project analysis. This was accomplished using data from a series of experiments

known as LoRho (low-density) that were conducted at the AEDC during the 1960s (Ref. 3). These experiments used an arc heater augmented with a linear Faraday MHD accelerator and N_2 for the working gas. An overview of the AEDC LoRho research and a thorough discussion of the validation analysis is presented in Appendix Section B.1.

4.1.1.2 MHD Accelerator Parametric Performance Analysis

A parametric variation of four independent parameters, one at a time, was performed to establish the variation in performance with each parameter. Applied electrical current density, channel operating temperature, MHD accelerator channel entrance conditions, and applied magnetic field were each varied through a range of values to assess their effects. The parametric study results are presented on Mollier diagrams where they are compared against the NASA specified test condition discussed above.

Conditions for hypersonic flight at flight dynamic pressures of 500, 1,000, and 2,000 lbf/ft^2 and flight Mach numbers from 6 to 22 are also indicated on the Mollier diagrams. Post-bowshock conditions for a 5° deflection angle are also included. Performance limits for advanced arc heaters at operating pressures up to 200 atm and data for combustor inlet conditions on these figures are taken from Reference 4.

All analyses in the parametric study were performed by varying one parameter value at a time using a nominal baseline parameter set, which included a magnetic field strength of 8 T, an applied current density of 50 A/cm^2, and a maximum channel gas temperature of 3,500 K. A 1% molar fraction of Cs was used for seeding in all cases.

Figure 4- 1 presents the results of magnetic field variations for values from 6 to 30 T. High field strength magnets will be necessary to attain high dynamic pressure test conditions, such as those required by NASA. Of the magnetic fields studied, accelerators using 24- and 30-T fields approached nearest to the NASA target test condition but still produced results that fell short of the high dynamic pressure required by NASA. However, as seen in the next section where multiple variable optimization results are presented, combining high magnetic field values with low current density and an optimum temperature distribution produced significantly better results.

MHD channel temperature was varied over a range from 2,700 K to 4,500 K in the parametric analysis. Higher temperature generally resulted in lower entropy conditions at the channel exit due to the higher electrical conductivity and the higher heat transfer to the channel walls. The increased electrical conductivity reduced the Joule heating term (j^2/σ), which is an entropy production term. The higher temperature caused a higher heat transfer rate, which reduced entropy. However, at the highest temperatures, the heat transfer rate was so large that more energy was lost through heat transfer than was added by the applied electrical power; therefore, the target enthalpy could not be reached.

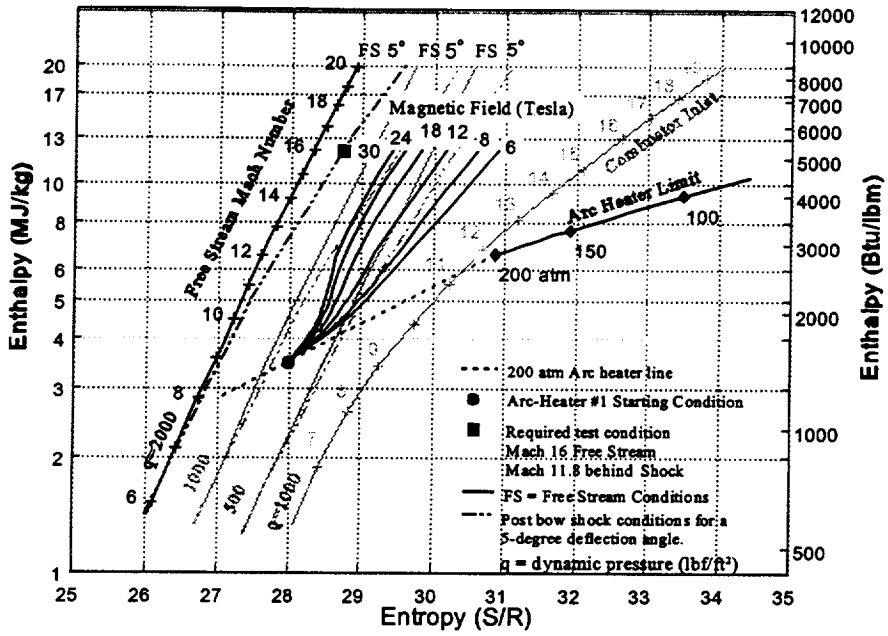

Figure 4- 1. Comparison of MHD performance for various magnetic field values.

Electrical current density values were varied from 25 to 100 A/cm^2. High values of current density resulted in the highest entropy due to the Joule dissipation term (j^2/σ). Thus, lower values of current density performed better, producing lower entropy values that approached closer to the NASA target test condition. However, at the lowest values of current density, power loss through heat transfer was larger than the applied power and again, the target enthalpy was unattainable.

4.1.1.3 Parametric Study Conclusions

The NASA-specified target operating conditions are, as expected, very difficult to achieve. The single variable parametric variation used in this study has provided valuable information on the performance effects of each of the individual variables. These effects have been characterized by variation about a baseline parameter set. None of these variations produced a solution that closely approached the NASA-specified condition. However, these solutions provide insight into ways in which an MHD-augmented driver can produce the higher enthalpy and lower entropy test conditions needed.

Performance analyses using three arc-heater conditions for MHD accelerator entrance properties were very enlightening. All arc-heater characteristics used in this study were of a 200-atm class but operated at various enthalpy levels. An arc heater referred to as Arc-Heater #2 was to the far right of the 200-atm performance envelope on the Mollier diagram. This arc heater provided the MHD channel with a high enthalpy flow; unfortunately, this was also at a high value of entropy.

The MHD channel performed well in this environment; however, the entropy was too high to allow the desired condition to be reached. The conditions for the arc heater referred to as Arc-Heater #3 was far to the left (low entropy); however, the enthalpy was too low to achieve adequate electrical conductivity for effective MHD operation. Thus, applied MHD power heated the working gas through Joule heating as an arc heater would, and the enthalpy vs. entropy curve for the solution followed the arc heater curve on the Mollier diagram (see Section B.1.5). Arc-Heater #1 was used for the remainder of the optimization analyses.

Increases in magnetic field strength offer the most benefit observed during this study. High strength magnetic fields present no problems for the high-pressure plasma of this application. Higher magnetic fields result in shorter channels and higher operating pressures. If technology permits, higher strength magnets could significantly improve the performance of MHD accelerator systems.

The parametric study considered only single parameter variations. These variations indicated that high values of the magnetic field strength, high channel temperature, and low current density individually lead to lower entropy solutions. Combinations of the best conditions can further improve the performance; therefore, a multiple variable performance optimization was performed and is summarized in the next section.

4.1.1.4 MHD Accelerator Optimization Analysis

Partial optimization of MHD accelerator performance to support the nation's hypervelocity propulsion wind tunnel testing requirements has been performed and is summarized in this section. These analyses extend the single parameter variation analysis that is summarized in the previous section and reported in Section B.1.4 by choosing the combination of parameter values that produces the highest accelerator design performance relative to the NASA target requirements discussed in Section 3.

Three design analyses have been completed in this study that are distinguished by the level of technology advancement required for the development of a facility. Throughout the analyses in Section B.1.4 and B.1.5, one parameter, magnetic field strength, stood out as the single most important factor in determining the limits of advanced MHD accelerator facility performance. For the high-pressure accelerators considered in this study, high strength magnets up to at least 30 T could be used to improve the performance without the detrimental effects due to high Hall parameter that would occur in lower pressure systems. Values of the magnetic field strength of 15, 24, and 30 T have been used in this analysis.

The results of performance calculations for the three magnetic fields are shown in Figure 4- 2. Each of the channels is 5 m long at the stagnation enthalpy level of the NASA-specified test condition (12.15 MJ/kg). This figure also shows the effect of extending these channels to a higher final stagnation enthalpy of 20 MJ/kg. To achieve this higher enthalpy, the channels are extended to lengths ranging from 6.65 to 6.9 m. Table 4- 1 lists the accelerator channel exit conditions for the 12.15-MJ/kg and 20.0-MJ/kg exits. Figure 4- 2 indicates the high dynamic

pressure test condition specified by NASA cannot be achieved using the seeded air, arc heater-driven, MHD accelerator designs considered in this study. These designs are unable to reach the required entropy level for the 2,000-lbf/ft^2 dynamic pressure specified by NASA but do provide test conditions for the same Mach number at lower dynamic pressure, which would correspond to flight at a higher altitude. The flight dynamic pressure and altitude were calculated for the Mach 16, post-bowshock test conditions that can be simulated using these MHD accelerator designs. These ranged from a flight dynamic pressure of 710 lbf/ft^2 at an altitude of 42.8 km (140.4 kft) for the 15-T design to 1,200 lbf/ft^2 at an altitude of 38.95 km (127.8 kft) for the 30-T design.

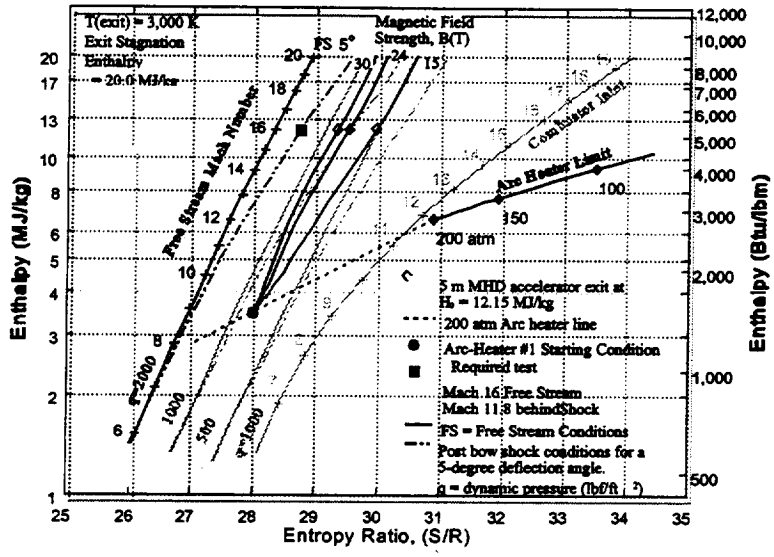

Figure 4- 2. MHD accelerator performance for selected accelerator designs.

Finally, Table 4- 1 also lists the channel exit conditions for an extension of the channel to a 30.0-MJ/kg exit. This design exit condition exceeds the 2,000-lbf/ft^2 dynamic pressure post-bowshock condition at a stagnation enthalpy level of 27.9 MJ/kg. At this point, an accelerator with a 30-T magnet can produce test conditions equivalent to the 2,000-lbf/ft^2 dynamic pressure, post-bowshock condition at a flight Mach number of 23.4 and an altitude of 40.8 km (133.7 kft).

Fortunately, for this application, high static pressure in the channel helps to maintain the Hall parameter at reasonably low values. For the 5-m channel designs (stagnation enthalpy of 12.15 MJ/kg in Fig. 4- 2), the maximum Hall parameter occurs in the 30-T case and is a moderate value of 1.65. A maximum transverse electric field (E_y) of 130.8 kV/m also occurs for this case. These values are very reasonable and should not cause any operational problems in this accelerator channel design.

Table 4- 1. Exit conditions for selected channel designs.[†]

Specifications		Accelerator Exit Conditions				Performance Data			
Magnetic Field Strength	Exit Stagnation Enthalpy (MJ/kg)	Entropy Ratio, S/R	Pressure (atm)	Mach Number	Velocity (m/s)	Channel Length	Current Density (A/cm^2)	Electrical Power Req'd.[††] (MW)	Wall Heat Loss (MW)
15	12.15	29.96	10.6	4.16	4,187	5.0	29.7	7,789	691
24	12.15	29.53	16.0	4.16	4,194	5.0	26.8	7,912	812
30	12.15	29.35	19.1	4.16	4,193	5.0	25.1	7,963	872
15	20.0	30.60	5.8	5.73	5,760	6.65	29.7	14,710	1,160
24	20.0	30.12	9.1	5.73	5,766	6.83	26.8	14,980	1,436
30	20.0	29.92	10.9	5.72	5,764	6.90	25.1	15,100	1,570
30	30.0	30.23	8.2	7.25	7,294	8.62	25.1	24,370	2,631

[†] Channel exit temperature was 3,000 K for these analyses.
[††] Does not include the electrical power into the arc heater.

If these accelerator designs are extended to the 20.0-MJ/kg exit stagnation enthalpy (end points of performance curves in Fig. 4- 2), the Hall parameters are somewhat higher due to the lower static pressure at the accelerator channel exit. Hall parameter values are moderately high and vary from 2.35 for the 15-T case to 2.70 for the 30-T case. Finally, for the 27.9-MJ/kg case, corresponding to the 2,000-lbf/ft^2 dynamic pressure and flight Mach number of 23.4 discussed above, a maximum Hall parameter value of 3.2 occurs at the exit[1]. Values of Hall parameter higher than about 2-3 can cause shorting and ionizational instabilities in some channel designs. However, there is experimental evidence that even Hall parameter values that exceed 3 may occur without detrimental effects. This is discussed further in Section B.1.5.

Based on extrapolation of current technology in superconducting magnets, it is estimated that magnets with a 15-T field strength could be developed for near-term applications (10 year); consequently, the accelerator designs based on these magnets are considered to be in a moderate risk category. The 24-T magnets may be available in the 20-year time frame, thus this value has been used for a higher risk, 20-year technology design. Further technology advancement to a 30-T magnet is considered to be high risk at present, and the future availability of these cannot yet be estimated. These are technically possible but are not expected to come to fruition in the foreseeable future. However, these could be available in the 20-year time frame if technology breakthroughs occur in the current research programs or if

[1]It should be noted that the Hall parameter varies from a minimum value of approximately 0.57 near the MHD accelerator channel entrance to the value of 3.2 at the 27.9-MJ/kg point and is less than 3.0 for approximately 95% of the channel length.

breakthroughs occur in the current research programs or if R&D programs are initiated to obtain this technology. An analysis based on the 30-T magnet is included in this study for comparison.

4.1.1.5 Optimization Analysis Conclusions

Accelerator designs evaluated in Appendix Section B.1.5 indicate that seeded MHD accelerators augmenting high-pressure arc heaters cannot produce the test conditions required in the MARIAH Project specifications (see Section 3). However, these show that flight simulations corresponding to high flight Mach number, post-bowshock conditions at lower dynamic pressures are obtainable. Several technologies that are beyond the current state-of-the-art are implied by the design values used in these analyses; however, in most cases, these technologies should be available in the 15- to 20-year time frame for development of a major new test facility. However, the prospect of large bore, high field strength magnets being available in the 15- to 20-year time frame is presently unknown. Six-Tesla superconducting magnets are available today, and 8- to 9-T magnets could probably be developed using present technology. Magnets having 10- to 12-T fields are projected for near-term development, and 15-T magnets may be available in the 15- to 20-year time frame. At present, 24- to 30-T magnet development cannot be projected in the foreseeable future. Analyses at these field values have been included to provide a basis for recommendations on future technology development.[2]

Higher temperature materials than what is available today would help to ensure the performance and reliability of these high performance accelerators; however, these devices could be fabricated with today's technology if new materials are not available. Finally, advances in arc-heater technology would be necessary before large, 200-atm arc heaters could be designed for this application. However, other higher pressure driver technologies are presently being studied for replacing arc heaters in the MHD accelerator applications, and these show excellent promise. Furthermore, use of the 150-atm arc heaters that are available today would result in some performance degradation but would still allow simulation of flight conditions close to those described herein.

4.1.2 Ohio State University MHD Accelerator Flow Train Analysis

OSU conducted an analysis of MHD accelerators as a part of the MARIAH Project for the purpose of investigating the performance limits of such devices. This research is summarized in this section and reported in Appendix Section B.2. The analysis is based on a 1-D simulation of the entire flow train starting at the plenum, passing through the nozzle and MHD accelerator, and continuing through the secondary expansion duct up to the inlet of the test section. Several issues have been investigated using this model such as: a) the question of pressures needed in the heater or plenum region; b) whether e-beam addition can be utilized in an unseeded flow to

2 Information obtained from conversations with personnel at the National High Magnetic Field Laboratory, Tallahassee, FL; Oxford Magnet Technology Ltd., Eynsham, U.K.; Wang NMR, Inc., Columbia University, NY; Fermilab, Batavia, IL; and the National Research Institute for Metals, Fengen, Japan.

enhance conductivity in the MHD duct; c) the question of seeded vs. unseeded flows; and d) issues relating to basic thermodynamic limits of such drivers. These issues are discussed and reported on in some depth in the following sections. Appendix Section B.2 also contains a discussion of several flow stability issues. This discussion has been omitted from the present summary in the interest of brevity.

There are several basic requirements that have been used to define the testing scenario and the performance objectives of this study. These are presented in Section 3 above and have been discussed in the literature (Refs. 24, 25, 26). Similar analytical studies have been conducted in the past by several researchers (Refs. 14, 27, 28). This study is unique in that the flow model incorporates several novel features, namely a) the inclusion of a Boltzmann equation solver for the electron distribution function; b) the ability to simulate the addition of e-beam energy directed into the MHD channel; c) the ability to simulate both chemical kinetics and vibrational nonequilibrium; and d) the ability to correctly account for all important ionization processes. These capabilities permitted us to systematically explore both the nonequilibrium and the equilibrium flow regimes across a wide spectrum of control parameters. Details of the kinetic model are given in Section 4.1.2.1.

The computer code developed on the basis of the kinetic model was run across a rather large set of control parameters, including variation of seed fraction and type, e-beam energy, plenum pressures and temperatures, and nozzle geometry (see Section B.2.3). The objective of the study was to demonstrate the possibility of placing points on the total enthalpy vs. entropy diagram corresponding to the post-bowshock, 2,000-lbf/ft^2 flight trajectory. This has been adopted as the limiting operating envelope for the hypothetical test facility. Conclusions of this study are given in Section 4.1.2.1.

4.1.2.1 Kinetic Equations

To simulate the gas dynamics and kinetics of both alkali-seeded and unseeded airflows in supersonic nozzles and MHD channels, we have used quasi-1-D nonequilibrium flow kinetic modeling. The model incorporates the following equation groups:

1. The equations of 1-D magnetogasdynamics for nonequilibrium reacting ionized real gases (Refs. 29, 30).
2. Chemical and ionization kinetics equations for a number of reacting species (including electrons, ions, and electronically excited metastable species).
3. Master equation for populations of vibrational levels of three diatomic species N_2, O_2, and NO (Ref. 31).
4. Boltzmann equation for symmetric part of electron energy distribution function $f(\varepsilon)$ (EEDF) in crossed electric and magnetic fields (Refs. 32, 33).
5. Generalized Ohm's Law (Ref. 30).

The full set of equations may be found in Appendix Section B.2. The effects of vibrational relaxation and chemical reactions are accounted for in the energy and motion equations. The chemistry-vibration coupling terms are incorporated into both the chemical kinetics and the master equation. Rates of electron impact processes used in kinetic equations (vibrational and electronic excitation, ionization, attachment, etc.), as well as electric conductivity are calculated based on the EEDF calculated by the Boltzmann equation. The latter takes into account superelastic processes, which couple vibrational and electron mode energies. Therefore, the system of solved equations is self-consistent.

In this quasi-1-D approach, the applied electric and magnetic fields are given as functions of the axial coordinate: $E_x(x)$, $E_y(x)$, and $B_z(x)$. Time and space derivatives in the Boltzmann equation are omitted since they are important only in extremely fast oscillating fields and in sheath areas. Therefore, the Boltzmann equation becomes a simple second-order differential equation with electron energy as an independent variable solved by standard iteration method (Ref. 33). The rest of the differential equations are first-order equations solved by a widely used stiff ordinary differential equations (ODE) system solver (LSODE) (Ref. 34).

The list of the neutral species chemical reactions (32 reactions for 12 species N, N_2, O, O_2, NO, O_3, NO_2, N_2O, NO_3, N_2O_4, N_2O_5, N_3), as well as the reaction rates at thermal equilibrium are taken from the Russian AVOGADRO database (Ref. 35) where the most reliable available data has been recommended in a wide temperature range. The vibration-chemistry coupling is modeled using the Macheret-Fridman-Rich nonequilibrium rate model (Refs. 36, 37), and the state-specific reaction rates $k(v\rightarrow,T)$ for the reactions

$$\begin{aligned} N_2(v) + M &\leftrightarrows N + N + M \\ O_2(v) + M &\leftrightarrows O + O + M \\ NO(v) + M &\leftrightarrows N + O + M \\ N_2(v) + O &\leftrightarrows NO + N \\ NO(v) + O &\leftrightarrows O_2 + N \end{aligned} \quad , \qquad (4\text{-}1)$$

used in chemical and vibrational kinetics equations are the same as in our previous paper (Ref. 38).

The list of ion-molecular reactions including ionization, recombination, ion conversion, attachment and detachment processes (more than 300 reactions for 13 species e^-, N^+, N_2^+, O^+, O_2^+, NO^+, O^-, O_2^-, N_2O^+, NO_2^-, Na^+, K^+, Cs^+), as well as most of the reaction rates were taken from the review (Refs. 39, 40, 41, 42, 43). The rates of electron impact ionization and electron attachment to the species N_2, O_2, NO, Na, K, Cs are calculated by the Boltzmann equation solver using the experimental cross-sections of these processes as functions of electron energy (Refs. 44, 45, 46, 47). The latter group of processes describes kinetics of nonequilibrium ionization and attachment of the plasma electrons in the presence of external electric and magnetic fields.

Note the thermochemical data for both neutral and charged species is incorporated into the code; therefore, the rates of reverse processes are evaluated from detailed balance. Consequently, the kinetic model correctly predicts the chemical composition of alkali-seeded air, including electron and ion concentrations, in thermodynamic equilibrium (with no fields applied). Thermochemical parameters such as enthalpies, entropies, and specific heats of the species in the temperature range 300-6,000 K are taken from References 48 and 49.

The rates of electronic excitation and dissociation of N_2 and O_2 by the plasma electrons, with the production of metastable species $N_2(A^3\Sigma_u^+)$, $N(^2D)$, $N(^2P)$, $O_2(a^1\Delta_g)$, $O_2(b^1\Sigma_g^+)$, $O(^1D)$, $O(^1S)$, are also calculated by the Boltzmann solver using the experimental cross-sections (Refs. 44, 45). Metastable species collisional quenching and chemical reaction rates are taken from the review (Ref. 39).

The rates of vibrational excitation of N_2 and O_2 by plasma electrons are evaluated by the Boltzmann solver using the experimental cross-sections $Q_{vib}^{0\to v}$ (Refs. 44, 45). The detailed cross-section matrix for N_2, $Q_{vib}^{v\to w}$, $0\le v,w\le 8$, needed for modeling of superelastic processes (Ref. 45), is calculated using the semi-empirical method (Ref. 50). The rates of vibration-translation (V-T) and vibration-vibration (V-V) rates for N_2 and O_2, including multiquantum processes, are taken the same as in Reference 38 where they have been evaluated using the forced harmonic oscillator (FHO) rate model (Ref. 51). These rates are in good agreement with the recent experiments and state-of-the-art close-coupled calculations in a wide temperature range (Ref. 51). The V-T rates for N_2-Na, N_2-K, and N_2-Cs are taken from Reference 52. As shown in Reference 53, these rates are consistent with the Na-seeded N_2 vibrational relaxation measurements behind shock waves.

The experimental electron transport cross-sections for N_2, O_2, NO, Na, K, and Cs that are necessary for the plasma electric conductivity calculations are taken from References 44 through 46 and 54).

In these calculations, we considered the use of a high-energy e-beam as a possible efficient way to sustain nonequilibrium ionization in the supersonic flow. Up to 50% of the relativistic e-beam power goes into electron impact ionization (Ref. 39). This external ionization method has been previously (and extensively) used to sustain a discharge in supersonic flows in gas dynamic lasers (Ref. 55). The e-beam power fractions going into ionization, dissociation, and electronic excitation of N_2 and O_2 in air (g-factors) are taken from the review (Ref. 39). The experimental secondary electron energy distribution in N_2 and O_2 for the beam energies 50 - 2,000 electronvolts (eV) are taken from References 44 and 45 and extrapolated toward the higher energies (Ref. 34). In this study, we do not address the high-power e-beam engineering issues (beam entering the high-pressure flow, focusing, X-ray radiation etc.). Our primary interest is the e-beam-initiated kinetics.

Wall heat transfer coefficient (c_h) and skin friction coefficient (c_f), as well as the boundary layer thickness (δ) are estimated based on the results of turbulent compressible boundary layer theory (Ref. 56). Heat fluxes to the electrode surfaces are estimated based upon the experimental heat transfer measurements in MHD accelerators (Ref. 3) (see Section 2.3).

4.1.2.2 Code Validation

Various parts of the kinetic model used in this study have been previously validated in modeling calculations. A more detailed description of these validation exercises may be found in the appendix. Two series of validation calculations were run for the entire simulation code, including the recently developed MHD accelerator model. The results of the first series were compared with the experimental data (somewhat scarce) that was obtained on the GE unseeded air MHD accelerator (Refs. 57, 58). In these experiments, air was heated to T_0=9,500 K at a pressure P_0=550 atm behind the reflected shock and expanded through a supersonic MHD channel (channel length L=30 cm, area ratio F_2/F_1=2.0, magnetic field B=4.2 T). The experimentally determined test area impact pressure in the MHD-augmented flow was approximately 1.5 - 2 times higher than in the isentropic flow in the same channel. Figure 4- 3 shows calculated axial profiles of the gas temperature and velocity in the channel for both MHD-augmented and isentropic flow, as well as the velocity profile obtained from the GE group 1-D equilibrium flow model (Ref. 57). The close agreement between these two models, both predicting about 15% velocity increase, is due to the fact that at the high temperature T≅6,800 K and pressure P=10-30 atm; the flow in the channel is very close to the LTE.

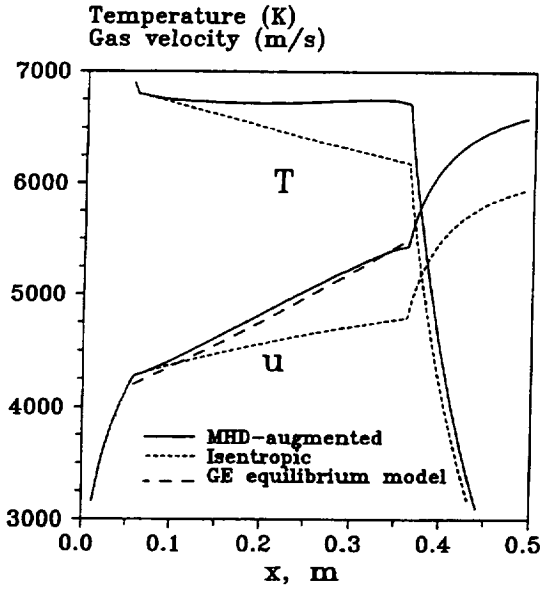

Figure 4- 3. Axial temperature and velocity profiles for the GE reflected shock unseeded air accelerator.

The second series of calculations was made for the AEDC continuous mode MHD accelerator operating with K-seeded (at 1.5%) N_2 (Accelerator B of Ref. 63). In these experiments, N_2 was heated by an arc heater up to a temperature of about T_0=6,000 K at a pressure P_0=3.3 atm and expanded through an MHD channel (channel length L=77 cm, area ratio F_2/F_1=2.1, magnetic field B=1.5 T). Figure 4- 4 shows the temperature and the flow velocity distributions along the

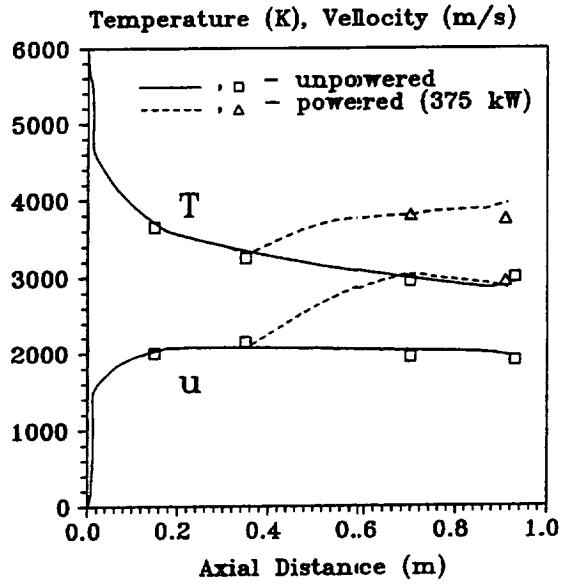

Figure 4- 4. Experimental and calculated temperature and velocity axial profiles for the AEDC K- seeded accelerator.

channel. Figure 4- 5 presents gas temperature and velocity at the channel exit as functions of the accelerator power.

The experimental and calculated data are in good agreement, and temperature and pressure in the MHD-augmented flow is up to 30 - 50% higher than in the isentropic flow. Nonequilibrium effects in the channel (N_2 vibrational disequilibrium) and chemical dissociation are both insignificant. The gas temperature in the channel T~3,000 - 4,000 K is not high enough to stimulate substantial thermal dissociation of N_2, while fast N_2 V-T relaxation on K atoms and quite slow expansion prevented freezing of N_2 vibrations. Again, the effective reduced electric field was low, $(E/N)_{eff} \cong 10^{-17}$ V×cm^2, so that $T_e \cong T$ in the channel. The experiments also show the boundary layers in the channel overlap (Ref. 3) so one has a fully developed channel flow.

In both series of calculations, the agreement with the experiments is quite good. However, we note that additional model validation is desirable, specifically for MHD flows where the flow is far from thermal and ionization equilibrium.

4.1.2.3 Results of Simulation Studies

We applied the kinetic model described and validated in Section 4.1.2.1 for modeling of both alkali-seeded and unseeded airflows in MHD accelerators in a wide range of plenum conditions and for various nozzle geometries. The main objective was to determine the feasibility and efficiency of using the MHD technology for the high Mach number energy addition wind tunnel.

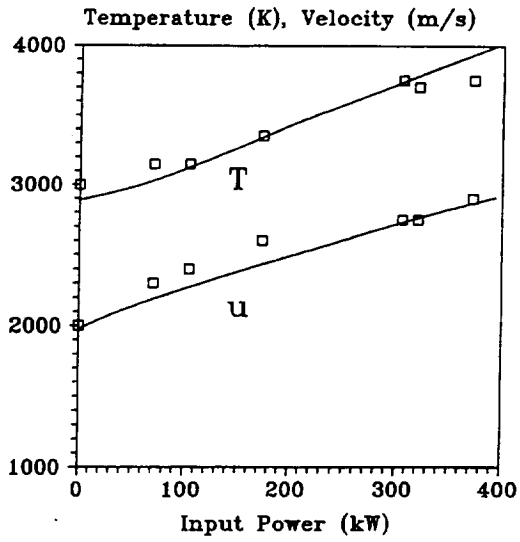

Figure 4- 5. Experimental and calculated exit temperature and velocity for the AEDC K-seeded accelerator.

All subsequent calculations are made for the nozzle throat cross-section area (F_{throat}=4 cm^2) and ideal Faraday accelerator [$E_x=\beta(E_y-uB_z)$, $j_x=0$ throughout the channel] with the magnetic field in the channel (B_z=10 T). The secondary expansion duct was assumed to be 2-m long with the exit area of 9 m^2.

4.1.2.3.1 *Unseeded Flows*

The first series of runs was made for the N_2: O_2=78: 22 air for the plenum temperatures T_0=3,000 - 6,000 K, and plenum pressures P_0=10 - 1,000 atm. The MHD channel length was L=30 cm, with the entrance cross-section area F_1=8 cm^2 and the area ratio F_2/F_1=2 (geometry similar to the MHD channel used in References 57 and 58). In all calculated cases, the Mach number at the MHD channel entrance was M=2, and the channel entrance pressure was about 10% of the plenum pressure (1, 10, and 100 atm, respectively). Constant loading parameter $K=E_y/uB_z$=2 was assumed. Ionization in the MHD channel was sustained by a relativistic e-beam. The e-beam loading per molecule D was in the range 0.0-1.0 keV/mol/s and was assumed to be constant.

Figures 4- 6 and 4- 7 summarize the obtained results. Figure 4- 6 shows the total enthalpy of the flow (H) as a function of the flow entropy (S), for the beam load D=1.0 keV/mol/s. The exceptions are Runs #6 and #3 for which the beam load was taken to be D=0.3 and 0.1 keV/mol/s, respectively, to avoid thermal instability. The total enthalpy increase is very small unless the plenum pressure is low. Note that all runs with D=0 did not show any enthalpy increase since the thermal ionization of air at these plenum temperatures is too small. Figure 4- 7 gives the ratio of the total enthalpy increase (ΔH) to the initial enthalpy (H_0) and also the ratio of

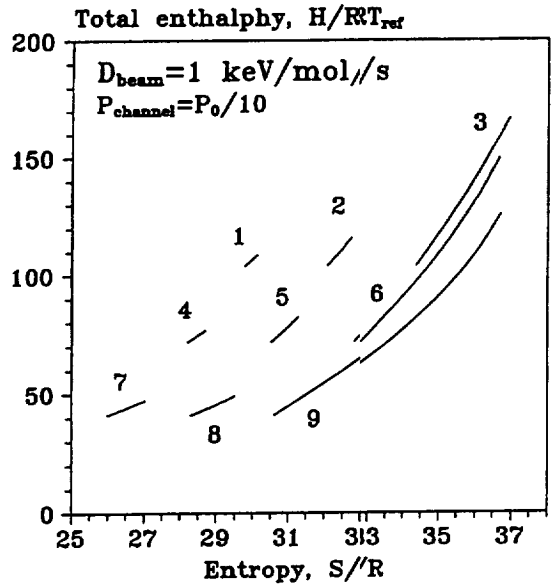

1- T_0=6000 K, P_0=1000 atm;
2- T_0=6000 K, P_0=100 atm;
3- T_0=6000 K, P_0=10 atm;
4- T_0=4,500 K, P_0=1,000 atm;
5- T_0=4,500 K, P_0=100 atm;
6- T_0=4,500 K, P_0=10 atm, D_{beam}=0.3;
7- T_0=3,000 K, P_0=1,000 atm;
8- T_0=3,000 K, P_0=100 atm;
9- T_0=3,000 K, P_0=10 atm, D_{beam}=0.

Figure 4- 6. Total enthalpy vs. entropy diagram for the MHD-augmented unseeded air flows, ionized by a high-energy e-beam (D_{beam}=1 keV/mol/s):

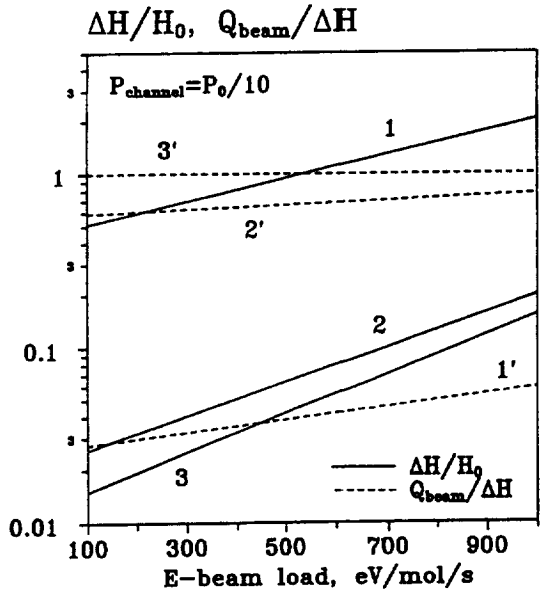

Figure 4- 7. Total enthalpy increase $\Delta H/H_0$ and beam efficiency $\Delta E_{beam}/\Delta H$ for the MHD-augmented unseeded air flows at T_0=3,000 K: 1,1'- P_0=10 atm, 2,2'- P_0=100 atm, 3,3'- P_0=1,000 atm.

the absorbed e-beam power to the enthalpy increase ($\Delta E_{beam}/\Delta H$ beam efficiency) for T_0=3,000 K. The nonequilibrium ionization sustained by the e-beam provides substantial flow power increase at reasonable efficiency ($\Delta H/H_0$=0.5-2 and $\Delta E_{beam}/\Delta H$=0.03-0.05) only for the plenum pressure of P_0=10 atm (channel pressure ≤ 1 atm). At higher plenum pressures, the power increase does not exceed 10 - 20% of the initial flow power ($\Delta H/H_0$<0.2), and it is mainly due to the e-beam stimulated gas heating in recombination processes ($\Delta E_{beam}/\Delta H$=0.6-1.0). At the high number densities, the recombination and electron attachment rates are so fast that the ionization fraction sustained by the beam in the MHD channel becomes far too low to produce a noticeable Lorentz force. For example, for the same beam load of 0.3 keV/mol/s, the ionization fraction in the channel is ~10^{-5} at the channel pressure of 1 atm, ~10^{-6} at 10 atm, and ~10^{-7} at 100 atm. Since the total power addition in the full-scale high-pressure wind tunnel facility has to be ΔH~1 GW and at the high channel pressure conditions $\Delta E_{beam}/\Delta H$ ~1, this would require the use of about a 1-GW e-beam (in a very inefficient way). It must be emphasized that the low efficiency of this method at high pressures is primarily due to the high rate of electron loss (recombination and attachment), which is independent of the particular method of nonequilibrium ionization. Since the high-energy e-beam is one of the most efficient ionization sources available (see Section B.2.2.2), the use of any other method of external ionization in the high-pressure MHD channels (P>1 atm) is also not feasible.

The only conceivable way to efficiently use e-beams (or any other ionization source) in high-plenum pressure flows appears to be expanding the flow down to the subatmospheric pressures prior to creating nonequilibrium ionization. We considered the feasibility of this mode of operation in the second series of calculations made for T_0=3,000 - 6,000 K, P_0=1,000 atm, and the beam load D=1 keV/mol/s. The MHD channel length was again L = 30 cm, with the entrance cross-section area F_1=170 cm^2, the area ratio F_2/F_1=2.35, and K=2=const. The channel entrance Mach number now was M=5, and the channel pressure was approximately 1 atm.

The results shown in Figure 4- 8 demonstrate a considerable total enthalpy rise (up to 70%) and reasonable beam efficiency (5 - 10%) for the high plenum and channel temperatures. Higher temperature in the channel leads to a) partial compensation of electron attachment by thermal detachment from the negative ions and b) slower recombination rates at the lower number density.

The slope of the H(S) curves on the Mollier charts (Figs. 4- 5 and 4- 7) is:

$$tan\theta = \frac{dH}{dS} = \frac{dQ_{total}}{dQ_{thermal}} T = \frac{j \cdot E}{j \cdot E - u \cdot (j \times B)} T = \frac{\sigma K(K-1) u^2 B_z^2}{\sigma (K-1)^2 u^2 B_z^2} T = \frac{K}{K-1} T \qquad (4\text{-}2)$$

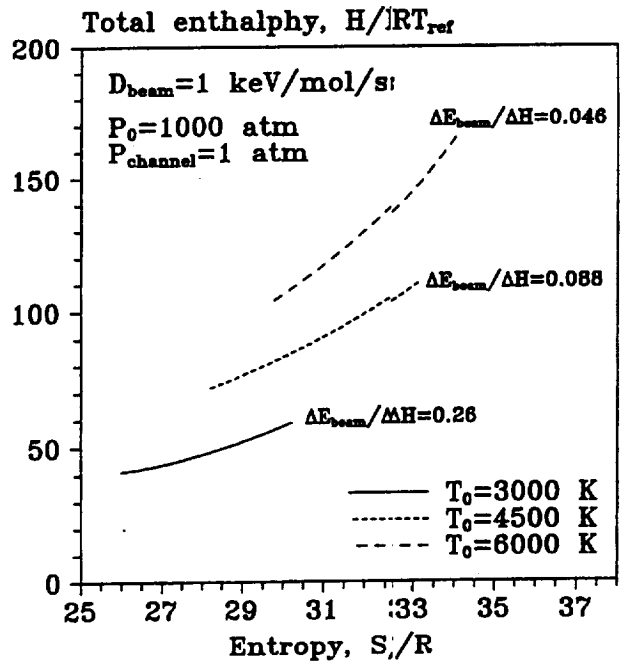

Figure 4- 8. Total enthalpy vs. entropy diagram for the high-plenum pressure (P_0=1,000 atm) MHD-augmented unseeded airflows, ionized by a high-energy e-beam (D_{beam}=1 keV/mol/s). The flow is expanded to P~1 atm before entering the MHD channel.

with the steepest slope dH/dS corresponding to the highest value of T_{avg}. Reducing the loading parameter would not increase since it would reduce the total power added to the flow proportional to K (K-1) [see Eq. (4- 2)] and inhibit the Joule heating, which would result in further reduction of T_{avg}.

The third series of calculations for the full-scale accelerator was made for T_0=5,000 K, P_0=1,000 atm, mass flow rate G=17.4 kg/s, and beam loads 0.0-2.0 keV/mol/s. The MHD channel length now was L=140 cm, with the entrance cross-section area F_1=200 cm^2, and the area ratio F_2/F_1=1.65 (channel entrance Mach number M=5, channel pressure P=1-2 atm). To prevent the large-scale thermal instability (see Section B.2.3.3) leading to excessive gas heating in the channel and increasing chemical dissociation, the loading parameter at high temperatures was reduced:

$$K = 1.5\,, \quad T < 2{,}500\ K$$
$$K = 1.0 + 0.5 \cdot (T / 2{,}500)\,, \quad T \geq 2{,}500\ K \qquad (4\text{- }3)$$

The results of calculations are shown in Figures 4- 9 - 4- 12. Figure 4- 9 presents the obtained H(S) curves, plotted together with the target values for TAV ("flight envelope"). Although the total enthalpy of the flow increases 1.5 - 2.5 times, the flow entropy is considerably larger than the target values. The main reason, as discussed above, is the low MHD channel entrance temperature [see Fig. 4- 10 and Eq. (4- 2)]. Therefore, while the calculated Mach numbers in the MHD-augmented flow are close to the target values and conditions, the flow pressure is more than an order of magnitude lower than the pressure behind the bowshock (see Table 4- 2).

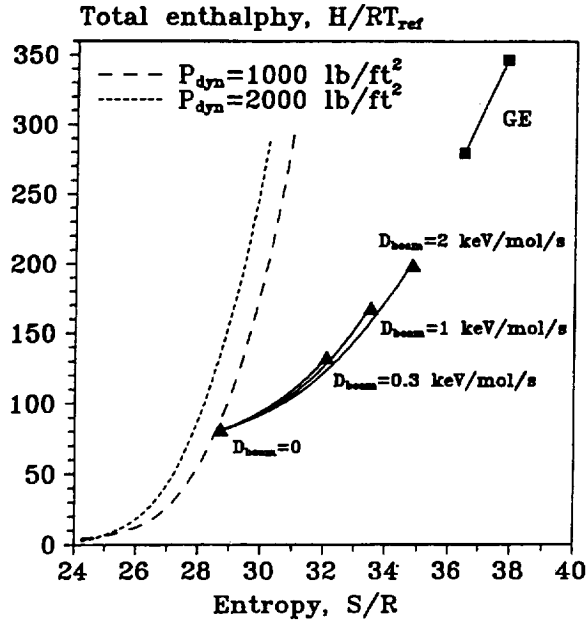

Figure 4- 9. Total enthalpy vs. entropy diagram for the full-scale unseeded air MHD accelerator with external ionization by an e-beam. P_0=1,000 atm, T_0=5,000 K, L=140 cm, F_y/F_1=1.65. Dashed lines - TAV flight envelope. Also shown H(S) for the GE reflected shock unseeded air accelerator.

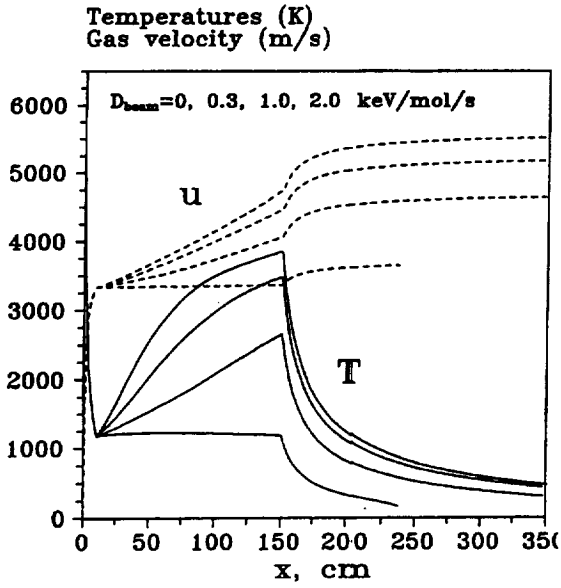

$T_0 = 5{,}000$ K,
$P_0 = 1{,}000$
$F_2/F_1 = 1.65$
L = 140 cm

Figure 4- 10. Axial temperature and velocity profiles for the accelerator of Fig. 4- 9 for different beam loads.

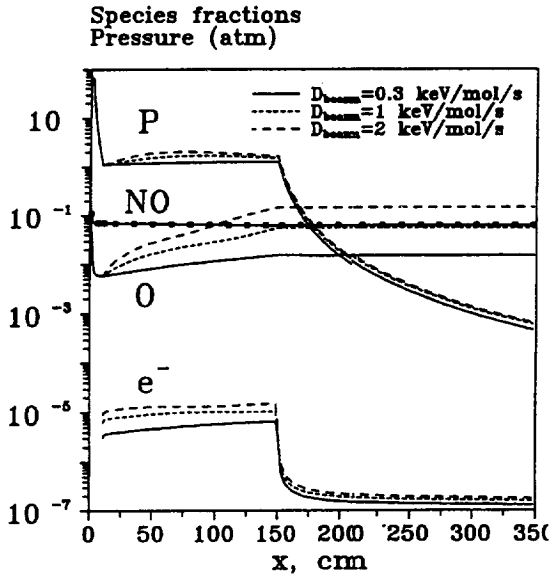

Figure 4- 11. Axial profiles of pressure and species mole fractions for the accelerator of Fig. 4- 9 for different beam loads.

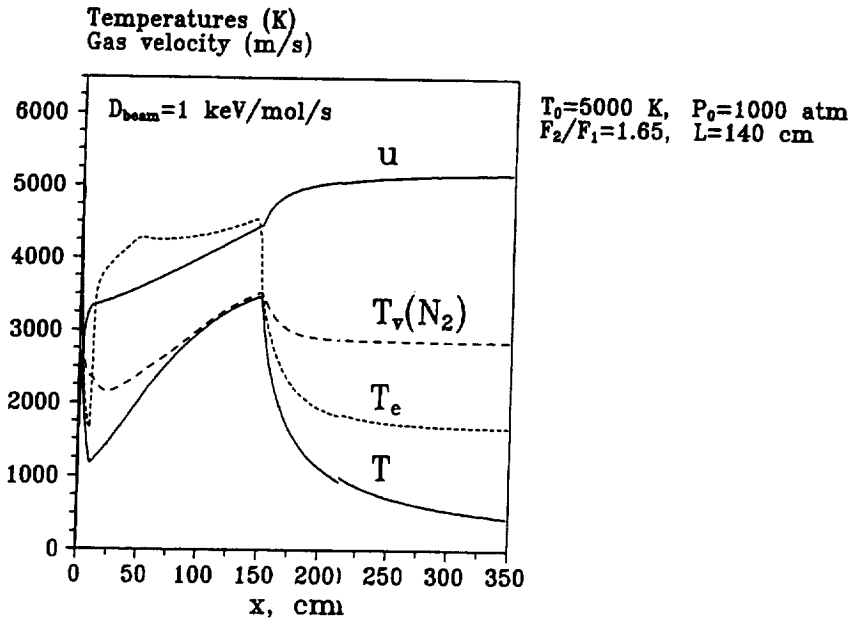

Figure 4- 12. Axial profiles of the translational temperature, vibrational temperature of N_2, and electron temperature for the accelerator of Figure 4- 9 for D_{beam}=1 keV/mol/s.

Table 4- 2. Unseeded air MHD accelerator performance.

Left and central subcolumns-target values for P_{dyn}=2,000 and 1,000 lbf/ft^2, respectively; right subcolumn – present calculations.

Case	H, MJ/kg			S/R			U, km/s			M		
1	7.2	7.0	6.9	27.9	28.6	28.9	3.76	3.64	6.3	9.4	9.0	8.9
2	11.6	11.0	11.4	28.7	29.3	32.1	4.78	4058	4.60	10.9	10.4	10.4
3	13.6	14.6	14.5	29.0	29.9	33.5	5.16	5.31	5.15	11.4	11.3	10.9
4	15.8	16.9	17.2	29.3	30.2	34.8	5.58	5.71	5.49	11.8	11.8	10.9

Case	P,mbar			y_o,%	Y_{NO},%	$T_V(N_2)$	D_{beam}, keV/mol/s	ΔE_{beam}, MW	ΔH, MW
1	41.1	21.4	12.8	0.4	7.0	1574	0.0	0.0	0
2	35.7	18.5	2.0	1.5	6.2	2776	0.3	6.5	77
3	34.4	17.2	1.3	5.6	6.2	2857	1.0	21	130
4	33.1	16.1	1.3	14.7	6.2	2455	2.0	41	176

Note that raising the beam load increases recombination losses (the ratio $\Delta E_{beam}/\Delta H$, (see Table 4- 2). In particular, this makes greater the average loading parameter K_{avg} defined as the ratio of the total power going into internal degrees of freedom to the total power into kinetic energy. For

this reason, the slope dH/dS actually decreases with the beam load despite the fact the T_{avg} becomes higher (see Figs. 4- 9 and 4- 10).

The calculated transverse current density in the channel did not exceed j_y=10 A/cm^2.

Finally, Table 4- 2 shows a tens of megawatt ionization source would be needed to operate the full-scale facility at the channel pressure of about 1 atm. The beam efficiency can be improved by further reducing the channel pressure, but this would lead to even greater flow entropy rise because of the lower channel entrance temperature according to Equation. (4- 2). The e-beam load (D) can be simply related to the beam current density (j_{beam}) and the energy of the beam electrons (ε_{beam}) that determines the penetration length:

$$l \approx 0.5 \cdot \frac{(\varepsilon_{beam}/300)^{1.35}}{(\rho/1.2)} \qquad (4\text{- }4)$$

where l is in m, ε_{beam} is in keV, and ρ is in kg/m^3 (Ref. 39). For the conditions of Table 4- 2, keeping in mind that $l \cong 2r \cong 0.2$ m, and the absorbed beam power $\Delta E_{beam}=eDN\times(Ll^2)\cong j_{beam}\,\varepsilon_{beam}\times(Ll)$, one has ε_{beam}~30 keV, and for D=1 keV/mol/s:

$$j_{beam} \cong \frac{eDNl}{\varepsilon_{beam}} \cong 0.3A/cm^2 \qquad (4\text{- }5)$$

4.1.2.3.2 *Seeded Flows*

The first series of runs was made for K-seeded (at 1%) air for the plenum temperatures T_0= 3,000 - 6,000 K and pressures P_0=10 - 1,000 atm. The MHD channel length was L=30 cm, with the entrance cross-section area F_1=8 cm^2, and the area ratio F_2/F_1=2-25. Again, in all calculated cases, the channel entrance Mach number was M=2, and the channel entrance pressure was about 10% of the plenum pressure. All runs for the K-seeded cases at T_0=3,000 K did not show any flow acceleration due to MHD augmentation since the thermal electric conductivity of the mixture was too low. Calculations for T_0=4,500 K demonstrated noticeable total enthalpy rise ΔH only for the plenum pressures of P_0=100 atm and lower. Since the results for the K-seeded cases were marginal in terms of MHD acceleration, these results are not shown. Plots for these cases may be found in Appendix Section B.2. We note the totally enthalpy rise ΔH also increases with the channel area ratio that results in the lower channel pressure. This is understandable since the term describing the flow acceleration in the motion equation is inversely proportional to the gas density:

$$\frac{du}{dt} \sim \frac{j_y B_z}{\rho} \sim \frac{\sigma(T)uB_z^2(K-1)}{\rho} \qquad (4\text{- }6)$$

where $\sigma(T)$ is proportional to the ionization fraction $\phi_e=n_e/N$. Thus, to produce the same acceleration at the higher pressure, higher ionization fraction (and therefore higher plenum temperature) is needed. Finally, substantial acceleration for P_0 = 1,000 atm was obtained only at the highest plenum temperature considered (T_0=6,000 K) and also for the large area ratio F_2/F_1=9-25. One can conclude from these results that the K-seeded MHD accelerator, which requires plenum pressures of approximately 1,000 atm (see Table 4- 2), should also operate at high-plenum temperatures of T_0~6,000 K. This limit can be somewhat lowered if a seed with lower ionization potential (e.g., Cs) is used.

The second series of runs was carried out for the full-scale Cs-seeded (at 0.5%) air accelerator for plenum conditions T_0=5,000 K and P_0=1,000 atm (mass flow rate G=17.4 kg/s). The MHD channel length was L=140 cm with the entrance cross-section area F_1=8 cm^2 and the area ratio F_2/F_1=36 (channel entrance Mach number M=2, entrance pressure P=120 atm). The loading parameter was again limited to prevent the developing of the thermal instability (see Section B.2.3.3) and the current density becoming too high:

$$K = 1.0 + \frac{j_{y\max}}{\sigma u B_z} \tag{4- 7}$$

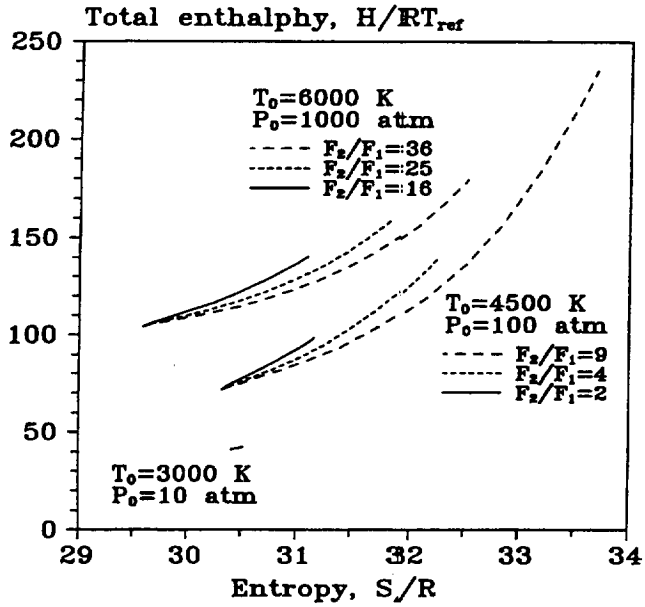

Figure 4- 13. Total enthalpy vs. entropy diagram for the MHD-augmented K-seeded (at 1%) air flows.

The calculated H(S) curves are shown in Figure 4- 14 for different values of j_{ymax}, plotted together with the target TAV trajectory data. One can see that at these conditions the total enthalpy can be increased up to 5 times if the maximum current density does not exceed

j_{ymax}=100 A/cm^2, while the flow entropy rise is considerably less than for the unseeded flows discussed in Section B.2.3.1 (see Fig. 4- 9). Although the flow entropy is still somewhat greater than the target value (see Fig. 4- 14), the seeded accelerator performance is clearly much better. NO and O fractions in the test section are much less than in the unseeded accelerator at comparable total enthalpy (Table 4- 2 and Table 4- 3). Also, the calculated flow pressure is now only 1.5 to 4 times less than the pressure behind the bowshock (see Table 4- 3).

Table 4- 3. Cs-seeded air MHD accelerator performance.

Left and central subcolumns – target values for p_{dyn}=2,000 and 1,000 lbf/ft^2 respectively, right subcolumn – present calculations.

Case	H, MH/kg			S/R			U,km/s			M		
1	7.2	7.0	6.7	27.9	28.6	28.3	3.76	3.64	3.53	9.4	9.0	9.1
2	13.6	14.6	14.1	29.0	29.9	30.8	5.16	5.31	5.14	11.4	11.3	11.5
3	18.4	19.4	19.7	29.6	30.4	31.4	6.02	6.14	6.07	12.3	12.2	12.3
4	24.8	25.7	25.2	30.2	31.0	31.9	6.99	7.07	6.88	13.1	13.0	13.1
5	33.2	33.8	33.9	30.9	31.6	32.5	8.08	8.12	7.98	13.9	13.8	13.7

Case	P, mbar			y_{cs},%	y_o,%	y_{NO},%	$T_v(N_2)$	J_{ymax},A/cm^2
1	41.1	21.4	14.5	0.5	0.01	4.5	1992	0
2	34.4	17.2	3.9	0.5	0.6	4.3	2630	30
3	32.1	16.1	5.4	0.5	1.6	4.1	2829	50
4	30.4	15.3	6.3	0.5	2.9	4.2	2944	70
5	29.1	14.7	9.6	0.5	5.1	4.9	3078	100

The latter result is in agreement with the criterion of Equation. (4- 2). First, the average channel temperature in the Cs-seeded MHD accelerator is generally higher than in the e-beam controlled channel even though it is being controlled to reduce chemical dissociation (see Figs. 4- 9 - 4- 16). Second, the average loading parameter in these runs is considerably lower ($K_{avg}\cong$1.1-1.3 vs. $K_{avg}\cong$1.6-1.8 for the unseeded runs); consequently, the greater part of the input power goes directly into the flow kinetic energy and does not contribute to the entropy rise. Figure 4- 16 shows the efficiency of the first half of the channel is less than that of the second (du/dx is lower) due to the higher gas density near the channel entrance [see Eq. (4- 6)]. The flow in the channel is very close to the thermochemical equilibrium, which is also confirmed by the equilibrium chemical composition calculations. However, freezing of molecular vibrations (despite the fast V-T relaxation of N_2 on Cs and oxygen atoms) and of chemical composition of the mixture in the test area is still well pronounced.

The boundary layer growth in the channel is quite significant. An estimate based on Schlichting (Ref. 56) gives $\delta/r\sim0.25$ at $x/L=1(Re_x=10^7)$. The calculated heat transfer losses, although quite large, did not exceed 15% of the initial flow power. However, the calculated local wall heat fluxes in the channel reach 10-20kW/cm^2 for j_{ymax}=100 A/cm^2, which may severely limit the operation time. It is noted that these heat fluxes are quite comparable to those observed

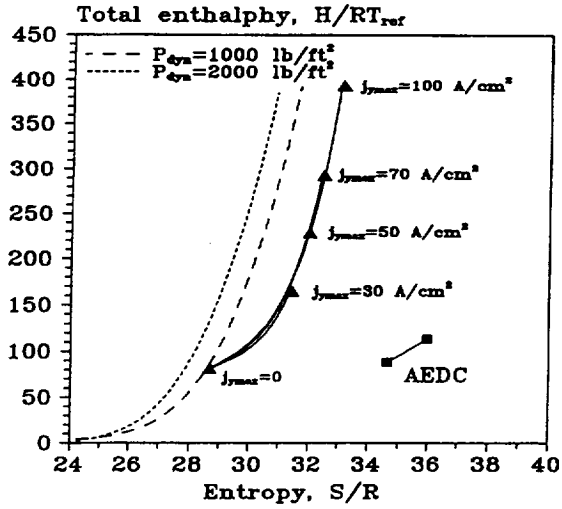

Figure 4- 14. Total enthalpy vs. entropy diagram for the full-scale Cs-seeded (at 0.5%) air MHD. P_0=1,000 atm, T_0=5,000 K, L=140 cm, F_2/F_1=1.65. Dashed lines - TAV flight envelope. Also shown H(S) for the AEDC K-seeded (at 1.5%) accelerator.

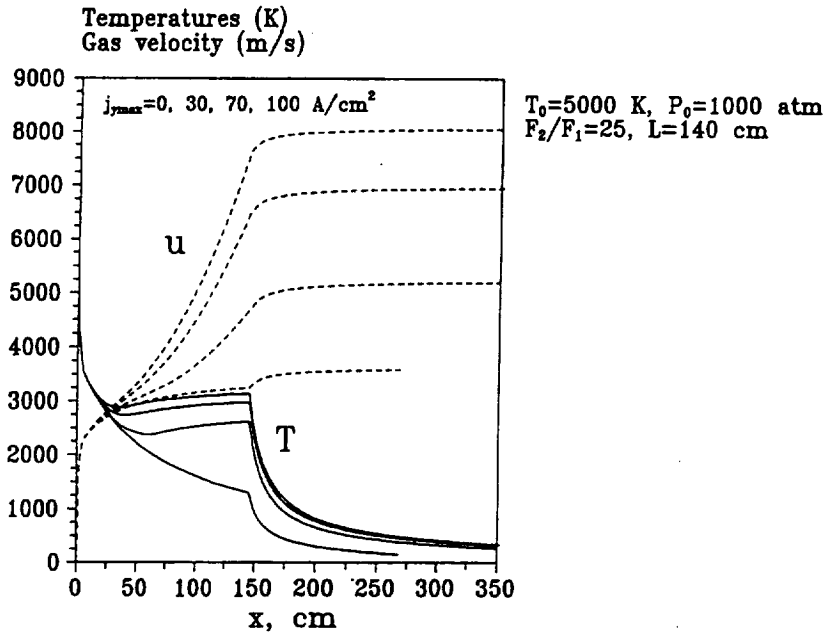

Figure 4- 15. Axial temperature and velocity profiles for the accelerator of Fig. 4- 14 for different maximum current densities.

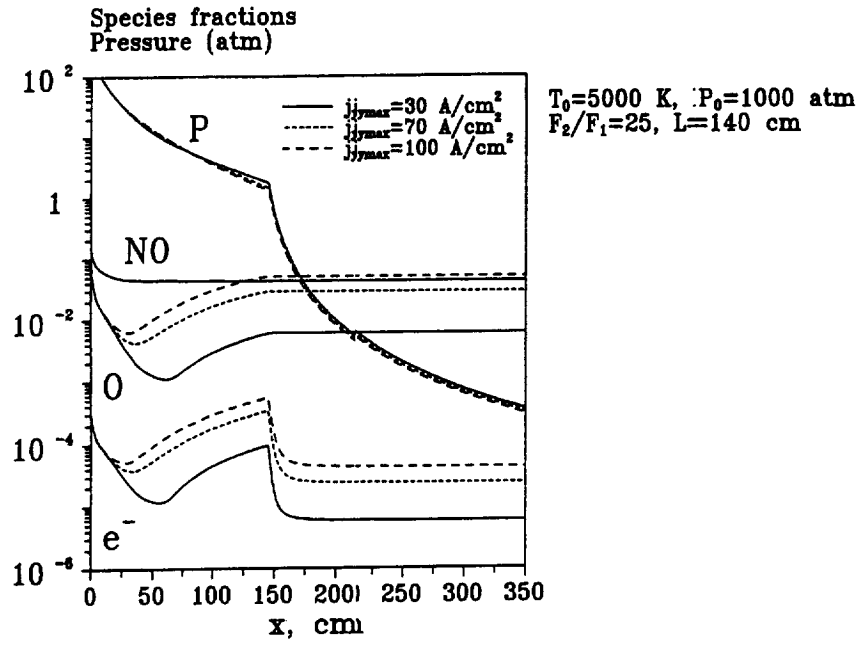

Figure 4- 16. Axial profiles of pressure and species mole fractions for the accelerator of Fig. 4- 14 for different maximum current densities.

experimentally by the Russian researchers (see Appendix E of this report). Run times reported in that facility are approximately 1 to 2 seconds, and reported electrode lifetimes are in the range of 10 – 15 seconds.

4.1.2.5 OSU One-Dimensional Analysis Conclusions

The results of the modeling calculations based on the quasi-1-D kinetic model described and validated in Section B.2.2 allow us to make the following conclusions:

1. The use of high-energy e-beams (or any other external ionization source) to sustain nonequilibrium ionization in high-pressure MHD channels is not feasible due to the fast electron loss in recombination and attachment processes. In the high-plenum pressure (P_0~1,000 atm) flows, e-beams can be efficiently applied to create nonequilibrium ionization only after the flow is expanded to low pressures $P \leq 1$ atm.
2. In the latter mode of operation, nonequilibrium ionization sustained by an e-beam allows considerable increase of the total enthalpy of the flow (1.5 - 2.5 times, M~11 in the test section) due to MHD augmentation. However, in this case, the static pressures in the test section are more than an order of magnitude lower than required by the TAV flight envelope.

3. The test section flow chemistry is poor and becomes steadily worse with the increase of the total enthalpy due to both e-beam initiated dissociation and thermal chemical reactions.

4. The high-plenum pressure (P_0~1,000 atm) alkali-seeded flows, which also require high-plenum temperatures ($T_0 \geq$ 5,000 - 6,000 K), look more promising for the wind tunnel application. Calculations for Cs-seeded flows predict up to a 5 times total enthalpy increase (test section Mach number M~14). Predicted test section static pressures are also closer to the reference values (although still 1.5 to 4 times lower). The calculated oxygen atom and NO concentrations in the test section are considerably lower than for the unseeded flows.

5. The predicted test section flow parameters can be obtained in a flow stable with respect to large-scale thermal instability.

6. Simple thermodynamic analysis shows the advantage of adding energy to the flow by means of a body force over the purely thermal energy addition.

Although the quasi-1-D model used in this study has the capability of analyzing nonequilibrium effects with respect to chemistry, electron energy distribution, and vibrational states, it nonetheless suffers from some inherent limitations. The most severe limitation is its inability to correctly simulate geometric effects. A correct multidimensional simulation will require the solution of a generalized Poisson partial differential equation to correctly predict the potential function across the duct and especially in the sheath and boundary layers. This subject is covered in Appendix Section B.3 of this report.

4.1.3 Enhancements to and Validation of Ohio State University Two-Dimensional Analysis Code

Reacting plasma flows occur in a wide variety of discharges. The characteristics of such discharges vary widely depending on operating conditions, geometry, and the characteristics of the gaseous medium. The experiments conducted by the NASA Ames researchers underscore the need for a simulation model that enables theoretical investigation of gaseous discharges in high-speed flows. A detailed simulation model allows the relative importance of various phenomena to be assessed for a given discharge configuration. It has the added quality of predicting parameters of interest that cannot be obtained experimentally. The research described below was conducted by the OSU computational plasma physics group and was primarily directed toward developing high-performance simulation tools to understand the physics of gaseous discharges occurring in high-speed reacting plasma flows. This research, including the code validation efforts, is summarized in Sections 4.1.3.1 through 4.1.3.5. A more complete, detailed description of this research can be found in Appendix Section B.3 and summarized in Section 4.1.3. This section is restricted in scope to a discussion of the code upgrades and the verification exercises that were conducted to validate the code. A discussion of the application of the code, which simulates the NASA Ames experiments, appears in Section 4.1.4.

4.1.3.1 Overview

The OSU 2-D reacting plasma flow code has been developed over a period of several years by the computational plasma physics group at OSU. This code solves the unsteady, compressible, Navier-Stokes equations coupled with an energy equation and a set of species equations describing the chemical kinetics. The unsteady equations describing flow, chemical kinetics, and electromagnetics are solved in a fully coupled manner. This enables transient, as well as steady-state solutions, to be obtained for a wide variety of flows, both subsonic and supersonic. The experiments conducted at NASA Ames involve unsteady, supersonic MHD flows with considerable air plasma chemistry. The OSU code has excellent capabilities in terms of being able to simulate both the high-speed gas dynamics and the chemical kinetics in time-dependent multidimensional flows. Prior to the MSE subcontract, the numerical algorithm and code had undergone several validation exercises, as explained in Section B.3.3.1 through B.3.3.3. The 2-D code developed at OSU was an ideal choice to model the complex interactions between electromagnetics, flow, and chemical reactions taking place in the shock tube experiments conducted at NASA Ames. Finally, the time-dependent capability of the code lends itself naturally to the simulation of the highly unsteady flows characteristic of impulse facilities. For these reasons, it was selected over other candidate codes as a starting point for the developmental efforts described below.

The OSU computational plasma physics group, under subcontract to MSE, conducted the research described in this section. Ultimately, the objectives of this research were to apply the upgraded code to simulate the NASA Ames testing scenario to use the code as an investigative tool to aid in the interpretation of the test data, and finally, to apply this validated code to realistic MHD accelerator problems. To accomplish this, several enhancements were developed and implemented in the code, as directed in the MSE/OSU Statement of Work (SOW). The primary tasks defined in the subcontract are described below.

1. Generalize and extend the OSU 2-D unsteady reacting flow code to study the chemical kinetics of air and "pseudo-air" plasmas in high-speed flows. This required the chemical rate database be upgraded to include rate data for the $N_2O + N_2$ reaction products ("simulated air") used in the NASA Ames Test Program.
2. Modify modules of the code to study the interaction of applied electric and magnetic fields with the charged species. This task required the modification of the Poisson solver developed earlier to accommodate the effects of an applied magnetic field as well as the tensorial constitutive relationship between current density and electric field (Generalized Ohm's Law). The derivation of the governing partial differential equation for the electric potential is given in Section B.3.2.
3. Modify the existing geometry to permit computations in rectangular ducts. The original code was restricted to axisymmetric geometries.
4. Upgrade the numerical algorithms. This involved the use of efficient block-tridiagonal matrix solvers for all of the high-level solution algorithms.

5. Validate the code against experimental data, especially the acquired data from the NASA Ames Test Program discussed in Section A.2.

As discussed in subsequent sections, Tasks 1 through 4 were fully accomplished. Task 5 was partially accomplished. A thorough analysis of the NASA Ames data was accomplished through the use of both the OSU 2-D code and the OSU 1-D nonequilibrium code described in Section B.2. However, in using the 2-D code, it was found that grid resolution and computer run time became significant problems largely due to the fact that very strong shocks were present in the NASA Ames experiments. The shock Mach numbers were as high as 10 - 12 in some cases, and the pressure ratios across the shock were as high as 350. Resolving the shock region adequately required the use of an extremely fine grid, which greatly increased the computing time. It should be noted that in its present form, the OSU code requires a uniform grid; consequently, if one refines the grid to accommodate a shock layer, the grid must be refined to the same level everywhere else.

Lack of knowledge of conditions upstream of the shock presented another source of difficulty in conducting the 2-D simulations. The computation appeared to be quite sensitive to the precise values of the input parameters (pressure, temperature, velocity) specified at the inlet to the skimmer tube. Incorrect specification of such parameters led to numerical difficulties or erroneous results. To resolve these issues, attempts were made to model the propagating shock in N_2 without chemical reactions. The conditions in these simulations were specified to be the same as in the NASA Ames experiments. This was performed as a test case solely for the purpose of investigating the fundamental convergence problems. In this mode, it was possible to reduce computing time and circumvent numerical problems arising due to stiffness of chemical reactions. Several simulations were conducted to study the effects of different inlet boundary conditions on numerical stability and the results of the simulations. The research is summarized in the following subsections. The reader is referred to Appendix Section B.3 for a more in-depth discussion of the results.

4.1.3.2 Model Description and Governing Equations

For present purposes, a continuum description is assumed to hold. This allows the plasma to be treated as a conducting fluid. This approximation is valid in the reacting plasma flows studied in this work since the mean-free paths are much less than any length scale of interest. The governing equations are essentially the compressible Navier-Stokes equations supplemented by species continuity equations and Maxwell's equations. A complete description of these flowing plasmas requires a coupling between the flow, chemical kinetics, and electromagnetics. The resulting set of governing equations describes the close interaction between several physical and chemical processes. In addition to the governing equations, appropriate initial and boundary conditions, transport properties, and rate coefficients are needed to complete the theoretical formulation of the problem. Solving this set of equations is a computationally intensive task that challenges the best numerical algorithms and available hardware. Variable properties, presence of jxB body forces, ohmic heating, species diffusion, and chemical reactions with ionization/ recombination processes render this system of equations extremely nonlinear and stiff, which makes them difficult to solve.

The governing equations for the OSU 2-D model consist of the following time-dependent equations.

1. Conservation of mass.
2. Conservation of the streamwise component of momentum.
3. Conservation of the transverse component of momentum.
4. Energy balance equation.
5. Equations for individual species balance.
6. A generalized Poisson equation for the electric potential (derived from Maxwell's equations). The derivation of this equation is presented in Appendix Section B.3.
7. Constitutive equations (such as the generalized Ohm's Law; the equation relating pressure, temperature, and density; and the empirical relationships that specify the kinetic rate data as a function of temperature and pressure).

The species conservation equations given in this section include effects of chemical kinetics only.[3] Since the gaseous medium in the NASA Ames experiments consist of a mixture of N_2O and N_2 (to reproduce the same composition as air for the post-shock conditions), the following species are modeled because they are the most important. The relative importance of the various neutral and ionic species was obtained by equilibrium calculations performed at the operating conditions of temperature and pressure in the NASA Ames experiments. On the basis of these calculations, the following species are included in this detailed study: N_2, O_2, N, O, NO, NO^+, N_2O, NO_2, and electrons. The set of chemical reactions associated with these species is:

$$
\begin{aligned}
N_2 + M &\Leftrightarrow N + M \\
O_2 + M &\Leftrightarrow O + O + M \\
NO + M &\Leftrightarrow N + O + M \\
N_2 + O &\Leftrightarrow NO + O \\
O_2 + N &\Leftrightarrow NO + O \\
NO_2 + M &\Leftrightarrow NO + O + M \\
N_2O + M &\Leftrightarrow N_2 + O + M \\
N + O &\Leftrightarrow NO^+ + e^-
\end{aligned}
$$

In the above reactions, M denotes any of the possible heavy particle species, hence, 48 chemical reactions are being modeled in the set of governing equations.

[3] Internal mode disequilibrium was not included in this model used to validate NASA AMES experiments.

Species continuity equations were written for seven species: atomic nitrogen, molecular nitrogen, atomic oxygen, molecular oxygen, NO, nitrogen dioxide (NO_2), and electrons. In each of the species conservation equations, the right-hand side represents the rate of change in concentration due to chemical reactions. Quasi-neutrality is assumed, and hence, the electron concentration is set equal to the concentration of NO^+. The concentration of nitrous oxide (N_2O) is then obtained from the equation relating mass density to the individual species concentrations. A detailed description of the rates used in the above equations is contained in Section B.3.4.

In implementing the code upgrades, the algorithm that computes the vibrational kinetics was developed separately from the algorithm that computes the chemical reactions for the air (or simulated air) species. This approach allowed evaluation of the computing time required for incorporating vibrational nonequilibrium in a molecular discharge. Such a development strategy also permits independent testing of the codes and thus enhances code reliability. The two separate modules can be combined to obtain a code capable of simultaneously studying vibrational nonequilibrium and chemical reactions in air plasmas. These modifications have thus laid the foundation to study chemical reactions and internal mode disequilibrium (vibrational modes) in high-speed air plasmas in some detail.

The computation for the electric potential (ϕ) proceeds on the assumption that at any stage in the computation: the electrical conductivity (σ), Hall Parameter (β), fluid velocity ($\vec{U}$), and the applied magnetic induction ($\vec{B}$) can be computed locally. Two other simplifying assumptions have been made, the first being the local charge density $e(n_i - n_e)$ is assumed to be negligible everywhere. This is the standard charge neutrality approximation commonly made in MHD problems. The approximation is likely to be invalid in the near-electrode sheath regions. For example, very close to the anode surface, electrons will be strongly drawn to the anode, whereas positive ions will be repelled. The presence of the electrode prevents the ions repelled from the sheath region to be readily replenished by diffusion processes as they are in the outer regions (i.e., there are few, if any, ions flowing from the anode into the gas). The net effect is a polarization of electric charge that is created, leading to a nonneutral charge density distribution in this thin layer. The problem is further complicated by the fact that properties of the electrode material (such as the work function) will influence the diffusion of electrons and ions across the sheath region. Thermionic emission or field-enhanced thermionic emission may also be important, implying the wall heat-transfer will be strongly coupled to electron emission. In view of the complexity of the problem and the limits on available resources, it was determined that only the core flow electric fields would be computed. These would be adequately simulated by the charge neutrality assumption.

The second simplifying assumption is that the magnetic Reynolds number is much less than one. This assumption is tantamount to assuming the currents induced in the plasma will not significantly alter the internal magnetic field. Thus, the local magnetic field is everywhere equal to the applied magnetic field. For purposes of simulating MHD accelerator problems, this approximation is generally valid.

Using the above assumptions, the governing equations for the electric potential are the Maxwell equations for electric field and the current conservation equation. The details of the derivation of

the governing partial differential equation for the electric potential are omitted here but may be found in Appendix Section B.3. The full set of governing partial differential and algebraic equations is given in Appendix Section B.3 but is not repeated here.

The above sets of governing equations describe flow, chemical kinetics, and electromagnetics. These equations are time-marched in a fully coupled manner to obtain spatial and temporal variations of parameters of interests such as mass density, velocities, temperature, species concentrations, and electric potential.

4.1.3.3 Method of Solution

The governing equations given in the previous section describe the interaction between several complex physical and chemical processes. This makes the system of equations very stiff; therefore, it is necessary to time-march the system of equations using implicit methods. However, implementation of implicit methods requires an intensive programming effort in contrast with explicit methods. Implicit methods aimed at solving a coupled system of equations are known as block-implicit methods developed originally by Lindemuth and Killeen, McDonald and Briley, Beam and Warming, and Briley and McDonald originally for solving the unsteady, compressible Euler and Navier-Stokes equations (Ref. 59). In the present study, the Linearized Block Implicit (LBI) method of Briley and McDonald is used to time-march the unsteady set of governing equations in an implicit, fully coupled manner (Ref. 60). Implicit methods allow stable time marching of the system of equations with larger time steps (as compared to explicit method), which makes it possible to obtain solutions within reasonable amounts of time. The LBI method essentially consists of an implicit scheme in which the solution is linearized by a Taylor expansion about the value at the previous time level. This produces a set of coupled, linear, difference equations that are valid for a given time step. The implementation of this method to reacting and plasma flows is explained in greater detail in Reference 61 and will be briefly described here.

The system of governing equations is transformed from the physical domain to the computational domain. The transformed equations are then linearized and discretized. In each coordinate direction, the time derivatives are discretized using the Crank-Nicholson method, whereas spatial derivatives are discretized using central differencing. The Douglas-Gunn Alternating Direction Implicit (ADI) method is used to split the 2-D operator self-consistently into two 1-D operators. This procedure gives rise to block tridiagonal matrices in each coordinate direction. Such matrices can be solved quite efficiently using LU decomposition methods (Ref. 62). A uniform, nonstaggered grid is used, and the dependent variables are treated implicitly in all the governing equations. Transport properties and rate equations (which depend on temperature and species concentrations) are treated explicitly. Explicit treatment of these quantities enables different models of transport properties to be used without extensive code modifications.

The governing equations are written in conservation-law form, and hence, shocks and discontinuities are obtained as part of the solution, thereby requiring no special treatment. The

shock is smeared over a few grid points; however, the simplicity of the approach greatly outweighs the slight compromise in results obtained using shock-capturing methods.

Based on the analysis and experimental results of Section 4.1.3 and Appendix Sections D.2 and D.3, it can be concluded that beamed energy addition may be used to provide substantial enhancement of ionization in an MHD accelerator channel. The main limitation on the use of lasers, microwaves, or e-beams for this purpose is that these technologies are all limited to subatmospheric pressures due to rapid electron-ion recombination rates at high pressures.

4.1.3.4 Verification and Validation

The complexity of the governing equations describing plasma flows makes it imperative to test the model and the code at every stage to ensure accurate results. The algorithm used to study reacting plasma flows is amenable to extension from quasi-1-D to 2-D and 3-D situations. Our efforts to develop a modular high-performance reacting flow code have progressed in stages of increasing complexity. The OSU 2-D code was used to simulate quasi-1-D cold flows. The results of these simulations were compared with analytical solutions for isentropic flow. These 1-D simulations are discussed in Section 4.1.3.4.1. This was followed by 2-D axisymmetric cold flow calculations. Next, the electromagnetics were included to simulate the presence of an arc in the 2-D axisymmetric formulation. These simulations were then applied to a variety of cases. Internal flow simulations in arcjet thrusters with hydrogen (H_2) as the propellant were studied for two different geometries corresponding to two different power levels; 30 kW (Ref. 63) and 1 kW (Ref. 64). These simulations included simple reactions in H_2 but disregarded internal mode disequilibrium. No analytical solutions exist for these flows. To verify the accuracy of the results of our simulations, detailed comparisons have been made with available experiments for the 1-kW arcjet geometry (Ref. 64). This model has also been used to study internal and external flows in welding plasmas to explore completely different plasma densities. Additional 2-D imulations on electric arc welders are also discussed in Section 4.3.4.2. The results of these simulations have also been compared with available experimental data. In the interests of brevity, only the isentropic quasi-1-D analyses are discussed below in any detail. The 2-D validation exercises are briefly summarized in Section 4.1.3.4.2. The reader is referred to Appendix Section B.3 for a detailed discussion of the 2-D results.

4.1.3.4.1 *Results for Quasi-1-D Isentropic Flow*

In this section, results for three case studies involving quasi-1-D flows are presented and compared with analytical solutions. The geometries used in these simulations have an exit-to-throat area ratio of 10, 100 and 225 (1-kW arcjet geometry). These three case studies bring to fore the ability of the numerical scheme to handle widely varying geometries and serve to identify the limits of the model's applicability. The area-ratio 10 and 100 configurations were each studied with two different grid sizes (150 and 1,500 grid points) for two different values of γ (ratio of specific heats): 1.4 (diatomic gases) and 1.67 (for monatomic gases). Flow in the 1-kW arcjet geometry (see Fig. 4- 20) was studied for two different grid sizes (150 and 1,500) for γ=1.4. The variation of Mach number in the streamwise direction obtained from these simulations was compared with analytical solutions for isentropic, quasi-1-D flows.

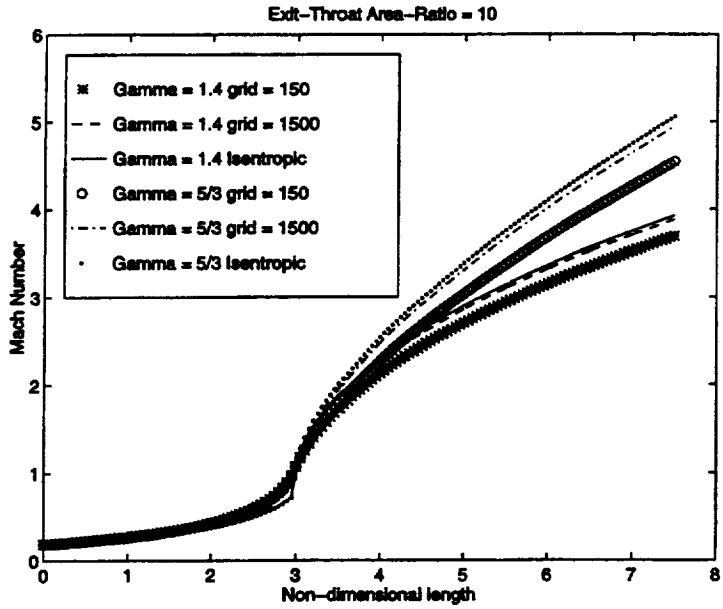

Figure 4- 17. Comparison of analytical and computed results (Area-Ratio = 10).

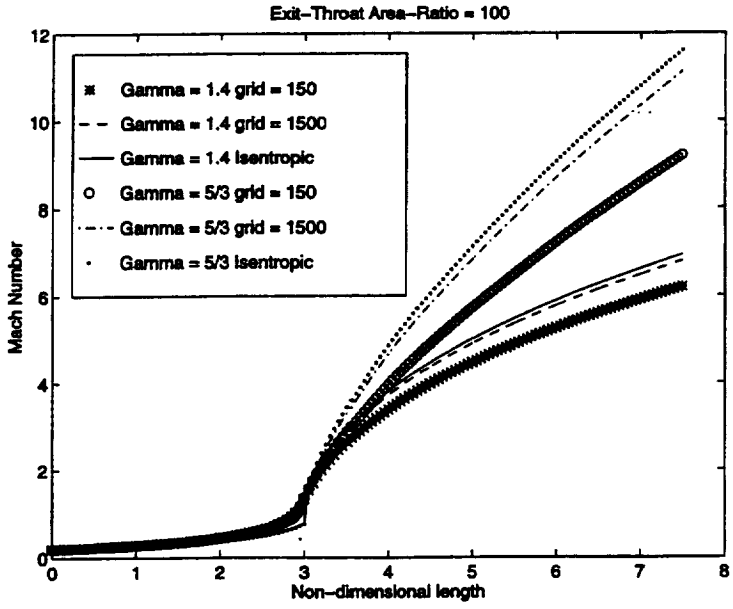

Figure 4- 18. Comparison of analytical and computed results (Area-Ratio = 100).

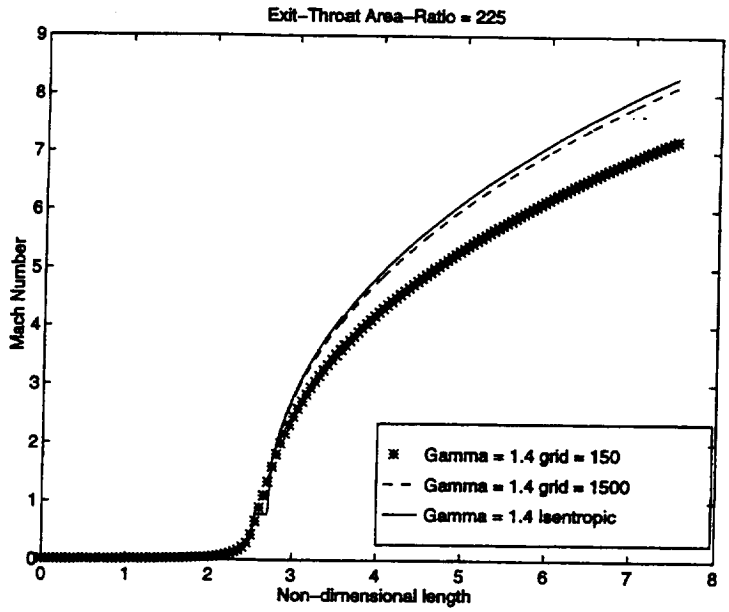

Figure 4- 19. Comparison of analytical and computed results (Area - Ratio = 225).

Figures 4- 17 through 4- 19 show comparisons between quasi-1-D code predictions and analytical relationships for the Mach number in an isentropic flow for exit-to-throat area ratios of 10, 100 and 225, respectively. The figures show the effects of different grid-sizes and γ. As can be seen, the calculated values match analytical solutions closely. The difference between the predicted values and theoretical values is largest in the supersonic region near the exit plane (approximately 10% in the case of the coarse grid), yet, with finer grid spacing, this discrepancy is reduced. Also, as area-ratios increase, the discrepancy increases. For a given area ratio, the error is greater for γ=1.67 than for γ=1.4 because larger gradients occur in the flow in the diverging section for monatomic gases compared to diatomic gases.

As Figures 4- 17 - 4- 19 show, the agreement between analytical results and the computations is quite good. The maximum discrepancy is about 10% for the case of coarse grids. This discrepancy is due to the effect of artificial dissipation (Ref. 65) and truncation errors. The artificial dissipation term used here is in the form $\varepsilon_x \partial^2\psi/\partial x^2$ where ε_x is given by $0.5\rho w dx$ with dx being the mesh spacing and ψ is any dependent variable. As expected (in all the case studies), the effect of numerical dissipation is larger for the coarser grids. It must be mentioned that the analytical results for isentropic flow do not take into consideration the effects of friction. However, the LBI scheme requires the addition of artificial dissipation for stability of the time-marching procedure. Addition of artificial dissipation introduces effects similar to viscous effects. It is well known that friction decelerates supersonic flows. Temperatures obtained from quasi-1-D computations are higher when compared to the analytical solutions. Axial velocities in the quasi-1-D simulations are lower than those values given by the analytical solution; therefore, the Mach numbers computed from the quasi-1-D simulations are lower than those

predicted by analytical solutions. The influence of artificial dissipation is highest in regions close to the exit plane where the discrepancy is largest. Reducing ε_x by a factor of 10 in the supersonic regions of the flow alone reduced the discrepancy to less than 1% for the nozzle geometry with an exit-to-throat-area ratio of 10.

The present code has the capability to provide results for quasi-1-D flow problems that converge to the twelfth decimal place within a few seconds or a few minutes of central processing unit (CPU) time on a Silicon Graphics Indigo Workstation. The CPU time depends on the initial guess and number of grid points. It is this highly efficient feature of the LBI algorithm that makes it attractive for computations involving multidimensions and large coupled sets of governing equations.

4.1.3.4.2 *Multidimensional Verification and Validation Exercises*

To validate the 2-D capabilities of the OSU code, two series of computations were run: one for an H_2 arcjet thruster and a second for an electric arc welder. In both cases, the geometry was axisymmetric, and their experimental data was available for comparison against the computational results. For the arcjet thruster, experimental data on H_2 atom concentration and streamwise velocities in the exit plan was available, and for the electric arc welder the available measurements were for radial pressure profile, total current, and total power input. Comparisons were conducted against both the computed and measured parameter sets.

Hydrogen Arcjet Thruster Simulations

Arcjet thrusters have primarily been targeted as low-power, high-specific-impulse (I_{sp}~1,000 s) space propulsion devices. These thrusters are currently used for North-South Station Keeping (NSSK) of communication satellites in geosynchronous orbits. Arcjet thrusters impart directed kinetic energy to a propellant stream by ohmically heating it and subsequently expanding to supersonic speeds. In addition to aerospace applications, the thrusters also have terrestrial applications in the area of materials processing. Arcjets are used commercially in the growth of freestanding diamond films and coatings.

Essentially, the device is comprised of an inlet plenum, a converging section, and a straight portion called the constrictor followed by a diverging section or supersonic nozzle. The propellant enters the inlet plenum relatively cold and unionized at subsonic speeds. The flow entering the plenum is randomly injected with swirl (which some believe stabilizes the arc). This cold, unionized gas is rapidly heated by an arc discharged between the cathode and the anode as a result of an electric field applied between the two electrodes. The heated gas reaches near-sonic speeds by the end of the constrictor and rapidly expands in the diverging section to supersonic speeds. The propellant in this study was molecular hydrogen (H_2).

The governing equations describing arcjet flow are similar to the conservation equations described in the section on model description. They are adapted to the case of H_2 arcjets and solved to obtain the velocity, temperature, and species concentrations. In this study, the following reactive processes are considered:

$$H_2 + H_2 \Leftrightarrow H + H + H_2$$
$$e^- + H \Leftrightarrow H^+ + e^- + e^-$$
$$H_2 + e^- \Leftrightarrow H + H + e^-$$
$$H + H_2 \Leftrightarrow H + H + H$$

The plasma in the H_2 arcjet is assumed to be composed of molecular hydrogen (H_2), atomic hydrogen (H), electrons (e^-), and singly ionized hydrogen atoms (H^+), H_2 is the only diatomic species. No vibrational states of H_2 are considered here, and a single temperature is used to describe the heavy particles and the electrons. Quasi-neutrality is assumed, which allows us to set the number density of e^- equal to that of H^+. Therefore, in this case study, the species conservation equations are written for H and electrons. The concentration of H_2 is then evaluated using the algebraic relationship between mass density and the species concentrations.

Flow through two different arcjet thrusters have been modeled, specifically a 30-kW arcjet thruster (Ref. 63) and a 1-kW (Ref. 64) arcjet thruster, with H_2 as the propellant. Unfortunately, no detailed experimental results for the 30-kW arcjet geometry exist. However, experimental measurements have been performed on 1-kW arcjet thrusters (see Fig. 4- 20) with H_2 as the propellant by groups at the U.S. Air Force's Phillips Laboratory (Edwards Air Force Base) (Ref. 66) and at Stanford University (Refs. 67, 68). The operating conditions for these experiments were a power level ~1.4 kW, current=10 A, and a mass flow rate of ~13 mg/s. Simulations for these experimental conditions (geometry, propellant, and operating conditions) were performed in order to compare directly with experimental measurements. In this subsection, results from numerical simulations are compared with experimental data.

In Appendix Section B.3 comparisons are made between the results of 2-D simulations with experimental measurements from References 66, 67, and 68, along the exit plane of the 1-kW H_2 arcjet thruster. A comparison of the predicted H_2 atom concentration at the exit plane against experimental data indicates quite good agreement across the exit plane. A comparison of the experimental vs. the computed stream-wise velocities along the exit plane also shows good agreement. The simulation under predicts the experimentally observed values along the centerline by about 10%. It must be mentioned that other single temperature models published in the literature also under predict velocities at the exit plane in a similar manner (Refs. 69, 70).

The arcjet computations are discussed in much greater detail in Appendix Section B.3. These computations are valuable because they provide a reasonably severe test of the ability of the OSU simulation code to correctly model a high-speed flow, which is characterized by a high degree of thermal and chemical nonequilibrium.

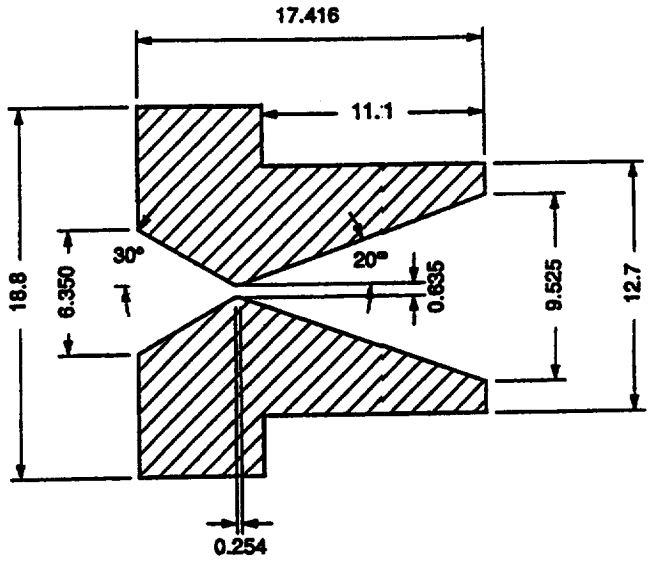

Figure 4- 20. Schematic of the 1-kW arcjet geometry (all dimensions in mm).

Electric Arc Welder Simulations

Electric arc-welding processes consist of an electrode and a workpiece of opposite polarities. An arc is struck by applying an electric field between two electrodes causing current flow through the partially ionized gas column (established between the electrodes). The heat generated in the arc produces the high temperatures needed to sustain the gas in its ionized state. The thermal energy is transferred to the workpiece primarily due to particle fluxes (Ref. 71) causing it to melt. Further details concerning the arc welding process are given in Appendix Section B.3.

A plasma-welding arc using Ar as both the plasma and shield gas was studied. A single reaction modeling electron impact ionization of Ar and its reverse (three-body recombination) was modeled. The Ar plasma was assumed to consist of Ar atoms, singly ionized Ar atoms (Ar^+) and electrons (e^-). A single equation describing the conservation of electrons is solved with the governing equations describing the flow and electromagnetics. Concentration of Ar^+ is equal to the electron concentration since quasi-neutrality is assumed. Concentration of Ar atoms is obtained from the overall mass density and electron concentration.

The plasma welding process was modeled in two separate stages, namely plasma flow within the torch body (internal flow) and the plasma jet impinging on the work piece (external flow). The governing equations describing these two situations are the same; however, the boundary conditions for the internal and external flows are different. A simple and inexpensive diagnostic technique is used in the present work for model validation. A radial pressure profile was measured on a water-cooled copper plate, while the plasma jet impinged on it.[4] This measured

[4] These experiments were conducted in the Department of Industrial, Systems, and Welding Engineering, at OSU (see Ref. 72 for details).

radial pressure distribution was compared with calculated pressure profiles. Model predictions were compared with experimental results at three different current levels. As in the case study on arcjets, the total stagnation pressure, total current, and power level were made to match experimental conditions to enable direct comparisons. Details of the geometry, boundary, and initial conditions are given in Reference 61.

The results of simulations are compared with the experiment for conditions listed in Table 4- 4.

Table 4- 4. Operating conditions for plasma welding torch.

Polarity	Straight
Plasma Gas	Argon
Shield Gas	Argon
Plasma Gas Flow Rate (CFH)	13
Shield Gas Flow Rate (CFH)	35
Current (Amps)	100 and 150
Stand-off Distance (in.)	3/8
Power (kW)	2.2

Spatial variations of temperature, velocity, and ionization fraction (in both the internal and external flows) are discussed in detail in Reference 61. In Appendix Section B.3 a comparison is made between the predicted radial distribution of static pressure along the surface of the cooled workpiece and experimental data for a total current of 100 and 150 A, respectively (Ref. 72). The experimental data in both these figures shows the plasma jet tends to remain collimated. The arc pressure (gauge) drops sharply to values close to zero within a distance of about three times the nozzle radius from the centerline. The simulations predict a broader pressure profile as compared to the experiment because of the combined effects of the simple heat-transfer model used to simulate the cooling of the copper plate and effects of numerical dissipation. Nevertheless, the results of the simulations agree with the experiment.

4.1.3.5 Ohio State University Two-Dimensional Analysis Conclusion

OSU's model and numerical technique have been rigorously tested to simulate a wide variety of discharges. The quasi-1-D ducts, the arcjet thruster, and the plasma torch differ widely in geometries, operating pressures, and gas compositions. Nevertheless, the model and the numerical scheme have been able to successfully simulate these different cases with reasonable accuracy. It is of importance to point out there are no adjustable constants in OSU's formulation; consequently, it is a truly predictive tool. Comparison with experiments for both cases studied show excellent agreement. The generality, stability, and accuracy of the numerical method/model make it a valuable tool to study reacting and plasma flows.

4.1.4 Analysis of the NASA Ames Experiments

This section summarizes the results of an analysis performed by the OSU, which addresses the interpretation of the experiments done at NASA Ames. These experiments are described in detail in Appendix Section A.2 and are summarized in Section 4.2.1. A more detailed discussion of this analysis is given in Appendix Section B.3.4.

The interpretation of the shock tube ionization data measurements at NASA Ames requires analysis of coupled vibrational relaxation, molecular dissociation, and ionization behind the shock. First consider nonequilibrium ionization behind shock waves in air. The kinetic mechanism of this process is well established. In particular, the principal mechanism of ionization for shock velocities of u_s<7 km/s is associative ionization in collisions of N and O atoms (Ref. 73):

$$N + O \rightarrow NO^{+} + e \tag{1}$$

The ionization process cannot begin until a sequence of dissociating reactions produces monatomic nitrogen and oxygen. The full reaction set is given in Appendix Section A.2. Here we note that the reaction of vibrationally excited O_2 with a heavy particle constitutes the bottleneck for the overall reaction set:

$$O_2(v) + M \rightarrow O + O + M \tag{2}$$

The symbol (v) behind a species indicates vibrational excitation of this particular species enhances the reaction rate. Since vibrational processes are important, it is essential to model the chemical kinetics coupled with the vibrational-translational (V-T) relaxation of N_2, O_2, and NO:

$$\mathrm{AB(v) + M \rightarrow AB(v + \Delta v) + M} \tag{3}$$

In Equation 3, AB stands for diatomic molecule, v is the vibrational quantum number, and Δv is its change in a collision (note that Δv is not necessarily equal to 1). In addition, vibration-vibration (V-V) energy exchange between the two most abundant air species is also of great importance:

$$\mathrm{N_2(v) + O_2(w) \rightarrow N_2(v + \Delta v) + O_2(w - \Delta w)} \tag{4}$$

As soon as atomic oxygen appears in the flow, NO and N atom production can begin in the chain reactions. The net rate of this chain process is strongly dependent on the vibrational temperature of N_2, which makes vibrational relaxation of N_2 another bottleneck. Note that other associative ionization processes such as:

$$N + N \rightarrow N_2^+ + e \text{ and } O + O \rightarrow O_2^+ + e \tag{5}$$

as well as charge transfer processes such as:

$$NO^+ + N_2 \rightarrow NO + N_2^+ \text{ and } NO^+ + O_2 \rightarrow NO + O_2^+ \tag{6}$$

are not important at shock velocities less than about 7 km/s because of the much greater ionization potentials of N_2 and O_2.

4.1.4.1 One-Dimensional Simulations

The kinetic processes discussed above have been extensively studied in the past. Both the experimental rates of dissociative reactions and theoretical models of coupled vibrational relaxation, dissociation, and ionization are available in the literature (Ref. 74). For the present study, a 1-D normal shock/nonequilibrium flow code is described in some detail in Section B.2. Briefly, the code solves master equations for the populations of each vibrational level of N_2, O_2, and NO, which is fully coupled with the set of chemical kinetics equations for a number of neutral and charged species, including N, N_2, O, O_2, NO, N_2O, NO_2, NO^+, and e^-, Boltzmann equation for the electron energy distribution function, and 1-D gas dynamics equations (see Refs. 17 and 75 and Appendix Section B.3.4 for details).

Calculations using this code show that ionization behind the shock proceeds in accordance with the well-known qualitative scenario discussed above. Figures 4- 21 and 4- 22 show translational and vibrational temperatures as well as species mole fractions behind the 4-km/s shock in air as functions of P_1t (i.e., the product of the static pressure ahead of the shock and the laboratory time). Figure 4- 23 compares the calculated ionization rise time τ (time to reach the equilibrium electron concentration behind the shock) with the available experimental data (Refs. 76, 77, 78, 79) showing satisfactory agreement. One can see that $P_1\tau$ does not exceed 1 Torr·μs for the shock velocities u_s>4 km/s. In other words, for the conditions of the NASA Ames experiments (u_s=4.5-5.0 km/s, P_1=5-35 Torr, P_2=2-13 atm), the ionization rise time should not exceed 0.1 μs. However, the measurements report ionization rise times of tens of microseconds (μs) (see Fig. 4-24).

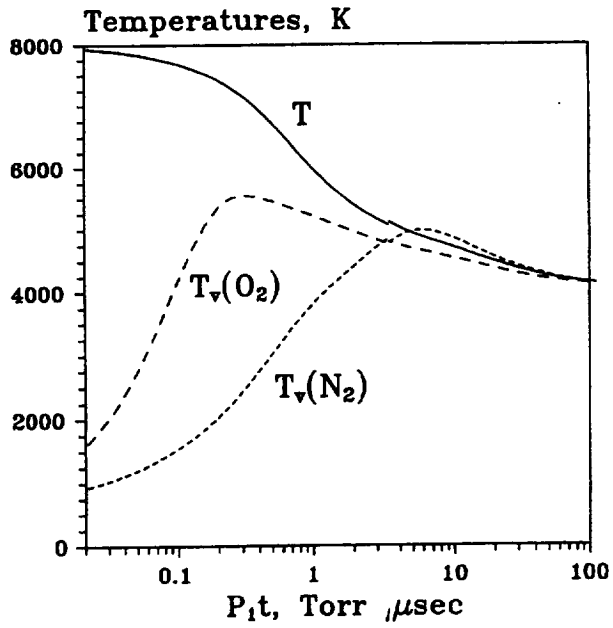

Figure 4- 21. Translational and vibrational temperature distributions behind the normal shock wave in air. Shock velocity u_s=4 km/s.

The fact that the NASA Ames ionization measurements have been made not in air but in N_2O-N_2=53.2:46.8 mixture to increase the available test time may considerably change the ionization kinetics. Can the presence of N_2O result in the increase of the ionization time up to tens of microseconds? We cannot directly model the process of N_2O vibrational relaxation and dissociation behind such strong shocks. The translational temperature overshoot immediately behind a 4.5-km/s shock wave in such a mixture exceeds T=10,000 K (the equilibrium temperature is T_{eq}=5,500 - 6,000 K), while the vibrational relaxation data for N_2O (to the best of our knowledge) is available only up to T=2,000 - 2,500 K.

Based on the low temperature data and the results of Reference 80, one can say that the vibrational relaxation time for N_2O is orders of magnitude less than that for either N_2 or O_2. For this reason, it can be assumed that N_2O behind the shock reaches equilibrium with the translational temperature instantaneously, as compared to N_2 and O_2 (let us call this assumption "case A").

On the other hand, the energy spacing between the N_2O level 00^01 and first vibrational level of N_2 is fairly small (107 cm^{-1}), which facilitates rather fast vibration/vibration energy exchange between these two modes. The rate of this process is induced by the dipole-quadruple interaction at T=2,000 K is $k_{vv}\sim10^{-11}$ cm^3/s (Ref. 80). Therefore, one can also make a somewhat opposed limiting assumption that the ν_3 mode temperature is equal to the vibrational temperature of N_2, while the other two modes are still in equilibrium with the translational temperature ("case B").

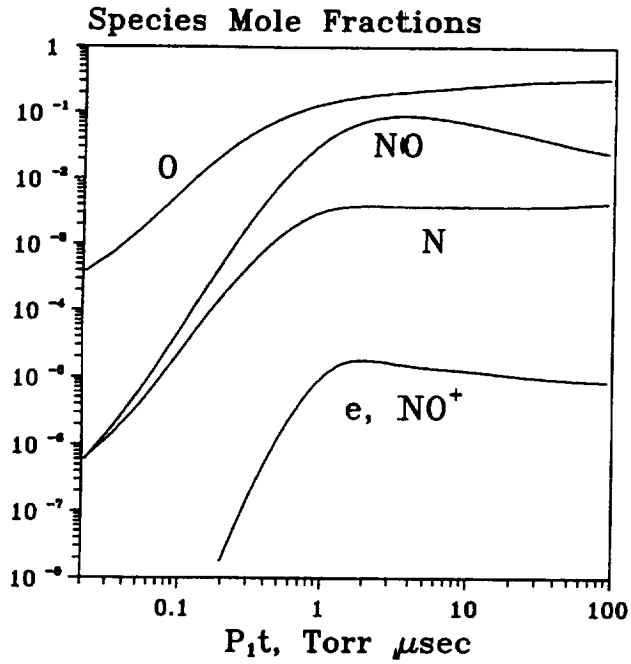

Figure 4- 22. Species mole fraction distributions behind the normal shock wave in air. Shock velocity u_s=4 km/s.

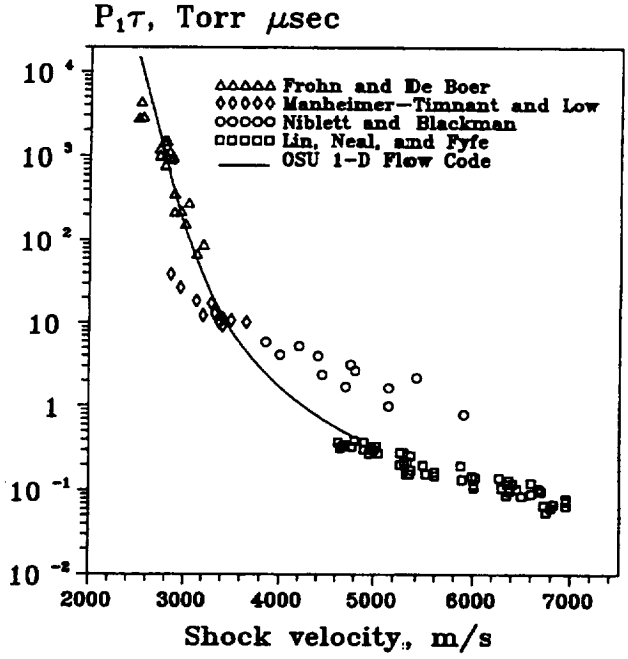

Figure 4- 23. Ionization rise time behind the shock wave in air.

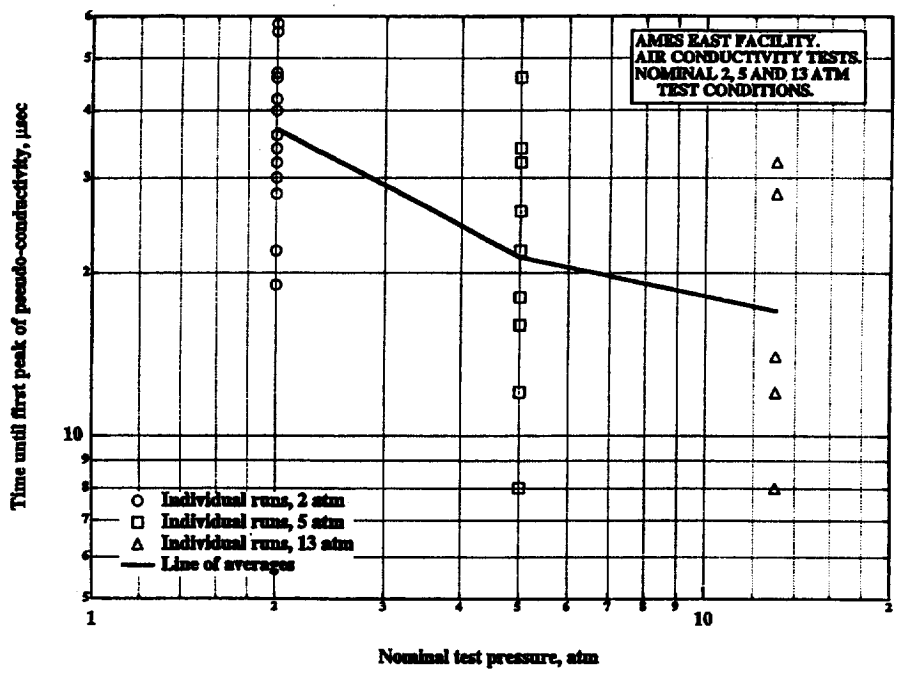

Figure 4- 24. Ionization rise time at the NASA Ames shock tube experiments.

In this case, the simplest phenomenological approach, widely used for modeling of nonequilibrium dissociation of diatomic molecules (Ref. 74), is to evaluate the N_2O dissociation rate using the "effective" temperature $T^* = [T \times T_v(N_2)]^{1/2}$. Note the dissociation energy of N_2O in Reaction (7)

$$N_2O + M \rightarrow N_2 + O + M \tag{7}$$

is much lower than that of N_2 (32,000 K as opposed to 113,000 K), and N_2O is expected to dissociate behind the shock much faster than N_2.

It is not clear which of the two processes (i.e., assumption A or B) would dominate at the high temperatures of T = 6,000 – 10,000 K: V-T self-relaxation of N_2O or V-V exchange $N_2O(v_3)$-N_2. However, the two opposite assumptions (cases A and B) permit estimates of the lower and upper limits for the ionization rise time in the N_2O-N_2 mixtures, respectively.

As is discussed in Appendix Section B.3.4, in both of these cases, the presence of the rapidly relaxing and dissociating N_2O results in a faster production of atomic species, which substantially accelerates ionization. For the shock velocities u_s=2-4 km/s, the calculated ionization rise times in the N_2O-N_2 mixture are always much shorter than in air. Therefore, we must conclude that the long ionization rise times observed in the NASA Ames experiments cannot be due to the relaxation processes in the flow behind the shock. The observed ionization

time, up to few tens of microseconds, must be pertinent to a particular method of conductivity measurements that involve strong perturbation of the flow by the applied electric field and the induced current.

Another observation made in the calculations was that, at these conditions, the flow reaches almost complete thermodynamic equilibrium at the temperature T_{eq} soon after the shock arrival (less than 1 μs), which is expected at these high temperatures and pressures.

In addition to calculation of vibrational distribution functions of the diatomic air species and species concentrations, the OSU 1-D nonequilibrium flow code also allows calculation of the electron swarm parameters of the high-enthalpy gas flows, including its electric conductivity. The conductivity is evaluated using EEDF, calculated by the Boltzmann solver, and the experimental values of the electron transport cross-sections for N_2, O_2, NO, N, and O as functions of electron energy. The comparison of the equilibrium electric conductivity of air calculated by the code with available experimental data and other theoretical calculations shows good agreement. In addition to showing it reaches the equilibrium value behind the shock extremely fast, the results of the 1-D conductivity calculations for the NASA Ames experiment conditions also show that the ionization level is unlikely to be enhanced by the applied fairly low electric field. Indeed, the estimated reduced electric field in the core flow (outside the sheath and the boundary layer) did not exceed $E/N \sim 0.5 \times 10^{-16}$ V cm^2, which is more than an order of magnitude lower than the breakdown threshold. Even for the applied voltage of V=400 V, the electron temperature exceeds the gas temperature (T~5,500-6,000 K) by only about 500 K. The resultant field-induced (electron impact) ionization rate in the core flow is minute compared to the thermal ionization rate in process (by 15 orders of magnitude) (Ref. 73). However, due to the large current drawn (current density up to j=100 A/cm^2), the ohmic heating of the flow may be substantial (also reaching a few hundred degrees K), which may result in a noticeable conductivity increase. Figures 4- 25 and 4-26 compare the calculated flow conductivity with the experimentally measured "pseudo-conductivity," defined as:

$$\sigma = \frac{jd}{U} \tag{4- 8}$$

where j is the current density, U is the applied voltage, and d = 3.1 cm is the interelectrode distance. First, at P_2 = 2 atm and U = 400 V, which is close to the maximum quasi-steady-state voltage applied in the experiment, the ohmic heating results in about 15 - 25% conductivity increase. As expected, at P_2=13 atm the effect is much smaller since the ohmic heating term is proportional to the factor $\sigma E^2/\rho u$, where ρ is the gas flow density. Second, one can observe that at the small-applied voltage, the measured pseudo-conductivity is much smaller than the theoretical value, approaching and sometimes exceeding it as the voltage increases.

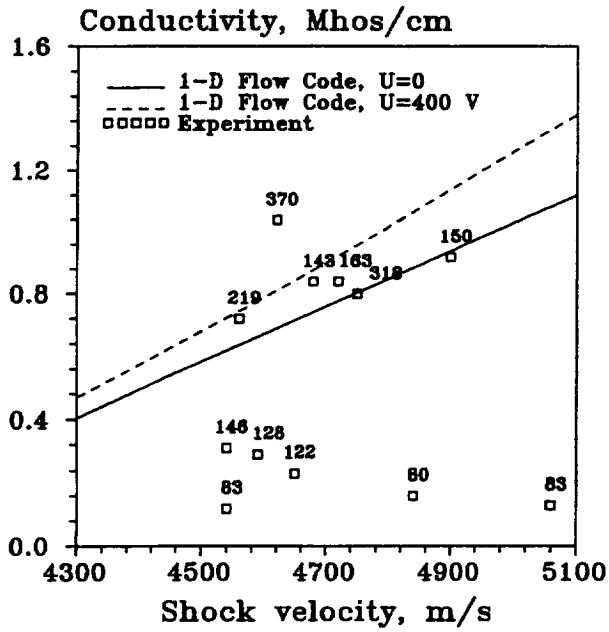

Figure 4- 25. Calculated and experimental flow conductivity in an N_2O-N_2=53:47 mixture. P_2=2 atm.

One can easily show the NASA Ames data demonstrates the presence of the field-induced ionization in the test section between the electrodes. Let us take as an example a run at $P_2 = 2$ atm, $u_s = 4.5$ km/s, $T_{eq} = 5{,}575$ K, and $n_e/N = 0.88 \cdot 10^{-4}$ (see Fig. 4- 27). The flux of electrons entering the test section with the flow is $Q = n_e d^2(u_s - u_2) \cong 8.7 \cdot 10^{20}$ 1/s, where $u_2 \cong 0.6$ km/s is the velocity of the compressed gas with respect to the shock velocity. If all of the electrons are removed from the flow by the applied field, the current would reach maximum. The maximum current that can be obtained without additional ionization produced in the test section is I_s=eQ=140 A. Most strikingly, this value of the current, which corresponds to the saturation current of the non-self-sustained Thomson discharge (Ref. 81), can be obtained only at enormously high-applied voltage (Ref. 82).

In Equation (4- 9), $\mu_+ \sim 10^{-3}$ $m^2/V/s$ is the ion mobility. The currents measured by NASA Ames at P_2=2 atm exceeded 1,000 A at voltages of 300 - 400 V (see Fig. 4- 28) unambiguously demonstrates that some additional ionization definitely occurs in the interelectrode region. Since we have already shown the core flow reduced electric field is far too low to produce any electron impact ionization, the boundary layer/sheath region is left as the only place where this ionization may occur. Thus, the electric discharge in the test section is clearly an intermediate case between a completely non-self-sustained Thomson-type discharge and a completely self-sustained discharge (such as a regular flow discharge). It is sustained both by the external ionization source (electrons arriving with the flow) in the core flow and by the electron production in the near-electrode regions, where the breakdown certainly must occur.

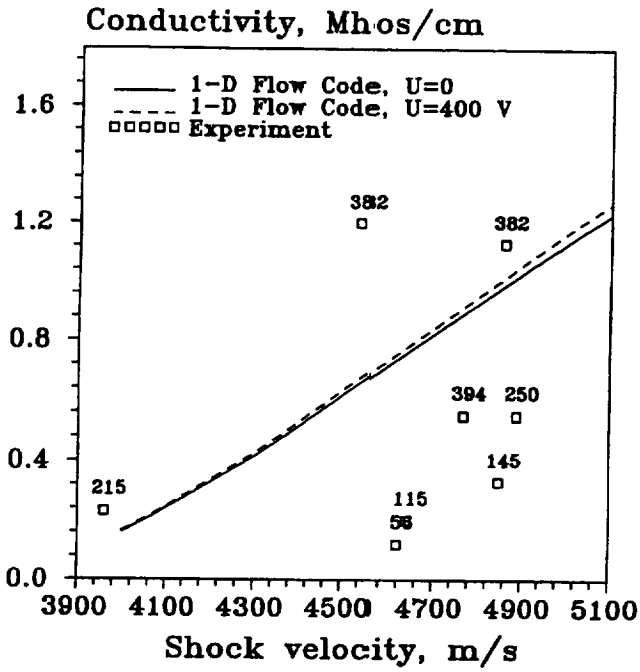

Figure 4-26. Calculated and experimental flow conductivity in an N_2O-N_2=53:47 mixture. P_2=13 atm.

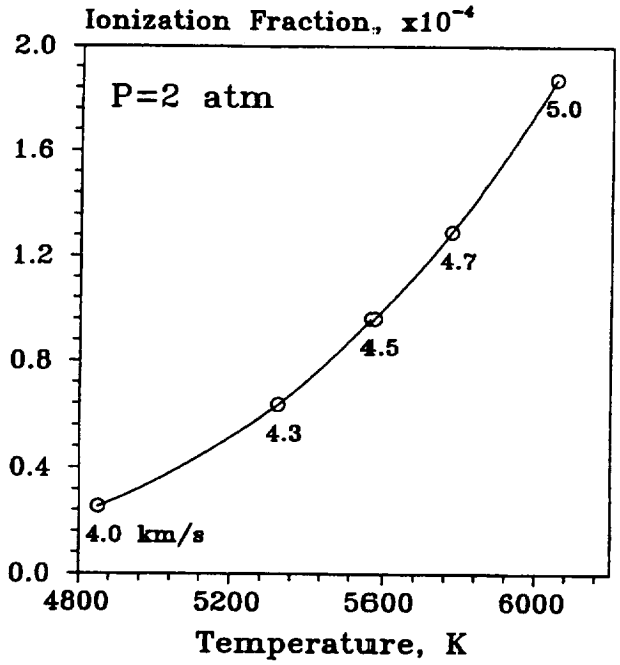

Figure 4- 27. Equilibrium ionization fraction as a function of temperature and the shock velocity in an N_2O-N_2=53:47 mixture. P_2=2 atm.

$$U_s = \frac{1}{2}\left(\frac{eQd}{\mu_+ \varepsilon_0}\right)^{1/2} \cong 10^7\ V \qquad (4\text{-}9)$$

Based on these elementary arguments, we can conclude that the core flow [like any discharge sustained by external ionization (e.g., by ultraviolet (UV) radiation or by e-beam)], should be fairly stable with respect to the ionization instabilities since there is no direct feedback between the electric field and the ionization rate for the core flow. The ohmic heating of the core flow, potentially leading to the greater thermal ionization, might be controlled by the supersonic flow expansion. On the contrary, the sheath region (where ionization is sustained by the strong electric field) may be unstable. In addition, ohmic heating of the slow flowing boundary layer is much more difficult to control. The core flow, where the electric field is far too weak to sustain the electron production, serves as a stabilizing factor so that an arc filament, even if developed in the sheath, cannot propagate across the channel. This, as well as a quite short flow residence time in the test section (<10 μs), may explain why breakdown was not observed in the NASA Ames experiments. The situation may be quite different if the electrodes are sectioned and not only transverse but also if axial electric fields are applied (to reduce the Hall current). This will generate strong axial field regions (between the edges of the closely spaced adjacent electrodes) located in potentially unstable high electric field sheath regions. For this reason, the "axial" arcing between sectioned electrodes located on the same wall appears to be much more probable than the "transverse" arcing, which was not observed by NASA Ames.

The qualitative interpretation of the NASA Ames pseudo-conductivity measurements appears to be quite straightforward and is mostly consistent with the conclusions suggested by the NASA Ames group. At low applied voltage, most of the voltage drop must occur in the sheath to sustain higher electric field and ionization. In this regime, space charge in the sheath is shielding the core flow so the electric field might be actually very low and much lower than the U/d ratio. This reason is why the conductivity determined from Equation. (4- 8) is much lower than the theoretical value for the core flow (see Figs. 4- 25 and 4-26) where the applied voltage is indicated beside the pseudo-conductivity value. As the voltage increases, the sheath voltage drop becomes an increasingly smaller fraction of the applied voltage, and the pseudo-conductivity value should be approaching the theoretical value. Since it is clear from Figures 4-25 and 4-26 that the ohmic heating of the flow cannot explain the higher-than-equilibrium values of the pseudo-conductivity, especially at high pressure, and the electron concentration in the core flow is at its equilibrium value, the effect of the current propagating along the hot sidewall boundary layers might be a likely explanation.

The anomalously long ionization rise times (see Fig. 4- 24) are at least partially due to the finite size of the electrodes. It takes the shock about 7 μs to pass the electrodes, and this time might be somewhat increased due to the edge effects. However, the rise time tends to decrease as the pressure increases (see Fig. 4- 24). The two main reasons for this long rise time are the thermal boundary layer buildup behind the shock (as has been pointed out by the NASA Ames) and also sheath formation, which is controlled by the drift of electrons and ions in strong fields near electrodes and the nonequilibrium ionization. The latter process also controls the electric field value in the core flow.

4.1.1.4.2 *Two-Dimensional Calculations*

To analyze the effects of the boundary layer, we have also attempted 2-D simulation of a propagating shock wave using the Navier-Stokes flow code developed at OSU (Ref. 83). For complete understanding of the ionization kinetics in the near-electrode regions of the test section of the NASA Ames experiments, analysis of coupled boundary layer and sheath effects, which requires solution of chemical kinetics equations and the Poisson equation for the electric field, needs to be performed. For example, it is not clear what would be the electron concentration near the cathode. The concentration may be affected by the boundary layer temperature as well as the strong repulsion from the cathode in a strong electric field. However, the effects of chemical reactions and electromagnetics were not included in the present simulations of very strong shocks. The purpose of this study was to determine the appropriate formulation (consistent set of initial and boundary conditions) that would allow a further numerical modeling of strong propagating shocks. This is a crucial first step following which effects of chemical reactions and electromagnetics can be included with confidence. Prescribing appropriate boundary conditions at the inlet of the skimmer tube is perhaps the most important issue in the formulation.

Shock propagation through a 45-cm-long tube (corresponding to the length of the skimmer tube and the electrode region in the NASA Ames experiment) containing N_2 was investigated. One of the main objectives was to reproduce the energy loading to the driver gas to match the shock velocity and static pressure (obtained experimentally) at the inlet of the skimmer tube, which is accomplished by the prescription of a stagnation pressure and stagnation temperature. In these simulations, it is assumed the diaphragm is at the inlet of the skimmer tube. These stagnation conditions would be related to temperature and pressure at the inlet of the skimmer tube using the following relationships:

1. The inlet velocity is obtained by setting $dw/dx = 0$ at the inlet, where w is the axial component of the flow velocity
2. $T_0 = T_{inlet} + w_{inlet}^2/2c_p$
3. $P_0/P_{inlet} = (T_0/T_{inlet})^{\gamma/\gamma-1}$

The first derivative of all dependent variables in the radial direction is set to zero along the wall and the centerline. The second derivative of all dependent variables in the axial direction is set to zero at the exit of the tube. A further discussion of the assumed initial conditions is given in Appendix Section B.3.4. It is also pointed out in that section that the major difficulty associated with accurately computing a numerical solution to the NASA Ames testing scenario is one of grid size and CPU time. Because of the presence of strong shocks, it is necessary to use a very fine grid in the region near the shock. Since the flow code is based on the use of uniform grids, this implies the grid must be very fine everywhere. The Courant condition dictates that the finer the grid, the finer must be the time step, hence a well-resolved solution for a strong shock will require dramatically increased computer run times compared to cases in which only weak shocks are present.

The results for the case of the driver tube being at 2 atm and the driven tube being at 5.2 atm are shown below. Centerline profiles of pressure, temperature, and gas velocity are shown in Figures 4- 28, 4- 29, and 4- 30. Each of the figures shows profiles at three instants of time as the shock propagates through the tube.

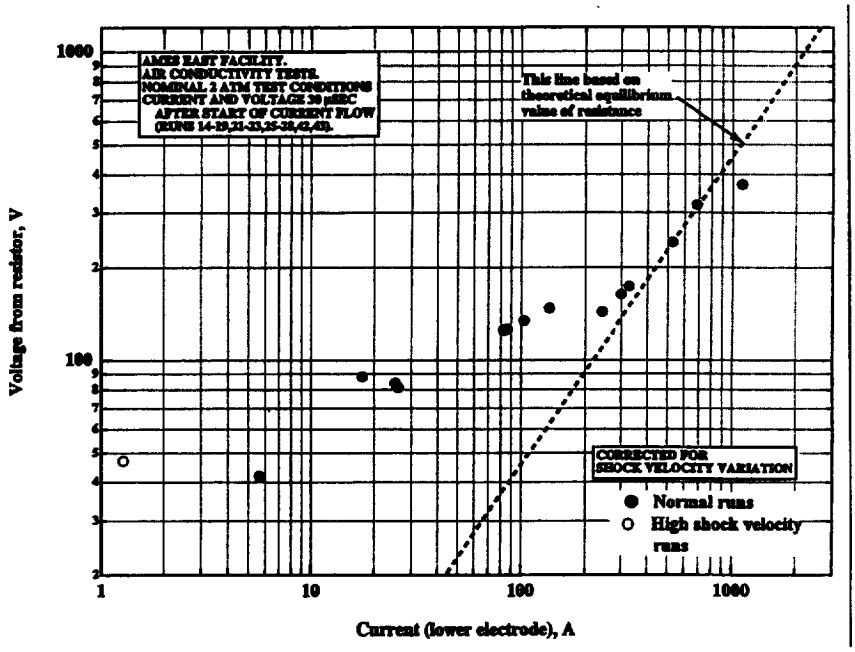

Figure 4- 28. Variation of gas velocity along the centerline at three different instants of time.

The pressure profile shows the drooping characteristics expected following the rupture of the diaphragm (Ref. 84). The velocity profiles follow the pressure profile; therefore, the pressure drop allows the acceleration of the gas behind the shock. The velocity profile also shows the relaxation of the gas velocity far downstream of the shock. The oscillations seen along the shock front are due to the simulations being carried out on a fixed grid and the use of central differencing of the spatial derivatives.

The pressure ratio along the shock front predicted by the simulations is about 1.3 atm as against the pressure of about 2.2 atm reported in the experiments. The reasons for this are discussed in detail in the appendix. Briefly, this pressure mismatch is due to: a) a mismatch between the actual diaphragm location and the simulated location, which was done to reduce computational time; b) the energy loading of the gas in the initial instants following diaphragm rupture may not be correctly simulated; and c) effects due to artificial dissipation that is introduced to stabilize the shock calculations.

Finally, Figures 4- 31 and 4- 32 show contour plots of the axial velocity and the translational temperature near the test section.

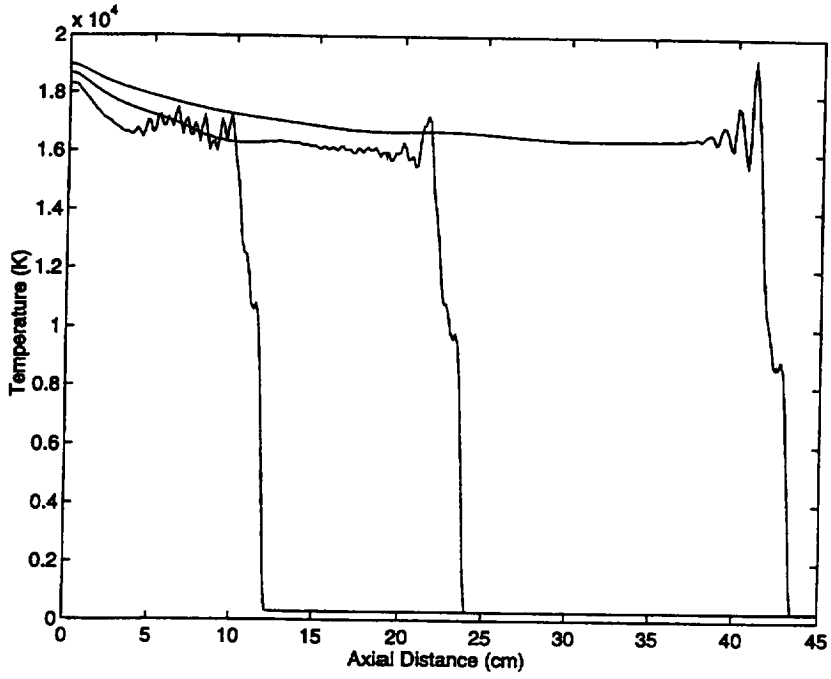

Figure 4- 29. Variation of temperature along the centerline at three different instants of time.

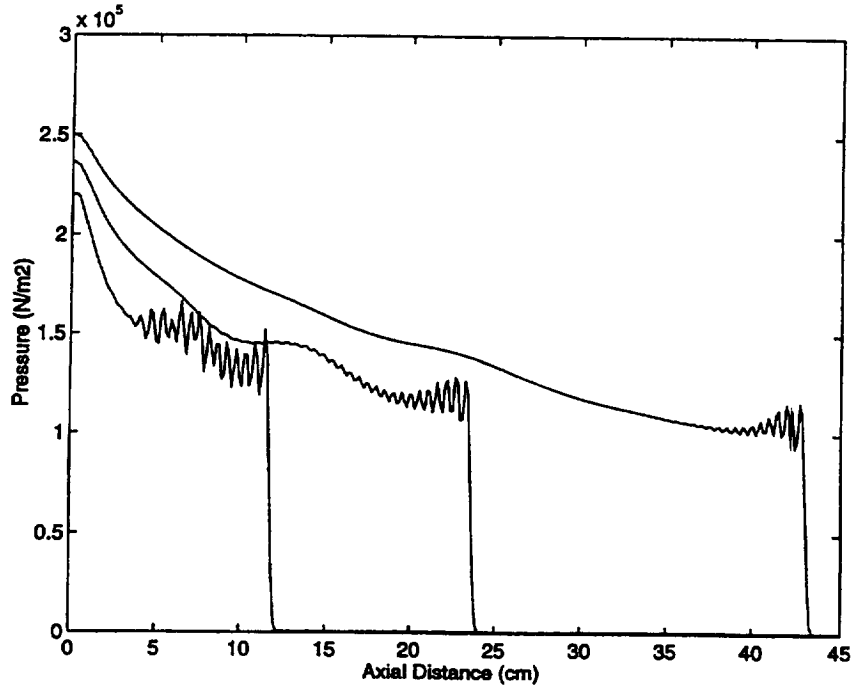

Figure 4- 30. Variation of pressure along the centerline at three different instants of time.

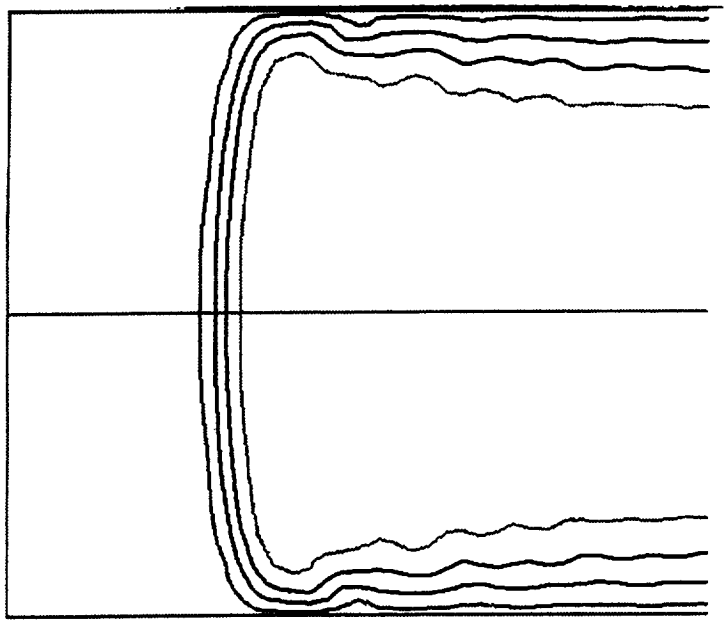

Figure 4- 31. Contour plot of the axial component of gas velocity near the test section. Outermost contour represents a velocity of 314 m/s; innermost contour represents a velocity of 2,519 m/s; the increment is 725 m/s. The region shown in the figure is 7.75 cm long.

Unlike in steady-state supersonic flows, the boundary layer behind the shock is initially cold since the shock front does not penetrate into the viscous layer. It takes quite a long time for the thermal boundary layer to heat up. For example, the flow in the test section at the pressure of 1.3 atm does not reach the steady state for at least 40 μs after the shock arrival (see Figs. 4- 31 and 4- 32). This confirms the explanation for the long ionization rise time we suggested in the previous section. Further development of the OSU Navier-Stokes code, which will extend its ability to model high-pressure discharges in reacting flows behind strong ionizing shocks, is currently underway. It is expected to provide new insight into the problem of stability and efficient control of such environments.

4.1.4.3 Ohio State University's Analyses of NASA Ames Experiment Conclusions

1-D and 2-D analysis of kinetics of vibrational relaxation, chemical reactions, and ionization behind the normal shock waves in air and in the N_2O-N_2 mixture showed:

1. In the shock tube ionization experiments performed at NASA Ames, the core flow reached vibrational, chemical, and ionization equilibrium extremely fast, over a period of less than 1 μs. The observed long ionization rise time cannot be explained by the relaxation phenomena. 2-D modeling suggests this anomalously long delay of ionization is due to the slow heating of the boundary layer behind the shock.

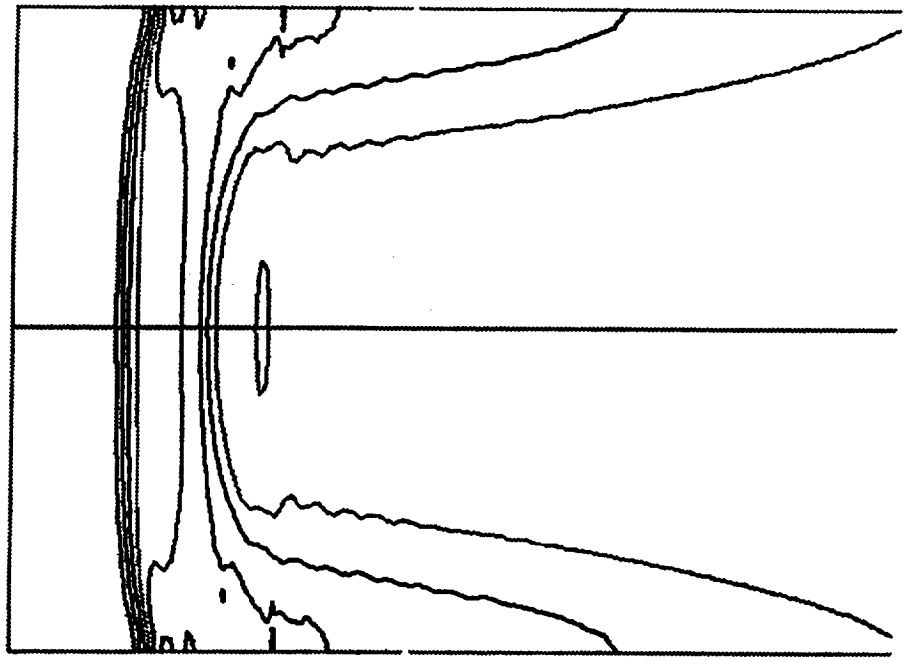

Figure 4- 32. Contour plot of the gas temperature near the test section. Outermost contour represents a temperature of 2,000 K; innermost contour represents a temperature of 16,000 K; the increment is 2,000 K. The region shown in the figure is 15.15 cm long.

2. The estimated reduced electric field in the core flow is very low ($E/N \leq 0.5 \times 10^{-16}$ V cm^2) even at the lowest pressure ($P_2 = 2$) atm and cannot result in any nonequilibrium ionization.
3. The measured current-voltage characteristic of the discharge in the flow indicates the presence of electron impact ionization in the sheath regions.
4. Core flow, where ionization is not self-sustained, is a stabilizing factor. The sheath regions, operating in a post-breakdown regime, are inherently unstable. This result indicates that the most likely instability scenario in a segmented electrode MHD accelerator appears to be the arcing between the adjacent same-wall electrodes due to axial component of the electric field.
5. The measured pseudo-conductivity is lower than the theoretical core-flow value at the low voltage (due to the voltage drop in the sheath) but exceeds the theoretical equilibrium limit (most likely due to the hot sidewall boundary layer currents after the steady-state temperature distribution is reached).

4.1.5 Effects of Seeding on Combustion

Evaluation of MHD accelerator capabilities for producing high Mach number, hypervelocity propulsion test conditions in ground test facilities is a primary objective of the MARIAH Project. For this application, it is critical the facility provides an adequate simulation of the in-flight operating environment, including flow chemistry. Since the flow chemistry is changed by the addition of an alkali metal to enhance ionization in the MHD accelerator, the effect of this contaminant on the propulsion-testing environment must be considered. The primary issues that arise with the addition of this seed material include the effect on the propulsion performance in the testing environment and the effect of molten alkali metal on seals and propulsion nozzle recombination catalysts. Specifically, the effect of adding an alkali metal seed on the ignition delay time in H_2-O_2 combustion is examined. A summary of this work is presented in this section and a detailed report on the topic is provided in Appendix Section C.3.

4.1.5.1 Overview

Efficient and effective operation of an MHD accelerator requires a high value of electrical conductivity, which can only be achieved in a plasma with significant ionization of the working fluid. A small amount of an alkali metal seed material is typically added to the working fluid in MHD accelerators to enhance the level of ionization and achieve a sufficient electrical conductivity. In equilibrium air accelerators, the alkali metal seed allows the desired ionization to be achieved at a temperature much lower than would be required in the air alone. However, for some applications, such as propulsion wind tunnels, the alkali metal can be an undesirable contaminate that may adversely affect the results of experiments. Thus, the use of a seed material must be carefully considered to ensure the accuracy of results.

It is critical the test facility does not introduce differences between the ground test simulation and the in-flight operation that are not well understood. High supersonic to hypersonic velocities in the combustor section of scramjets, coupled with engine size and weight limitations for flight vehicles, results in short residence time in these engines. Thus, the performance of scramjets will likely be limited by either the time required for mixing of the fuel with the incoming air at hypervelocity or by the reaction rates and ignition rates of the fuel and air mixture at lower hypersonic speeds. For this reason, it is crucial such tests closely reproduce the chemistry and fluid dynamics of the environment a full-scale engine would see in flight.

Three important questions arise in this connection: a) do small amounts of an alkali metal seed change the ignition delay times in a scramjet combustor by changing either the reaction rates or the set of important reactions? b) if addition of the seed does appear to increase the ignition delay times, will the delay times approach or exceed the turbulent mixing times? and c) does the presence of a small amount of seed affect the mixing rate in the turbulent, supersonic airflow?

A study conducted to address the first issue is reported in Appendix Section C.3 and summarized in this section. Presently, combustion in full-scale, operational scramjets is thought to be mixing limited.[5] Thus, small changes to the reaction kinetics would not affect performance, but large changes could cause the combustion to be limited by the chemical kinetics. Although this study does not address the second and third issues, some preliminary conclusions about the significance of this work in the context of supersonic combustion are presented in Section 4.1.5.3 below.

To simplify the problem, an assumption was made that the presence of seed in small amounts has no affect on the mixing times. Further simplification was achieved by assuming the primary variable of interest is the change in the ignition delay time as a function of the alkali metal mole fraction in the flow. A general set of reactions and reaction rates that adequately describe combustion in the presence (or absence) of an alkali metal seed material was determined based on research reported in the literature, and computations were done for a series of seed mole fractions ranging from 0 to 5 mole percent. Further details of the kinetic model are presented in Appendix Section C.3, while a summary of this work is given in this section. The effect of varying amounts of atomic oxygen and NO on ignition time was also evaluated.

4.1.5.2 Analysis

Results of ignition delay time calculations in a stoichiometric mixture of H_2 and air (or O_2) with admixtures of other species such as O, NO, K, and Na are summarized in this section. All calculations are for an adiabatic combustion process at a constant pressure of 1 atm. Ignition times are determined as the time required for the temperature to increase to 100 K above the initial value.

The kinetic mechanism of H_2 ignition in O_2 or in air (without the admixtures specified above) is well known (Refs. 85, 86). This kinetic model includes 19 species and approximately 80 chemical reactions (see Appendix Section C.3 for details). It is based upon the well-known Warnatz mechanism of H_2 - O_2 combustion combined with the well-known Zel'dovich mechanism of N_2 oxidation and reactions of $H_xN_yO_z$ species (Ref. 87). Only a few of the large number of reactions considered are critical for H_2 combustion. For example, in an H_2-O_2 mixture with no radicals present (such as O, H, and OH), the most important initiation reaction is:

$$H_2 + O_2 \quad \rightleftharpoons \quad HO_2 + H \tag{8}$$

This reaction has quite large activation energy, which explains why H_2-O_2 mixtures do not ignite spontaneously at low temperatures. It produces the H_2 atoms that initiate the chain reaction mechanism:

[5] Personal communication, Mr. Gordon Nelson, MSE with Dr. Phil Drummond, NASA LaRC, April 1996.

$$O_2 + H \rightleftharpoons OH + O \quad (9)$$

$$H_2 + O \rightleftharpoons OH + H \quad (10)$$

A small amount of hydrogen or oxygen atoms present in the gas mixture starts the self-accelerating chain reaction (Reactions 9, 10), while the initial reaction (Reaction 8) is a bottleneck for the entire chain process. Finally, water is produced in Reactions 11 and 12.

$$H_2 + OH \rightleftharpoons H_2O + H \quad (11)$$

$$O_2 + H + M \rightleftharpoons H_2O + M \quad (12)$$

The last reaction releases a large amount of energy, thereby heating the mixture and accelerating the combustion process. This is a classical, well-established mechanism.

Addition of N_2 to the mixture does not qualitatively change this scenario in spite of the addition of many chemical reactions. In this case, however, the ignition time is always greater than for the H_2 - O_2 mixture (see Fig. 4- 33).

Quite obviously, the ignition time steeply decreases with temperature in the temperature range 1,000 - 2,000 K but increases again above 2,000 K (see Fig. 4- 33). This happens because of the reverse radical reactions that become important at the high temperatures and decrease the overall water production and energy release rates.

This analysis also shows that the presence of NO in the mixture, even in considerable concentrations (a few percent), does not substantially affect the O, H, and OH radical concentrations in the mixture. Therefore, it does not appreciably change the ignition delay time at any temperature within the range considered (see Fig. 4- 33).

Atomic oxygen, however, results in a well-pronounced effect. In the presence of oxygen atoms, the initial reaction (Reaction 8) is no longer a bottleneck, and the chain mechanism (Reactions 9, 10) starts instantaneously. This is especially important at temperatures less than 2,500 K when there are no other fast processes of oxygen atom formation. Therefore, in this temperature range, the ignition time is reduced by about an order of magnitude if the atomic oxygen concentration is 0.1-1.0% (see Fig. 4- 34).

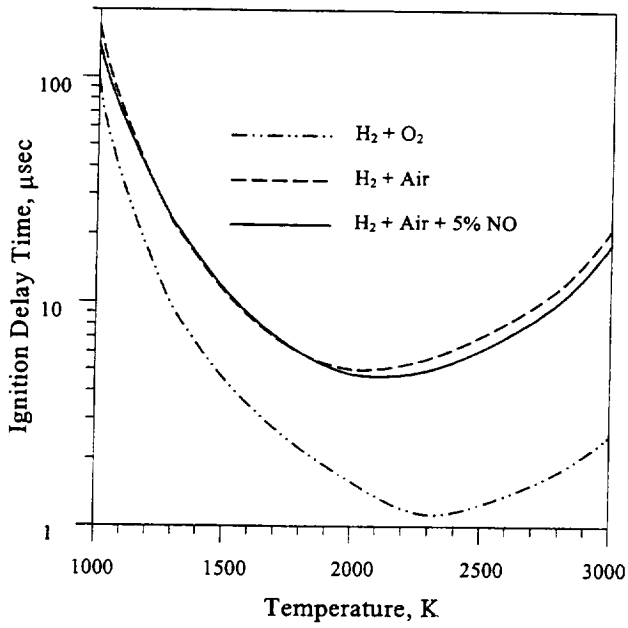

Figure 4- 33. Effect of NO on ignition delay in H_2 - air mixture.

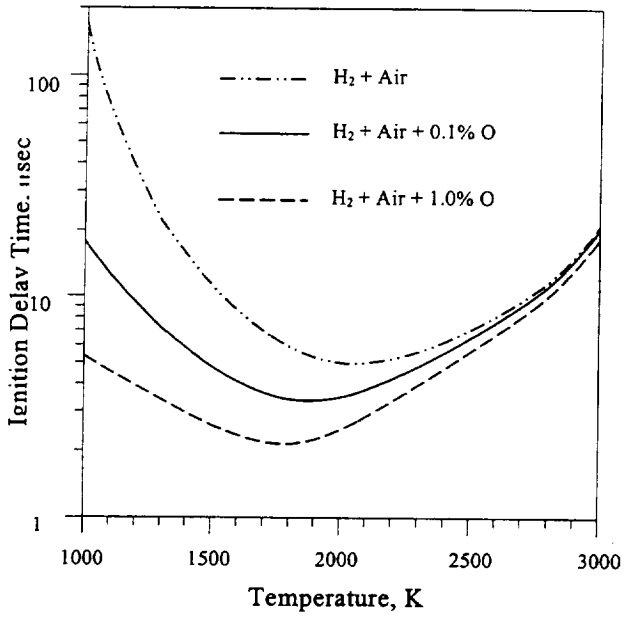

Figure 4- 34. Effect of atomic oxygen on ignition delay in H_2 - air mixture.

Of course, these are unrealistically high concentrations for airflow expanding from a high temperature plenum, unless nonequilibrium ionization is sustained in the supersonic section of the nozzle (by an e-beam or by seeding the gas). Then, related chemical processes can increase the amount of oxygen atoms up to a few percent (Ref. 17). Therefore, the presence of atomic oxygen can substantially accelerate the ignition in energy addition flows at temperatures less than 2,500 K. In other words, an air mixture contaminated with oxygen atoms would have a shorter ignition delay in a wind tunnel experiment than would occur in a real flight where there are almost no oxygen atoms present in the flow. The catalytic effect of oxygen atoms becomes much weaker, however, at temperatures greater than 2,500 K (see Fig. 4- 34).

Alkali atom effects on H_2 ignition appear to be quite straightforward. The global kinetic mechanism for K and Na reactions in H_2-O_2 flames by Jensen (Refs. 88, 89) (Reactions 13a and 14a for K, 13b and 14b for Na) is sustained by the later studies of Na and K kinetics in flames (Refs. 90, 91), although with some corrections.

Slack et al. (Ref. 91) refines this two-reaction mechanism by replacing it by a five-reaction scheme that produces quite similar results (see Appendix Section C.3). In these calculations, the global Jensen mechanism for both K and Na is assumed.

$$K + OH + M \rightleftharpoons KOH + M \qquad (13a)$$

$$Na + OH + M \rightleftharpoons NaOH + M \qquad (13b)$$

$$KOH + H \rightleftharpoons K + H_2O \qquad (14a)$$

$$NaOH + H \rightleftharpoons Na + H_2O \qquad (14b)$$

At temperatures less than 1,500 K, the rates of the shuffle reactions (Reactions 9, 10) are not very fast, and the radical concentrations increase quite slowly. Then, Reactions 13 and 14 result in removal of radicals (H and OH) from the mixture, which tends to terminate the chain process (Reaction 9, 10) and delay the ignition (see Fig. 4- 35). Reactions 13 and 14 are exothermic; however, the energy release is very slow at these temperatures. Alkali atoms act as inhibitors in this temperature regime.

At the high temperatures, the radical production rate by the chain mechanism (Reactions 9, 10) becomes much faster, and Reactions 13 and 14 can no longer keep up. These reactions now act as an additional exothermic channel of water production, and both K and Na act as catalysts. The presence of K or Na at a 1% level for temperatures greater than 2,000 K can then be seen to reduce the ignition delay time by about a factor of 2 (see Fig. 4- 35). If Slack's recommendations are followed, the effect of either metal on the ignition time is almost identical.

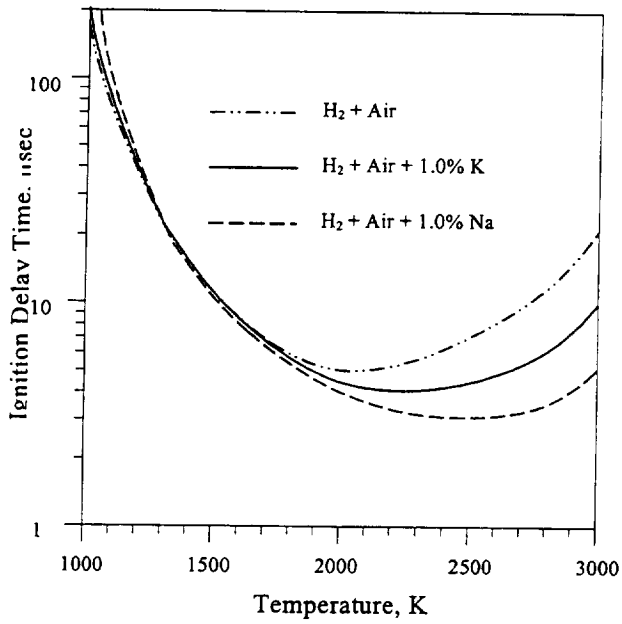

Figure 4- 35. Effect of alkali atoms on ignition delay in H_2 - air mixture.

4.1.5.3 Analysis Limitations

Since the kinetic model used here for the ignition delay time calculations it is not coupled with the flow, it is not applicable to modeling the entire supersonic flow combustion process. First, the assumption of adiabaticity is justified only at the initial stage of combustion (i.e., ignition), when the energy released into the flow is small, but, is not valid when the combustion process is well under way. Secondly, the model does not take into account the turbulent mixing of the species that, in fact, may control the chemical reaction rates.

For these reasons, the calculated ignition delay time for a particular gas mixture (scaled as 1/P, if necessary) should be compared with the turbulent mixing time, experimentally measured for a particular combustor as a function of temperature, pressure, and Mach number (e.g., see Ref. 92). This would answer the question as to whether the chemical kinetic processes or turbulent mixing controls the combustion rate for a particular flow. Obviously, reaction kinetics, including the effect of alkali seeds is only relevant in the former case. Effects of pressure were not considered in this study, and all calculations were performed at a constant pressure of 1 atm. However, ignition delay time scales with pressure as approximately 1/P (see Table 4- 5). A slight deviation from the 1/P law results from the three-body reactions involved.

Table 4- 5. Ignition delay time in $H_2:O_2 = 2:1$ mixture as a function of pressure.		
P (atm)	T(K)	Ignition Delay time, μs
0.01	2,000	187.0
0.03	2,000	60.9
0.1	2,000	17.6
0.3	2,000	5.64
1	2,000	1.6
3	2,000	0.50

4.1.5.4 Effects of Seeding on Combustion Conclusion

Conclusions from Figures 4- 33 through 4- 35:

1. NO has very little effect on H_2 ignition throughout the entire temperature range considered;
2. Atomic oxygen strongly decreases ignition time at low temperatures by removing a radical production bottleneck (Reaction 8); and
3. K and Na both decrease the ignition time at high temperatures due to the catalytic effects in Reactions 13 and 14.

No attempt was made in this study to model the turbulent mixing of the fuel and air. For scramjet flow regimes that are mixing limited, the effect on scramjet performance of small additions of K seed may not be significant. However, if the flow is limited by the chemical kinetic rates rather than by mixing, the decrease of the ignition delay time due to the presence of an alkali metal seed would most likely affect the scramjet performance in the ground test simulation.

4.1.6 Reproducing Flight Conditions in Hypersonic Wind Tunnels

4.1.6.1 Overview

This section is a summary of research performed under subcontract to the ENGO organization during the fall of 1995 and extending into the spring of 1996. ENGO is a private Russian consortium headquartered in Moscow comprised of researchers from a number of Russian scientific, academic, and technical agencies. The Principal Investigator (PI) for this subcontract was Dr. Vadim Alfyorov, a noted MHD researcher at TsAGI. In the 1960s, Dr. Alfyorov and his colleagues developed an MHD accelerator facility that included a small aerodynamic test

section. The facility is the only hypersonic, MHD-driven aerodynamic test facility in existence. The full report, as received from ENGO, may be found in Appendix Section E.3. The ENGO subcontract had the primary objective of evaluating the potential for advanced arc-heated, seeded MHD accelerator systems to serve as drivers for ground test facilities capable of testing advanced air-breathing engines. The term "advanced MHD accelerator systems" was somewhat arbitrarily defined as one that relied on a 12-T magnet and was driven by an arc heater operating at a 200-atm stilling chamber pressure. Both of these components are somewhat beyond state-of-the-art technology.

The ENGO report does not specifically address the TsAGI MHD facility, nor was it intended to develop recommendations for an upgraded Russian MHD test facility. The research is of a more general nature and addresses the question of what performance gains might be realized from a hypothetical, high-performance MHD facility driven by advanced arc heater and magnet systems.

4.1.6.2 Problem Definition and Scope of the ENGO Study

The ENGO report characterizes the basic limitations of existing ground test facilities with respect to their capability for supporting testing of air-breathing engines. Performance data on several gas piston-driven facilities, such as the Stalker tube at the AEDC and the high-pressure Russian facility at the TSNIIMASH research center, is cited. Although these facilities have somewhat higher performance envelopes compared to arc-heated facilities, they suffer from very short run times. This renders gas-piston facilities unsuitable for advanced engine testing, leaving only arc-heated facilities as candidates. The term "arc-heated facility" is used here to include MHD accelerator facilities driven by arc heaters.

As noted in Section 3 of this report, a major technical issue for arc-heated facilities is the problem of adding sufficient enthalpy to the flow while maintaining the entropy within the bounds of the targeted flight envelope. Additionally, materials problems become an issue for MHD accelerators. Since accelerators such as the one at TsAGI operate close to LTE, they must rely on thermal ionization of an alkali metal seed to achieve the requisite electrical conductivities. This generally implies that the accelerator must operate at temperatures above 2,700 K with substantially higher temperatures in the plenum.

A major shortcoming of the present TsAGI MHD facility (and similar facilities) is the arc heater operates at a maximum stilling chamber pressure of 20 atm and a temperature of about 3,800 K. Figure 4- 59 shows the approximate region of operation that can be achieved in the present facility. This region represents the total enthalpy-entropy conditions achievable in the test section. Note that it lies well to the right of the target 2,000 lbf/ft^2 post-bowshock flight envelope, implying there is a pressure and Mach number mismatch between the test section conditions and the in-flight, post-bowshock conditions. In this respect the TsAGI facility is typical of all arc-heated facilities whether or not they employ MHD acceleration downstream.

Since entropy scales inversely with the logarithm of pressure, the most straightforward way to improve this situation is to increase the operating pressure of the arc heater (maintaining a fixed temperature), thus reducing the starting entropy. This will result in a corresponding reduction in the final entropy for a fixed amount of heat addition. Alternatively, one can operate the accelerator with an increased magnetic field. This will have the effect of increasing the slope of the H-S curves describing the flow through the accelerator system. Both of these strategies were considered in the work described in Appendix Section E.3.2, which is the translated ENGO report.

Testing requirements are also addressed. The ENGO study makes the assumption that so-called "combustor inlet" conditions must be reproduced in the test section to obtain an adequate engine testing environment. These conditions are tabulated as a function of free-stream Mach number in Table 4- 6.

Table 4- 6. Flight Mach numbers vs. scramjet combustor inlet conditions for an assumed dynamic pressure of 1,500 lbf/ft^2. The table has been reproduced from the ENGO report in Appendix Section E.3.2.

M_{inf}	5	8	10	12	15	20
M_2	1.75	3	3.75	4.4	5.2	6.1
P_2	2.5	1.8	1.5	1.15	0.8	0.5
T_2	800	1,100	1,400	1,500	2,000	2,250
u_2	978	1,900	2,720	3,270	4,480	5,500
P_{02}	14	80	100	700	1,500	3,000
T_{02}	1,200	2,000	3,500	5,000	7,200	9,000

According to the authors of Reference 93, it must be noted that achieving combustor inlet conditions in the test section will not provide an adequate testing scenario for conducting an engine development program. It is worth quoting the major conclusions of Reference 93 with respect to testing requirements:

"In either case, ground testing of such engines presents unique facility requirements that are daunting compared to simulation requirements for hypersonic aerodynamics. These include the need to do the following:

1. Duplicate the internal flow path, stream velocity, pressure, temperature, chemical composition, and turbulence in order to replicate the fluid physics and chemistry of the combustor.
2. Duplicate the inlet shock wave system swallowed by the engine since it will interact directly with the fuel injection and combustion mechanisms in the diffusive-burning engine, or it will become the combustion mechanism itself in the detonation wave engine, and the resulting internal shock system will emerge from the combustor and affect the nozzle performance.

3. Duplicate the heat load imposed on the engine internal structures by the captured airstream, which exceeds that imposed by the fuel combustion per se, as well as the associated aerodynamic and aeroelastic loads.

4. Provide sufficient test time to evaluate material thermal soaks, unstart, and controls.

The above discussion is the basis for the requirement stated in Section 3, namely that the facility must be capable of simulating post-bowshock conditions. This requirement is much more severe than the combustor inlet conditions assumed in the ENGO study.

As implied in the report, there were three basic questions that defined the scope of the study:

1. What are the performance limits of arc-heated, seeded MHD accelerator systems assuming modest extrapolations in arc heater and magnet technology from state of the art?

2. What are the primary air chemistry effects in the test section? These effects are induced both by the introduction of seed and by the nonequilibrium chemistry created by the presence of strong electric fields in the MHD accelerator and the arc heater. Both of these processes create a chemically confounded airstream different from what an actual vehicle or engine inlet would see in flight.

3. What are the effects of a nonequilibrium flow stream contaminated by alkali metal seed and alien species, such as nitrogen oxide, on the combustion processes in a scramjet engine?

4.1.6.3 Working Assumptions and Method

A 1-D simulation code was used to model the MHD problem, including the gas dynamics, the MHD interaction, and the chemical kinetics. The chemistry model included five equations for the O_2- N_2 reactions, as well as rate equations for ionization, reattachment, and dissociation processes. Vibrational excitation and relaxation was simulated only for the lower vibrational states. The computer code was run for a range of stagnation temperatures, seed fractions, and magnetic fields. It was assumed the seed material was K in all cases. The assumed range of parameters of the study is shown below.

- Plenum Conditions: $P_0 = 200$ atm, $T_0 = 4{,}700$ K (held fixed)
- Magnetic field: B = 12 T (fixed).
- Seed fractions: 0.25 - 2.0% (mole % K)
- Current densities: 20 - 200 A/cm^2
- Channel Lengths: 1.0 - 1.7 meter
- Secondary Expansion Duct Length: 0.6 meter

A total of 16 cases were run, representing parameter sweeps in the above variables. The gas dynamics code was capable of predicting the molar concentrations of monatomic oxygen and nitrogen oxide at the exit of the MHD channel.

This phase of the analysis provided provisional answers to questions 1) and 2) above. The third question, relating to the effects of alien chemical species on combustion, was answered by use of a chemical kinetics code that modeled the combustion process using a reaction set of 43 reactions. A shortcoming of the model is that the reaction set did not include any ionic species or free electrons.

4.1.6.4 Study Results

Table 4- 7, taken from the ENGO report, summarizes the results of the parametric MHD study.

Table 4- 7. Summary of results of the MHD parametric analysis.

P_1 At	A_1	C_K %	L M	P_L KPa	T_L K	U_L m/s	P_2 KPa	T_2 K	U_2 m/s	C_O %	C_{NO} %	F_2 cm^2
20	0.66	1.0	1.1	356	3,150	4,241	83.1	2,265	4,502	2.23	5.35	380
20	0.66	1.0	1.5	246	3,306	5,224	52.3	2,312	5,460	3.43	5.70	509
20	0.66	1.0	1.7	1.0	3,400	5,784	51.0	2,448	5,990	4.28	5.94	510
20	0.15	0.5	1.1	345	3,058	4,235	82.9	2,208	4,483	1.68	5.25	370
20	0.15	0.5	1.5	238	3,211	5,211	53.0	2,262	5,434	2.43	5.48	491
20	0.15	0.5	1.7	203	3,309	5,768	50.1	2,380	5,965	2.99	5.69	506
16	0.15	0.5	1.0	306	3,064	4,314	82.1	2,267	4,542	1.70	5.15	321
16	0.15	0.5	1.35	214	3,213	5,265	53.0	2,317	5,473	2.35	5.41	426
16	0.15	0.5	1.55	181	3,320	5,880	51.4	2,468	6,060	2.91	5.63	420
16	0.66	1.0	0.95	330	3,150	4,200	81.2	2,290	4,455	2.24	5.36	340
16	0.66	1.0	1.35	224	3,322	5,276	53.1	2,383	5,496	3.44	5.72	436
16	0.66	1.0	1.55	187	3,415	5,890	51.2	2,523	6,080	4.36	5.97	433

The subscript "1" in the first row indicates conditions at the inlet of the MHD channel, subscript "L" indicates the MHD channel exit, and subscript "2" indicates conditions at the exit of the

secondary expansion duct (i.e., the test section inlet plane). The symbol "C" stands for molar concentration. Thus "C_{NO}" indicates the molar concentration of nitrogen oxide at the exit of the secondary expansion duct. The parameter a_1 is a dimensionless parameter characterizing electrode geometry. F_2 is the cross-sectional area at the exit plane of the expansion nozzle.

The table shows some clear trends. As might be expected, longer channels provide greater gas acceleration but at the cost of increased O_2 dissociation. There is also a trend of increasing NO production with respect to channel length, but the effect is small. Detailed plots (not shown here) indicate the flow is essentially frozen chemically at the exit of the expansion nozzle but is vibrationally close to equilibrium.

As noted above, question 3 was analyzed using a chemical kinetics code. Two cases were considered:

1. The gas composition entering the combustion chamber was assumed to be stoichiometric air.
2. The incoming airstream contained monatomic oxygen at a 1.7% molar concentration and nitrogen oxide at 5.15%. This condition corresponds to the first row in the P_1 = 16 atm series in Table 4- 7.

One parameter of interest was the induction length. This was defined as the distance along the combustion chamber at which the concentration of monatomic hydrogen reached a local maximum. The computations were run for a chamber pressure of 82 kPa, temperature of 2,267 K, and flow velocity of 4,542 m/s. These initial computations were run without a seed species. The results of the computations are presented as plots of monatomic hydrogen concentration vs. distance (not shown here). The most significant conclusion is that there is essentially no difference in induction lengths between the two different gas compositions 1) and 2).

A second set of calculations was run to investigate the effects of seed on combustion. The seed species was assumed to be Na. Since the original reaction equation set contained no alkali metal species, it was augmented by a set of six additional reactions involving Na, water, O_2, neutral OH, and unspecified heavy particles. Sodium was selected over other alkali metals because of the better rate data available and because the reaction chemistry is somewhat better understood. The lack of any ionization reactions or rate data in the model in the analysis is again noted.

The single plot that is presented in the report again indicates no difference in induction length between cases 1) and 2). In fact, all three of the plots shown in the report show the induction length to be essentially invariant at a value of 1.0 cm.

4.1.6.5 ENGO Study Conclusions

With respect to the gas kinetic combustion study, the conclusions were quite similar to those of the OSU study (Appendix Section C.4). The presence of small amounts of alkali metal in the flow stream of a supersonic combustion system does not significantly alter the chemical kinetics

or the ignition delay times. However, it should be noted that both of these studies made the assumption of a premixed flow stream. Although it seems probable the mixing process would be essentially unaffected by the presence of small amounts of seed material, this question was not investigated in the MARIAH Project. It should also be mentioned that through most of the combustion regimes of interest, the mixing process is the factor that limits ignition (see footnote 4).

Other conclusions reached by the authors of the ENGO report are paraphrased below.

1. Presently, there are no hypersonic facilities that offer the capability of reproducing flight conditions in the Mach 12 to 20 flight regime. MHD offers some promise for doing so.
2. The MHD parametric study conducted by ENGO shows that an advanced arc-heated MHD system operating with a 12-T magnet and at reservoir conditions of 4,700 K and 200 atm could provide test section conditions corresponding to combustor inlet conditions (direct connect mode).
3. The presence of alkali metal atoms in the MHD flow has no significant effect on either the induction time or the gas dynamic parameters in the combustion chamber.

4.1.7 Evaluation of Electron Attachment

When free electrons in an ionized gas attach to neutral atoms and molecules in the gas, negative ions are formed that reduce the overall mobility of the charge carriers and the electrical conductivity. Singly charged ions having the same magnitude of charge as an electron will experience the same force as an electron in an electric field; however, its acceleration will be far less due to its larger mass as compared to the electron mass. Furthermore, their random thermal velocity will be far less than that of the electrons at the same temperature. Thus, ions are much less mobile and far less effective at the transport of electrical energy than the light mass electrons; the electrical conductivity contribution of ions will be nearly insignificant compared to an equal concentration of free electrons in a gas. The major effect of electron attachment is through the reduction of the electrical conductivity of the plasma. High values of electrical conductivity are essential to achieving good performance from an MHD accelerator, and electron attachment can substantially reduce the electrical conductivity.

Macheret, Miles, and Nelson (Ref. 23; see also Appendix E of this report) defined an MHD conversion efficiency, η, as

$$\eta = \frac{< j_y u B_z >}{< j_y E_y + j_x E_x >} \qquad (4\text{-}10)$$

where the brackets < > denote an average across the duct. For a 1-D, uniform flow approximation, the brackets can be removed and can then be rewritten for a Faraday accelerator as:

$$\eta = \frac{j_y u B_z}{\left(\frac{j_y^2}{\sigma} + j_y u B_z \right)} \qquad (4\text{-}11)$$

From this, the importance of the push-work term is evident:

$$\eta = \frac{\sigma j_y u B_z}{j_y^2 + \sigma j_y u B_z} = \frac{\sigma u B_z}{j_y + \sigma u B_z} \qquad (4\text{-}12)$$

For large values of σ, the term resulting from the push-work (σuB) will dominate, and the conversion efficiency can approach unity. For low values of σ, the current density (resulting from the Joule-heating term) will dominate, and the conversion efficiency will be low. Thus, large values of electrical conductivity are clearly desirable since these will allow better MHD performance while low values will constrain the device to perform little better than conventional arc heaters.

Rosa (Ref. 94) presents an elementary derivation of electrical conductivity in an ionized gas for electrical conduction by electrons and shows this to be proportional to the number density of electrons in the gas:

$$\sigma_e = \frac{n_e e^2}{m_e n Q c_e} \qquad (4\text{-}13)$$

Electron attachment to atomic and molecular species in the flow reduces the number of free electrons and increases the number of ions. Thus, electrical conductivity could be reduced significantly by electron attachment in a plasma, and it is this mechanism by which the MHD performance would be reduced.

Electron attachment is insignificant in the 1% seeded, 1-atm air plasma. However, concentrations of Cs decrease and those of the negative ions increase with increasing pressure. This can more readily be seen in Figure 4- 36, showing the electron-to-Cs ion ratio (e^-/Cs^+) for the 1% Cs-seeded air. This is the fraction of available electrons still free in the 1-atm plasma. The ratio of these concentrations can be seen to approach a value of 1 at temperatures above 2,000 K, indicating that most of the electrons are free or not attached to other air species. At 3,000 K (see the inset in Fig. 4- 36), approximately 97% of the available electrons are seen to be free in a 1-atm plasma while this drops to 85% at 10 atm and 42% at 100 atms. Thus, the percentages of electrons attached in negative ions are 3%, 15%, and 58% for these three pressures. Since electrical conductivity is proportional to the number of free electrons, the 1-atm plasma would be expected to have a reasonably high conductivity with an ionization fraction approaching 10% and very few electrons lost to negative ion formation. However, at a 100-atm pressure, the ionization fraction is only 1%, and 58% of the electrons are lost to attachment;

therefore, the conductivity would be expected to be low. The 1-atm plasma has an electrical conductivity of approximately 165 mho/m, and the 100-atm plasma conductivity is only 17 at 3,000 K.

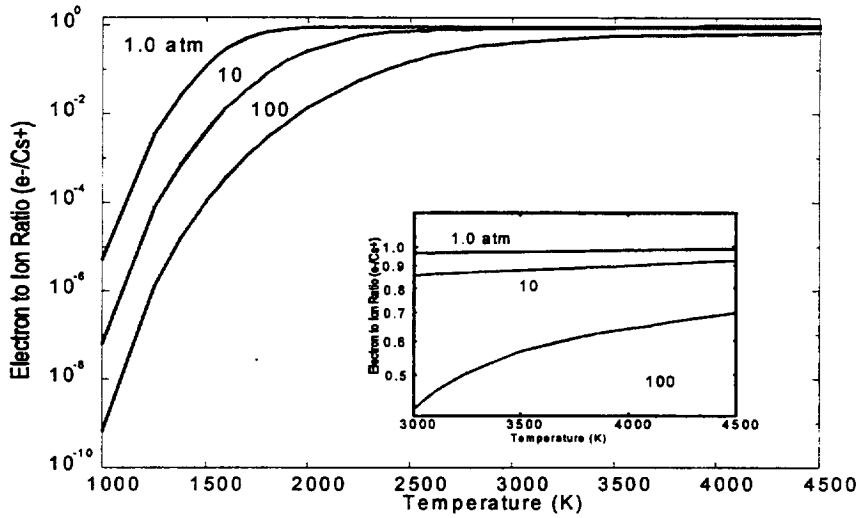

Figure 4- 36. Electron-to-Cs ion fraction for Cs-seeded air.

The electron attachment trends are very similar at a seed fraction of 0.01% to those discussed above for the 1% seed fraction, except the mole fractions for the electrons and all ions are considerably lower due to the smaller amount of seed available. When Figure 4- 36 was created, showing the electron-to-Cs ion ratio (e^-/Cs^+), data for both 1% and 0.01% seed were plotted; however, the lines for the two cases could not be distinguished at this scale. Therefore, the seed fraction, at least in the range of 0.01-1.0%, has no significant effect on the electron-ion ratio, which is equivalent to saying that the seed fraction has no significant effect on electron attachment. Electrical conductivity for the 0.01% seed fraction is compared to the 1% seed fraction in Figure 4- 37. As would be expected, the electrical conductivity values are lower for the lower seed fraction at 3,000 K and 1 atm. The 0.01% seeded plasma has an electrical conductivity of approximately 28 compared to 165 mho/m noted earlier for the 1.0% seed case.

The effect of electron attachment on electrical conductivity can be estimated by comparing the Cs-seeded air conductivity with values for Cs-seeded N_2 since significant negative ion formation does not occur in the N_2. Electrical conductivity for seeded N_2 and air plasmas is compared for two pressures and two seed fractions in Figure 4- 38. As expected, electrical conductivity values for seeded N_2 are higher than those for air, especially at high pressure and low temperature where electron attachment was shown to be most dominant in the above discussions. At low pressure, the electrical conductivity values in N_2 and air are almost identical. However, at high pressure, the electrical conductivity of the seeded N_2 is significantly higher than that of the

seeded air. Electrical conductivity values at low, moderate, and high temperatures are presented in Table 4- 8 for comparison.

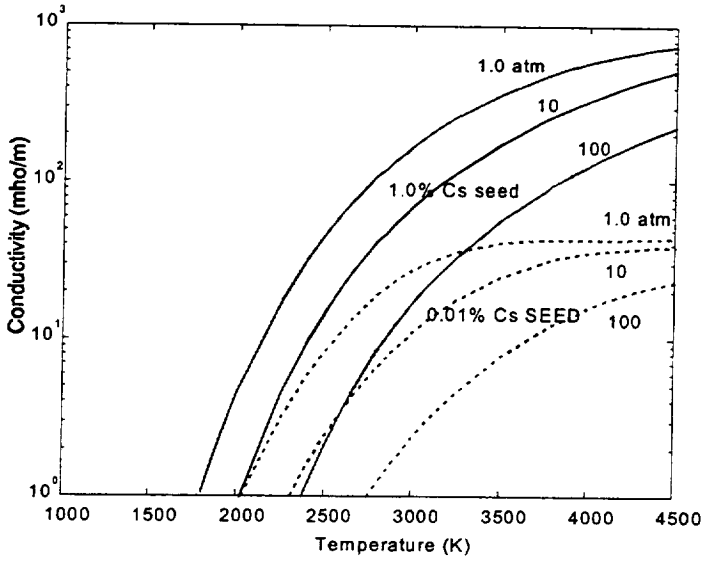

Figure 4- 37. Electrical conductivity for Cs-seeded air.

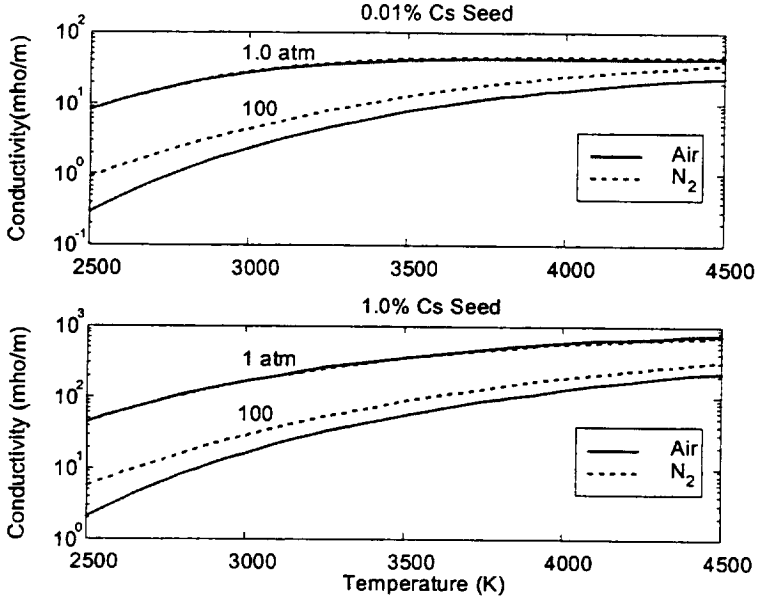

Figure 4- 38. Comparison of electrical conductivity for Cs-seeded N_2 and Cs-seeded air.

Table 4- 8. Comparison of seeded air and N_2 electrical conductivity for 100-atm pressure.						
	1.0% Cs			0.01% Cs		
Temperature (K)	Electrical Conductivity (mho/m)		% Decrease In Air	Electrical Conductivity (mho/m)		% Decrease in Air
	Air	N_2		Air	N_2	
4,500	225.1	318.5	29%	23.2	35.7	35%
3,500	56.9	88.0	35%	7.7	12.8	39%
2,500	2.1	5.8	63%	0.3	0.9	68%

As seen in Table 4- 8 and Figure 4- 38, the electrical conductivity of seeded air can be depressed significantly by electron attachment in some temperature and pressure regimes. The large depression of the conductivity at the lowest temperature is inconsequential since the magnitude of the electrical conductivity at this high-pressure, low temperature condition is so low that MHD, using equilibrium ionization, would not be considered for this regime. At the highest temperature and with 1% Cs seeding, the conductivity is depressed less than 30%.

4.1.1.7.1 *Electron Attachment Conclusions*

Electron attachment is insignificant in low-pressure air but can be quite important in high-pressure air for some temperature regimes. Depression of electrical conductivity is most important in the moderate temperature ranges where the electrical conductivity value is large enough to be significant and the electron-to-ion ratio is significantly less than 1. At high temperature, the electron-to-ion ratio approaches unity, and electron attachment becomes much less important.

In the temperature range of 2,500 – 3,500 K (typical of MHD accelerator operation), comparison of seeded air and N_2 electrical conductivity values indicates that depression of the electrical conductivity is strongly pressure dependent. Differences between 1% Cs-seeded N_2 and air are negligible for a pressure of 1 atm; however, for a pressure of 100 atm, air electrical conductivity is 35% lower than N_2 at 3,500 K and 63% below N_2 at 2,500 K. This electrical conductivity reduction is predominantly due to electron attachment by monatomic and diatomic oxygen.

4.2 EXPERIMENTAL STUDIES

Two experimental studies were performed for the MARIAH Project. UTA performed experiments with a detonation-driven shock tube to investigate the electrical conductivity of

seeded air and N_2 at high pressure. NASA Ames performed experiments to investigate the physics of electrical conduction and breakdown in high-pressure, high temperature air plasma. The following sections describe the test configurations, test operations, and obtained results.

4.2.1 NASA Ames Research Center Test Program

4.2.1.1 Overview

A test program was initiated at the NASA Ames Electric Arc Shock Tube (NASA Ames EAST) facility to determine the effects of gas pressure, ionization fraction, and electric field strength on current discharges in shock-heated, high-pressure air. These tests were designed to provide useful information on air conductivity and electron dynamics. Data from the experiments will aid in the development of computational plasma/fluid dynamic models of MHD accelerators for airflow applications.

Experimental investigations in the EAST Facility included: a) measurement of current and voltage across a pair of electrodes in a square channel to determine the gas conductivity; b) study of the diffuse discharge/arc transition at these conditions; and c) spectroscopic investigations to attempt measurement of electron density and temperature. Test section static pressure for these experiments ranged from 2 to 13 atm, and static temperatures of 5,500 – 6,000 K produced ionization fractions of about 10^{-4}, typical of seeded MHD accelerators. Some testing was accomplished at a lower shock-induced ionization fraction on the order of 10^{-5} to focus on nonequilibrium effects. Applied electrode voltage was varied over a range of 5 to 1 or more for each condition tested. The test section was designed to vary boundary layer thickness by varying the length of the skimmer section upstream of the electrodes; however, this was not used during the course of this study.

4.2.1.2 Test Hardware Description

A diagram of the MARIAH Project test section installed in the EAST Facility is shown in Figure 4- 39. This facility is a 10.16-cm internal diameter, electric arc-driven shock tube. For these experiments, He was heated in the 76-cm-long driver section with an electric discharge from a capacitor bank rated for a maximum energy of 1.24 MJ. The 550-cm driven tube was separated from the driver with a double diaphragm Ar buffer section. A 3.5-cm inside diameter skimmer tube, projecting 23 cm into the driven tube, was used to remove the boundary layer and direct the core flow into the electrical conductivity test section. A Delrin™ plastic-lined conductivity channel had a 3.1-cm-square cross-section and was connected to the skimmer through a round entrance-to-square exit transition section. A pair of 3.1-cm-square brass electrodes were located flush with the internal walls of the channel approximately 40 cm downstream of the skimmer tube inlet. The Delrin liner, which extended 9 cm upstream and 40 cm downstream of the electrodes, provided electrical insulation between the high temperature, electrically conducting gas and the steel walls of the test section.

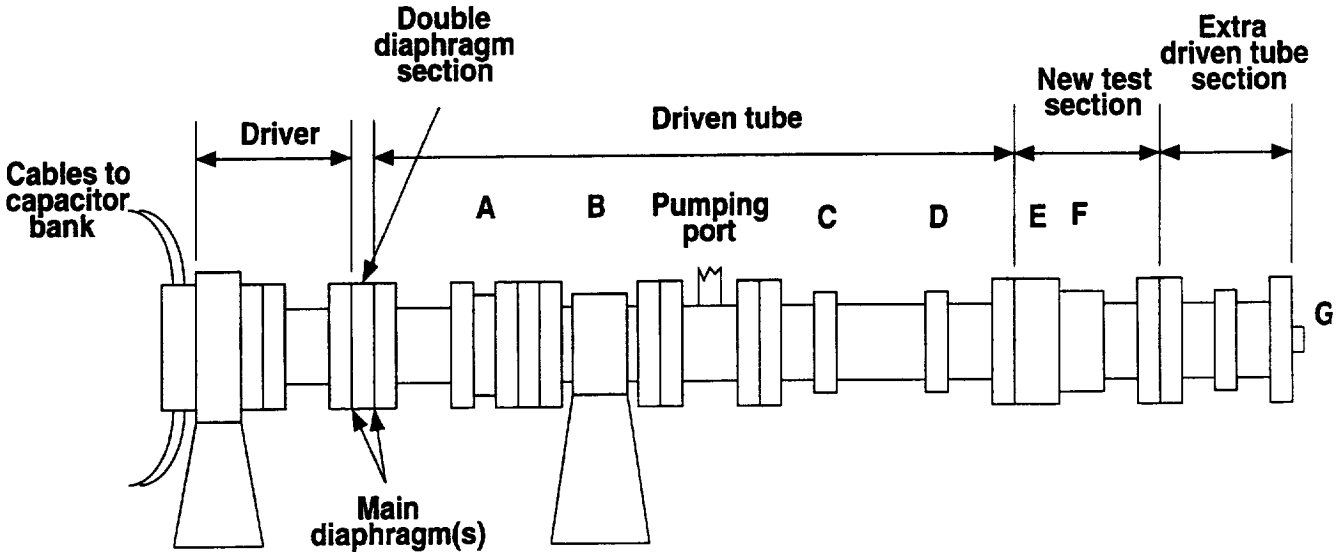

Figure 4- 39. NASA Ames EAST shock tube facility (not to scale).

Figure 4- 40 shows a cross-section of the 62-cm-long test section parallel to the axis and the diagnostic ports. Three interchangable skimmer tubes were designed and fabricated having different lengths (13, 23, and 33 cm) to allow the entry length to be changed and provide different boundary layer thicknesses at the electrode position in the test section. However, only the mid-length skimmer was used during the MARIAH Project testing.

A mixture of nitrous oxide and nitrogen ($2N_2O + 1.76N_2$) was used in the driven tube to simulate air. This mixture was chosen to provide the same N/O atom ratio as air after shock heating and to increase test time. A nominal shock velocity of 4.65 km/s was chosen to produce an ionization fraction of approximately 10^{-4}. Unfortunately, the shock velocity was found to vary as much as ±6% between successive, nominally identical tests. The driven tube fill pressures were chosen to provide nominal aftershock pressures of 2, 5, and 13 atm, thus providing three basic test conditions. A total of 51 test runs were made, including 36 satisfactory runs with current between the electrode pair.

Current to the electrodes was provided by a 720-μfd capacitive power supply that could be charged up to 4,500 V. The capacitor bank was connected to the electrodes through a salt-water ballast resistor. Another salt-water resistor was placed in parallel with the electrode gap. An ignitron tube was used as the switch to apply power from the charged capacitor bank to the electrode circuit. Initial voltages across the electrode pair at the instant power was applied ranged from 45 to 1,060 V, and the maximum electrode currents ranged from approximately 5 to 3,000 A, depending upon the applied voltage, driven tube pressure, and shock velocity.

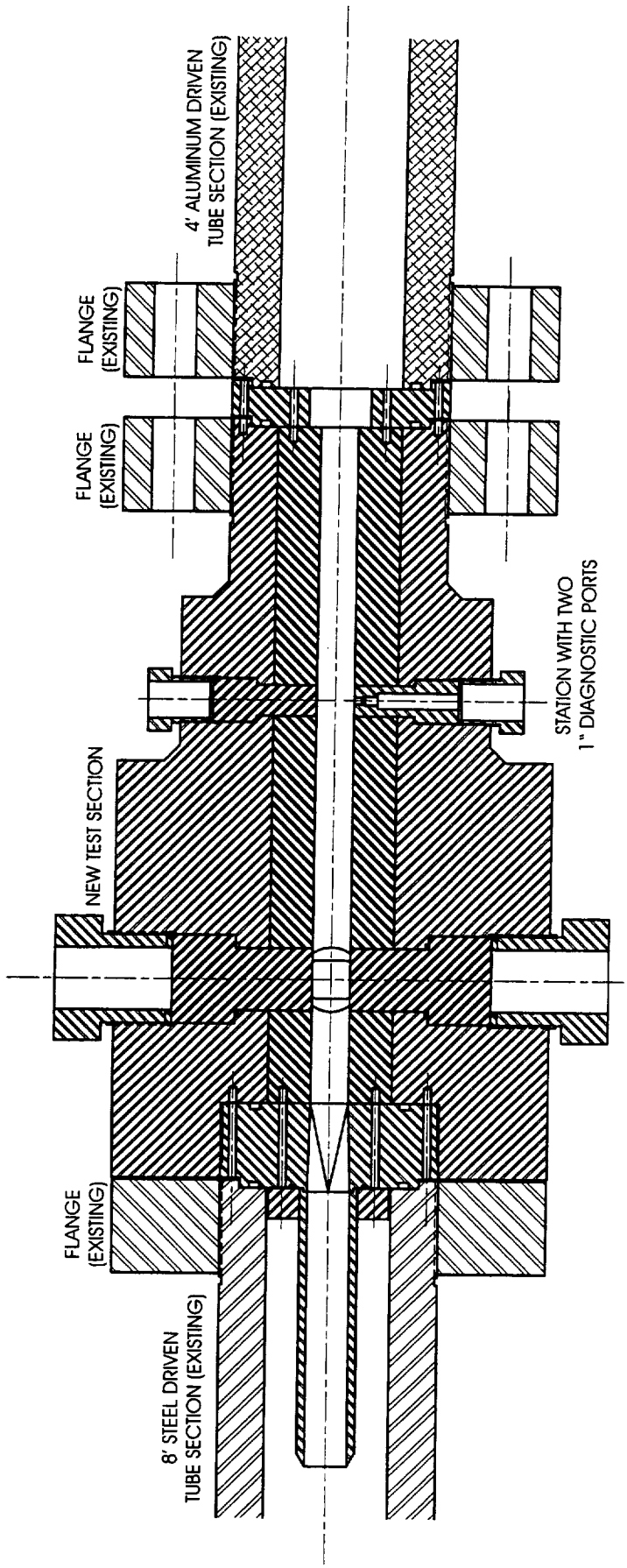

Figure 4- 40. Section through new test section parallel to channel axis and diagnostic ports.

4.2.1.3 Measurements and Diagnostics

The main diagnostic station, with four 2-inch nominal diagnostic ports, is located 10 cm downstream from the end of the transition section. Electrodes were located in two of these ports, and the remaining two ports were used to provide optical access to the plasma discharge. A pair of 1-inch nominal diagnostic ports were located 23 cm downstream of the electrodes to provide access for a pressure transducer and a photomultiplier tube, allowing measurement of the shock velocity and the test time duration in the square channel. This gave a measurement of the change in shock velocity that took place as the shock moved from the 10.16-cm-diameter driven tube to the 3.1-cm-square channel.

Routine shock tube diagnostics included ionization gauge shock detectors; quartz crystal, piezoelectric pressure gauges; and photomultiplier tubes (used to measure the total light emission). These diagnostics provided a measurement of the shock velocities and pressures and provided an indication of the arrival of additional shock waves, compression waves, rarefactions, and driver gas contamination. Diagnostics at the electrode station included electrical current and voltage measurements, nonspectroscopic optical measurements, high-speed video, and spectroscopic measurements.

Voltage across the electrode pair was measured using a voltage divider and also by measuring the current through a resistor connected in parallel to the electrodes. Electrical currents at both the top and bottom electrodes were measured using current transformers. Two 5-cm-diameter Plexiglas windows permitted the region between the electrodes to be viewed. Total light emission from the electrode region was initially measured using a photomultiplier tube. Later, this diagnostic was replaced by two monochromators tuned to look at a He line and 10 nanometers (nm) to one side of the He line to detect the arrival of the He driver gas contamination. Images of the flow in the region between the electrodes were obtained using an image converter camera (IMACON™) to provide up to eight frames at 4-μs intervals. Determination of the electron density from a measurement of the H-β line width was attempted. However, no reliable data was obtained due to the difficulty of making these measurements in the high-test section pressure (13 atm) and to an overlapping iron (Fe) line resulting from flow contamination from the tube walls or the diaphragm.

4.2.1.4 Test Results

Tests were conducted at a range of applied voltages for each pressure condition in order to evaluate the effect of electric field on the electrical properties of the plasma. Current and voltage histories were obtained from these runs and used to calculate an approximation to the plasma electrical conductivity. This "pseudo-conductivity" is obviously not the true electrical conductivity since it includes the voltage drops across the electrode fall regions. Figure 4- 41 shows some pseudo-conductivity histories for the 2-atm condition; these are typical of those at other test conditions.

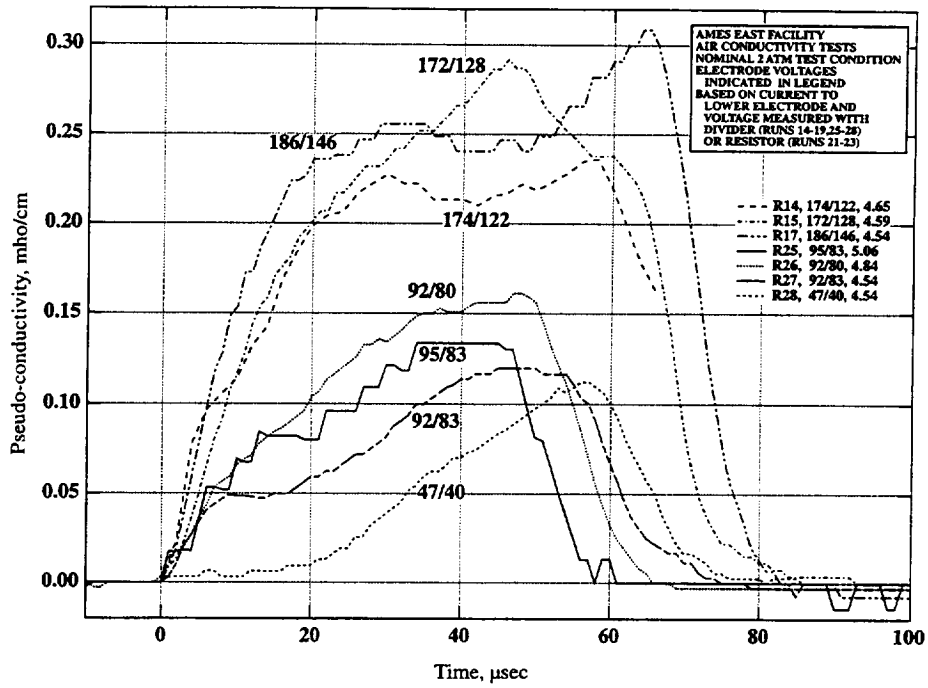

Figure 4- 41. Pseudo-conductivity histories for 2-atm nominal test condition.

A fraction of the current from the upper electrode (at a potential above ground) was found to be leaking to ground through the hot, electrically conductive plasma to the driven tube upstream of the insulating Delrin liner. The fraction of the diverted current was typically about 10% for runs with heavy currents but can be as much as 50 - 60% at the lowest currents, particularly towards the beginning of the current flow. Since the current flowing directly across the test section between the electrodes was of primary importance, almost all of the study results were based on the current flowing to the lower electrode. "Pseudo-conductivity" values were calculated using the measured voltage across the electrodes and the current to the lower electrode.

Most of the "pseudo-conductivity" histories show the following general features (see Fig. 4- 41). Pseudo-conductivity rises very rapidly for the first 7 to 30 μs, and this rise is generally followed by a region of high conductivity usually lasting about 20 to 50 μs. This high conductivity region can be fairly flat but can also be sloped or show a hump or humps at the beginning and/or end of the period. These various features in the high-conductivity region are thought to be due to conductivity changes consequent to the arrival of additional compression or rarefaction waves and the resulting temperature changes. The pseudo-conductivity starts to fall steeply 40 to 60 μs after the start of current flow.

At a nominal shock velocity of 4.6 km/s, the shock wave takes approximately 7 μs to cross the electrode face. Thus, the first part of the initial steep rise in pseudo-conductivity is probably due to the 7 μs required for the shock wave to completely fill the region between the electrodes with

heated gas. However, the pseudo-conductivity continues to rise substantially between 7 and 15 - 30 μs after the start of current flow. Two possible explanations are offered: a) The electron population may take this long after the shock wave passage to come up to a value that is in equilibrium with the gas temperature at the prevailing electric field; and b) the current may be flowing mainly in the boundary layers along the sidewalls extending between the electrodes. These boundary layers will initially thicken very rapidly with passing time; however, later on, they will tend to stabilize at a constant thickness. Finally, the rapid drop in pseudo-conductivity is believed to be due to the arrival of the much cooler driver gas 40 to 60 μs after the start of current flow.

The test time available from the start of current flow until the arrival of driver gas contamination was estimated from the time of the start of the final, rapid drop in pseudo-conductivity. This data showed the test times dropping from 50 - 70 μs at shock velocities of 4.5 km/s to 40 - 50 μs at 5.0 km/s and to approximately 30 μs at 6.3 km/s. Using the monochromators at the electrode station that are tuned on and to one side of a He line, it appeared the He driver gas contamination arrives roughly 10 μs before the start of the final (steep) drop in pseudo-conductivity is observed.

At each of the three test conditions, current, voltage, and pseudo-conductivity data at 15 and 30 μs after start of current flow were used to evaluate the effect of the applied voltage and current on the discharge characteristics. The voltages applied across the electrodes at the start of current flow ranged from 45 to 1,060 V. However, the voltage data 15 and 30 μs after the start of current flow were lower (from 40 to 490 V), due to the inability of the power supply to maintain the voltage during heavy current flow.

For each test condition, a theoretical equilibrium conductivity was calculated, and this was used as a benchmark against which to compare the experimentally measured values. Generally, the data from all three test conditions showed the following characteristics (see Fig. 4- 42). In the current range from approximately 2 to 300 A, the measured pseudo-conductivities were below the calculated equilibrium conductivity, being as much as 50 times less at currents of approximately 2 A. This ratio dropped to approximately 15 at currents of about 10 A and approximately 3 at currents of about 100 A. In these current ranges, it is believed that the bulk gas has a conductivity close to the theoretical equilibrium value; however, the resistance values of the electrode voltage drop regions increase very significantly at low current. In general, in the current ranges of 300 - 700 A, the pseudo-conductivity was found to be relatively close to the theoretical equilibrium conductivity.. In this current range, it is believed that the resistance of the voltage drop regions at the electrodes is very much smaller due to the heavier current, and the conductivity of the core flow gas predominates. Finally, in the current range of 700 – 3,000 A, the pseudo-conductivity is 30 - 100% above the theoretical core flow gas equilibrium conductivity. For the 2- and 5-atm test conditions, this increase can in part be explained by ohmic heating of the core gas. This explanation will not suffice for the 13-atm test condition. It is possible the high electric fields produce some nonequilibrium ionization under the high-current conditions, and this may be responsible for some of the observed increase in the pseudo-conductivity at the higher currents. This would seem less likely to be a possible explanation at the 13-atm condition where it should be much more difficult to obtain nonequilibrium.

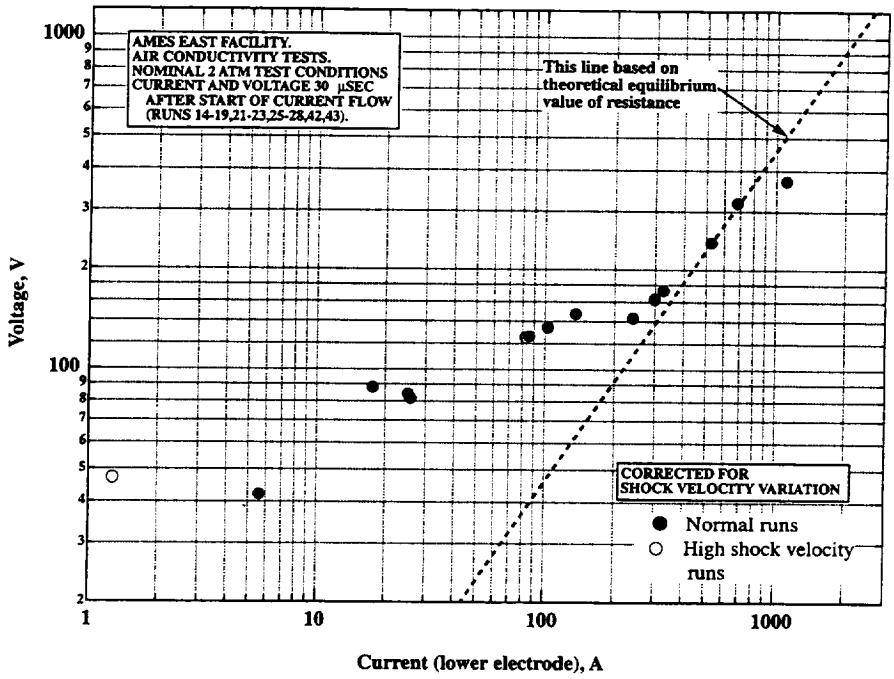

Figure 4- 42. 2-atm test conditions, voltages across electrodes 30 μs after start of current flow plotted vs. current to lower electrode 30 μs after the start of current flow. Corrected for shock velocity effect.

At the 2-atm test condition, there is a region in the voltage-current characteristics of the electrode gap where there is a large change in current (from approximately 100 A to 250 A) with almost no voltage change at the time that the current was measured. (The voltage was essentially constant at 140 V for this current range.) However, there was a voltage change at the beginning of the current flow between the runs with approximately 100 A and the runs with approximately 250 A. Hence, in these cases, 15 and 30 μs after the start of current flow, the electrode gap is likely responding to the voltages impressed on the gap at the start of current flow. (As mentioned previously, there is a considerable difference between the voltages at the start of current flow and the voltages 15 and 30 μs after the start of current flow because of the inability of the power supply to maintain the voltage during heavy current flow.)

The voltage-current characteristics of the electrode gap 15 and 30 μs after the start of current flow were generally found to be fairly similar for the three pressure conditions; however, at the lower voltages, considerably more current was drawn at the higher pressures. On comparing the pseudo-conductivity histories for the three pressure conditions, it was found that the conductivity values rose considerably more rapidly at the higher pressures. This is believed to be due to the more rapid approach to the equilibrium electron densities at the higher pressures.

A number of interesting features were observed in the IMACON photographs of the discharge region. An example IMACON Polaroid photograph for Run 18 at the 2-atm test condition is shown in Figure 4- 43. The run number, date, and test conditions are given at the top of the figure. Flow is from left to right in this photo, and the frame sequence is identified below the figure. Times given below the frames are measured from the start of current flow. A shock wave image first appears in the first frame and a second image of the shock appears in the second frame, allowing a determination of the shock velocity to be 4.4 km/s ±0.30 for this run. The oblique shock waves emanating from the leading edge of the electrodes are clearly visible in frames 2 through 5. Flow Mach number, determined from the shock wave angles, ranged from 2.24 to 2.48 for this test. Glow from the flow region near the electrode surfaces begins to overwhelm the rest of the field in the last three frames. The large dynamic range of the light emission over this 28-μs period is evident from a comparison of the faintness of the first two frame images with the near saturation in the last two. This aspect of the testing meant that a complete flow visualization of the total test period was rarely achieved.

Oblique shock waves were seen to emanate from the leading edges of the electrodes. The Mach numbers of the flow between the electrodes can be readily calculated from the angles of these shock waves. The theoretical Mach numbers in equilibrium flow behind a shock wave at the observed velocity in the electrode region were also calculated. In general, the experimentally observed Mach numbers are 0.20 to 0.45 less than the theoretical values. There are several possible explanations for this. Boundary layer growth, both natural growth without electrical energy deposition and enhanced growth due to electrical energy deposition, may help to throttle the flow somewhat and thus to reduce the Mach number. At higher currents, energy deposition in the bulk gas may result in a Mach number reduction. Further, the relatively low experimental Mach numbers may be due, in part, to the fact that the gas may not reach equilibrium prior to the photographs being taken and may not, therefore, have all of the degrees of freedom excited. This would lead to a specific heat ratio larger than the equilibrium value and a Mach number smaller than the equilibrium value.

Perhaps the most interesting feature observed in the IMACON photographs was the presence of "hot spots" on the electrode surfaces. For some test conditions, discrete, bright light sources could be seen on the electrodes. At the 2-atm test condition, fixed spots of bright light were frequently visible at the edges of both electrodes where the radii of the electrodes will produce an electric field increase. In addition, at the 2-atm test condition and the highest current levels, moving spots of light were visible on the lower electrode (the cathode). These were not observed at lower voltage and currents at the 2-atm test conditions and were not observed at all at the 5- and 13-atm test conditions. In general, a smooth glow was seen along the electrodes at the 5-atm and 13-atm test conditions. It was noted that this glow became progressively more intense after the shock wave passed in all three test conditions. However, the rate of increase of the electrode glow became progressively more rapid as the pressure increased. This may be due to the faster approach to equilibrium at higher pressures and densities and may well be closely connected with the more rapid current and pseudo-conductivity rises seen at higher pressures.

Run no: 18 **Date:** 5/8/97 **Shock press. At D:** 2.55 atm
Shock vel. At E: 4.72 km/s **Voltage at start of current flow:** 277 V

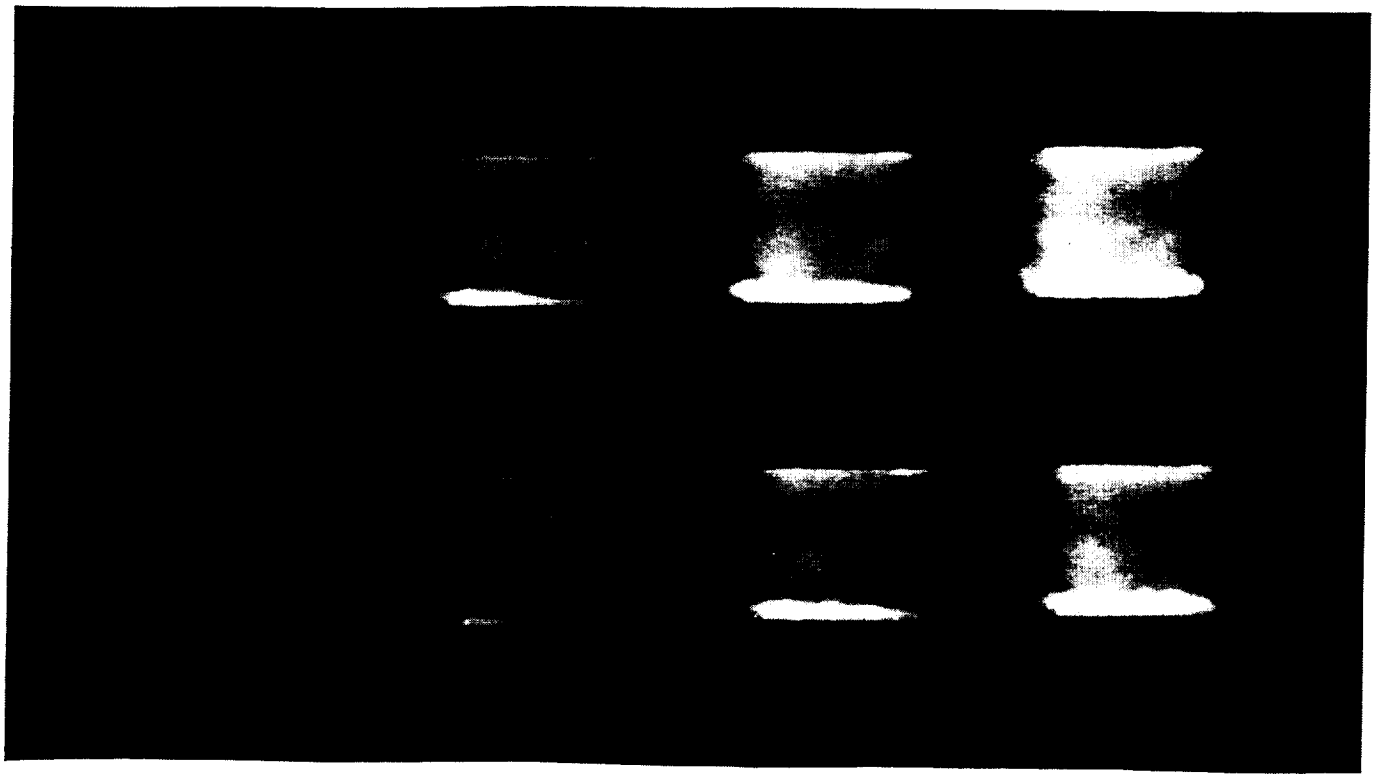

Frame:	**2**	**4**	**6**	**8**
Time:	5.2	13.2	21.2	29.2
Mach no:	2.24	2.32		
Frame:	**1**	**3**	**5**	**7**
Time:	1.2	9.2	17.2	25.2
Mach no:		2.42	2.48	

V_I: 4.6 km/s V_{CAV}: 4.96 km/s

Figure 4- 43. IMACON image of the shock-heated test gas flow in the electrode region. The time is measured from the start of the current flow. Mach numbers and velocities are deduced from the image as explained in Section 4.2.1.4.

4.2.1.5 NASA Ames Test Program Conclusions

From all of the data taken, including current and voltage histories, total light emission, monochromator histories, and the IMACON photographs, there appears to be no solid evidence of breakdown in the gas. Some of the current histories do show late increases in current prior to the final and steep drop in current. However, there are generally other runs at nearby conditions with higher voltages that show no evidence of such late increases in current. In addition, as stated previously, there is no indication of breakdown in any of the other diagnostics, including no indication of a sudden drop in voltage. The gas spends only approximately 7 μs traversing the electrode region and is continually renewed. This is believed to be the reason that the maximum voltages of approximately 1,050 V are not sufficient to cause breakdown in this flow geometry.

An electrical pseudo-conductivity was calculated for each test. Pseudo-conductivity values were generally found to be significantly less than theoretical equilibrium values in the core for applied electrical current in the 2- to 300-A range. For electrical current in the range of 300 – 700 A, pseudo-conductivity was found to be relatively close to theoretical values, and for the range 700–3,000 A, pseudo-conductivity was generally higher than theoretical. Low pseudo-conductivity values in the low current range are believed to be due to the resistance of the electrode sheath and boundary layer regions. Pseudo-conductivity values that are higher than the theoretical values for the high current tests are believed to be due to ohmic heating, which raises the gas temperature and electrical conductivity in the core region. However, at the highest pressure (13 atm), ohmic heating would not be sufficient to cause the change in electrical conductivity observed.

Further documentation of the research conducted at the NASA Ames EAST Facility is included in Appendix Section A.2. Graphs of the data for all powered tests, including measured voltage and current and the calculated pseudo-conductivities, are provided for all powered tests at the end of Section A.2. It is worth emphasizing that the joint MSE/NASA Ames test program represents one of the few experimental efforts in which data for conductivity in air at high temperatures and pressures has been systematically collected.

4.2.2 University of Texas at Arlington Test Program

4.2.2.1 Overview

A principal objective of the MARIAH Project was to investigate the feasibility of using MHD augmentation of high-pressure arc heaters as the basis for development of a continuous-flow hypervelocity wind tunnel optimized for testing advanced air-breathing hypervelocity propulsion systems. In particular, the facility should be capable of providing post-bowshock conditions for testing advanced concepts such as the Pre-Mixed, Shock-Induced Combustor (PM/SIC) Engine (Ref. 93). In order to simulate this test environment in an MHD-augmented test facility, preliminary design studies indicate that accelerator channel static pressures on the order of

100 atm may be required (Ref. 95). Unfortunately, the previous operational experience base for MHD accelerator operation was at pressures on the order of 0.5–5 atm (Refs. 3, 96). Development of MHD accelerators capable of operating at high pressures will require improved understanding of a variety of technical issues. These include the effect of high pressures on the electrical conductivity and Hall parameter for equilibrium and nonequilibrium plasmas, the structure and stability of the current discharge, and plasma electrical breakdown characteristics.

In support of the MARIAH Project, UTA conducted an experimental investigation of critical electrical phenomena associated with operation of MHD accelerators at high pressure. The objectives of the UTA investigation were to:

1. Develop an experimental apparatus for measuring the electrical conductivity of high-pressure seeded plasma.
2. Conduct an experimental investigation of the effect of applied electric field, static temperature and pressure, and seed concentration on the bulk electrical conductivity of the plasma.
3. Perform these experimental investigations using K-seeded air as the working gas and repeat the experiments at selected conditions using N_2 for comparison to determine the effects of electron attachment to O_2 on the electrical conductivity.

The results of this research are summarized in this section and discussed in more detail in Appendix Section A.1.

4.2.2.2 Test Hardware Description

The UTA shock tunnel facility, prior to modification for the MARIAH Project, is shown schematically in Figure 4- 44 and is described in detail in References 97 and 98. The shock tube is composed of a 15.2-cm-diameter (6-in.), 3.05-m-long (10-ft) driver tube, and a 15.2-cm-diameter (6-in.), 8.23-m-long (27-ft) driven tube, each rated for a pressure of 41.3 MPa (6,000 psi). A double-diaphragm section separates the two tubes.

In its original configuration, the UTA shock tube could not produce the high test section pressure and temperature required to support the MARIAH Project testing. To provide the necessary conditions, UTA converted its existing pressure-driven hypersonic shock tunnel into a detonation-driven shock tube. Other concepts for enhancing the performance of the existing facility were briefly considered, including the use of an electrical (Refs. 99, 100) or combustion-heated (Refs. 101, 102) light gas driver and a free piston driver (Ref. 103). Although the free piston driver probably has the highest performance capability, Bakos and Erdos (Ref. 104) have shown that the detonation driver offers somewhat comparable performance at a lower cost. Furthermore, a substantial experience base had been developed at UTA to support this approach via an ongoing research program to develop Pulse Detonation Engine (PDE) concepts (Refs. 105, 106). Much of the technology developed as part of that program was directly applicable to the detonation-driven shock tunnel.

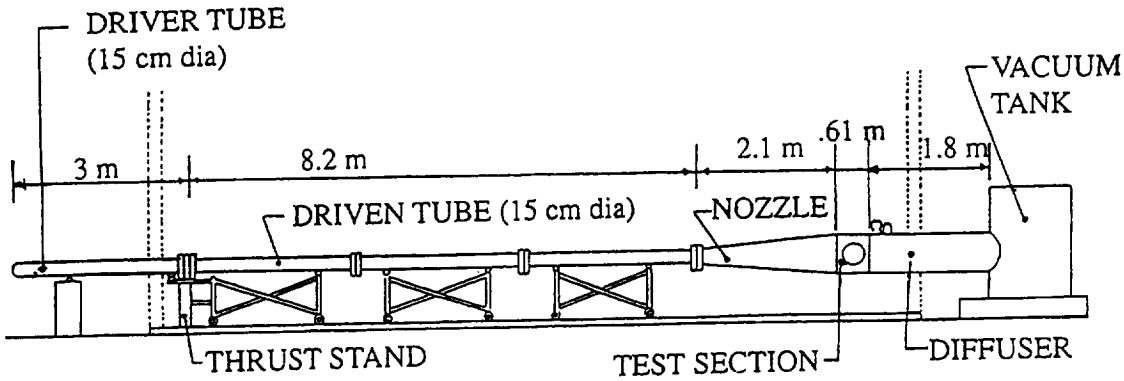

Figure 4- 44. Schematic of UTA shock tunnel.

The detonation-driven shock tube was first proposed by Bird in 1957 (Ref. 107) and has been subsequently studied by several investigators (Refs. 104, 108, 109, 110, 111, 112, 113, 114, 115). A detonation process is typically established in a driver tube filled with a near-stoichiometric mixture of N_2 and O_2, although other gas combinations are possible. Initial pressure levels prior to detonation can be quite low, thus eliminating the need for thick metal diaphragms. A relatively low molecular weight driver gas at high temperature and pressure levels is produced from the detonation process. The detonation wave produces a sudden pressure rise causing the primary diaphragm to rupture, thus establishing a shock wave in the driven tube filled with air.

This device may be operated in either an "upstream propagation" or a "downstream propagation" mode. In the "upstream propagation" mode, the ignition source is placed just upstream of the primary diaphragm producing a detonation wave that propagates from the diaphragm, upstream through the driver tube. The pressure rise following the detonation wave ruptures the primary diaphragm to establish the flow in the driven tube. In the "downstream propagation" mode, the ignition source is located at the upstream end of the driver tube, producing a detonation wave that travels from the upstream end wall of the tube, downstream through the driver tube, rupturing the primary diaphragm on impact. For either mode, further performance enhancement is possible by adding He dilution to the H_2/O_2 driver tube mixture. Helium dilution raises the sonic speed in the driver gas and also somewhat reduces the danger associated with premature detonation of the H_2/O_2 mixture. Performance calculations by Yu et al. (Ref. 111) indicate the performance degradation caused by the slight lowering of the detonation temperature due to He dilution is more than adequately offset by the increased sonic speed of the driver tube gas.

Detonation Driver (Arc-Ignition Mode)

The driver from the existing shock tunnel was modified to serve as the detonation driver, and ports for four surface-mounted pressure transducers were installed to monitor the behavior of the detonation wave. Ports were also installed for an ignition plug at each end so both upstream and downstream propagation modes could be evaluated. The tube had two ports for injecting gases. These were used for injecting H_2, O_2, air, and He as well as for vacuuming out the initial air and venting the combustible mixture in case of an aborted run. The shock tube retained the same pressure rating converted to a detonation driver.

Arc Ignition System

An arc ignition system was constructed from an adaptation of the ignition system developed at UTA for the PDE program (Refs. 105, 106). A single high-voltage, high-current arc plug, driven by a capacitor bank power supply, was used for the ignition source. A high frequency unit in the arc-ignition power supply initially ionizes a path between two flush-mounted, pin electrodes, and capacitors then discharge through the ionized path in a high current arc to provide the necessary ignition energy. The arc ignition system is discussed further in Appendix Section A.1.

Driven Tube

The original driven tube was replaced with a new tube of type 304 stainless steel with a 4.12-cm (1.62 in.) internal diameter and a 9.14-m (30 ft) length. The tube was commercially available and had a pressure rating of 19 MPa (2,800 psi), sufficient for nonreflected mode needed to support the MARIAH Project testing. This combination of driver and driven tube produced a driver-to-driven tube area ratio of 14.7, thereby providing an additional improvement in performance.

Initial Test Results (Arc-Ignition Mode)

The initial operation of the modified shock tube consisted of a series of test runs at increasing pressure levels to verify the design and refine operating procedures. The first test run was with a stoichiometric mixture of H_2 and O_2 in the driver at an initial pressure of 1 atm. The driven tube contained atmospheric air and was separated from the driver tube by a 0.381-mm-thick (0.015 in.) Mylar™ diaphragm. Thin Mylar could be used since the initial pressures were low and the post-detonation pressure is typically about 20 times the initial level. Subsequent tests increased the initial detonation tube pressure to 8 atm. Both upstream and downstream propagation modes were examined.

The overall performance map of the modified shock tube was obtained by conducting a parametric variation of both driver and driven tube pressures and by introducing varying amounts of He dilution. Test results are summarized in Figure 4- 45. The performance was

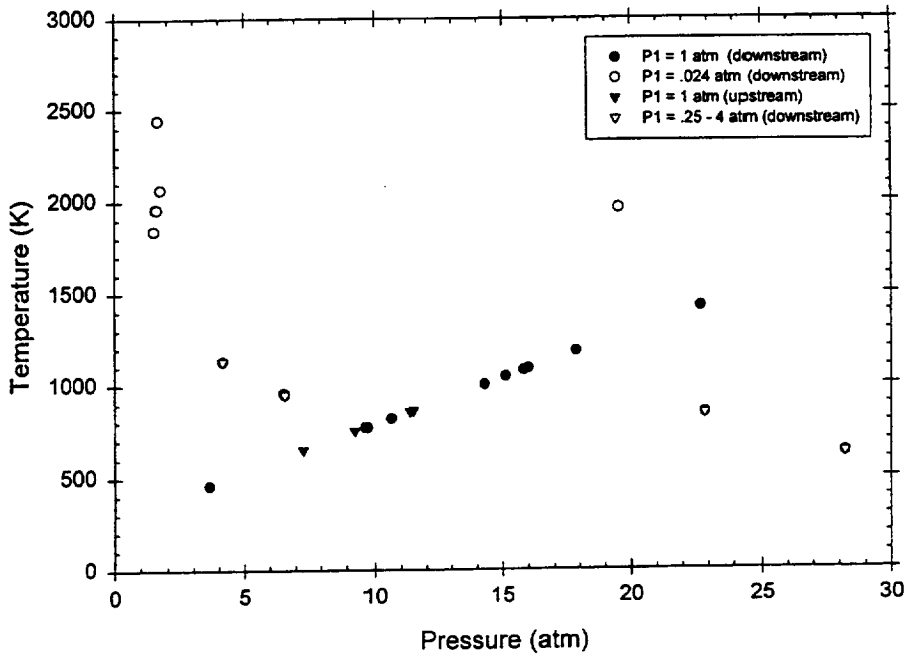

Figure 4- 45. Experimental performance map, electrical arc-ignition.

considerably less than predicted. An analysis of the test data for the downstream propagation mode suggested the following reasons for the low performance. A strong expansion wave, generated to satisfy the zero velocity boundary condition at the closed end of the tube, followed the incident detonation wave. This expansion wave caused an immediate drop in pressure from the Chapman-Jouguet level generated by the incident detonation wave, and the interaction of this expansion wave with the reflected detonation wave appeared to drastically lower the pressure level behind the reflected detonation wave. It is this pressure that initiates and sustains the incident shock wave propagation in the driven tube, and as a result, very rapid attenuation of the incident shock wave is suspected.

A somewhat different cause is suspected for the reduced performance with the upstream propagation mode of operation. A detailed analysis of the pressure data indicated the initial wave formation is a weak detonation wave ($M_D \sim 1.7$) that transitions to a fully developed CJ detonation wave ($M_D \sim 5.3$) about 50 cm (20 in.) from the ignition source. The fact that a CJ wave does not form immediately upon ignition probably interferes with the formation of a strong incident shock wave in the driven tube. A further adverse effect may arise from the fact that the upstream propagation mode induces a flow following the incident detonation wave in the opposite direction to the flow induced in the driven tube, and additional loss of momentum is required to reverse this flow direction.

Recommendations for Modification of Detonation Driver

Unfortunately, as a result of the reduced performance of the detonation-driven shock tube, it was concluded that the original performance goals could not be met with this configuration. Detailed analysis of the test data from the calibration suggested the shock speeds were considerably lower than predicted, thus drastically lowering the pressure and temperature levels generated by the incident shock wave. An analysis of these test results, as well as discussions with Drs. John Erdos and Robert Bakos of GASL and Dr. Dave Bogdanoff of NASA Ames, identified two reasons for the poor performance. The primary reason was attributable to the Taylor rarefaction wave associated with the arc-ignition process for the downstream mode and the combined effects of reduced pressure due to the inability to directly initiate a CJ detonation wave and the required flow reversal for the upstream mode. A secondary factor can be attributed to shock attenuation due to an overly long driven tube, which can be quite easily remedied.

Thus, the poor performance of the UTA detonation-driven shock tube was attributable to the arc-ignition process for initiating the detonation. To alleviate this problem, a modified ignition process based on the "light gas driver tube" concept implemented by GASL in their expansion tube facility (Refs. 114, 115) was adopted. The arc-ignition process was then replaced with the light gas driver tube to generate the detonation wave in the combustible mixture by rupture of a diaphragm between the driver tube and the detonation tube. This concept is summarized in the following section and discussed in detail in Appendix Section A.1.

Shock-Induced Detonation Driver

Figure 4- 46 (adapted from Ref. A.1-115) is an illustration of the light-gas, shock-induced detonation mode concept. A high-pressure air or He driver, upstream of the detonation tube, drives a shock wave into the detonation tube when the diaphragm between the tubes is ruptured. This shock wave should quickly transition to a CJ detonation wave; however, the rarefaction wave associated with the closed-end operation of the detonation tube should be drastically reduced because of a reduction of the strength of the Taylor rarefaction wave, thus resulting in a higher pressure behind the detonation wave. In effect, the driver tube exhaust acts like a "gas piston" to sustain the pressure behind the incident detonation wave. In fact, in the "perfectly driven" mode (discussed further in Appendix Section A.1), the full CJ pressure level can be maintained behind the detonation wave.

Facility Modifications

The necessary facility modifications were implemented by reconfiguring the detonation driver tube back to its original pressure-driven mode of operation and converting one of the original 2.74-m- (9-ft), 15.2-cm-diameter (6-in.) driven-tube sections to become the detonation tube section. The original double-diaphragm section was reinstalled between the upstream driver tube and the detonation tube, and the 4.12-cm-diameter (1.62-in.) driven tube was shortened to a length of 3.05 m (10 ft) to reduce shock attenuation due to boundary layer growth behind the

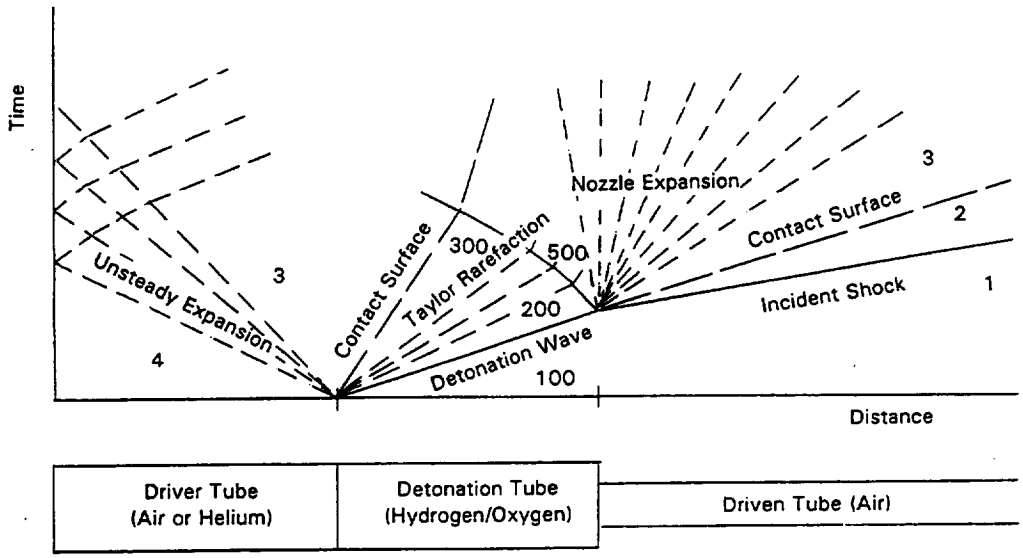

Figure 4- 46. Wave diagram depicting shock-expansion tube operation with a shock-induced detonation driver.

incident shock. The new detonation tube was also modified to allow insertion of four pressure transducers to monitor the detonation wave development.

Test Results from Shock-Induced Detonation Mode of Operation

After modification to operate in the shock-induced detonation mode, the detonation tube was tested using both air and He for the driver. For these tests, the detonation tube contained a stoichiometric mixture of H_2 and O_2 at various pressures. These tests indicated that near perfectly driven detonations could be achieved with a He driver, and the pressure drop due to the Taylor rarefaction wave could be considerably reduced or eliminated. Furthermore, the pressure level achieved by the reflected detonation wave was much higher, and the corresponding driven-tube Mach numbers were increased to as high as 7.65. Thus, it appears the shock-induced detonation mode offers substantial gains in performance by reduction or possible elimination of the Taylor rarefaction wave.

The composite performance map for the shock-induced detonation driver is shown in Figure 4-47. The peak shock Mach number obtained with the air driver was 10.71, resulting in a post-shock temperature and pressure of 4,190 K and 9.8 atm, respectively. The highest post-shock pressure attained with the air driver was 21 atm, with a corresponding temperature of 2,058 K. As anticipated, use of He in the upstream driver resulted in considerable improvement in performance. There was a general increase in both temperature and pressure over that attainable

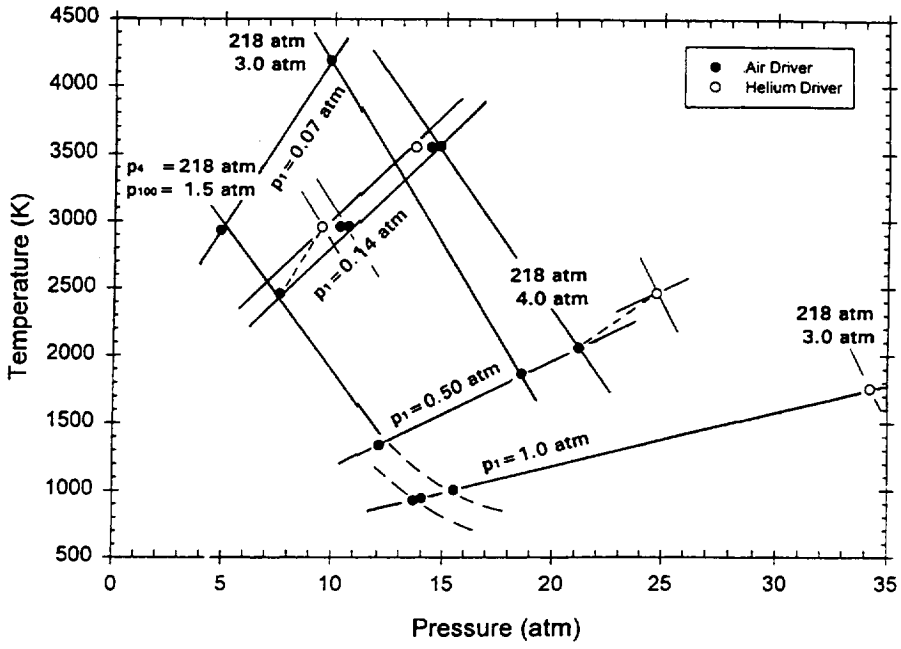

Figure 4- 47. Composite performance map, shock-induced detonation mode.

with the air driver for comparable conditions. A comparison of Figures 4- 45 and 4- 47 shows that a significant enhancement in shock tube performance was realized by incorporation of the shock-induced detonation mode over that attainable with the arc-initiated detonation.

Conductivity Measurement Channel

The plasma electrical conductivity was measured in a channel connected to the end of a 3.05-m (10-ft) driven tube section. The conductivity measurement channel was adapted from a design by Garrison (Ref. 116) and consisted of a pair of powered electrodes to provide an axial electrical field and 20 probe electrodes, separated by insulators, to measure the axial voltage distribution. The major components are displayed in Figure 4- 48. The inside and outside diameters of all electrodes were 40.0 mm (1.576 in.) and 139.7 mm (5.5 in.) respectively, and their thicknesses were 9.53 mm (0.375 in.) for the powered electrodes and 3.18 mm (0.125 in.) for the probe electrodes. Teflon™ insulator rings of the same inside and outside diameters were interspersed with the electrodes to electrically isolate all electrodes.

The total length of the measurement channel, including the powered electrodes, the probe electrodes, and the insulators was 115.9 mm (4.56 in.). As shown in Figure 4- 48, the electrodes and insulators were clamped together with four threaded steel rods, which isolated them from the

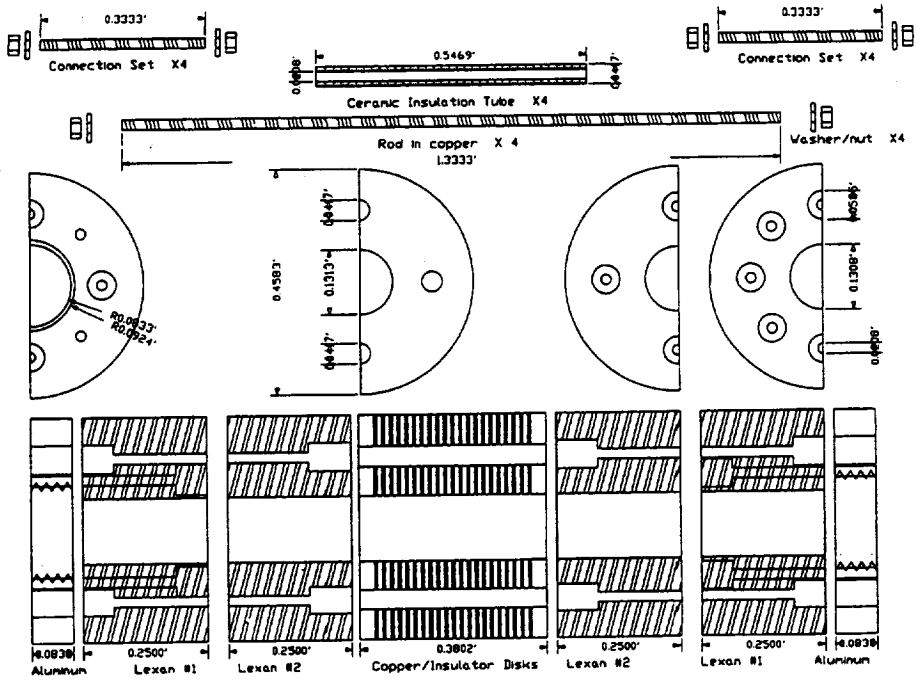

Figure 4- 48. Electrical conductivity channel.

electrodes by sheathing them with ceramic tubing. Lexan™ insulator segments 15.2 cm (6 in.) in length were mounted on both ends of the conductivity channel to prevent the applied voltage from shorting to ground. A 2.61-m (8.57-ft) section of driven tube was also installed downstream of the conductivity channel to prevent shock reflections from the downstream diaphragm returning to the test section prior to termination of the test window.

Initial tests of the conductivity channel installed in the detonation-driven shock tube resulted in two separate incidents that exposed several design deficiencies in the channel. These incidents occurred when the channel was subjected to higher pressures than were anticipated in the original design. When the mode of operation was changed from the arc-ignition to the shock-induced detonation mode, the pressures behind the incident shock remain the same; however, the channel was subjected to much higher pressures during the blowdown process. The first incident occurred when peak internal pressures on the order of 10.2 MPa [1,500 pounds per square inch absolute (psia)] were generated within the conductivity channel during the blowdown process and resulted in tensile failure of the Teflon insulators. The second incident occurred when high-pressure gas leaked between the insulators and copper plates causing an axial loading sufficient to create a tension failure of the axial tie rods and damaged the copper electrode plates and insulators beyond repair.

These design deficiencies were corrected by fabricating a containment structure of aluminum (Al) to accommodate the radial pressure loads and increasing the tie rod strength and diameter to support the axial load. Also, two steel plates were fabricated for each end of the channel, which were also tied together with high-strength bolts for application of compressive stresses to the channel. Finally, the plates were anchored to the shock tube thrust stand with high-strength chains. A photograph of the final assembly is shown in Figure 4- 49. These modifications proved to be adequate, and no mechanical problems were encountered in subsequent tests.

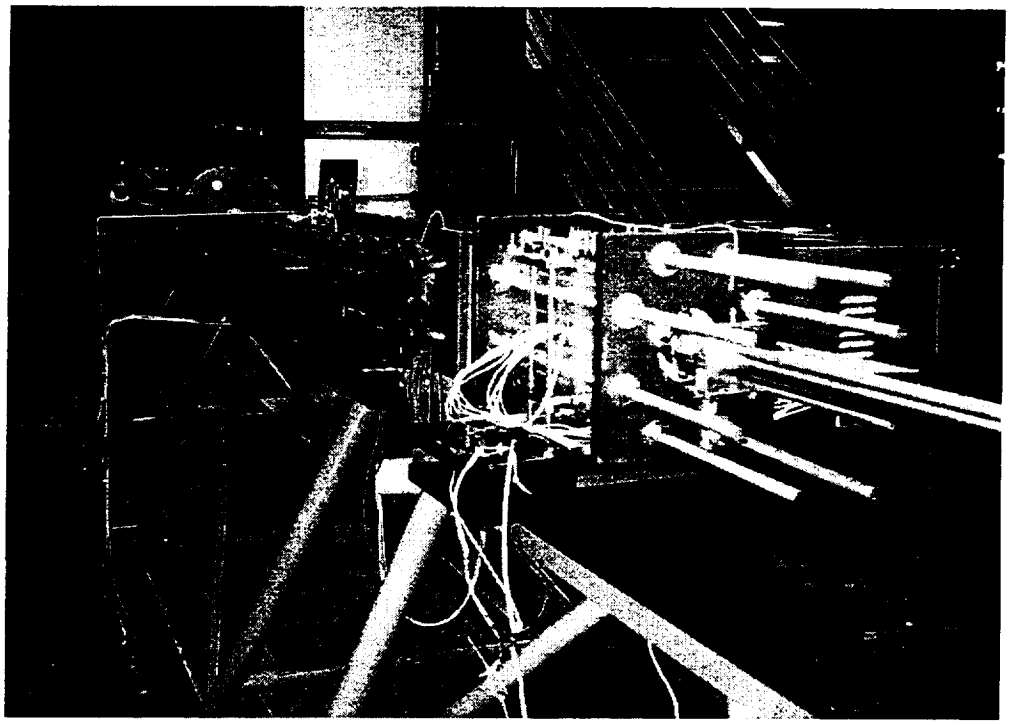

Figure 4- 49. Photograph of final conductivity channel installation.

Seed Injection System

Since the focus of the UTA research program was to investigate the electrical properties of seeded, high-pressure plasmas, a method was developed for injecting an alkali metal seed material uniformly throughout the driven tube prior to initiating the flow through the shock tube. The seed injection apparatus was designed to inject either K_2CO_3 or cesium carbonate (Cs_2CO_3) in dry powder form into the driven tube upstream of the electrical conductivity channel; however, only K_2CO_3 was used during the test program.

Two solenoid valves were used to control the inlet and outlet air through the seed injector column. The entire seed injection system was mounted on a vibration mechanism to prevent coagulation of the seed. The seed was injected into the driven tube through a nozzle assembly designed to inject the seed parallel to the axis of the tube in both upstream and downstream

directions in order to spread the seed material uniformly throughout the driven tube. The nozzle assembly was inserted into the tube from a cavity in the side of the driven tube by the applied air pressure. Once the pressure was removed, a spring retracts the nozzle assembly into the cavity to remove it from the flow path during operation.

4.2.2.3 Experimental Program Results

Test Objectives

The objectives of the conductivity tests were to conduct an experimental investigation of the effect of applied electric field, static temperature, static pressure, and seed fraction on the electrical conductivity of a seeded air plasma. Also, seeded N_2 experiments were to be conducted to examine the effect of electron attachment to oxygen ions. Finally, a test was to be conducted to match the fluid density and electron mole fraction in the UTA facility to one of the NASA Ames test points that used unseeded air so that a comparison of the data from the two facilities could be made. The resulting test plan is shown in Table 4- 9.

Table 4- 9. Proposed test matrix.

RUN SERIES	p_2 (atm)	T_2 (K)	SEED	V_2 (v)	COMMENTS
1	9.5-11	3,000	1%	400 600 800	Test to define *V-I* curve
2	9.5-11	3,000	2%	600	Effect of increased seed fraction
3	9.5-11	2,500 2,500	1%	600	Effect of temperature on conductivity
4	TBD	TBD	TBD	600	Test to match Ames electron mole fraction
5	9.5-11	3,000 2,500 2,500	1%	600	N_2 test series
6	20-25	3,000	1%	400 600 800	*V-I* curve at increased pressure
7	20-25	3,500 2,500	1%	800	Effect of temperature on conductivity at elevated pressure
8	20-25	3,000	2%	800	Effect of increased seed fraction
9	9.5-11	3,000	1%	1,000 1,200 1,400	Effect of Joule heating on conductivity

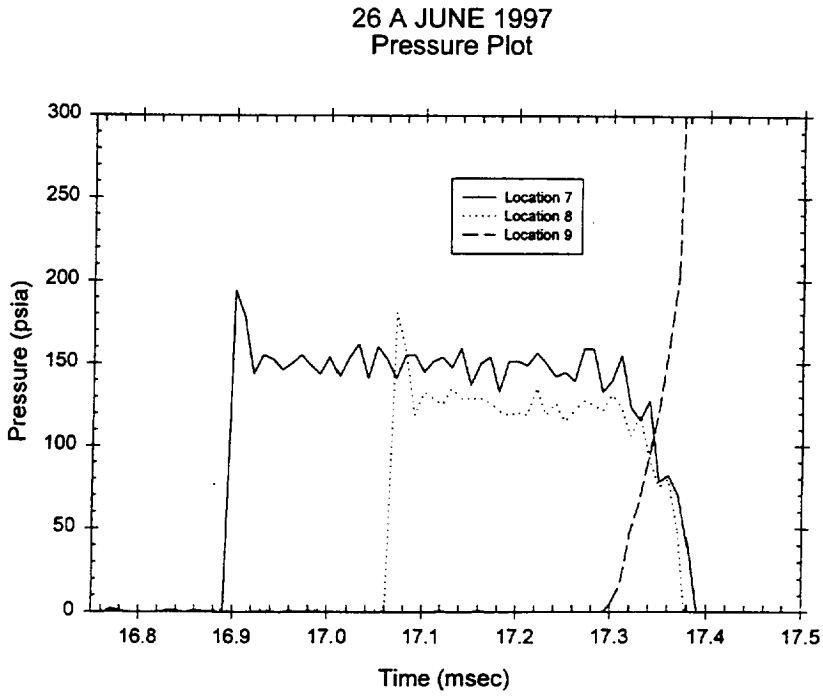

Figure 4- 50. Driven tube pressure vs. time for June 26A test.

Summary of Test Results

Results from a typical conductivity test run (Run 26A June) are illustrated in Figures 4- 50 through 4- *53*. The conditions for this run were a shock Mach number of 7.76, T_2 of 3,010 K, p_2 of 8.5 atm, applied voltage of 417 V, and seed rate of 1% by weight. The pressure traces from the three pressure transducers located in the driven tube are shown in Figure 4- 50. The traces from the first two transducers were used to determine the shock speed. The pressure p_2 and temperature T_2 following the incident shock were calculated as a function of the initial pressure and temperature in the driven tube and the calculated shock speed.

The unusual behavior observed at t≈17.3 ms is thought to be the result of interference induced in the piezoresistive pressure transducers from the current flow in the channel. This phenomenon was not observed at low currents. The abrupt change in pressure transducer output at t≈17.3 ms coincides with the initiation of current flow in the channel, and the transducer output returns to a steady pressure level at t≈18.1 ms (not shown), which approximately coincides with the decay of the current to near zero.

Figure 4- 51 shows the voltage vs. time traces. The top curve is the total applied voltage across the powered electrodes. The probe electrodes do not sense any voltage until passage of the incident shock. Their voltage levels quickly reach a maximum value in about 20 μs and then

drop as the initiation of current flow from the capacitor bank causes a slight drop in the power supply output voltage and the formation of the electrode voltage drops. The voltages then rise to a second peak after the arrival of the contact surface when the electrical conductivity begins to rapidly drop. An examination of the current vs. time trace (Fig. 4- 52) shows the peak current occurs at about 17.6 ms, which coincides with the minimum applied voltage.

Finally, the average conductivity was calculated as a function of time from the Ohm's Law relation:

$$\sigma^* = \frac{j}{E} = \frac{I / A}{\Delta V_C / \Delta x} \qquad (4\text{- }14)$$

and is shown in Figure 4- 53. The conductivity variation appears to closely follow the measured current variation.

The rate of current rise is slower than the designed rate. This was initially thought to be due to an impedance mismatch between the power supply and the plasma load. However, a simulation of the transient characteristics of the power supply indicated the current rise time should be on the order of 10-20 μs for a constant load. This analysis suggested that a more probable cause of the slow rise time is an actual variation in plasma resistance with time. Two possible reasons for the plasma resistance variation with time could be the finite times required for vaporization, dissociation, and ionization of the K_2CO_3 seed material, as well as a nonuniform distribution of seed material in the driven tube. The estimated duration of the test window, defined as the region between the incident shock and the contact surface, was 185 μs for this run, which means that the peak current occurs approximately 200 μs after the theoretical time of passage of the contact surface through the conductivity channel. The electrical conductivity of unseeded combustion products would be very low compared to that of seeded air, yet the peak current and peak electrical conductivity occurred after passage of the contact surface. This implies that some of the seed must have been entrained in the detonation products following the contact surface rather than being evenly distributed in the test gas slug (region 2 on Fig. 4- 45).

As can be seen in Fig. 4- 52, the current does not drop to zero, and the voltage distribution over the probe electrodes stabilizes to a near constant level. During this period, the unseeded detonation tube combustion products, which have a small but measurable conductivity, are passing through the conductivity channel.

The voltage vs. time data was then cross-plotted to determine the axial voltage gradients vs. distance for the time corresponding to the theoretical passage of the contact surface and the time corresponding to the peak current. These results are shown in Figure 4- 54. The voltage gradient data was then used to calculate the axial electric field.

$$E = -\frac{\Delta V_c}{\Delta x} \qquad (4\text{- }15)$$

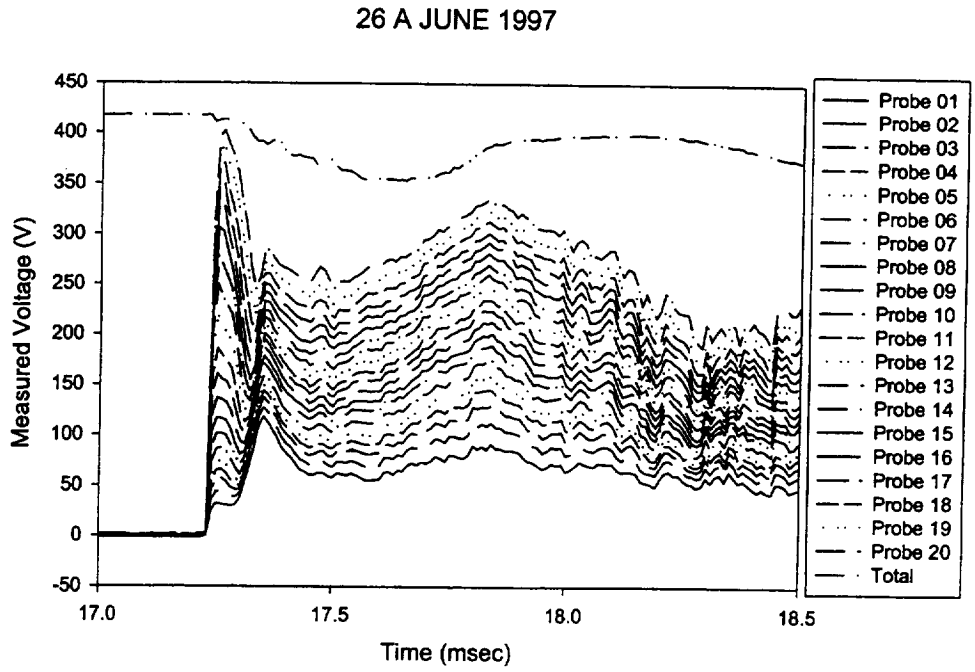

Figure 4- 51. Voltage vs. time for June 26A test.

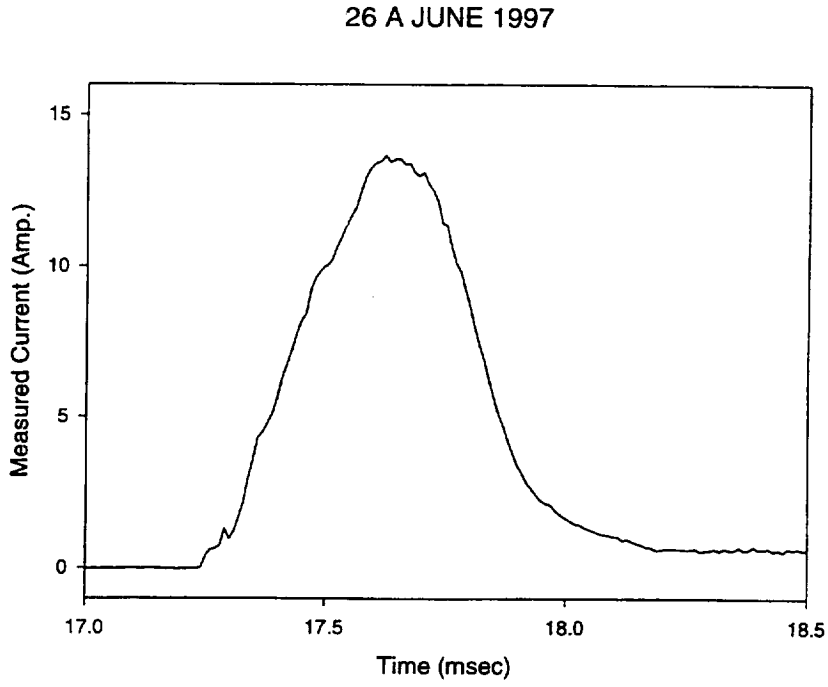

Figure 4- 52. Current vs. time for June 26A test.

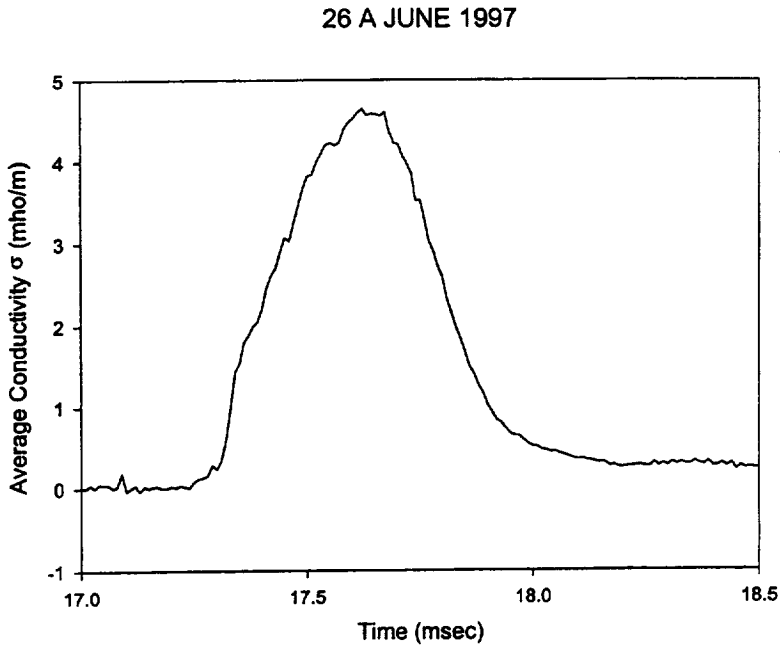

Figure 4- 53. Average conductivity vs. time for June 26A test.

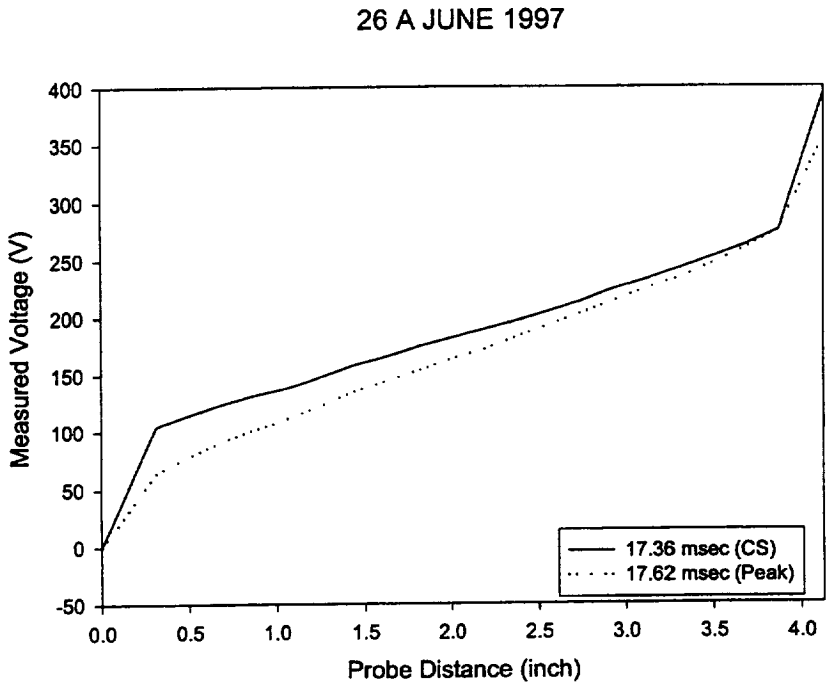

Figure 4- 54. Voltage vs. distance for June 26A test.

The electric field calculation was based on the voltage gradient between probe electrodes 1 and 20 since the higher gradients at the front and rear of the channel (Fig. 4- 54) correspond to the end effects in the powered electrode regions. These 2-D end effects include surface work functions, voltage drops across the boundary layers, and curvature of current filament lines in the powered electrode region.

A summary of all experimental results and test data for all powered tests is presented in Appendix Section A.1. Testing was accomplished in a moderate pressure regime (9.5-11 atm) and the higher pressure regime (20 - 25 atm) with various values of applied voltage and seed fraction. Unfortunately, the test program was terminated prematurely during the high-pressure test series when an electrical breakdown apparently occurred in the channel. Testing at high values of applied voltage to assess the effects of Joule heating on the electrical conductivity was not accomplished. However, some Joule heating effects were noted at the lower values of applied voltage and are reported in Appendix Section A.1.

Comparison with Theoretical Models

The calculated values of average conductivity based on the experimental measurements are compared with theoretical calculations of conductivity in Figure 4- 55 for the nominal 10-atm data. The theoretical values were calculated with the modified version of the NASA chemical equilibrium code, using the Demetriades and Argyropoulos conductivity model (Ref. 117). The conductivity values calculated from the experimental measurements, both at contact surface passage and at peak current, are shown in Figure 4- 55. In general, the measured conductivities are lower than the theoretical values, with the experimental conductivities ranging from a factor of 2 above theory at low temperatures to a factor of 4 below theory at the highest temperatures using the peak current. The experimental results are uniformly lower than theory using the current measured at the passage of the contact surface. The experimental results ranged from a factor of 5 below the theory at low temperatures to a factor of 13 below the theory at high temperatures.

A plot of average conductivity vs. temperature for the nominal 20-atm test runs is presented in Figure 4- 56. The absolute levels of conductivity are considerably higher than the theoretical predictions for this set of data. A much flatter trend with increased temperature is also observed. The measured current levels were much higher for these cases, but an analysis of the temperature rise due to Joule heating again showed the conductivity increase should be quite small. Also, the possibility of leakage current due to a breakdown of the insulators cannot be discounted as it was during this sequence of runs that the electrical breakdown occurred.

Finally, a comparison between experimental and theoretical conductivities for seeded N_2 plasma is presented in Figure 4- 57 for a nominal pressure of 10 atm. The experimental conductivities for seeded N_2 are considerably higher than for seeded air, whereas the theoretical values for the two plasmas are roughly comparable for the Demetriades and Argyropoulos model. The measured values of conductivity ranged from 85% of theory for the peak current and 75% of theory at the contact surface current at higher temperatures to 3.3 times the theory for the peak current and 2.3 times the theory for the contact surface current at low temperatures. Thus, the phenomenon of electron attachment by positive oxygen ions appears to have some degree of validity.

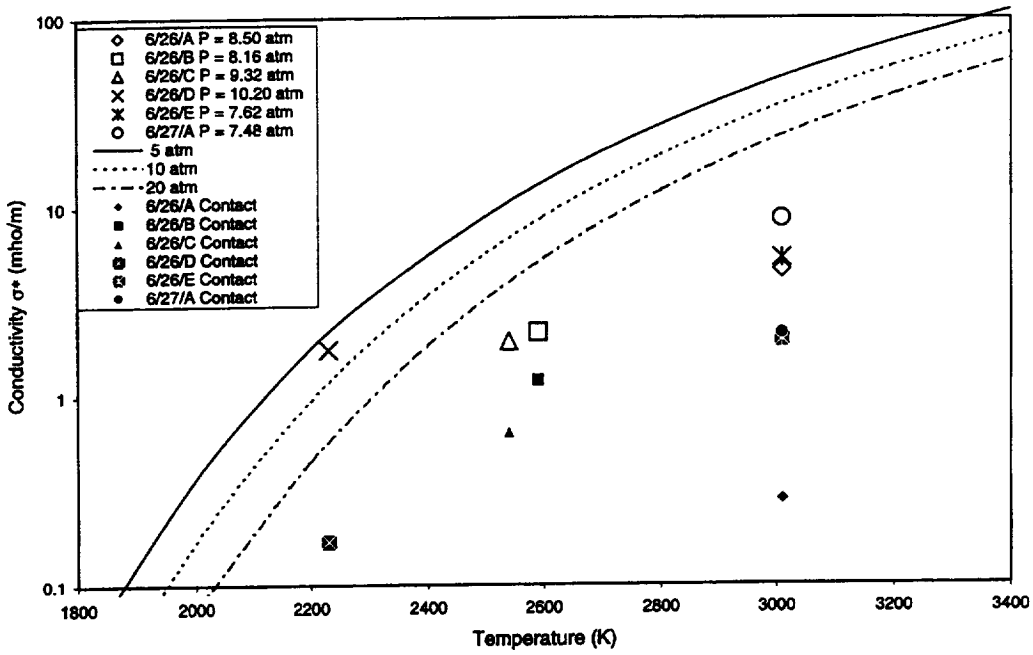

Figure 4- 55. Comparison of experimental and theoretical conductivity of 1% weight fraction K_2CO_3-seeded air plasma for nominal pressure of 10 atm.

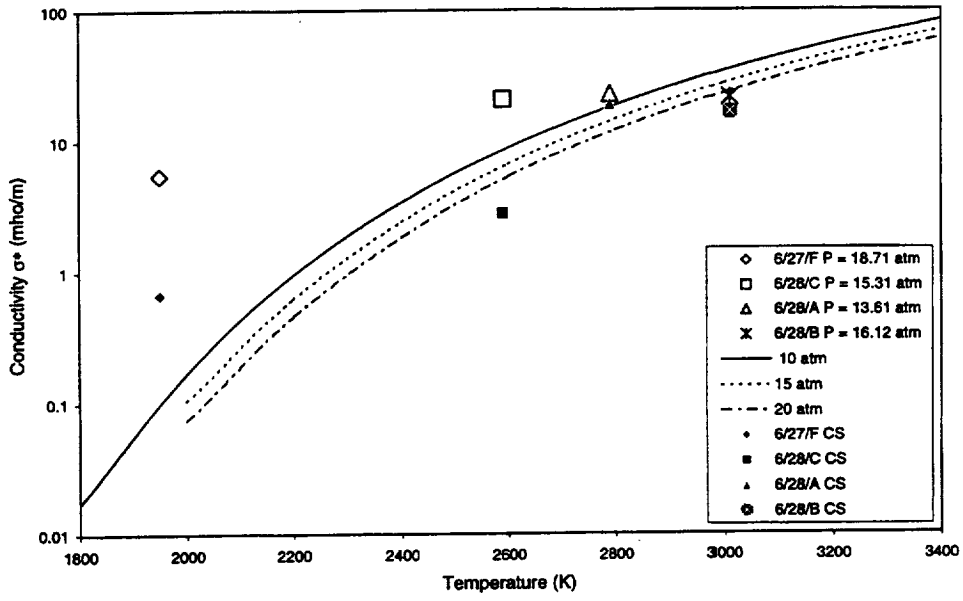

Figure 4- 56. Comparison of experimental and theoretical conductivity of 1% weight fraction K_2CO_3-seeded air plasma for nominal pressure of 20 atm.

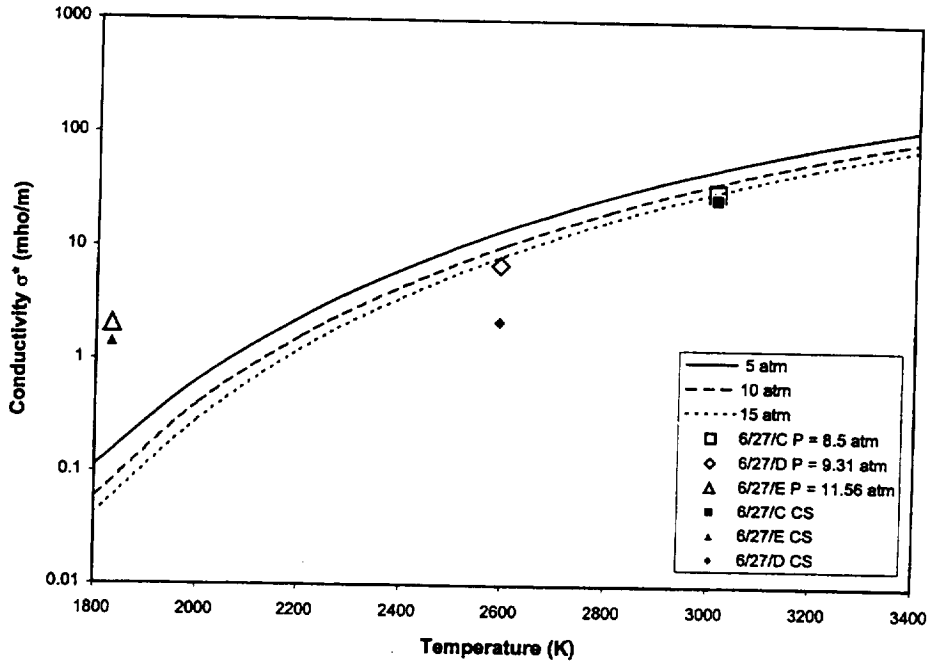

Figure 4- 57. Comparison of experimental and theoretical conductivity of seeded N_2 plasma (1% K_2CO_3) at a nominal pressure of 10 atm.

4.2.2.4 University of Texas Test Program Conclusions

A new detonation-driven shock tube facility was developed to support the MARIAH Project research program conducted at UTA. The new facility provided significantly increased performance over the former pressure-driven facility. The performance of the facility with the original arc-ignition mode was considerably lower than predictions based on ideal shock and detonation wave models. This reduced performance was shown to be a result of the interaction between the Taylor rarefaction wave and the reflected shock wave for the downstream propagation mode of operation. For the upstream mode, the gradual rise in end-wall pressure resulting from the failure to directly initiate a Chapman-Jouguet detonation wave is the most likely cause of the lower performance.

Implementation of the shock-induced detonation mode proposed by Bakos and Erdos of GASL (Refs. 115, 116) provided a considerable increase in performance. Peak shock Mach numbers of 10.7 have been achieved. Furthermore, by proper tailoring of conditions, the trailing Taylor rarefaction wave associated with the arc-ignition mode can be eliminated.

The basic approach proposed by Garrison (Ref. 116) was implemented for measurement of the electrical conductivity of seeded air and N_2 plasma for this research. Generally consistent results were obtained; however, the interpretation of these results was complicated by the observation of

current flow after the theoretically estimated time of passage of the contact surface through the conductivity channel. The contact surface should separate the seeded air plasma from the unseeded detonation products; however, the detonation products apparently also contained seed in these experiments since the estimated conductivity for unseeded detonation products is too low to explain the continued rise in current after the predicted contact surface passage.

The observed variation of conductivity with temperature for the seeded air plasma resulted in a lesser rate of increase than the theory would predict. Also, the observed magnitude of conductivity was considerably lower than the theoretical magnitude for the 10-atm data. In contrast, fairly good agreement was achieved for high pressures and high temperature.

The results of the conductivity measurements with seeded N_2 plasma appear to give some support to the theory of electron attachment by the positive oxygen ions in seeded air plasma. Measured conductivities for the N_2 plasma were on the order of 2 to 3 times larger than comparable measurements for the air plasma, whereas the theoretical values calculated from the CEC code using the Demetriades and Argyropoulos conductivity model (Ref. 117) produced comparable results for the two plasmas with only a slightly higher electrical conductivity in the N_2.

4.1.2.3 Russian MHD Facility Research

This section summarizes work performed under subcontract to TsAGI, a Russian government technology organization contracted to conduct aerodynamic testing across a wide spectrum of test conditions, Mach numbers, and altitudes. The product of the subcontract was a set of two reports dealing with a) the problem of upgrading the facility to support MHD accelerator experiments at increased channel pressure; and b) MHD channel electrode characterization. The PI for the subcontract was Dr. Vadim Alfyorov, a noted MHD researcher at TsAGI. In the 1960s, Dr. Alfyorov and his colleagues developed an MHD accelerator facility that included a small aerodynamic test section. As of this writing, the facility is still operational and has been used to characterize the hypersonic flow around various small-scale models, including models of the Russian Buran Space Shuttle vehicle. Model sizes are limited to lengths or diameters of 15 cm or less. The reports were originally written in Russian and then translated into English; they appear in unedited form in Appendix E of this document as Sections E.1 and E.2.

The TsAGI subcontract had several objectives:

1. Summarize and document all of the operating characteristics and capabilities of the TsAGI MHD test facility and describe recent operating experience. This included an explanation of the significant facility limitations, such as electrode lifetimes, power requirements, and magnet limitations.

2. Provide descriptions and cost estimates of new equipment required in upgrading the facility. The specific envisioned facility upgrades, as described above, include: 1) improved seed injection system, 2) special MHD accelerators for diagnostics on electrode walls, and 3) a 7.5-T superconducting magnet.

3. Investigate the electrode phenomena in the TsAGI MHD channel. This was understood to include a description of the basic modes of conduction within the sheath layers and electrode wall boundary layers, along with experimental investigations to characterize the mode of conduction in the near-wall region (i.e., whether arc mode or diffuse mode). No new experiments were conducted for this phase of the research. Instead, data from past Russian papers, reports, and previous electrode tests were researched.

Objectives 1) and 2) were addressed in the first TsAGI report (Section E.1.2), and Objective 3) was the subject of the second TsAGI report (Section E.2.2).

Subsections 1 and 2 of the TsAGI facilities report give a reasonably detailed description of the test capabilities and operating conditions of the existing facility. The MSE Summary (Section E.1.3) supplements this information, which includes photographs of the facility in addition to a discussion of some of the salient features of the facility. TsAGI supplied the photographs at the request of MSE.

The proposed facility modifications described in the report are divided into two stages. Stage 1 addresses the issue of upgrading the seed injection system and constructing the new MHD channels, and Stage II addresses the costs for upgrading the magnet to a 7.5-T superconducting magnet. Conclusions and findings of the report are presented in the Summary.

The two subsections below (Sections 4.2.3.1 and 4.2.3.2) provide a synopsis of the facility capabilities, the costs of upgrading the facility, and the major results of the MHD electrode study. Additional details and photographs may be found in Appendix E. A third study appearing in Appendix Section E.3 is entitled "ENGO Report on the Feasibility of MHD for Simulating Flows over Transatmospheric Vehicles." This was conducted under a separate subcontract and is not addressed here. A summary level description of this study may be found in Section 4.1.1.3.

4.2.3.1 TsAGI Facility Capabilities and Facility Upgrades

The photograph of the TsAGI Hypersonic MHD Facility is an end-to-end view of the entire facility. The flow direction is from right to left, away from the observer. The main components, starting at the upstream end include: a) the arc heater; b) the MHD accelerator enclosed by one half of the magnet in place; c) the test cabin with the large diagnostic window clearly visible; and d) the ejector system that conducts the exhaust gases into a storage tank.

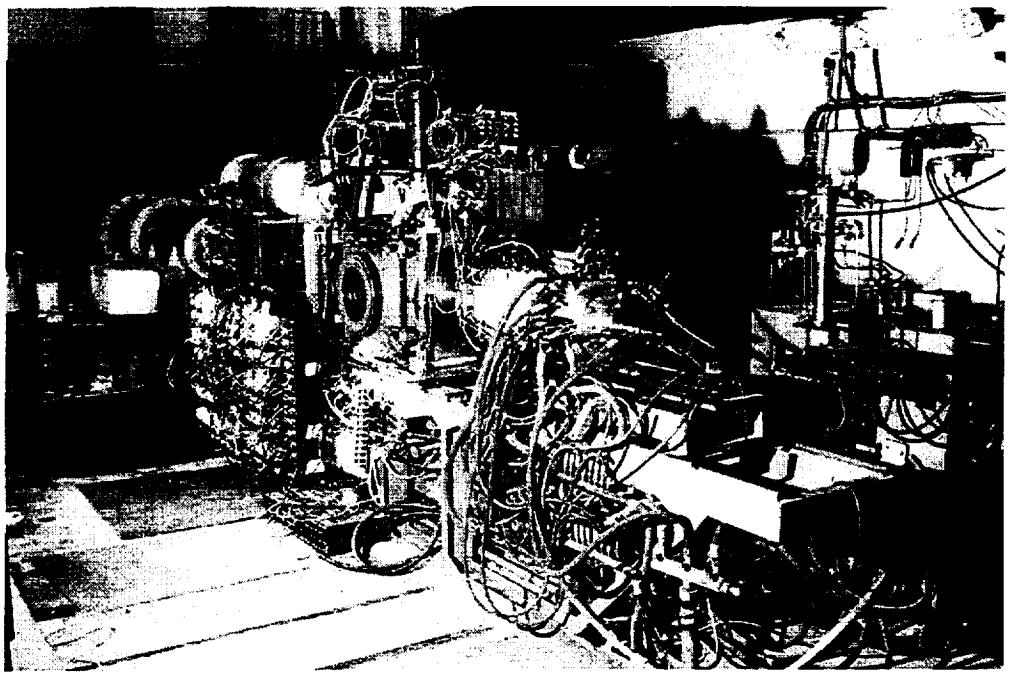

Figure 4- 58. Photograph of the TsAGI hypersonic MHD facility.

The overall performance capabilities of the system are shown in Figure 4- 59. The triangular points on this diagram represent projections made in a separate study conducted by the ENGO organization (see Section 4.1.1.3 and Appendix Section E.3). The present facility capability is represented by the elliptical region on Figure 4- 59. As is typical of arc-heated facilities, the exit flow conditions from the MHD accelerator lie too far to the right of the q = 1,000 or q = 2,000 lbf/ft^2 curves to permit dynamic pressure matching between test section conditions and actual post-bowshock conditions. The implication is that, for a specified altitude, the test section Mach numbers or static pressures will be consistently lower than the corresponding post-bowshock quantities.

Because the TsAGI system is a small-scale, 30-year-old device, it was realized it would be difficult and expensive to upgrade the facility to anything resembling a pilot-scale (i.e., large-scale) MHD-driven aerodynamic test facility. However, the facility could potentially be utilized for the investigation of several fundamental design and performance issues if adequate diagnostic capabilities were available. Several such issues were identified:

- Flow chemistry issues, including the formation of monatomic oxygen and nitrogen oxide within the arc heater and accelerator.
- Thermal management questions, such as the demonstration of gas cooling by means of injecting He or Ar at critical points along the electrode wall. These "gas curtains" might reduce the effective wall temperature and wall heat fluxes while providing a conductive

path through the boundary layer regions. Another study, which would be useful for future MHD accelerator system designs, would be to characterize the wall heat fluxes as a function of power input and applied magnetic field.

- Characterization of the nature of the conduction mechanism within the electrode sheath layers. Such studies would require special diagnostics and specially constructed electrode wall sections, which would permit the photographing of arc patterns and the characterization of the arc structure and current densities as a function of magnetic field, temperature, and static pressure.

These studies would require a number of upgrades to the TsAGI facility including a) improved diagnostics, b) special MHD accelerator channels, c) special diagnostic wall sections, d) improved seed injection system, and e) a higher field strength magnet. The identification of these required facility upgrades and their costs constituted one of the primary tasks of the TsAGI subcontract.

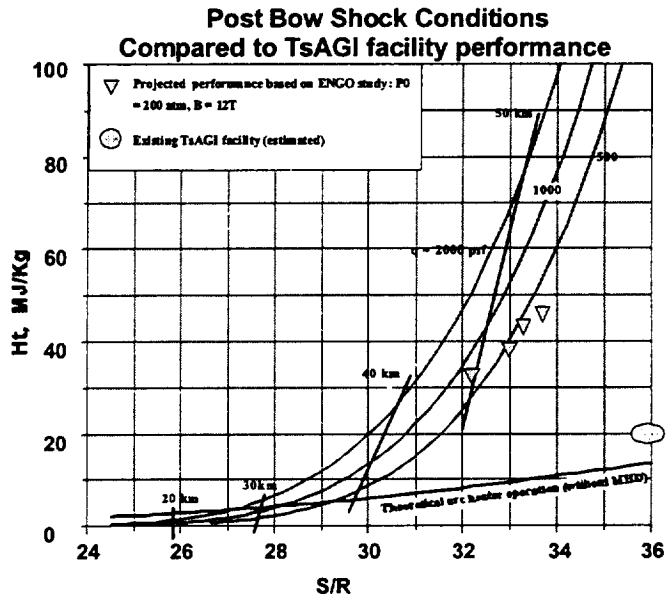

Figure 4- 59. Post-bowshock conditions.

Several points in the above report merit emphasis or further discussion. First, the cost of the proposed upgrades amounted to approximately $400,000 for the Stage I modifications (high-pressure facility utilizing the existing magnet) and $500,000 to $1 million for Stage II. The large uncertainty in the cost estimate for Stage II is primarily due to the uncertainty of magnet costs. The total cost for all proposed upgrades would be in the range $900,000 to $1.4 million. Since

this exceeded the available funds for experimental work in the MARIAH Project, these facility upgrades were not pursued.

A brief description of key facility hardware components and facility operating characteristics is found below. A more detailed description, as well as additional photographs, may be found in Appendix E. Some of the information below has also been derived from observation of the facility during a visit to the site by MSE in 1995.

Seed Material and Seed Injection System

The seed material used in virtually all of the TsAGI testing has been a eutectic mixture of Na and K with a mixture ratio of 77/23 by mass of K/Na. This mixture is commonly referred to as NaK. The advantage of NaK over more common seed materials such as Cs or K is it is liquid at room temperature. This permits the seed to be injected by means of a pressurized injection system. The quartz ampoule containing the NaK is shown near the center of the photograph. Seed flow is initiated when a mechanical plunger breaks the glass near the base of the ampoule. Pressurization of the seed is achieved by use of the gas cylinders shown in the photograph.

Liquid injection of the seed eliminates many of the problems associated with the use of powdered seed materials. It is also superior to other liquid systems, such as the K_2CO_3 plus water mixture, which was briefly used in the DOE MHD power generation program. The major failing of this scheme was that the introduction of water depressed the flame temperature in the combustor.

Arc Heater

The arc heater is a Huels segmented electrode heater. The arc is spin stabilized using a coaxial magnetic field. The heater is water cooled and operates at a stilling chamber temperature of 3,700 K and a pressure of approximately 20 atm.

MHD Accelerator

Several different accelerators have been built and tested in recent years. Typical accelerators are 55 - 70 cm in length, designed to run in the Faraday mode, and contain 40 - 45 electrodes. An important feature of the TsAGI accelerators is they run in the heat sink mode (i.e., without active cooling). This, coupled with the high heat fluxes (10 - 50 MW/m^2), implies very short lifetimes for the electrodes and insulators. As noted in the report, typical electrode-insulator lifetimes are in the range of 5 - 10 seconds. The most common failure mode is erosion of the interelectrode insulators along the anode wall. Channels are commonly operated at maximum currents of 55 A and Faraday voltages in the range 200-400 V. The input power to the accelerator is in the range 0.5 to 1.0 MW.

Sequence of Operation

The sequence of events for a typical test is as follows:

1. Cooling water flow is initiated in the arc heater and other downstream components (excluding the accelerator).
2. Magnet power supply is activated.
3. Airflow is initiated.
4. Power to the arc heater is activated.
5. Seed flow is initiated.
6. Power to the MHD accelerator is activated. A typical powered run time is 1-2 seconds.
7. Measurements and diagnostics in the test section are recorded.
8. Power to the accelerator is terminated.
9. Seed flow is terminated.
10. Arc heater power is terminated.
11. Airflow is terminated.
12. Magnet power is terminated.
13. Cooling water flow is terminated.

A summary of key operating parameters is shown in Table 4- 10.

Table 4- 10. Summary of the TsAGI MHD facility operating parameters.	
ARC HEATER	
Power Input	200 - 260 kW
Stilling Chamber Temperature	3,700 K
Stilling Chamber Pressure	20 - 30 atm
Mass Flow Rate	7.0 to 22.5 gram/s
ACCELERATOR	
Inlet Dimensions	1.5 × 1.0 or 1.5 × 1.5 cm^2
Channel Length	Variable, 14.5 to 72.5 cm
Inlet Flow Velocity	1,800 m/s
Inlet Mach Number	1.9 (variable, depending on choice of nozzle)
Magnetic Field	2.4 T
Gas Conductivity in Stilling Chamber (Nominal)	150 mho/m
Electrode Pitch (Longitudinal)	8.0 mm
Electrode Width (in Longitudinal Direction)	4.5 mm
Number of Active Electrode Pairs	45
Maximum Current Per Electrode Pair	55 A
Applied Voltage Per Electrode Pair	200 - 400 V
Total Input Electric Power	0.5 - 1.0 MW
Heat Flux	10 - 50 MW/m^2
Powered Run Times	1 - 2 s
TEST SECTION	
Dimensions (cross section)	50 cm × 50 cm
Maximum Flow Velocity	7.5 km/s
Densities	10^{-4} - 10^{-2} kg/m^3
Mach Number	15 (for sec. nozzle exit area of 20 × 20 cm^2)

The report develops several important conclusions summarized below.

1. The most severe barrier to increasing the run times of the MHD accelerator is the extremely high wall heat flux, which is typically in the range 10 - 50 MW/m^2. Such high heat fluxes imply very short electrode wall lifetimes (typically 10 - 12 seconds). The most common failure mode that was observed in the TsAGI experimental program was erosion of the anode wall insulators at the electrode-insulator interface. According to the report, the use of active cooling instead of relying on heat sink operation will not significantly improve the problem.

2. The chemical composition of the gas leaving the MHD accelerator will generally be different from the in-flight composition. The molar concentration of monatomic oxygen increases strongly with the applied MHD currents. At a reservoir pressure of 20 atm and an applied field of 3 T, the molar monatomic oxygen content was computed to be 27%. As the report notes, such high concentrations of this species will almost certainly confound the combustion chemistry occurring in a scramjet test module.

3. One of the recommendations made by MSE during a visit to TsAGI in the fall of 1995 was to investigate the feasibility of modifying the facility to operate at substantially higher pressures. This would improve the overall performance of the system, permitting the test section conditions (Mach number and static pressure) be moved somewhat closer to the post-bowshock conditions. According to the report, (see Section 4): "Increasing the pressure (and the mass flow rate, accordingly) implies substantial losses in output parameters as compared with those implemented by now. The velocity V = 6,000 m/s is necessary to simulate conditions inherent in the combustion chamber for M = 15 - 20, may be realized (while maintaining a suitable length of the MHD channel) at B > 5 T only. The highest results may be obtained at B = 7.5 T."

The high cost associated with the design and implementation of facility modifications to support higher pressure, higher magnetic field operation of the facility was the primary reason MSE decided not to pursue these recommendations further.

4.2.3.2 TsAGI Report on MHD Electrode Study

This section describes experimental work done at TsAGI to characterize the various modes of current transport in the vicinity of the MHD accelerator electrode walls. The report is a review and compilation of work previously accomplished at TsAGI under separately funded efforts. The intent of the discussion below is to provide the background and objectives of the TsAGI experimental investigations.

Current flow through an MHD accelerator is a complex process for many reasons. First, even in the ideal case where the pressure, temperature, velocity, and magnetic field are everywhere

uniform, the current density and electric field vectors will not be parallel to each other due to the tensorial character of the generalized Ohm's Law relationship. Nonuniformities in temperature and velocity further complicate the current flow patterns. The TsAGI report (Section E.1.2) addresses these issues in the context of three distinct zones within the flow stream in which the current flow and current nonuniformities are dominated by different mechanisms. In Appendix E, several such nonuniformities are identified. The reader is referred to Sections E.3.1. and E.3.2 for a description.

One type of nonuniformity is a result of thermal overshoot within the boundary layer. It occurs only in high Mach number flows where the wall recovery temperatures may be substantially higher than the core flow static temperatures. In a high-speed flow, the temperature of an adiabatic wall can be estimated knowing the core flow properties from the equation:

$$\frac{Taw}{T} = 1 + \frac{r(\gamma - 1)}{2} M^2 \qquad (4\text{-}16)$$

where T is the static temperature in the core flow, and M is the core flow Mach number.

The parameter r is the recovery factor, a number which depends on the Prandtl number and is generally close to, but less than 1. For a high Mach number flow, equation (4- 16) indicates the adiabatic wall temperature may be significantly higher than the core flow temperature. In a real accelerator, the actual wall temperature will be lower than the adiabatic wall temperature; however, the overall result is that thermal overshoots can occur in high Mach number flows due to the conversion of kinetic energy to thermal energy through the mechanism of viscous dissipation. The term "thermal overshoot" simply means that a local maximum occurs in the static temperature profile somewhere within the boundary layer.

Because electrical conductivity is a very strong function of temperature, the existence of such a thermal nonuniformity will have the effect of locally increasing the electrical conductivity, thereby causing a local increase in the current density (Jy). Increased Jy will result in an increased body force (JyB) on the fluid, leading to an increase in the flow velocity. Therefore, in a high Mach number MHD accelerator flow, one can expect overshoots of both temperature and velocity within the boundary layer.

It should be noted the velocity overshoot phenomenon is unique to MHD accelerators. In an MHD generator, the body force acts in the upstream direction, and the current Jy is in the opposite direction from what occurs in an accelerator. The local increase in conductivity will cause the current density to be more negative, thus retarding the flow in the boundary layer more than in the core region. It is also true that Mach numbers in generators are usually somewhat lower than in accelerators; therefore, the recovery temperatures are closer to the core flow temperature. Consequently, the mechanism leading to thermal overshoots is somewhat diminished in generators, and due to the opposite direction of the current density, there is no mechanism for velocity overshoots in MHD generators.

The above discussion concerning the various mechanisms for current and field nonuniformities suggests the design of electrodes for MHD accelerators must take into account a number of factors. Some of these mechanisms are not well understood and can only be resolved by recourse to experiment. These considerations were the primary motivating factor for the TsAGI study on electrode phenomena.

4.2.3.3 TsAGI Electrode Study Conclusions

Although not clearly noted in the report, the schematic of the experimental rig (Fig. E.3.2, Appendix Section E.3) shows the special electrode wall sections installed in the test chamber of the facility with a separate magnet coil for applying the magnetic field. Therefore, the test rig was separate from the MHD channel used for flow acceleration in the TsAGI facility.

The primary objective in these investigations was to investigate the mode of current transport from the hot core flow through the boundary layer and near-wall sheath layer. The major concern is to understand how the transverse current flows from the hot core and thermal overshoot regions, through the cold sublayer, and into the electrodes. A second objective was to characterize the current distribution along the electrode face as a function of both the streamwise coordinate and the magnetic field. To this end, special wall sections containing segmented electrodes were fabricated. Both the total current and the current through each segment were measured as the magnetic field was varied. By observing how the current through each of the segmented electrodes varied as a function of applied field, it was possible to deduce a relationship between the applied B field, the segment number, "i", and the segment current I_i.

The photographs taken inside the test channel (Appendix Section E.2.2) clearly show the presence of a thin, highly luminescent layer close to the wall. This is not caused by the electric discharge but corresponds to the thermal overshoot region as described above. The core Mach numbers in the test channel ranged from 2 to 4. At a Mach number of 3, using a recovery factor of 0.9, the estimated ratio Taw/T in Equation (4- 16) is 2.6, indicating the temperature within the boundary layer may be substantially higher than in the core. This is entirely consistent with the observation of the luminescent region close to the channel walls. Although the wall is not adiabatic, the regions near the insulator faces are close to adiabatic, and one would expect substantial elevation in static temperatures within the boundary layer.

The conclusions of this experimental work may be summarized as follows:

1. In a high Mach number flow through MHD accelerators, the thermal recovery process near the electrode walls, in combination with the Joule heating from the injected power, can drive a thermal instability that results in the formation of microarcs in the sheath (near-wall) regions. Evidence for this comes from the photographs employing a high-speed framing camera. Estimated current in a typical microarc was 5 - 10 A. The number of microarcs grows in rough proportion to the total current.

2. The experiments that employed quadruple-segmented electrodes show the current transport in the sheath region on the anodes is primarily due to microarcs that have observed lifetimes in the range 10^{-5} to 0.01 seconds. The microarcs concentrate along the downstream edge near the electrode-insulator interface at the higher currents. At low currents (less than 5 A), the current distribution with respect to streamwise distance is nearly uniform. The microarcs concentrate on the downstream edge of the anodes and on the upstream edge of the cathodes. This arc concentration phenomenon leads to arc erosion of the anodes at the electrode-insulator interfaces. Arc erosion damage was clearly visible in the photograph (see Appendix E, Fig. E.1-6).

3. Microarcs were also observed at the cathode. In this case, the current concentration was along the upstream electrode-insulator interface. The more severe erosion damage appeared to be along the anode as opposed to the cathode face.

4. The application of a magnetic field changes the current distribution on the anode considerably. At a field strength of 2.4 T, most of the current passed through the downstream segment. The report gives an exponential decay law for the current Ii on the i-th segment in terms of the streamwise coordinate X_i:

$$I_i = I_{i0} \exp\left(-kB^2 X_i\right) \qquad (4\text{-}17)$$

Therefore, the current decay with an e-folding distance is inversely proportional to the square of the magnetic field.

5. The report indicates that intense Joule heating in the boundary layer can lead to localized gasdynamic flow disturbances, including shocks. It is not clear if this is a theoretically predicted or observed result.

4.2.3.4 MSE Perspective

One of the key unresolved issues raised by the TsAGI electrode investigations is the question of what is the primary mechanism of wall failure. Destruction of the electrode walls can be explained by several possible mechanisms: a) high heat fluxes, b) arc erosion, and c) rapid oxidation due to the very high temperatures and the presence of O_2. It would appear, based upon the observed failure modes, that mechanism c) may not be as important as a) and b) but may still be a contributing factor. The common mode of failure observed in the TsAGI channels was the burnout or destruction of the boron nitride insulator material at the on the anode wall insulator-electrode interface. If oxidation had been the primary mechanism of destruction, one would expect the more reactive metallic electrodes to have failed first. This typically did not happen.

The fact the damage was usually concentrated near the downstream edge of the anode insulator suggests that arc erosion may be playing an important role since it is at this interface where current will be most highly concentrated.

The statement in the report to the effect that active cooling cannot significantly extend wall lifetimes must be contrasted with the experience gained in the AEDC LoRho program, in which run times for water-cooled MHD accelerator channels were in the range of tens of minutes or more. Because there were several significant differences in the operational and design parameters between these two experimental programs, it is not clear that active cooling alone can explain the much greater channel lifetimes experienced in the LoRho program. We note the following:

- The TsAGI MHD channels were run at significantly higher magnetic fields. (2.4 T vs. 1.5 T in the LoRho experiments). This implies, according to Equation (4- 17), current concentrations will be much higher in the Russian channels. Higher current concentrations will imply higher arc erosion rates.
- The LoRho program used N_2 rather than air as the working gas. This eliminates oxidation as a mechanism for wall degradation in the LoRho channels. The TsAGI program has always relied on air as the working gas.
- The TsAGI MHD channels were designed to run at somewhat higher Mach numbers. Typical Mach numbers in the TsAGI program were in the range 2 - 4, whereas in the LoRho program they were nearly always below 2. This implies, according to equation (4- 16), the peak temperatures in the boundary layer will be substantially higher in the TsAGI channels compared to the LoRho channels. Note the Mach number enters as a squared term; therefore, a Mach number of 3 yields a thermal overshoot of 2.6 vs. a value of 1.4 for a Mach number of 1.5. These much higher boundary layer temperatures in the TsAGI channels imply correspondingly higher heat fluxes.

4.3 SYSTEMS ISSUES

In this section several supporting technologies for MHD accelerators are evaluated. The topics considered include: a) technologies for enhancing ionization and conductivity in MHD accelerators are presented in Section 4.3.1 and Appendices Sections D.2 and D.3; b) an evaluation of the possible use of fullerenes for use as an MHD seed material is reported in Section 4.3.2 and Appendix Section C.1; c) a study to characterize the advantages and disadvantages of several alkali metal seed materials is given in Section 4.3.3 and Appendix Section C.2; and d) a section addressing the thermal management and thermal protection issues for MHD accelerators is presented in Section 4.3.4 and Appendix Section D.1. In some cases, especially for the ionization technology study, new technologies have been recommended as candidates for improving accelerator performance. The potential use of beamed energy addition in the MHD channel opens the possibility of achieving the necessary electrical conductivity

without operating at extremely high core temperatures. This mode of operation has the potential to alleviate the high heat fluxes to the walls, which were characteristic of the TsAGI MHD accelerator. The studies on seed materials and thermal protection are significant because they characterize the state of the art in these two areas. All of these technologies are critical to the task of designing and operating an MHD accelerator system that is efficient, reliable, and durable.

4.3.1 Ionization Technologies

As part of the overall MARIAH Project, MSE has attempted to characterize and evaluate several technologies that may have the potential to enhance the electrical conductivity within a MHD accelerator or to improve the channel efficiency. The purpose of this section is to provide a synopsis of a number of candidate technologies that have been or are being evaluated for possible application to MHD-augmented wind tunnels. Such technologies include e-beams, microwave sources, heavy-charged particle beams, neutral particle beams, x-rays, gamma radiation, laser irradiation, microwaves, and radio frequency (rf) sources. Each has its own unique characteristics and operating regime. Likewise, each has its own advantages, disadvantages, and technology issues. These are addressed in greater depth in the following sections.

4.3.1.1 Problem Statement

The purpose of the MHD accelerator is to augment the total enthalpy of the flow by accelerating an incoming airstream to high velocities. To accomplish this, it is necessary to substantially increase the total enthalpy through the addition of work or heat. As discussed in Section 3 of this report, to simulate conditions representative of hypervelocity flight will require that large amounts of energy (typically tens of megawatts per kg) be added to the gas stream while keeping the entropy of the gas within sharply defined limits. A problem with conventional arc-heated MHD has been its tendency to exceed these entropy limits due to the low plenum pressures and the high-plenum temperatures. Ideally, one would like to operate the plenum of an MHD system at low temperatures and high pressures because this would permit starting the entire process at much lower entropy levels. In arc-heated MHD systems, there is a sharply defined temperature limit of about 2,600 - 2,700 K below which the expansion from the primary nozzle must not fall. The requirement for high temperatures in the channel is due to the "necessity" of relying on thermal ionization of an alkali metal seed. To ionize any of the alkali metals in this way requires temperatures of at least a few tenths of an electron volt or at least 2,600 K.

On the other hand, if a way could be found to ionize the seed (or a constituent of air) at low temperatures, then high temperatures would no longer be required. Low temperature operation would yield a significant payoff in terms of air chemistry. The dissociation of O_2 and the generation of nitrogen oxide would be greatly reduced if the working temperatures in the accelerator could be maintained below approximately 2,500 K. Materials issues also become

easier to address if the channel temperatures are reduced. Thus, there are several reasons for investigating the possibility of low temperature operation of an MHD channel. Although temperatures of 2,600 K may seem high, it should be pointed out the Russian accelerator channel at TsAGI is estimated to operate at core temperatures close to 4,000 K.

4.3.1.2 Technology Evaluation

The most obvious way to produce ionization at low temperatures is to use some type of beamed energy such as e-beams, heavy particle beams, microwaves, or lasers. As is shown in Reference 17, any of these technologies is capable of producing ionization, but to sustain appreciable free electron number density downstream of the ionizing source will require the channel be run at low pressures of the order of a few tenths of an atmosphere or less. Otherwise recombination and attachment processes will cause the free electron number density to drop to essentially zero in the space of a few centimeters or less. It thus appears that practical application of beamed energy addition implies temperatures and pressures in the channel are low. In the following subsections, the merits and deficiencies of each of the beamed energy technologies are summarized. The reader is referred to Appendix Section D.2 for more detailed discussions. We note that Appendix Section D.2 contains data on microwaves and e-beam ionization for a spectrum of pressures and temperatures ranging from 0.01 to 1,000 atm in pressure and from 300 to 3,000 K in temperature. Since it was convincingly demonstrated in Reference 17 that beamed energy addition is practical only at low to moderate temperatures and low pressures, we confined ourselves to that regime in the discussion below.

4.3.1.2.1 *Electron Beams*

As part of this study, MSE has evaluated e-beams as a means of enhancing the ionization of air within the MHD accelerator. E-beams have been employed successfully in gas lasers where they have been used to create a population inversion in the vibrational modes of gases such as carbon dioxide (CO_2) (Refs. 118, 119). That application represents a much more benign environment from the standpoint of creating ion-electron pairs because in all of the laser applications, the working pressures are very low, usually of the order of a few torr whereas in typical MHD accelerators, the pressures may be a few tenths of an atmosphere. The static pressure is a critical parameter in any ionization scheme that relies on impact ionization.

In a general sense, there are three essential issues with respect to the propagation of e-beams in air: a) What kinetic energies are necessary to ensure the beam penetrates the gas to a sufficient depth? b) How much ionization occurs per unit path length assuming the beam can propagate? and c) What is the availability and capability of e-beam sources?

The first question can be answered quite completely based on the formulas for particle ranges as a function of kinetic energy, originally derived by Hans Bethe. These formulas include the relativistic effects that come into play at high beam energies and are valid under the assumption

that the beam scattering is due to Coulomb forces. The range formulas are summarized in the book by Turner (Ref. 120). Evaluation of the range parameter involves evaluation of an integral over the energy spectrum from the lower limit zero up to the specified incident beam energy. Details of the computational method may be found in Reference 120. Table 4- 11 is an abbreviated version of Table D.2-1. It shows computational results using these formulas for the particular case of ambient air.

Table 4- 11. Range of electrons in air.

CASE	Pressure (atm)	Temp (K)	β	Kin. Energy (MeV)	Range (cm)
A.	1	300	0.506	0.0816	10
			0.800	0.342	100

The parameter β is the ratio of the incident beam velocity to the speed of light in a vacuum.

Figure 4- 60 shows range calculations for electrons and heavy particles in low-pressure air at 300 K. These computations show that beam energies in the range 10 to 100 keV will be necessary to penetrate the gas to depths of a few centimeters up to about a meter. The more detailed computations in Appendix Section D.2 show the particle range scales inversely with the pressure or heavy particle number density and increases more or less uniformly with beam energy. Another important conclusion is, for any of the selected low-pressure low temperature conditions, the heavy particles have significantly lower penetrating power than do electrons at the same kinetic energy. However, it would be premature to dismiss the possible use of heavy particles since at this point, nothing has been said about their ability to create ion-electron pairs through impact ionization.

The question regarding the number of ion-electron pairs created per unit of path length can be answered by appealing to the notion of an ionization mean-free path. The mean-free path is a simple function of the ionization cross section. This parameter was measured for electron impact ionization in N_2, NO, and O_2 by Rapp (Ref. 121) in the 1960s up to energies of roughly 1 keV (Ref. 120). Although Rapp's data is for the low energy limit, it can serve to illustrate the general approach to the problem. The results for NO are shown in Figure 4- 61. The data for N_2 and O_2 are quite similar. In all cases, the measured cross section data has been converted into mean-free path numbers using the formula:

$$l = \frac{1}{n\Sigma}$$

where l is the mean-free path (in cm) for impact ionization, n is the number of target molecules (NO in this case) per cubic cm, and Σ is the measured ionization cross section.

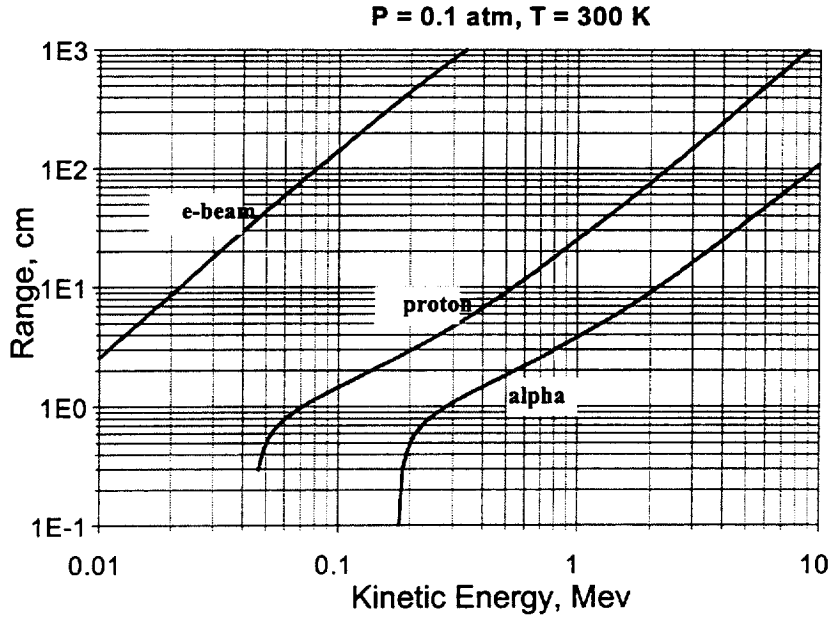

Figure 4- 60. Range of charged particles in air at low pressure.

The problem of computing the steady-state conductivity in a gas irradiated by an e-beam of known intensity can be formulated using a set of rate equations into which empirically known or theoretically computed rate coefficients are introduced. This model was used in Reference 23 to analyze the MARIAH II concept flow train consisting of an ultrahigh-pressure gas piston driver, followed by an expansion region into which beamed energy was directed. Downstream of the beamed energy region the flow entered an MHD accelerator. Electrical conductivity in the accelerator was assumed to be sustained by an e-beam having a beam current density (j_b).

In Reference 23, the authors analyzed the e-beam interaction for the case of low pressures and moderate temperatures through the accelerator (p~0.1 atm, T<1,500 K). A set of five chemical kinetics equations was developed that describe the interaction of electrons with the air molecules. The flow was assumed to be unseeded. Nitrogen oxide was taken to be the ionizing species. The reader is referred to Appendix F for further details of the kinetics model. By assuming steady conditions in the MHD channel, the authors of Reference 23 were able to deduce an approximate expression for the electrical conductivity in the channel as a function of the beam parameters, pressure, and rate constants describing electron-neutral impact ionization and dissociative recombination. The result is:

$$\sigma = \frac{e^2\left(M/m\right)}{\rho K_{en}}\sqrt{\frac{j_b \rho y}{e W_i K_{dr}}}$$

where M is the average mass of an air molecule; m is the electron mass; y is the mass stopping power of air; ρ is the mass density; e is the electron charge; K_{en} and K_{dr} are the rate constants for

electron–neutral ionization and dissociative recombination, and σ is the electrical conductivity. To illustrate the ability of an e-beam to augment the conductivity of air, we consider a 30-keV beam propagating through air at a pressure of 1 atm and a temperature of 1,500 K.

E	=	30 keV
T	=	1,500 K
P	=	1 atm
j_b	=	1.0 A/cm^2
W_i	=	9.26 eV (ionization energy for NO)
ρ	=	0.232 kg/m^3
dE/dx	=	ρY = 1.97 × 10^{-3}MeV/cm (Ref. 120)
M/m	=	5.29 × 10^4 (assuming the molecular weight of air is 28.8)
K_{en}	=	5.8 × 10^{-9}cm^3/s
K_{dr}	=	1.5 × 10^{-7} cm^3/s

Substituting these values into the above formula for σ yields a value of 95 mho/m. Thus, this nonequilibrium model shows that reasonable conductivity levels can be achieved through the use of e-beams. It should be emphasized the above computation for σ is valid only in the vicinity of the beam. Outside the beam, j_b is zero, and the conductivity may rapidly decrease due to electron-ion recombination. To maintain acceptable levels of conductivity through the MHD accelerator will require the heavy particle number density be kept low to suppress recombination. This generally implies operation at low pressures (Ref. 119).

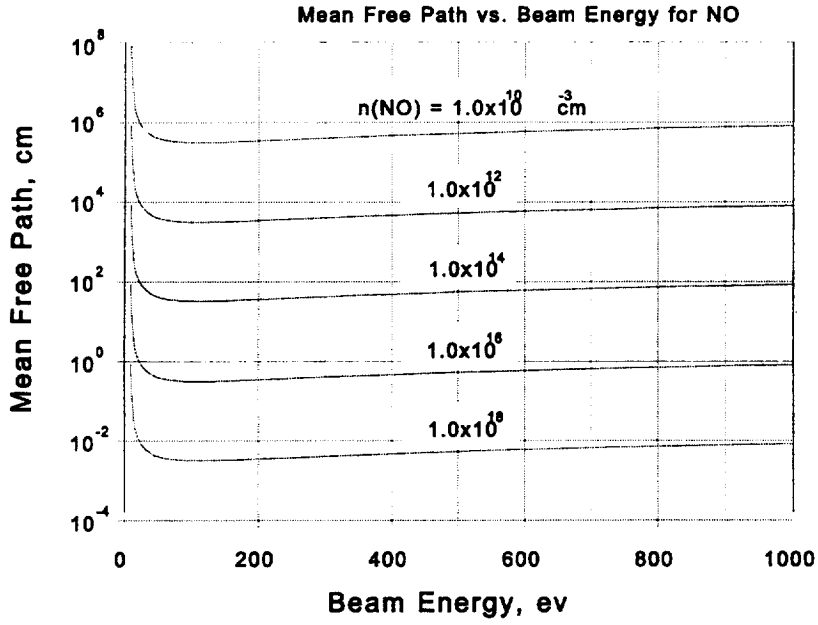

Figure 4- 61. Mean-free path vs. beam energy for nitrogen oxide.

In Reference 17, the e-beam problem was addressed somewhat differently using a 1-D computational model that incorporated all of the important chemical kinetics and ionization processes. The electron energy distribution function was computed using a numerical solution to the Boltzmann equation for the electron energy distribution function. The conclusions of that paper are that e-beams are useful for MHD only in the low-pressure limit, i.e., only for channel pressures below approximately 1 atm. For high-pressure operation in the range of 50 -100 atm, the authors concluded that recombination would be so rapid as to render the process useless. However, if the MHD duct could be operated at subatmospheric pressures, the recombination rates drop dramatically, and the e-beam ionization process would become attractive.

A more practical issue in the use of e-beams is the question of window design. Based on knowledge gained to date, it appears there are two major problems with regard to design of the foil windows that are used to isolate the working gas from the incoming e-beam. First, the window material may be subjected to high current densities, which often implies a very rapid temperature rise. The equation relating the rate of temperature rise to e-beam parameters may be derived from a simple heat transfer analysis:

$$\frac{dT}{dt} = \frac{j_b}{e\rho Cp}\frac{dE}{dx}$$

In the above equation, T is the temperature in degrees K; t is the time; j_b is the e-beam current; e is the electron charge; ρ is the mass density; Cp is the specific heat of the window material; and dE/dx is the stopping power of the window material measured in eV per cm. The last parameter has been tabulated for many materials (Ref. 120). Typical values for dE/dx are in the range 1-4 MeV/cm. The following representative numbers illustrate the magnitude of the problem. For a current density of 48 A/cm^2, mass density of 1 gram/cm^3, dE/dx = 1.86 MeV/cm, and a heat capacity of 1 calorie per gram, the predicted temperature rise is 21.3 million degrees per second. Judicious choices of foil materials along with various schemes for actively cooling the foil can alleviate the problem to some extent; however, in general it is not possible to operate in a continuous mode at very high current densities, irrespective of the foil material. The heating problem is the primary consideration that dictates a pulsed mode of e-beam operation when high current densities are required.

Another problem relating to window design is the pressure standoff problem. Because the foils must be very thin to avoid absorbing significant numbers of electrons, they are unable to withstand large pressure differentials. In practice, this restricts most e-beam windows to a pressure difference of 1-2 atm, and in many cases, substantially less.

With respect to cost and availability of e-beam hardware, according to Dr. Lou Rosocha of Los Alamos National Laboratory (LANL), there is off-the-shelf hardware available capable of delivering electrons at the beam energies required for MHD (0.5-5 MeV). One class of such devices is Linear Accelerators (LINACCS), which are used widely in the medical imaging field. They have typical ratings of 1 kW of beam power and can deliver particles with kinetic energies up to 10 MeV. Dr. Rososcha indicated a used LINACC suitable for our use would cost in the

neighborhood of $1 million. He also stated there is a new technique called fusion bonding in which titanium is bonded to the wall material, giving a composite that has greater strength than the foil alone. Aerodynamic windows have been used only for small apertures (approximately ¼-in. dia.). Diamond has also been used as a window material for windows up to approximately 1½-in. diameter.

Dr. Rosocha cited Textron Defense Systems of Everett, Massachusetts, and the Boeing North American Corporation Rocketdyne Division as two companies that have built cooled windows for laser weapons applications. Finally, he mentioned that graphite fiber has been used for e-beam windows. This material can take high stress but not high temperature.

MSE has also communicated with Dr. Ron Gielgenbach at the University of Michigan on the same topic. Dr. Gielgenbach mentioned a company called AECL in Ontario, Canada. AECL has built high power, continuous wave e-beams that operate at up to 13 MeV for materials deposition applications. Dr. Gielgenbach mentioned there is an ongoing effort by the workers in the field of flue gas processing to utilize e-beams for ionizing particulates so they can be removed in electrostatic precipitators. Reference 122 describes this concept in some depth. He also cited the "Nike" project at the Naval Research Laboratory as having utilized high-energy e-beams in a pulsed mode. The pulse widths were about 100 nanoseconds (ns). Dr. Gielgenbach indicated he was uncertain whether pulse repetition at high repetition rates would be feasible.

4.3.1.2.2 *Microwaves*

Microwave beams have been suggested as a means of achieving enhanced ionization. From experimental work done in the postwar years, it is known that microwaves can be used to ionize gases. The work of MacDonald is noteworthy (Ref. 123). MacDonald measured the breakdown fields of microwaves in low temperature air, H_2, N_2, and O_2 as a function of pressure, with pressures ranging from about 0.1 to 100 mm mercury (Hg). Plots of the breakdown field amplitude vs. cavity pressure typically exhibit a minimum at a critical pressure in the range 1-40 mm Hg. This critical pressure is dependent on the frequency and the gas type; however, the dependence generally appears to be weak for both of these parameters. Data for high pressures (above 1–atm) seems to be quite scarce.

Based on the work of MacDonald and others, it is well established that the predominant ionization mechanism in most gases of interest is electron impact. The collision frequency (ν_c) of an electron with neutral particles is a fundamental parameter. To achieve ionization by microwaves, the collision frequency must be substantially higher than the beam frequency:

$$\nu_c >> \nu_b$$

If this condition does not hold, the electrons will typically undergo many periods of oscillation before colliding with a neutral, and therefore, on the average, will gain no net energy from the electric field. Conversely, the electrons will gain net energy if the ac field does not change

appreciably over one collision time. If the collision time is long enough (but still smaller than the beam period), sufficient kinetic energy will be imparted to the electrons to ionize a neutral particle upon impact. This is the basic mechanism of microwave ionization.

The wave propagation vector k of a microwave is given by:

$$k = \beta + i\alpha$$

and the real quantities α and β are the attenuation and phase constants, respectively. Both have the units of inverse length. The skin depth (or absorption length) is then defined as the inverse of α. The absorption length is a fundamental parameter that characterizes the distance to which microwave energy can penetrate a material or a gas.

Mitchner and Kruger (Ref. 124) derive the relation which gives α as a function of the frequency and other parameters. Details may be found in Appendix Section D.2. A key parameter characterizing the plasma is the plasma frequency, ω_p, defined as:

$$\omega_p = \sqrt{\frac{n_e \ e^2}{\varepsilon_0 \ m_e}}$$

Pressure and temperature dependence is a significant issue. For MHD applications, subatmospheric pressures and temperatures in the range 300 – 2,500 K are of greatest interest. Figure 4- 61 is a plot of the microwave beam absorption length at 0.01 atm and 1,000 K. The absorption length is plotted as a function of beam frequency for three selected beam energies. For conditions corresponding to MHD accelerator operation, the free electron densities for adequate electrical conductivity should be in the range of 10^{-5} to 10^{-4} of the heavy particle density. This is the situation depicted in Figure 4- 62. One can conclude that frequencies in the range 7 – 8 gigahertz (GHz) and beam energies in the range of a few tenths to a few eV will be adequate for sustaining ionization at the indicated conditions.

It should be noted the conclusions regarding microwave absorption depth are based on a highly simplified model of the gas-microwave interaction. The electron density in this model is a specified parameter, whereas in an experimental sense, it is determined by the impact kinetics of electrons being accelerated and then colliding with and ionizing neutral molecules. Further simulations need to be done taking into account the kinetics and the gas-wave interactions before microwaves can be considered to be a useful technology for ionization enhancement.

Micci (Ref. 125) has demonstrated microwave heating and plasma creation in several gases, including He and N_2, at pressures up to 3 atm using a 2.2-kW microwave thruster operating at 2.45 GHz. His device was a resonant cavity into which gas was introduced after a standing wave had been set up in the cavity. He further describes laser-induced fluorescence equipment that has been used to measure exit flow velocities from the exit of the microwave thruster. This technology appears to be reliable and practical for the lower pressures at which Micci has worked.

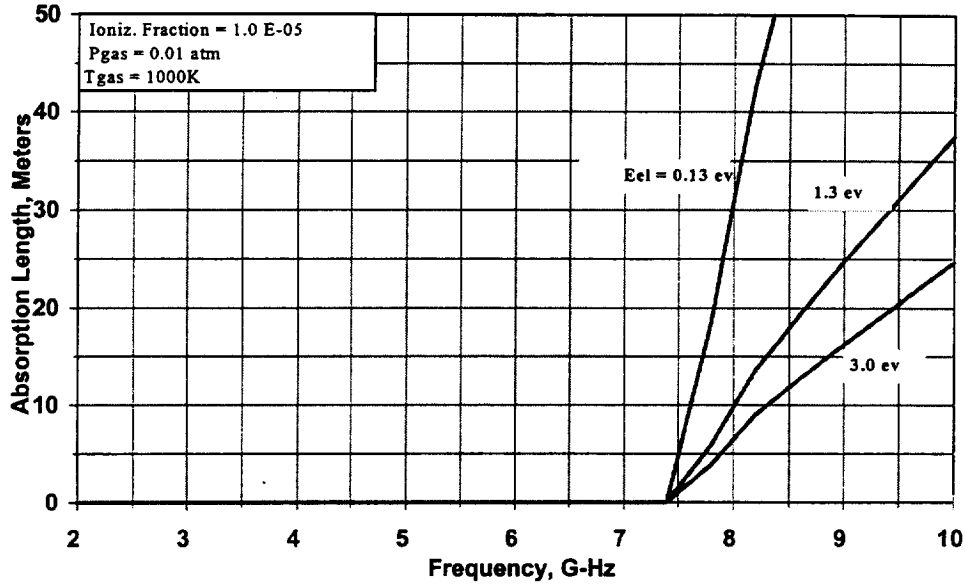

Figure 4- 62. Microwave absorption length vs. beam frequency at T = 1,000 K and low pressure.

4.3.1.2.3 *Heavy Particle Beams*

Heavy particle beams include alpha particles, proton beams, neutrons, and more exotic species such as pions. To date, we have only examined the first two in a preliminary manner. Figure 4-61 shows the range calculations for air at selected temperature and pressures. As previously noted, the ranges for two particle types shown (protons and alpha particles) are consistently lower than for electrons. Collision cross-section data for impact ionization by these heavy particle species has not yet been collected. A more detailed mode, similar to the kinetic rate model described in Reference 23 for electron impact ionization, should be developed for heavy particle ionization.

4.3.1.2.4 *Laser Beam Energy Addition*

In Reference 126, Macheret described a mechanism by which air can strongly absorb CO_2 laser radiation at high pressures and low temperatures. 1-D modeling of this mechanism indicates the characteristic absorption lengths will be of the order of a meter or less. The mechanism is a two-step process in which a small amount of CO_2 in the flow first absorbs the laser radiation by way of a vibrational absorption process. Then, the excited CO_2 molecule must rapidly transfer its vibrational energy to an N_2 molecule through a V-V transfer of energy. The laser energy is added in the exit region of a contoured nozzle, where the pressure is a few atm, and the

temperatures (through the energy addition region) range from approximately 1,000 up to 6,000 K. The analysis of Reference 4- 22 did not address the use of lasers for ionizing air. Rather, the application was to use a CO_2 laser to add energy in the nozzle expansion region of an RDHWT.

The use of lasers to directly increase the ionization in or upstream of an MHD duct is somewhat problematic. To ionize a Cs atom or an nitrogen oxide molecule will require 3.89 or 9.26 eV, respectively. For a laser beam to accomplish this will in the simplest case require that a single photon of at least the ionization energy be absorbed by the particle, followed by the ejection of an electron from the valence orbital. A photon having 3.89 eV of energy corresponds to a frequency of 9.4×10^{14} Hz, a frequency in the UV spectrum. Ionization of nitrogen oxide will likewise require photons in the UV region. This appears to be feasible in principle. UV lasers (excimers) are well developed. The primary question is one of conversion efficiency. The UV lasers presently available operate at low conversion efficiencies. Although they cannot be ruled out as ionization sources, they do not appear as attractive as the more efficient microwave and e-beam technologies.

4.3.1.3 Pulsatron Study on Ionization Methods for MHD Accelerators

Pulsatron Inc., is a company headquartered in the United States with a scientific staff consisting of Russian scientists residing in Moscow. Past research by the Pulsatron staff includes investigation of gas discharge phenomena, application of corona discharges to the problem of pollutant removal from gas streams, and high-voltage discharges in long air gaps. The research performed by Pulsatron under the MARIAH Project was motivated by the fact that electrical conductivity is one of the basic parameters that limits the performance of MHD accelerators. This subcontracted research had the primary objective of investigating various schemes for creating a favorable conductivity regime within MHD accelerators. The study was limited to computational modeling and analysis.

As part of the scope of the work, a target flight regime was established for the purpose of focusing the investigation. For simplicity, a free-stream condition corresponding to an altitude of 31 km and 2,000 lbf/ft^2 dynamic pressure was adopted as a target simulation point. The temperature, Mach number, static pressure, and total enthalpy shown on page 5 of this report correspond to this free-stream condition.

In preliminary discussions with Pulsatron, MSE emphasized that one of the gasdynamic regimes of interest to NASA was the high-pressure regime, characterized by static pressures of 100 atm or higher in the MHD channel. This is the basis for Pulsatron's selection of a very high-pressure reservoir with a stagnation pressure of 1,000 atm. If one specifies a pressure of 100 atm at the inlet of the MHD accelerator channel and an inlet Mach number of at least 2, the required reservoir pressures must be at least 800 atm to satisfy the isentropic expansion relations. While reservoir pressures in the range of 800 - 1,000 atm are far beyond present arc heater capabilities, it is not completely unreasonable to assume that a 100-atm static pressure condition, with

temperatures of at least 2,500 K, could be achieved at the accelerator inlet. Methods for realizing such high-pressure inlet conditions are the focus of the MARIAH II concept discussed in Section F.

The approach adopted by Pulsatron consisted of investigating three different MHD acceleration schemes:

- An MHD accelerator that operates in the LTE regime and for which alkali metal seed is required. The required electrical conductivity is achieved through nonequilibrium ionization of the seed. Pulsatron selected Cs as the seed material.
- Nonequilibrium gas ionization by means of e-beams. This technique has been roposed in the past and was studied analytically by Macheret et al. (Ref. 23) and experimentally by Shair and Sherman (Ref. 127). The Pulsatron analysis assumes a beam energy of 40 keV, which according to the curves shown in Figure D.2-2 (Appendix Section D.2) should be adequate to penetrate air to a distance of several cm.
- Plasma acceleration by means of the so-called "snow plow" technique. This method relies on creating a highly localized sheet of very high conductivity plasma and utilizing the MHD process to accelerate the sheet. The supposed advantage of this scheme over conventional MHD processes is the plasma is produced through a series of arc filaments within which the current density and the conductivities are extremely high, leading to very high JyB body forces. The proposed scheme is not without both theoretical and practical difficulties. Difficulties include: a) electrode erosion due to the high current densities impinging on the electrodes; b) the problem of generating many such sheets at a high pulse repetition rate to accelerate the gas more or less continuously; c) and the problem of controlling the instabilities, which are characteristic of this type of localized plasma.

It should be noted this technique did not originate with Pulsatron. The scheme has been often referred to in the literature as the T-layer concept. A number of researchers in Russia and the United States have investigated the T-layer scheme in the context of MHD. An excellent analysis and description of the process has been given in the Ph.D. dissertation of Lin (Ref. 128), which also contains numerous references to recent work in this area.

All three of the above cases were analyzed using a set of 1-D equations representing the momentum balance, energy balance, and mass conservation. Details on the analysis may be found in Appendix Section D.3.

The three different ionization schemes considered by Pulsatron are discussed in separate subsections below.

4.3.1.3.1 *Nonequilibrium Ionization Scheme*

In the usual configuration of MHD accelerator systems, electrical conductivity is obtained through the thermal ionization of a seed material, usually an alkali metal. Because all of the alkali metals have ionization potentials of 3.8 eV and higher, elevated temperatures of the order of 2,700 K and higher are required to sustain thermal ionization in the MHD channel. Such temperatures are undesirable because they lead to high wall heat fluxes and high entropy levels. The high temperatures that are required for conventional MHD accelerators are the fundamental reason that upstream drivers must operate at high pressures. The high pressure provides some compensation in entropy for the high temperatures.

The MHD accelerator system proposed by Pulsatron in this section would solve the high temperature problem by using very high applied electric fields to obtain elevated electron temperatures and high conductivities in the MHD accelerator. The bulk gas would be at a substantially lower temperature than the electrons. This approach is unusual because of the high pressures and number densities involved.

Table 4- 12 summarizes the operating characteristics.

Table 4- 12. Operational characteristics of an MHD system which relies on nonequilibrium ionization of Cs.

Mass Flow Rate	40 kg/s	Channel Exit Pressure	70 atm
Heater Temperature	2,800 K	Channel Inlet Velocity	2,020 m/s
Heater Pressure	980 atm	Channel Exit Velocity	1,750 m/s
Molar Fraction of Cs	0.01%	Channel Inlet Total Enthalpy	3.5 MJ/kg
Magnetic Field	6.0 T	Channel Exit Total Enthalpy	6.4 MJ/kg
Channel Inlet Temperature	1,200 K	Applied Transverse Elec. Field	3,400 V/cm
Channel Exit Temperature	2,900 K	MHD Channel Length	17 cm
Electron Temperature (approx.)	5,800 K	MHD Channel Hydraulic Diameter	5.2 cm
Channel Inlet Pressure	25 atm		

One of the more interesting conclusions of the Pulsatron analysis is that the targeted free-stream conditions could theoretically be obtained using very small seed fractions. Since the ionization scheme does not rely on thermal ionization, it is possible to ionize nearly all of the seed atoms.

The assumed molar seed fraction adopted by Pulsatron was 0.01%, or about 50 to100 times smaller than is commonly used in conventional MHD systems.

The elevation in electron temperature is substantial. Electron temperatures of 0.5 eV (5,800 K), are mentioned, while Figure 2- 1 in the report shows the bulk gas temperature to be everywhere less than 3,000 K, and at the inlet to be only 1,200 K. At the same time, the computed pressures through the channel are in the range 25 - 70 atm. Because the static pressures are quite high and the temperatures moderate, the heavy particle number densities will be appreciably above that of ambient air. This would preclude the possibility of substantial elevation in electron temperature unless very high electric fields were employed, as Pulsatron assumed in their analysis. Electric fields of 3,400 V/cm are quoted. This is to be compared to the MHD analysis done by MSE (Appendix Section B.1) in which the pressures and temperatures in the channel are comparable to those just quoted; however, typical electric fields are in the range of a few hundred V/cm.

The TsAGI MHD facility provides a useful reference point for comparison of electric fields. In that facility, the applied electric fields in the channel were of the order of 200 V/cm. Therefore, the proposed Pulsatron channel would be operated at approximately 17 times the applied electric fields of the TsAGI MHD channel. The high electric fields in the Pulsatron channel suggests the possibility of avalanche breakdown in the interelectrode air gap. The parameter that determines the onset of avalanche breakdown is the ratio E/N, where E is the local electric field in V cm, and N is the number density of heavy particles in cm^{-3}. For air, the critical value of E/N is given by Raizer (Ref. 55) as 1.23×10^{-17} V cm^2. The heavy particle number density N may be estimated from the relationship P = NkT, and E is given in Table 4- 12 as 3,400 V/cm. The pressure and temperature data in the table yield a value for E/N of approximately 2.2×10^{-17} V cm^2, which is nearly twice the breakdown value. Based on this analysis, it appears the MHD channel proposed by Pulsatron may operate in an arcing mode, at least through some part of the accelerator.

The Pulsatron method for computing the nonequilibrium conductivity was based on the nonequilibrium parameter ζ, which is the difference in electron and heavy gas temperatures. This value was determined using empirical data for cold air; however, the details of this part of the model are somewhat sketchy. It is unclear, for example, whether the parameter ζ properly accounts for recombination and electron attachment processes. It would be desirable to attempt to reproduce the Pulsatron results by using a nonequilibrium model for conductivity, which includes all of the important kinetics processes and relies on a more "first principles" approach to the computation of electrical conductivity.

Although the idea of nonequilibrium ionization at high pressures is an interesting one, the concept is largely unproven experimentally. Questions of scale also are important and were not considered in the Pulsatron analysis. The mass flow rate through the Pulsatron accelerator was 40 kg/s. In a full-scale wind tunnel system, the mass flows will be as high as 800 kg/s. Thus, the MHD channel cross sections must be scaled by a factor of 20 in area or a factor of 4.5 in the two transverse dimensions. To obtain the same electric field with an electrode separation 4.5 times larger will require the applied voltage to be increased by the same factor. Thus, the applied

voltages for the full-scale device may be as high as 70,000 to 80,000 V across each electrode pair. Such high voltages may create practical problems in system design, such as the problem of maintaining electrical isolation in a very confined space. The high-voltage problem may be mitigated somewhat by resorting to channels having a low height-to-width ratio (i.e., nonsquare cross sections); however, this may create additional problems in magnet design.

4.3.1.3.2 *Ionization by Electron Beams*

The two methods discussed above for obtaining the necessary electrical conductivity in the accelerator are ordinary thermal ionization and nonequilibrium electric field-enhanced ionization. A third method is to use high-energy e-beams to create additional free electrons through impact ionization of the heavy gas particles.

The Pulsatron analysis of the interaction of an e-beam in a high temperature flow is formulated through a set of gasdynamic equations supplemented by a constitutive equation for pressure (ideal gas law), the Ohm's Law relation for a plasma, and a rate equation that balances free electron creation due to impact ionization against the sum of electron losses due to dissociative recombination and three body attachment to O_2. The analysis is reasonably complete, and the authors give estimates of the attachment rate and recombination rate coefficients. Based on this nonequilibrium conductivity model, the case of an MHD channel employing reservoir conditions of 1,800 K and 1,000 atm is simulated. Because it is more energetically favorable to ionize at low gas densities rather than high ones, the gas was expanded to approximately 0.6 atm at the MHD accelerator inlet. An e-beam having energy of 40 keV and current density of 1 A/cm^2 was assumed to be injected along the axis of the accelerator. Table 2.3.1 in the report illustrates the results of the computations based on the above model. At the test section, the target conditions of 0.01-atm pressure and Mach number of 11.6 were met.

Table 4- 13 and Table 4- 14 below show the main operating parameters of the system. Table 4-14 has been reproduced from Table 2.3.1 of the report.

Table 4- 13. Operating characteristics of an MHD accelerator system which employs e-beams.

Section	Cross section cm^2	Pressure Atm	Temp. K	Velocity m/s	Mach #
Heater		1,000	1,800		
Nozzle Throat	2.1 × 2.1	536	1,528	773	1.0
Channel Entrance	16.7 × 16.7	0.54	242	1,858	5.9
Channel Exit	16.7 × 16.7	1.00	830	3,418	6.2
Test Section	85.5 × 85.5	0.01	228	3,595	11.6

Table 4- 14. Additional system data for an MHD accelerator system.	
Mass Flow Rate	40 kg/s
Magnetic Field	6 T
Transverse Applied Voltage	6.5 kV
Electron Beam Current Density	1 A/cm^2
Electron Beam Energy	40 keV
Electron Beam Power	6.0 MW
Power to MHD Accelerator	200 MW

It was suggested that dielectric walls be used for the sidewalls. For the e-beam system, 12 hollow cathode sources were recommended. These would be placed downstream of the MHD accelerator, and the e-beam would be aimed upstream.

This simulation is important not only because it shows the possibility of enhanced MHD performance through the use of e-beams but also because it shows the general approach to be taken in formulating the problem of e-beam interaction in high temperature air. This model should be capable of being easily generalized to two and three dimensions. The major uncertainties in the model are uncertainties in the rate coefficients for electron attachment and dissociative recombination. Ultimately, one must have recourse to experiments to demonstrate the feasibility of using e-beams to achieve enhanced MHD accelerator performance.

4.3.1.3.3 *Snowplow Method*

As noted above, the snowplow method is not a novel idea, and considerable study has been devoted to it in the recent past. The work of Lin (Ref. 128), Bityurin (Refs. 129, 130), and Veefkind (Ref. 131) is noteworthy. The last two researchers have studied the problem experimentally. It is known from these studies that T-layers can be formed in a time scale of a few milliseconds and can propagate for some distance. It is also known that a sheet of hot plasma being accelerated into a cooler region ahead of it will be subject to the Raleigh-Taylor instability and will have a pronounced tendency to disintegrate. Thus, a major challenge for the T-layer scheme is to demonstrate the layer can cohere for a sufficiently long time to provide a more or less uniform acceleration to the gas in the channel.

Another problem is the question of how a localized plasma sheet can be used to provide uniform and continuous flow conditions in an aerodynamic or combustion test facility. The proposed

solution is to provide multiple rail electrodes along the walls of the accelerator, which would permit multiple plasma sheets to propagate through the channel simultaneously spaced at more or less uniform intervals from each other. It is also recommended in the report that the T-layer concept be combined with a gas ejector system, which would help to damp out the nonuniformities. This concept is a novel one but will require experimental demonstration before it can be seriously considered as a candidate for driving an MHD accelerator for the purpose of reproducing hypervelocity flight conditions.

Finally, there is the question of entropy generation. The very high current densities inside the plasma sheet may have the effect of increasing the entropy generation to intolerable levels, resulting in exit conditions, which are far to the right of the desired Ht-vs.-S trajectory. Although the Pulsatron computations indicate this should not be the case, there are several questions concerning the model equations that were used and are the subject of ongoing discussions between MSE and Pulsatron.

4.3.1.4 Ionization Technologies Conclusions

The conclusions on the feasibility of beamed energy addition for ionization enhancement in MHD accelerators are summarized below:

Electron Beams

For operation at or below atmospheric pressures and temperatures of a few hundred Kelvin, e-beams appear to be quite feasible. Beam energies in the range 20 - 200 keV will be adequate for achieving the necessary electrical conductivity. Theoretical estimates of 100 mho/m at a pressure of 1 atm and a temperature of 1,500 K were cited in the literature. Higher conductivities than this appear to be attainable by operating at subatmospheric pressures. For operation at high pressures (100 atm or higher), recombination and electron attachment processes will be extremely fast. As a result, e-beams appear not to be feasible for high-pressure operation.

One of the major issues for e-beam energy is foil heating. For beam current densities of 1 A/cm^2 and higher, typical temperature rise times for the foil material will be approximately hundreds of thousands of degrees Kelvin per second or more. Two possible methods for alleviating this problem are active cooling and aerodynamic window technology. The latter will be workable only for small apertures (of the order of 1 cm).

Heavy Particle Beams

Heavy particle beams such as alpha particles and protons have much smaller ranges in air than e-beams at the same energy. However, the number of ion-electron pairs produced per unit path length by heavy particles as a function of beam energy has not been determined. For this reason, heavy particle beams cannot be ruled out as a means of ionization enhancement.

Lasers

Lasers also appear to be potentially useful. Assuming the "seed" material is either an alkali metal or nitrogen oxide, the required laser beam wavelength will be in the ultraviolet spectrum. Excimer lasers appear to be good candidates for such applications.

Microwave Beams

For microwave energy to be a feasible method of enhancing ionization, it is necessary to roughly match the absorption length to the physical dimension of the accelerator channel. For air at standard conditions, beam frequencies of a few tens of GHz will penetrate to depths of 0.2 - 2 meters. In the case of an MHD channel operating at high pressures and high temperatures (greater than 100 atm and 2,500 K), the required beam frequencies are in the range 10^{11} - 10^{12} Hz, which is well outside the microwave spectrum. Thus, microwaves are only good candidates in the low-pressure regime. For pressures close to atmospheric, the feasibility of a continuous wave microwave-sustained discharge in N_2 and other gases has been demonstrated experimentally by Micci. This experiment used a readily available microwave source operating at 2.45 GHz.

4.3.2 Seed Studies

4.3.2.1 Carbon-60 and Other Fullerenes

Fullerenes are a recently discovered class of carbon molecules that have high molecular weight, a high degree of structural symmetry, remarkable impact resilience, an even number of carbon atoms, and unusual chemical properties (Refs. 132, 133, 134, 135). Fullerenes are the third form of pure carbon; the other two pure forms are diamond and graphite. The best known and most prevalent representative of this class is an isomer of carbon-60 called Buckminster Fullerene. This molecule possesses symmetry similar to a geodesic sphere and is named for the architect and scientist, Richard Buckminster Fuller (1895-1983), who first described the geodesic dome structure. Typically, fullerene structures have 12 pentagons, with differing numbers of hexagons and an even number of carbon atoms. The pentagons allow the curvature and eventual closure of the surface upon itself. The second most prevalent fullerene is the C_{70}. The lighter C_{20} is widely accepted as the smallest fullerene, and quantum mechanical calculations project fullerenes as large as C_{600}. Bucky tubes (hollow carbon tube-like fullerenes) and bucky-onions, or concentric spherical shells of carbon, have also been observed.

MSE has investigated the use of fullerenes as a seed to enhance the ionization characteristics of MHD accelerators. The properties of fullerenes, which include their high mass, low ionization potential, and extreme resilience, suggests these molecules could be an excellent source of ions for ion thrusters (Refs. 136, 137, 138, 139). Fullerenes were proposed as a possible seed material by MSE since seed materials for MHD accelerators require some of the same

characteristics as those reported for fullerenes in the ion thruster application. For fullerenes to be viable as an MHD seed material in wind tunnel applications, they must be stable and nonreactive in high temperature, high-pressure air, and must have a sufficiently low ionization potential that will provide adequate electrical conductivity for efficient and effective MHD operation.

The first ionization potential of the C_{60} molecule is reported to be 7.61 to 7.8 eV. This could be marginally satisfactory for MHD application. However, this study found that fullerenes would decompose and combust in the high temperature air-operating environment of MHD accelerators. Negative ion formation is another problem in the MHD application as the fullerene molecules have an affinity for electron attachment.

The MSE study on the use of fullerenes for this application is further reported in Appendix Section C.1 and in *The Properties, Behavior and Applications of Fullerene Molecules* (Ref. 140).

4.3.2.2 Cesium, Rubidium, and Potassium Seed Materials

Traditionally, K_2CO_3 has been the most commonly used seed material for gas-phase MHD accelerators and generators. However, Cs and Rb each have lower ionization potential than K; therefore, their use will result in higher performance for most MHD applications. Other factors that require consideration (beyond the lower ionization potential) include the cost, availability, handling properties, and safety.

Cesium has the lowest ionization potential (3.894 eV) and is the most electropositive and most alkaline element. It is one of only three metals that are liquid at room temperature. Cesium reacts explosively with cold water and the carbonate form can cause skin irritation. If inhaled, CsO can be fatal. Canada is the major source of raw Cs ore; however, the market is very small resulting in no active trading and no official market price. Although the current production rate is low, the availability of Cs appears to be sufficient to support the operation of a major wind tunnel facility at a reasonable cost.

Rubidium has an ionization potential of 4.177 eV and is the second most electropositive and alkaline element. Rubidium ignites spontaneously in air and reacts violently in water. Safety issues for Rb are similar to those of Cs; the carbonate form causes skin irritation and the oxide may be fatal if inhaled. Cost and availability factors of Rb mirror those for Cs resulting in it having no official market price. MHD performance using Rb would be lower than with Cs due to its low ionization potential, and since its cost and availability are essentially the same as for Cs, Rb would be a poor choice for MHD applications.

Potassium metal reacts vigorously with O_2, water, and acids, and its toxicity characteristics are similar to both Cs and Rb. Potassium has an ionization potential of 4.342 eV, which is lower than either Cs or Rb. Thus, Cs and Rb would both perform better than K in most MHD applications. However, K's availability is greater than the others since it is the seventh most abundant metal in the world and is widely used in various industries. The world's potash

industry is presently in a state of overcapacity and has been subject to price supports and operation at partial capacity to maintain prices.

A detailed discussion of these seed materials is contained in Appendix Section C.2 of this report.

4.3.2.3 Seed Study Conclusions

Although fullerenes may be promising for other MHD applications with a less harsh environment, they are not practical for the high performance air accelerators needed for hypervelocity propulsion testing applications. However, designer molecules are being developed from fullerenes that may have characteristics that would allow them to be useful for MHD accelerator applications. Thus, future studies may need to revisit fullerenes to assess their viability in other applications.

Potassium's availability in large quantity and its low cost have typically made it the favored choice for seeding in past MHD generator and accelerator experiments. For most applications, and especially for commercial power generation, the small performance degradation that results from using K rather than Cs is overshadowed by the higher cost of the Cs. However, for high performance applications where small performance improvements can be significant, Cs would be the better choice. Since Rb has lower performance than Cs, although its cost and availability are similar, either K or Cs would be preferred.

4.3.3 Thermal Management of MHD Hypervelocity Accelerators

4.3.3.1 Overview

MHD accelerators for hypervelocity propulsion ground test facilities will operate in a very challenging thermal environment due to the high stagnation pressure and temperature required. Thus, a thermal management study is essential to identify the requirements for the MHD accelerator walls and methods and materials that can be applied to alleviate the thermal problems. A preliminary study was conducted under the MARIAH Program (Ref. 141), and the results are summarized in this section and Appendix Section D.1.

The primary objective of this work was a preliminary investigation of thermal management issues for MHD hypervelocity accelerators. Initial literature review and relevant analyses suggest the MHD-induced hypervelocity flow may produce recovery temperatures in the boundary layer that approach 10,000 K. The objective includes the following: a) define the thermal environment; b) identify possible materials that can be used in that environment, with or without active cooling; and c) identify innovative methods of cooling (passive or active) that can improve the thermal management for future, high performance MHD accelerator systems.

4.3.3.2 MHD Accelerator Hypervelocity Flow High Temperature Environment

Aerodynamic heating in an MHD accelerator is produced from radiative and convective heat transfer resulting from the high-velocity, high temperature ionized plasma. Although the magnitude of the heating is primarily dependent on the plasma flow velocity, density, and temperature, it can also depend on the channel geometry, the electrode insulator sidewall materials, and the wall cooling method. The degree of ionization of the plasma and the presence of metal ions and/or particles in the flow can also have a substantial effect on the rate of radiative heat transfer to the walls. In a hypervelocity flow, the high-velocity gas contains a large amount of kinetic energy, which when converted to thermal energy in the boundary layers results in very high recover temperatures (approaching 10,000 K) that occur very close to the wall surface. Electrical energy dissipation in the boundary layer and the electron and ion dynamics in the electrode sheath layers can also increase the electrode heat rate considerably. Thus, the walls, electrodes, and insulators exposed to the hypervelocity flow in MHD accelerators can experience an extremely harsh thermal environment, and the performance and reliability of these devices depend on the development of methods and materials to protect the exposed surfaces.

MHD accelerator research aimed at developing drivers for various aerospace testing applications was very active in the 1960s (see MHD Accelerator Technology Background, Section 2). Two otherwise similar programs, one in the United States and one in Russia, used very different approaches to thermal management. An arc heater-driven MHD accelerator experimental program known as LoRho was conducted at AEDC during the 1960s (Ref. 3) (see also Appendix Section B.1.3). Active cooling was used for the walls of this MHD accelerator as discussed below. During this same period, Russian researchers at TsAGI developed an arc heater-driven MHD accelerator of about the same scale as LoRho; however, this device used passive cooling (heat sink) for thermal control (Ref. 142).

Three small POC accelerator channels were tested during the LoRho program with a K-seeded N_2 plasma at power levels up to 400 kW and power densities on the order of 1 MW/m^3. The accelerator channel known as LoRho Accelerator B was 0.77 m long with entrance dimensions of 2.54 cm by 2.98 cm and exit dimensions of 2.54 cm by 6.22 cm. This accelerator had 117 electrode pairs, but only the center 60 electrode pairs were powered. At the high power level, centerline gas temperature exceeded 5,000 K, and the total heat transfer exceeded 200 kW or approximately 50% of the applied power. Average heat flux to the walls was on the order of 2 MW/m^2. Typically, the centerline Mach number was in the neighborhood of 2 for these tests. Electrodes were water-cooled, uncoated copper, and the sidewalls were water-cooled copper coated with a plasma-sprayed BeO. Maximum current densities on the LoRho accelerator electrodes approached 20 A/cm^2 for the high power tests.

The LoRho BeO insulation and copper electrodes reportedly survived very well in this environment. No appreciable damage was noted after minutes of run time for normal operation.

Several MHD accelerators have been built and tested at TsAGI. The TsAGI accelerators have been actively used for aerospace testing applications since the 1960s. Typical accelerators were 55-70 cm in length with 40-45 electrodes. These accelerators operate with centerline Mach numbers from 2 to 4 and centerline gas temperatures from 4,000 to 5,000 K. No active cooling is provided for these channels, thus they operate in a heat sink mode for run times on the order of 10 seconds or less with high heat fluxes of 10-50 MW/m^2. Channels are commonly operated at maximum currents of 55 A and Faraday voltages in the range 200-400 V, with total input power to the accelerator in the range 0.5 to 1.0 MW.

Typical electrode-insulator lifetimes are in the range of 5 to 10 seconds, and the most common failure mode is erosion of the interelectrode insulators along the anode wall.

These are small and low-power accelerators compared to the devices that will be needed for the next generation of full-scale, hypervelocity propulsion wind tunnel facilities. Preliminary analyses discussed in Appendix Section B.1 of this report indicate that seeded MHD accelerator designs for full-scale, hypervelocity propulsion test facilities would have dimensions on the order of a ½- to 1-m-square cross-section and 2 to 7 meters long. Applied electrical power for these accelerators may be on the order of 1 to 10 GW with wall heat losses of 0.5 to 1 GW. The thermal management problems for these accelerators will be enormous compared to the MHD accelerators of the 1960s. New materials for electrodes, insulators, and sidewalls, as well as sophisticated new methods for active cooling and thermal recycling (effective use of the thermal energy removed from the device) will need to be developed to enable these devices to perform to the required level.

4.3.3.3 Thermal Protection Systems

Some general methods for protecting the electrodes and walls of MHD accelerator channels from the harsh thermal environment will be briefly discussed in this section. There are two broad types of thermal protection systems: a) systems based on heat dissipation (active and radiative cooling) and b) systems based on heat absorption (passive cooling or heat sink).

Active cooling systems that have been used in many MHD accelerator and generator devices since the 1960s are one of the best examples of heat dissipation systems. In these systems, water or another cooling fluid is circulated through passages to transfer heat by convection from the hot exposed surfaces in the MHD device. The cooling fluid then transfers the heat to a low temperature system away from the MHD system. These systems are generally very effective but have disadvantages in their complexity and the loss of efficiency of the device being cooled. Since the objective of MHD acceleration is to increase the stagnation enthalpy of the working fluid, cooling the fluid is counter productive but most often necessary to protect the device.

Another form of heat dissipation would be radiation from the surfaces to be cooled. This is effectively used in many applications but may not be possible in the MHD accelerator environment due to the high temperature core flow.

Heat absorption methods can be either intrinsic or extrinsic. Intrinsic methods use the material that is exposed to the high temperature environment (walls, electrodes, nozzle, etc.) to absorb the heat and store the energy (heat sink) or remove the heat by ablation. Extrinsic methods transfer the heat to another medium and include such methods as transpiration and film cooling.

Heat sink methods can be used when the exposure times are short and the thermal capacity of the heat sink material is sufficient to prevent an excessive rise in the material temperature. This method may not be practical for T & E facilities, where long run times will be necessary and high facility productivity is desirable. Various forms of sacrificial (ablative) electrodes have been considered for MHD applications. This method can theoretically provide a solution to both the electrode heat transfer problem and electrode arc erosion; however, there are practical problems and disadvantages that must be overcome.

Transpiration cooling methods remove heat by vaporization of a coolant at the surface to be protected. Liquid coolant is pumped through porous surfaces into the slow moving flow along the wall; it is then heated and vaporized as it absorbs the heat from the flow before the heat reaches the wall surface. Film cooling is a closely related method in which a liquid film is introduced and allowed to flow over the area being protected. Transpiration and film cooling methods may be suitable for MHD accelerator applications if an appropriate cooling fluid is used that will both provide the necessary cooling and not detrimentally contaminate the flow. These methods are discussed further in Appendix Section D.1.

4.3.3.4 Search for a Suitable Material

One of the most demanding tasks in the development of an advanced, high-performance, hypervelocity MHD accelerator will be that of finding suitable materials, suitable cooling methods, or a combination of both to manage the extremely harsh thermal environment of these devices. The availability of suitable materials and cooling methods will be a significant factor in the feasibility of MHD accelerators for this application. The extreme thermal environment demands the exploration of state-of-the-art materials and methods. One candidate material for possible use in MHD accelerator sidewalls, if coupled with an appropriate cooling system, is discussed below. Other materials that should be investigated further for this application are also identified.

Hypervelocity vehicles and reentering vehicles experience boundary layer temperatures in about the same range as expected for the proposed MHD accelerator. These vehicles undergo a large range of heating conditions during the excursion through the atmosphere. As such, much research has been done for the design of reusable thermal protection systems (TPS) for these

vehicles. A typical TPS is composed of a combination of high temperature reusable materials and ablative materials and can involve active cooling systems as well.

The Space Shuttle is an example of a successful application of a reusable TPS. Anderson reports that when the Space Shuttle reenters the earth's atmosphere at Mach 25, it experiences a boundary layer temperature behind the shock wave of about 8,000 K (Ref. 143). Thus, Space Shuttle tiles, especially at the nose region, experience very high boundary layer temperature yet are reused without much damage and replacement. This is due in part to the reradiation of energy from the tile surface to the cooler environment beyond the Shuttle's hypersonic flow. In fact, the Space Shuttle tiles release most of the heat they receive from the boundary layer back to the atmosphere by reflection and reradiation, thereby keeping the surface temperature to a value in the neighborhood of 2,000 K.

Although the boundary layer temperature of Space Shuttles at reentry and the boundary layer temperature of the proposed MHD accelerator are expected to be in approximately the same range, the two surfaces may experience two very different heat transfer mechanisms. In the case of MHD channels, reradiation of energy from the surface might occur; yet, it would require much higher surface temperature since even the core flow will have a temperature in excess of 3,000 K. However, Shuttle tile material or its derivatives may be useful in MHD accelerators if these can be supplemented with other forms of cooling. For this reason, a brief overview of the Shuttle tile material, its fabrication, and its thermal and mechanical properties is included in Appendix Section D.1.

Space Shuttle tiles are made from a material called carbon-carbon composite, also known as reinforced carbon-carbon (RCC) material. Since the mid-1960s, RCC began replacing fine-grained graphite as nose tips in rockets because they represented significant improvement in thermoshock and erosion behaviors. The RCC structure is composed of a carbonaceous or graphitic matrix, which in turn is reinforced by carbon and graphite. This material has most of the desirable properties of monolithic graphite, but in addition, it has the high strength and versatility of a composite material. Additionally, this material has some unusual combination of properties including high temperature resistance, low thermal stress due to low thermal expansion, retention of properties at elevated temperature, high strength, high stiffness, and chemical inertness. These properties are of special interest for specialized high temperature applications like aeronautical, space, missile, propulsion, chemical, and nuclear fields, and may be of interest for MHD applications.

Carbon-carbon composite is a generic term that refers to a class of materials composed of carbon (or graphite) fibers with carbon (or graphite) matrix. A further discussion of the Space Shuttle material, carbon-carbon composite material, and other advanced materials that may be useful for thermal management are discussed in Appendix Section D.1.

4.3.3.5 Thermal Management Conclusions

A preliminary review of thermal management methods and materials that may be applied to MHD accelerators for producing hypervelocity flow conditions was performed as a task in the MARIAH Project. This review is summarized in this section and reported in Appendix Section D.1. Heat exchange mechanisms were explored, and also different thermal protection systems for surfaces exposed to very high temperature were investigated. It was concluded that to withstand the severe thermal environment in an MHD channel, the electrodes and the channel walls must use state-of-the-art materials coupled with a suitable cooling method. Several cooling methods in this regard were discussed. In search of a suitable material, important information about a state-of-the-art material used as the heat shield in Space Shuttles was discussed in detail. Guidelines and information on other possible materials are also given in the report.

Space Shuttle tile material was explored in some detail because of its unique physical and mechanical properties. This material has anisotropic properties and can withstand considerably high temperatures without losing its structural integrity. It has high thermal and electrical conductivities in one direction of the fibers and low values of the conductivities in the other direction. Oxidation of this material can be avoided at elevated temperatures with an appropriate and already known coating. However, due to the possibility of a higher surface temperature of the MHD channel walls than the surface temperature of a Space Shuttle, additional cooling mechanisms will definitely be required to keep the temperature to an acceptable level.

Development of a thermal management system to be used in the harsh environment of an MHD accelerator, including selection of appropriate materials for the walls and electrodes, is a very challenging problem. Numerical modeling can help define the thermal environment and the response of advanced materials and cooling systems when used in this application.

4.4 MARIAH II CONCEPT

The MARIAH Project was undertaken for the purpose of conducting studies into the feasibility of using MHD accelerators to produce true air simulation for hypervelocity propulsion in ground testing facilities. The MARIAH II concept is an outgrowth of that effort and is based upon MHD augmentation of UHP drivers with radiative energy addition. The RDHWT concept is a hybrid theory that employs the UHP technology with beamed energy addition in a supersonic expansion following a nozzle. The MARIAH II concept is also a hybrid that has the RDHWT as the primary driver and MHD as a second-stage driver.

Results of a preliminary study into the benefits of this hybrid technology are summarized in this section and reported in further detail in Appendix F and Reference 23. The primary issues addressed are: the overall conversion efficiencies; potential advantages of the MARIAH II scheme compared with the stand-alone RDHWT; the optimal range of parameters (pressure, temperature, velocity) for the MHD channel operation in the overall MARIAH II scheme; the requirements on electric and magnetic fields as well as an ionizer; and the required plenum

conditions for the first stage. The key technical issues are identified, and some recommendations for an R&D program to further demonstrate the feasibility of the MARIAH II scheme are given.

4.4.1 Overview

The problem of duplicating (in a ground test facility) the high enthalpy, high dynamic pressure, high Mach number regime characteristic of hypervelocity flight has been a challenge to airframe and engine designers for the past 40 years. In continuous flow testing (i.e., simulations that last several seconds or more), the primary means of generating such flows has been the arc heater. While arc-heater technology has progressed significantly in the last two decades, it continues to be limited to operation at reservoir pressures below 150 atm. Arc heaters also suffer from high entropy values at their exit due to the addition of energy completely by Joule dissipation. This fact, coupled with a reasonably well-defined hypersonic flight envelope, imposes second law limitations on the amount by which the total enthalpy can be increased without crossing the targeted flight envelope. These fundamental limitations have prompted researchers to search for alternatives to arc-heater technology.

In the recent past, both MHD and UHP drivers with downstream radiative energy addition have been proposed as alternatives for augmenting the total enthalpy of air (Refs. 2, 14, 17, 25, 28, 126, 127, 144, 145) While MHD accelerators have been applied in the past to arc heated flows, they are not intrinsically limited to such flows. The UHP drivers with radiative energy addition RDHWT have been described in some detail in References 144-126, while MHD augmentation of airflows has been described in References 2, 14, 17, 25, 28, and 127. Each of these technologies has limitations associated with both hardware and fundamental physics. Second law limitations (specifically, limitations due to Joule dissipation or the thermalization of beamed energy) are common to both technologies. However, each offers unique advantages when compared to arc heaters. For the RDHWT scheme, the proposed resolution of the entropy problem is to start the process at very low entropy levels by pressurizing the gas in a reservoir to 20,000 atm or more while maintaining temperature at modest levels (below 1,500 K, for instance). For the MHD concept, the problem of Joule heating is mitigated in some sense by the push work done on the gas by the MHD body forces. The latter contribution adds no entropy to the flow, and this fact constitutes the primary argument for MHD over other energy addition methods.

In this section, the MARIAH II concept, which would employ the UHP technology with beamed energy addition as the primary driver and MHD as a second-stage driver is investigated. The primary issues that are addressed below include: a) overall conversion efficiencies; b) potential advantages of the MARIAH II scheme compared with the stand-alone RDHWT; c) the optimal range of parameters (pressure, temperature, velocity) for the MHD channel operation in the overall hybrid scheme; d) the requirements on electric and magnetic fields on an ionizer; and e) required plenum conditions for the first stage. The key technical issues are identified and some recommendations are given for an R&D program to further demonstrate the feasibility of the MARIAH II scheme.

4.4.2 Basis for the MARIAH II Concept

Figure 4- 63 is a Mollier diagram showing total enthalpy and entropy corresponding to post-bowshock conditions experienced by a hypersonic aircraft at various flight altitudes. As the diagram shows, to duplicate these conditions in a ground test facility will require the total enthalpy of the gas to be increased from ambient levels to tens of millions joules per kg.

The limiting envelope for arc-heater operation (Ref. 2) is also shown on Figure 4- 63. Arc heaters have been the primary means of creating high enthalpy continuous flows for hypersonic testing for the past 30 years. These devices operate at relatively low plenum pressure (below 150 atm) and high temperature and rely on a complete conversion of electrical power to heat by way of Joule dissipation. This results in very high entropy levels at the heater exit. While the total enthalpy is limited only by the amount of added electrical power, the thermodynamic end point is typically too far to the right on the H-S diagram, as can be seen in Figure 4- 63. The overall result is the test section pressures and/or Mach numbers are lower than those corresponding to in-flight, post-bowshock conditions.

This situation has prompted researchers to investigate alternative technologies for simulating hypervelocity flight. One such alternative is the UHP gas piston driver. This technology, originally developed in Russia, relies on the creation of a reservoir of extremely high-pressure gas that is subsequently released through a narrow throat into a downstream expansion region (Refs. 146, 147, 148, 149). Experience with this technology in both Russia and the U.S. indicates that reservoir pressures of 20,000 atm are attainable. The advantage of using such high-plenum pressures to drive a high-speed flow is the low entropy that results since the entropy scales as the logarithm of the inverse of the reservoir pressure.

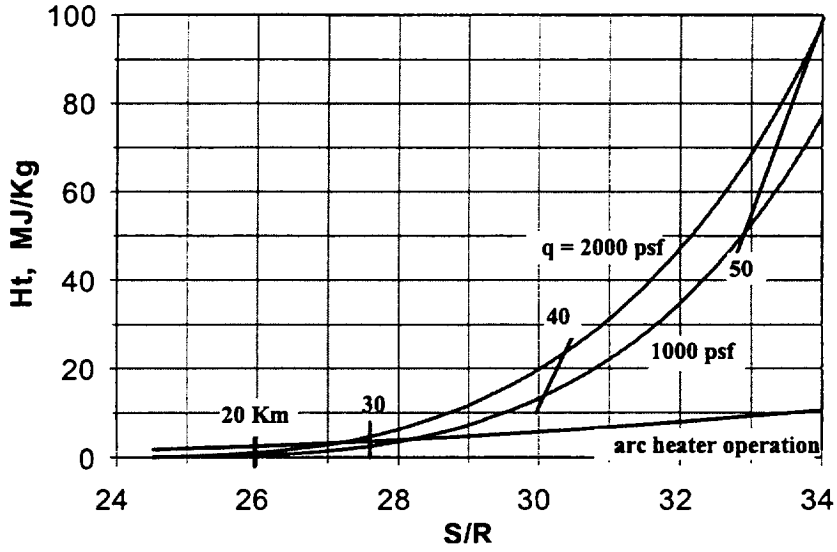

Figure 4- 63. Hypersonic test facility performance requirements in terms of entropy, total enthalpy, and dynamic pressure.

High-plenum pressures thus correspond to greatly reduced starting entropy levels in comparison to arc heaters. The RDHWT concept (Refs. 126, 144, 145) combines the UHP driver with beamed energy addition in the form of laser, microwave, or relativistic electrons to significantly improve its performance and broaden its capabilities. A key element of the RDHWT concept is that the beamed energy is added to the expanding supersonic flow downstream of the throat. This provides a large increase in the total enthalpy while at the same time greatly reducing the maximum static temperatures attained when compared to more conventional technologies. This in turn alleviates the materials problems downstream of the nozzle throat. The overall thermodynamic process of such a device is illustrated in Figure 4- 64, which shows a representative path on the Mollier diagram.

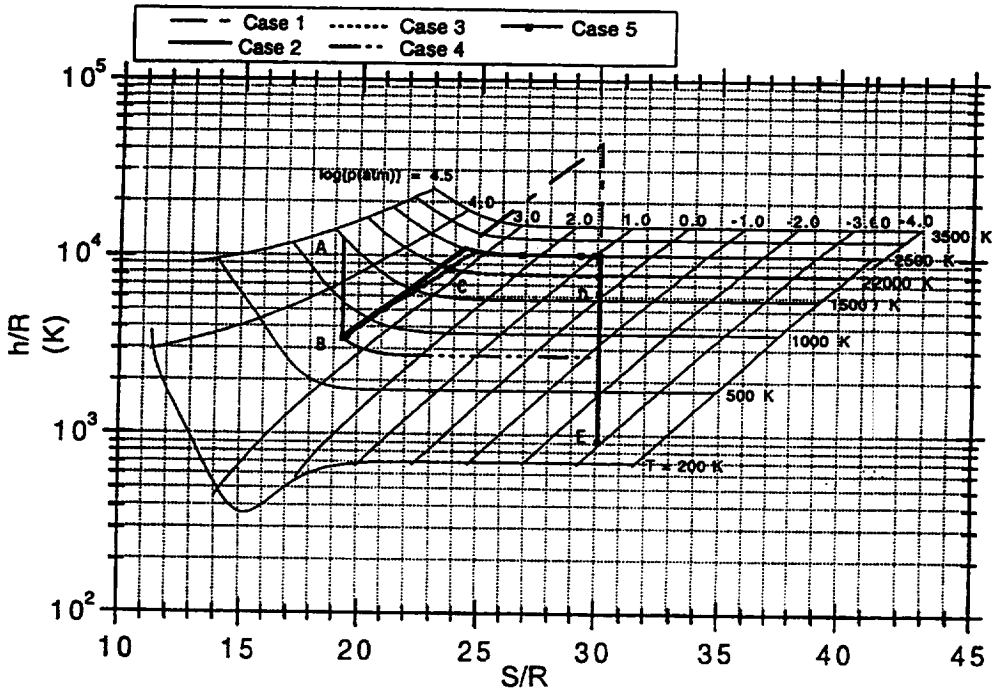

Figure 4- 64. Mollier diagram for air, showing typical process paths for the RDHWT (Ref. 145). The baseline Case 3 is the line ABCDE.

The other driver technology to be considered is MHD. It should be emphasized that the important feature that differentiates MHD energy addition from energy addition by means of an arc heater or beamed energy is an MHD accelerator adds a significant fraction of the input electric power as push work, which does not contribute to an entropy increase. The fraction of energy that is added as push work is referred to as the conversion efficiency, η. Therefore, the quantity $(1 - \eta)$ is the fraction of input power added through Joule dissipation. Since an arc heater adds all of its energy through Joule dissipation, the MHD conversion efficiency is obviously zero.

The MHD energy conversion efficiency (η) can be defined as the ratio of the push work ($<j_y uB>$) to the total electric power per unit volume applied to the accelerator ($<j \cdot E>$):

$$\eta = \frac{< j_y uB >}{< j_y E_y + j_x E_x >} \tag{4- 18}$$

Where the brackets < > denote an average across the duct, j_y and j_x are the transverse and axial current densities, u is the flow velocity, B is the applied magnetic field, and E_y and E_x are the transverse and axial electric fields.

For a Faraday accelerator, the streamwise or axial current j_x, is zero, and with the aid of the Ohm's law relationships (see Ref. 150), the conversion efficiency can be reduced to:

$$\eta = 1 / K \tag{4- 19}$$

Where the Faraday load factor K, is defined as:

$$K = \frac{< E_y >}{< uB >} \tag{4- 20}$$

(see Appendix F for further details.)

It is apparent from Equation (4- 19) that K must be close to unity for high efficiency. Of course, if $K = 1$, then the transverse current density will be zero and there will be no push work ($j_y uB = 0$). In fact, there will be no power applied to the accelerator. Thus, for any real MHD accelerator, the load factor must be greater than unity and the conversion efficiency must be less than unity. In practice, the channel length required to increase the enthalpy by a specified quantity will be found to be dependent on the load factor, and load factors too close to unity will result in very long channels.

Then, if $L_{\Delta H}$ is the length of MHD duct required to increase the total enthalpy by an amount ΔH, it can be shown this can be approximated by:

$$L_{\Delta H} = \frac{\dot{m}\,\Delta H}{\left\langle K(K-1)\sigma\, u^2\, B^2\, A \right\rangle - \left\langle q_w\, P_{ch} \right\rangle} \tag{4- 21}$$

where q_w is the heat flux to the walls, m is the mass flow rate, $P_{ch}(x)$ is the channel perimeter, and $A(x)$ is the channel cross-section. Viscous dissipation has been neglected. If heat transfer is neglected, this expression indicates that a value of K equal to 1 results in an infinite channel length. This also suggests that for minimum channel length, the accelerator should be operated

at the maximum possible load factor. However, as noted above, this corresponds to maximum Joule dissipation and low conversion efficiency. In practice, values of K in the range 1.1 to 3 may represent a reasonable compromise between achieving a workable duct length and minimizing Joule dissipation.

As Equation (4- 21) shows, to increase the MHD efficiency (i.e., to make K close to 1) and to restrict the channel length (L) for minimizing boundary layer effects, the value of the term $\sigma u^2 B^2$ must be high. Of course, overly strong magnetic fields and low densities may result in very large Hall parameters (Refs. 17, 150), which would be undesirable. One of the benefits of combining RDHWT with MHD is the potential for RDHWT to produce much higher gas velocities at the MHD duct entrance than those created by conventional arc heaters. Creating the high values of electrical conductivity required for efficient MHD operation presents a great challenge, especially at high densities and/or low temperatures. However, the beamed energy addition for the RDHWT may assist with this by creating and sustaining nonequilibrium ionization.

Potential advantages of the MARIAH II scheme can be better understood by looking at basic thermodynamic constraints imposed on the RDHWT performance envelope. Certainly, RDHWT modeling performed in References 126, 144, and 145 has demonstrated that the UHP driver combined with laser, microwave, or e-beam heating of the dense supersonic stream is potentially capable of achieving Mach numbers of 12 and above at high dynamic pressure with long run times and relatively low contamination of the flow. However, the concept still has inherent limitations dictated by the second law of thermodynamics.

An acceptable entropy increase (Δs) for an RDHWT driver is limited since the final entropy is set by the required test section conditions while the minimal initial entropy is essentially defined by the incompressibility of high-density fluids (RDHWT operates close to that limit). The enthalpy that can be added to the flow by heating (to be then converted into kinetic energy through expansion) is obviously related to the average temperature (T_a) at which the heat is added and to the entropy increase (Δs) by the second law:

$$\Delta H = T_a \Delta s \tag{4- 22}$$

Despite the fact it is thermodynamically advantageous to operate at high temperatures, the average temperature (T_a) cannot be very high because of the need to minimize air dissociation and wall erosion.

Using MHD acceleration in the RDHWT expansion nozzle could improve the performance, thereby increasing Mach number and/or dynamic pressure in the test section. This is due to the fact that at least a part of the energy addition in the MHD channel is in the form of push work, which directly increases the kinetic energy of the flow without generation of entropy. As can be easily shown, the total enthalpy that can be added in the MHD channel for a given entropy change depends on the loading parameter K (Ref. 17):

$$\Delta H = \frac{K}{K-1} \cdot T_a \Delta s \qquad (4\text{-}23)$$

Thus, if a sufficiently high value of the conductivity can be created, then the MHD channel can operate with a value of K close to 1, and a significant augmentation of flow enthalpy, test section Mach number, and pressure could be expected.

Several advantages can be realized using the RDHWT concept as a first-stage driver to provide the entrance conditions for the MHD channel. Indeed, the RDHWT is very flexible (Refs. 126, 144), and by varying UHP pressure and temperature, supersonic nozzle geometry, and the heating power, a wide range of conditions can be reached at the MHD channel entrance. For example, velocity and Mach number at the MHD channel entrance can be high with a moderate gas pressure. Furthermore, preionization of air, when high-energy e-beams are used as an energy source for the RDHWT, can be an additional advantage for the MHD. A preliminary analysis presented in Appendix F indicates this combination could be advantageous for MHD augmentation and compares favorably with the conventional arc heater, which is limited to lower pressure operation. This version of a MARIAH II wind tunnel facility is shown schematically in Figure 4- 65.

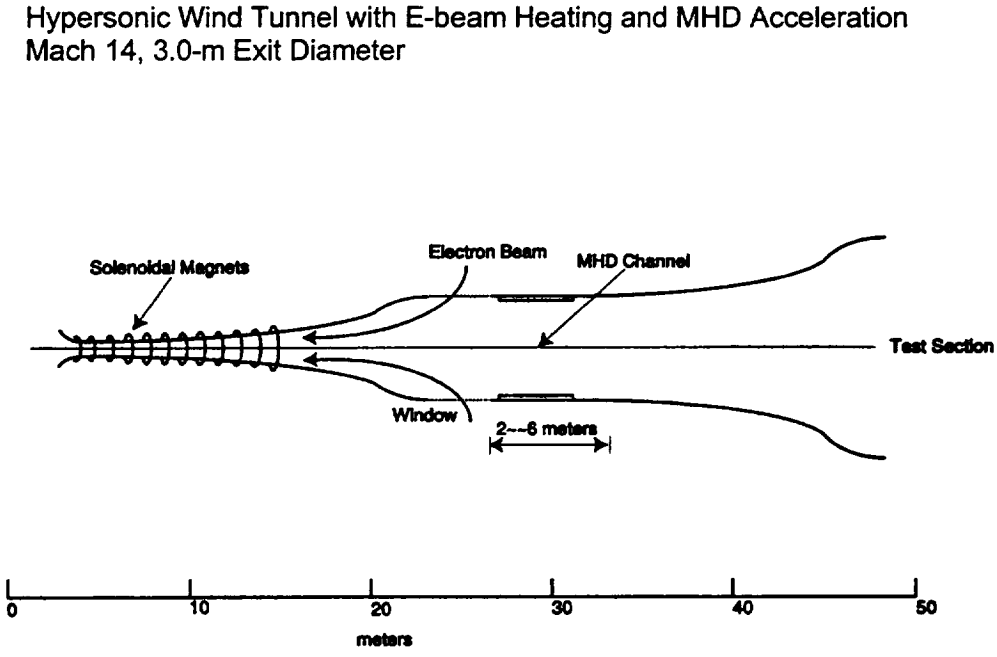

Figure 4- 65. A schematic picture of a MARIAH II wind tunnel. Relativistic e-beams focused by solenoidal magnets add energy to air at high pressures, followed by acceleration in an MHD duct at low pressures.

4.4.3 Two Regimes of MHD Channel Operation

Efficient operation of an MHD accelerator requires high values of the electrical conductivity (σ) as discussed in the previous section. However, simulation of high Mach number, high dynamic pressure conditions in the test section requires low entropy, which in turn requires high pressure and/or low temperature in the MHD channel. For conventional MHD operation (even with K or Cs seed), the temperature in the channel must be on the order of 3,000 K, which results in MHD channel static pressures on the order of tens to hundreds of atmospheres, depending on the flight conditions to be simulated. Sufficiently high electrical conductivity is extremely difficult to achieve under these conditions.

Therefore, two "unconventional" modes of MHD acceleration have been suggested: a) high-pressure operation with highly nonuniform ionization; and b) low-pressure, low temperature operation with an external ionization source.

4.4.3.1 MHD Acceleration at High Pressure: A Guided Arc Concept

In this regime, the flow exiting the UHP driver will be directly passed into an MHD channel. The pressure in this channel would be high, on the order of a few hundred atmospheres, and the temperature, although high, is below that needed for conventional MHD operation. Thus, the flow will have to be ionized and the discharge stabilized to develop MHD augmentation. Since it is all but impossible to get a uniformly high conductivity at these conditions, a possible approach may be a guided arc accelerator.

In this case, a bright arc would be initiated across the channel along a line defined by either a laser or an e-beam. This arc will be sustained by two thin linear electrodes on each side of the flow extending in the flow direction. In the absence of a magnetic field, the arc will propagate downstream and move along the electrodes to the end of the channel. It has been shown by Topchiyan et al. (Refs. 146, 147) that such arcs can be initiated and maintain their integrity as they move downstream in high-pressure hypersonic flows. In the presence of a magnetic field, the arc will be accelerated due to the high electric current and will serve as a fluid accelerator.

A single arc will not suffice to accelerate the entire flow. An interesting possibility would be to examine initiating an array of arcs as a flow driver, each with its own pair of linear electrodes. The spatial separation between these arcs should be small enough to generate uniform flow acceleration but large enough to minimize magnetic interaction between them. With axial segmentation of the electrodes, arcs could be passed from one pair of electrodes to the next as the flow moves downstream, and a new set of arcs could be initiated.

Thus, a rapid-fire sequence of arcs can be formed to more effectively drive the flow and to minimize flow nonuniformity. The approach will create fundamentally nonuniform air and the implications of this must be studied. With a high enough repetition rate and a close enough separation, this nonuniformity may hopefully thermalize before the air enters the test section.

The high pressure also enhances the recombination rate of electric charges and nonequilibrium species, thereby helping to minimize NO and ozone formation.

The high temperature in the arc allows the electrical conductivity to be sustained and enhances the $\Delta H/\Delta s$ ratio. Of course, there will be additional entropy generated by the arc moving through the air, which also has to be evaluated to determine the actual work-to-heat ratio. These issues need to be addressed in future research.

4.4.3.2 MHD Acceleration at Low Pressure and Temperature with E-Beam Ionization

Because of difficulties of sustaining high uniform conductivity at high densities, it would be advantageous if an acceptable MHD channel performance at low densities could be demonstrated. Again, the second law imposes an important constraint here. The entropy at the channel entrance has to be significantly less than the required entropy at the test section. Since entropy increases with temperature and decreases with pressure, low pressures in the channel would all but preclude operation at high temperatures. This, in turn, creates two difficult problems.

First, low temperatures mean only a small amount of enthalpy can be added in the form of heat ($T\Delta s$). According to Equation (4- 23), this must be compensated by the loading parameter K (close to 1) so almost all of the enthalpy is added directly as kinetic energy.

Secondly, the low temperature operation of the MHD channel requires adequate conductivity be created by means other than conventional thermal ionization. Because the requirement $K\approx 1$ restricts the maximum value of the electric field (E), the effective field $(E - uB)$ in the channel will be small and incapable of sustaining the discharge. This leaves only an external ionization source as a method of creating the conductivity. Specifically, beams of high-energy electrons could be used for the ionization of the gas.

The MARIAH II tunnel in this scenario would have an UHP front end. After expansion to supersonic velocity, air will be heated using lasers, microwaves, or relativistic e-beams, and its velocity increased while still at very high pressure (from thousands of atmospheres down to about 1,000 or perhaps several hundred atmospheres). The air will then be isentropically expanded to low pressure (on the order 0.1 atm) and low temperature (perhaps about 300 K). Further acceleration will be provided by the MHD channel, perhaps in the form of a Faraday accelerator with ionization sustained by high-energy e-beams injected parallel to the magnetic field. The entropy at the channel exit should match the test section entropy so the gas can reach the required conditions by isentropic expansion after the MHD channel. Figure 4- 65 is a schematic diagram of such a wind tunnel, and Figure 4- 66 shows a representative thermodynamic path of air in the tunnel.

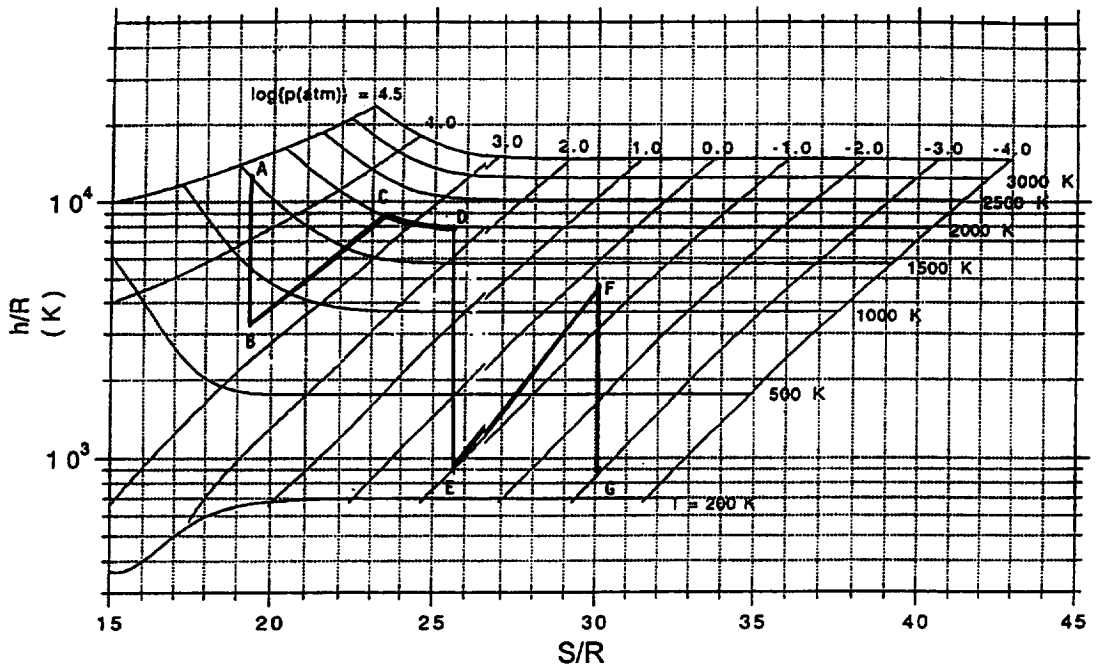

Figure 4- 66. Thermodynamic path (ABCDEFG) of the example case of a MARIAH II type facility. A – ultrahigh pressure plenum; AB, DE, FG – isentropic expansion regions; BCD – heating by beamed energy sources; EF – low-pressure MHD accelerator; G – test section.

4.4.3.3 MARIAH II Concept Conclusions

The preliminary analysis performed in Appendix F and summarized in this section shows a flow train consisting of a UHP driver, beamed energy heating, and an MHD accelerator offers interesting possibilities for future high dynamic pressure, long run time hypervelocity wind tunnels. The MARIAH II scheme draws upon the strengths of each of the components and benefits from their synergism. The UHP driver, with RDHWT, adds a large amount of enthalpy to air when the density is high and entropy is low. This relaxes requirements on MHD performance and creates favorable gas conditions in the MHD channel. Conversely, MHD acceleration is capable, in principle, of significantly extending the performance envelope (Mach number, dynamic pressure, etc.) of the RDHWT.

Two MARIAH II type facility concepts were suggested. One is the guided arc concept, which at this time is in the early, qualitative stage. Some of the principal issues to be addressed in future experimental and theoretical developments of the concept are:

1. How multiple arcs can be controlled and stabilized by lasers or e-beams and accelerated in crossed electric and magnetic fields.

2. How effective a moving region of hot gas can be in imparting momentum to the bulk flow.
3. The level of efficiency this scheme can achieve in terms of entropy generation.
4. Whether the resulting flow nonuniformity and chemistry inside arcs can produce acceptable flow quality for test facilities.

The other MARIAH II concept relies on using an MHD duct as an "afterburner," augmenting the energy addition of the RDHWT. In this scheme, MHD would operate at low pressure and temperature with ionization created by beams of energetic (30 - 60 keV) electrons. Simple analysis and estimates performed (see Appendix F) show such a scheme might significantly augment the Mach number and dynamic pressure as compared with the pure beamed energy, RDHWT case. It may also be possible to significantly reduce the ultrahigh pressure in the plenum, thus helping to scale the facility to larger volumes and longer run times. Among many issues to be resolved in the development of this concept are:

- coupling of ionizing e-beams into the duct where strong magnetic and electric fields are present;
- control of gas flow and ionization processes in the boundary layer (in conjunction with designing a system of segmented electrodes to avoid breakdown and short-circuiting due to high electric fields in the slow-moving gas near the electrodes); and
- chemical quality of the flow subjected to the flux of energetic electrons.

Other issues related to ultrahigh-pressure drivers and beamed energy addition must be addressed in the development of the MARIAH II concept. Scaling of the UHP drivers to very large volumes and long run times, survivability of throat materials, selection of energy sources (lasers, microwaves, or e-beams), and their coupling to dense supersonic flow are among those critical issues. A multidisciplinary effort aimed at resolution of the technical issues could result in development of the new advanced concept of hypervelocity test facilities.

5. CONCLUSIONS AND RECOMMENDATIONS

5. CONCLUSIONS AND RECOMMENDATIONS

Three distinct MHD accelerator concepts have been addressed during the MARIAH Project. The first (and most extensively evaluated) is the equilibrium, seeded MHD accelerator augmenting advanced, high-pressure arc heaters. Cesium was used exclusively as the seed material for these analyses. Other seed materials were reviewed, including fullerenes, a high molecular weight form of carbon. Fullerenes were found to be impractical for seeding high temperature air since they would decompose at the high temperature and the carbon would combine with O_2 in the air environment (see Appendix Section C.1). Other alkali metal species were considered (K and Rb) but were rejected in favor of the higher performance available from the low ionization potential of Cs (see Appendix Section C.2).

The effect of seed contamination on hypervelocity propulsion testing has been a concern of researchers. Two studies were conducted to assess the effects of seed on combustion in supersonic flow. These studies concluded that if scramjet combustion is mixing limited (as most researchers believe it is), then the small effects the MHD seed material will have on the combustion kinetics will be negligible (see Appendix Section C.3 and Appendix E).

Unseeded MHD accelerator concepts have been evaluated by MSE in previous studies and were the original basis for initiation of the MARIAH Project. The analytical studies conducted by OSU also addressed the unseeded accelerator concept. The results and conclusions of the unseeded studies are discussed in this section. Unseeded MHD has the potential to produce test conditions in a limited range of hypervelocity propulsion test regimes and can produce clean, true air chemistry for those conditions.

Finally, the third concept to be addressed is the use of a UHP driver with beamed energy addition to provide suitable conditions for an MHD accelerator. The accelerator thus augments the energy addition to produce the desired test section conditions. The MARIAH II concept is discussed in Appendix F and is summarized in Section 4.1.4.5. Conclusions and recommendations relative to this concept are discussed in Section 5.1.3.

Following these MHD technology conclusions, open issues that should be addressed in future research are discussed in Section 5.2 and are divided into a discussion of the technology deficiencies identified during the MARIAH Project in Section 5.2.1 and the currently unresolved issues in Section 5.2.2. Finally, recommendations for future research are provided in Section 5.3.

MHD accelerator technology has been evaluated to determine if it can produce the high-stagnation enthalpy, high dynamic pressure conditions necessary for large-scale ground testing of air-breathing hypersonic propulsion engines at hypervelocity free-jet conditions. This research has been conducted under the NASA MARIAH Project. The objectives of the MARIAH Project were to investigate the feasibility of MHD augmentation of other hypersonic wind tunnel driver technologies to provide the high Mach number, low entropy test conditions required for a hypervelocity T&E facility. Specifically, NASA provided a target test condition for comparison

against predicted MHD accelerator capabilities. This T&E facility should produce test conditions equivalent to the post-bowshock conditions for a 5° deflection angle at a flight Mach number of 16 and a flight dynamic pressure of 2,000 lbf/ft^2.

5.1 MHD TECHNOLOGY CONCLUSIONS

Conclusions from the evaluation of three MHD accelerator concepts are addressed in this section. Primary emphasis in the MARIAH Project has been on assessing the capabilities of Cs-seeded MHD accelerators augmenting high-pressure arc heaters. Conclusions of the Cs-seeded MHD studies are discussed in Section 5.1.1. Results from analytical evaluations of unseeded, nonequilibrium MHD accelerators used to augment arc heater test conditions are given in Section 5.1.2. Finally, the assessment of MHD used in the MARIAH II arrangement with a UHP driver and beamed energy addition is provided in Section 5.1.3.

5.1.1 Cesium-Seeded MHD Augmentation of Advanced Arc Heaters

Several analytical studies were conducted evaluating the performance of seeded MHD accelerators augmenting advanced arc heaters. MHD parametric and optimization studies were conducted and reported in Appendix Sections B.1.4 and B.1.5, respectively, and summarized in Section 4.1.1. Advanced arc heater and high field strength magnet technologies projected to be available in the 15- to 20-year development time for a major test facility were used in these analyses. Relatively conventional, linear, segmented Faraday MHD channel technology was assumed.

Cesium seeding, at a 1.0-molar percent level, was used for all of the analyses conducted with the MSE ACCEL 1-D MHD code. Cesium has the lowest ionization potential and produces the highest level of electrical conductivity of available seed species. An evaluation of the cost and availability of Cs (see Appendix Section C.2) indicated it would be available in the quantities required for a major facility but would be a significantly higher cost seed than K. There were no factors indicated in this study that would preclude the use of Cs; yet, selection of a practical seed based on performance, cost, and availability tradeoffs should be conducted in a facility design study at the appropriate time.

Magnets with field strengths of 15, 24, and 30 T were evaluated in this study. Magnetic field strength had the most pronounced effect of any parameter evaluated. Today, 6-T superconducting magnets are available, and 8-T magnets could probably be developed using present technology. Magnets having 10- to 12-T fields are projected for near-term development, and 15-T magnets could be available in the 15- to 20-year time frame. At present, 24- and 30-T magnet development cannot be projected in the foreseeable future. Analyses at these field values have been included to provide a basis for recommendations on future technology development. Cesium-seeded MHD, augmenting advanced 200-atm arc heaters, were not capable of producing test conditions to simulate the NASA specified flight condition. High-pressure operation of the

MHD accelerator channel contributed significantly to the performance difficulties encountered. Pressures in the MHD channel ranged from about 10 atm to 80 or 90 atm, depending on other conditions in the simulation. The high pressure contributed to a large increase in entropy by several mechanisms. First, high channel pressures resulted in low values of electrical conductivity. A study of ionization and electron attachment for Cs-seeded air (see Appendix Section C.4) indicated that both a reduced ionization fraction and an increased electron attachment to O_2 species at the high pressure were the reasons. Experimental investigations at the UTA confirmed the equilibrium electrical conductivity reduction due to electron attachment (see Appendix Section A.1). Low values of electrical conductivity cause large entropy increases because of the increased Joule heating. High pressure also caused higher wall heat losses, resulting in longer channels to reach the desired enthalpy level and, thus, higher entropy production due to wall friction losses.

Thus, for the NASA-specified, Mach 16 flight condition, entropy was always too high in the MHD simulations. Higher entropy conditions correspond to lower dynamic pressure flight conditions at higher altitude. For example, the NASA specification for a flight dynamic pressure of 2,000 lbf/ft^2 corresponds to a flight altitude of 35.3 km. With a 200-atm arc heater and a magnetic field of 15 T, an MHD accelerator was capable of producing post-bowshock conditions equivalent to Mach 16 flight with a dynamic pressure of 710 lbf/ft^2, which corresponds to an altitude of 42.8 km. In using a 30-T magnet (which is beyond presently foreseeable technology capabilities), MHD could simulate flight at a dynamic pressure of 1,200 lbf/ft^2 and Mach 16, corresponding to post-bowshock conditions at 39-km altitude.

At low pressures, Hall parameter (electron mobility times magnetic field strength) can grow to large values and cause ionizational instabilities in the plasma that cause a reduction in performance. But, at the high pressure required for the attempts at simulation of the NASA condition, Hall parameter was within reasonable bounds and would not present any problems to the MHD performance, even at the 30-T magnetic field.

Although arc-heater driven MHD was unable to reach the required NASA flight conditions, these devices clearly produced simulations of flight conditions that cannot be obtained using other technologies. For example, with a 15-T magnetic field, MHD could simulate Mach 16 free-stream conditions at a flight dynamic pressure of 500 lbf/ft^2 and MHD-produced conditions that were significantly lower in entropy (higher pressure) than required for combustor inlet conditions for all Mach numbers evaluated (up to 20, although the data easily extrapolates beyond this).

A few simulations were conducted using MHD starting conditions equivalent to lower pressure, lower enthalpy arc-heater exit conditions. These did not produce significantly different solutions to those of the baseline 200-atm arc heaters. Thus, it is concluded that higher pressure arc heaters could enable only marginally higher MHD performance. At the high pressure required for producing the high dynamic flight pressure and the high Mach number conditions specified by NASA, developments in magnet technology that lead to higher field strength provided far more benefits than increases in arc-heater pressure limits.

The NASA specifications for the MARIAH Project study required a test section area of 80 ft^2. At the flight conditions specified, this leads to a mass flow rate of 820 kg/s. Stagnation enthalpy at this condition is 12.15 MJ/kg. Thus, the total thermal power at test section conditions is 9.96 GW. This is the minimum power required to be added to ambient air by any means to reach test section conditions. Since wall heat loss for the optimum performance cases was usually on the order of ½ to 1 GW and about 2.5 GW thermal power is provided by the arc heater, electrical power to the MHD channel was typically 8-9 GW. Thus, including an estimate of the total power required by the arc heater, total electrical power for this facility would be approximately 12-13 GW. If electrical energy storage was available and 10 tests (2-minutes duration each) were run per day, this represents an average power use of approximately 85 MW. Although not impossible to obtain, a power system for an MHD facility of this scale would be a significant investment, and the operational costs would be equally large.

The large power requirements of an MHD facility are due primarily to the high energy and large scale of the specified flight simulation condition. Simulation of lower energy conditions (lower flight Mach number) at a smaller scale would considerably reduce the power requirements.

Although seeded MHD augmentation of arc heaters can produce lower pressure (higher entropy) test conditions, this technology cannot produce the high-pressure test conditions required by the NASA specifications for the MARIAH Project (see Section 3). These investigations indicated that simulation of flight conditions at a dynamic pressure of 500 lbf/ft^2 may be possible. However, even using magnetic field strength values well beyond those available in the foreseeable future, the analyses indicated that a dynamic pressure of 2,000 lbf/ft^2 at a Mach 16 flight condition is unachievable using seeded MHD augmentation of arc heaters.

5.1.2 Unseeded MHD Augmentation of Conventional Arc Heaters

Unseeded, nonequilibrium MHD acceleration was evaluated in previous analytical studies (Refs. 14, 17, 24) and was found to be a potentially viable technology for producing the higher entropy test conditions, such as hypersonic propulsion combustor inlet conditions. Using a 200-atm arc-heater entrance condition and a 10-T magnetic field, MHD was capable of producing hypersonic propulsion combustor inlet conditions for flight Mach numbers up to 20 and flight dynamic pressure of 500 lbf/ft^2 or greater. Two different mechanisms for producing the nonequilibrium ionization were considered. Both involve elevated, nonequilibrium electron temperatures that produce nonequilibrium ionization through molecular collisions. In both cases, the equilibrium population of NO in the air is the predominant species ionized since it has the lowest ionization potential of the naturally occurring air species.

In one analysis, high values of the applied electric fields created nonequilibrium electron temperature through acceleration of the electrons in these fields. This analysis indicated combustor inlet conditions for a 500 lbf/ft^2 dynamic pressure were possible using this technique. The other analysis assumed that arbitrary electron temperature values could be maintained in the MHD channel using a combination of the high electric field acceleration of electrons and

external enhancement by beamed energy addition (microwave or e-beam). This analysis indicated higher performance, and the simulated conditions approached combustor inlet conditions at a dynamic pressure of 1,000 lbf/ft^2.

Aside from the MSE studies cited, OSU also investigated the feasibility of unseeded, nonequilibrium MHD. This study is described in Reference 17 and also in Appendix Section B.2. Briefly, the conclusions of the study were that the total enthalpy increases through the MHD accelerator will be quite small, even if e-beams are used for ionization enhancement. This is due to the very rapid electron-ion recombination rates associated with the assumed high-pressure inlet conditions. In most of the cases studied by the OSU group, the inlet pressure was in the range 10-100 atm. These cases all showed only slight enthalpy increases within the MHD channel. In one series of runs, plenum conditions were taken to be 1,000 atm and 6,000 K. An e-beam was employed in the channel inlet region for conductivity enhancement, and the flow was expanded out of the arc heater to 1 atm pressure. For this case, it was found the total enthalpy could be augmented by approximately 70%. As stated in the report, "The only conceivable way of efficient use of e-beams (or other ionization sources) in high-plenum pressure flows appears to be expanding the flow down to the low pressures prior to creating the nonequilibrium ionization." This scheme does not have the inherent pressure limits associated with conventional, thermal ionization. Presumably it should be possible to expand the flow from the heater to tenths of an atmosphere if necessary. In the nonequilibrium approach, the expansion may proceed down to very low temperatures and therefore much lower pressures because the ionization no longer depends on temperature.

The basic conclusion of the OSU nonequilibrium study was similar to the MSE studies, namely this concept is not capable of reaching the very high enthalpy, low entropy conditions specified by NASA for the MARIAH Project. However, the concept could provide a clean air testing environment for testing at higher entropy levels such as for tests requiring simulation of combustor inlet conditions.

The conclusion from these three studies is that the arc-heated, unseeded, nonequilibrium ionization concept cannot produce test conditions approaching those specified by NASA for the MARIAH Project analyses. In the low-pressure channel flow with high electric field values, uncorrected electrical conductivity values were reasonably high. In a typical analysis, electrical conductivity entrance values were between 50-100 mho/m and increased to several hundred at the exit. However, in the low-pressure flow with high magnetic field strength, Hall values grew very large creating concerns about ionizational instabilities. A simple correction was used to calculate an effective Hall parameter and an adjusted electrical conductivity (see Appendix Section B.1.2). These corrections considerably depressed the conductivity, resulting in low values that reduced the MHD performance.

At the higher pressure required to reach high dynamic pressure, post-bowshock condition, Hall parameter will be much lower, and correction of the electrical conductivity will not be necessary. However, electrical conductivity will also be lower due to the difficulties of maintaining nonequilibrium ionization at the high pressure. Two mechanisms will lower the degree of

ionization and the electrical conductivity. First, the electron mean-free path in the gas will be much shorter in the higher pressure, thus, the electrons will not be able to gain as much kinetic energy accelerating in the electric field and will have a much lower temperature. Secondly, the more frequent collisions in the higher density gas will result in faster equilibration of the nonequilibrium ionization. Lower performance can then be expected at the high pressure, and the nonequilibrium MHD channel will not be capable of reaching the low entropy conditions selected by NASA.

There is a relatively high degree of uncertainty in these analyses due to the simplistic approach to the nonequilibrium ionization and high Hall parameter corrections used. However, this analysis does provide a technical basis for further consideration of this concept if the need for clean-air testing in the combustor entrance regime warrants development of a new test facility. However, augmentation of arc heaters with an unseeded, nonequilibrium MHD accelerators cannot reach the high pressure necessary to simulate the conditions required by the NASA specifications for the MARIAH Project (see Section 3). In fact, this technology cannot produce even the lower pressure conditions for post-bowshock conditions at a dynamic pressure of 500 lbf/ft^2. Use of this technology will be limited to simulating conditions equivalent to low dynamic pressure, combustor inlet flow.

5.1.3 MARIAH II Concept

The MARIAH II concept, which incorporates a UHP driver, beamed energy, and MHD augmentation, was the subject of a preliminary feasibility study completed jointly by MSE and Princeton University (Ref. 23). Appendix F an edited version of an original American Institute of Aeronautics and Astronautics (AIAA) technical paper. Section 4 contains a summary description of the concept. A number of advantages of the MARIAH II concept were cited in Appendix F. These include the following:

- The MARIAH II concept takes advantage of the UHP driver to dramatically reduce the reservoir entropy compared to typical entropy values in arc heaters.
- Joule heating is minimized by taking advantage of MHD. This point is discussed in Appendix F.
- By exploiting beamed energy in the supersonic expansion region, the MARIAH II concept offers the possibility of much lower temperatures through the flow train compared to either arc-heater technology or conventional MHD accelerators. This approach will alleviate many of the materials problems. The reduced temperatures also alleviate the problems of air chemistry. Species concentrations of monatomic oxygen and nitrogen will be significantly reduced if the flow train can be run at temperatures below 2,100 K.
- As noted in Reference 23, there is a natural synergy between the high-pressure driver and the MHD accelerator. By relying on MHD to do part of the flow acceleration, the required reservoir pressures can be substantially reduced, perhaps to values close to 10,000 atm. This will alleviate many materials and structural problems associated with the primary piston driver and will reduce technical risk accordingly.

- Finally, the UHP driver together with MHD offers the possibility of covering a much wider range of the H-S diagram of interest to the hypersonic testing community. Because it is not nearly so entropy-limited as other driver technologies, it opens up new possibilities for achieving true air simulation at high dynamic pressures.

Based on the preliminary research completed (see Appendix F), the MARIAH II concept appears promising. However, there are a number of technical questions that must be answered, including questions relating to run times, MHD channel operations, magnet requirements, and others. These are briefly addressed in Section 5.2. To fully resolve all of these technical issues will require a substantial, multidisciplinary, multiyear program of analytical and experimental investigation. The scope and nature of such a program are addressed in Section 5.3.

The MARIAH II concept has the potential to alleviate the air chemistry problem because the temperatures throughout the flow train will be lower than typical MHD channel or arc-heater temperatures. The success of this approach will depend on demonstrating low temperature operation of the MHD channel. Preliminary analysis has indicated that this concept can potentially reach the high enthalpy, low entropy conditions specified by NASA for the MARIAH Project. Furthermore, it has other advantages, including low air temperature in the MHD accelerator and less power required for the MHD acceleration, which make this technology very attractive for the high-pressure, propulsion testing applications.

5.2 OPEN ISSUES

Each of the MHD concepts discussed in the MHD Technology Conclusions above will require further research to address open issues identified but not resolved during the MARIAH Project. Various technology deficiencies, i.e., necessary technologies that are not presently available or beyond the present state-of-the-art, were also identified during this project. The identified technology deficiencies and unresolved issues are listed in this section.

5.2.1 Technology Deficiencies

5.2.1.1 Seeded and Unseeded MHD, Arc Heater Augmentation

5.2.1.1.1 *High Field Strength, Large Bore Magnets*

Magnets with a field strength on the order of 6-8 T can be constructed with currently available technology. Some projections have indicated 10- to 12-T magnets will be available in the 10- to 15-year time frame, and perhaps 15-T magnets will be available in 15 - 20 years. Parametric studies have clearly shown the benefit of using high-strength magnets for the high-pressure MHD applications while the Hall parameter remains low with even high field magnets. The parametric and optimization studies (see Appendix Sections B.1.4 and B.1.5) indicated that

magnets with fields up to 30 T produce significant gains in performance. Magnets with bore sizes sufficient for a ½- to 1-m-square channel cross-section and 2 to 7 meters in length are required to support MHD accelerator technology on the scale specified by NASA's requirements.

Analyses performed for the unseeded, nonequilibrium concept indicated much lower pressures in the channel and thus much higher Hall parameters likely resulting in ionizational instabilities. The unseeded, nonequilibrium accelerator probably would not benefit from the higher strength magnet technology.

5.2.1.1.2 *High Power Availability, Power Supplies, and Energy Storage*

Facilities on the scale specified by NASA for the MARIAH Project will require short bursts (1 - 2 minutes) of power at the 10- to 15-GW level. The power demands of these facilities will be far more than could be obtained from a commercial power grid without some form of storage and load leveling. Power supply options include: a) a dedicated, on-demand power source that would produce the necessary power from a chemical fuel; b) a dedicated, continuous operating power source with storage for the burst-demand; or c) commercial power source with storage. For a 2-minute burst, this facility will require approximately 1.5 TJ of energy. Power sources, load leveling, and storage of this magnitude will be a very major acquisition and the technology on which it is based may not exist. These requirements and technology availability should be reviewed to determine if R&D efforts are required.

5.2.1.1.3 *High-Pressure, High-Power Arc Heaters*

Current technology arc heaters can operate up to pressures on the order of 150 atm, and higher pressure operation can provide some improvement in MHD accelerator performance. Studies in this report were conducted assuming the availability of a 200-atm arc heater. However, power levels for current generation arc heaters are far below those needed for a facility of the scale specified by NASA. The thermal power of the exit gas stream for the arc heaters in this study were on the order of 2.5 GW. Since a large fraction of the input power to arc heaters is lost to the cooling water, an arc heater of this class would need to operate with an electrical power input of 4 to 5 GW.

5.2.1.1.4 *High-Temperature Materials for Electrode and Sidewalls*

High Mach number flight simulations require high stagnation enthalpy flow and produce very high recovery enthalpy (and temperature) levels in the boundary layers near the channel walls. This produces high heat flux to the walls for cold walls or extremely high temperature walls for adiabatic walls. High temperature wall materials would allow higher efficiency channel operation by reducing the thermal energy lost to the cooling water. Furthermore, electrode

erosion is frequently a problem with MHD systems, thus more durable electrode designs and materials would be beneficial.

5.2.1.1.5 *High-Power Microwave and/or E-Beam Devices (Unseeded MHD Only)*

Unseeded, nonequilibrium MHD accelerator performance could be improved through the use of external ionization sources. High-power devices sufficient for this application and windows or other means of introducing these beams into the channel should be developed if unseeded MHD accelerator systems are to be developed.

5.2.1.1.6 *Electrogasdynamic Effects on Engine Performance*

Preliminary analyses documented in Section 4 and in the appendices have indicated the presence of small amounts of alkali metal in the airstream will not cause a significant change in induction length or ignition delay times. However, for nonequilibrium MHD channel operation, the use of e-beam technology may result in elevated levels of O_2 species in the test cell. Indeed, the larger question of air chemistry effects due to e-beams has not yet been adequately addressed. This problem should receive much more attention in any future MHD accelerator studies.

5.2.1.1.7 *Other Downstream Issues*

There are a number of unresolved issues relating to the unique effects of MHD accelerator operation on the conditions and chemistry in the test cell. These include possible effects of molten alkali metal on engine seals, the effects of the MHD accelerator chemistry on accelerants and catalysts used to enhance engine performance, and questions of electron recombination and vibrational relaxation through the secondary nozzle. The latter issue was addressed to some degree in the OSU kinetics study (Appendix C.3) and in the ENGO MHD accelerator study (Appendix E.3).

5.2.1.2 MARIAH II Concept

Appendix F also notes there are a number of key technology issues that must be resolved before the MARIAH II system can be built with confidence. Most of these are discussed in the Appendix and are summarized below.

5.2.1.2.1 *High Field Strength, Large Bore Magnets*

Large magnet systems will be required for the MHD accelerator. Since the accelerator will be operated at lower pressure and temperature (higher Mach number), it will probably be larger than

accelerators for the arc-heated MHD, thereby requiring larger magnets. However, lower field strength magnets may be acceptable for this application. The large bore size required is beyond the magnet fabrication capability available today and will require some development.

5.2.1.2.2 *Run Times*

The testing requirements defined in Section 3 specified run times of tens of seconds to minutes. The gas piston driver must confine the entire slug of test gas in the main cylinder and compress it to pressures of 10,000 to 20,000 atm before releasing it through the nozzle. To simulate the Mach 16, 2,000 lbf/ft^2, post-bowshock conditions for a 10-s duration will require 8,200 kg of air. By contrast, the Russian A-4 facility under design at the Laurentyev Institute will be capable of handling a few tens of kg of air (see Ref. 151) and will have a run time of approximately 0.1 s. Clearly the scaleup of the primary driver is a major technology issue.

5.2.1.2.3 *MHD Channel Operation*

As explained in Appendix F, the MHD accelerator must operate with a minimum of Joule heating. To provide a "true air" flow stream and to avoid erosion of the electrode walls, it will be necessary to maintain low temperatures in the channel. This mode of operation rules out conventional seeded MHD. Based on the preliminary study described in Appendix F, there are two possible modes in which the MHD accelerator channel might operate.

Guided Arc Mode

This regime is characterized by inlet pressures of several hundred atm and temperatures below 2,200 K. A key issue for this option will be to demonstrate significant MHD acceleration using arc discharges within the channel.

Low-Pressure, Low Temperature MHD Acceleration with Beamed Energy Addition

The key parameter is the electrical conductivity in the channel. Because the temperature must remain low to minimize the entropy rise and reduce electrode erosion, this mode of MHD gas acceleration must rely on some type of beamed energy addition either within or upstream of the accelerator. Operation at subatmospheric pressure will be essential to minimize recombination of free electrons. A more detailed discussion of this issue is given in Appendix F.

5.2.1.2.4 *Beamed Energy Addition to a Supersonic Air Flow*

A key idea of the RDHWT scheme is to add beamed energy to the supersonic flow in the nozzle expansion region. This approach minimizes the temperature rise of the airstream, which in turn mitigates materials and air chemistry problems. A key question is: Can a supersonic airstream

absorb substantial energy from a laser, microwave, or e-beam? This issue is discussed in greater depth in Appendix F. To prove the feasibility of the MARIAH II concept, an experimental demonstration of the absorption of beamed energy in a supersonic airstream will be necessary.

5.2.1.2.5 *Air Chemistry Issues*

Chemistry issues were addressed in Appendix Sections B.2 and E.3. The primary species of concern are monatomic oxygen and nitrogen oxide. Alkali metal seed, if required for the MHD accelerator, will also be of some concern. As noted in the ENGO study (Appendix E.3), monatomic oxygen may reach levels as high as 4 - 5% molar, and nitrogen oxide levels may be as high as 6% for typical combustor inlet conditions. A similar kinetics study done by AEDC (Ref. 28) indicated monatomic oxygen levels could be as high as 15% molar under some conditions. Note this corresponds to high temperature operation in the channel. In some cases the core temperatures in the MHD channel were 3,500 K or higher.

5.2.2 Unresolved Issues

5.2.2.1 Multidimensional Phenomena

All analyses in this study were conducted with 1-D computer codes. Various multidimensional electrical and fluid dynamic phenomena occur in high-power MHD accelerators that should be investigated with multidimensional computer codes. Some of these phenomena include electrical shorting through the sidewall boundary layers, current constriction in the core flow, axial shorting between electrodes, Hall eddy currents, and 3-D fluid phenomena.

5.2.2.2 Flow Uniformity (Thermal and Velocity) and Quality (Chemistry)

Flow nonuniformities result from wall boundary layer effects and nonuniform acceleration due to electrical conductivity and current nonuniformities in the channel. These could be investigated through the use of multidimensional computer codes and experiments. Flow quality deficiencies could result from high temperature dissociation and formation of NO and other contaminate species. Problems associated with flow quality could be investigated using 1-D and multidimensional chemical kinetics codes.

5.3 RECOMMENDATIONS FOR FUTURE RESEARCH IN HYPERVELOCITY FACILITIES

National facilities studies in recent years (Refs. 21, 22, 152) have prioritized the needs for major national aerospace testing facilities and assigned development responsibilities to the

governmental organizations having interests in the facilities. National hypervelocity T & E facilities (an MHD-augmented, hypervelocity propulsion testing facility is an example) are now under the auspices of the USAF, and all future R&D will be conducted under its direction. USAF personnel have been reviewing the progress and results of the NASA MARIAH Project since its inception. At the conclusion of the MARIAH Project, the USAF will direct all future MHD research. For this reason, MSE had worked with USAF personnel to identify requirements for facilities to support their present and future missions.

Based on preliminary discussions between MSE and the USAF, it appears the test capabilities required to support the USAF mission in the near term will be for flight Mach numbers in the range of 8 – 16, with a requirement for conducting advanced engine testing at dynamic pressures in the range 1,000 to 2,000 lbf/ft^2. A facility capable of supporting such testing must have run times of the order of tens of seconds or greater.

The set of high level tasks shown below is suggested as a basis for developing a multiyear R&D program leading to a national hypervelocity test facility operating on the MARIAH II concept (see Section 4.1.4.5 and Appendix F). This concept, as discussed in Reference 23, takes advantage of synergistic features of RDHWT.

1. Define the testing regimes (run times, test section Mach numbers, pressures, and temperatures) of interest to the hypersonic testing community. This will require extensive discussions with government agencies and aerospace companies. Because of the long lead times involved in completing the necessary developmental work and designing a facility, it is recommended that the focus of this task be on long-term hypervelocity testing needs as opposed to the needs in the immediate future.
2. Upgrade and validate analytical tools that can adequately simulate the UHP driver, beamed energy addition in the nozzle expansion region, and MHD accelerator performance. Assemble a computational tool that can analyze the entire flow train.
3. Conduct parametric analytical studies to identify feasible pressure-temperature-Mach number regimes. The exit flow stream from the primary nozzle must be shown to be compatible in terms of pressure, temperature, and electrical conductivity with the inlet conditions in the MHD channel.
4. Demonstrate substantial beamed energy absorption in a supersonic airflow exiting from a UHP driver. This demonstration must be done experimentally after analytic studies have established an optimal range of pressures, velocities, and Mach numbers.
5. Demonstrate experimentally that one of the two options described below is feasible for operation of an MHD accelerator channel:

    a) High-pressure, moderate temperature gas acceleration using MHD:
    This is the "guided arc" mode of MHD acceleration considered in Reference 23. Inlet pressures of several hundred atmospheres and temperatures in the range

6. REFERENCES

6. REFERENCES

1. "United States Air Force Scientific Advisory Board, Report of the Ad Hoc Committee on Requirements for Hypersonic Test Facilities," Vol. 1, Study Report, May 1989.

2. Whitehead, G.L.; Mac Dermott, W.N.; Siler, L.G.; and Roepke, R.G., "Assessment of MHD Applications to Hypersonic Propulsion Testing Facilities," AEDC-TMR-87-V54, Arnold Engineering Development Center (AEDC), Dec. 1987.

3. Rittenhouse, L.E.; Pigott, J.C.; Whoric, J.M.; and Wilson, D.R., "Theoretical and Experimental Results with a Linear Magnetohydrodynamic Accelerator Operated in the Hall Current Neutralized Mode," AEDC-TR-67-150, Arnold Engineering Development Center (AEDC), Nov. 1967.

4. Pate, S.R.; Siler, L.G.; Stallings, D.W.; and Wagner, D.A., "Development of an MHD-Augmented, High Enthalpy, Shock Tunnel Facility," *AIAA Journal*, Vol. 12, No. 3, Mar. 1974, pp. 289-297.

5. Carter, A.F.; Wood, G.P.; McFarland, D.R.; and Weaver, W.R., "Research on a One-Inch Square Linear D-C Plasma, Accelerator," AIAA Paper 64-699, Aug./Sept. 1964.

6. Carter, A.F.; Wood, G.P.; McFarland, D.R.; Weaver, W.R.; and Park, S.K., "Operating Characteristics, Velocity and Pitot Distribution, and Material Evaluation Tests in the Langley One-Inch Square Plasma Accelerator," AIAA Paper 66-180, Mar. 1966.

7. Harris, C.J.; Marston, C.H.; and Warren, W.R., Jr., "MHD Augmented Shock Tunnel Experiments with Unseeded, High Density Air Flows," *AIAA Journal*, Vol. 13, No. 2, pp. 229-231, Feb. 1975.

8. Wood G.P. and Carter, A.F., "NASA Considerations in the Design of Steady D.C. Plasma Accelerators," NASA Langley Research Center, Hampton, VA, 1963.

9. Grabowsky, W.R.; Durran, D.A.; and Mirels, H., "Performance of a 500-kJoule MHD Wind Tunnel," *AIAA Journal*, Vol. 7, No. 10, pp. 1846-52, Oct 1969.

10. "MHD Program Summary Report," 2DOE-MHD, MSE Technology Applications, Inc., March 1977.

11. *Proceedings of the 31st Symposium on the Engineering Aspects of MHD*, Whitefish, MT, June 1993.

12. *Proceedings of the 32nd Symposium on the Engineering Aspects of MHD,* Pittsburgh, PA, June 1994.

13. Starr, R.F.; Christensen, L.S.; Whitehead, G.L.; Garrison, G.W.; Seiber, B.L.; and Lowry, R.L., "Report on the MHD Performance Demonstration Experiment for the Period Oct. 1, 1979 to Sept. 30, 1980," AEDC ET2895-10, Arnold Engineering Development Center (AEDC), Oct. 1980.

14. Simmons, G.A.; Nelson, G.L.; Lee, Y.M., "Analysis of an Unseeded, Nonequilibrium MHD Accelerator for Hypersonic Propulsion Ground Testing Applications," AIAA Paper 92-3994, July 1992.

15. Lineberry J. and Chapman, J., "MHD Accelerators for Hypersonic Applications," AIAA Paper 91-0384, 1991.

16. Cole, J.; Campbell, J.; and Robertson, A., "Rocket-Induced Magnetohydrodynamic Ejector - A Single - Stage - to - Orbit Advanced Propulsion Concept," AIAA Paper 95-4079, 1995.

17. Adamovich, I.V.; Rich, J.W.; and Nelson, G.L., "Feasibility Study of MHD Acceleration of Unseeded and Seeded Air Flows," AIAA Paper 96-2347, June 1996.

18. Wilson, D.R.; Lu, F. K.; Stuessy, S.; and Burge, K.R., "Development of a High-Pressure Detonation-Driven Shock Tube Facility," AIAA Paper 96-0853, Jan. 15-18, 1996.

19. Laster, M.L., and Bushnell, D.M., "A National Study for Hypersonic Facility Development," AIAA Paper 94-2473, June 1994.

20. Liu, C.J., "Preliminary Design of the MHD Accelerator for an Arc-Heated, MHD-Augmanted Hypersonic Wind Tunnel," Thesis for Master of Science in Aerospace Engineering at the University of Texas at Arlington, December 1989.

21. Chinitz, W.; Erdos, J.; Rizkalla, O.; Anderson, G.; and Bushnell, D., "Facility Opportunities and Associated Stream Chemistry Considerations for Hypersonic Air-Breathing Propulsion," *Journal of Propulsion and Power*, Vol. 10, No. 1, Jan.-Feb. 1994.

22. Richey, K and McKinney, "Hypersonic Test Investment Plan (HTIP): A Developmental Plan and Investment Strategy for U.S. Hypersonic Test Capabilities and Facilities, AEDC-TR-94-4, Dec. 1994.

23. Macheret, S.O.; Miles, R. B.; and Nelson, G. L., "Feasibility Study of a Hybrid MHD/Radiatively Driven Facility for Hypersonic Ground Testing," AIAA Paper 97-2429, June 1997.

24. Simmons, G.; Nelson, G.L.; Hiers, R; and Western, A., "An Unseeded Air MHD Accelerator Concept for High Mach Number Hypersonic Propulsion," AIAA Paper 89-2535, July 1989.

25. Nelson, G.L. and Simmons, G.A., "Augmentation of Hypersonic Propulsion facilities Using MHD," AIAA Paper 95-1937, June 1995.

26. Simmons, G.A.; Nelson, G.L.; and Lee, Y.M., "Feasibility Study of a Nonequilibrium MHD Accelerator Concept for Hypersonic Propulsion Ground Testing," AIAA Paper 95-2720, July 1995.

27. Lineberry, J. and Chapman, J., "MHD Accelerators for Hypersonic Applications," AIAA Paper 91-0384, Jan. 1995.

28. Crawford, R.A.; Chapman, J.N.; and Rhodes, R.P., "Potential Application of Magnetohydrodynamic Acceleration for Hypersonic Environment Testing," AEDC-TR-90-6, August 1990.

29. Clark, J.F. and McChesney, *Dynamics of Real Gases*, Butterworths, London, 1976.

30. Sutton, G.W. and Sherman, A., *Engineering Magnetohydrodynamics*, McGraw-Hill, New York, 1965.

31. Gordiets, B.F. and Zhdanok, S., *Analytical Theory of Vibrational Kinetics of Anharmonic Oscillators, Nonequilibrium Vibrational Kinetics*, M. Capitelli (ed.), Springer, Berlin, 1986, pp. 47-83.

32. Huxley, L.G.H. and Crompton, R.W., *The Diffusion and Drift of Electrons in Gases*, Wiley, New York, 1974.

33. Dyatko, N.A.; Kochetov, I.V.; and Napartovich, A.P., *Journal of Physics D.: Applied Physics*, Vol. 26, 1993, p. 418.

34. Suhre, D.R. and Verdeyen, J.T., *Journal Applied Physics*, Vol. 47, 1976, p. 4484.

35. Krivonosova, O.E.; Losev, S.A.; Nalivaiko, V.P.; Mukoseev, Yu.K.; and Shatalov, O.P., "Recommended Data on Rates of Chemical Reactions between Molecules Consisting of N and O Atoms," *Khimiya Plazmy (Plasma Chemistry)*, B.M. Smirnov (ed.), Vol. 14, Nauka, Moscow, 1987, pp. 3-31.

36. Macheret, S.O.; Fridman, A.A.; and Elkin, A.A., *Sov. Chem. Phys.*, Vol. 9, 1990, p. 174.

37. Macheret, S.O. and Rich, J.W., *Chem. Phys.*, Vol. 174, 1993, p. 25.

38. Treanor, C.E.; Adamovich, I.V.; Williams, M.J.; and Rich, J.W., *Thermophys. Heat Trans.*, Vol. 10, 1996, p. 193.

39. Matzing, H., "Chemical Kinetics of Flue Gas Cleaning by Irradiation with Electrons," *Advances in Chemical Physics*, Vol. 80, pp. 315-403.

40. Cool, T.A. and Zukoski, E.E., *Physics of Fluids*, Vol. 9, 1966, p. 780.

41. Ashton, A.F. and Heyhurst, A.N., *Combustion and Flame*, Vol. 21, 1973, p. 69.

42. Olson, R.E., *Journal of Chemical Physics*, Vol. 56, 1972, p. 2979.

43. Torr, D.G., "The Photochemistry of Upper Atmosphere," *The Photochemistry of Atmospheres*, J.S. Levine (ed.), Academic Press, New York, 1985, Chap. 5.

44. Itikawa, Y.; Hayashi, M.; and Ichimura, A., et al., *Journal of Physical and Chemical Reference Data*, Vol. 16, 1986, p. 985.

45. Itikawa, Y.; Hayashi, M.; and Ichimura, A., et al., *Journal of Physical and Chemical Reference Data*, Vol. 18, 1989, p. 23.

46. Mojarrabi, B.; Gulley, R.J.; and Middleton, A.G., et al., *Journal of Physics - B: Atomic Molecular and Optical Physics*, Vol. 28, 1995, p.487 and references therein.

47. Lennon, M.A.; Bell, K.L.; and Gilbody, H.B., et al., *Journal of Physical and Chemical Reference Data*, Vol. 17, 1988, p. 1988.

48. Glushko, V.P., (ed.), *Thermodynamic Properties of Individual Substances*, Nauka, Moscow, 1976.

49. "JANAF Thermochemical Tables," *Journal of Physical and Chemical Reference Data*, Vol. 14, Suppl. 1, 1985.

50. Chen, J.C.Y., *Journal of Chemical Physics*, Vol. 40, 1964, p.3507.

51. Adamovich, I.V.; Macheret, S.O.; Rich, J.W.; and Treanor, C.E, AIAA Paper 95-2060.

52. Fisher, E. and Smith, G., *Chemical Physics Letters*, Vol. 13, 1972, p. 448.

53. Eremin, A.V.; Kulikovsky, A.A.; and Naboko, I.M., *Chemical Physics Letters*, Vol. 45, 1976, p. 351.

54. Perel, J.; Englander, P.; and Bederson, B., *Physics Review*, Vol. 128, 1962, p. 1148.

55. Raizer, Yu. P., *Gas Discharge Physics*, Springer-Verlag, Berlin, 1991, Chap.14.

56. Schlichting, H., *Boundary Layer Theory*, McGraw-Hill, New York, 1960, Chap. 21.

57. Warren, W.R.; Harris, C.J., et al.,"Feasibility Study of a High Density Shock Tunnel Augmented by a Magnetohydrodynamic Accelerator," AEDC-TR-65-225, Arnold Engineering Development Center (AEDC), Oct. 1965.

58. Harris, C.J.; Marston, C.H.; and Warren, W.R., *AIAA Journal*, Vol. 13, 1975, p. 229.

59. Oran, E.S. and Boris, J. P., *Numerical Simulation of Reactive Flow*, Elsevier, 1987.

60. Briley, W.R. and McDonald, H. *Journal of Computational Physics*, Vol. 24, 1977, pp. 372-397.

61. Aithal, S.M., "Numerical Simulation of Plasma and Reacting Flows,"doctoral dissertation, Ohio State University, Mar. 1997.

62. Isaacson, E. and Keller, H.B., *Analysis of Numerical Methods*, Wiley, New York, 1966.

63. Babu, V.; Aithal, S.M.; and Subramaniam, V.V., "Numerical Simulation of a Hydrogen Arcjet," *J. Propulsion & Power*, Vol. 12, No. 6, Nov.-Dec. 1996.

64. Aithal, S.M.; Subramaniam, V.V.; and Babu, V., "Effects of Arc Attachment on Arcjet Flows," AIAA Paper 96-3295, July 1996.

65. Roache, P.J., *Computational Fluid Dynamics*, Hermosa, Albuquerque, New Mexico, 1972.

66. Pobst, J.A.; Wysong, I.J.; and Spores, R.A., "Laser-Induced Fluorescence of Ground State Hydrogen Atoms in an Arcjet Plume," Paper IEPC-95-28, 24th International Electric Propulsion Conference, Moscow, Russia, Sept. 1995.

67. Storm, P. V. and Cappelli, M. A., "High Spectral Resolution Emission Study of a Low Power Hydrogen Arcjet Plume," AIAA Paper 95-1960, June 1995.

68. Storm, P.V. and Cappelli, M.A., "Fluorescence Velocity Measurements in the Interior of Hydrogen Arcjet Nozzle," *AIAA Journal*, Vol. 34, No. 4, Mar. 1996, pp. 853-855.

69. Boyd, I., "Monte Carlo Simulation of Non-Equilibrium Flow in Low Power Hydrogen Arcjets," AIAA Paper -96-2022, June 1996.

70. Butler, G.W.; Boyd, I.D.; and Cappelli, M.A. "Non-Equilibrium Flow Phenomena in Low Power Hydrogen Arcjets," AIAA Paper 95-2819 presented at the 31st AIAA/ASME/SAE/ASEE Joint Propulsion Conference and Exhibit, San Diego, CA, July 10-12, 1995.

71. Dowden, J.; Kapadia, P.; and Fenn, B., "Space Charge in Plasma Arc Welding and Cutting," *Journal of Physics - D: Applied Physics*, Vol. 26, 1993.

72. Pagan, J. M., Master's Thesis, Ohio State University, Columbus, OH, June 1996.

73. Lin, S.C. and Tear, J.D., *Physics of Fluids*, Vol. 6, 1963, p. 355.

74. Park, C., *Nonequilibrium Hypersonic Aerodynamics*, Wiley, New York, 1990.

75. Treanor, C.E.; Adamovich, I.V.; Williams, M.J.; and Rich, J.W., *Journal of Thermophysics and Heat Transfer*, Vol. 10, 1996, p. 193.

76. Frohn, A. and De Boer, P.C.T., *Physics of Fluids Supplement I*, 1969, p. I54.

77. Manheimer-Timnant, Y. and Low, W., *Journal of Fluid Mechanics*, Vol. 6, 1959, p. 449.

78. Niblett, B. and Blackman, V.H., *Journal of Fluid Mechanics*, Vol. 4, 1958, p. 191.

79. Lin, S.C.; Neal, R.A; and Fyfe, W.I., *Physics of Fluids*, Vol. 5, 1962, p. 1633.

80. Biryukov, A.S.; Yu, A.; Volkov, Demin; A.I., Kudryavtsev; E.M., Kulagin; Sobolev, N.N.; and Shelepin, L.A., *Soviet Physics – JETP*, Vol. 41, 1975, p. 834.

81. Thomson, J.J. and Thomson, G.P., *Conduction of Electricity Through Gases*, Vol. 1, Cambridge, University Press, 1928.

82. Adamovich, I.; Hiltner, J.; Macheret, S.; and Rich, J.W., AIAA Paper 92-3028, June 1992.

83. Babu, V.; Aithal, S.M.; and Subramaniam, V.V., *AIAA Journal*, Vol. 12, 1996, p. 1114.

84. Anderson, D. A.; Tannehill, J. C.; and Pletcher, R. H., *Computational Fluid Mechanics and Heat Transfer*, Taylor & Francis, 1984.

85. Maas, U. and Warnatz, J., "Detailed Numerical Modeling of H_2-O_2 Ignition by Hot Spots," *Progress in Astronautics and Aeronautics*, Vol. 131, *Dynamics of Deflagrations and Reactive Systems: Flames*, Kuhl A.L.; Leyer, J.C.; Borisov, A.A.; and Sirignano, W.A. (eds.), AIAA, Washington, D.C., 1991, pp. 3-19.

86. Trevino, C., "Ignition Phenomena in H_2-O_2 Mixtures," *Progress in Astronautics and Aeronautics*, Vol. 131, *Dynamics of Deflagrations and Reactive Systems*: *Flames*, Kuhl, A.L.; Leyer, J.C.; Borisov, A.A.; Sirignano, W.A.(eds.), AIAA, Washington, D.C., 1991, pp. 19-44.

87. Mallard, W.G., "NIST Chemical Kinetics Database," NIST Standard Reference Database 17, National Institute of Standards and Technology (NIST), Gaithersburg, MD, Nov. 1994.

88. Jensen, D.E., *Journal of Chemical Society Faraday Transactions I*, Vol. 78, 1982, p. 2835.

89. Jensen, D.E. and Jones, G.A., *Journal of Chemical Society Faraday Transactions I*, Vol. 78, 1982, p. 2843.

90. Haynes, A.J.; Steinberg, M.; and Schofield, K., *Journal of Chemical Physics*, Vol. 8, 1984, p. 2585.

91. Slack, M.; Cox, J.W.; Grillo, A.; and Ryan, R., *Combustion and Flame*, Vol. 77, 1989, p. 311.

92. Dimotakis, P.E., "Turbulent Free Shear Layer Mixing and Combustion," *Progress in Astronautics and Aeronautics*, Vol. 137, *High Speed Flight Propulsion Systems*, Murthy, S.N.B.; and Curran, E.T. (eds.), AIAA, Washington, D.C., 1991, pp. 265-340.

93. Chinitz, W.; Bakos, R.J.; and Erdos, J.I., "Experimental Requirements for the Study of Shock-Induced Premixed Combustion," AIAA Paper 94-3099, 1994.

94. Rosa, R.J., *Magnetohydrodynamic Energy Conversion,* McGraw-Hill, New York, 1968.

95. "Proceedings of the Magnetohydrodynamics (MHD) Technical Review and Planning Workshop," NASA, Washington, D.C., Feb. 1995.

96. Pate, S.R.; Siler, L.G.; Stallings, D.W.; and Wagner, D.A., "Development of an MHD-Augmented, High Enthalpy, Shock Tunnel Facility," *AIAA Journal,* Vol. 12, No. 3, Mar. 1974, pp. 289-297.

97. Stuessy, W.S.; Murtugudde, R.G.; Lu, F.K.; and Wilson, D.R., "Development of the UTA Hypersonic Shock Tunnel," AIAA Paper 90-0080, 1990.

98. Lu, F.K., "Initial Operation of the UTA Shock Tunnel," AIAA Paper 92-0331, 1992.

99. "Summary of Capabilities of Hypersonic Shock Tunnels at Calspan ATC," Calspan Advanced Technology Center, Buffalo, NY.

100. "Description of the Aachen Shock Tunnel TH2," Shock Wave Laboratory, Technical University of Aachen, Aachen, Germany, January 1991.

101. Namagatsu, H.; Sheer, R.; Osberg, L.; and Cary, K., "Design Features of the General Electric Research Laboratory Hypersonic Shock Tunnel," GE Research Lab Report No. 61-RL-2711C, May 1961.

102. Eitelburg, G.; McIntyre, T.J.; Beck, W.H.; and Lacey, J., "The High Enthalpy Shock Tunnel at Göttingen," AIAA Paper 92-3942, 1992.

103. Deiwert, G.S.; Cavalowsky, J.A.; and Loomis, M.P., "Large Scale Scramjet Testing in the Ames 16-Inch Shock Tunnel," AIAA Paper 94-2519, 1994.

104. Bakos, R.J. and Erdos, J.I., "Options for Enhancement of the Performance of Shock-Expansion Tubes and Tunnels," AIAA Paper 95-0799, 1995.

105. Stanley, S.B; Stuessy, W.S.; and Wilson, D.R., "Experimental Investigation of Pulse Detonation Wave Phenomena," AIAA Paper 95-2197, 1995.

106. Stanley, S.; Burge, K.; and Wilson, D., "Experimental Investigation of Pulse Detonation Wave Phenomena as Related to Propulsion Application," AIAA Paper 95-2580, 1995.

107. Bird, G.A., "A Note on Combustion Driven Shock Tubes," In "Hypersonic Facilities in the Aerodynamics Department, Royal Aircraft Establishment," P.A. Hufton (ed.), AGARD Report 146, 1957.

108. Coates, P.B. and Gaydon, A.G., "A Simple Shock Tube With Detonating Driver," *Proceedings of the Royal Society of London*, A283, pp.18-32, 1965.

109. Balcarzak, M.J. and Johnson, M.R., "The Gaseous-Detonation Driver and Its Application to Shock Tube Simulation Techniques," *Proceedings of the 5th International Shock Tube Symposium,* Z.I. Slawsky, J.F. Moulton and W.S. Filler (eds.), U.S. Naval Ordinance Lab, White Oak, MD, 1966, pp. 1111-1128.

110. Lee, B. "Detonation Driven Shocks in a Shock Tube," *AIAA Journal,* Vol. 5, No. 4, Apr. 1967, pp. 791-792.

111. Yu, H.R.; Esser, B.; Lenartz, M.; and Gronig, H., "Gaseous Detonation Driver for a Shock Tunnel," *Shock Waves,* Vol. 2, 1992, pp. 245-254.

112. Tamagno, J.; Calleja, J.F; and Erdos, J., "Exploratory Tests of Detonation-Driven Expansion Tube Performance," NASA CR-191580, General Applied Science Laboratories, Ronkonkoma, NY, Mar. 1994.

113. Engers, R.J.; Calleja, J.F.; and Bakos, R.J., "A Detonation Driven Injectant Heater for Pulse Facility Testing Applications," AIAA Paper 95-3153, 1995.

114. Bakos, R.J.; Castrogiovanni, A.; Calleja, J.F.; Nucci, L.; and Erdos, J.I., "Expansion of the Scramjet Ground Test Envelope of the HYPULSE Facility," AIAA Paper 96-4506, 1996.

115. Erdos, J.I; Bakos, R.J.; Castrogiovanni, A.; Calleja, J.F.; and Rogers, R.C., "Dual Mode Shock-Expansion/Reflected-Shock Tunnel," AIAA Paper 97-0560, 1997.

116. Garrison, G. W., "Electrical Conductivity of a Seeded Nitrogen Plasma," *AIAA Journal*, Vol. 6, No. 7, July 1968, pp. 1264-1270.

117. Demetriades, S.T and Argyropoulas, G.S., "Ohm's Law in Multicomponent Nonisothermal Plasmas with Temperature and Pressure Gradients," *Physics of Fluids*, Vol. 8, No. 11, November 1966, pp. 2136-2149.

118. Webb, C.E., "The Fundamental Discharge Physics of Atomic Gas Lasers," presented at the Conference on High Power Gas Lasers, 1975, pp. 1-28. Published by the Institute of Physics, Conference Series number 29. Lectures given at a summer school organized by the International College of Applied Physics, Capri, Italy, Sept. 23 – Oct. 4, 1975.

119. Judd, O., "The Fundamental Discharge Physics of Atomic Gas Lasers," presented at the Conference on High Power Gas Lasers, 1975, pp. 29-43. Published by the Institute of Physics, Conference Series number 29. Lectures given at a summer school organized by the International College of Applied Physics, Capri, Italy, Sept. 23 – Oct. 4, 1975.

120. Turner, J., *Atoms, Radiation, and Radiation Protection*, John Wiley, 1995.

121. Rapp, D. and Englander-Golden, P., "Total Cross Sections for Ionization and Attachments in Gases by Electron Impact, I. Positive Ionization," *Journal of Chemical Physics*, Vol. 43, No. 5, Sept. 1965, pp. 1464-79.

122. Matzing, H., "Chemical Kinetics of Flue Gas Cleaning by Irradiation with Electrons," *Advances in Chemical Physics*, Vol. 80, pp. 315-403.

123. MacDonald, A.D., *Microwave Breakdown in Gases*, John Wiley, 1968.

124. Mitchner, M. and Kruger, C.H., *Partially Ionized Gases*, Wiley-Interscience Publication, reprinted in 1992.

125. Sullivan, D.J. and Micci, M. M., "Performance Testing and Exhaust Plume Characterization of the Microwave Arcjet Thruster," presented at the AIAA/ASME/SAE Joint Propulsion Conference, Indianapolis, IN, June 1994.

126. Macheret, S.; Meinrenken, C.; Williams, G.; Gillespie, W.; Lempert, W.; and Miles, R., "Radiative Energy Addition to High Pressure Supersonic Air," AIAA Paper 96-1984, June 1996.

127. Shair, F.H. and Sherman, A. "Electron Beam Preionization in an MHD Generator," *6th Symposium on Engineering Aspects of Magnetohydrodynamics (SEAM)*, Apr. 1965, pp. 7-12.

128. Lin, B.C., "A Study of the T layer MHD Generator/Accelerator Using Nonequilibrium Plasma," doctoral dissertation, University of Tennessee Space Institute, Tullahoma, TN, 1991.

129. Bityurin, V.A., et al., "On the Dynamics of a Nonuniform Conducting Flow in an MHD Generator", *Magnetohydrodynamics, on International Journal*, Vol. 2, No. 2-3, 1989.

130. Butyurin, V.A. and Likhachev, A.P., "High Efficiency MHD Generator With Space and Time Dependent Current Carrying Nonuniformities," *10th International Conference on MHD Electrical Power Generation*, Vol. 2, p. 191, Tirchirappalli, India, Dec. 4-8, 1989.

131. "Shock Tube Experiments on Non-Uniformities in Combustion MHD Generators", *31st Symposium on Engineering Aspects of MHD*, III.4.1, Whitefish, MT, June 1993.

132. Bunshah, R.F.; Jou, S.; Prakash, S.; and Doerr, H.J., "Production of Fullerenes by Electron Beam Evaporation," Patent Number 5,316,636, May 31, 1994.

133. Smith, R.L., *Fullerenes*, McGraw-Hill, New York, 1993, pp 312-314.

134. Goran, S.M., "Method of Making Metal Fulleride," Patent Number 5,324,495, June 28, 1994.

135. Curl, R.F. and Smalley, R.E., "Fullerenes," *Scientific American,* Vol. 60, Oct. 1991, pp. 57, 60.

136. Leifer, S., "Characterization of Fullerenes for Electrostatic Propulsion Associations," doctoral dissertation, California Institute of Technology, Pasadena, CA, 1995.

137. Takegahara, H. and Nakayama, Y., "C60 Feasibility Study on Application to Ion Thruster," AIAA 95-2665, July 1995.

138. Leifer, S.D. and Rapp, D., "Assessment of C60 as a Propellant Material for Ion Thrusters," *NASA Tech Brief*, Vol. 19, No. 5, Item #59, June 1995.

139. Anderson, J.R.; Fitzgerald, D.; Leifer, S.; and Mueller, J., "Design and Testing of a Fullerene RF Ion Engine," AIAA Paper 95-2664, July 1995.

140. Wagner, K., "Properties, Behavior, and Applications of Fullerene Molecules," MSE Technology Applications, Inc., Technical Report MSE-18, Apr. 1996.

141. Amin, M.R. "Thermal Management of Magnetohydrodynamics (MHD) Hypersonic Accelerators - Final Report," MSE Technology Applications, Inc., Report No. MSE-23, Oct. 1996.

142. "A Program of Experiments for Investigating Into Performance of MHD Accelerator with Increased Pressure in Its Channel by Using the TsAGI SMGDU Facility," Final Report on work completed under subcontract to MSE, Inc., in support of the NASA MARIAH Project, ENGO, Moscow, June 1996.

143. Anderson, J.D., *Hypersonic and High Temperature Gas Dynamics*, McGraw Hill Book Company, 1989.

144. Miles, R.B.; Brown, G.L.; Lempert, W.R.; Yetter, R.; Williams, G.J. Jr.; Bogdonoff, S.M.; Natelson, D.; and Guest, J.R., "Radiatively Driven Hypersonic Wind Tunnel," *AIAA Journal*, Vol. 33, No. 8, pp. 1463-1470; see also AIAA Paper 94-2472, 1995.

145. Macheret, S.; Meinrenken, C.; Williams, G.; Gillespie, W.; Lempert, W.; and Miles, R. "Energy Addition and Thermalization Issues in a Radiatively Driven Hypersonic Wind Tunnel," AIAA Paper 95-2142.

146. Topchiyan, M.E. and Kharitonov, A.M., "Wind Tunnels for Hypersonic Study (Achievements, Problems, Outlooks)," *The Science Report No. 8-93 of the International Center of Aerophysical Studies, Institute of Theoretical and Applied Mechanics*, Russian Academy of Sciences Siberian Branch, 1993.

147. Topchiyan, M.E.; Rychkov, V.N.; Pinakov, V.I.; and Meshcheryakov, A.A., "Creation and Use of Adiabatic Compression Units for Producing Dense Hypersonic Flows," *International Symposium IUTAM,* Marseille, France, Sept. 1-4, 1992.

148. Meshcheryakov, A.A.; Pinakov, V.I.; and Topchiyan, M.E., "On Stress Distribution in Locking Piston and Tube of an Adiabatic Compression Unit," *Zhurnal Prikladnoi Mekhaniki i Tekhnicheskoi Fiziki (Journal of Applied Mechanics and Technical Physics)*, No. 2, [In Russian], 1980.

149. Pinakov, V.I.; Rychkov, V.N.; and Topchiyan, M.E., "Simulation of Hypersonic Flows in Gasdynamic Facilities with High Pressure," *Zhurnal Prikladnoi Mekhaniki i Tekhnicheskoi Fiziki (Journal of Applied Mechanics and Technical Physics)*, [In Russian], No. 1, 1981.

150. Jahn, R.G., *Physics of Electric Propulsion*, McGraw-Hill, 1968.

151. Constatino, Marc, Dr., Presentation at RDHWT/MHD Meeting, April 23-24, 1997, Tullahoma, TN.

152 Wagner, D.A.; Varner, M.O.; Williams, R.R.; and Griffith, B.J., "Hypersonic Facility Requirements and Design Considerations," AIAA paper 88-1991, Sverdrup Technology, Inc., Tulahoma, TN, May 1988.

APPENDIX A

CONTENTS

SECTION A.1

FIGURES

TABLES

SECTION A.2

FIGURES

TABLES

APPENDIX A, SECTION A.1

A.1 UNIVERSITY OF TEXAS AT ARLINGTON TESTING PROGRAM

Experimental research was conducted at UTA to assess the properties of high-pressure, K-seeded air for magnetohydrodynamics (MHD) accelerator applications. Since MHD research has historically been conducted at much lower pressures, experimentally measured electrical property data is not available for seeded air in the high-pressure, hypervelocity testing regime specified for the MARIAH Project. In order to obtain the development of these high performance accelerators, an experimental program was conducted at UTA to investigate the effect of high-pressure on the equilibrium and nonequilibrium electrical conductivity of seeded air. The effects of temperature, seed fraction, and electric field on these properties at high-pressure were also investigated. Electrical conductivity in N_2 plasma was also investigated under similar conditions to assess the effects of the loss of electrons through attachment to oxygen (O_2) and other species in air.

This appendix discusses the facility modifications and experimental program to perform the high-pressure, seeded air, and electrical property measurements. Electrical conductivity measurements at various pressures, temperatures, and seed fractions are reported. Potassium-seeded N_2 electrical properties data are compared to seeded air data to investigate the effects of electron attachment to O_2 species in air. Finally, a compendium of all data measurements obtained during the UTA research is included at the end of this appendix.

NOMENCLATURE

A	Area
A^*_c	Effective core area for oxial current
C_{FD}	Computational fluid dynamics
C_p	Specific heat at constant pressure
C_t	Total power supply capacitance
E	Electrical field
E	Energy
e	Electron charge
h_t	Total enthalpy
h_t	Total enthalpy
I	Current
j	Current Density
k	Boltzmann constant
L	Inductance
L	Length
$\dot{m}$	Mass flow rate
L_t	Total power supply inductance
N	Number of loops
M_D	Detonation Mach number

M_S	Shock Mach number
m_S	Seed mass
p	Pressure
q	Charge
R	Function, Radius
S	Seed mass fraction
T	Temperature
t	Time
t_d	Discharge time
T_t	Total temperature
U	Velocity
U_S	Shock speed
V	Voltage
V_A	Applied voltage
ΔV_C	Voltage drop between probe electrodes 1 and 20
x	Distance
Z	Load impedance
Λ	Ratio of Debye shielding distance to impact parameter for ion scattering
σ	Electrical conductivity
σ^*	Average electrical conductivity
σ_{add}	Additive electrical conductivity
σ_{ei}	Electrical conductivity due to electron-ion collision
σ_{en}	Electrical conductivity due to electron-neutral collision
ρ	Density
μ	Permeability
δ	Boundary layer thickness
δ^*_J	Boundary layer current density displacement thickness
ω_R	Uncertainty of function r

A.1.1 Overview

The need for ground test facilities capable of testing advanced hypervelocity propulsion system concepts has generated renewed interest in the use of MHD accelerators for augmentation of high-pressure arc heaters. A critical problem in the development of this concept is the need for increased understanding of the electrical properties of high-pressure plasmas. Experimental data is needed to validate theoretical models for calculating the electrical conductivity of seeded plasmas at high-pressure levels. Furthermore, the electrical breakdown characteristics of high-pressure plasmas subjected to intense electric fields are not well understood. Both of these issues are critical to the development of MHD accelerator channels capable of operating at the pressure levels thought to be necessary in order to duplicate the flow conditions required for hypervelocity engine testing (Ref. 1).

As part of the MARIAH Project, UTA conducted an experimental investigation of critical electrical phenomena associated with operation of MHD accelerators at high pressure. The objectives of the UTA investigation were to:

- Develop an experimental apparatus for measuring the electrical conductivity of high-pressure seeded plasmas.
- Conduct an experimental investigation of the effect of applied electric field, static temperature, static pressure and seed concentration on the bulk electrical conductivity of the plasma.
- Perform these experimental investigations using K-seeded air as the working gas and repeat the experiments at selected conditions using N_2 for comparison to determine, at selected conditions, the effects of electron attachment to O_2 on the electrical conductivity.

The results of the UTA Phase 1A study to design the test apparatus and develop a detailed plan for experiments to be conducted were presented as part of the MARIAH Workshop held by MSE at Butte, Montana, on November 20-21, 1995 and were summarized in Reference 2. The results of this experimental program are presented in the following sections. The development of the original detonation-driven shock tube, together with the initial performance results is described in Section A.1.2. Based on the performance results from these tests, a change in the mode of detonation initiation was proposed, and the subsequent modifications to the shock tube facility and resulting performance enhancement are described in Section A.1.3. The design of the conductivity channel and power supply is discussed in Section A.1.4, and the seeding system is described in Section A.1.5. The test program objectives, test matrix, and uncertainty analyses are presented in Section A.1.6, and the test results are presented in Section A.1.7. Section A.1.8 presents the comparison between experimental data and available theoretical models, and a summary of results, conclusions, and recommendations for future studies are presented in Section A.1.9. References are listed in Section A.1.10, and a compilation of data plots for each individual test run is given in Section A.1.11.

A.1.2 Detonation-Driven Shock Tube Development (Arc Ignition Mode)

A.1.2.1 Existing Shock Tunnel Facility

The existing UTA shock tunnel facility is shown schematically in Figure A.1- 1 and is described in detail in References 3 and 4. The shock tube is composed of a 15.2-cm diameter [6-inch (in.)], 3-meter (m) long [10-foot (ft)] driver tube and a 15.2-cm diameter (6-in.), 8.23-m long (27-ft) long driven tube. The two tubes are separated by a double-diaphragm section. Both tube sections are rated for a pressure of 41.3 mega pascal (MPa) [6,000 pounds per square inch (psi)]. The diaphragms are normally constructed from 10 or 12 gauge [3.42 or 2.66 millimeters (mm)] hot-rolled type 1008 steel plate scored to various depths in a cross pattern. A 7.5° half-angle conical nozzle with interchangeable throat inserts for Mach numbers of 5 to 16 is attached to the end of the driven tube. The exit diameter of the nozzle is 33.6 centimeters (cm) (13.25 in.).

Previous operation of the shock tunnel employed the reflected-mode of operation with the nozzle configured for Mach 8. A secondary diaphragm constructed from 0.127 mm (0.005 in.) thick aluminum sheet was located in the nozzle throat region and used to separate the driven-tube gas from that in the test section. The test section is a semi-free jet design, 53.6 cm long (21.1 in.) and 43.8 cm in diameter (17.25 in.). Two 23-cm diameter (9 in.) optical windows are located on opposite sides of the test section. The diffuser is 30.5 cm in diameter (12 in.), 213 cm long (84 in.), and connects the test section to a 4.25-cubic meters (m^3) [150-cubic foot (ft^3)] vacuum tank. The test section and diffuser contain model mounting and instrumentation ports.

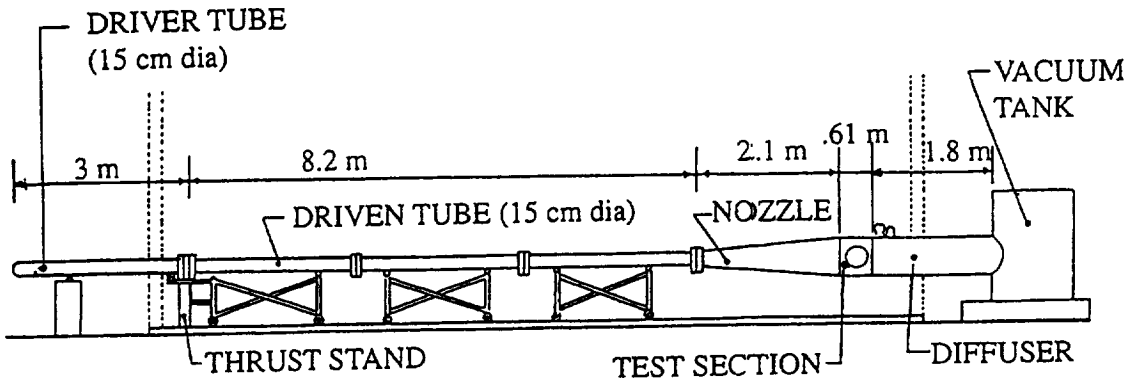

Figure A.1- 1. Schematic of UTA shock tunnel.

The pneumatic system consists of a Haskell model 55696 two-stage gas-driven booster pump capable of charging the driver tube to 41.3 MPa (6,000 psi). The Haskell pump is normally connected to the facility air compressor system consisting of a Clark CMB-6 5-stage air compressor, twin-tower desiccant drier, and 14.5 MPa (2,100 psi) storage bottles. Alternatively, the Haskell pump can be fed from a manifold of 15.2 MPa (2,200 psi) helium (He) storage bottles. The vacuum system consists of a Sargent-Welch model 1376 [300-liters per minute (l/min)] pump used to evacuate the driven tube and a Sargent-Welch model 1396 (2,800-l/min) pump used to evacuate the test section/diffuser/vacuum tank. In addition, there is a vacuum pressure measurement system, consisting of two Baratron type 127A pressure transducers and the associated valving system to enable full range coverage from 10,000 to 0.001 torr [1.33 Mpa to 0.133 Pascal (Pa)].

A.1.2.2 Detonation-Driven Shock Tube Concept

A principal objective of the MARIAH Project was to investigate the feasibility of using MHD augmentation of high-pressure arc heaters as the basis for development of a continuous-flow hypervelocity wind tunnel optimized for testing advanced air-breathing hypervelocity propulsion systems. In particular, the facility should be capable of providing post-bowshock conditions for

testing advanced concepts such as the Pre-Mixed, Shock-Induced Combustor (PM/SIC) Engine (Ref. 5). In order to simulate this test environment in an MHD-augmented test facility, preliminary design studies indicate that accelerator channel static pressures on the order of 100 atmospheres (atm) may be required (Ref. 1). Unfortunately, the previous operational experience base for MHD accelerator operation was at pressures on the order of 0.5–5 atm (Refs. 6, 7). Development of MHD accelerators capable of operating at high pressures will require improved understanding of a variety of technical issues. These issues include the effect of high pressures on the electrical conductivity and Hall parameter of equilibrium and nonequilibrium plasmas, the structure and stability of the current discharge, and the plasma electrical breakdown characteristics.

In order to provide an experimental capability able to investigate some of the relevant phenomena associated with the operation of MHD accelerators at high pressures, UTA proposed to convert its existing pressure-driven hypersonic shock tunnel into a detonation-driven shock tube. Other concepts for enhancing the performance of the existing facility were briefly considered, including the use of an electrical (Refs. 8, 9) or combustion-heated (Refs. 10, 11) light gas-driver and a free piston driver (Ref. 12). Although the free piston driver probably has the highest performance capability, Bakos and Erdos (Ref. 13) have shown the detonation driver offers somewhat comparable performance at a lower cost. Furthermore, a substantial experience base had been developed at UTA to support this approach via an ongoing research program to develop Pulse Detonation Engine (PDE) concepts (Refs. 14, 15). Much of the technology developed as part of that program would be directly applicable to the detonation-driven shock tunnel.

The detonation-driven shock tube was first proposed by Bird in 1957 (Ref. 16) and has been subsequently studied by several investigators (Refs. 13, 17, 18, 19, 20, 21, 22, 23, 24). A detonation process is typically established in a driver tube filled with a near-stoichiometric mixture of hydrogen (H_2) and O_2, although other gas combinations are possible. The initial pressure level prior to detonation can be quite low, thus eliminating the need for thick metal diaphragms. The detonation process produces a relatively low molecular weight driver gas at high temperature and pressure levels. The sudden pressure rise produced by the detonation wave causes the primary diaphragm to rupture, thus establishing a shock wave in the air-filled driven tube. Two modes of operation are possible. In the "upstream propagation" mode (Figure A.1-2), the ignition source is placed just upstream of the primary diaphragm and produces a detonation wave that propagates from right to left through the driver tube. The pressure rise following the detonation wave ruptures the primary diaphragm to establish the flow in the driven tube. The effective driver tube conditions for this mode are the pressure and temperature at state 4′ on the wave diagram in Figure A.1- 2. In the "downstream propagation" mode (Figure A.1-3), the ignition source is located at the upstream end of the driver tube and produces a detonation wave that travels from left to right through the driver tube, rupturing the primary diaphragm on impact. The effective driver tube conditions for this mode are those for state 4′′ on the wave diagram shown in Figure A.1- 3. For either mode, further performance enhancement is possible by adding He dilution to the H_2/O_2 driver tube mixture. Helium dilution raises the sonic speed in the driver gas and also somewhat reduces the danger associated with premature detonation of the H_2/O_2 mixture. Performance calculations by Yu et al. (Ref. 20) indicate the performance

degradation caused by the slight lowering of the detonation temperature due to He dilution is more than adequately offset by the increased sonic speed of the driver-tube gas.

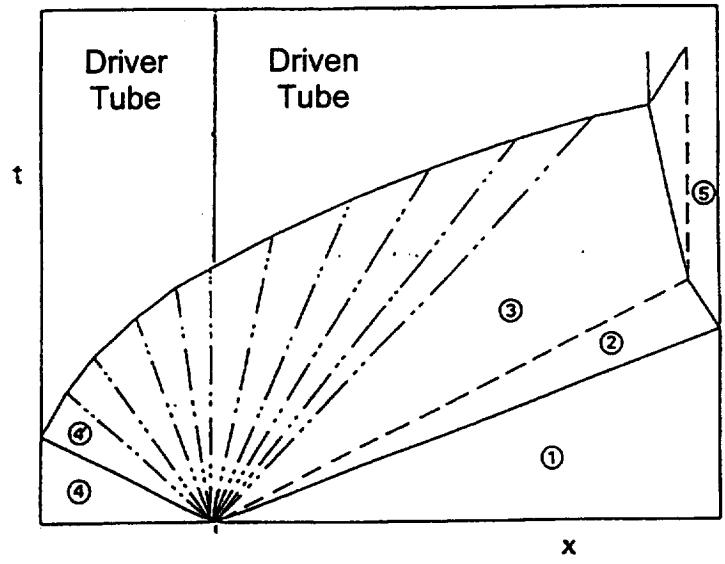

Figure A.1- 2. Wave diagram of upstream propagating detonation wave.

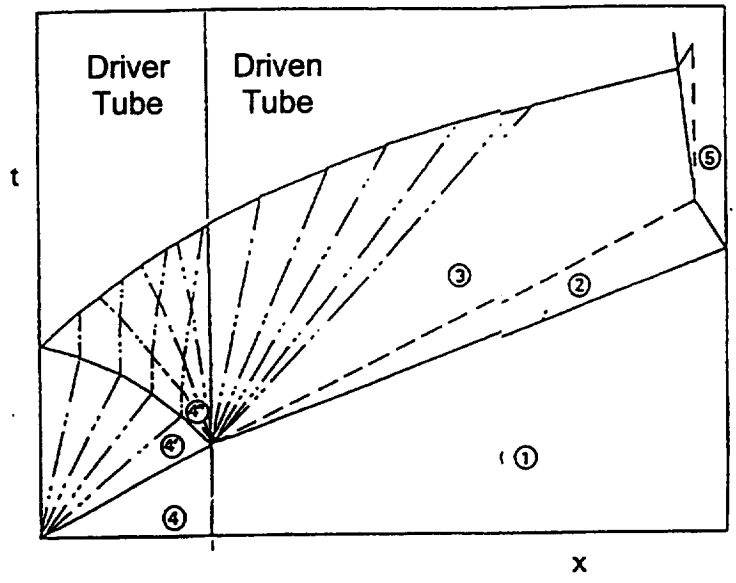

Figure A.1- 3. Wave diagram of downstream propagating detonation wave.

A.1.2.3 Facility Design/Performance Analysis

The initial design concept was based on a reflected mode of operation. In this mode, a secondary diaphragm is located at the end of the driven tube to reflect the incident shock wave and temporarily stagnate the flow. The high-pressure (p_5) created by the shock reflection ruptures the secondary diaphragm to establish flow in a downstream nozzle. This nozzle was designed to expand the flow to a Mach number of 2.0 at the entrance to the conductivity channel. Venable (Ref. 25) performed a quasi-one-dimensional (1-D) computational fluid dynamics (CFD) simulation of the starting characteristics of this configuration, together with a simulation of the transient aspects of the flow through the conductivity channel. Venable's analysis showed the time interval between the incident shock and the contact surface was extremely short as a result of the high gas temperatures behind the contact surface produced by the detonation mode of operation. This fact, together with the nature of the starting process in the Mach 2 nozzle, precluded any possibility of steady flow establishment in the conductivity channel. On the basis of Venable's results, the decision was made to modify the shock tunnel to operate in a nonreflected mode of operation. In this approach the detonation driver would be used to initiate the flow in a driven tube that would directly exhaust the flow to atmosphere at the downstream exit. Preliminary estimates of run time for this mode were on the order of 0.5 to 1.0 milliseconds (ms), which was deemed to be more than adequate for the proposed conductivity experiments. One benefit of this mode is the flow is not stagnated as in the reflected mode of operation, thus problems associated with dissociation of the air coupled with possible freezing of the flow in the subsequent nozzle expansion are to some extent mitigated. Furthermore, the Mach numbers following the incident shock for high incident shock Mach numbers are on the order of 1.75–2.0. Therefore, it appeared possible to closely match the required entrance Mach number representative of MHD accelerator operation, as well as matching the required pressure and temperature levels.

The performance estimates for the detonation driver were made with the TEP™ Computer Code (Ref. 26), a Windows™ version of the NASA CEC76 Code (Ref. 27). Calculations were based on an equilibrium flow assumption. The TEP™ Code was first used to calculate detonation tube performance for stoichiometric mixtures of H_2 and O_2 for a range of initial pressures and different amounts of He dilution. These results were then input into an existing perfect gas code (Ref. 28) to calculate the driven-tube pressure ratio, p_2/p_1, and shock speed, u_S, as a function of the shock tube pressure ratio, p_4/p_1, gas properties, and shock tube area ratio. Prior comparisons with real gas codes indicate that, p_2/p_1, and, u_S, are generally within 5% of perfect gas calculations. The calculations were made for a range of driver-to-driven-tube area ratios. An area reduction has been shown to increase the shock Mach number for a given driver-to-driven-tube pressure ratio (Ref. 29). Furthermore, it was necessary to reduce the area of the driven tube to permit a more realistic size for the conductivity channel. The TEP™ Code was then used to calculate the temperature ratio across the incident shock wave using the perfect gas value of shock speed as an input to the code.

Performance calculations for the downstream-propagation mode are shown in Figure A.1- 4 for a driver-to-driven-tube area ratio of 14.7. The performance envelope was obtained for a stoichiometric O_2 and H_2 mixture at initial driver pressures ranging from 1 to 9 atm and a driven

tube filled with air at initial pressure from 0.063 to 10 atm. The initial gas temperature was 300 Kelvin (K). Also included for comparison are the performance maps of cold air and cold He drivers, with the driver operated at its maximum rating of 400 atm. The downstream-propagating mode of operation was chosen since test conditions behind the driven-tube incident shock wave in excess of 100 atm and 4,000 K were predicted for this mode. The upstream-propagating mode resulted in pressure levels behind the reflected detonation wave in excess of the 400-atm pressure rating of the driver tube to produce comparable test conditions.

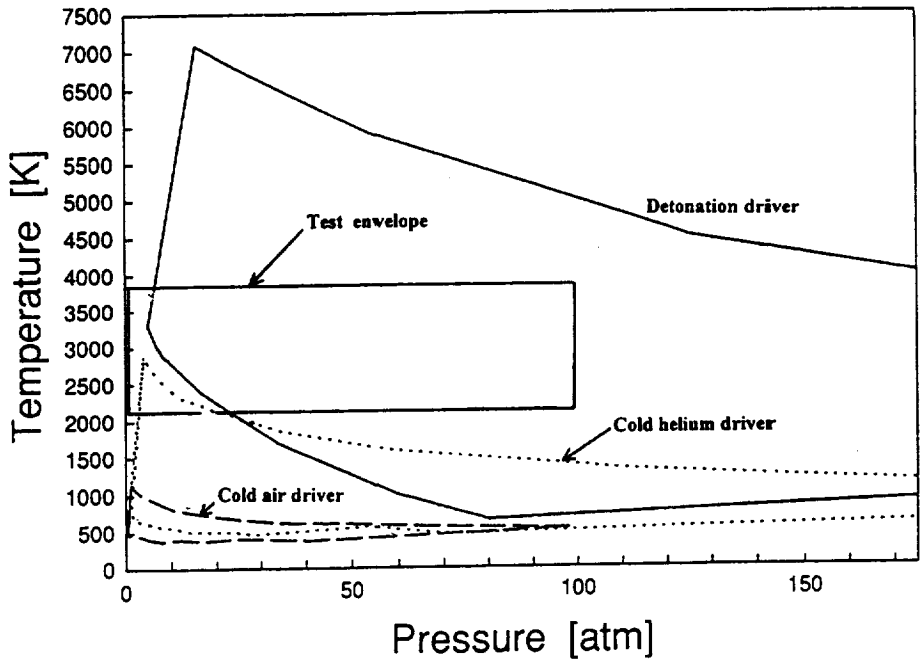

Figure A.1- 4. Performance map of detonation driver, $A_4/A_1 = 14.7$.

A.1.2.4 Preliminary Simulation Experiments

UTA, in collaboration with Lockheed Martin Tactical Aircraft Systems and the Rocketdyne Division of the Boeing North American Corporation, has been actively involved in an on-going PDE research program funded by the State of Texas Advanced Technology Program and NASA-Langley Research Center (NASA-LaRC). The PDE developed as part of this program was reconfigured as a detonation-driven shock tube in order to generate experimental data to validate the choice of operating modes.

A.1.2.4.1 *PDE Research Facility*

A schematic diagram of the PDE Research Facility is shown in Figure A.1- 5. Principal components include the detonation chamber, fuel/oxidizer system, fuel/air system, ignition system, purge air system, vacuum system, and data acquisition/control system. The detonation chamber was constructed from 7.62-cm diameter (3-in.) steel tube sections of varying lengths. Each section had provisions for mounting pressure transducers, heat flux sensors, and thermocouples at 7.62-cm intervals along the principal axis of the tube. One section of 7.62-cm length contained the arc igniter plug and could be placed at either end of the tube, or at intermediate locations. The fuel and oxidizer, as well as the purge air were admitted into the chamber through an end flange that also contains a pressure transducer. Mylar diaphragms of 0.254–0.381 mm (0.01–0.015 in.), thickness are used to seal the open end of the tube. These diaphragms rupture upon impact of the detonation wave, and the combustion products are exhausted into the facility's exhaust system. The vacuum system was used to pump the sealed chamber to a pressure about 690 Pa [0.1 pounds per square inch absoulute (psia)], and the fuel and oxidizer were then admitted to the chamber from standard high-pressure storage bottles through a regulation system. Matheson series 6103 flash arrestors were installed in the lines to prevent flashback into the fuel and oxidizer tanks in the event of a premature ignition during the filling operation. The pressure in the chamber was monitored during the filling operation by a precise Baratron Model 127A vacuum pressure transducer, and the method of partial pressures was used to set the mixture ratio. The fuel/oxidizer mixture was ignited by a high-energy electric arc ignition system (Ref. 14).

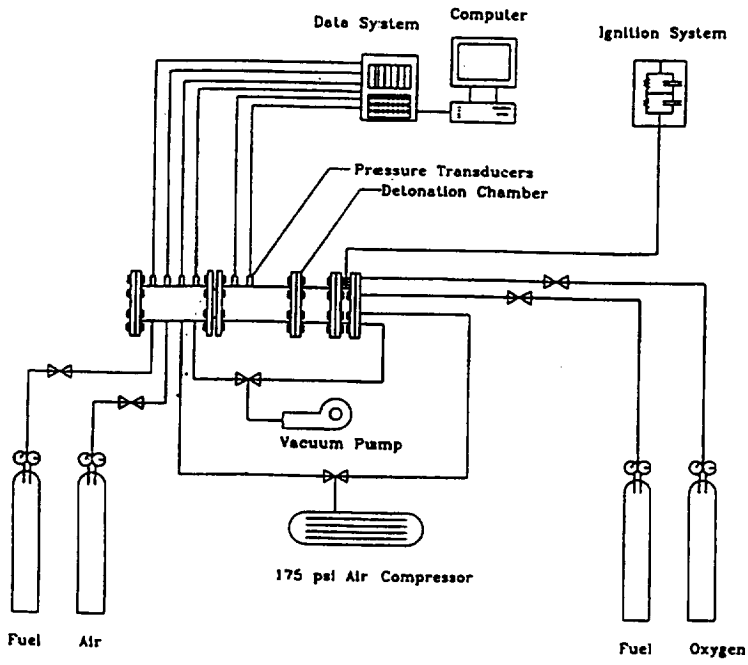

Figure A.1- 5. Schematic diagram of PDE test facility.

A DSP Technology Data Acquisition/Control System was used to gather data during a test firing. This system provides 48 channels containing independent amplifiers, a 100 kilohertz (kHz) analog-to-digital converter, and 512 kilobyte (kB) of sample memory unit. All channels are sampled simultaneously. Transient chamber pressures were measured with PCB Model 111A24 dynamic pressure transducers rated at 6.89 MPa (1,000 psi) and having a response time of 1 microsecond (μs). The Data Acquisition System (DAS) was connected to a 486-DX 33 megahertz (MHz) IBM-compatible PC via a GPIB 488 bus.

The PDE detonation chamber was reconfigured as a detonation-driven shock tube by using a Mylar diaphragm at a flange interface to separate the driver-tube section containing the appropriate fuel/oxidizer/diluent mixture from the driven tube containing air. The length of the driver tube was 53.3 cm (21 in.), and the driven tube was 30.5 cm (12 in.). A 3.49 cm (1.37 in.) section containing the diaphragm was inserted between the driver and driven tube. The driver tube contained two transducers located 15.24 cm (6 in.) apart whereas the driven tube contained 4 transducers located at 7.62 cm (3 in.) intervals. The first transducer in the driven tube was 5.4 cm (2.12 in.) downstream of the diaphragm. Tests were conducted with the 7.62-cm (3-in.) igniter section located at both upstream and downstream ends of the driver tube.

A.1.2.4.2 *Experimental Results*

For the simulated detonation-driven shock tube experiments, the driver tube was filled with near-stoichiometric mixtures of H_2 and O_2. The initial pressure in the driver tube was limited to 2 atm to prevent over pressurization of the pressure transducers resulting from reflection of the detonation wave from the end wall or primary diaphragm. A 0.381-mm (0.015-in.) thick Mylar diaphragm separated the driver and driven tubes. The driven tube was open to atmosphere for the shock tube simulation experiments. Both "upstream propagation" and "downstream propagation" modes were simulated. Also investigated were turbulence enhancement in the driver tube and He dilution of the H_2/O_2 mixture.

Transient pressure traces at selected axial stations for the "upstream propagation" mode are shown in Figure A.1- 6. The two traces to the left of Figure A.1- 6 are from transducers located in the driver tube whereas the other four traces are from transducers in the driven tube. Although a large pressure rise was generated by the upstream propagating detonation wave, the diaphragm did not rupture until the reflected detonation wave from the upstream end wall of the detonation tube impacted the diaphragm. The results from Figure A.1- 6 were converted to a plot of wave propagation speed vs. distance, which is shown in Figure A.1- 7. The wave propagation speed was determined by measuring the time interval between the occurrence of the rapid pressure rise from adjacent transducers. Also shown in Figure A.1- 7 are the sonic velocity and the theoretical Chapman-Jouguet (CJ) detonation wave speed for the H_2/O_2 mixture. These values were calculated from the TEP™ Code. The velocity plot based on time-of-flight measurements shows that transition to a CJ detonation wave occurred in the vicinity of 27 cm from the ignition source, which is comparable to measurements of detonation wave formation distance from the basic PDE experiments (Refs. 14, 15). The CJ detonation wave was clearly not established prior to passage of the wave past the first transducer upstream of the diaphragm, and it was speculated the gradual

rise in pressure associated with the detonation wave formation was insufficient to cause diaphragm rupture. A thinner diaphragm was clearly needed in this case. Diaphragm rupture did occur upon impact of the reflected detonation wave, thereby generating a strong shock wave ($M_S \cong 3.5$) in the driven tube. Notice the abrupt rise in pressure upon passage of the shock wave as compared to the gradual rise in pressure associated with passage of the detonation wave. This "precompression" phenomenon appears to be a characteristic of weak detonation waves and generally disappears when a full CJ detonation wave is formed (Ref. 15). Good agreement was observed between wave propagation speeds in the driven tube based on time-of-flight measurements and values calculated from the measured shock pressure ratio using classical shock tube theory in the front part of the driven tube. However, the pressure ratio calculations indicate an attenuation of wave speed that is not observed from the time-of-flight measurements. Tests conducted with turbulence enhancement in the detonation tube via a Shchelkin spiral (Ref. 30) produced rather surprising results; turbulence enhancement actually delayed the formation of a CJ detonation wave in the driver tube, with a maximum wave propagation velocity of approximately 2,000 meters per second (m/s), as compared to the nearly 3,000 m/s achieved for the CJ detonation wave. The driver tube pressure levels were actually higher and little difference was seen in the strength of the shock wave generated in the driven tube.

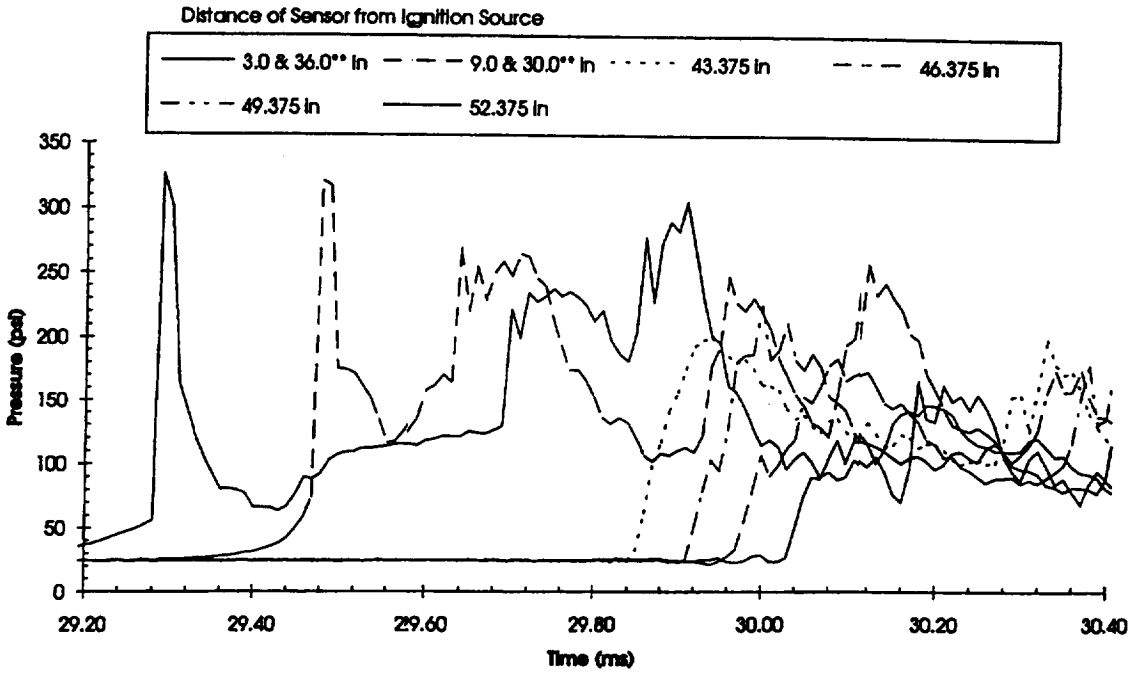

Figure A.1- 6. PDE shock tube pressure plot for $H_2/O_2 = 2.0$ at an initial pressure of 2 atm.

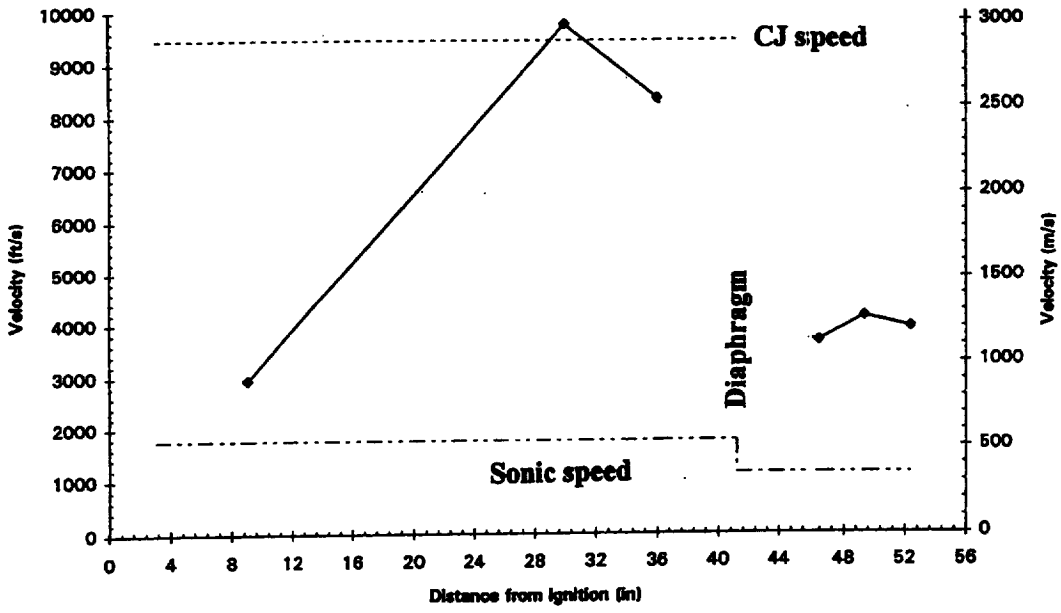

Figure A.1- 7. PDE velocity plot for $H_2/O_2 = 2.0$ at an initial pressure of 2 atm.

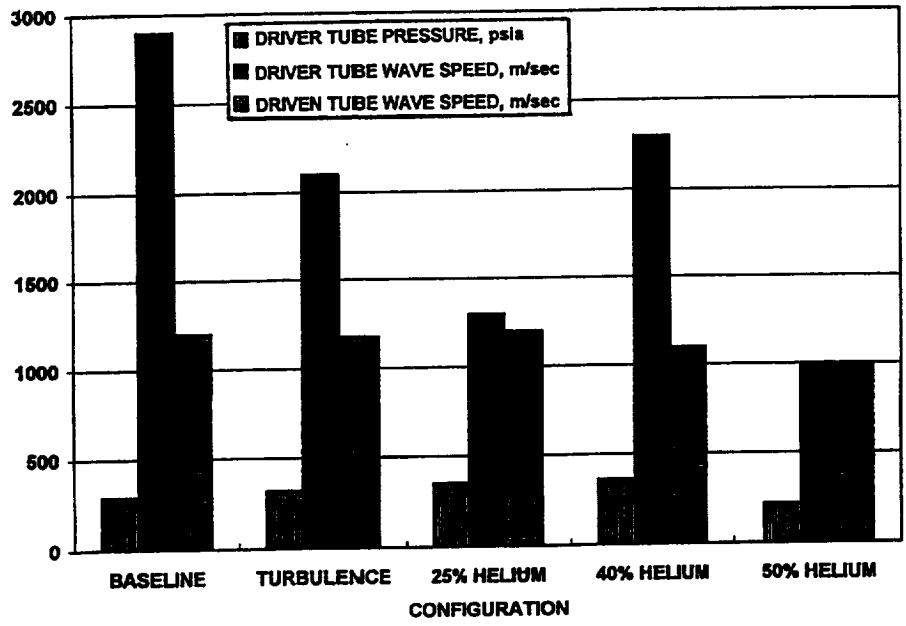

Figure A.1- 8. Summary of upstream propagation test runs.

A summary of measured driver tube pressure levels, driver, and driven-tube wave propagation speeds is shown in the form of a velocity histogram in Figure A.1- 8 for the upstream propagation mode. The shock speed in the driven tube for the upstream mode appears to correlate better with the maximum pressure level attained in the detonation tube rather than the detonation wave speed. Helium dilution did not exhibit the anticipated performance enhancement, and in fact, shock velocities were actually lower. Furthermore, examination of the pressure traces for the He dilution runs indicated a rather irregular wave pattern in both the driver and driven tubes and it appeared that inadequate mixing of the gases might be a principal factor. Other investigators have emphasized the importance of achieving good mixing to obtain strong detonation wave fronts (Refs. 22, 31).

Similar results were obtained for the "downstream propagation" mode, although lower driven-tube shock speeds were observed for this mode. In general, CJ detonation waves did not form in the driver tube, probably due to the shorter distance traveled by the wave. This was not considered to be a problem for the full-scale detonation tube, since the total length would be approximately a factor of 10 greater than the distances required for transition to a CJ detonation wave in the basic PDE experiments. The pressure rise behind a downstream-propagating CJ detonation wave should be more than adequate to rupture the diaphragm and initiate a strong shock wave in the driven tube.

The results of the preliminary simulation experiments were inconclusive in so far as providing a clear validation of the choice of operating modes. In general, the performance for the downstream mode was lower than for the upstream mode, which is inconsistent with the theoretical predictions discussed in Section A.1.2.3. However, this may be due to the very short length of driver tube, which obviously prevented attainment of CJ detonation speeds. Thus, in developing the design modifications required to convert the existing pressure driver to a detonation driver, the decision was made to provide mounting ports for insertion of the arc igniter plug at both ends of the driver and to test both concepts with the full-scale facility.

A.1.2.5 Shock Tunnel Modifications

A.1.2.5.1 *Detonation Driver*

The driver from the existing shock tunnel was modified to serve as the detonation driver. Ports for four surface mounted pressure transducers were installed to monitor the behavior of the detonation wave. Ports were also installed for an ignition plug at each end; therefore, both upstream and downstream-propagation modes could be evaluated. The tube had two ports for injecting gases, specifically H_2, O_2, air, and He; as well as for vacuuming out the initial air and venting the combustible mixture in case of an aborted run. The conversion to a detonation driver retains the same pressure rating.

A.1.2.5.2 *Arc Ignition System*

The arc ignition system (Figure A.1- 9) was an adaptation of the ignition system developed for the PDE program (Refs. 14, 15). The ignition source is a single high-voltage, high-current arc plug driven by a capacitor bank. The high frequency welding unit ionizes a path between the two electrodes of the arc plug using high frequency, high-voltage, and low-current energy. A spark gap limits the voltage and produces a spectrum of frequencies. When the path is ionized sufficiently, the capacitors are discharged as a high-current arc. The capacitor bank consists of two 11 millifarad (mF), 75 volt direct current (VDC) capacitors connected in series and charged to 135 VDC. The capacitors are charged by an 88 volt alternating current (VAC), 50-milliampere (mA) transformer and a rectifying diode bridge. The charging transformer is kept small to avoid driving the arc directly once the capacitors are discharged. A diode is also connected across the arc-plug leads to eliminate ringing of the discharge current. This eliminates reverse voltage on the capacitor bank and reduces the maximum voltage differential seen by many of the components, thus leading to longer component life. A timer circuit provides a fixed-width pulse to limit the operational time of the controls of the high frequency unit. The timer circuit is isolated from the high frequency unit by an infrared diode-transistor pair.

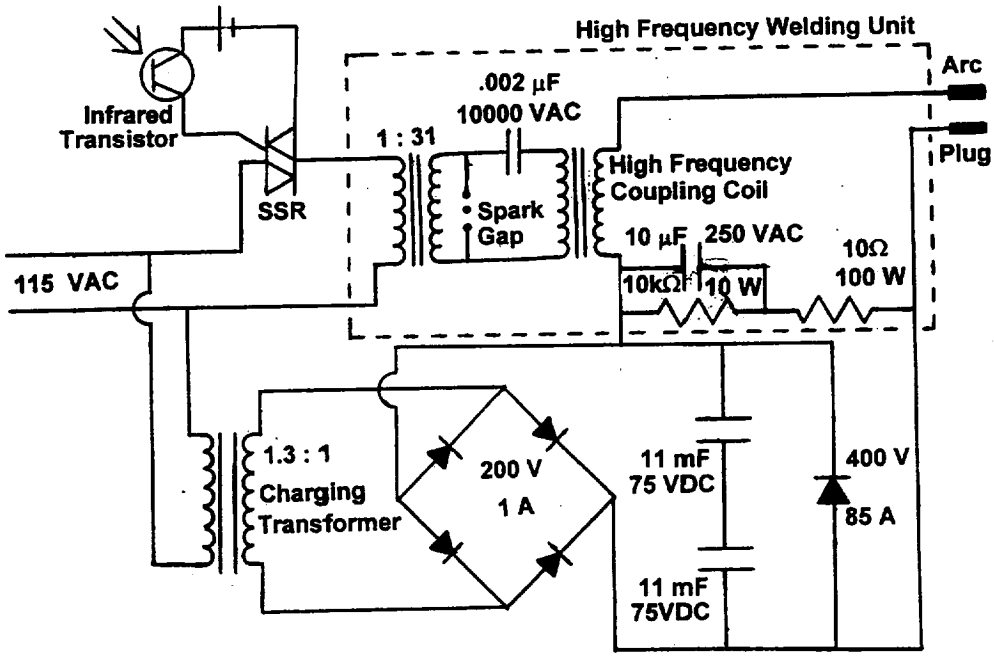

Figure A.1- 9. Circuit diagram of ignition system.

The energy from the capacitor bank is discharged through an arc plug constructed of two tungsten electrodes in a ceramic holder. The assembly is mounted in a threaded steel housing. The ends of the electrodes are flush with the surface of the plug. The threaded housing assembly is then installed into the sidewall of the driver tube of the facility. The ends of the electrodes are nearly flush with the inner wall of the chamber.

A.1.2.5.3 *Driven Tube*

The original driven tube was replaced with a new tube of type 304 stainless steel with 4.12 cm internal diameter (1.62 in.) and 9.1 m in length (30 ft). The tube was commercially available and had a pressure rating of 19 MPa (2,800 psi). The detonation-driven shock tube was designed for operation in the non-reflected mode for the MARIAH Project; thus the driven tube was designed for a lower pressure rating. The existing downstream diaphragm section and hypersonic nozzle were removed, and the end of the driven tube was extended into the existing vacuum tank. The tank was not used for vacuum, but actually used to collect the exhaust before releasing it to the atmosphere. This combination of driver and driven tube produces a driver-to-driven tube area ratio of 14.7, thereby providing an additional improvement in performance.

A.1.2.5.4 *Pneumatic Injection System*

The H_2, O_2, and He are injected through the sidewall of the driver. Two tubes are available for this purpose. The H_2 and O_2 are injected through separate tubes for safety reasons. Helium and purge air are injected through the O_2 line. The initial air is evacuated through the H_2 line and the combustible mixture is also vented through the H_2 line. Both lines contain Matheson series 6103 flash arrestors for added safety.

A.1.2.5.5 *Instrumentation/Data Acquisition System*

The detonation driver instrumentation includes four PCB Model 111A22 dynamic pressure transducers and a MKS Model 127A Baratron pressure transducer. The Baratron has a maximum pressure range of 1.33 MPa (10,000 torr) and is used to set the mixture ratio during filling of the detonation driver using partial pressures. The PCB transducers are mounted in the driver tube with the sensing diaphragm flush with the inside wall. Each one has a full-scale range of 68.9 MPa (10,000 psi), a rise time of 2 μs, and a time constant of 1,000 s. The Baratron is used to provide an initial pressure reading as the PCB's are dynamic transducers.

The driven tube instrumentation also includes four PCB transducers. Two of these are PCB model 111A23, which have a full-scale pressure range of 34.4 MPa (5,000 psia), a rise time of 2 μs, and a time constant of 500 s. These transducers are used primarily for shock speed measurements, as they are upstream of the test area and separated by a precisely measured distance. The other two PCB transducers are either model 111A23 or 111A24, depending upon the conditions in the driven tube. The model 111A24 transducers have a full-scale range of 6.89

MPa (1,000 psia), a response time of 2 μs, and a time constant of 100 s. An MKS Model 127A Baratron pressure transducer also measures the initial pressure in the driven tube. This transducer has a maximum pressure range of 133 kilopascal (kPa) (1,000 torr), provides a very accurate measure of the initial driven-tube pressure, and also provides an initial pressure for the dynamic PCB pressure transducers.

The pressure transducers were connected to a DSP Technology DAS; which has 48 channels capable of 100 kHz sampling rate and 12 bits of accuracy, with each channel having its own amplifier and analog to digital converter to allow for simultaneous sampling of all channels. The system has 512 kilosamples of memory available for distribution between the channels being utilized. Eight channels are also available with the capability of 1 MHz sampling rate, 12 bits of accuracy, and each with separate analog to digital converters for each channel. Two megasamples of memory are available for these eight channels. The DAS is controlled by a personal computer (PC) that retrieves the data through an IEEE-488 interface. The data is then stored for later analysis.

The pressure transducers provided direct measurement-of-pressure ratios upon passage of the detonation or shock waves. Furthermore, time-of-flight measurements were used to calculate wave propagation speeds by determining the time between passage of the detonation or shock wave between successive transducers. Since the transducers are a known distance apart, the shock or detonation velocity can be determined from the measured time interval between adjacent pressure transducers. This provides an important indication of the properties of the detonation wave, primarily that the wave has indeed transitioned to a fully developed CJ wave.

A.1.2.6 Initial Test Results (Arc-Ignition Mode)

The initial operation of the modified shock tube consisted of a series of test runs at increasing pressure levels to verify the design and refine operating procedures. The first test run was with a stoichiometric mixture of H_2 and O_2 in the driver at an initial pressure of 1 atm. The driven tube contained atmospheric air and was separated from the driver tube by a 0.381 mm (0.015 in.) thick mylar diaphragm. Thin mylar could be used since the initial pressures were low and the post detonation pressure is typically about 20 times the initial level. Subsequent tests increased the initial detonation tube pressure to 8 atm. Both upstream-and downstream-propagation modes were examined. A typical detonation tube pressure trace for the upstream-propagation mode is shown in Figure A.1- 10 for an initial detonation tube pressure of 6 atm. The sensor closest to the ignitor (Location 4) detects some precompression ahead of the detonation wave and is an indication that the detonation wave has not reached full CJ velocity. The precompression phenomena was observed in experiments reported by Helman (Ref. 32) and was also observed in our own experiments with a smaller detonation tube being used for PDE research (Refs. 14, 15). The next sensor passed by the detonation wave (Location 3), as well as subsequent sensors (not shown in Figure A.1- 10 for clarity), did not detect any precompression; also, the time of flight calculations indicate the detonation wave had reached CJ velocity. A similar plot for the downstream-propagation mode is shown in Figure A.1- 11 for an initial pressure of 6 atm. The time-of-flight measurements indicate CJ velocity was achieved by the time the detonation wave

reached the first pressure sensor. The rapid fall-off in pressure following passage of the detonation wave for both cases is due the Taylor rarefaction wave that follows the incident detonation wave (Ref. 33).

The overall performance map of the modified shock tube was obtained by conducting a parametric variation of both driver- and driven-tube pressures, as well as introducing varying amounts of He dilution. Test results are summarized in Figure A.1- 12. The performance was considerably less than predicted. Furthermore, contrary to initial predictions, the data indicated the upstream propagation mode (downstream ignition location) provided better performance. An analysis of the test data suggests the following reasons for the low performance. Figure A.1- 13 illustrates the wave process for the downstream-propagation mode of operation, resulting from ignition of the detonable mixture at the upstream end of the detonation tube. The incident detonation wave is followed by a strong expansion wave that is generated to satisfy the zero velocity boundary condition at the closed end of the tube. This expansion wave causes an immediate drop in pressure from the CJ level generated by the incident detonation wave, as shown in Figure A.1- 11, and the interaction of this expansion wave with the reflected detonation wave appears to drastically lower the pressure level behind the reflected detonation wave.

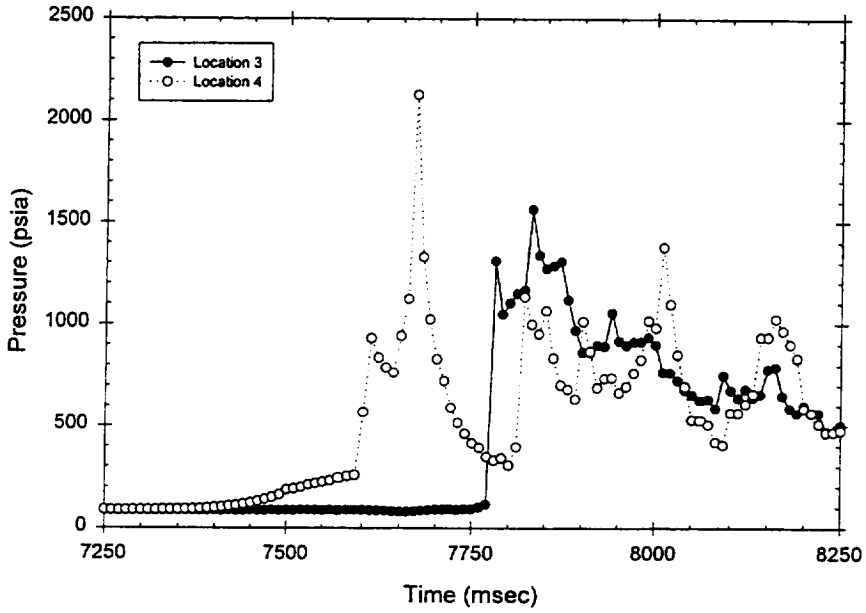

Figure A.1- 10. Detonation tube pressure traces, upstream propagating mode at an initial pressure of 6 atm, electric arc-ignition.

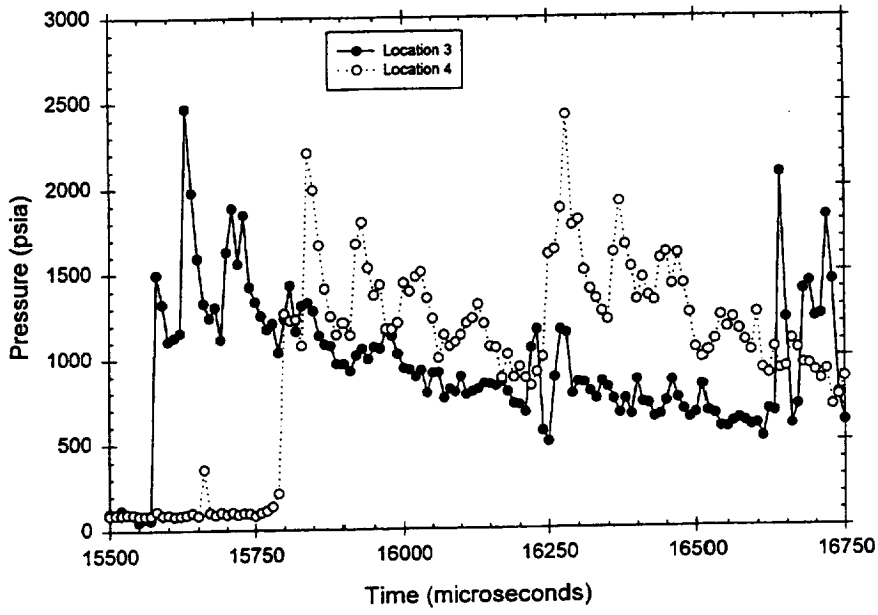

Figure A.1- 11. Detonation tube pressure traces, downstream propagating mode at an initial pressure of 6 atm, electric arc-ignition.

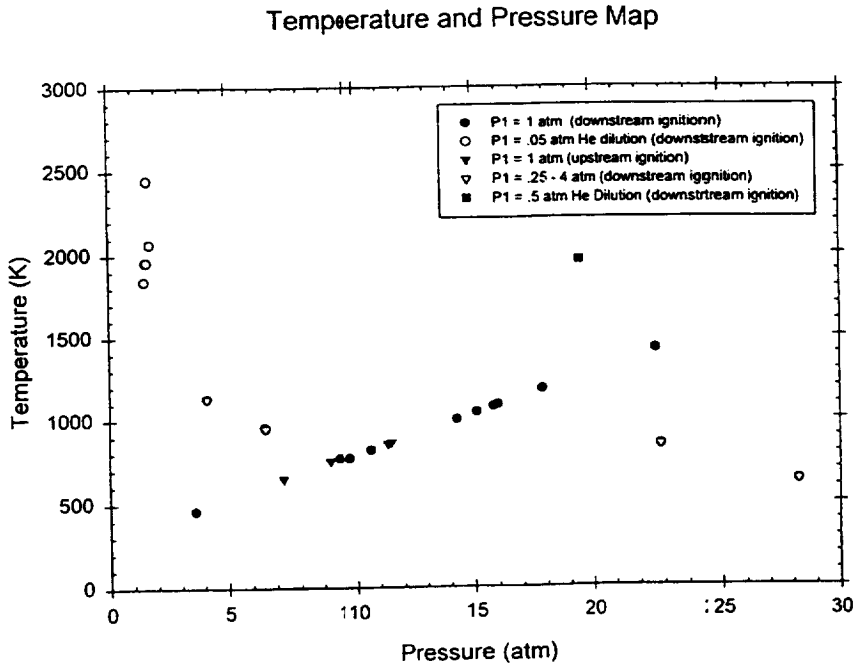

Figure A.1- 12. Experimental performance map, electrical arc-ignition.

This pressure initiates and sustains the incident shock wave propagation in the driven tube and consequently, rapid attenuation of the incident shock wave is suspected. The performance predictions described in Section A.1.2.3 were based on a simple model that did not have the capability of analyzing the complex flow patterns resulting from wave interactions and thus did not predict this effect. Funding restrictions prevented the development of an adequate numerical simulation capability; thus the problem was not detected until the test results from the full-scale detonation driver were obtained.

A somewhat different cause is suspected for the reduced performance with the upstream-propagation mode of operation. A typical pressure trace in the detonation tube for this mode was shown in Figure A.1- 10. A detailed analysis of the pressure data indicates the initial wave formation is a weak detonation wave ($M_D \sim 1.7$) that transitions to a fully developed CJ detonation wave ($M_D \sim 5.3$) about 50 cm (20 in.) from the ignition source. This observation is consistent with results observed in the PDE experiments (Ref. 15). Figure A.1- 13 shows an end-wall pressure trace from a similar test conducted as part of the PDE program. This data was from a 7.62-cm diameter (3-in.) chamber containing a stoichiometric mixture of H_2 and O_2, initially at a pressure level of 1 atm. Transition to a fully developed CJ detonation wave for this case was triggered by a Shchelkin spiral (Ref. 30) inserted into the detonation chamber.

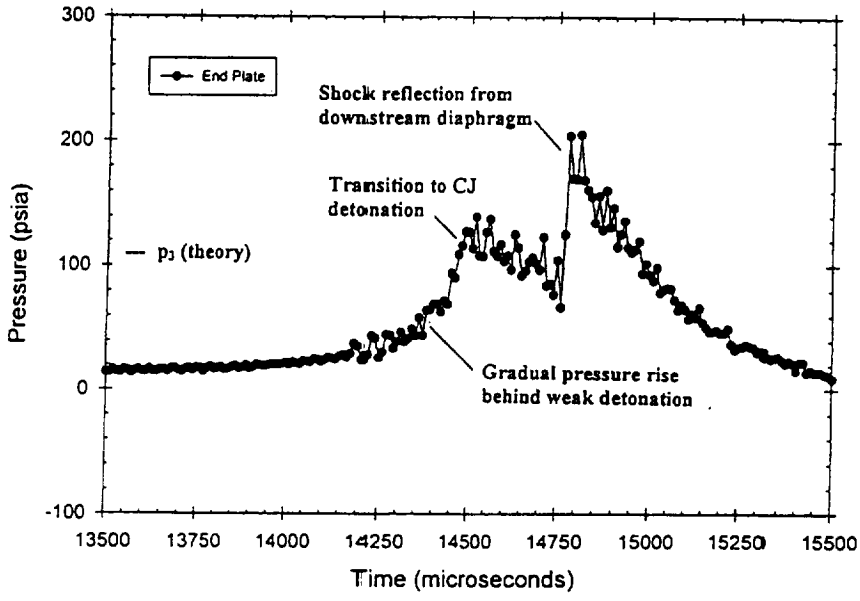

Figure A.1- 13. End wall pressure trace from PDE experiment.

Moreover, similar results have been observed for cases at higher initial pressure or with different fuels that naturally transitioned to CJ detonation wave propagation speeds without turbulence enhancement. The end-wall pressure is seen to gradually increase to a level of about 70 psia; and

then abruptly increase to a level of about 110 psia, which corresponds to the transition in wave propagation from a weak to a CJ detonation wave. This pressure level is in close agreement with the predicted end-wall pressure using the Zeldovich-von Neumann-Doring (ZND) detonation model (Ref. 33); however, the fact that a CJ wave does not form immediately upon ignition probably interferes with the formation of a strong incident shock wave in the driven tube. Another adverse effect may arise from the fact that the upstream-propagation mode induces a flow following the incident detonation wave in the opposite direction to the flow induced in the driven tube, and additional loss of momentum is required to reverse this flow direction. Again, a method of characteristics or CFD code would have predicted this phenomena prior to conducting the tests.

A.1.2.7 Recommendations for Modification of Detonation Driver

Unfortunately, as a result of the reduced performance of the detonation-driven shock tube, it was concluded the original performance goals could not be met with the current configuration. Detailed analysis of the test data from the calibration suggested the shock speeds were considerably lower than predicted, therefore drastically lowering the pressure and temperature levels generated by the incident shock wave. An analysis of our test results and discussions with Drs. John Erdos and Robert Bakos of GASL, as well as Dr. Dave Bogdanoff of NASA Ames, led us to conclude that there were two reasons for the poor performance. The primary reason was attributed to the Taylor rarefaction wave associated with the arc-ignition process for the downstream mode, as well as the combined effects of reduced pressure due to the inability to directly initiate a CJ detonation wave and the required flow reversal for the upstream mode. A secondary factor can be attributed to shock attenuation due to an overly long driven tube, which can be remedied quite easily.

In order to improve the performance of the shock tube, a modification of the ignition process by adopting the "light gas driver tube" concept implemented by GASL in their expansion tube facility (Refs. 23, 24) was proposed. Thus, the arc ignition process would be replaced by a light gas driver tube that generates the detonation wave in the combustible mixture by rupture of a diaphragm between the driver tube and the detonation tube. This concept is discussed in some detail in the following section.

A.1.3 Shock-Induced Detonation Driver Development

A.1.3.1 Basic Concept

The reduced performance of the detonation-driven shock tube prevented attainment of the shock Mach numbers required to meet the original goals of the program. After evaluation of several proposed options for upgrading the shock tube performance, the shock-induced mode of detonation being incorporated by Bakos et al. of GASL (Refs. 23, 24) was selected to expand the

performance of the HYPULSE facility. The concept is illustrated in Figure A.1- 14 (adapted from Ref. 24).

A high-pressure air or He driver is placed upstream of the detonation tube and used to drive a shock wave into the detonation tube. This shock wave should quickly transition to a CJ detonation wave; but the rarefaction wave associated with the closed-end operation of the detonation tube should be drastically reduced because of a reduction of the strength of the Taylor rarefaction wave which results in a higher pressure behind the detonation wave. In effect, the driver tube exhaust acts like a gas piston to sustain the pressure behind the incident detonation wave. In the "perfectly-driven" mode, the full CJ pressure level can ideally be maintained behind the detonation wave, as shown in Figure A.1- 15 (from Ref. 24).

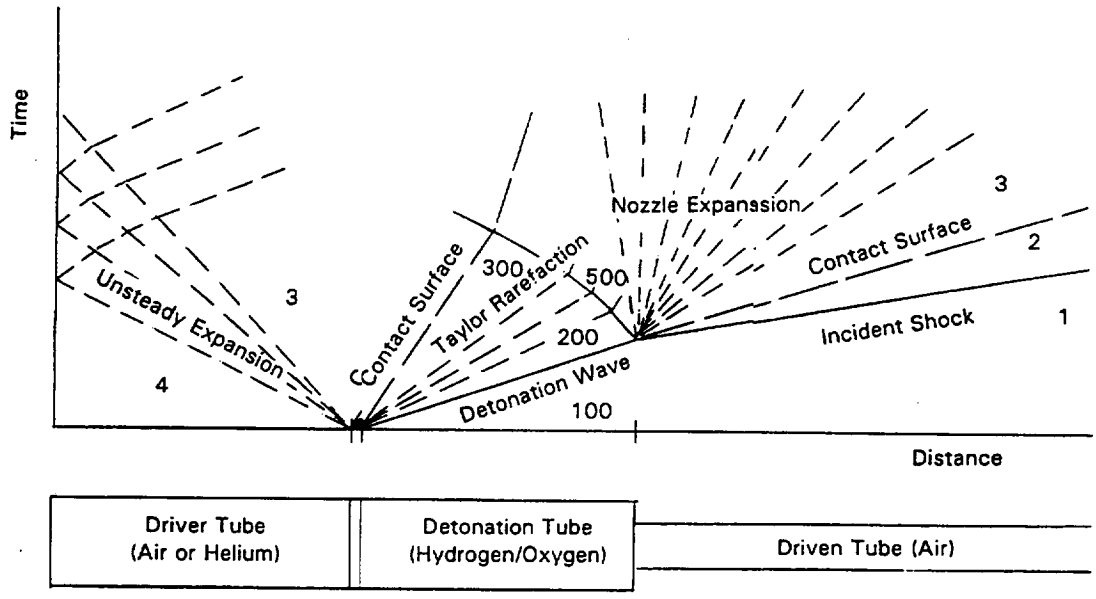

Figure A.1- 14. Wave diagram depicting shock-expansion tube operation with a shock induced detonation driver

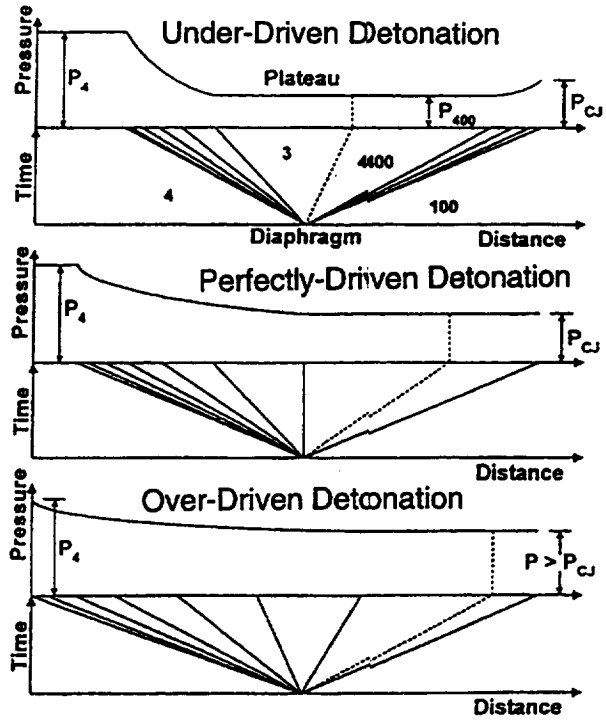

Figure A.1- 15. Operation of a light-gas driven tube in under driven, perfectly driven, and over driven modes.

A.1.3.2 Facility Modifications

Development of the shock-induced detonation driver concept was proposed to MSE as an extension to the existing contract and subsequently approved. The necessary facility modifications were implemented by reconfiguring the detonation driver tube back to its original pressure-driven mode of operation and converting one of the original 2.74-m (9-ft), 15.24-cm diameter (6-in.) diameter driven-tube sections to become the detonation tube section. The original double-diaphragm section was reinstalled between the upstream driver tube and the detonation tube, and the 4.12-cm diameter (1.62-in.) driven tube was shortened to a length of 3 m (10 ft) to reduce shock attenuation due to boundary layer growth behind the incident shock. The new detonation tube was also modified to allow insertion of four pressure transducers to monitor the detonation wave development. A sketch of the modified shock tube showing pertinent instrument locations is shown in Figure A.1- 16.

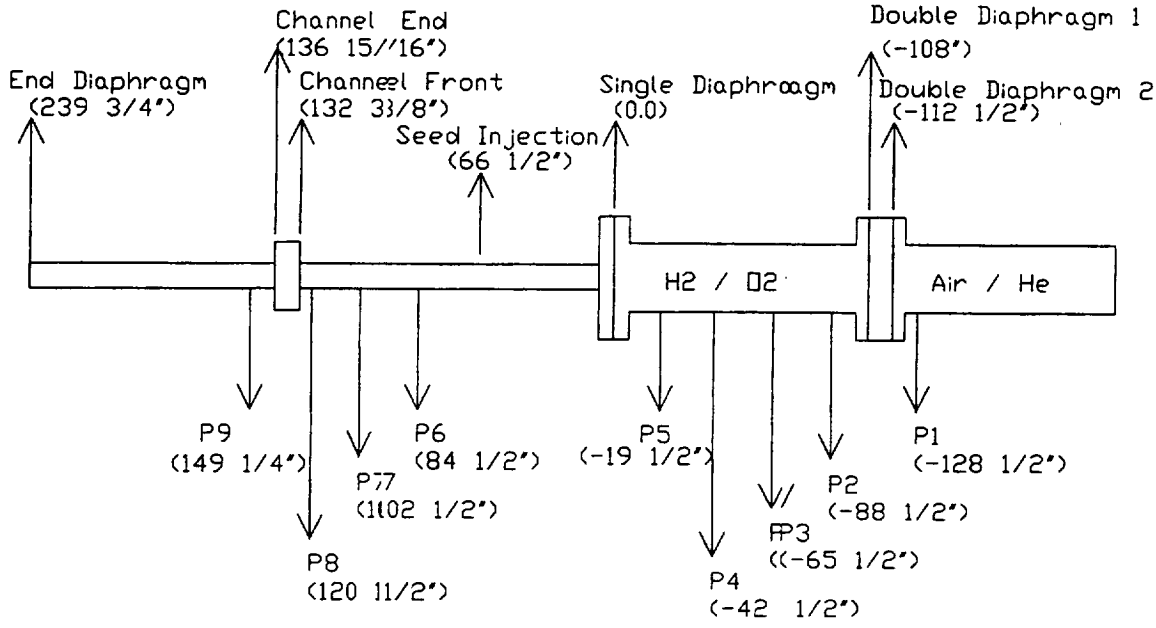

Figure A.1- 16. Schematic of modified shock tube showing instrumentation locations.

A.1.3.3 Test Results from Shock-Induced Detonation Mode of Operation

A typical detonation tube pressure trace from the shock-induced mode is shown in Figure A.1-17. The initial conditions in the detonation tube were a stoichiometric mixture of H_2 and O_2 at 4 atm. Air at a pressure of 217 atm was loaded into the upstream driver tube. The time-of-flight measurements indicate a detonation wave propagation speed of 2,920 m/s, which is almost identical to the theoretical CJ detonation wave speed for these conditions. This particular test corresponded to the under-driven mode (Figure A.1- 15) in which the incident detonation wave is followed by a moderate-strength Taylor rarefaction wave that lowers the pressure. The reflected detonation wave increases the pressure by a factor of about 2.3, which is in good agreement with theoretical considerations. Unfortunately, the reduction in pressure caused by the rarefaction wave lowers the peak pressure behind the reflected detonation wave, although not as much as observed for the arc-initiated detonation wave. The pressure trace in the driven tube for this test is shown in Figure A.1- 18. The time-of-flight measurements indicate a shock Mach number of 5.95.

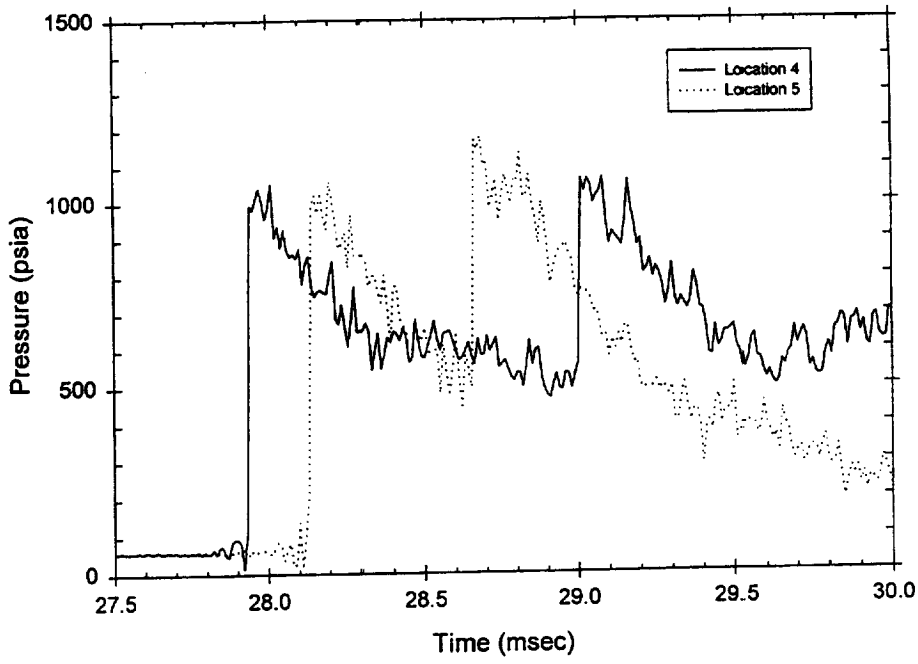

Figure A.1- 17. Detonation tube pressure traces for an initial detonation tube pressure of 4 atm shock induced detonation (air driver pressure = 217 atm).

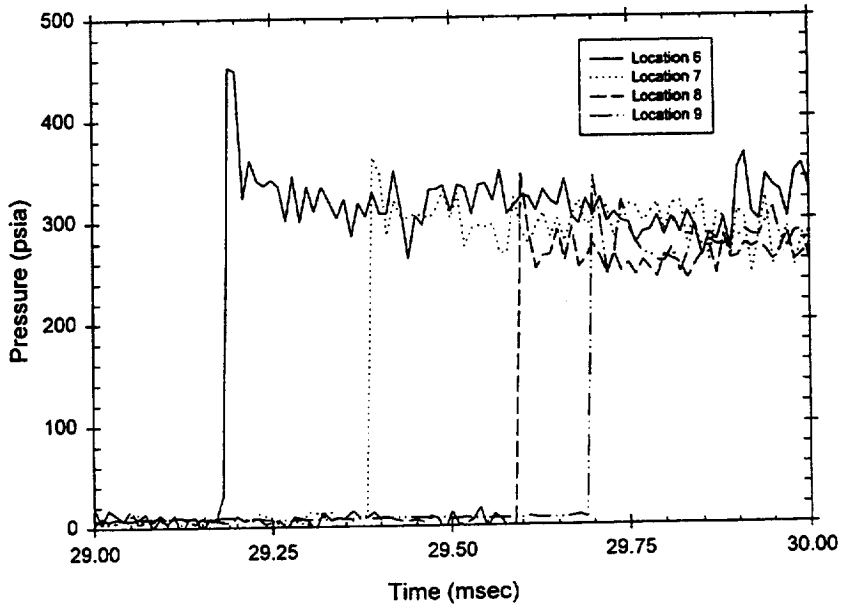

Figure A.1- 18. Driven tube pressure traces for an initial detonation tube pressure of 4 atm, shock induced detonation (air driver pressure = 217).

Results from two tests comparing air and He drivers at nominal driver tube pressures on the order of 210 atm are shown in Figures A.1- 19 and A.1- 20. The detonation tube contained a stoichiometric mixture of H_2 and O_2 at a pressure of 1.5 atm, and the initial pressure in the driven tube was nominally 0.14 atm. The test run shown in Figure A.1- 19, using air in the driver is typical of the under-driven mode and is characterized by the drop in pressure through the Taylor rarefaction wave. In contrast the test run shown in Figure A.1- 20 with He as the driver gas is nearly perfectly driven, and the pressure drop through the Taylor rarefaction wave was considerably reduced. Furthermore, the pressure level achieved by the reflected detonation wave is much higher, and the corresponding driven-tube Mach numbers are increased from 6.70 to 7.65. Driven-tube pressure traces for these two cases are shown in Figure A.1- 21 (air driver) and A.1-22 (He driver). Thus, it appears the shock-induced detonation mode offers substantial gains in performance by reduction or possible elimination of the Taylor rarefaction wave.

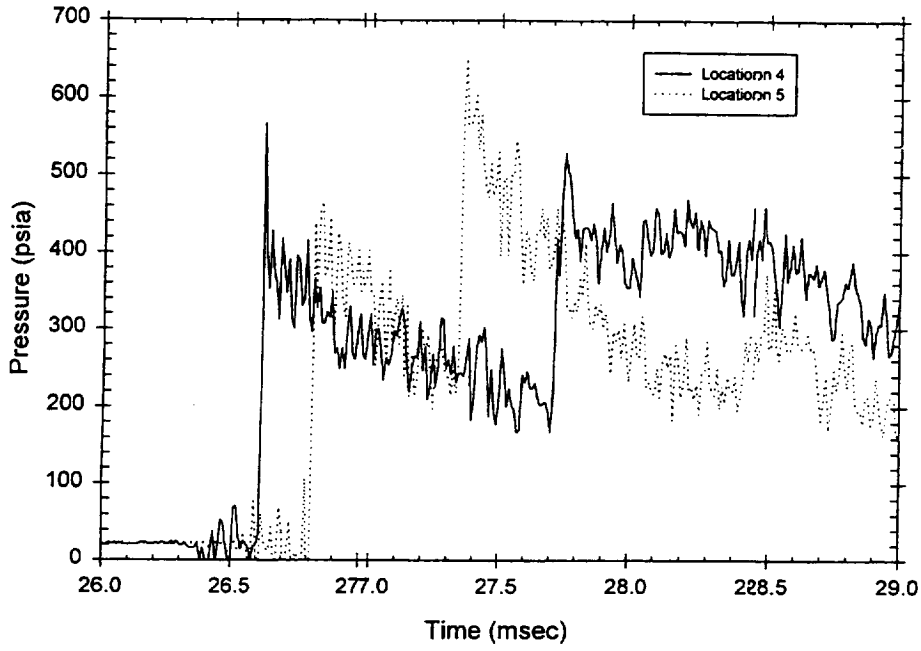

Figure A.1- 19. Detonation tube pressure traces for an initial detonation tube pressure of 1.5 atm, shock induced detonation (air driver pressure = 219 atm).

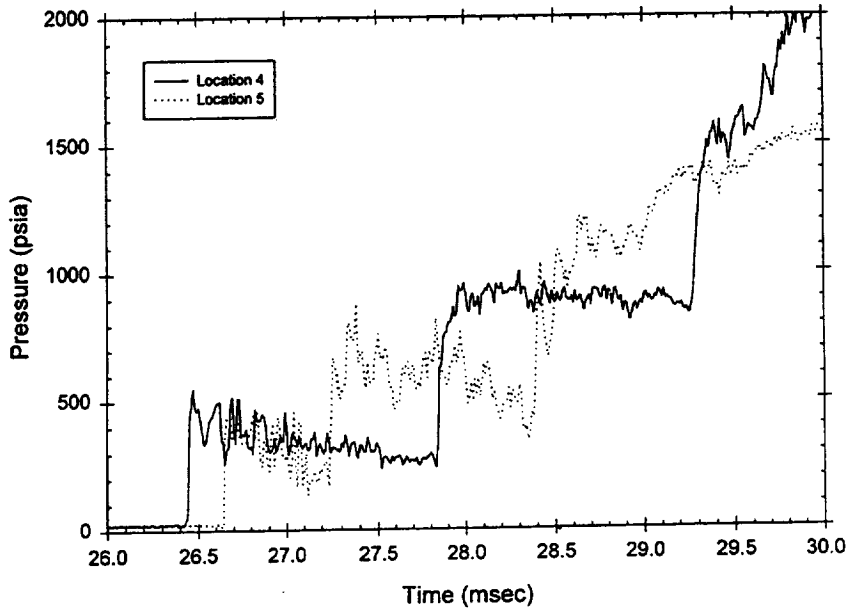

Figure A.1- 20. Detonation tube pressure traces for an initial detonation tube pressure of 1.5 atm, shock induced detonation (He driver pressure = 201 atm).

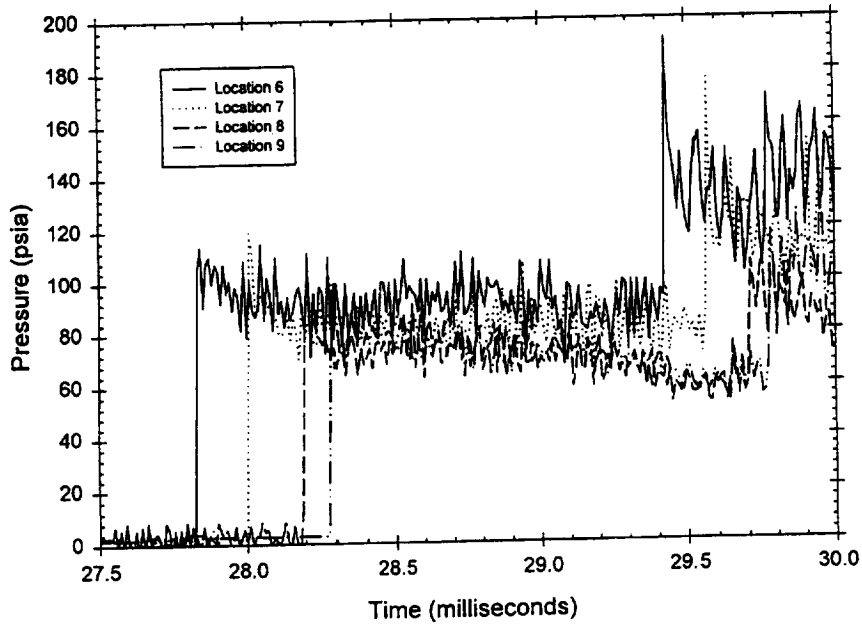

Figure A.1- 21. Driven tube pressure traces for an initial driver tube pressure of 1.5 atm (air driver pressure = 219 atm).

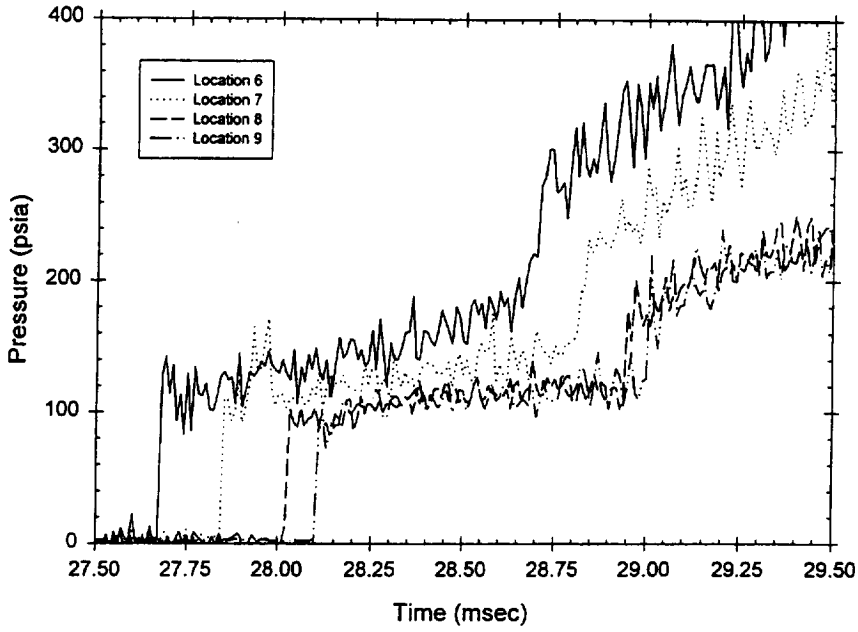

Figure A.1- 22. Driven tube pressure traces for an initial driver tube pressure of 1.5 atm (He driver pressure = 201 atm).

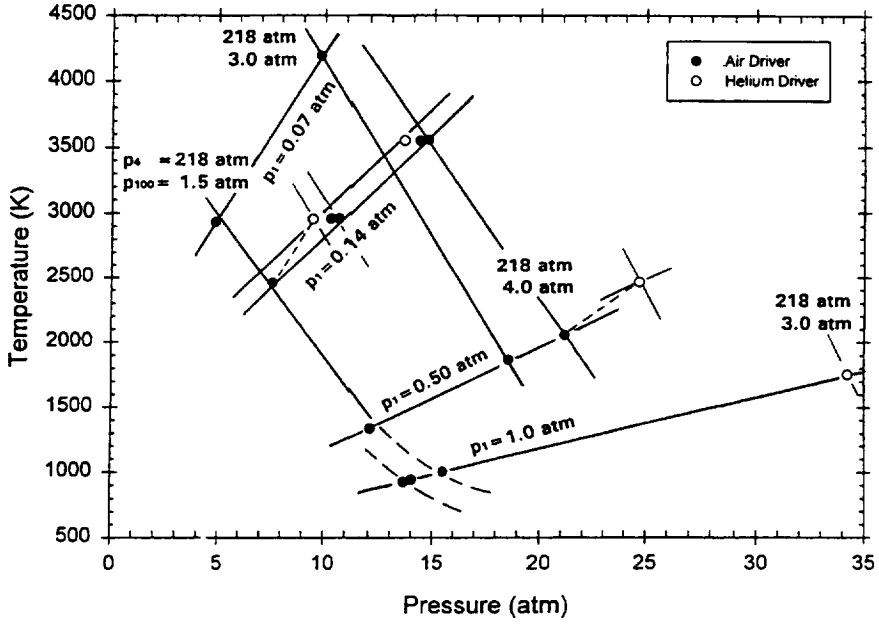

Figure A.1- 23. Composite performance map.

The composite performance map obtained to date is shown in Figure A.1- 23. The peak shock Mach number obtained with the air driver was 10.71, resulting in a post-shock temperature and pressure of 4,190 K and 9.8 atm, respectively. The highest post-shock pressure attained with the air driver was 21 atm, with a corresponding temperature of 2,058 K. As anticipated, use of He in the upstream driver resulted in considerable improvement in performance. There was a general increase in both temperature and pressure as compared to that attainable with the air driver for similar conditions. A comparison of Figures A.1- 23 and A.1- 12 shows that a significant enhancement in shock tube performance was realized by incorporation of the shock-induced detonation mode, as compared with the arc-initiated detonation.

A.1.4 Conductivity Channel and Power Supply

A.1.4.1 Theoretical Considerations

Theoretical expressions for the electrical conductivity have been developed for a singly ionized plasma in Lin et al. (Ref. 34). A collision-mixing model was used to determine the effect of temperature on the electrical conductivity at pressures on the order of 1 atm. The electrical resistivity can be written as the sum of the resistivity of two effects, namely, those due to electron-neutral and electron-ion collisions,

$$\frac{1}{\sigma_{add}} = \frac{1}{\sigma_{en}} + \frac{1}{\sigma_{ei}} \qquad \text{(A.1- 1)}$$

Spitzer and Harm (Ref. 35) proposed the electron-ion conductivity could be expressed as:

$$\sigma_{ei} = 1.913 \times 10^4 \frac{(kT/e)^{3/2}}{\ln \Lambda} \qquad \text{(A.1- 2)}$$

The quantity kT/e is the gas temperature expressed in electron volts while Λ is a parameter equal to the ratio of Debye shielding distance to the impact parameter for 90° scattering by an ion. The conductivity due to electron-neutral collisions σ_{en} can be calculated as a function of the electron density from the Saha equation (Ref. 36). However, it is believed the conductivity calculated by this method is overestimated by 70% under some circumstances. Thus, more accurate models are needed.

Nevertheless, the collision-mixing model was used by Garrison (Ref. 37) to evaluate the conductivity of air for a low-pressure MHD accelerator. Theoretical results were obtained for

the effect of temperature on electrical conductivity for pressures from 0.1 to 5 atm. However, this pressure range is inadequate for facility simulation of air-breathing hypervelocity flight. The collision-mixing model was replaced by a chemical equilibrium model (Ref. 27) modified for electrical conductivity calculations by Demetriades and Argyropoulos (Ref. 38) to obtain high-pressure results. Typical results for pressures from 1.0 to 100 atm and temperatures from 1,800 to 4,200 K are shown in Figures A.1- 24 and A.1- 25, respectively, for K-seeded and cesium (Cs)-seeded air. As can be seen in the figures, the electrical conductivity increases dramatically with temperature but decreases with increased pressure. Furthermore, Cs seeding increases the gas conductivity over that attainable with K.

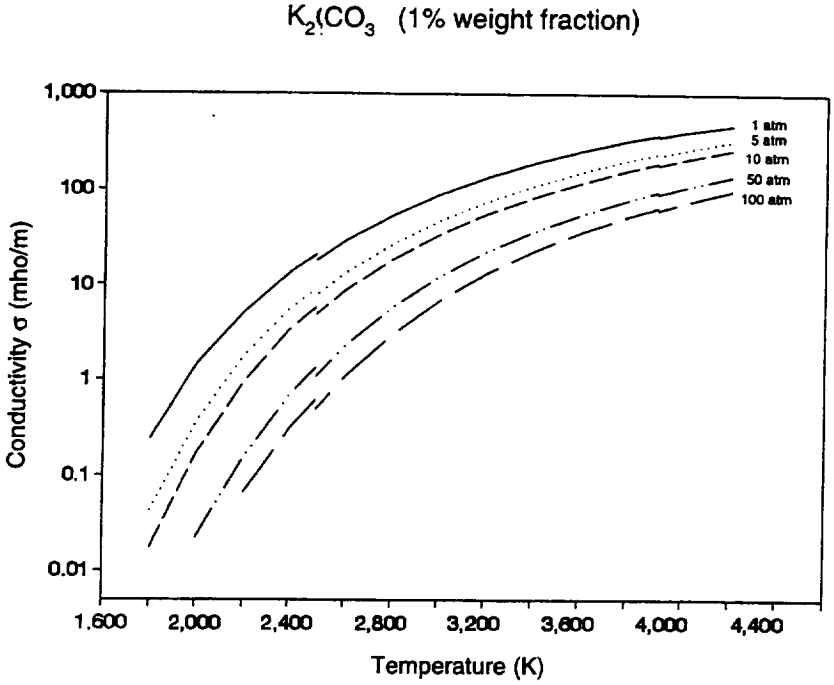

Figure A.1- 24. Electrical conductivity with 1% weight fraction K-seeded air.

The theoretical results discussed above indicate there might be difficulties in achieving adequate ionization levels under high-pressure conditions. Thus, the experiments conducted by UTA and reported in the following sections were proposed to provide information needed for the analysis and design of future high-pressure MHD accelerators. In the following paragraphs, the conductivity channel and other hardware required to perform the experiments are described.

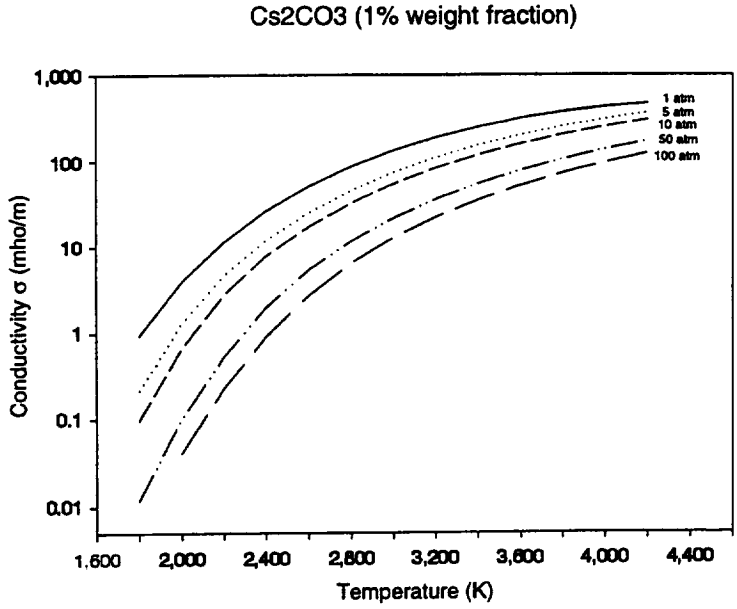

Figure A.1- 25. Electrical conductivity with 1% weight fraction Cs-seeded air.

A.1.4.2 Conductivity Measurement Channel

The plasma electrical conductivity was measured in a channel connected to the end of a 3.05-m (10-ft) driven tube section. The conductivity measurement channel consisted of a pair of powered electrodes and 20 probe electrodes separated by insulators in a design adapted from Garrison (Ref. 37). The major components are displayed in Figure A.1- 26. These electrodes were made of O_2-free copper (Cu) that had an electrical resistivity of 1.69 μΩ-cm at 300 K. The pair of powered electrodes provided an axial electrical field. Their inner and outer diameters were 40.03 mm (1.58 in.) and 140 mm (5.5 in.); respectively, and their thickness was 9.53 mm (0.375 in.).

Between the power electrodes at the ends of the measurement channel, there were 20 probe electrodes for measuring the voltage drop along the channel. The probe electrodes had the same dimensions as the powered electrodes except they were only 3.18 mm (0.125 in.) thick. Insulator rings made originally from Zircar Type RS 100 ceramic fiber reinforced aluminum (Al) composite sheets 1.59 mm (1/16 in.) thick were used to insulate between the copper electrodes. This material was made of 75% alumina (Al_2O_3) and 16% silicon dioxide (SiO_2) with other minor constituents. It had a volume resistivity of 4.6×10^9 Ω-cm and a dielectric strength of 2.8 kV/mm (71 V/mil). The insulator material was subsequently replaced with Teflon™ because of the tendency of the Zircar to absorb moisture from the combustion products passing through the conductivity channel from the detonation chamber exhaust. The Zircar was also porous, which prevented maintaining the desired pressure level.

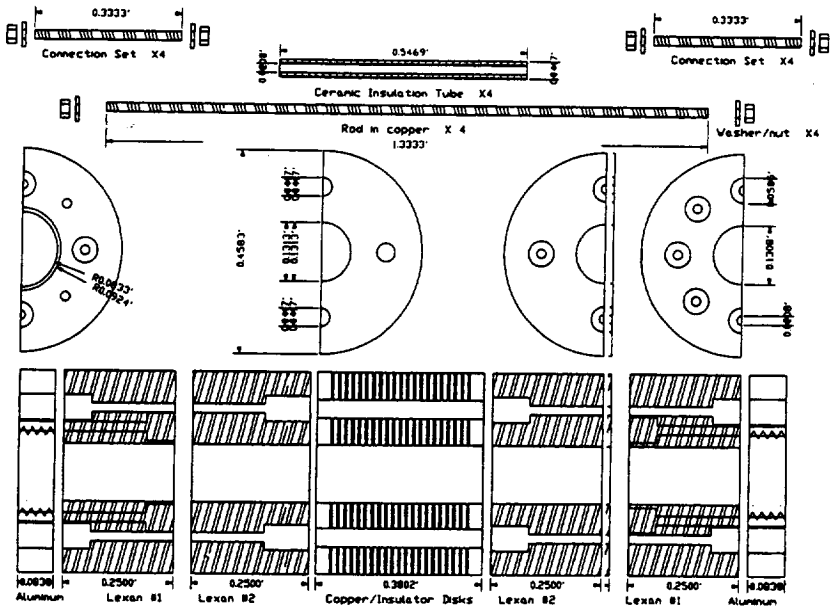

Figure A.1- 26. Conductivity channel.

The total length of the measurement channel including the powered electrodes, the probe electrodes, and the insulators was 115.9 mm (4.56 in.). The channel dimensions were used to size the power supply, which will be discussed in the next section. The electrodes and insulators were assembled together by clamping them with four threaded steel rods. These rods were isolated from the electrodes by sheathing them with ceramic tubing, as shown in Figure A.1- 26. Lexan insulator segments 15.24 cm (6 in.) in length were mounted on both ends of the conductivity channel to prevent shorting of the applied voltage to ground. A 2.61-m (8.57-ft) section of driven tube was also installed downstream of the conductivity channel to prevent shock reflections from the downstream diaphragm returning to the test section prior to termination of the test window.

The initial test run with the conductivity channel installed in the detonation-driven shock tube resulted in two separate incidents that exposed several design deficiencies in the channel. Both incidents were caused by the channel being subjected to higher pressures than were anticipated in the original design. This was caused in part, by the change in mode of operation from the arc-ignition to shock-induced detonation mode of operation. The pressures behind the incident shock remain the same for the two modes, but the channel is subjected to much higher pressures during the blowdown process in the shock-induced detonation mode. The first incident occurred during the first test with the channel in which the shock-induced detonation mode was used. Peak internal pressures on the order of 10.2 MPa (1,500 psia) were generated within the conductivity channel during the blowdown process and resulted in tensile failure of the Teflon insulators. The failure appeared to originate at the holes cut in the insulators for insertion of the axial tie rods. This problem was solved by building a containment structure of Al to

accommodate the internal pressure loads. The portion of the containment covering the conductivity measurement channel is shown schematically in Figure A.1- 27. The conductivity channel was encased in two layers of Teflon™ prior to insertion into the containment structure to prevent shorting of the applied voltage. The containment structure extends beyond the conductivity channel on both upstream and downstream ends to also encase the Lexan insulator rings.

The second problem was more serious in nature because it resulted in the destruction of the conductivity channel. A tension failure of the axial tie rods occurred causing the channel and downstream driven tube section to separate from the upstream driven tube section. The individual copper plates and insulators were damaged beyond repair. It appears that sufficient leakage of high-pressure gas between the insulators and copper plates occurred to load the channel axially to a level sufficient to cause the axial tie rods to fail. Fortunately, enough copper was on hand to fabricate a second channel, and the Lexan segments were not damaged to any extent. Design changes were implemented to increase both tie rod strength and diameter. Also, two steel plates were fabricated for each end of the channel, which were also tied together with high-strength bolts for application of compressive stresses to the channel. Finally, the plates were anchored to the shock tube thrust stand with high-strength chains. A photograph of the final assembly is shown in Figure A.1- 28. These modifications proved to be adequate, and no further mechanical failures were encountered in subsequent tests with the channel.

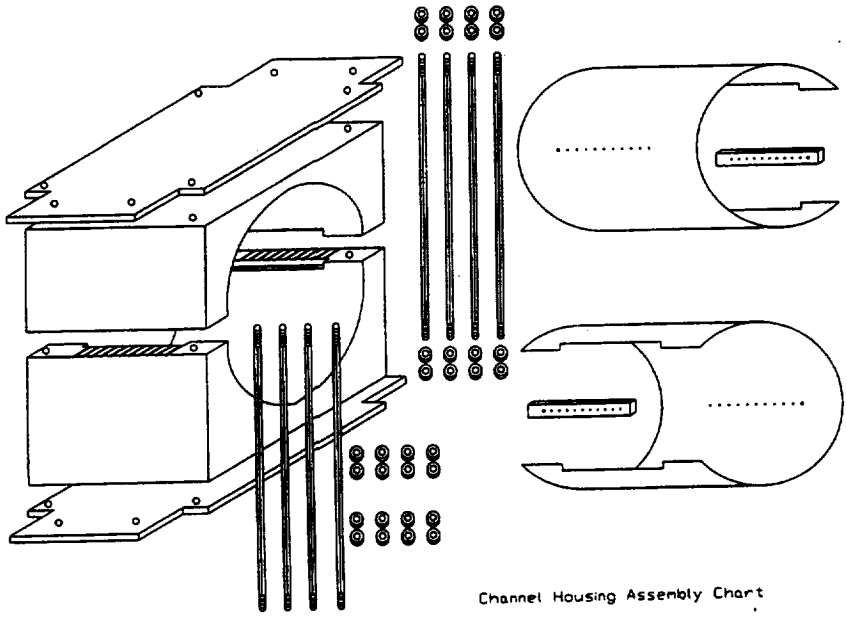

Figure A.1- 27. Pressure containment structure for conductivity channel.

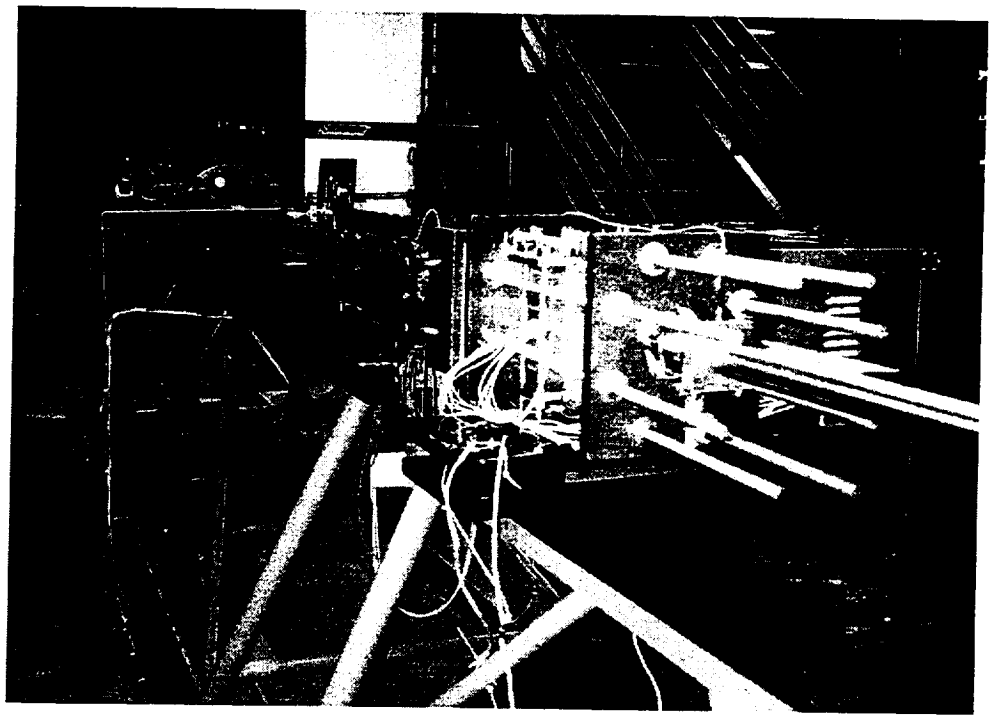

Figure A.1- 28. Photograph of final conductivity channel installation.

A.1.4.3 Conductivity Channel Power Supply

A.1.4.3.1 *Design Considerations*

The design of the electrode power supply required an estimate of the volt-amp curves for the anticipated range of test conditions. Ohm's Law (Ref. 34) gives the electrical field as a linear function of electrical conductivity; that is,

$$E = \frac{I}{\sigma A} \tag{A.1- 3}$$

This equation can be rearranged to yield:

$$V = \frac{IL}{\sigma A} \tag{A.1- 4}$$

where V is the voltage drop along the channel, I is the total input current, L is the length of the measurement channel and A is the effective area of current conduction. For a measurement channel with a 40.0-mm (1.58-in.) bore and a 115.9-mm (4.56-in.) length, the voltage drop is

directly proportional to current for a given electrical conductivity of the plasma. An example of such a calculation for air at 3,000 K, with a 1% Cs-seeding, is displayed in Figure A.1- 29, which shows the current and voltage as a function of gas pressure. From Equation (A.1- 4), given the dimensions of the measurement channel A and L, the theoretical estimates of electrical conductivity at a given pressure and temperature enables the current and voltage characteristics of the channel to be calculated. Thus, the power supply can be sized.

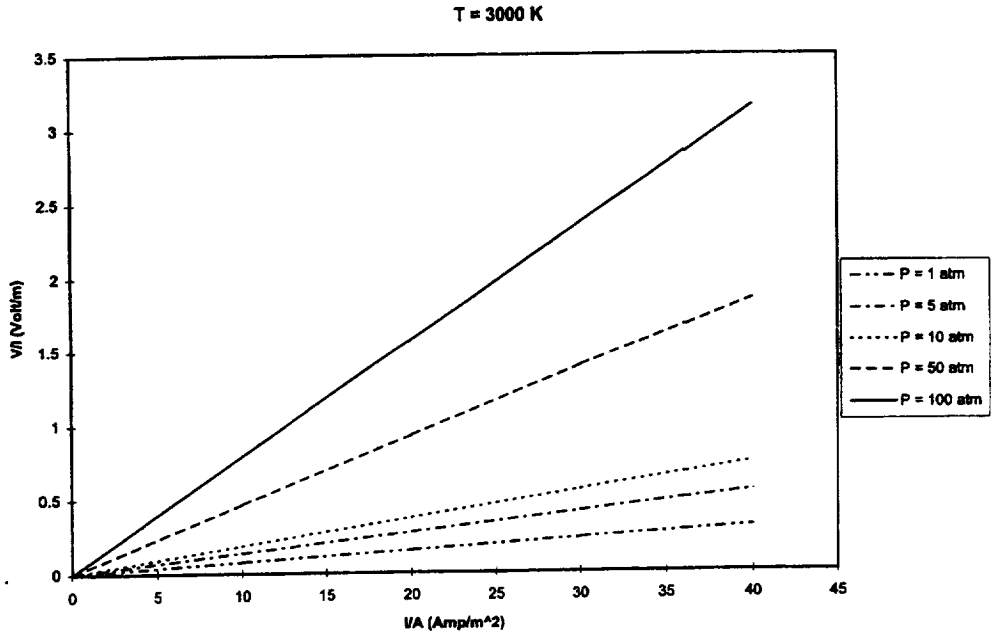

Figure A.1- 29. Electric field vs. current density for air seeded with 1% weight fraction Cs at 3,000 K.

A.1.4.3.2 *Power Supply Design*

The method presented in Adler (Ref. 39) was used to design the power supply. The impedance of the seeded plasma was obtained from the conductivity computations described in the previous section. This provides the load impedance for the power supply design. To cover a wide range of impedances arising from the design pressure and temperature ranges, a variable capacitance power supply was selected. The power supply capacitances and inductances were calculated from:

$$\frac{t_d}{2} = ZC_t = \frac{L_t}{Z} \qquad \text{(A.1- 5)}$$

where t_d is the desired discharge time (which was set to a maximum of 1 ms for the anticipated tunnel operation) Z is the load impedance, C_t the total power supply capacitance, and L_t the total power supply inductance. For a 1 ms discharge time, a network of 5 capacitors and inductors was chosen, each being ⅕ of the value calculated in Equation (A.1-5). Table A.1- 1 (taken from Ref. 40) lists several operating parameters for the design of the power supply. The load voltages shown are for a current of 100 A. Lower current levels would require lower voltage levels. The voltages shown in the last column are those required by the conductivity channel. The table illustrates the capacitor bank must be variable and that the capacitance varies inversely with the voltage. The relationship between capacitance and voltage is beneficial because it allows off-the-shelf capacitors to be connected in series or parallel combinations to obtain the correct configuration. The capacitors used were 440 V with capacitance values of 40, 50 and 55 μ F and are assembled in different combinations to obtain the design capacitances for the five assemblies. The capacitors were connected in series to provide the higher voltage and lower capacitance assemblies, as well as in parallel to provide the lower voltage and higher capacitance assemblies. The inductors were formed by wrapping copper wire around a cylindrical iron core. The inductance was calculated by:

$$L = N^2 A \mu / l \qquad \text{(A.1- 6)}$$

The inductance calculation assumes the magnetic field lines are contained in the core. A cylindrical core does not completely contain the magnetic field lines over their entire length; therefore, the value of the permeability (μ) must be corrected to account for this. The terms in the equation are the length of the core (l) in m, the cross sectional area of the core (A) in m^2, and the number of turns (N). The inductance calculated is in Henrys (H). The equation is used to construct an inductor, near the desired value, that is then modified using an inductance meter to obtain the desired value.

Table A.1- 1. Power supply design parameters.

T, K	p, atm	σ, mho/m	z, Ω	C_t, μF	L_t, mH	V, V
4,000	1	423	.218	2,300	.109	22
4,000	100	95.3	.966	517	.483	97
3,000	1	132	.698	716	.349	70
3,000	100	12.7	7.25	69.0	3.63	725
2,500	1	37.6	2.45	204	1.22	245
2,500	100	1.62	56.8	8.80	28.4	5,680
2,500	25	6.23	14.8	33.8	7.40	1,480
2,500	50	3.36	27.4	18.2	13.7	2,750
2,500	75	2.22	41.5	12.0	20.8	4,150

The power supply, which is a capacitor bank with inductors arranged in a pulse-forming network is shown in Figure A.1- 30. The capacitor bank was designed for a maximum charge voltage of 8 kV. The inductors reduce both the rate of discharge of the capacitors to the time required and the amount of overshoot of the current from the steady state value. The current will tend to

oscillate at the end of the discharge time; therefore, a diode is connected across the output leads to eliminate this and reduce the voltage seen by the capacitors, resulting in increased capacitor life. The capacitor bank open circuit voltage was applied to the conductivity channel prior to firing the shock tube, and the seeded air plasma following the incident shock wave served as the switch to initiate current flow.

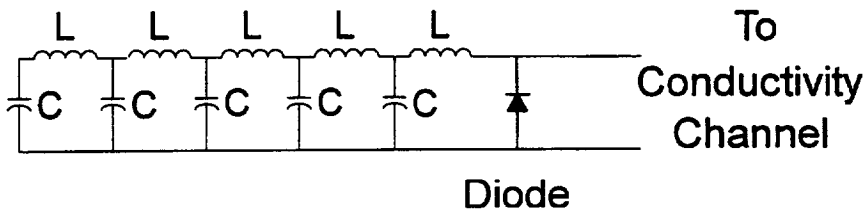

Figure A.1- 30. Capacitor bank.

The capacitor bank was charged between shock tube firings. A charging unit (Figure A.1- 31) was designed to charge capacitor assemblies up to 2.5 kV. For voltages above this, the capacitors were separated by switches to allow them to be charged as assemblies and then reconnected in the proper configuration for operation. This allowed the charging unit to be smaller, less expensive, and constructed with off-the-shelf components.

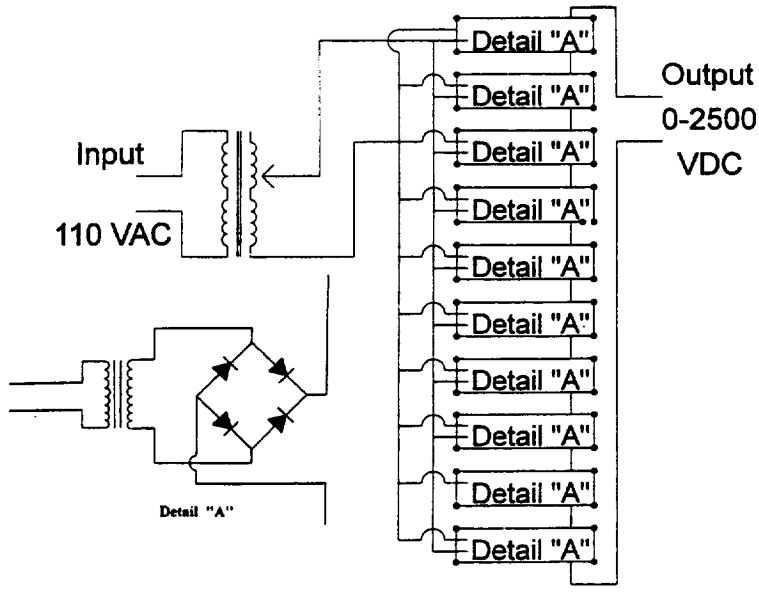

Figure A.1- 31. Charging circuit.

A.1.4.4 Instrumentation

The basic instrumentation and data acquisition systems for the detonation-driven shock tube were described in Section A.1.2.5.5. For the conductivity test, two of the driven tube pressure transducers were installed upstream of the conductivity channel, and one was located downstream of the channel (see Figure A.1- 16 for location of the transducers). Also two Medtherm Type S Model TCS-031-S thermocouples with a full-scale range of 1,000 °C and a response time of 1 μs were located just upstream and downstream of the conductivity channel for measuring the surface temperature. A voltage divider circuit was used to measure the voltage drop across each electrode pair (Figure A.1- 32). Current flow was measured using a F. W. Bell IHA-150 high frequency current sensor that measured the magnetic field generated by the electrical current in the wire. This sensor is electrically isolated from the circuit, which eliminates the error caused by the inductance of other current measurement devices such as a current shunt. The sensor has a response time of less than 1 μs, a frequency response from DC to 50 kHz, and a full-scale range ±150 amperes with a full-scale output of ±5 VDC. Linearity is ±1% over the compensated temperature range of 0 °C to 75 °C with an excitation voltage of ±12 VDC.

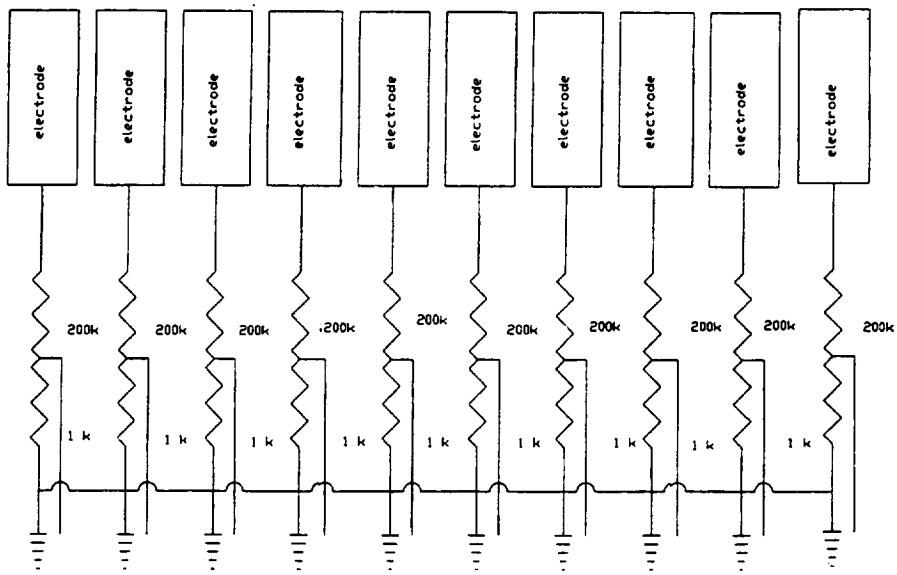

Figure A.1- 32. Voltage divider circuit.

All the sensors were connected to the DSP Technology DAS, which contained eight channels capable of simultaneous 1 MHz per channel sampling rates with 12-bit accuracy, as well as 48 channels with a sampling rate of 100 kHz per channel. The DAS was connected to a 486-DX 33 MHz IBM-compatible PC via a GPIB-488 bus for data retrieval, storage, and manipulation.

A.1.5 Seeding System

A.1.5.1 Seed Injection System

The focus of the UTA research program was to investigate the electrical properties of seeded, high-pressure plasmas. Thus, it was necessary to develop a method for injecting seed material uniformly throughout the driven tube prior to initiating the flow through the shock tube. The seed injection apparatus, shown schematically in Figure A.1- 33, was designed to inject either K_2CO_3 or Cs_2CO_3 in dry powder form into the driven tube upstream of the electrical conductivity channel (Figure A.1- 16). Nominal seed fractions were to be on the order of 1% by weight. An Acculab V-1mg model scale, with a resolution of 10^{-3} grams (g) and maximum capacity of 120 g, was used to measure the desired amount of seed material.

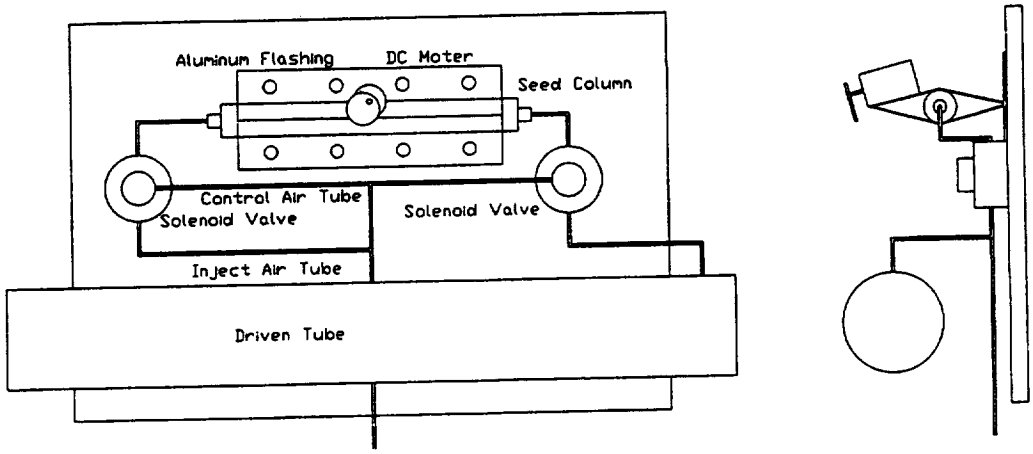

Figure A.1- 33. Seed injection system.

A chromatography column 8.628-cm (3.937-inch) in length and a 1.111-cm (0.4375-inch) inside diameter was used to hold the seed. The pressure rating of the column is 4,135 kPa (600 psi), and it is sealed by two endpieces to O-rings. PTFE cone-type connectors were used to connect PTFE tubing to the column. The PTFE tube has a 0.1588-cm inside diameter (ID) (0.0625-inch) and 0.3175-cm outside diameter (0.125-inch) OD, and it is rated for 3,466 kPa (500 psi).

Two solenoid valves were used to control the inlet and outlet air through the seed injector column. The maximum control air pressure was set at 276 kPa (40 psi) and 24 V AC electrical power was used to activate these valves. During the seed injection operation, the outlet valve was opened first to let the seed be drawn into the driven tube due to the vacuum conditions within the tube. The inlet valve was then opened for few seconds to provide 276 kPa (40 psi) air to force the seed material into the driven tube. Preliminary bench tests of the system indicated that an inlet valve opening of about 10 s was sufficient to inject the required amount of seed

material into the driven tube. The pressure in the driven tube during the injection procedure was raised by less than 6.89 kPa (1 psi).

The entire seed injection system was mounted on a panel that could be vibrated to prevent coagulation of the seed. The vibration mount consisted of two aluminum plates. One end of the two plates was mounted to the wall of the injector system, and the other end of the plates was clamped together. The seed column was placed between the aluminum plates. A 9-V DC motor was set on the upper side of the plate with an off-center rubber wheel attached to the shaft. When a 9-V battery activated the motor, the off-center wheel induced a vibration in the plates that helped keep the seed from settling in the bottom of the chromatography column.

The seed was injected into the driven tube through a nozzle assembly designed to inject the seed parallel to the axis of the tube in both upstream and downstream directions in order to spread the seed material uniformly throughout the driven tube. The nozzle assembly was inserted into the tube from a cavity in the side of the driven tube by the applied air pressure. Once the pressure was removed a spring retracted the nozzle assembly into the cavity to remove it from the flow path during operation.

Bench testing of the system showed that higher inlet air pressure or longer injection times resulted in a more uniform distribution of the seed material in the driven tube. However, the need to control the initial pressure in the driven tube to achieve the desired test conditions placed a limit on both inlet air pressure and seed injection time.

A.1.5.2 Seed Material

The seed system was designed for use with either potassium carbonate (K_2CO_3) or cesium carbonate (Cs_2CO_3) in dry powder form. Lots of each were obtained with a 99.9% purity level and a particle size equivalent to #20 mesh. Each was stored in glass bottles with a desiccant to prevent moisture absorption by the seed. Potassium carbonate was the only seed material used during the MARIAH Project test program.

A.1.6 Conductivity Test Program

A.1.6.1 Test Objectives

The objectives of the conductivity tests were to conduct an experimental investigation of the effect of applied electric field, static temperature, static pressure, and seed fraction on the electrical conductivity of a seeded air plasma.

During the course of the project, MSE also requested that experiments with seeded N_2 be conducted to complement the seeded air experiments. The purpose of these experiments was to examine the effect of electron attachment to O_2 ions. Also a test was suggested in which UTA would attempt to match the fluid density and electron mole fraction in the UTA facility to one of the NASA Ames test points that used unseeded air. The resulting test plan is shown in Table A.1- 2.

Table A.1- 2. Proposed test matrix.

TEST RUN SERIES	P_2 (atm)	T_2 (K)	SEED	V_2 (v)	COMMENTS
1	9.5-11	3,000	1%	400 600 800	Test to define *V-I* curve
2	9.5-11	3,000	2%	600	Effect of increased seed fraction
3	9.5-11	2,500 2,500	1%	600	Effect of temperature on conductivity
4	TBD	TBD	TBD	600	Test to match NASA Ames electron mole fraction
5	9.5-11	3,000 2,500 2,500	1%	600	N_2 test series
6	20-25	3,000	1%	400 600 800	*V-I* curve at increased pressure
7	20-25	3,500 2,500	1%	800	Effect of temperature on conductivity at elevated pressure
8	20-25	3,000	2%	800	Effect of increased seed fraction
9	9.5-11	3,000	1%	1,000 1,200 1,400	Effect of Joule heating on conductivity

A.1.6.2 Test Procedure

The detailed test procedure used during the conductivity test program is described in the following steps:

- Determine target conditions for the specific test; p_1, T_1, p_{100}, p_4, driver gas (air or He), seed percent, and applied voltage.

- Install the diaphragms.
- Pull a vacuum on the detonation driver tube.
- Fill the seed injection cartridge with the desired amount of seed material.
- Set the capacitor bank for the desired applied voltage.
- Fill the detonation driver with the correct mixture of H_2 and O_2.
- Activate the seed system vibrator.
- Charge the upstream driver and the double diaphragm section with air or He to the desired pressure level.
- Pull a vacuum on the driven tube and inject the correct amount of seed material into the driven tube. Continue to fill the driven tube to the desired p_1 level by pumping air through the seeding system (Note: this procedure was revised during the test program to inject seed plus air through the seed system to fill the driven tube to a pressure of 1 atm, and then use the vacuum pump to evacuate the driven tube to the desired p_1 level).
- Close the valve to the Baratron transducer to prevent damage from the high-pressure detonation wave and activate the DAS.
- Fire the shock tube by opening the vent valve in the double diaphragm section.

A.1.6.3 Data Analysis

Eight high-speed data acquisition channels (1 MHz sampling rate) were used to sample the current and voltages from seven probe electrodes. All of the voltage measurements, as well as data from the eight pressure transducers, were captured by the slower 100 kHz data acquisition channels. Data were taken during the entire duration of the test firing, but the test window of interest begins when the incident shock enters the conductivity channel. The incident shock Mach number is determined from the time of flight measurements using pressure versus time traces from two pressure transducers located upstream of the conductivity channel,

$$u_s = \frac{\Delta x}{\Delta t} \qquad \text{(A.1- 7)}$$

where Δx is the distance between the transducers and Δt is the time interval between shock arrival at the two transducer locations. The current and voltage data were stored in a matrix as functions of time. The voltage data were then cross-plotted at discrete times to generate voltage versus distance plots. The plots of voltage versus distance were used to calculate the average electric field in the conductivity channel. This calculation was based on the voltage and separation distance between electrodes 1 and 20. The voltage drop between the powered electrodes and the adjacent probe electrodes was considered to be due to a combination of boundary layer and two-

dimensional (2-D) end effects. The average conductivity was then calculated as a function of time from the Ohm's Law relation

$$\sigma^* = \frac{j}{E} = \frac{I / A}{\Delta V_C / L} \tag{A.1- 8}$$

A.1.6.3 Uncertainty Analysis

The uncertainty analysis was based on the method of Kline and McClintock (Ref. 41). Given a function R of the independent variables $x_1, x_2 \ldots x_n$,

$$R = R(x_1, x_2, \ldots, x_n), \tag{A.1- 9}$$

let ω_R be the uncertainty in the function R, and $\omega_1, \omega_2, \ldots, \omega_n$ be the individual uncertainties in the independent variables. Then the uncertainty ω_R is given by

$$\omega_R = \left[\left(\frac{\partial R}{\partial x_1} \omega_1 \right)^2 + \left(\frac{\partial R}{\partial x_2} \omega_2 \right)^2 + \ldots + \left(\frac{\partial R}{\partial x_n} \omega_n \right)^2 \right]^{1/2} \tag{A.1- 10}$$

The uncertainty analysis was applied to the pressures p_1 and p_2, temperatures T_1 and T_2, shock speed u_S, initial driven tube air mass m_1, seed mass m_S, seed mass fraction S, current I, voltage V and average conductivity σ^*. The zero order uncertainties for each primary measurement were estimated from manufacturer's specifications for the transducers and sensors using the root-mean-squares method (Ref. 41). The error propagation was then estimated for the data processing operations using Eq. (A.1- 10). The resulting uncertainties are

- Pressure, p_1: ±16.1%
- Temperature, T_1: ±1.0%
- Shock speed, u_S: ±1.4%
- Pressure, p_2: ±5.4%
- Temperature, T_2: ±5.5%
- Seed mass, m_S: ±1.3%
- Seed mass fraction, S: ±1.3%
- Current, I: ±1.0%
- Voltage, V: ±1.0%
- Average conductivity, σ^* ±4.6%

The high uncertainty in initial pressure p_1 is due to the inability to accurately measure the initial pressure due to the necessity of isolating the Baratron pressure transducer prior to firing the tunnel to prevent damage resulting from over pressurization. Normally this would not be a problem; however, there were small leaks in the conductivity channel that allowed the pressure to rise an unknown amount between isolation of the transducer and rupture of the diaphragm to initiate the flow. This did not affect the accuracy of the shock speed measurements but did have an adverse effect on the ability to precisely set the pressure ratio to achieve a desired shock speed. The uncertainty in average conductivity is principally due to the uncertainty in separating the precise break point on the voltage gradient plots between the electrode regions and the "uniform core" region. The uncertainty in seed fraction is based on the assumptions of uniform entrainment of seed in the air with no setting, and the seed fraction remains constant during evacuation of the driven tube.

A.1.7 Conductivity Test Results

A run log is presented in Table A.1- 3 (Section A.1.11) together with the data plots from the individual tests. The actual test program followed the proposed test plan presented in Table A.1-2 except for the first series of tests that were made with much lower seed rates than planned due to an error in calculation of the required seed material.

Results from a typical conductivity test run (Run 26A June) are illustrated in Figures A.1- 34 through A.1- 42. The conditions for this test are a shock Mach number of 7.76, T_2 of 3,010 K, p_2 of 8.5 atm, applied voltage of 417 V, and seed rate of 1% by weight. The pressure traces from the three pressure transducers located in the driven tube are shown in Figure A.1- 34. The traces from the first two transducers were used to determine the shock speed from Equation A.1-7.

The pressure p_2 and temperature T_2 following the incident shock were calculated as a function of the initial pressure and temperature in the driven tube and the calculated shock speed. Prior experience obtained during the detonation-driven shock tube calibration had indicated the measured and calculated values for p_2 were usually in close agreement. Unfortunately, the seals between the electrodes and insulators tended to leak, particularly at low p_1 levels. Since it was necessary to isolate the Baratron transducer prior to firing the tunnel, a precise repeatable p_1 level could not be set. Thus, for these test series, the measured value for p_2, together with the measured shock speed was used to calculate the p_1 levels using the TEP™ code (Ref. 26), as shown in Table A.1- 3. Since the initial temperature T_1 was accurately known, the final temperature T_2 was calculated from the shock speed as described above. This procedure resulted in an accurate determination of test conditions for each run but precluded being able to closely match the desired test conditions due to the sensitivity of shock speed to initial pressure ratio.

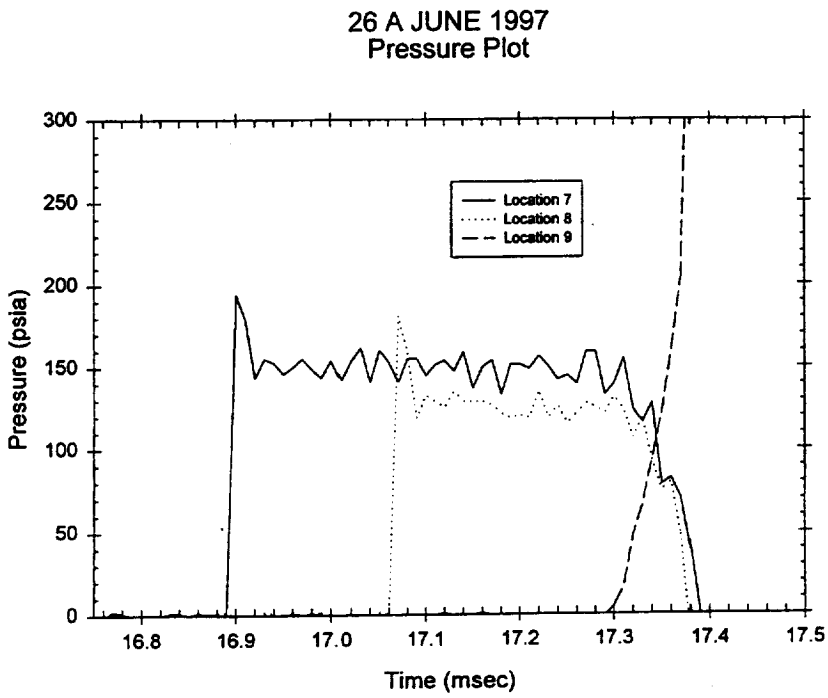

Figure A.1- 34. Driven tube pressure vs. time.

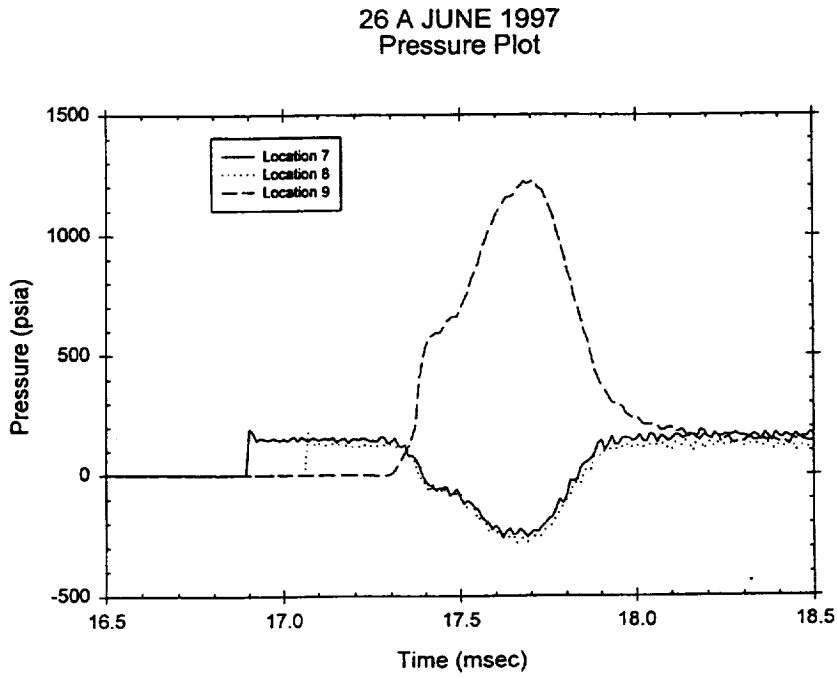

Figure A.1- 35. Extended plot of pressure vs. time showing current-induced interference.

The unusual behavior observed at t≈17.3 ms is thought to be the result of interference induced in the piezoresistive pressure transducers from the current flow in the channel. This phenomenon was not observed at low currents. An expanded time plot of the pressures is shown in Figure A.1- 35. The abrupt change in pressure transducer output at t≈17.3 ms coincides with the initiation of current flow in the channel, and the return to a steady pressure level at t≈18.1 ms approximately coincides with the decay of the current to near zero.

Figure A.1- 36 shows the voltage vs. time traces. The top curve is the total applied voltage across the powered electrodes. The probe electrodes do not sense any voltage until passage of the incident shock. Their voltage levels quickly reach a maximum value in about 20 μs and then drop as the initiation of current flow from the capacitor bank causes a drop in the power supply output voltage. The voltages then rise to a second peak as the applied voltage from the capacitor bank increases.

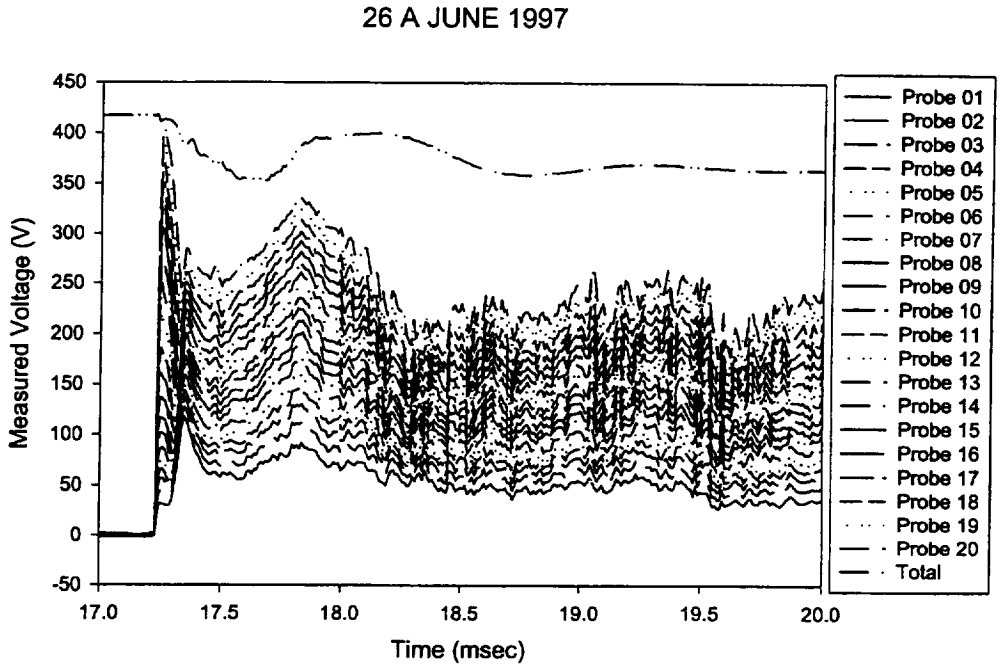

Figure A.1- 36. Voltage vs. time.

An examination of the current vs. time trace (Fig. A.1- 37) shows that the peak current occurs at about 17.6 ms, which coincides with the minimum applied voltage. The rate of current rise is slower than the designed rate and was initially thought to be due to an impedance mismatch between the power supply and the plasma load. However, a simulation of the transient

characteristics of the power supply conducted by G. A. Simmons of MSE[1] indicated that the current rise time should be on the order of 10 - 20 μs. The estimated rise times calculated during the design of the power supply were approximately 80 - 100 μs. Simmons' analysis suggested a more probable cause of the slow rise time is an actual variation in plasma resistance with time. One possible reason for the plasma resistance variation with time could be the finite times required for vaporization, dissociation, and ionization of the K_2CO_3 seed material. A second possibility could be non-uniform distribution of seed material in the driven tube. Note the current does not drop to zero, and the voltage distribution over the probe electrodes stabilizes to a near constant level. This period is undoubtedly associated with the passage through the conductivity channel of the detonation tube combustion products that have a small but measurable conductivity.

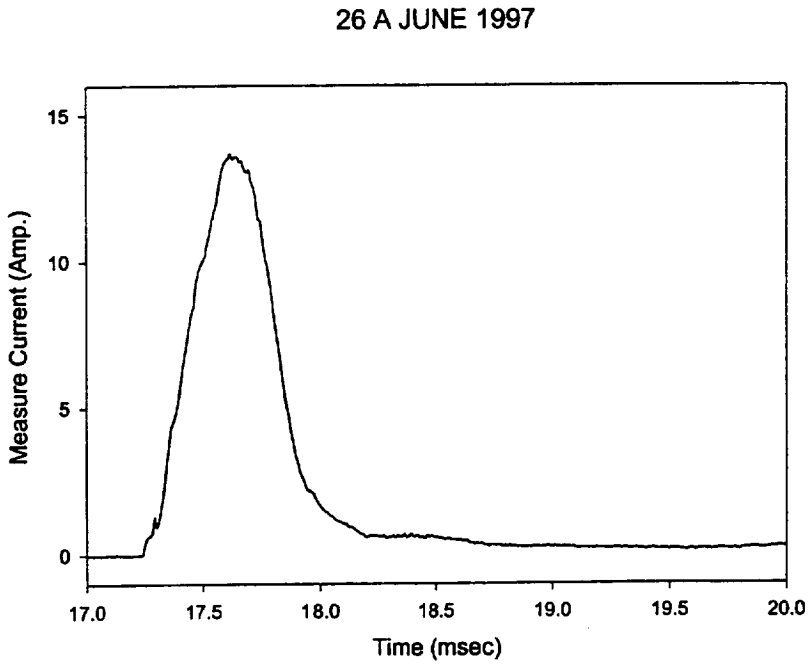

Figure A.1- 37. Current vs. time.

The actual test window of interest is the time period between passage of the incident shock and the trailing contact surface through the conductivity channel. Thus, the voltage and current traces are shown on an expanded time scale covering a period of 1,500 μs in Figures A.1- 38 and A.1- 39, respectively. The voltage versus time data were then cross-plotted to determine the axial voltage gradients versus distance for the time corresponding to the theoretical passage of the contact surface and the time corresponding to the peak current and results are shown in Figure A.1- 40. These voltage gradient data were used to calculate the axial electric field:

[1] Simmons, G.A., MSE, Inc., Private Communication, July 31, 1997.

$$\vec{E} = -\frac{\Delta V_c}{\Delta x} \qquad \text{(A.1- 11)}$$

The electric field calculation was based on the voltage gradient between probe electrodes 1 and 20 since the higher gradients at the front and rear of the channel (Fig. A.1- 40) correspond to the end effects in the powered electrode regions. These 2-D end effects include surface work functions, voltage drops across the boundary layers, and curvature of current filament lines in the powered electrode region. A plot of the total electrode voltage drop vs. time is shown in Figure A.1- 41. The magnitude of the voltage drop quickly rises to a peak level of 250 V, then drops to a value of about 135 V, as the current rises to its peak value at t≈17.6 ms. This trend is in general agreement with the Nottingham Model, that gives the following relation for the electrode voltage drop (Ref. 42):

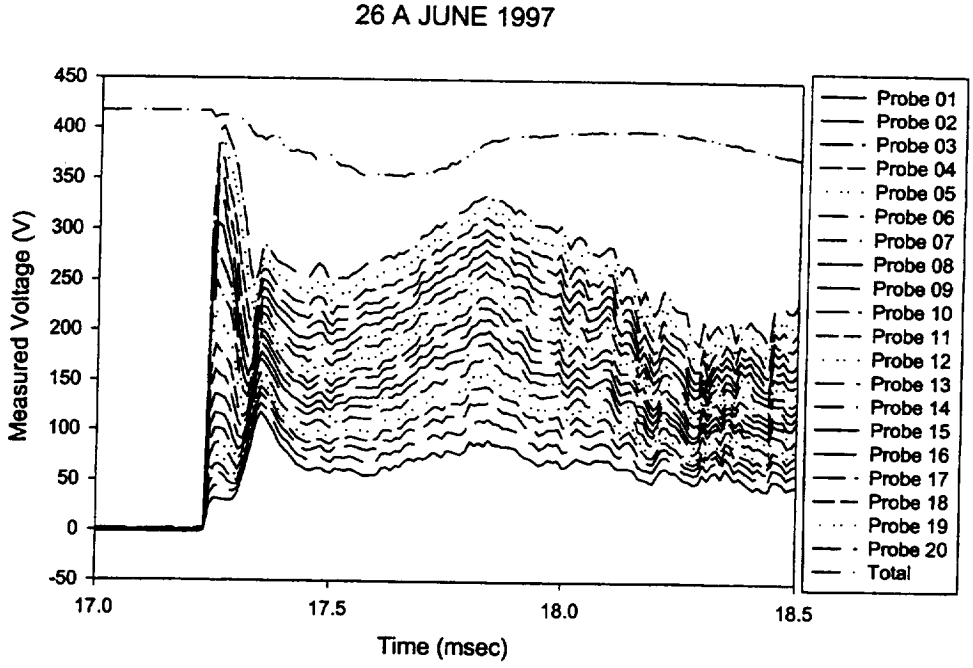

Figure A.1- 38. Expanded plot of voltage vs. time for primary test window.

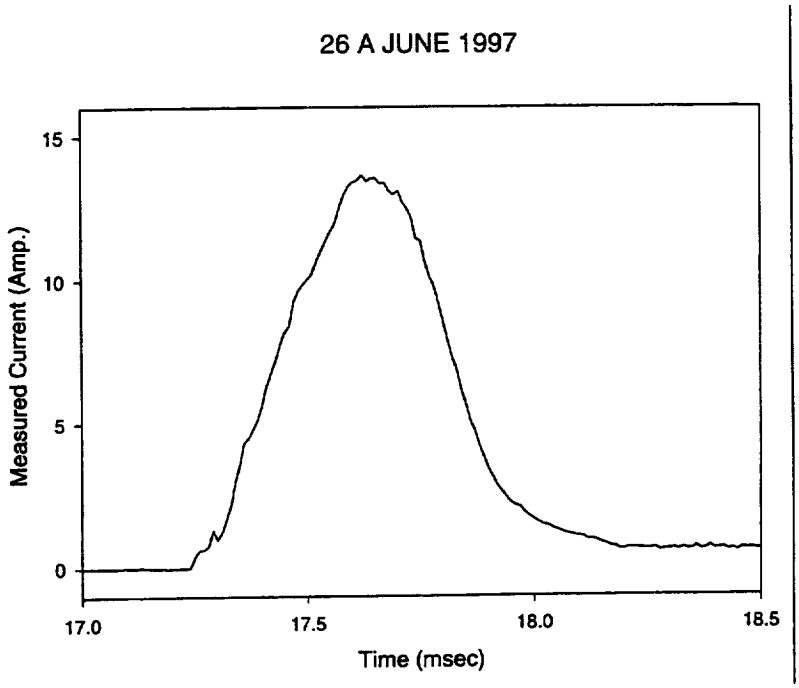

Figure A.1- 39. Expanded plot of current vs. time for primary test window.

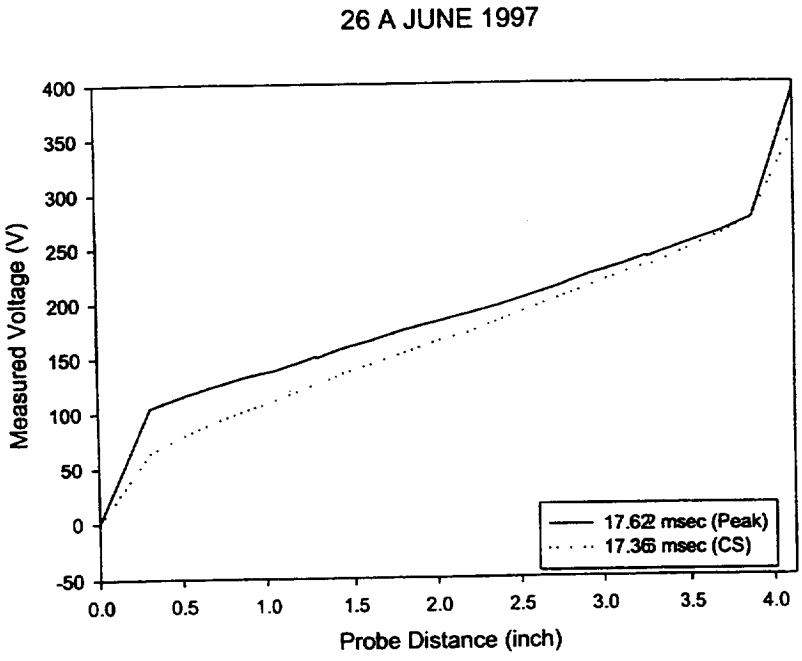

Figure A.1- 40. Voltage vs. distance.

$$\Delta V = C_1 + \frac{C_2}{I^n} \qquad \text{(A.1- 12)}$$

The voltage drop then rises as the current decays to near zero.

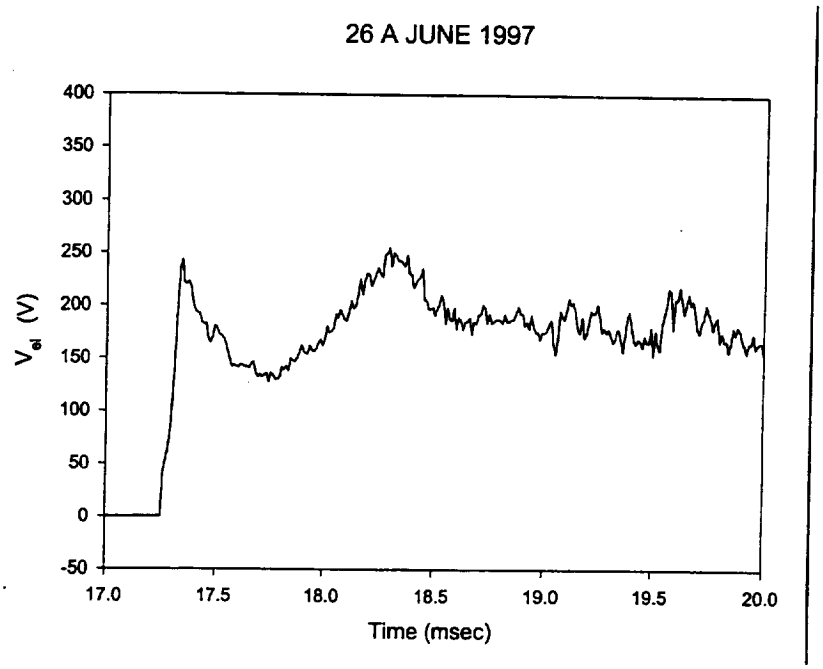

Figure A.1- 41. Electrode voltage drop vs. time.

Finally, the average conductivity was calculated as a function of time from the Ohm's Law relation:

$$\sigma^* = \frac{j}{E} = \frac{I / A}{\Delta V_C / \Delta x} \qquad \text{(A.1- 13)}$$

and is shown in Figure A.1- 42. The conductivity variation appears to closely follow the measured current variation. The estimated duration of the test window (defined as the region between the incident shock and the contact surface), was 185 μs for this run, which means that the peak current occurs approximately 200 μs after the theoretical time of passage of the contact surface through the conductivity channel. This implies that some of the seed must be entrained in the detonation products following the contact surface rather than being entrained in the test gas slug (Region 2 on Fig. A.1- 14). To test this hypothesis, an analysis was conducted to investigate the effect of seed entrainment in the detonation products following the contact surface. This analysis was based on estimating the division of seed material in Region 2 and 3 by integrating the current versus time trace (Fig. A.1- 37) to calculate the charge in each region.

$$q_2 = \int_{t_1}^{t_2} \sigma \, dt \tag{A.1- 14}$$

$$q_3 = \int_{t_2}^{t_3} \sigma \, dt \tag{A.1- 15}$$

where t_1 = time of initiation of current flow from Fig. A.1- 37;
t_2 = estimated time of passage of the contact surface through the conductivity channel;
t_3 = time corresponding to decay of the current to near zero.

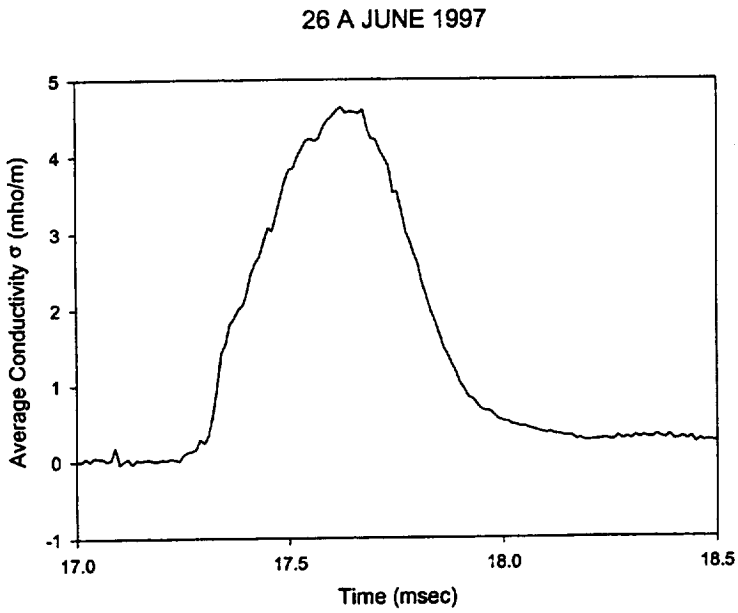

Figure A.1- 42. Average conductivity vs. time.

The seed mass distribution was calculated by assuming:

$$\frac{m_{s_2}}{m_s} \cong \frac{q_2}{q_2 + q_3} \tag{A.1- 16}$$

$$\frac{m_{s_3}}{m_s} \cong \frac{q_3}{q_2 + q_3} \tag{A.1- 17}$$

The seed mass fractions were then calculated from:

$$s_2 = \frac{m_{s_2}}{m_{air}} \tag{A.1- 18}$$

$$s_3 = \frac{m_{s_3}}{m_{dp}} \tag{A.1- 19}$$

where

$$m_{air} = \int_{t_1}^{t_2} \rho_2 u_2 A dt \tag{A.1- 20}$$

$$m_{dp} = \int_{t_2}^{t_3} \rho_3 u_3 A dt \tag{A.1- 21}$$

Note from classical shock tube theory,

$$\rho_2 u_2 = \rho_3 u_3 \tag{A.1- 22}$$

The results were $S_2 = 0.72\%$ and $S_3 = 2.29\%$. Figure A.1- 43 shows the results of theoretical calculations of σ versus T for air + 0.72% seed and detonation products + 2.29% seed. The estimated temperatures for Region 2 and 3 are 3,010 K and 3,330 K; respectively, and the resulting conductivities are 27 mho/m in Region 2 and 16.5 mho/m in Region 3.

The theoretical conductivity calculations suggest the conductivity in Region 3 is less than that in Region 2 but the results are based on the assumptions the seed material is distributed uniformly throughout the length of the driven tube and the seed material vaporizes, dissociates, and ionizes instantaneously as the incident shock passes. Figure A.1- 39 shows the current continually rises after the theoretical passage of the contact surface, suggesting that some of the seed remain in the driven tube after the contact surface passage. The distribution of seed material from t_1 to t_3 will determine the trend of the curves in Figure A.1- 43; the larger the percentage of the seed left behind after the contact surface, the closer together the curves will be. Theoretically, the current in Figure A.1- 39 should be a step function but the electronics introduce a small delay in the current rise and the finite rate of seed vaporization, dissociation, and ionization will result in a gradual increase in the conductivity throughout the test window.

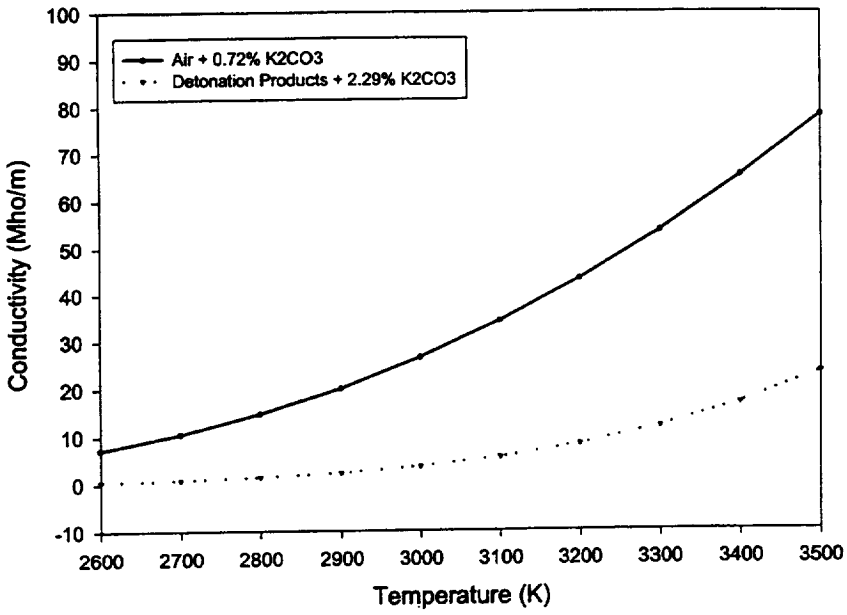

Figure A.1- 43. Conductivity of air and detonation products.

A similar analysis procedure was applied to all of the tests, and conductivity versus time plots are presented in Section A.1.11. A summary of the experimental results is presented in Section A.1.8, and comparisons are made with theoretical predictions. Unfortunately, the test program was terminated prematurely during the high-pressure test series when an electrical breakdown apparently occurred in the channel. A voltage plot from Run 28B June is shown in Figure A.1-44. Note that voltages are observed on a number of the probe electrodes prior to abrupt rise in voltage for all of the probes at a time of 19.05 ms. A careful examination of similar plots for all of the tests prior to this showed, with the sole exception of one test (Run 27F June) in which a slight voltage was observed on several electrodes, the voltage on all of the probe electrodes was zero prior to passage of the incident shock through the channel. An examination of the current trace for this test showed no current prior to 19.05 ms, but it appears that sufficient leakage current was flowing to at least establish a voltage distribution through the channel. One more test (Run 28C June) was conducted. During the setup for the next test (as the voltage was being applied to the channel during the setup procedure) a breakdown occurred at 400 V. Subsequent attempts to reapply voltage resulted in the same breakdown occurrence, and it was decided to terminate the test program until the channel could be disassembled for inspection. As a result, it was not possible to complete all of the planned test runs, particularly the high-pressure tests and the test sequence to match the NASA Ames test conditions.

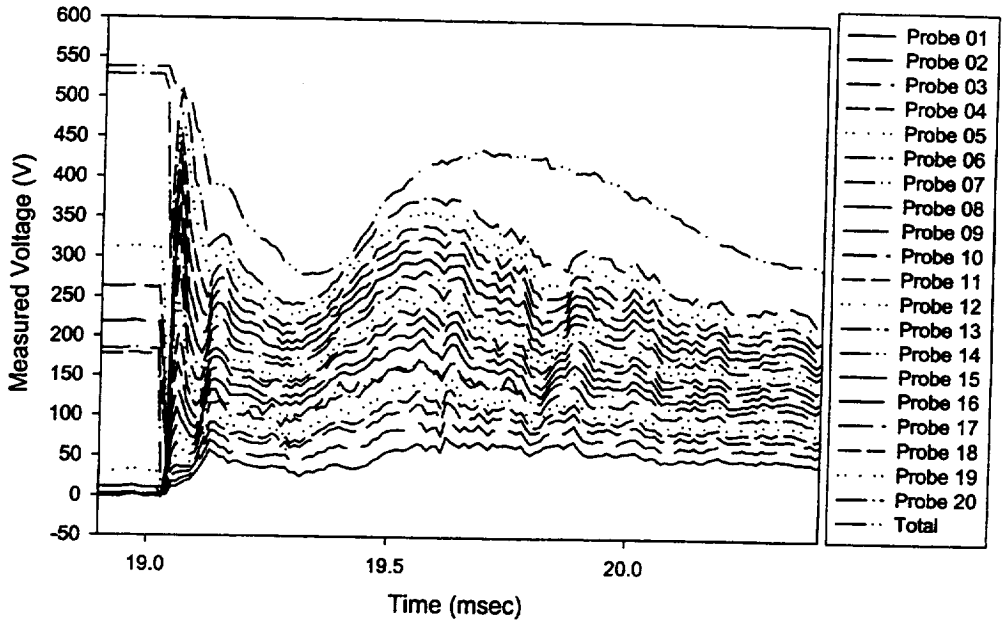

Figure A.1- 44. Voltage vs. time plot for test run with incipient electrical breakdown.

A.1.8 Comparison with Theoretical Models

The calculated values of average conductivity based on the experimental measurements are compared with theoretical calculations of conductivity in Figure A.1- 45 for the nominal 10-atm data. The theoretical values were calculated with the modified version of the NASA CEC Code, using the Demetriades and Argyropoulos conductivity model (Ref. 38). The conductivity values calculated from the experimental measurements both at contact surface passage and at peak current are shown in Figure A.1- 45. In general, the measured conductivities are lower than the theoretical values, with the experimental conductivities ranging from a factor of 2 above theory at low temperatures to a factor of 4 below theory at the highest temperatures using the peak current. The experimental results are uniformly lower than theory using the current measured at the passage of the contact surface. The experimental results ranged from a factor of 5 below at low temperatures to a factor of 13 below the theory at high temperatures.

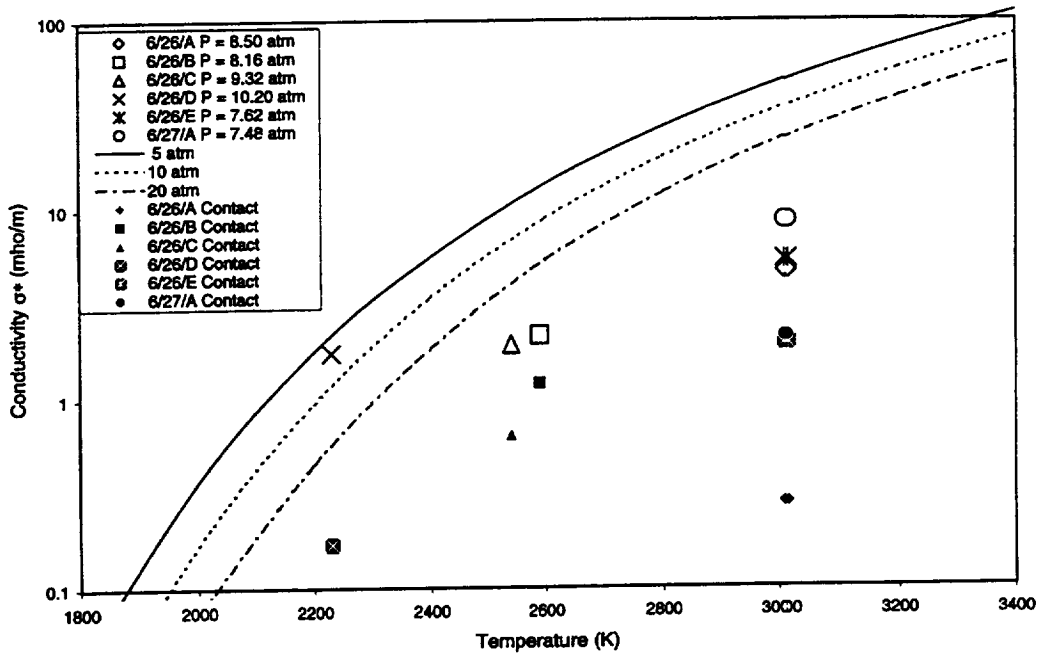

Figure A.1- 45. Comparison of experimental and theoretical conductivity of 1% weight fraction K_2CO_3 seeded air plasma for nominal pressure of 10 atm.

Note the experimental conductivity values have not been corrected for boundary layer blockage effects, although as discussed above, the data were corrected for electrode voltage drops. Applying a boundary layer blockage correction would increase the values of the experimental conductivities. The effective core area for current transport is given by:

$$A_c^* = \left(R - \delta_J^*\right)^2 \tag{A.1- 23}$$

where the oxial electrical current displacement thickness is:

$$\delta_J^* = \int_0^{\delta} \left(1 - \frac{j_x}{j_{xc}}\right) dy \tag{A.1- 24}$$

and the effective core conductivity is:

$$\sigma_c = \frac{IL}{VA_c^*} \tag{A.1- 25}$$

The effect of conductivity depression in the boundary layer is illustrated in Figure A.1- 46, which shows the influence of δ^*_j/R on the ratio of conductivity in the uniform core of the flow to the average conductivity. This curve shows that correcting for the effect of current depression in the boundary layer will improve the agreement. However, at the higher temperatures it is obvious that an unrealistic correction would be required to bring the measured values (Fig. A.1- 45) in line with the theory.

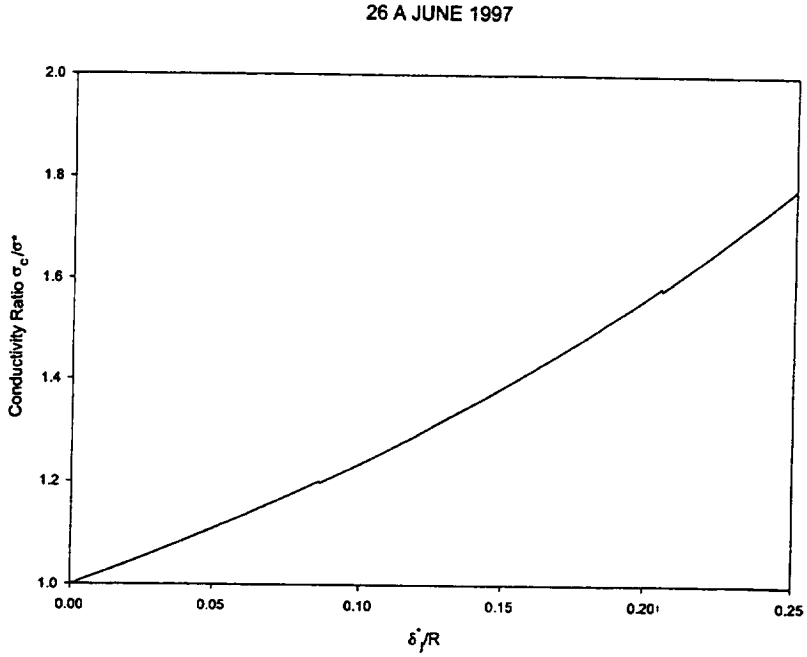

Figure A.1- 46. Variation of σ/σ^* with δ^*_j/R for test conditions of Run 26A June 1997.

A volt-amp curve for the nominal 10-atm data at 1% seed rate is shown in Figure A.1- 47. Curves are shown representing the electrical current trend with increased voltage for both the applied voltage and the effective core voltage. In general, the shapes of the curves are quite similar. Note that the curves would be linear if the electrical conductivity were constant, since:

$$V = \frac{I}{A}\frac{L}{\sigma^*} \qquad \text{(A.1- 26)}$$

All three data points were at the same estimated temperature T_2, thus the break in the curve is consistent with (but not a confirmation of) an increase in conductivity due to Joule heating. This is evaluated further in the following paragraphs.

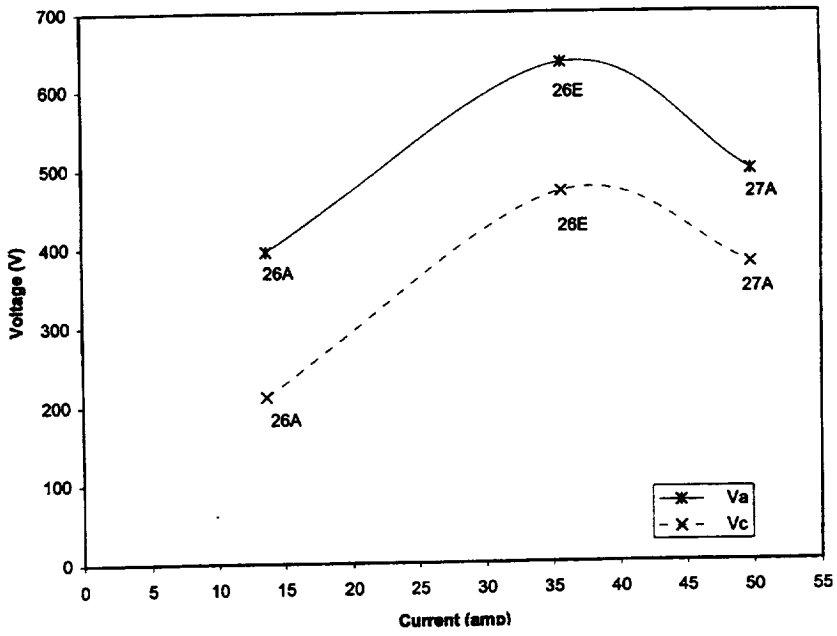

Figure A.1- 47. Volt-Amp curve for 1% K_2CO_3 seed air plasma at nominal pressure of 10 atm.

Two simple models made estimates of the temperature increase due to Joule heating. In the first, the increase in temperature was calculated by performing an energy balance (neglecting heat loss to the walls) on the slug of gas passing through the channel during the period of time for which measurable current flux was observed. From Figure A.1- 39, this period is approximately 185 μs. The energy added to the slug is given by:

$$E = \int I(t)\Delta V_c(t)dt \cong 0.28J \qquad \text{(A.1- 27)}$$

for Run 26A June 1997. Similarly, the mass of the slug passing through the channel during this period is:

$$m = \int \rho_2 u_2 A dt \cong 4.2\times10^{-4}\,\text{kg} \qquad \text{(A.1- 28)}$$

For a relatively small change in temperature, a perfect gas approximation can be used to estimate the temperature increase:

$$\Delta T = \frac{\Delta H}{Cp} = \frac{E/m}{Cp} \cong 0.34K \qquad \text{(A.1- 29)}$$

for this run. A similar calculation for Run 27A June 1997 gives a temperature rise of only 0.58 K. By using the steady flow energy equation (again neglecting heat loss to the walls), a second estimate was made.

$$\int h_t \rho \mathbf{v} \cdot n dA = \dot{W} \tag{A.1-30}$$

For a quasi-1-D perfect gas approximation, this approach gives an increase in total temperature.

$$\Delta T_{t_{max}} = \frac{\dot{W}_{max}}{\dot{m} C_p} \cong 3.21 K \tag{A.1-31}$$

Thus, Joule heating does not appear to be sufficient to explain the break in the *V-I* curve. If we calculate the average conductivity for the test points shown in Figure A.1- 47, values of 4, 5, and 8 mho/m are obtained for test points 26A, 26E and 27A, respectively. The increase in conductivity from 5 to 8 mho/m only requires a temperature change of about 100 K that is within the estimated uncertainty in T_2 (Section A.1.6.3). Thus, the shape of the *V-I* curve is likely to be influenced more by run-to-run variations in T_2 than by Joule heating.

A plot of average conductivity vs. temperature for the nominal 20-atm tests is presented in Figure A.1- 48. The absolute levels of conductivity are considerably higher than the theoretical predictions for this set of data. A much flatter trend with increased temperature is also observed. The measured current levels were much higher for these cases but an analysis of the temperature rise due to Joule heating again showed the conductivity increase should be quite small. Also, the possibility of leakage current due to a breakdown of the insulators cannot be discounted as it was during this sequence of tests in which the electrical breakdown occurred.

Figures A.1- 49 and A.1- 50 present an estimate of the conductivity variation throughout the length of the conductivity measurement channel from the entrance to the exit. A nominal 10-atm condition (Run 26A June) was analyzed in Figure A.1- 49 using the first five electrode probes to determine the inlet conditions and the last five electrode probes to determine the exit conditions. A similar procedure was used on a nominal 20-atm case (Run 28C June) and presented in Figure A.1-50. The low-pressure case (Figure A.1- 49) has no increase in conductivity throughout the length of the measurement channel, suggesting the Joule heating was negligible. For the high-pressure case, (Figure A.1- 50), the exit conductivity measurements were slightly higher than at the entrance. The increase in conductivity was small compared with the overall magnitude of the conductivity, indicating very small amounts of Joule heating.

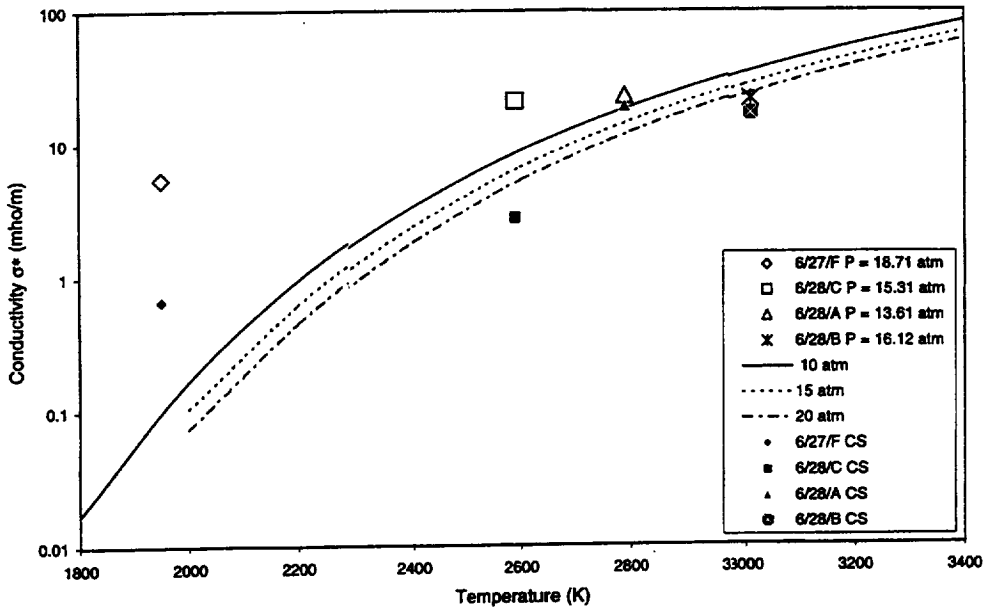

Figure A.1- 48. Comparison of experimental and theoretical conductivity of 1% weight fraction K_2CO_3 seeded air plasma for nominal pressure of 20 atm.

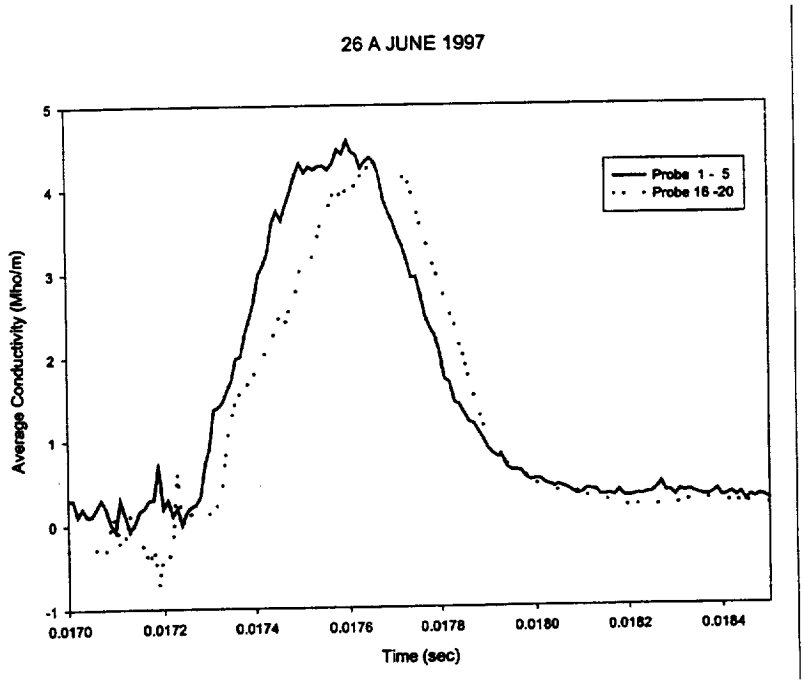

Figure A.1- 49. Conductivity comparison between inlet/outlet measurement channel at low pressure condition (8.5 atm).

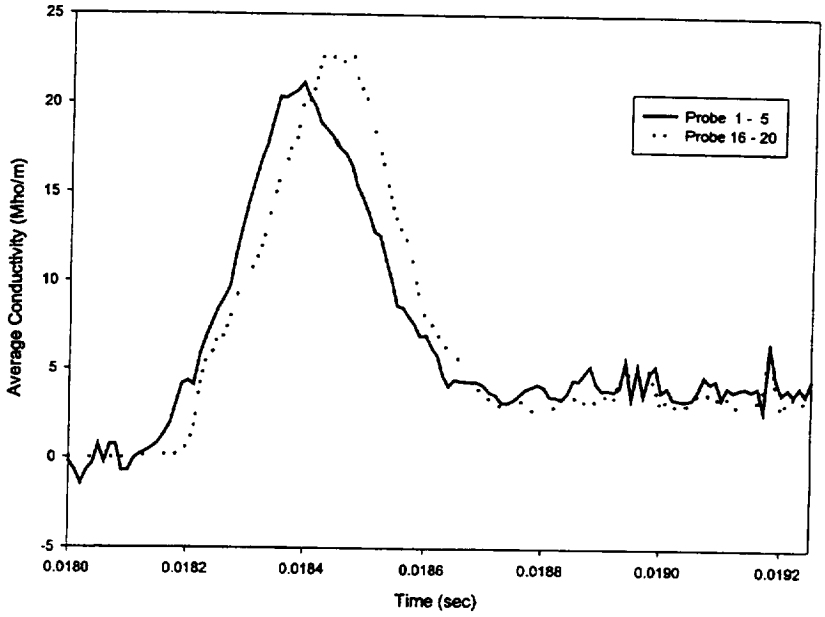

Figure A.1- 50. Conductivity comparison between inlet/outlet measurement channel at high-pressure condition (15.3 atm).

Figure A.1- 51 represents a plot of experimental and theoretical conductivity vs. temperature for a seed rate of 0.046%. The nominal pressure for this data set is 10 atm. A cross plot of conductivity vs. seed percent is shown in Figure A.1- 52. The accuracy in seed mass fraction at the lower levels is somewhat questionable since these values are at the lower limit of the resolution capability of the seed injection system. The trends are certainly realistic with the exception of the 2% seed rate point that would suggest enhancement due to Joule heating since the peak current level for this test was 71.3 amps. Based on the conditions at the time of peak current and of passage of the contact surface, analysis of the high seed rate test (27B June 1997) indicated temperature rises of 24.0 K and 13.4 K, respectively. Thus, the effects of Joule heating should be minimal.

A comparison between experimental and theoretical conductivities for a seeded N_2 plasma is presented in Figure A.1- 53 for a nominal pressure of 10 atm. The experimental conductivities for seeded N_2 are considerably higher than for seeded air whereas the theoretical values for the two plasmas are roughly comparable for the Demetriades and Argyropoulos model. The measured values of conductivity ranged from 85% of theory for the peak current and 75% of theory at the contact surface current at higher temperatures to 3.3 times the theory for the peak current and 2.3 times theory for the contact surface current at low temperatures. Thus, the phenomenon of electron attachment by positive O_2 ions postulated by MSE appears to have some degree of validity.

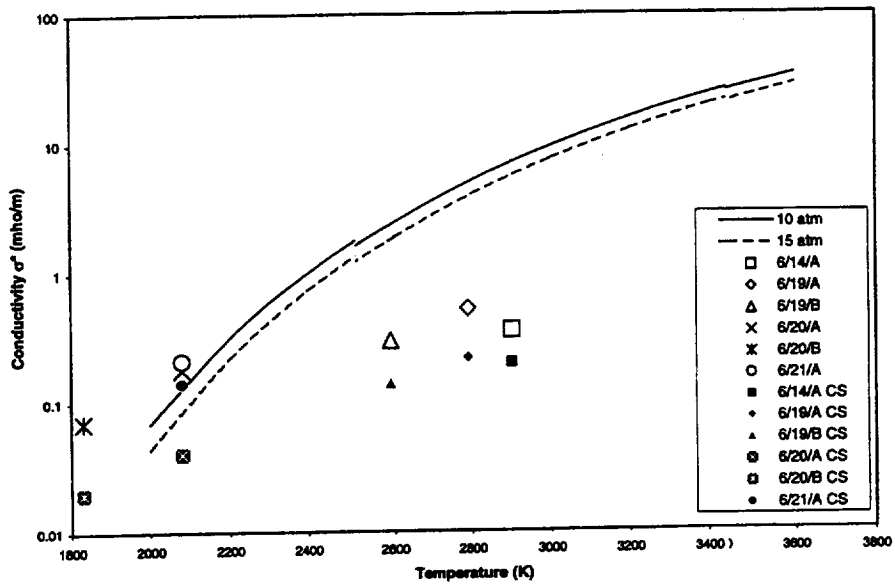

Figure A.1- 51. Comparison of experimental and theoretical conductivity of 0.046% weight fraction K_2CO_3 seeded air plasma for nominal pressure of 10 atm.

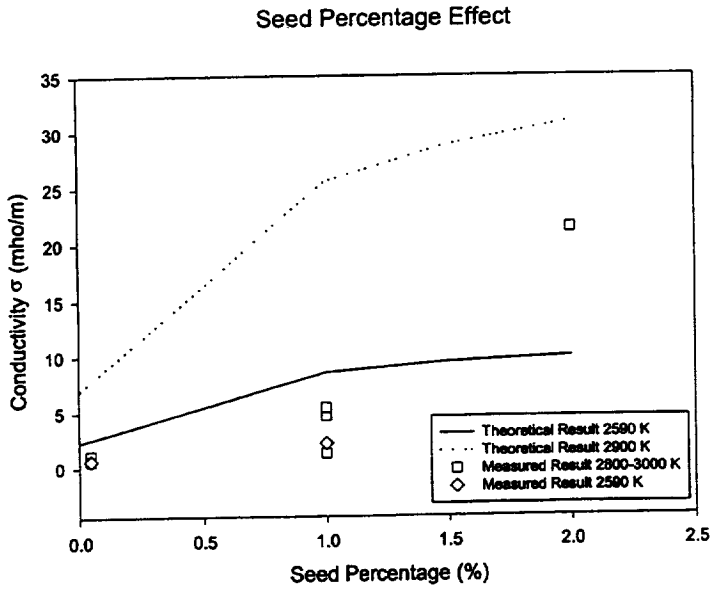

Figure A.1- 52. Effect of seed rate on electrical conductivity.

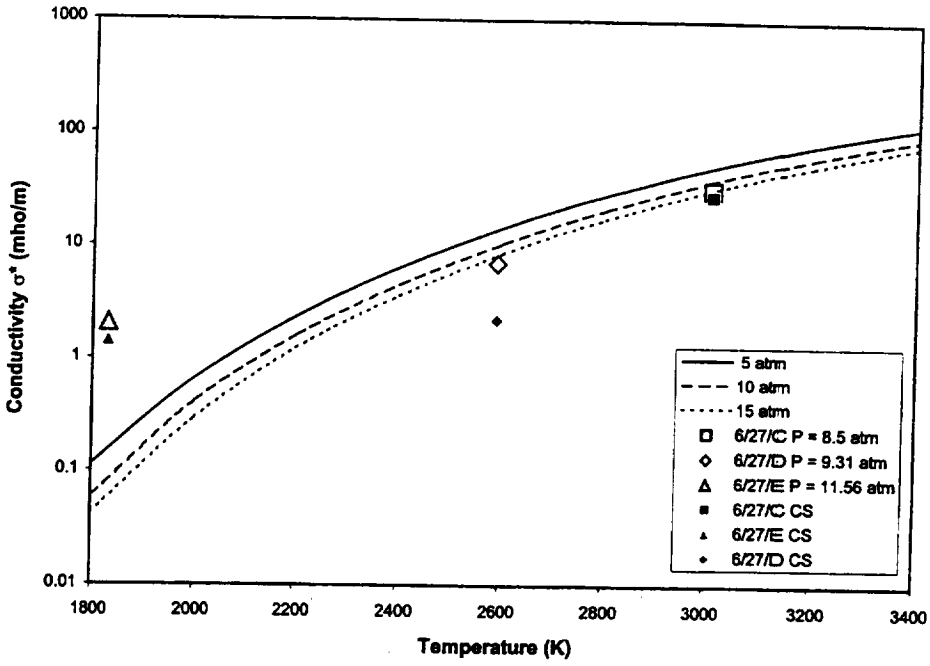

Figure A.1- 53. Comparison of experimental and theoretical conductivity of seeded N_2 plasma (1% K_2CO_3) at a nominal pressure of 10 atm.

A.1.9 Summary

The research program conducted at UTA resulted in the development of a new detonation-driven shock tube facility with increased performance over the existing UTA pressure-driven facility. The performance of the facility with the original arc ignition mode was considerably lower than predictions based on ideal shock and detonation wave models. This reduced performance was shown to be a result of the interaction between the Taylor rarefaction wave and the reflected shock wave for the downstream propagation mode of operation. For the upstream mode, the gradual rise in end-wall pressure resulting from the failure to directly initiate a CJ detonation wave is the most likely cause of the lower performance. Furthermore, in this mode the initial flow behind the incident detonation wave is in the upstream direction, and requires a stronger expansion wave to reverse the direction of flow.

Implementation of the shock-induced detonation mode proposed by Bakos and Erdos of GASL (Refs. 23 and 24) provided a considerable increase in performance. Peak shock Mach numbers of 10.7 have been achieved to date. By proper tailoring of conditions, it is possible to eliminate the trailing Taylor rarefaction wave associated with the arc ignition mode. This concept has far-reaching potential for improving shock tube and shock tunnel performance at reasonable capital investment, and UTA plans to implement it into a reconfiguration of their hypersonic shock tunnel upon completion of this effort.

The basic approach proposed by Garrison (Ref. 37) for measurement of the electrical conductivity of seeded air plasmas was implemented in a shock tube environment. Generally consistent results were obtained but the interpretation of these results was complicated by the observation of current flow after the theoretical estimated time of passage of the contact surface through the conductivity channel. The contact surface should separate the seeded air plasma from the unseeded detonation products but obviously the detonation products must also contain seed in the mixture. The estimated conductivity for unseeded detonation products is too low to explain the continued rise in current after the predicted contact surface passage.

An analysis was conducted to determine the effect of seed entrainment in both the air test gas and the detonation products. This analysis was based on the assumptions of uniform seed distributions in both regions for the duration of observed current flow and instantaneous vaporization, dissociation, and ionization of the seed. The relative seed mass fractions in the two regions were based on an integration of the current versus time for each region to calculate the representative amounts of electric charge. This model helps to explain the continued rise in current following passage of the contact surface; however, the shape of the current vs. time curves suggest that finite rates of vaporization, dissociation, and ionization of the seed are influencing the shape of the curve. Furthermore, the effect of non-uniform seed distribution in the driven tube cannot be ruled out. An analysis was also conducted for estimating the effect of Joule heating on the measurements. In general, the effect of Joule heating was minimal.

The observed variation of conductivity with temperature for the seeded air plasma resulted in a slower rate of increase than the theory would predict. Also, the observed magnitude of conductivity was considerably lower than the theoretical magnitude for the 10-atm data. In contrast, fairly good agreement was achieved for higher pressures.

The results of the conductivity measurements with a seeded N_2 plasma appear to give some support to the theory of electron attachment by the positive O_2 ions in a seeded air plasma. Measured conductivities for the N_2 plasma were on the order of 2 to 3 times larger than comparable measurements for the air plasma whereas the theoretical values calculated from the CEC code using Demetriades and Argyropoulos conductivity model (Ref. 38) produced comparable results for the two plasmas.

Two methods are currently being investigated for estimating the core conductivity from the measured average conductivity values. One uses an existing steady flow MHD channel flow code (Ref. 43) to calculate boundary layer growth as a function of distance from the channel entrance. This length would then be used as a representation of the distance between the incident shock wave and the conductivity channel in the actual transient conductivity channel flow. This representation should give an approximation to the boundary layer blockage effect but it is not a correct physical model. The other approach uses a time-accurate Navier Stokes Code developed as part of the NASA/UTA Center for Hypersonic Research Program (Ref. 44) for analysis of hypersonic equilibrium and nonequilibrium flow fields. This code includes MHD terms and is being modified to incorporate the correct thermodynamic and transport property model to simulate the flow in the conductivity channel. These results will be reported at a later date; however, it is not anticipated these corrections will substantially change the results presented in

this report. The boundary layers should be relatively thin due to the high pressures and the short distance traveled by the incident shock wave. For example in the test run analyzed in Section A.1.1.7, the incident shock should be about 0.8 m downstream of the conductivity channel by the time the current has risen to its peak value. The time-accurate Navier-Stokes Code should answer the question regarding the effect of finite dissociation and ionization rates on the observed current versus time plots.

Further testing is needed to provide more data at the higher-pressure levels. This will require refurbishment of the UTA channel. Also, an extended section of driver tube ahead of the conductivity channel should give longer test duration between the incident shock wave and the contact surface. The current length was selected to minimize shock attenuation due to boundary layer effects but a longer tube length would allow more time for the vaporization, dissociation, and ionization reactions to approach equilibrium.

A.1.10 References

1. *Proceedings of the Magnetohydrodynamics (MHD) Technical Review and Planning Workshop*, NASA, Washington, D.C., Feb. 1995.

2. Wilson, D.R. and Lu, F.K., "Experimental Apparatus and Procedures Development for the Hypersonic Ground Test Facility, Phase 1A (Design Phase)," Final Report for MSE Contract No. 95-C294-F, The University of Texas at Arlington, Dec. 1995.

3. Stuessy, W.S.; Murtugudde, R.G.; Lu, F.K.; and Wilson, D.R., "Development of the UTA Hypersonic Shock Tunnel," AIAA Paper 90-0080, 1990.

4. Lu, F.K., "Initial Operation of the UTA Shock Tunnel," AIAA Paper 92-0331, 1992.

5. Chinitz, W.; Bakos, R.J.; and Erdos, J.I., "Experimental Requirements for the Study of Shock-Induced Premixed Combustion," AIAA Paper 94-3099, 1994.

6. Rittenhouse, L.E.; Piggot, J.C.; Whoric, J.M.; and Wilson, D.R., "Theoretical and Experimental Results with a Linear Magnetohydrodynamic (MHD) Accelerator Operated in the Hall Current Neutralized Mode," AEDC-TR-67-150, 1967.

7. Pate, S.R.; Siler, L.G.; Stallings, D.W.; and Wagner, D.A., "Development of an MHD-Augmented, High Enthalpy, Shock Tunnel Facility," *AIAA Journal,* Vol. 12, No. 3, Mar. 1974, pp. 289-297.

8. "Summary of Capabilities of Hypersonic Shock Tunnels at Calspan ATC," Calspan Advanced Technology Center, Buffalo, NY.

9. "Description of the Aachen Shock Tunnel TH2," Shock Wave Laboratory, Technical University of Aachen, Aachen, Germany, Jan. 1991.

10. Namagatsu, H.; Sheer, R.; Osberg, L.; and Cary, K., "Design Features of the General Electric Research Laboratory Hypersonic Shock Tunnel," GE Research Lab Report No. 61-RL-2711C, May 1961.

11. Eitelburg, G.; McIntyre, T.J.; Beck, W.H.; and Lacey, J., "The High Enthalpy Shock Tunnel at Göttingen," AIAA Paper 92-3942, 1992.

12. Deiwert, G.S.; Cavalowsky, J.A.; and Loomis, M.P., "Large Scale Scramjet Testing in the Ames 16-Inch Shock Tunnel," AIAA Paper 94-2519, 1994.

13. Bakos, R.J. and Erdos, J.I., "Options for Enhancement of the Performance of Shock-Expansion Tubes and Tunnels," AIAA Paper 95-0799, 1995.

14. Stanley, S.B; Stuessy, W.S.; and Wilson, D.R., "Experimental Investigation of Pulse Detonation Wave Phenomena," AIAA Paper 95-2197, 1995.

15. Stanley, S.; Burge, K.; and Wilson, D., "Experimental Investigation of Pulse Detonation Wave Phenomena as Related to Propulsion Application," AIAA Paper 95-2580, 1995.

16. Bird, G.A., "A Note on Combustion Driven Shock Tubes," In "Hypersonic Facilities in the Aerodynamics Department, Royal Aircraft Establishment," P.A. Hufton (Ed.), AGARD Report 146, 1957.

17. Coates, P.B. and Gaydon, A.G., "A Simple Shock Tube With Detonating Driver," *Proceedings of the Royal Society of London,* A283, 1965, pp.18-32.

18. Balcarzak, M.J. and Johnson, M.R., "The Gaseous-Detonation Driver and Its Application to Shock Tube Simulation Techniques," *Proceedings of the 5th International Shock Tube Symposium,* Slawsky, Z.I.; Moulton, J.F.; and Filler, W.S., (Eds.), U.S. Naval Ordinance Lab, White Oak, MD, 1966, pp. 1111-1128.

19. Lee, B. "Detonation Driven Shocks in a Shock Tube," *AIAA Journal,* Vol. 5, No. 4, Apr. 1967, pp. 791-792.

20. Yu, H.R.; Esser, B.; Lenartz, M.; and Gronig, H., "Gaseous Detonation Driver for a Shock Tunnel," *Shock Waves,* Vol. 2, 1992, pp. 245-254.

21. Tamagno, J.; Calleja, J.; and Erdos, J., "Exploratory Tests of Detonation-Driven Expansion Tube Performance," NASA CR-191580, General Applied Science Laboratories, Ronkonkoma, NY, Mar. 1994.

22. Engers, R.J.; Calleja, J.F.; and Bakos, R.J., "A Detonation Driven Injectant Heater for Pulse Facility Testing Applications," AIAA Paper No. 95-3153, 1995.

23. Bakos, R.J.; Castrogiovanni, A.; Calleja, J.F.; Nucci, L.; and Erdos, J.I., "Expansion of the Scramjet Ground Test Envelope of the HYPULSE Facility," AIAA Paper 96-4506, 1996.

24. Erdos, J.I; Bakos, R.J.; Castrogiovanni, A.; Calleja, J.F.; and Rogers, R.C., "Dual Mode Shock-Expansion/Reflected-Shock Tunnel," AIAA Paper 97-0560, 1997.

25. Venable, B.; Anderson, D.; and Wilson, D., "A Numerical Investigation of a Shock-Tube-Driven Electrical Conductivity Channel," AIAA Paper 96-4590, 1996.

26. *Thermal Equilibrium Program for Windows: User's Manual*, Software and Engineering Associates, Inc., 1992.

27. Gordon, S. and McBride, B.J., "Computer Program for Calculation of Complex Chemical Equilibrium Composition, Rocket Performance, Incident and Reflected Shocks, and Chapman-Jouguet Detonations," NASA SP-273, 1976.

28. Angelone, J.P., "Shock Tube-High Temperature Gasdynamics Studies," doctoral dissertation, The University of Texas at Arlington, 1978.

29. Alpher, R.A. and White, D.R., "Flow in Shock Tubes with Area Change at the Diaphragm Section," *Journal of Fluid Mechanics*, Vol. 3, 1958, pp. 457-470.

30. Shchelkin, K.I., *Soviet Journal of Technical Physics*, Vol. 10, 1940, pp. 823-827.

31. Hinkey, J.B.; Bussing, T.R.A; and Kaye, L., "Shock Tube Experiments for the Development of a Hydrogen-Fueled Pulse Detonation Engine," AIAA Paper 95-2578, 1995.

32. Helman, D.; Shreeve, R.P.; and Eidelman, S., "Detonation Pulse Engine," AIAA Paper 86-1683, 1986.

33. Bussing, T. and Pappas, G., "An Introduction to Pulse Detonation Engines," AIAA Paper 94-0263, 1994.

34. Lin, S.C.; Resler, E.L.; and Kantrowitz, A., "Electrical Conductivity of Highly Ionized Argon Produced by Shock Waves," *Journal of Applied Physics*, Vol. 26, No. 1, Jan. 1953, p. 95.

35. Spitzer, L. and Harm, R., "Transport Phenomena in a Completely Ionized Gas," *The Physical Review*, Vol. 89, 1963, p. 977.

36. Vincenti, W.G. and Kruger, C.H., *Introduction to Physical Gas Dynamics*, Krieger, Huntington, NY, 1977.

37. Garrison, G.W., "Electrical Conductivity of a Seeded Nitrogen Plasma," *AIAA Journal*, Vol. 6, No. 7, July 1968, pp. 1264-1270.

38. Demetriades, S.T. and Argyropoulas, G.S., "Ohm's Law in Multicomponent Nonisothermal Plasmas with Temperature and Pressure Gradients," *Physics of Fluids*, Vol. 8, No. 11, Nov. 1966, pp. 2136-2149.

39. Adler, R.J., "Pulse Power Formulary," North Star Research Corporation, Albuquerque, NM, 1989.

40. Stuessy, W.S.; Liu, H.C.; Lu, F.K.; and Wilson, D.R., "Detonation Wave Driver for Enhancing Shock Tube Performance," AIAA Paper 96-2195, 1996.

41. Figliola, R.S. and Beasley, D.E., *Theory and Design for Mechanical Measurements,* 2nd Ed., New York, John Wiley and Sons, 1995.

42. Nottingham, W.B., "A New Equation for the Static Characteristic of the Normal Electric Arc," *Transactions of the A.I.E.E.*, Feb. 1923, pp. 302-310.

43. Wilson, D.R. and Simmons, G.A., "MHD Generator Off-Design Performance and NO_x Chemical Kinetics Analysis," NASA CR-156187, June 1980.

44. Munipalli, R.; Kim, H.; Anderson, D.A.; and Wilson, D.R., "Computation of Unsteady Nonequilibrium Propulsive Flowfields," AIAA Paper 97-3164, 1997.

A.1.11 Data Plots

Data plots for each test run are presented in this section. The sequence of plots for each test run include

- Pressure vs. time from transducers located in the driven tube
- Voltage vs. time for the probe and powered electrodes for primary test window
- Current vs. time for primary test window
- Voltage vs. distance obtained by cross-plotting the voltage vs. time curves
- Average conductivity vs. time

The run log for the test program is presented in Table A.1- 1

Table A.1- 1. Test program run log.

Date	Gas	K_2CO_3	VA	P1 *	T1	Vs #	M *	T2 *	P2 #	C_S	TCS	Ics #	ΔV_{cs}	σ_{cs}	Tmax.	Imax	ΔV_{max}	σ_{max}	RM	GN
		%	Volt	atm	K	m/sec		K	atm	μsec	msec	Amp	Volt	Mho/m	msec	Amp	Volt	mho/m		
6/11 *	Air	0.05	600	0.13	298	2390	6.94	2590	7.48	225	11.00	2.52	605	1.01	11.12	3.92	609	1.29	X	1
6/13 A	Air	0.05	400	0.89	298	1520	4.40	1310	20.41	477	11.67	0.08	429	0.02	12.02	0.03	430	0.04	I a	8
6/13 B	Air	0.05	800	0.06	298	3270	9.42	3790	6.80	133	9.62	18.13	690	3.18	9.74	18.13	774	3.72	X	8
6/14 A	Air	0.05	400	0.12	298	2610	7.54	2900	8.50	187	10.20	0.50	185	0.20	10.43	1.27	250	0.36	R	8
6/16 A	Air	0.09	600	0.11	298	2540	7.33	2790	7.96	198	11.09	0.94	259	0.26	11.29	2.32	289	0.58	D	8
6/19 A	Air	0.05	600	0.11	297	2540	7.33	2790	7.82	198	11.31	0.74	238	0.22	11.51	1.90	260	0.53	I-V	1(
6/19 B	Air	0.05	800	0.16	297	2410	6.95	2590	9.32	220	8.39	0.91	476	0.14	8.57	2.14	517	0.30	I-V	1(
6/20 A	Air	0.05	700	0.28	299	2080	5.58	2080	11.90	284	10.82	0.24	451	0.04	11.05	1.17	478	0.18	I-V	1(
6/20 B	Air	0.05	600	0.26	299	1910	5.49	1830	9.32	303	8.16	0.07	284	0.02	8.58	0.33	343	0.07	T	1(
6/21 A	Air	0.05	600	0.26	298	2080	6.00	2080	11.22	284	11.22	0.62	323	0.14	11.46	1.07	369	0.21	R	8
6/21 B	Air	0.05	600	0.15	298	2540	7.33	2790	9.52	198	6.96	0.44	303	0.10	7.27	2.97	345	0.62	T	8
6/21 C	Air	0.05	600	0.15	298	2410	6.94	2590	8.50	220	6.49	0.17	178	0.07	6.88	1.46	390	0.27	T	8
6/21 D	N2	0.05	600	0.15	298	2290	6.59	2400	8.16	243	11.01	0.18	185	0.07	11.29	0.85	375	0.16	N2	8
6/21 E	N2	0.05	600	0.16	298	2410	6.94	2590	8.84	220	11.42	0.42	208	0.15	11.69	1.23	359	0.25	N2	8
6/24 A	N2	0.05	630	0.19	296	2410	6.98	2590	11.02	220	10.00	0.29	187	0.11	10.20	1.13	336	0.24	N2	3:
6/25 A	Air	1	571	0.16	296	2540	7.33	2790	10.20	198	9.19	0.88	312	0.20	9.44	1.69	364	0.33	X	
6/25 B	Air	1	600	X	296	X	X	X	X	X	X	X	X	X	X	X	X	X	X	
6/25 C	Air	1	675	0.12	296	2690	7.76	3010	8.50	185	21.99	5.02	322	1.18	22.13	8.24	385	1.54	X	
6/25 D	Air	1	815	0.10	296	2690	7.76	3010	7.48	185	24.23	4.66	563	0.90	24.36	5.54	441	0.90	X	
6/26 A	Air	1	417	0.12	296	2690	7.76	3010	8.50	185	17.43	2.70	193	2.70	17.62	13.66	211	4.65	I-V	
6/26 B	Air	1	721	0.14	296	2410	6.94	2590	8.16	220	23.26	1.21	234	2.04	23.58	12.91	429	2.16	T	
6/26 C	Air	1	713	0.17	296	2290	6.85	2540	9.32	243	23.69	0.64	264	1.07	24.01	12.43	463	1.93	R	
6/26 D	Air	1	709	0.22	296	2180	6.28	2230	10.20	285	19.81	0.17	200	0.29	20.26	10.35	411	1.75	T	
6/26 E	Air	1	778	0.10	296	2690	7.76	3010	7.62	185	20.86	1.96	367	1.88	21.12	35.68	466	5.37	I-V	
6/27 A	Air	1	703	0.10	298	2690	7.76	3010	7.48	185	19.51	2.11	535	3.97	19.77	49.80	393	8.95	I-V	
6/27 B	Air	2	618	0.11	298	2540	7.33	2790	6.80	198	15.92	17.16	242	0.48	16.16	71.33	241	21.32	D	
6/27 C	N2	1	580	0.12	298	2690	7.76	3010	8.50	185	17.63	72.21	186	27.94	17.76	81.81	184	31.91	N2	
6/27 D	N2	1	585	0.17	298	2290	6.94	2590	9.31	243	23.64	7.22	235	2.21	23.94	26.85	278	6.94	N2	
6/27 E	N2	1	586	0.32	298	1910	5.49	1830	11.56	303	23.68	0.62	167	0.62	24.04	9.58	335	2.05	N2	
6/27 F	Air	1	584	0.29	298	1990	5.74	1950	18.71	297	25.83	0.66	262	0.66	26.15	25.40	334	5.46	HP	
6/28 A	Air	1	575	0.21	298	2540	7.33	2790	13.61	198	23.42	2.80	287	2.80	23.66	67.54	232	20.90	HP	
6/28 B	Air	1	538	0.22	298	2690	7.76	3010	16.12	185	19.26	19.05	221	19.05	19.34	69.22	218	22.82	HP	
6/28 C	Air	1	750	0.26	298	2410	6.94	2590	15.31	220	18.34	16.69	318	16.69	18.41	95.51	320	21.48	HP	

11 A JUNE 1997

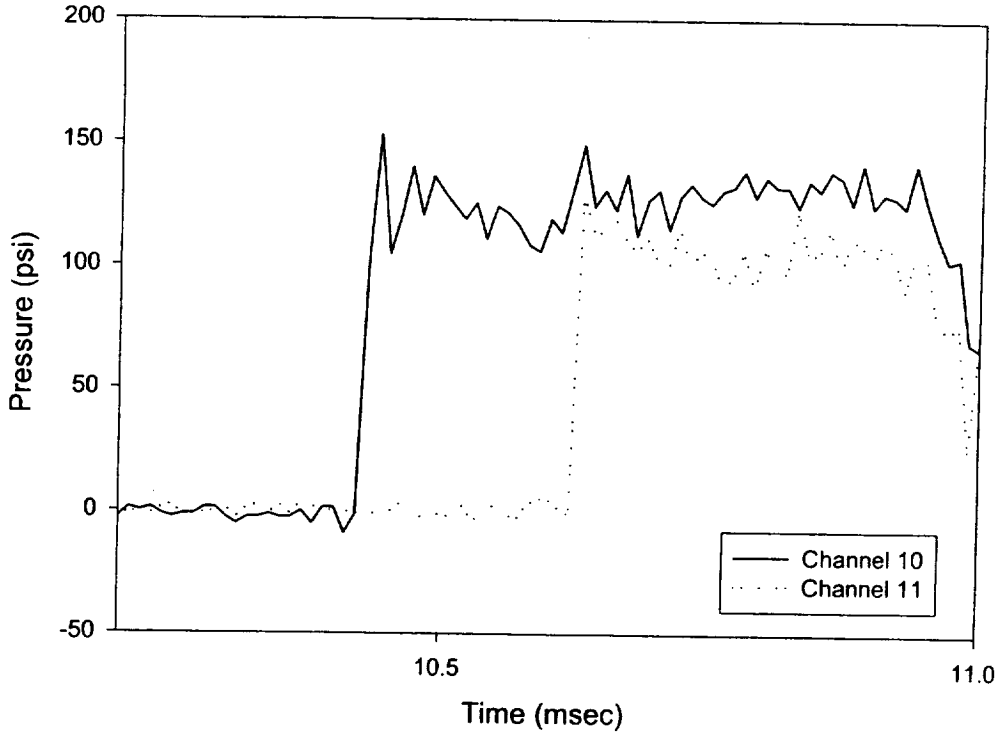

11 A JUNE 1997

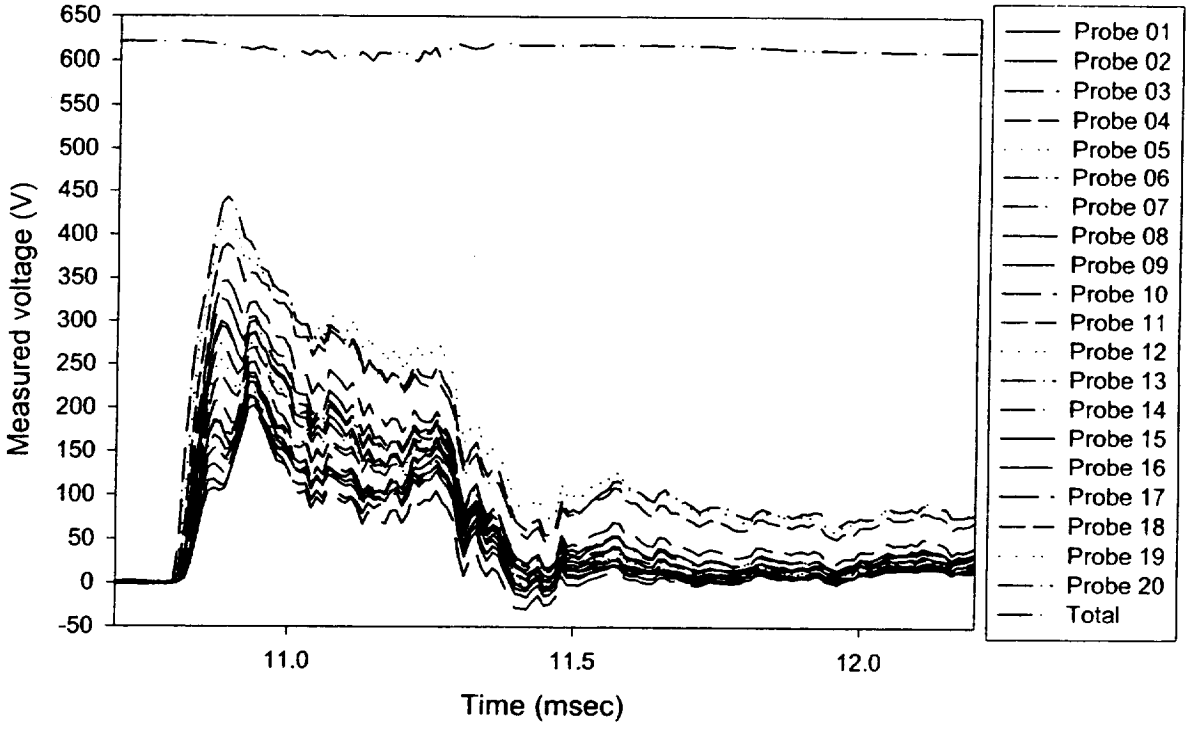

11 A JUNE 1997

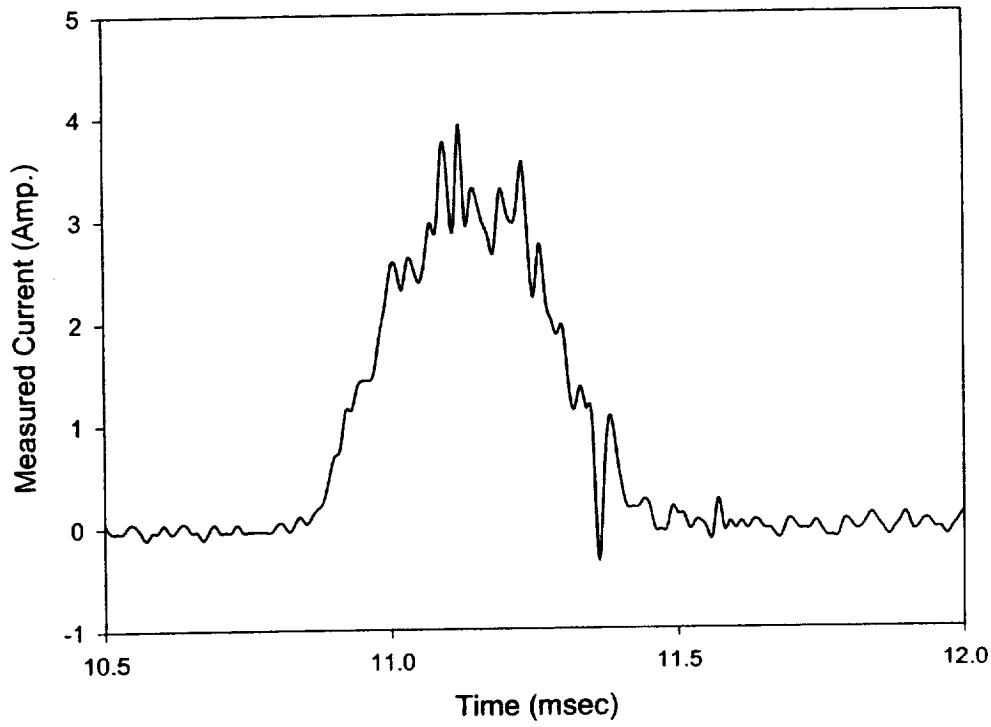

11 A JUNE 1997

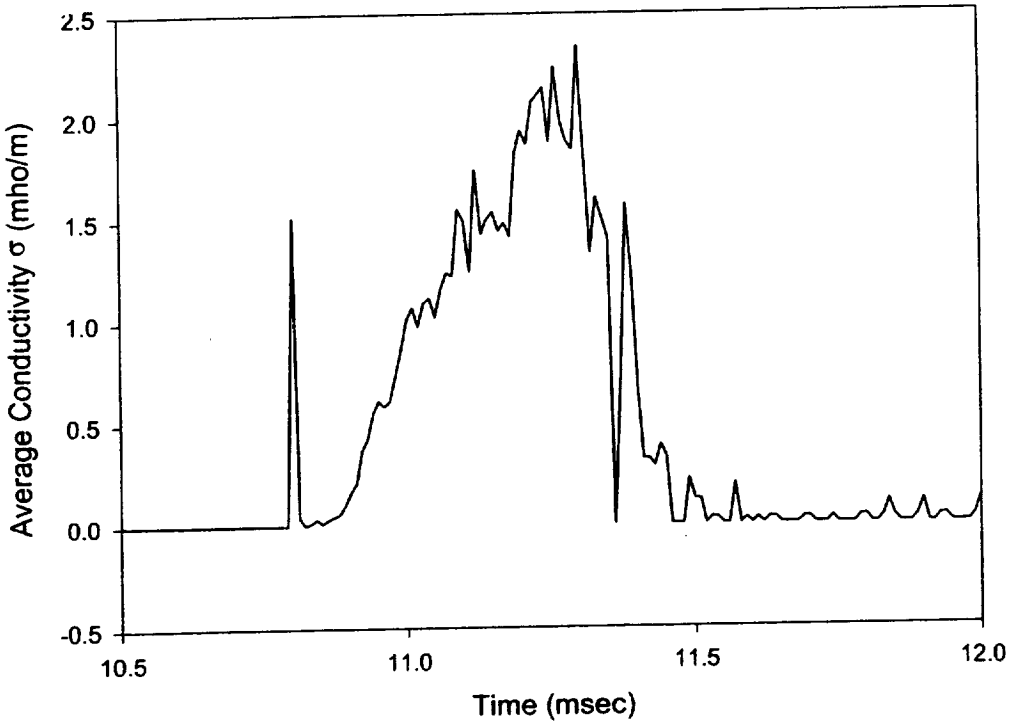

11 A JUNE 1997

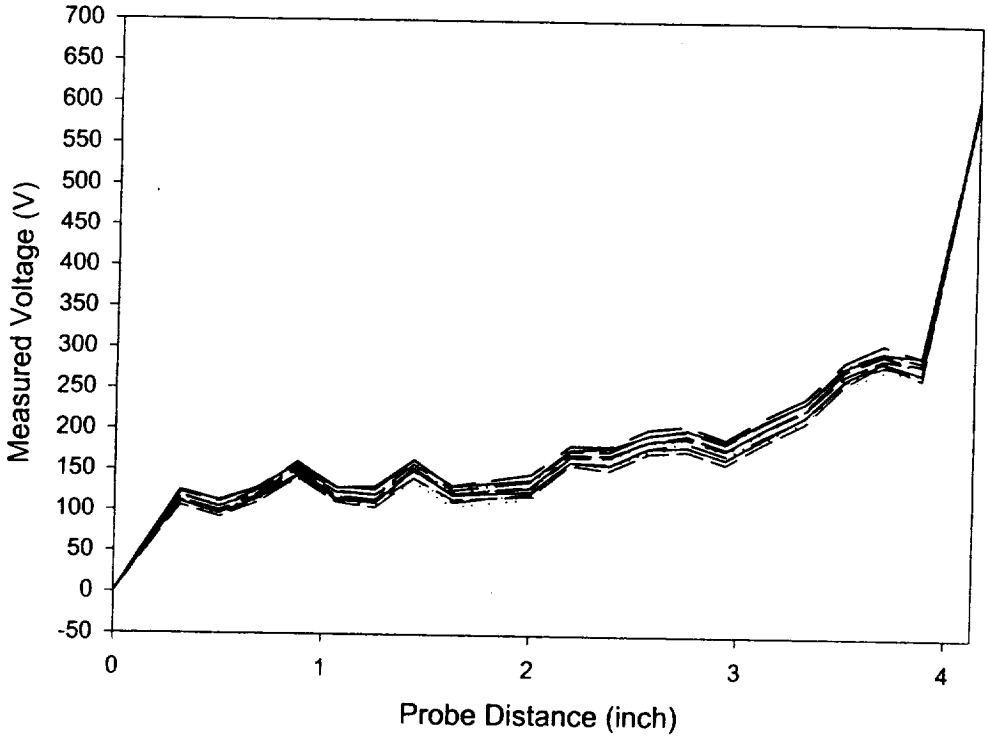

13 A JUNE 1997

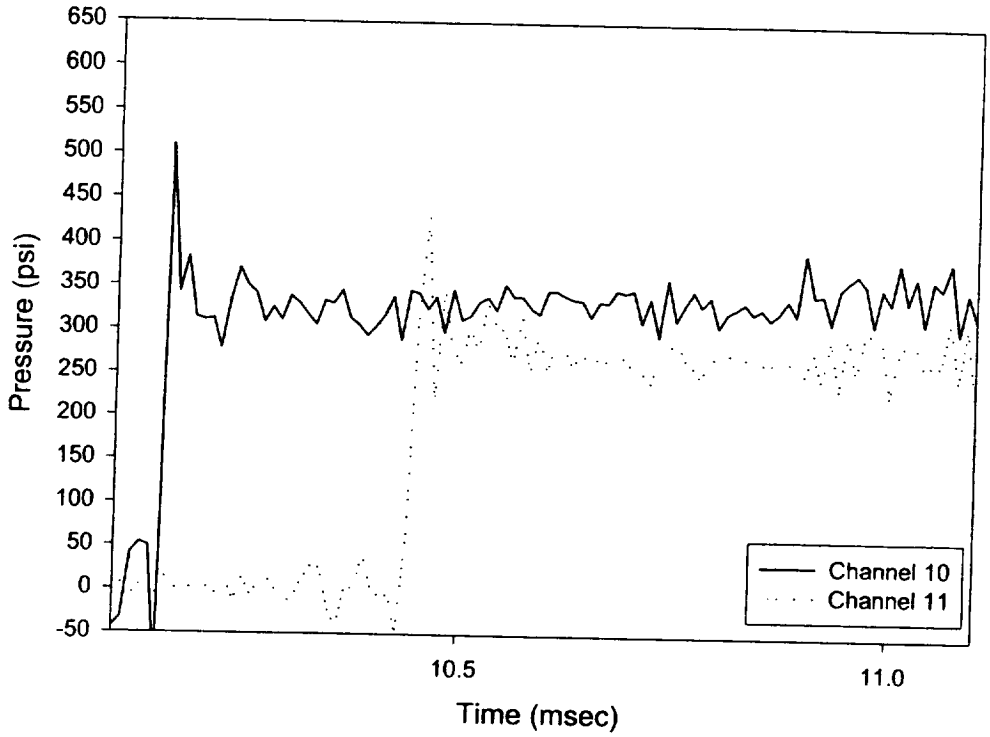

13 A JUNE 1997

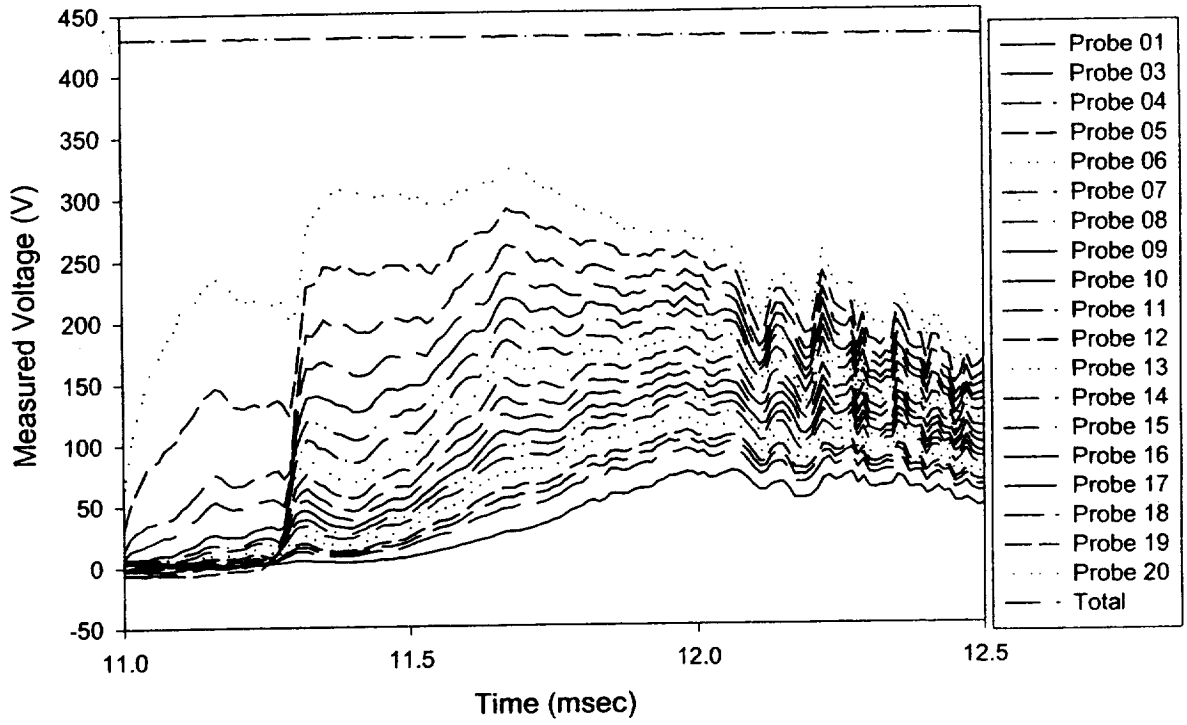

13 A JUNE 1997

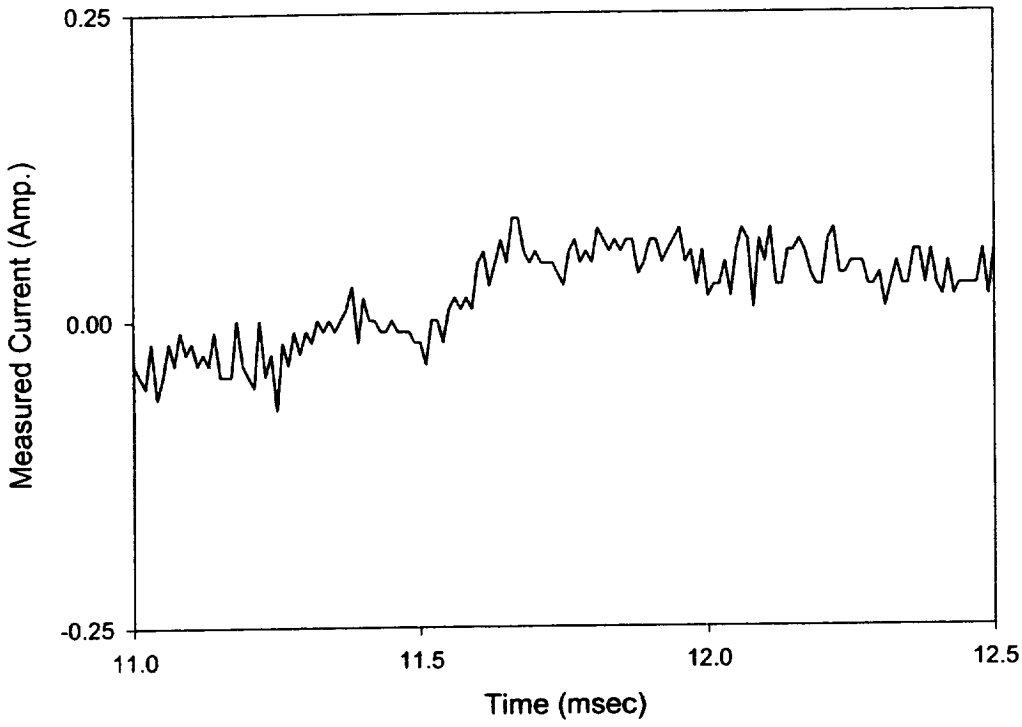

13 A JUNE 1997

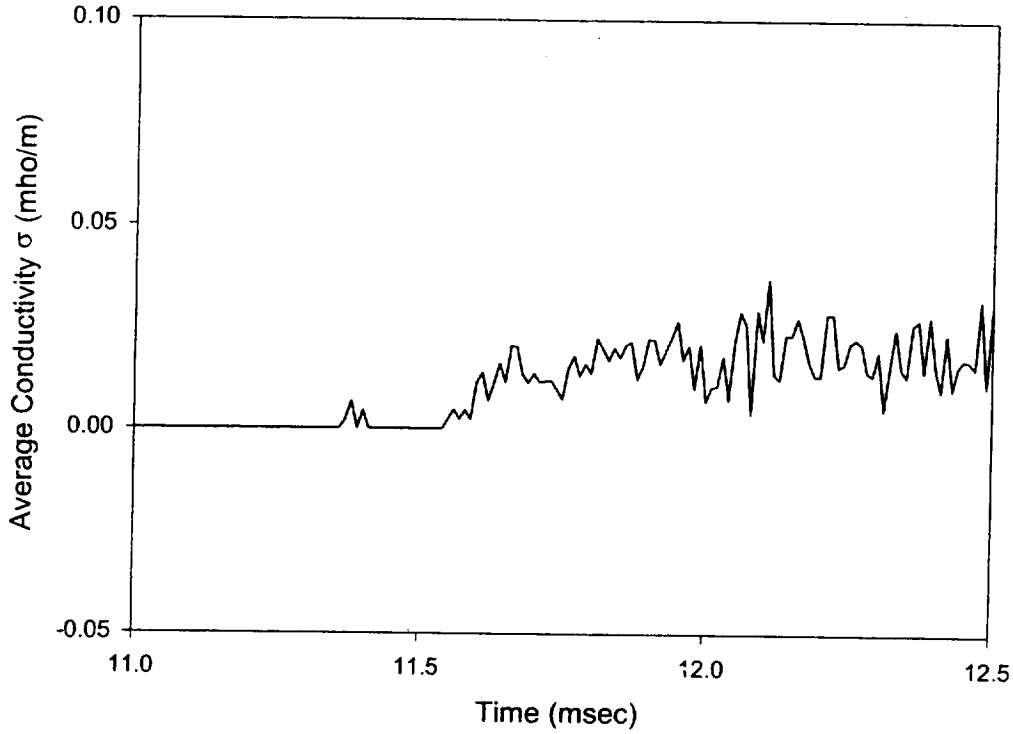

13 A JUNE 1997

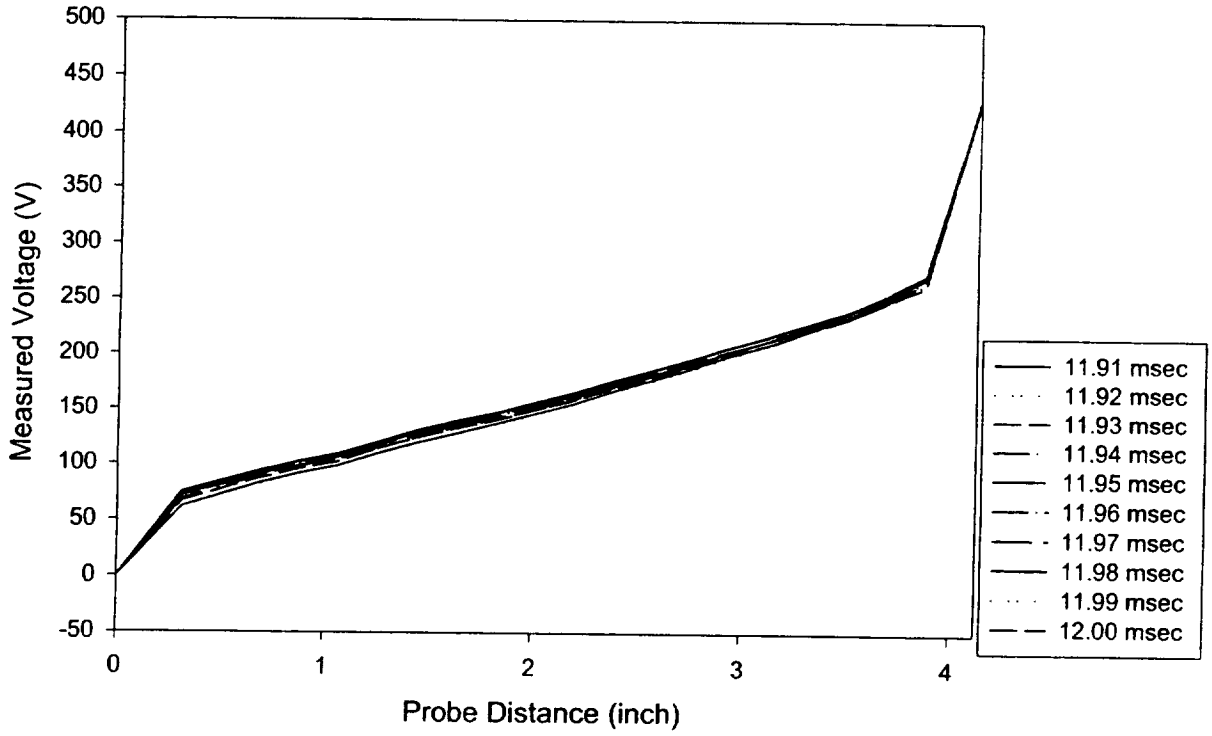

13 B JUNE 1997

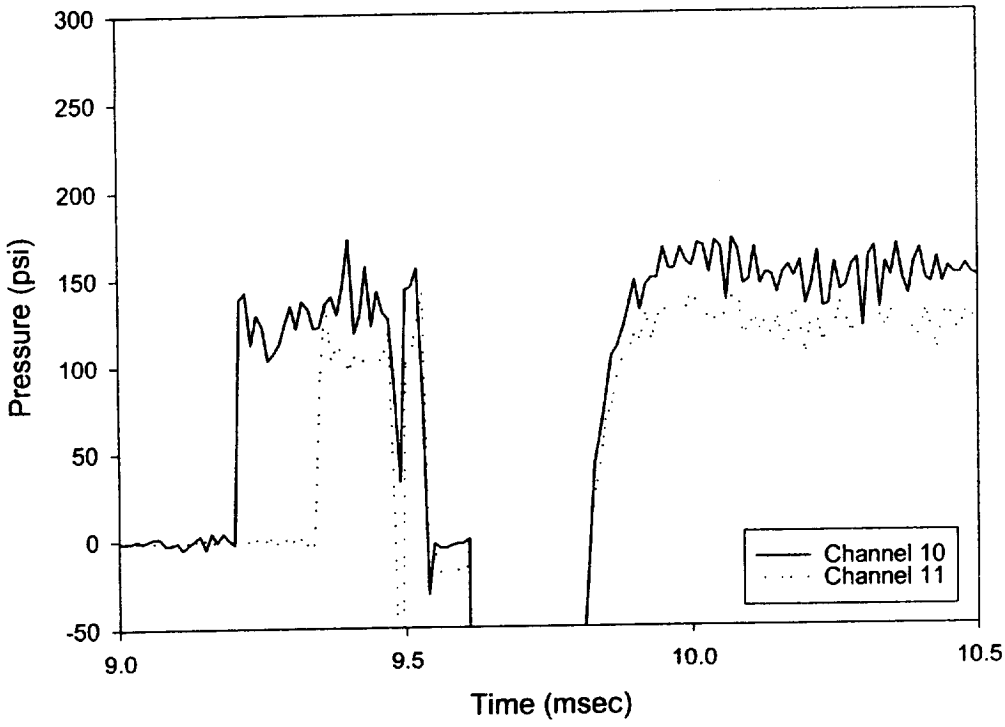

13 B JUNE 1997

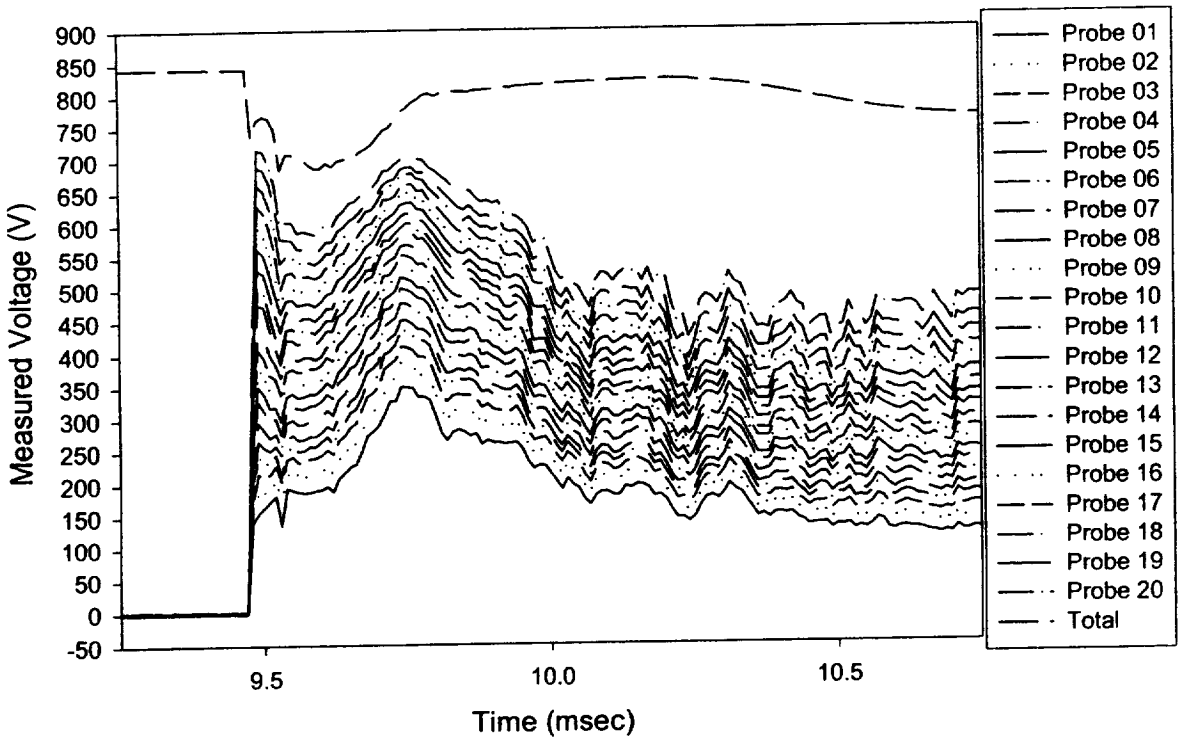

13 B JUNE 1997

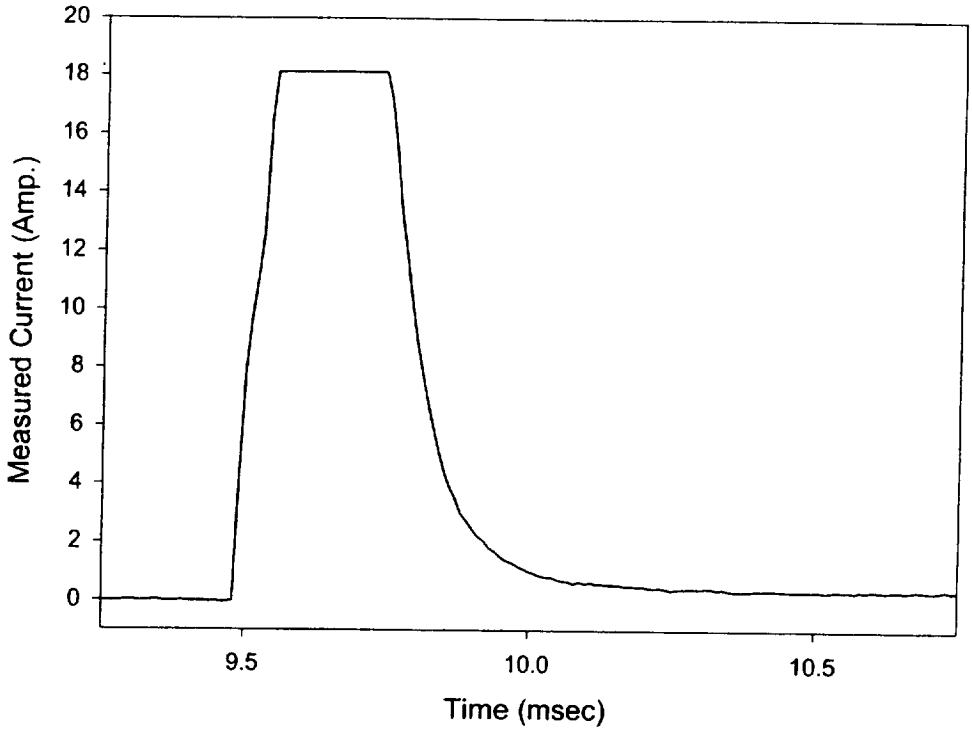

13 B JUNE 1997

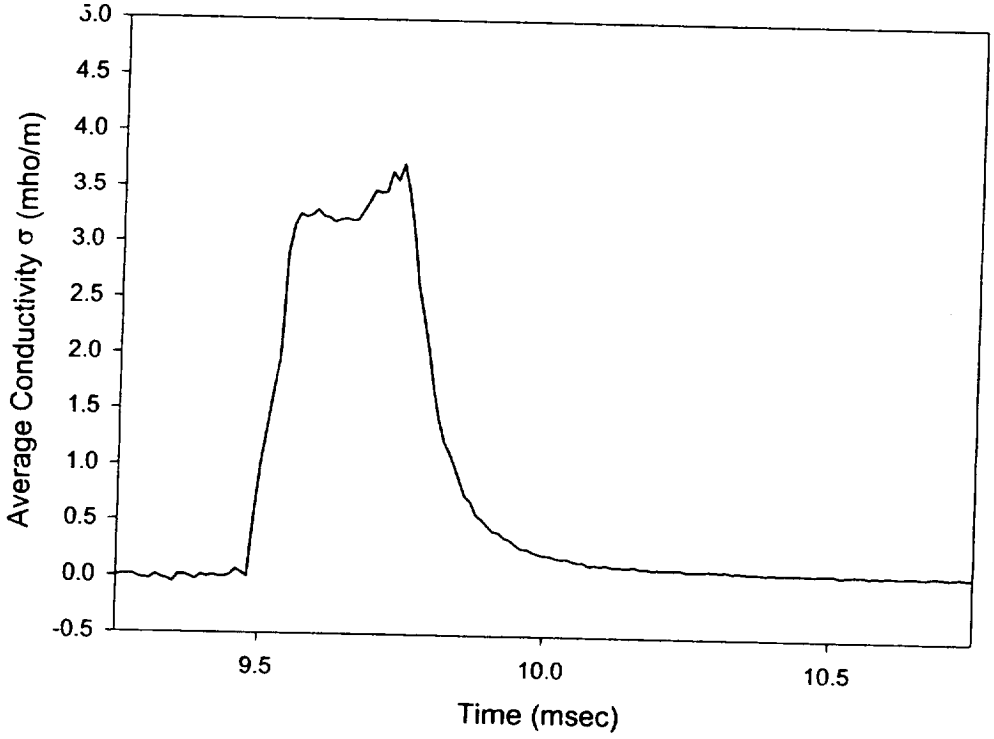

13 B JUNE 1997

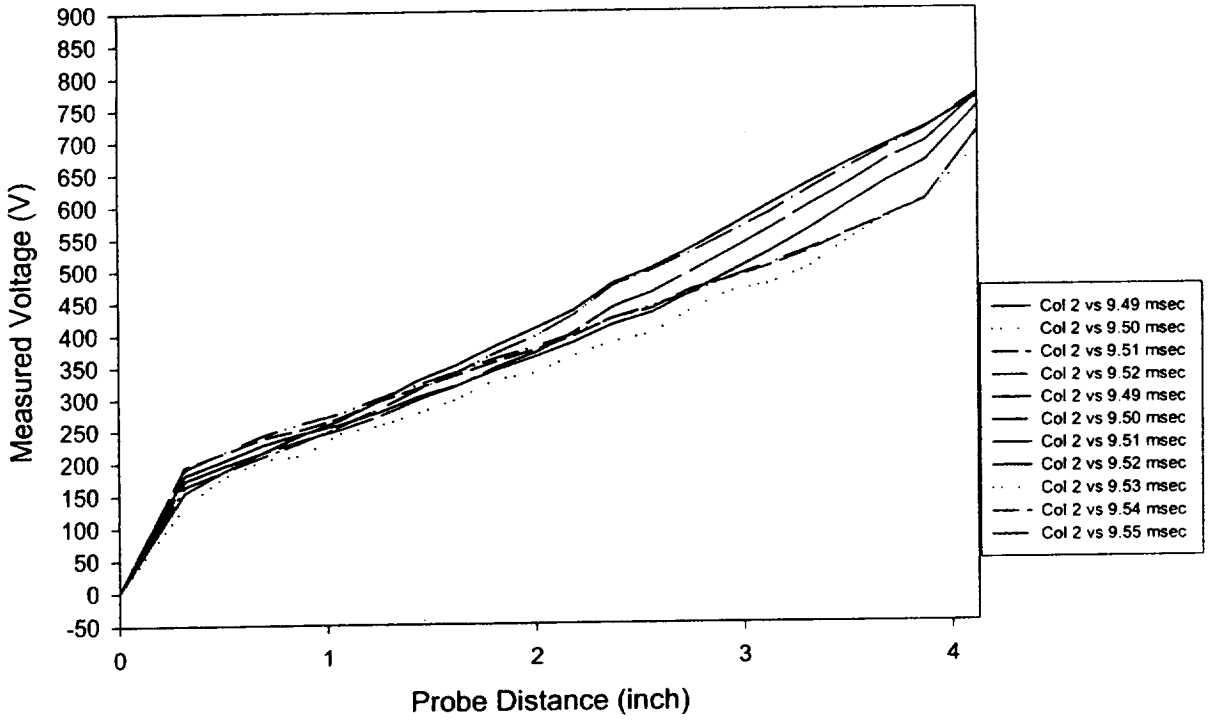

14 A JUNE 1997

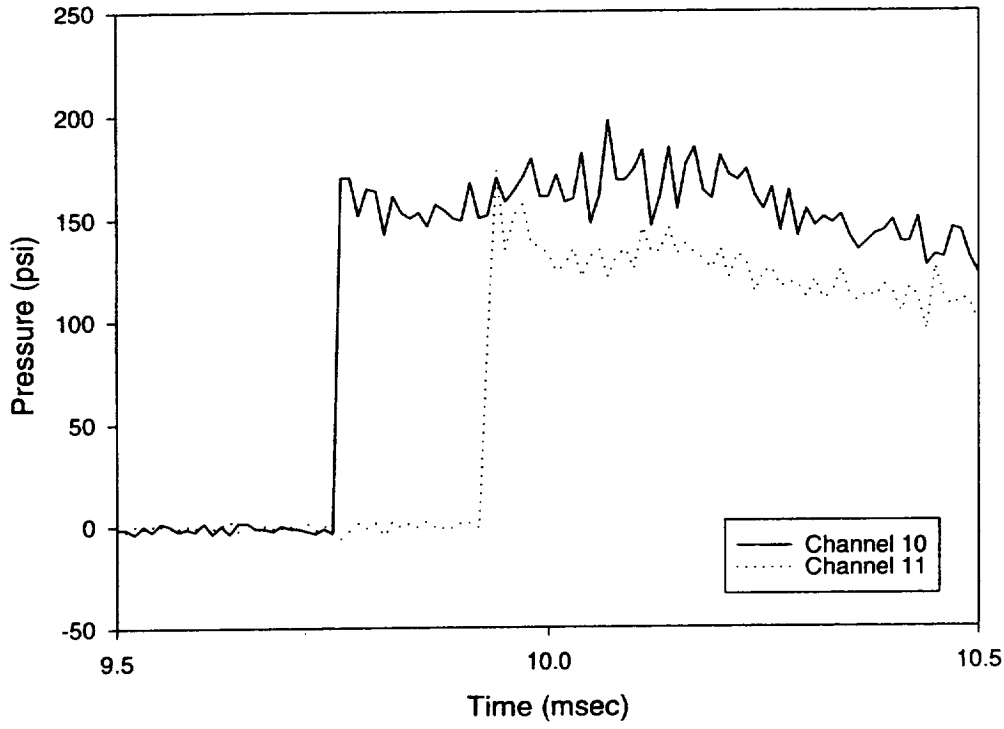

14 A JUNE 1997

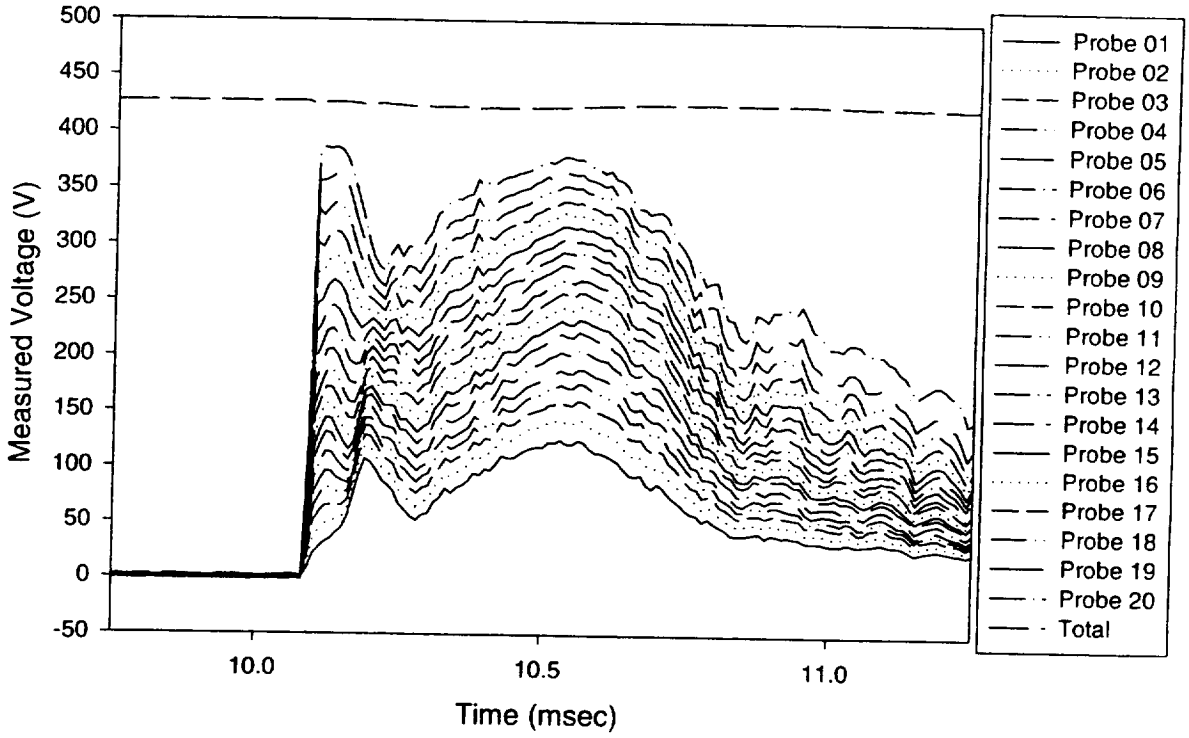

14 A JUNE 1997

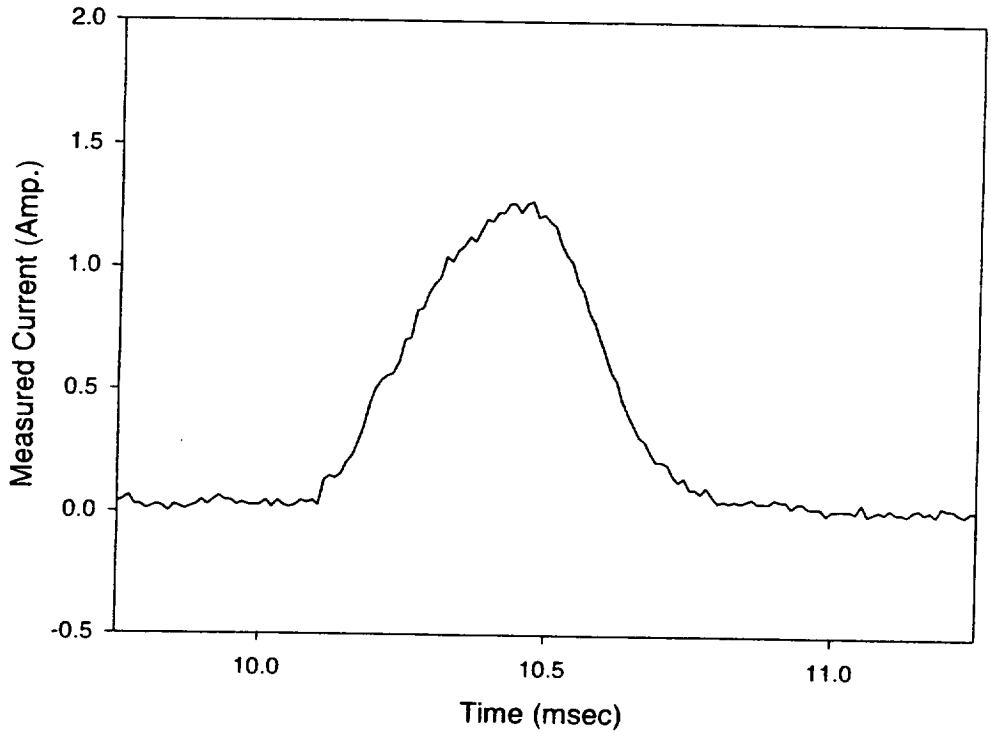

14 A JUNE 1997

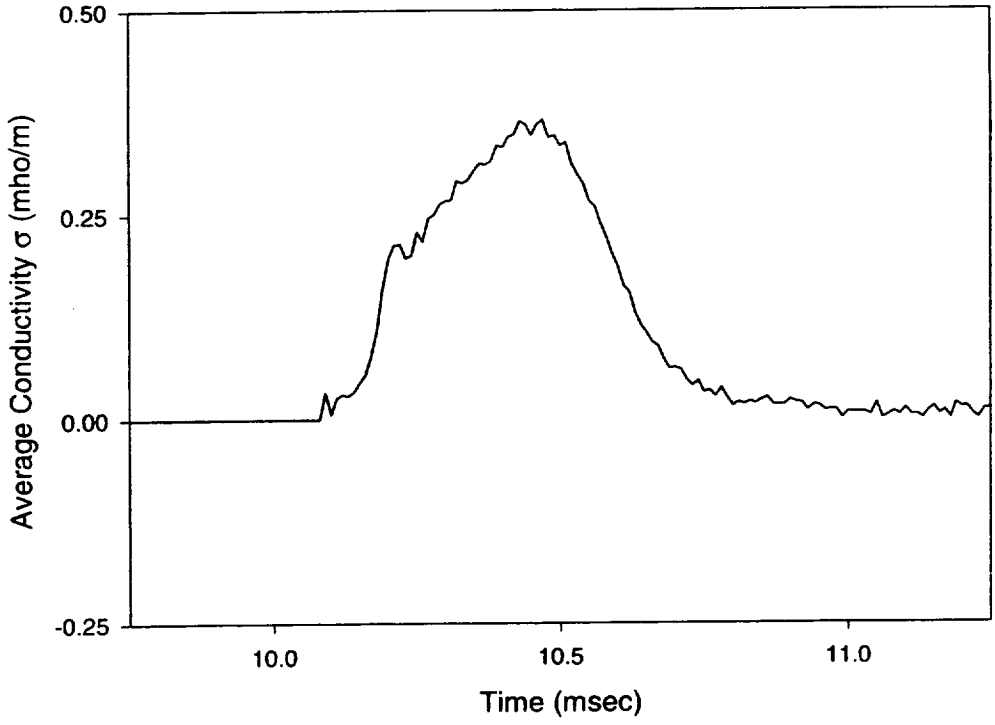

14 A JUNE 1997

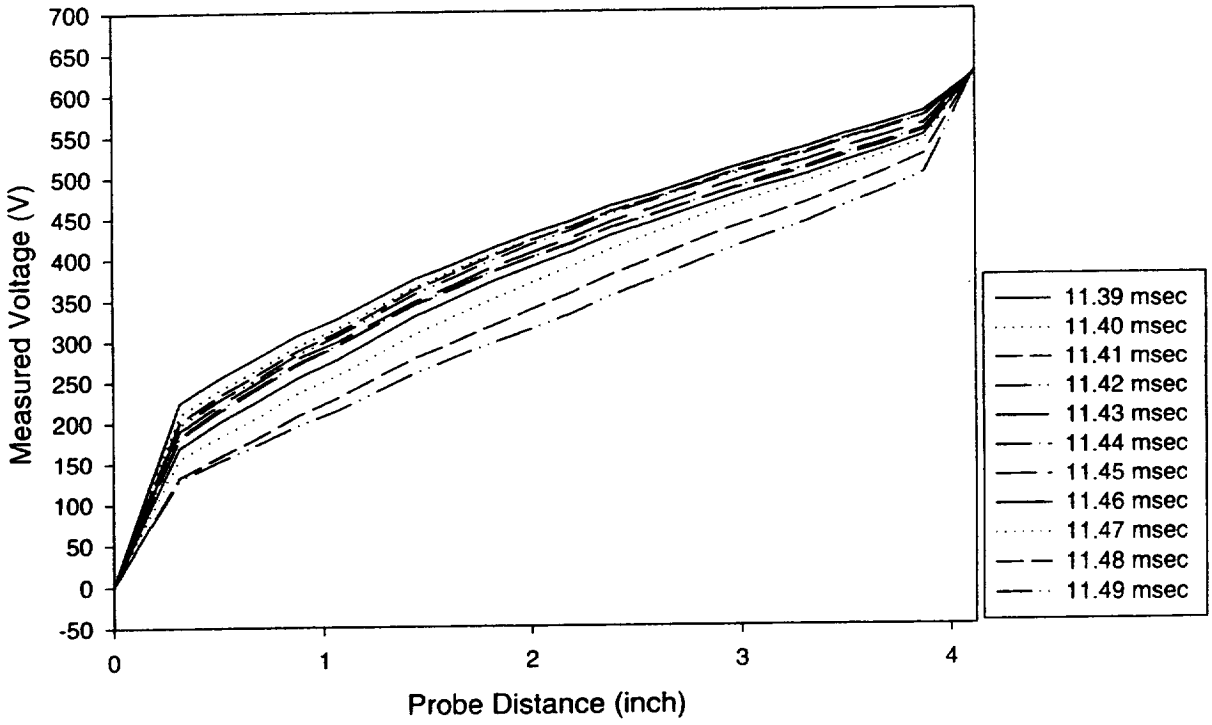

16 A JUNE 1997

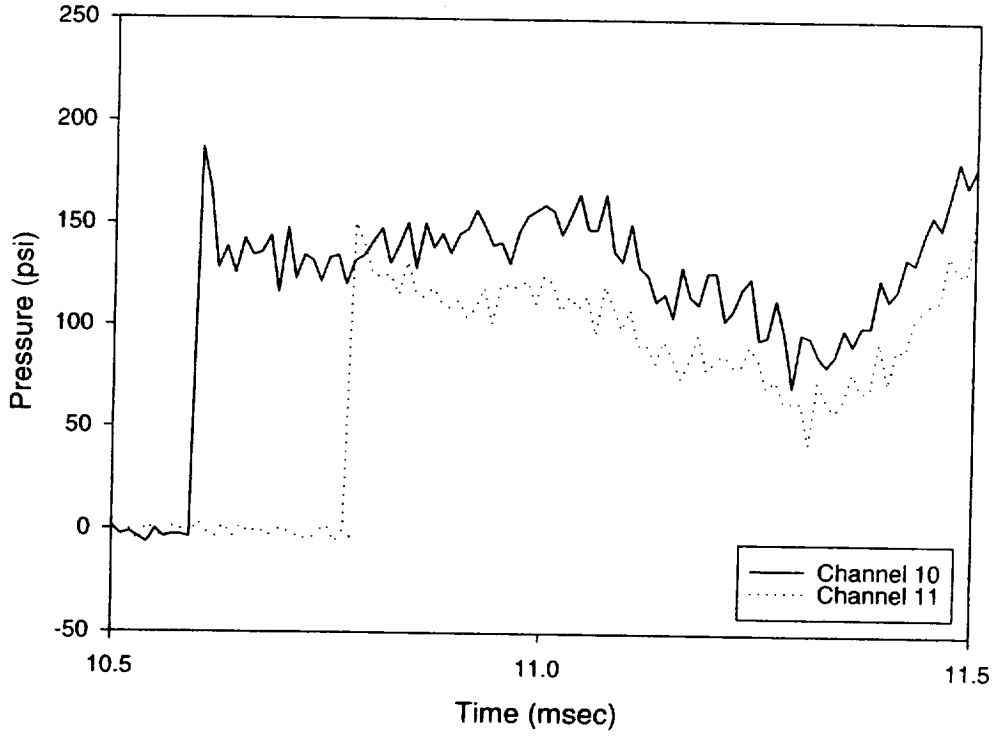

16 A JUNE 1997

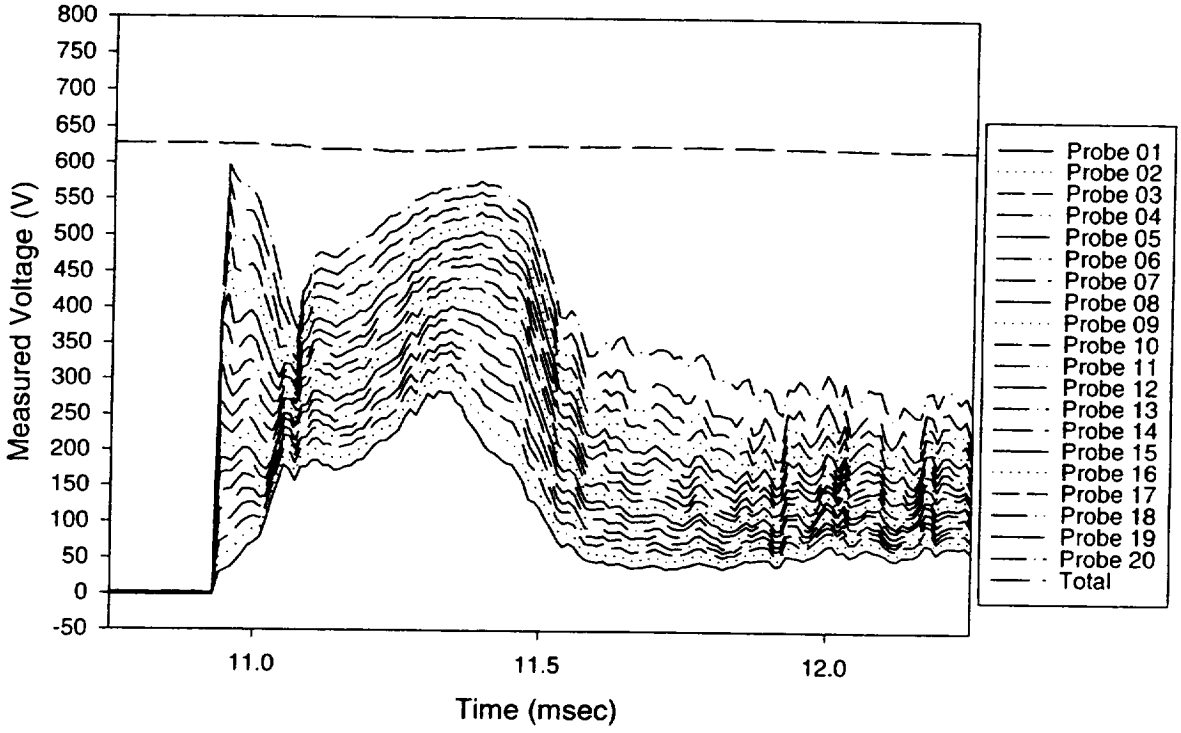

16 A JUNE 1997

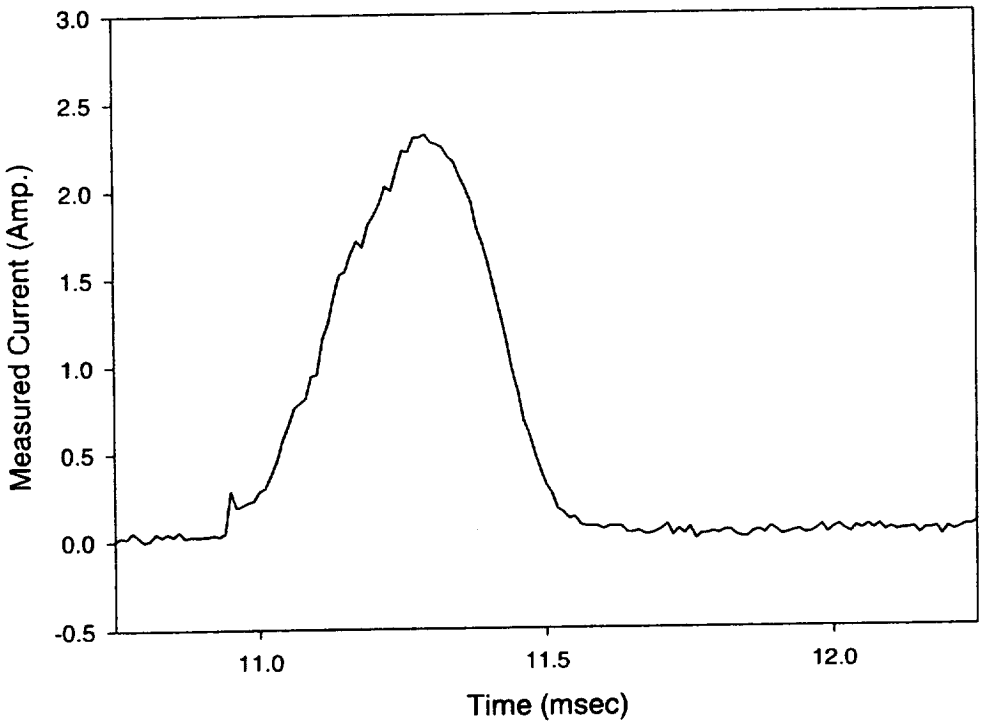

16 A JUNE 1997

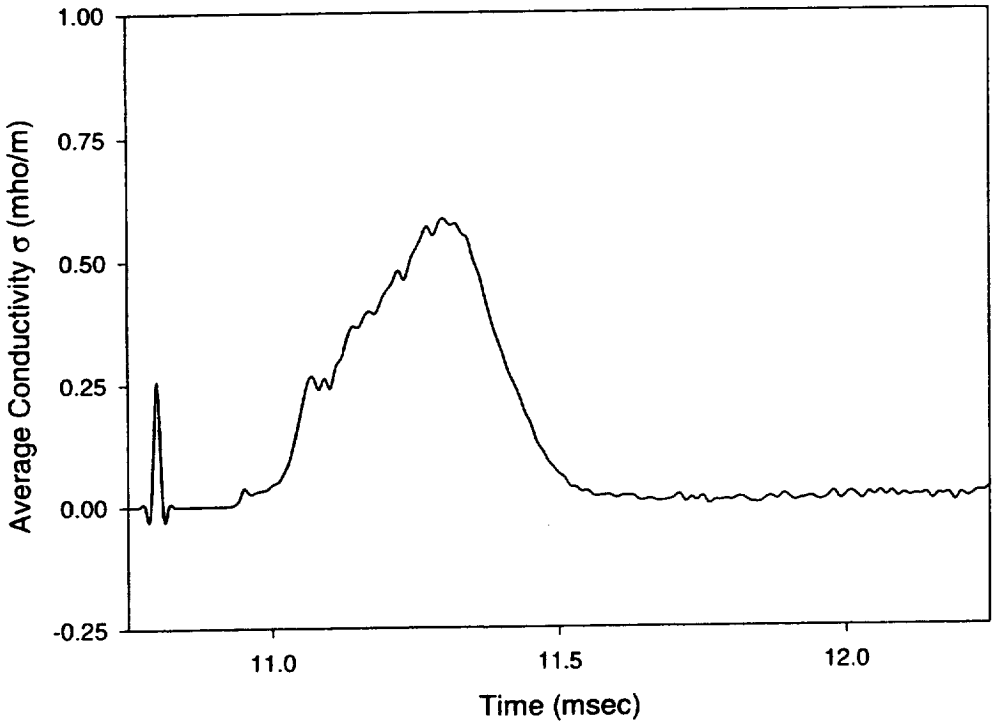

16 A JUNE 1997

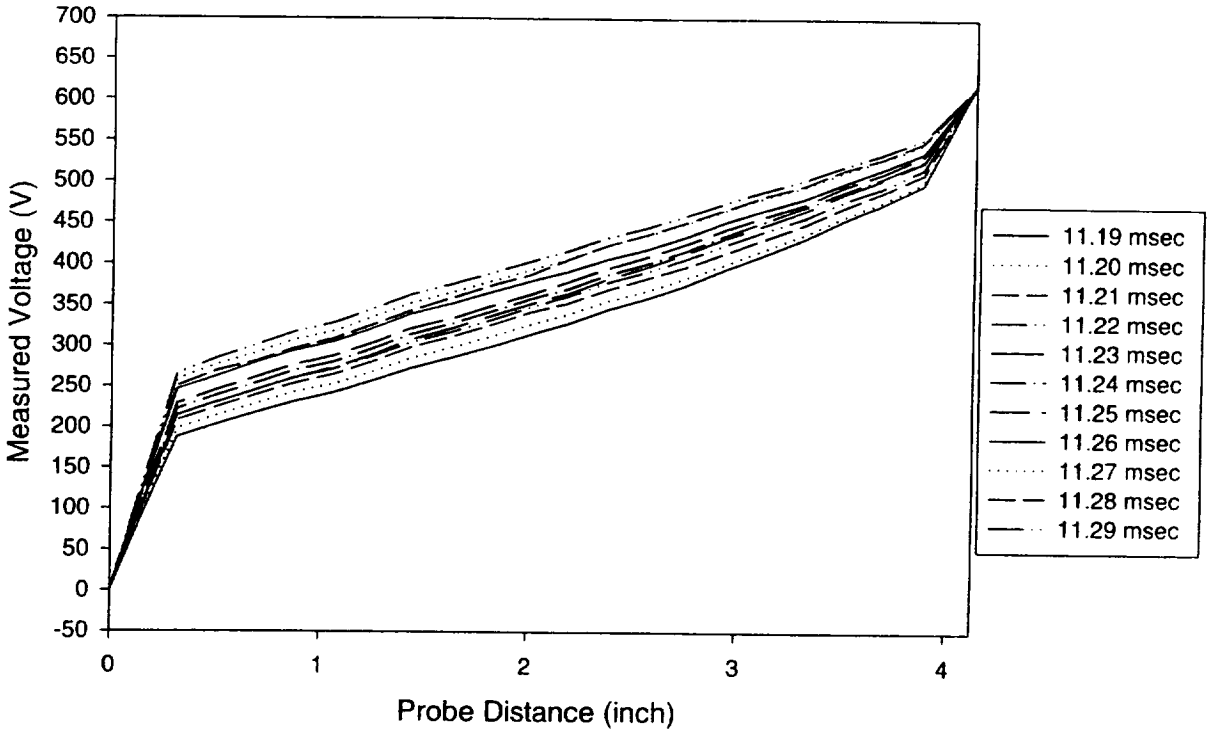

19 A JUNE 1997

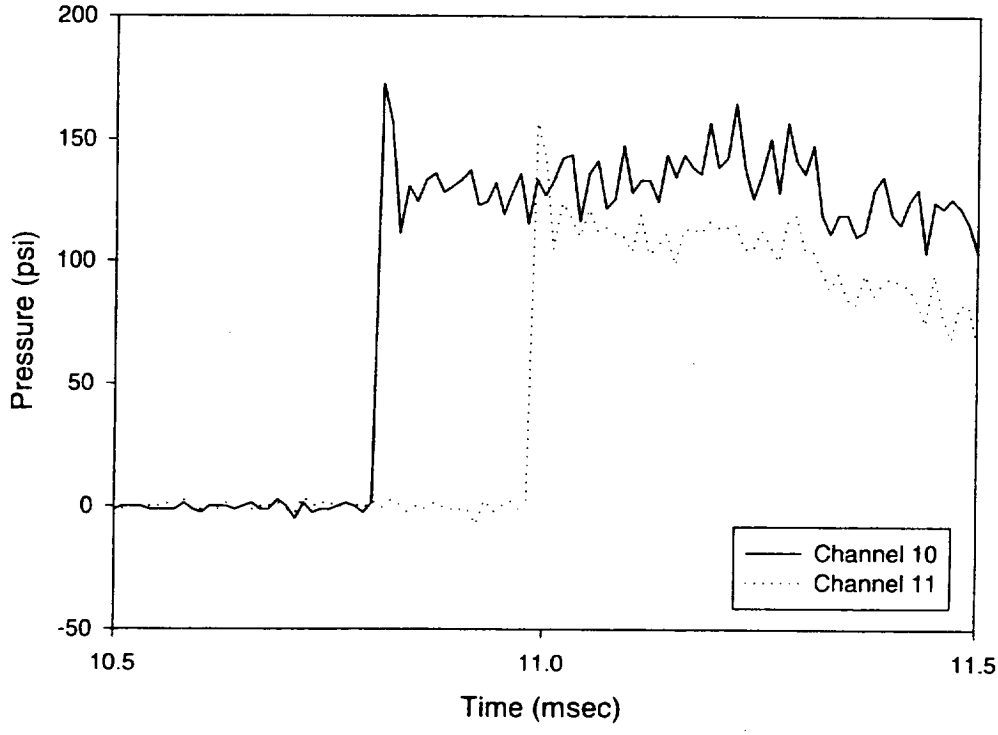

19 A JUNE 1997

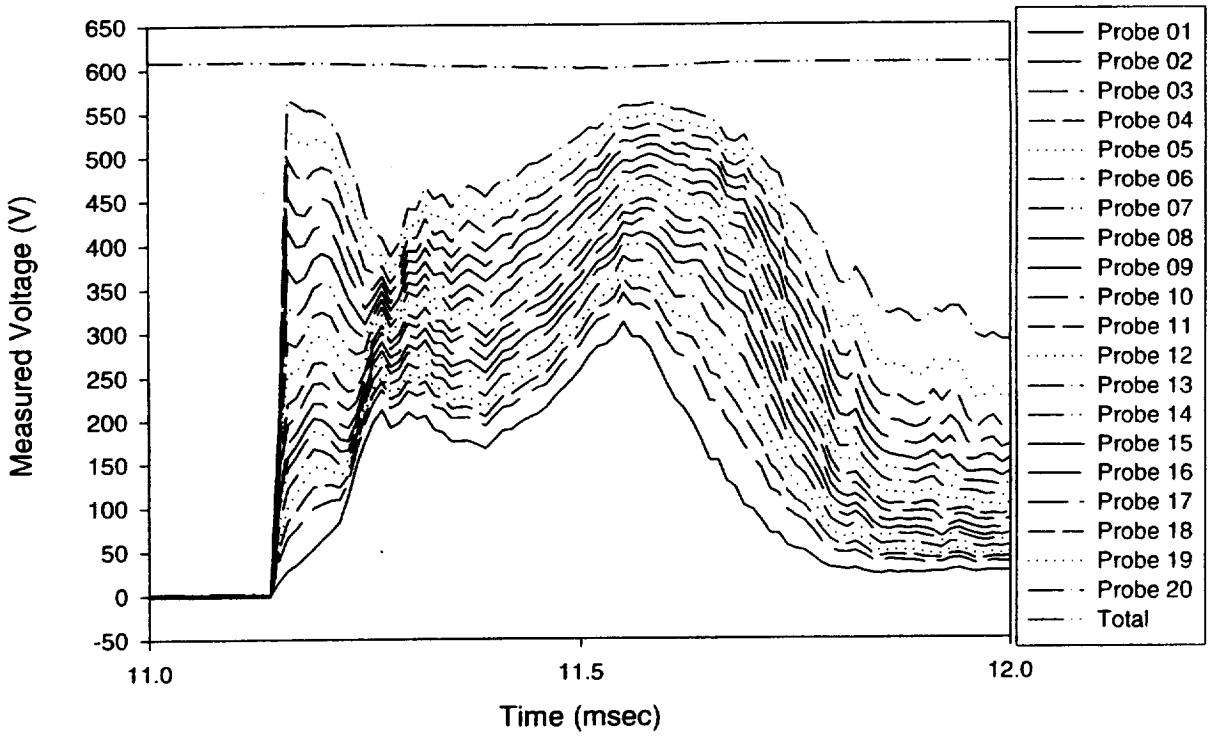

19 A JUNE 1997

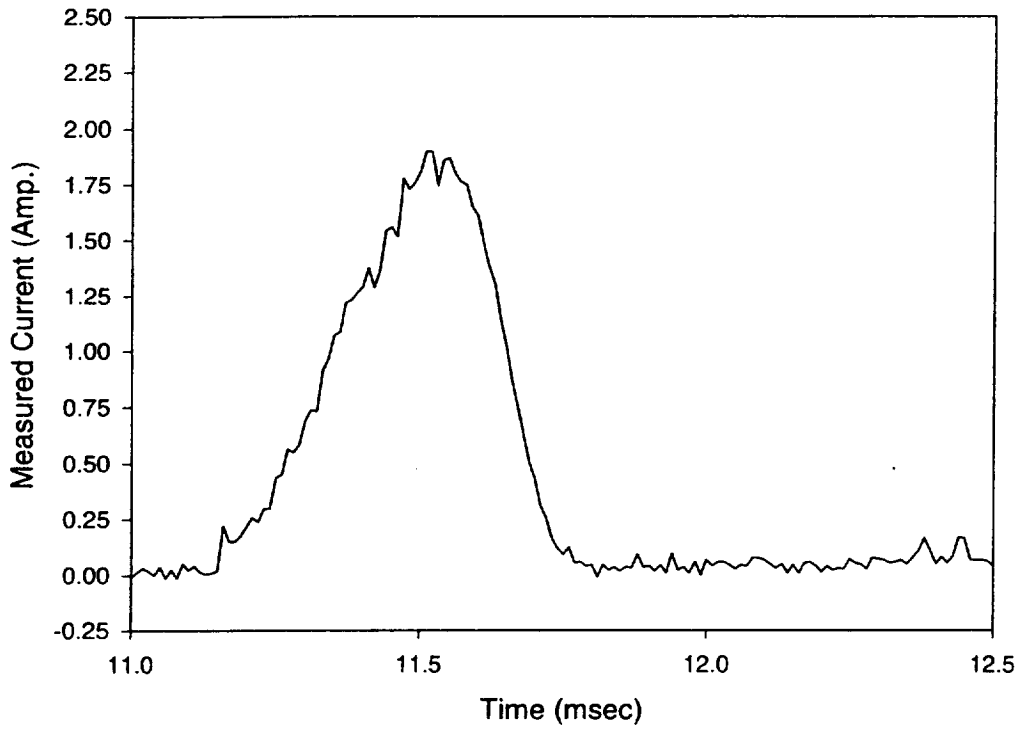

19 A JUNE 1997

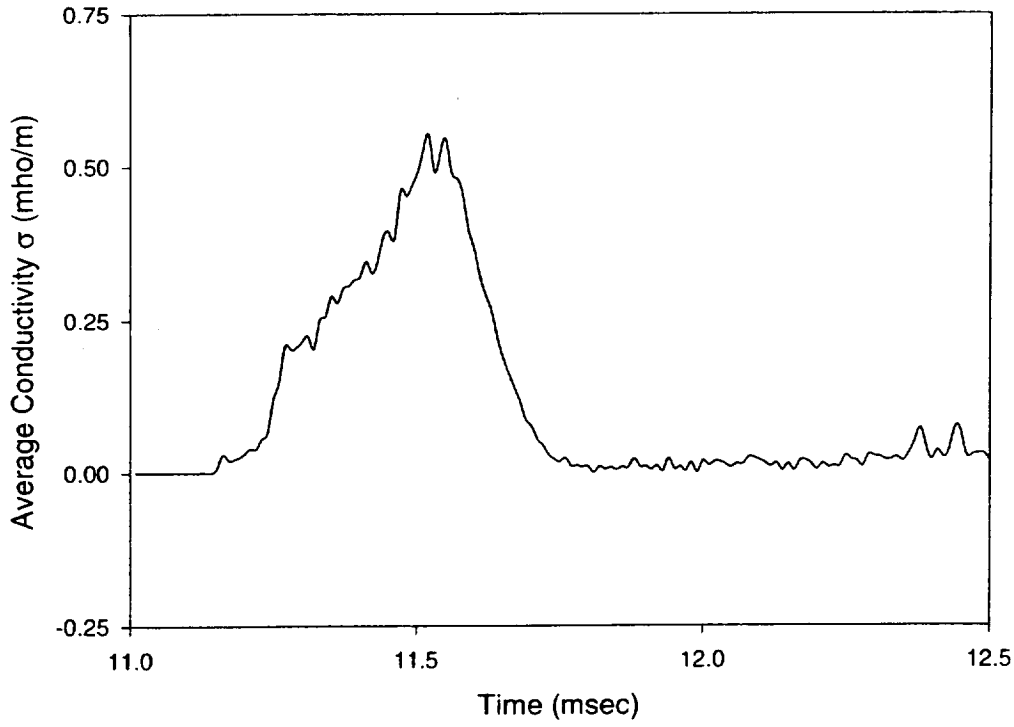

19 A JUNE 1997

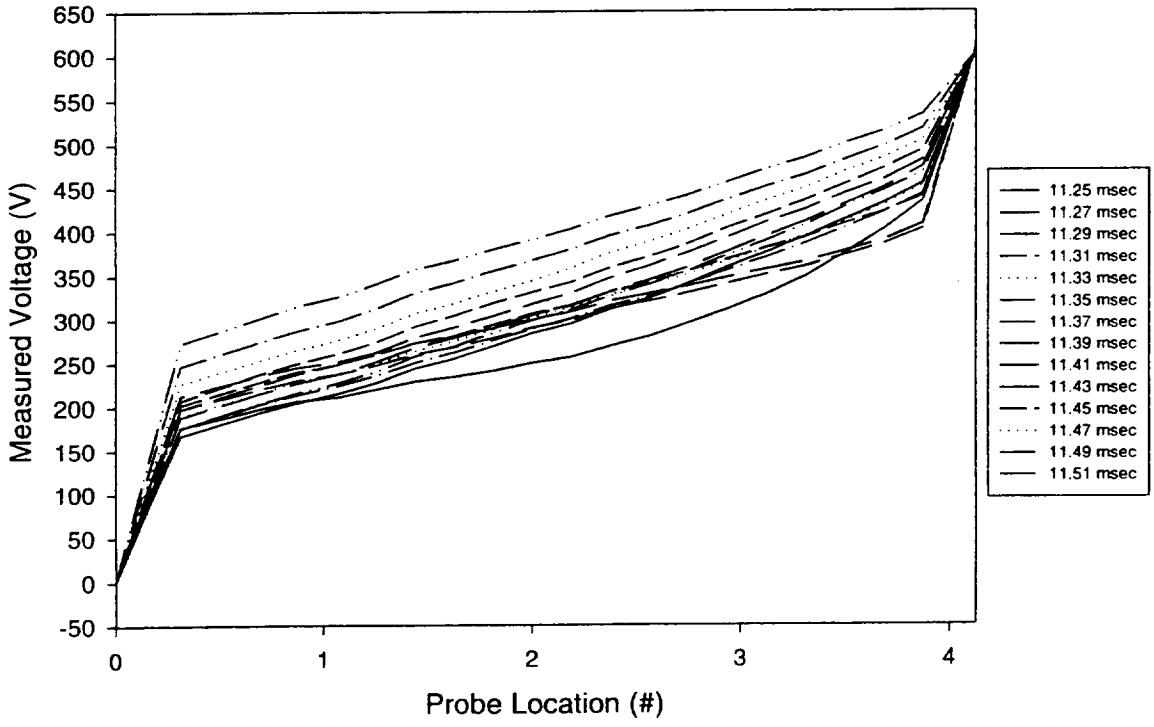

19 B JUNE 1997

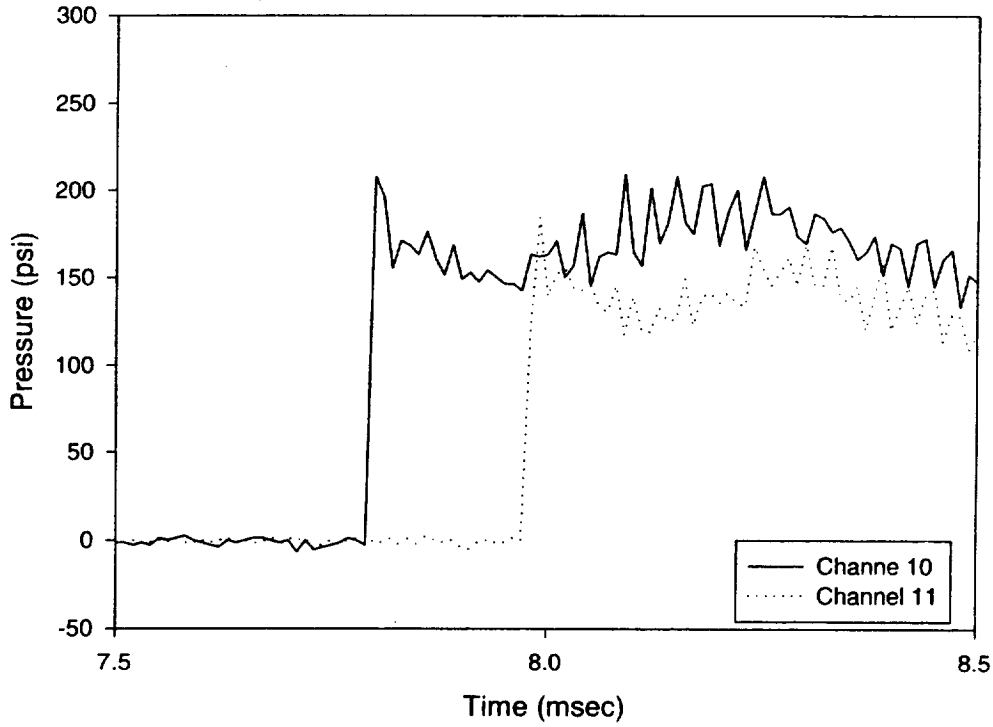

19 B JUNE 1997

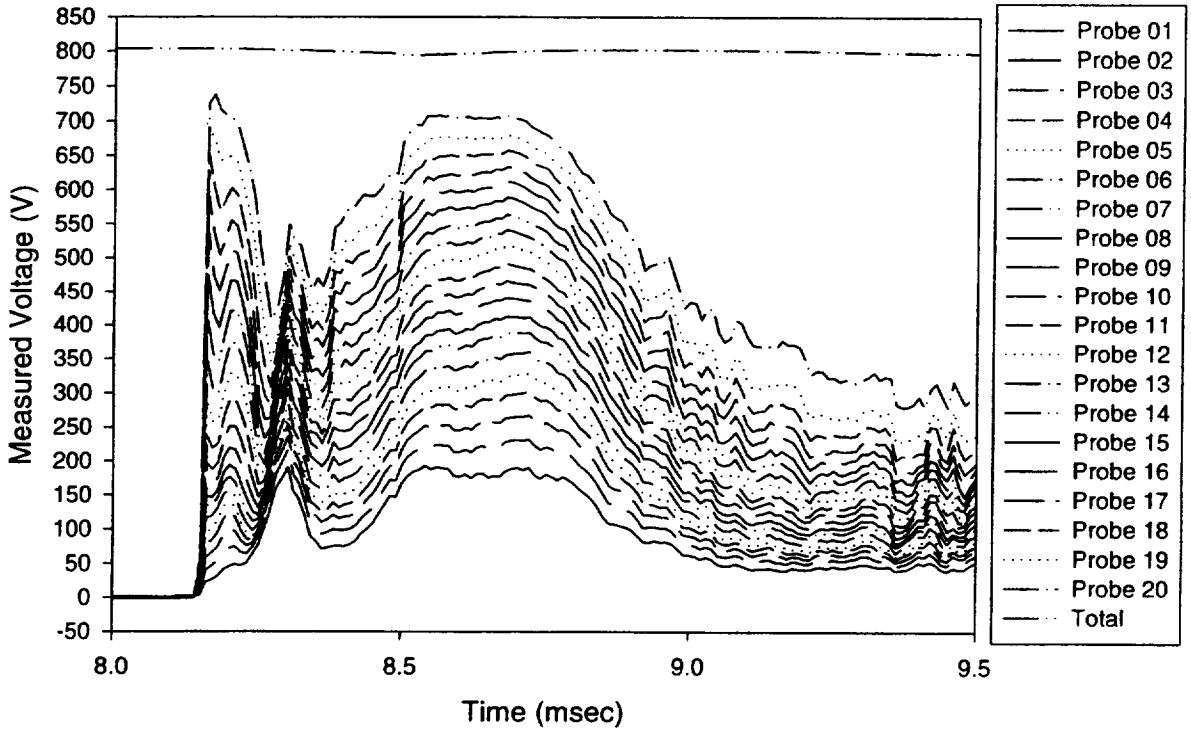

19 B JUNE 1997

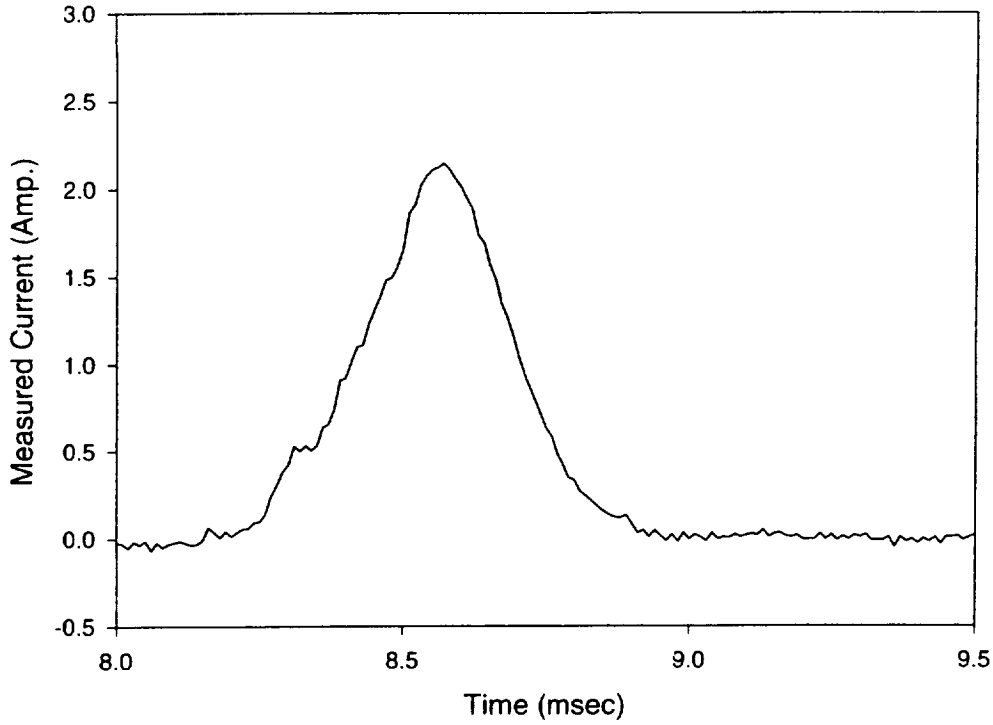

19 B JUNE 1997

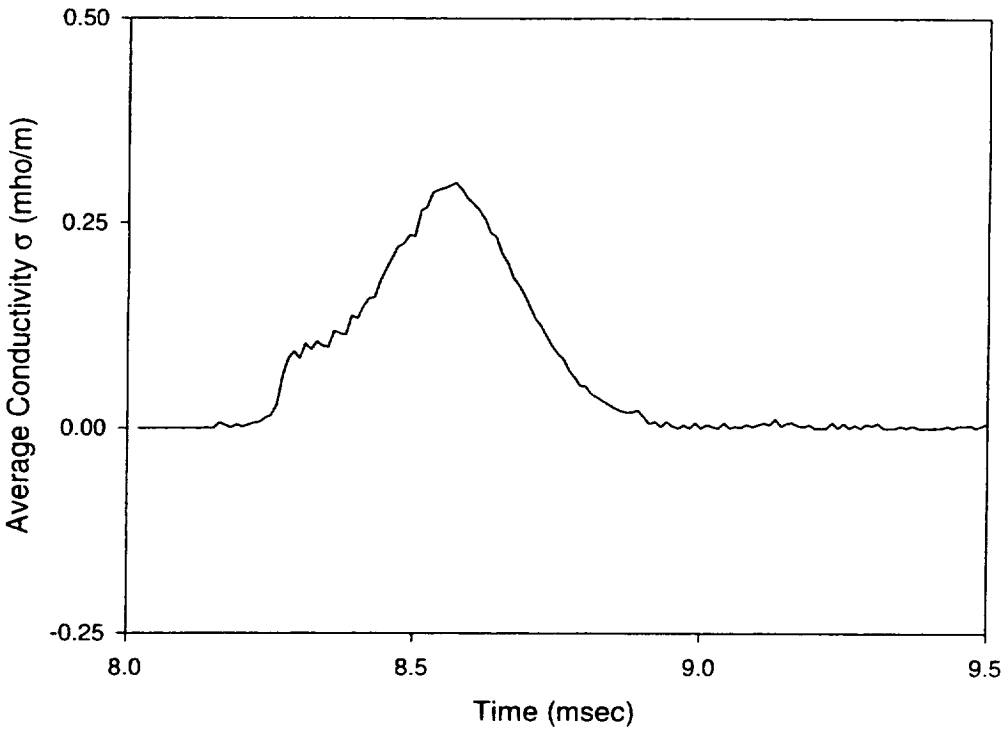

19 B JUNE 1997

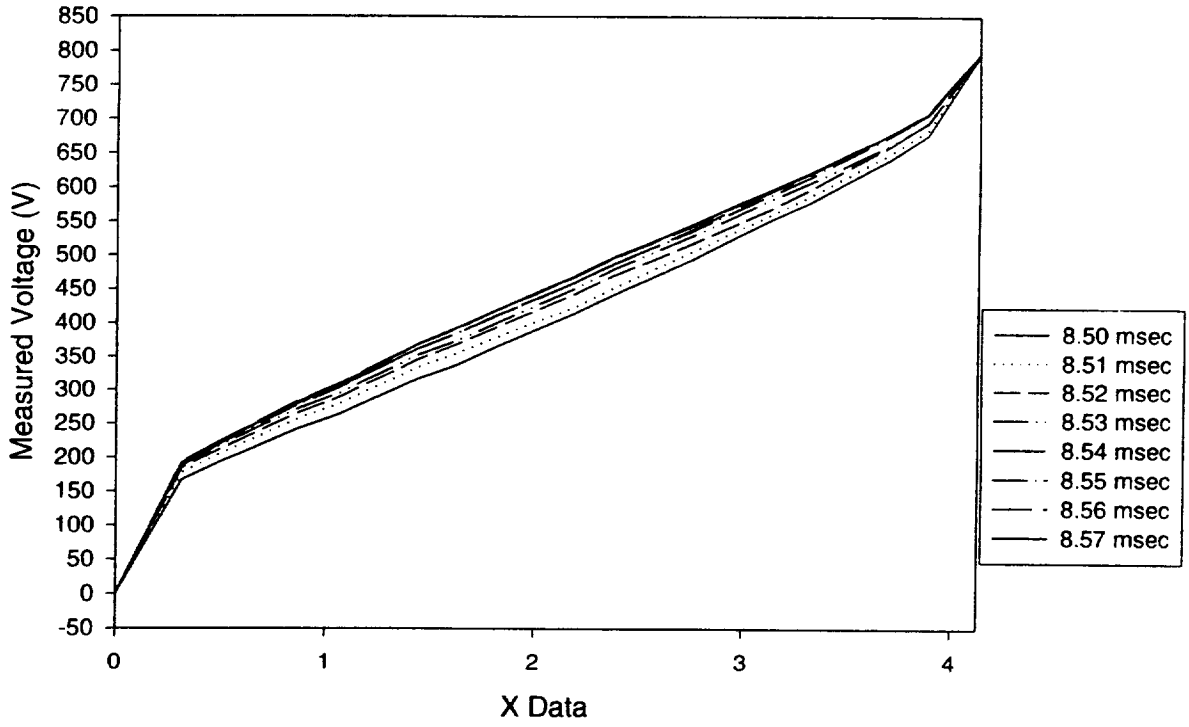

20 A JUNE 1997

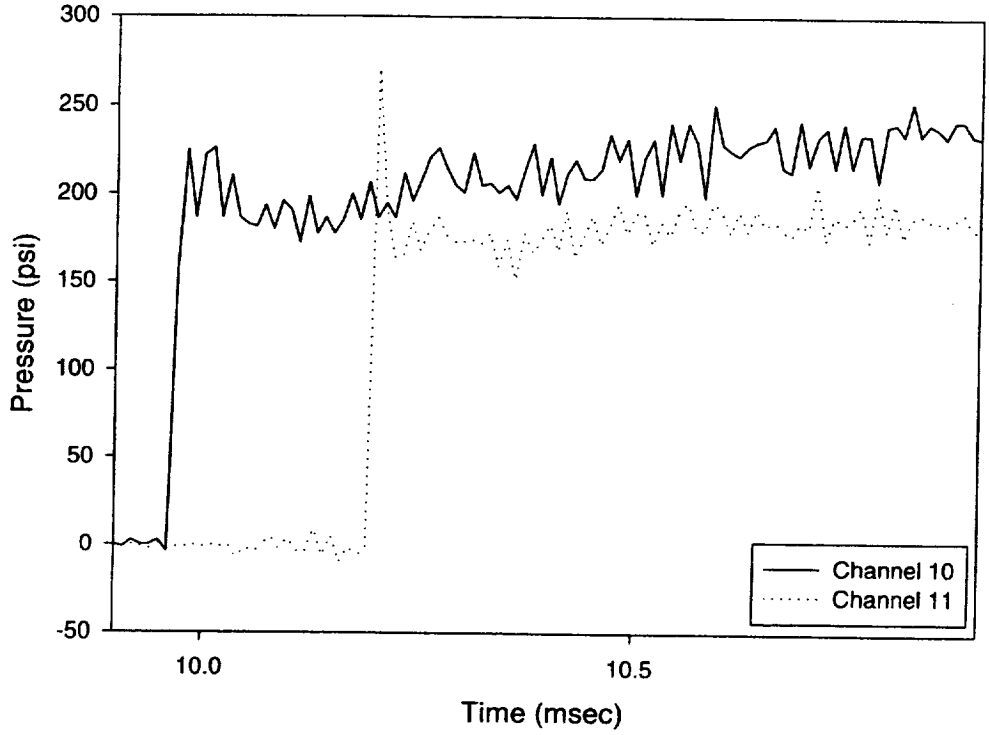

20 A JUNE 1997

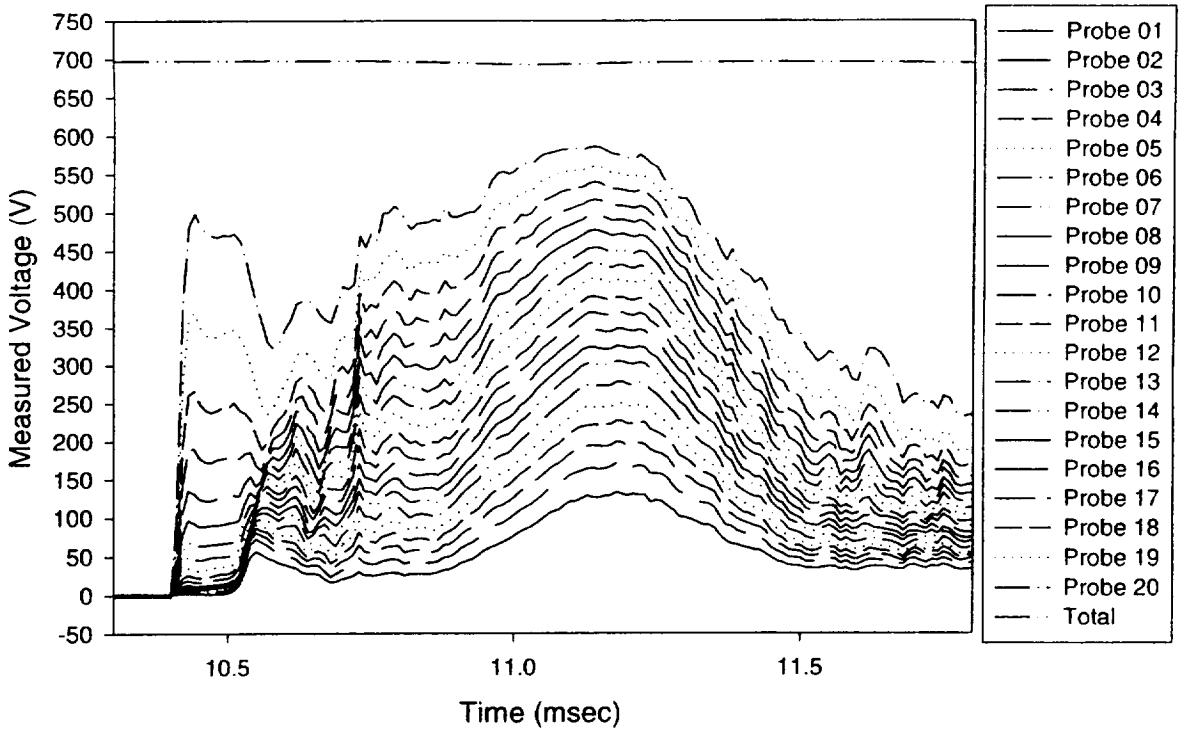

20 A JUNE 1997

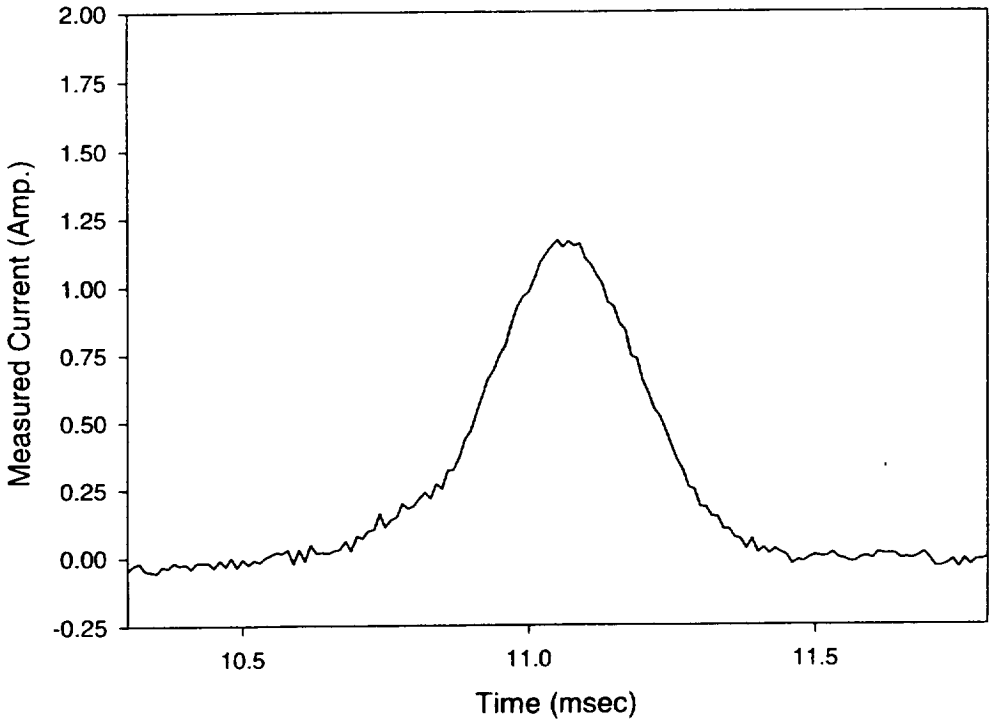

20 A JUNE 1997

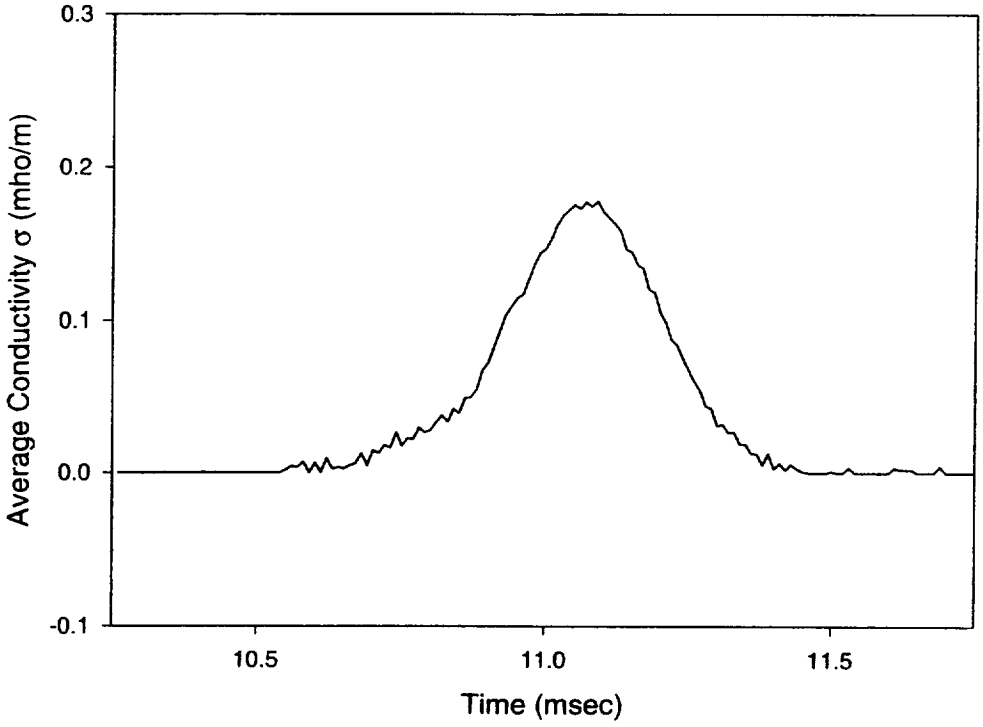

20 A JUNE 1997

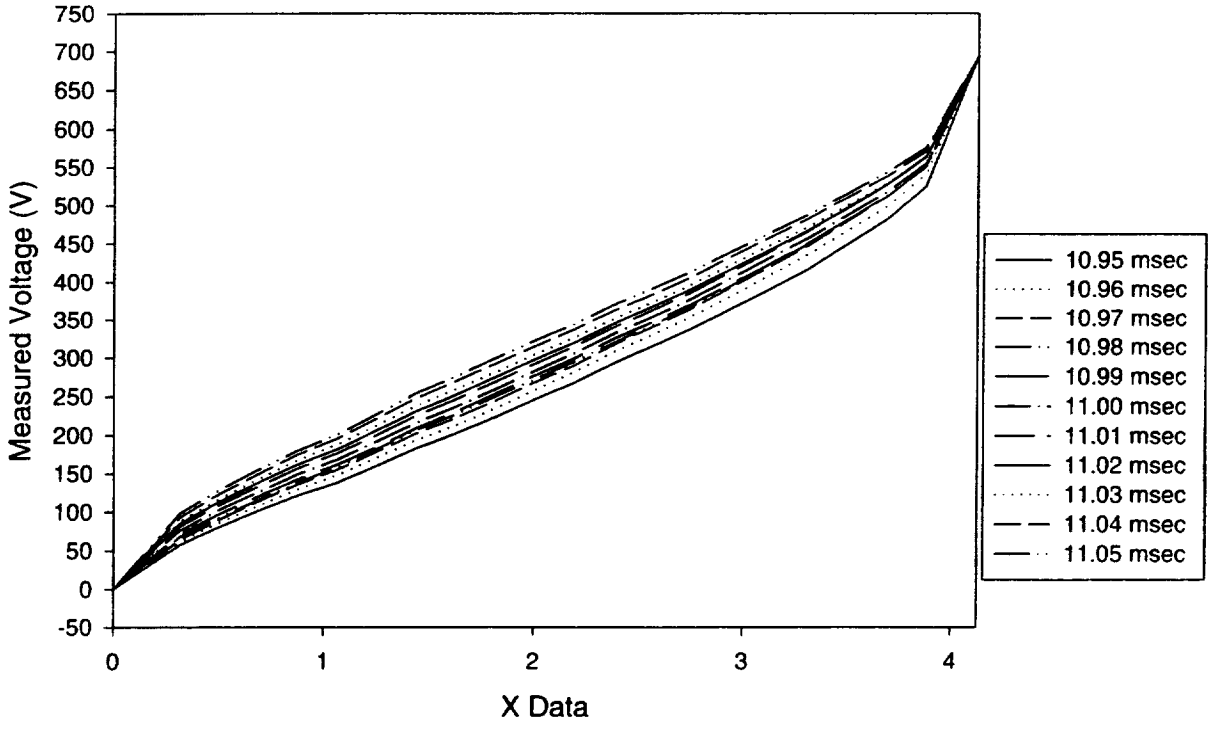

20 B JUNE 1997

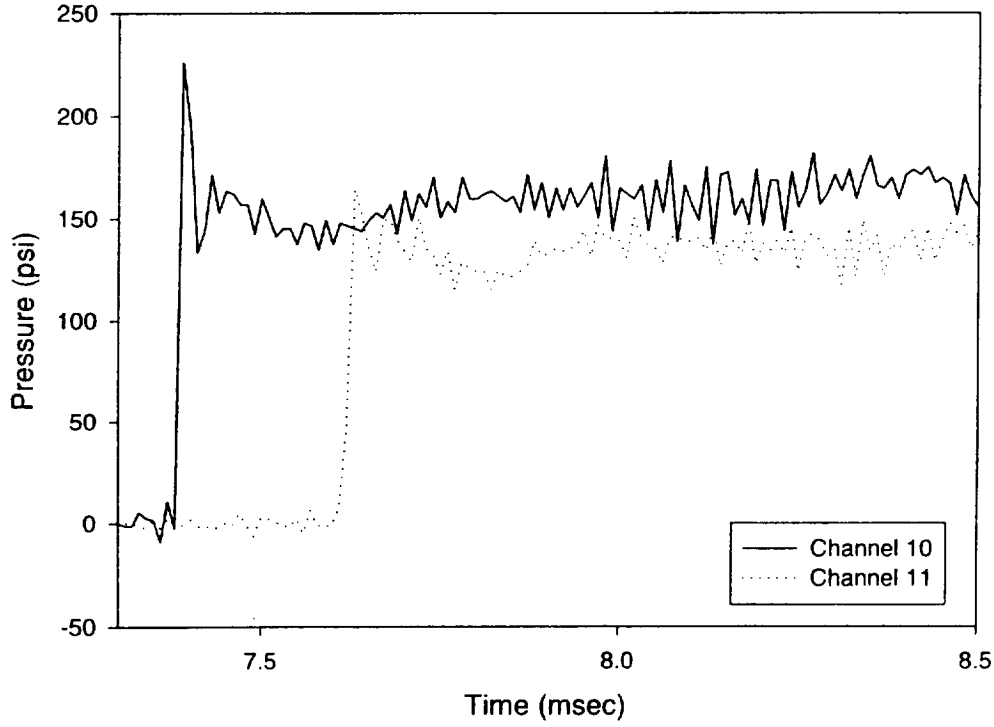

20 B JUNE 1997

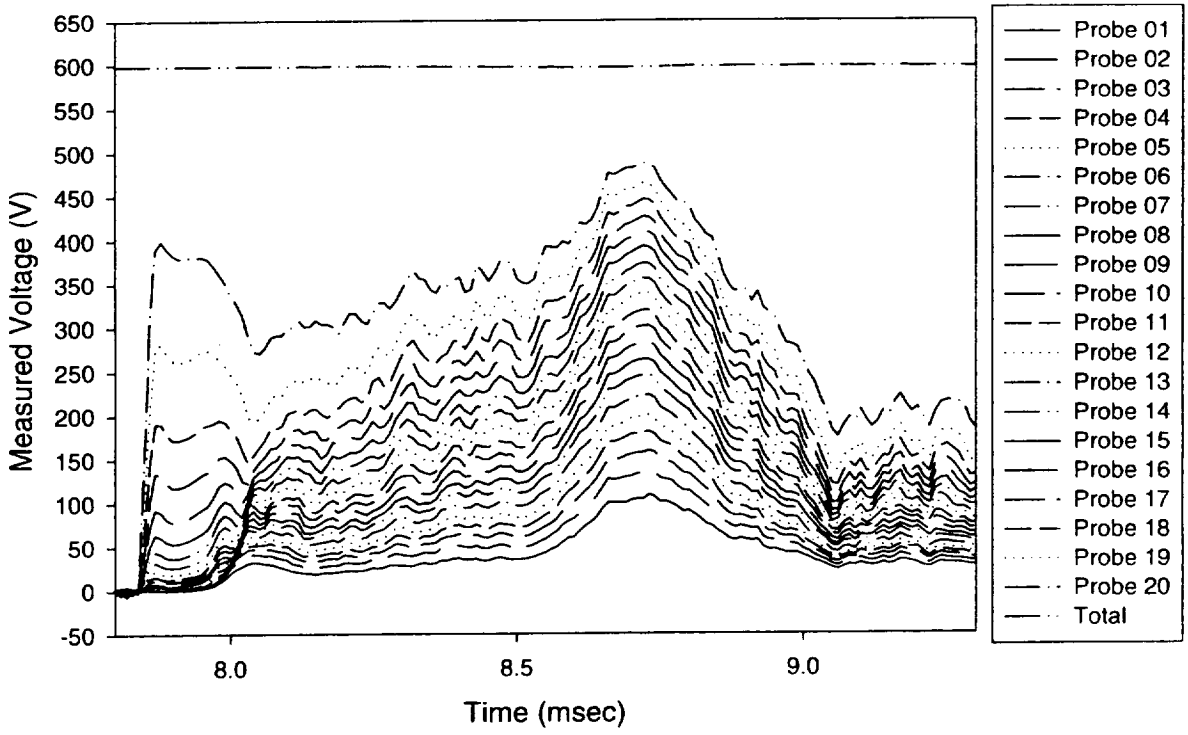

20 B JUNE 1997

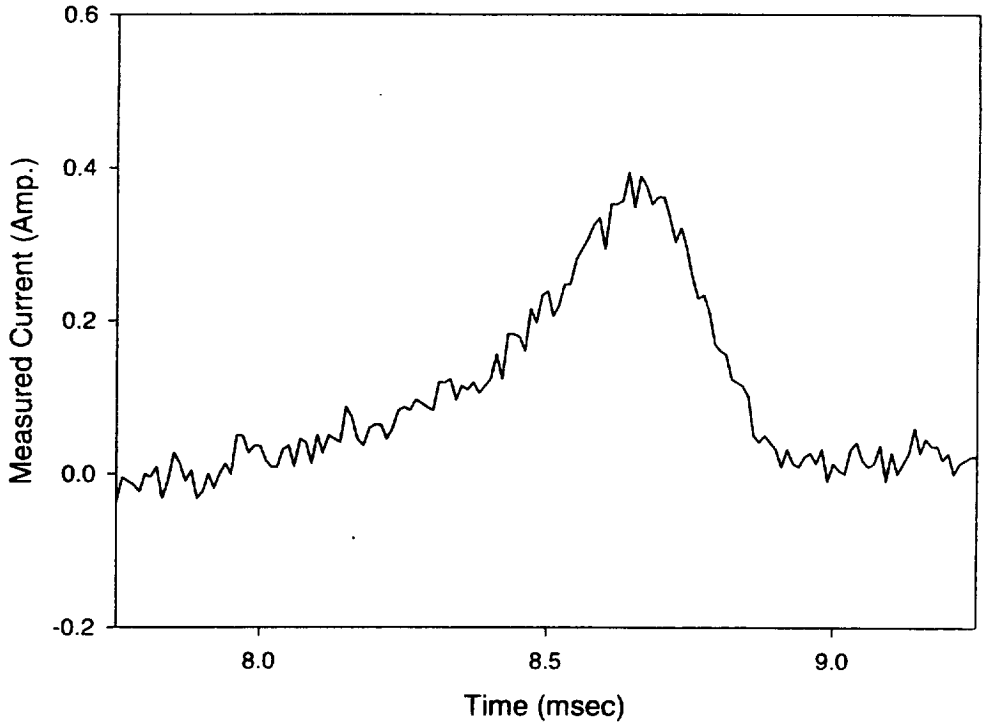

20 B JUNE 1997

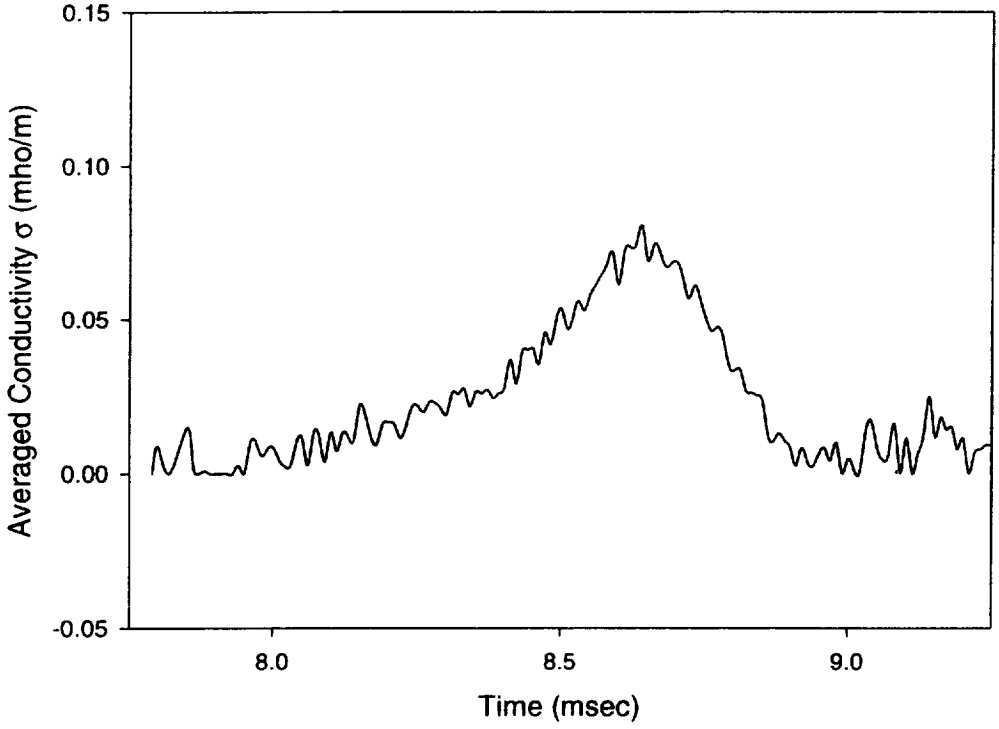

20 B JUNE 1997

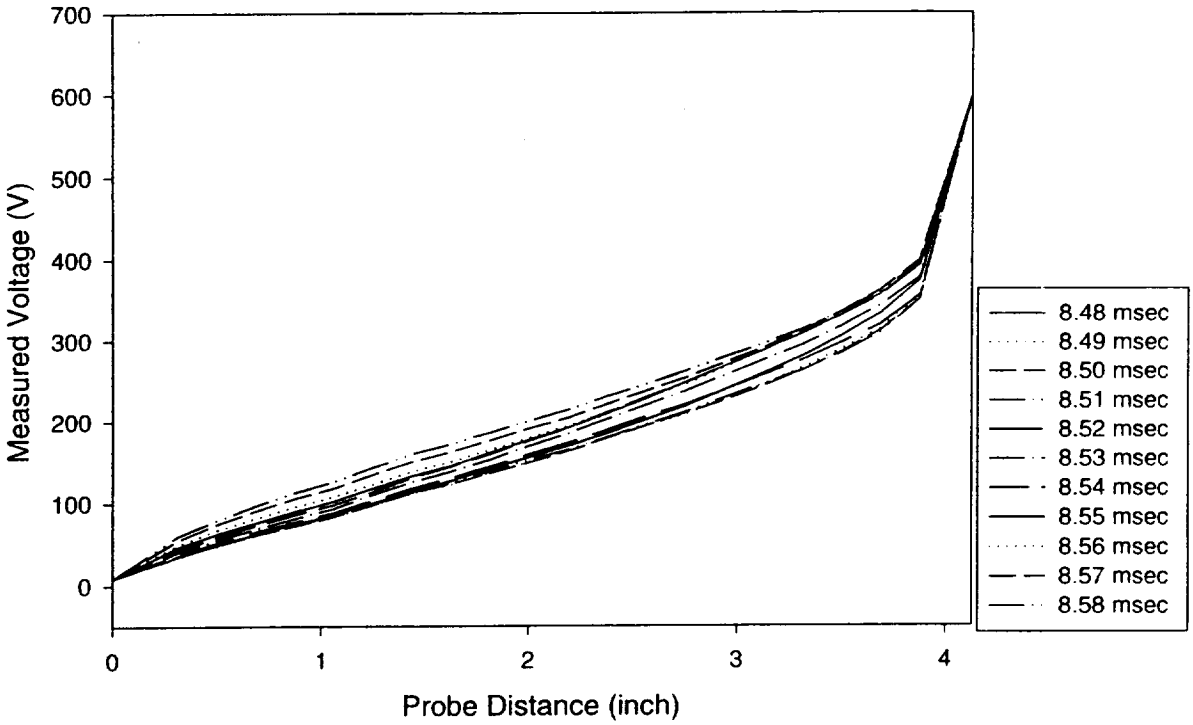

21 A JUNE 1997

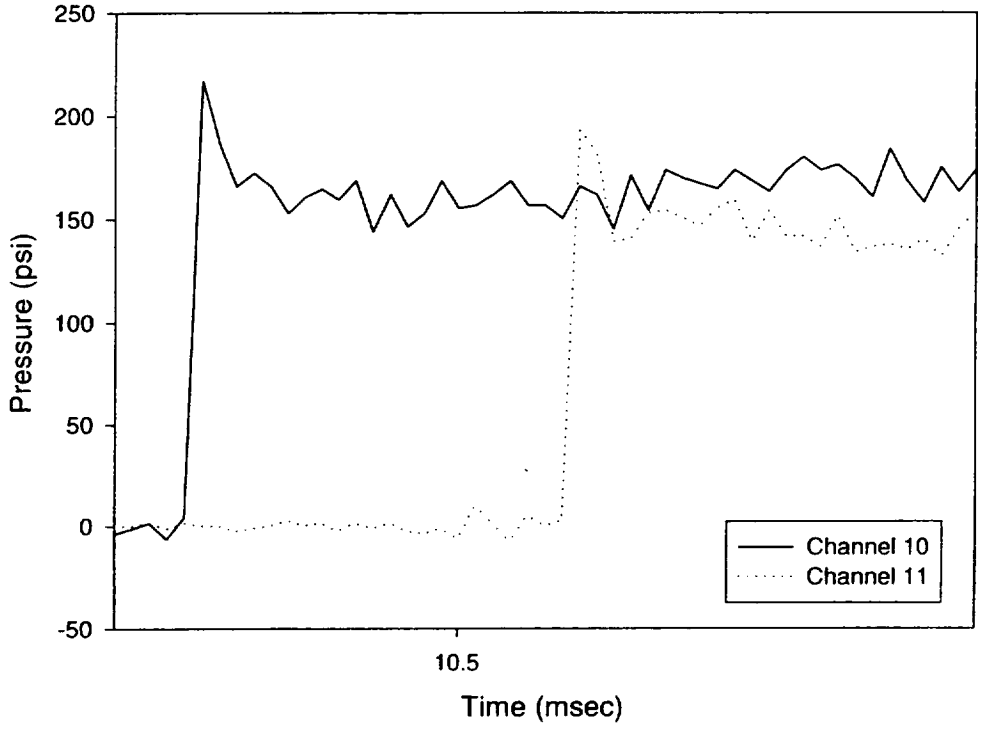

21 A JUNE 1997

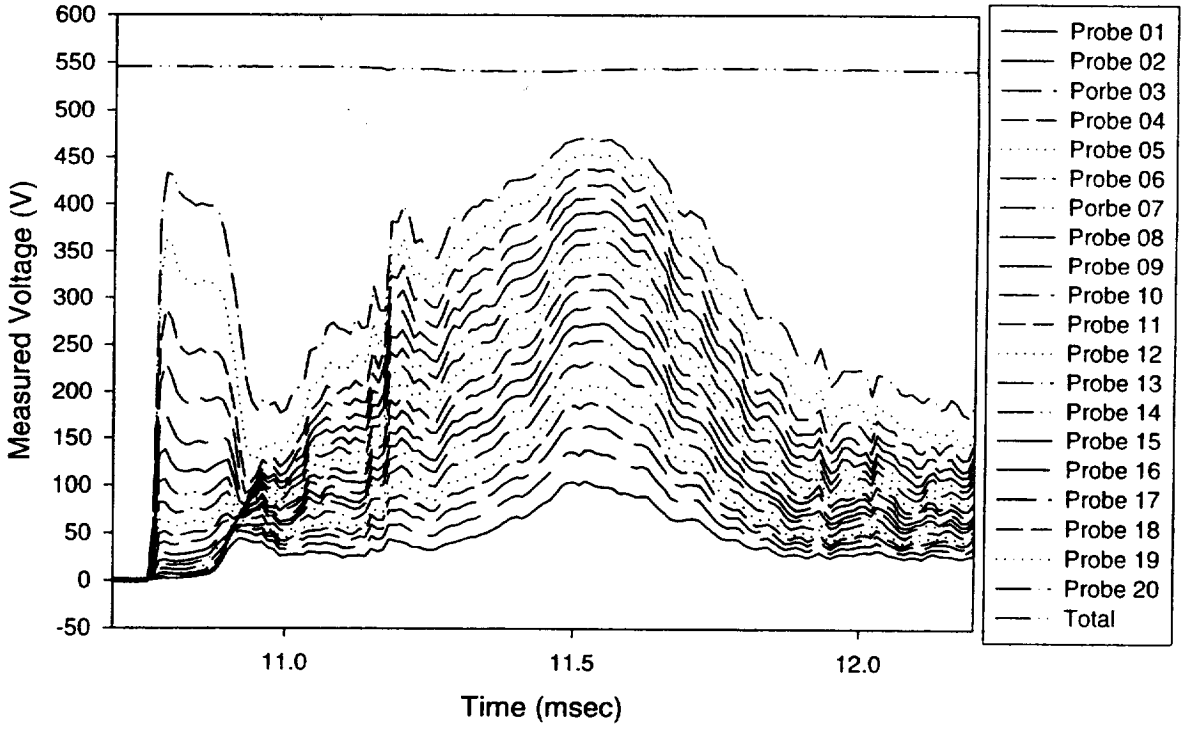

21 A JUNE 1997

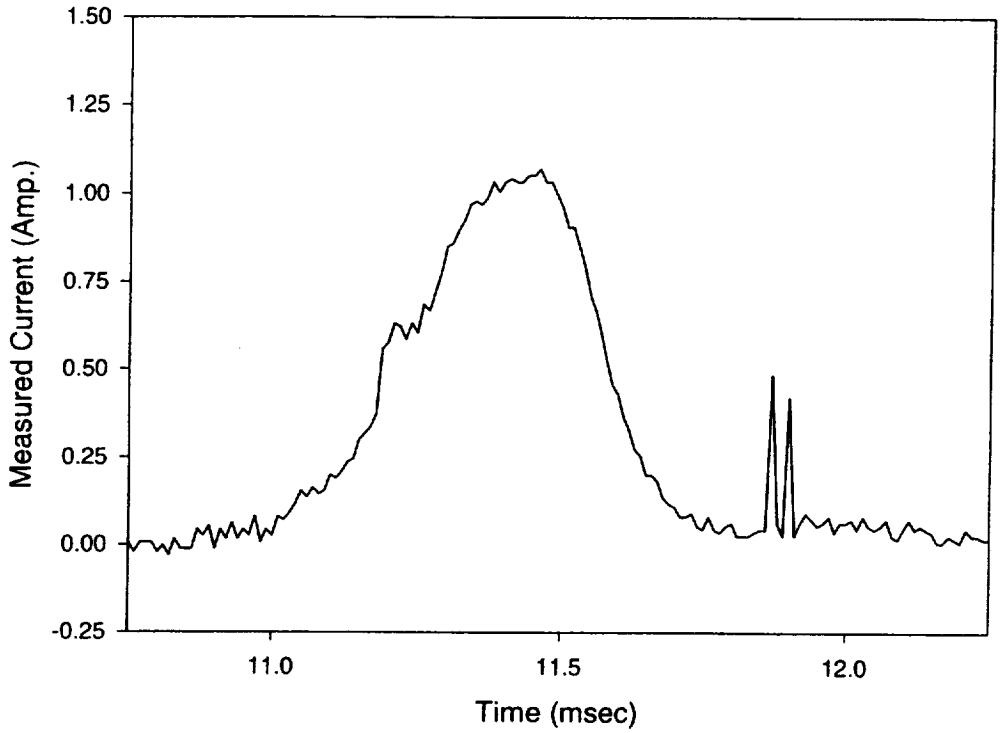

21 A JUNE 1997

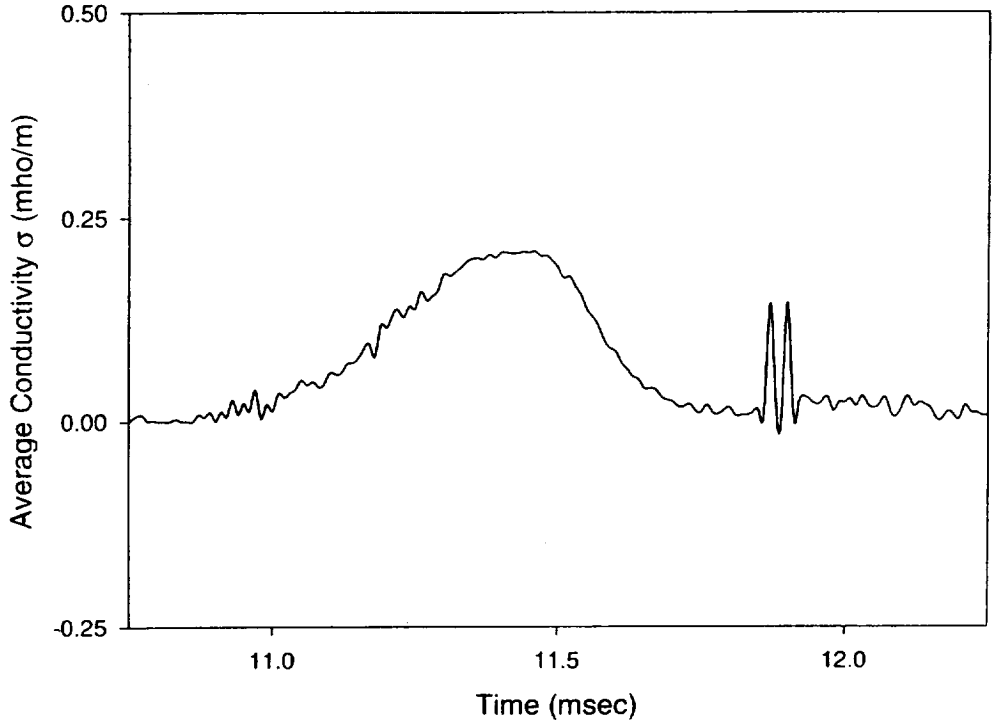

21 A JUNE 1997

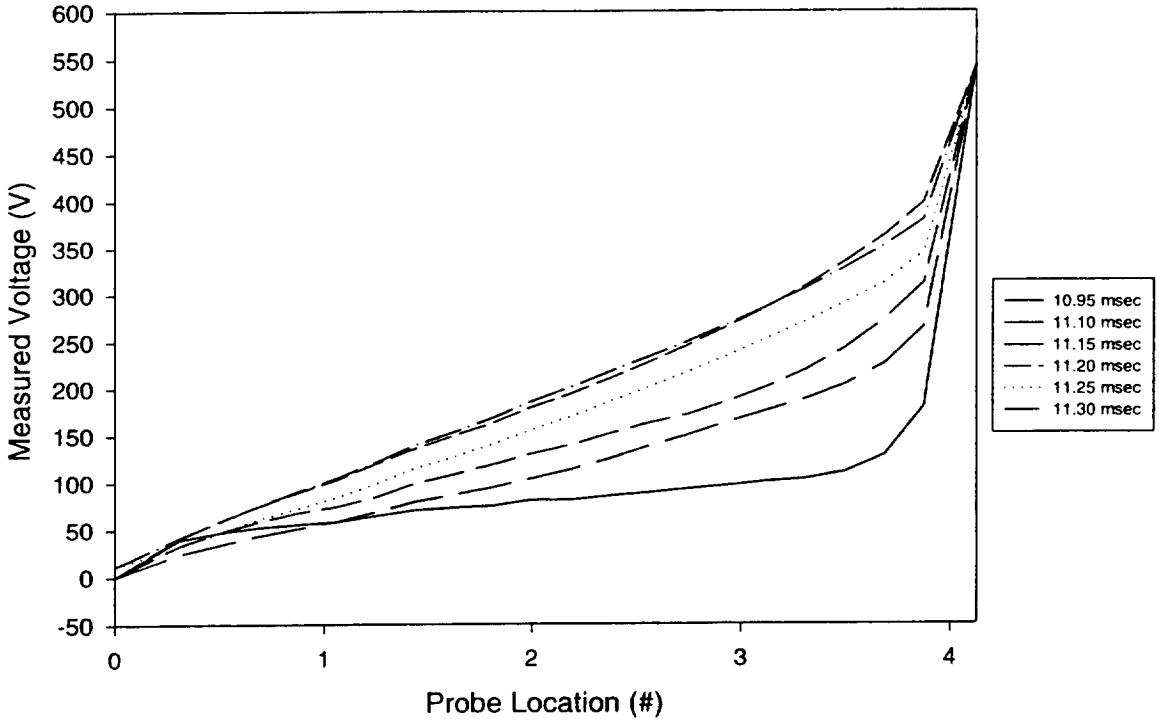

21 B JUNE 1997

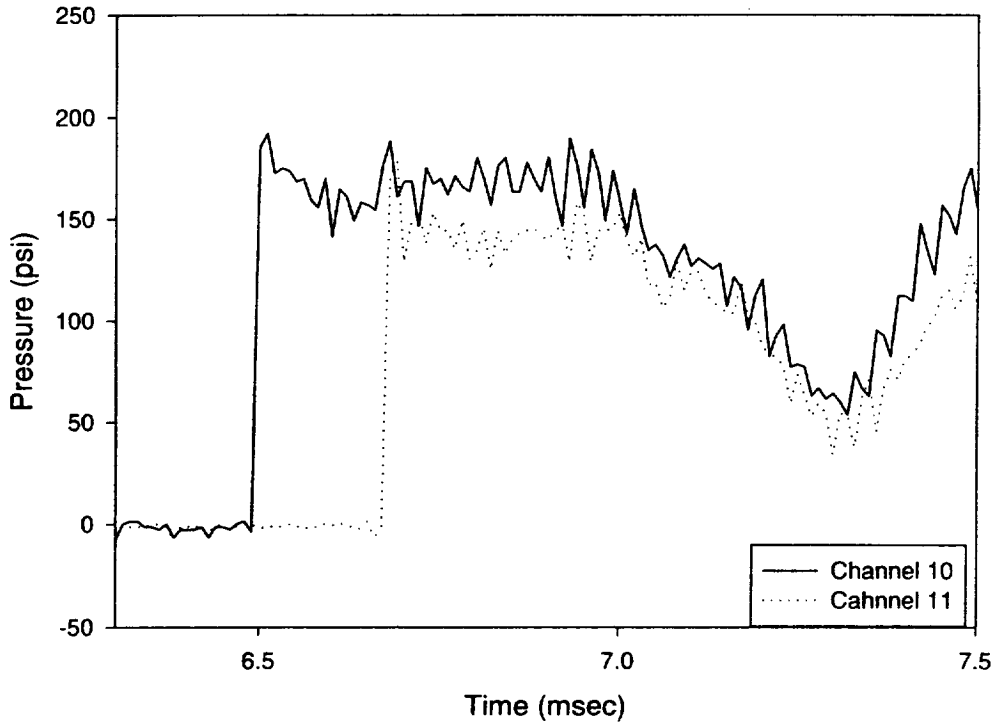

21 B JUNE 1997

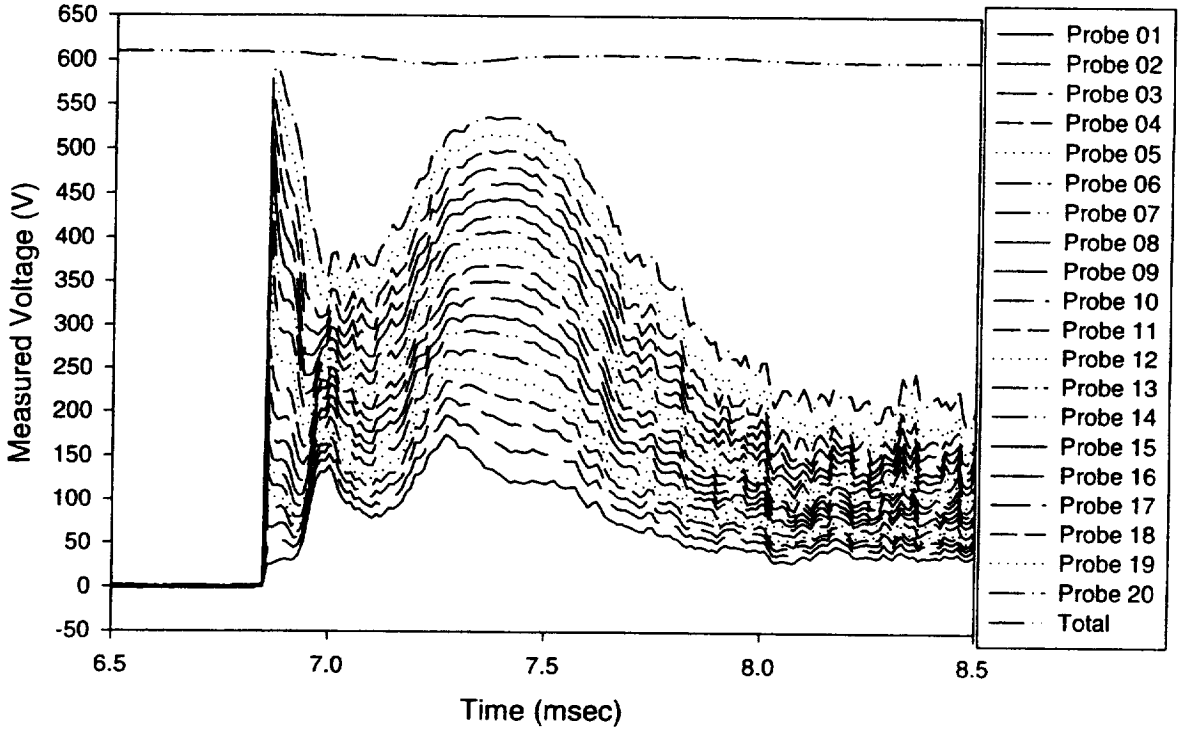

21 B JUNE 1997

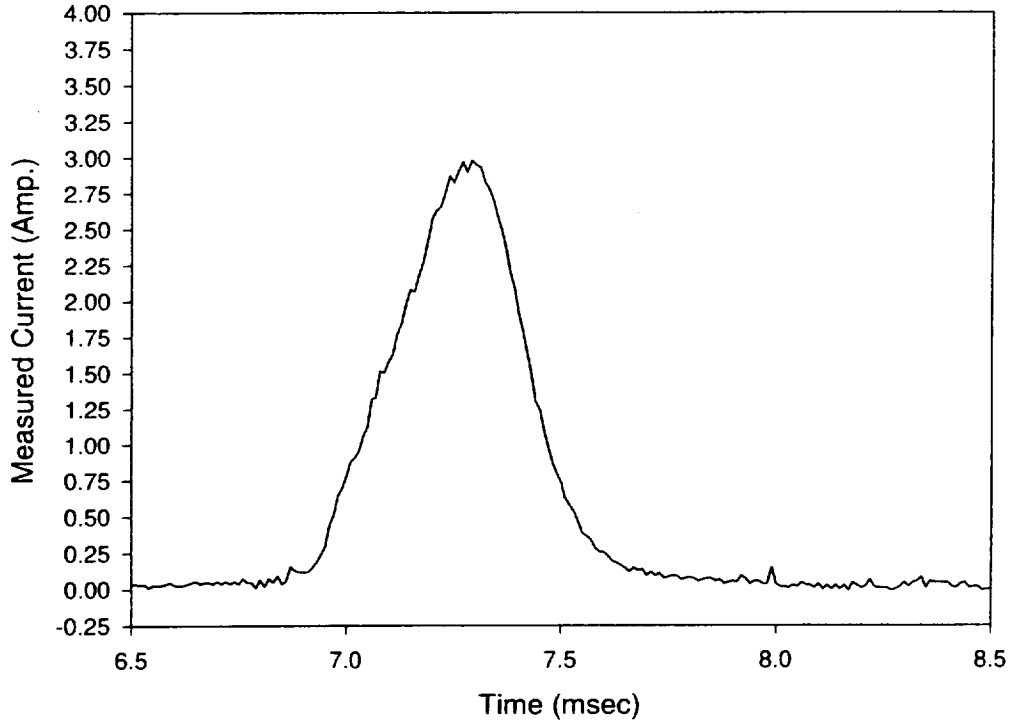

21 B JUNE 1997

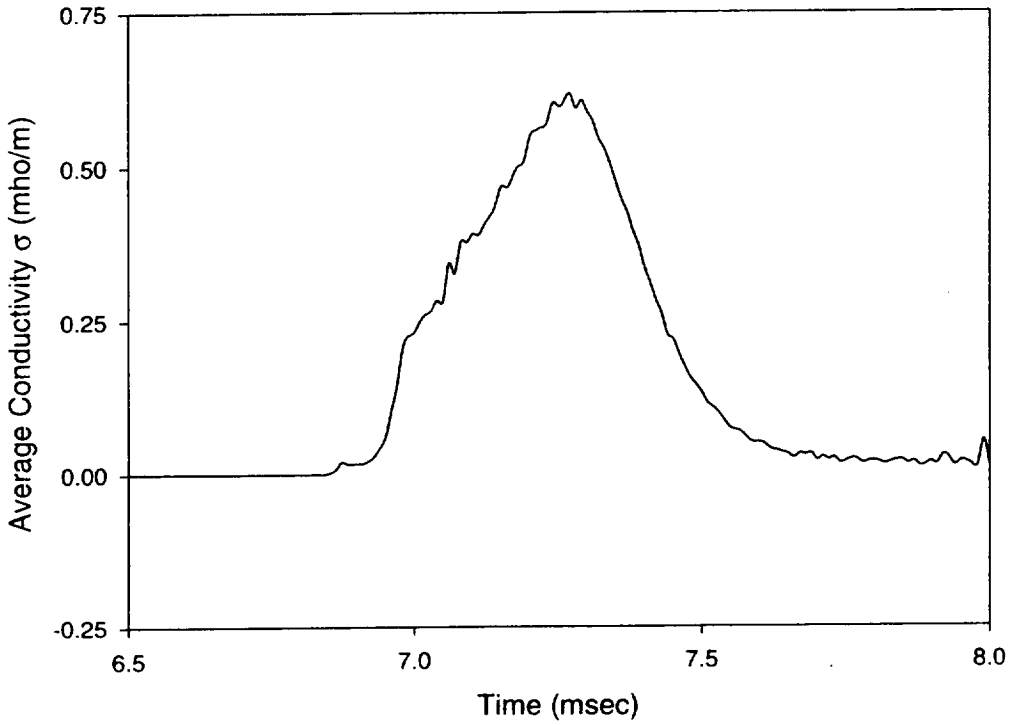

21 B JUNE 1997

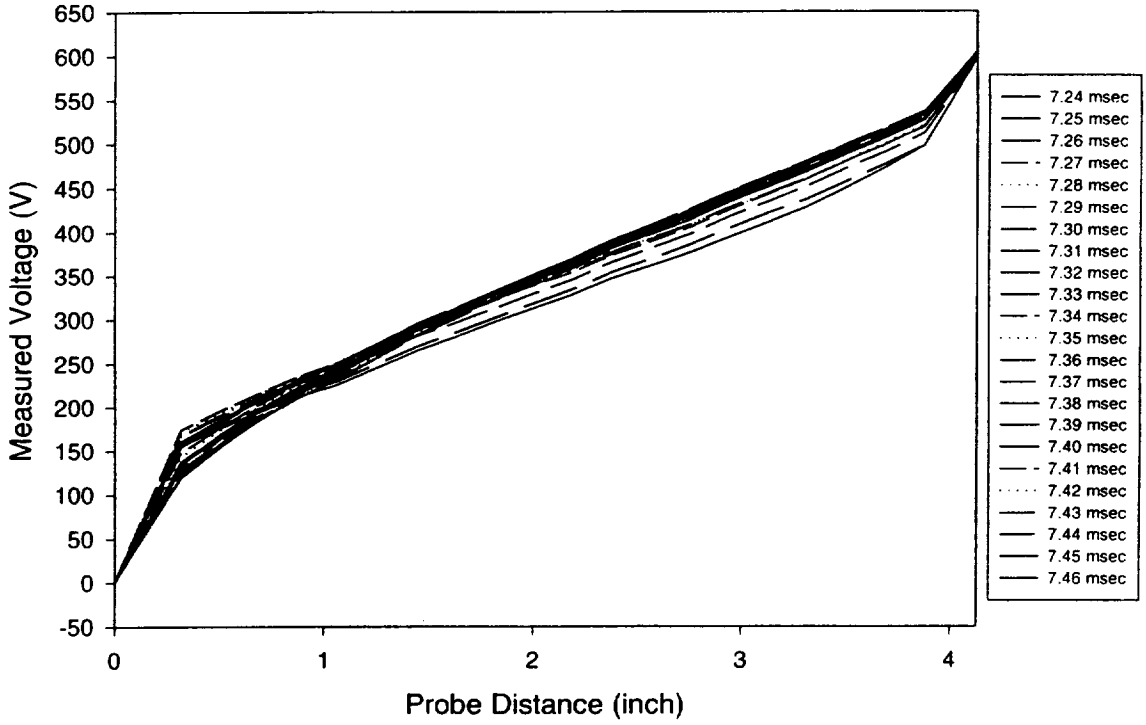

21 C JUNE 1997

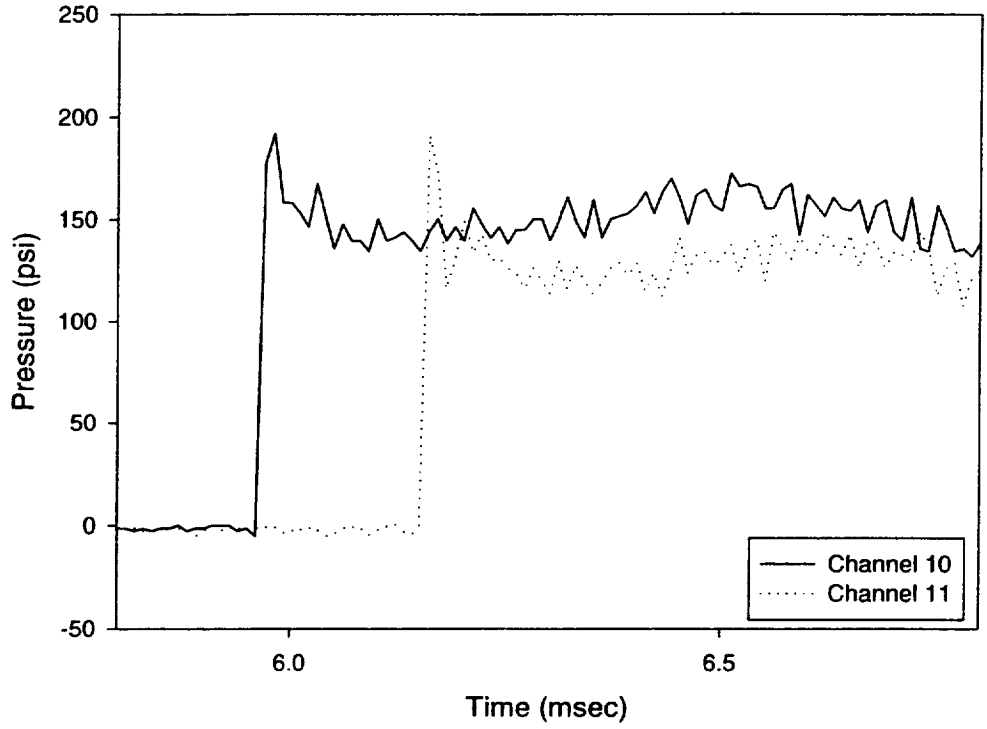

21 C JUNE 1997

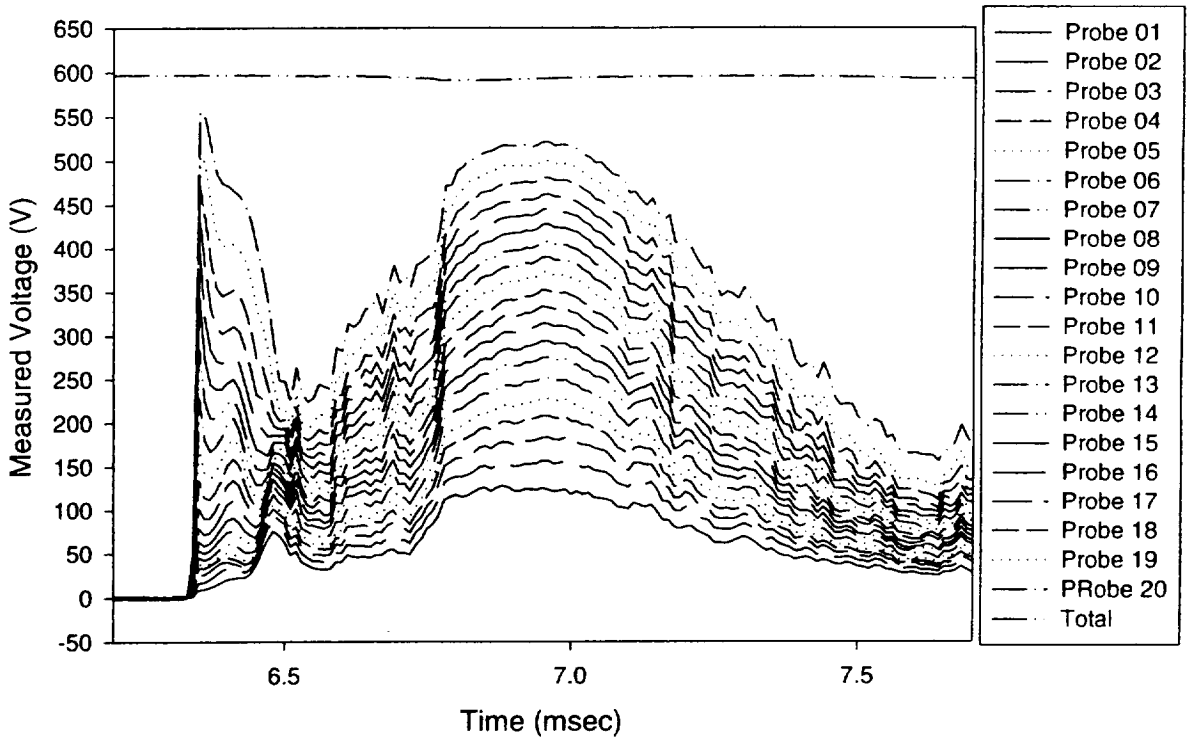

21 C JUNE 1997

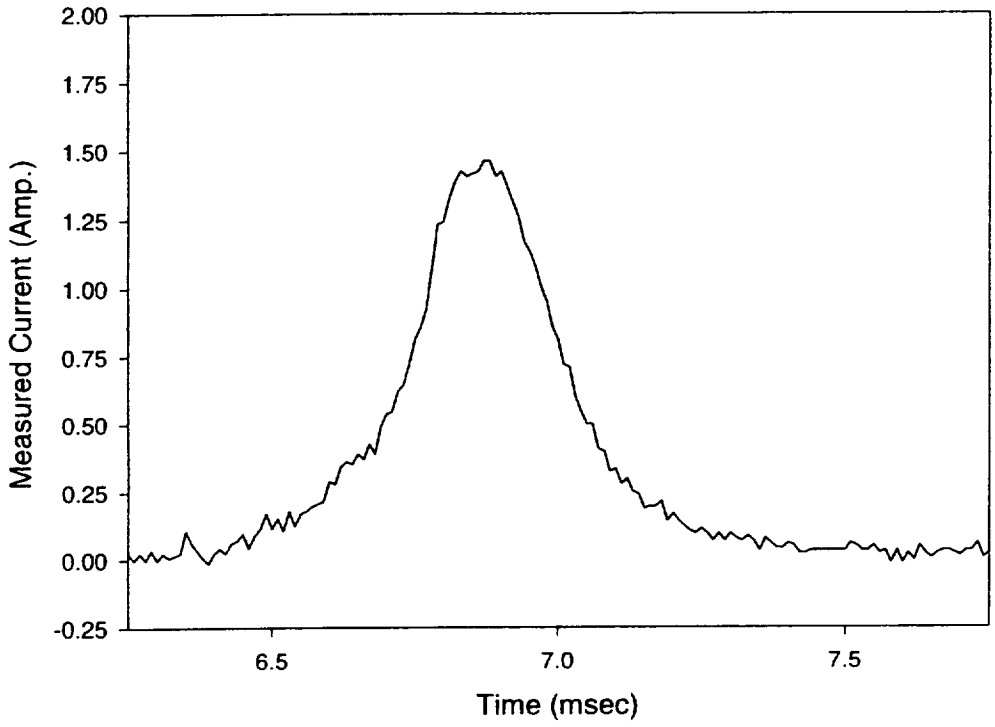

21 C JUNE 1997

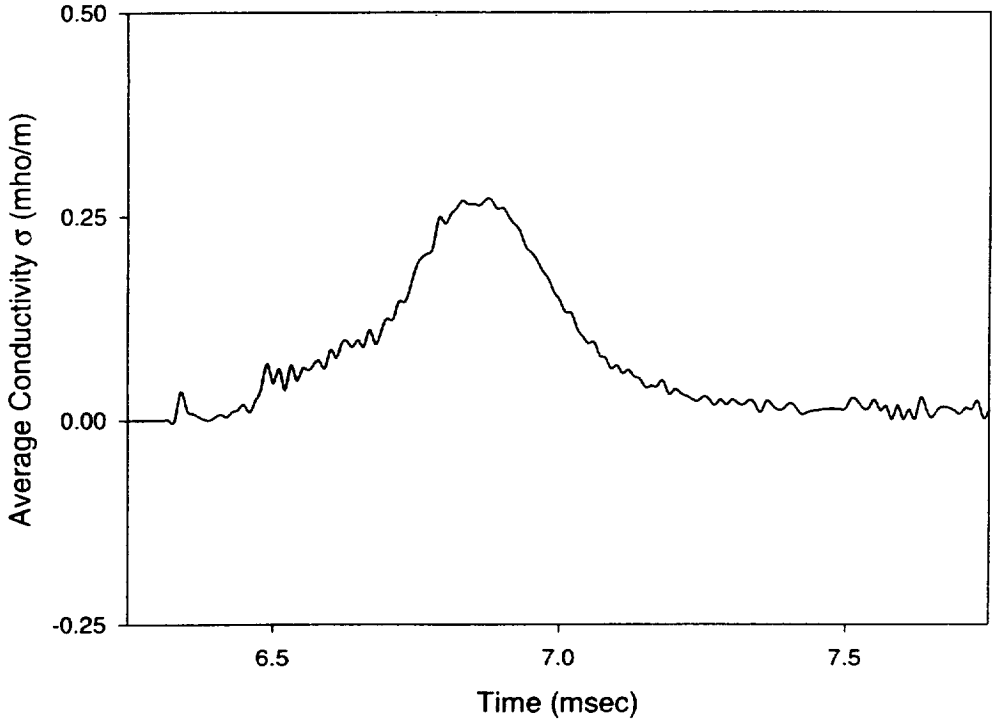

21 C JUNE 1997

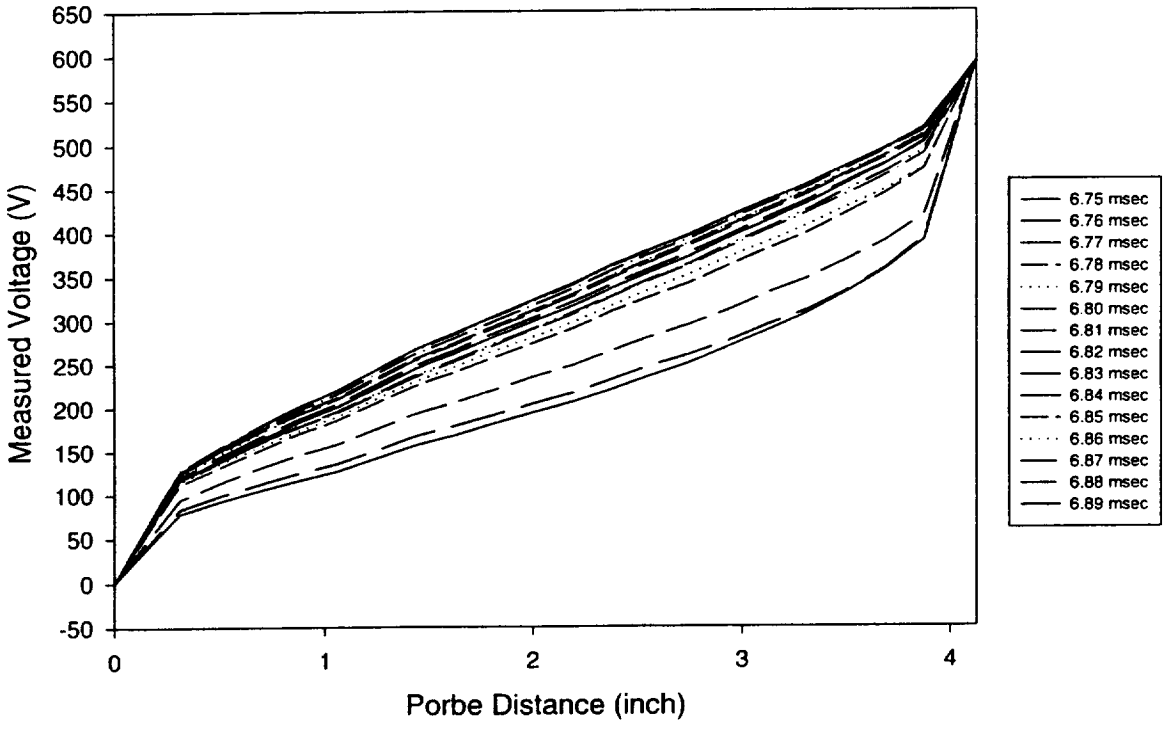

21 D JUNE 1997

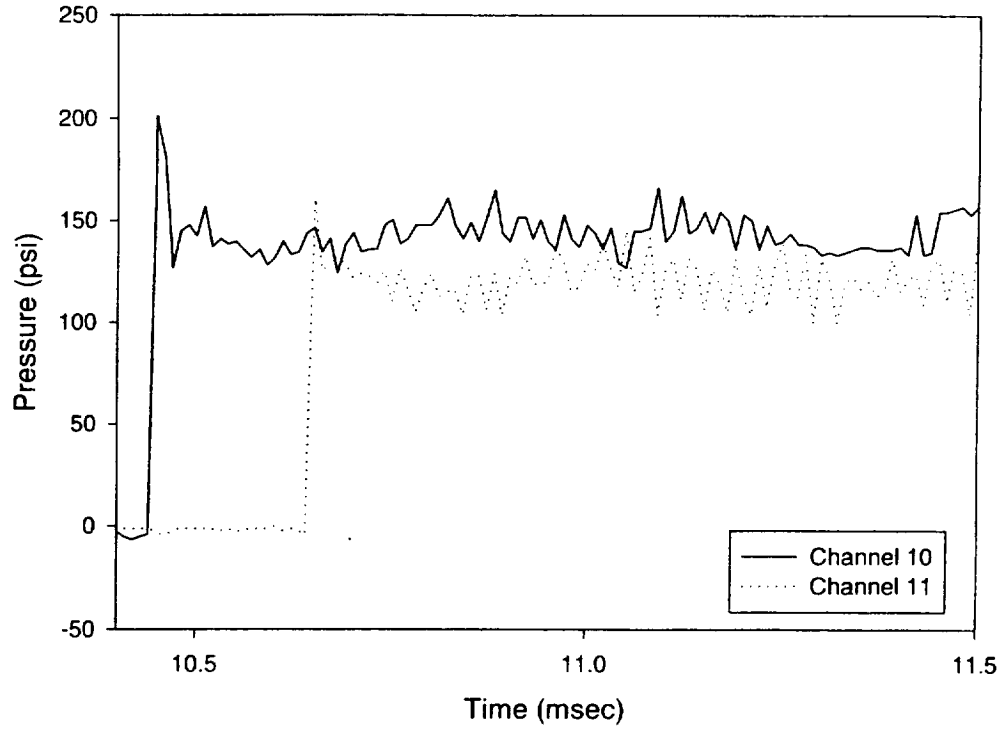

21 D JUNE 1997

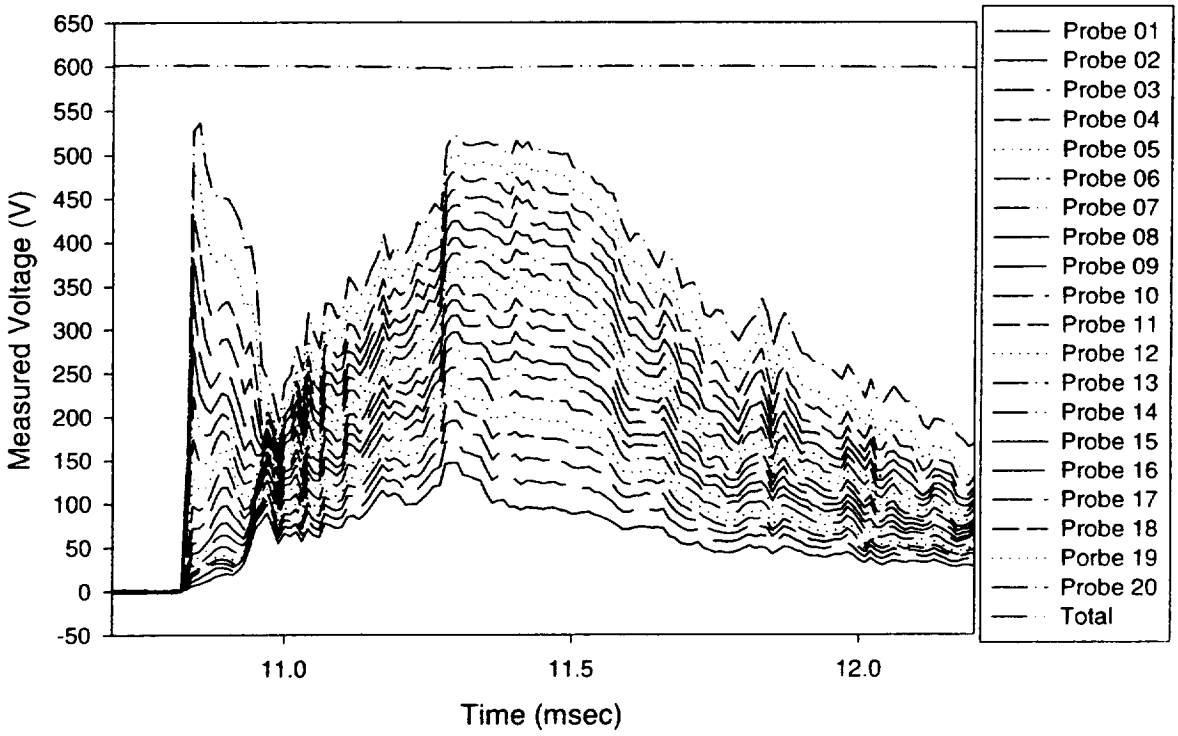

21 D JUNE 1997

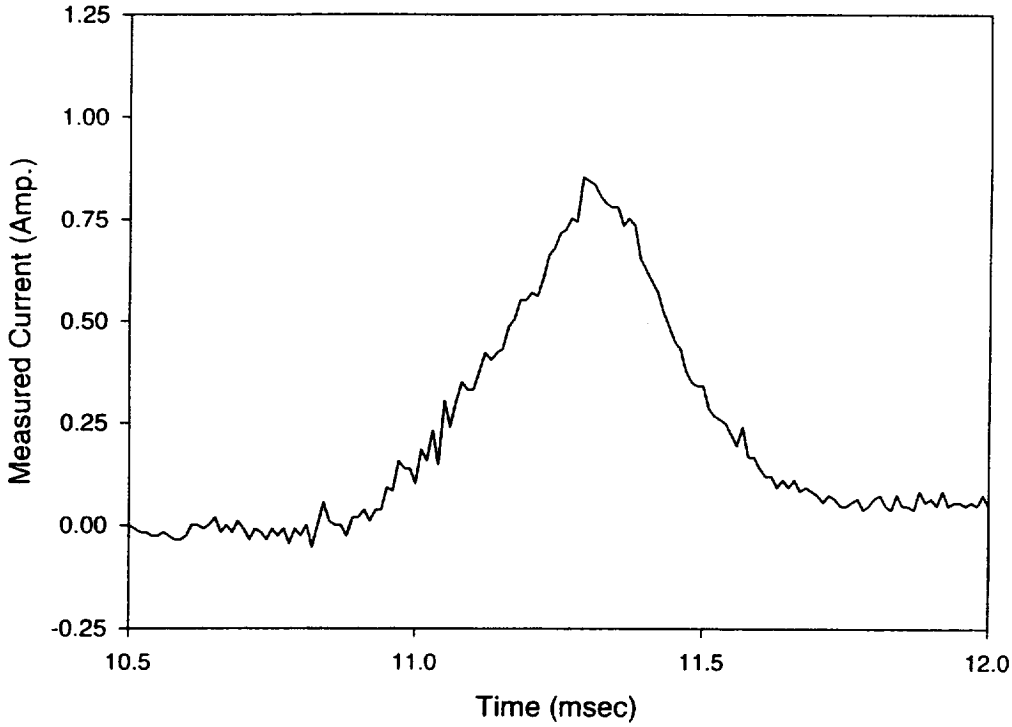

21 D JUNE 1997

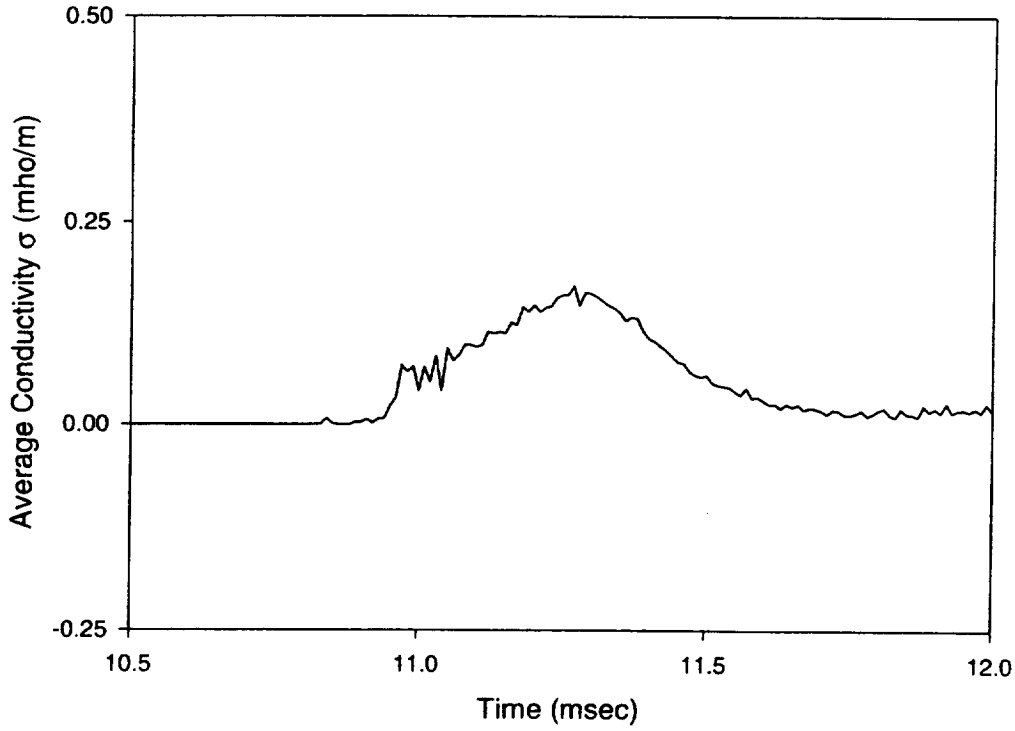

21 D JUNE 1997

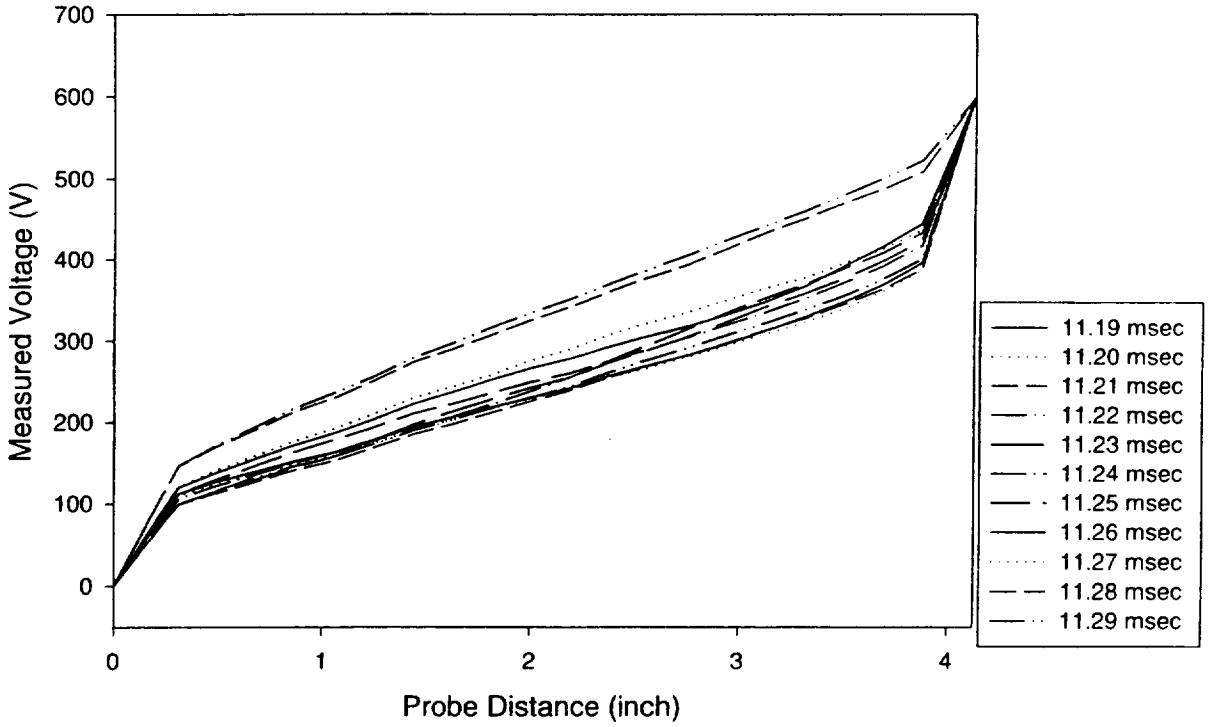

21 E JUNE 1997

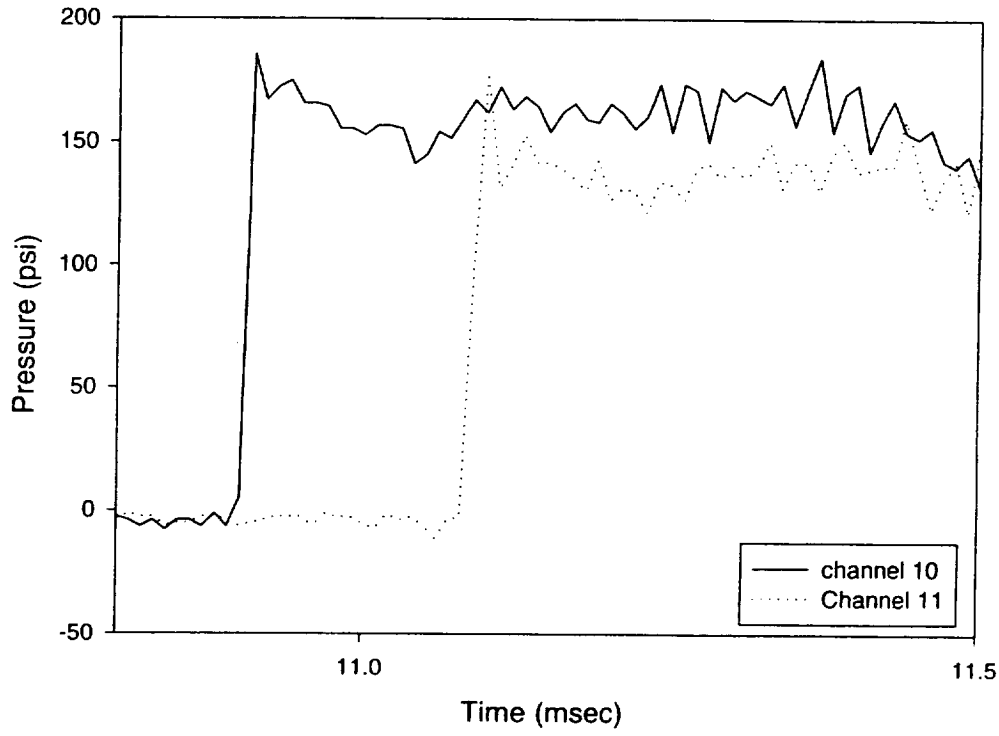

21 E JUNE 1997

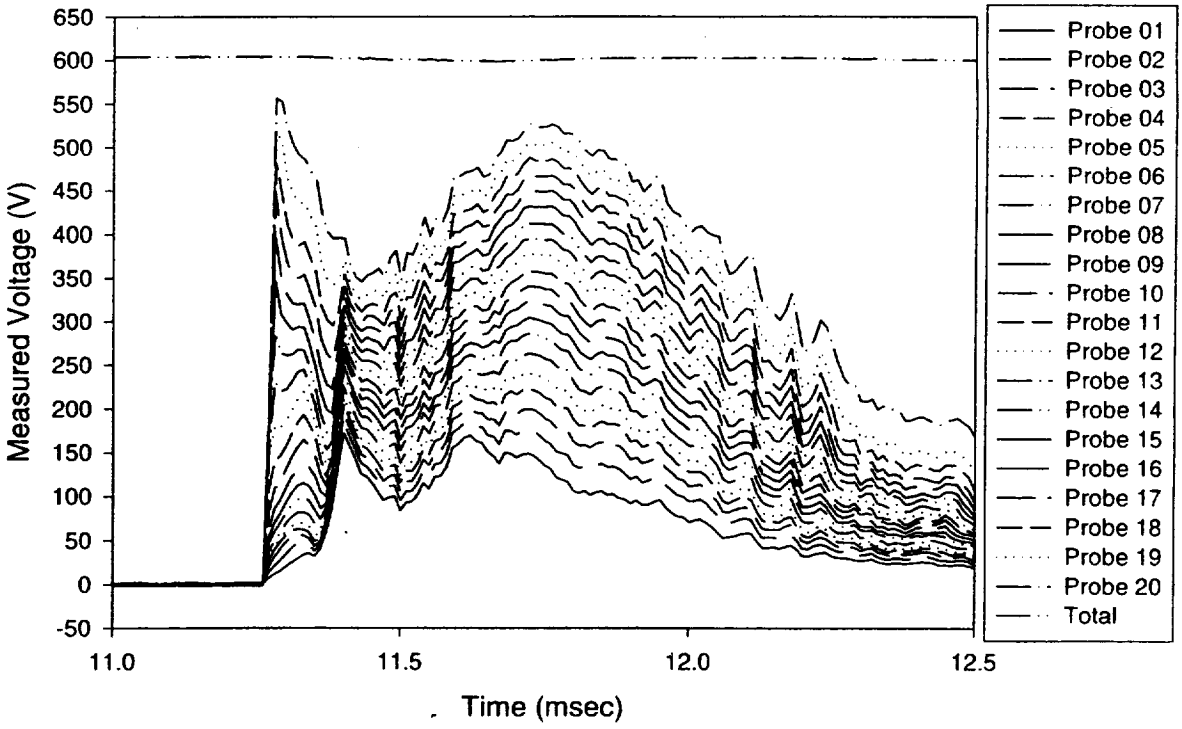

21 E JUNE 1997

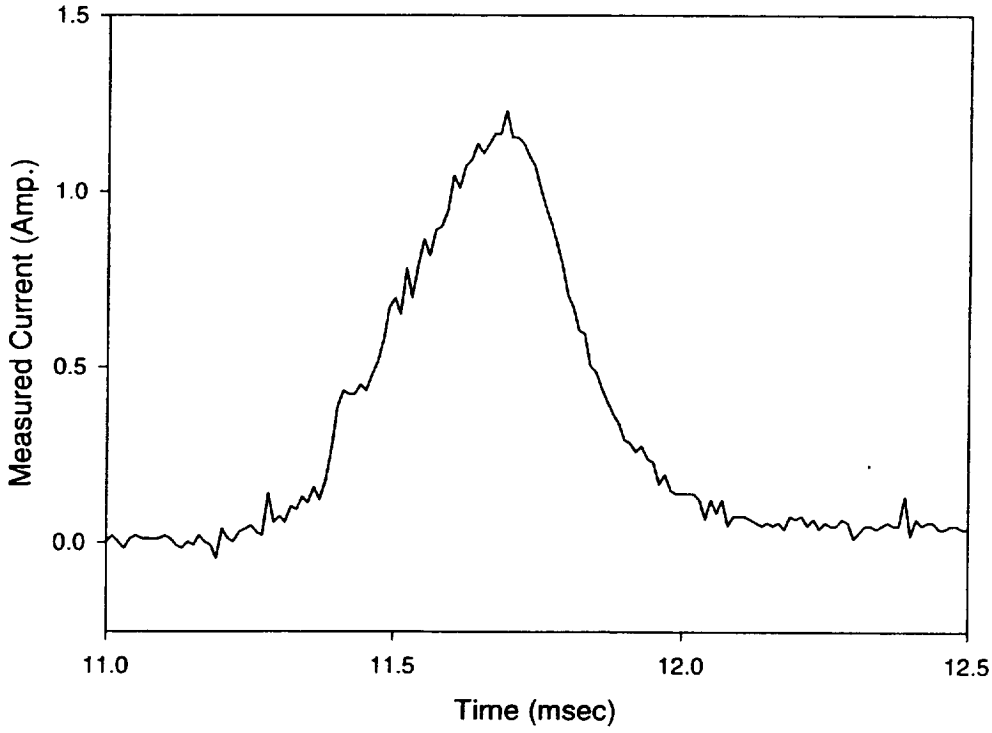

21 E JUNE 1997

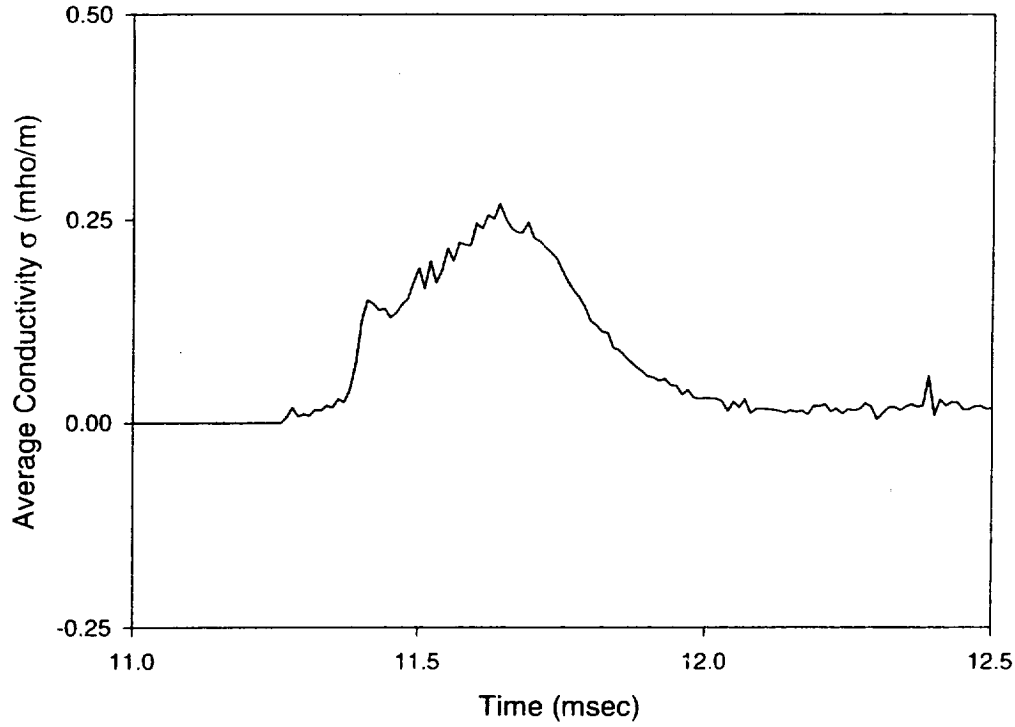

21 E JUNE 1997

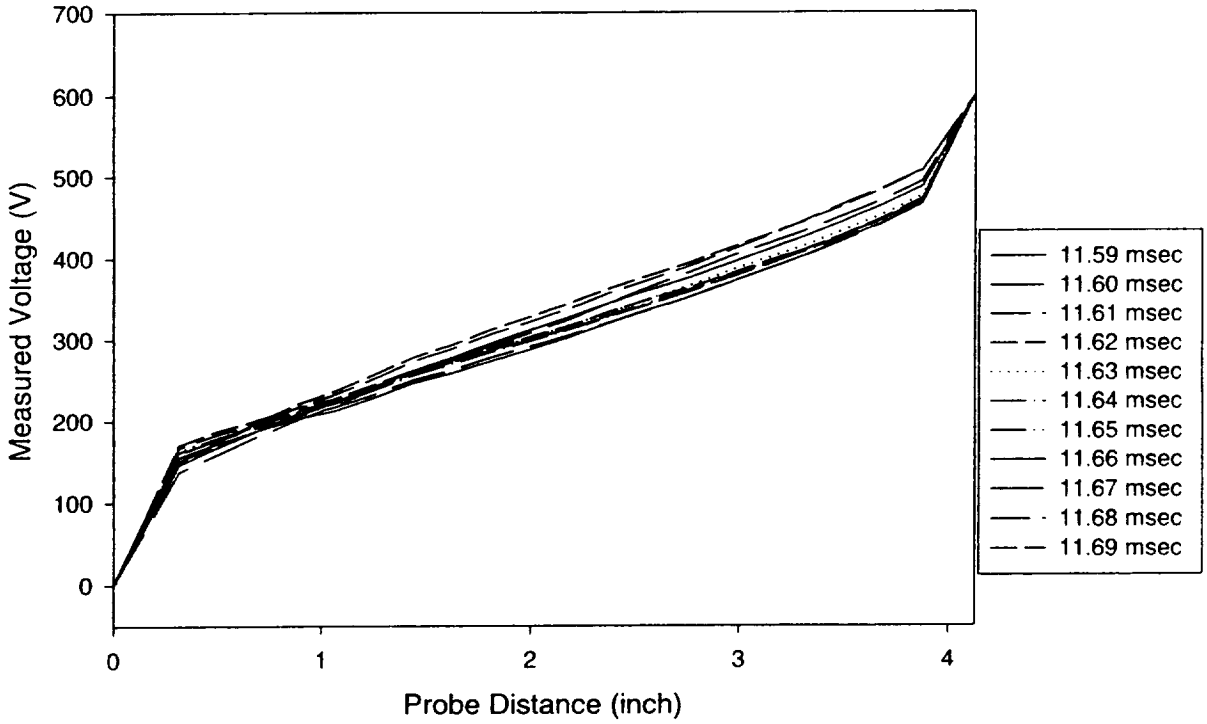

24 A JUNE 1997

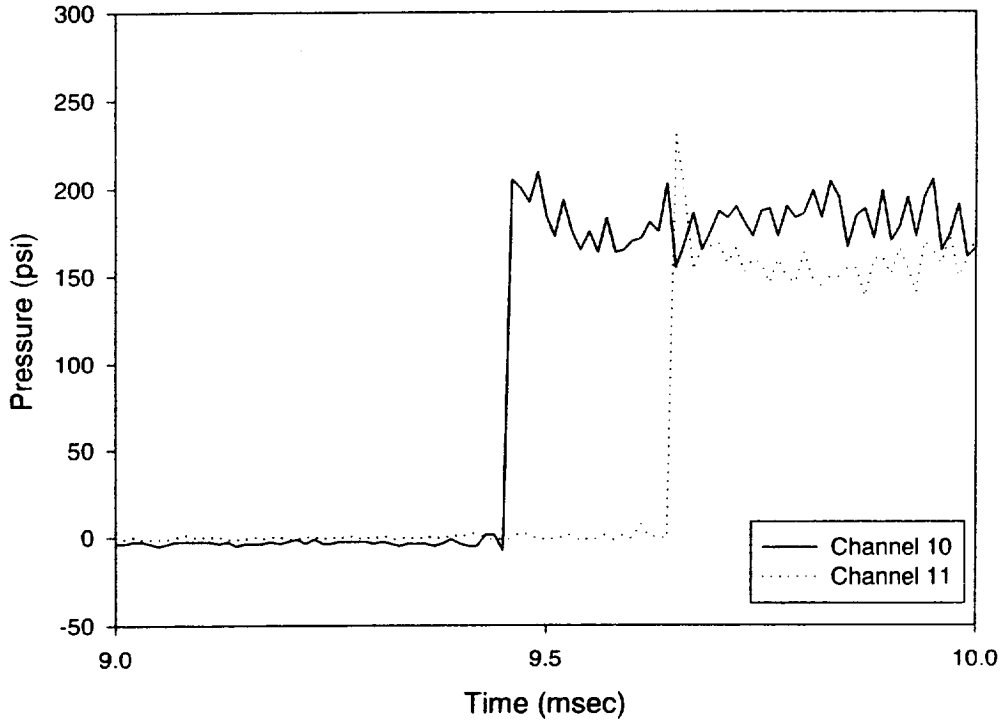

24 A JUNE 1997

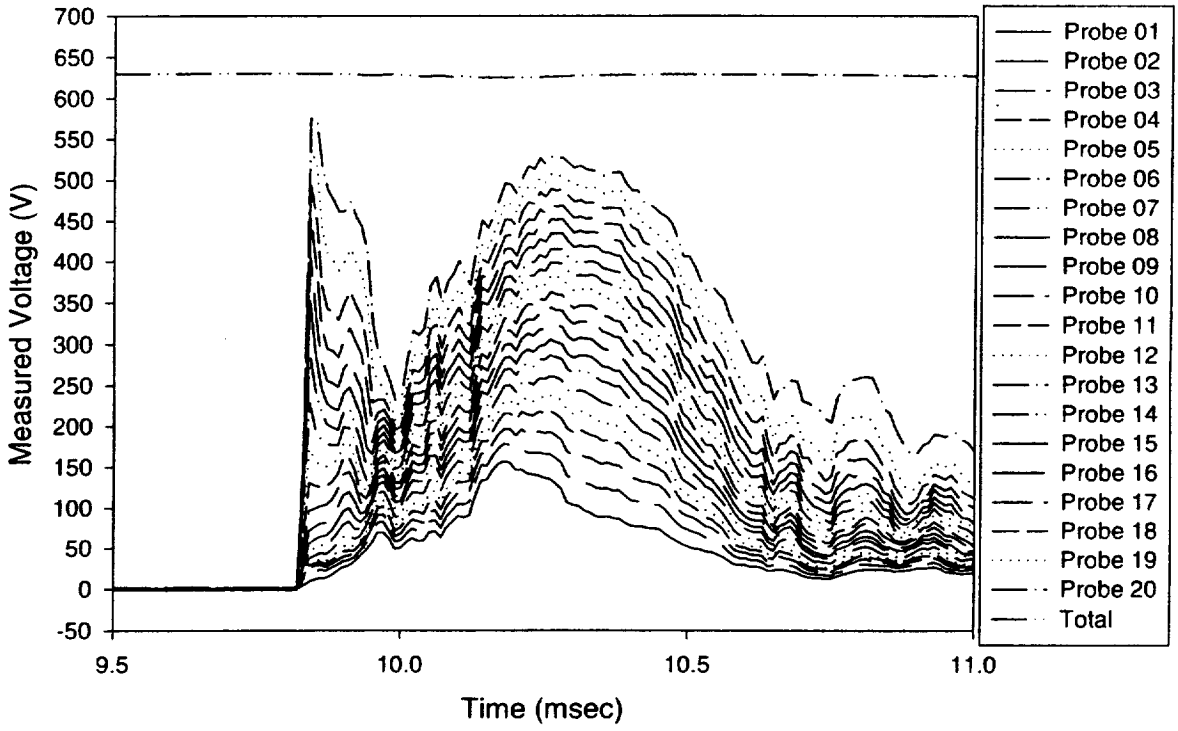

24 A JUNE 1997

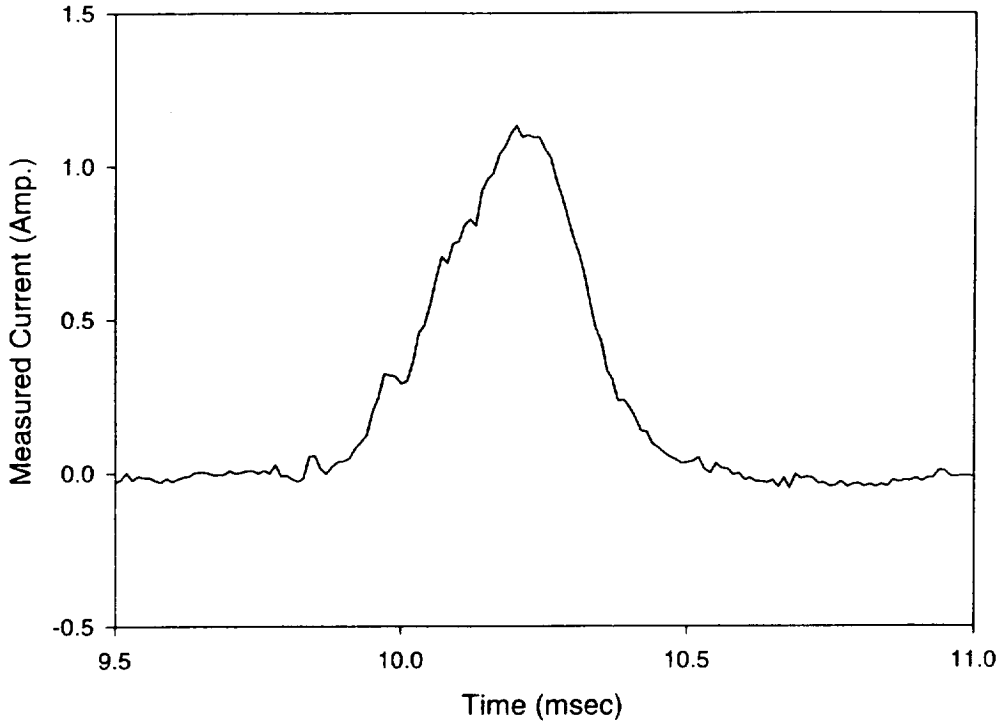

24 A JUNE 1997

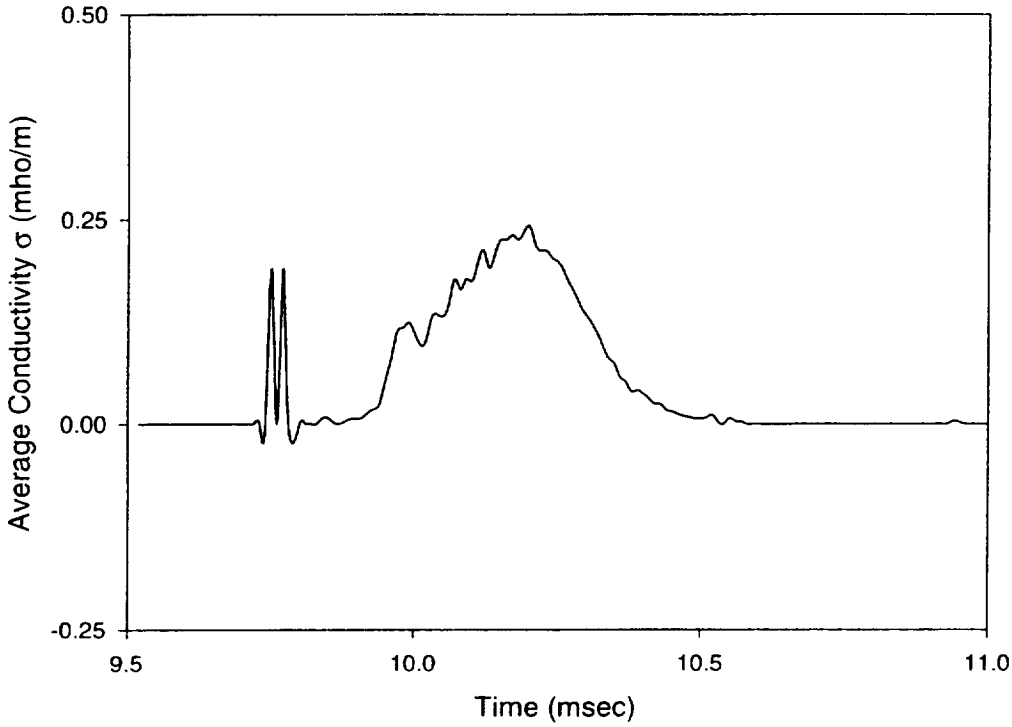

24 A JUNE 1997

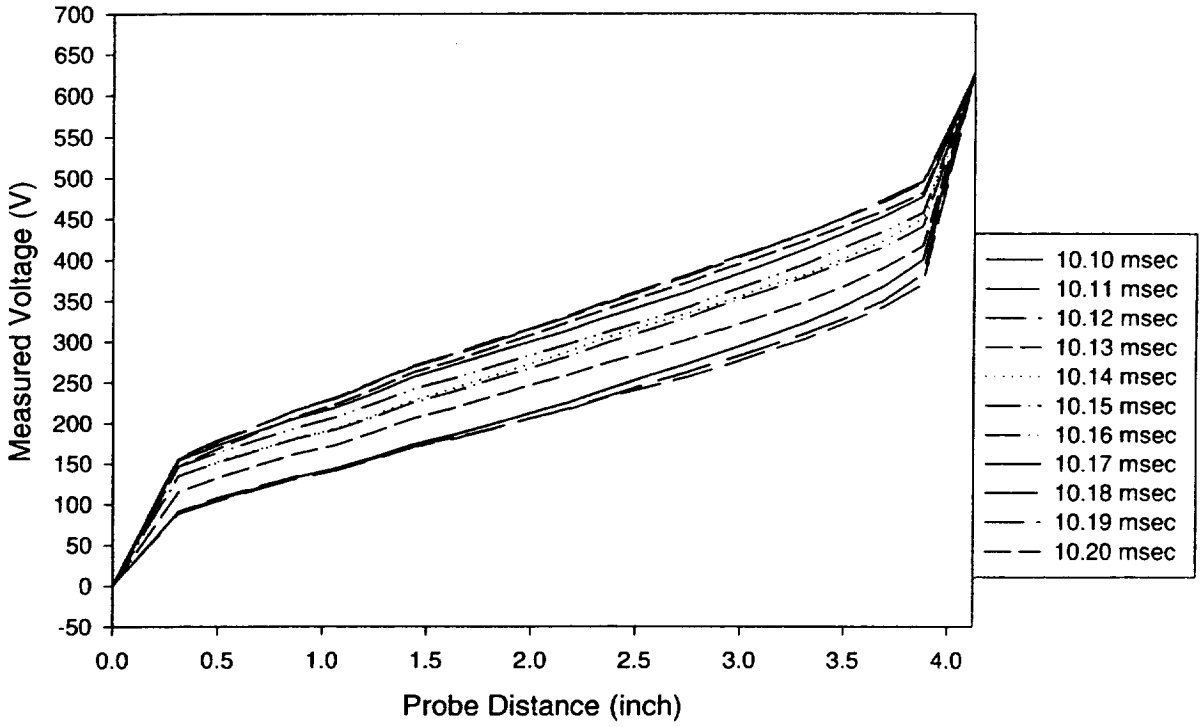

25 A JUNE 1997

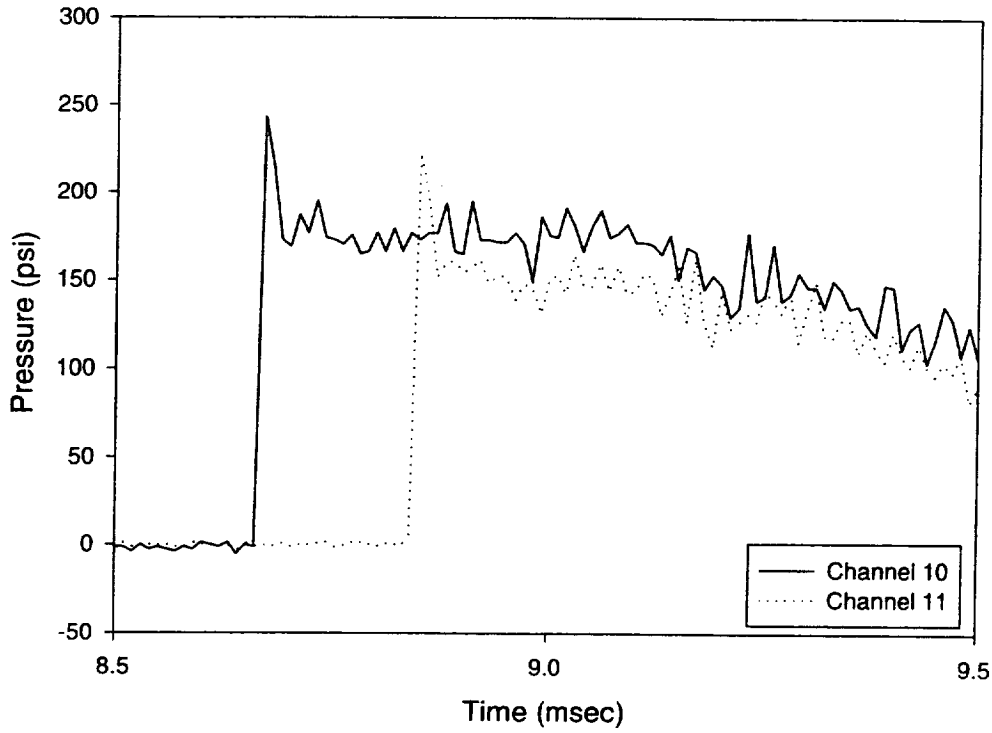

25 A JUNE 1997

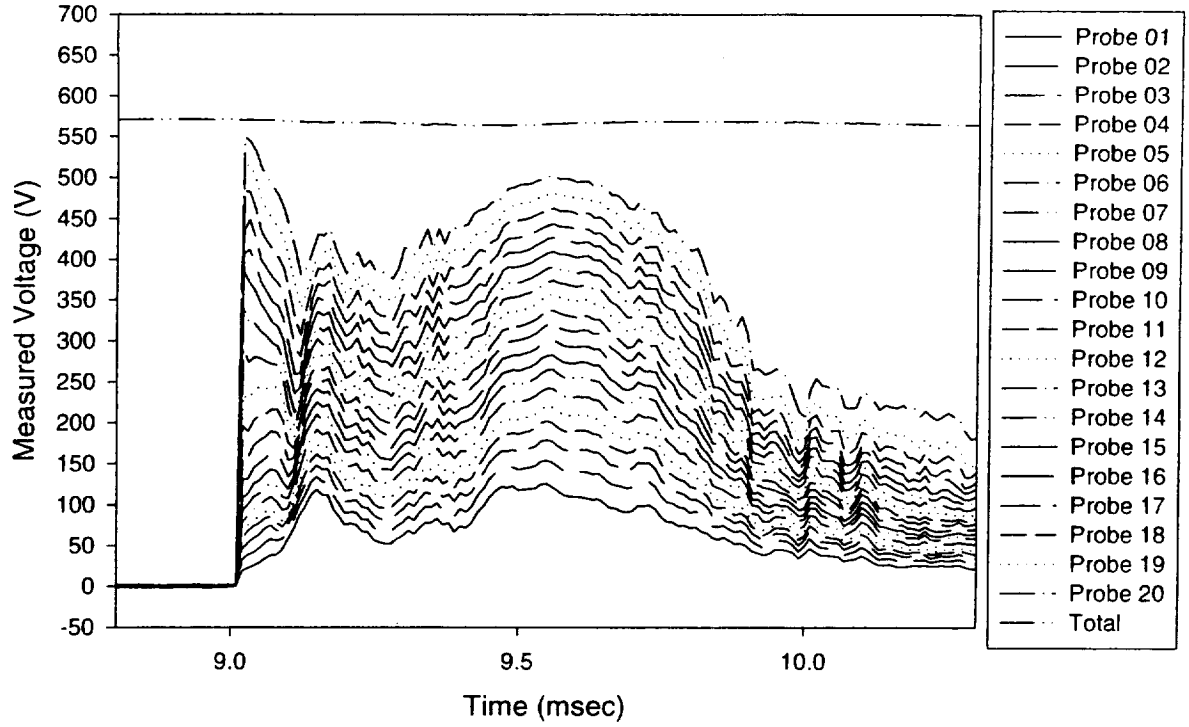

25 A JUNE 1997

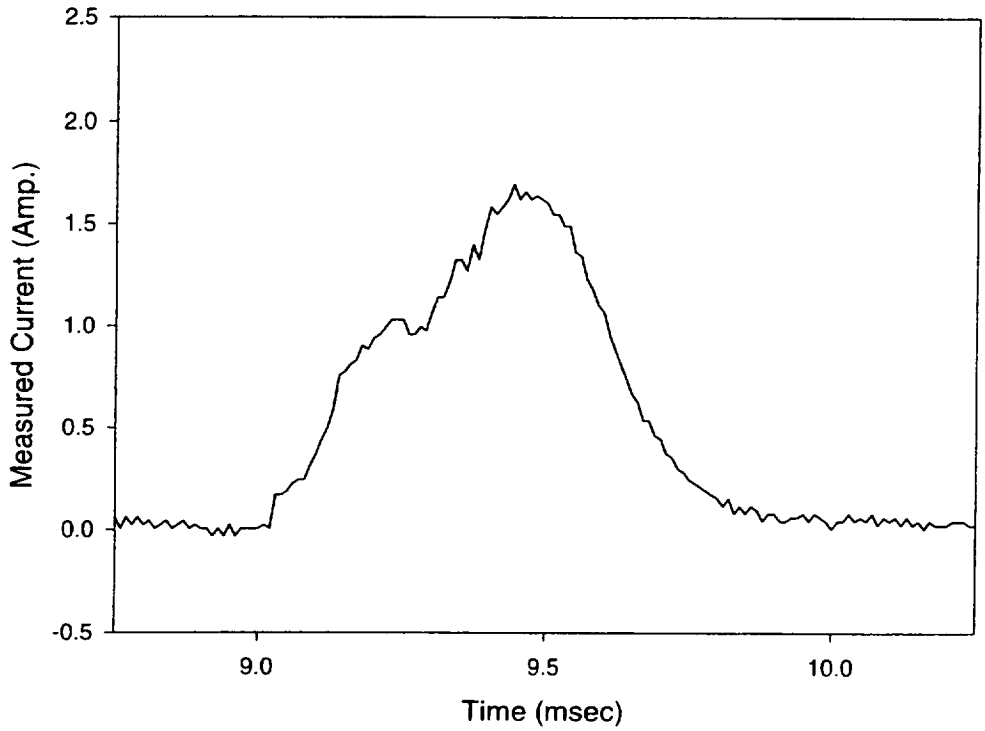

25 A JUNE 1997

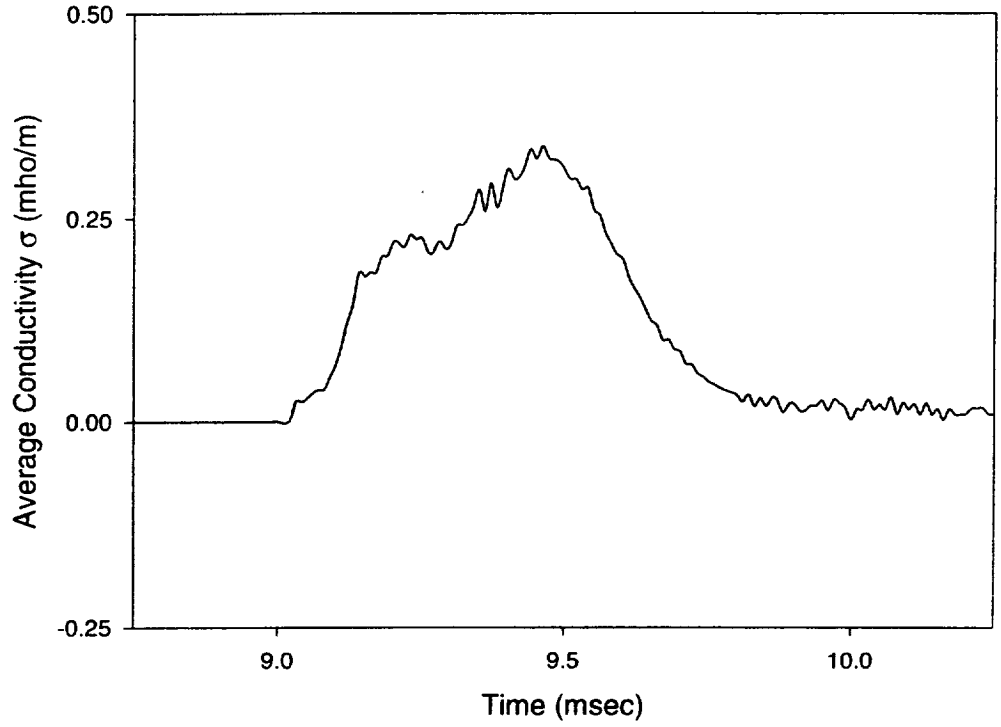

25 A JUNE 1997

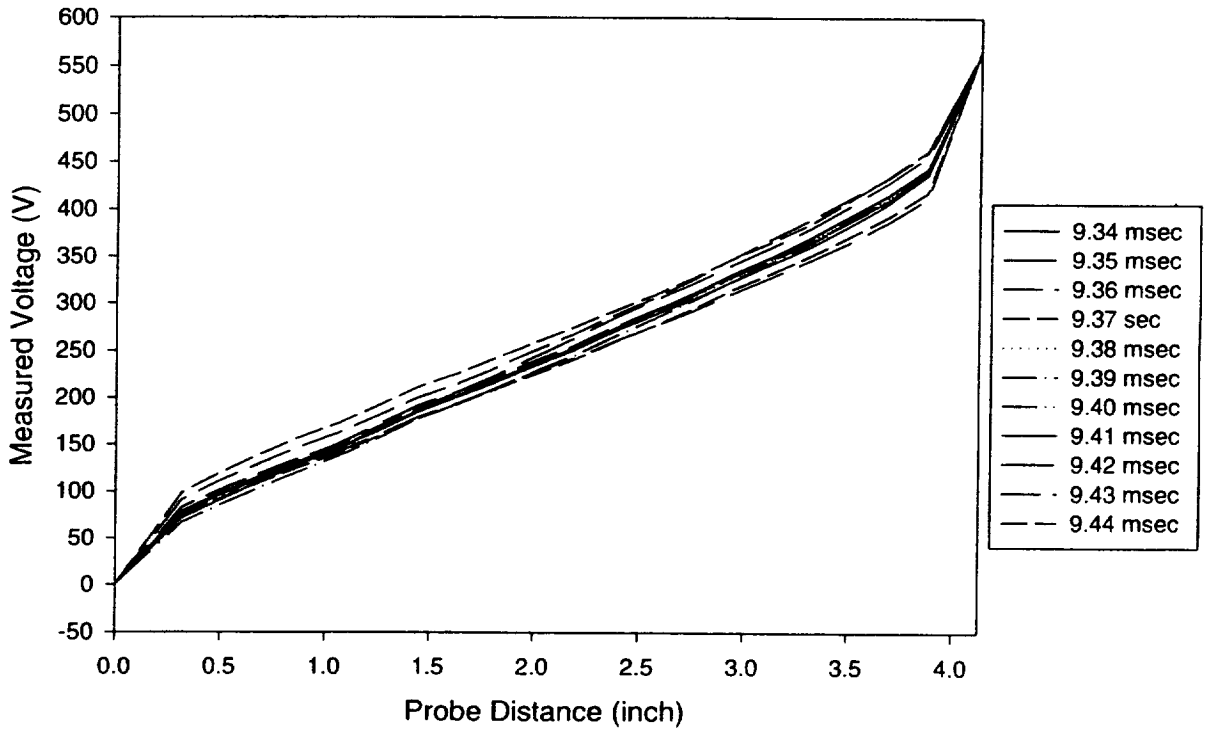

25 C JUNE 1997

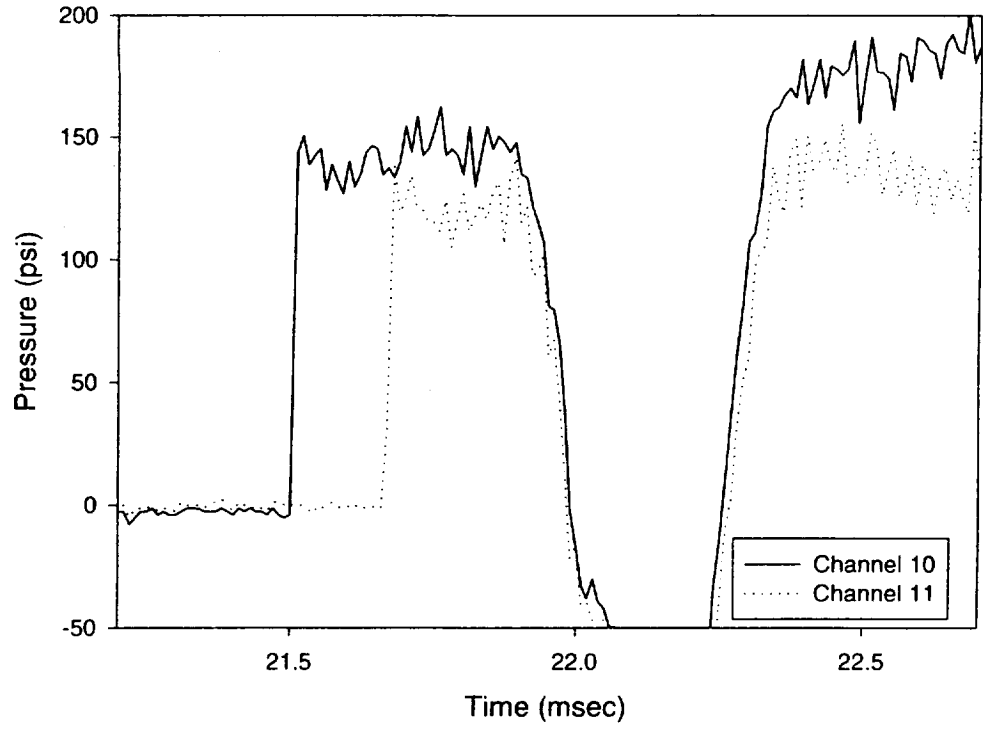

25 C JUNE 1997

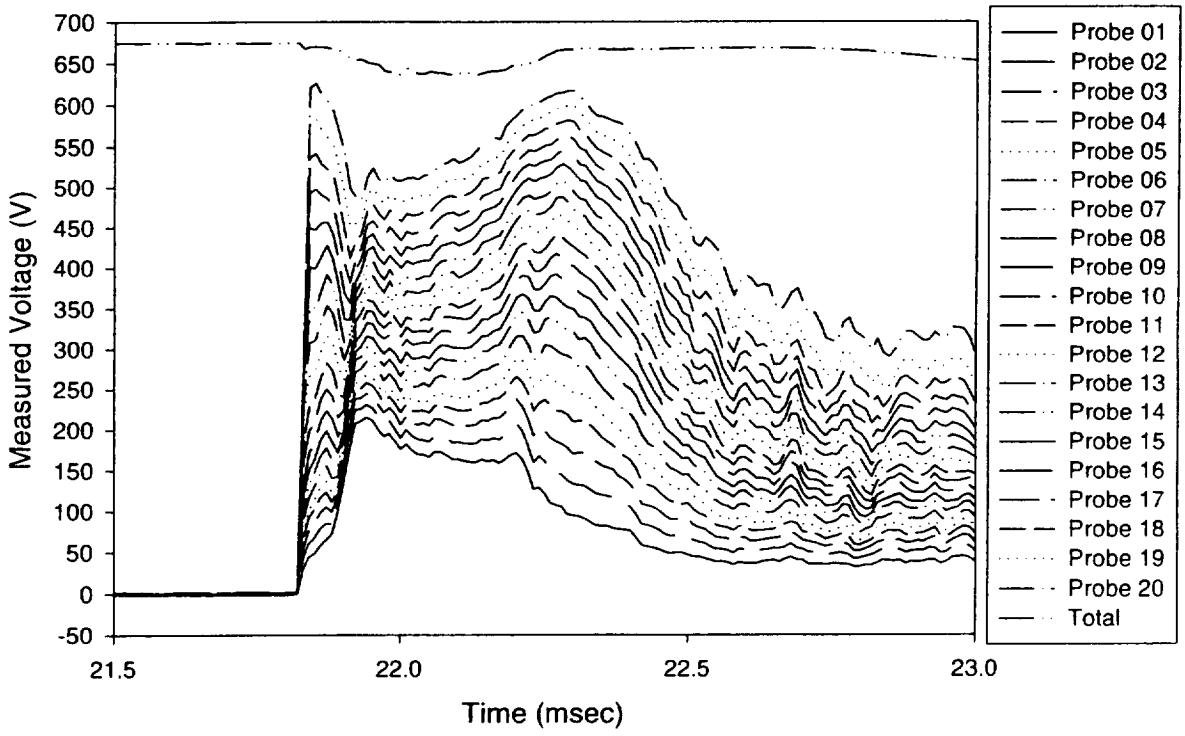

25 C JUNE 1997

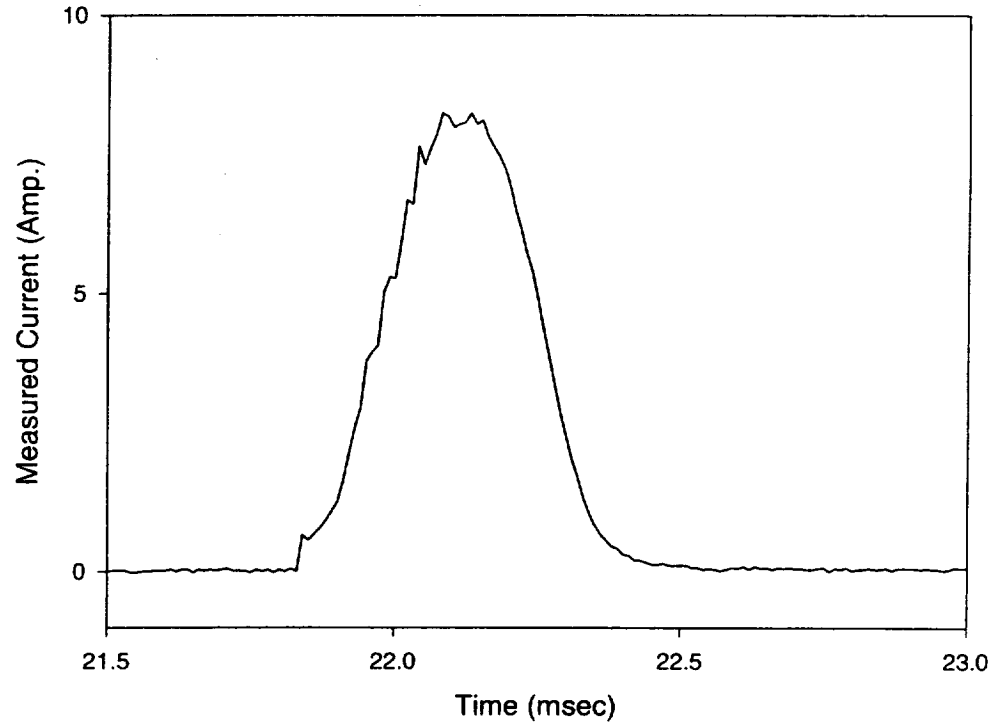

25 C JUNE 1997

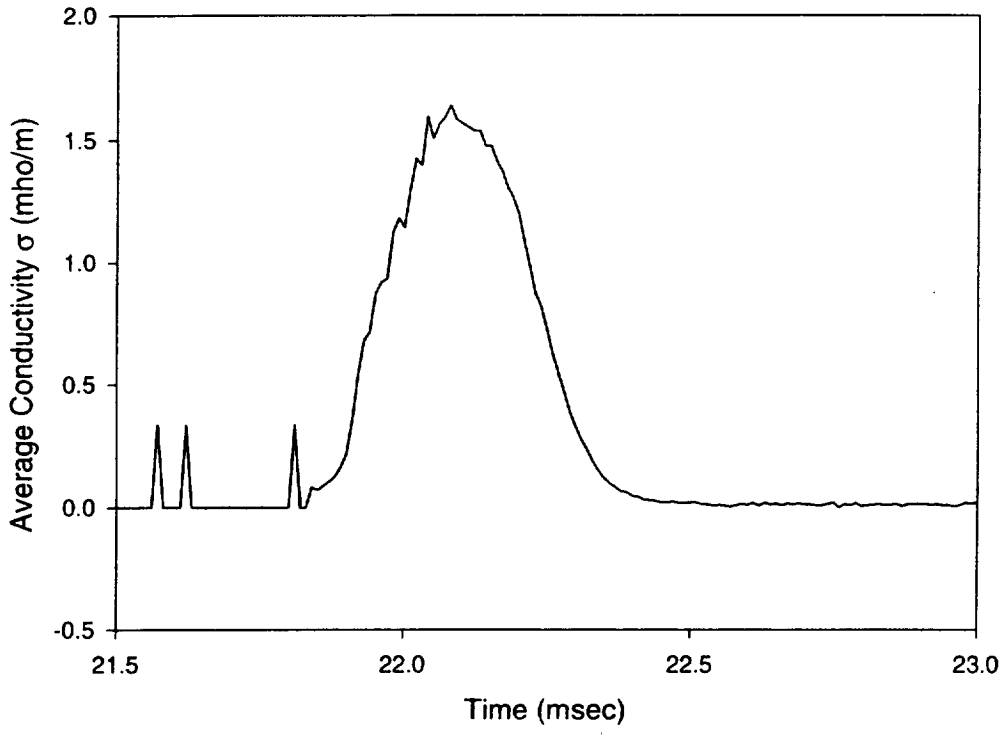

25 C JUNE 1997

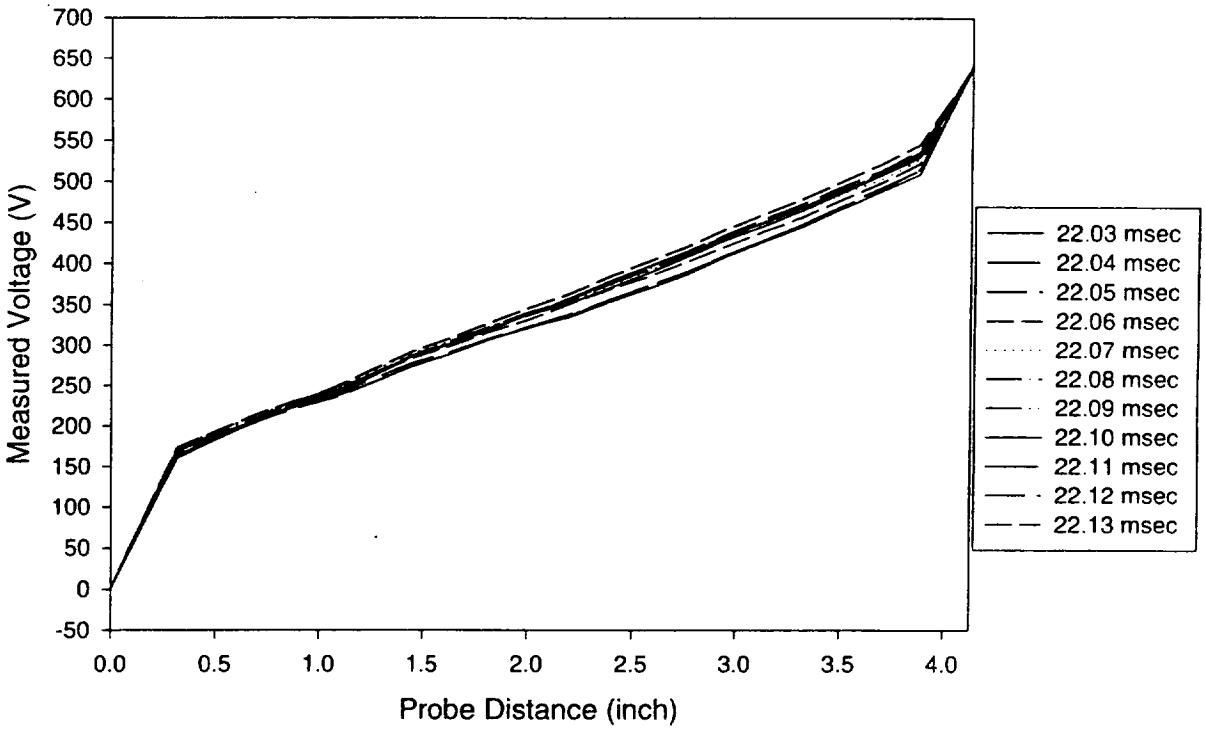

25 D JUNE 1997

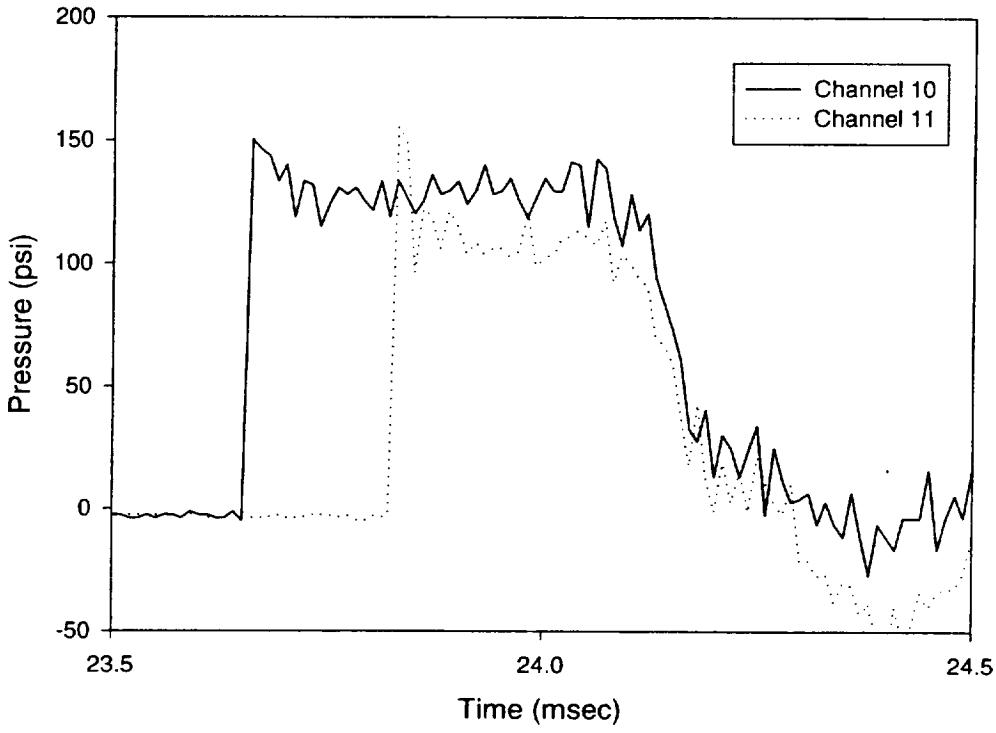

25 D JUNE 1997

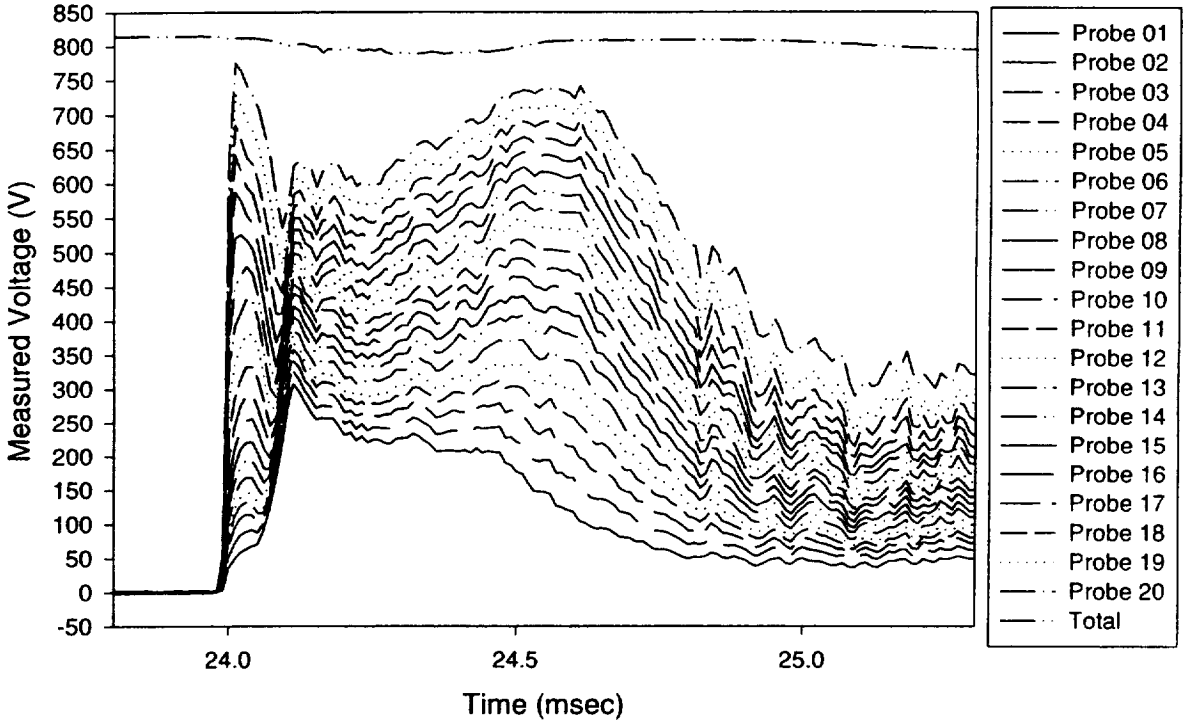

25 D JUNE 1997

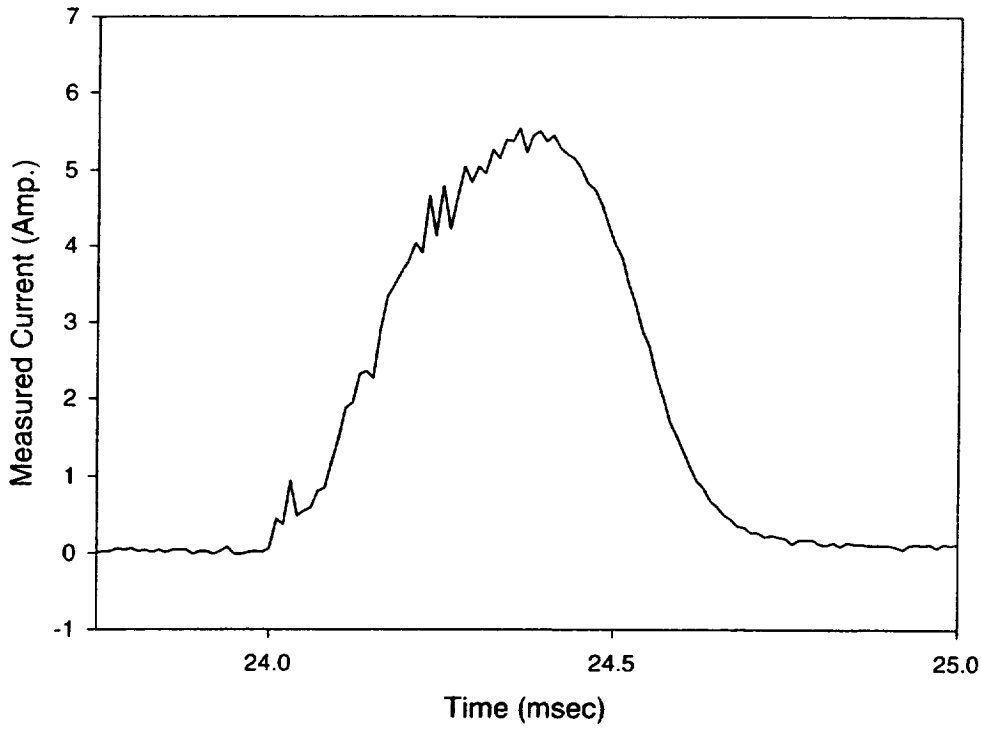

25 D JUNE 1997

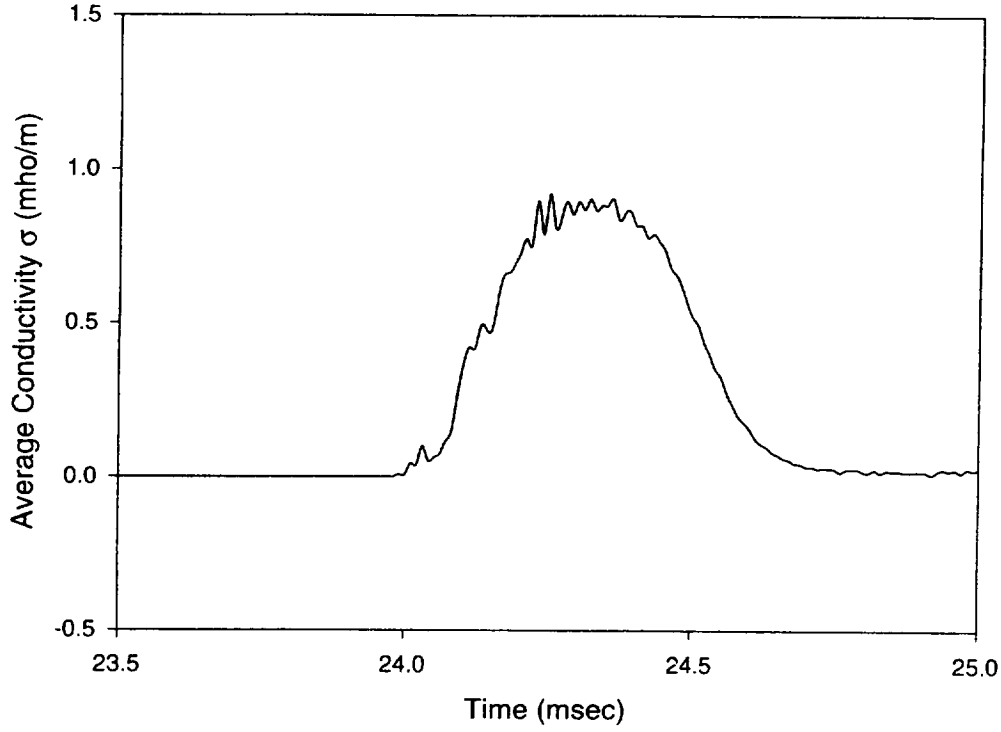

25 D JUNE 1997

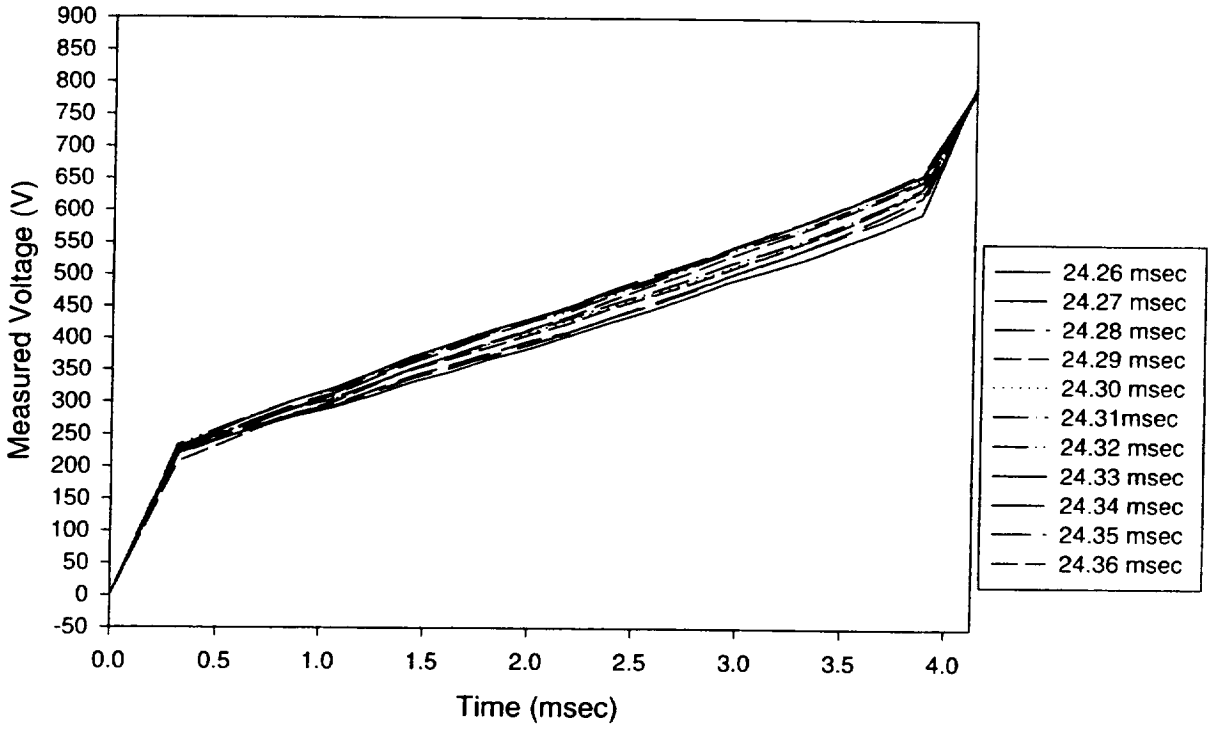

26 A JUNE 1997

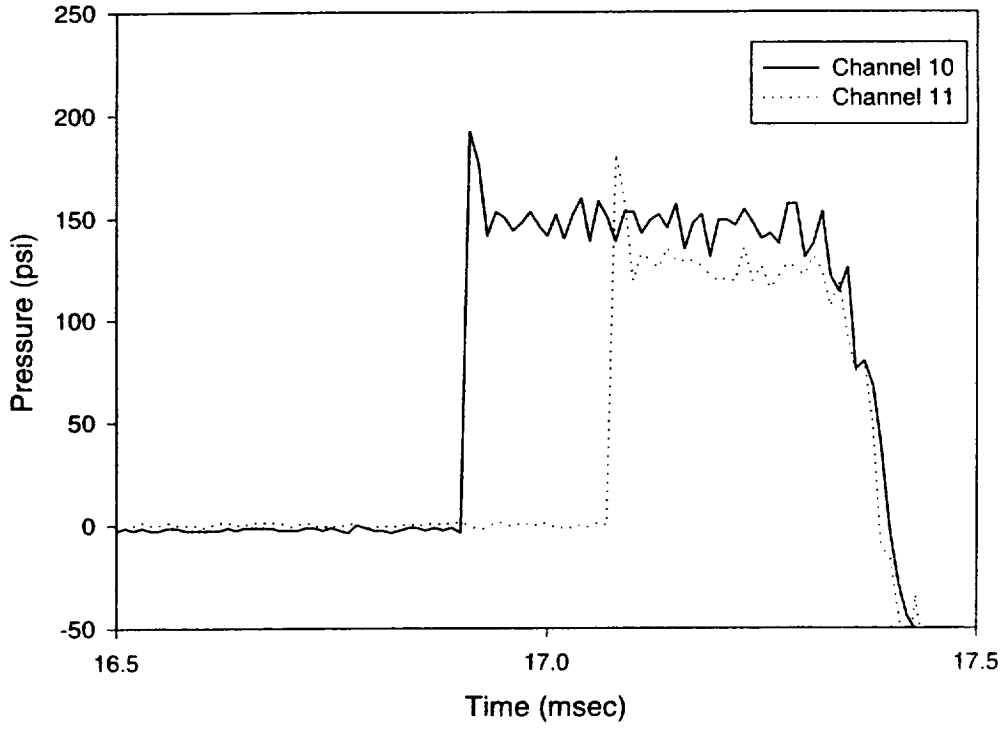

26 A JUNE 1997

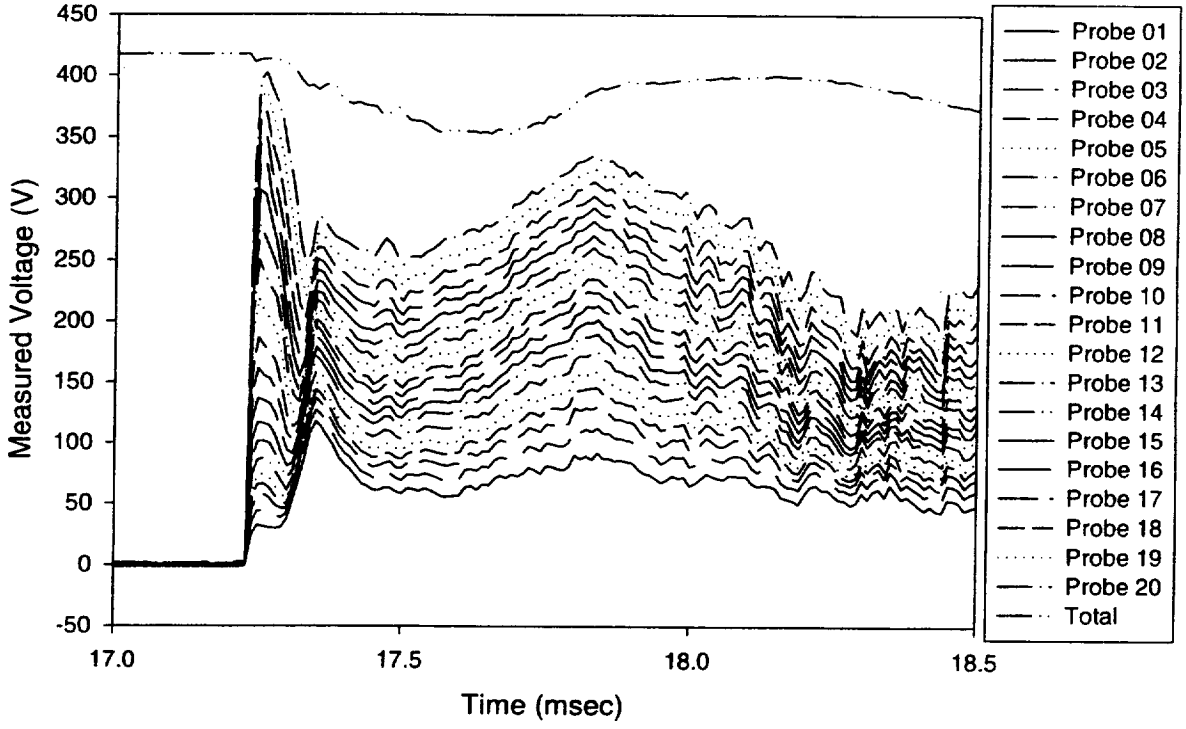

26 A JUNE 1997

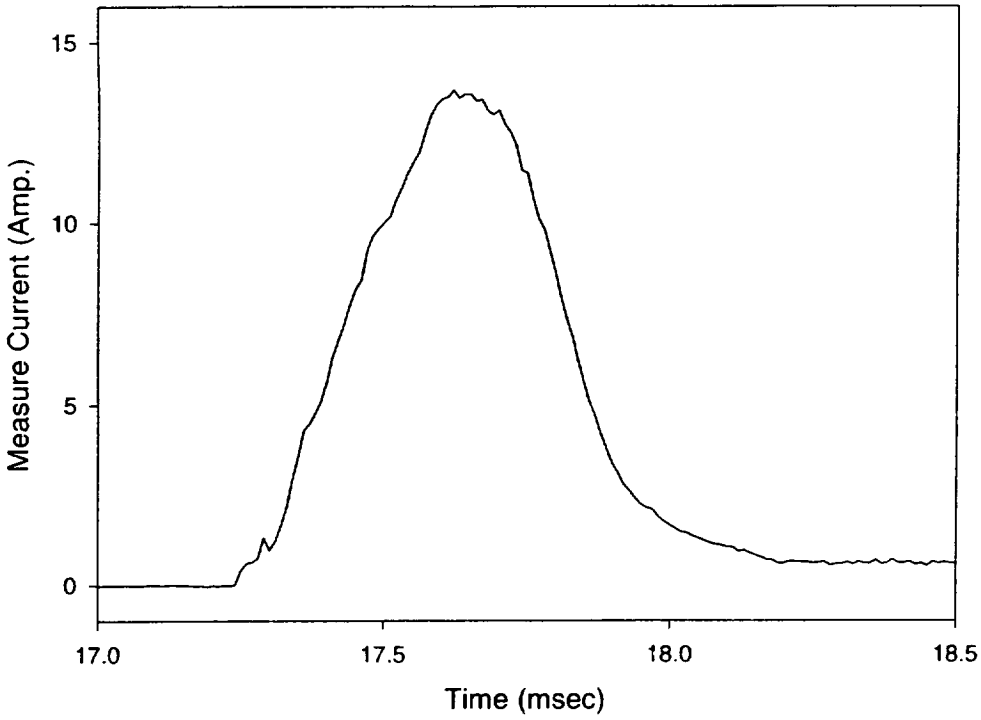

26 A JUNE 1997

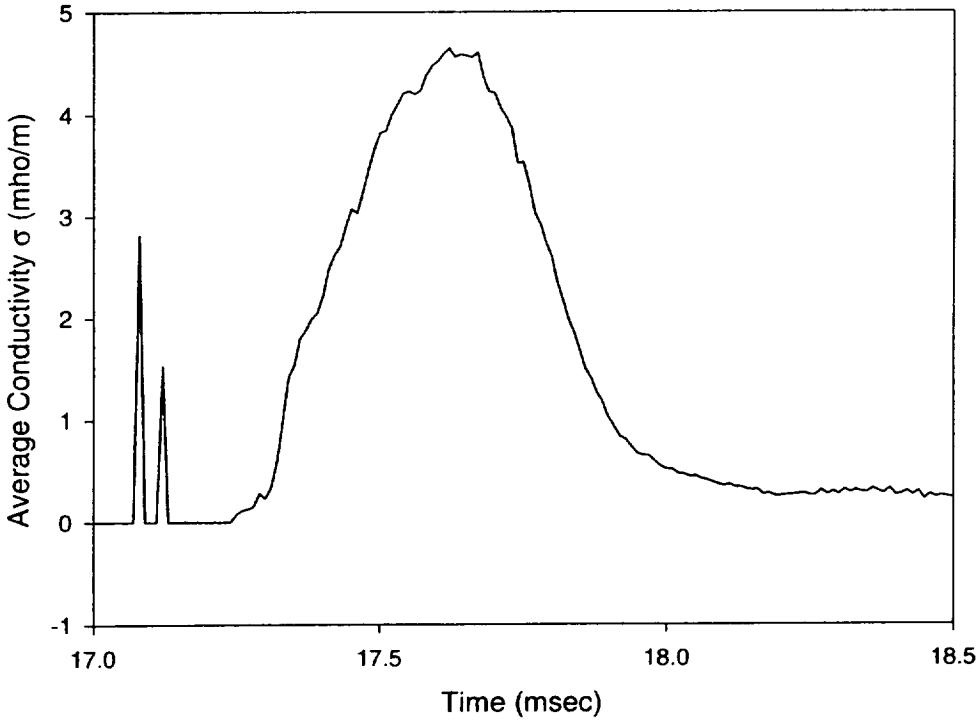

26 A JUNE 1997

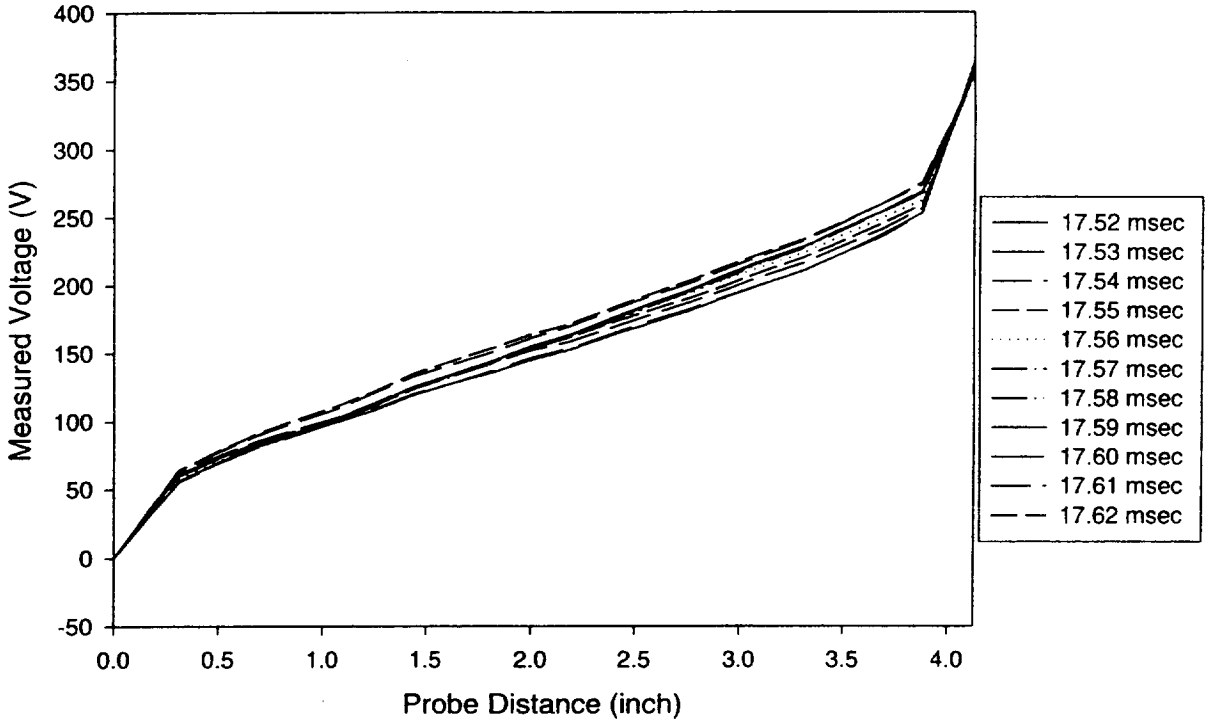

26 B JUNE 1997

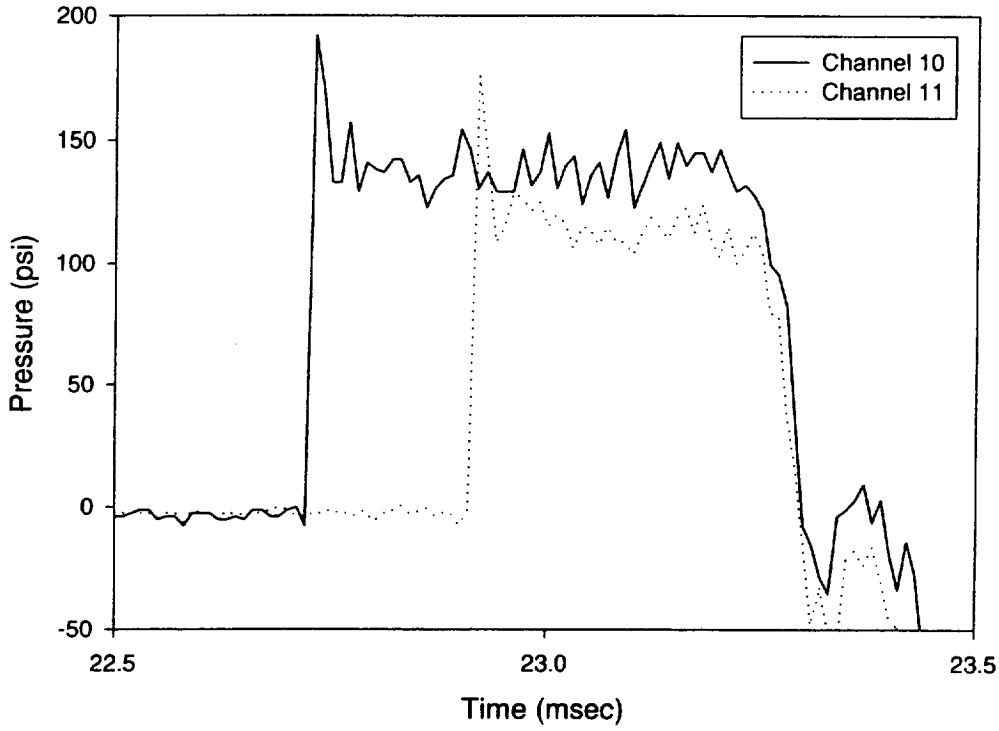

26 B JUNE 1997

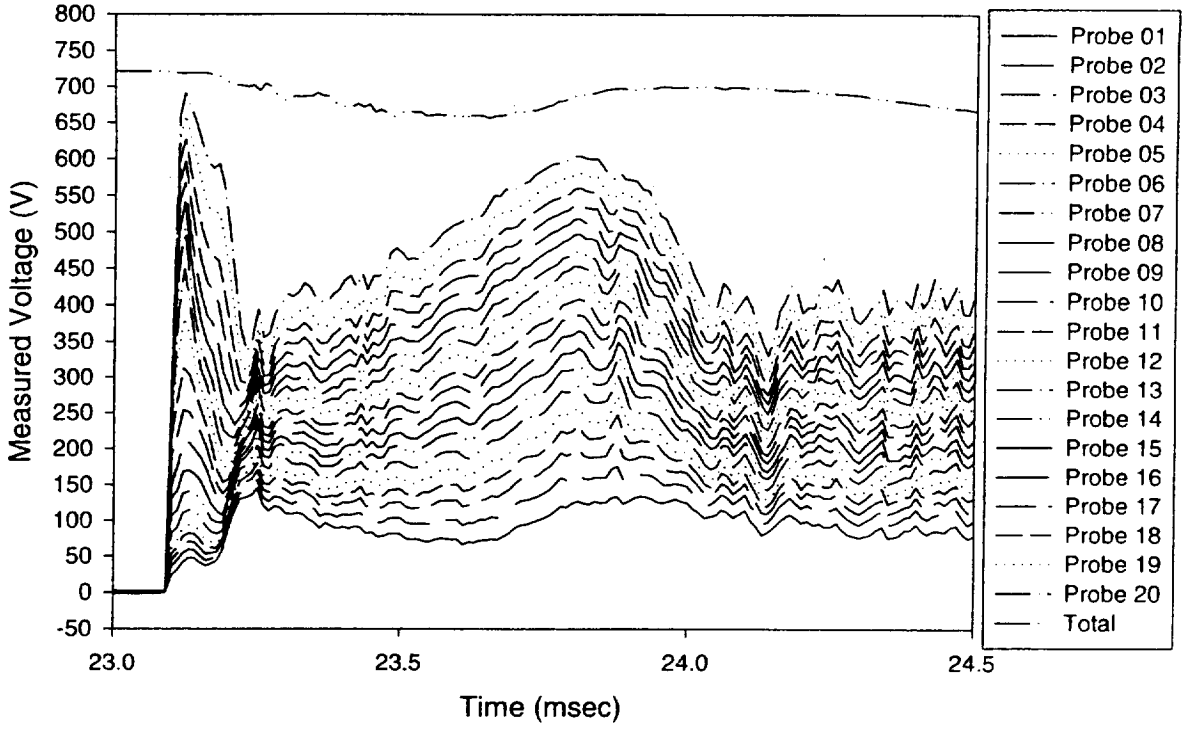

26 B JUNE 1997

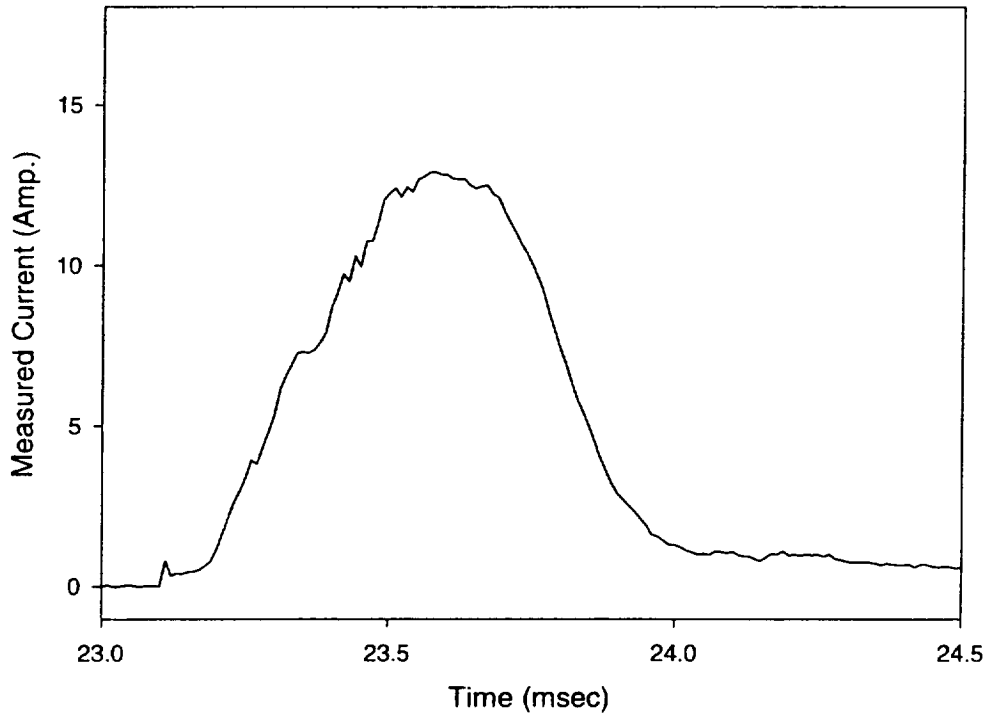

26 B JUNE 1997

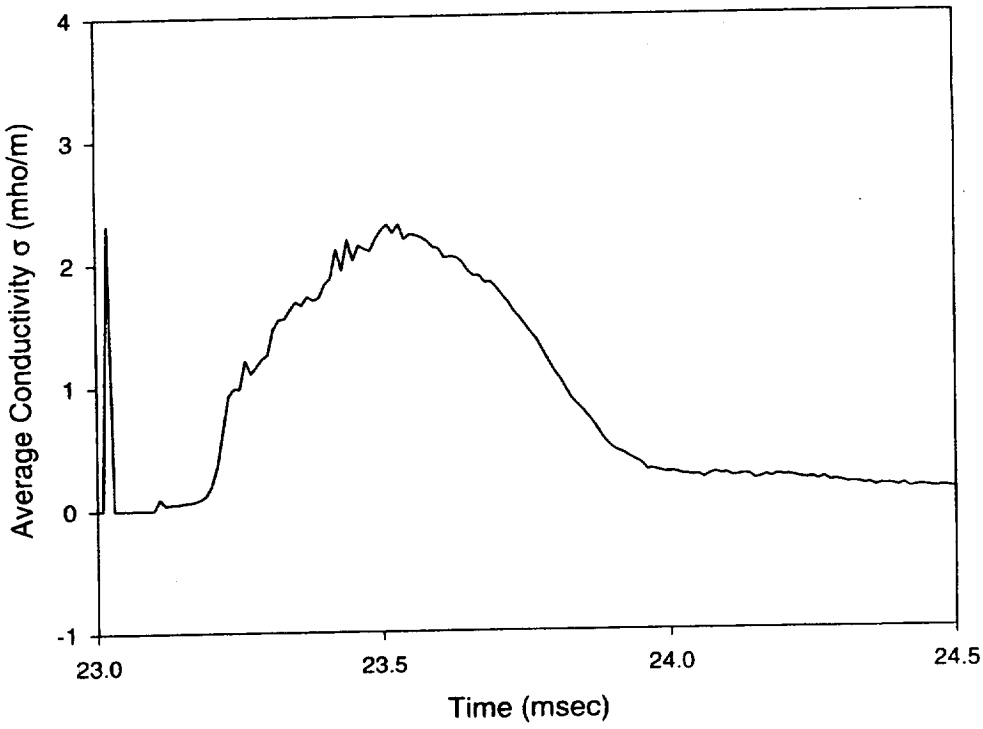

26 B JUNE 1997

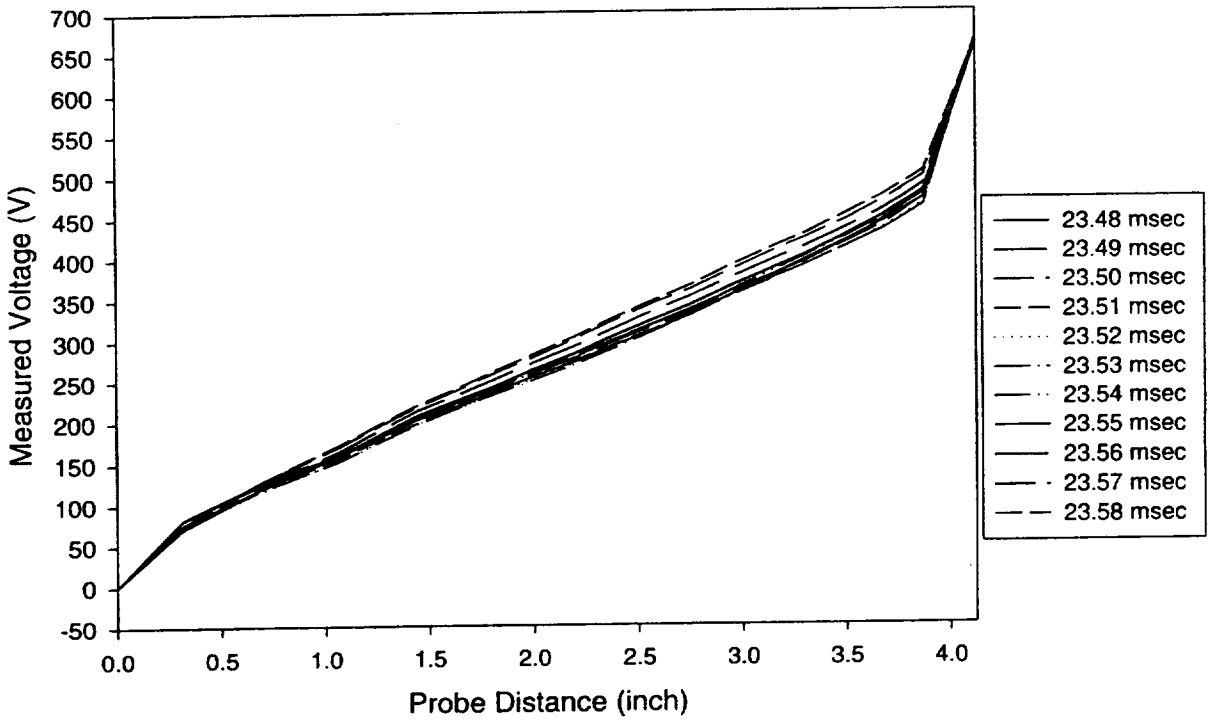

26 C JUNE 1997

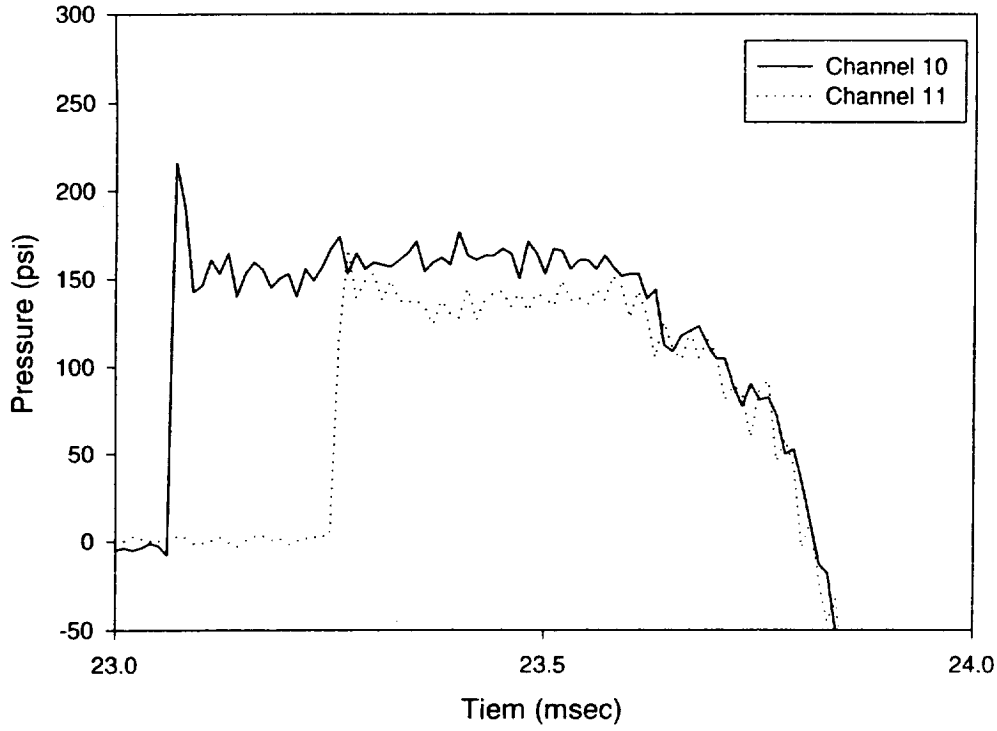

26 C JUNE 1997

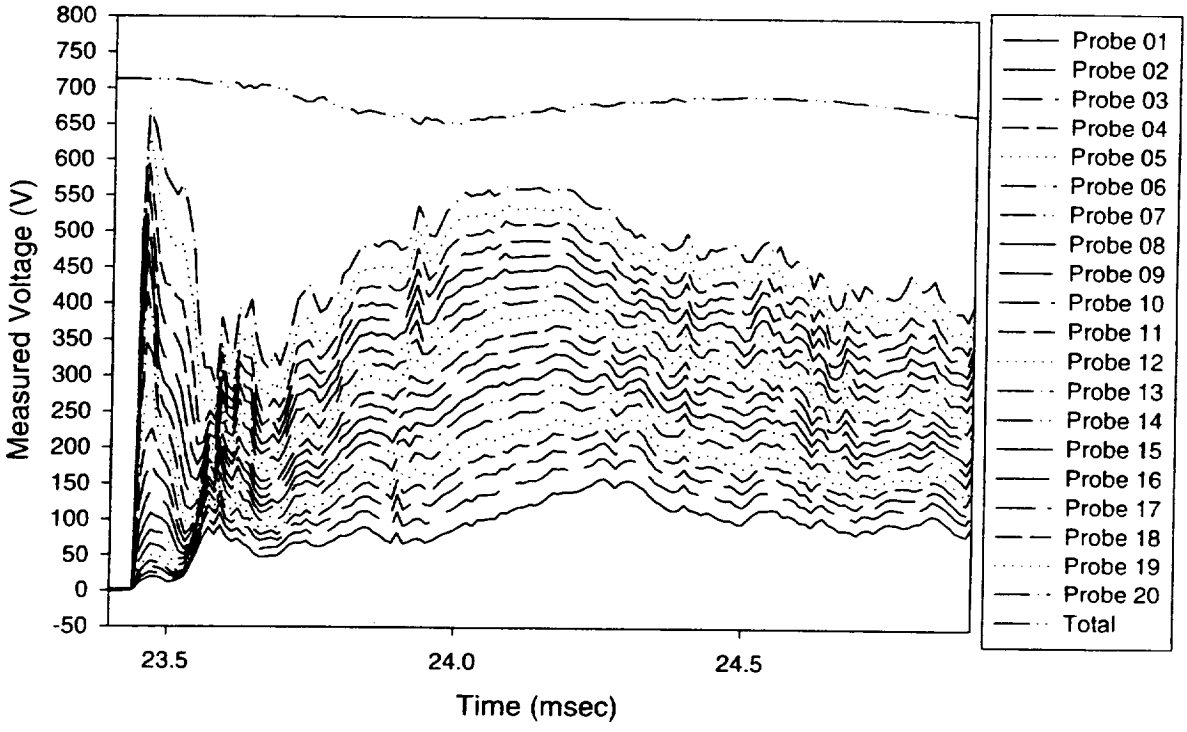

26 C JUNE 1997

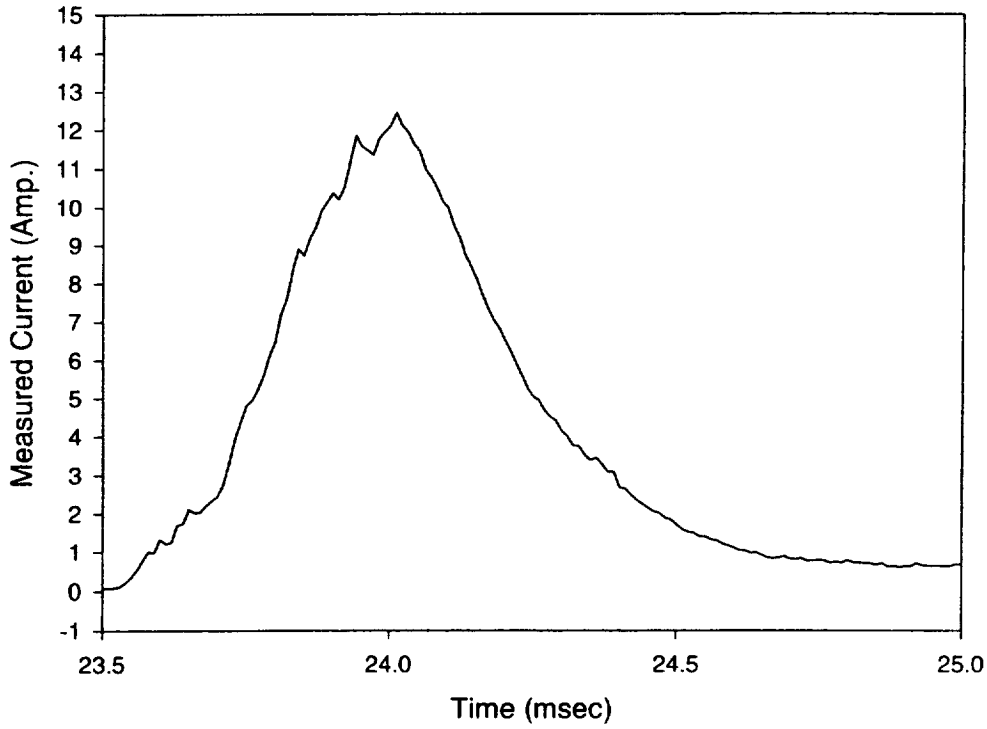

26 C JUNE 1997

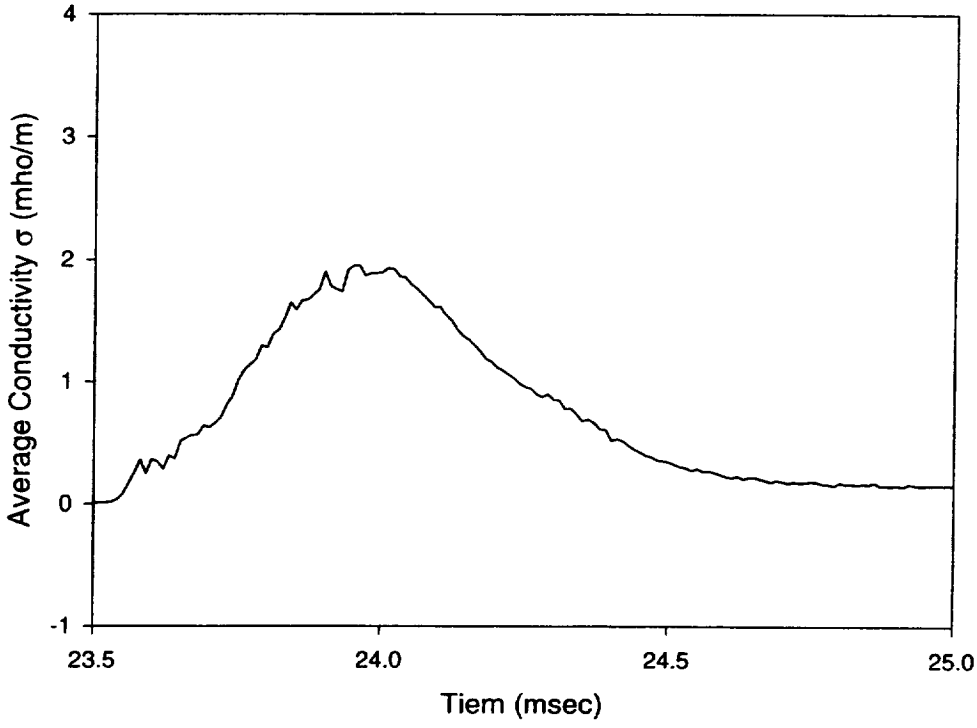

26 C JUNE 1997

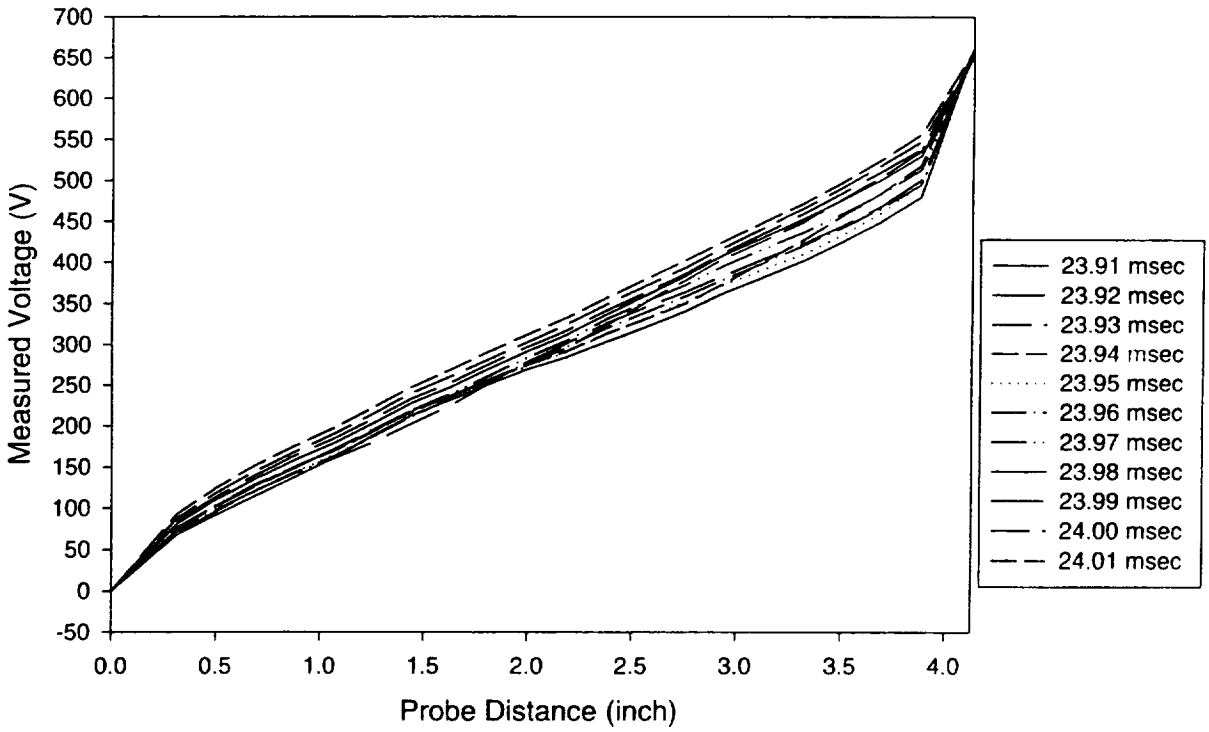

26 D JUNE 1997

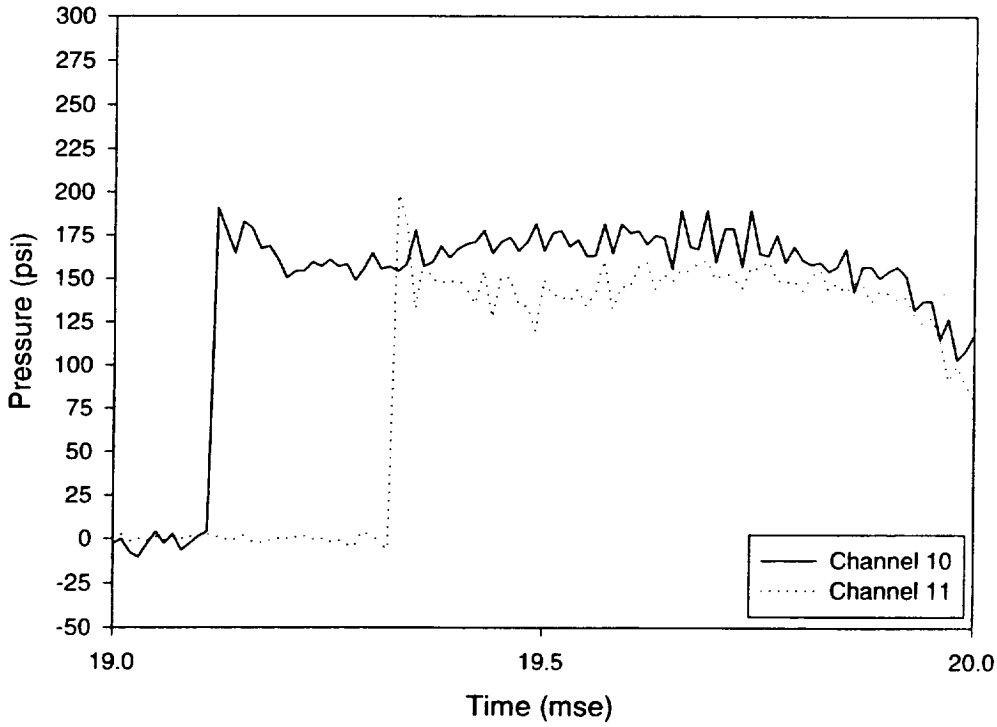

26 D JUNE 1997

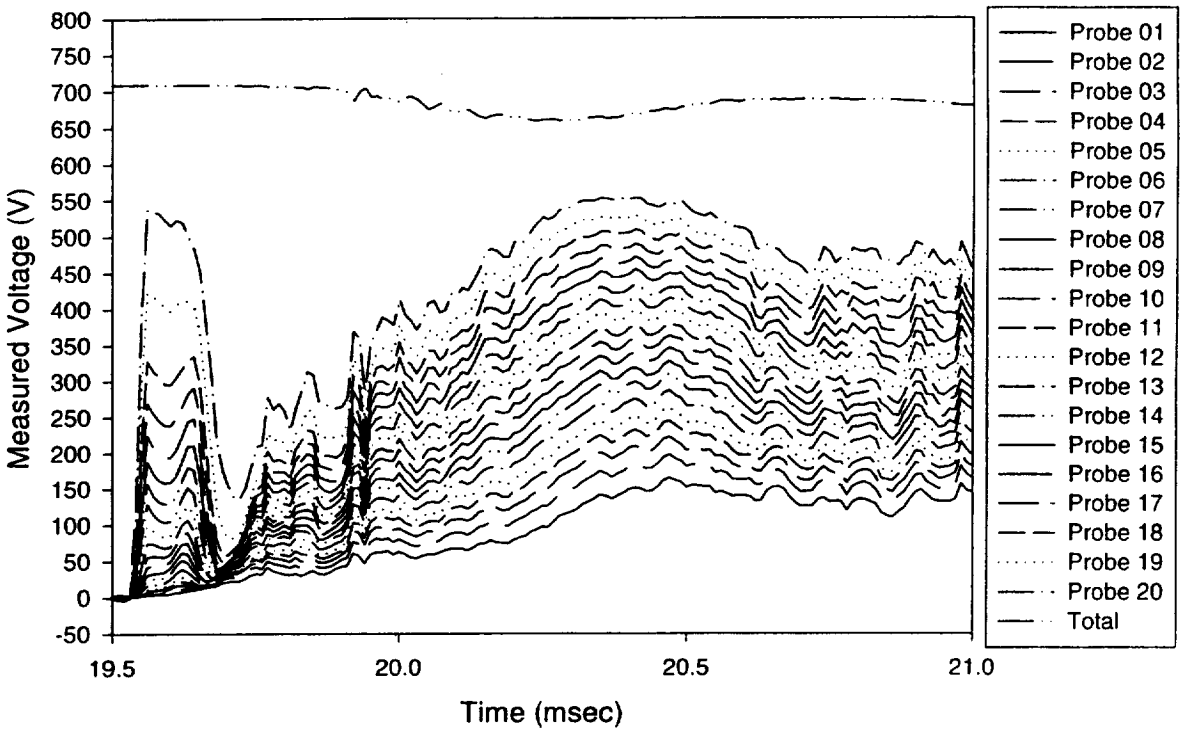

26 D JUNE 1997

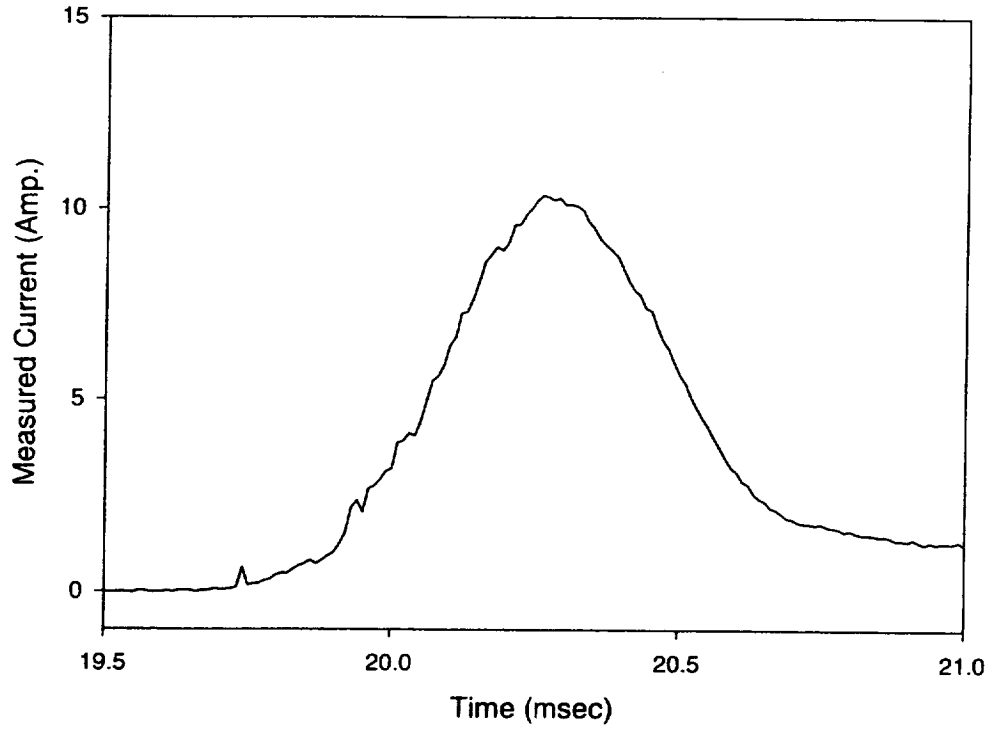

26 D JUNE 1997

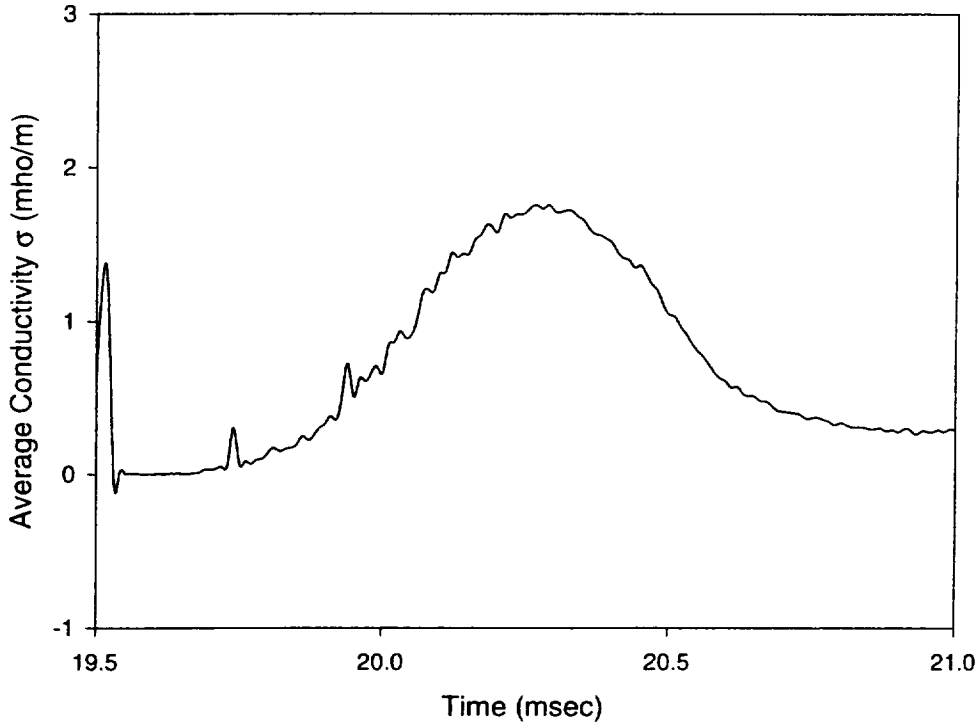

26 D JUNE 1997

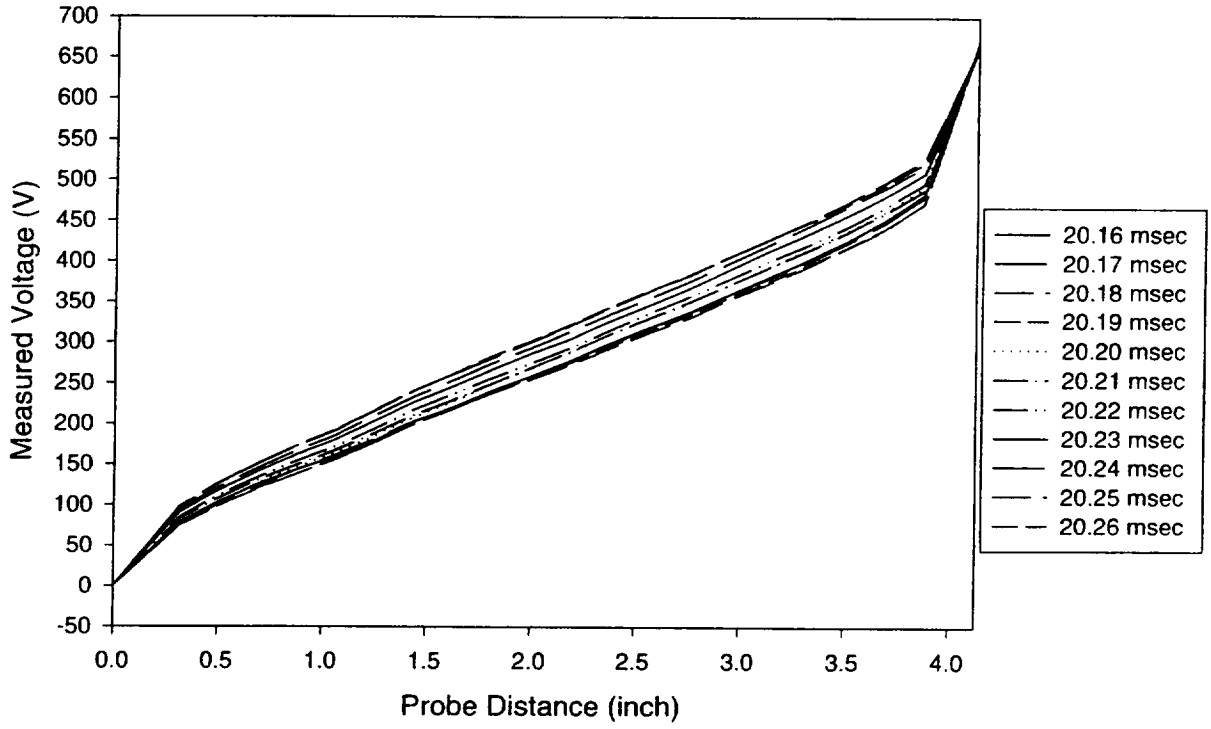

26 E JUNE 1997

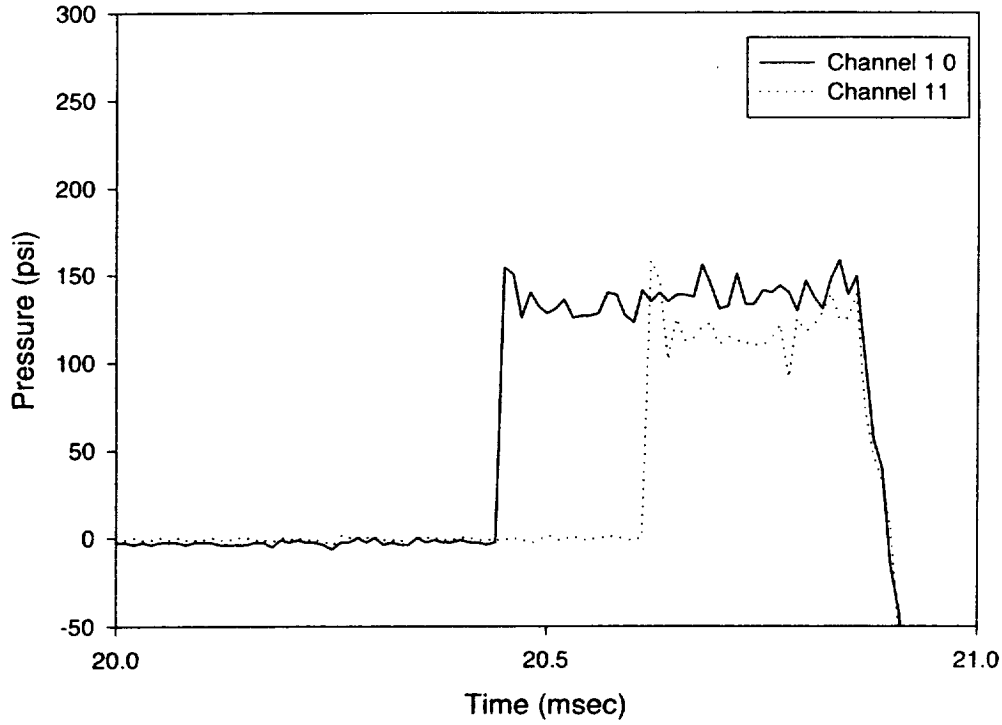

26 E JUNE 1997

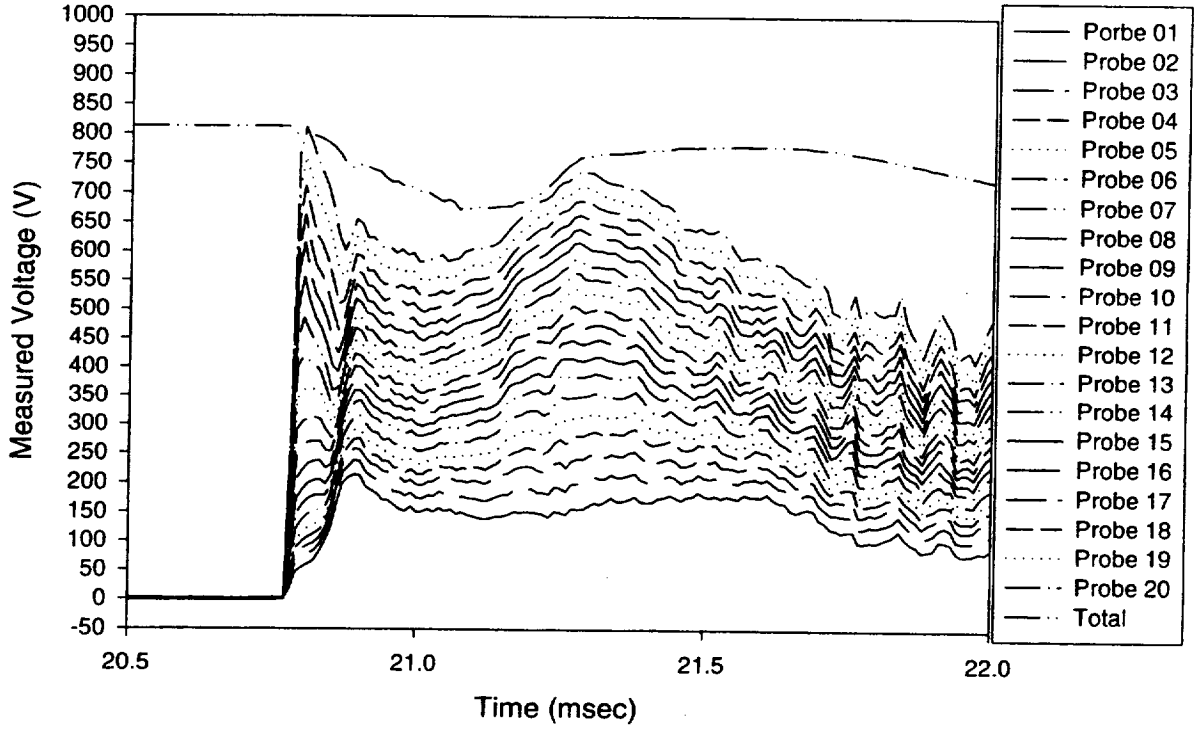

26 E JUNE 1997

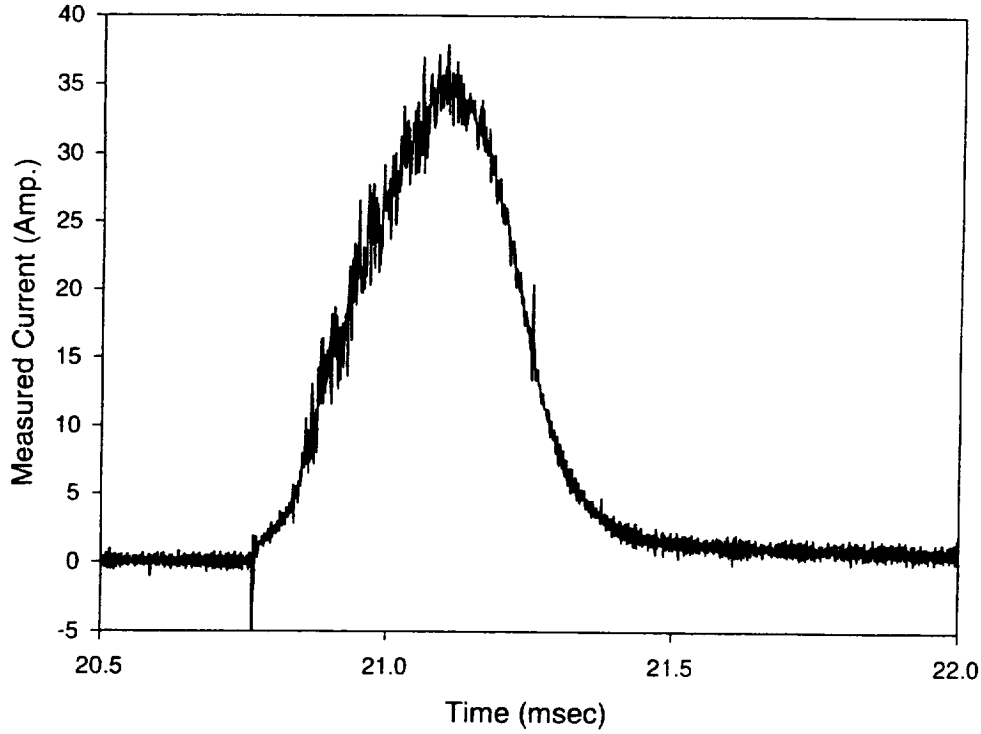

26 E JUNE 1997

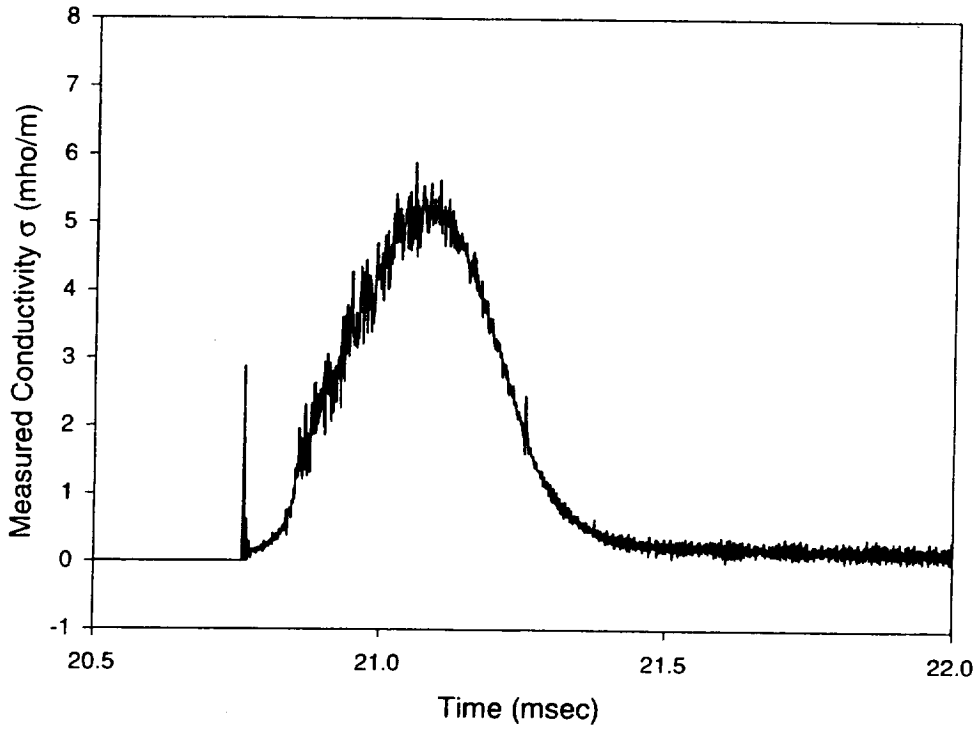

26 E JUNE 1997

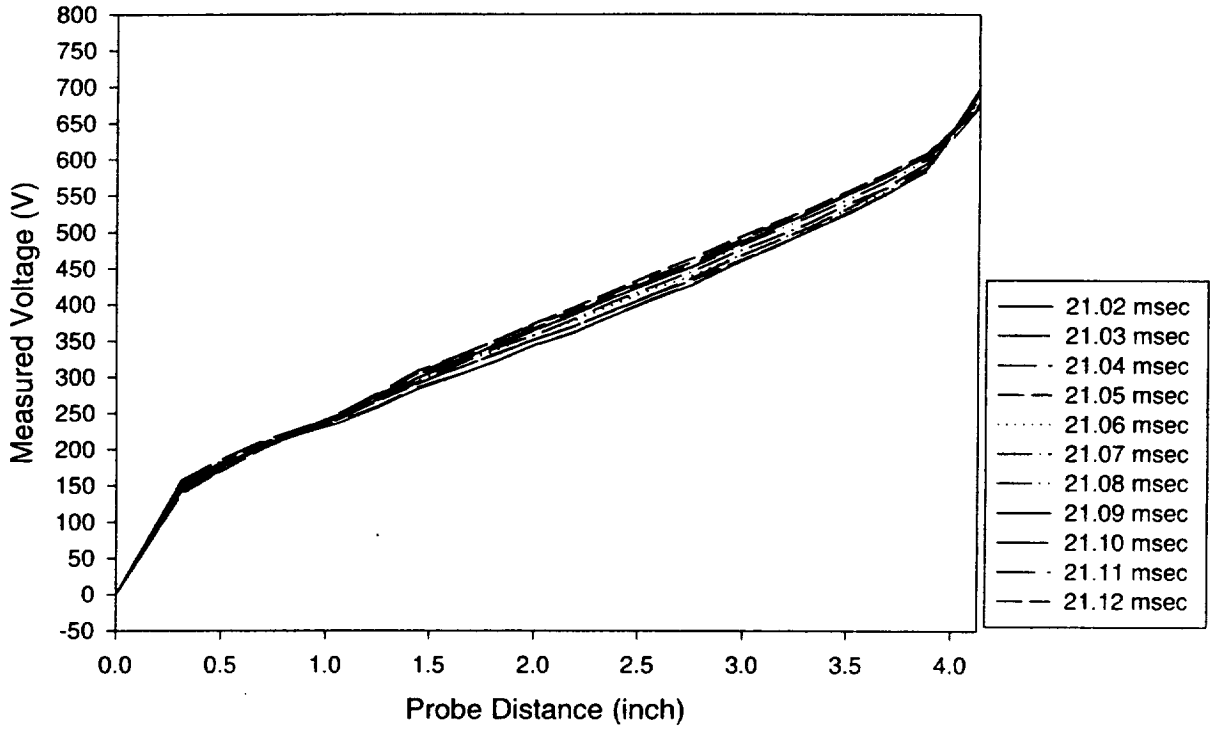

27 A JUNE 1997

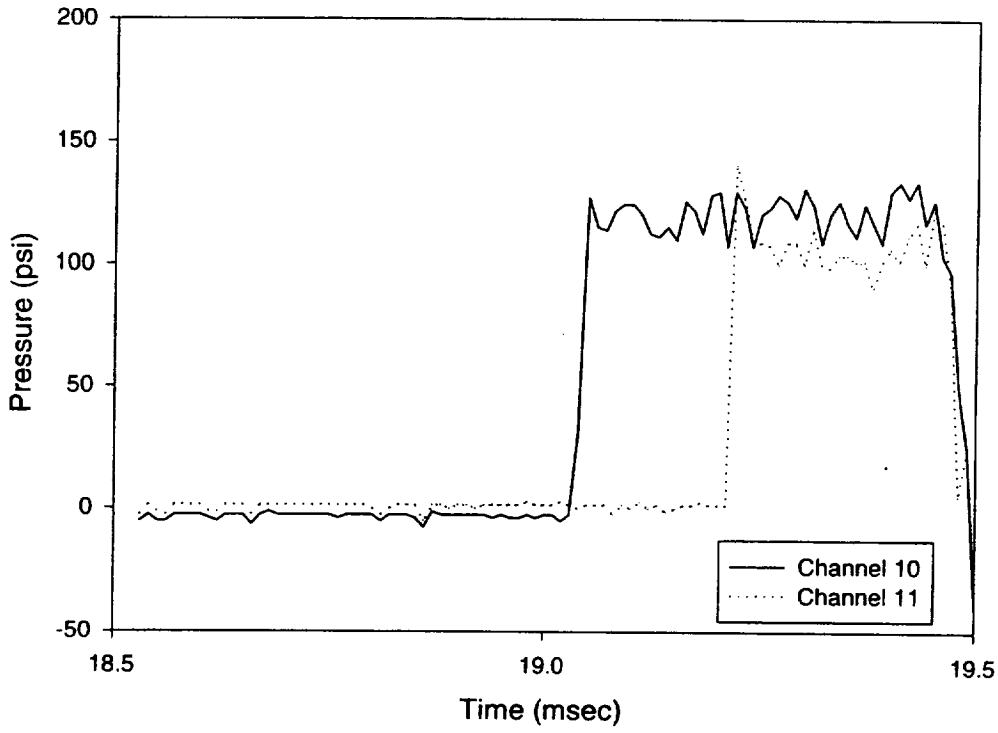

27 A JUNE 1997

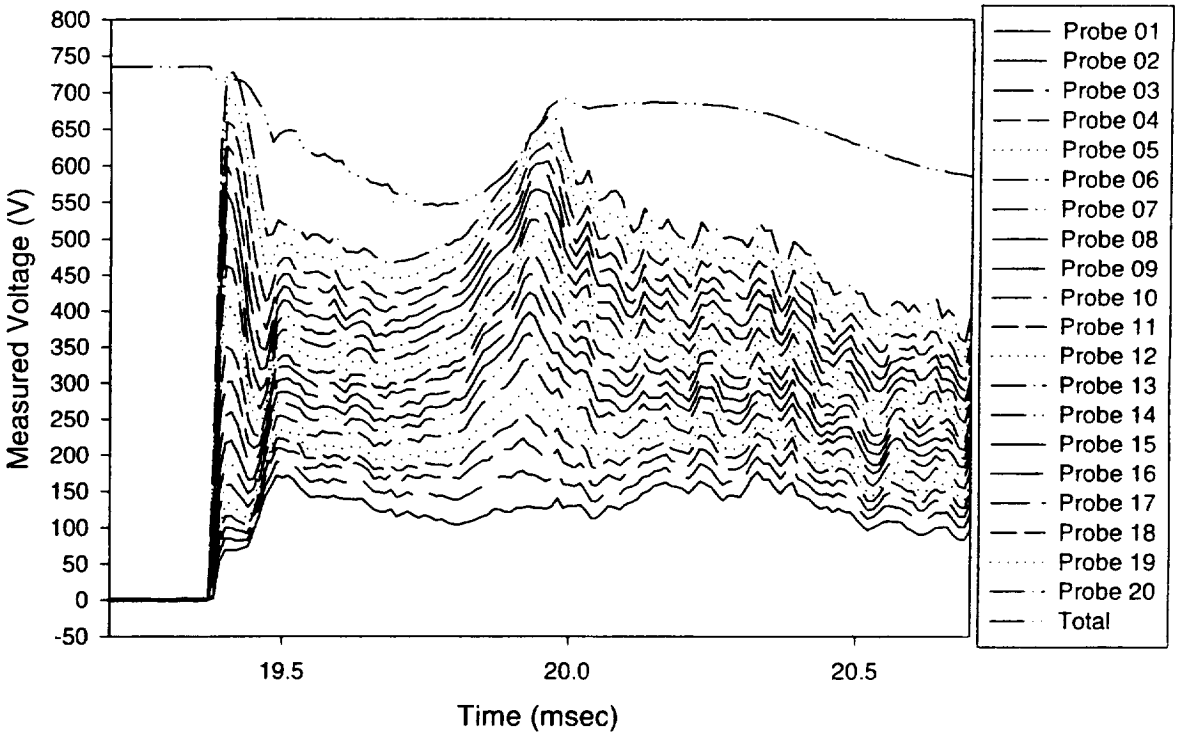

27 A JUNE 1997

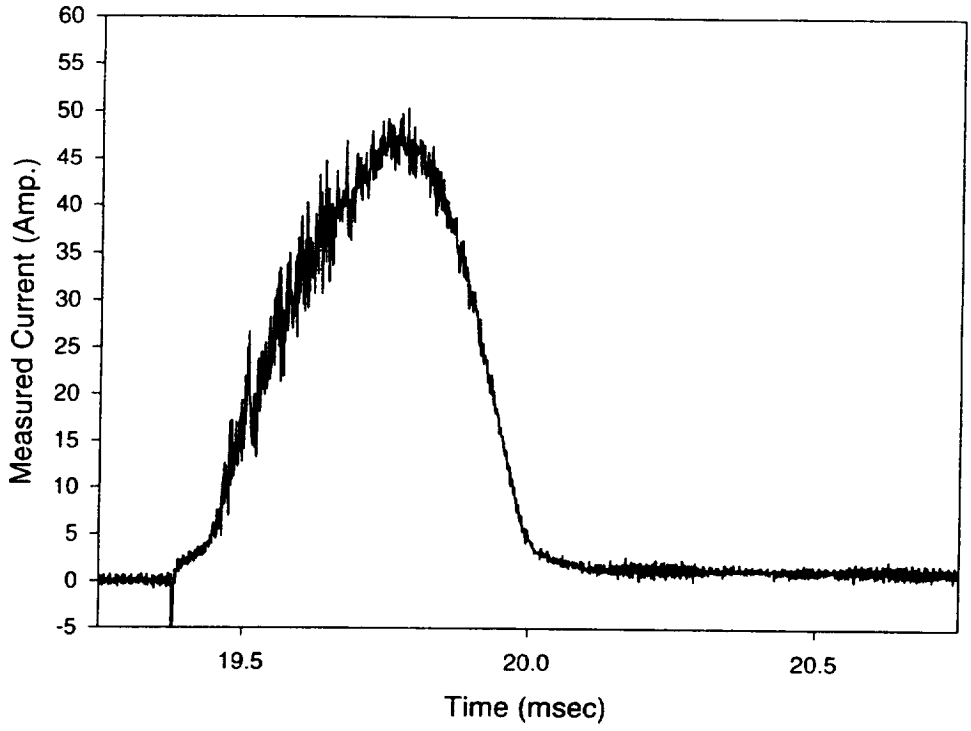

27 A JUNE 1997

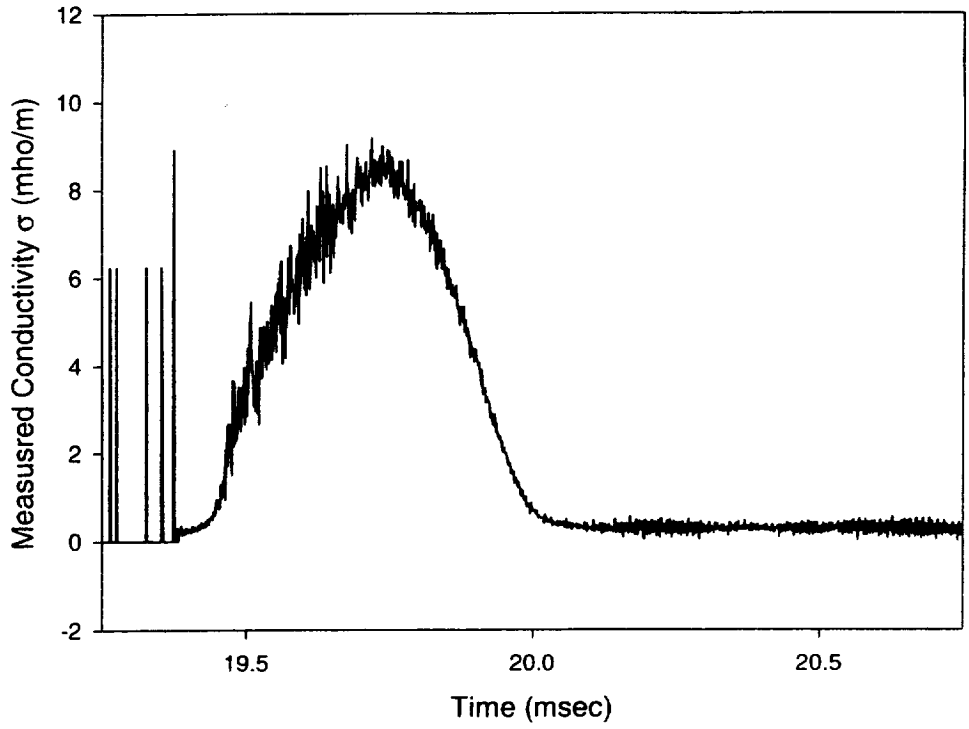

27 A JUNE 1997

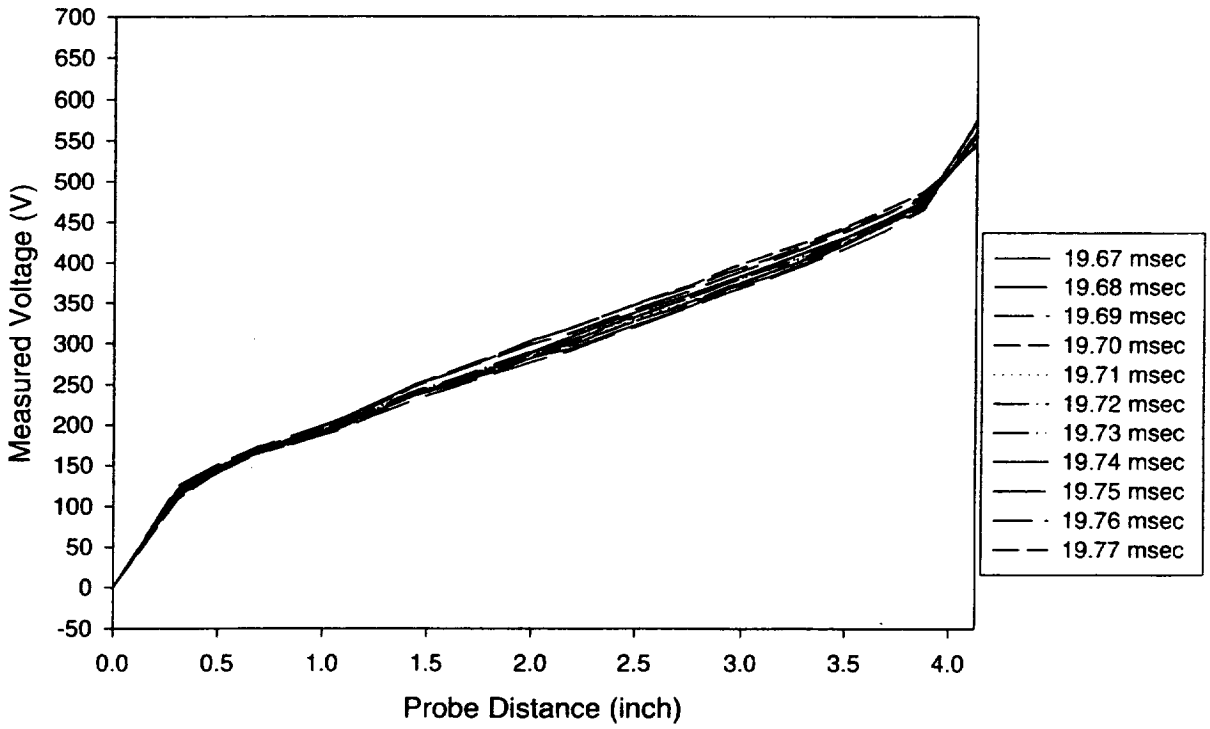

27 B JUNE 1997

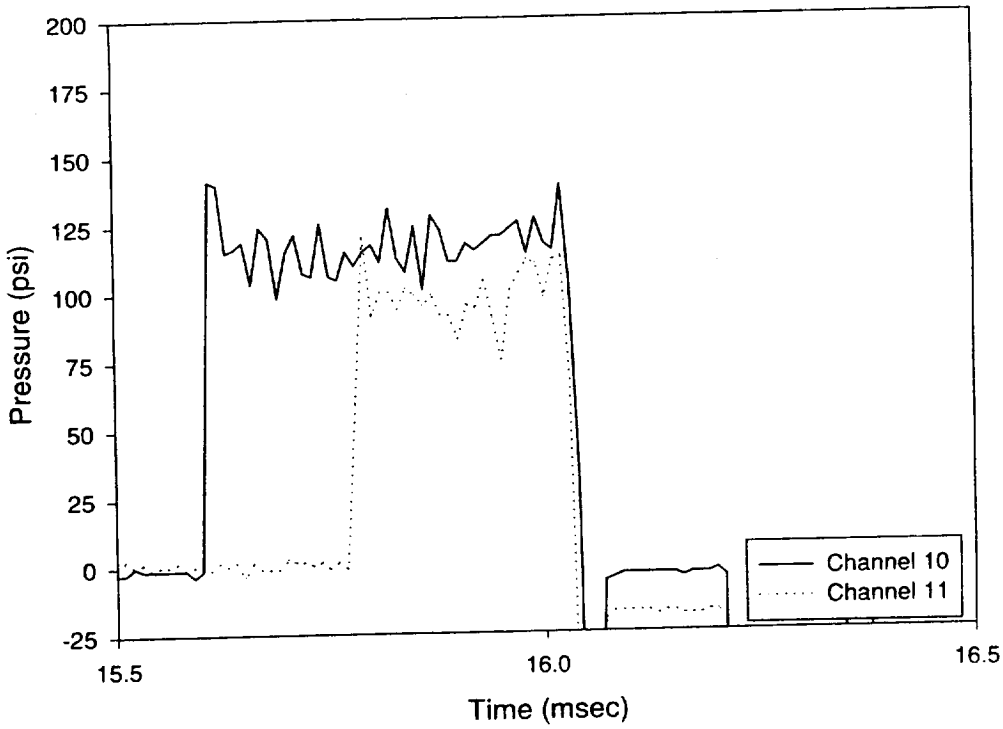

27 B JUNE 1997

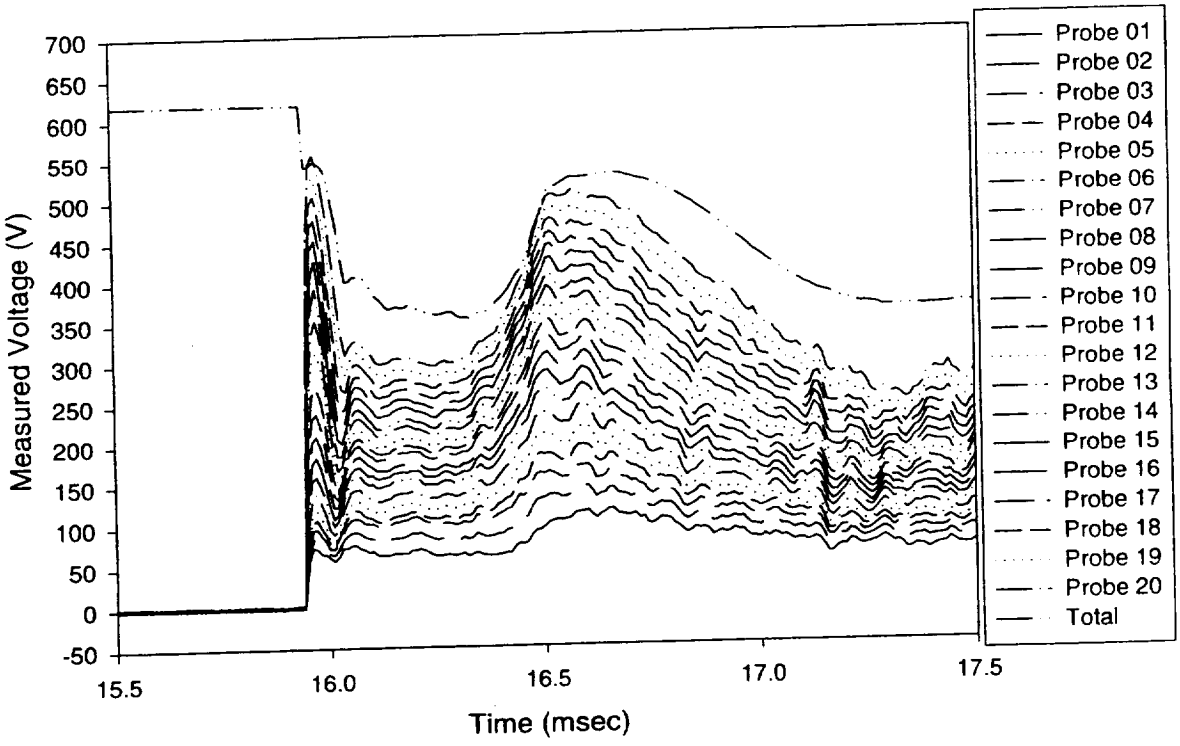

27 B JUNE 1997

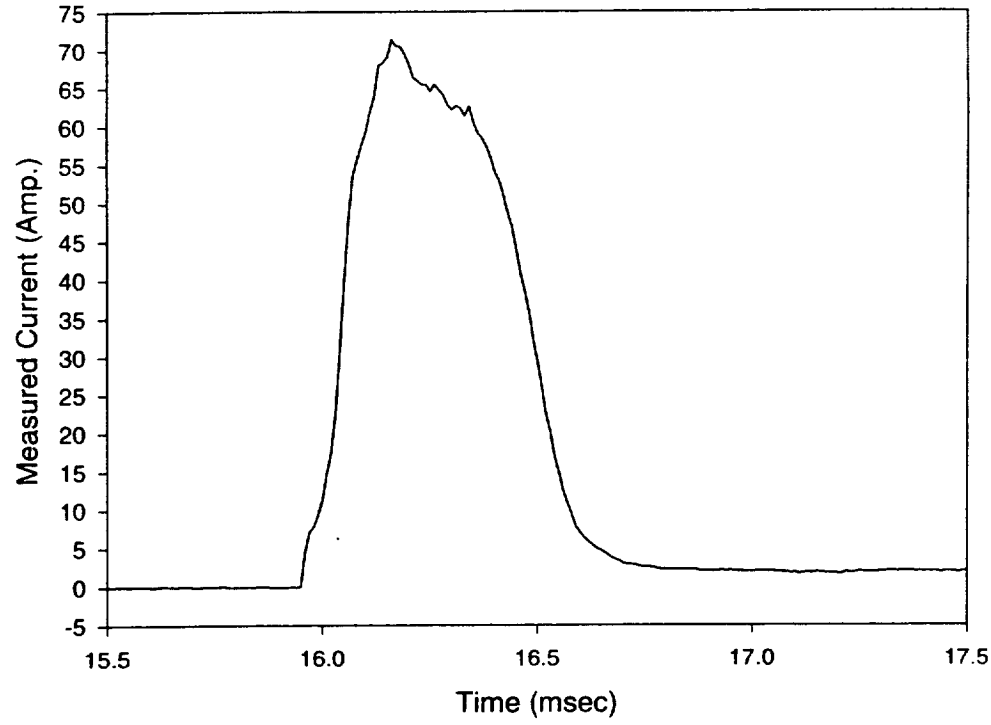

27 B JUNE 1997

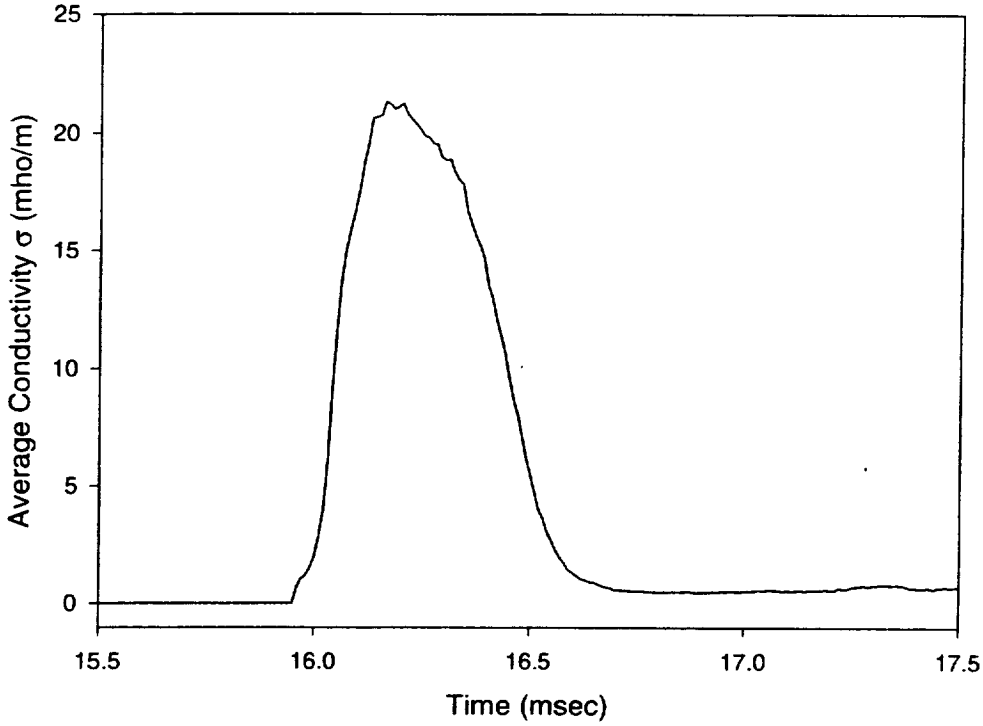

27 B JUNE 1997

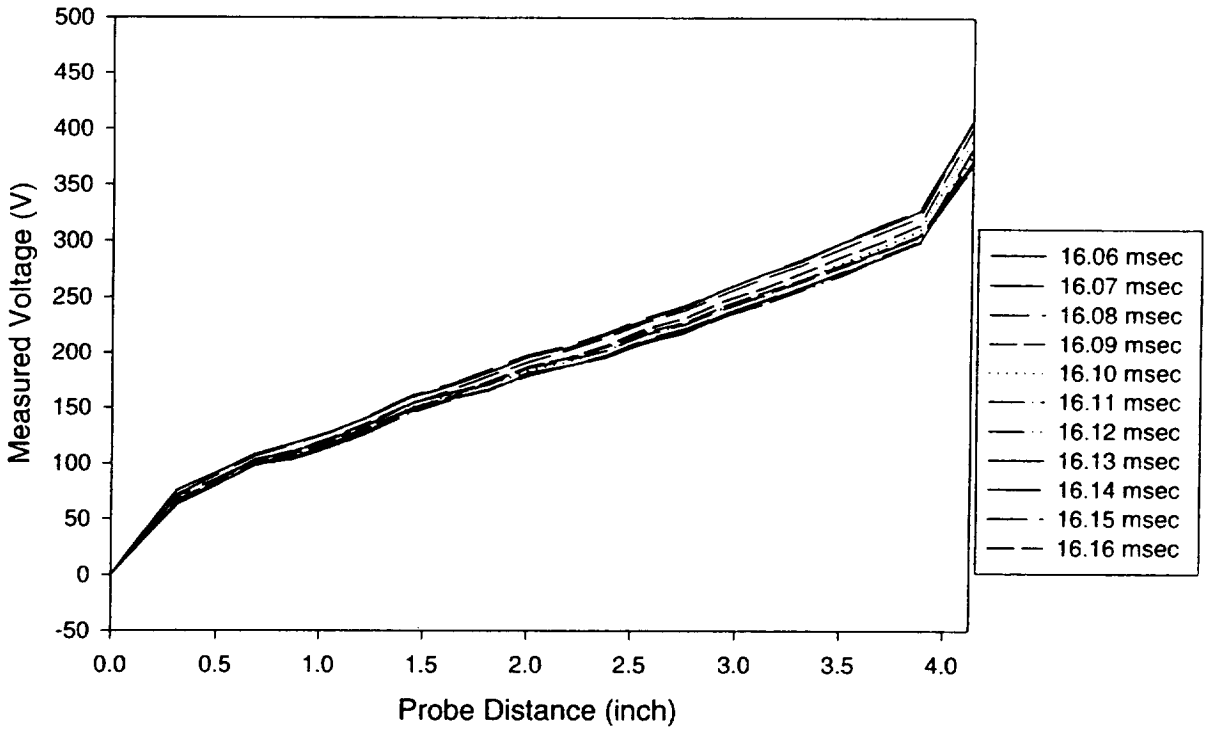

27 C JUNE 1997

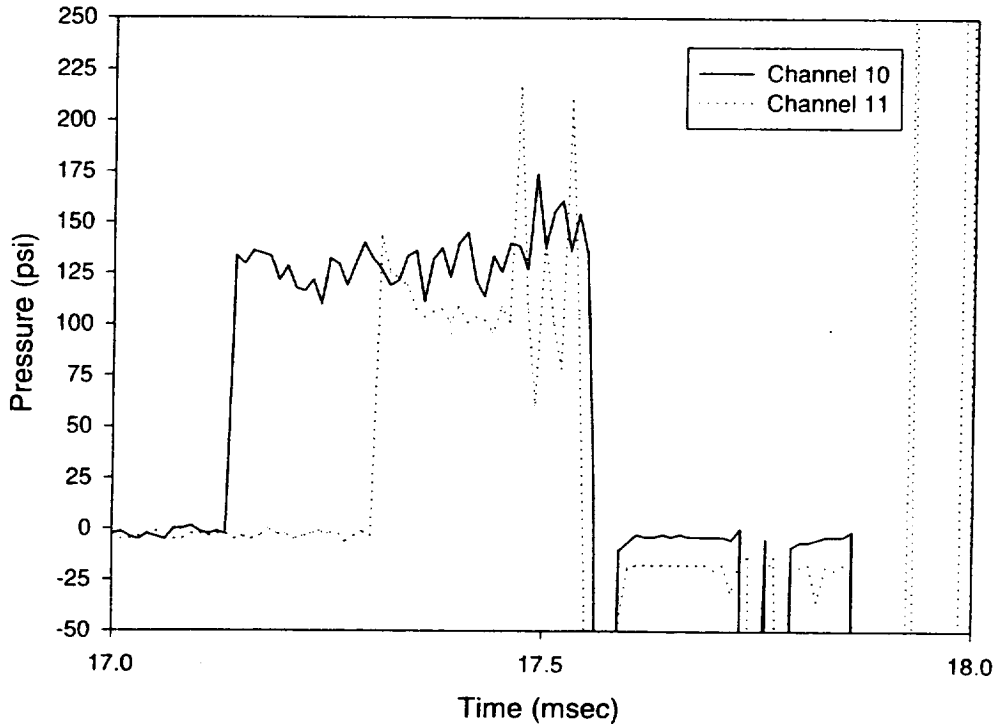

27 C JUNE 1997

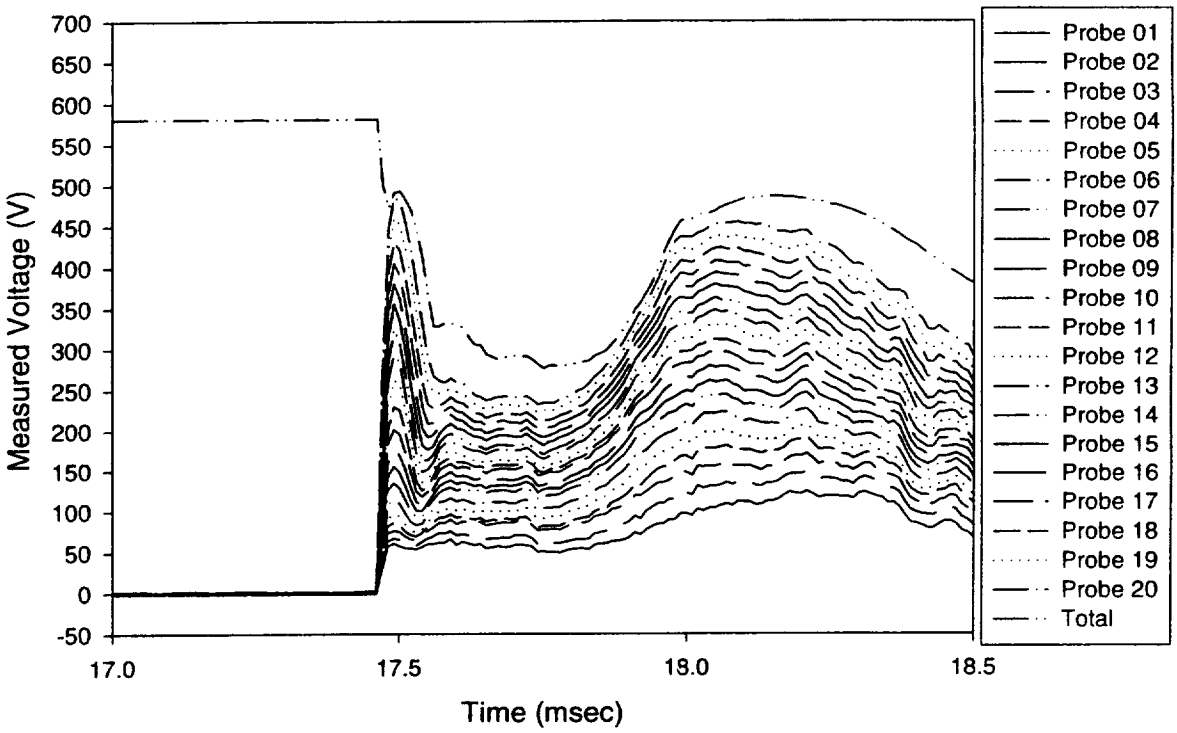

27 C JUNE 1997

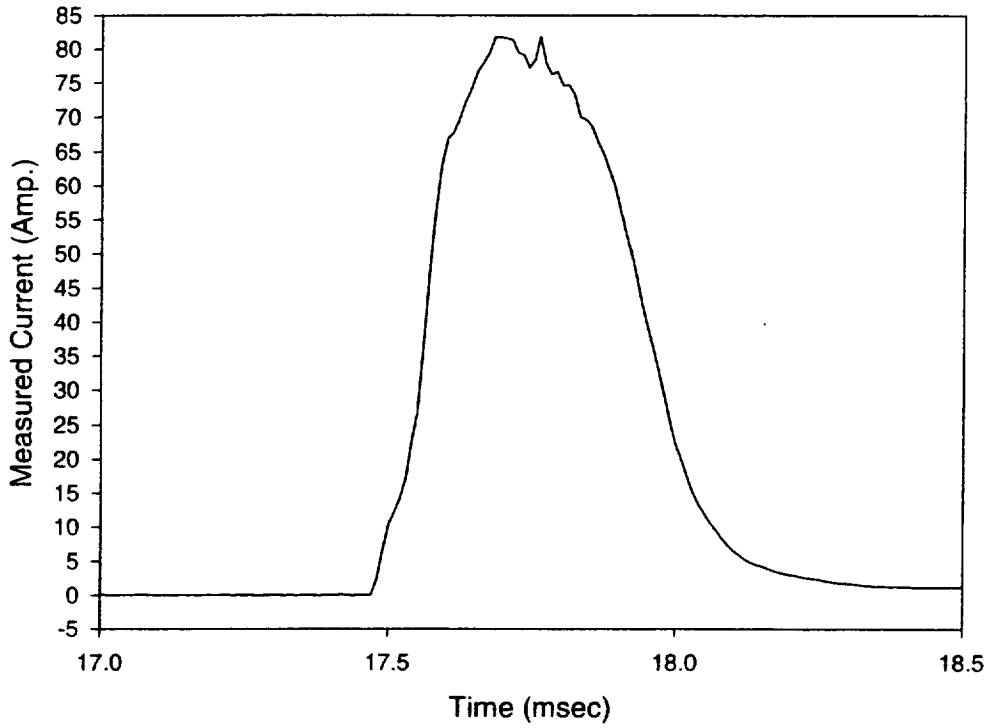

27 C JUNE 1997

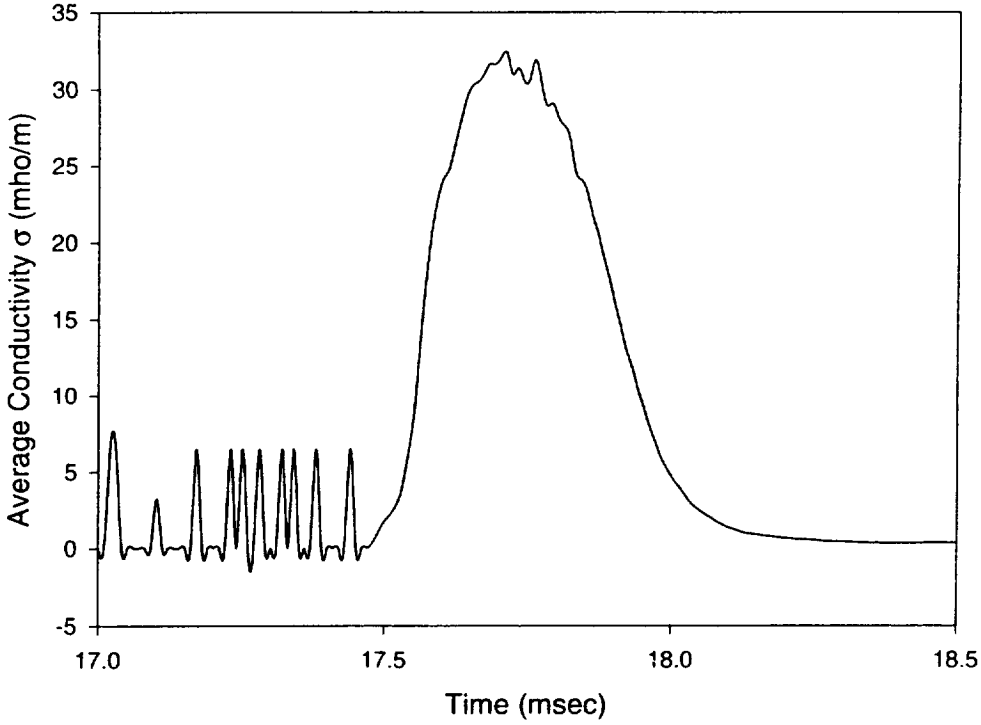

27 C JUNE 1997

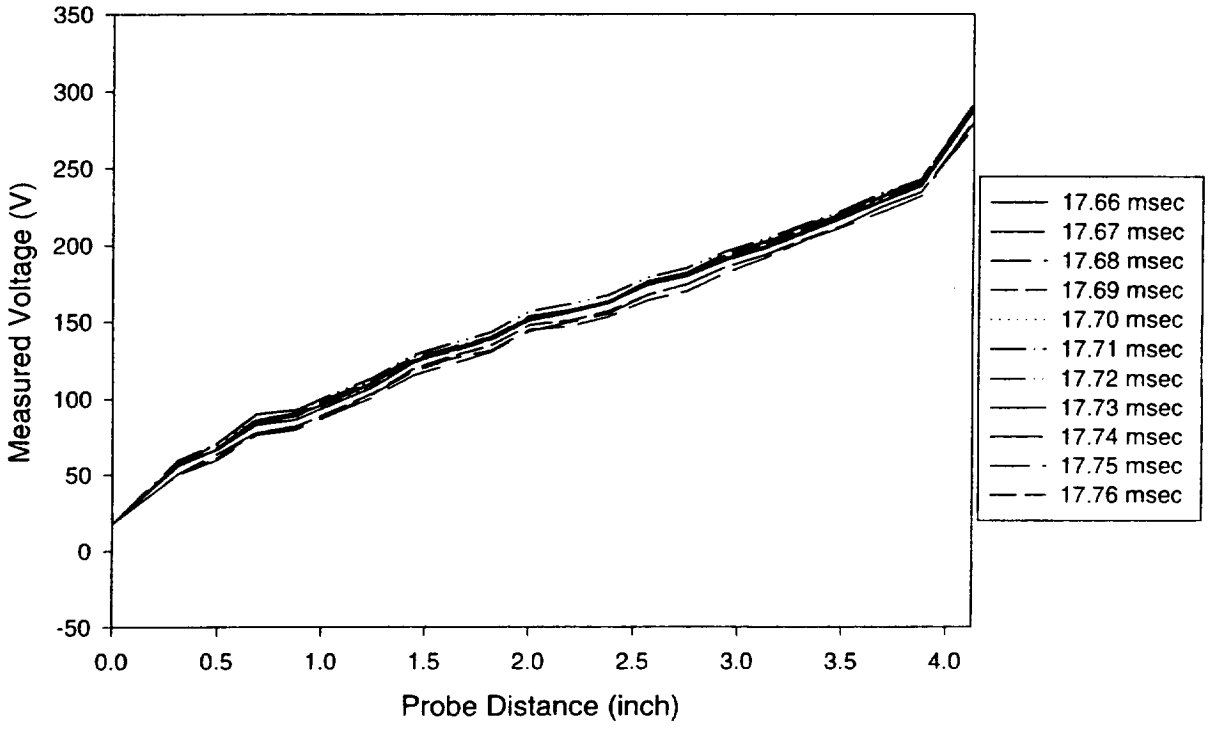

27 D JUNE 1997

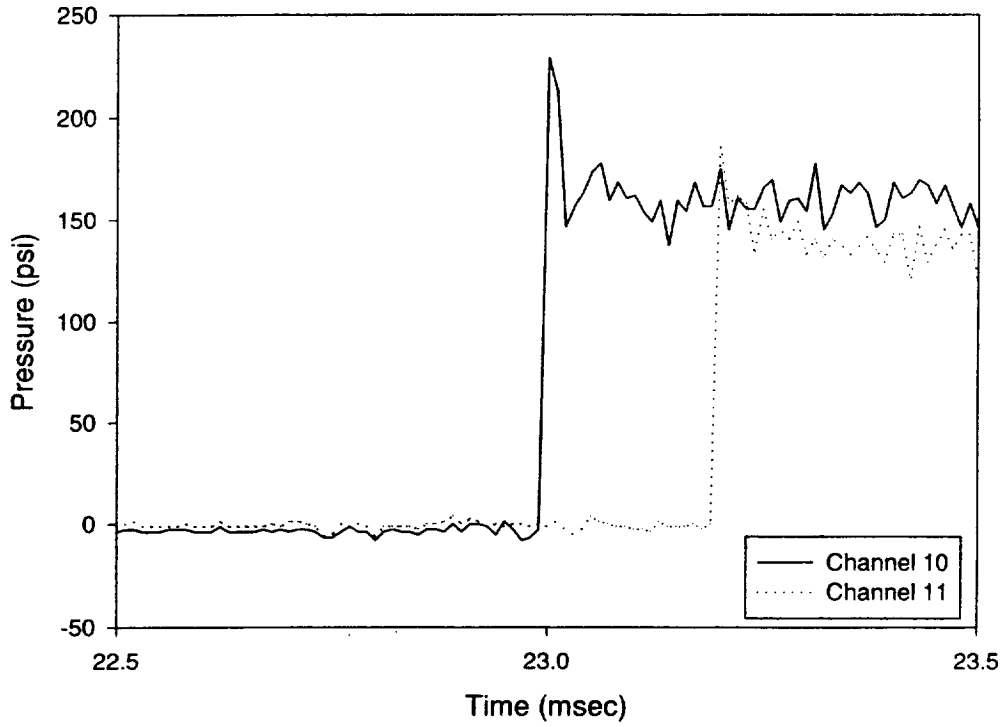

27 D JUNE 1997

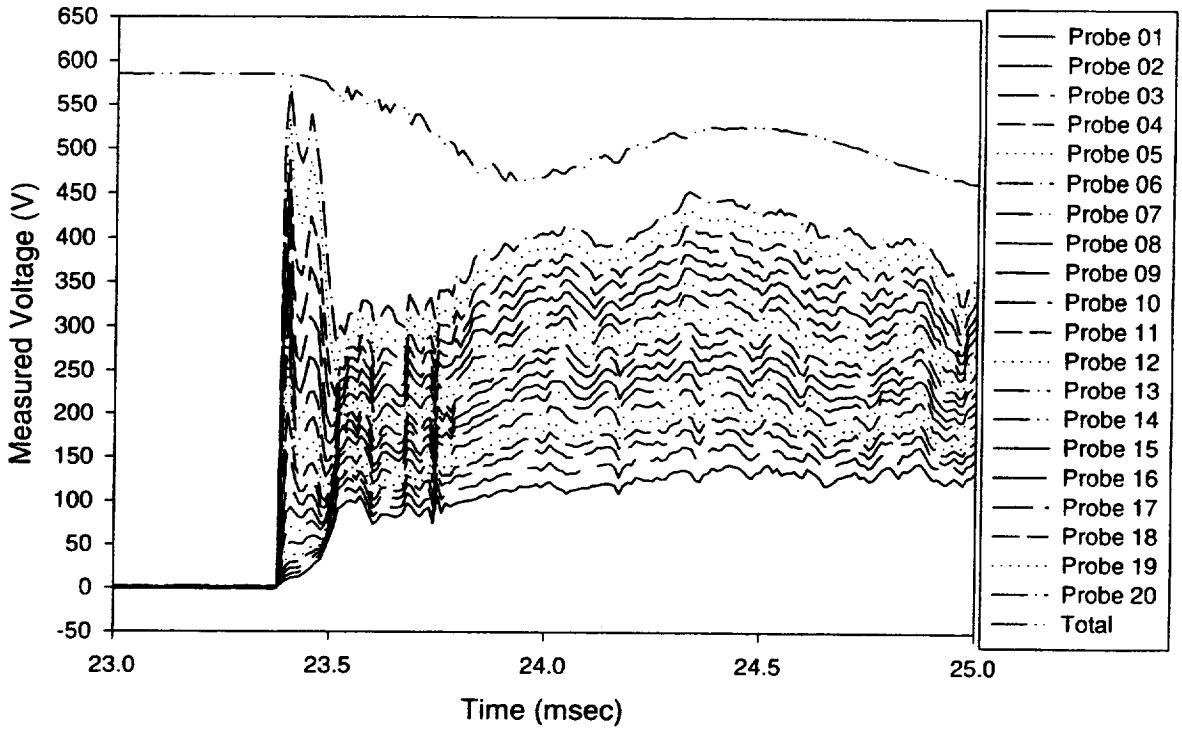

27 D JUNE 1997

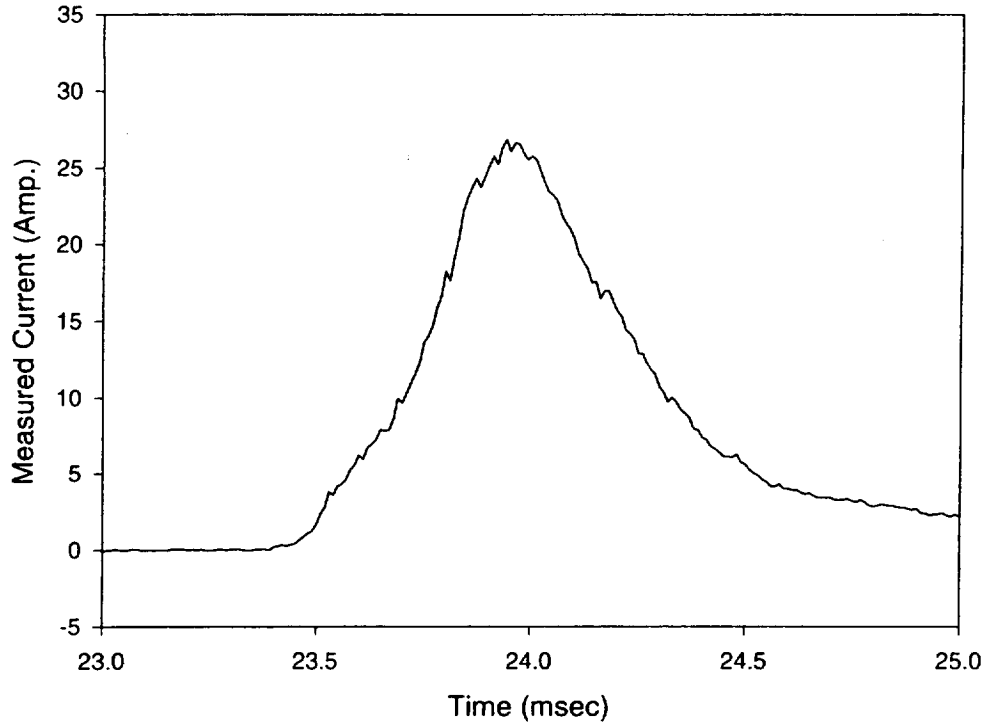

27 D JUNE 1997

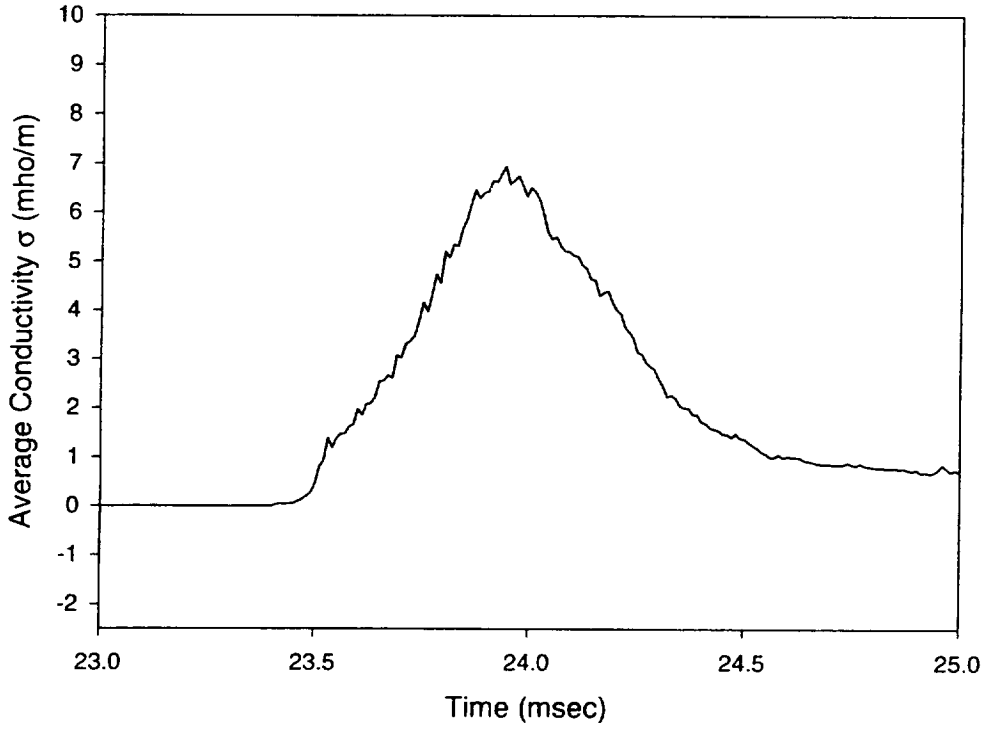

27 D JUNE 1997

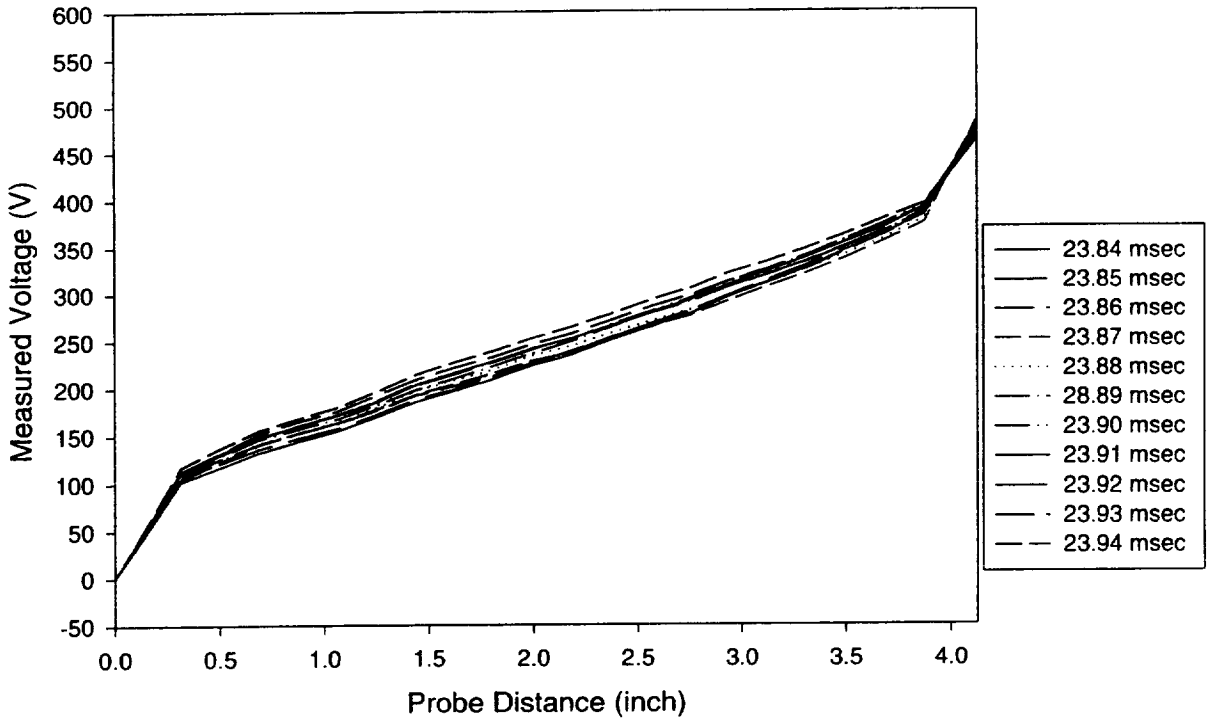

27 E JUNE 1997

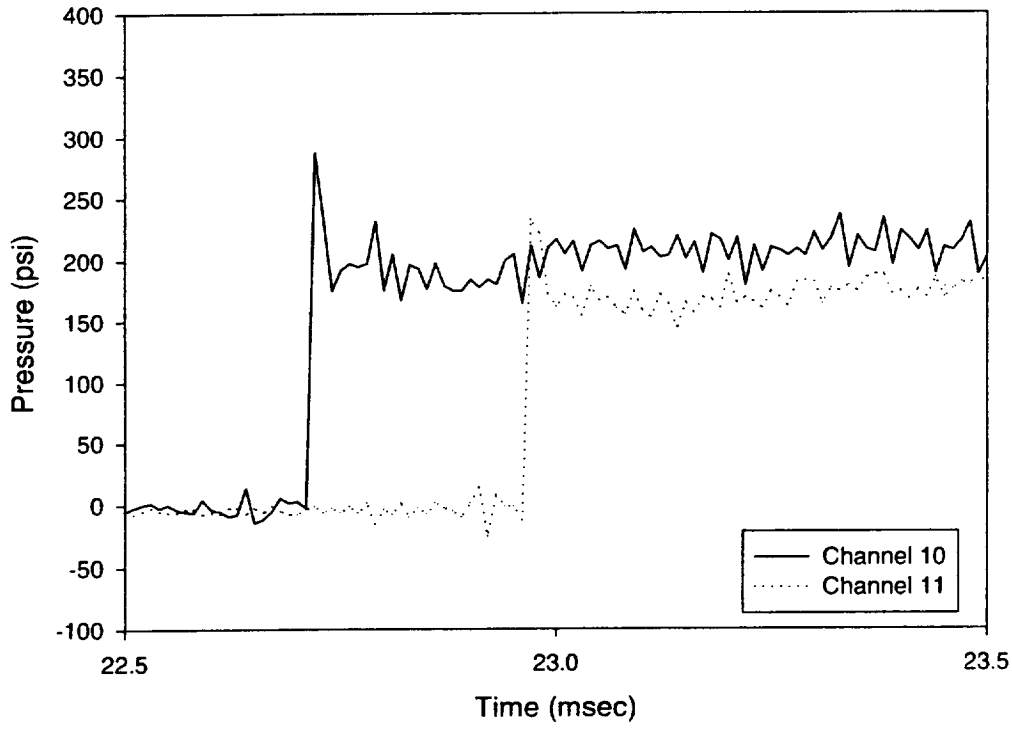

27 E JUNE 1997

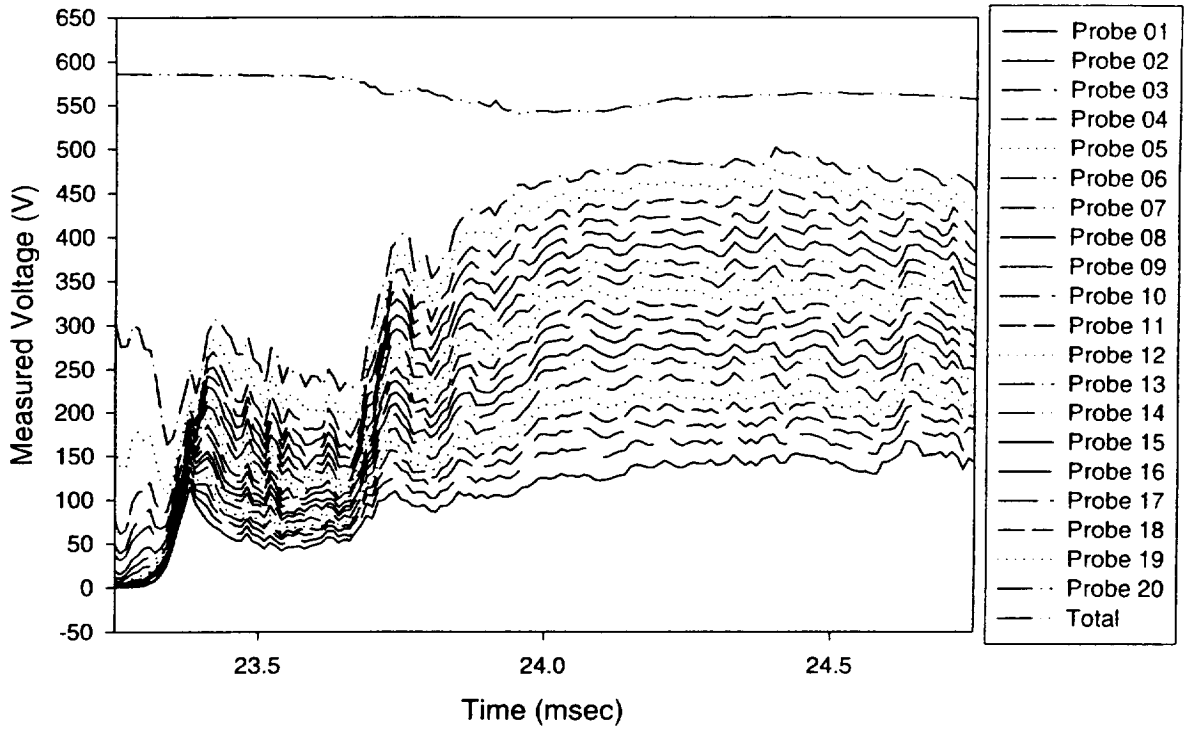

27 E JUNE 1997

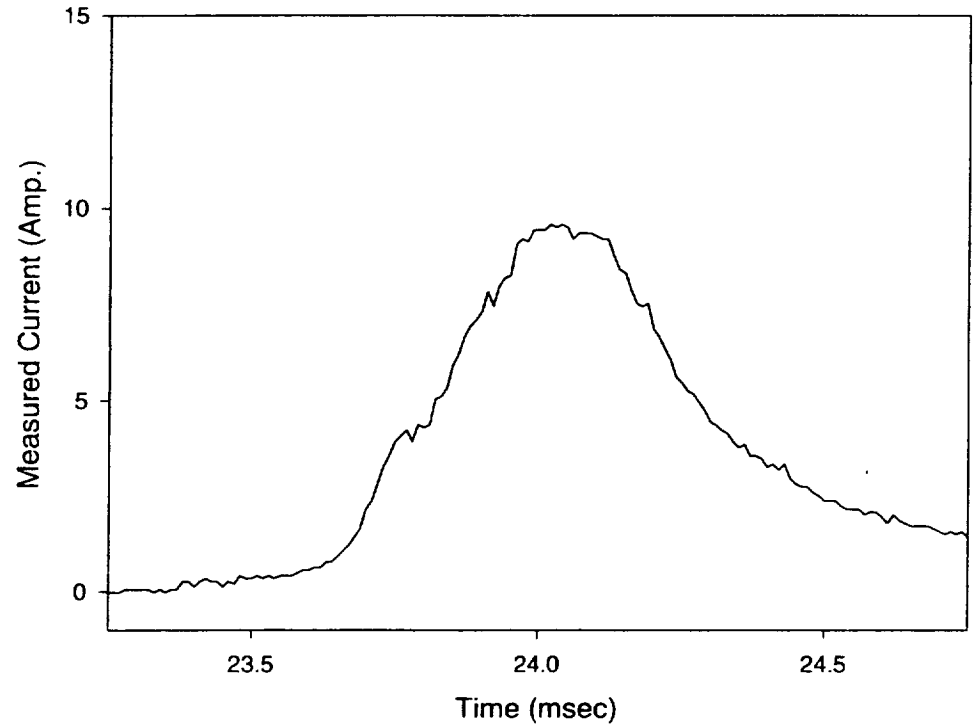

27 E JUNE 1997

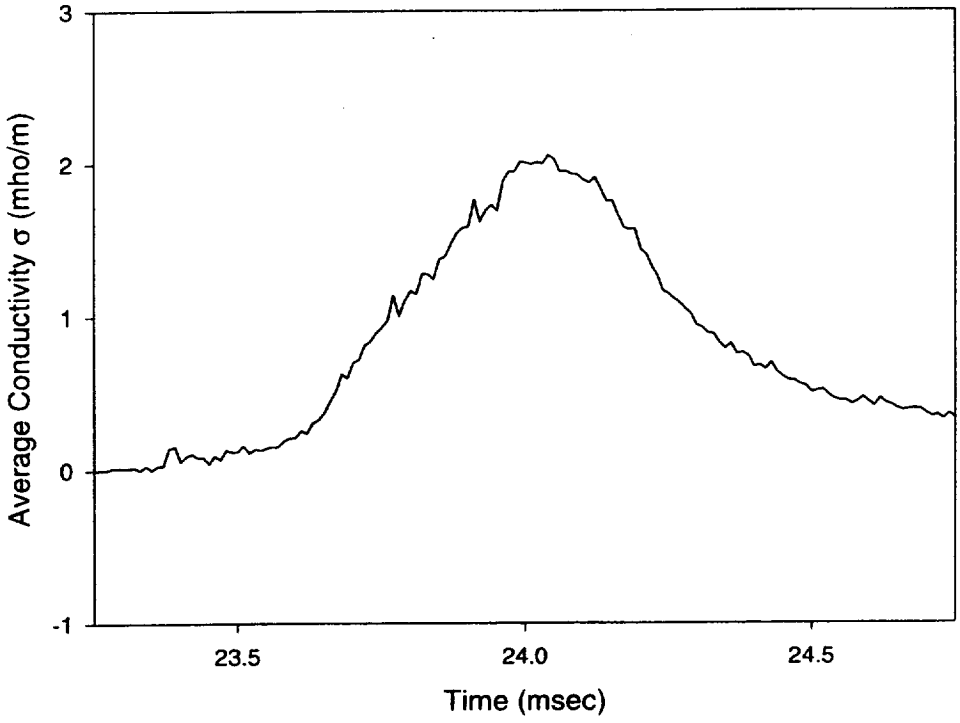

27 E JUNE 1997

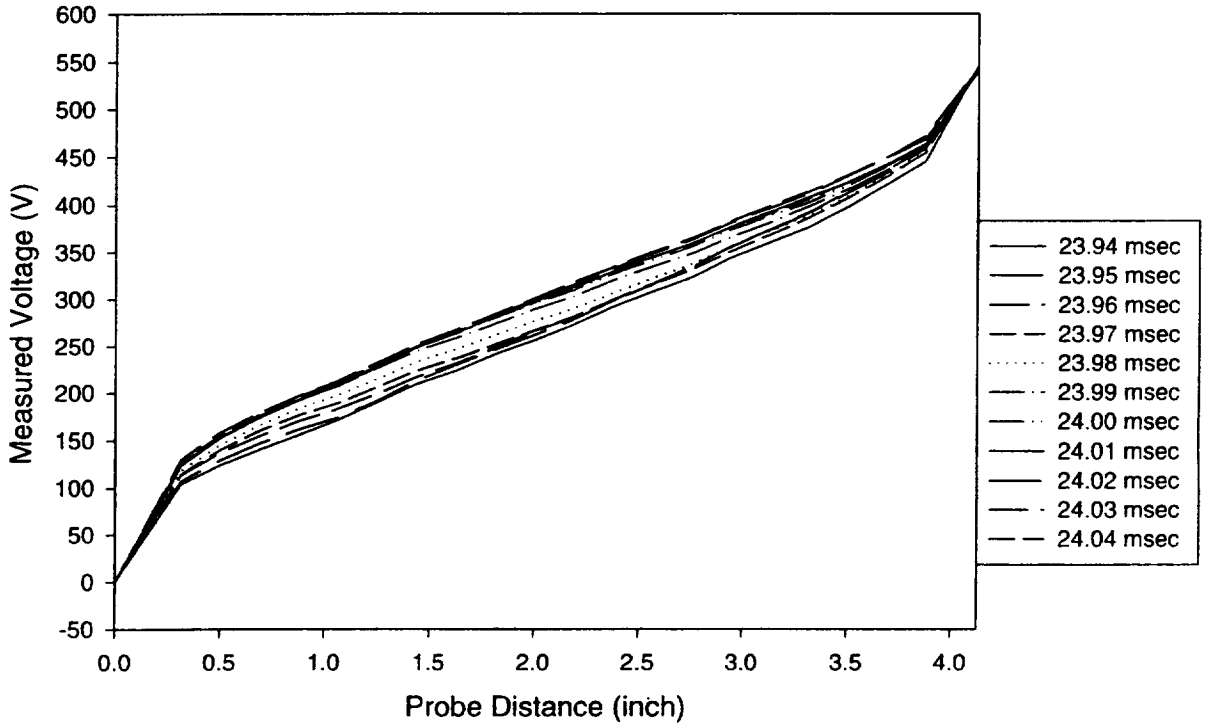

27 F JUNE 1997

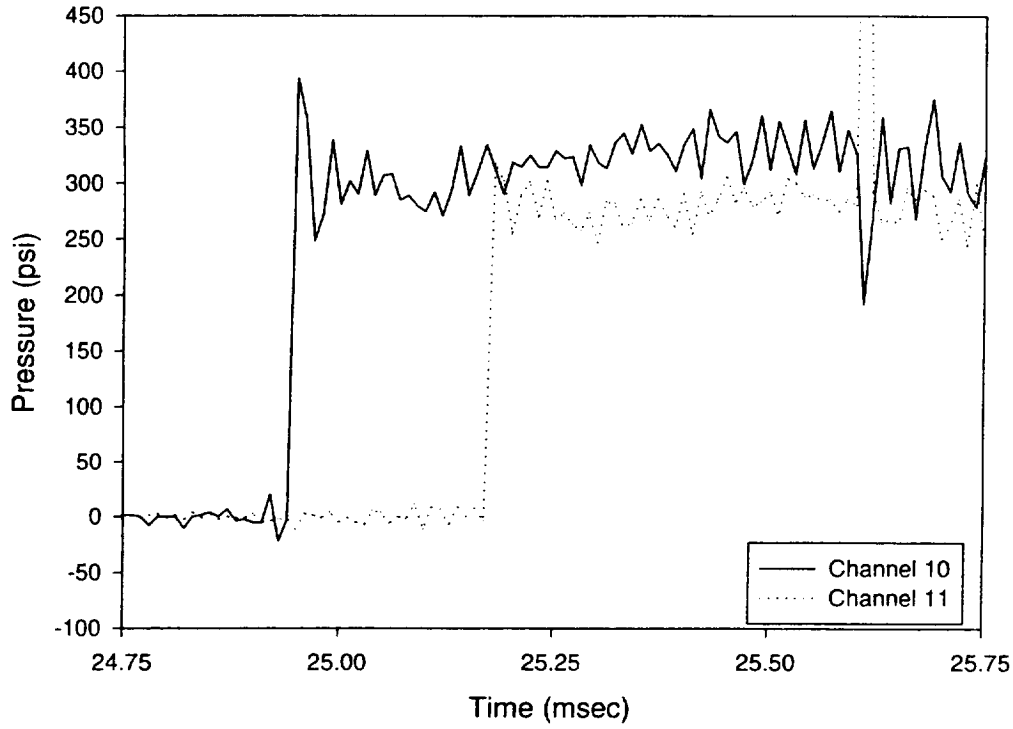

27 F JUNE 1997

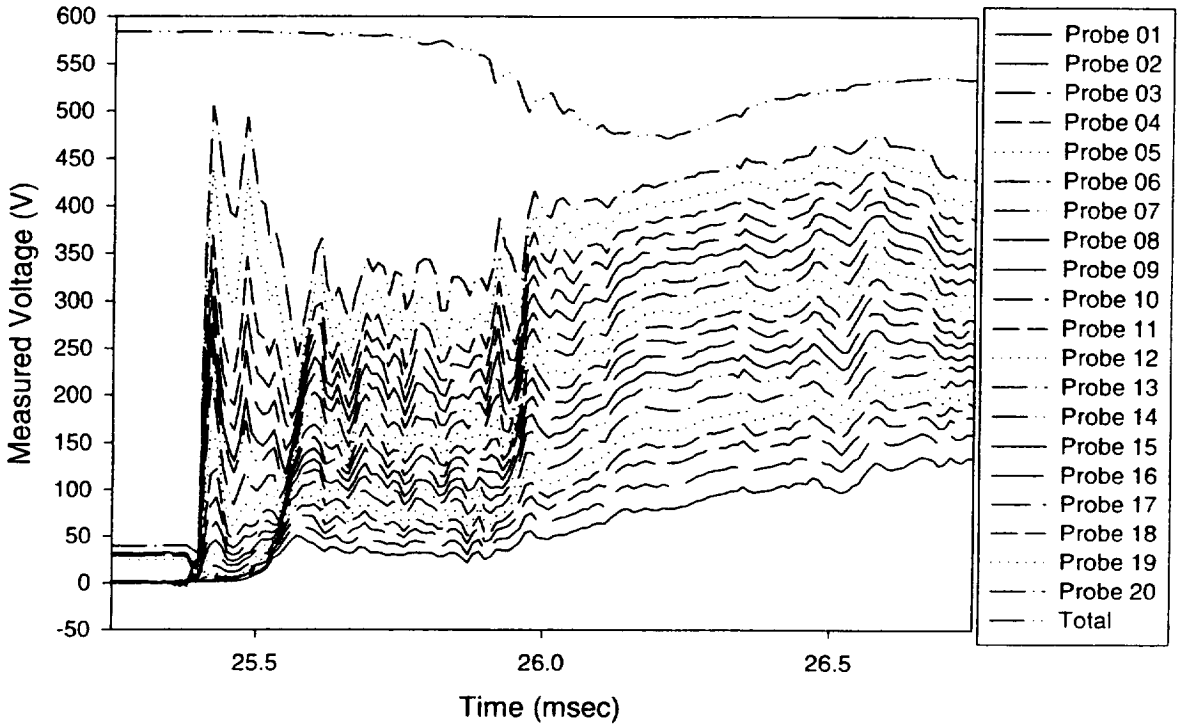

27 F JUNE 1997

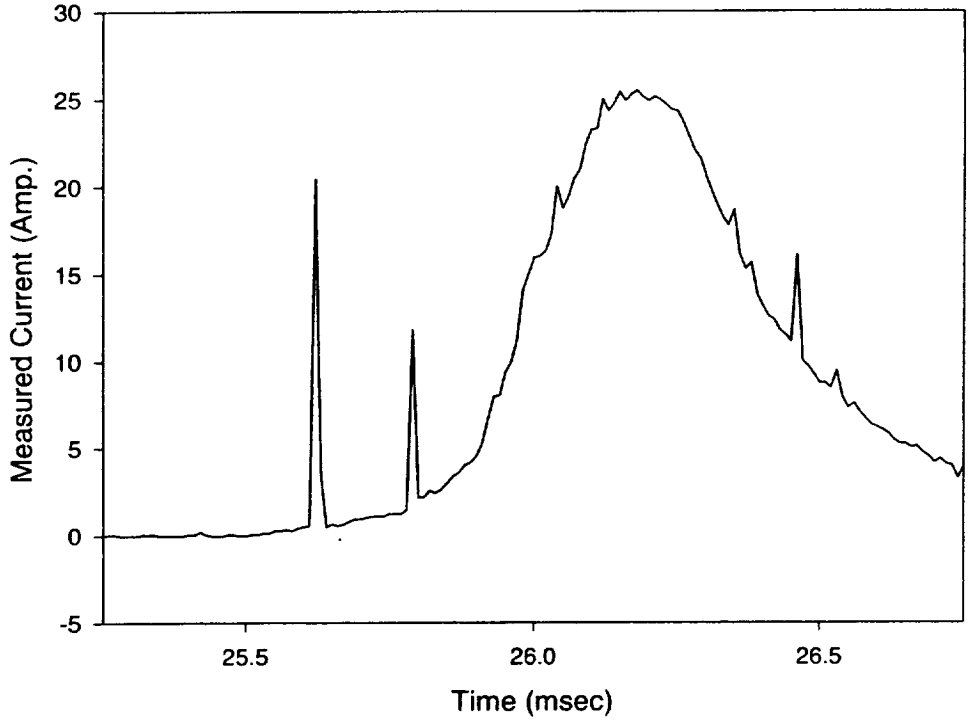

27 F JUNE 1997

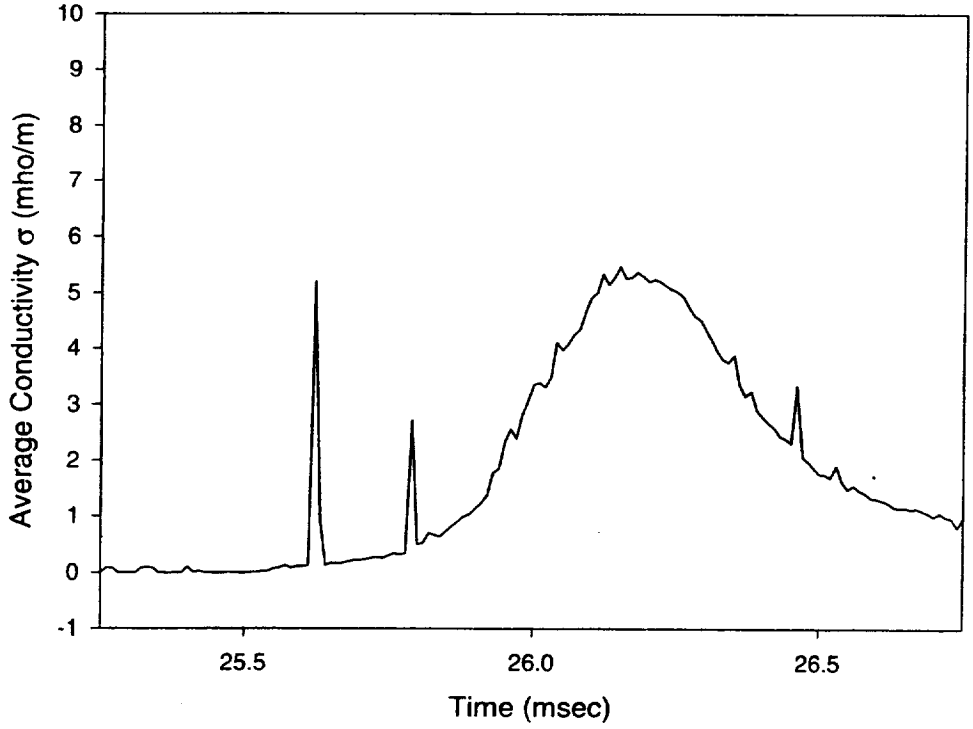

27 F JUNE 1997

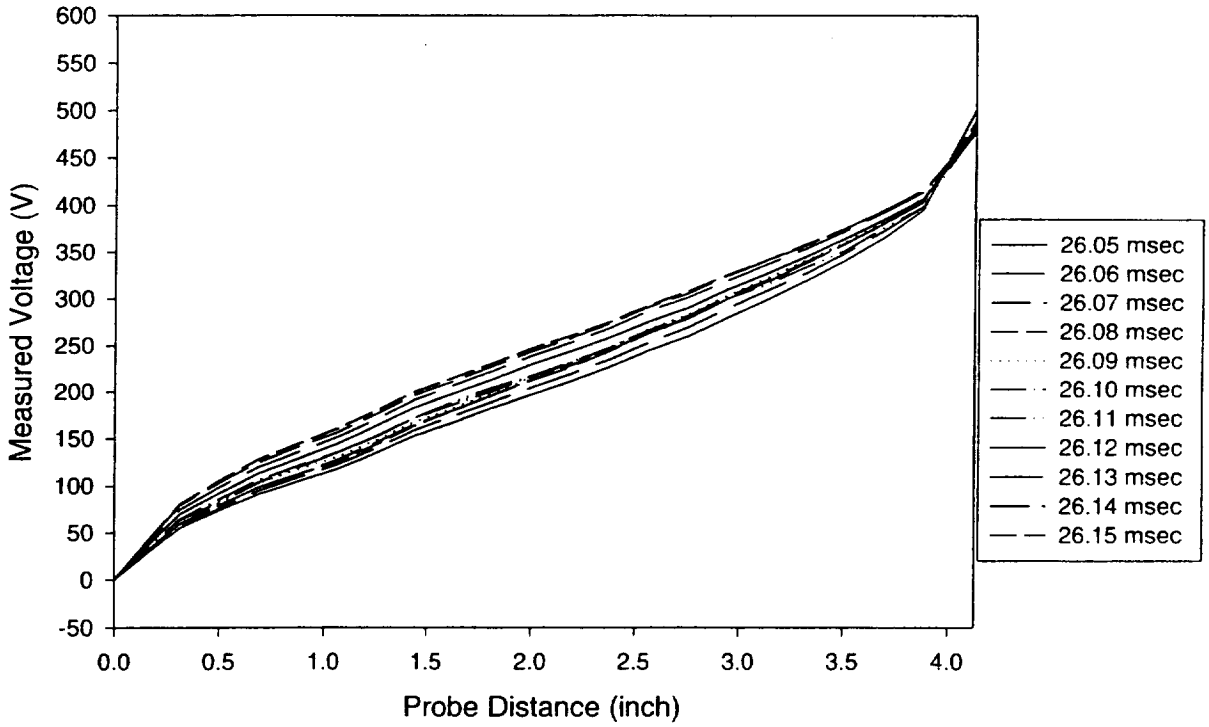

28 A JUNE 1997

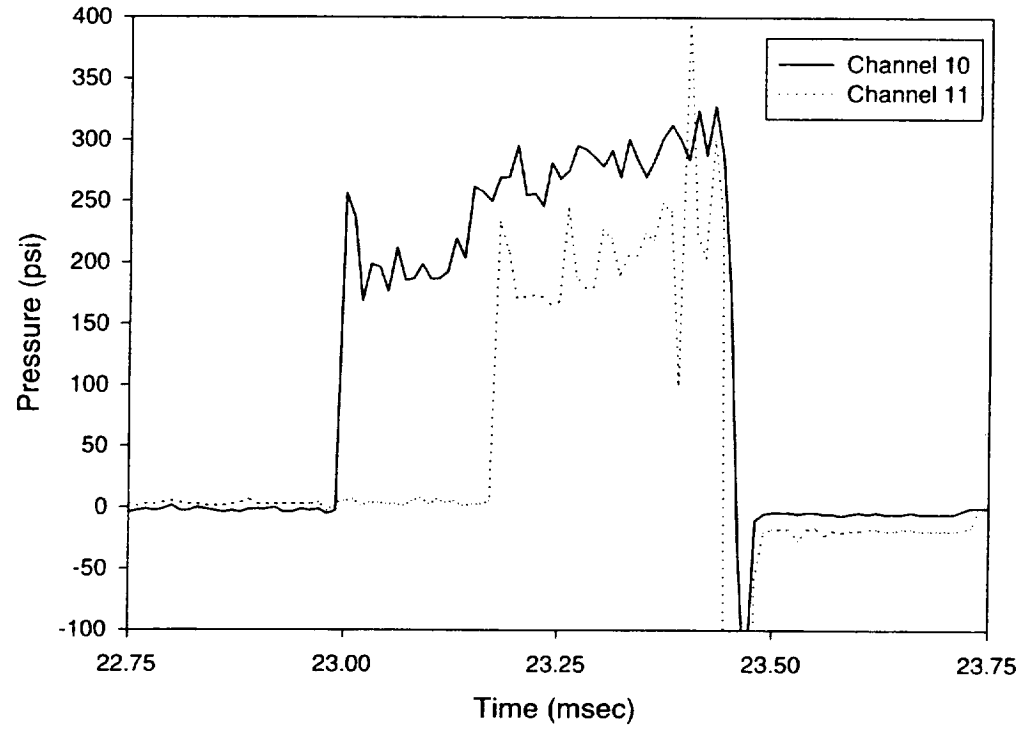

28 A JUNE 1997

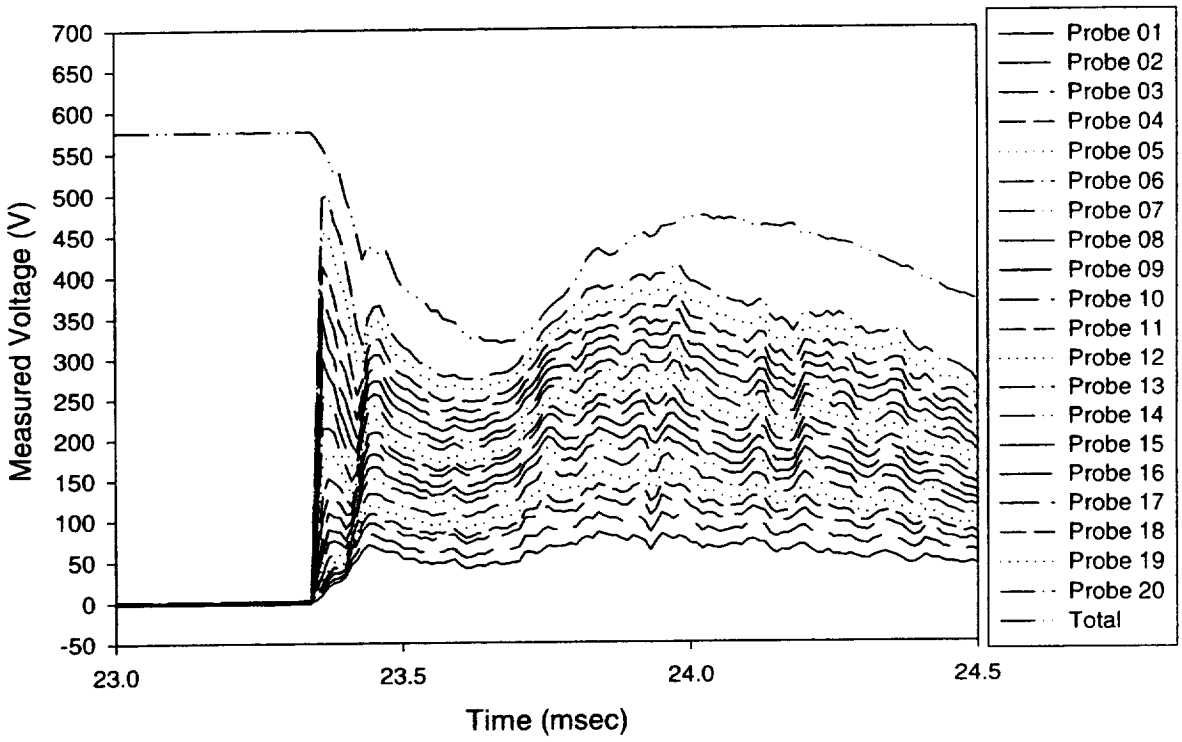

28 A JUNE 1997

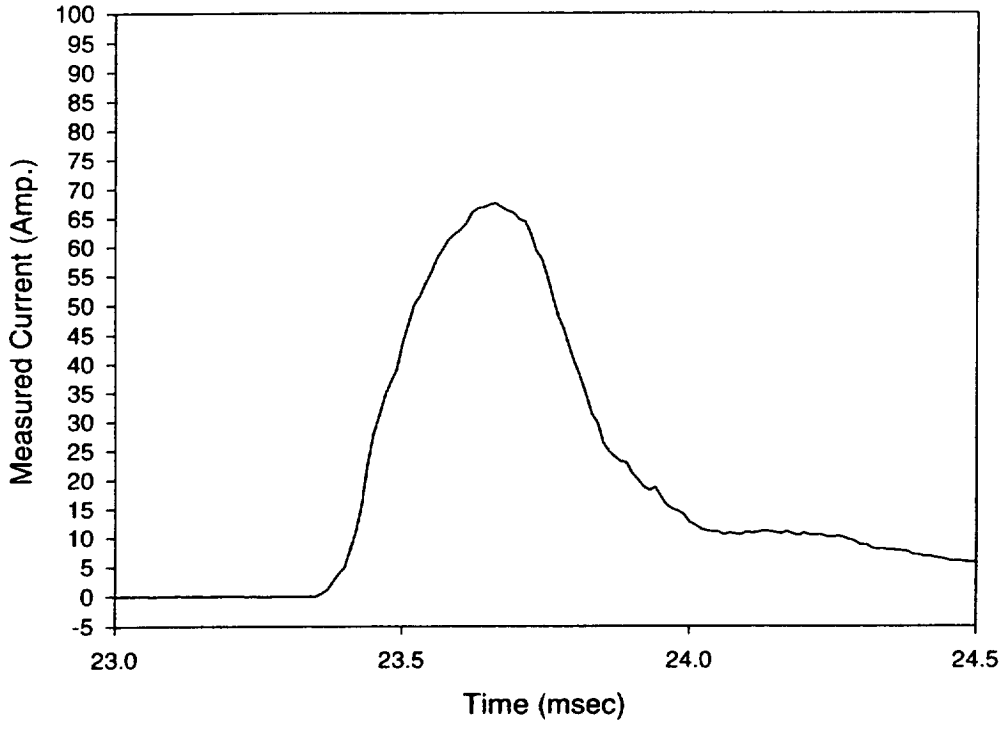

28 A JUNE 1997

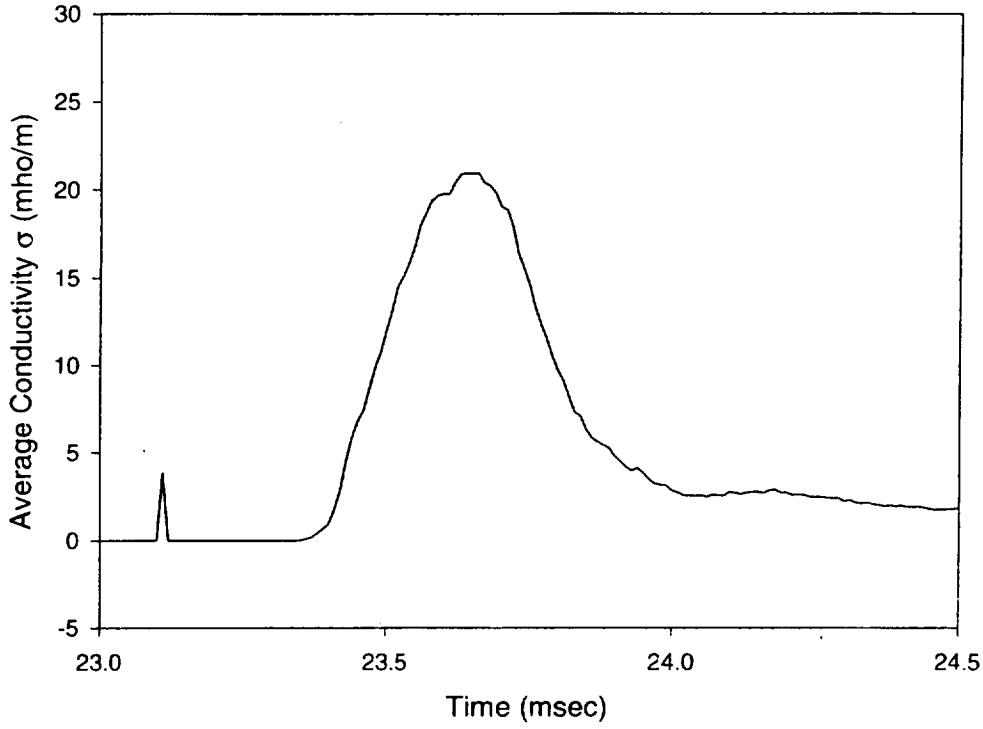

28 A JUNE 1997

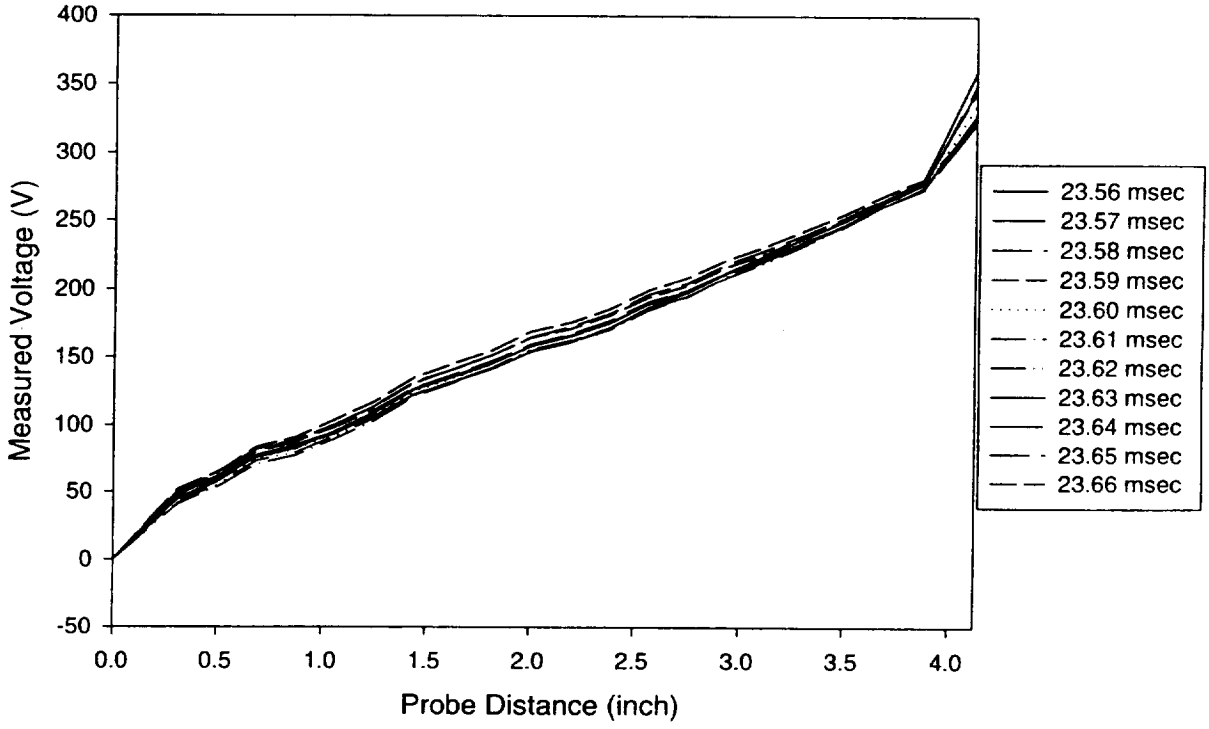

28 B JUNE 1997

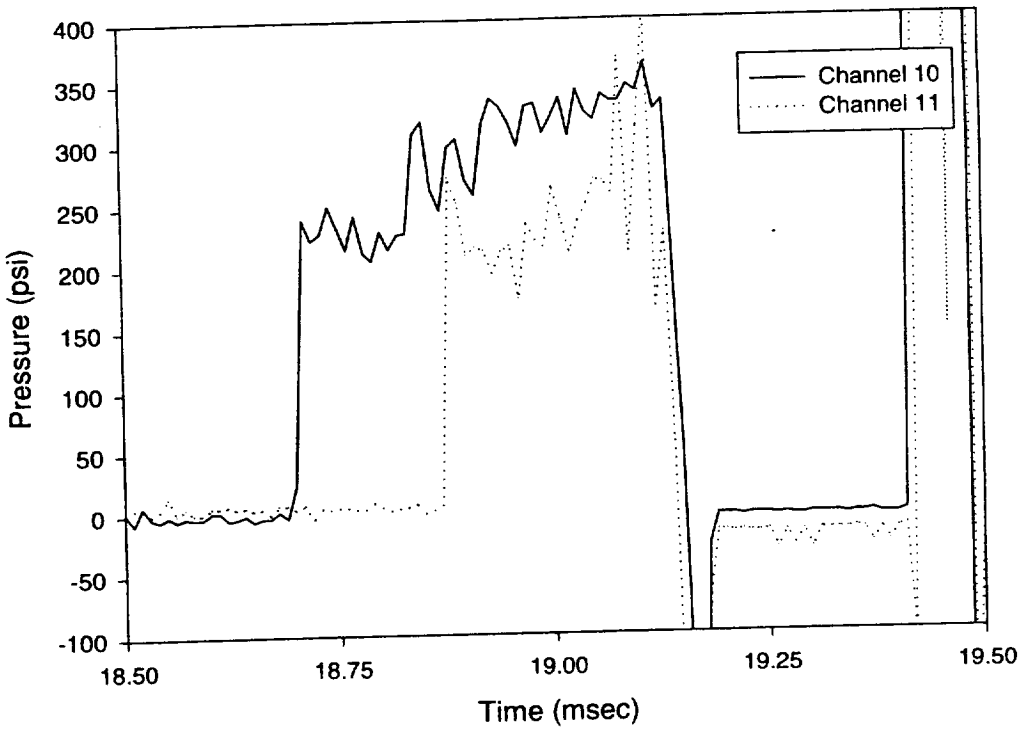

28 B JUNE 1997

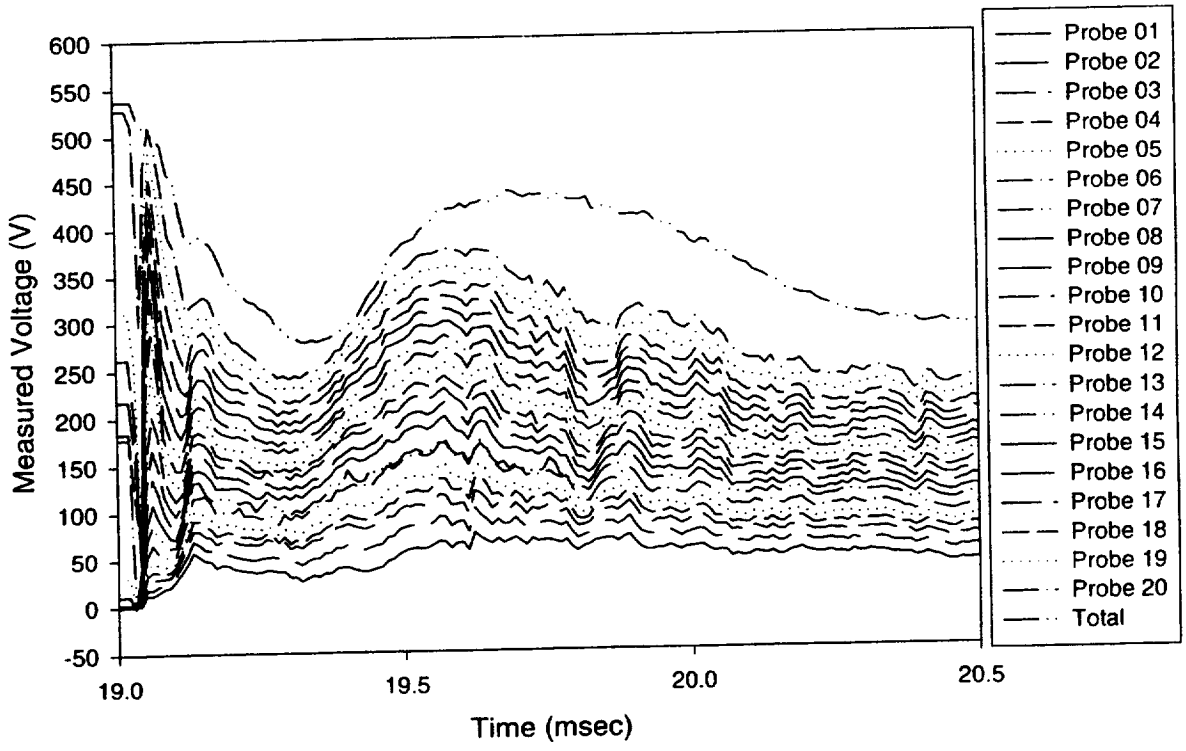

28 B JUNE 1997

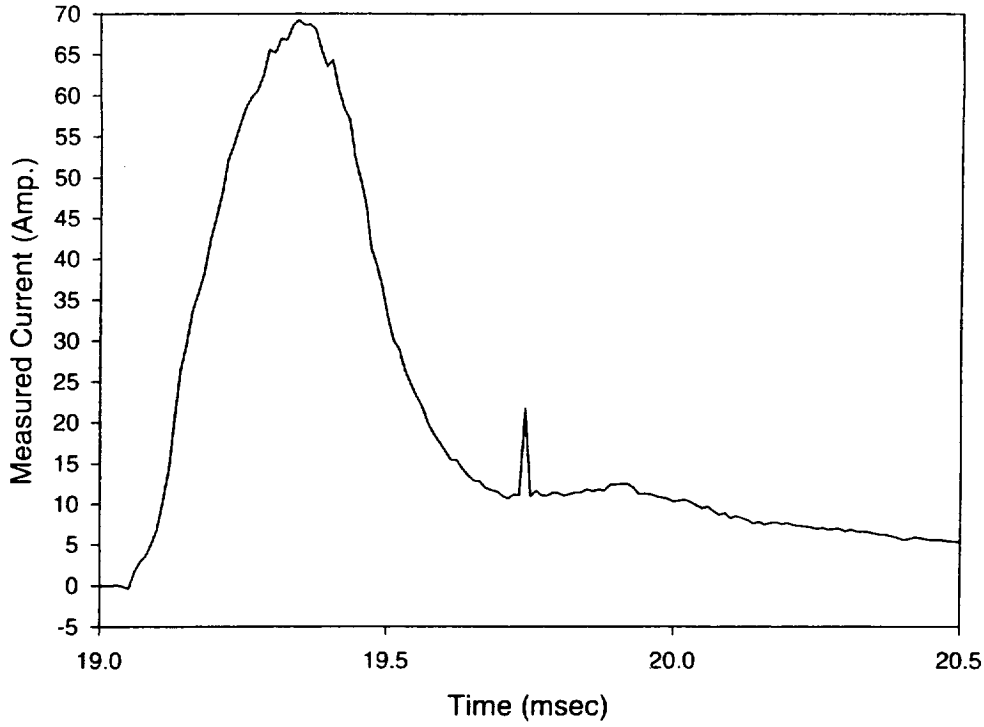

28 B JUNE 1997

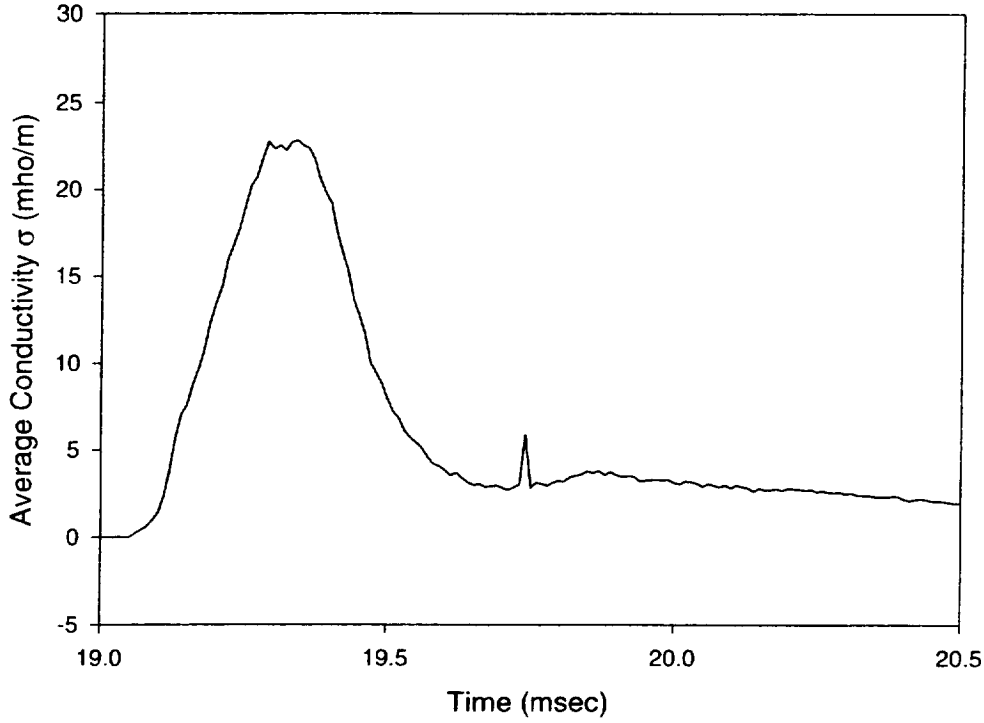

28 B JUNE 1997

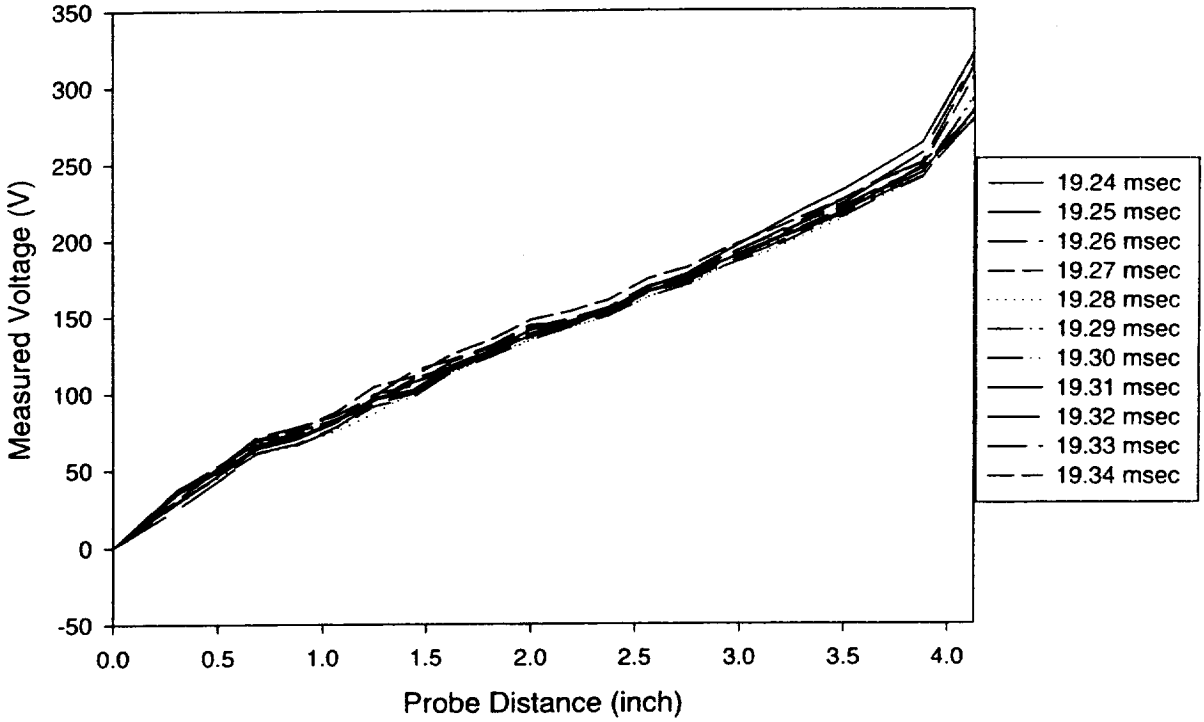

28 C JUNE 1997

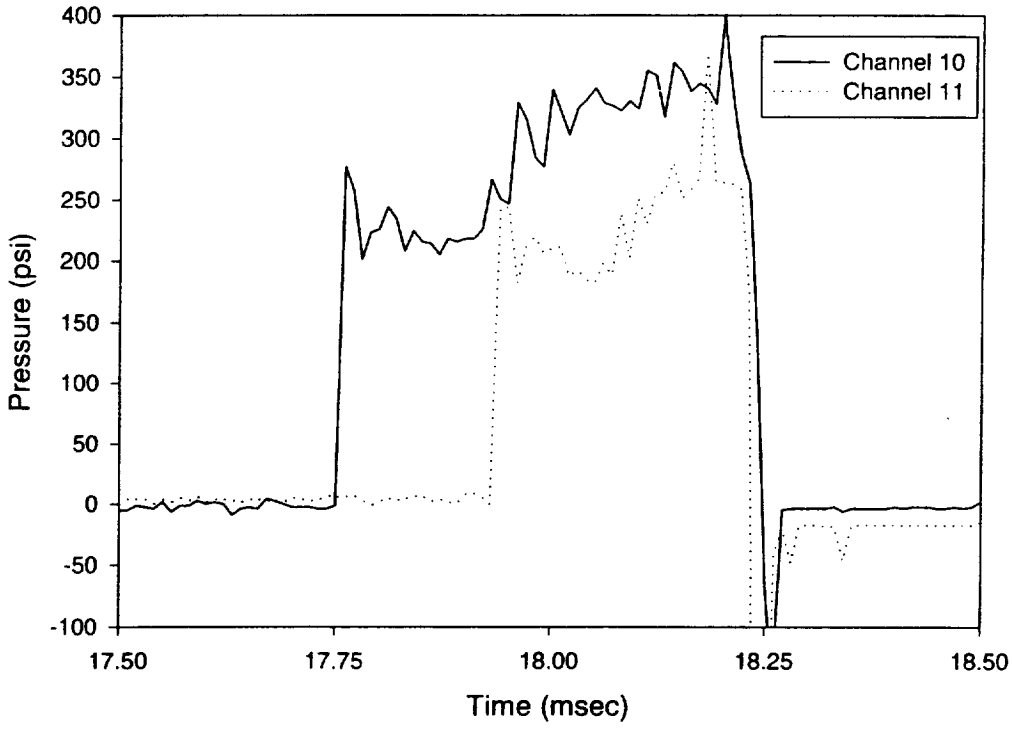

28 C JUNE 1997

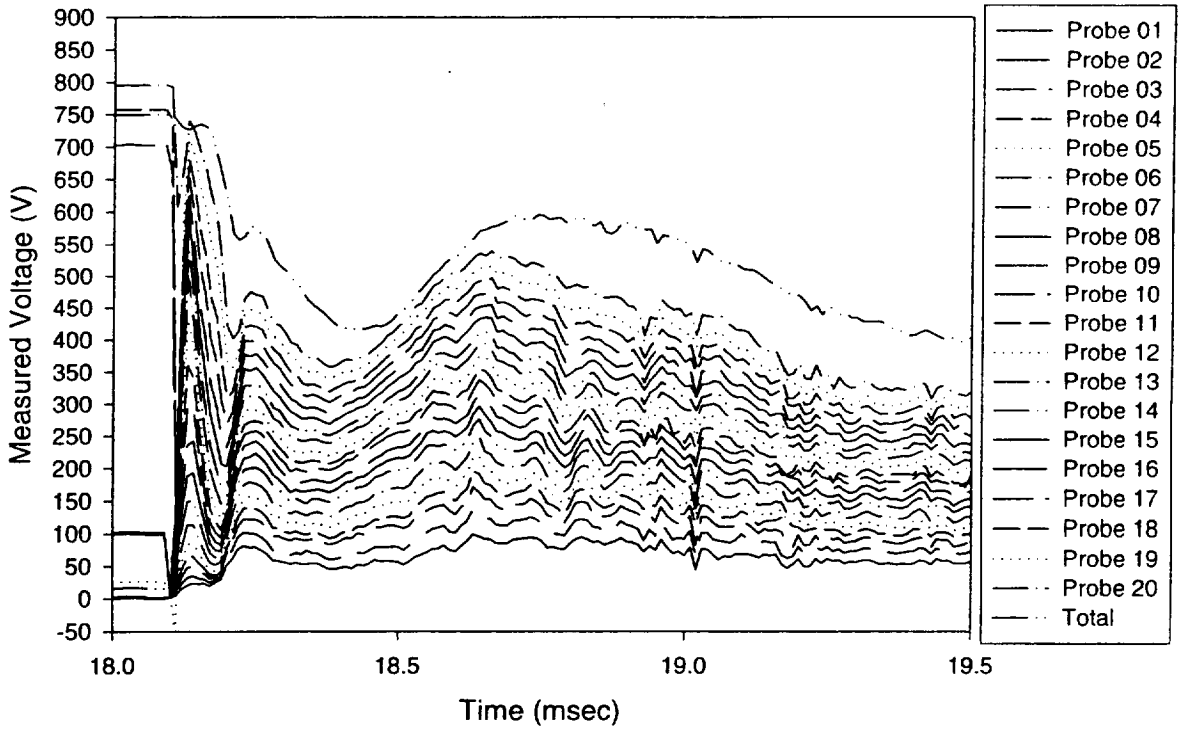

28 C JUNE 1997

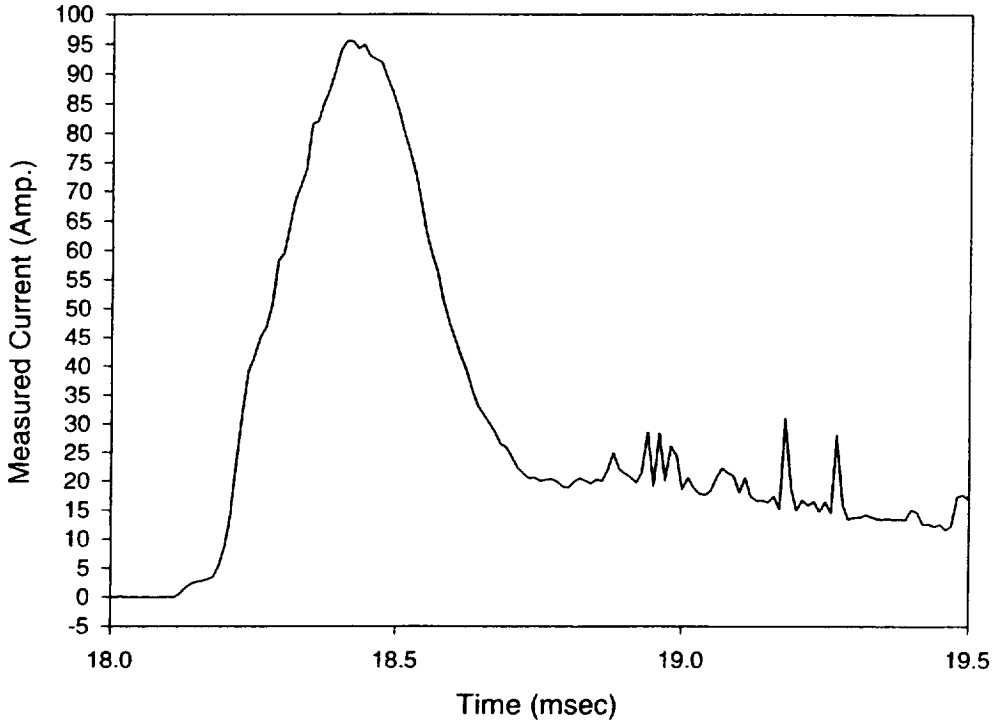

28 C JUNE 1997

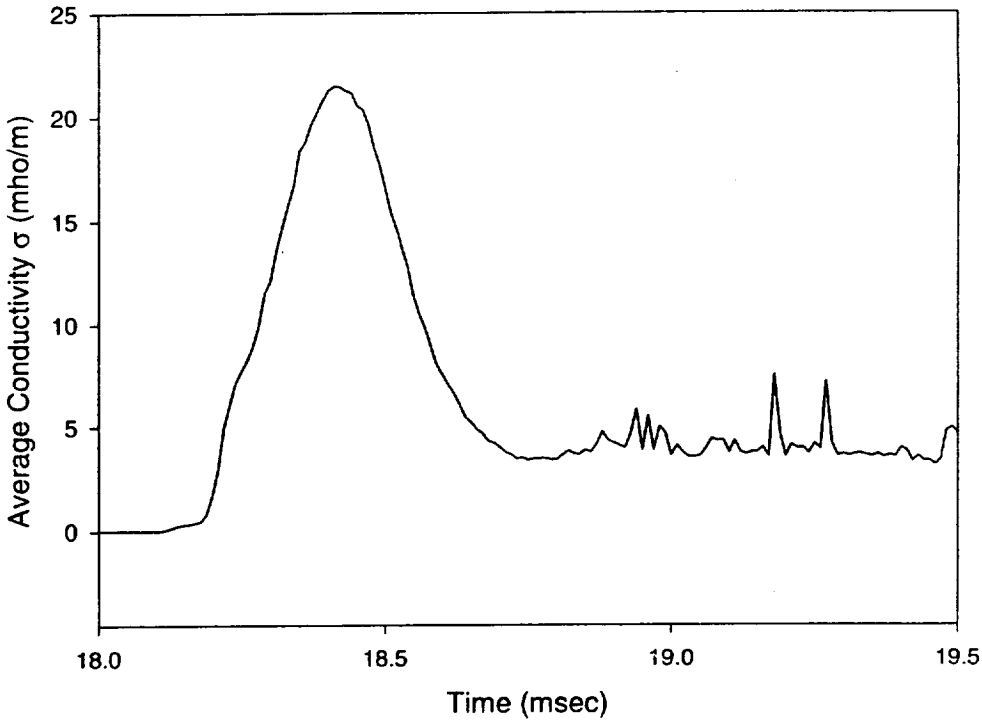

28 C JUNE 1997

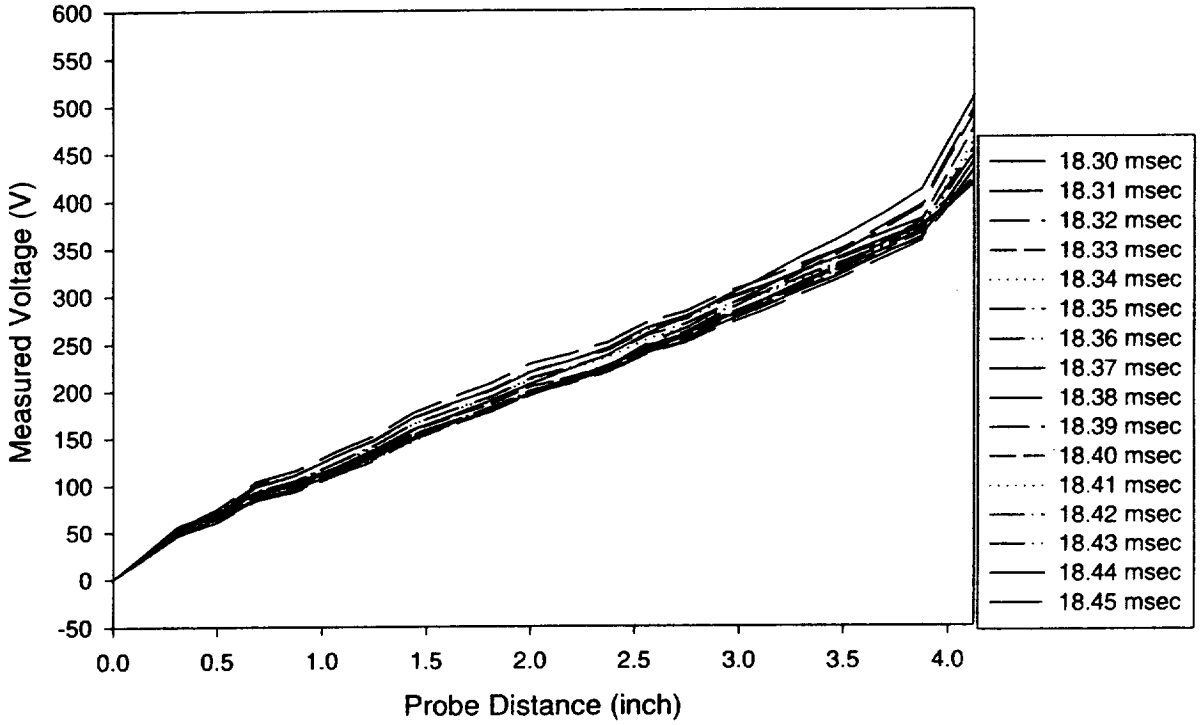

APPENDIX A, SECTION A.2

A.2 NASA AMES RESEARCH CENTER TEST PROGRAM

The results of experimental research conducted at NASA Ames for investigating the effects of pressure, ionization fraction, and electric field strength on the electrical conductivity and discharge characteristics in high-pressure, unseeded air are reported in this section. Experimentally measured electrical property data is generally not available for air in the high-temperature, high-pressure, and hypervelocity testing regime of interest in the MARIAH Project. The experiments at NASA Ames were designed to provide insight into the electrical discharge physics of high-pressure air.

Alkali metal seed materials, usually used to achieve ionization at low-temperature in MHD accelerators, cannot be used in the spectroscopically-clean shock-tube facility used for these experiments. Therefore, these experiments were conducted at high-temperature to thermally achieve the same ionization fractions in air that would typically be achieved from the seed species; thereby simulating experiments that simulate the electrical properties of the lower seeded air.

Current and voltage were measured and high-speed photography and spectroscopic investigations were performed to evaluate the electrical conductivity and discharge characteristics under various conditions. The results of investigations at pressures up to 13 atm are discussed. This appendix discusses the NASA Ames facility modifications to incorporate an electrical conductivity channel as well as the experimental program for the investigation of the high-temperature electrical discharge physics for pressures up to 13 atm. Electrical pseudo-conductivity measurements at various pressures and applied voltages are reported. A compendium of all data measurements obtained at the NASA Ames is included at the end of this appendix.

A.2.1 Overview

The purpose of the test program in the NASA Ames Electric Arc-Driven Shock Tube (NASA Ames EAST) facility was to determine the effects of gas pressure, ionization fraction (temperature), and electric field strength on current discharges in shock-heated, high-pressure (1 to 13 atm) air flows. These tests provided useful information on air conductivity and electron dynamics and also allowed investigation of the influence of boundary layers on the discharges. Data from the experiments aided in the development of computational plasma/fluid dynamic models of MHD accelerators for airflow applications.

The investigations included:

1. Measurement of current and voltage across a pair of electrodes in a square channel to measure the gas conductivity.
2. Study of the diffuse discharge/arc transition at these conditions using photomultiplier tube light emission histories, high-speed videos, as well as current and voltage histories.

3. Study of nonequilibrium effects.
4. Spectroscopic investigations to measure electron density and temperature.

High-pressure testing (up to 25 atm) was included in the original test plan; however, several factors resulted in limiting test section static pressure to a maximum value of 13 atm. Thus, actual test section static pressures ranged from 1 to 13 atm. Most testing was performed at temperatures of 5,500 - 6,000 K with shock-induced ionization fractions of about 10^{-4} that would be typical for MHD accelerators. Some testing was performed at lower shock-induced ionization fractions such as 10^{-5}, to focus on nonequilibrium effects. Voltage across the electrodes was varied over a range of 5 to 1 or more for each post-shock pressure setting. A replaceable skimmer section was designed and fabricated in various lengths to allow the boundary layer thickness to be varied in the test section, however, only one length was used during the course of this testing.

A.2.2 Test Section Hardware Development

Before describing the test section, a brief overall description of the EAST facility is presented. This facility is a 10.16-cm-diameter shock tube with an electric arc-heated driver. Figure A.2- 1 shows a sketch (not to scale) of the facility. The arc in the driver is supported by a capacitor bank, which can store up to 1.24 megajoules (MJ) of energy at 40 kilovolts (kV). The driver gas is usually H_2, He, or He/Ar mixtures. Reflected shock pressures up to 50 MPa can be obtained and shock velocities ranging from 1.5 to 50 kilometers per second (km/s) have been obtained. Further description of the facility is given in Refs. 1 and 2.

For these experiments, the facility was configured as follows: the driver- and driven-tube lengths were 76.2 and 550 cm, respectively. A double diaphragm section was located between the driver and driven tubes. The test section was approximately 62 cm long and was located at the end of the driven tube. Finally, a 122-cm long extension was installed on the downstream side of the test section. Using the diagnostic ports in this tube section, one could look directly up the conductivity channel from the downstream end.

Figure A.2- 2 shows a cross-section view of the test section parallel to the axis and the diagnostic ports. Figure A.2- 3 shows a cross-section normal to the axis and through the four 2-in. diagnostic ports. Finally, Figure A.2- 4 shows an enlarged view of the upstream half of Figure A.2- 2 and two views of the brass electrodes. The test section was 62 cm long and contained a 3-cm- square channel inside an insulating Delrin™ liner. The maximum (reflected shock) pressure rating of the test section was 27.5 MPa. A skimmer tube used to skim off the shock tube boundary layer was located upstream of the panel. Three skimmer tubes of lengths 13, 23, and 33 cm were available to vary the boundary layer thickness in the square channel section. A 7-cm-long round-to-square transition section was located downstream of the skimmer tube.

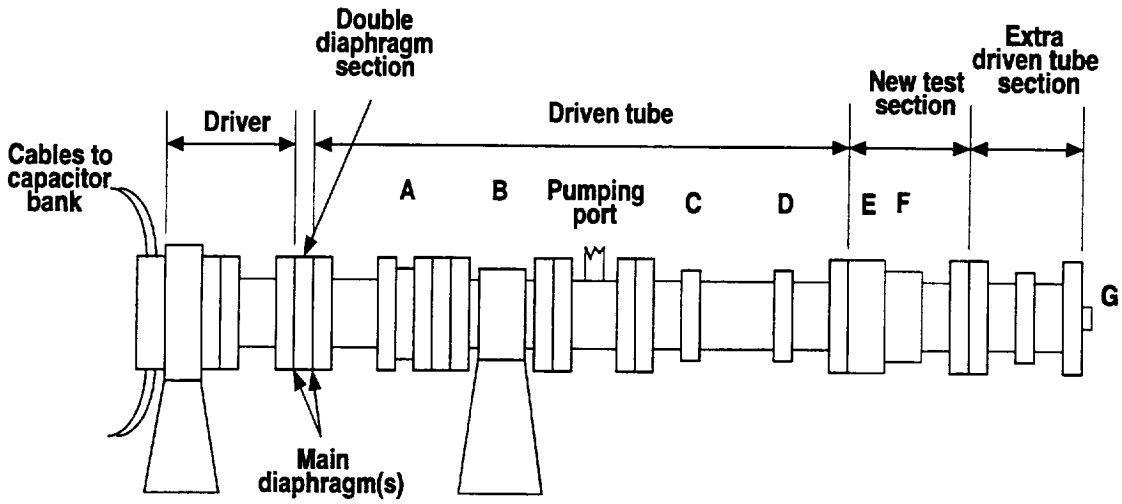

Figure A.2- 1. NASA Ames EAST shock tube facility (not to scale).

The main diagnostic station with four 2-in. diagnostic ports was located 10 cm downstream from the end of the transition section. A pair of 3-cm-square electrodes (see Figures A.2- 3 and A.2-4) were mounted in two of these ports. The remaining two ports were used to provide optical access to the plasma discharge. However, it was possible to mount a pressure transducer in one of the ports usually used for optical access. A pair of 1-in. diagnostic ports was located 23 cm downstream of the electrodes. These were generally provided with a pressure transducer and a photomultiplier tube to allow the measurement of the shock velocity and the test time duration in the square channel. In this way, one could measure changes that may have taken place as the shock moves from the 10.16-cm-diameter driven-tube to the 3-cm-square channel.

A.2.3 Diagnostics

The diagnostics were divided into four main groups, as follows:

1. Standard shock tube diagnostics - quartz crystal pressure transducers, ionization gauge shock detectors, and photomultiplier tubes (PMTs).
2. Voltage and current measurements for the plasma discharge.
3. Nonspectroscopic optical measurements of the discharge involving light emission histories using PMTs and high-speed videos.
4. Spectroscopic optical measurements of the discharge utilizing techniques designed to measure electron density and the arrival of driver gas contamination.

The initial proposed deployment of diagnostics, referring to the diagnostic stations shown in Figure A.2- 1, is listed below.

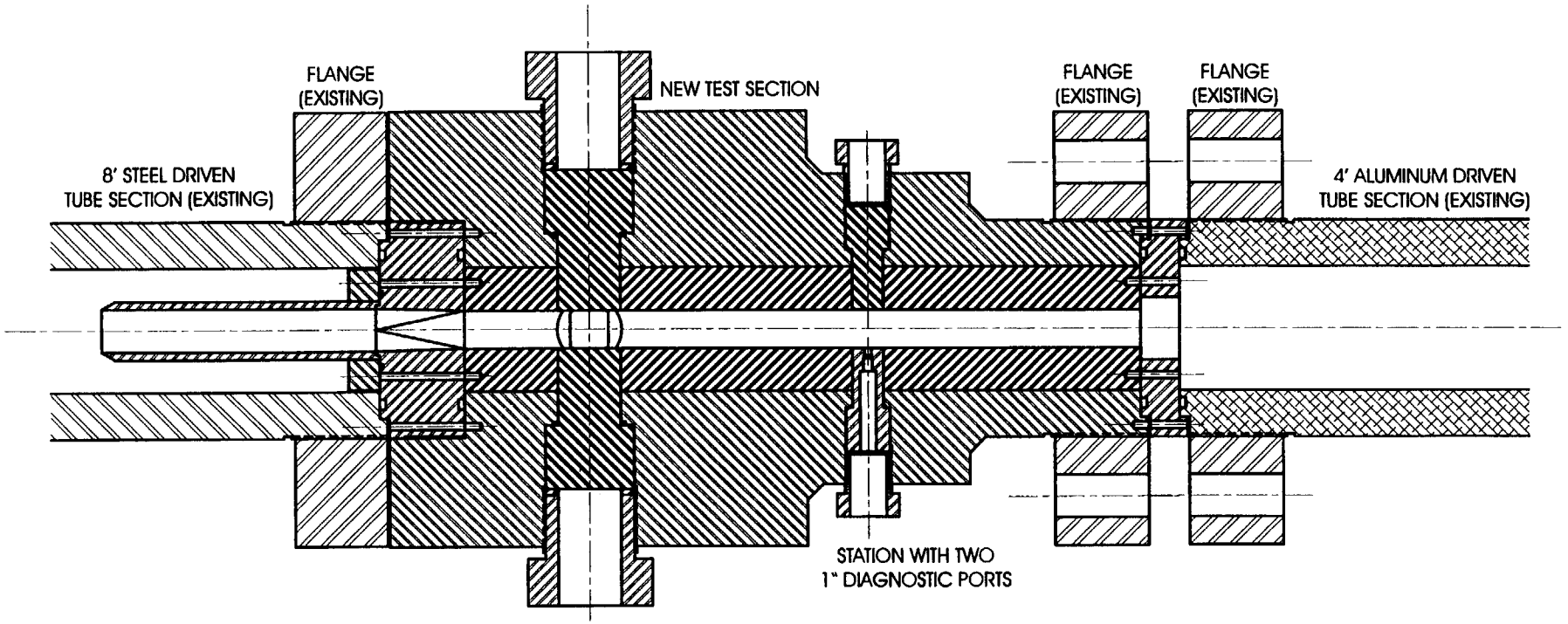

Figure A.2- 2. Section through test section parallel to channel axis and diagnostic ports.

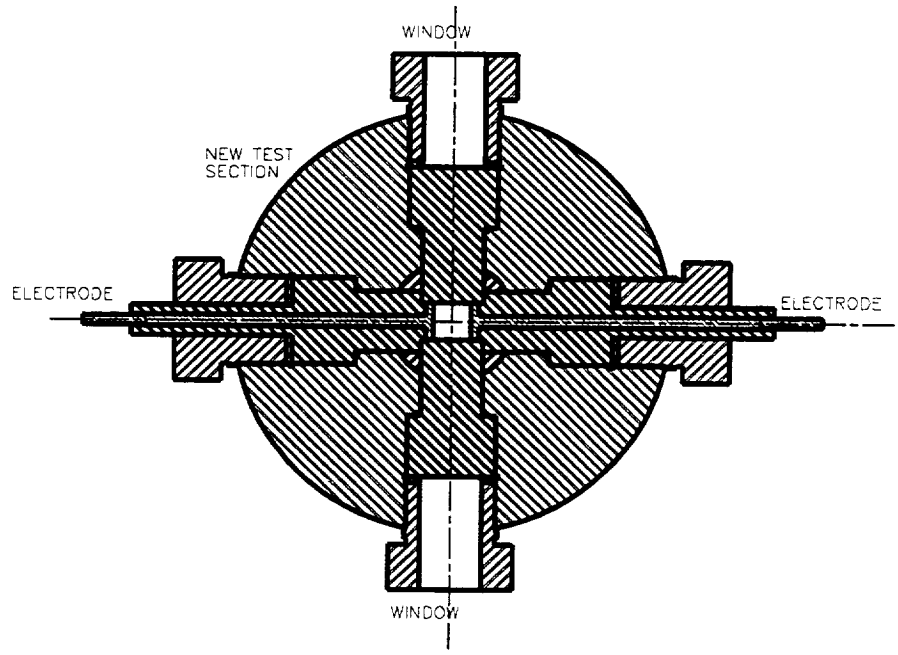

Figure A.2- 3. Section through test section normal to channel axis and through 2'' diagnostic ports.

Station A - no diagnostics
Station B - ionization gauge shock detector
Station C - quartz crystal pressure transducer and PMT
Station D - quartz crystal pressure transducer and PMT or ionization gauge
Station E - discharge current and voltage
- PMT and/or high-speed video
- spectroscopic diagnostics
Station F - quartz crystal pressure transducer and PMT.
Station G - no diagnostics

PCB Corporation quartz crystal piezoelectric pressure transducers were utilized. Transducer model numbers 111A22, 113A24, and 113A21, with sensitivities of 1, 5, and 25 millivolts per pound per square inch (mV/psi), respectively, were available. Each pressure transducer was connected to a PCB Model 484B amplifier unit. The ionization gauge consisted of two 0.13-cm-diameter wire electrodes that protruded 0.05 cm into the flow. A voltage of 50 V was applied across the electrodes and upon arrival of the incident shock wave the sudden conduction of electric current through the shock-heated gas produced a very abrupt voltage change at the ion gauge output yielding a precise time for the passage of the shock. The PMT were types 1P21, 1P28, and RA56. For the shock velocity measurements at stations C, D, and F; the PMTs viewed the shock tube flow through two slits of width 0.005 to 0.0125 cm oriented perpendicular to the direction of shock motion. The slits were separated by distances of 7.5 to 15 cm and were

mounted in a small tube that was placed just outside an acrylic window in the wall of the tube. The discharge current measurements (currents to top and bottom electrodes) were made using Pearson current transformer models 101, 1025, and 110. The sensitivities of these transformers were 0.01 volts per amps (V/A), 0.025 V/A, and 0.10 V/A, respectively. The discharge voltage was measured with a voltage divider with the large resistance being about 120 K and the small resistance being between 2 K and 12 K, as required. A second voltage measurement is obtained by placing a 130-ohm resistor in parallel with the discharge and measuring the current through it with a Pearson Model 110 current transformer (sensitivity 0.10 V/A).

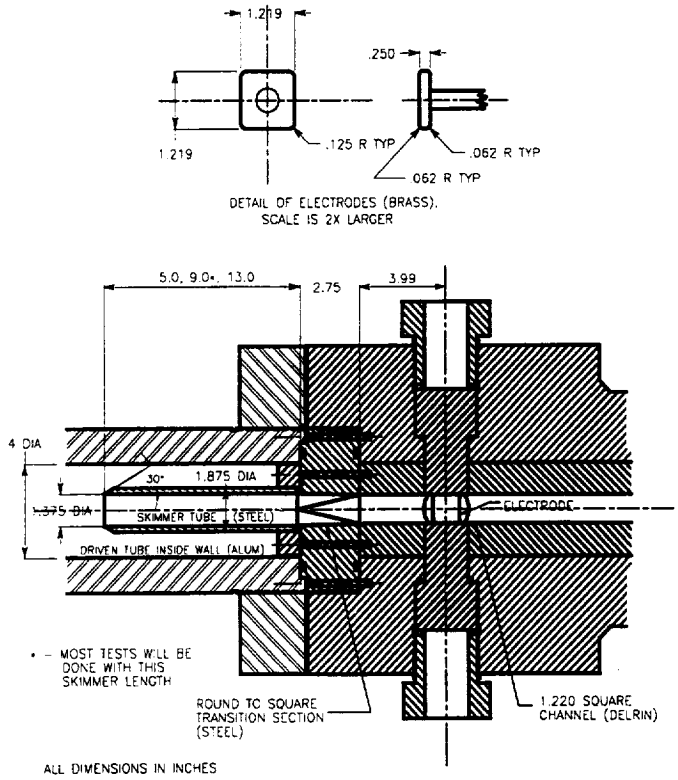

Figure A.2- 4. Channel in test section and electrodes.

In Runs 10 – 27, with current between the electrodes, the light emission history from the discharge was recorded from station E using the 1P21 PMT mentioned above, but with the slit nearest the test section (used for the measurements of shock velocity) replaced with three sheets of paper. For Runs 29 - 51, the light emission history at station E was analyzed using two monochromators. (A single monochromator was used for Run 28.) The monochromators used are Bausch and Lomb™ instruments with input and output slits 0.25 to 0.50 mm wide and 1.1 cm high. The distances from the slits to the mirror are 25 cm and those from the mirrors to the gratings are 21 cm. The mirror diameters are 9.4 cm, and the gratings are square with 5-cm sides. The gratings have 600 grooves/mm with a blaze angle of 13° and blaze wavelength of 750 nm. The distance between the test section and the entrance slits of the monochromators was 109

cm, and either one or two lenses with focal lengths of 250 mm and clear apertures of 4.44 cm were used to image the test section on the entrance slits of the monochromators. A single lens approximately 54 cm from the test section was used for Runs 28 – 41, and two lenses located 25 and 75 cm from the test section were used for Runs 42 - 51. Monochromator #1 was tuned to look at a He line and used a Fairchild PMT with an S1 photocathode and an applied voltage of 800 V. Monochromator #2 was tuned to look 10 nm to one side of a He line to determine the broadband background radiation utilizing a PMT with an S20 photocathode and an applied voltage of 1,000 V. Follow-on amplifiers with 15-V power supplies were used after both PMTs to boost the signal levels. By ratioing the monochromator output time histories (i.e., forming the ratio of the output of the monochromator tuned to the He line to the output of the monochromator tuned to one side of the He line) an indication of the arrival time of He driver gas contamination at the electrodes can be obtained. An abrupt increase in this ratio indicates the arrival of driver gas contamination.

The high-speed videos taken at station E were obtained using a Hadland IMACON™ Standard Model electronic camera with a P856 image converter tube and a s11photocathode. This can capture a maximum of 12 frames during a run. The interval between the frames is 4 μs. These videos were to search for breakdown paths or concentrations of discharge current. They also give information regarding the main shock wave, oblique shock waves off the leading edges of the electrodes, damage to the leading edges of the windows, the electrode glow regions, and hot spots in these regions.

Figure A.2- 5 shows a schematic of the setup of a spectrometer for planned spectroscopic studies at station E in the test section. In some cases, two spectrometers have been used to allow narrow band and wide band spectroscopy to be performed simultaneously. To measure the electron number density the Stark broadening of the 486.1-nm Hydrogen Balmer β line caused by the electrons was determined. The driven-tube gas is typically seeded with approximately 5×10^{-3}-mole fraction of H_2 to allow these measurements to be made. The electron number density, N_e, can be related to the full width at half maximum of the H-β line, $\Delta\lambda_s$, as follows:

$$N_e = C(N_e, T)\Delta\lambda_s^{2/3} \qquad \text{(A.2- 1)}$$

where $C(N_e,T)$ varied only slightly with N_e and T (temperature).

The spectroscopic measurements can be made in two ways. With the slit perpendicular to the axis of the flow channel, wavelength is in one direction and distance across the channel is in the other direction. This allows the variation of the spectra across the channel to be studied. With the slit aligned parallel to the channel axis, the variation of the spectra in the direction along the channel axis is obtained. In this case the variation of the spectra for up to 5 cm along the direction of the shock motion can be observed. This allows study of the development of nonequilibrium processes after shock passage. Nonequilibrium studies at distances greater than 5 cm behind the shock wave could be made by delaying the time at which the spectra were taken with respect to the time of passage of the shock wave.

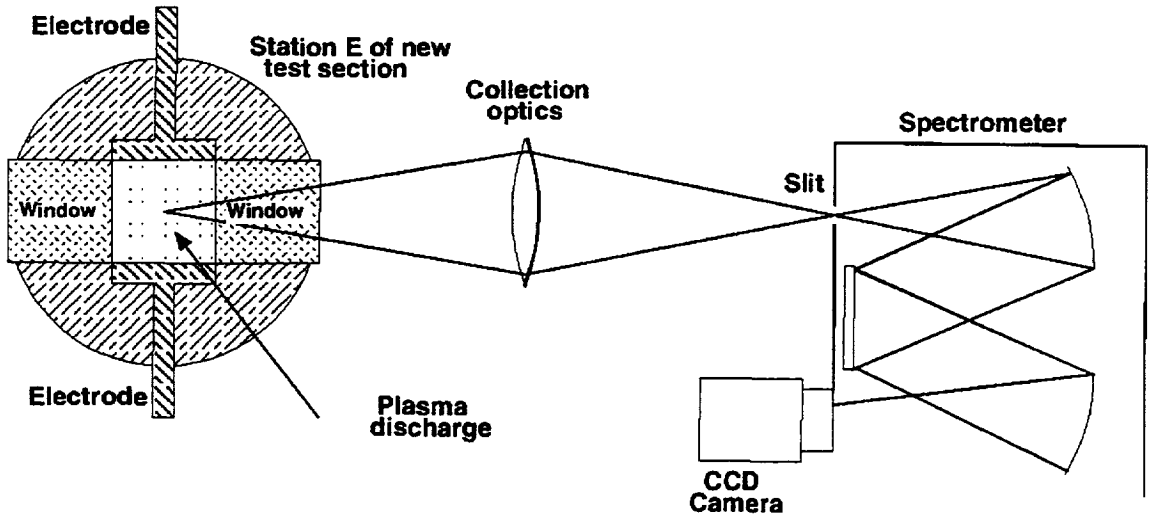

Figure A.2- 5. Arrangement of spectrometer, CCD camera, etc., for spectroscopy at station E in the test section. Sketch is schematic only and not to scale.

The signals from the pressure transducers, photomultiplier tubes, ionization gauges, and the discharge current and voltage pickups were digitized and recorded using a data acquisition system comprised of 12 high-speed digitizers made by the DSP Corporation.

The following additional data was taken for each test. Driver- and driven-tube pressure, as well as pressure between the two diaphragms were measured before each test. The voltage on the main driver capacitor bank was measured before and after the discharge. An oscilloscope trace of the capacitor bank discharge current history was also obtained for each test, and voltage on the plasma discharge capacitor bank was measured before each test.

A.2.4 Power Supply

The power supply was a Faraday rotator power supply obtained from the Lawrence Livermore National Laboratory. A considerable amount of refurbishment was performed by NASA Ames to make this unit operational. It contained a bank of three 240-microfarad (μf) capacitors that could be charged to 5,000 V. For these tests the power supply was operated with all three capacitors, and the capacitors were switched by a National #NL-7703NP ignitron tube. The minimum rated voltage of the power supply was 500 V.

The circuit used in the NASA Ames air conductivity and breakdown experiments is shown in Figure A.2- 6. Three elements were added for this application: a) a ballast resistor; b) a voltage-clamping device; and c) a parallel resistor. The ballast resistor limits the maximum current through the plasma discharge and makes the V-I characteristic of the overall circuit stable. The voltage-clamping device was a highly nonlinear resistor (metal oxide varistor or MOV) that tended to maintain the voltage across itself constant as the capacitor discharged. The parallel

resistor is used to avoid placing a very high voltage across the electrodes before the shock wave arrives and gas conduction starts.

The ballast and parallel resistors had to be able to handle large energy deposition, have very low inductance, and be variable. These requirements were met by designing and building two saltwater resistors with electrode spacings of 5.3 cm and electrode areas of 248 cm^2. By varying the concentration of salt, the resistance of these resistors was varied from 0.1 to 12 or more ohms, which was sufficient for these tests. The MOVs were purchased from Harris Semiconductors. At least two of each of the following model number units were obtained; and consequently, there was at least one spare available for each type.

V881BA60	V150LA20A
V481BA60	V100RA16
V251BA60	V39RA16
V131BA60	

The characteristics of these units covered a sufficiently wide range to permit voltage clamping to be used for all proposed test conditions.

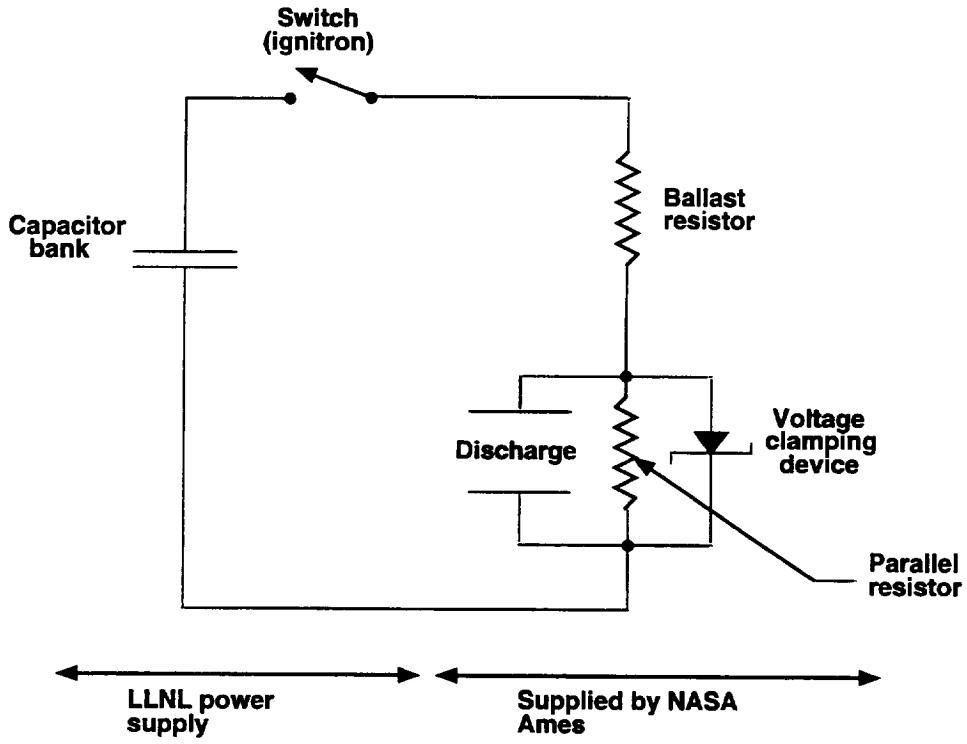

Figure A.2- 6. Electrode power supply circuit.

A.2.5 Integration, Verification, and Characterization

A.2.5.1 Mechanical Integration

The integration of the test section into the EAST facility can best be described using Figure A.2- 2. The test section was made with the same end diameters, alignment steps, and O-ring grooves as the existing driven tube sections and was integrated into the EAST facility as shown in Figure A.2- 2. The test section was fastened on both ends to existing driven tube sections using eight 1.25-7 bolts or studs. The holes for the bolts are visible at the right end of the test section in Figure A.2- 2. The holes for the studs are not visible at the left end of the test section in Figure A.2- 2 because they are rotated 22.5° out of the section plane. After the test section was integrated into the facility, electrodes, windows, transducer holders, etc. were inserted into the six diagnostic ports of the test section. The complete facility was then closed up and a vacuum check to the required base pressure was run without difficulty.

A.2.5.2 Power Supply Integration

The power supply and the grounded cabinet containing the salt water resistors were located about 1.5 meters away from the test section and were connected together using RG-213 high voltage cable.

A.2.5.3 Diagnostic Development

The voltages applied to the electrodes and the currents passing between the electrodes were found to produce considerable electrostatic and electromagnetic noise on the data channels. The main current leads to the electrodes were arranged to the fullest extent possible to provide magnetic field cancellation to reduce the electromagnetic noise pick-up. A voltage divider was used to determine the voltage across the electrodes. The large resistor of the divider was 120 kilohms (kohms) and the small resistor was varied between 2 k and 12 kohms (as required) to provide the proper signal output levels. To reduce noise pickup the divider was placed in a shielded box. One side of the divider was connected to the electrode at high potential, and this was believed to produce noise problems at the digitizers used to collect the data. A second method for measuring the voltage across the electrodes utilized a 127-ohm resistor placed across the electrodes, and the current through the resistor was measured with a Pearson Model 110 current transformer. With this technique the input to the recording digitizer has no direct connection with the electrodes in the test section. In general, the voltage histories from the two techniques were found to agree reasonably well with each other. However, at very high currents, the voltages from the divider were sometimes found to run 15 - 20% below those from the current transformer during the period of heavy current draw that was believed to be due to noise picked up in the instrumentation cables or in the digitizers. In these cases, the voltage data from the current transformer was used in the data analysis.

It was found that under some circumstances a certain amount of current was passing from the upper electrode at high potential to the grounded part of the shock-tube upstream of the insulating Delrin liner rather than to the lower electrode at ground potential. The insulating Delrin liner extends about 9 cm upstream of the leading edges of the electrodes, beyond this the tunnel wall is steel and can provide a return current path to ground. Downstream of the electrodes the Delrin liner extends for about 40 cm; therefore, there should be very little problem with current flowing downstream to ground since the length of the conducting slug of gas is roughly 25 cm. When higher voltages are applied to the electrodes and heavier currents are drawn, the fraction of the current passing upstream to the tunnel ground is typically about 10%. For voltages of 40 - 90 V applied to the electrodes, the fraction of the current flowing to the tunnel wall ground can be significantly larger (up to 50 - 60%) particularly during the first half of the current conduction time. Since the objective of this study was to investigate only currents passing directly between the two electrodes, all pseudo-conductivities were calculated based on the current to the bottom electrode, i.e., the current passing directly between the two electrodes.

For the photomultiplier tubes, monochromators, spectrometers, and the Hadland IMACON camera, signal levels and film exposures were noted on the first shot or two, then neutral density filters and digitizer sensitivities were adjusted to provide the best signal levels and exposures.

A high-speed camera was used to obtain images of the shock-heated airflow through the discharge region. The camera was an early IMACON model designated by the manufacturer as a "Standard Model" (circa 1970) consisting of a P856 image converter tube with an S11 photocathode. Images were relayed to the photocathode from the test section by a 90-mm f/2.8 Zoomar lens. Although variable framing rate plug-in modules are available for the camera, a 200,000 frame/s unit was used for all tests conducted during this investigation.

The camera images were recorded on Polaroid Type 57 film, and the image record was triggered by an SRS DG535 delay generator that was activated by a signal from an ionization gauge at Station D, 77.37 cm upstream of the electrode location. The trigger delay to the IMACON was set so the shock would arrive within the second frame for a nominal shock velocity of 4.65 km/s. Both the trigger signal and a monitor signal from the IMACON that coincided with the first image were recorded on a digital oscilloscope for each test. This provided an independent determination of the delay generator setting and the internal delay of the camera. Before each test, the camera focus was checked, and the view was aligned through one of the Plexiglas windows. Neutral density filters of various attenuation were used to try to minimize film saturation.

Measurements were conducted before and after the shock tube tests to determine the actual interframe and exposure times of the IMACON. The delay generator was configured to control both the IMACON and a Xenon pulser, and the delay was varied in 0.1 μs steps to determine when the image appeared and disappeared from successive frames on the Polaroid photos. The internal delay to the first frame was 1.2 μs, the interframe rate was nominally 4.0 ± 0.1 μs, and the exposure time was typically 1.0 ± 0.1 μs.

Depending on the test conditions and the actual trigger timing for a given run, several flow quantities could be determined from the images. The first quantity was the flow Mach number that was measured from the angles of the oblique shocks emanating from the discontinuity between the tunnel wall and the electrode. In all but the most overexposed images, these shock waves were easily discernable on both the top and bottom electrodes. Angles were determined from a tangent measurement wherever possible, using a precision rule and dividers. For an oblique shock wave, the Mach number can be determined from the Mach angle, μ, using the following relation (Ref. 3).

$$M = [(tan\ \mu)^2 + 1]^{1/2} \qquad \text{(A.2- 2)}$$

Frequently, measurements from multiple frames for both the upper and lower shocks were averaged to improve precision since individual determinations of the Mach number were uncertain by $\pm$ 0.15.

The other flow properties that could be determined from the images were related to the shock velocity. For all recorded images (except the first two) the time-averaged shock velocity from Station D to the test region could be measured. This was accomplished by determining the shock location relative to the center of the electrode in the frame in which it first appears and resolving the total time from the trigger, including the internal camera delay, time to the first image, interframe timing, and frame exposure time. The average shock velocity determined from the images is referred to as V_{CAV} (velocity, camera-average) in the following tables and figures. The precision of this measurement was quite high since the time between the trigger and the shock image was large, and the distance traveled was also large, so that small errors in either had minimal impact. However, note that the instantaneous shock velocity can be substantially different from V_{CAV}.

The instantaneous shock velocity, which is more valuable than the average velocity, could only be determined for tests where an image of the shock wave was captured in successive frames. By referencing the locations of the shock images to the known distance of the imaged electrode spacing, the interframe travel distance was determined. This distance was then divided by the framing interval (4 μs) to obtain the shock velocity, herein referred to as V_I, as it passes over the electrodes. As expected, the precision of this measurement is less than that of V_{CAV}, since the distances are quite small. The estimated precision of the values of V_I are $\pm$ 0.30 km/s.

Examples of the Polaroid photographs will be given for each of the three test conditions and will be discussed in the sections to follow. Tables summarizing the measured quantities for all of the tests at each test condition will also be presented.

A second camera system was implemented during the tests to attempt to measure the electron number density in the shock-heated test gas flow. This instrumentation, consisting of an intensified CCD camera and 218-mm focal length spectrometer with a 2,400-line/mm grating, was installed during the tests and brought on line for measurements at the higher pressures. Spatially and spectrally resolved images of the light emitted from the electrode region were

recorded during some of the 13-atm test runs. The dominant spectral features were from Iron (Fe) and Chromium (Cr) transitions. These elements were probably introduced to the flow from the walls and diaphragm, which are made of stainless steel. H-β emission from the H_2 added to the driven gas was discernable, but the line width could not be resolved owing to the presence of a strong overlapping Fe transition. This measurement will be repeated at more favorable, lower pressure conditions in the future.

A.2.5.4 Characterization of Facility with Test Section

Table A.2- 1 shows the facility operating conditions that were found to produce the desired shock velocity of 4.65 km/s at the electrodes. Of course the desired shock velocity is not achieved on the first test at any condition. One starts with a rough-cut at the facility operating conditions, and then the capacitor bank voltage, the main diaphragm thickness, and score depth are adjusted to produce the desired shock velocity. This was done for the 2 and 5-atm test conditions. For the 13-atm test condition, the driver and main diaphragm conditions were held fixed, and the driven-tube fill pressure was varied to achieve the desired shock velocity.

Table A.2- 2 shows the range of shock velocities obtained while the facility was operated at the nominal operating conditions for each of the three different nominal test pressures. The variation in shock velocities is rather wide, up to ±6.5% for the 5-atm test condition. There are two main reasons for this rather large shock velocity range. First, the diaphragm breaks not at a controlled pressure but simply when sufficient electrical energy has been deposited in the driver to raise the pressure to the diaphragm rupture pressure that typically has a ±5-10% variation. Second, electrical energy continues to be added to the driver after diaphragm rupture, leading to additional compression and shock waves that follow the main shock wave and can combine with it in an unpredictable manner. The shock velocities obtained during operation of the facility under off-nominal operating conditions are given in the last rows of Table A.2- 2. Some of these shock velocities were obtained at the beginning of the test series while searching for the nominal operating condition. The highest velocities were obtained by deliberately increasing the capacitor bank voltage or reducing the driven tube fill pressure. The low velocity shot at the 13-atm condition was obtained when the driver arc penetrated the insulating driver liner and destroyed it.

In the following paragraphs the slowing down of the shock wave as it travels down the facility and the methods used to calculate the shock velocity at the electrodes is discussed. Table A.2- 3 shows key dimensions along the facility. Note that the skimmer nose station moved back about 1.9 cm in the course of the test entry because it had to be re-machined several times after having been struck by thrown diaphragm petals. Shock velocities were measured using a shock detector at station B and PCB quartz crystal pressure transducers at stations C, D, E, and F. Measured shock velocities for Runs 2 - 4 and 6 - 9 is given in Table A.2- 4. (The main diaphragm did not break in Run 1 and a spurious trigger pulse caused the loss of all data in Run 5.) At the heads of the columns the shock velocities are identified by the stations between which they are measured. It was noted the ratio between the BC and CD shock velocities was variable, likely due to

additional shock waves and compression waves catching up to the main shock wave between stations B and D.

Table A.2- 1. Facility operating conditions used to obtain the desired shock velocity at the electrodes.			
Nominal test pressure (atm)	2	5	13
Driver			
Gas	He	He	He
Fill pressure (MPa)	0.851	2.13	2.41
Capacitor bank capacitance (microfarad)	861	1530	1530
Capacitor bank voltage (kV)	19.7	24.9	32.5
Main diaphragm			
Material	304 SS	304 SS	304 SS
Thickness (cm)	0.160	0.160	0.229
Score depth (%)	45	20	25
Nominal burst pressure (MPa)	9.66	35.2	35.9
Buffer			
Gas	Ar	Ar	Ar
Fill pressure (kPa)	137	341	931
Buffer-driven diaphragm			
Material	Mylar	Mylar	Mylar
Thickness (cm)	0.00635	0.0153	0.0305
Driven tube			
Gas	N_2O/N_2*	N_2O/N_2*	$N_2O/N_2/H_2$†
Fill pressure (kPa)	0.694	1.73	4.72

*53.2%N_2O, 46.8% N_2 by partial pressure.
†52.925%N_2O, 46.575% N_2, 0.5% H_2 by partial pressure.

Table A.2- 2. Shock velocity ranges obtained for the three different nominal test pressures.			
Nominal test pressure (atm)	2	5	13
Shock velocity range, nominal operating condition (km/s)	4.52 - 4.90	4.35 - 4.95	4.54 - 4.89
Percent deviation from nominal shock Velocity	-2.8/+5.4	-6.5/+6.5	-2.4/+5.2
Additional shock velocity range, off-nominal operating condition (km/s)	3.79 - 4.37*, 5.06†	4.16 - 4.22*, 5.38 - 6.29†	3.96**

*Obtained at beginning of test series while searching for nominal operating condition.
†Facility deliberately operated at high shock velocity conditions.
**Bad shot, driver liner penetrated by arc and destroyed.

Table A.2- 3. Key dimensions along the NASA Ames EAST facility.			
Stations	Distance from main Diaphragm (cm)	Delta distances, Identification	Delta distances (cm)
B	101.679		
C	255.19	BC	153.511
D	377.11	CD	121.92
Skimmer nose	414.495-416.400		
E (electrodes)	454.475	DE	77.365
F	474.795	EF	20.32

Table A.2- 4. Shock velocity measurements.						
Run no.	Shock vel., BC (km/s)	Shock vel., CD (km/s)	Shock vel., DE (km/s)	Shock vel., EF (km/s)	Shock vel., DF (km/s)	Slow down ratio
2	4.582	4.618			4.481	
3	5.221	5.188			4.835	
4	4.029	4.024			3.876	
6	4.767	4.618			4.284	
7	5.197	5.233	5.090	4.726	5.009	7.07
8	4.992	5.059	4.959	4.618	4.884	7.52
9	4.680	4.618	4.524	4.233	4.461	6.30

On the other hand, the shock velocities CD, DE, EF, and DF showed much more consistent ratios when the results for the various runs were compared. The shock wave slowed down 0.2-0.3 km/s between the CD and DF measurements and 0.4-0.5 km/s between the CD and EF measurements. In Runs 7 - 9, a pressure transducer was installed at station E allowing accurate measurements of the EF shock velocity to be made. By plotting up the shock velocities of Table A.2- 4, it was determined that the rate of slow down of the shock wave (km/s/cm) was about 7 times as much in the skimmer tube and Delrin conductivity channel as in the 10 cm diameter driven tube. These "slow down ratios" are shown in the last column for Runs 7 - 9 and are fairly consistent from among tests. From the same plots it was determined that the shock velocity at station E (at the electrodes), v_E, could be very well estimated as $v_E = 0.9622 \times v_{DF}$, (where v_{DF} is given in Table A.2- 4). With windows installed at station E to allow the discharge to be observed, it was no longer possible to have a pressure transducer at station E; hence, with current flowing between the electrodes, the above correlation between v_E and v_{DF} was used to estimate the shock velocity at the electrodes.

For some runs with very heavy currents, electromagnetic noise pickup on the histories of the pressure transducer at station F made it difficult or impossible to determine the time of shock passage at station F. However, with lower currents it was found that there was a very consistent

ratio between the time intervals between the shock passages at stations D and F and that between the shock passage at station D and the start of the current between the electrodes. This ratio was then established for a large number of runs with currents that were not too large. For the runs with very large currents and poorly defined (or undefined) times of shock passage at station F, this ratio was used to allow the DF time interval to be estimated from the time of shock passage at station D and the time of the start of current flow. With this estimated DF time interval in hand, the shock velocity at the electrodes was then estimated using the correlation between v_E and v_{DF} given in the previous paragraph.

The test time available from the start of current flow until the arrival of driver gas contamination was estimated in two ways. Since the driver gas is much cooler than the driven tube gas its arrival at the electrodes should result in a rapid drop in conductivity and current passing between the electrodes. In fact, such a rapid drop in current was observed in all of the tests. Figure A.2- 7 shows a plot of the test times estimated from the start of current flow to the bottom electrode until the start of the final, rapid drop in current flow. The results shown in Figure A.2- 7, for the three nominal test section pressures, are plotted versus the shock velocity at the electrodes. The data show test times dropping from 50 - 70 μs at shock velocities of 4.5 km/s to 40 - 50 μs at 5.0 km/s to ~30 μs at 6.3 km/s.

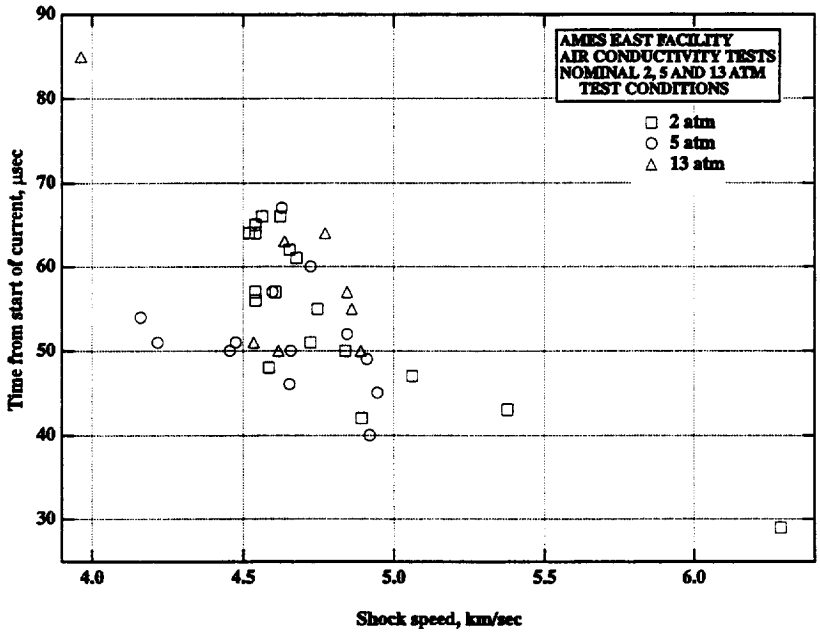

Figure A.2- 7. Times until driver gas arrival, estimated from the time of the start of the final, steep drop in current to the bottom electrode.

A second method of determining the time of driver gas arrival was to use two monochromators viewing the region between the electrodes at station E. These two monochromators, their optical train, photomultiplier tubes, and amplifiers, etc., are described in Section A.2.3. The driver gas

is pure He; and therefore, one monochromator (monochromator #1) was tuned to a He line, while the second monochromator (monochromator #2) was tuned to a wavelength either 10 nm above or below that of the He line chosen. Runs were made using the He lines at 501.6, 587.6 and 706.5 nm. The outputs of the two monochromators were ratioed in the postprocessing, and the He driver gas arrival was taken to occur when the ratio (signal from monochromator #1)/ (signal from monochromator #2) showed an abrupt increase. Monochromator data was taken on Runs 30 - 51. Examining the data from Runs 30 - 46 (17 runs), 8 runs appeared to show fairly definite increases in the monochromator output ratio at times ranging from 28 μs before the start of the final, steep current drop to 4 μs after the start of the current drop. Unfortunately, the remaining 9 runs often showed no indication of increase in the monochromator signal ratio at the appropriate time or even showed drops in the monochromator ratio about the time when the He gas should be arriving.

It was observed that electromagnetic noise pickup on the monochromator histories was severe, and it was believed that this pickup was confounding and, at times overwhelming the actual spectroscopic information conveyed from the monochromators. During the time period covering Runs 30 - 46, a number of changes were made to attempt to improve signal-to-noise ratio of the monochromator signals. The signal cables for the monochromators were initially rather long and passed fairly close to the leads for the electrodes at station E; these cables were shortened and moved away from the electrodes. Much of the spectroscopic work was done with monochromator #1 tuned to the 706.5-nm line that was later shifted to the 587.6-nm line, which is about 2.5 times stronger. The slits of monochromator #1 had been set at 0.50 mm or 0.25 mm for most of the earlier runs; it turned out that a setting of 0.30 mm is considerably superior, providing good rejection of broadband background radiation and 2 or more times as much output as when the slits are set at 0.25 mm. For the last 8 runs the slits were set to 0.3 mm. Finally, for the last 11 runs the top electrode (rather than the center of the flow) was imaged on the monochromator-input slits. This images the high-electric field electrode fall region (rather than the low-electric field free-stream region) on the monochromator-input slits. With these changes at the 13-atm test condition, definitive increases in the monochromator signal ratio were observed for Runs 47 and 49 through 51. (For Run 48 the slits were set to 0.25 mm and the increase in the signal ratio was smaller and not as definitive.) For Runs 47 and 49 through 51, the helium driver gas contamination was observed to arrive 7 to 14 μs before the start of the final, steep drop in the current to the bottom electrode. Based on these results, it would appear to be advisable to consider the final 10 μs of data before the final, steep drop in current to be suspect; due to the possible presence of driver gas contamination.

This section ends with a discussion of the state of the conductivity channel elements during and after the 51 test runs of this test entry. At the end of the test entry, the brass electrodes showed absolutely no signs of pitting, melting, arcing or damage of any kind. The interior of the Delrin conductivity channel did not show any sign of physical damage, erosion, scoring, etc. to the surface; however, the surface had turned from white to black apparently coated with a tough residue of material originating in the driver. This coating, however, did not provide a conductivity path large enough to support measurable current since it was determined that the current observed before the shock wave arrival (with the maximum applied voltage) was always zero. The Plexiglas windows survived up to 20 runs with minimum surface damage at the 2-atm

test condition; however, at the 5 and 13-atm test conditions the window surfaces facing the hot gas would begin the show fine surface cracking (without loss of material) after 1 to 3 runs. This cracking was likely due to the intense thermal shock applied to the windows during the tests. At the higher-pressure test conditions when the windows were judged to have been sufficiently damaged by cracking, they were removed and refinished on a lathe. Since there were four sets of Plexiglas windows available, a set of windows in good condition could always be dropped into the facility while a damaged set was being refinished.

A.2.6 Results

A.2.6.1 At Nominal 2-Atm Test Condition

Table A.2- 5 gives the test conditions for the runs with current between the electrodes at the nominal 2-atm facility operating condition. Runs 1 through 9, 20, and 24 were omitted since these were made without current between the electrodes. Other runs were also omitted including Runs 10 through 12, which were made with current measurements only to the top electrode, and Run 13 for which the bottom electrode was inadvertently left disconnected. Runs 29 through 41 were made at the nominal 5-atm test condition, and therefore are not included in this table. Since the descriptions at the heads of the columns are necessarily somewhat telegraphic, the data of Table A.2- 5 will be reviewed by columns. Column 1 gives the identifying run number. Column 2 gives the driven tube gas, with "N_2O/N_2" denoting 53.2%N_2O, 46.8% N_2 by partial pressure and "$N_2O/N_2/H_2$" denoting 52.925%N_2O, 46.575% N_2, 0.5% H_2 by partial pressure. Column 3 gives the driven tube fill pressure. The temperature of the driver and driven tube fill gases would always be about 295 K, the laboratory room temperature. Column 4 gives the shock velocity at the electrodes, estimated as described in Section A.2.5.4. Columns 5 and 6 give the shock pressures measured using the quartz crystal pressure transducers at stations D and F. The pressures given at station D should be quite accurate and are higher than 2 atm because the shock wave slows down between station D and the electrodes. The shock pressures given from the pressure transducer located at station F, downstream of the electrodes, are often rather uncertain or sometimes completely unavailable due to the very large noise pickup from the large current between the electrodes on this transducer. In column 6, "(N)" and "(EN)" denote noisy and extremely noisy pressure histories from the transducer at F. Where there is no entry in column 6, the electromagnetic noise on the pressure history at F was so large that no information on the shock strength at this station could be obtained. Finally, columns 7 and 8 give the voltage across the electrodes measured using the current in the 127-ohm parallel resistor (see Section A.2.5.3) at the beginning of current flow and 30 μs after the beginning of current flow.

Figures A.2- 8 - A.2- 12 present representative data histories for Run 17 at the 2-atm nominal test condition. Figures A.2- 8 - A.2- 9 show the voltage histories from the voltage divider and from the current through the 127-ohm parallel resistor. Figure A.2- 10 - A.2- 11 show the current histories to the top and bottom electrodes. Note that the current to the top electrode is about

10% greater than that to the bottom electrode and likely a result of the current flowing from the top electrode to the steel wall of the shock tube upstream of the Delrin insulator of the conductivity channel. (See discussion in Section A.2.5.3.) In certain tests there is also some suggestion that a small fraction of the current (5 - 10%) may be flowing from the top electrode to the pressure transducer holder about 20 cm downstream of the electrodes. However, this can only occur after about 45 μs after the start of current flow when the conducting gas behind the shock wave reaches the pressure transducer holder.

Table A.2- 5. Test conditions for runs at the nominal 2-atm test condition.

Test no.	Dn tube gas	Dn tube fill pressure (kPa)	Shock v at E (km/s)	Shock p at D (atm)	Shock p at F (atm)	Voltage at 0 μs (V)	Voltage at 30 μs (V)
14	N_2O/N_2	0.694	4.653	2.44	1.80 (N)	174	122
15	N_2O/N_2	0.694	4.585	2.42	1.72 (N)	172	128
16	N_2O/N_2	0.694	4.895	2.75	2.00 (N)	324	150
17	N_2O/N_2	0.694	4.540	2.33	1.40 (EN)	186	146
18	N_2O/N_2	0.694	4.723	2.55	1.47 (EN)	277	163
19	N_2O/N_2	0.694	4.563	2.29	2.19 (EN)	371	219
21	N_2O/N_2	0.694	4.676	2.86		229	143
22	N_2O/N_2	0.694	4.747	2.76		509	318
23	N_2O/N_2	0.694	4.623	2.72		712	370
25	N_2O/N_2	0.694	5.062	3.39		95	83
26	N_2O/N_2	0.694	4.840	3.07		92	80
27	N_2O/N_2	0.694	4.541	2.60	2.60 (EN)	92	83
28	N_2O/N_2	0.694	4.541	2.68	1.91 (N)	46.6	40.3
42	$N_2O/N_2/H_2$	0.686	6.286	4.78		45.5	44.5
43	$N_2O/N_2/H_2$	0.841	5.377	3.97		187	115

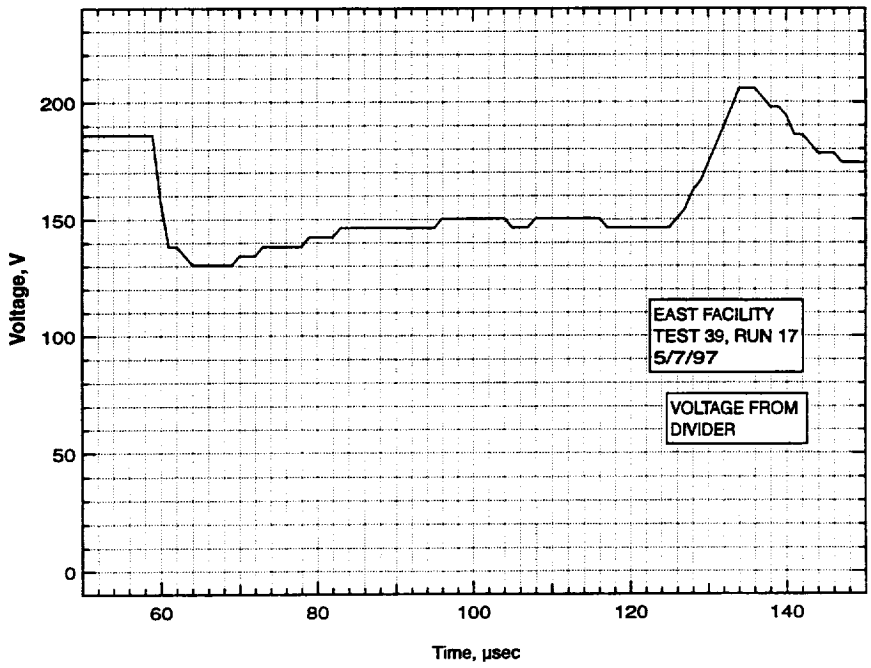

Figure A.2- 8. Run 17, voltage across electrodes determined by divider.

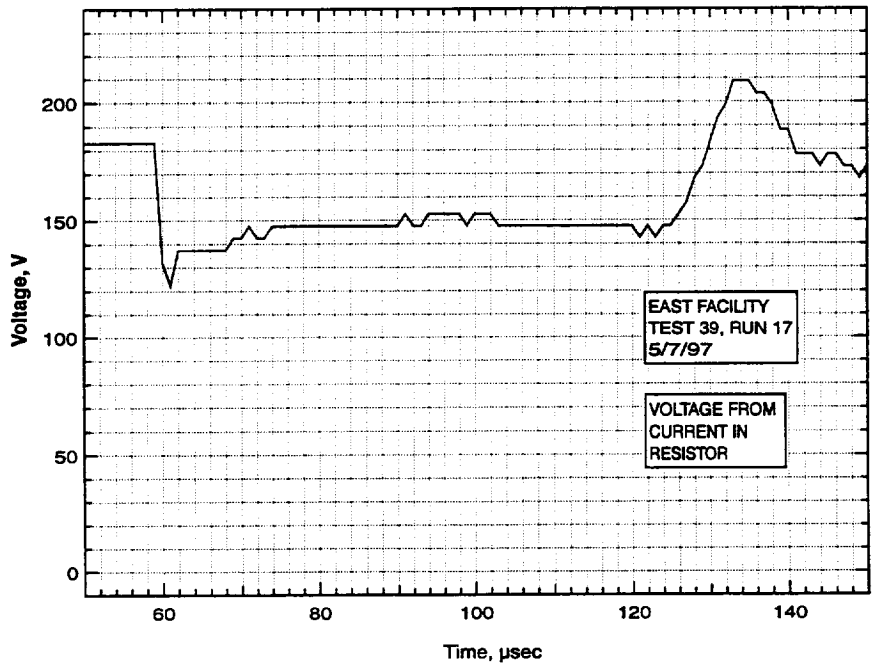

Figure A.2- 9. Run 17, voltage across electrodes determined by current in resistor.

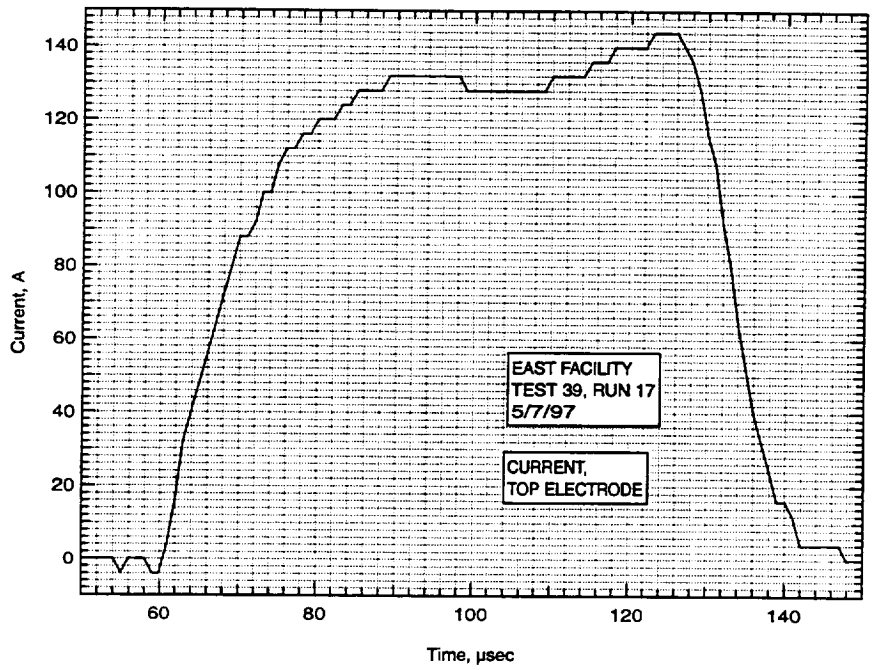

Figure A.2- 10. Run 17, current to top electrode.

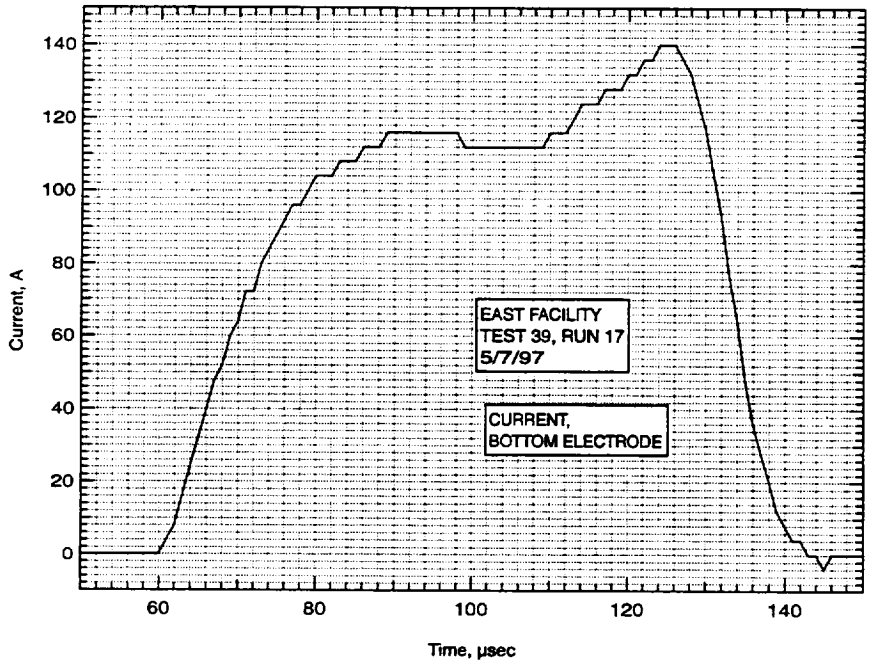

Figure A.2- 11. Run 17, current to bottom electrode.

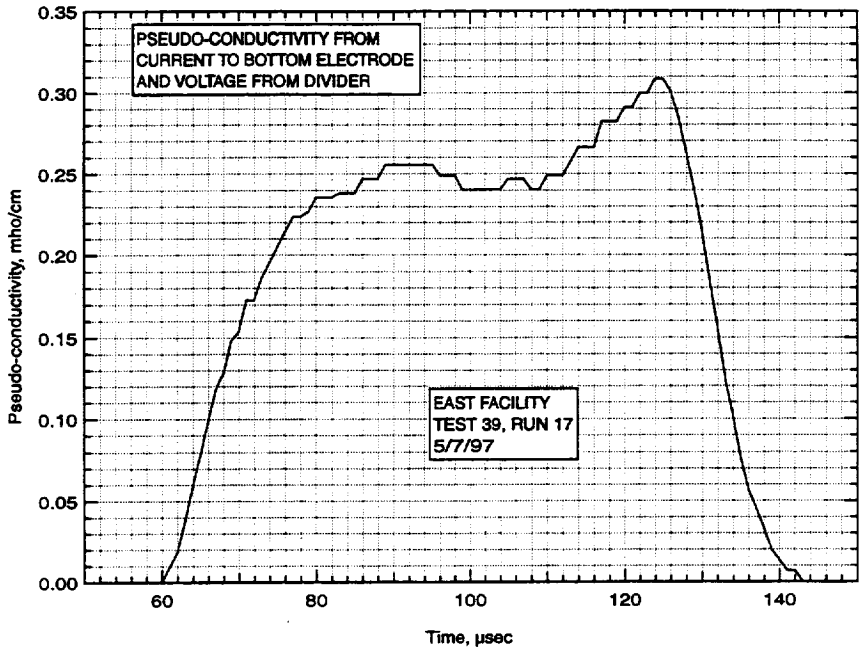

Figure A.2- 12. Run 17, pseudo-conductivity calculated from current to bottom electrode and voltage from divider.

Figure A.2- 12 shows the history of the "pseudo-conductivity," σ, as calculated from the following equation,

$$\sigma(t) = \frac{L I(t)}{A E(t)} \tag{A.2-3}$$

where $\sigma(t)$ is the pseudo-conductivity, L is the spacing between the electrodes, $I(t)$ is the current to the bottom electrode, A is the electrode area, and $E(t)$ is the voltage across the electrodes. Because it more accurately represents the current between the electrodes, $\sigma(t)$ was calculated using $I(t)$ from the bottom electrode, $E(t)$ from the voltage divider at lower and moderate currents and from the current through the 127-ohm resistor for the heaviest currents, L=3.1 cm and A=9.61 cm^2. Obviously $\sigma(t)$ is not the true conductivity since it is calculated including the voltage drops across the electrode fall regions. At this point in time, without additional floating potential electrodes, the true conductivity cannot be obtained.

For the histories given above, note that the origins of the abscissae are arbitrary and simply reflect the time of the stop trigger of the data acquisition system. However, in all cases the time spanned by the range of the abscissae is 100 μs.

Figures A.2- 13 through A.2- 16 present compilations of the histories of the pseudo-conductivities based on the current data for the bottom electrode. The voltages measured at the beginning of current flow and 30 μs after the start of current flow as well as the shock wave velocity at the electrodes are given in the legend. The voltages are also given on each curve.

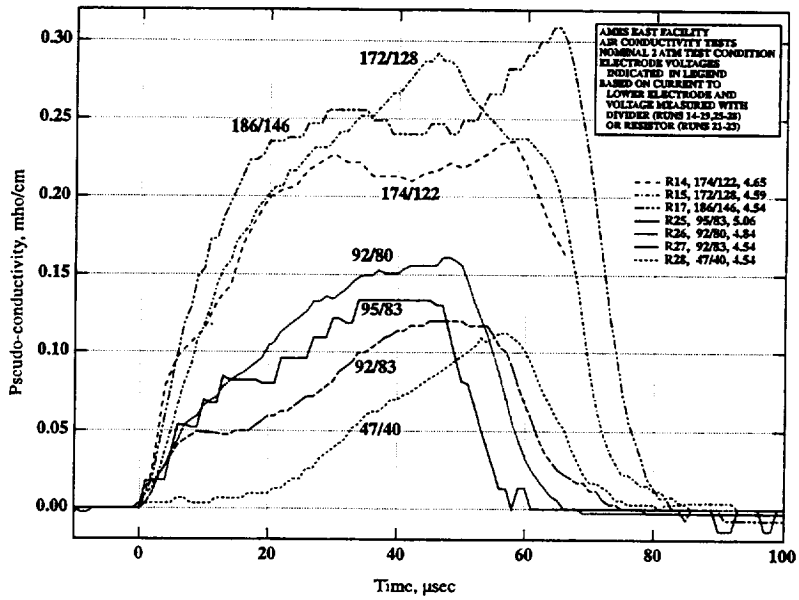

Figure A.2- 13. Pseudo-conductivity histories for 2-atm nominal test condition.

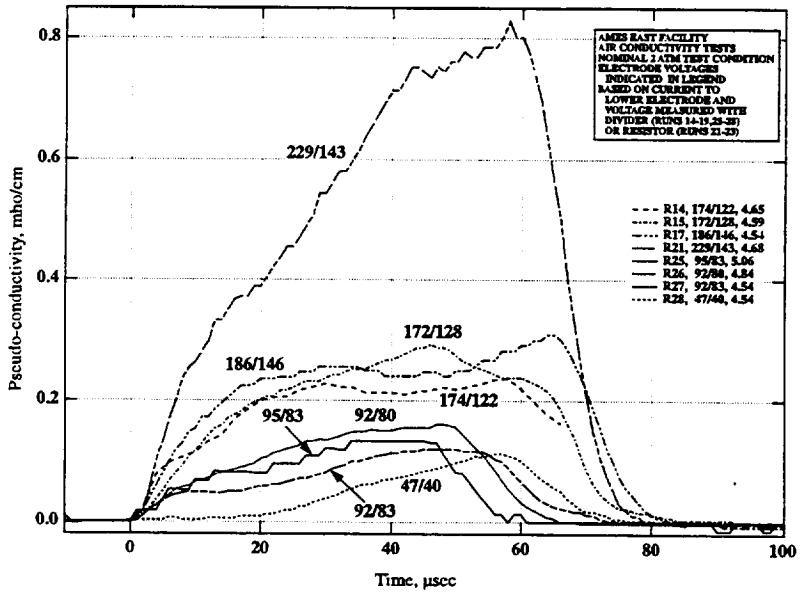

Figure A.2- 14. Pseudo-conductivity histories for 2-atm nominal test condition.

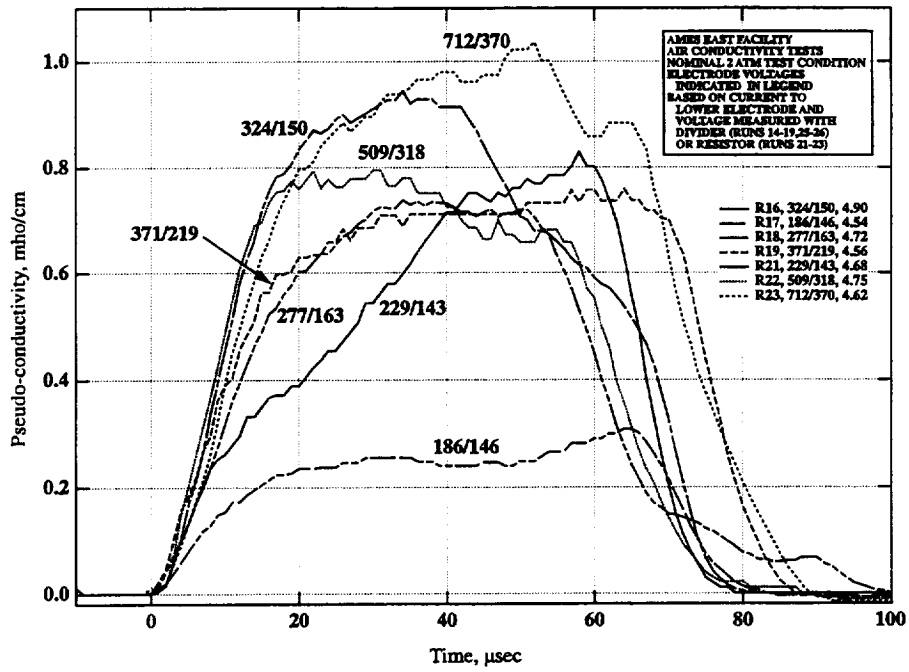

Figure A.2- 15. Pseudo-conductivity histories for 2-atm nominal test condition.

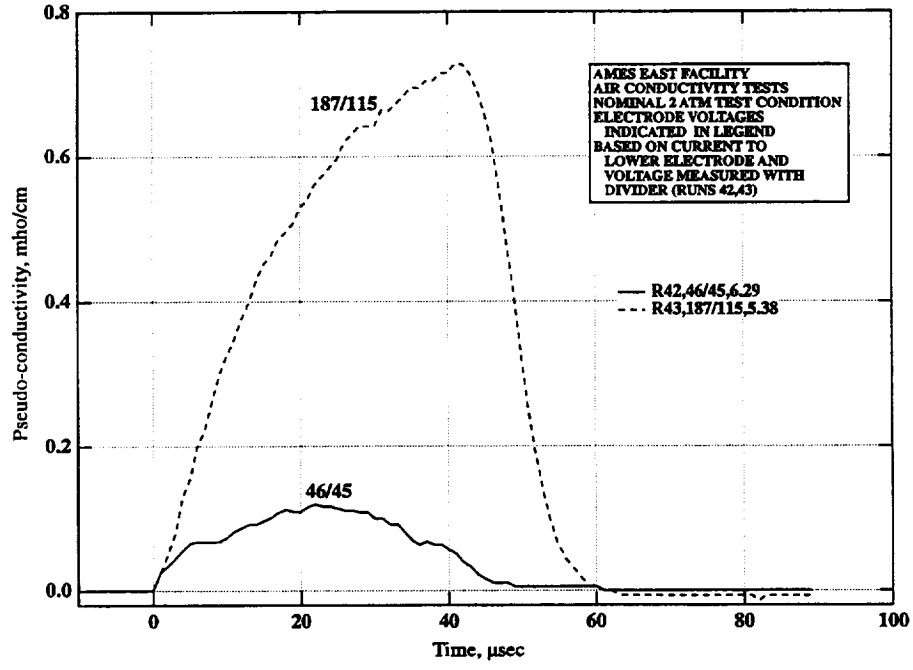

Figure A.2- 16. Pseudo-conductivity histories for 2-atm nominal test condition.

Figures A.2- 13 - A.2- 15 show the pseudo-conductivities for the first 13 runs shown in Table A.2- 5, plotted with three different ordinate scales of pseudo-conductivity. There is some overlap of the pseudo-conductivity curves between the three figures to allow the effect of the applied voltage to be more clearly seen. The results for Runs 42 and 43 are shown separately in Figure A.2- 16 because of the considerably higher shock velocities deliberately chosen for these runs.

Most of the histories show the following features (with times now measured from the start of current flow): the pseudo-conductivities rise very rapidly for the first 7 - 20 μs, then rise more slowly for a period that is usually between 15 and 30 μs, but can range from 7 to 35 μs. The rise in pseudo-conductivity is generally followed by a plateau in conductivity lasting usually 15 to 20 μs, but occasionally up to 30 μs. The pseudo-conductivity then starts to fall steeply 40 - 60 μs after the start of current flow. Note that at a nominal shock velocity of 4.6 km/s, it takes the shock wave about 7 μs to cross the electrode face. Thus, the first part of the initial steep rise in pseudo-conductivity likely reflects the fact that it takes about 7 μs for the shock wave to completely fill the region between the electrodes with heated gas. However, the pseudo-conductivity continues to rise substantially between 7 and 20 - 40 μs after the start of current flow. Two possible explanations are as follows: a) the electron population may take this long after the shock wave passage to come up to a value that is in equilibrium with the gas temperature and the prevailing electric field; b) the current may be flowing mainly in the boundary layers that extend between the electrodes and these boundary layers will initially thicken very rapidly with passing time but will tend to stabilize at a constant thickness. Finally, the rapid drop in pseudo-conductivity is believed to be due to the arrival of the much cooler driver gas 40 to 60 μs after the start of current flow. (See discussion of Section A.2.5.4.)

As mentioned at the beginning of this section, the above-described behavior is typical for most of the tests. For Run 28 with the very low applied voltage of 47 V, the pseudo-conductivity shows a somewhat different behavior. The pseudo-conductivity remains very low for approximately the first 20 μs and then begins to rise. This behavior may occur because the electron population may take 30 - 40 μs to arrive at a value that is in equilibrium with the gas temperature.

Figure A.2- 17 shows the pseudo-conductivities 30 μs after the start of current flow plotted versus shock velocity at the electrodes for all test runs at the 2-atm test condition. The voltage (in Volts) across the electrodes 30 μs after the start of current flow is shown beside each experimental data point. The smooth curves give the calculated equilibrium electron mole fractions behind the shock wave for the 2 atm and the 5-atm test conditions. These mole fractions were calculated using the computer program of McBride and Gordon (Ref. 4). The gas conductivity should be nearly proportional to the electron mole fraction. Unfortunately, there was sufficient spread in the shock velocities (see Table A.2- 5 and Figure A.2- 17) to potentially produce significant variations in gas conductivity due to the shock velocity effect alone, thus obscuring the effect of the changes in the voltage applied across the electrodes. Using the data shown in Figure A.2- 17, the following technique was developed to correct for, to some extent, the shock velocity variations. Four lines were drawn in Figure A.2- 17, each line joining points with similar applied voltages. One line was drawn between the 40- and 45-V data points; a

second line fit the trend of the 80-, 83- and 83-V data points; a third line between the 122- and 115-V data points; and a fourth line fit the trend of the 143-, 163-, and 150-V data points.

The slopes of the three highest of these lines were determined to be reasonably close. The average of the three slopes was chosen, and the following correction factor was determined to correct the data to the nominal shock velocity of 4.65 km/s:

$$f_c = 818.24 \exp(-1.4424 u_s) \qquad \text{(A.2-4)}$$

where u_s is the shock velocity in km/s, and f_c is the correction factor. The correction factor is applied to the current between the electrodes; the voltage across the electrodes is left unchanged.

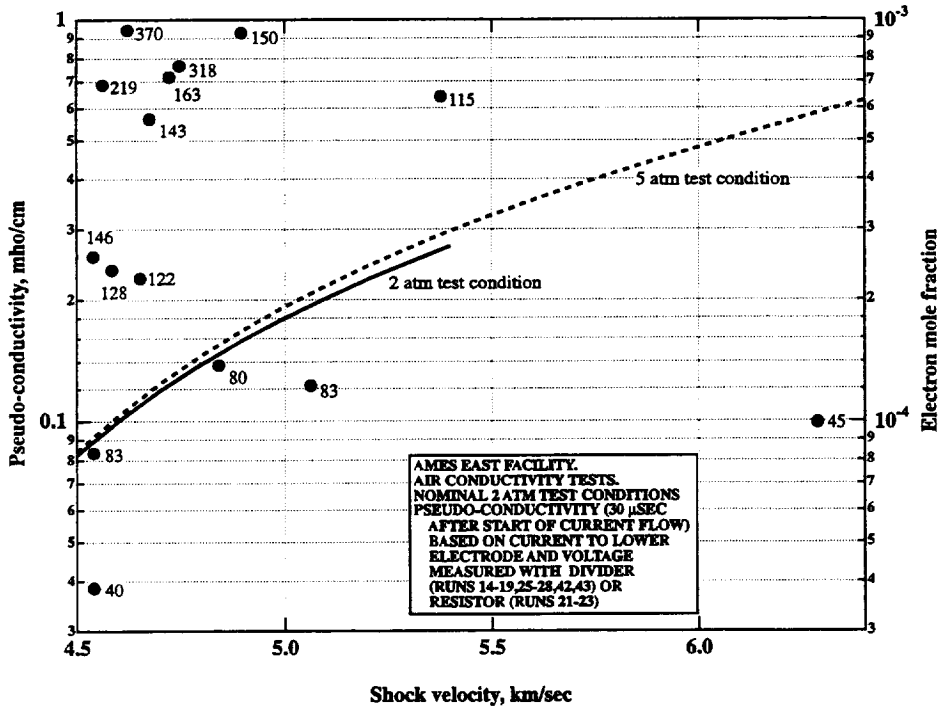

Figure A.2- 17. 2-atm test conditions, pseudo-conductivities 30 μs after start of current flow plotted versus shock velocity. Voltages across electrodes are shown next to data points. Curves show calculated equilibrium electron mole fractions behind shock wave for the 2-atm and 5-atm test conditions.

Figure A.2- 18 shows the pseudo-conductivities 30 μs after the start of current flow plotted versus the voltage across the electrodes 30 μs after the start of current flow. In Figure A.2- 18, the pseudo-conductivities have not been corrected for the shock velocity effect. Figure A.2- 19

shows the data of Figure A.2- 18 with the pseudo-conductivities now corrected for the shock velocity effect. The scatter of the data is considerably reduced by the application of the shock velocity correction. Many graphs to be presented later will have the shock velocity correction applied to the data. Figure A.2- 20 shows the pseudo-conductivities 30 μs after the start of current flow plotted versus the voltage across the electrodes at the start of current flow. Figures A.2- 21 and A.2- 22 correspond to Figures A.2- 19 and A.2- 20, but represent the conductivities measured for 15 rather than 30 μs after the start of current flow. The correction factor for the shock velocity effect in this case was:

$$f_c = 413.45\exp(-1.2956u_s) \qquad \text{(A.2- 5)}$$

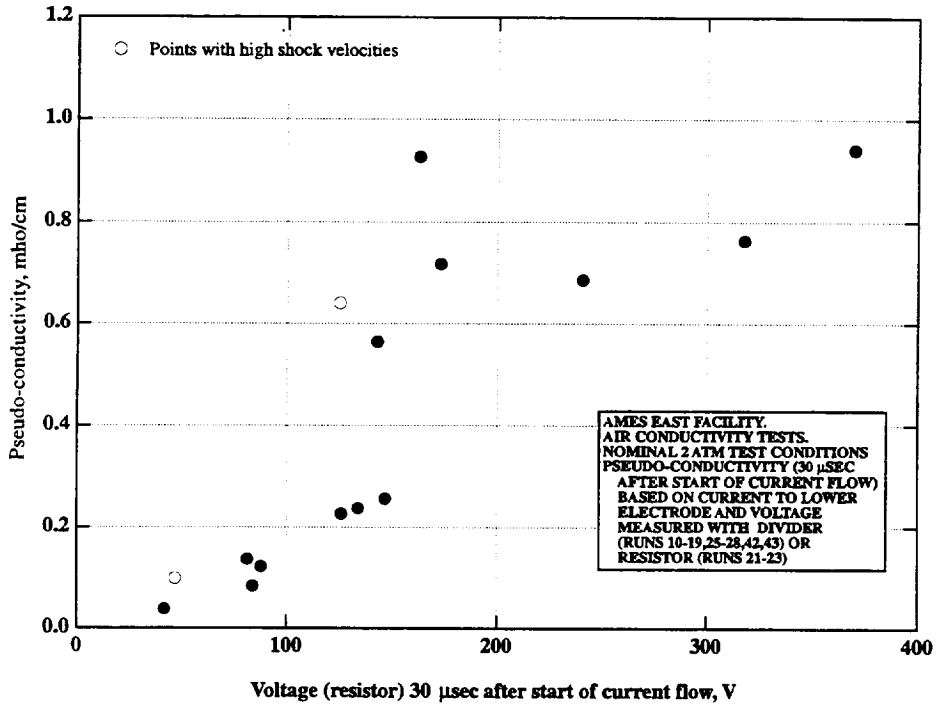

Figure A.2- 18. 2-atm test conditions, pseudo-conductivities 30 μs after start of current flow plotted versus voltage applied across electrodes 30 μs after start of current flow. Not corrected for shock velocity effect.

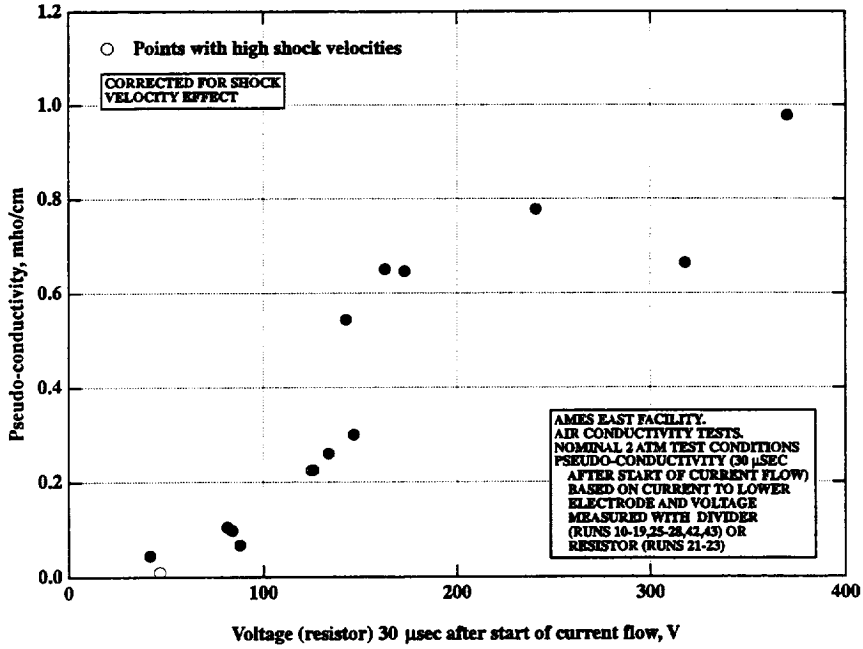

Figure A.2- 19. 2-atm test conditions, pseudo-conductivities 30 μs after start of current flow plotted versus voltage applied across electrodes 30 μs after start of current flow. Corrected for shock velocity effect.

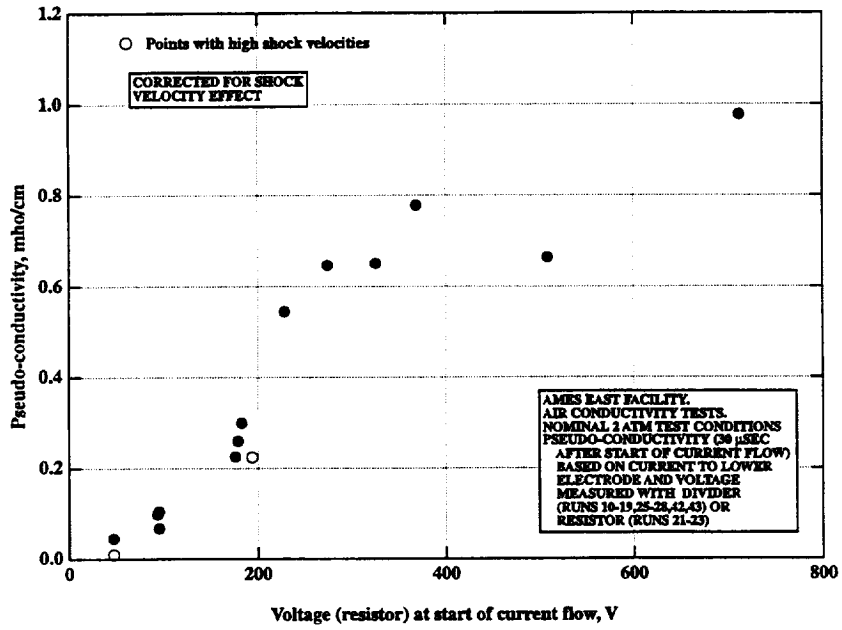

Figure A.2- 20. 2-atm test conditions, pseudo-conductivities 30 μs after start of current flow plotted versus voltage applied across electrodes at start of current flow. Corrected for shock velocity effect.

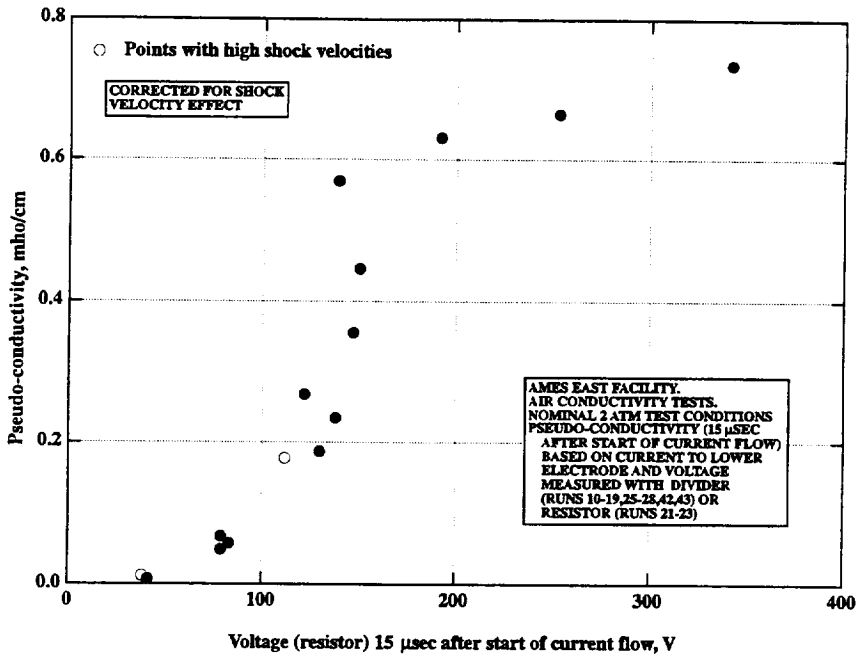

Figure A.2- 21. 2-atm test conditions, pseudo-conductivities 15 μs after start of current flow plotted versus voltage applied 15 μs after the start of current flow. Corrected for shock velocity effect.

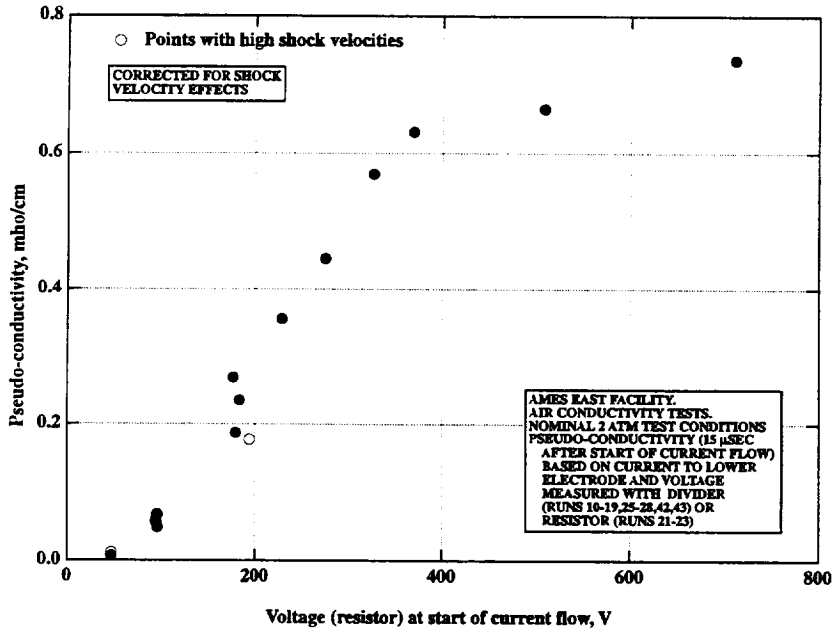

Figure A.2- 22. 2-atm test conditions, pseudo-conductivities 15 μs after start of current flow plotted versus voltage applied across electrodes at start of current flow. Corrected for shock velocity effect.

Figures A.2- 19 and A.2- 21, which show the pseudo-conductivities plotted versus the voltages at the times the pseudo-conductivities were calculated, also show the following characteristics. The conductivities rise from values of 0.01 - 0.04 Mhos/cm at voltages of about 40 V to values of 0.2 - 0.3 Mhos/cm at voltages of 100 - 130 V. At about 140 V, the conductivities rise very steeply to about 0.6 Mhos/cm and then rise much more slowly to values of 0.75 - 1.0 Mhos/cm at the maximum voltages of about 350 V. The rise at a voltage of about 140 V is very abrupt, the conductivity doubling or tripling over a voltage range of 10 - 20 V, or less. The data of Figures A.2- 20 and A.2- 22, where the conductivities are plotted versus the voltage applied at the start of current flow show fairly similar trends to the data of Figures A.2- 19 and A.2- 21 with the following differences. The voltages are now considerably higher, particularly at the higher conductivities (i.e., at higher current draws) due the inability of the available power supply to maintain the voltage at the heavier current draws. Further, the abrupt rises in conductivity at a voltage of about 140 V in A.2- 19 and A.2- 21 are replaced by somewhat gentler rises in conductivity between voltages of 180 and 350 V in Figures A.2- 20 and A.2- 22. This may indicate that the conductivity values 15 and 30 μs after the start of current flow are responding in part, to the higher voltages applied at the start of current flow, as well as to voltage applied at the instant the conductivity was calculated. While undesirable, this effect could not be avoided with the power supply available to us during this test entry. Note that the increases in pseudo-conductivity obtained as the applied voltage is increased from the minimum to the maximum values are very large, by a factor of about 25 for Figures A.2- 19 and A.2- 20 and by a factor of about 100 for Figures A.2- 21 and A.2- 22.

In general, the conductivities at 30 μs after the start of current flow are about 20 - 30% larger than those at 15 μs after the start of current flow, possibly because of the increase in electron density in the time period between 15 and 30 μs after the start of current flow while the electron density is approaching a value in equilibrium with the gas temperature and the prevailing electric field. Such increases in electron density have been observed after the passage of shock waves travelling into Ar at shock velocities and tube fill pressures in the ranges of those of the EAST facility's experiments (Ref. 5). In the experiments of Reference 5 at a shock velocity of 4.2 km/s and a tube fill pressure of 0.688 kPa, the electron number density was observed to take about 20 μs to approach a fairly constant value. An additional reason for the increase in the conductivity between 15 and 30 μs after the start of current flow may be the increase in the thickness of the boundary layers with time. The electrode boundary layers may become less resistive when they are thicker; and/or the sidewall boundary layers, if they carry a significant fraction of the current flow, may offer better current paths as they become thicker. More detailed work is required in these areas.

Figure A.2- 23 shows the pseudo-resistivity (the pseudo-resistivity is equal to 1/pseudo-conductivity) 30 μs after the start of current flow plotted versus the current to the bottom electrode 30 μs after the start of current flow. Figure A.2- 24 shows the voltage across the electrodes 30 μs after the start of current flow plotted versus the current to the bottom electrode 30 μs after the start of current flow. Figures A.2- 25 and A.2- 26 correspond to Figures A.2- 23 and A.2- 24 but are for data 15 instead of 30 μs after the start of current flow. Each of these four graphs also shows a line based on the theoretical equilibrium gas conductivity behind a shock wave at the nominal shock velocity of 4.65 km/s. The resistance value used to generate the lines

in Figures A.2- 24 and A.2- 26 was based on the theoretical equilibrium conductivity behind the shock wave, the electrode area of 9.61 cm^2, and the electrode spacing of 3.10 cm. With the theoretical equilibrium conditions behind the shock wave calculated using the computer program of Reference 4, the equilibrium conductivities were obtained by interpolating between the values given in Reference 6. At low to moderate voltages (40 - 140 V) and currents (1 - 300 A), the pseudo-resistivity is above the value corresponding to the equilibrium bulk gas conditions behind the shock wave being as much as 50-100 times this value at currents of ~1 A.

This ratio drops to about 15 at currents of ~10 A and about 3 at currents of ~100 A. Between voltages of 140 and 330 V and currents of 300 and 700 A, the pseudo-resistivity appears to be about equal to the value corresponding to the equilibrium bulk gas conditions behind the shock wave; while at the highest current (1,100 A) 30 μs after the start of current flow, it appears to be about 30% below this value.

Consider the low to moderate (1 - 300 A) current range where the pseudo-resistivity increases steeply as the current drops. If it is assumed that the conductivity of the bulk gas (away from the electrodes) is not far from the calculated equilibrium value, it is clear that the resistivity of the electrode fall regions must rise steeply as the current drops. This would appear to be in line with negative voltage - current characteristics of electric arcs reported in Nottingham (Ref. 7) and Cobine (Ref. 8).

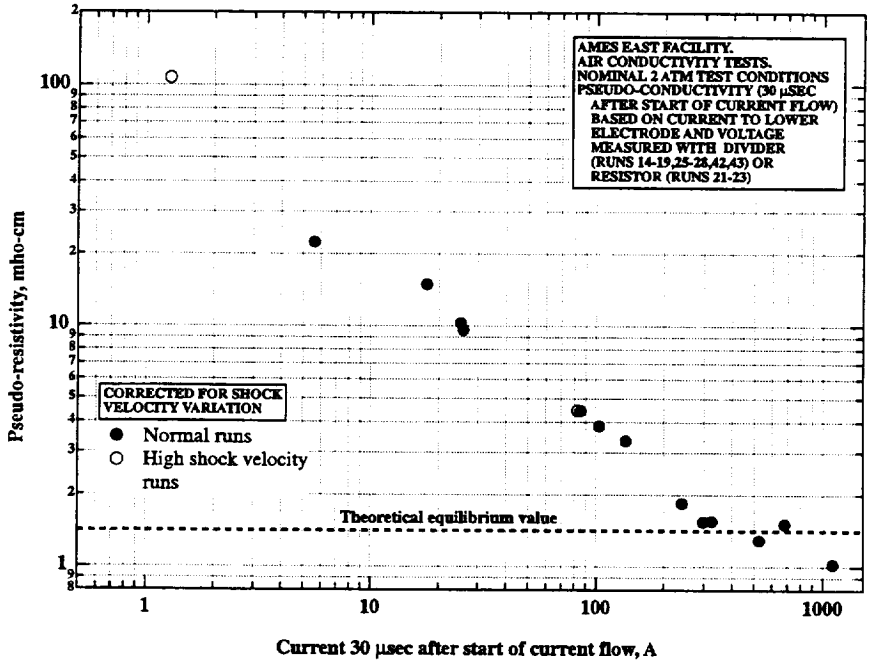

Figure A.2- 23. 2-atm test conditions, pseudo-resistivities 30 μs after start of current flow plotted versus current to lower electrode 30 μs after the start of current flow. Corrected for shock velocity effect.

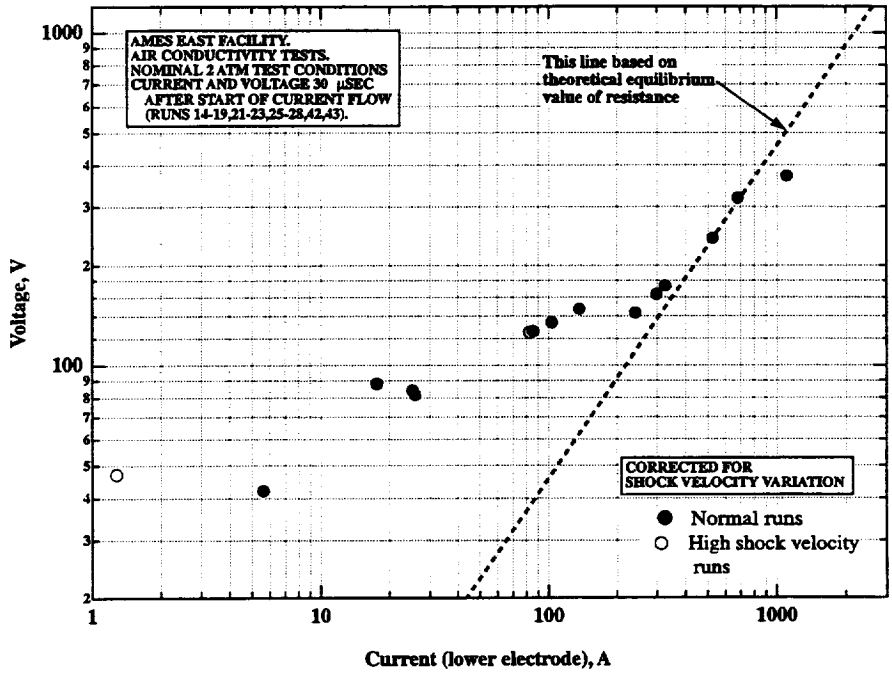

Figure A.2- 24. 2 atm test conditions, voltages across electrodes 30 μs after start of current flow plotted versus current to lower electrode 30 μs after the start of current flow. Corrected for shock velocity effect.

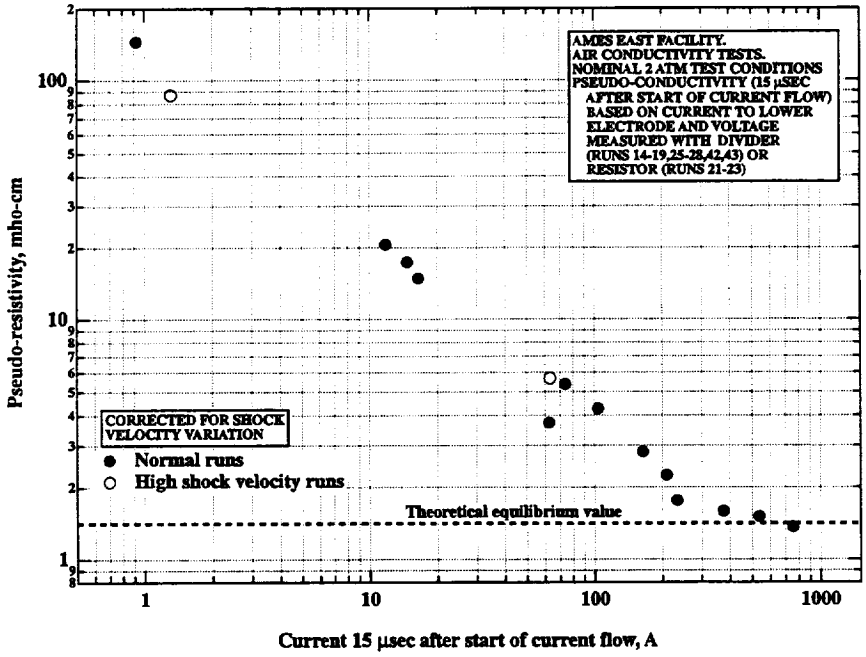

Figure A.2- 25. 2 atm test conditions, pseudo-resistivities 15 μs after start of current flow plotted versus current to lower electrode 15 μs after the start of current flow. Corrected for shock velocity effect.

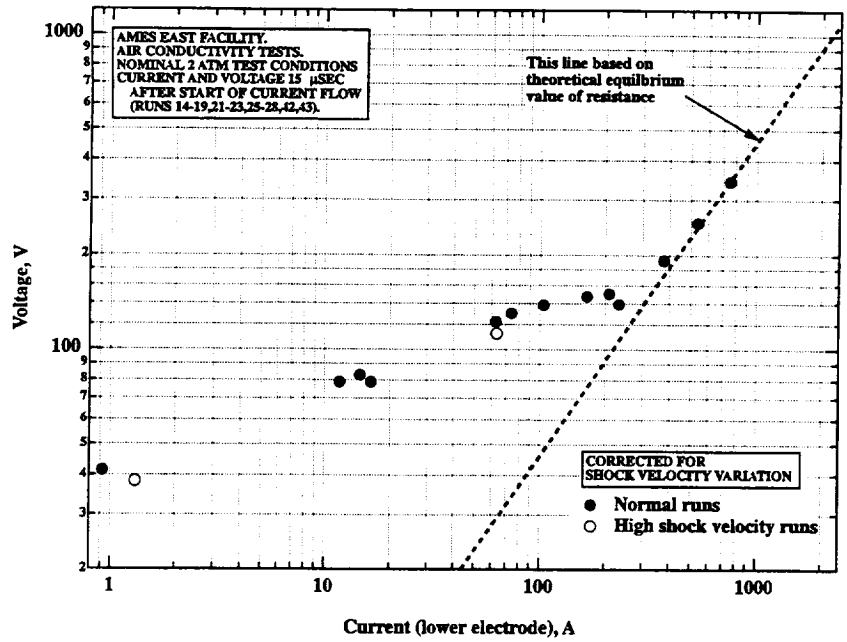

Figure A.2- 26. 2-atm test conditions, voltage across electrodes15 μs after the start of current flow plotted versus current to lower electrode 15 μs after the start of current flow. Corrected for shock velocity effect.

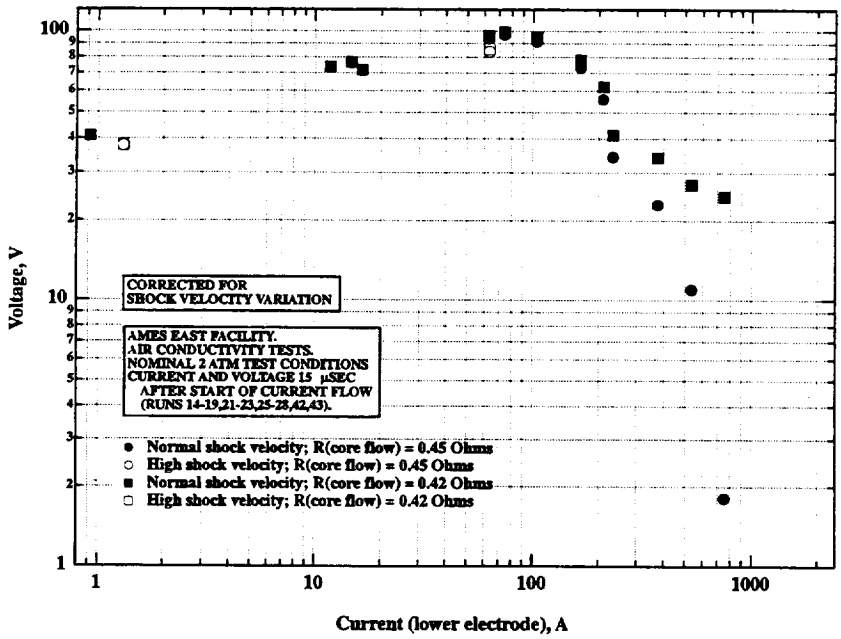

Figure A.2- 27. 2-atm test conditions, estimated electrode fall voltage 15 μs after start of current flow plotted versus current to lower electrode 15 μs after the start of current flow. Corrected for shock velocity effect.

In Reference 9, use is made of the Nottingham equations to estimate the anode and cathode falls in an MHD channel. Therein, it is postulated that the electrode fall regions being very near the cold electrodes and away from the shock-heated free stream flow, behave as they do in a normal electric arc. In the current range between 300 and 700 A, it is suggested the electrode fall voltages have become so small compared to the IR drop in the bulk gas that the pseudo-resistivity is essentially dominated by the bulk gas conductivity and hence, is reasonably given by 1/(bulk gas conductivity). Such an interpretation would appear to be supported by Figures A.2- 23 - A.2- 26.

At the very highest current (1,100 A) 30 μs after the start of current flow, the pseudo-resistivity appears to be about 30% below this calculated equilibrium value. Such a phenomenon is supported by only one data point at the 2-atm test condition but will later be shown to occur also for the 5 and 13-atm test conditions. For this data point the power input to the gas can easily be calculated to be ~0.40 MW. From the equilibrium calculations of the conditions behind the shock wave made using the program of Reference 4, the density, velocity and specific heat behind the shock wave can be obtained. Hence, knowing the cross-sectional area of the flow channel, the average temperature rise of the gas as it transits the electrode region can be calculated. Allowance must be made for the slowing of the flow caused by the bulk heating, which converts a small fraction of the kinetic energy of the flow into an additional static enthalpy rise. The gas temperature rise calculated in this way is 280 K. The increases expected in equilibrium conductivity for temperature rises of 280 and 140 K will be calculated. The equilibrium calculations of conditions behind the shock wave for various shock velocities produce different temperatures behind the shock wave. Using these results, the temperature increases of 280 and 140 K can be shown to produce an increase in the electron mole fraction of 47 and 21%, respectively. The increase in the pseudo-conductivity (over the calculated equilibrium value) for the 1,100 A data point 30 μs after the start of current flow is 38%. Hence, simple ohmic heating of the gas may be able to explain a substantial portion of the observed decrease in the pseudo-resistivity for this data point. It is also possible that the higher electric field at this high current condition could be producing some nonequilibrium ionization in the bulk gas.

From the data of Figure A.2- 26, an attempt to separate out the voltage drops across the electrode fall regions and what will be separated out will be the sum of the voltage drops across the two electrode fall regions will now be made. This is done by taking the voltages from Figure A.2- 26 and subtracting IR drops for the core flow assuming various (constant) core flow resistances. The resulting voltage drops across the electrode fall regions for assumed core flow resistances of 0.45 and 0.42 ohms are shown in Figure A.2- 27 plotted against the current to the bottom electrode. To the left side of the peak voltage in Figure A.2- 27, the voltages are essentially independent of the value chosen for the core flow resistance. Note that the voltage drop across the electrodes apparently increases as the current increases from 1 to 100 A and then decreases as the current further increases to ~700 A. For assumed core flow resistances near 0.42 ohms and currents above ~100 A, it appears that one might be able to fit the experimental V-I characteristics of the voltage drop across the electrode fall regions with a Nottingham (Ref. 7) type expression, i.e.,

$$V = C_1 + \frac{C_2}{I^{.67}} \qquad \text{(A.2- 6)}$$

where V is voltage, I current, and C_1 and C_2 are constants. Nottingham gives values of the current exponent for 10 different pairs of electrode materials. He also gives an exponent of 0.67 for two copper electrodes, which is as close as can be achieved to the two brass electrodes. To obtain the best fit of the Nottingham curve to this part of the voltage drop across the electrode fall region would also involve finding the best value for the assumed core flow resistance. In essence this would be equivalent to fitting the part of the data of Figure A.2- 27 for currents above ~100 A with an equation of the form:

$$V = C_1 + \frac{C_2}{I^{.67}} + IR_c \qquad \text{(A.2- 7)}$$

where R_c is the core flow resistance. For lack of time, this data was not completed for this test entry; however, it may be worth attempting. As mentioned previously, Figure A.2- 27 suggests that a core flow resistance of about 0.42 ohms would allow a Nottingham type of equation to be fit to the portion of the data for currents above 100 A. This value is rather close to the value 0.46 ohms, estimated as described earlier from the calculations of Viegas and Peng (Ref. 6) for equilibrium flow behind the shock wave. However, it is clear that a Nottingham-type equation is not going to apply to the portion of the curve of Figure A.2- 27 to the left of the voltage maximum. From examining Figure A.2- 24 and the figures corresponding to Figures A.2- 24 and A.2- 26 for the 5 and 13-atm test conditions, it is clear that the general nature of the estimated voltage drops across the electrode fall regions for all test conditions is fairly similar to that shown in Figure A.2- 27. In other words, in the low to moderate current ranges the apparent voltage drops across the electrode fall regions appear to show a positive rather than negative V-I characteristic for all test conditions.

An example IMACON™ Polaroid photograph for test 18 at the 2-atm test condition is shown in Figure A.2- 28. The test number, date, and test conditions are given at the top of the figure. The flow is from left to right, and the frame sequence is identified below the figure. The times given below the frames are measured from the start of current flow. The shock wave image first appears in the first frame. A second image of the shock appears in the second frame, which allowed a determination of V_I. For this particular test, V_I = 4.4 km/s and V_{CAV} = 4.96 km/s. The oblique shock waves emanating from the leading edge of the electrodes are clearly visible in frames 2-5, and Mach numbers determined from a measurement of the oblique shock angle are given for each frame. In the images of frames 4 and 5, the shock waves are seen to cross and a slight bend from this interaction is discernable. Glow from the flow region near the electrode surfaces begins to overwhelm the rest of the field in the last three frames. The large dynamic range of the light emission over this 28-μs record period is evident from a comparison of the faintness of the first two frame images with the near saturation in the last two. This aspect of the testing meant that a complete flow visualization of the total test period was rarely achieved.

A summary of all photographs for the 2-atm case and the parameters measured from them is given in Table A.2- 6 and Table A.2- 7. The shock velocities, pressures, and voltages were taken from Table A.2- 5 with the exception of those for tests 13, 20, and 24. The time given is the time of frame number 1 after the start of current flow. The remaining parameters in the Table A.2- 6

are the velocities inferred from the photographs. Table A.2- 7 gives the Mach numbers read from the oblique shock waves. Columns 2 through 5 give the experimental Mach numbers themselves and column 7 gives the frames in which they were measured. Column 6 gives the theoretical Mach numbers in equilibrium flow behind a shock wave at the observed velocity at the electrodes. These theoretical Mach numbers were calculated using the computer program of Reference 4. Note that, in general, the observed Mach numbers are 0.20 to 0.45 less than the theoretical values. There are several possible explanations for this, which include boundary layer growth, natural growth without electrical energy deposition, and enhanced growth due to electrical energy deposition may help to throttle the flow somewhat and thus to reduce the Mach number. At higher currents, energy deposition in the bulk gas may result in a Mach number reduction. Furthermore, the relatively low experimental Mach numbers may also be due in part, to the fact that the experimental flow may not be in equilibrium. From the formulas of Reference 10, it may easily be shown that the theoretical Mach number behind a strong shock in an ideal gas is given by:

$$M_{\text{after shock}} = \sqrt{\frac{2}{\gamma(\gamma - 1)}} \qquad \text{(A.2- 8)}$$

where γ is the specific heat ratio. $M_{\text{after shock}}$ rises from 2.26 to 2.89 as γ drops from 1.3 to 1.2. Hence, the Mach number behind the shock wave would be expected to be less than the equilibrium value if all of the degrees of freedom of the gas are not excited, which would tend to produce a γ value greater than the equilibrium value.

Table A.2- 6. Results from IMACON photographs for runs at the nominal 2-atm test condition.

Run no.	Shock vel. at E (km/s)	Shock press at D (atm)	Voltage at start of current (V)	Time of fr. #1 after start of current (μs)	V_I from Photo (km/s)	V_{CAV} from Photo (km/s)
13	4.85	2.57	174	?	----	----
14	4.65	2.44	176	-1.5	----	4.90
16	4.89	2.75	324	5.2	----	5.05
17	4.54	2.33	186	-5.8	----	4.80
18	4.72	2.55	277	1.2	4.6	4.96
19	4.56	2.29	371	-4.6	4.6	4.84
20	4.61	2.43	0	-3.1	4.6	4.82
22	4.75	2.76	520	-1.1	----	----
23	4.62	2.72	714	-5.6	4.5	4.75
24	4.72	2.84	0	0.7	4.5	4.97
25	5.06	3.39	95	-2.1	4.6	5.37
26	4.84	3.07	92	-8.2	4.6	5.14
27	4.54	2.60	92	-5.6	----	4.77
28	4.54	2.68	46.6	-6.2	4.8	4.76
43	5.38	3.97	187	-12.5	----	5.77

Table A.2- 7. Results from IMACON photographs for runs at the nominal 2-atm test condition.						
Run no.	Mach no.	Mach no.	Mach no.	Mach no.	Theoretical Mach no.	Frame numbers
13	2.59	2.69	2.42		2.78	1,2,3
14	2.85	2.46			2.71	3,4
16	2.57	2.69			2.79	1,2
18	2.24	2.42	2.32	2.48	2.73	2,3,4,5
19	2.33	2.33			2.68	5,6
20	2.42	2.46	2.42	2.42	2.70	3,4,5,6
24	2.46	2.26			2.73	3,4
25	2.31	2.40	2.40		2.84	2,3,4
26	2.39	2.30			2.77	5,6
28	2.39				2.67	5
43	2.69	2.69			2.93	7,8

Although no evidence of breakdown due to the electrical discharges was found in any IMACON photographs images, some interesting qualitative features were observed. The most interesting feature observed in the images was the presence of "hot spots" on the electrode surfaces. For some of the highest current test cases where the attenuation of light from the test section was sufficient, discrete, bright light sources could be seen on the electrodes. To illustrate these features, images from two 2-atm runs are shown in Figure A.2- 29. The top image is from Run 23, which had the highest current measured during the 2-atm tests. (The maximum current to the bottom electrode was 1,180 A.) Fixed spots of bright light are visible at the edges of both electrodes, where the radii of the electrodes will produce an electric field increase. In addition, moving spots of light are visible on the lower electrode (the cathode) and were also observed on the cathode in Runs 19 and 22, which were the runs with the second and third highest voltages and currents at the 2-atm test conditions. The voltages at the start of current flow for these two runs were 371 and 509 V, and the maximum currents to the lower electrode were 575 and 800 A. However, the moving spots of light were not observed at lower voltage and currents. An example of the IMACON photographs for lower current conditions is shown in the lower half of Figure A.2- 29. This photograph is from Run 14 with a maximum current of 96 A to the lower electrode. These images show less bright emission near the electrodes (when the neutral density filters used in front of the camera are taken into account) and the bright spots at each end of the electrode are likely due to the higher electric fields in these regions, as discussed earlier. There is no trace of moving hot spots on the cathode surface. In general, radiation from the center of the flow is quite weak in comparison to the emission from the regions close to the electrodes. In Reference 11 (Figure A.2- 6), oblique photographs were taken of the cathode of e-beam sustained discharges in static, room-temperature nitrogen at pressures of 13.3 and 40 kPa and the duration of the discharges was 20 μs. In the two photographs shown in Reference 11, the cathode is covered with a large number of glowing spots that are smaller at the higher pressure. The gas densities in the work of Reference 11 were 1.5 to 5 times greater than those at the EAST facility, whereas the EAST facility's current densities were 10 to 25 times greater than those for the work of Reference 11. It was speculated that the moving hot spots may be related to the glowing spots seen in the work of Reference 11 but without further experimental study, little more can be said about any such relation.

Run no: 18 **Date:** 5/8/97 **Shock press. At D:** 2.55 atm
Shock vel. at E: 4.72 km/s **Voltage at start of current flow:** 277 V

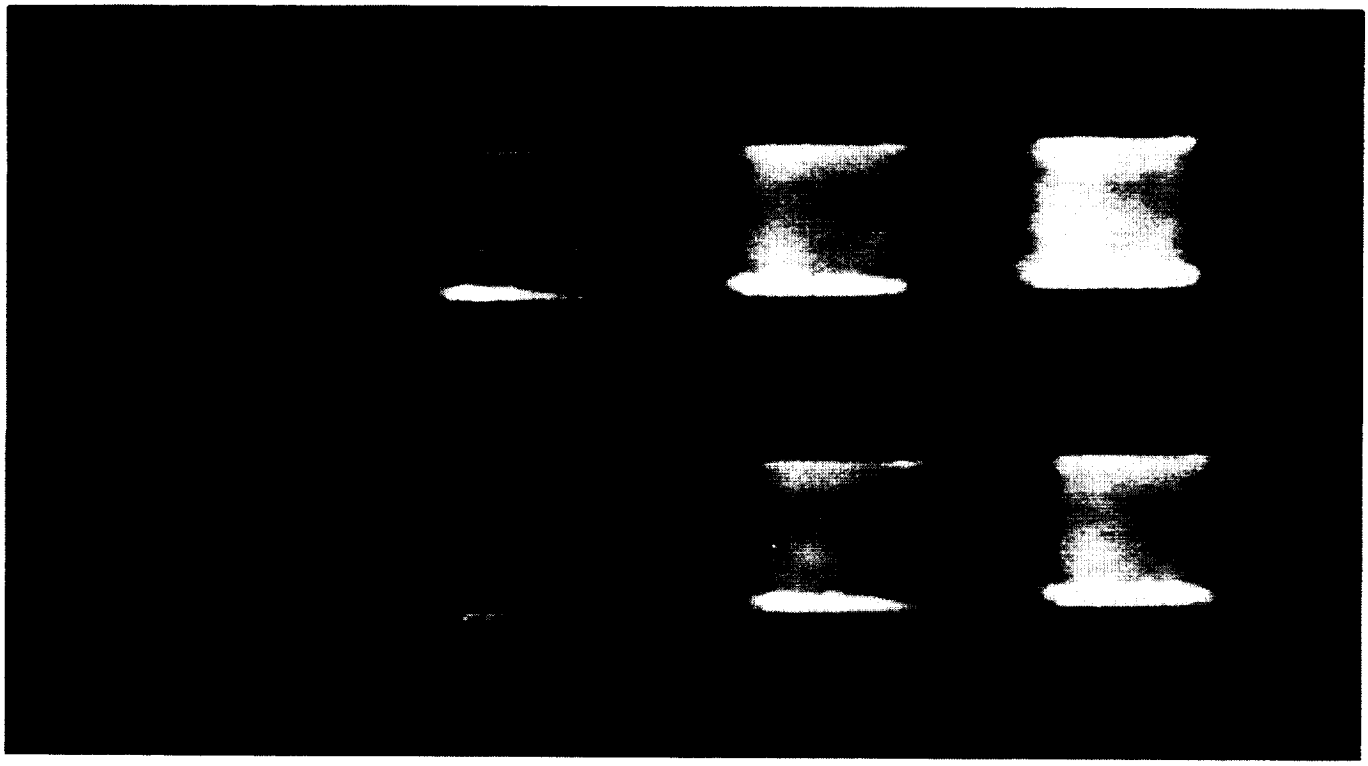

Frame:	**2**	**4**	**6**	**8**
Time:	5.2	13.2	21.2	29.2
Mach no:	2.24	2.32		
Frame:	**1**	**3**	**5**	**7**
Time:	1.2	9.2	17.2	25.2
Mach no:		2.42	2.48	

V_I: 4.6 km/s V_{CAV}: 4.96 km/s

Figure A.2- 28. IMACON image of the shock-heated test gas flow in the electrode region. The time is measured from the start of the current flow. Mach numbers and velocities are deduced from the image as explained in Section A.2.5.3.

Run no: 23 **Date:** 5/14/97 **Shock press. At D:** 2.72 atm
Shock vel. at E: 4.62 km/s **Voltage at start of current flow:** 714 V
Max. current, lower elect.: 1180 A **Time of first frame after start of current:** -5.6 μs

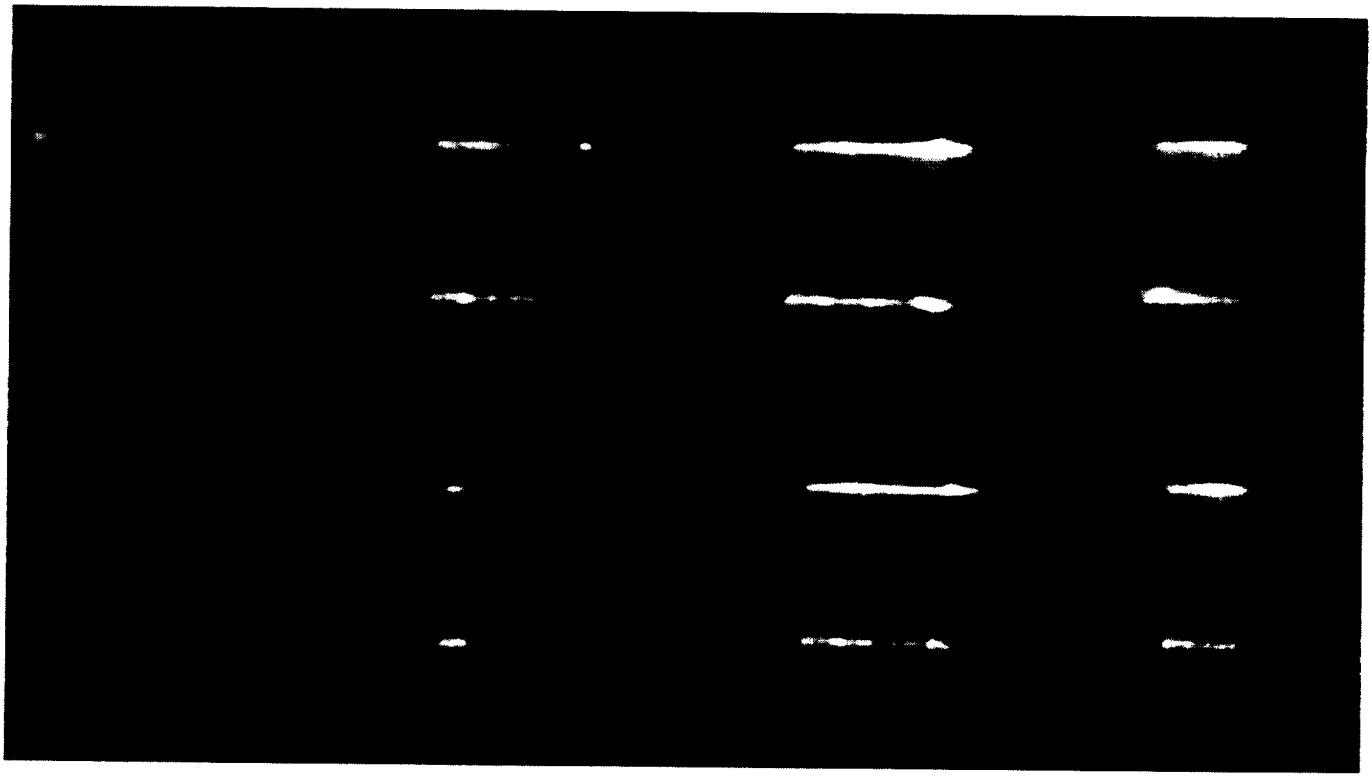

Run no: 14 **Date:** 5/2/97 **Shock press. At D:** 2.44 atm
Shock vel. at E: 4.65 km/s **Voltage at start of current flow:** 176 V
Max. current, lower elect.: 96 A **Time of first frame after start of current:** -1.5 μs

Figure A.2- 29. The upper set of images, from a high current test run, shows the presence of bright "hot spots" at the cathode (lower electrode) surface. The lower images, which are from a low current run, show essentially none of these features.

A.2.6.2 At Nominal 5-Atm Test Condition

Table A.2- 8 gives the test conditions for the runs at the nominal 5-atm facility operating condition. The various columns of Table A.2- 8 present data in exactly the same manner as in Table A.2- 5(see Section A.2.6.1) for the 2-atm test condition. Representative data histories for the voltages, currents and pseudo-conductivities will not be provided for the 5 and 13-atm test conditions, since they show data in exactly the same formats as the data histories presented in Figures A.2- 8 and A.2- 12 for the 2-atm test conditions.

Table A.2- 8. Test conditions for runs at the nominal 5-atm test condition.

Run no.	Dn tube gas	Dn tube fill pressure (kPa)	Shock v At E (km/s)	Shock p at D (atm)	Shock p at F (atm)	Voltage at 0 μs (V)	Voltage at 30 μs (V)
29	N_2O/N_2	1.73	4.159	4.72	5.36 (N)	91	80.6
30	N_2O/N_2	1.73	4.215	4.99	5.64 (N)	92	84
31	N_2O/N_2	1.73	4.653	7.08	4.90 (N)	92	86
32	N_2O/N_2	1.73	4.921	7.61	6.58 (N)	92	88
33	N_2O/N_2	1.73	4.475	5.80	7.11 (EN)	188	143
34	N_2O/N_2	1.73	4.597	5.97	5.43 (EN)	270	210
35	N_2O/N_2	1.73	4.912	7.15		469	310
36	N_2O/N_2	1.73	4.627	6.17		700	406
37	N_2O/N_2	1.73	4.455	6.17		1024	490
38	N_2O/N_2	1.73	4.846	7.21		1020	482
39	N_2O/N_2	1.73	4.657	6.49		469	310
40	N_2O/N_2	1.73	4.946	8.00		190	151
41	N_2O/N_2	1.73	4.723	7.28		45.5	40.3

Figures A.2- 30 - A.2- 32 present compilations of the histories of the pseudo-conductivities based on the current data for the bottom electrode. The voltages measured at the beginning of current flow and 30 μs after the start of current flow, as well as the shock wave velocity are given in the legend. The voltages are also given on each curve.

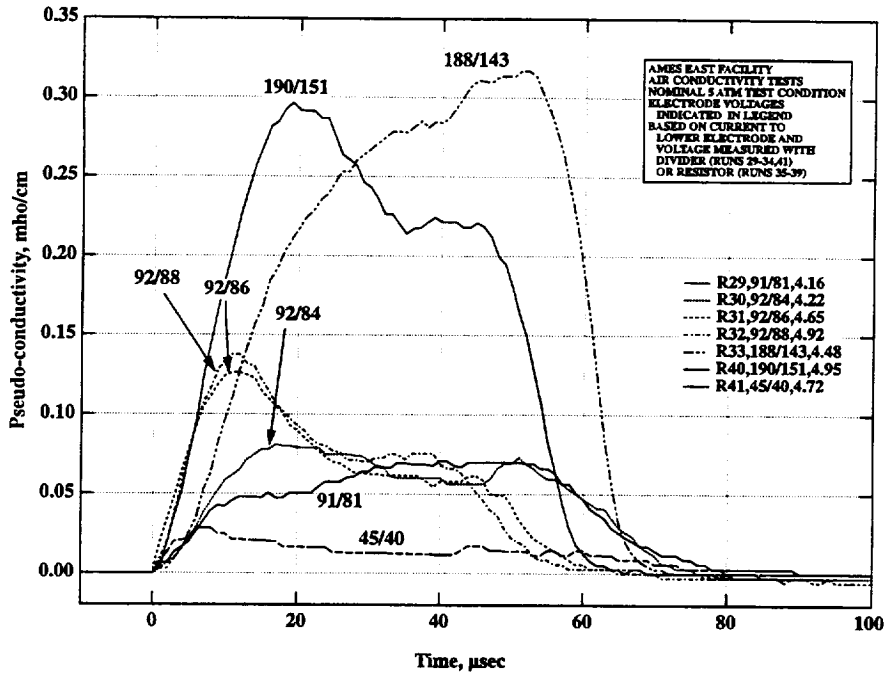

Figure A.2- 30. Pseudo-conductivity histories for 5-atm nominal test condition.

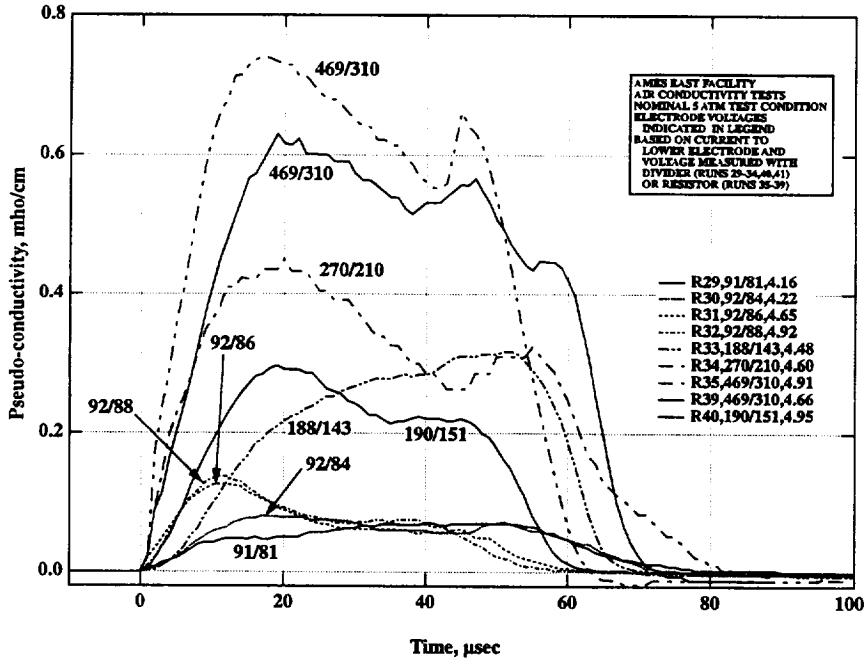

Figure A.2- 31. Pseudo-conductivity histories for 5-atm nominal test condition.

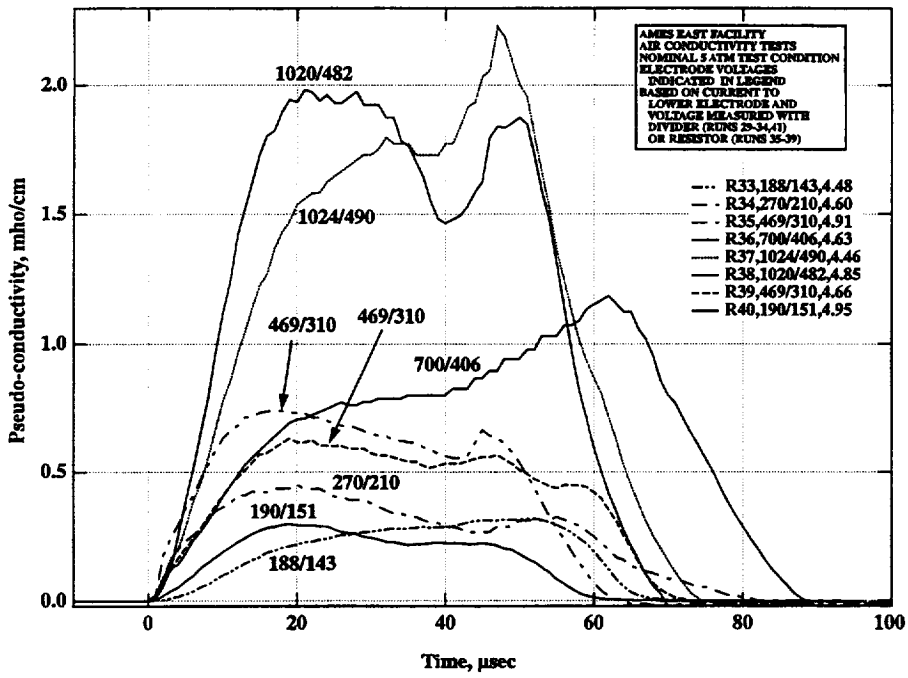

Figure A.2- 32. Pseudo-conductivity histories for 5-atm nominal test condition.

The following is a general description of the histories (with times now measured from the start of current flow). The pseudo-conductivities rise very rapidly for the first 7 - 20 μs. After this period some of the histories then show a plateau that lasts roughly 40 μs, while others show a 20 - 50% drop in pseudo-conductivity for 15 - 25 μs, followed by a period of roughly constant conductivity lasting 20 - 25 μs. The pseudo-conductivity then starts to fall steeply 40 to 60 μs after the start of current flow. Some of the tests at the higher applied voltages also show a rise of pseudo-conductivity of 10 - 20% in the 10 - 12 μs preceding the final, steep drop.

The discussion in the present paragraph is for the most part, repeated verbatim from the corresponding discussion in Section A.2.6.1 regarding Figures A.2- 13 - A.2- 16. Note that at a nominal shock velocity of 4.65 km/s, it takes the shock wave about 7 μs to cross the electrode face. Thus, the first part of the initial steep rise in pseudo-conductivity likely reflects the fact that it takes about 7 μs for the shock wave to completely fill the region between the electrodes with heated gas. However, the pseudo-conductivity continues to rise substantially between 7 and 10 - 30 μs after the start of current flow. The explanation may involve one or both of the following phenomena: a) the electron population may take this long after the shock wave passage to come up to a value that is in equilibrium with the gas temperature and the prevailing electric field; b) the current may be flowing mainly in the boundary layers that extend between the electrodes and these boundary layers will initially thicken very rapidly with passing time, but will tend to stabilize at a constant thickness. Currently, there is no explanation for the drops (followed in some cases by rises) in conductivity occurring after the first peak 10 to 20 μs after the start of current flow and before the final, steep drop in pseudo-conductivity. Finally, the

large and rapid drop in pseudo-conductivity is believed to be due to the arrival of the much cooler driver gas 40 to 60 μs after the start of current flow.

Figure A.2- 33 shows the pseudo-conductivities 30 μs after the start of current flow plotted versus the voltage across the electrodes 30 μs after the start of current flow. Figure A.2- 35 shows the pseudo-conductivities 30-μs after the start of current flow plotted versus the voltage across the electrodes at the start of current flow. When the plot of the pseudo-conductivities 30-μs after the start of current flow versus shock velocities (corresponding to Figure A.2- 17 for the 2-atm test condition) was made for the 5-atm test condition, little or no shock velocity effect could be seen. Hence, Figures A.2- 33 and A.2- 34 are not corrected for the shock velocity effect. Figures A.2- 35 and A.2- 36 correspond to Figures A.2- 33 and A.2- 34 but are for the conductivities measured for 15 rather than 30 μs after the start of current flow. A consistent shock velocity effect was found in this case and the correction factor used to correct for it was

$$f_c = 72.19\exp(-0.9202u_s) \qquad \text{(A.2- 9)}$$

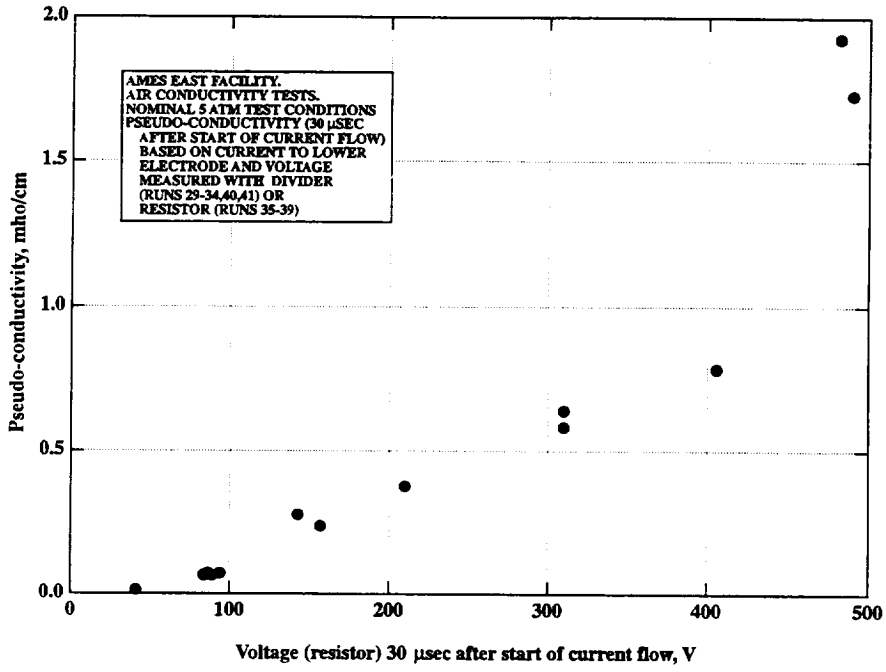

Figure A.2- 33. 5-atm test conditions, pseudo-conductivities 30 μs after start of current flow plotted versus voltage applied across electrodes 30 μs after start of current flow.

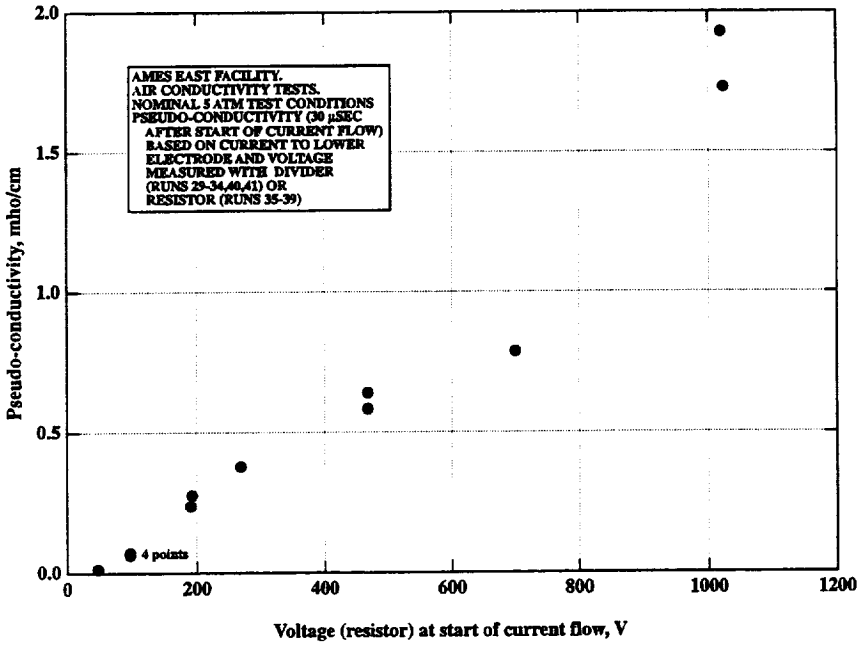

Figure A.2- 34. 5-atm test conditions, pseudo-conductivities 30 μs after start of current flow plotted versus voltage applied across electrodes at start of current flow.

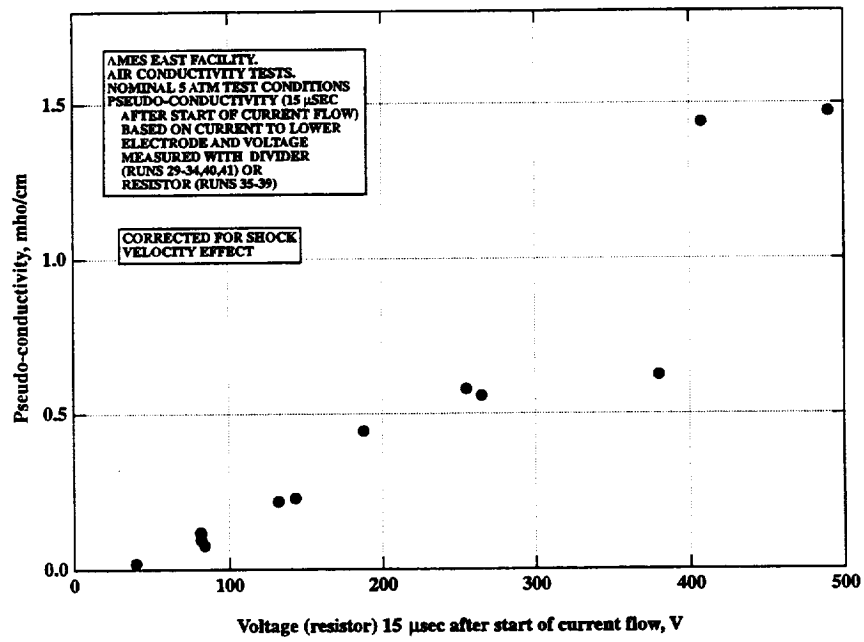

Figure A.2- 35. 5-atm test conditions, pseudo-conductivities 15 μs after start of current flow plotted versus voltage applied across electrodes 15 μs after start of current flow.

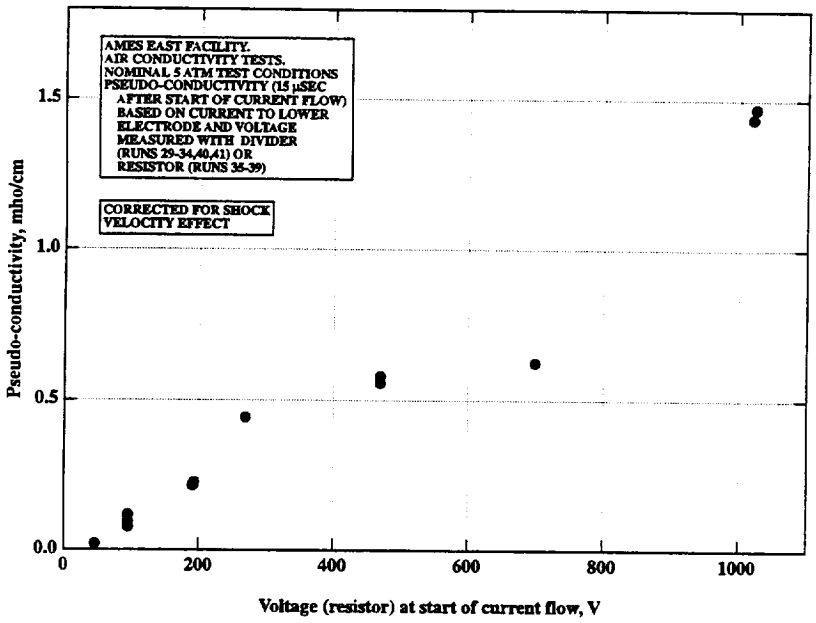

Figure A.2- 36. 5-atm test conditions, pseudo-conductivities 15 μs after start of current flow plotted versus voltage applied across electrodes at start of current flow. Corrected for shock velocity effect.

Figures A.2- 33 and A.2- 35, which show the pseudo-conductivities plotted versus the voltages at the times the pseudo-conductivities were calculated, show the following characteristics. The conductivities rise from values of 0.02 Mhos/cm at voltages of about 40 V to values of 0.6 Mhos/cm at voltages of 250 - 300 V. The conductivities are relatively constant at about 0.6 Mhos/cm between 250 to 400 V. At about 400 V, the conductivities rise steeply to 1.4 - 1.9 Mhos/cm. At the maximum applied voltage of just under 500 V, the conductivities are at their maximum values of 1.5 to 1.9 Mhos/cm. The data of Figures A.2- 34 and A.2- 36, where the conductivities are plotted versus the voltage applied at the start of current flow generally show fairly similar trends to the data of Figures A.2- 33 and A.2- 35 with following differences. The voltages are now considerably higher, particularly at the higher conductivities (i.e., at higher current draws) due the inability of the available power supply to maintain the voltage at the heavier current draws. The abrupt rises in conductivity at a voltage of about 400 V shown in Figure A.2- 35 may be replaced by a somewhat gentler rise in conductivity between voltages of 700 and 1,000 V in Figure A.2- 36, but insufficient data is available in Figure A.2- 36 to establish this for certain.

This smoothing out of the abrupt conductivity rise when one shifts from plotting the conductivity versus the voltage at the moment the conductivity is calculated to plotting it versus the voltage at the start of current flow was observed at the 2-atm test condition (see Figures A.2- 19 - A.2- 22); however, as already remarked, cannot be established with certainty for the 5-atm test condition. Note that the increases in pseudo-conductivity obtained as the applied voltage is increased from

the minimum to the maximum values are very large by a factor of about 100 for Figures A.2- 33 through A.2- 36.

The conductivities 30-μs after the start of current flow are about 10 - 30% larger than those 15 μs after the start of current flow for the highest two voltage levels, but these differences become less consistent at the lower voltages. As can be seen by examining the histories shown in Figures A.2- 30 - A.2- 32, the pseudo-conductivity decreases between 15 and 30 μs after the start of current flow for a number of test runs. At this point there is no explanation for this drop in conductivity between 15 and 30 μs after the start of current flow.

Figure A.2- 37 shows the pseudo-resistivity 30-μs after the start of current flow plotted versus the current to the bottom electrode 30-μs after the start of current flow. Figure A.2- 38 shows the voltage across the electrode 30-μs after the start of current flow plotted versus the current to the bottom electrode 30-μs after the start of current flow. Figures A.2- 39 and A.2- 40 correspond to Figures A.2- 37 and A.2- 38, but are for data 15 instead of 30 μs after the start of current flow. Each of these four graphs also shows a line based on the theoretical equilibrium gas conductivity behind a shock wave at the nominal shock velocity of 4.65 km/s. These lines were constructed as described in Section A.6.2.1 with regard to Figures A.2- 23 through A.2- 26. In addition, Figures A.2- 38 and A.2- 40 have added constant resistance lines, which pass through the experimental data point on the "knee" or inflection point of the trend of the data. In general, Figures A.2- 37 through A.2- 40 for the 5-atm test condition show rather similar characteristics to those of Figures A.2- 23 through A.2- 26 for the 2-atm test condition, as follows. At low to moderate voltages (40 - 220 V) and currents (2 - 400 A), the pseudo-resistivity is above the value corresponding to the equilibrium bulk gas conditions behind the shock wave; as much as 50 times this value at currents of ~2 A. This ratio drops to about 10 at currents of ~20 A and 3 at currents of ~100 A.

Between voltages of 300 and 400 V and currents of 500 and 800 A, the pseudo-resistivity appears to be about equal to the value corresponding to the equilibrium bulk gas conditions behind the shock wave, while at the highest currents (1,000 - 3,000 A), it appears to be 10% (at 1,000 A) to 50-60% (at 2,000 – 3,000 A) below this value. The region of "constant" pseudo-conductivity appears to be less well defined for the 5-atm test condition, especially 30 μs after the start of current flow, than for the 2-atm test condition (compare Figures A.2- 37 and A.2- 39 with A.2- 23 and A.2- 25.). However, this appearance may be due to the lack of sufficient data to define the curves in Figures A.2- 37 through A.2- 40.

As for the case of the 2-atm data of Figures A.2- 23 through A.2- 26, the data of Figures A.2- 37 through A.2- 40 imply that in the low to moderate (2 - 400 A) current range, the resistivity of the electrode fall regions must rise steeply as the current drops. This would appear to be in line with negative voltage - current characteristics of electric arcs reported in References 7 - 9.

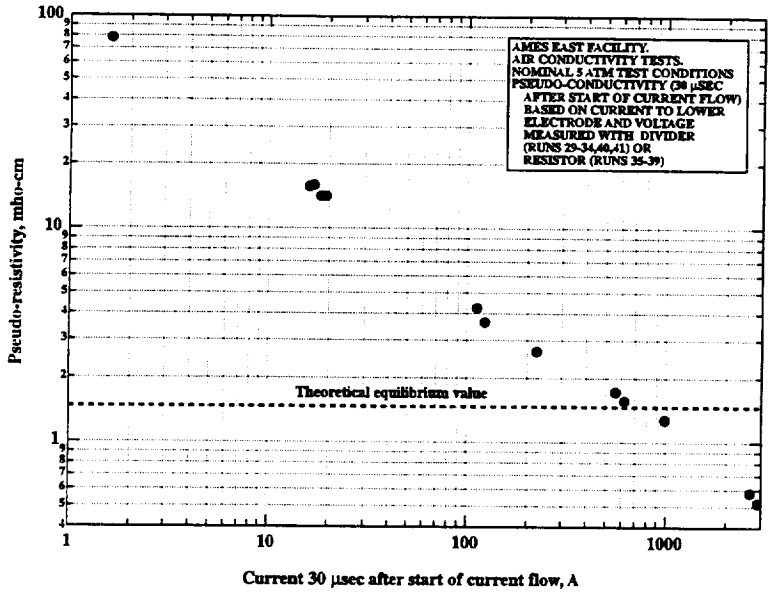

Figure A.2- 37. 5-atm test conditions, pseudo-resistivities 30 μs after start of current flow plotted versus current to lower electrode 30 μs after the start of current flow. Corrected for shock velocity effect.

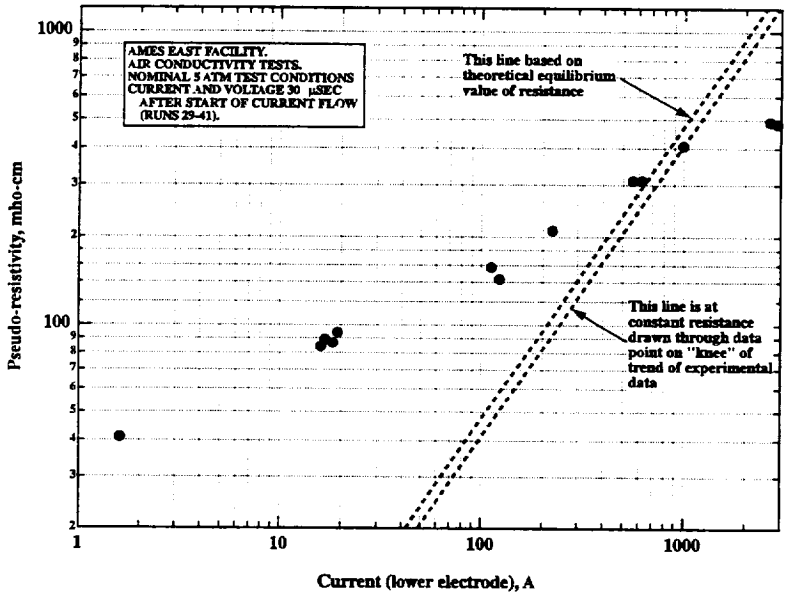

Figure A.2- 38. 5-atm test conditions, voltages across electrodes 30 μs after start of current flow plotted versus current to lower electrode 30 μs after start of current flow. Corrected for shock velocity effect.

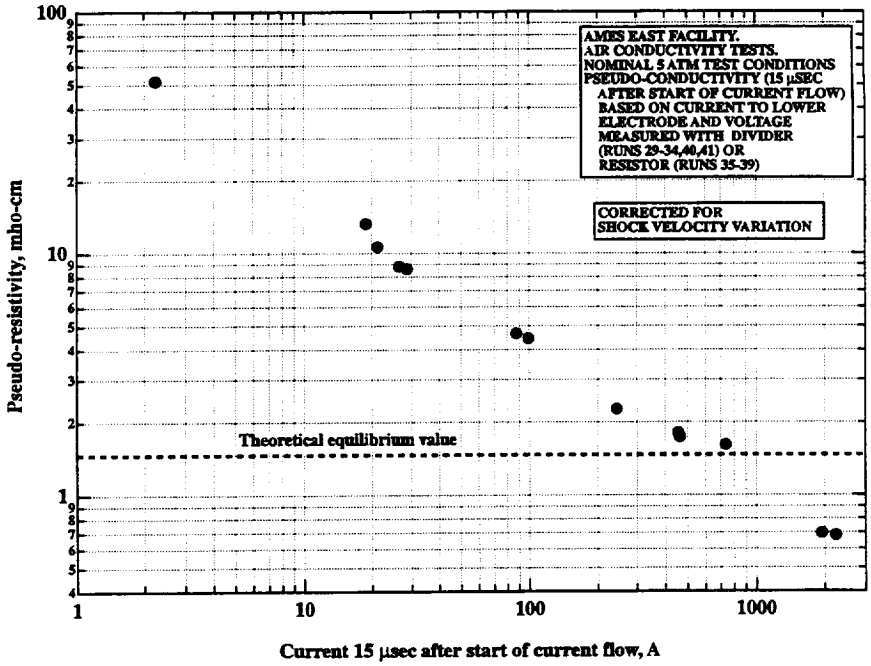

Figure A.2- 39. 5-atm test conditions, pseudo-resistivities 15 μs after start of current flow plotted versus current to lower electrode 15 μs after start of current flow. Corrected for shock velocity effect.

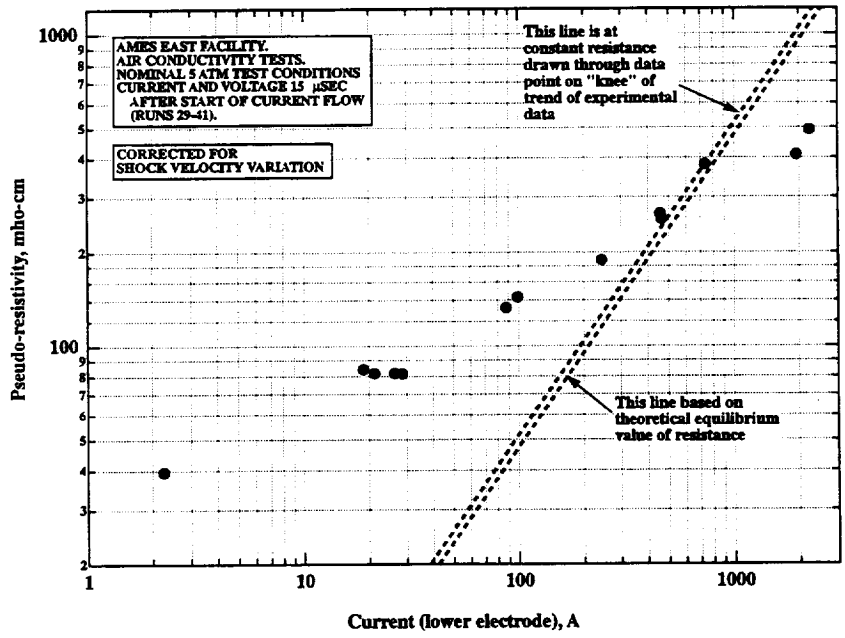

Figure A.2- 40. 5-atm test conditions, voltages across electrodes 15 μs after start of current flow plotted versus current to lower electrode 15 μs after start of current flow. Corrected for shock velocity effect.

In the current range between 500 and 800 A, it is suggested that the electrode fall voltages have become so small compared to the IR drop in the bulk gas that the pseudo-resistivity is essentially dominated by the bulk gas conductivity and hence, is closely given by 1/(bulk gas conductivity). Such an interpretation would appear to be reasonably consistent with the data of Figures A.2- 37 through A.2- 40, although as stated earlier, the region of "constant" pseudo-conductivity appears to be less well defined at 5 atm than at 2 atm.

At the very highest currents (1,000 – 3,000 A), the pseudo-resistivities are 10 - 60% below the calculated equilibrium value. The input powers to the gas can readily be calculated to be between 0.27 and 1.40 MW. Following the technique described in Section A.2.6.1, the expected gas temperature rise due to the electric energy input as the flow passes between the electrodes for each of these cases can be calculated. The corresponding expected increase in the equilibrium electron mole fraction could then be easily calculated. (See Section A.2.6.1 for details of the calculation techniques.) The conductivity of the gas should be very nearly proportional to the electron mole fraction. The calculated increases in electron mole fraction due to the electric heating of the gas will then be compared to the observed increases in the pseudo-conductivity above the calculated equilibrium value (calculated without electric heating of the gas) shown in Figures A.2- 37 and A.2- 39. The results of this comparison are shown in Table A.2- 9. The comparisons are made for the five points seen in Figures A.2- 37 and A.2- 39 that have pseudo-resistivities below the calculated equilibrium value. The first column of the table gives the run number. The second column gives the time after the start of current flow at which the data was taken. The third column gives the calculated ratio of the electron mole fraction after half of the discharge power is absorbed by the gas to that before any power is absorbed by the gas. Column 4 is similar to column 3, except that the ratio is based on the absorption of all of the discharge power by the gas. Finally, column 5 gives the observed increase in the pseudo-conductivity over the calculated equilibrium value - that can be obtained from Figures A.2- 37 and A.2- 39. For the first three rows of the table, it appears the ohmic heating of the gas could account for a significant fraction (30 - 60%) of the observed conductivity increase if the conductivity in the current path were assumed to respond on the average to half of the full energy deposition by the discharge. For the data of the last two rows of the table, this fraction is not as large (~15%). The conductivity may also be enhanced by the production of nonequilibrium ionization in the bulk gas at the high electric fields of the higher current conditions.

Table A.2- 9. Comparison of calculated electron mole fraction ratios and observed conductivity ratios.

Run no.	Time from start of current flow (μs)	Calculated electron mole fraction ratios, half T rise	Calculated Electron mole Fraction ratios, full T rise	Observed Conductivity Ratio
36	30	1.093	1.231	1.149
37	15	1.355	1.789	2.150
37	30	1.513	2.171	2.525
38	15	1.160	1.326	2.105
38	30	1.230	1.500	2.816

An example IMACON Polaroid photograph for Run 39 at the 5-atm test condition is shown in Figure A.2- 41. The test number, date, and test conditions are given at the top of the figure. The flow is from left to right, and the frame sequence is identified below the figure. The times given below the frames are measured from the start of current flow. The shock wave image is barely visible in the second frame although a second image of the shock appears in the third frame, which allowed a determination of V_I. For this particular run, $V_I = 4.5$ km/s and $V_{CAV} = 4.85$ km/s. The oblique shock waves emanating from the leading edge of the electrodes are clearly visible in frames 3 - 7, and Mach numbers determined from a measurement of the oblique shock angle are given for frames 4 and 6. Glow from the flow region near the electrode surfaces begins to overwhelm the rest of the field in the last two frames.

A summary of all photographs for the 5-atm case and the parameters measured from them is given in Table A.2- 10 and Table A.2- 11. The shock velocities, pressures, and voltages were taken from Table A.2- 8. The time given is the time-of-frame number 1 after the start of current flow. The remaining parameters in the Table A.2- 10 are the velocities inferred from the photographs and Table A.2- 11 gives the Mach numbers read from the oblique shock waves. Columns 2 through 5 give the experimental Mach numbers themselves and column 7 gives the frames in which they were measured. Column 6 gives the theoretical Mach numbers in equilibrium flow behind a shock wave at the observed velocity at the electrodes. These theoretical Mach numbers were calculated using the computer program of Reference 4. Note that in general, the observed Mach numbers are 0.10 to 0.50 less than the theoretical values. Several possible explanations for this are discussed in Section A.2.6.1 in connection with the discussion of the photographs taken at the 2-atm test condition.

As mentioned in Section A.2.6.1, no evidence of breakdown due to the electrical discharges was found in any IMACON photographs images. The moving hot spots seen on the cathode at high current conditions at the 2-atm test condition were not seen at the 5-atm test condition. Also, the fixed hot spots at the edges of the electrodes at the 2-atm test condition were much less prominent at the 5-atm test condition. In general, a smooth glow is seen along the electrodes at the 5-atm test conditions. It was noted that this glow becomes progressively more intense after the shock wave passes in both the 2- and 5-atm test conditions. However, the rate of increase of the electrode glow is more rapid at the 5-atm test condition. This may be due to the faster approach to equilibrium at higher pressures and densities and may well be closely connected with the more rapid current rise at higher pressures (see Section A.2.6.4).

Table A.2- 10. Results from IMACON photographs for runs at the nominal 5-atm test condition.

Run no.	Shock vel. at E (km/s)	Shock press. at D (atm)	Voltage at start of current (V)	Time of fr. #1 after start of current (μs)	V_I from Photo (km/s)	V_{CAV} from photo (km/s)
31	4.65	7.08	92	-3.1	4.3	4.89
32	4.92	7.61	92	4.9	----	5.08
33	4.47	5.80	188	-8.4	4.8	4.68
34	4.60	5.97	270	-4.6	----	4.80
35	4.91	7.15	469	3.4	----	5.06
36	4.63	6.17	700	-5.4	----	4.80
37	4.45	6.17	1024	-11.7	4.2	4.63
38	4.85	7.21	1020	0.1	4.5	4.96
39	4.66	6.49	469	-2.8	4.5	4.85
40	4.95	8.00	190	3.3	----	5.09
41	4.72	7.28	45.5	-0.9	----	4.92

Table A.2- 11. Results from IMACON photographs for runs at the nominal 5-atm test condition.

Run no.	Mach no.	Mach no.	Mach no.	Mach no.	Theoretical Mach no.	Frame numbers
33	2.53	2.40			2.61	5,6
34	2.60	2.37	2.24		2.64	5,6,7
36	2.32	2.14	2.14		2.65	5,6,7
38	2.42	2.27	2.31		2.72	2,3,4
39	2.24	2.42			2.66	4,6
40	2.33	2.40			2.75	2,3
41	2.24	2.24			2.68	3,4

Run no: 39 **Date:** 6/5/97 **Shock press. At D:** 6.49 atm
Shock vel. at E: 4.66 km/s **Voltage at start of current flow:** 472 V

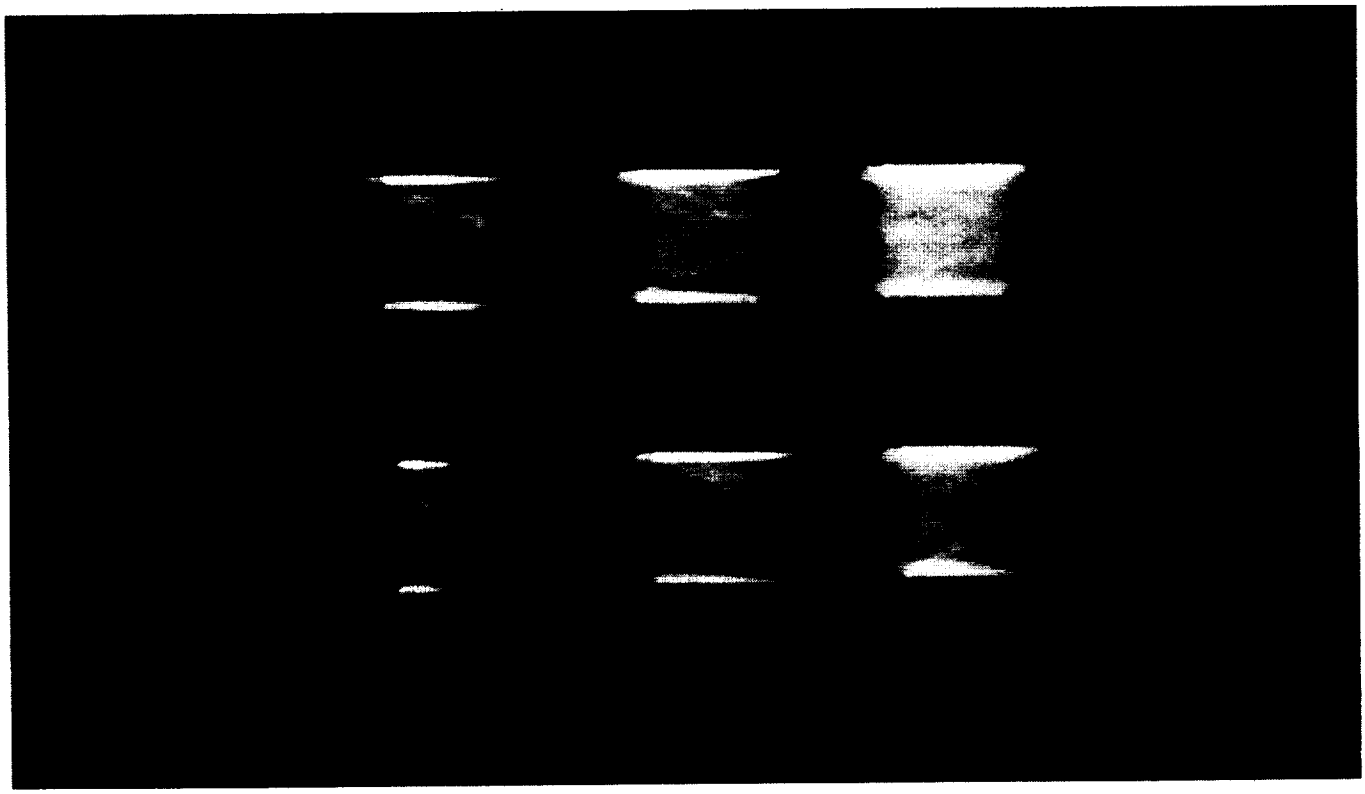

Frame:	**2**	**4**	**6**	**8**
Time:	1.2	9.2	17.2	25.2
Mach no:		2.24	2.42	
Frame:	**1**	**3**	**5**	**7**
Time:	-2.8	5.2	13.2	21.2
Mach no:				

V_I: 4.5 km/s V_{CAV}: 4.85 km/s

Figure A.2- 41. IMACON image of the shock-heated test gas flow in the electrode region. The time is measured from the start of the current flow. Mach numbers and velocities are deduced from the image as explained in Section A.2.5.3.

A.2.6.3 At Nominal 13-Atm Test Condition

Table A.2- 12 gives the test conditions for the runs at the nominal 13-atm facility operating condition. The various columns of Table A.2- 12 present data in exactly the same manner as in Table A.2- 8 for the 2-atm test condition and Table A.2- 5 for the 5-atm test condition (see Sections A.2.6.1 and A.2.6.2). Representative data histories for the voltages, currents, and pseudo-conductivities will not be provided for the 13-atm test conditions since they show data in exactly the same formats as the data histories presented in Figures A.2- 8 - A.2- 12 for the 2-atm test conditions.

Table A.2- 12. Test conditions for runs at the nominal 13-atm test condition.

Run no.	Dn tube gas	Dn tube fill pressure (kPa)	Shock v At E (km/s)	Shock p at D (atm)	Shock p at F (atm)	Voltage at 0 μs (V)	Voltage at 30 μs (V)
44	$N_2O/N_2/H_2$	4.16	4.846	17.90	11.46 (N)	186	145
45	$N_2O/N_2/H_2$	4.72	4.637	19.68	14.95 (EN)	186	115
46	$N_2O/N_2/H_2$	4.72	3.964	13.39	7.30 (EN)	312	215
47	$N_2O/N_2/H_2$	4.72	4.892	20.65	20.71 (EN)	325	250
48	$N_2O/N_2/H_2$	4.72	4.772	18.45		572	394
49	$N_2O/N_2/H_2$	4.72	4.536	14.88		1020	382
50	$N_2O/N_2/H_2$	4.72	4.862	19.22		764	382
51	N_2O/N_2	4.72	4.617	18.10	9.51(EN)	73.2	56.4

Note that seven of the eight tests were performed with the addition of 0.5% H_2 gas to the usual N_2O/N_2 driven tube to allow development of the electron number density technique. No H_2 was added to the driven tube gas for test Run 51. Equilibrium calculations were made for the conditions behind the main shock wave both with and without the addition of H_2, and it was found that the concentrations of nonhydrogen containing species, including electrons, differed by only a maximum of 2-4% for the two different driven tube fill gases (i.e., with and without H_2). It was concluded there would be only minor differences in the conductivities between the two different types of driven tube gas; therefore, it would be justified to compare the test data at the 13-atm nominal test condition (with H_2) with 2 and 5-atm conditions (without H_2, for the most part).

Figures A.2- 42 - A.2- 43 present compilations of the histories of the pseudo-conductivities based on the current data for the bottom electrode. The voltages measured at the beginning of current flow and 30 μs after the start of current flow, as well as the shock wave velocity are given in the legend. The voltages are also given on each curve. The following is a general description of the histories (with times measured from the start of current flow). The pseudo-conductivities rise very rapidly for the first 7-30 μs. After this time period, some of the histories then show a plateau, which lasts roughly 20-40 μs, while others show a 20-40% drop in pseudo-conductivity

for 15-25 μs followed by a period of roughly constant conductivity or a 20-40% rise in conductivity lasting 20-25 μs. The pseudo-conductivity then falls steeply, (40-60 μs), after the start of current flow. The general behavior of the pseudo-conductivity histories for the 13-atm test condition is very similar to those for the 2 and 5-atm test conditions.

The discussions of the rise of the conductivity, the relatively flat or double-humped region near the conductivity maximum and the final fall of the conductivity presented in Sections A.2.6.1 and A.2.6.2 in connection with the 2 and 5-atm test conditions apply; essentially without modification to the data of Figures A.2- 42 and A.2- 43, and therefore will not be repeated here.

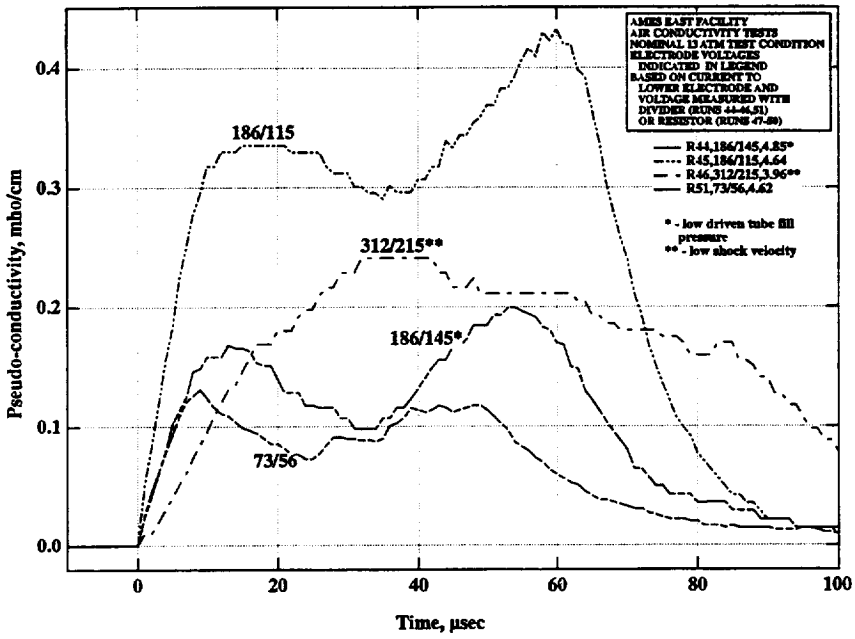

Figure A.2- 42. Pseudo-conductivity histories for the 13-atm nominal test condition.

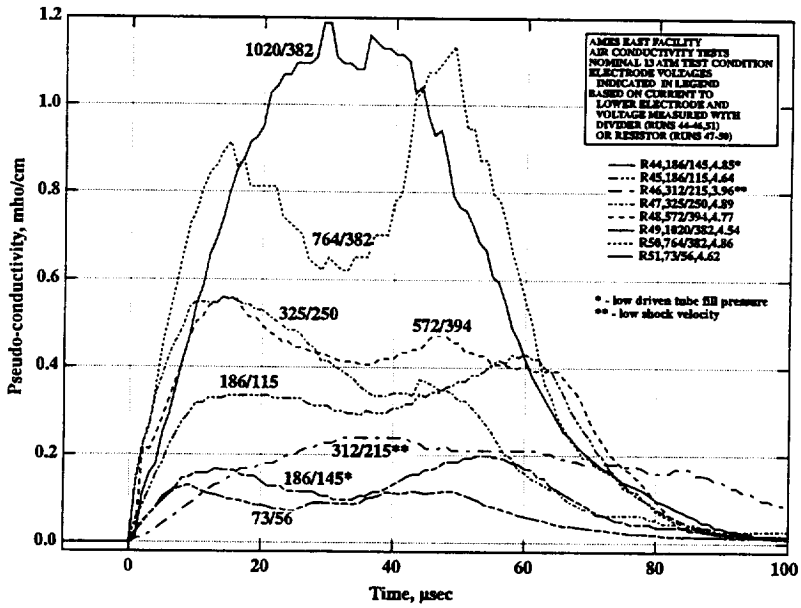

Figure A.2- 43. Pseudo-conductivity histories for the 13-atm nominal test condition.

As has been done for the 2- and 5-atm test conditions, the pseudo-conductivities taken from Figures A.2- 42 and A.2- 43 at 15 and 30 μs after the start of current flow will be used to make comparisons among the various tests. These pseudo-conductivities were first plotted versus shock velocity to attempt to separate out the shock velocity effect. Unfortunately, with only eight data points for the 13-atm test condition, it was nearly impossible to identify a shock velocity effect with the exception of the comparison of the data for Runs 46 and 47. The data points for these two runs were taken with nearly the same voltage applied to the electrodes, and the conductivities at the higher shock velocity appear to be about 1.8 - 3.8 times those at the lower shock velocity. However, with only one pair of runs showing a clear shock velocity effect, it was decided not to derive and apply any shock velocity correction to the data for the 13-atm test condition, as was done for 3 of the 4 data sets for the 2 and 5-atm test conditions.

Before proceeding with the analysis of the pseudo-conductivities 15 and 30 μs after the start of current flow, some experimental difficulties that occurred during the runs at the 13-atm test condition will be discussed. This operating condition could be obtained only by operating the driver at essentially its maximum rated energy deposition capability that led to rapid destruction of various insulating elements inside the driver. A number of polycarbonate insulating and sealing components surrounds the high voltage electrode at the blind end of the driver, and can typically survive 40 or more tests at the 2 or 5-atm test conditions. Some of these components were destroyed after one or two runs at the 13-atm test condition. Only six or seven sets of the polycarbonate components existed; therefore, the number of tests possible at the 13-atm condition was limited without the fabrication of additional components. In addition, the driver is lined with a rubber-coated fiberglass tube to prevent the arc from short-circuiting directly to the driver wall from the high voltage electrode. This rather expensive component also typically survives 40 or

more tests at the lower energy test conditions. Two of these liners were destroyed in the course of the eight runs made at the 13-atm test condition. At the termination of the test entry only one spare driver liner remained available. Finally, the surfaces of the windows used to observe conditions at the electrodes typically remained satisfactory for six to twenty runs at the 2 or 5-atm test conditions. At the 13-atm conditions the window surfaces had to be remachined after one or two tests. This does not mean that testing cannot be completed at the 13-atm condition; however, extensive testing at such severe conditions will require substantial quantities of the "expendable" components to be on hand.

In Figures A.2- 44 and A.2- 45, the pseudo-conductivities 30 μs after the beginning of current flow are plotted versus the voltage-applied 30 μs after the beginning of current flow (Figure A.2- 41) and at the beginning of current flow (Figure A.2- 42). Before proceeding with the discussion, it is necessary to note that there are difficulties with the data from two of the eight tests; therefore, most of the following discussion will involve only six of the eight data points shown in each graph. In Run 46, the electric arc in the driver penetrated the rubber-lined fiber glass driver liner, thereby destroying it and resulting in a shock velocity of about 3.9 km/s rather than the nominal value of 4.65 km/s. Hence, the conductivity data from this run lie well below the trends established by the six good tests. The data points from Run 46 will be shown in the figures to follow, but will be marked with the notation "LV" denoting the low-shock velocity. Run 44 was made with a driver-fill pressure of 31.2 torr rather than 35.35 torr, which was used for Runs 45 - 51. The shock velocity for this run was rather high (about 4.84 km/s); however, the conductivity values were well below the trends for the six good runs for reasons that are not understood. The data points from Run 44 will also be shown in the figures to follow but will be marked with the notation "LP" denoting the low driven-tube fill pressure.

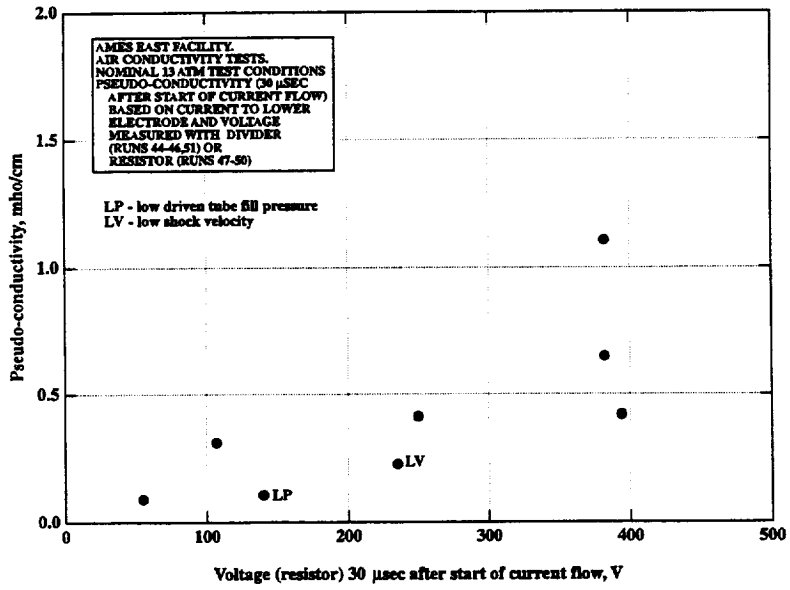

Figure A.2- 44. 13-atm test conditions, pseudo-conductivities 30 μs after start of current flow plotted versus voltage applied across electrodes 30 μs after start of current flow.

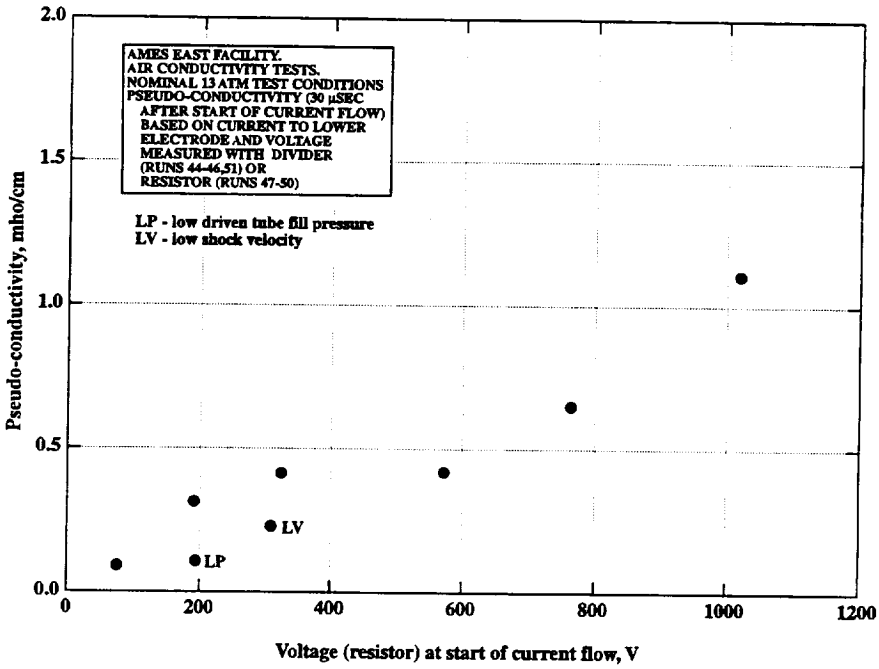

Figure A.2- 45. 13-atm test conditions, pseudo-conductivities 30 μs after start of current flow plotted versus voltage applied across electrodes at start of current flow.

The discussions to follow will be based on the six good data points of each graph and will essentially ignore the data points marked "LV" and "LP".

In Figure A.2- 44, the first four good data points show a fairly consistent rise in conductivity from ~0.1 to ~0.4 Mhos/cm as the voltage increases from 50 to ~380 V with a plateau in conductivity between voltages of 250 and 380 V. The three points at the highest conductivities show a substantial change in conductivity with almost no change in the voltage (~380 V) at 30 μs after the start of the current. The conductivity differences for these three points may be due to the substantial differences in the voltages that were applied at the start of the current flow (refer to Figure A.2- 45 to be discussed in the next paragraph to see these voltages). Such a phenomenon was noted also for the 2 atm (see Figures A.2- 19 and A.2- 21) and 5-atm (see Figures A.2- 33 and A.2- 35) test conditions.

Figure A.2- 45 presents the same conductivity values plotted versus the voltage at the start of current flow. In Figure A.2- 45, the pseudo-conductivity rises from ~0.1 Mhos/cm at an applied voltage of ~60 V to ~1.1 Mhos/cm at a voltage of ~1,000 V. There appears to be a plateau of conductivity between applied voltages of ~300 and ~600 V. The abrupt rise in conductivity for the three highest current data points seen in Figure A.2- 44 is now replaced by a much smoother rise. The voltages are now higher, especially for the higher voltage and current conditions, due to the inability of the available power supply and resistor network to maintain the voltage with very heavy current draws.

Figures A.2- 46 and A.2- 47 correspond with Figures A.2- 44 and A.2- 45, but now the pseudo-conductivity is measured at 15 rather than 30 μs after the start of current flow. Figure A.2- 43 presents the conductivity values plotted versus the voltage at 15 μs after the start of current flow.

Figure A.2- 46 is in general form, rather similar to Figure A.2- 44 with a plateau in the pseudo-conductivity between 200 and 330 volts, followed by an abrupt rise in pseudo-conductivity at a nearly constant voltage of about 330 volts. The main difference between Figures A.2- 44 and A.2- 46 is the last data point (with the highest voltage at the start of current flow) in Figure A.2-46 and does not show a further rise in pseudo-conductivity.

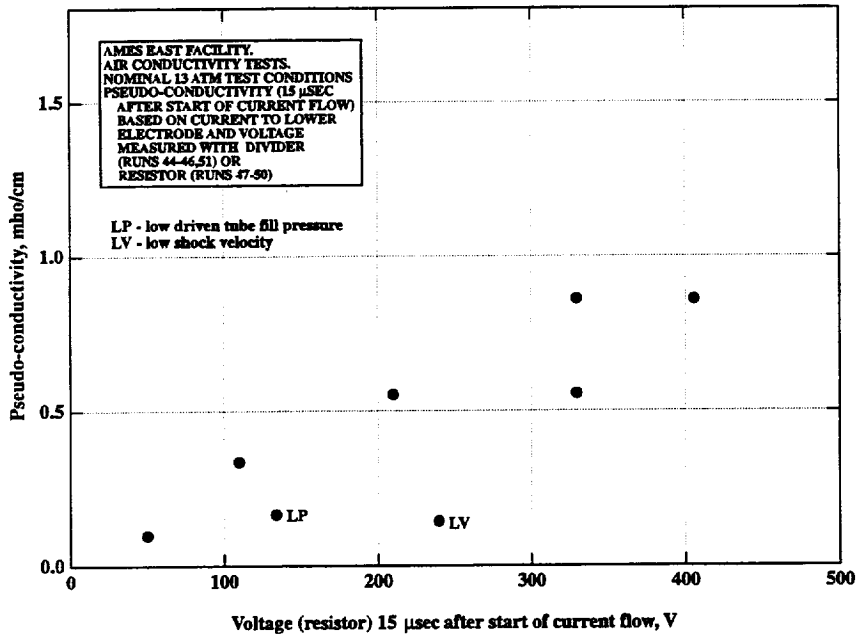

Figure A.2- 46. 13-atm test conditions, pseudo-conductivities 15 μs after start of current flow plotted versus voltage applied across electrodes 15 μs after start of current flow.

Figure A.2- 47 presents the same conductivity values plotted versus the voltage at the start of current flow. Figure A.2- 47 is in general form, rather similar to Figure A.2- 45 with a plateau in the pseudo-conductivity between 300 and 600 volts. There now appears to be an additional plateau between 800 and 1,000 V; however, this is defined by only two data points and more data points would be needed to confirm its existence.

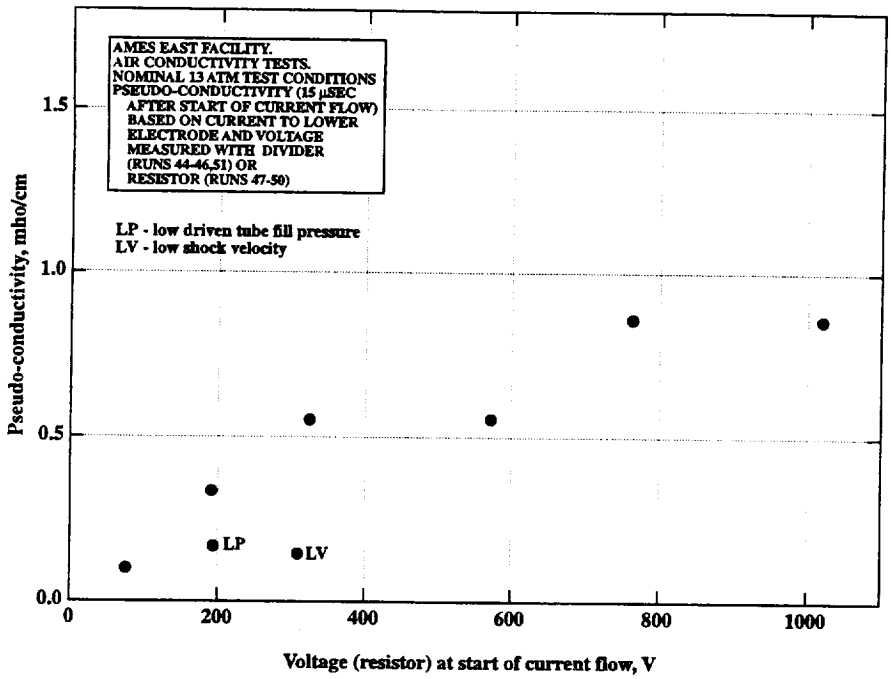

Figure A.2- 47. 13-atm test conditions, pseudo-conductivities 15 μs after start of current flow plotted versus voltage applied across electrodes at start of current flow.

In general, the pseudo-conductivities 30 μs after the start of current flow are approximately 6 to 30% less than those at 15 μs after the start of current flow, which is in marked contrast to those for the 2- and 5-atm test conditions where the pseudo-conductivities tend to be higher for the data taken 30 μs after the start of current flow. This can readily be seen from Figures A.2- 42 through A.2- 47. However, this is not true for the data taken at the very highest applied voltage. Many of the histories shown in A.2- 42 and A.2- 43 do show a late rise in conductivity with a second maximum occurring between 40 and 60 μs after the start of current flow. This data cannot be used to study the effect of the applied voltage because it is highly likely that much of this data was compromised by contamination of the test gas with driver gas. (See discussion of this problem in Section A.6.2.1.) At present, there is no explanation for the reduced conductivities at 30 μs after the start of current flow for the 13-atm test conditions.

Figure A.2- 48 shows the pseudo-resistivity at 30 μs after the start of current flow plotted versus the current to the bottom electrode at 30 μs after the start of current flow. Figure A.2- 49 shows the voltage across the electrodes at 30 μs after the start of current flow plotted versus the current to the bottom electrode at 30 μs after the start of current flow. Figures A.2- 50 and A.2- 51 correspond to A.2- 48 and A.2- 49, but are for data at 15 instead of 30 μs after the start of current flow. Each of these four graphs also show a line based on the theoretical equilibrium gas conductivity behind a shock wave at a shock velocity of 4.72 km/s. This shock velocity is not the nominal shock velocity of 4.65 km/s, but rather is the average shock velocity of Runs 45 and 47 through 51. These lines were constructed as described in Section A.6.2.1 with regard to Figures A.2- 23 through A.2- 26. In addition, in Figures A.2- 49 and A.2- 51, constant resistance

lines have been added that pass through the experimental data point on the "knee" or inflection point of the trend of the data. In general, Figures A.2- 48 and A.2- 51 for the 13 -atm test condition show rather similar characteristics to those of Figures A.2- 23 through A.2- 26 for the 2-atm test condition and Figures A.2- 37 and A.2- 40 for the 5-atm test condition. However, there are only six good data points for the 13-atm test condition, as compared to 15 and 13 for the 2- and 5-atm test conditions, respectively. Hence, the trends of the data are less well defined for the 13-atm data in general; in particular, the 13-atm data contains only a single data point at currents less than 100 A versus seven for each of the data sets at 2 and 5. However, the trends of the 13-atm data appear to closely follow those of the larger 2- and 5-atm data sets. At low to moderate voltages (50 - 200 V) and currents (15 - 300 A), the pseudo-resistivity is above the value corresponding to the equilibrium bulk gas conditions behind the shock wave being as much as seven times this value at currents of ~15 A.

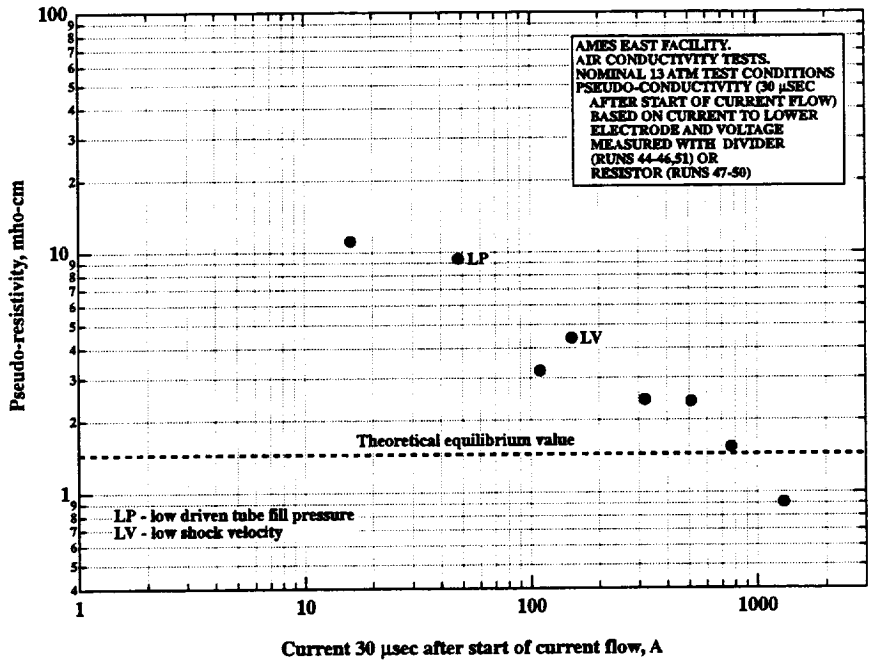

Figure A.2- 48. 13-atm test conditions, pseudo-resistivities 30 μs after start of current flow plotted versus current to lower electrode 30 μs after start of current flow.

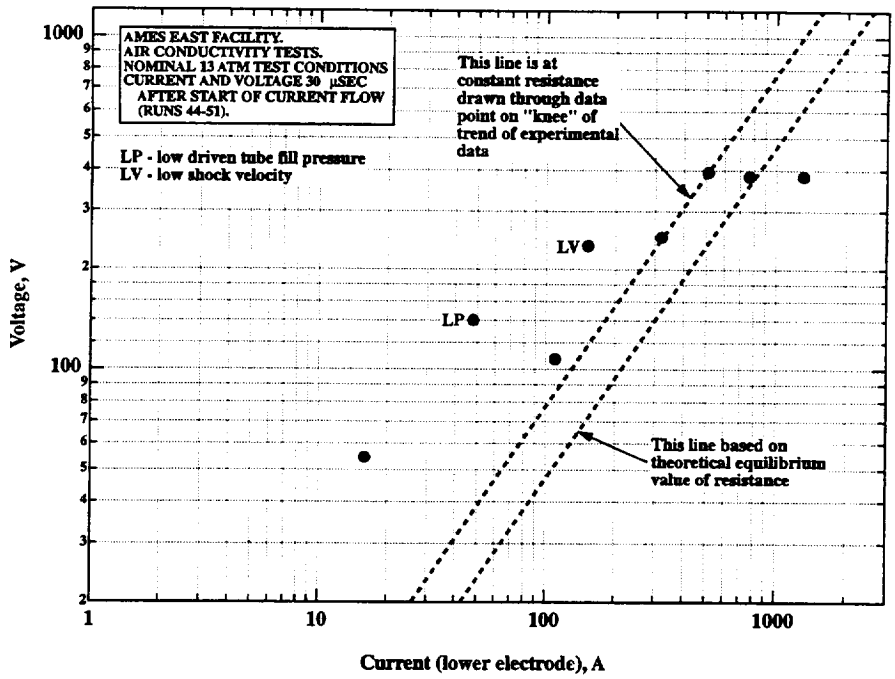

Figure A.2- 49. 13-atm test conditions, voltage across electrodes 30 μs after start of current flow plotted versus current to lower electrode 30 μs after start of current flow.

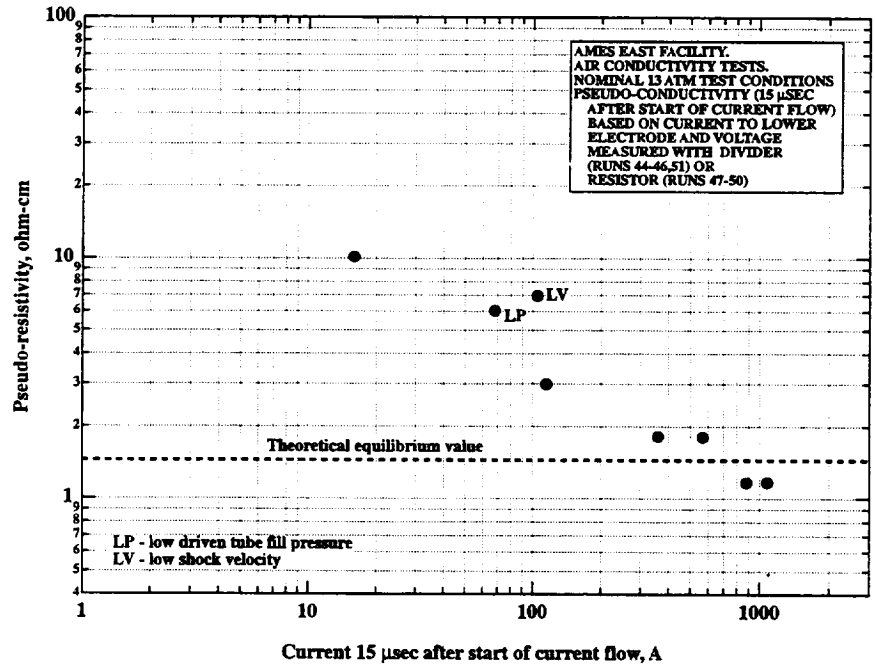

Figure A.2- 50. 13-atm test conditions, pseudo-resistivities 15 μs after start of current flow plotted versus current to lower electrode 15 μs after start of current flow.

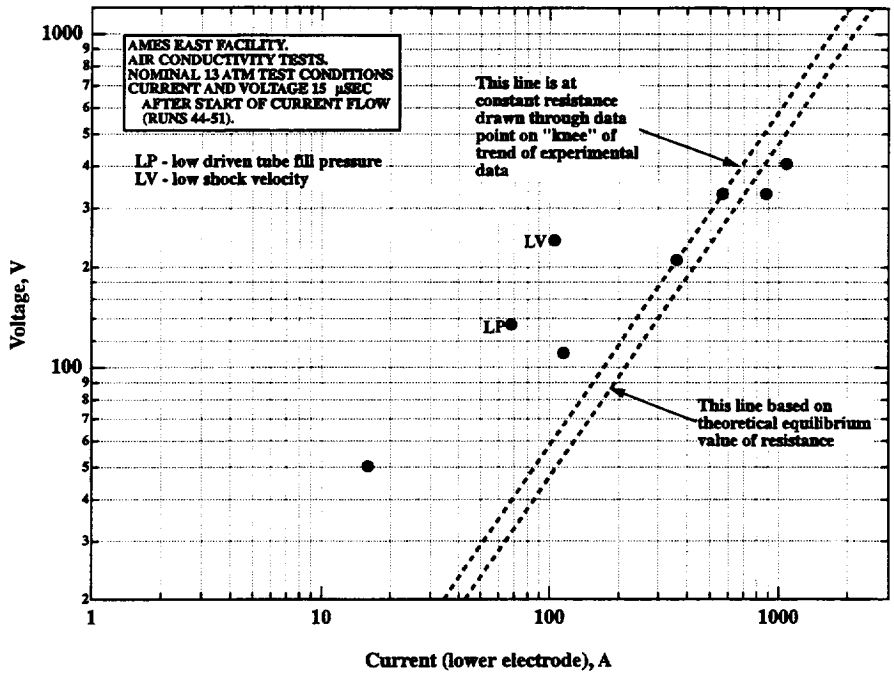

Figure A.2- 51. 13-atm test conditions, voltage across electrodes 15 μs after start of current flow plotted versus current to lower electrode 15 μs after start of current flow.

This ratio drops to about 2 at currents of ~100 A. Between voltages of 200 and ~350 V and currents of 300 and 600 A, the pseudo-resistivity appears to be roughly constant at values 65% (30 μs data) and 25% (15 μs data) above the value corresponding to the equilibrium bulk gas conditions behind the shock wave. At the highest currents (~1,000 A), it appears to be 20 - 40% below this value.

The constant pseudo-conductivity regions show conductivities somewhat below the theoretical equilibrium value, particularly for the data 30-μs after the start of current flow. At this point the meaning of this is unclear. More data (perhaps 2 or 3 times as much in total) is needed to define the experimental shapes of the data curves shown in Figures A.2- 48 through A.2- 51. Also, it would be desirable to re-examine the theoretical techniques for calculating the equilibrium conductivity values. In general, the shapes of the curves of Figures A.2- 48 through A.2- 51 for currents less than 800 A appear to be reasonably consistent with those for the 2 and 5-atm data sets.

For the highest currents (~1,000 A), the data of Figures A.2- 48 - A.2- 51 show a drop in resistivity below the calculated equilibrium value. A similar phenomenon was observed for the 2- and 5-atm data sets. For the 2- and 5-atm data sets, it was concluded that at least part of this phenomenon could be explained by an ohmic heating-induced increase in the conductivity of the bulk gas. This explanation will not work for the 13-atm data sets. In comparing Figures A.2- 48 through A.2- 51 for the 13-atm test condition to Figures A.2- 37 through A.2- 40 for the 5-atm

test condition, it can immediately be seen that for the high current data points, the maximum power deposited in the gas for the 13-atm condition is 0.35 - 0.50 times that for the 5-atm test condition. On the other hand, the gas density is 2.6 greater for the 13-atm test condition. Hence, the ohmic heating-induced temperature rises will be five or more times smaller for the 13-atm test condition that can easily be shown to be far to small to explain the conductivity increases observed in Figures A.2- 48 through A.2- 51 for the data at the highest currents. It may be possible that the conductivity increase involves the production of nonequilibrium ionization in the bulk gas at the higher electric fields; however, this seems less likely to occur at the 13-atm test condition than at the 2- or 5-atm test conditions. On the whole, caution must be used in the interpretation of the 13-atm data set due to the paucity of data.

An example IMACON Polaroid photograph for Run 49 at the 13-atm test condition is shown in Figure A.2- 52. The run number, date, and test conditions are given at the top of the figure. The flow is from left to right, and the frame sequence is identified below the figure. The times given below the frames are measured from the start of current flow. The shock wave image is just barely visible in the third frame. A second image of the shock appears in the fourth frame that allowed a determination of V_I. For this particular run, $V_I = 4.2$ km/s and $V_{CAV} = 4.68$ km/s. The oblique shock waves emanating from the leading edge of the electrodes are clearly visible in frames 4 an 5, and a Mach number determined from a measurement of the oblique shock angle is given for frame 5. Glow from the flow region near the electrode surfaces and the hot core flow test gas overwhelms the rest of the field in the last three frames. This was the case for most of the 13-atm IMACON photographs since the attenuation was kept sufficiently low to allow a determination of the shock locations.

A summary of all photographs for the 13-atm case and the parameters measured from them is given in Table A.2- 13 and Table A.2- 14. The shock velocities, pressures, and voltages were taken from Table A.2- 12. The time given is the time-of-frame number 1 after the start of current flow. The remaining parameters in the Table A.2- 13 are the velocities inferred from the photographs. Table A.2- 14 gives the Mach numbers read from the oblique shock waves. Columns 2 through 5 give the experimental Mach numbers themselves and column 7 gives the frames in which they were measured. Column 6 gives the theoretical Mach numbers in equilibrium flow behind a shock wave at the observed velocity at the electrodes. These theoretical Mach numbers were calculated using the computer program of Reference 4. Note that in general, the observed Mach numbers are 0.10 to 0.40 less than the theoretical values. Several possible explanations for this are discussed in Section A.2.6.1 in connection with the discussion of the photographs taken at the 2-atm test condition.

Table A.2- 13. Results from IMACON photographs for runs at the nominal 13-atm test condition.

Run no.	Shock vel. at E (km/s)	Shock press. at D (atm)	Voltage at start of current (V)	Time of fr. #1 after start of current (μs)	V_I from photo (km/s)	V_{CAV} from Photo (km/s)
44	4.85	17.90	186	6.1	----	5.03
45	4.64	19.68	186	-2.6	4.8	4.87
46	3.96	13.39	312	-26.9	----	4.24
47	4.89	20.65	325	4.5	----	5.08
48	4.77	18.45	572	1.1	4.2	4.96
49	4.54	14.88	1020	-4.2	4.2	4.68
50	4.86	19.22	764	3.0	----	5.05
51	4.62	18.10	73.2	-5.0	----	4.74

Table A.2- 14. Results from IMACON photographs for runs at the nominal 13-atm test condition.

Run no.	Mach no.	Mach no.	Mach no.	Mach no.	Theoretical Mach no.	Frame Numbers
44	2.36				2.66	1
48	2.24				2.64	3
49	2.24				2.57	5
50	2.24	2.40			2.66	2,3
51	2.48				2.60	5

As mentioned in Section A.2.6.1, no evidence of breakdown due to the electrical discharges was found in any IMACON photographic images. The moving hot spots seen on the cathode at high current conditions at the 2-atm test condition were not seen in either the 5-atm or the 13-atm test conditions. Also, the fixed hot spots at the edges of the electrodes at the 2-atm test condition were much less prominent at the 5-atm and 13-atm test conditions. In general, a smooth glow is seen along the electrodes at the 5-atm and 13-atm test conditions. It was noted that this glow becomes progressively more intense after the shock wave passes in all three test conditions. However, the rate of increase of the electrode glow becomes progressively more rapid as the pressure increases. This may be due to the faster approach to equilibrium at higher pressures and densities and may well be closely connected with the more rapid current rise at higher pressures (see Section A.2.6.4).

Run no: 49 **Date:** 6/19/97 **Shock press. at D:** 14.88 atm
Shock vel. at E: 4.54 km/s **Voltage at start of current flow:** 1040 V

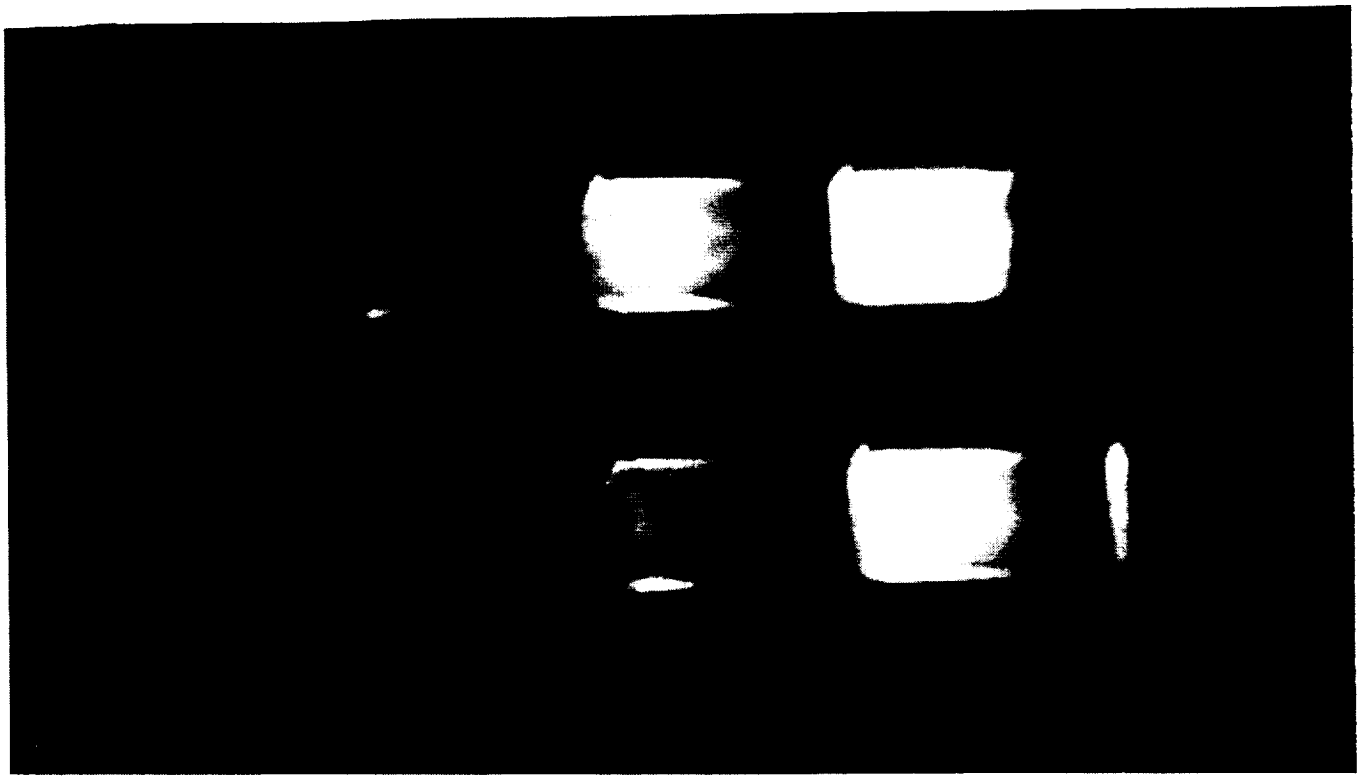

Frame:	**2**	**4**	**6**	**8**
Time:	-0.2	7.8	15.8	23.8
Mach no:				
Frame:	**1**	**3**	**5**	**7**
Time:	-4.2	3.8	11.8	19.8
Mach no:			2.24	

V_I: 4.2 km/s V_{CAV}: 4.68 km/s

Figure A.2- 52. IMACON image of the shock-heated test gas flow in the electrode region. The time is measured from the start of the current flow. Mach numbers and velocities are deduced from the image as explained in Section A.2.5.3.

A.2.6.4 Comparisons of Data

In this section, the data taken under the three different test conditions - 2, 5 and 13 atm is compared. First, refer back to Figure A.2- 7 (Section A.2.5.4), which shows test times estimated from the time of the start of the final and steep drop in current to the bottom electrode for all the runs with current between the electrodes. Three different symbols are used in the figure to indicate the data from the three different test conditions. There appears to be no significant difference between the test times for the 3 different test conditions. The trend of all of the data shows test times dropping from 50 - 70 μs at shock velocities of 4.5 km/s to 40 - 50 μs at 5.0 km/s to ~30 μs at 6.3 km/s. This is in agreement with the well-known (Ref. 12) tendency of uncontaminated test times in shock tunnels to drop as the shock velocity increases. In Section A.2.5.4, it was also mentioned that a limited number of spectroscopic measurements taken at the 13-atm test condition suggest that He driver gas contamination arrives about 10 μs before the start of the final and steep drop in current to the bottom electrode.

The conductivity histories presented previously for the three test conditions, Figures A.2- 13 through A.2- 16, A.2- 30 through A.2- 32, and A.2- 42 through A.2- 43 will now be re-examined. These histories generally have a rapid rise in conductivity lasting 10 - 30 μs, a region of high conductivity lasting 20 - 50 μs followed by a rapid fall in conductivity. The first part of the initial rise in pseudo-conductivity simply reflects the fact that it takes about 7 μs for the shock wave to completely fill the region between the electrodes with heated gas. However, the pseudo-conductivity continues to rise substantially between 7 and 10 - 30 μs after the start of current flow. As stated earlier, the electron population may take this long after the shock wave passage to come up to a value that is in equilibrium with the gas temperature and the prevailing electric field. Also, the current may be flowing mainly in the boundary layers that extend between the electrodes, and these boundary layers will initially thicken very rapidly with passing time. However, they will tend to stabilize at a constant thickness. The rapid drop in pseudo-conductivity is believed to be due to the arrival of the much cooler driver gas at 40 to 60 μs after the start of current flow. The widths of the high conductivity regions of the pseudo-conductivity curves are believed to essentially follow the trend of test time versus shock velocity discussed in the previous paragraph and shown in Figure A.2- 7.

The shapes of the high conductivity regions of the pseudo-conductivity histories for all of the runs with current between the electrodes have been examined and the frequencies with which the various shapes occur have been noted in Table A.2- 15. The shapes in the table are for the high conductivity regions of the conductivity histories. There is a tendency for the "flat top", "rounded top" and "long slope upwards" shapes to prevail at the 2-atm condition, whereas shapes with a definite early peak ("early hump, then lower flat region" and "double hump - camel") become more common at the higher-pressure conditions. However, at all conditions the shapes are highly variable from run to run and show little or no correlation with the applied voltage. It is believed that this variability may well be due to the varying conditions behind the main shock wave.

Table A.2- 15. Shapes of the high conductivity regions of the pseudo-conductivity histories.			
Shape of pseudo-conductivity history	Number of runs with stated shape at various test pressures		
	2 atm	5 atm	13 atm
Flat top	5	1	1
Rounded top	3	--	2
Long slope upwards	6	1	--
Flat top, then late hump	1	3	--
Early hump, then lower flat region	--	5	1
Double hump, "camel"	--	3	4

The main shock wave is followed by smaller shock waves and/or compression or rarefaction waves that are highly variable from run to run. This can easily be seen to be so in the pressure histories obtained at station D, well upstream of the electrodes. However, as it was not possible to obtain pressure histories at the electrodes when current was being passed between the electrodes, it was not possible to make a definitive correlation between the shapes of the conductivity histories and the pressure history at the electrodes.

The changes in the dominant shapes of the conductivity histories between the various run conditions shown in Table A.2- 11 were reexamined by noting the time from the start of current flow to the first definite maximum of the conductivity for each test run. This data is presented in Figure A.2- 53. All of the results for the individual runs are shown in the figure, as well as a curve that joins the three average values for the three test conditions. There is a wide range of variation of these times for each test condition likely due to the effects of additional shock waves, compression waves, and rarefaction waves as discussed above. Nevertheless, there is a definite tendency for the first peak in conductivity to arrive earlier as the pressure increases. This is likely to be due to a more rapid approach to an equilibrium electron concentration after the shock wave as the pressure increases.

In Figures A.2- 54, the electrode gap voltage-current characteristics 30-μs after the start of current flow for the 3 test pressures will be compared. The three lines in the figure for the data for 2, 5 and 13 atm were taken from the data presented in Figures A.2- 24, A.2- 38, and A.2- 49. To create the trend lines in Figure A.2- 54, blocks of data points in Figures A.2- 24, A.2- 38, and A.2- 49 were grouped together. The line based on the theoretical equilibrium value of the conductivity was calculated for the average equilibrium conductivity for the three test conditions. However, the maximum variation of the three equilibrium values from the average value is less than 2% and would scarcely be detectable on the figure. Figure A.2- 55 corresponds to Figure A.2- 54, except that the data is now taken at 15 μs after the start of current flow, and the data of Figure A.2- 55 was obtained from Figures A.2- 26, A.2- 40, and A.2- 51.

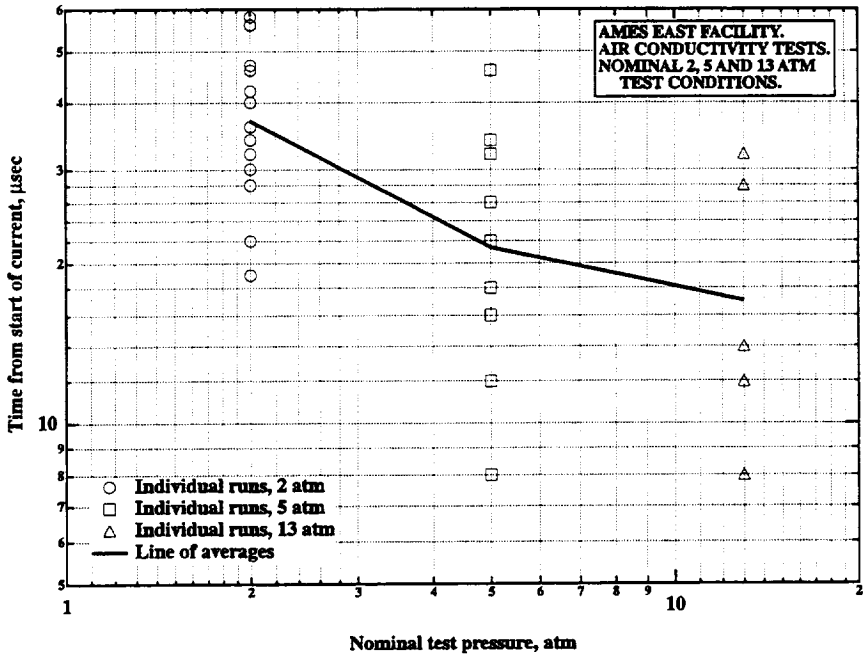

Figure A.2- 53. Time until first peak of pseudo-conductivity versus nominal test pressure.

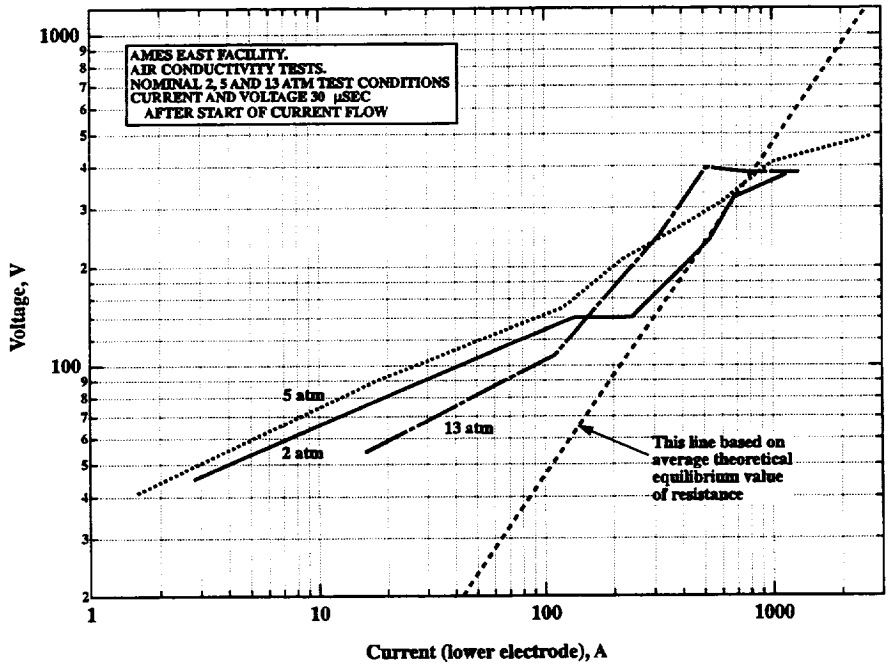

Figure A.2- 54. Electrode gap voltage-current characteristics, 30 μs after start of current flow.

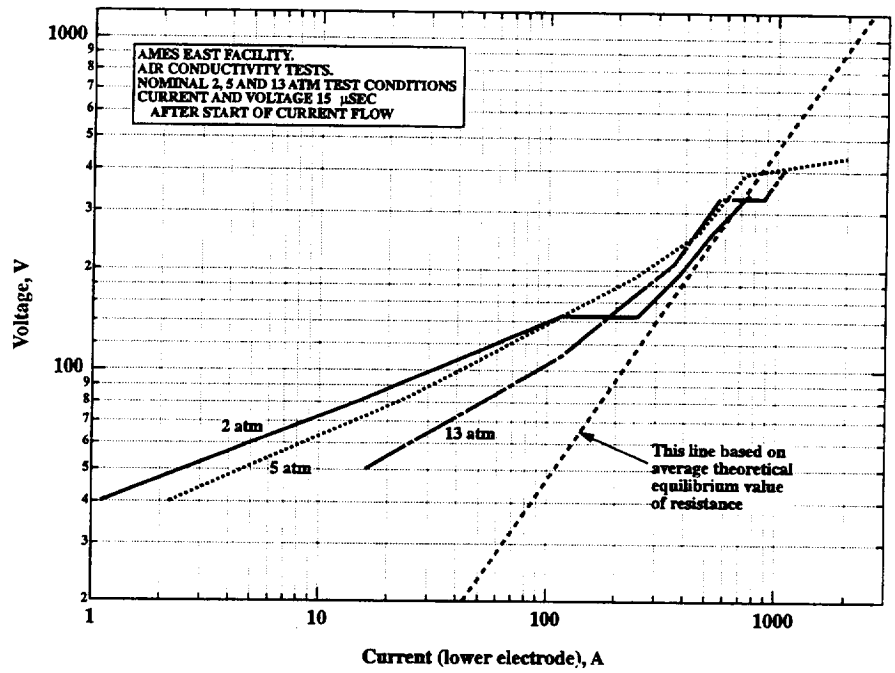

Figure A.2- 55. Electrode gap voltage –current characteristics, 15 μs after start of current flow.

In the voltage range from 40 to 140 V, the resistance of the gap is much greater than the value corresponding to the equilibrium conductivity, and likely due to the large voltage drops in the electrode fall regions discussed earlier. In general, the current drawn in this region increases with pressure at given voltage (except for the 2- and 5-atm curves at 30 μs after the start of current flow). This may well be due to the more rapid approach to the equilibrium electron concentration at higher pressures discussed previously. In both figures the data for the 2-atm condition shows a rapid increase in current at an essentially constant voltage of ~140 V. Such increases in current may reflect a response of the electrode gap to the voltage applied at the beginning of current flow, which continues to increase as the current shown in Figures A.2- 54 and A.2- 55 increases. This was discussed earlier in Section A.2.6.1. No such increase in current at nearly constant voltage are observed at the 5- and 13-atm test conditions until voltages of 330 to 400 V are reached. The increases in current at the higher voltages of 330 - 400 V can be, in part, explained by ohmic heating of the gas at the 2- and 5-atm test conditions; however, this explanation will not apply for the 13-atm test condition. (See discussions in Sections A.2.6.1, A.2.6.2 and A.2.6.3.) Fifteen μs after the start of current flow, the three-test conditions show a region (between voltages of 140 and 400 V, but with different voltage ranges for each test condition), which follows fairly closely the line based on theoretical equilibrium conductivity. Thirty μs after the start of current flow, this correspondence is still quite good between 140 and 330 V for the 2-atm test condition; unlike the other test conditions. The data for the 5-atm test condition is only close to the theoretical line near 350 V, while the curve for the 13-atm data runs

parallel to the theoretical line between 110 and 400 V, implying a constant resistance about 1.8 times the theoretical value.

Another issue of importance is the breakdown in the gas. From the data taken (including current and voltage histories, total light emission, monochromator histories, and the image converter photographs) there appears to be no solid evidence of breakdown in the gas. Some of the current histories do show late increases in current before the final and steep drop in current. These are the histories that yield the "flat top, then late hump" and "double hump-camel" pseudo-conductivity histories noted in Table A.2- 11. They could be interpreted to indicate the start of breakdown. However, there are other runs at nearby conditions with higher voltages that show no evidence of such late increases in current. In addition, as stated previously, there is no indication of breakdown in any of the other diagnostics, including no indication of a sudden drop in voltage. Also, as mentioned earlier, it is believed that the late increases in current are likely due to the arrival of additional shock or compression waves, causing further heating of the gas. The gas spends only ~7 μs traversing the electrode region and is continually renewed and for this reason it is believed that the maximum voltages of ~1,050 V are not sufficient to cause breakdown in the flow geometry. If a region of the flow much longer than the3.1 cm electrode length were subjected to the same voltages, it would seem more likely that breakdown would occur.

A.2.7 Summary

Air conductivity experiments were carried out in the NASA Ames EAST facility. This facility has a 10-cm diameter tube and was configured with a 76-cm long driver section and 445-cm long driven tube section. The He driver gas is heated by an electric discharge from a 1.2 MJ capacitor bank. For these experiments a skimmer tube projecting 23 cm into the driven tube from the blind end with a 3.5-cm inside diameter was used to remove the boundary layer in the driven tube and direct the core flow into the conductivity channel. The conductivity channel was 3.1 cm square and was lined with Delrin plastic. A pair of 3.1-cm square brass electrodes were located flush with the walls of the Delrin-lined channel about 40 cm downstream of the skimmer tube inlet. The insulating Delrin extended 9 cm upstream and 40 cm downstream of the electrodes.

The initial driven tube fill gas was $2N_2O + 1.76N_2$, chosen to provide the same N/O atom ratio as air after shock heating and to provide an increased test time when compared to operation of the facility with air as the driven tube fill gas. The nominal shock velocity was 4.65 km/s, chosen to produce an ionization fraction of $\sim 10^{-4}$. Unfortunately, the shock velocity was found to vary as much as ±6% between successive nominally identical test runs. The driven-tube fill-pressures were chosen to provide nominal after-shock pressures of 2, 5, and 13 atm, thus providing three basic test conditions. A total of 51 tests were conducted, including 36 satisfactory runs with current between the electrode pair.

The current to the electrodes was provided by a power supply with a 720 μfd capacitor bank that could be charged up to 4,500 V. The capacitors were connected to the electrodes through a salt-water ballast resistor and a second salt-water resistor was placed in parallel with the electrode

gap. The pre-charged capacitor bank was switched across the electrode gap-resistor network by using an ignitron tube. The voltages initially across the electrodes ranged from 45 to 1,060 V, and the maximum currents ranged from ~5 to ~3,000 A depending upon the applied voltage, driven tube pressure, and shock velocity.

Diagnostics included routine shock tube diagnostics and special diagnostics at the electrode station. The routine shock tube diagnostics included ionization gauge shock detectors, piezoelectric quartz crystal pressure gauges, and photomultiplier tubes that are used to measure the total light emission. These diagnostics allow the measurement of the shock velocities and pressures, while watching for additional shock waves, compression waves, and rarefactions; along with the arrival of driver gas contamination. At the electrode station, the voltage across the electrodes was measured using a voltage divider and by measuring the current through a resistor connected in parallel to the electrodes. The current to the top and bottom electrodes was measured using current transformers. Two 5-cm diameter Plexiglas™ windows permitted a view of the area between the electrodes. The total light emission from the electrode region was initially measured using a photomultiplier tube and this diagnostic was later replaced by two monochromators tuned to look at a He line and 10 nm to one side of the He line. These two monochromators were used to detect the arrival of He driver gas contamination. An image converter camera (IMACON) was used to obtain up to 8 frames at 4-μs intervals of the flow between the electrodes. A technique to measure the electron density by measuring the width of the H-β line was attempted, but was made difficult by the high-pressure (13-atm) test condition that was being conducted when the diagnostic was first tried, and by an overlapping Fe spectural line caused by contamination from the tube walls or the diaphragm. This diagnostic will be tried again later at a lower-pressure test condition.

At each pressure condition, runs were conducted at a number of different applied voltages, and current and voltage histories were obtained. It was determined that a certain fraction of the current from the upper electrode (at a potential above ground) was returning to ground in the driven tube upstream of the insulating Delrin liner, rather than to the lower (ground potential) electrode. The fraction of the diverted current was typically about 10% for runs with heavy currents, but was as much as 50 - 60% at low currents, particularly towards the beginning of the current flow. Since it was desired to study the current flowing directly across the electrode gap, almost all of the studies were done based on the current flowing to the lower electrode. "Pseudo-conductivities" were calculated based of the voltage across the electrodes, the current to the lower electrode, and the electrode gap and area. The "pseudo-conductivities" are obviously not the true conductivities since they include the voltage drops across the electrode fall regions.

Most of the pseudo-conductivity histories show, in general, the following features. The pseudo-conductivities rise very rapidly for the first 7- to 30-μs. The rise in pseudo-conductivity is generally followed by a region of high conductivity lasting usually 20- to 50-μs. This high conductivity region can be fairly flat, but can also be sloped or show a hump(s) at the beginning and/or end. These various features that can be found in the high conductivity region of the history are thought to be due to conductivity changes consequent to the arrival of additional compression or rarefaction waves and the resulting temperature changes. The pseudo-conductivity starts to fall steeply 40- to 60-μs after the start of current flow. Note that at a

nominal shock velocity of 4.6 km/s, it takes the shock wave about 7 μs to cross the electrode face. Thus, the first part of the initial steep rise in pseudo-conductivity more than likely reflects the fact that it takes about 7 μs for the shock wave to completely fill the region between the electrodes with heated gas. However, the pseudo-conductivity continues to rise substantially between 7 and 15 - 30 μs after the start of current flow. Two possible explanations are as follows: a) the electron population may take this long after the shock wave passage to come up to a value that is in equilibrium with the gas temperature and the prevailing electric field; b) the current may be flowing mainly in the boundary layers that extend between the electrodes; and these boundary layers will initially thicken rapidly, but will stabilize at a constant thickness. Finally, the rapid drop in pseudo-conductivity is believed to be due to the arrival of the much cooler driver gas 40 to 60 μs after the start of current flow.

The test time available from the start of current flow until the arrival of driver gas contamination was estimated from the time of the start of the final and rapid drop in pseudo-conductivity. These data showed test times dropping from 50-70 μs at shock velocities of 4.5 km/s to 40-50 μs at 5.0 km/s to ~30 μs at 6.3 km/s. Using the monochromators at the electrode station tuned on and to one side of a He line, it appeared that the He driver gas contamination arrives roughly 10 μs before the start of the final and steep drop in pseudo-conductivity is observed.

At each of the three test conditions; current, voltage, and pseudo-conductivity data 15 and 30 μs after the start of current flow were used to evaluate the effect of the applied voltage and current on the discharge characteristics. (Note the voltages applied across the electrodes at the start of current flow ranged from 45 to 1,060 V; however, the voltage data 15 and 30 μs after the start of current flow were lower, from 40 to 490 V, due to the inability of the power supply to maintain the voltage at heavy current draws.) For each test condition, theoretical equilibrium conductivity was calculated, and was used as a benchmark against which to compare the experimentally measured values. Generally, the data from the three test conditions showed the following characteristics. In the current range from ~2 to ~300 A, the measured pseudo-conductivities were below the calculated equilibrium conductivity, being as much as 50 times less at currents of ~2 A. This ratio dropped to ~15 at currents of ~10 A and ~3 at currents of ~100 A. In these current ranges, it is believed that the bulk gas has a conductivity close to the theoretical equilibrium value; but that the resistance of the voltage drop regions at the electrodes increases very rapidly as the current drops. In general, in the current ranges of 300-700 A, the pseudo-conductivites were found to be relatively close to the theoretical equilibrium conductivities. In this current range it is believed that the resistances of the voltage drop regions at the electrodes are much smaller due to the heavier currents and the conductivity of the core flow gas predominates. Finally, in the current range 700 – 3,000 A, the pseudo-conductivities are 30 - 100% above the theoretical core flow gas equilibrium conductivities. For the 2- and 5-atm test conditions, this increase can be somewhat explained by ohmic heating of the core gas. This explanation will not suffice for the 13-atm test condition. It is possible that the high-electric fields produce some nonequilibrium ionization under the high-current conditions, and this may be responsible for some of the observed increase in the pseudo-conductivity over the equilibrium values at the higher currents. This would seem less likely to be a possible explanation at the 13-atm condition where it should be much more difficult to obtain nonequilibrium.

At the 2-atm test condition, there is a region in the voltage-current characteristics of the electrode gap where there is a large change in current (from ~100 A to ~250 A) with almost no voltage change at the time that the current was measured. (The voltage was essentially constant at 140 V for this current range.) However, there was a voltage change at the beginning of the current flow between the runs with ~100 A and the runs with ~250 A. Hence, in the cases at 15 and 30 μs after the start of current flow, the electrode gap is likely responding to the voltages impressed on the gap at the start of current flow. (As mentioned previously, there is a considerable difference between the voltages at the start of current flow and the voltages at 15 and 30 μs after the start of current flow because of the inability of the power supply to maintain the voltage at heavy current draws.)

The voltage-current characteristics of the electrode gap 15 and 30 μs after the start of current flow were generally found to be fairly similar for all three pressure conditions. However, at the lower voltages, considerably more current was drawn at the higher pressures. On comparing the pseudo-conductivity histories for the three pressure conditions, it was found that the conductivities rose considerably more rapidly at the higher pressures. This is believed to be due to the more rapid approach to the equilibrium electron densities at the higher pressures.

A number of interesting features were observed in the IMACON photographs of the discharge region. Oblique shock waves were seen to emanate from the leading edges of the electrodes. Mach numbers of the flow between the electrodes can readily be calculated from the angles of these shock waves. The theoretical Mach numbers in equilibrium flow behind a shock wave at the observed velocity at the electrodes have also been calculated. In general, the experimentally observed Mach numbers are 0.20 to 0.45 less than the theoretical values. There are several possible explanations for this, which include boundary layer growth, both natural growth without electrical energy deposition and enhanced growth due to electrical energy deposition, may help to throttle the flow somewhat and thus to reduce the Mach number. At higher currents, energy deposition in the bulk gas may result in a Mach number reduction. Further, the relatively low experimental Mach numbers may also be partially due to the fact that the experimental gas flow may not yet be in equilibrium when the photographs are taken, and therefore, may not have all of the degrees of freedom of the gas excited. This would lead to a specific heat ratio larger than the equilibrium value and a Mach number smaller than the equilibrium value.

Perhaps the most interesting feature observed in the IMACON photographs was the presence of "hot spots" on the electrode surfaces. For some test conditions, discrete light sources could be seen on the electrodes. At the 2-atm test condition fixed spots of bright light are frequently visible at the edges of both electrodes, where the radii of the electrodes will produce an electric field increase. In addition, also at the 2-atm test condition and at the highest currents, moving spots of light are visible on the lower electrode (the cathode). The moving spots of light were not observed at lower voltages and currents at the 2-atm test conditions and were not observed at the 5- and 13-atm test conditions. In general, a smooth glow is seen along the electrodes at the 5- and 13-atm test conditions. It was noted that this glow becomes progressively more intense after the shock wave passes in all three test conditions; however, the rate of increase of the electrode glow becomes progressively more rapid as the pressure increases. This may be due to the faster

approach to equilibrium at higher pressures and densities and may well be closely connected with the more rapid current and pseudo-conductivity rises seen at higher pressures.

From all of the acquired data, including current and voltage histories, total light emission, monochromator histories and the IMACON photographs there appears to be no solid evidence of breakdown in the gas. Some of the current histories do show late increases in current, before the final and steep drop in current. However, there are other runs at nearby conditions with higher voltages that show no evidence of such late increases in current. In addition, as previously stated, there is no indication of breakdown in any of the other diagnostics, including no indication of a sudden drop in voltage. Note that the gas spends only ~7 μs traversing the electrode region and is continually renewed and for this reason it is believed that the maximum voltages of ~1,050 V are not sufficient to cause breakdown in the flow geometry.

A.2.8 References

1. Sharma, S.P., and Park, C., "Operating Characteristics of a 60- and 10- cm Electric Arc-Driven Shock Tube - Part I: The Driver," *Journal of Thermophysics and Heat Transfer*, Vol. 4, No. 3, July 1990, pp. 259-265.

2. Sharma, S.P., and Park, C., "Operating Characteristics of a 60- and 10- cm Electric Arc-Driven Shock Tube - Part II: The Driven Section," *Journal of Thermophysics and Heat Transfer*, Vol. 4, No. 3, July 1990, pp. 266-272.

3. Liepmann, H.W., and Roshko, A., *Elements of Gasdynamics,* Wiley, New York, 1957, p. 92.

4. McBride, B.J., and Gordon, S., "Computer Program for Calculation of Complex Chemical Equilibrium Compositions and Applications: II. Users Manual and Program Description," NASA Reference Publication 1331, June 1996.

5. Glass, I.I., Liu, W.S., Takayama, K. and Brimelow, P.I., "Interactions of Shock Structure with Shock-Induced Quasi-Steady Laminar Sidewall and Flate-Plate Boundary-Layer Flows in Ionizing Argon," in *Proceedings of the 12th International Symposium on Shock Tubes and Waves*, Jerusalem, July 16-19, 1979, pp. 232-241.

6. Viegas, J.R., and Peng, T.C., "Electrical Conductivity of Ionized Air in Thermodynamic Equilibrium," ARS *Journal*, May 1961, pp. 654-657.

7. Nottingham, W.B., *A New Equation for the Static Characteristics of the Normal Electric Arc, Transactions of AIEE*, Feb. 1923, pp. 302-310.

8. Cobine, J.D., *Gaseous Conductors*, Dover, New York, 1958, pp. 292-300.

9. Rittenhouse, L.E., Pigott, J.C., Whoric, J.M., and Wilson, D.R., *Theoretical and Experimental Results with a Linear Magnetohydrodynamic Accelerator Operated in the Hall Current Neutralized Mode*, Arnold Engineering Development Center Report AEDC-TR-67-150, November, 1967, pp. 45-46.

10. Shapiro, A.H., *The Dynamics and Thermodynamics of Compressible Fluid Flow*, Ronald, New York, 1954, p. 1002.

11. Margalith, E. and Christiansen, W.H., "Interactions Between an E-Beam Sustained Discharge and Supersonic Flow," *Proceedings of the 12th International Symposium on Shock Tubes and Waves, Jerusalem*, July 16-19, 1979, pp. 376-385.

12. Copper, J.A., Miller, H.R. and Hameetman, F.J., "Correlation of Uncontaminated Test Durations in Shock Tunnels," *Fourth Hypervelocity Techniques Symposium, Arnold Air Force Station,* Nov. 1956, pp. 274-310.

Data Compendium

This data compendium consists of a condiderable fraction of the data obtained for each of Runs 13 - 51. The data is, for the most part, presented run by run. The order of the data presented for each run is as follows:

1. Data sheet.
2. Voltage history from voltage divider.
3. Voltage history from current in resistor.
4. Current history to top electrode.
5. Current history to bottom electrode.
6. Pseudo-conductivity history from current to bottom electrode and one of the voltage histories.
7. Image converter photograph of the region between the electrodes.

Data is not provided for Runs 1 - 9, which were performed without current passing between the electrodes. Data is also not provided for Runs 10 - 12, for which current was only measured to the top electrode. The seven items listed above were not all available for all of runs 13 - 51. Since there was no current for Runs 20 and 24, items 2 - 6 are lacking for these runs. For Run 13, the bottom electrode was not connected, hence items 5 and 6 are lacking for this run. Finally, image converter photographs were not obtained for Runs 15, 21, 29, 30 and 42.

The data sheet giving the test conditions starts (Sec. 1) by giving the driven tube gas mixture, fill pressure and estimated shock velocity at the electrodes. This latter velocity is frequently estimated from the average velocity measured between stations D and F. The correlation between the average velocity between stations D and F and the shock velocity at the electrodes was established during early runs without current, when there was a pressure transducer at the electrode station to allow the shock velocity at the electrodes to be determined very accurately. Under some conditions (with very heavy currents), the time of shock passage of station F cannot be determined due to severe EM noise pickup on the pressure transducer at station F. In these cases, the shock velocity was determined by noting the time interval between the shock passage of station D and the start of the current to the electrodes. This time interval was found to be very accurately related to the time interval between the shock passage between stations D and F in the many test runs when the shock passage time at station F could be accurately determined.

The measured shock pressure at station D, upstream of the test section, is given next. This value should be quite accurate and is considerably higher than the nominal pressure because the shock wave slows down between station D and the electrodes. The shock pressures given from the pressure transducer located at station F, downstream of the electrodes are to be regarded as rather uncertain, on account of the very large noise pickup, from the large current between the electrodes, on this transducer.

A number of critical facility dimensions are then presented (Sec. 2). Section 3 gives the nominal pressure condition and the voltages across the plasma at the beginning of current flow and after 30 μsec of current flow. Finally, Sec. 4 gives an assessment of whether breakdown appears to have occurred.

Following all of the run by run sets of data for Runs 13 - 51, six tables are presented which give data regarding the image converter photographs. The first two tables are for the 2 atm nominal test condition, the next two tables for the 5 atm condition and the last two tables for the 13 atm test condition. The first table for each of the three run conditions contains the following, in order:

Run number
Shock velocity at station E
Shock pressure at station D
Voltage at start of current
Time of frame number 1 after start of current
Interframe shock velocity from photograph
Shock velocity from station D to appearence of shock in photograph

The interframe time interval is 4 μsec. If the shock appears in more than one frame, an interframe shock velocity can be calculated and is given in the sixth column of the table. The methods of calculating this velocity and the velocity in column seven are discussed in the report.

The second table for each of the three run conditions contains the following, in order:

Run number
Experimental flow Mach numbers (four columns)
Theoretical flow Mach number.
Frame numbers for the experimental flow Mach numbers.

The experimental flow Mach numbers are calculated from the observed shock wave angles, as described in the report. The theoretical flow Mach numbers are calculated for equilibrium flow behind the main vertical shock wave, again as described in the report.

Run Number	Run Date	Nominal Pressure	Comments
13	5/1/97	2	Lower electrode not connected
14	5/5/97	2	
15	5/5/97	2	
16	5/6/97	2	
17	5/7/97	2	
18	5/8/97	2	
19	5/9/97	2	
20	5/12/97	2	No current to electrodes
21	5/13/97	2	
22	5/13/97	2	
23	5/14/97	2	
24	5/15/97	2	No current to electrodes
25	5/15/97	2	
26	5/16/97	2	
27	5/19/97	2	
28	5/20/97	2	
29	5/22/97	5	
30	5/23/97	5	
31	5/27/97	5	
32	5/28/97	5	
33	5/29/97	5	
34	5/30/97	5	
35	5/30/97	5	
36	6/2/97	5	
37	6/3/97	5	
38	6/4/97	5	
39	6/5/97	5	
40	6/6/97	5	
41	6/9/97	5	
42	6/10/97	2	High shock velocity
43	6/11/97	2	High shock velocity
44	6/12/97	13	0.5% H_2 added to driven tube
45	6/13/97	13	0.5% H_2 added to driven tube
46	6/16/97	13	0.5% H_2 added to driven tube
47	6/17/97	13	0.5% H_2 added to driven tube
48	6/18/97	13	0.5% H_2 added to driven tube
49	6/19/97	13	0.5% H_2 added to driven tube
50	6/20/97	13	0.5% H_2 added to driven tube
51	6/20/97	13	

AIR CONDUCTIVITY MEASUREMENT IN AMES EAST FACILITY

RUN 39/13, 5/1/97

1. Driven tube conditions:

53.2% N_2O, 46.8% N_2,
Total pressure - 5.20 Torr
Measured shock velocity between stns D and F - 5.035 km/sec
Estimated shock velocity at electrodes - 4.845 km/sec
Measured shock pressure at stn D - 2.57 atm
Measured shock pressure at stn F - 1.53 - very uncertain
due to large EM noise pickup

2. Electrodes, driven tube dimensions:

Electrode size - 3.10 cm square
Electrode spacing - 3.10 cm
Main diaphragm to electrodes - 454.475 cm
Skimmer nose to electrodes - 39.979 cm
Driven tube diameter - 10.16 cm
Stn D (dn tube) to electrodes (channel) - 77.365 cm
Electrodes (channel) to stn F (channel) - 20.32 cm

3. Nominal test conditions:

Pressure - 2 atm
Voltage across electrodes - 174/122 V
Lower electrode not connected

4. Breakdown:

Little or no indication of breakdown.

Run no: 13 **Date:** 5/1/97 **Shock press. at D:** 2.57 atm
Shock vel. at E: 4.85 km/sec **Voltage at start of current flow:** 174 V

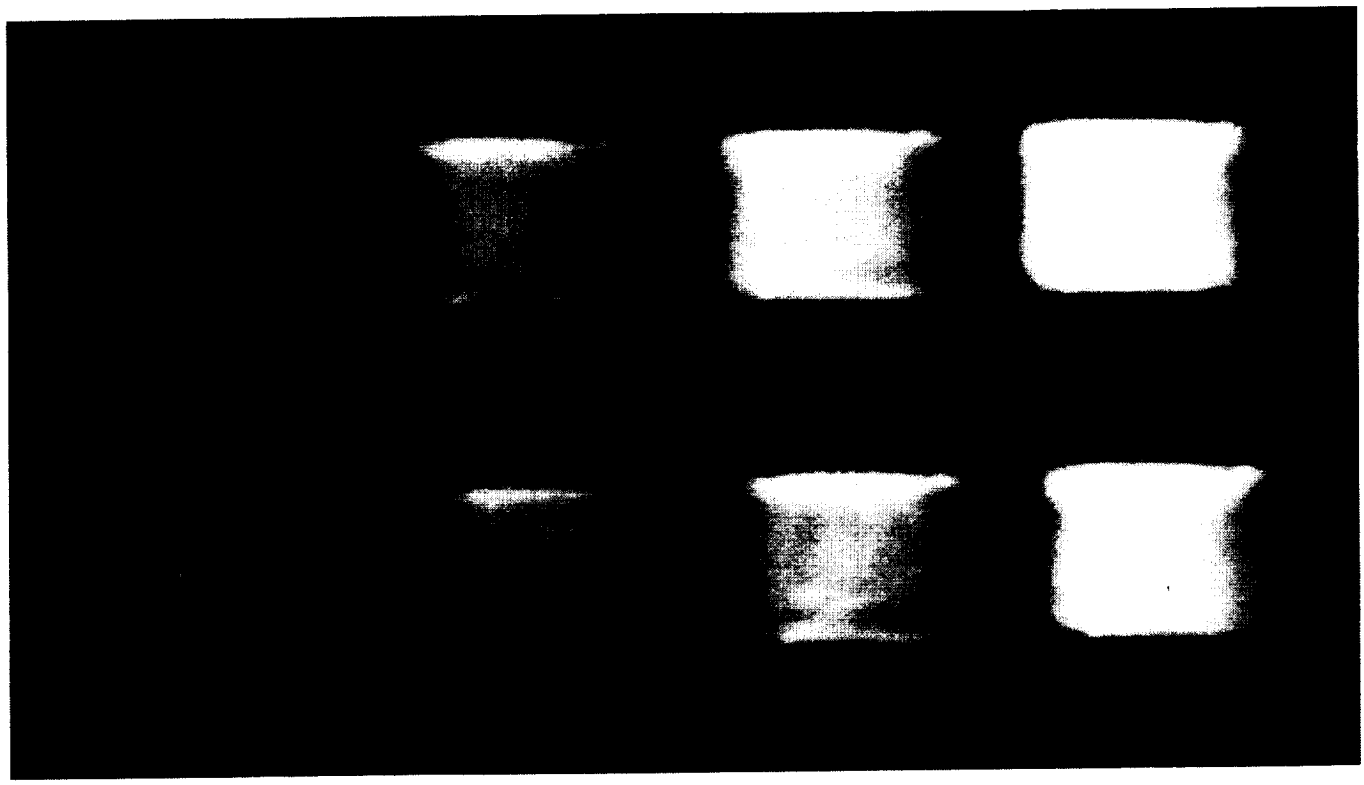

Frame:	**2**	**4**	**6**	**8**
Time:				
Mach no:	2.69			
Frame:	**1**	**3**	**5**	**7**
Time:				
Mach no:	2.59	2.42		

V_I: km/sec V_{CAV}: km/sec

IMACON image of the shock-heated test gas flow in the electrode region. The time is measured from the start of the current flow. Mach numbers and velocities are deduced from the image as explained in section A.2.5.3.

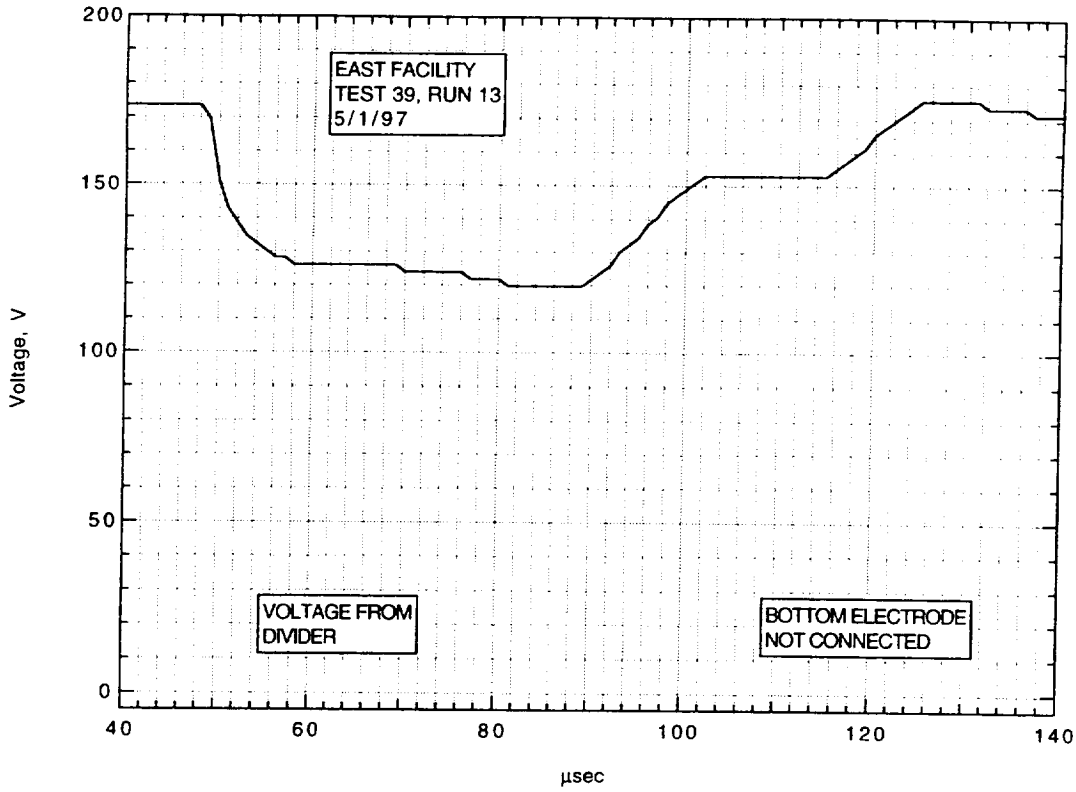

Run 13. Voltage from divider.

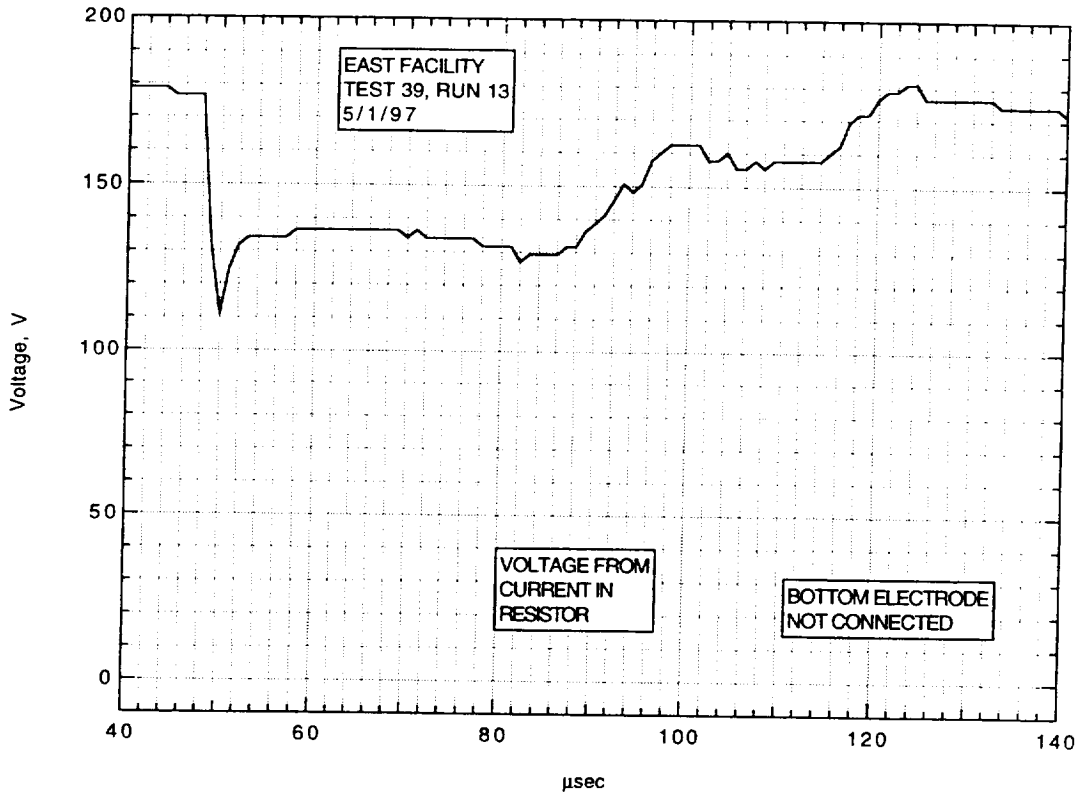

Run 13. Voltage from current in resistor.

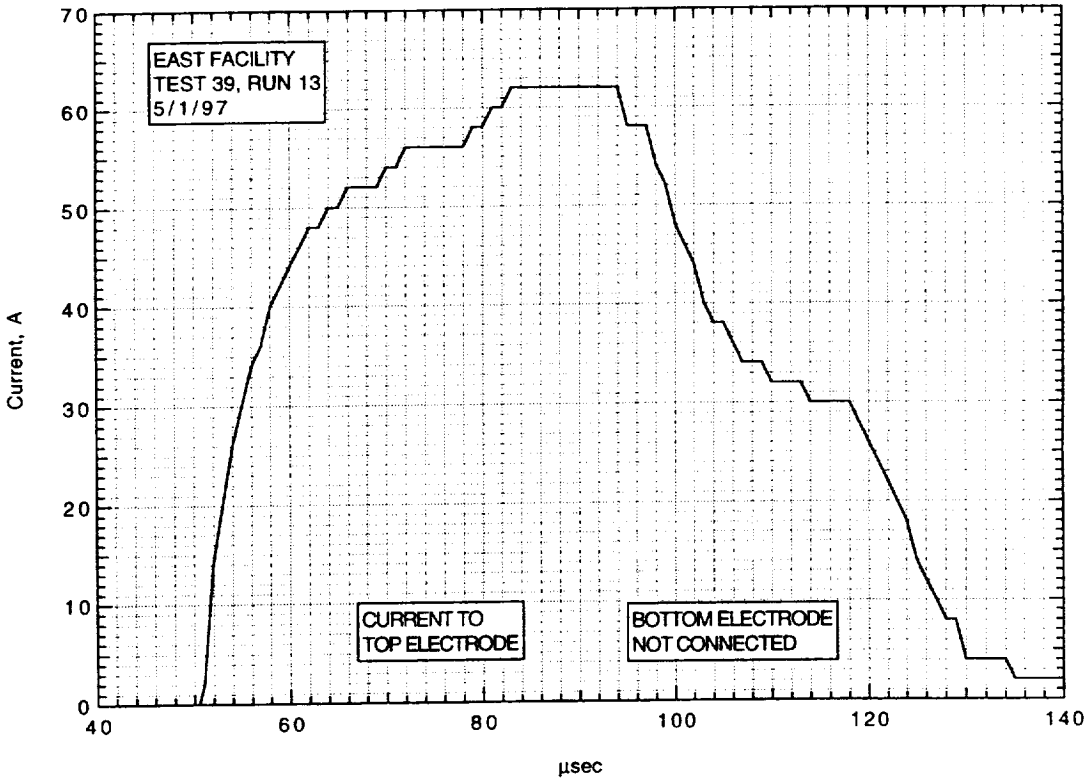

Run 13. Current to top electrode.

AIR CONDUCTIVITY MEASUREMENT IN AMES EAST FACILITY

RUN 39/14, 5/5/97

1. Driven tube conditions:

53.2% N_2O, 46.8% N_2,
Total pressure - 5.20 Torr
Measured shock velocity between stns D and F - 4.836 km/sec
Estimated shock velocity at electrodes - 4.653 km/sec
Measured shock pressure at stn D - 2.44 atm
Measured shock pressure at stn F - 1.80 - very uncertain
due to large EM noise pickup

2. Electrodes, driven tube dimensions:

Electrode size - 3.10 cm square
Electrode spacing - 3.10 cm
Main diaphragm to electrodes - 454.475 cm
Skimmer nose to electrodes - 39.979 cm
Driven tube diameter - 10.16 cm
Stn D (dn tube) to electrodes (channel) - 77.365 cm
Electrodes (channel) to stn F (channel) - 20.32 cm

3. Nominal test conditions:

Pressure - 2 atm
Voltage across electrodes - 176/122 V

4. Breakdown:

Little or no indication of breakdown.

Run no: 14 **Date:** 5/5/97 **Shock press. at D:** 2.44 atm
Shock vel. at E: 4.65 km/sec **Voltage at start of current flow:** 174 V

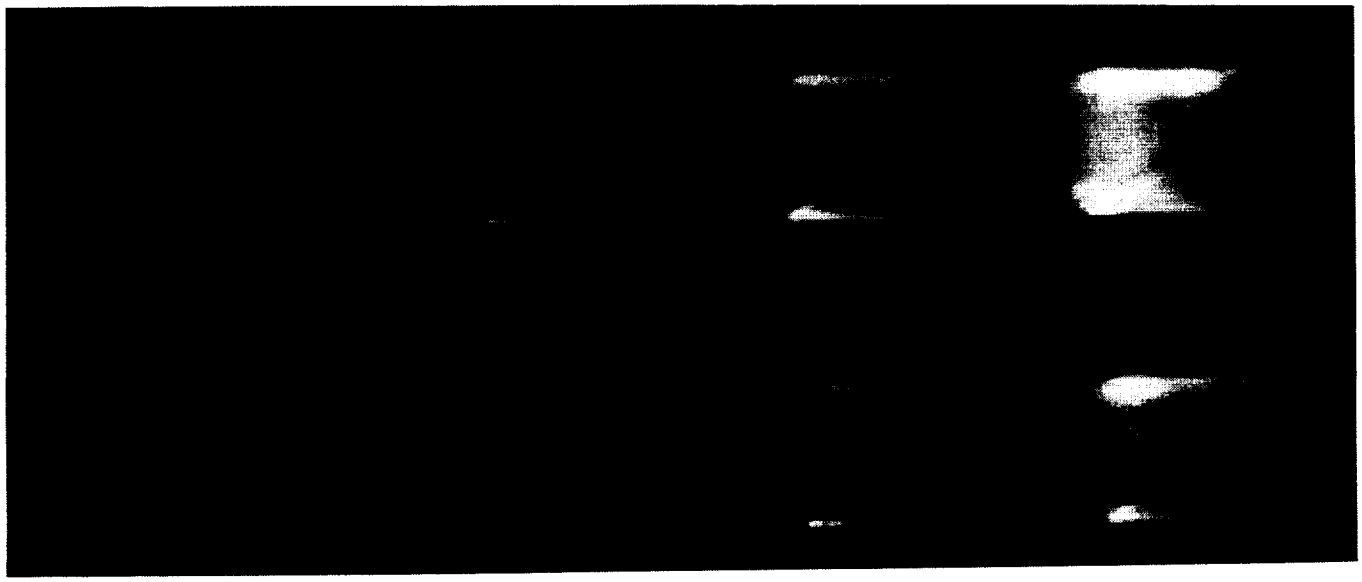

Frame:	**2**	**4**	**6**	**8**
Time:	2.5	10.5	18.5	26.5
Mach no:		2.46		
Frame:	**1**	**3**	**5**	**7**
Time:	-1.5	6.5	14.5	22.5
Mach no:		2.85		

V_I: km/sec V_{CAV}: 4.90 km/sec

IMACON image of the shock-heated test gas flow in the electrode region. The time is measured from the start of the current flow. Mach numbers and velocities are deduced from the image as explained in section A.2.5.3.

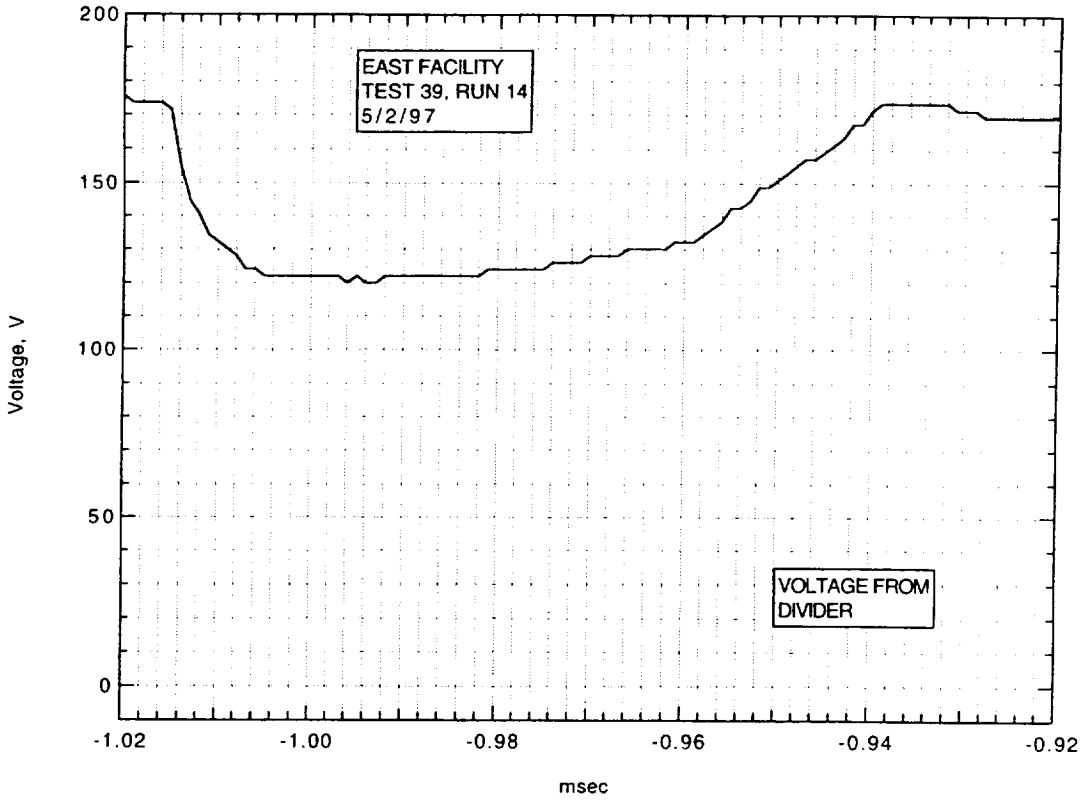

Run 14. Voltage from divider.

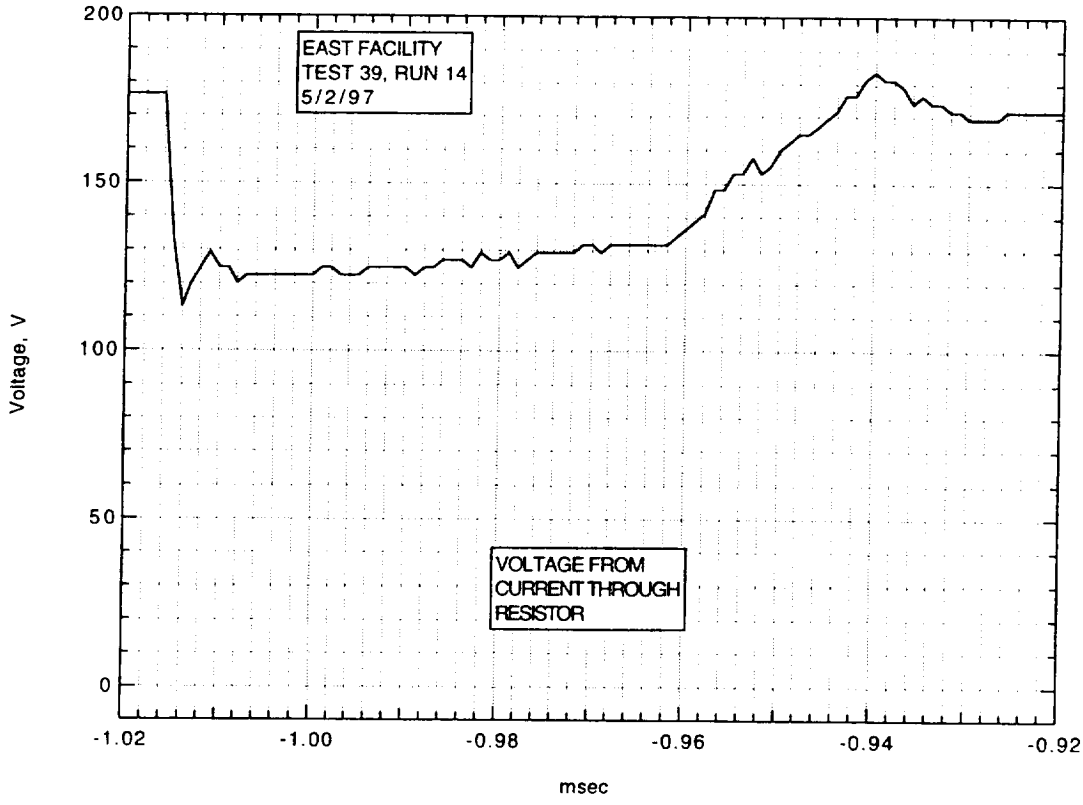

Run 14. Voltage from current in resistor.

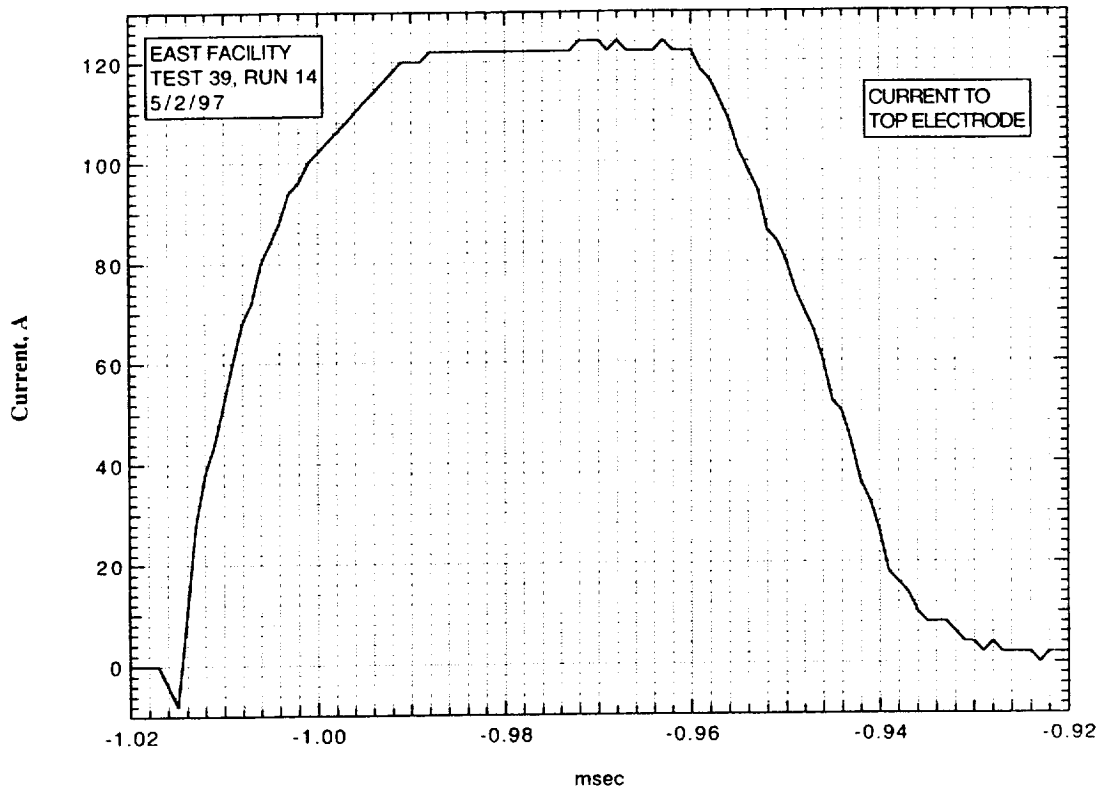

Run 14. Current to top electrode.

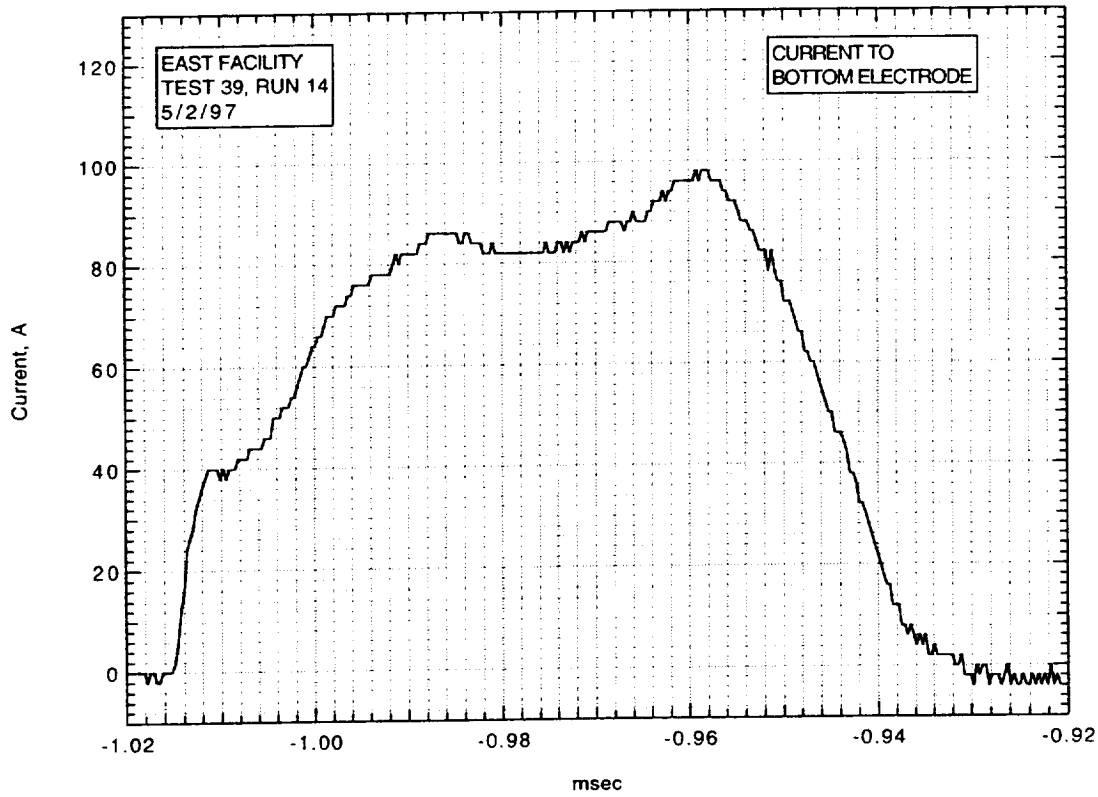

Run 14. Current to bottom electrode.

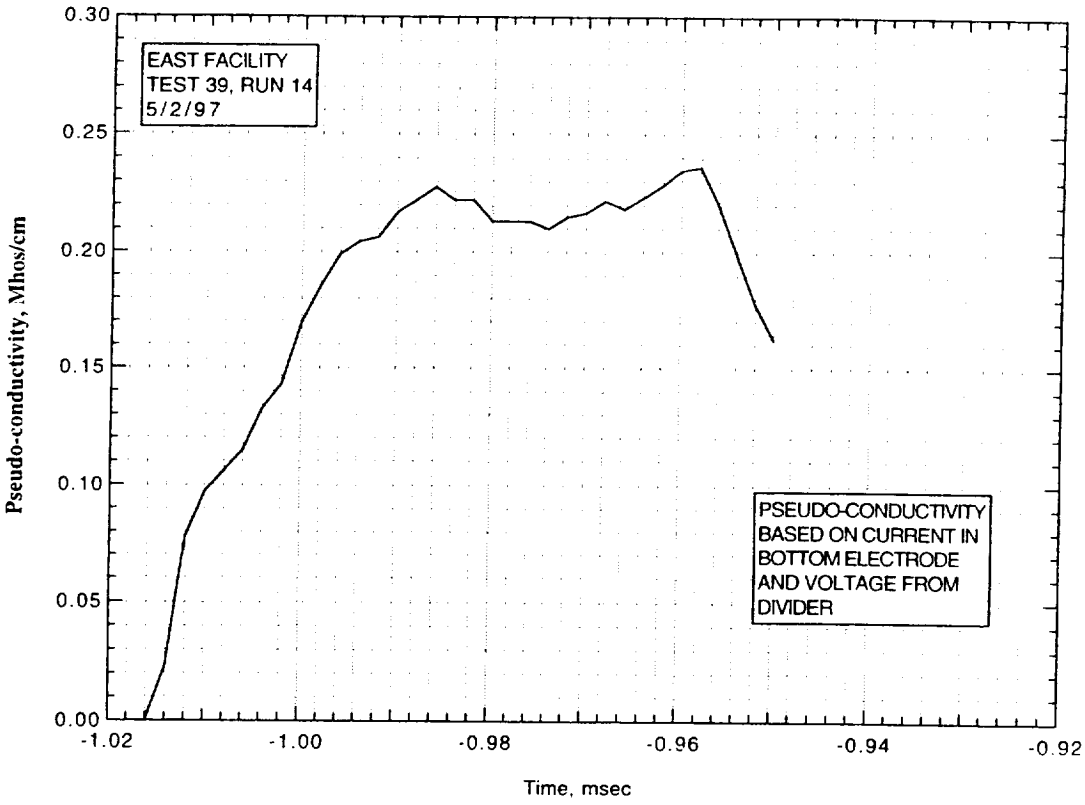

Run 14. Pseudo-conductivity based on current to bottom electrode and voltage from divider.

AIR CONDUCTIVITY MEASUREMENT IN AMES EAST FACILITY

RUN 39/15, 5/5/97

1. Driven tube conditions:

53.2% N_2O, 46.8% N_2,
Total pressure - 5.20 Torr
Measured shock velocity between stns D and F - 4.765 km/sec
Estimated shock velocity at electrodes - 4.585 km/sec
Measured shock pressure at stn D - 2.42 atm
Measured shock pressure at stn F - 1.72 rather uncertain due to large EM noise pickup

2. Electrodes, driven tube dimensions:

Electrode size - 3.10 cm square
Electrode spacing - 3.10 cm
Main diaphragm to electrodes - 454.475 cm
Skimmer nose to electrodes - 39.979 cm
Driven tube diameter - 10.16 cm
Stn D (dn tube) to electrodes (channel) - 77.365 cm
Electrodes (channel) to stn F (channel) - 20.32 cm

3. Nominal test conditions:

Pressure - 2 atm
Voltage across electrodes - 173/128 V

4. Breakdown:

Little or no indication of breakdown.

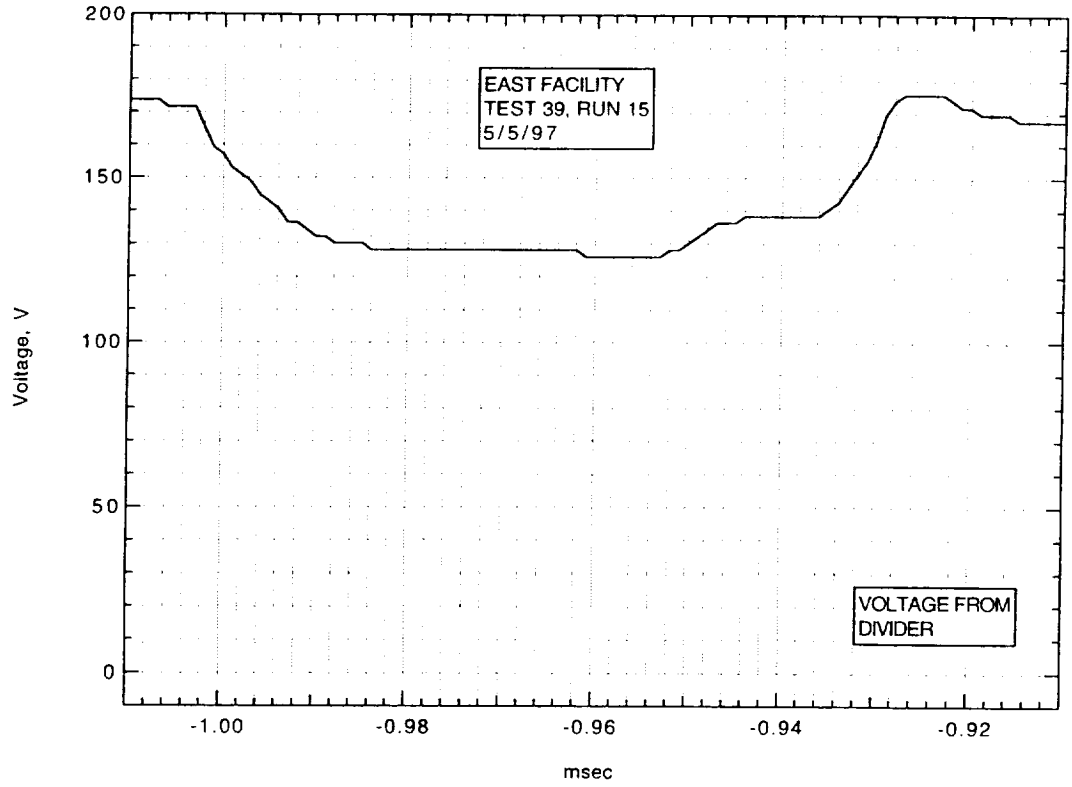

Run 15. Voltage from divider.

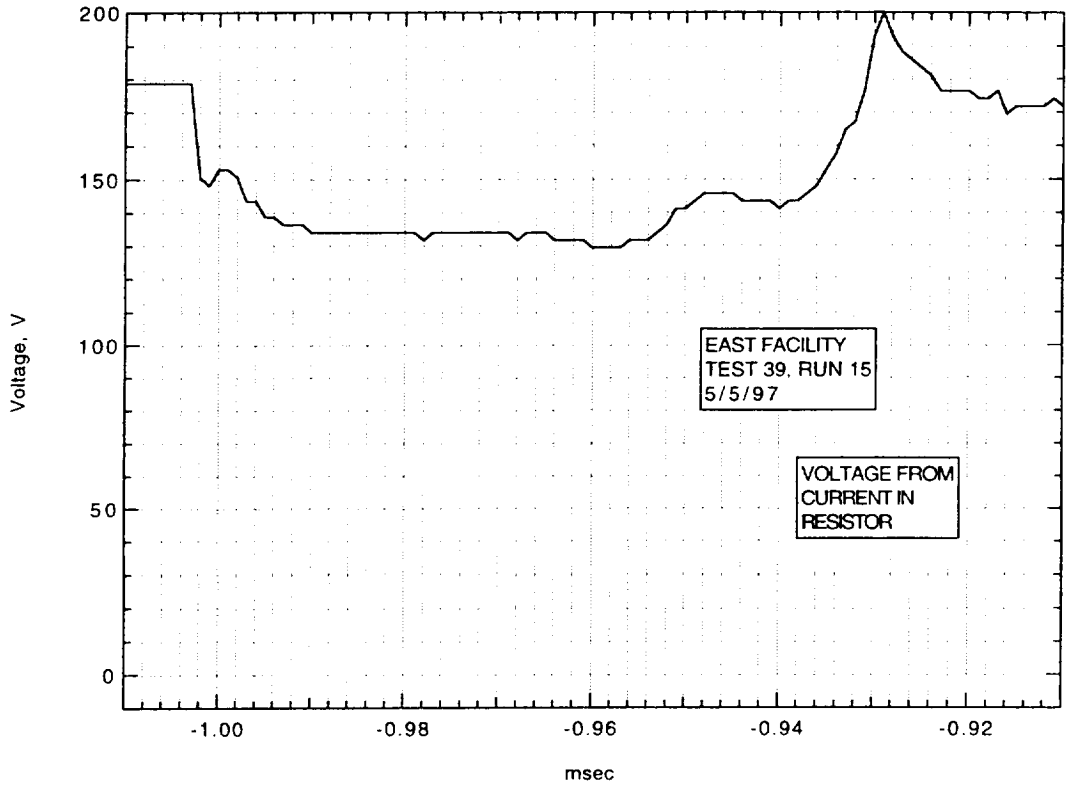

Run 15. Voltage from current in resistor.

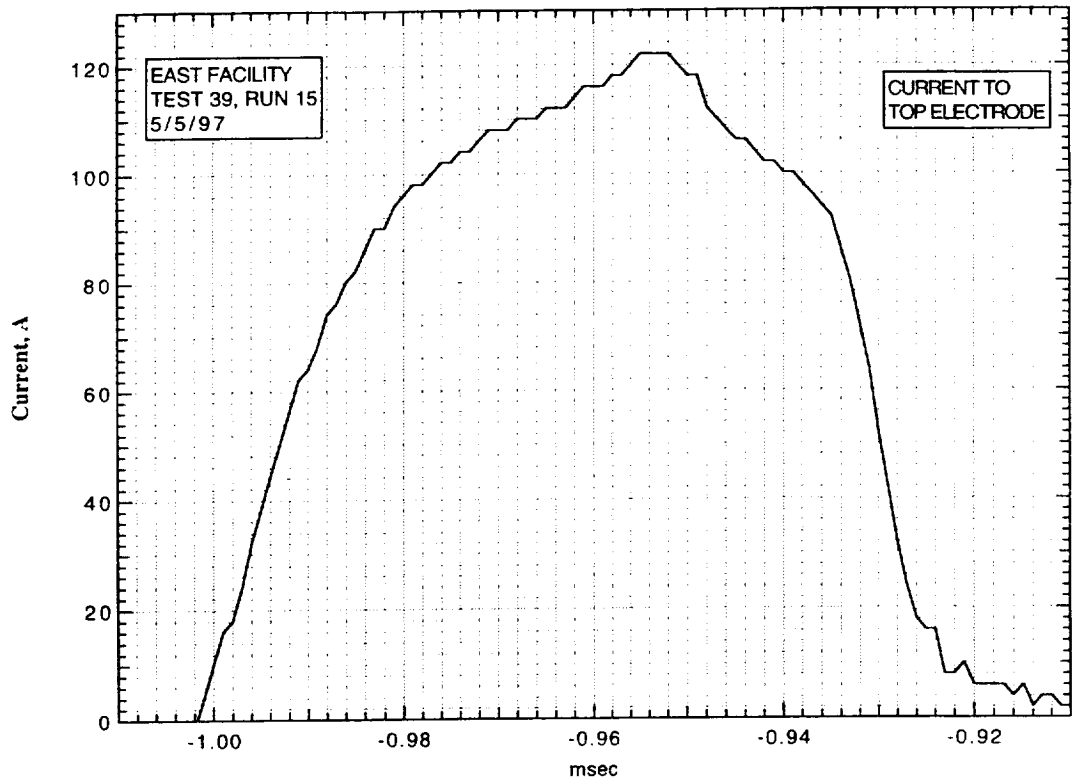

Run 15. Current to top electrode.

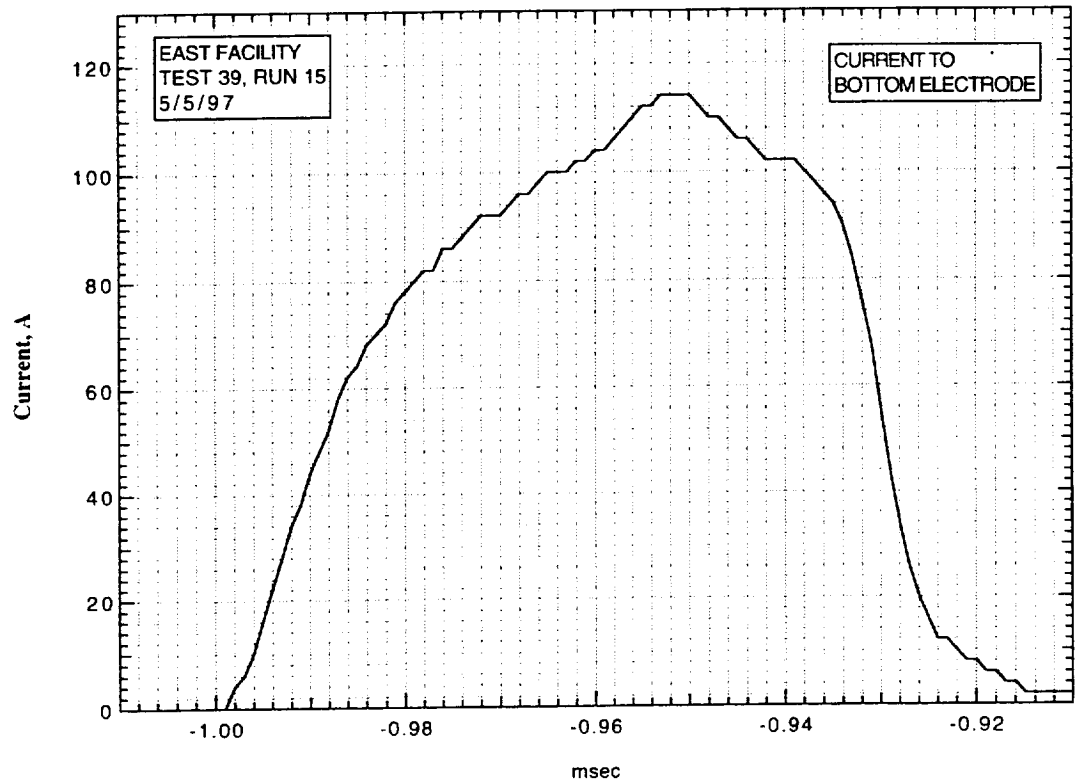

Run 15. Current to bottom electrode.

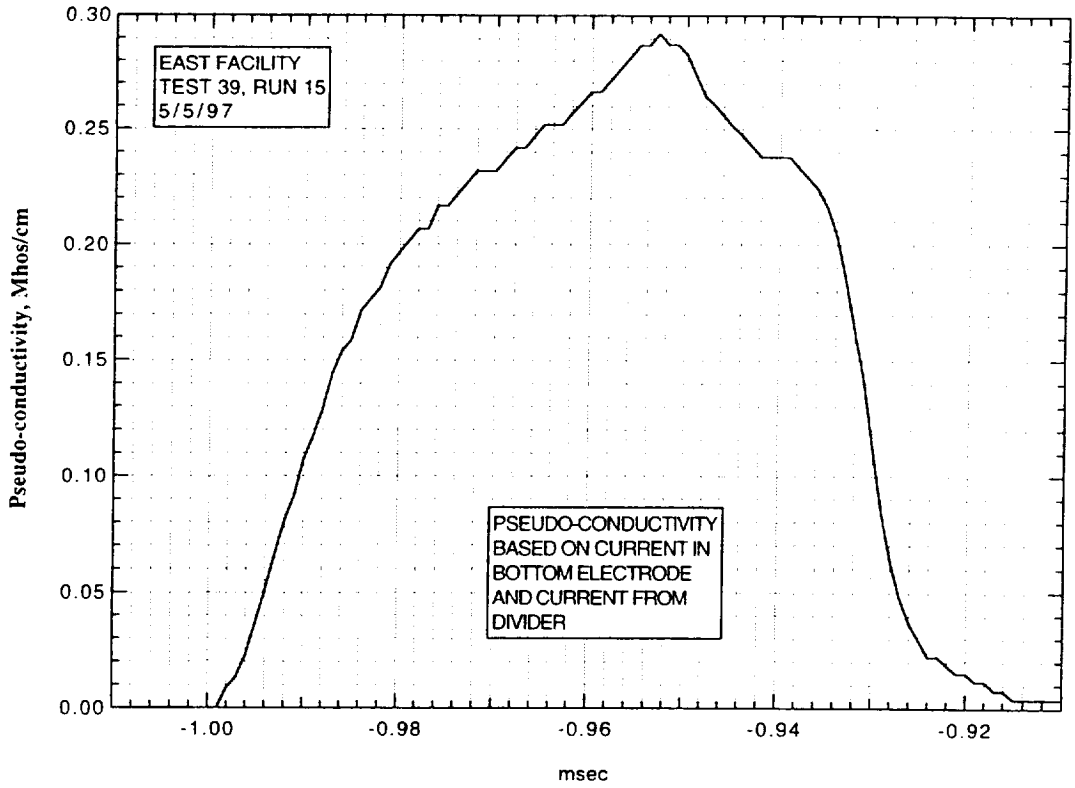

Run 15. Pseudo-conductivity based on current to bottom electrode and voltage from divider.

AIR CONDUCTIVITY MEASUREMENT IN AMES EAST FACILITY

RUN 39/16, 5/6/97

1. Driven tube conditions:

53.2% N_2O, 46.8% N_2,
Total pressure - 5.20 Torr
Measured shock velocity between stns D and F - 5.087 km/sec
Estimated shock velocity at electrodes - 4.895 km/sec
Measured shock pressure at stn D - 2.75 atm
Measured shock pressure at stn F - 2.00 very uncertain
due to large EM noise pickup

2. Electrodes, driven tube dimensions:

Electrode size - 3.10 cm square
Electrode spacing - 3.10 cm
Main diaphragm to electrodes - 454.475 cm
Skimmer nose to electrodes - 39.979 cm
Driven tube diameter - 10.16 cm
Stn D (dn tube) to electrodes (channel) - 77.365 cm
Electrodes (channel) to stn F (channel) - 20.32 cm

3. Nominal test conditions:

Pressure - 2 atm
Voltage across electrodes - 324/150 V

4. Breakdown:

Little or no indication of breakdown.

Run no: 16 **Date:** 5/6/97 **Shock press. at D:** 2.75 atm
Shock vel. at E: 4.89 km/sec **Voltage at start of current flow:** 324V

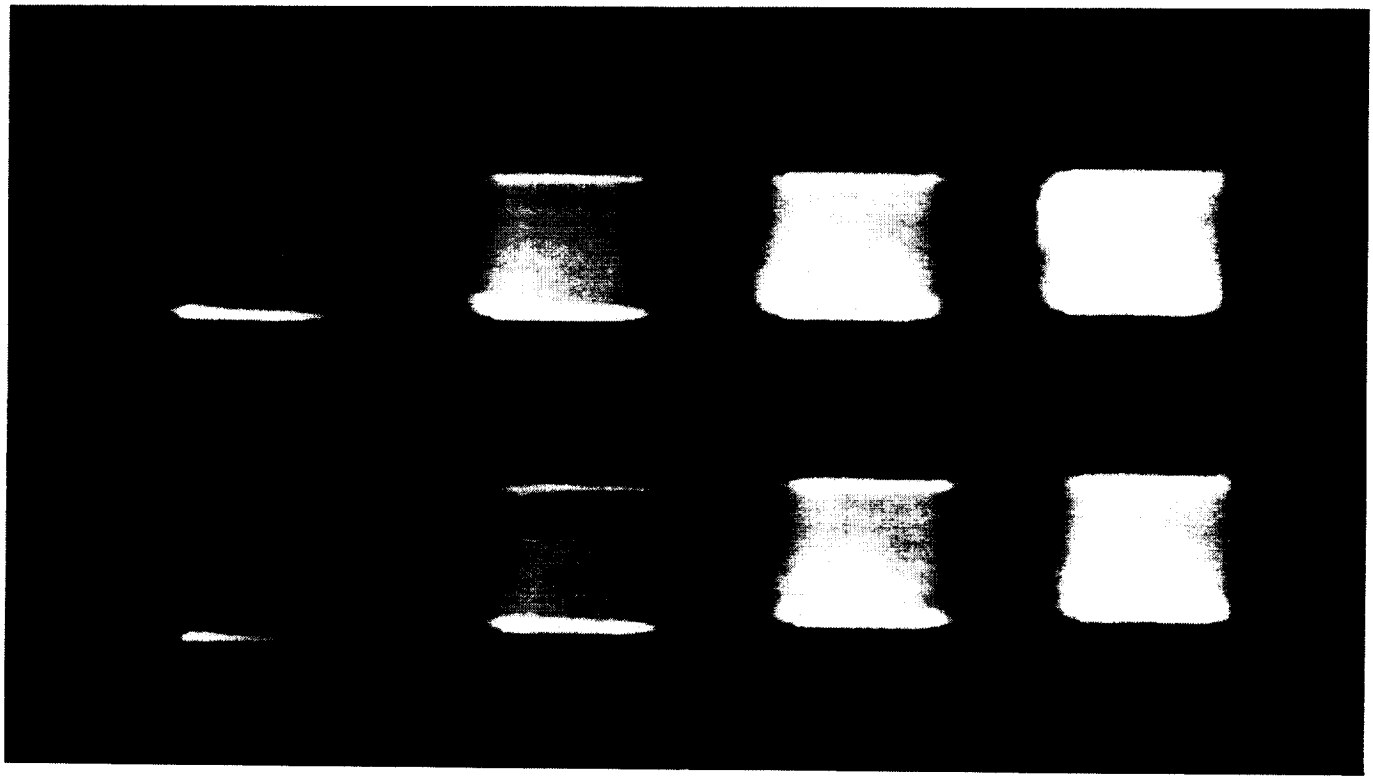

Frame:	**2**	**4**	**6**	**8**
Time:	9.2	17.2	25.2	33.2
Mach no:	2.69			
Frame:	**1**	**3**	**5**	7
Time:	5.2	13.2	21.2	29.2
Mach no:	2.57			

V_I: km/sec V_{CAV}: 5.05 km/sec

IMACON image of the shock-heated test gas flow in the electrode region. The time is measured from the start of the current flow. Mach numbers and velocities are deduced from the image as explained in section A.2.5.3.

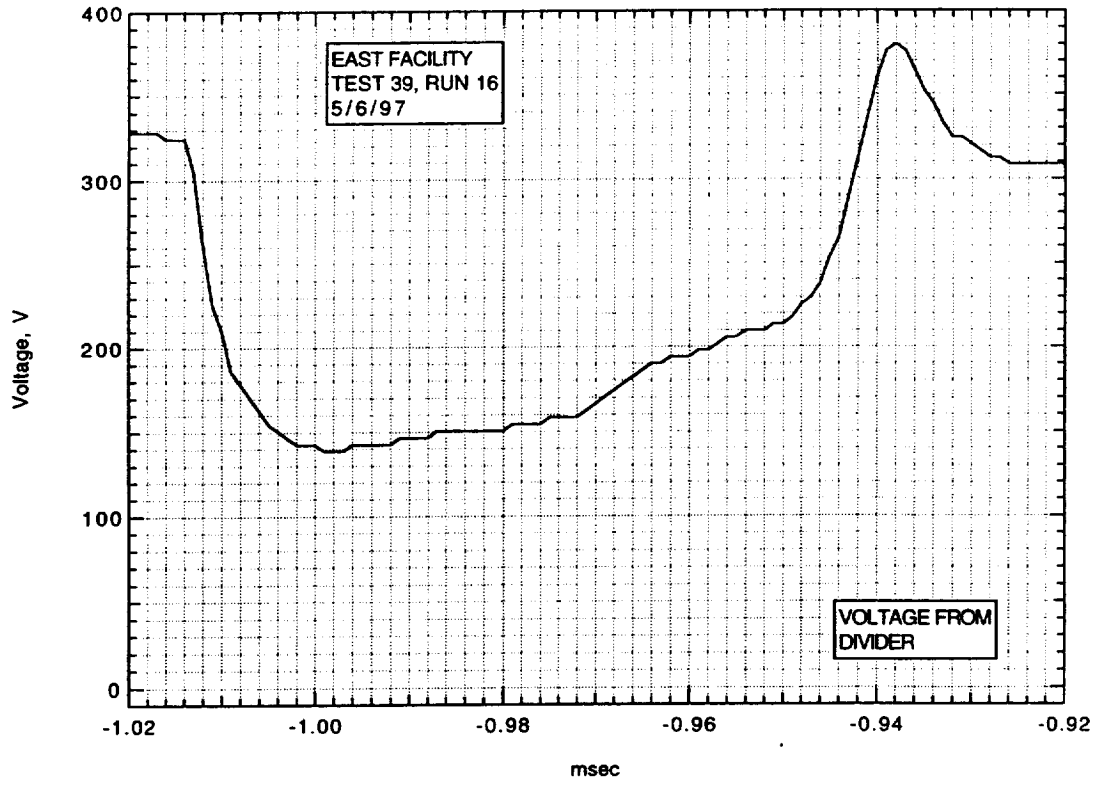

Run 16. Voltage from divider.

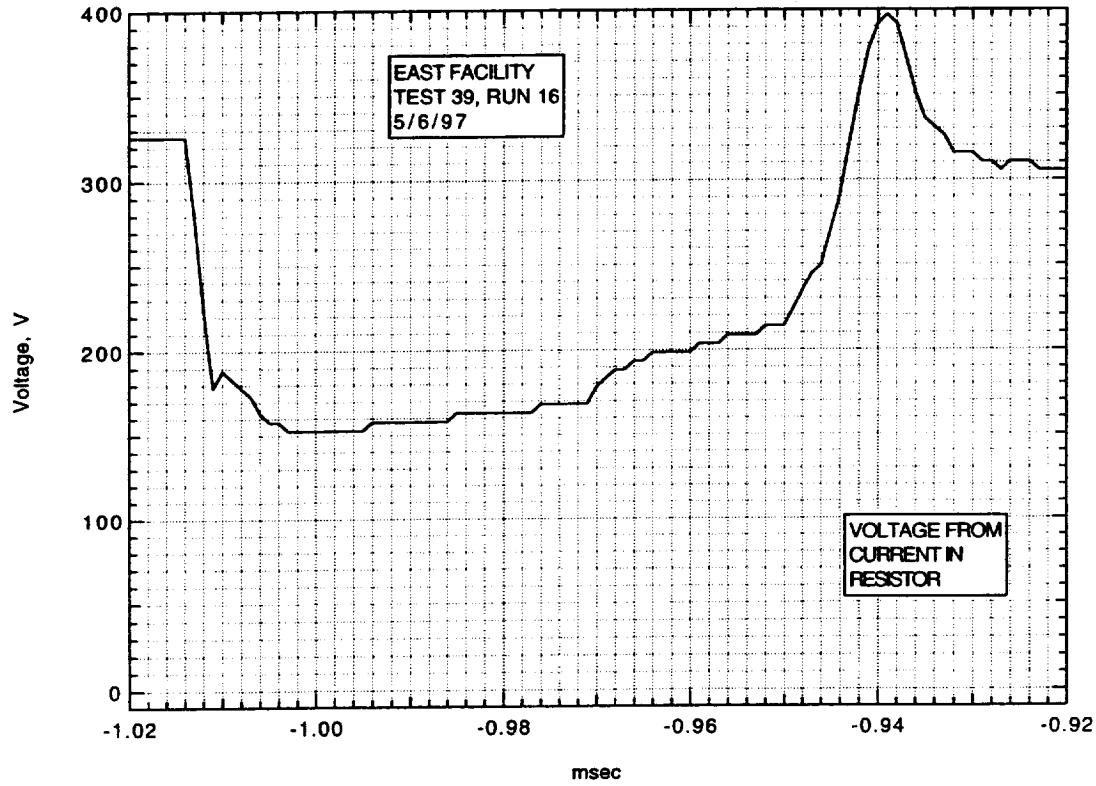

Run 16. Voltage from current in resistor.

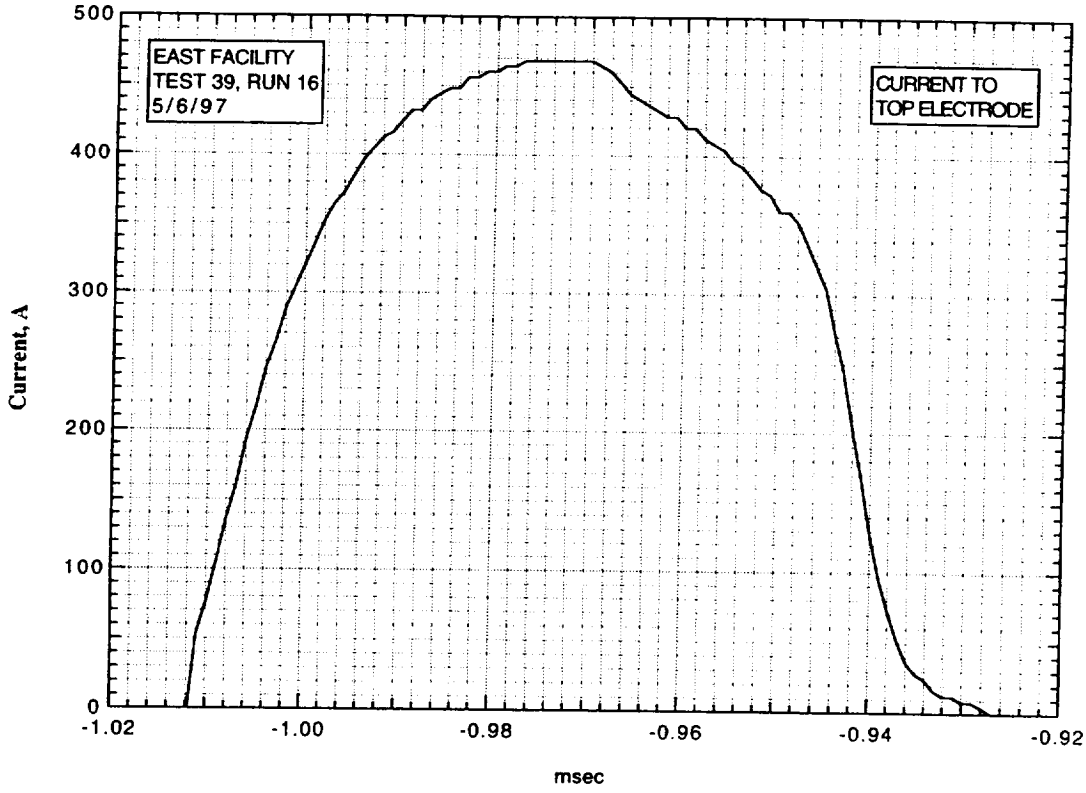

Run 16. Current to top electrode.

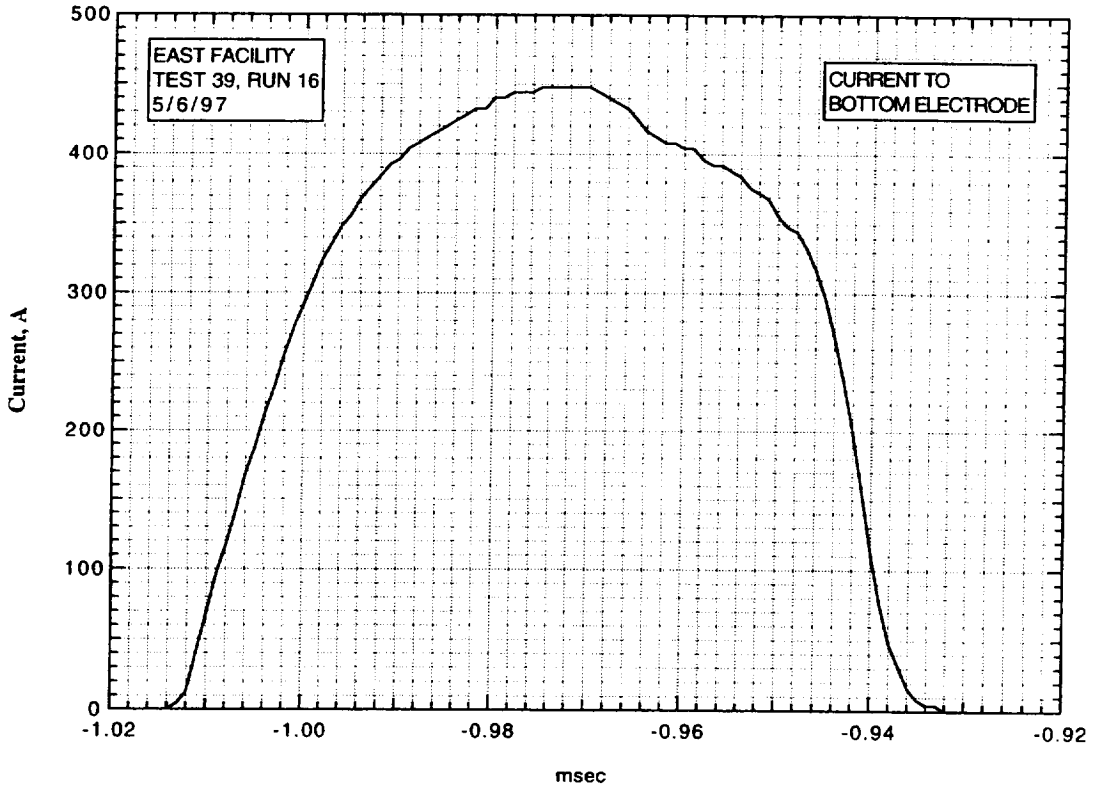

Run 16. Current to bottom electrode.

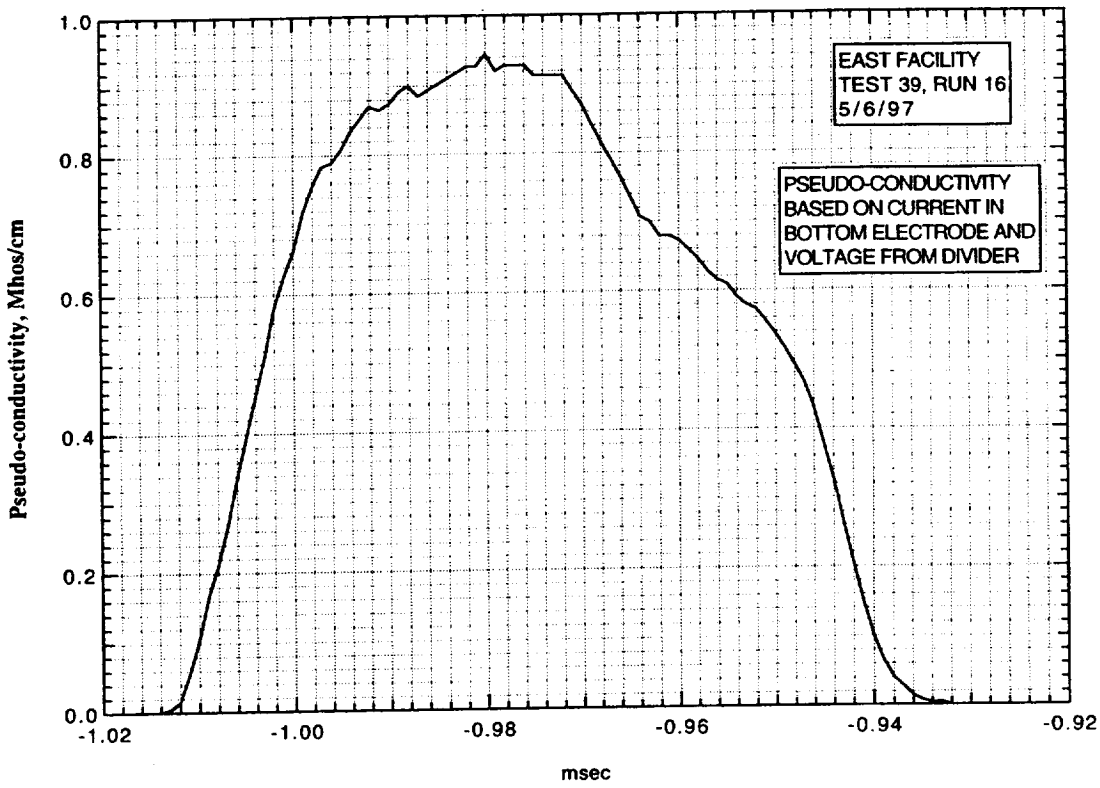

Run 16. Pseudo-conductivity based on current to bottom electrode and voltage from divider.

AIR CONDUCTIVITY MEASUREMENT IN AMES EAST FACILITY

RUN 39/17, 5/7/97

1. Driven tube conditions:

53.2% N_2O, 46.8% N_2,
Total pressure - 5.20 Torr
Measured shock velocity between stns D and F - 4.719 km/sec
Estimated shock velocity at electrodes - 4.540 km/sec
Measured shock pressure at stn D - 2.33 atm
Measured shock pressure at stn F - 1.40 very uncertain
due to large EM noise pickup

2. Electrodes, driven tube dimensions:

Electrode size - 3.10 cm square
Electrode spacing - 3.10 cm
Main diaphragm to electrodes - 454.475 cm
Skimmer nose to electrodes - 39.979 cm
Driven tube diameter - 10.16 cm
Stn D (dn tube) to electrodes (channel) - 77.365 cm
Electrodes (channel) to stn F (channel) - 20.32 cm

3. Nominal test conditions:

Pressure - 2 atm
Voltage across electrodes - 186/146 V

4. Breakdown:

Little or no indication of breakdown.

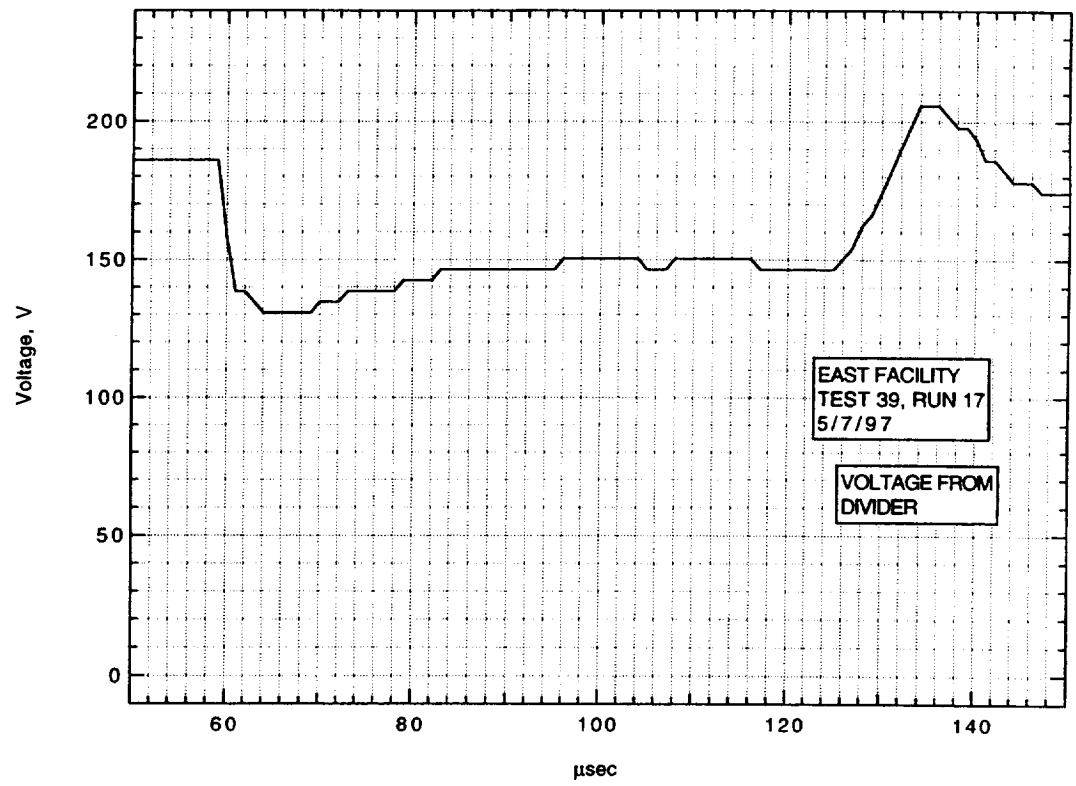

Run 17, voltage across electrodes from divider.

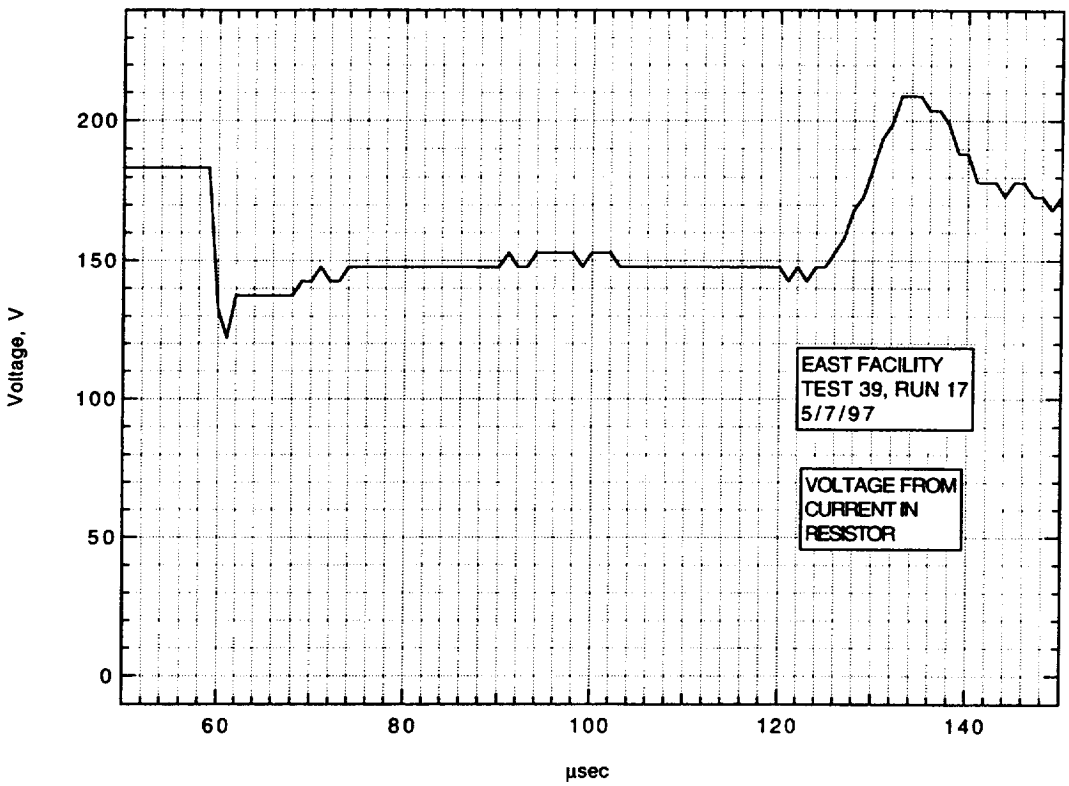

Run 17, voltage across electrodes from current in resistor.

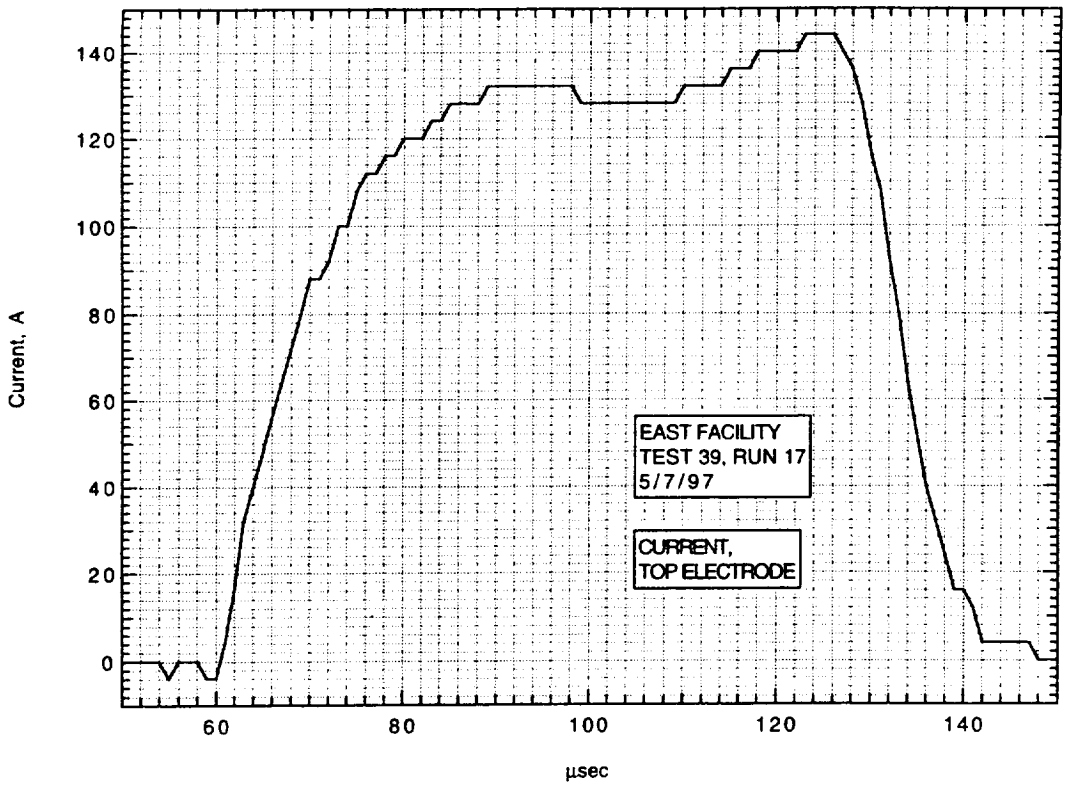

Run 17, current to top electrode.

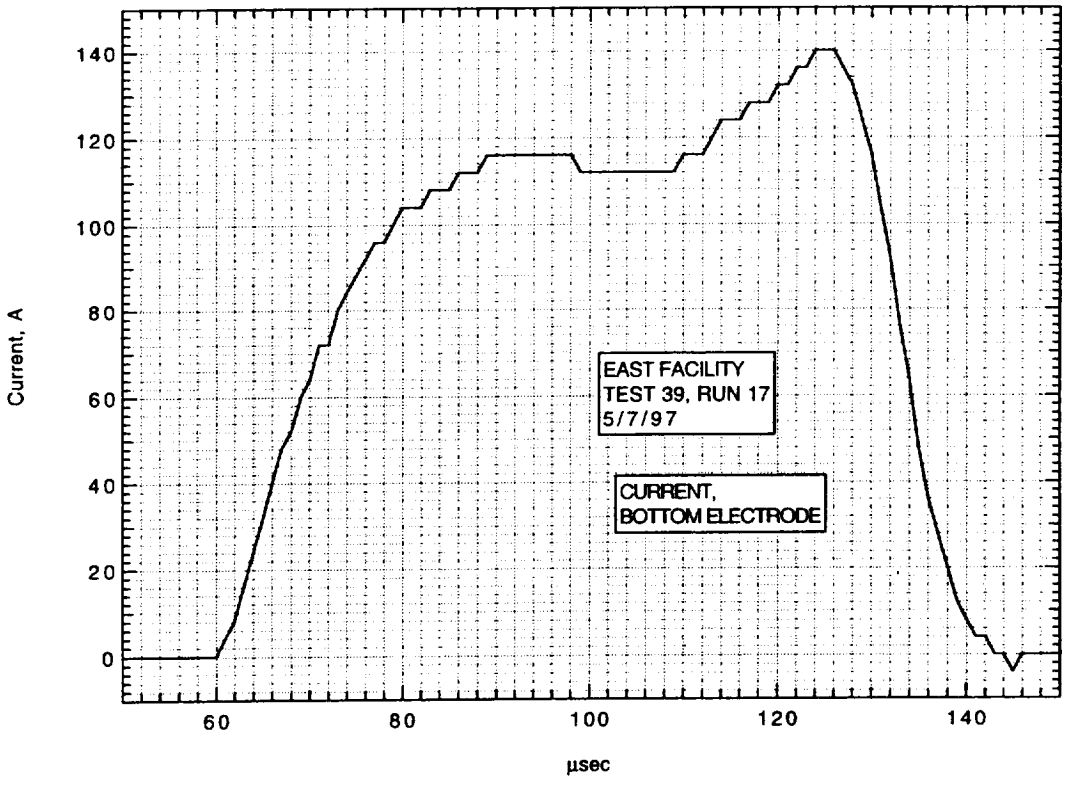

Run 17, current to bottom electrode.

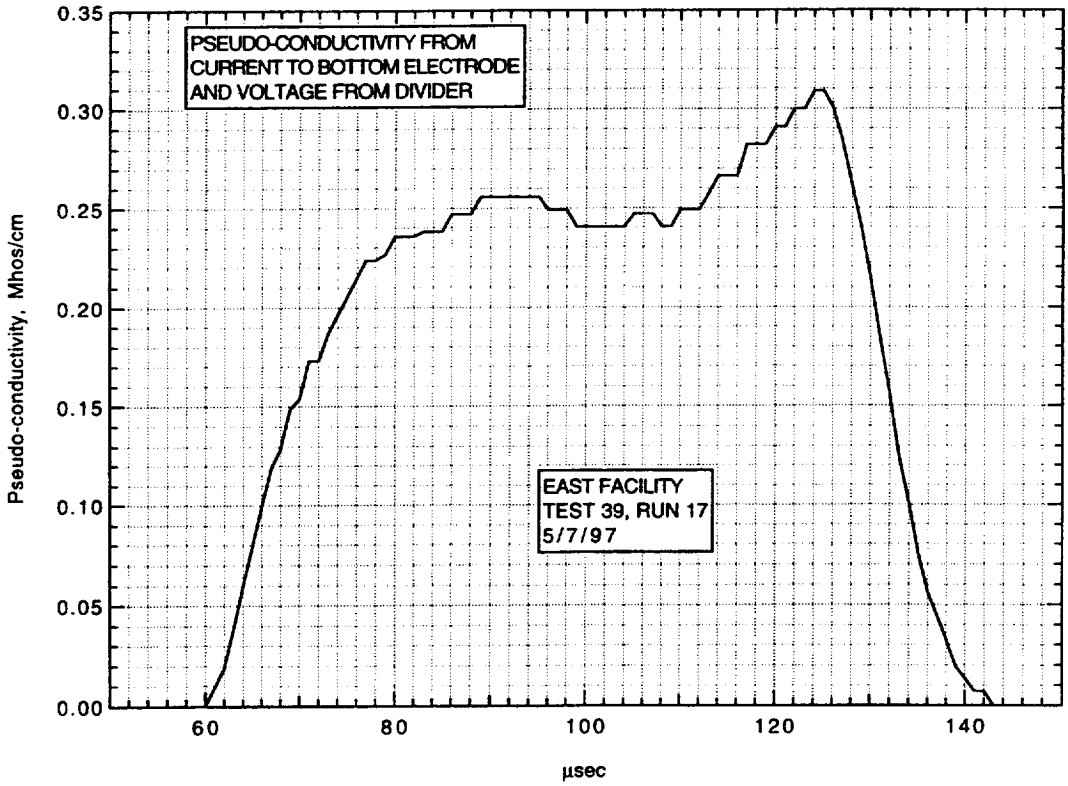

Run 17, pseudo-conductivity from current to bottom electrode and voltage from divider.

AIR CONDUCTIVITY MEASUREMENT IN AMES EAST FACILITY

RUN 39/18, 5/8/97

1. Driven tube conditions:

53.2% N_2O, 46.8% N_2,
Total pressure - 5.20 Torr
Measured shock velocity between stns D and F - 4.909 km/sec
Estimated shock velocity at electrodes - 4.723 km/sec
Measured shock pressure at stn D - 2.55 atm
Measured shock pressure at stn F - 1.47 very uncertain
due to large EM noise pickup

2. Electrodes, driven tube dimensions:

Electrode size - 3.10 cm square
Electrode spacing - 3.10 cm
Main diaphragm to electrodes - 454.475 cm
Skimmer nose to electrodes - 39.979 cm
Driven tube diameter - 10.16 cm
Stn D (dn tube) to electrodes (channel) - 77.365 cm
Electrodes (channel) to stn F (channel) - 20.32 cm

3. Nominal test conditions:

Pressure - 2 atm
Voltage across electrodes - 277/163 V

4. Breakdown:

Little or no indication of breakdown.

Run no: 17 **Date:** 5/7/97 **Shock press. at D:** 2.33 atm
Shock vel. at E: 4.54 km/sec **Voltage at start of current flow:** 186 V

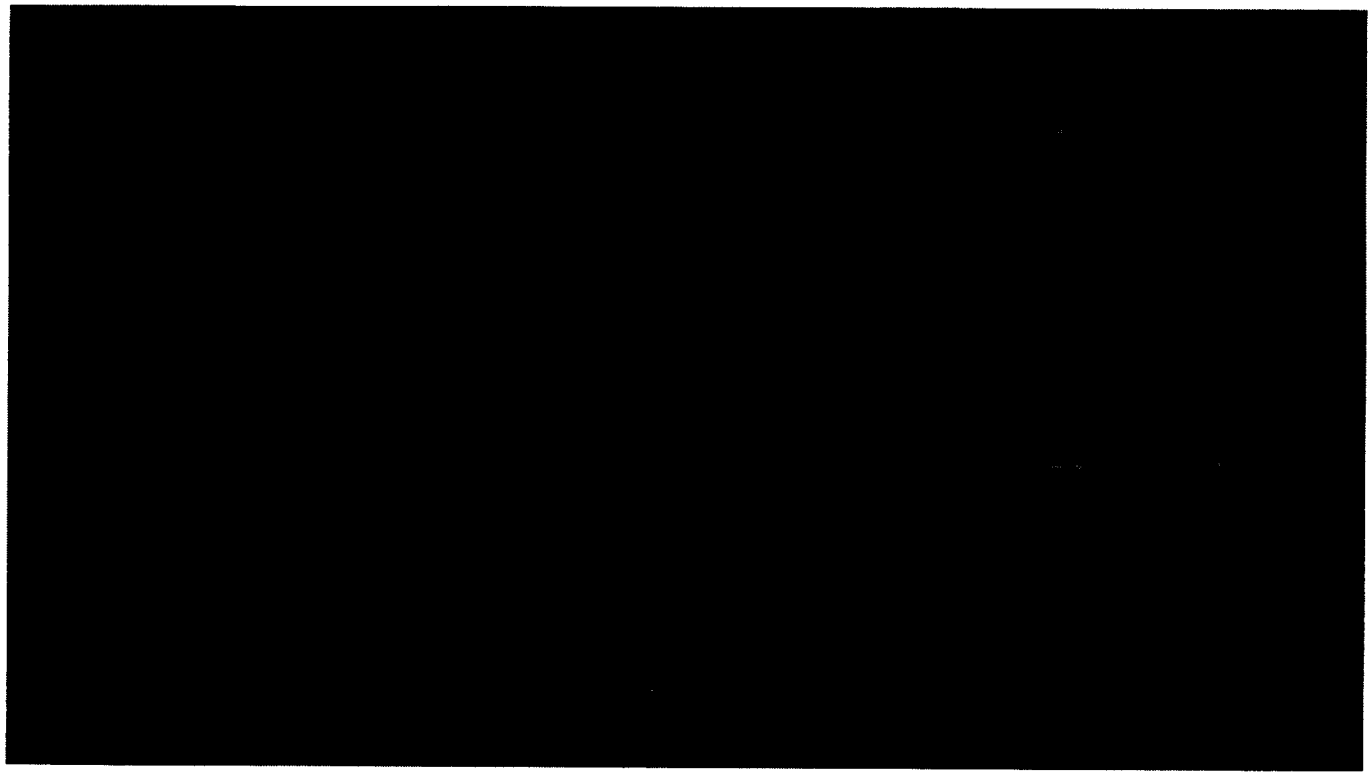

Frame:	**2**	**4**	**6**	**8**
Time:	-1.8	6.2	14.2	22.2
Mach no:				
Frame:	**1**	**3**	**5**	7
Time:	-5.8	2.2	10.2	18.2
Mach no:				

V_I: km/sec V_{CAV}: 4.8 km/sec

IMACON image of the shock-heated test gas flow in the electrode region. The time is measured from the start of the current flow. Mach numbers and velocities are deduced from the image as explained in section A.2.5.3.

Run no: 18 **Date:** 5/8/97 **Shock press. at D:** 2.55 atm
Shock vel. at E: 4.72 km/sec **Voltage at start of current flow:** 277 V

Frame:	**2**	**4**	**6**	**8**
Time:	5.2	13.2	21.2	29.2
Mach no:	2.24	2.32		
Frame:	**1**	**3**	**5**	**7**
Time:	1.2	9.2	17.2	25.2
Mach no:		2.42	2.48	

V_I: 4.6 km/sec V_{CAV}: 4.96 km/sec

IMACON image of the shock-heated test gas flow in the electrode region. The time is measured from the start of the current flow. Mach numbers and velocities are deduced from the image as explained in section A.2.5.3.

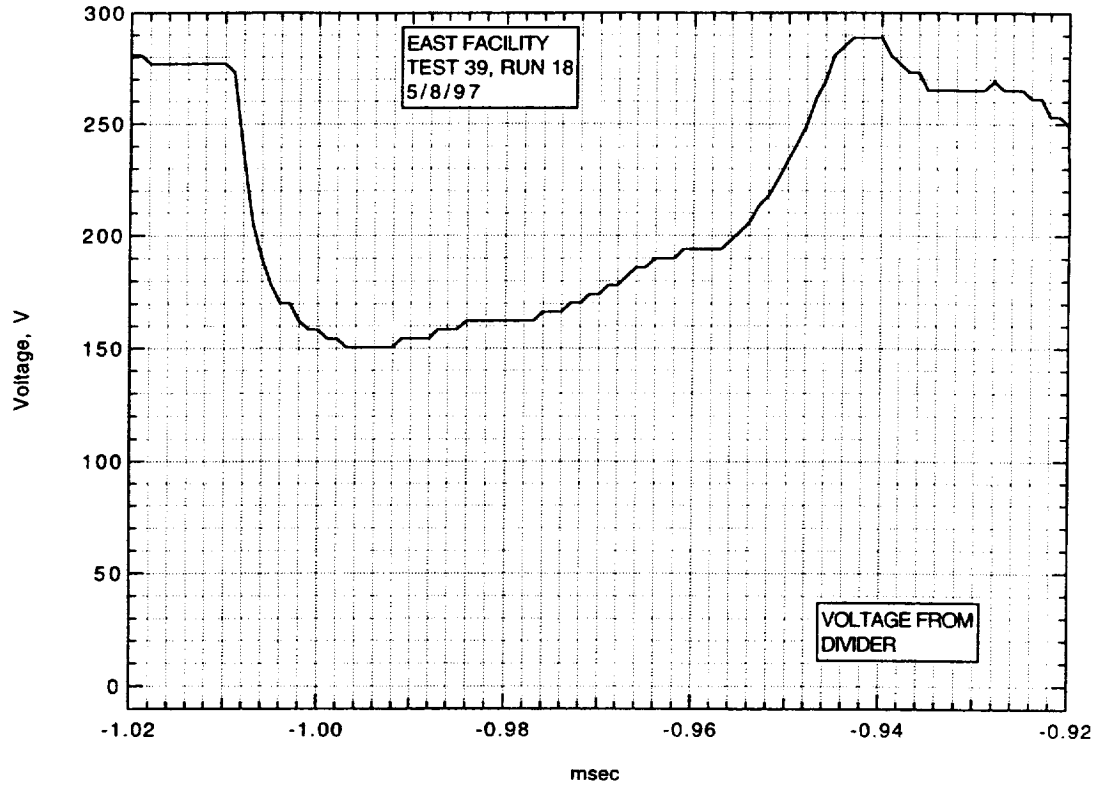

Run 18. Voltage from divider.

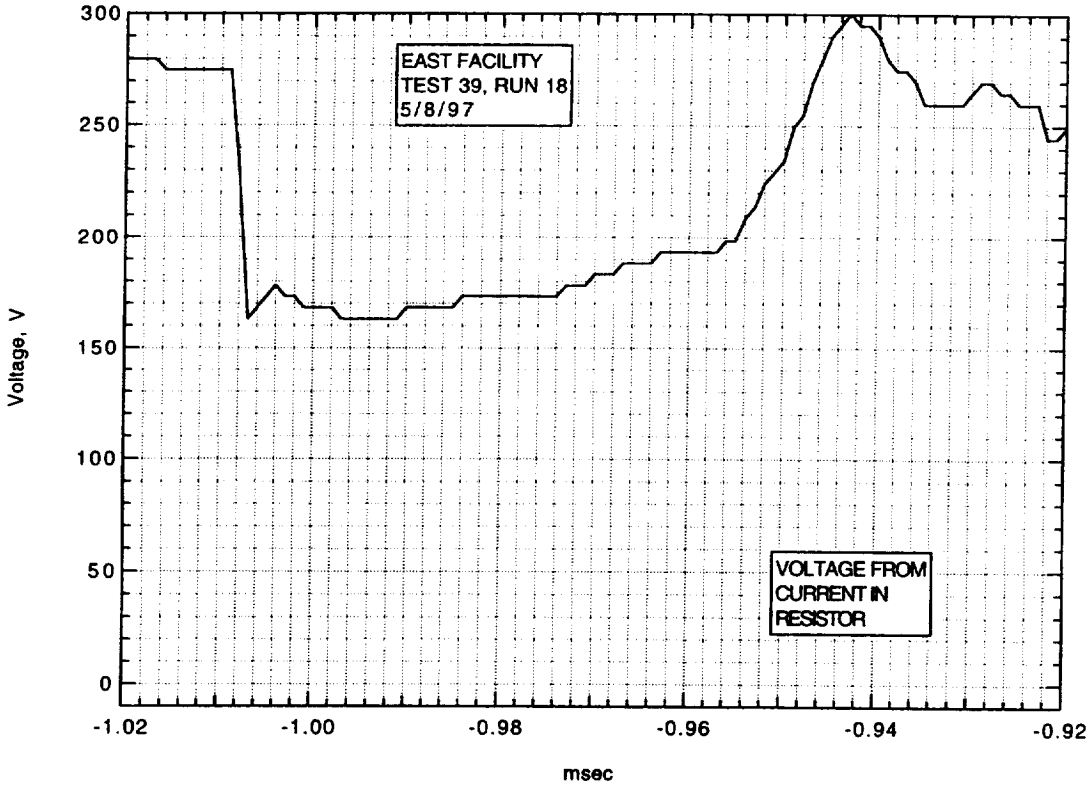

Run 18. Voltage from current in resistor.

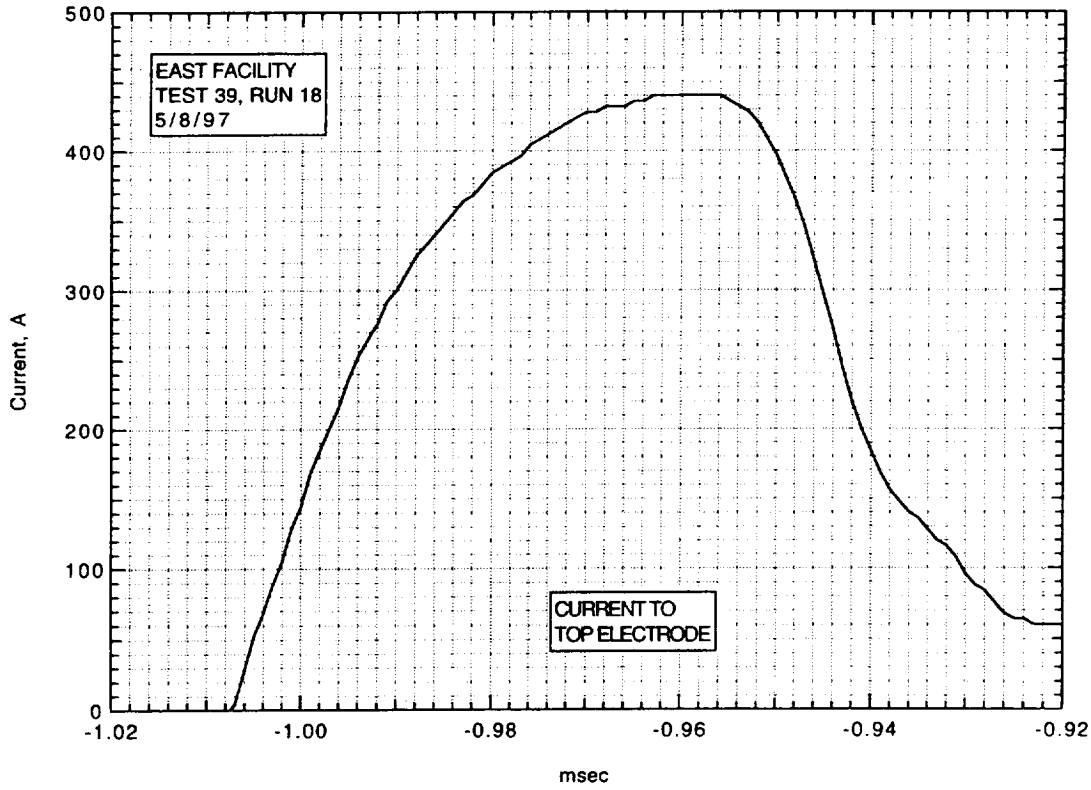

Run 18. Current to top electrode.

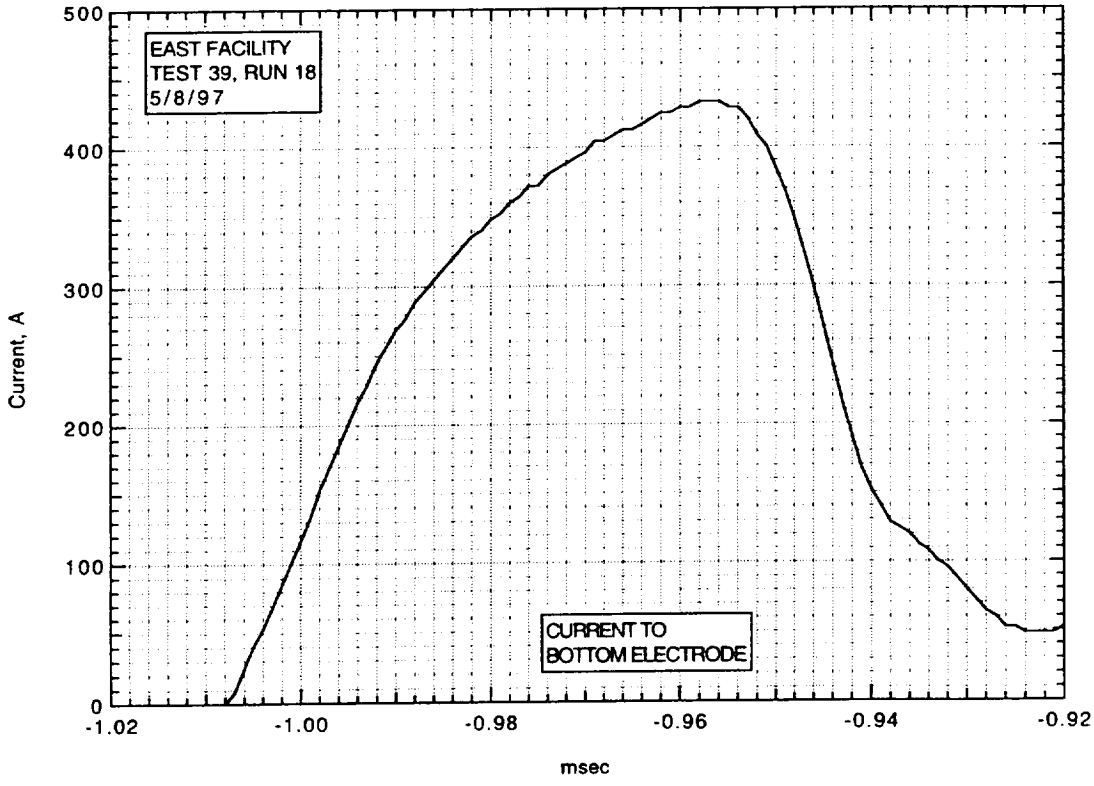

Run 18. Current to bottom electrode.

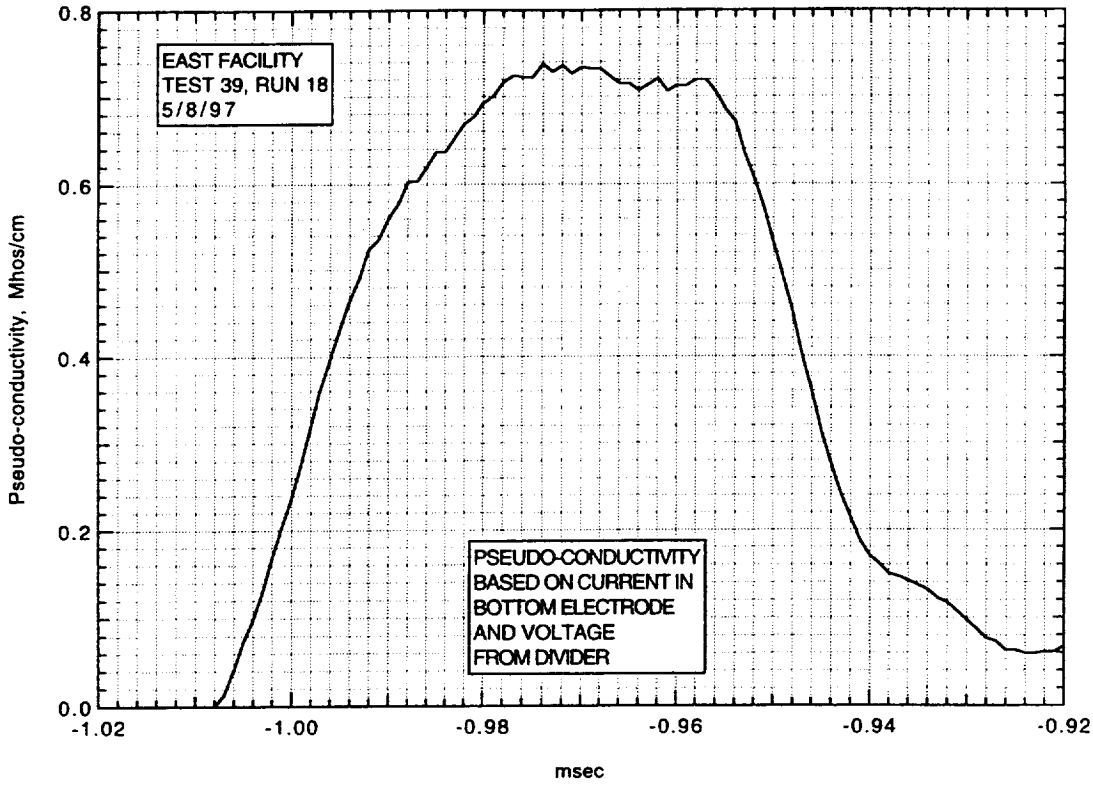

Run 18. Pseudo-conductivity based on current to bottom electrode and voltage from divider.

AIR CONDUCTIVITY MEASUREMENT IN AMES EAST FACILITY

RUN 39/19, 5/9/97

1. Driven tube conditions:

53.2% N_2O, 46.8% N_2,
Total pressure - 5.20 Torr
Measured shock velocity between stns D and F - 4.742 km/sec
Estimated shock velocity at electrodes - 4.563 km/sec
Measured shock pressure at stn D - 2.29 atm
Measured shock pressure at stn F - 2.19 very uncertain
due to large EM noise pickup

2. Electrodes, driven tube dimensions:

Electrode size - 3.10 cm square
Electrode spacing - 3.10 cm
Main diaphragm to electrodes - 454.475 cm
Skimmer nose to electrodes - 39.979 cm
Driven tube diameter - 10.16 cm
Stn D (dn tube) to electrodes (channel) - 77.365 cm
Electrodes (channel) to stn F (channel) - 20.32 cm

3. Nominal test conditions:

Pressure - 2 atm
Voltage across electrodes - 371/219 V

4. Breakdown:

Little or no indication of breakdown.

Run no: 19 **Date:** 5/9/97 **Shock press. at D:** 2.29 atm
Shock vel. at E: 4.56 km/sec **Voltage at start of current flow:** 371 V

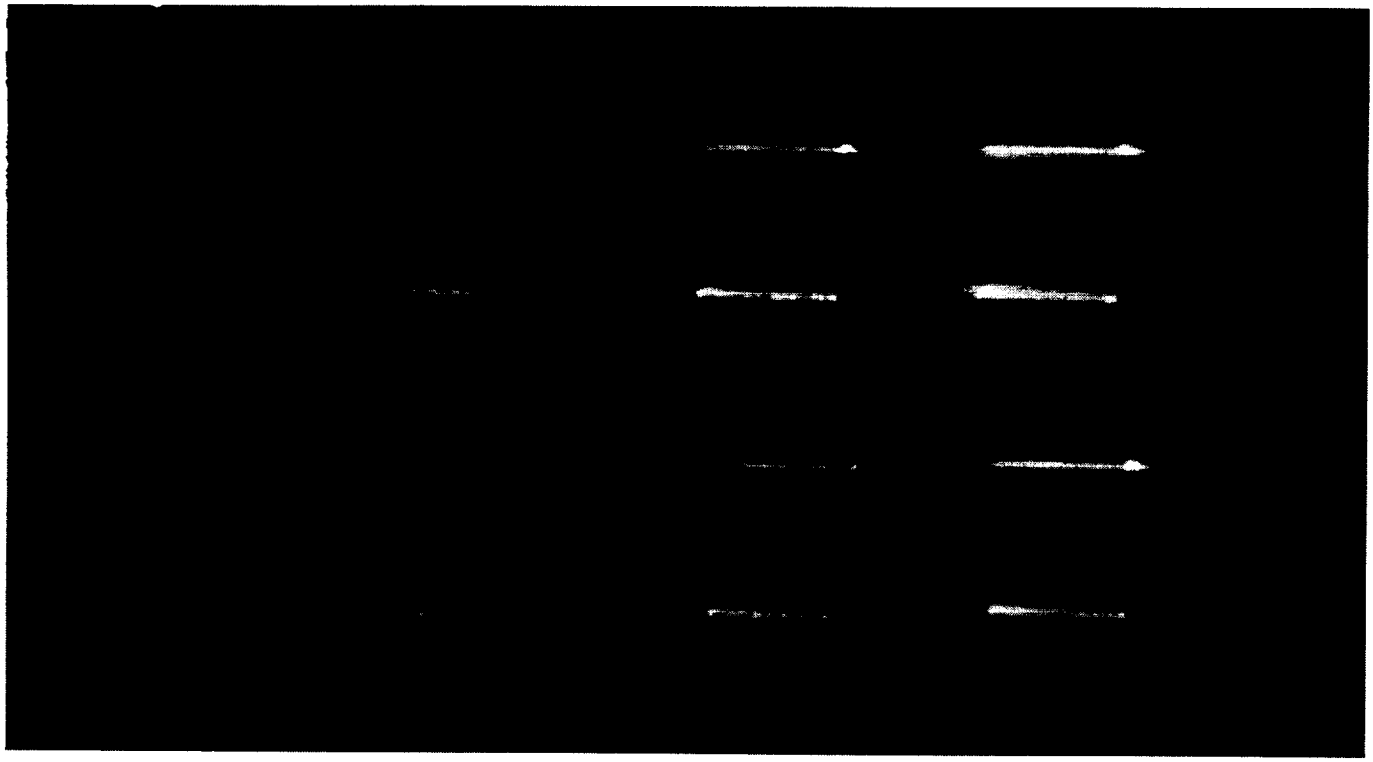

Frame:	**2**	**4**	**6**	**8**
Time:	-0.6	7.4	15.4	23.4
Mach no:			2.33	
Frame:	**1**	**3**	**5**	7
Time:	-4.6	3.4	11.4	19.4
Mach no:			2.33	

V_I: 4.6 km/sec V_{CAV}: 4.84 km/sec

IMACON image of the shock-heated test gas flow in the electrode region. The time is measured from the start of the current flow. Mach numbers and velocities are deduced from the image as explained in section A.2.5.3.

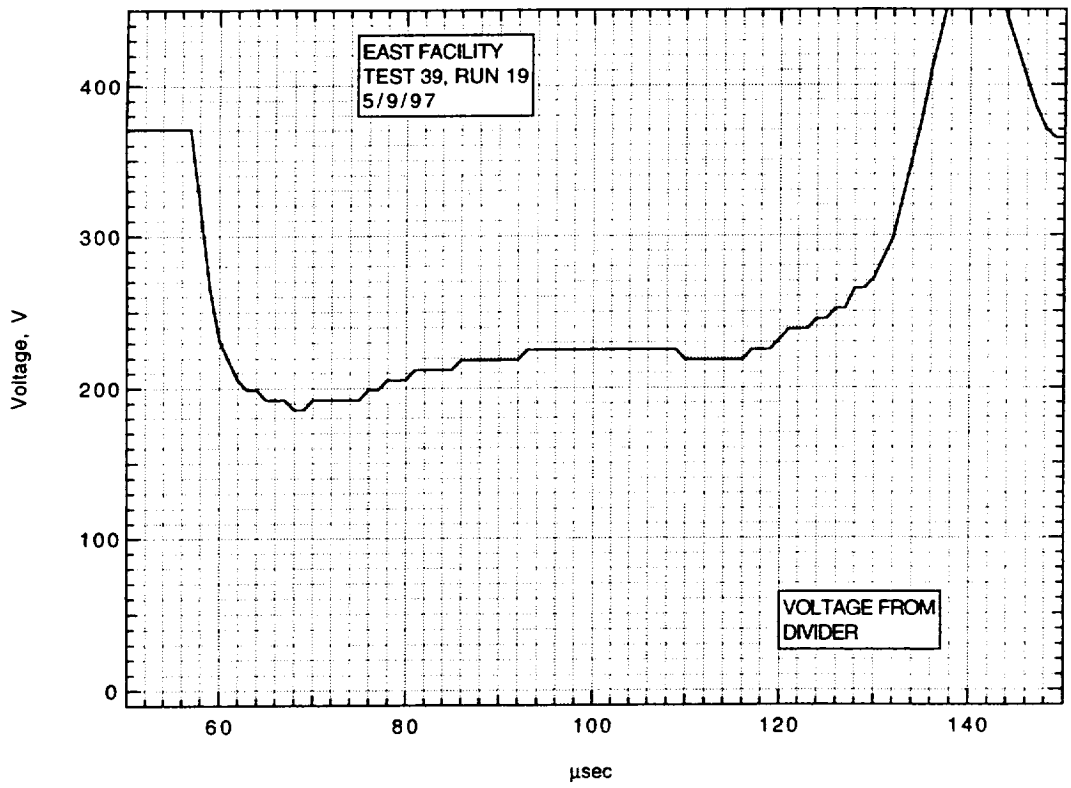

Run 19. Voltage from divider.

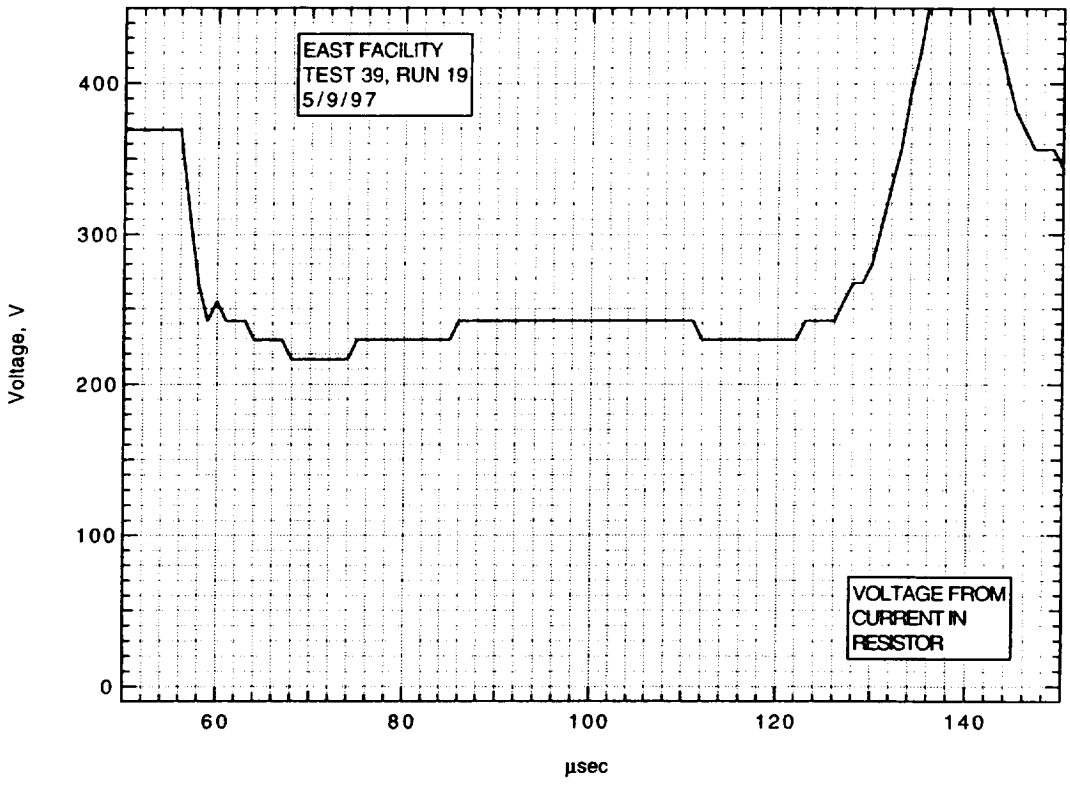

Run 19. Voltage from current in resistor.

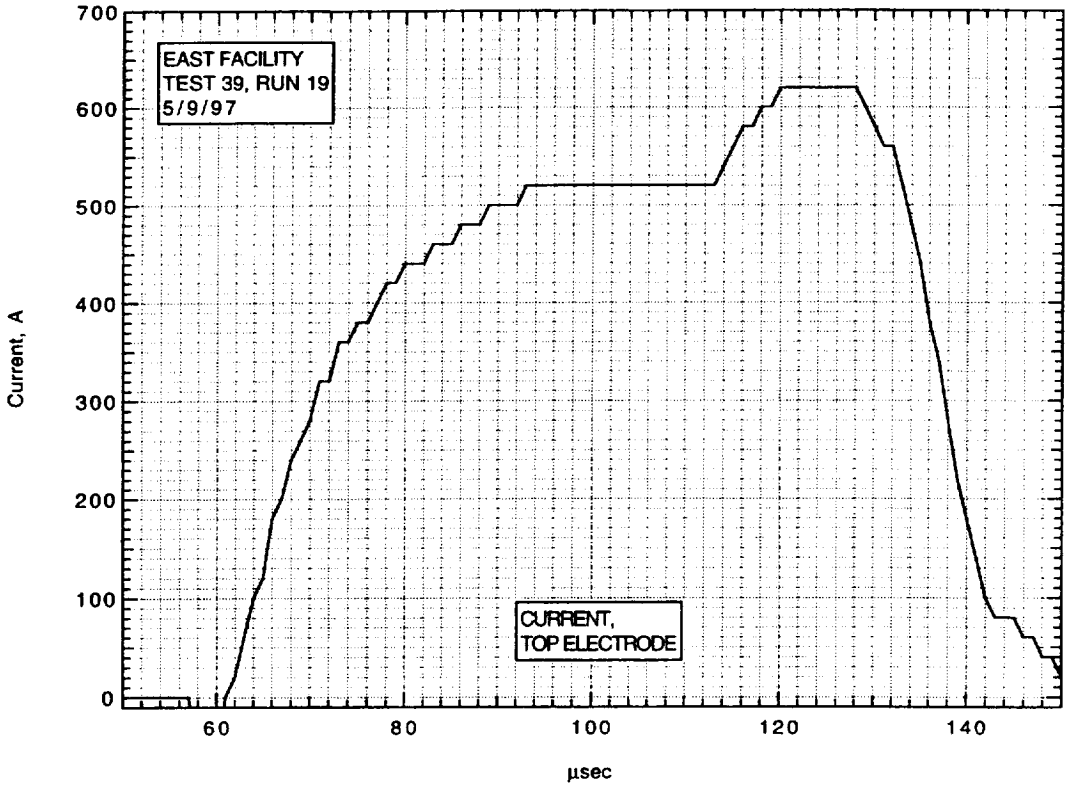

Run 19. Current to top electrode.

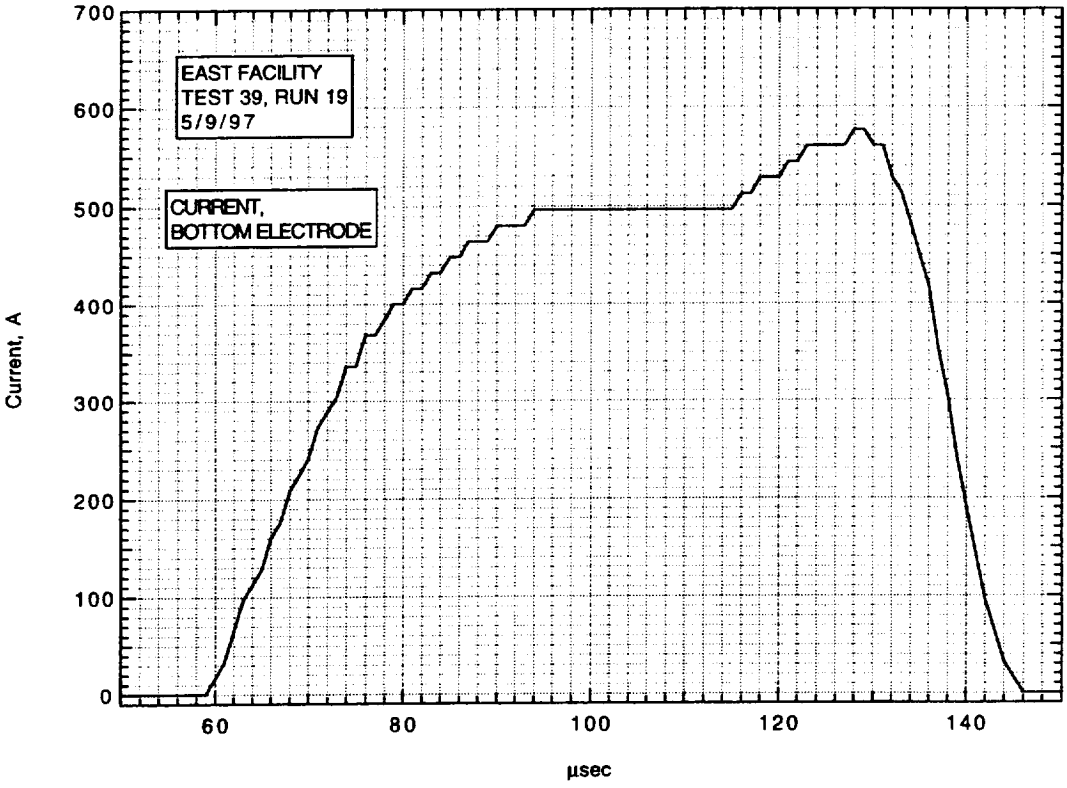

Run 19. Current to bottom electrode.

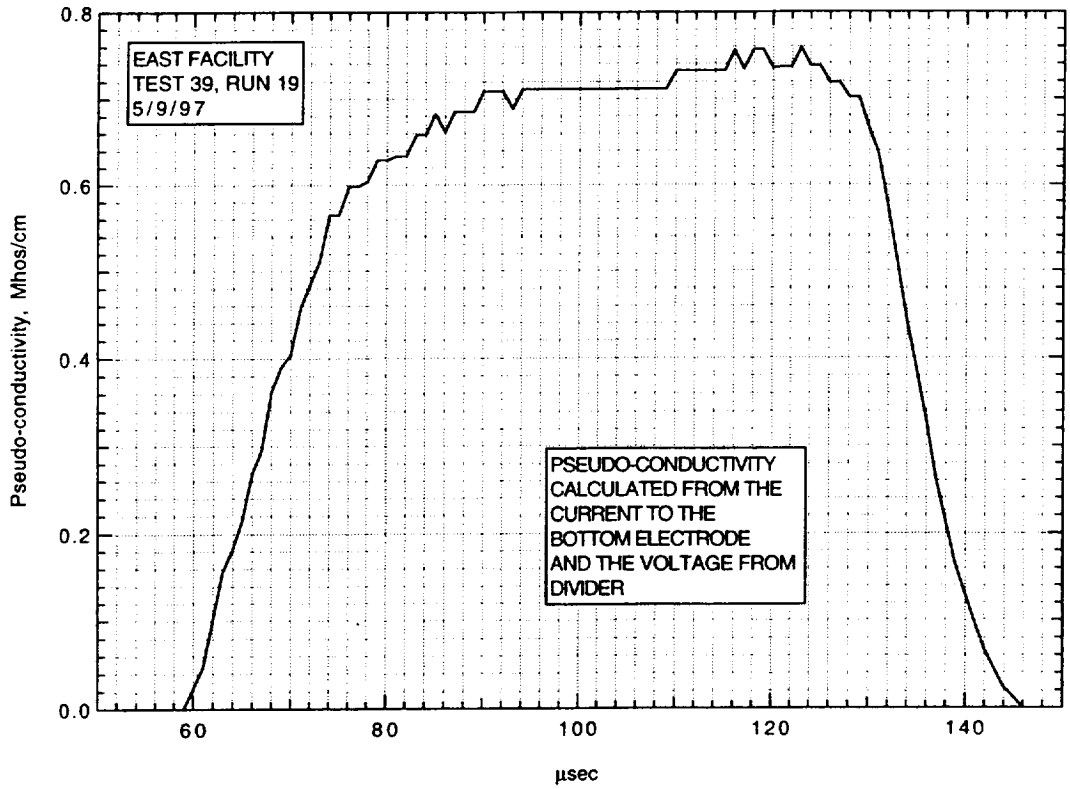

Run 19. Pseudo-conductivity based on current to bottom electrode and voltage from divider.

AIR CONDUCTIVITY MEASUREMENT IN AMES EAST FACILITY

RUN 39/20, 5/12/97

1. Driven tube conditions:

53.2% N_2O, 46.8% N_2,
Total pressure - 5.20 Torr
Measured shock velocity between stns D and F - 4.788 km/sec
Estimated shock velocity at electrodes - 4.607 km/sec
Measured shock pressure at stn D - 2.43 atm
Measured shock pressure at stn F - 2.23 atm

2. Electrodes, driven tube dimensions:

Electrode size - 3.10 cm square
Electrode spacing - 3.10 cm
Main diaphragm to electrodes - 454.475 cm
Skimmer nose to electrodes - 39.979 cm
Driven tube diameter - 10.16 cm
Stn D (dn tube) to electrodes (channel) - 77.365 cm
Electrodes (channel) to stn F (channel) - 20.32 cm

3. Nominal test conditions:

Pressure - 2 atm
Voltage across electrodes - 0/0 V

4. Breakdown:

No voltage applied to electrodes.

Run no: 20 **Date:** 5/12/97 **Shock press. at D:** 2.43 atm
Shock vel. at E: 4.61 km/sec **Voltage at start of current flow:** 0 V

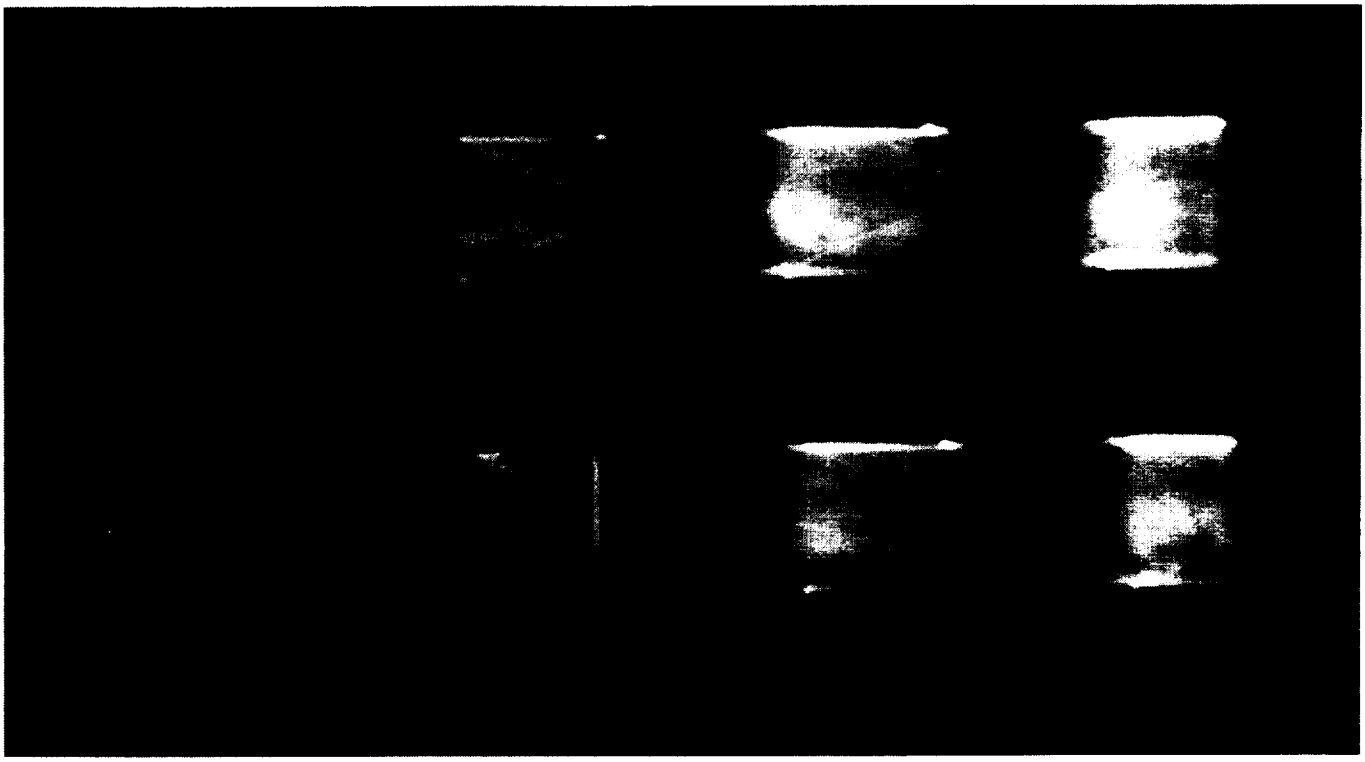

Frame:	**2**	**4**	**6**	**8**
Time:	0.9	8.9	16.9	24.9
Mach no:		2.46	2.42	
Frame:	**1**	**3**	**5**	**7**
Time:	-3.1	4.9	12.9	20.9
Mach no:		2.42	2.42	

V_I: 4.6 km/sec V_{CAV}: 4.82 km/sec

IMACON image of the shock-heated test gas flow in the electrode region. The time is measured from the start of the current flow. Mach numbers and velocities are deduced from the image as explained in section A.2.5.3.

AIR CONDUCTIVITY MEASUREMENT IN AMES EAST FACILITY

RUN 39/21, 5/13/97

1. Driven tube conditions:

53.2% N_2O, 46.8% N_2,
Total pressure - 5.20 Torr
Measured shock velocity between stns D and F - 4.860 km/sec
Estimated shock velocity at electrodes - 4.676 km/sec
Measured shock pressure at stn D - 2.86 atm
Measured shock pressure at stn F - N/A due to large EM noise pickup

2. Electrodes, driven tube dimensions:

Electrode size - 3.10 cm square
Electrode spacing - 3.10 cm
Main diaphragm to electrodes - 454.475 cm
Skimmer nose to electrodes - 39.979 cm
Driven tube diameter - 10.16 cm
Stn D (dn tube) to electrodes (channel) - 77.365 cm
Electrodes (channel) to stn F (channel) - 20.32 cm

3. Nominal test conditions:

Pressure - 2 atm
Voltage across electrodes - 229/143 V

4. Breakdown:

Little or no indication of breakdown.

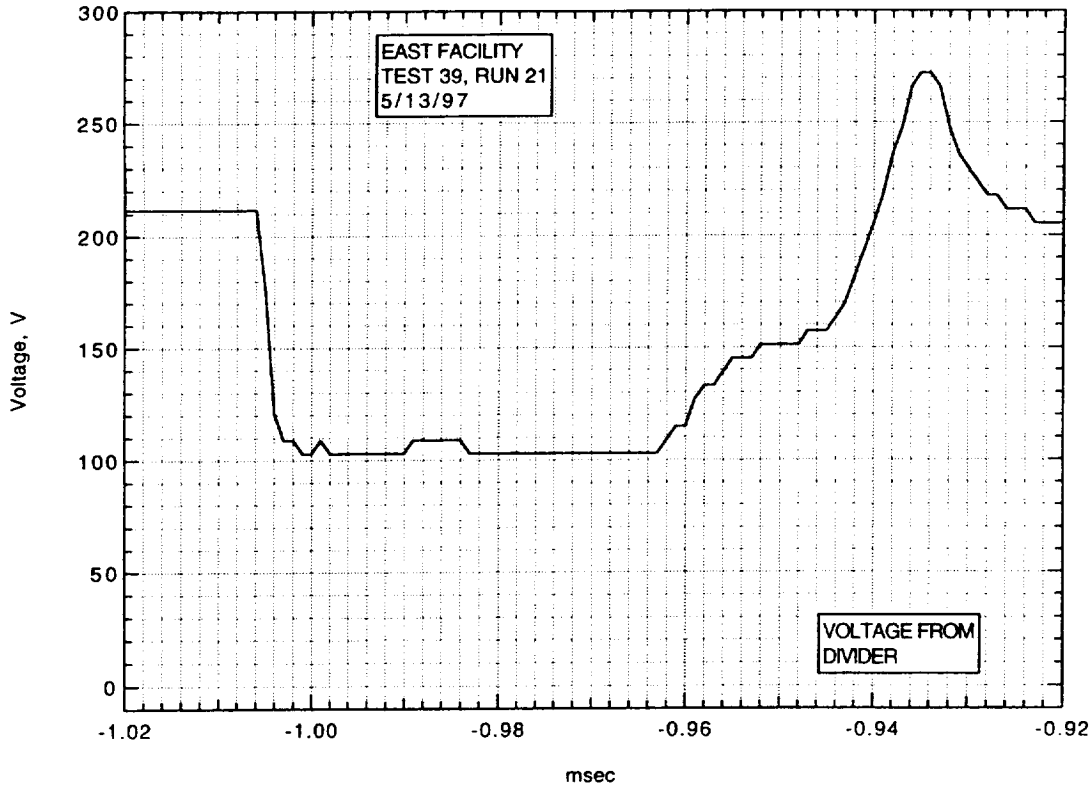

Run 21. Voltage from divider.

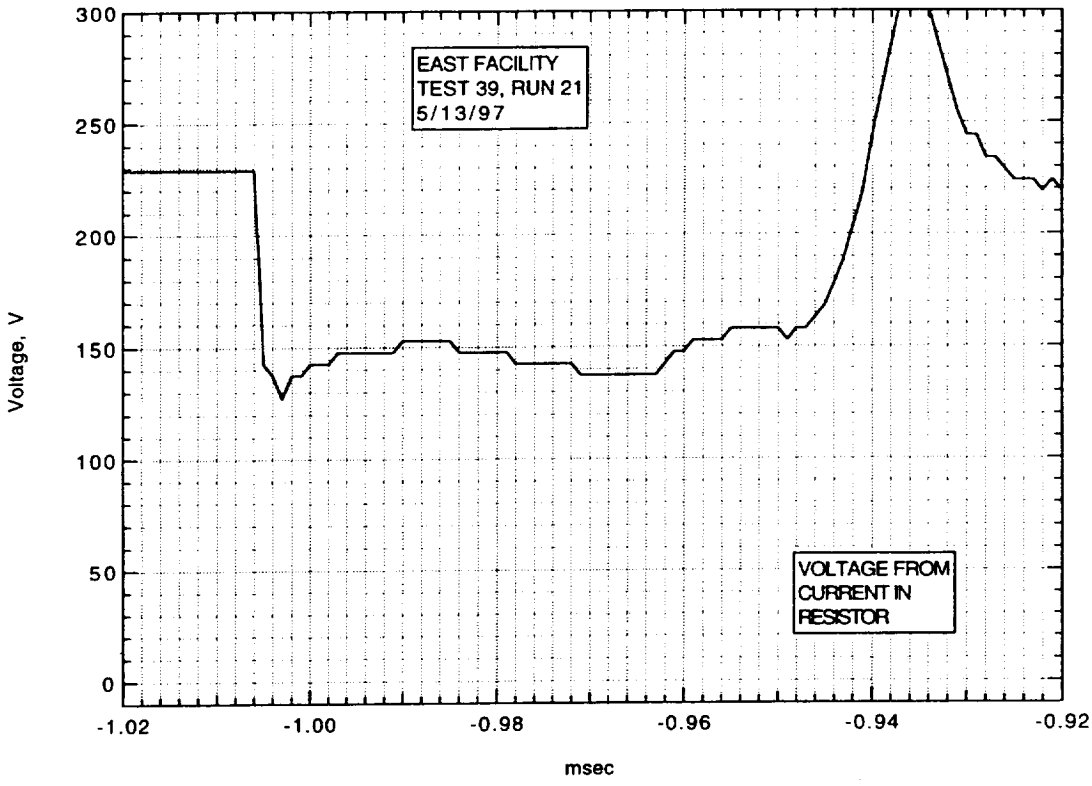

Run 21. Voltage from current in resistor.

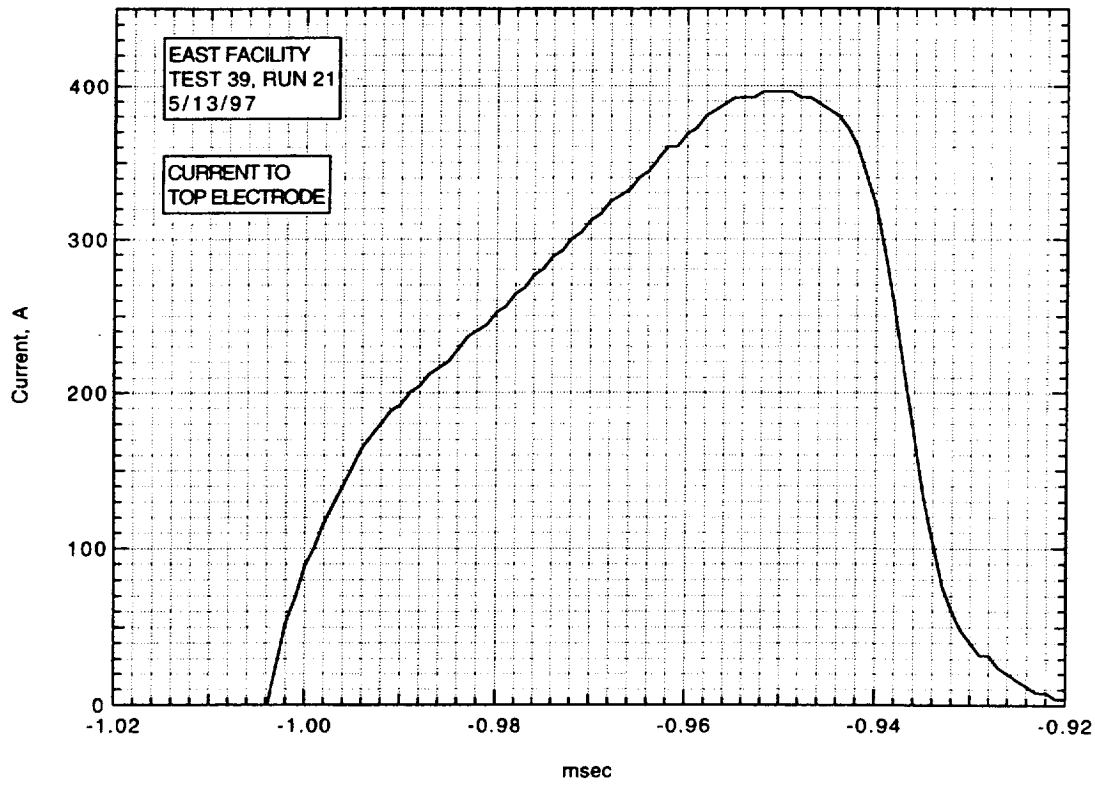

Run 21. Current to top electrode.

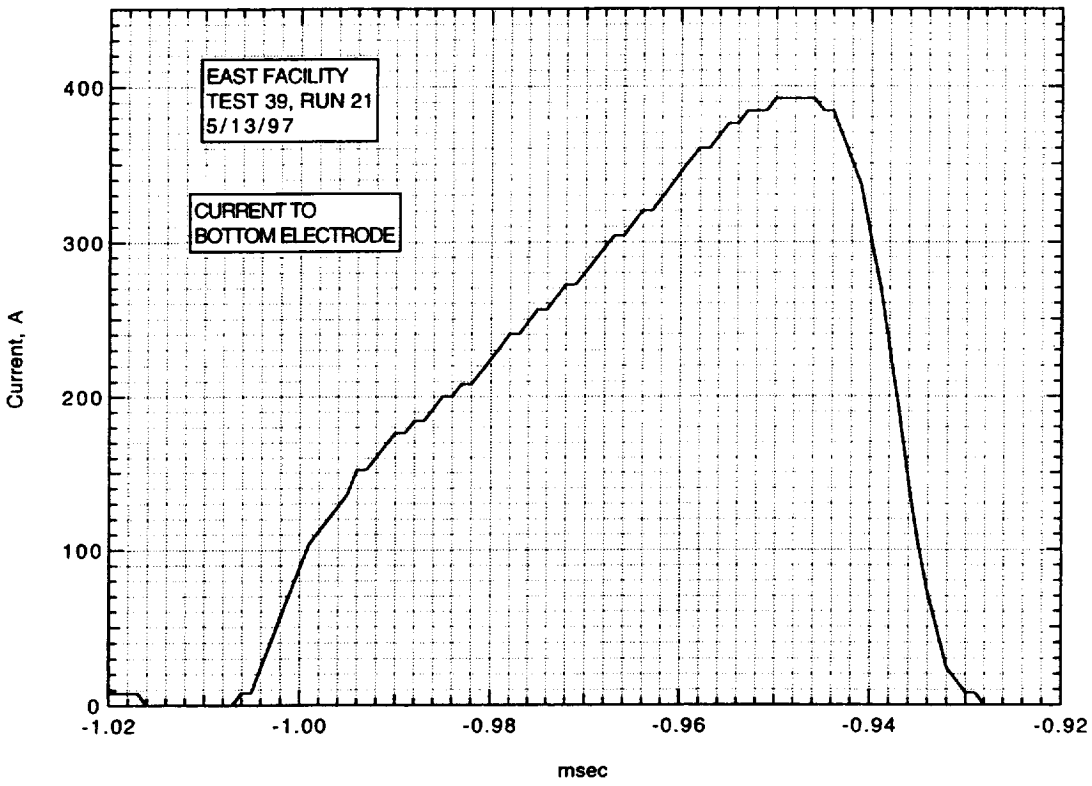

Run 21. Current to bottom electrode.

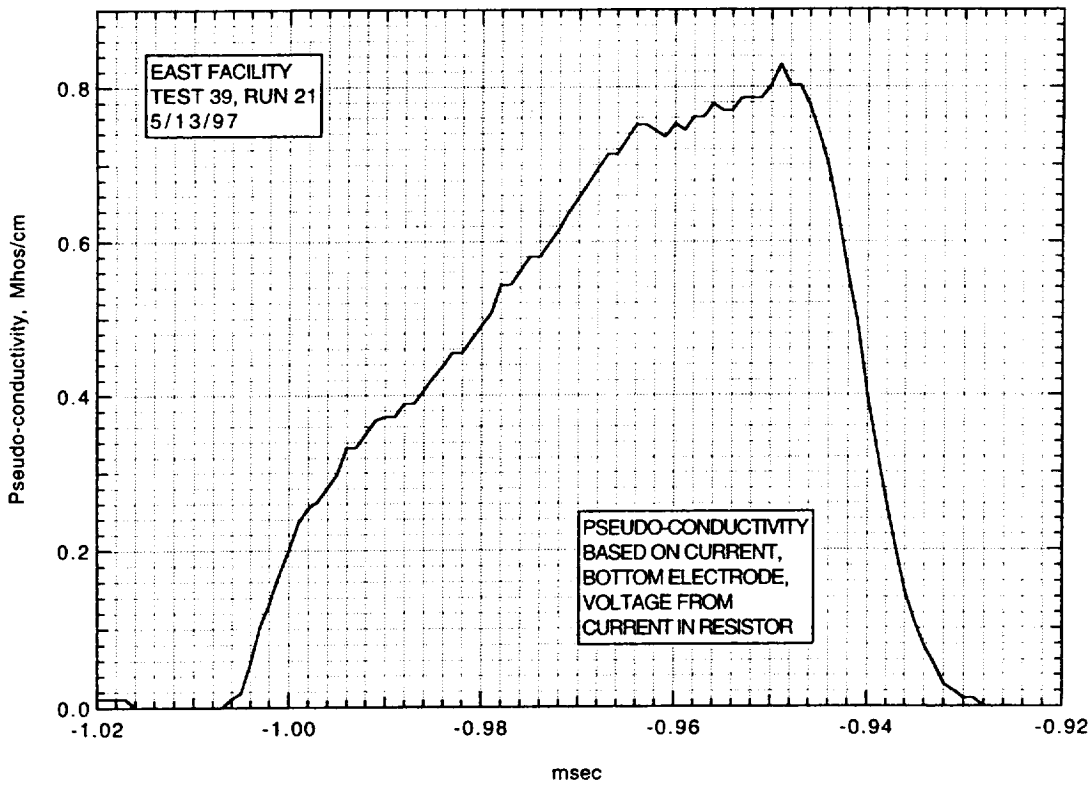

Run 21. Pseudo-conductivity based on current to bottom electrode and voltage from current in resistor.

AIR CONDUCTIVITY MEASUREMENT IN AMES EAST FACILITY

RUN 39/22, 5/13/97

1. Driven tube conditions:

53.2% N_2O, 46.8% N_2,
Total pressure - 5.20 Torr
Measured shock velocity between stns D and F - 4.933 km/sec
Estimated shock velocity at electrodes - 4.747 km/sec
Measured shock pressure at stn D - 2.76 atm
Measured shock pressure at stn F - N/A due to large EM noise pickup

2. Electrodes, driven tube dimensions:

Electrode size - 3.10 cm square
Electrode spacing - 3.10 cm
Main diaphragm to electrodes - 454.475 cm
Skimmer nose to electrodes - 39.979 cm
Driven tube diameter - 10.16 cm
Stn D (dn tube) to electrodes (channel) - 77.365 cm
Electrodes (channel) to stn F (channel) - 20.32 cm

3. Nominal test conditions:

Pressure - 2 atm
Voltage across electrodes - 520/318 V

4. Breakdown:

Little or no indication of breakdown.

Run no: 22 **Date:** 5/13/97 **Shock press. at D:** 2.76 atm
Shock vel. at E: 4.75 km/sec **Voltage at start of current flow:** 509 V

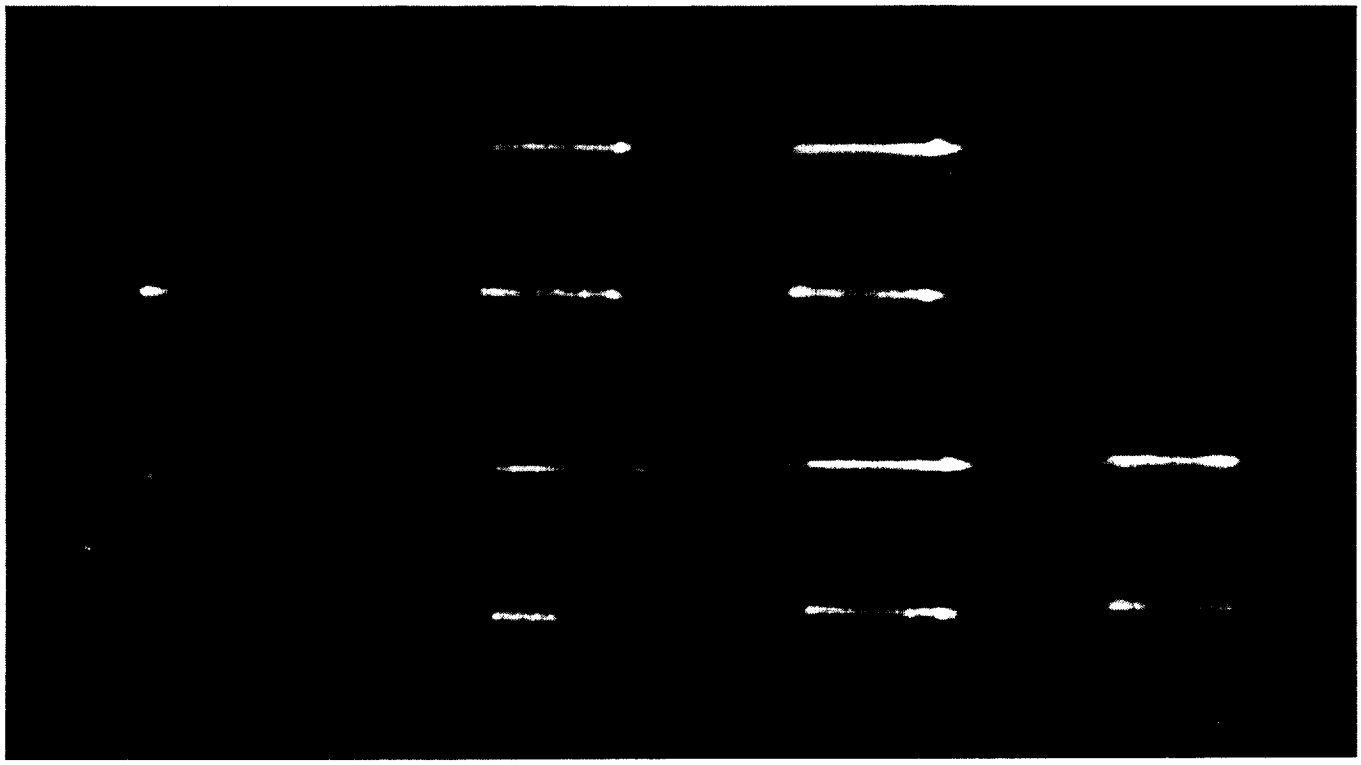

Frame:	**2**	**4**	**6**	**8**
Time:	2.9	10.9	18.9	26.9
Mach no:				
Frame:	**1**	**3**	**5**	**7**
Time:	-1.1	6.9	14.9	22.9
Mach no:				

V_I: km/sec V_{CAV}: km/sec

IMACON image of the shock-heated test gas flow in the electrode region. The time is measured from the start of the current flow. Mach numbers and velocities are deduced from the image as explained in section A.2.5.3.

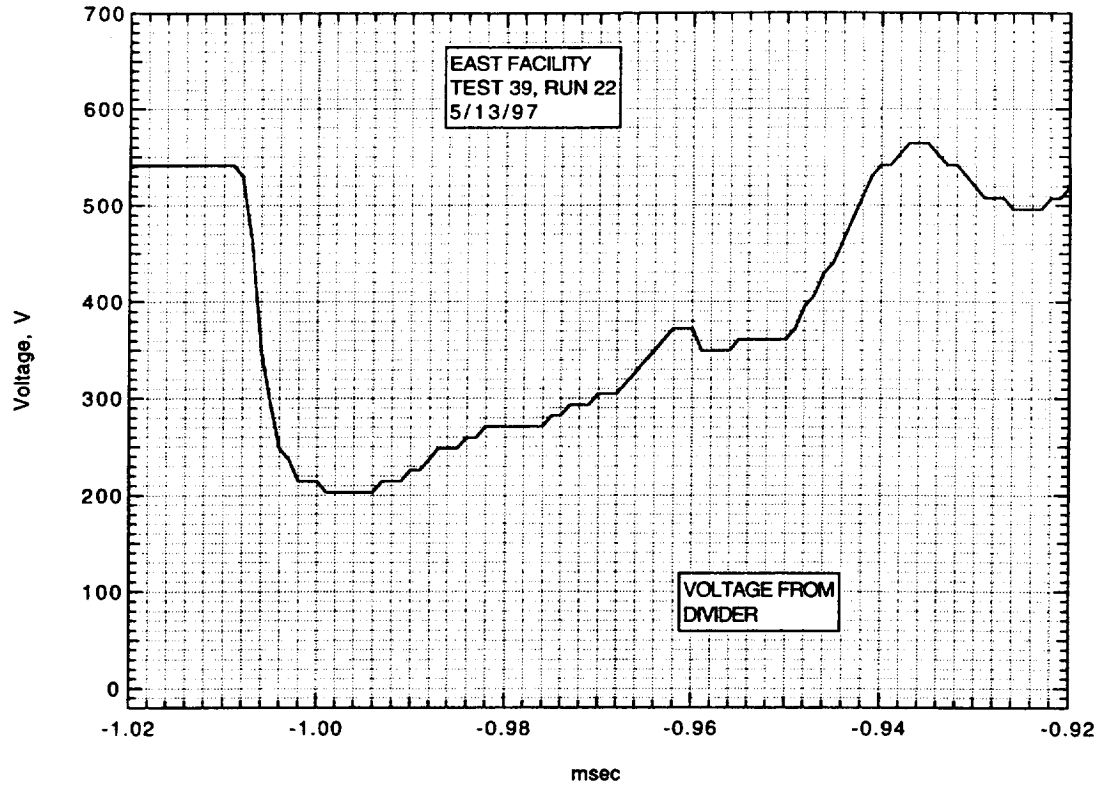

Run 22. Voltage from divider.

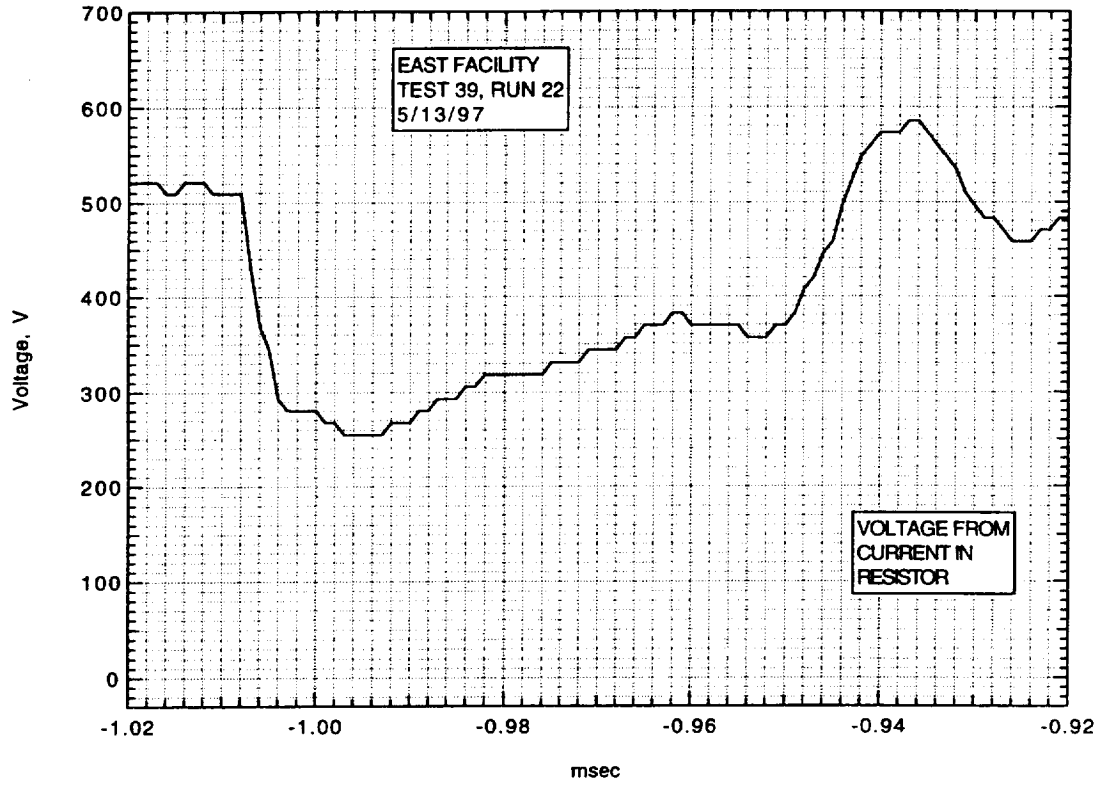

Run 22. Voltage from current in resistor.

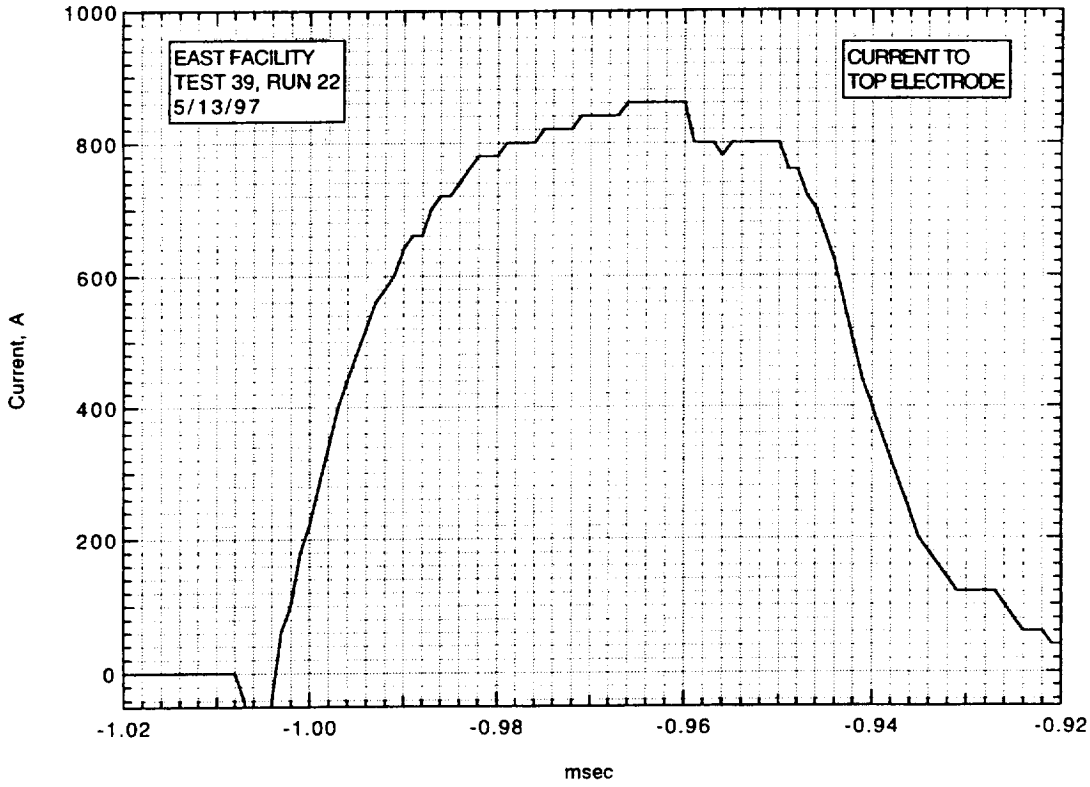

Run 22. Current to top electrode.

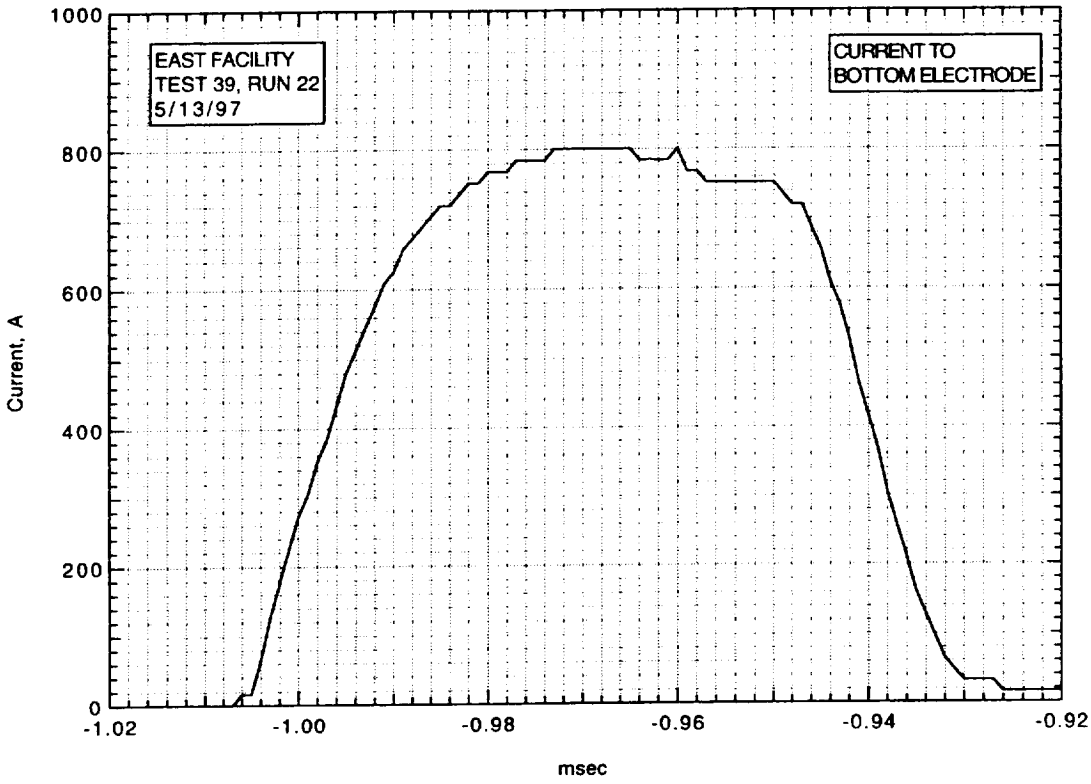

Run 22. Current to bottom electrode.

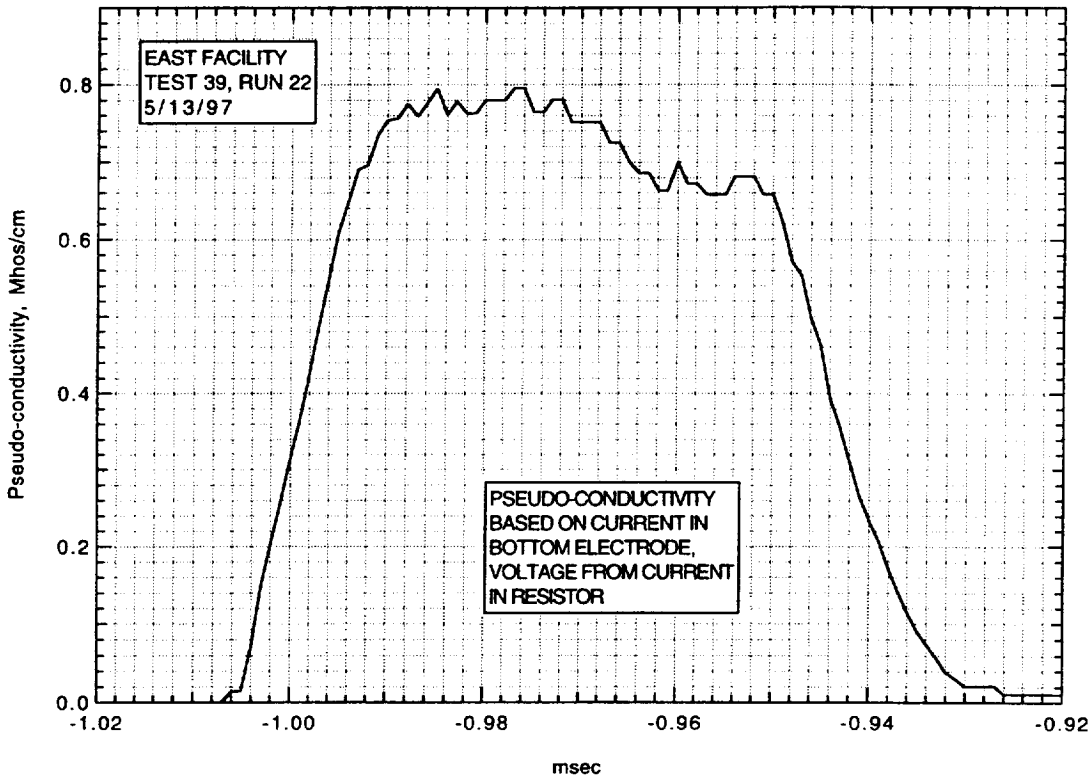

Run 22. Pseudo-conductivity based on current to bottom electrode and voltage from current in resistor.

AIR CONDUCTIVITY MEASUREMENT IN AMES EAST FACILITY

RUN 39/23, 5/14/97

1. Driven tube conditions:

53.2% N_2O, 46.8% N_2,
Total pressure - 5.20 Torr
Measured shock velocity between stns D and F - N/A
Estimated shock velocity at electrodes - 4.623 km/sec
(Scaled from shot 22 using D to E times.)
Measured shock pressure at stn D - 2.72 atm
Measured shock pressure at stn F - N/A

2. Electrodes, driven tube dimensions:

Electrode size - 3.10 cm square
Electrode spacing - 3.10 cm
Main diaphragm to electrodes - 454.475 cm
Skimmer nose to electrodes - 39.979 cm
Driven tube diameter - 10.16 cm
Stn D (dn tube) to electrodes (channel) - 77.365 cm
Electrodes (channel) to stn F (channel) - 20.32 cm

3. Nominal test conditions:

Pressure - 2 atm
Voltage across electrodes - 714/370 V

4. Breakdown:

Little or no indication of breakdown.

Run no: 23 **Date:** 5/14/97 **Shock press. at D:** 2.72 atm
Shock vel. at E: 4.62 km/sec **Voltage at start of current flow:** 712 V

Frame:	**2**	**4**	**6**	**8**
Time:	-1.6	6.4	14.4	22.4
Mach no:				
Frame:	**1**	**3**	**5**	**7**
Time:	-5.6	2.4	10.4	18.4
Mach no:				

V_I: 4.5 km/sec V_{CAV}: 4.75 km/sec

IMACON image of the shock-heated test gas flow in the electrode region. The time is measured from the start of the current flow. Mach numbers and velocities are deduced from the image as explained in section A.2.5.3.

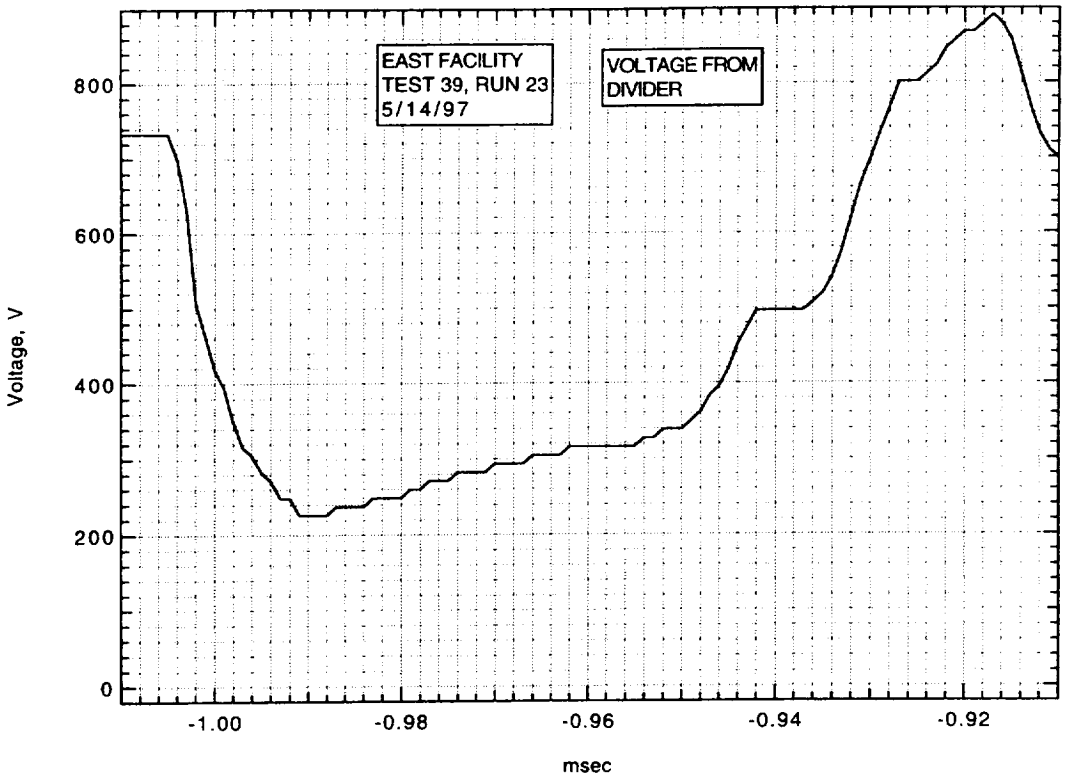

Run 23. Voltage from divider.

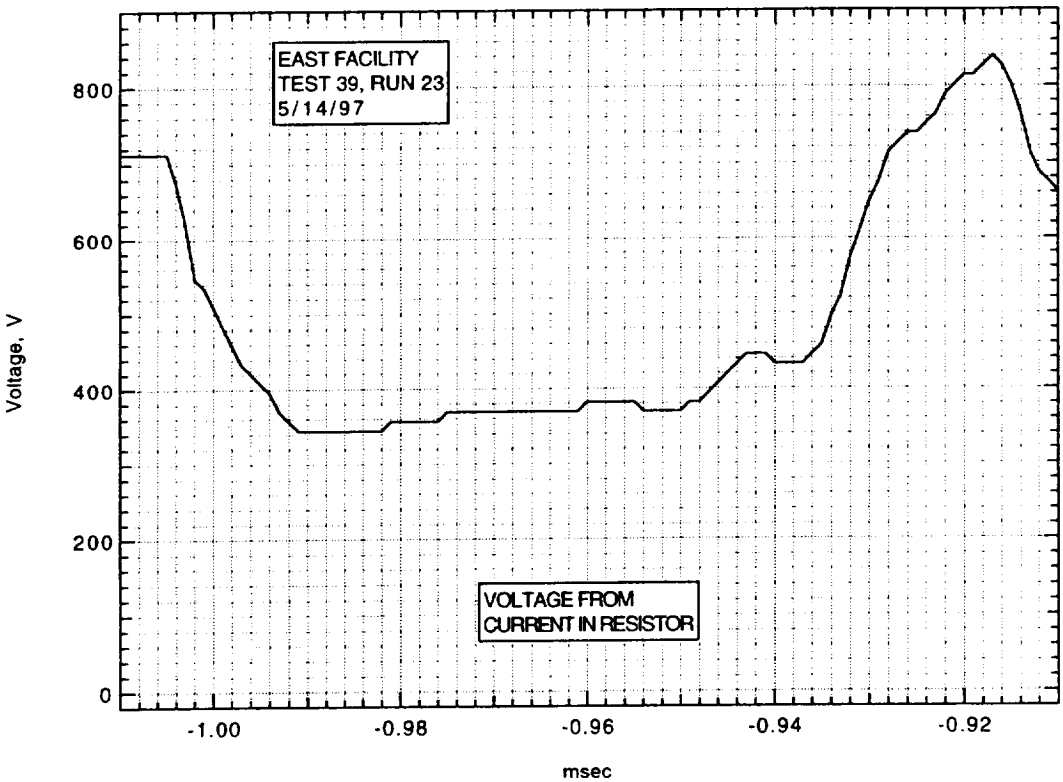

Run 23. Voltage from current in resistor.

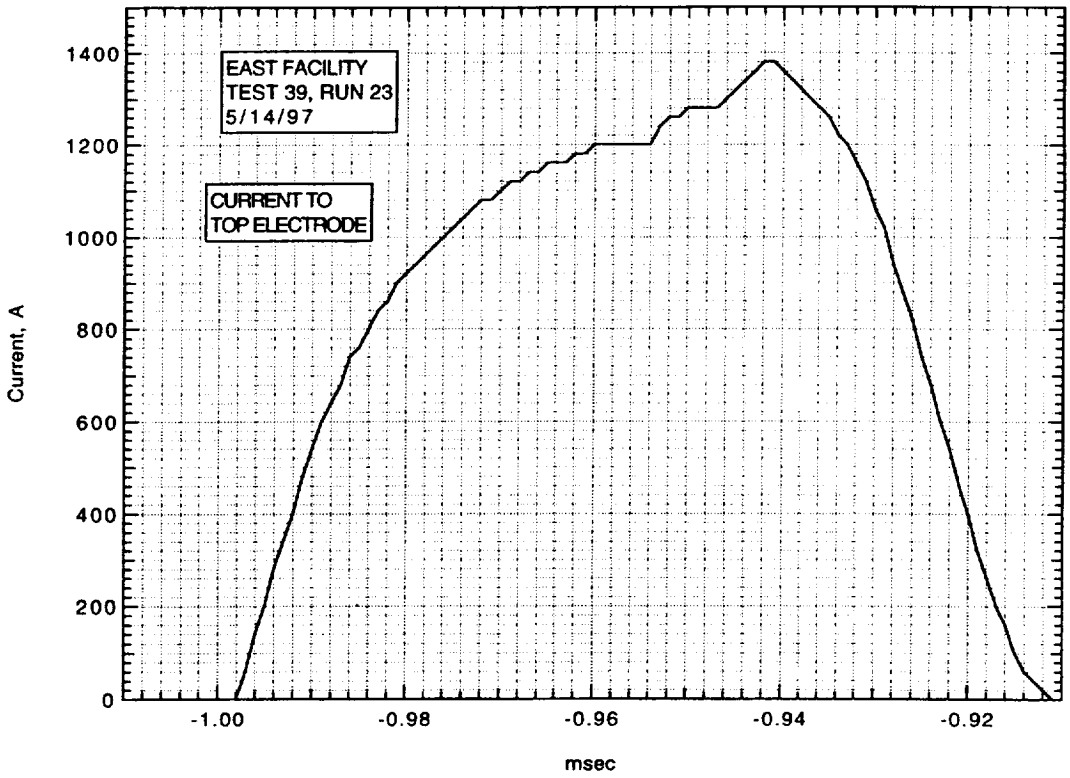

Run 23. Current to top electrode.

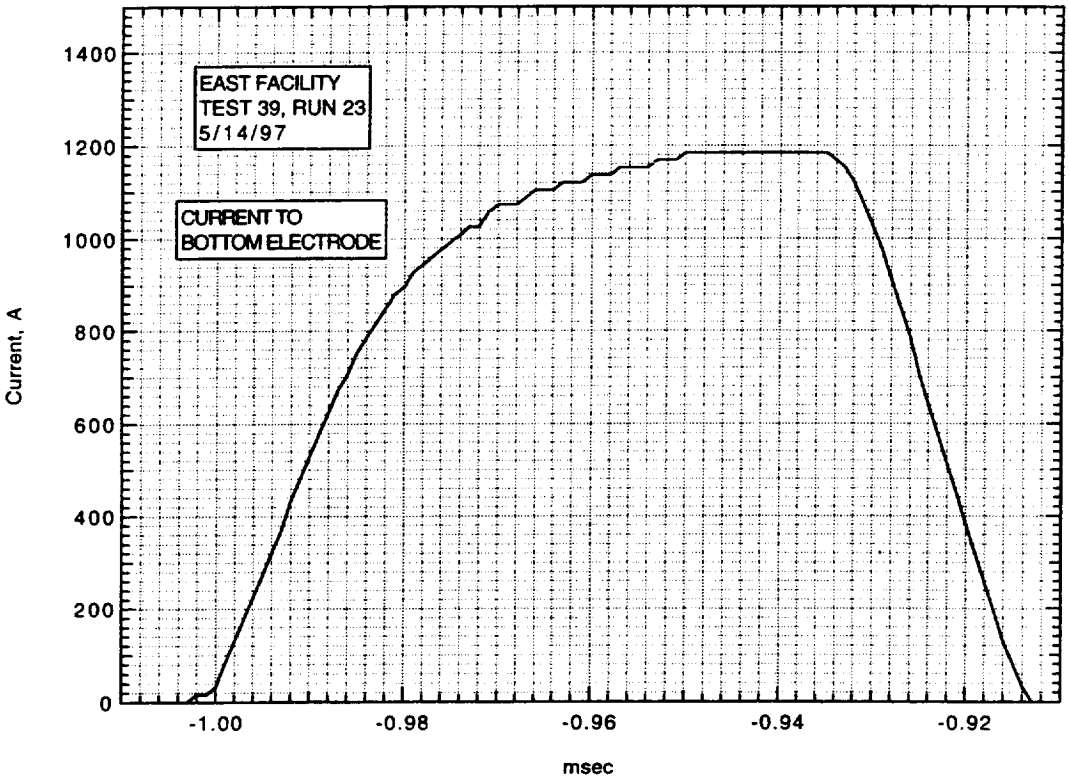

Run 23. Current to bottom electrode.

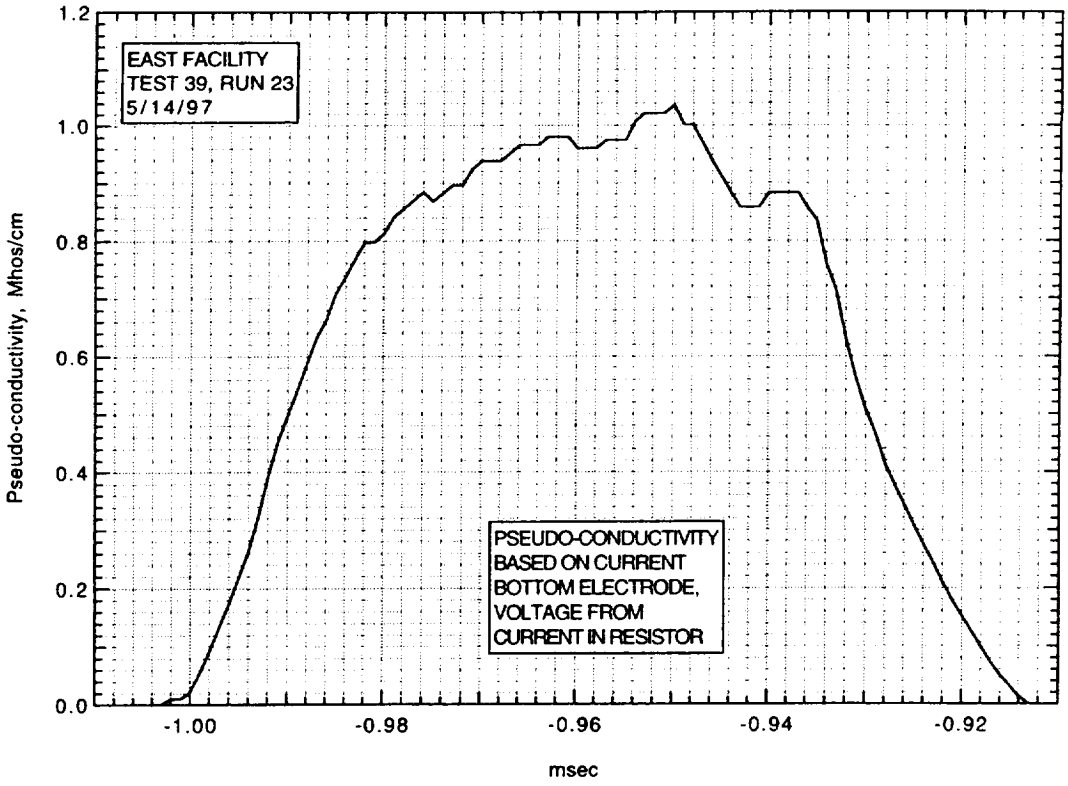

Run 23. Pseudo-conductivity based on current to bottom electrode and voltage from current in resistor.

AIR CONDUCTIVITY MEASUREMENT IN AMES EAST FACILITY

RUN 39/24, 5/15/97

1. Driven tube conditions:

53.2% N_2O, 46.8% N_2,
Total pressure - 5.20 Torr
Measured shock velocity between stns D and F - 4.909 km/sec
Estimated shock velocity at electrodes - 4.723 km/sec
Measured shock pressure at stn D - 2.84 atm
Measured shock pressure at stn F - 2.38 atm

2. Electrodes, driven tube dimensions:

Electrode size - 3.10 cm square
Electrode spacing - 3.10 cm
Main diaphragm to electrodes - 454.475 cm
Skimmer nose to electrodes - 39.979 cm
Driven tube diameter - 10.16 cm
Stn D (dn tube) to electrodes (channel) - 77.365 cm
Electrodes (channel) to stn F (channel) - 20.32 cm

3. Nominal test conditions:

Pressure - 2 atm
Voltage across electrodes - 0/0 V

4. Breakdown:

No voltage applied to electrodes.

Run no: 24 **Date:** 5/15/97 **Shock press. at D:** 2.84 atm
Shock vel. at E: 4.72 km/sec **Voltage at start of current flow:** 0 V

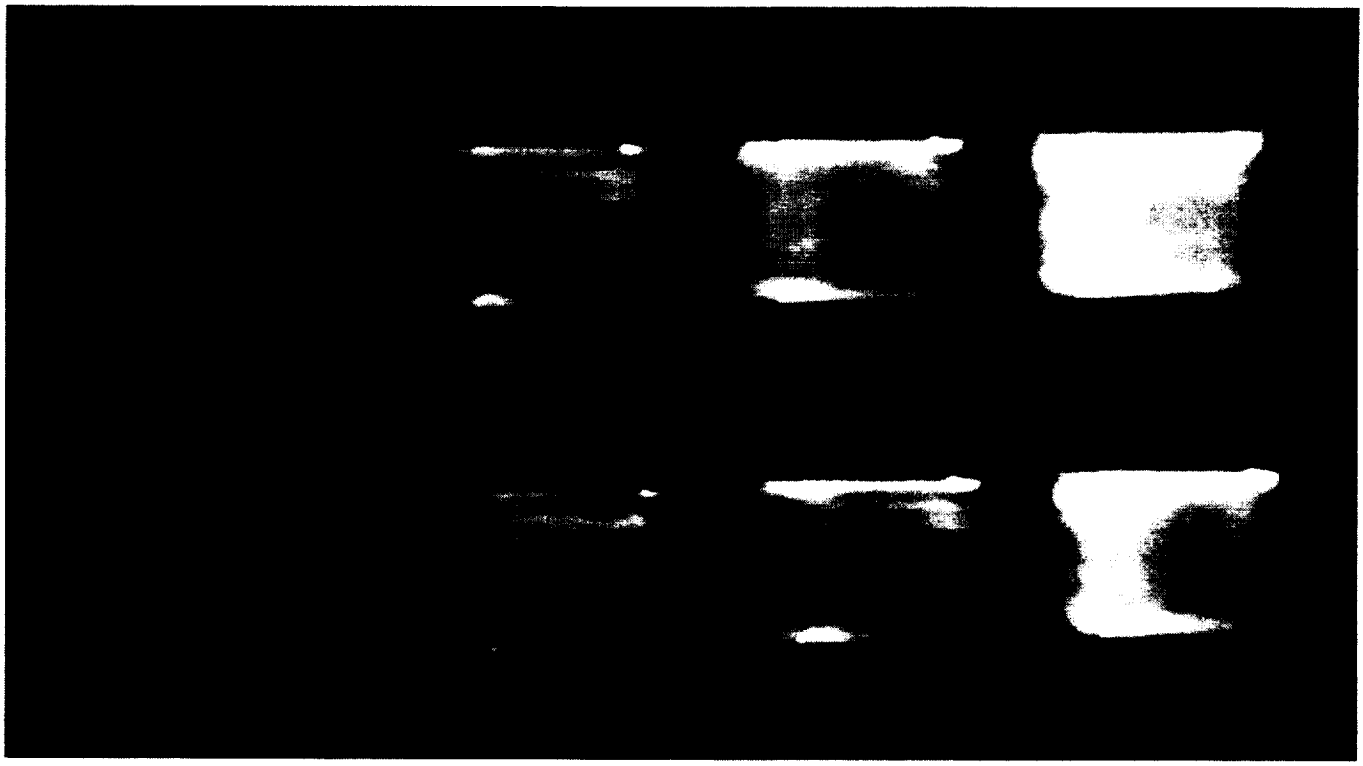

Frame:	**2**	**4**	**6**	**8**
Time:	4.7	12.7	20.7	28.7
Mach no:		2.26		
Frame:	**1**	**3**	**5**	**7**
Time:	0.7	8.7	16.7	24.7
Mach no:		2.46		

V_I: 4.5 km/sec V_{CAV}: 4.97 km/sec

IMACON image of the shock-heated test gas flow in the electrode region. The time is measured from the start of the current flow. Mach numbers and velocities are deduced from the image as explained in section A.2.5.3.

AIR CONDUCTIVITY MEASUREMENT IN AMES EAST FACILITY

RUN 39/25, 5/15/97

1. Driven tube conditions:

53.2% N_2O, 46.8% N_2,
Total pressure - 5.20 Torr
Measured shock velocity between stns D (pressure) and F (light) - 5.3.08 km/sec
Estimated shock velocity at electrodes - 5.062 km/sec
(Scaled from shot 22 using D to E times + speed from pressure transducer at D to light at F for this run.)
Measured shock pressure at stn D - 3.39 atm
Measured shock pressure at stn F - N/A

2. Electrodes, driven tube dimensions:

Electrode size - 3.10 cm square
Electrode spacing - 3.10 cm
Main diaphragm to electrodes - 454.475 cm
Skimmer nose to electrodes - 39.979 cm
Driven tube diameter - 10.16 cm
Stn D (dn tube) to electrodes (channel) - 77.365 cm
Electrodes (channel) to stn F (channel) - 20.32 cm

3. Nominal test conditions:

Pressure - 2 atm
Voltage across electrodes - 95/83 V

4. Breakdown:

Little or no indication of breakdown.

Run no: 25 **Date:** 5/15/97 **Shock press. at D:** 3.39 atm
Shock vel. at E: 5.06 km/sec **Voltage at start of current flow:** 95 V

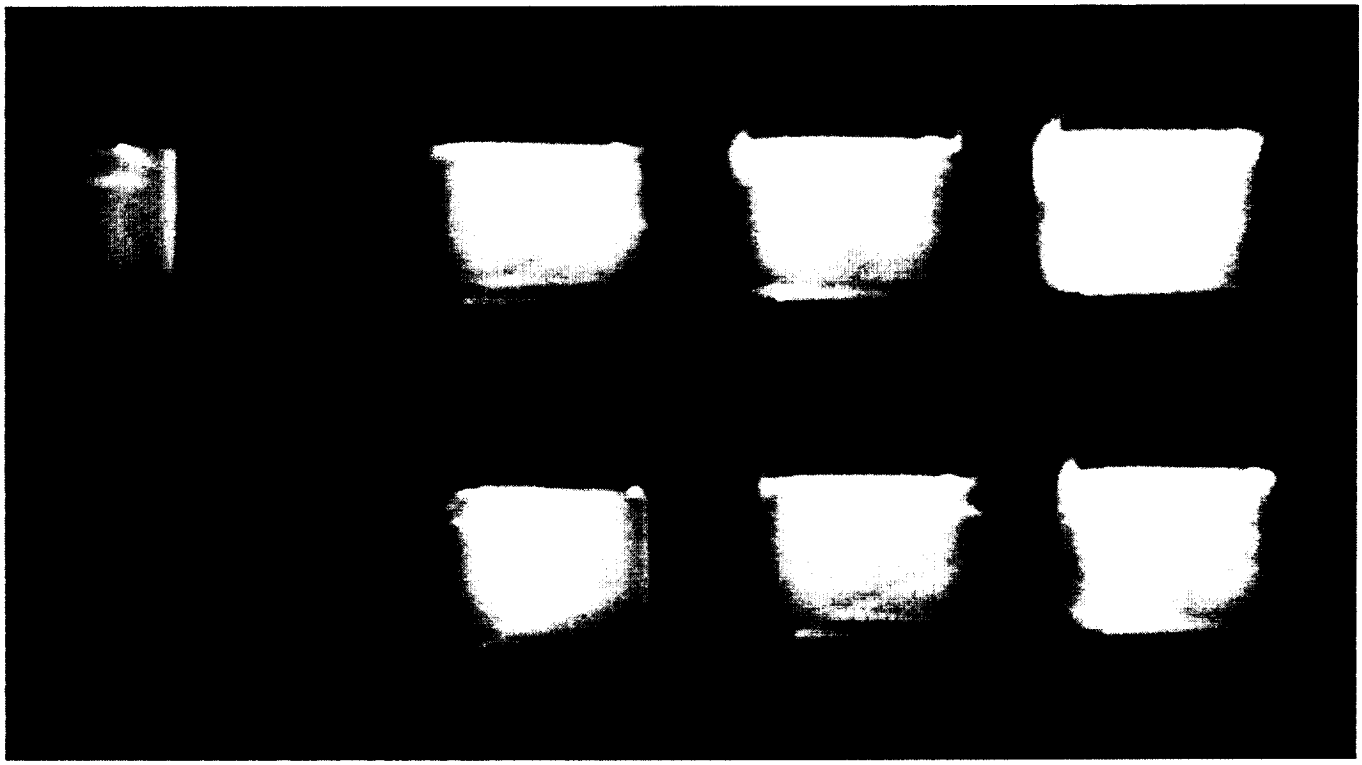

Frame:	**2**	**4**	**6**	**8**
Time:	1.9	9.9	17.9	25.9
Mach no:	2.31	2.40		
Frame:	**1**	**3**	**5**	**7**
Time:	-2.1	5.9	13.9	21.9
Mach no:		2.40		

V_I: 4.6 km/sec V_{CAV}: 5.37 km/sec

IMACON image of the shock-heated test gas flow in the electrode region. The time is measured from the start of the current flow. Mach numbers and velocities are deduced from the image as explained in section A.2.5.3.

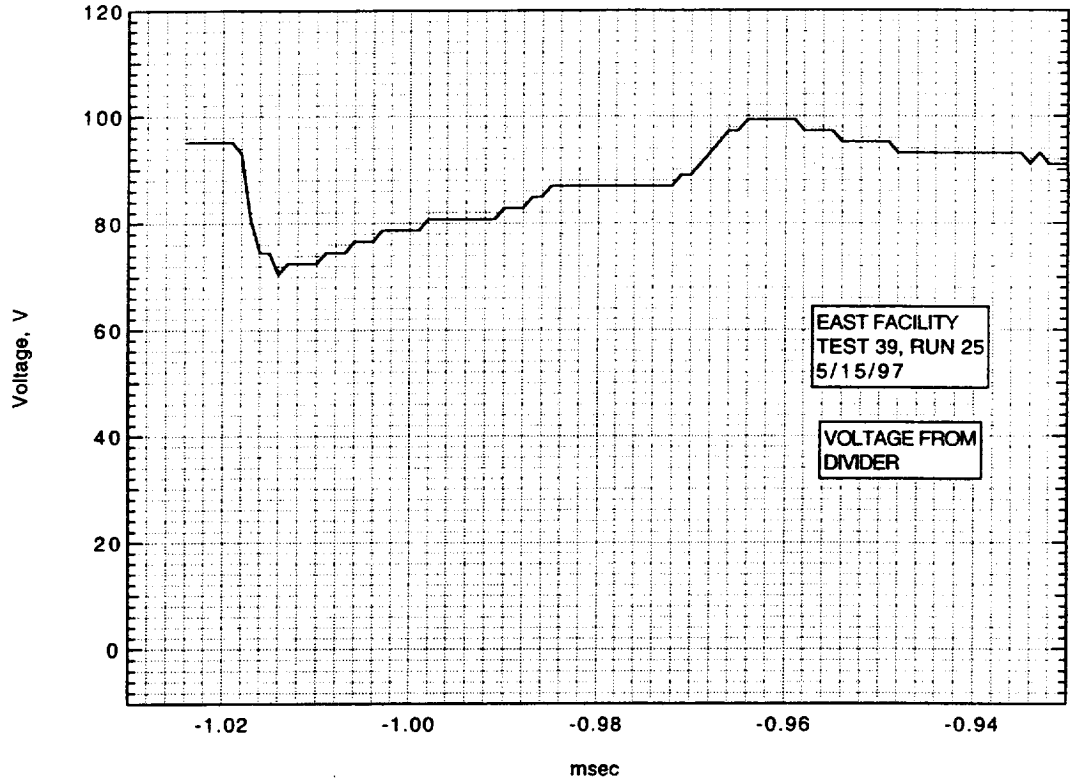

Run 25. Voltage from divider.

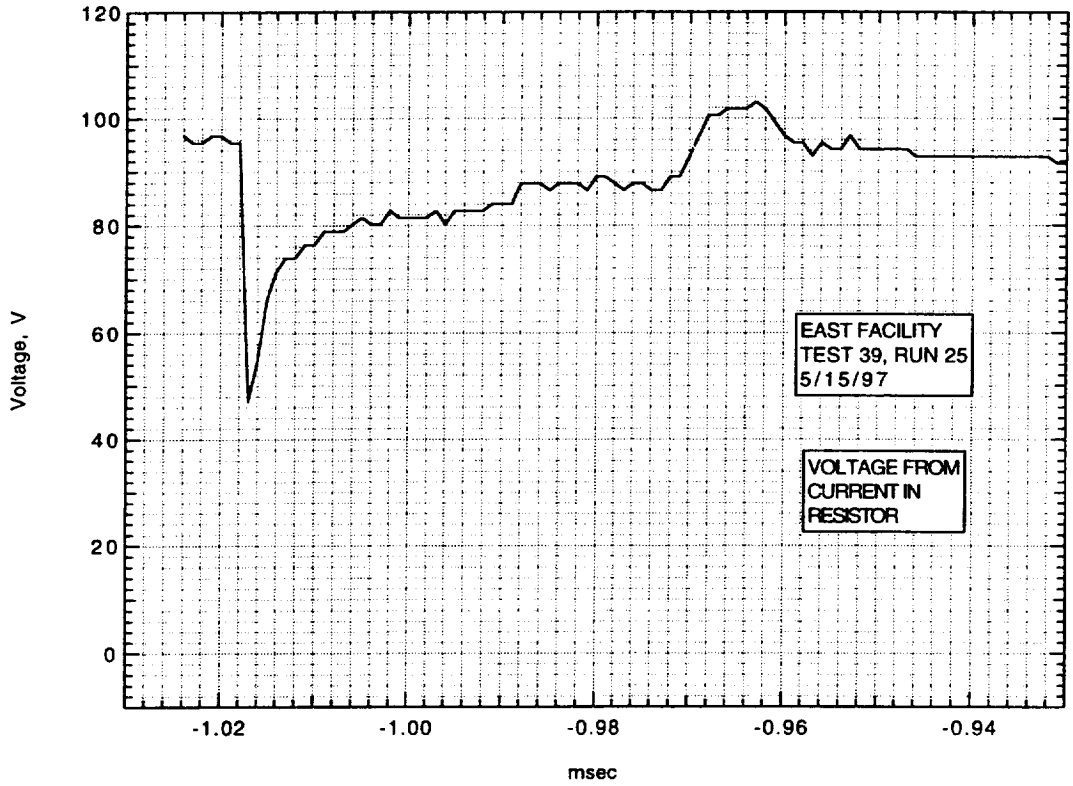

Run 25. Voltage from current in resistor.

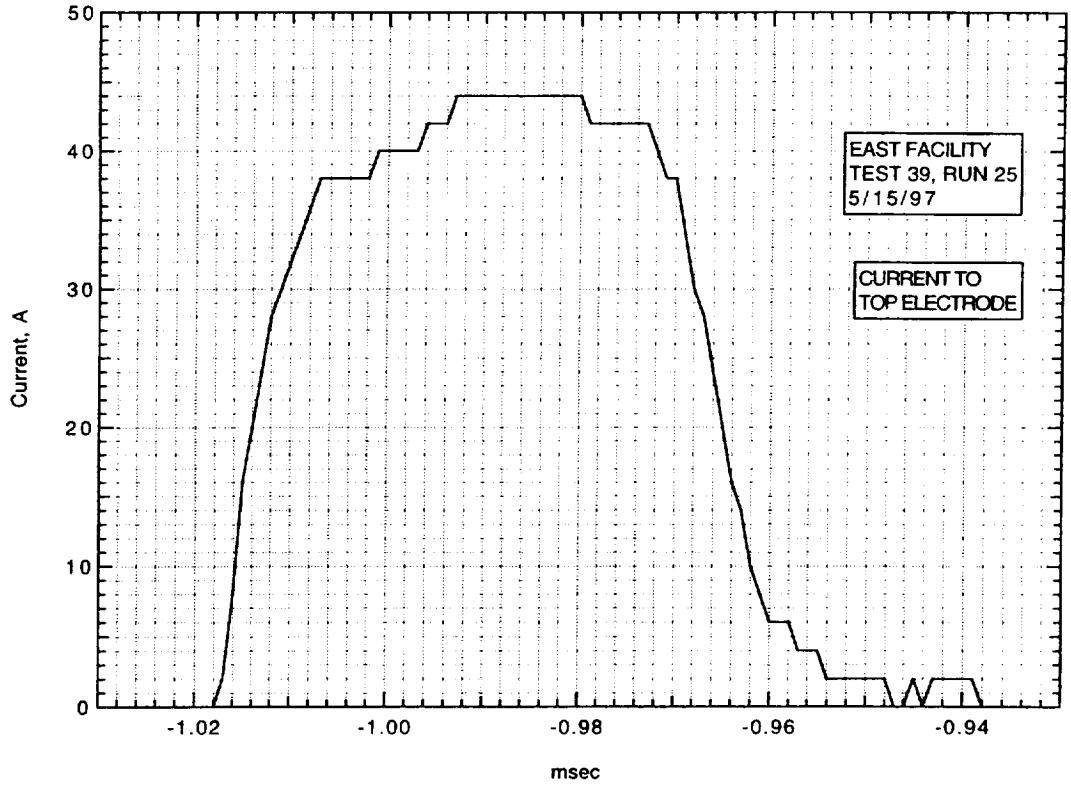

Run 25. Current to top electrode.

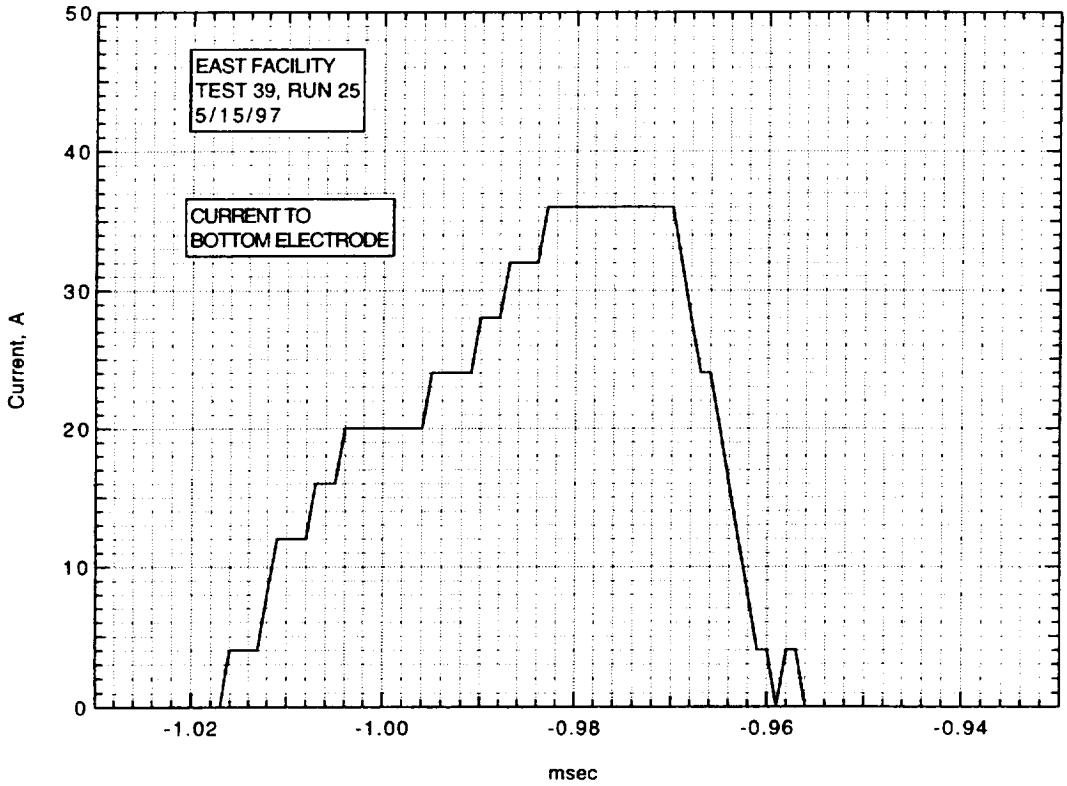

Run 25. Current to bottom electrode.

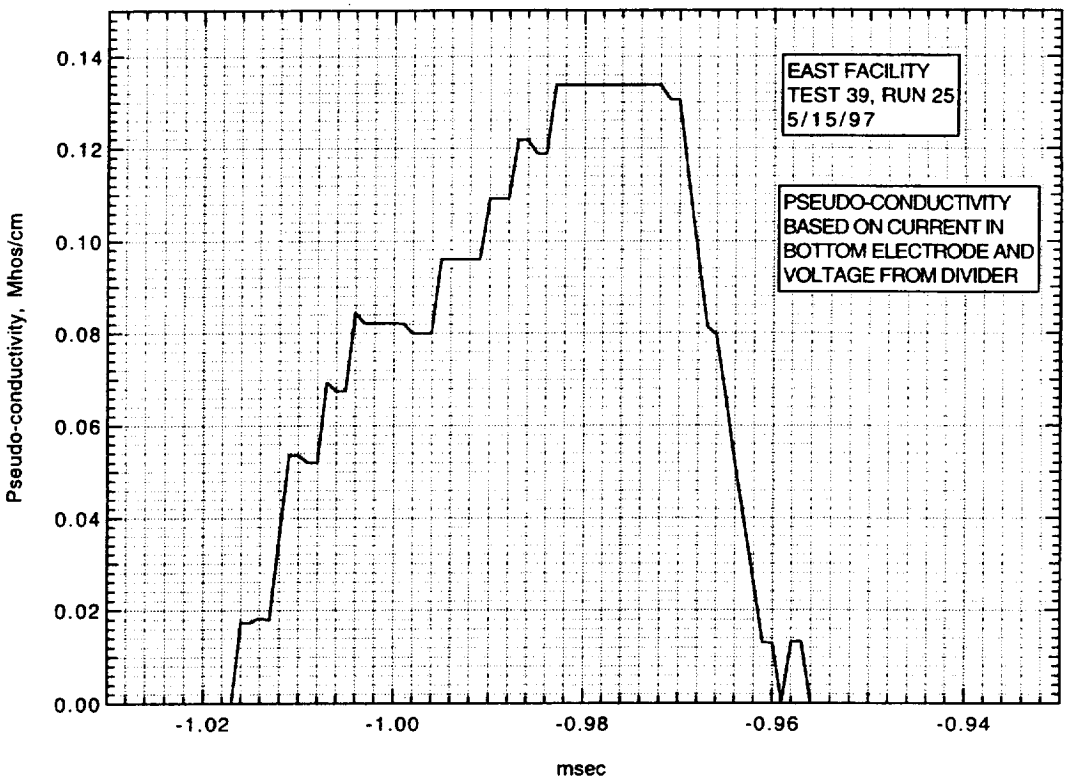

Run 25. Pseudo-conductivity based on current to bottom electrode and voltage from divider.

AIR CONDUCTIVITY MEASUREMENT IN AMES EAST FACILITY

RUN 39/26, 5/16/97

1. Driven tube conditions:

53.2% N_2O, 46.8% N_2,
Total pressure - 5.20 Torr
Measured shock velocity between stns D (pressure) and F (light) - 5.061 km/sec
Estimated shock velocity at electrodes - 4.840 km/sec
(Scaled from shot 22 using D to E times + speed from pressure transducer at D to light at F for this run.)
Measured shock pressure at stn D - 3.07 atm
Measured shock pressure at stn F - N/A

2. Electrodes, driven tube dimensions:

Electrode size - 3.10 cm square
Electrode spacing - 3.10 cm
Main diaphragm to electrodes - 454.475 cm
Skimmer nose to electrodes - 39.979 cm
Driven tube diameter - 10.16 cm
Stn D (dn tube) to electrodes (channel) - 77.365 cm
Electrodes (channel) to stn F (channel) - 20.32 cm

3. Nominal test conditions:

Pressure - 2 atm
Voltage across electrodes - 92/80 V

4. Breakdown:

Little or no indication of breakdown.

Run no: 26 **Date:** 5/16/97 **Shock press. at D:** 3.07 atm
Shock vel. at E: 4.84 km/sec **Voltage at start of current flow:** 92 V

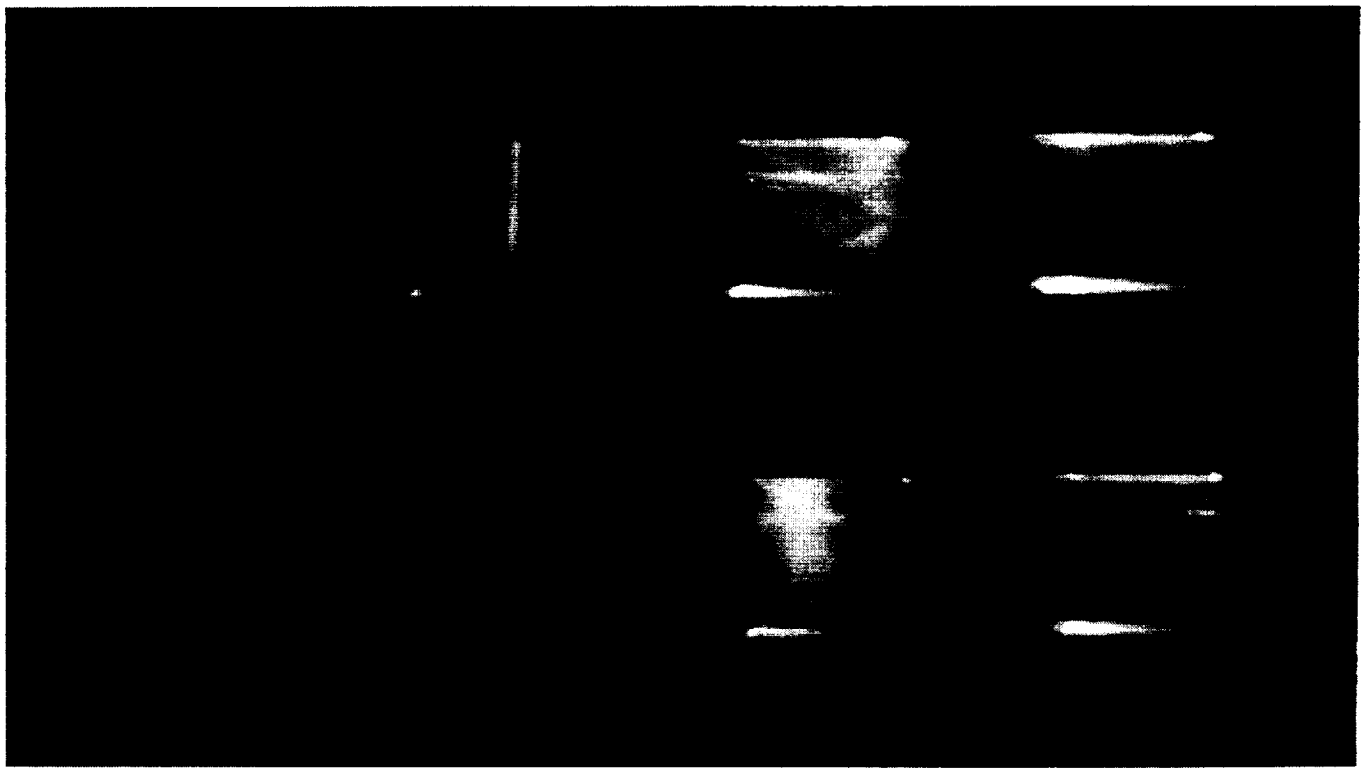

Frame:	**2**	**4**	**6**	**8**
Time:	-4.2	3.8	11.8	19.8
Mach no:			2.30	
Frame:	**1**	**3**	**5**	**7**
Time:	-8.2	-0.2	7.8	15.8
Mach no:			2.39	

V_I: 4.6 km/sec V_{CAV}: 5.14 km/sec

IMACON image of the shock-heated test gas flow in the electrode region. The time is measured from the start of the current flow. Mach numbers and velocities are deduced from the image as explained in section A.2.5.3.

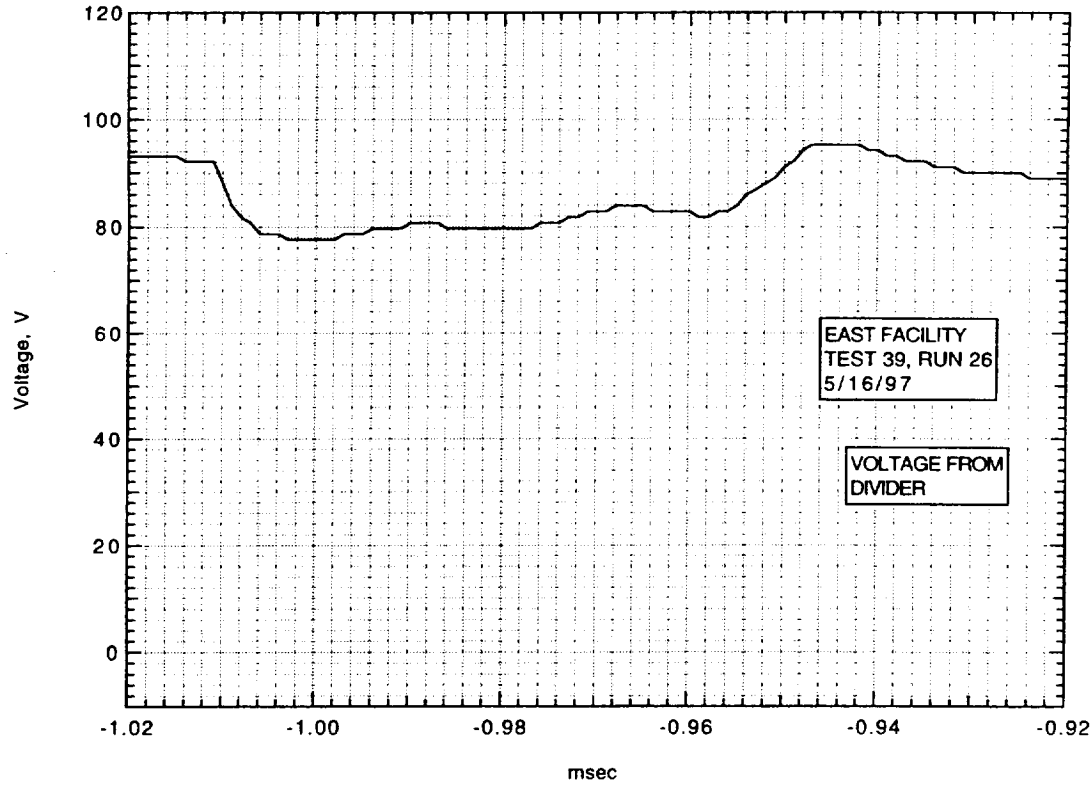

Run 26. Voltage from divider.

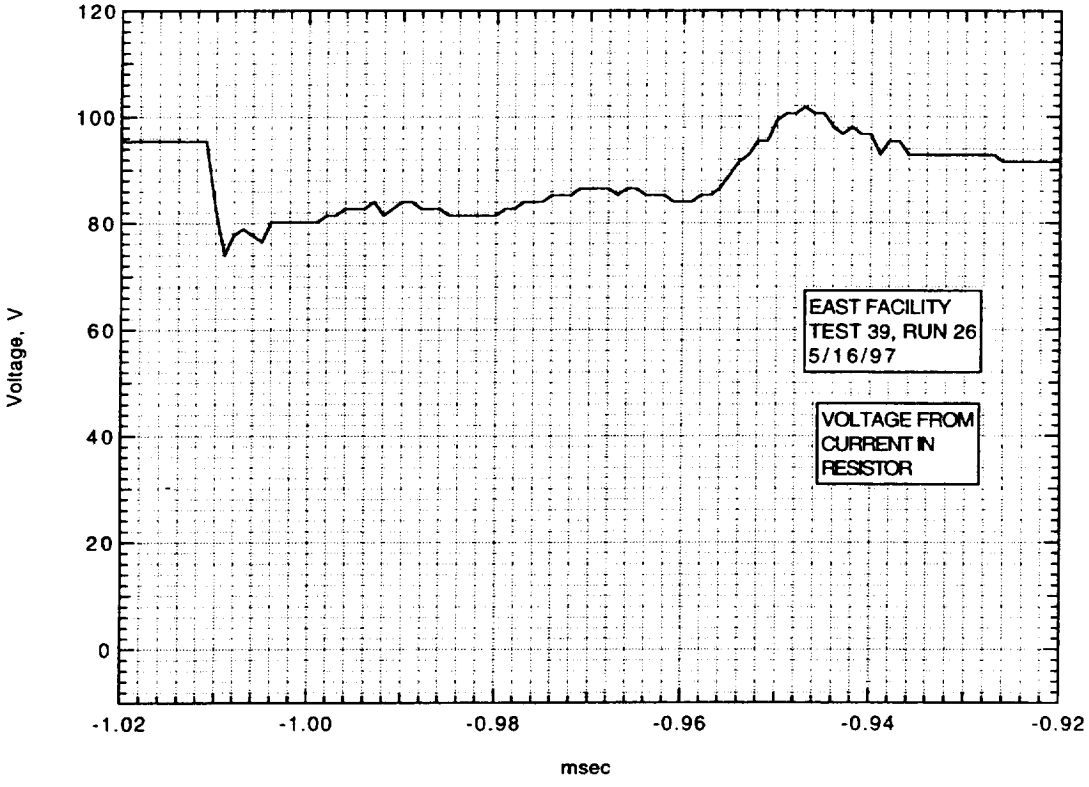

Run 26. Voltage from current in resistor.

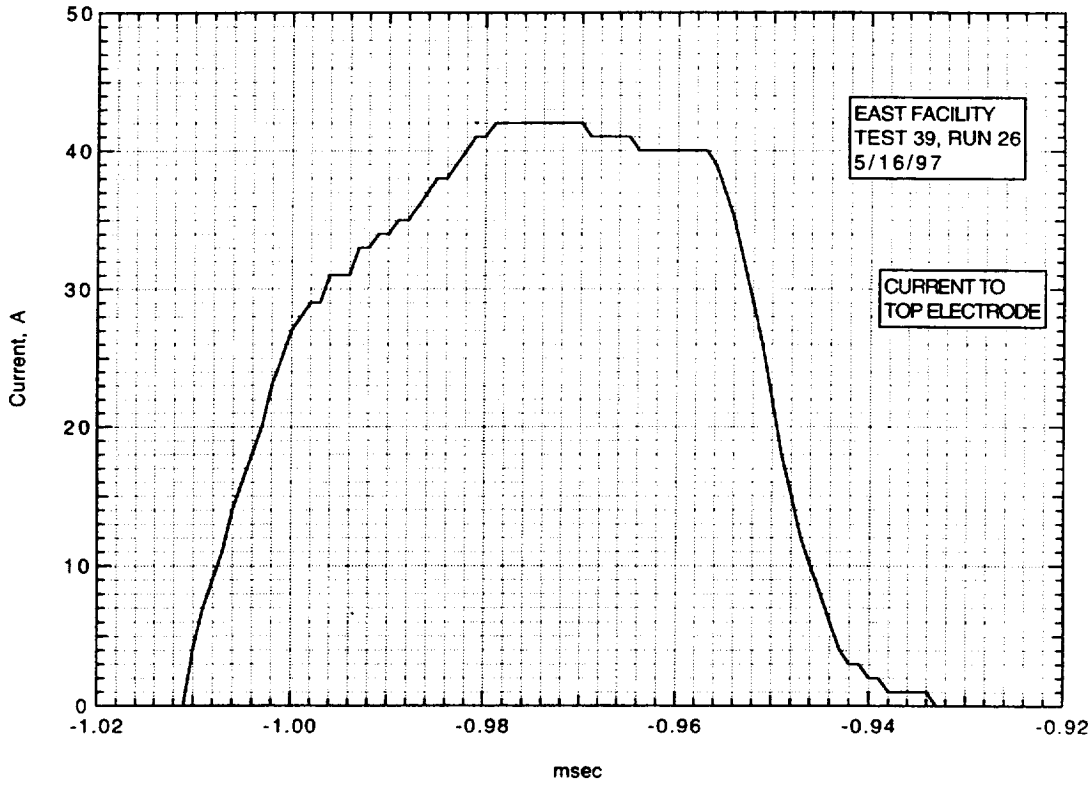

Run 26. Current to top electrode.

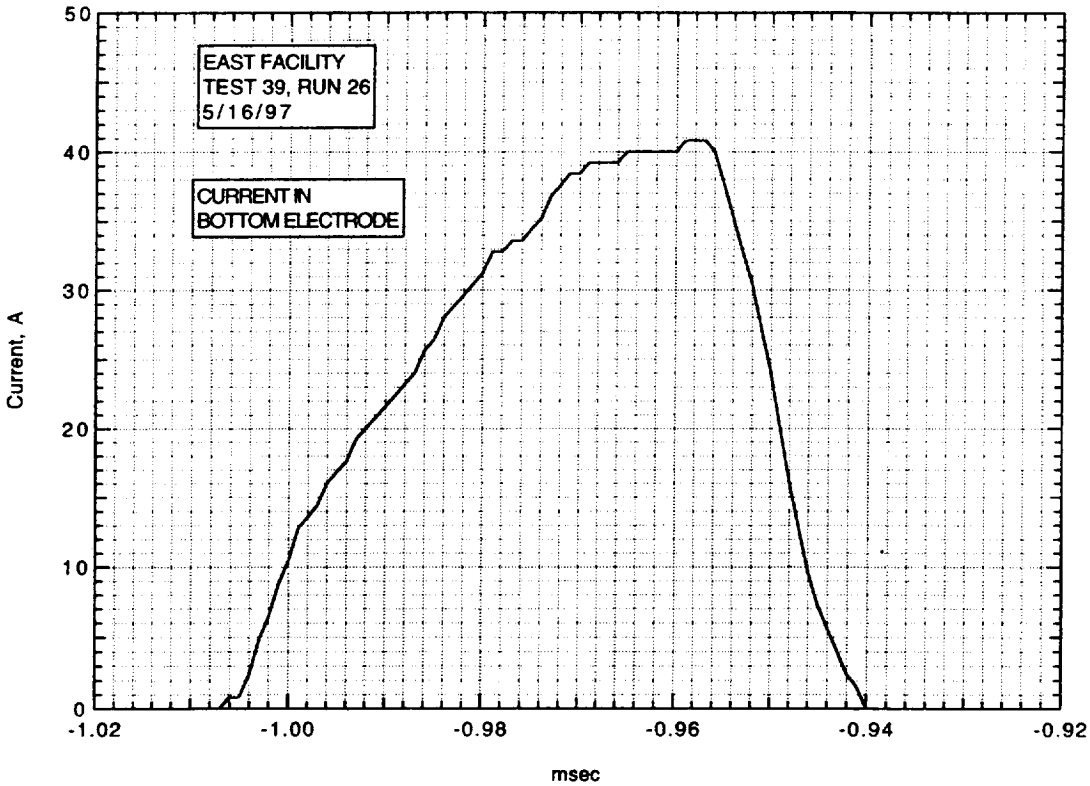

Run 26. Current to bottom electrode.

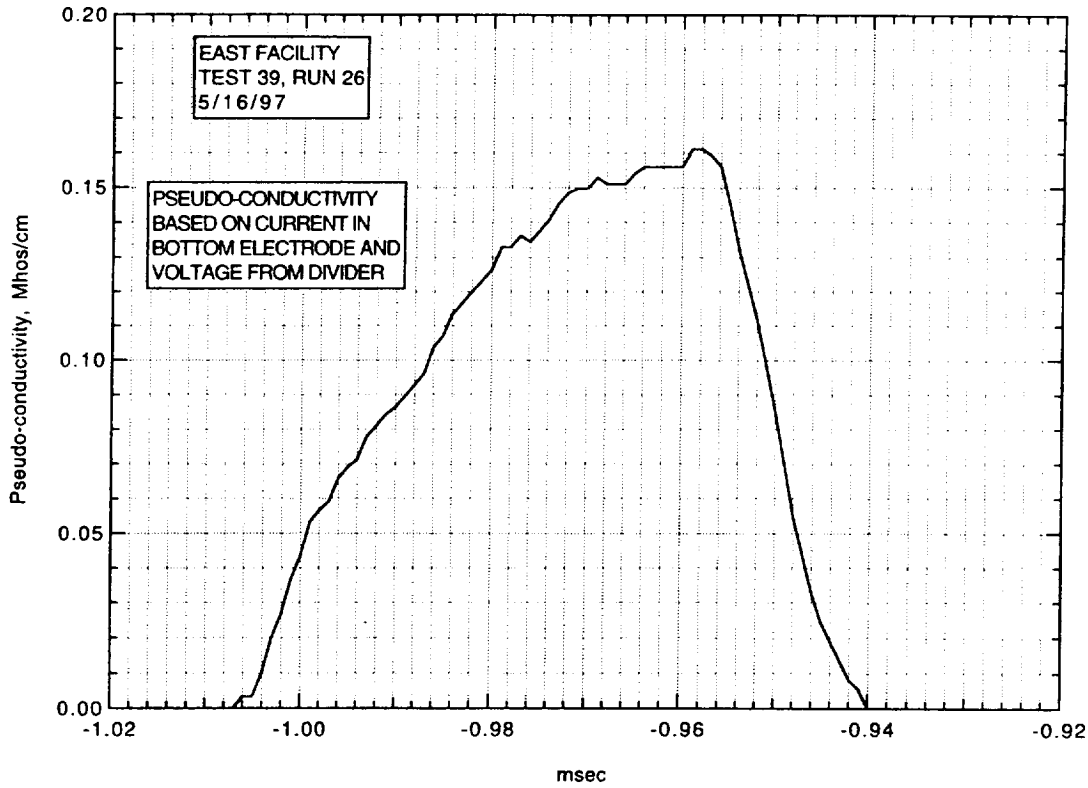

Run 26. Pseudo-conductivity based on current to bottom electrode and voltage from divider.

AIR CONDUCTIVITY MEASUREMENT IN AMES EAST FACILITY

RUN 39/27, 5/19/97

1. Driven tube conditions:

53.2% N_2O, 46.8% N_2,
Total pressure - 5.20 Torr
Measured shock velocity between stns D and F - 4.719 km/sec
Estimated shock velocity at electrodes, from Δt(DF) - 4.541 km/sec
Measured shock pressure at stn D - 2.60 atm
Measured shock pressure at stn F - 2.60 atm; this value rather uncertain due to large EM noise pickup

2. Electrodes, driven tube dimensions:

Electrode size - 3.10 cm square
Electrode spacing - 3.10 cm
Main diaphragm to electrodes - 454.475 cm
Skimmer nose to electrodes - 39.979 cm
Driven tube diameter - 10.16 cm
Stn D (dn tube) to electrodes (channel) - 77.365 cm
Electrodes (channel) to stn F (channel) - 20.32 cm

3. Nominal test conditions:

Pressure - 2 atm
Voltage across electrodes - 92/83 V

4. Breakdown:

Little or no indication of breakdown.

Run no: 27 **Date:** 5/19/97 **Shock press. at D:** 2.60 atm
Shock vel. at E: 4.54 km/sec **Voltage at start of current flow:** 92 V

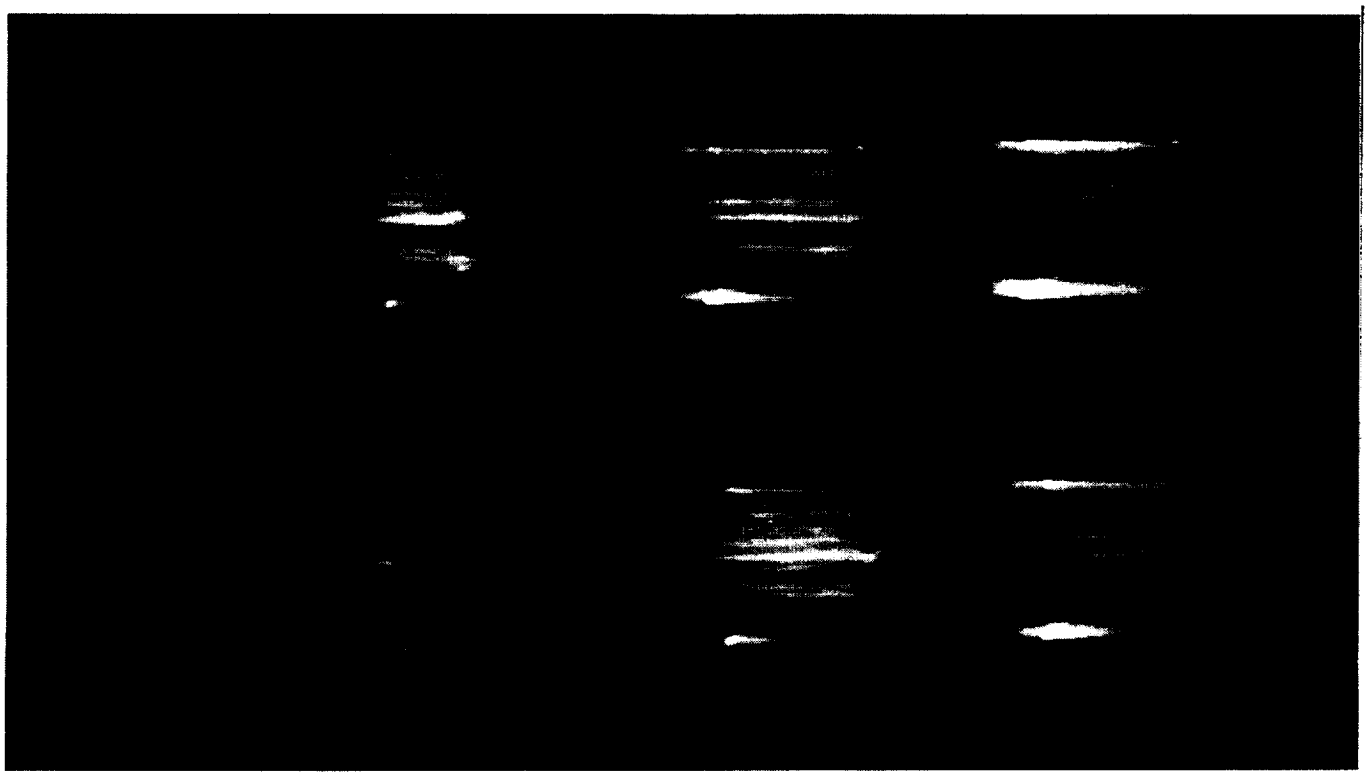

Frame:	**2**	**4**	**6**	**8**
Time:	-1.6	6.4	14.4	22.4
Mach no:				
Frame:	**1**	**3**	**5**	**7**
Time:	-5.6	2.4	10.4	18.4
Mach no:				

V_I: km/sec V_{CAV}: **4.77** km/sec

IMACON image of the shock-heated test gas flow in the electrode region. The time is measured from the start of the current flow. Mach numbers and velocities are deduced from the image as explained in section A.2.5.3.

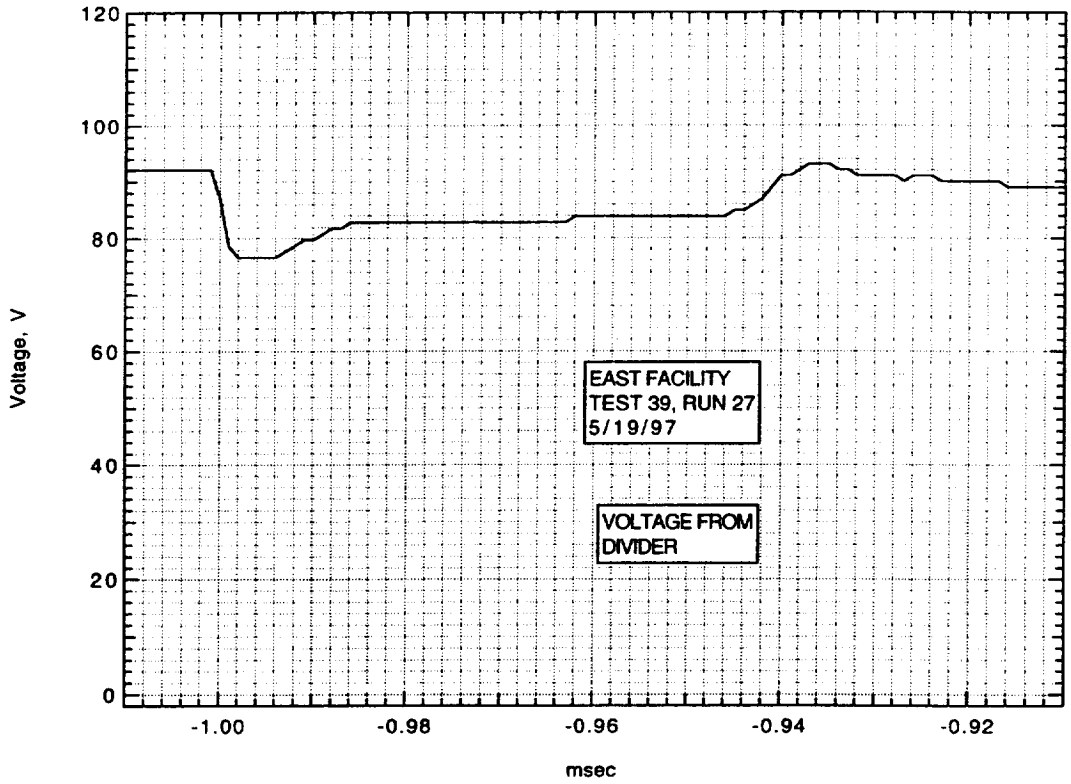

Run 27. Voltage from divider.

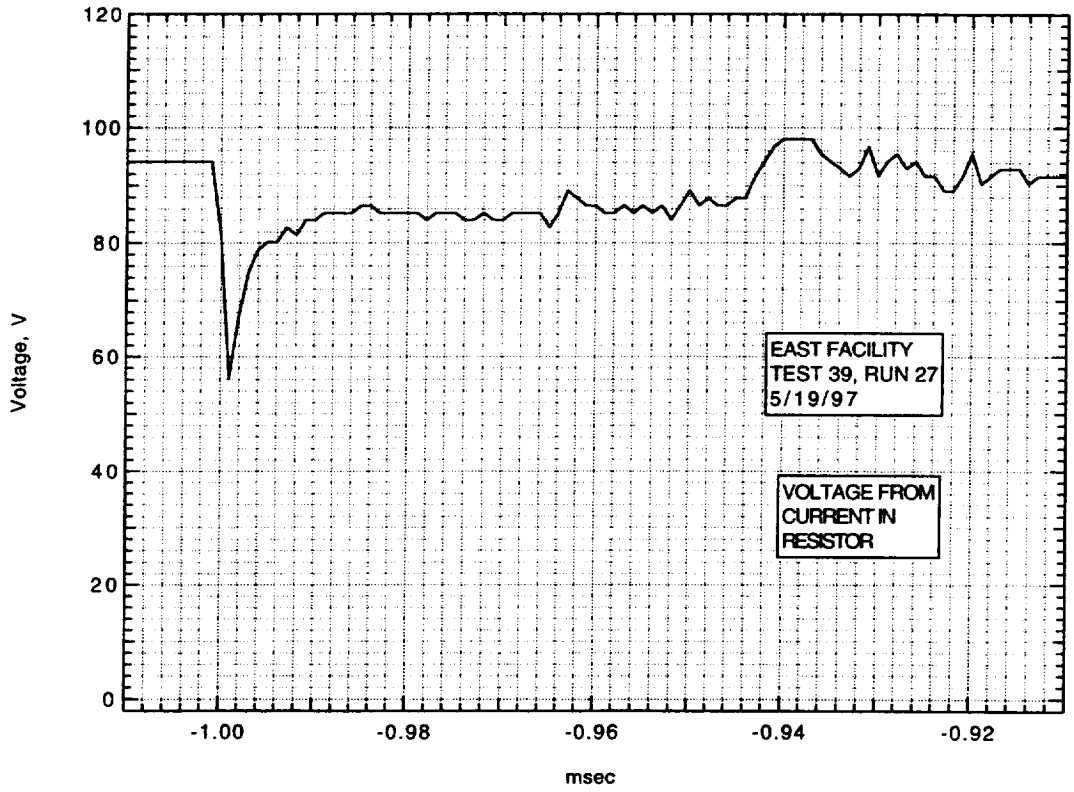

Run 27. Voltage from current in resistor.

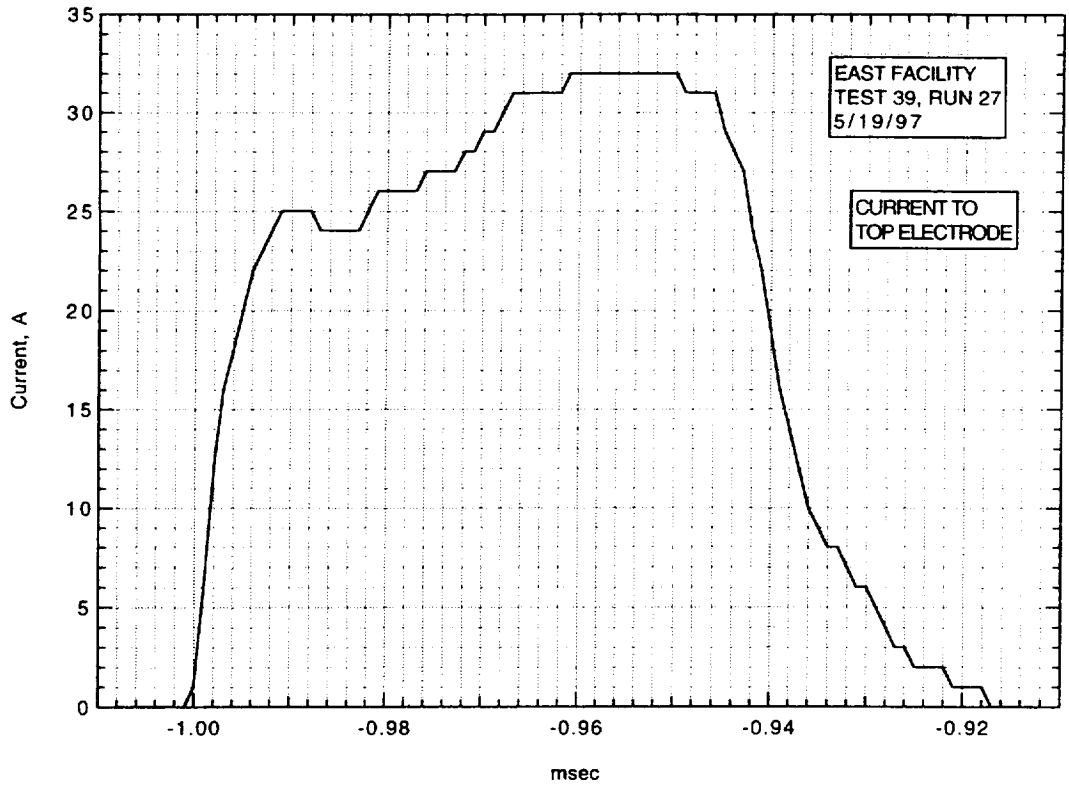

Run 27. Current to top electrode.

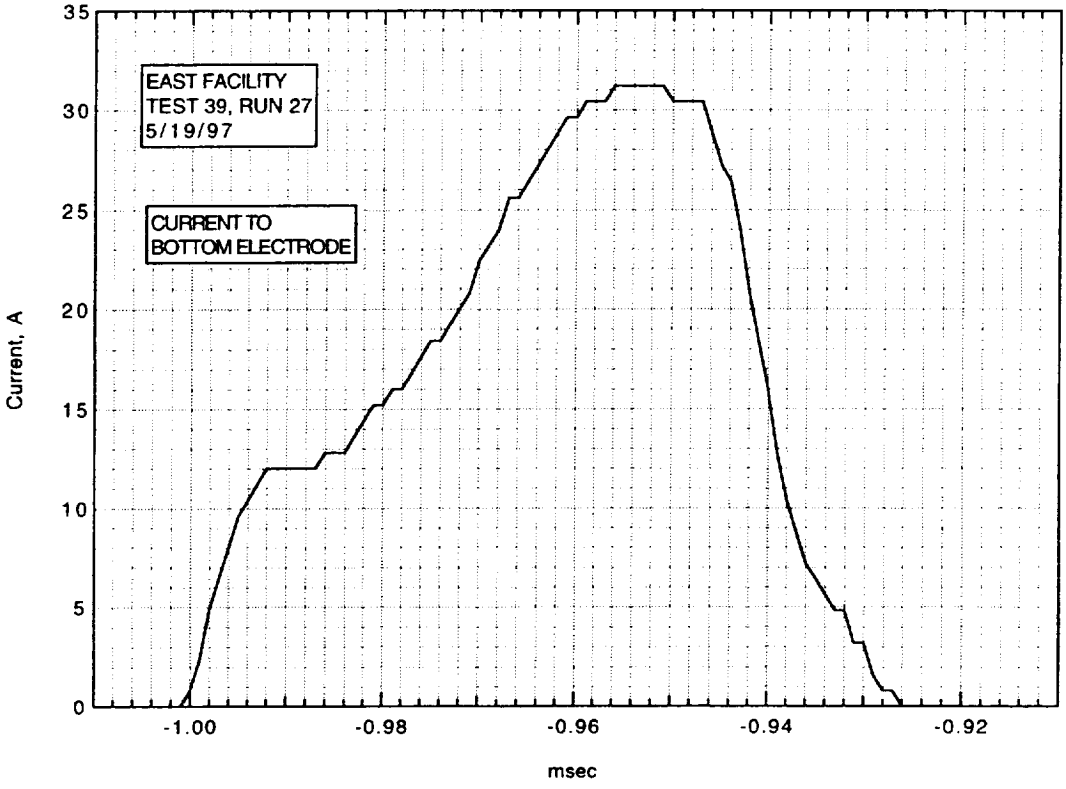

Run 27. Current to bottom electrode.

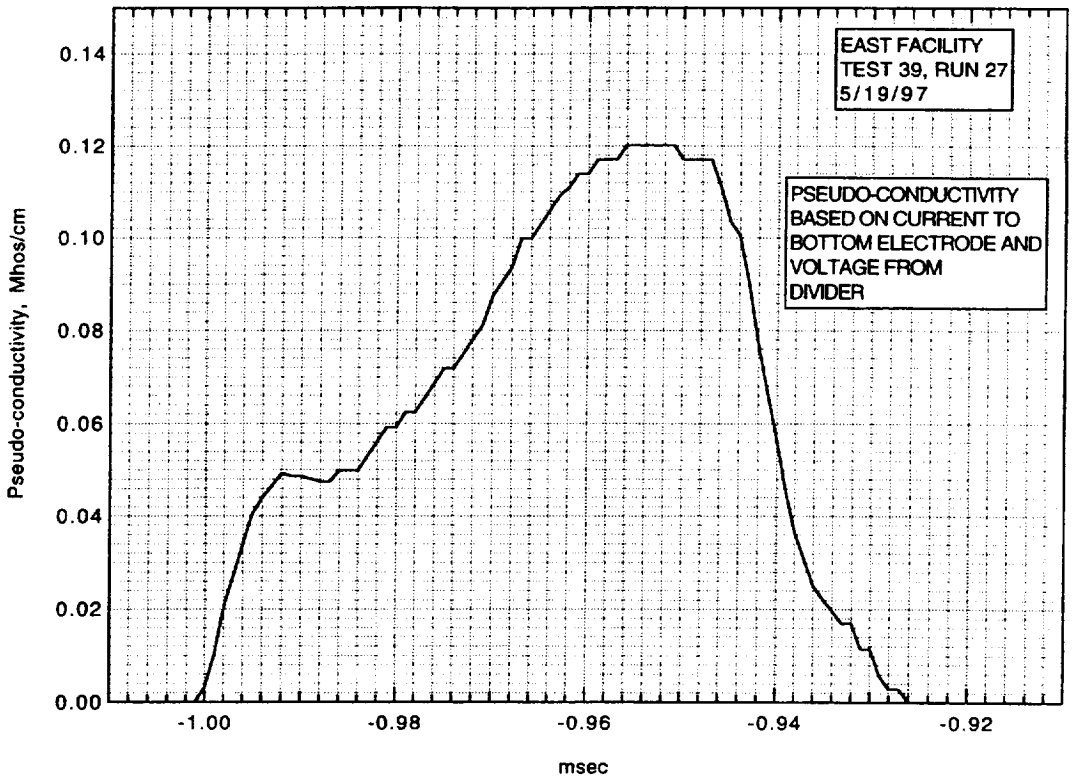

Run 27. Pseudo-conductivity based on current to bottom electrode and voltage from divider.

AIR CONDUCTIVITY MEASUREMENT IN AMES EAST FACILITY

RUN 39/28, 5/20/97

1. Driven tube conditions:

53.2% N_2O, 46.8% N_2,
Total pressure - 5.20 Torr
Measured shock velocity between stns D and F - 4.719 km/sec
Estimated shock velocity at electrodes, from $\Delta t(DF)$ - 4.541 km/sec
Measured shock pressure at stn D - 2.68 atm
Measured shock pressure at stn F - 1.91 atm; this value rather uncertain due to large EM noise pickup

2. Electrodes, driven tube dimensions:

Electrode size - 3.10 cm square
Electrode spacing - 3.10 cm
Main diaphragm to electrodes - 454.475 cm
Skimmer nose to electrodes - 39.979 cm
Driven tube diameter - 10.16 cm
Stn D (dn tube) to electrodes (channel) - 77.365 cm
Electrodes (channel) to stn F (channel) - 20.32 cm

3. Nominal test conditions:

Pressure - 2 atm
Voltage across electrodes - 46.6/40.3 V

4. Breakdown:

Little or no indication of breakdown.

Run no: 28 **Date:** 5/20/97 **Shock press. at D:** 2.68 atm
Shock vel. at E: 4.54 km/sec **Voltage at start of current flow:** 46.6 V

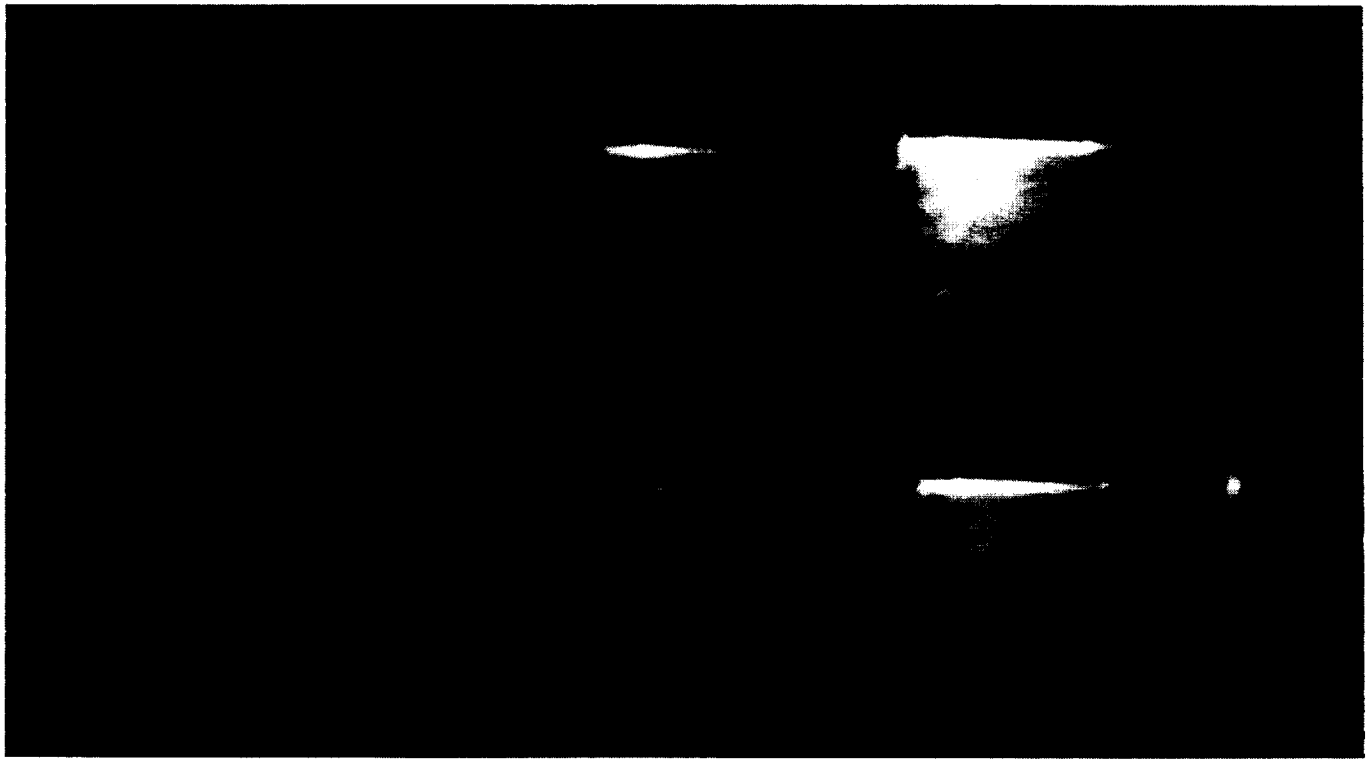

Frame:	**2**	**4**	**6**	**8**
Time:	-2.2	5.8	13.8	21.8
Mach no:				
Frame:	**1**	**3**	**5**	**7**
Time:	-6.2	1.8	9.8	17.8
Mach no:			2.39	

V_I: 4.8 km/sec V_{CAV}: 4.76 km/sec

IMACON image of the shock-heated test gas flow in the electrode region. The time is measured from the start of the current flow. Mach numbers and velocities are deduced from the image as explained in section A.2.5.3.

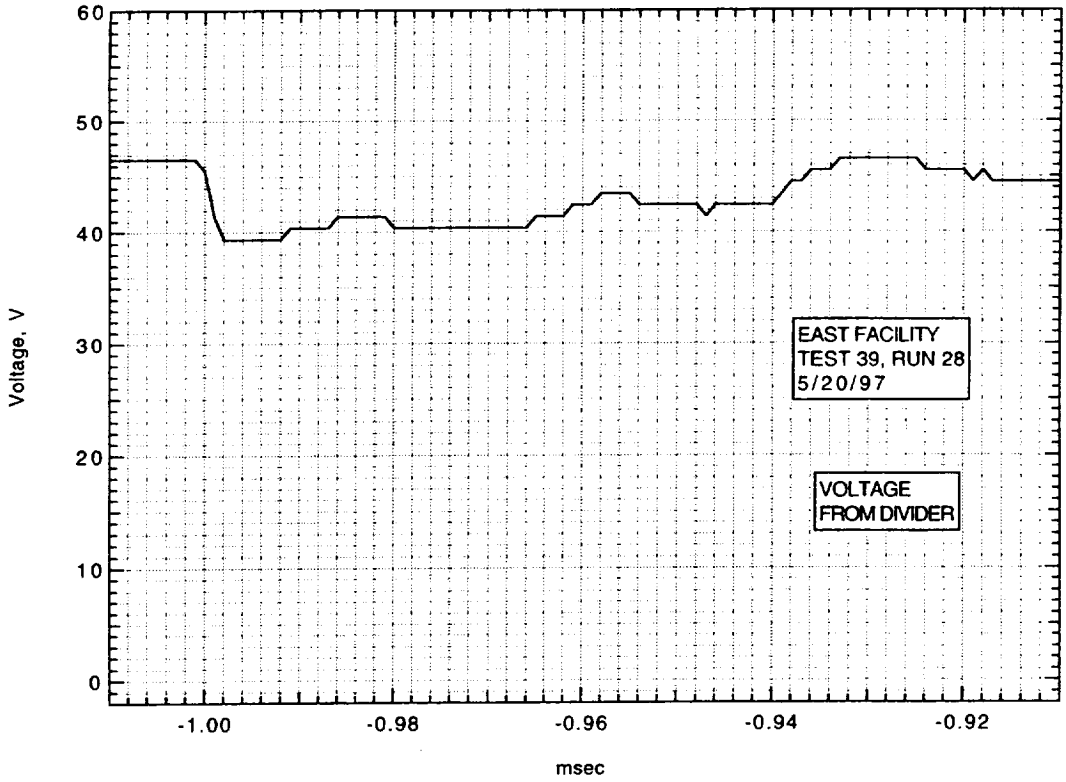

Run 28. Voltage from divider.

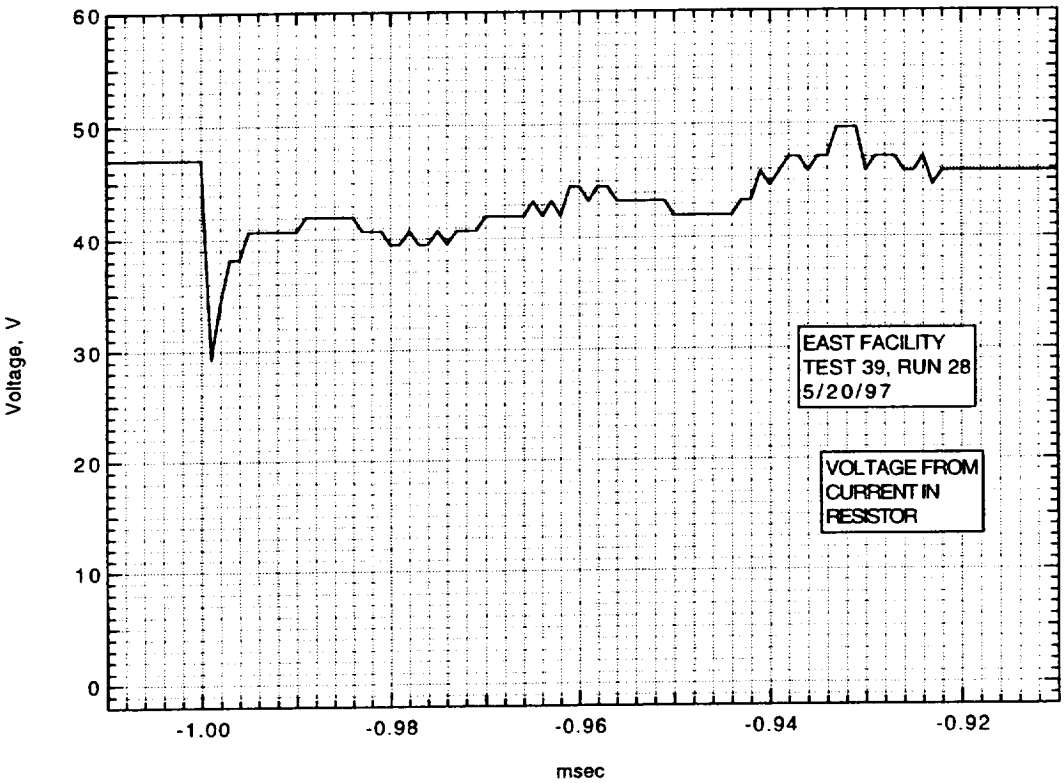

Run 28. Voltage from current in resistor.

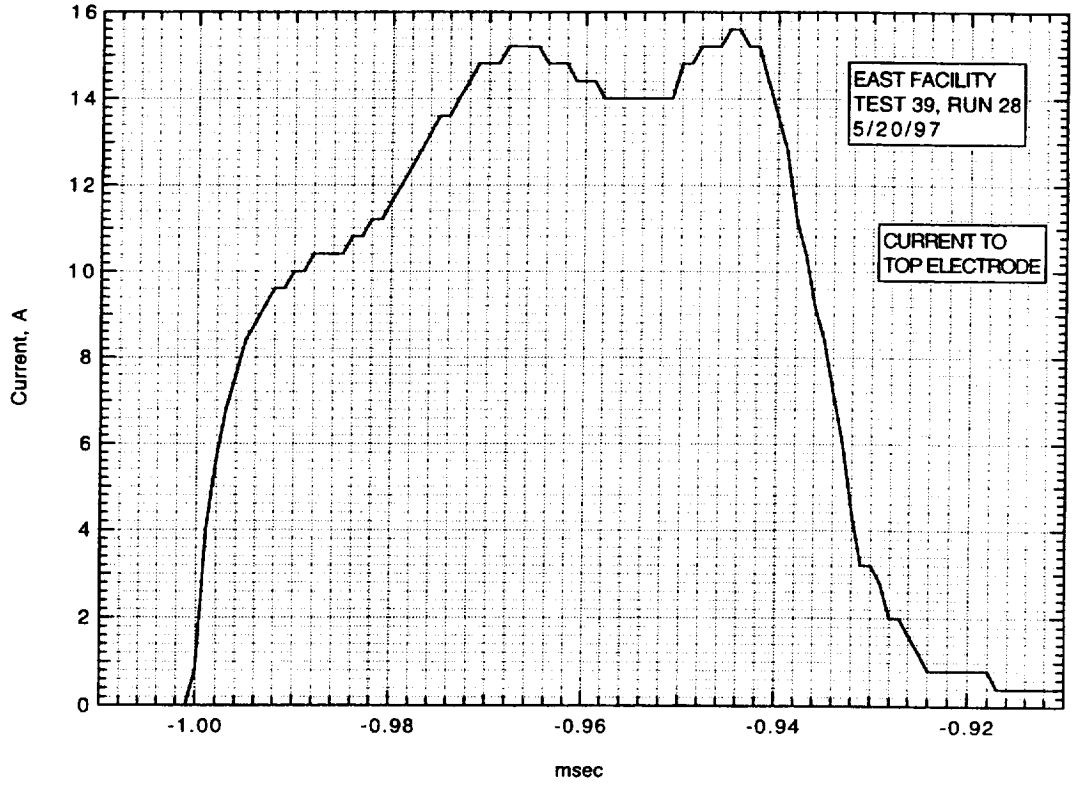

Run 28. Current to top electrode.

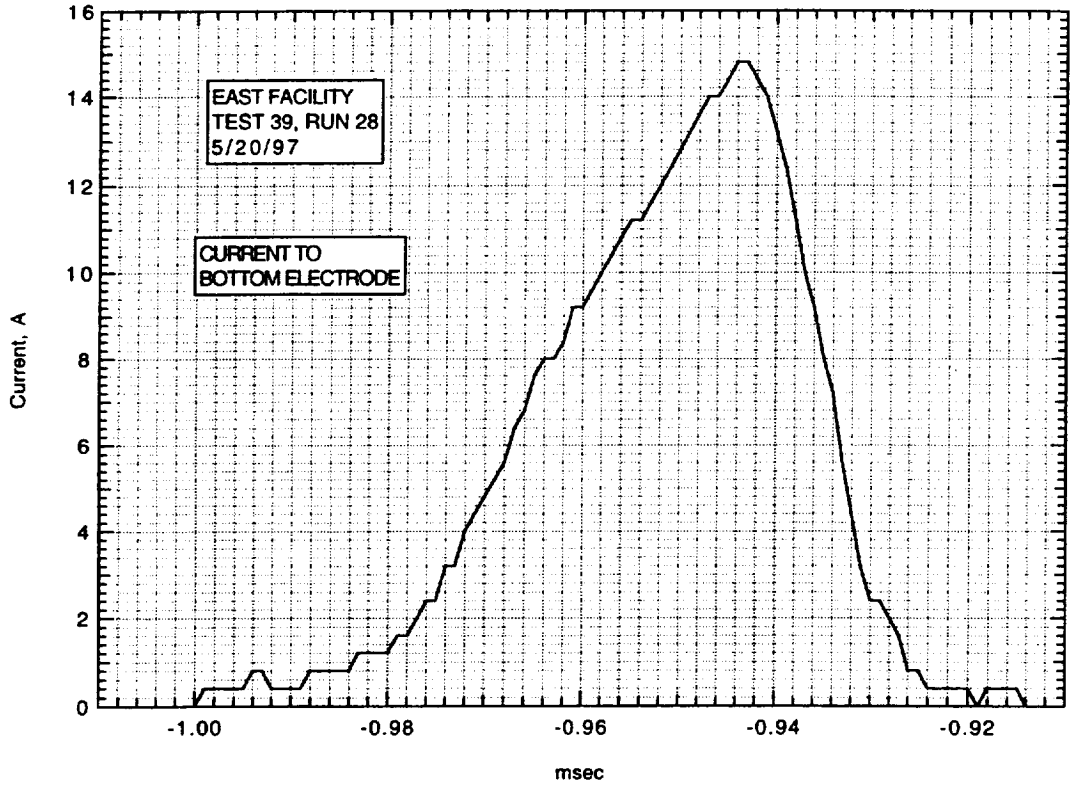

Run 28. Current to bottom electrode.

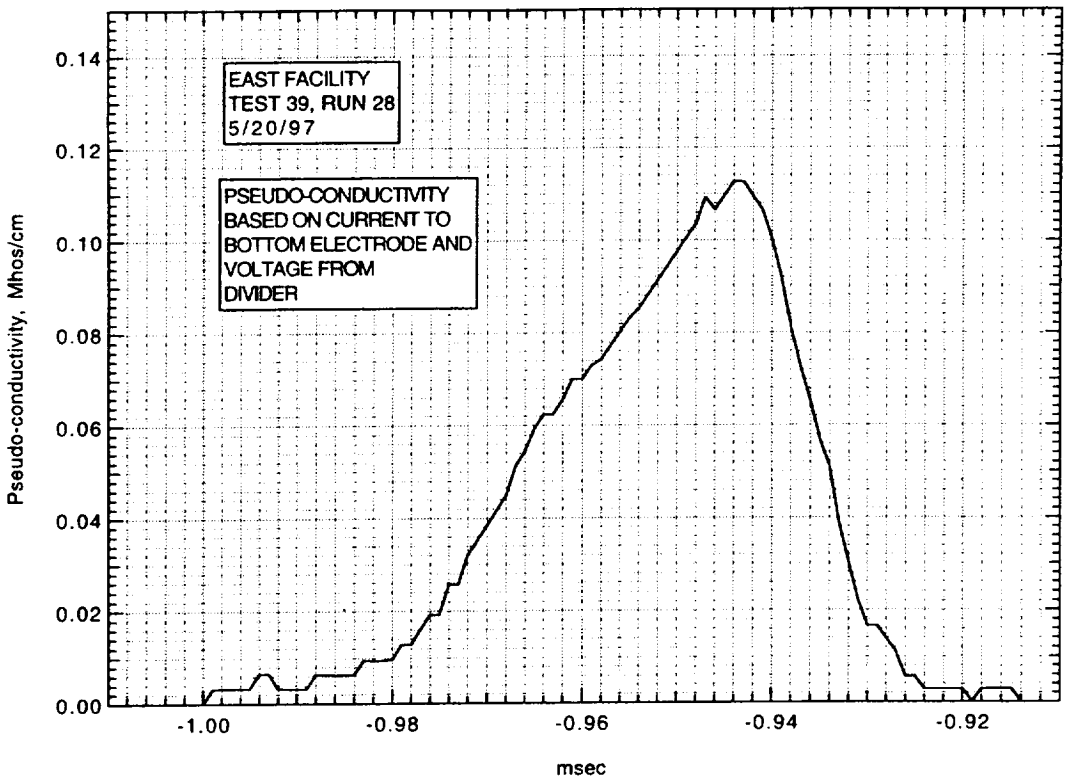

Run 28. Pseudo-conductivity based on current to bottom electrode and voltage from divider.

AIR CONDUCTIVITY MEASUREMENT IN AMES EAST FACILITY

RUN 39/29, 5/22/97

1. Driven tube conditions:

53.2% N_2O, 46.8% N_2,
Total pressure - 13 Torr
Measured shock velocity between stns D and F - 4.322 km/sec
Estimated shock velocity at electrodes, from Δt(DF) - 4.159 km/sec
Measured shock pressure at stn D - 4.72 atm
Measured shock pressure at stn F - 5.36 atm; this value rather uncertain due to large EM noise pickup

2. Electrodes, driven tube dimensions:

Electrode size - 3.10 cm square
Electrode spacing - 3.10 cm
Main diaphragm to electrodes - 454.475 cm
Skimmer nose to electrodes - 39.979 cm
Driven tube diameter - 10.16 cm
Stn D (dn tube) to electrodes (channel) - 77.365 cm
Electrodes (channel) to stn F (channel) - 20.32 cm

3. Nominal test conditions:

Pressure - 5 atm
Voltage across electrodes - 91/81 V

4. Breakdown:

Little or no indication of breakdown.

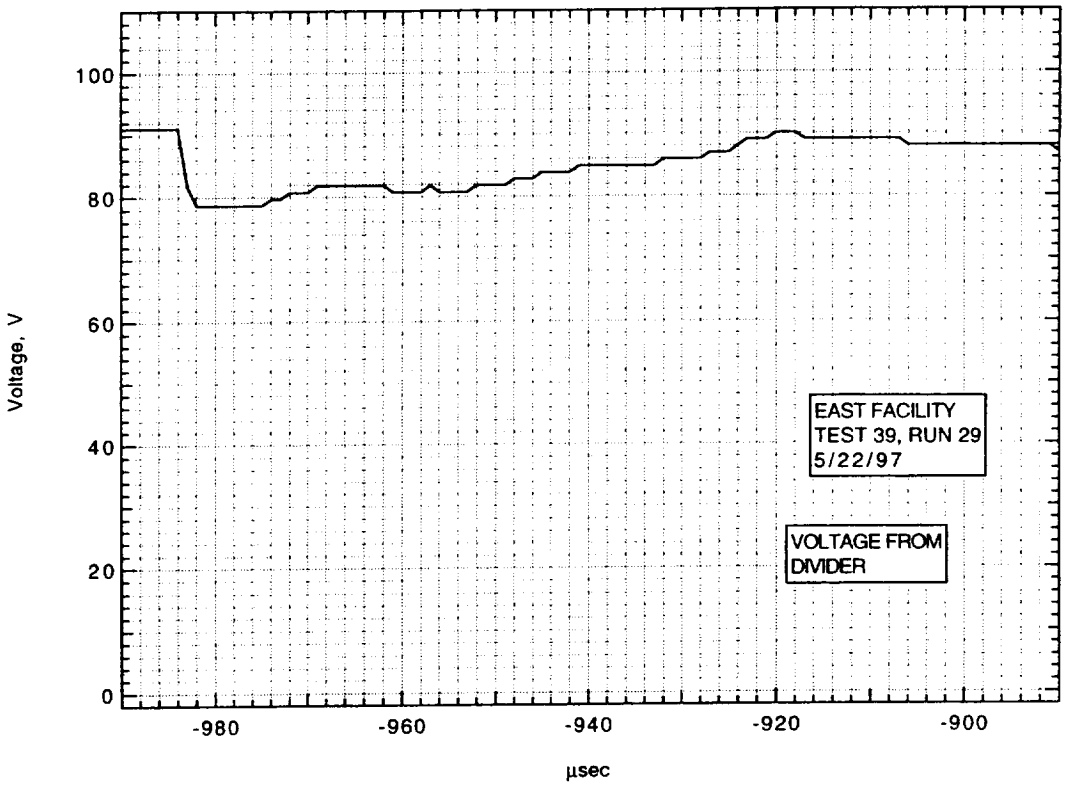

Run 29. Voltage from divider.

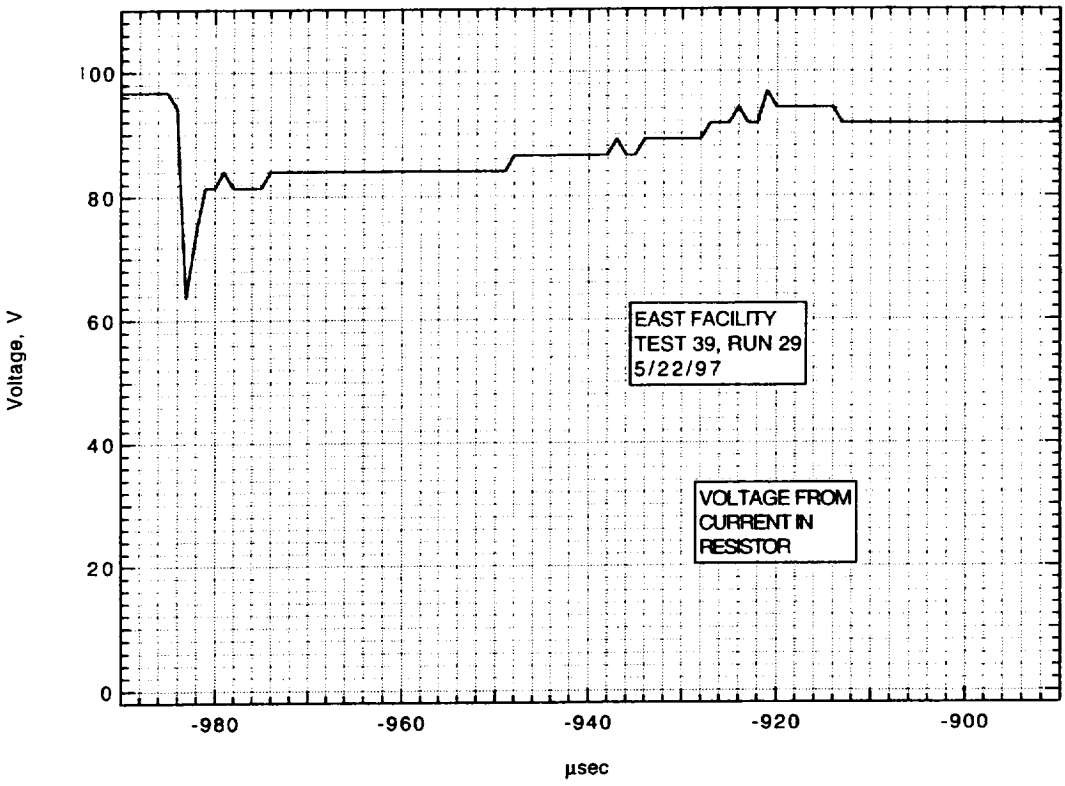

Run 29. Voltage from current in resistor.

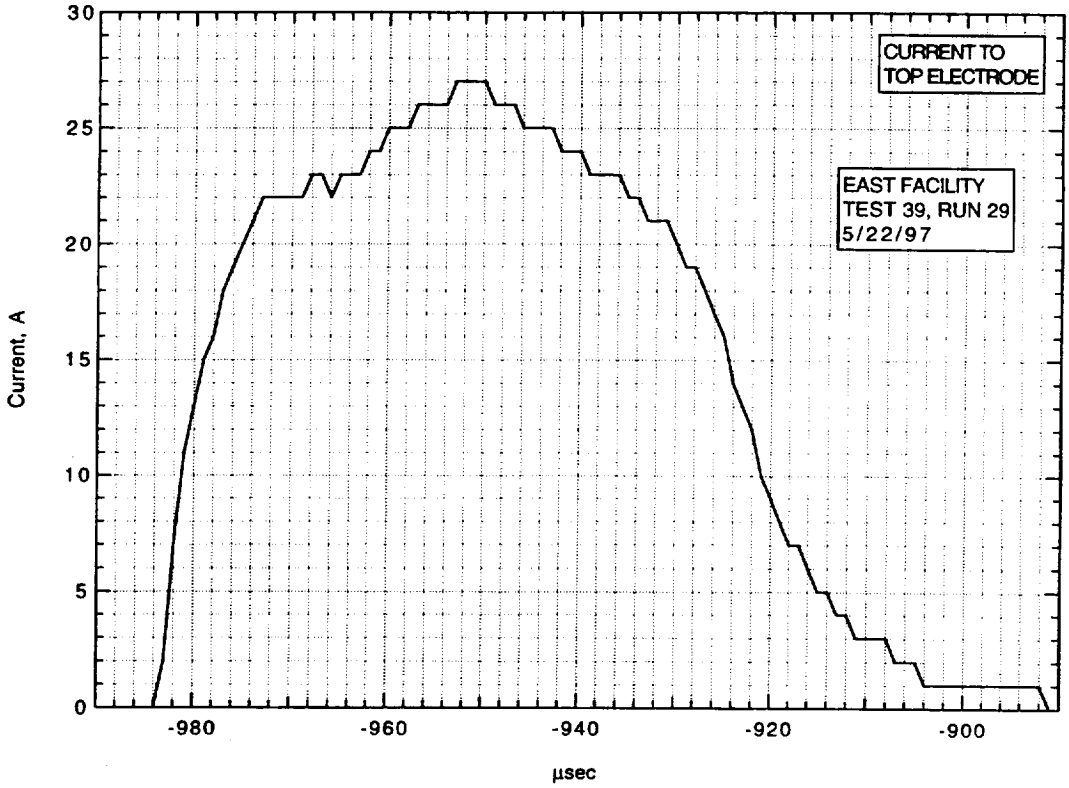

Run 29. Current to top electrode.

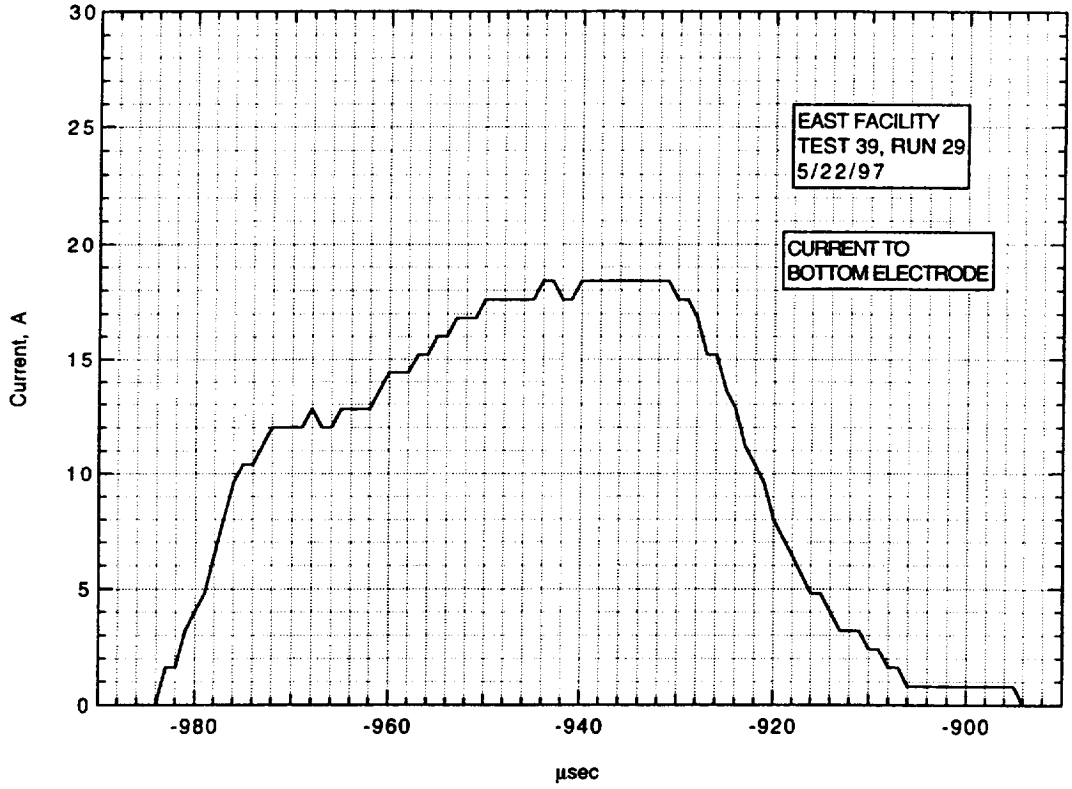

Run 29. Current to bottom electrode.

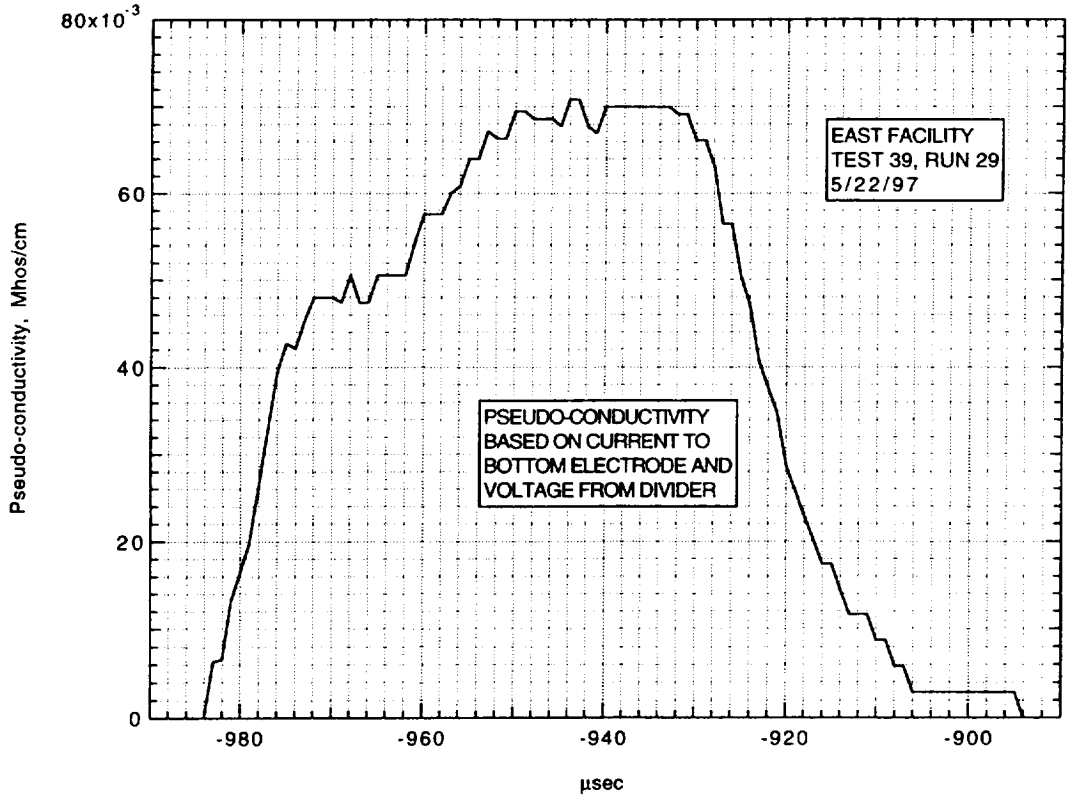

Run 29. Pseudo-conductivity based on current to bottom electrode and voltage from divider.

AIR CONDUCTIVITY MEASUREMENT IN AMES EAST FACILITY

RUN 39/30, 5/23/97

1. Driven tube conditions:

53.2% N_2O, 46.8% N_2,
Total pressure - 13 Torr
Measured shock velocity between stns D and F - 4.380 km/sec
Estimated shock velocity at electrodes, from Δt(DF) - 4.215 km/sec
Measured shock pressure at stn D - 4.99 atm
Measured shock pressure at stn F - 5.64 atm; this value rather uncertain due to large EM noise pickup

2. Electrodes, driven tube dimensions:

Electrode size - 3.10 cm square
Electrode spacing - 3.10 cm
Main diaphragm to electrodes - 454.475 cm
Skimmer nose to electrodes - 39.979 cm
Driven tube diameter - 10.16 cm
Stn D (dn tube) to electrodes (channel) - 77.365 cm
Electrodes (channel) to stn F (channel) - 20.32 cm

3. Nominal test conditions:

Pressure - 5 atm
Voltage across electrodes - 92/84 V

4. Breakdown:

Little or no indication of breakdown.

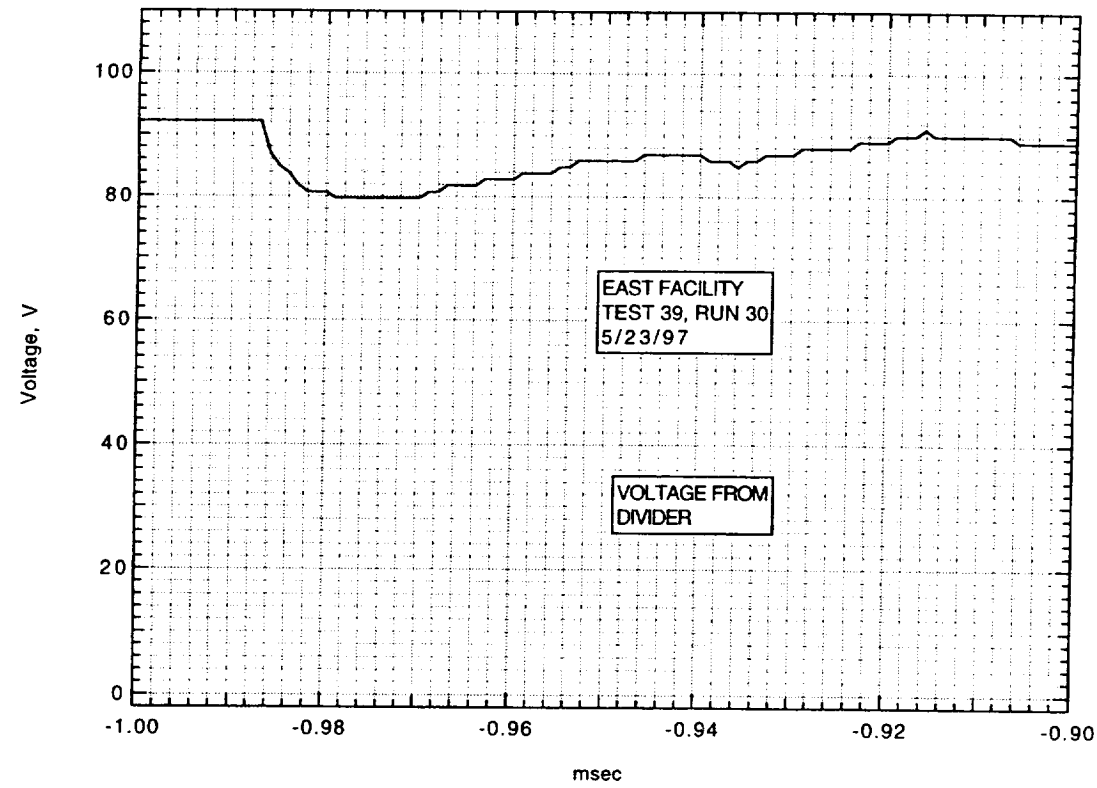

Run 30. Voltage from divider.

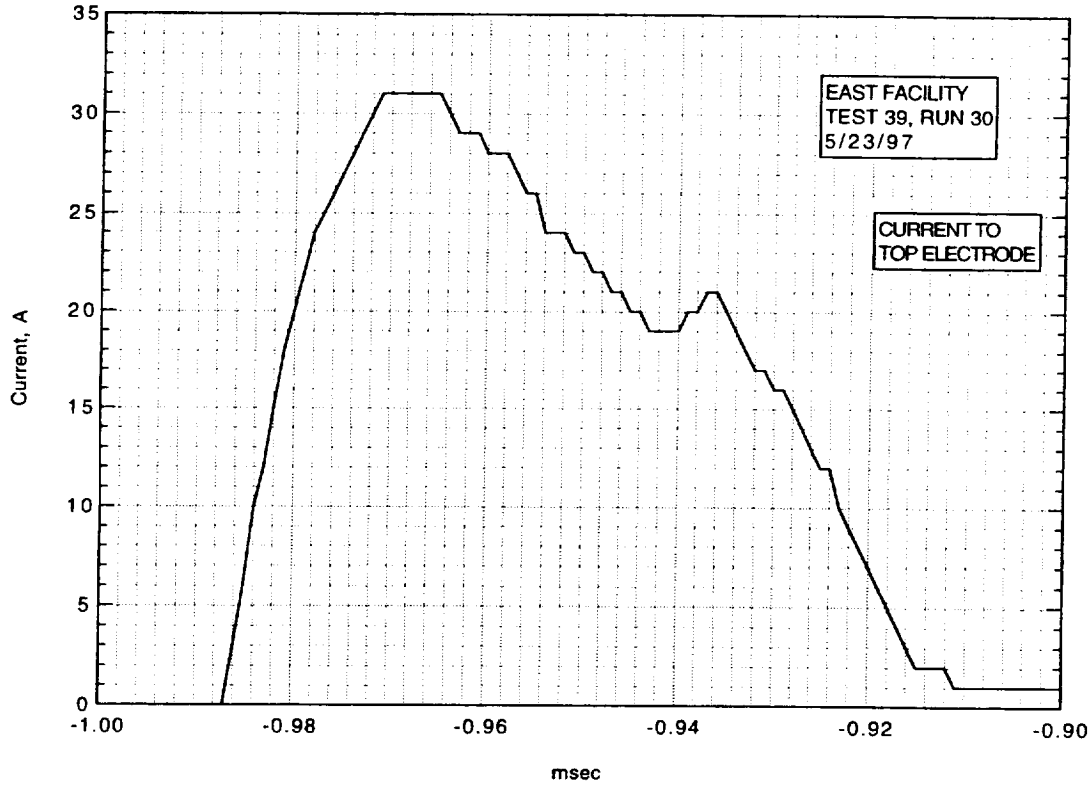

Run 30. Voltage from current in resistor.

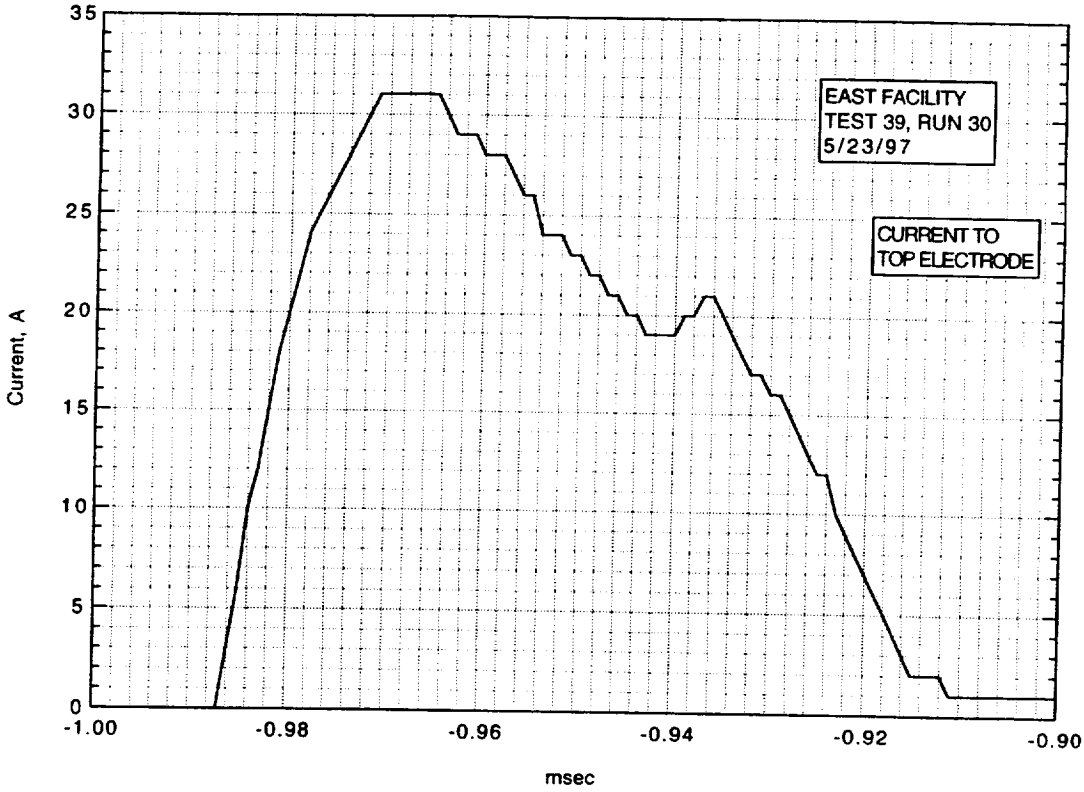

Run 30. Current to top electrode.

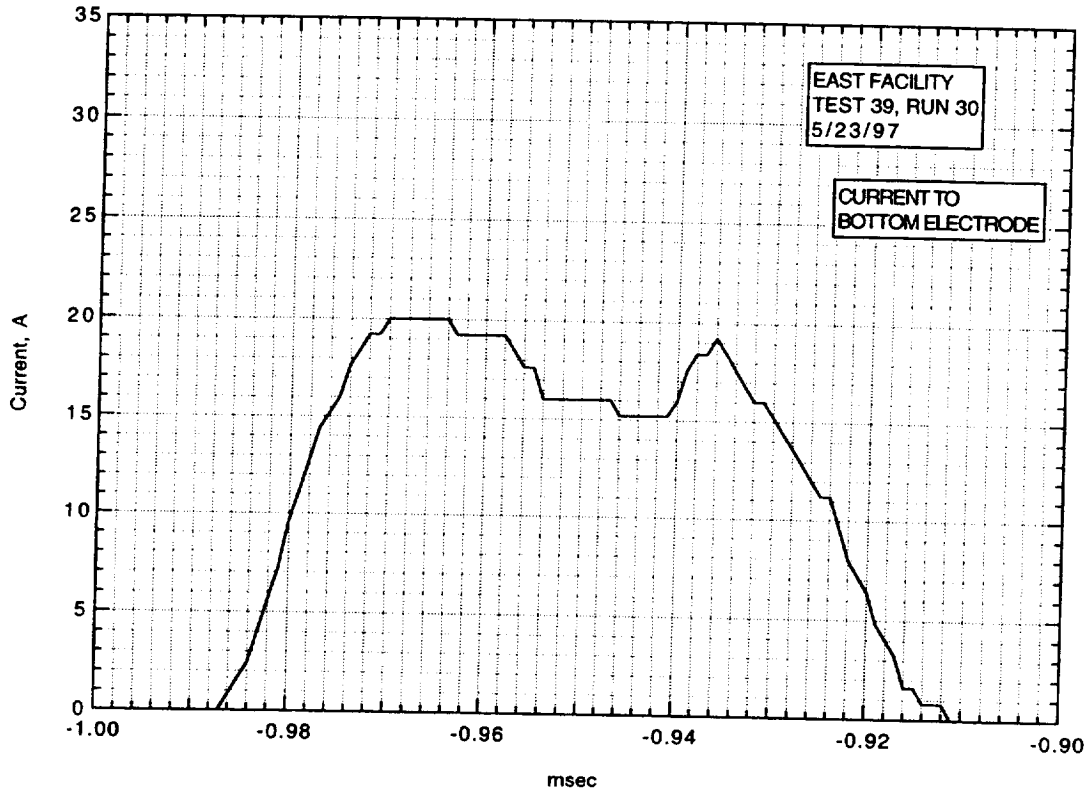

Run 30. Current to bottom electrode.

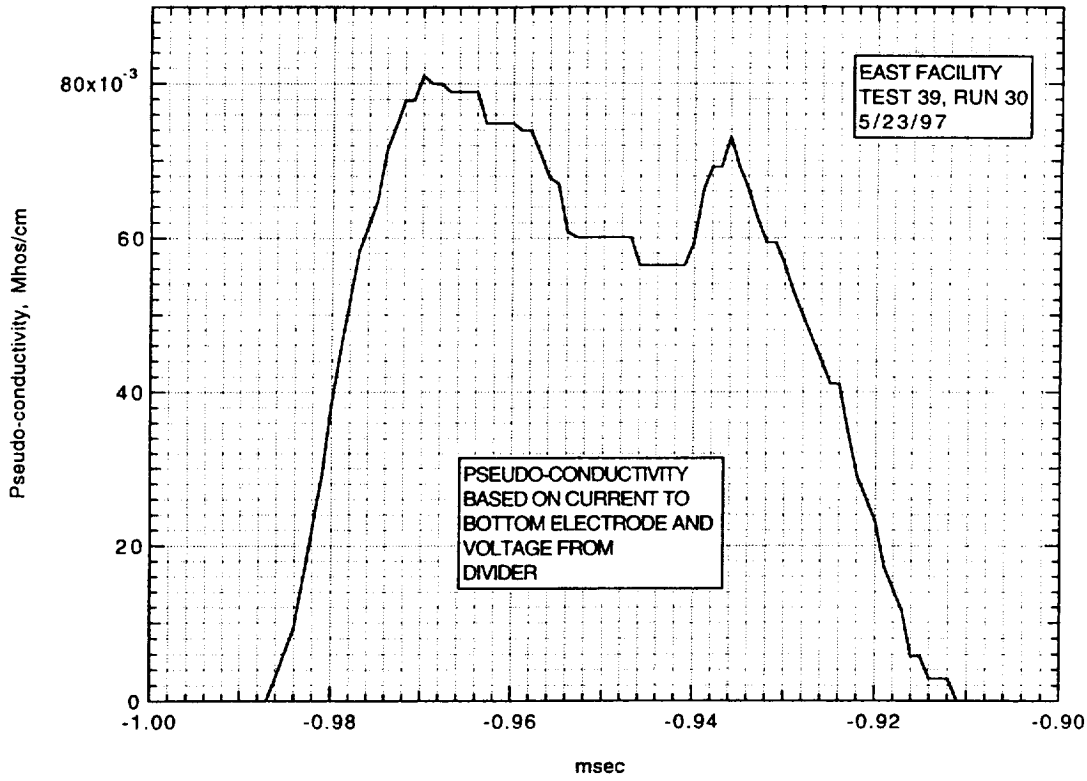

Run 30. Pseudo-conductivity based on current to bottom electrode and voltage from divider.

AIR CONDUCTIVITY MEASUREMENT IN AMES EAST FACILITY

RUN 39/31, 5/27/97

1. Driven tube conditions:

53.2% N_2O, 46.8% N_2,
Total pressure - 13 Torr
Measured shock velocity between stns D and F - 4.835 km/sec
Estimated shock velocity at electrodes, from Δt(DF) - 4.653 km/sec
Measured shock pressure at stn D - 7.08 atm
Measured shock pressure at stn F - 4.90 atm; this value rather uncertain due to large EM noise pickup

2. Electrodes, driven tube dimensions:

Electrode size - 3.10 cm square
Electrode spacing - 3.10 cm
Main diaphragm to electrodes - 454.475 cm
Skimmer nose to electrodes - 39.979 cm
Driven tube diameter - 10.16 cm
Stn D (dn tube) to electrodes (channel) - 77.365 cm
Electrodes (channel) to stn F (channel) - 20.32 cm

3. Nominal test conditions:

Pressure - 5 atm
Voltage across electrodes - 92/86 V

4. Breakdown:

Little or no indication of breakdown.

Run no: 31 **Date:** 5/27/97 **Shock press. at D:** 7.08 atm
Shock vel. at E: 4.65 km/sec **Voltage at start of current flow:** 92 V

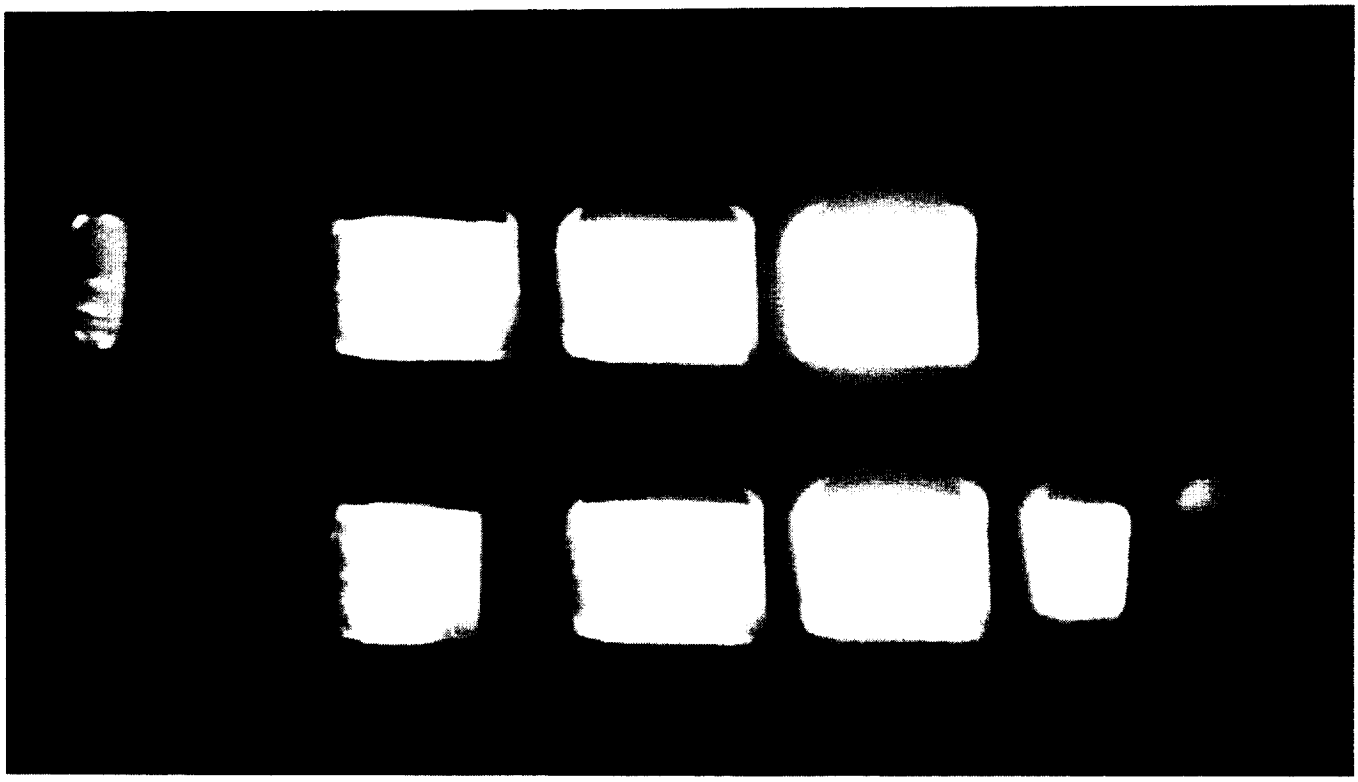

Frame:	**2**	**4**	**6**	**8**
Time:	0.9	8.9	16.9	24.9
Mach no:				
Frame:	**1**	**3**	**5**	**7**
Time:	-3.1	4.9	12.9	20.9
Mach no:				

V_I: 4.3 km/sec V_{CAV}: 4.89 km/sec

IMACON image of the shock-heated test gas flow in the electrode region. The time is measured from the start of the current flow. Mach numbers and velocities are deduced from the image as explained in section A.2.5.3.

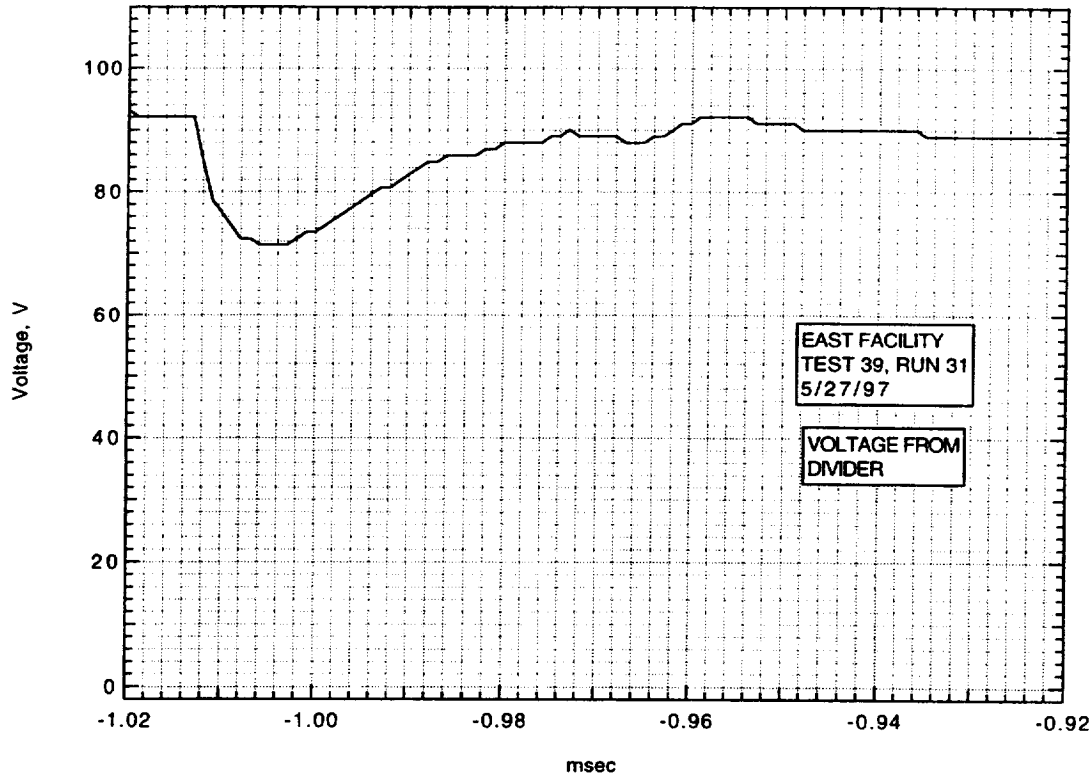

Run 31. Voltage from divider.

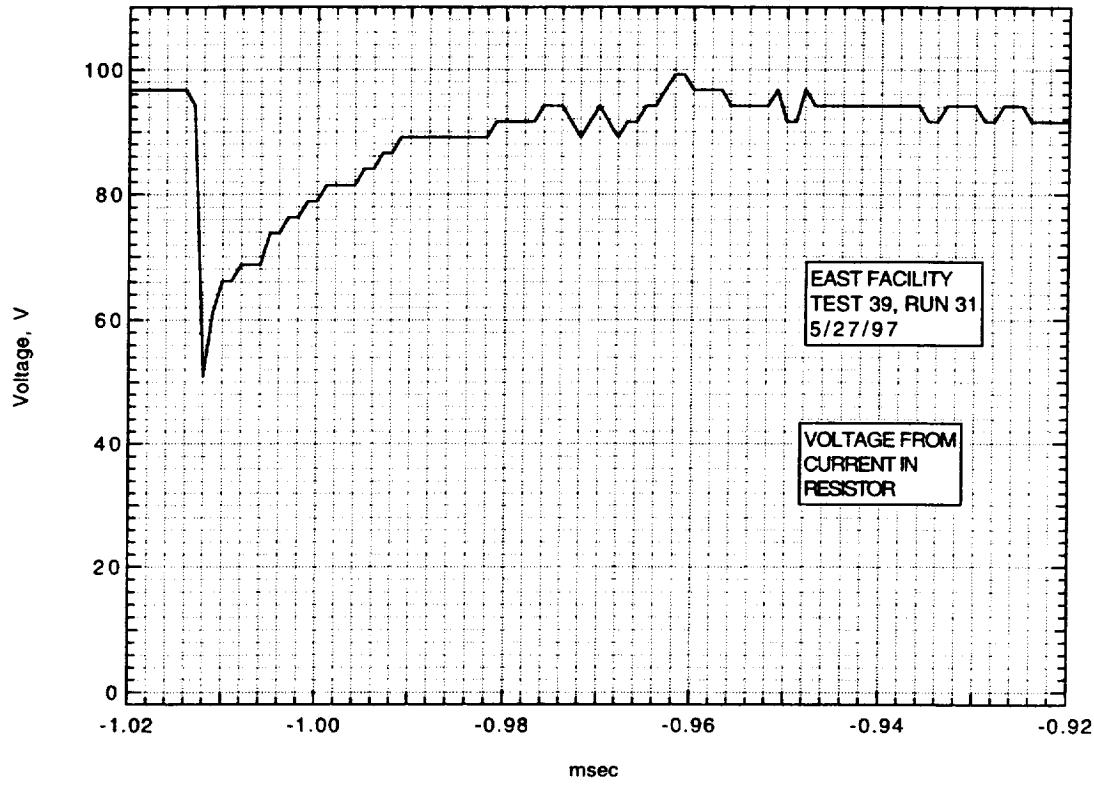

Run 31. Voltage from current in resistor.

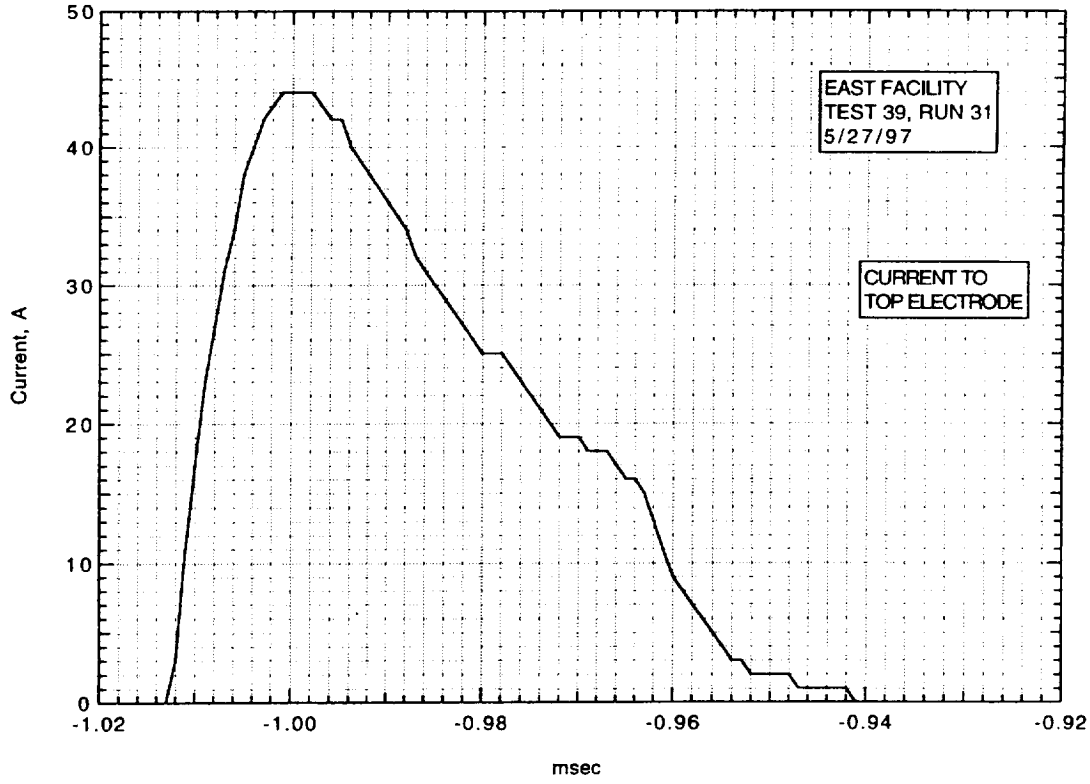

Run 31. Current to top electrode.

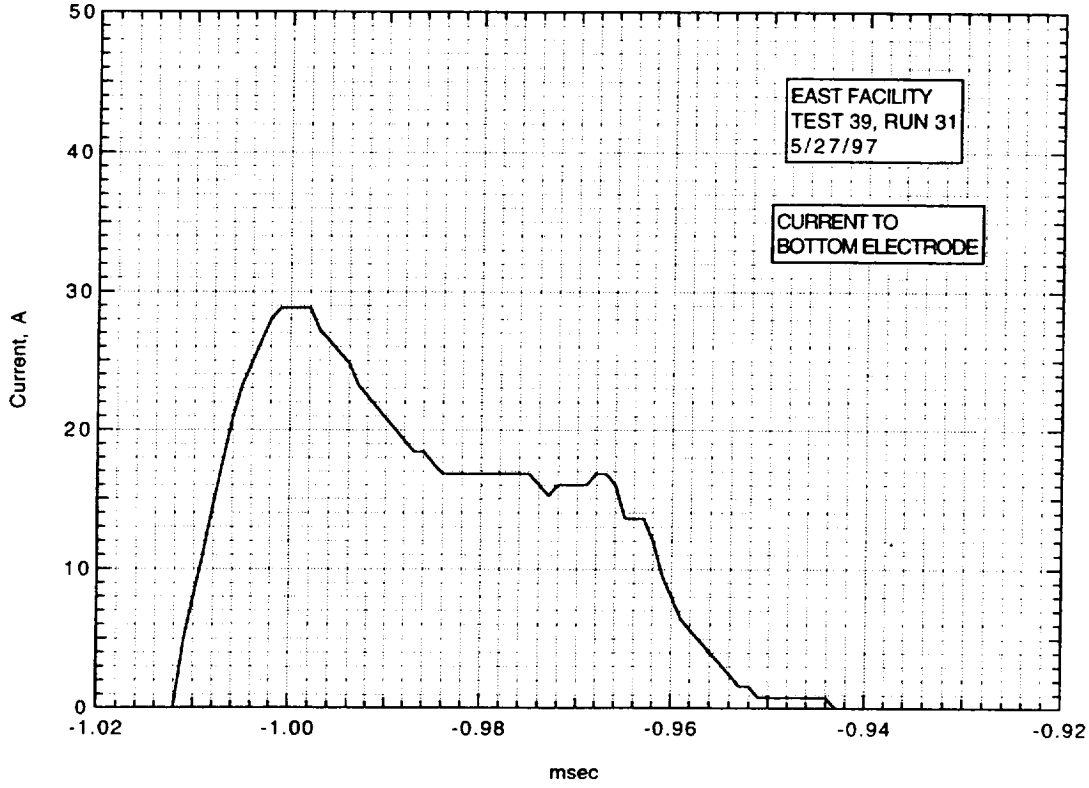

Run 31. Current to bottom electrode.

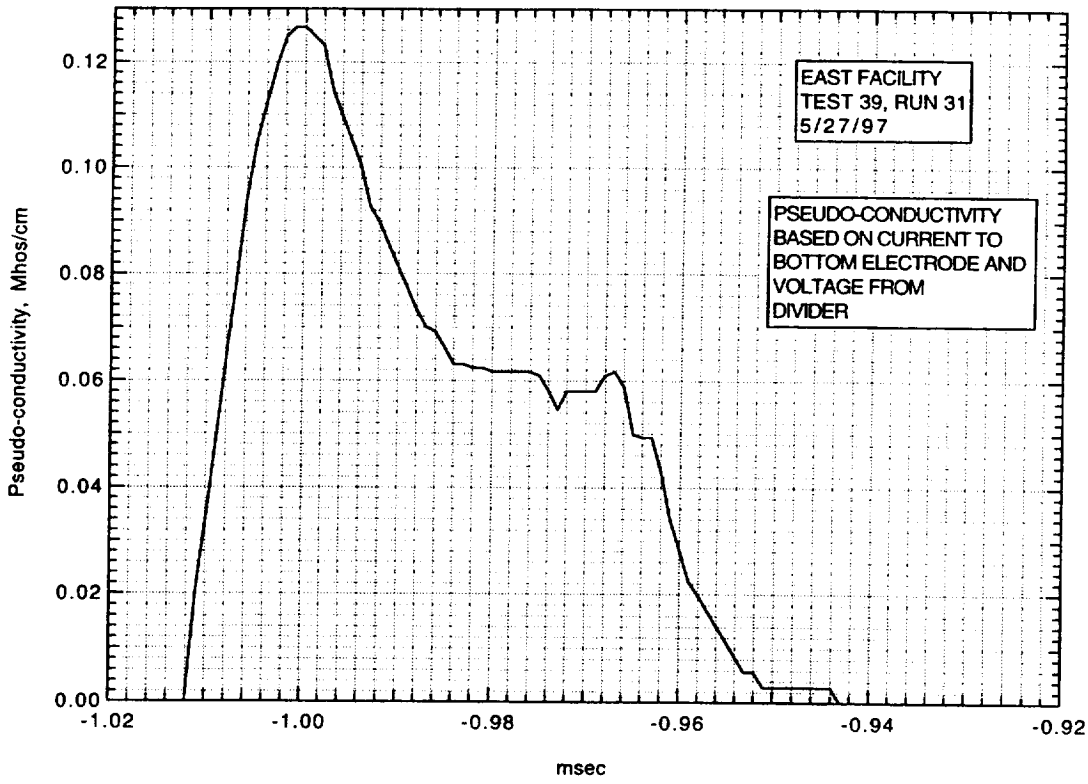

Run 31. Pseudo-conductivity from current to bottom electrode and voltage from divider.

AIR CONDUCTIVITY MEASUREMENT IN AMES EAST FACILITY

RUN 39/32, 5/28/97

1. Driven tube conditions:

53.2% N_2O, 46.8% N_2,
Total pressure - 13 Torr
Measured shock velocity between stns D and F - 5.114 km/sec
Estimated shock velocity at electrodes, from $\Delta t(DF)$ - 4.921 km/sec
Measured shock pressure at stn D - 7.61 atm
Measured shock pressure at stn F - 6.58 atm; this value
very uncertain due to large EM noise pickup

2. Electrodes, driven tube dimensions:

Electrode size - 3.10 cm square
Electrode spacing - 3.10 cm
Main diaphragm to electrodes - 454.475 cm
Skimmer nose to electrodes - 39.979 cm
Driven tube diameter - 10.16 cm
Stn D (dn tube) to electrodes (channel) - 77.365 cm
Electrodes (channel) to stn F (channel) - 20.32 cm

3. Nominal test conditions:

Pressure - 5 atm
Voltage across electrodes - 92/89 V

4. Breakdown:

Little or no indication of breakdown.

Run no: 32 **Date:** 5/28/97 **Shock press. at D:** 7.61 atm
Shock vel. at E: 4.92 km/sec **Voltage at start of current flow:** 92 V

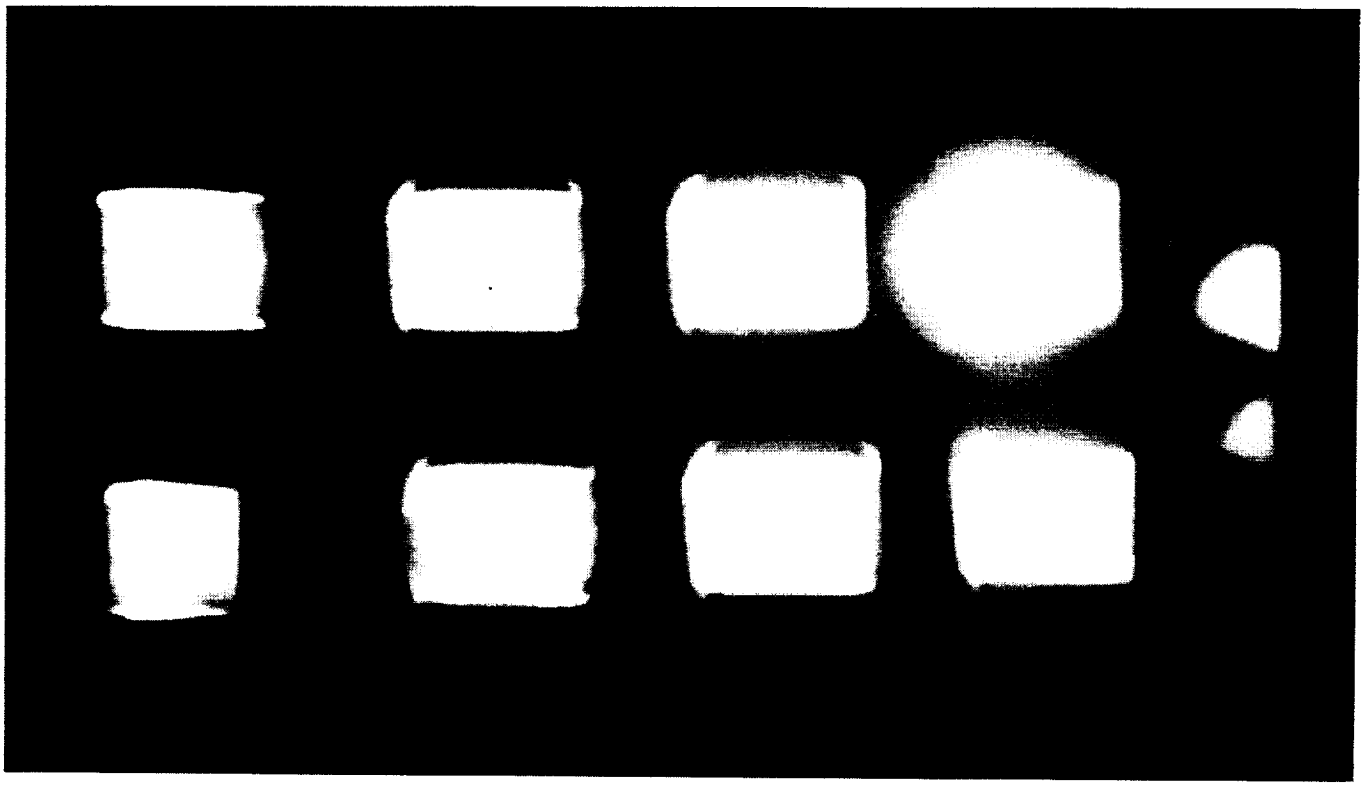

Frame:	**2**	**4**	**6**	**8**
Time:	8.9	16.9	24.9	32.9
Mach no:				
Frame:	**1**	**3**	**5**	**7**
Time:	4.9	12.9	20.9	28.9
Mach no:				

V_I: km/sec V_{CAV}: 5.08 km/sec

IMACON image of the shock-heated test gas flow in the electrode region. The time is measured from the start of the current flow. Mach numbers and velocities are deduced from the image as explained in section A.2.5.3.

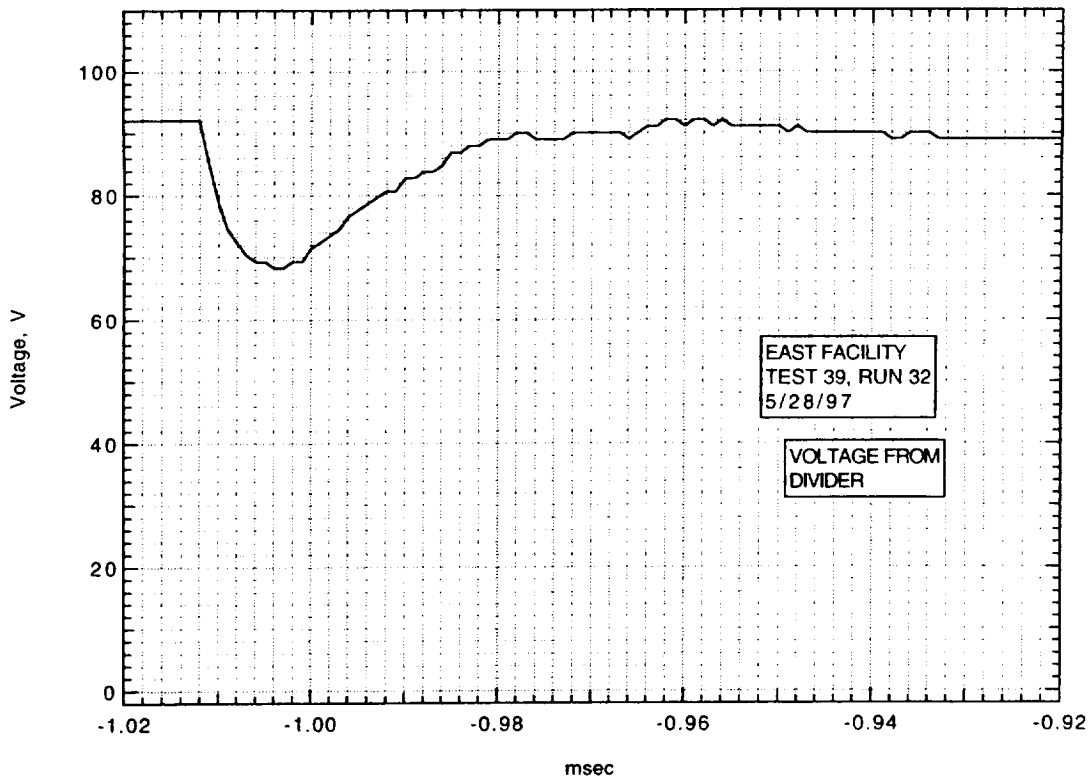

Run 32. Voltage from divider.

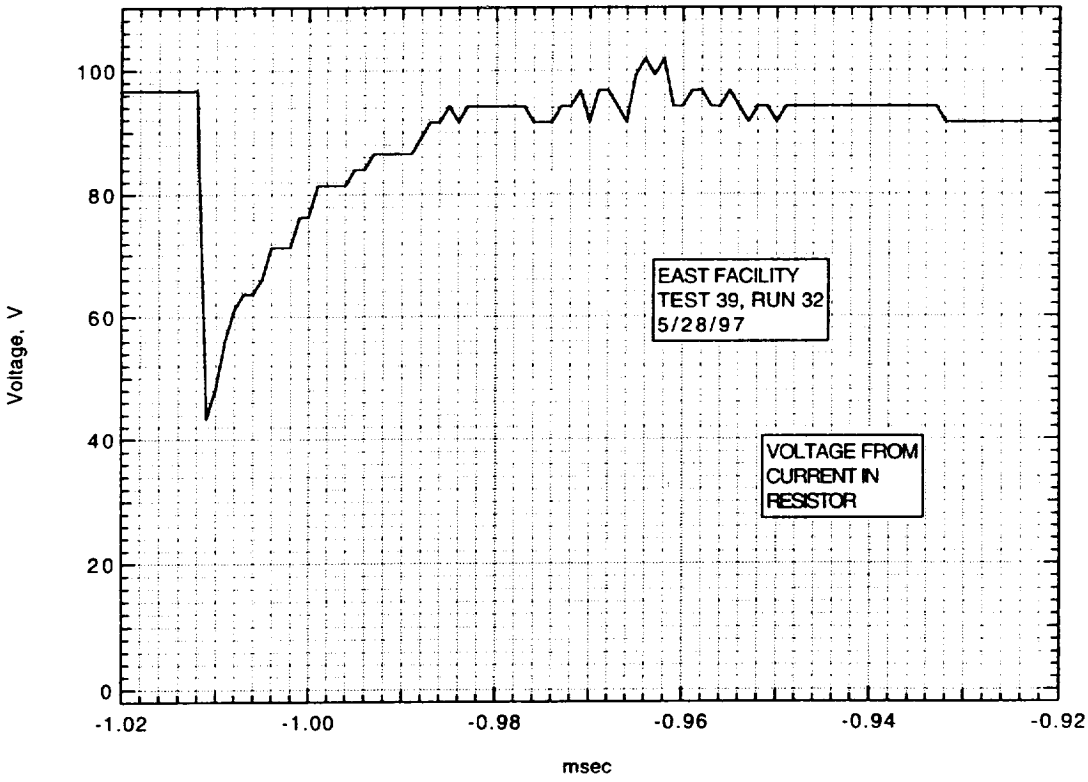

Run 32. Voltage from current in resistor.

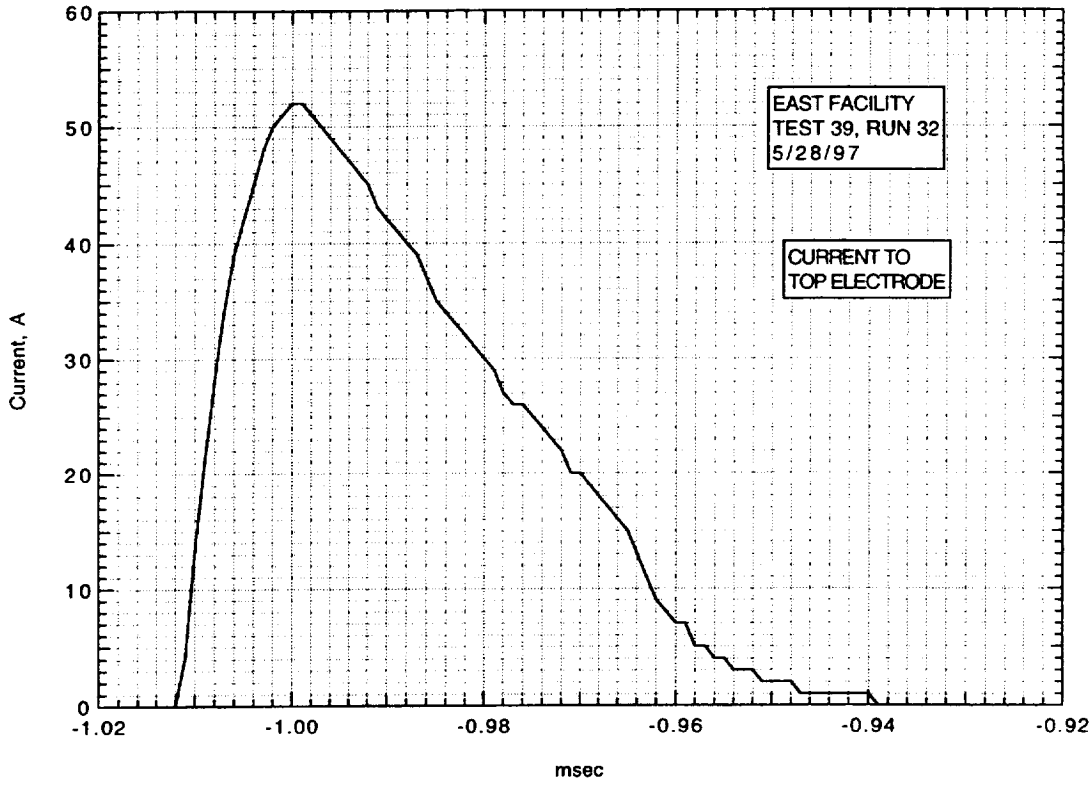

Run 32. Current to top electrode.

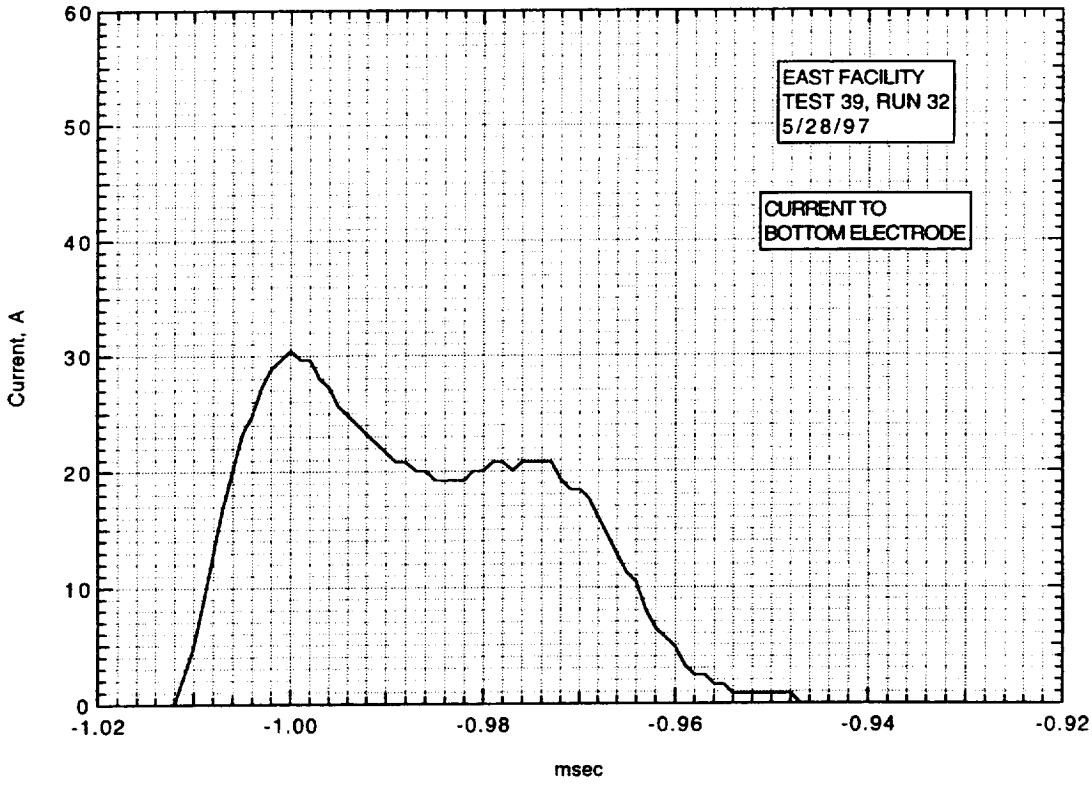

Run 32. Current to bottom electrode.

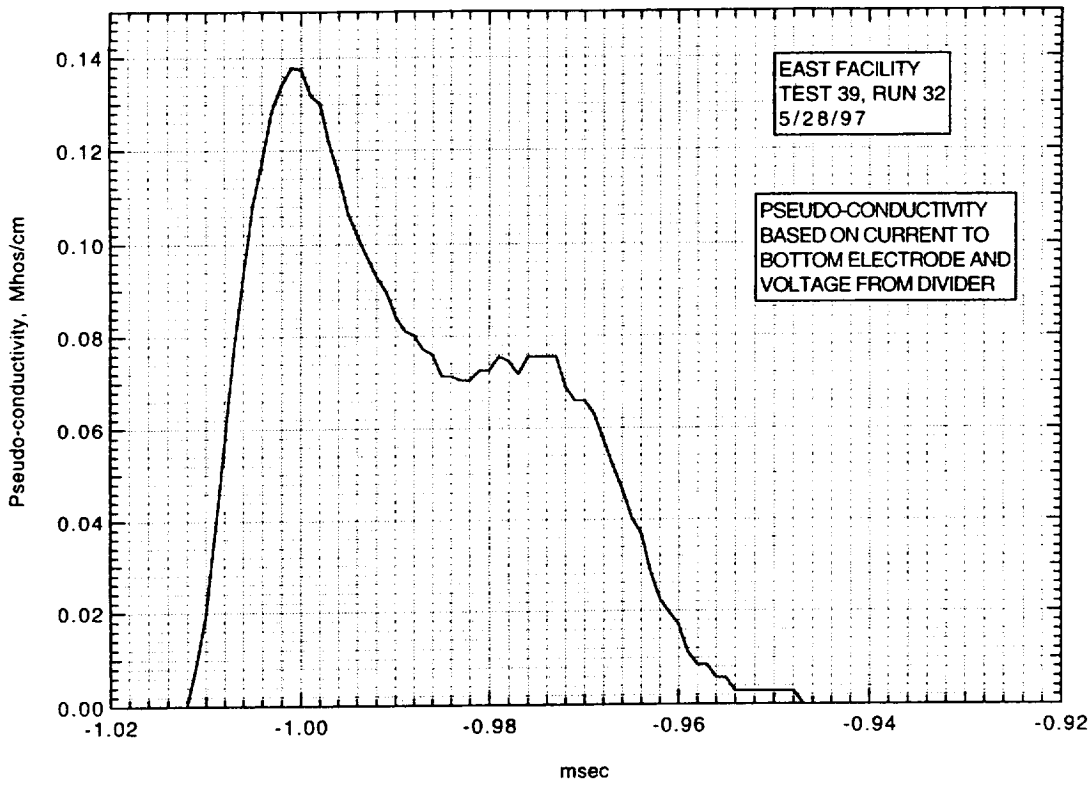

Run 32. Pseudo-conductivity based on current to bottom electrode and voltage from divider.

AIR CONDUCTIVITY MEASUREMENT IN AMES EAST FACILITY

RUN 39/33, 5/29/97

1. Driven tube conditions:

53.2% N_2O, 46.8% N_2,
Total pressure - 13 Torr
Measured shock velocity between stns D and F - 4.651 km/sec
Estimated shock velocity at electrodes, from Δt(DF) - 4.475 km/sec
Measured shock pressure at stn D - 5.80 atm
Measured shock pressure at stn F - 7.11 atm; this value
very uncertain due to large EM noise pickup

2. Electrodes, driven tube dimensions:

Electrode size - 3.10 cm square
Electrode spacing - 3.10 cm
Main diaphragm to electrodes - 454.475 cm
Skimmer nose to electrodes - 39.979 cm
Driven tube diameter - 10.16 cm
Stn D (dn tube) to electrodes (channel) - 77.365 cm
Electrodes (channel) to stn F (channel) - 20.32 cm

3. Nominal test conditions:

Pressure - 5 atm
Voltage across electrodes - 188/143 V

4. Breakdown:

Little or no indication of breakdown.

Run no: 33 **Date:** 5/29/97 **Shock press. at D:** 5.80 atm
Shock vel. at E: 4.47 km/sec **Voltage at start of current flow:** 188 V

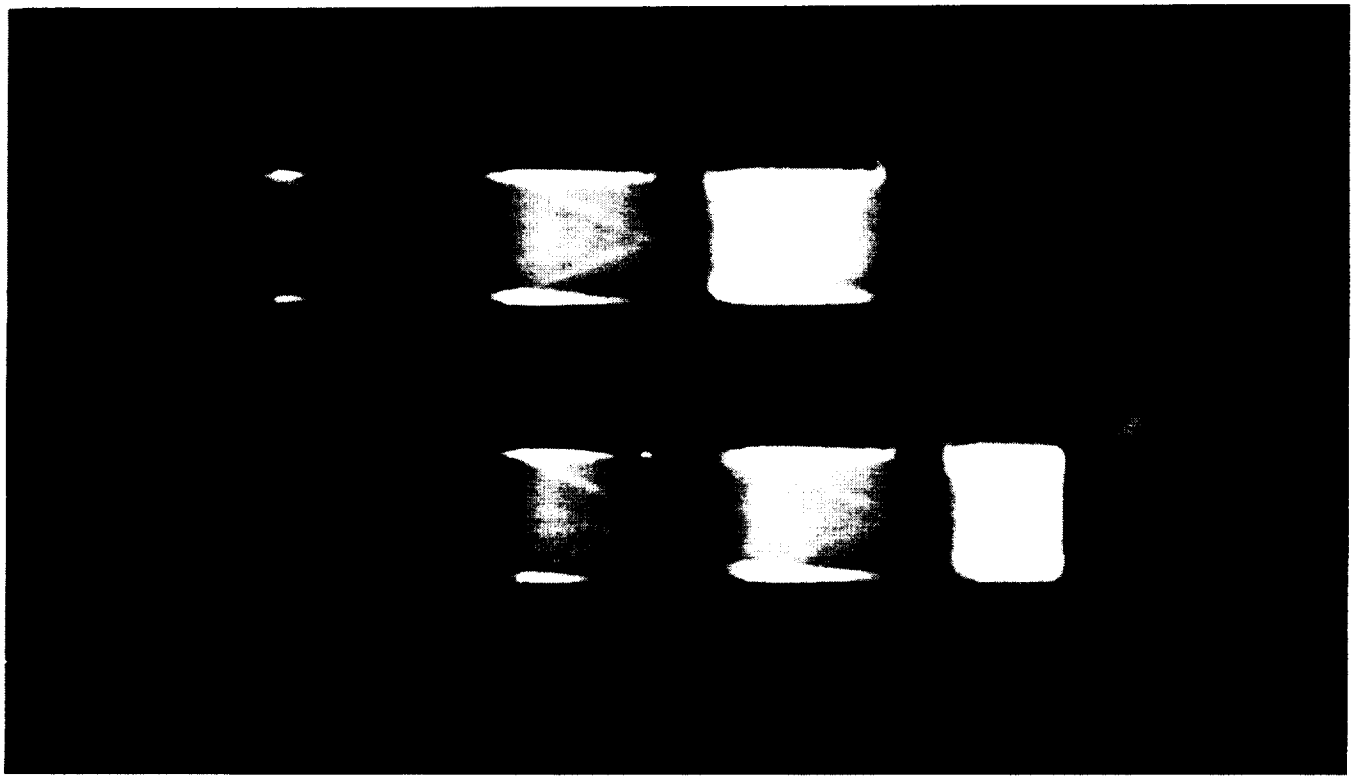

Frame:	**2**	**4**	**6**	**8**
Time:	-4.4	3.6	11.6	19.6
Mach no:			2.40	
Frame:	**1**	**3**	**5**	**7**
Time:	-8.4	-0.4	7.6	15.6
Mach no:			2.53	

V_I: 4.8 km/sec V_{CAV}: 4.68 km/sec

IMACON image of the shock-heated test gas flow in the electrode region. The time is measured from the start of the current flow. Mach numbers and velocities are deduced from the image as explained in section A.2.5.3.

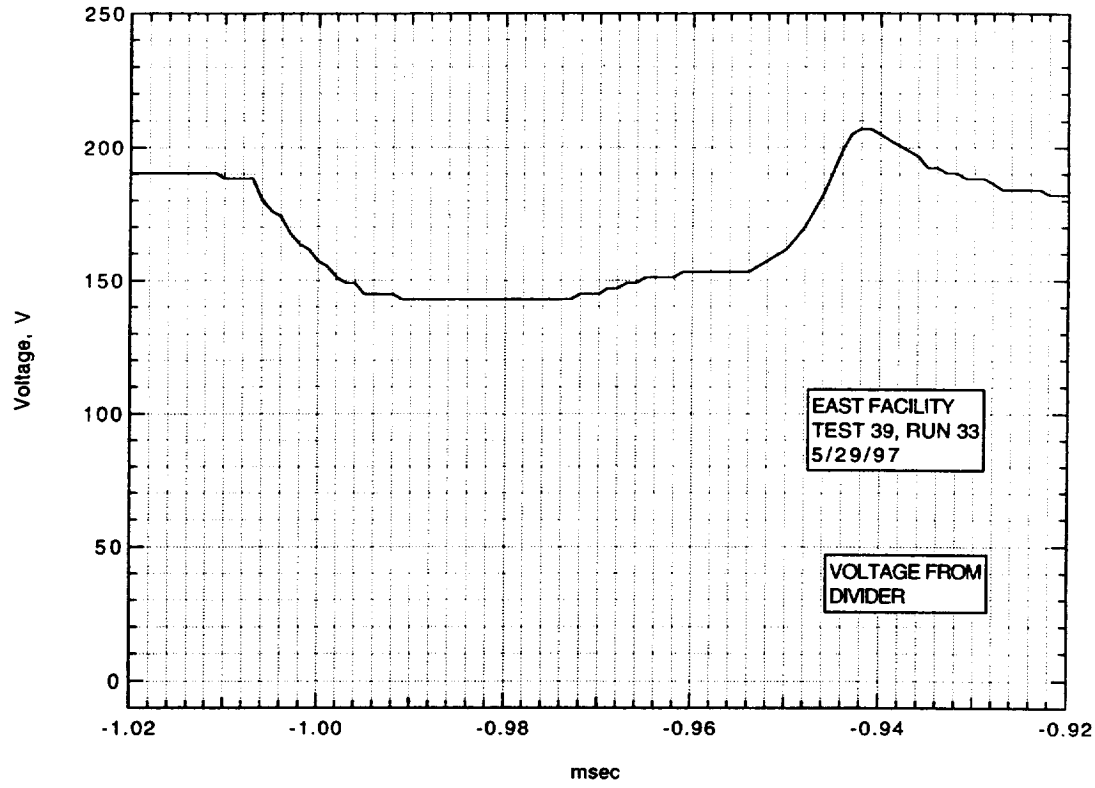

Run 33, Voltage from divider.

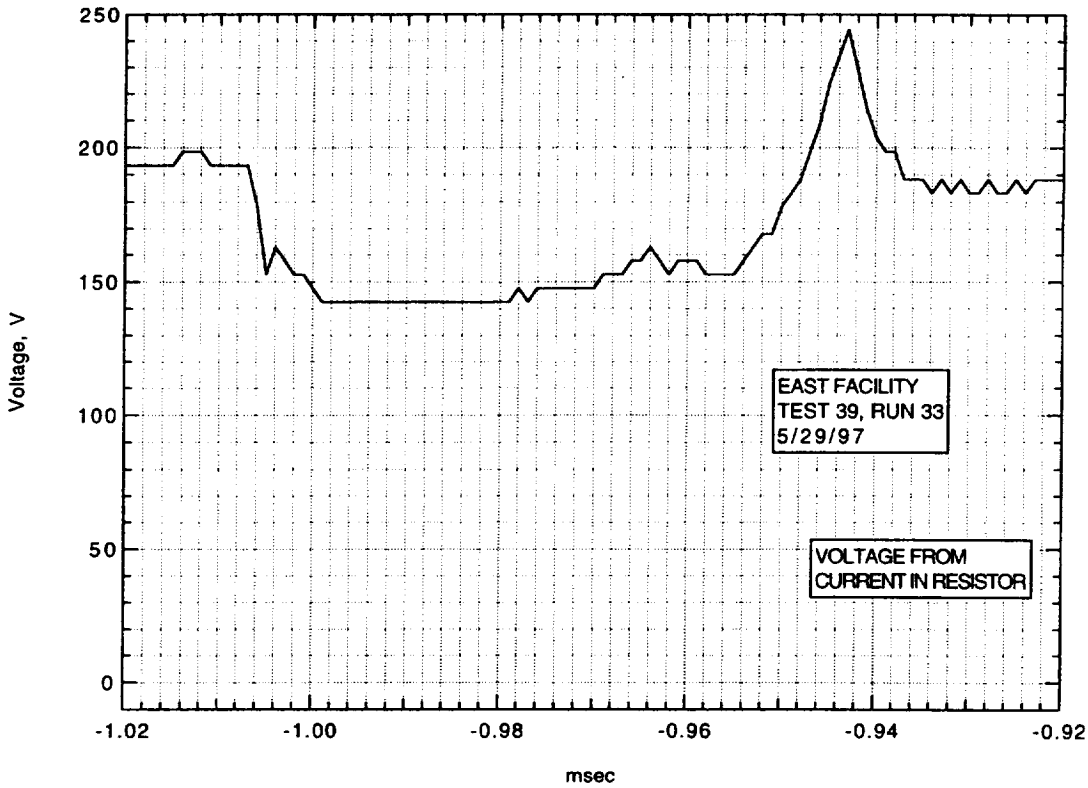

Run 33. Voltage from current in resistor.

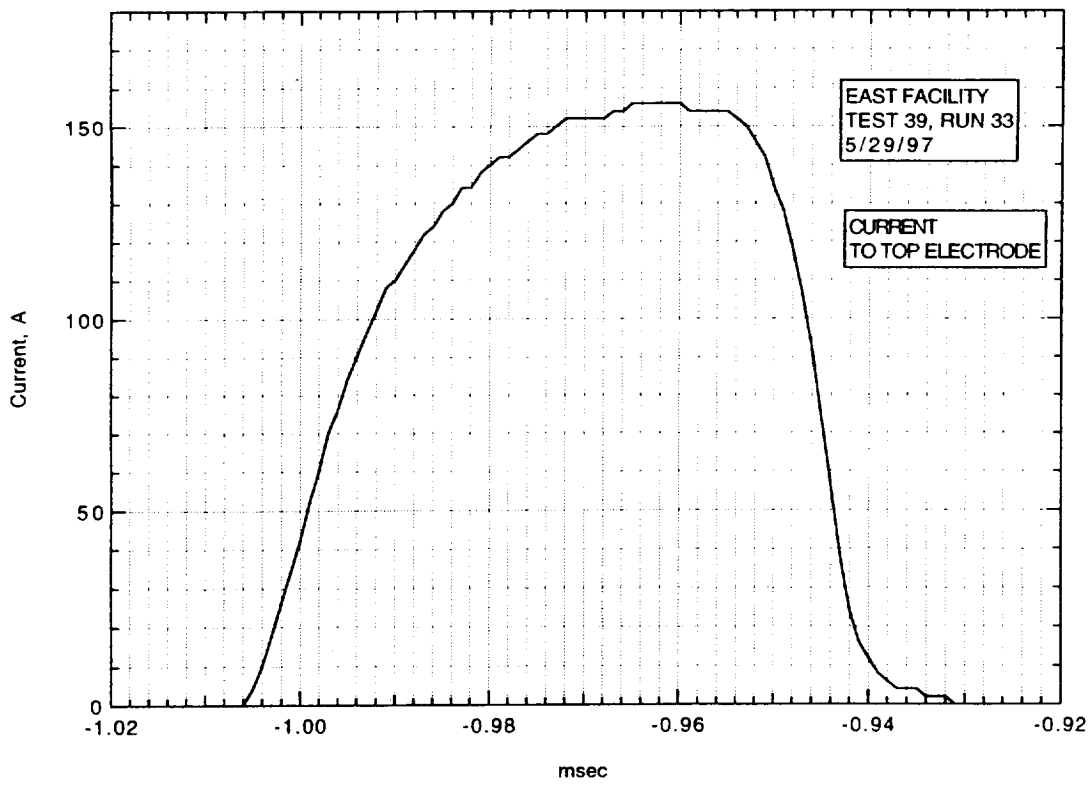

Run 33, Current to top electrode.

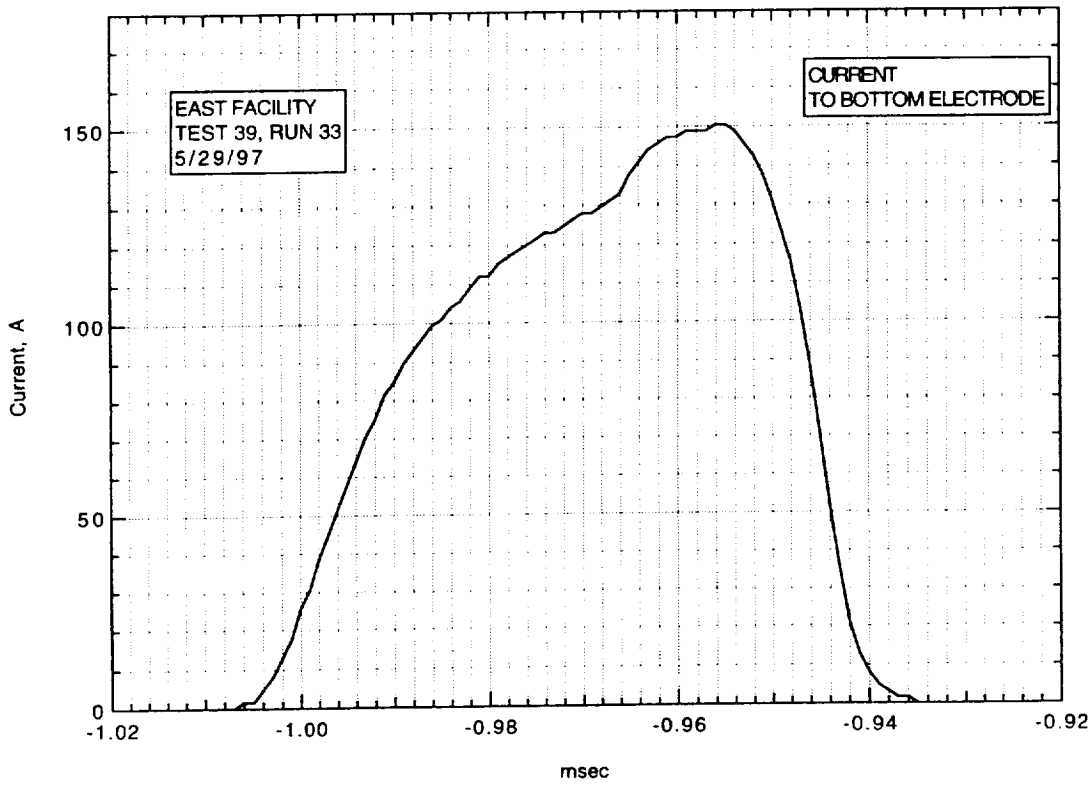

Run 33, Current to bottom electrode.

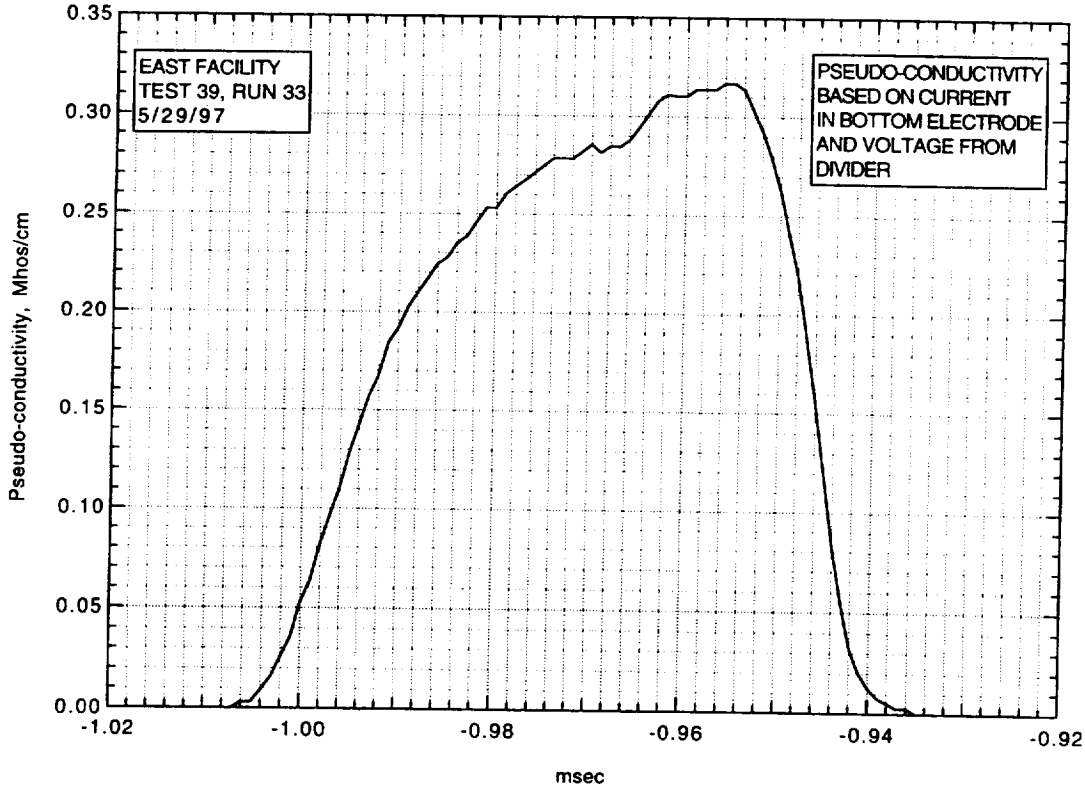

Run 33, Pseudo-conductivity based on current to bottom electrode and voltage from divider.

AIR CONDUCTIVITY MEASUREMENT IN AMES EAST FACILITY

RUN 39/34, 5/30/97

1. Driven tube conditions:

53.2% N_2O, 46.8% N_2,
Total pressure - 13 Torr
Measured shock velocity between stns D and F - 4.741 km/sec
Estimated shock velocity at electrodes, from Δt(DF) - 4.562 km/sec
Measured shock pressure at stn D - 5.97 atm
Measured shock pressure at stn F - 5.43 atm; this value
very uncertain due to large EM noise pickup

2. Electrodes, driven tube dimensions:

Electrode size - 3.10 cm square
Electrode spacing - 3.10 cm
Main diaphragm to electrodes - 454.475 cm
Skimmer nose to electrodes - 39.979 cm
Driven tube diameter - 10.16 cm
Stn D (dn tube) to electrodes (channel) - 77.365 cm
Electrodes (channel) to stn F (channel) - 20.32 cm

3. Nominal test conditions:

Pressure - 5 atm
Voltage across electrodes - 269/191 V

4. Breakdown:

Little or no indication of breakdown.

Run no: 34 **Date:** 5/30/97 **Shock press. at D:** 5.97 atm
Shock vel. at E: 4.60 km/sec **Voltage at start of current flow:** 270 V

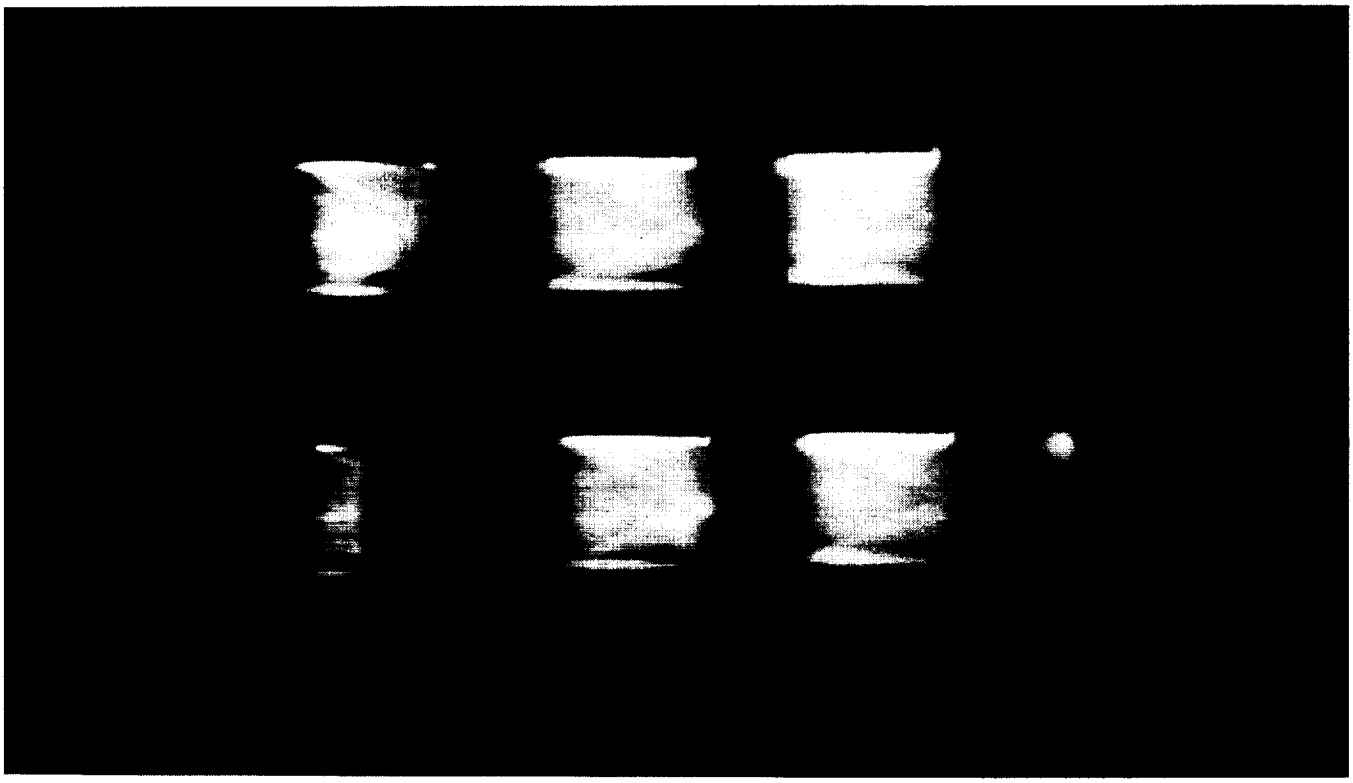

Frame:	**2**	**4**	**6**	**8**
Time:	-0.6	7.4	15.4	23.4
Mach no:			2.37	
Frame:	**1**	**3**	**5**	**7**
Time:	-4.6	3.4	11.4	19.4
Mach no:			2.60	2.24

V_I: km/sec V_{CAV}: 4.80 km/sec

IMACON image of the shock-heated test gas flow in the electrode region. The time is measured from the start of the current flow. Mach numbers and velocities are deduced from the image as explained in section A.2.5.3.

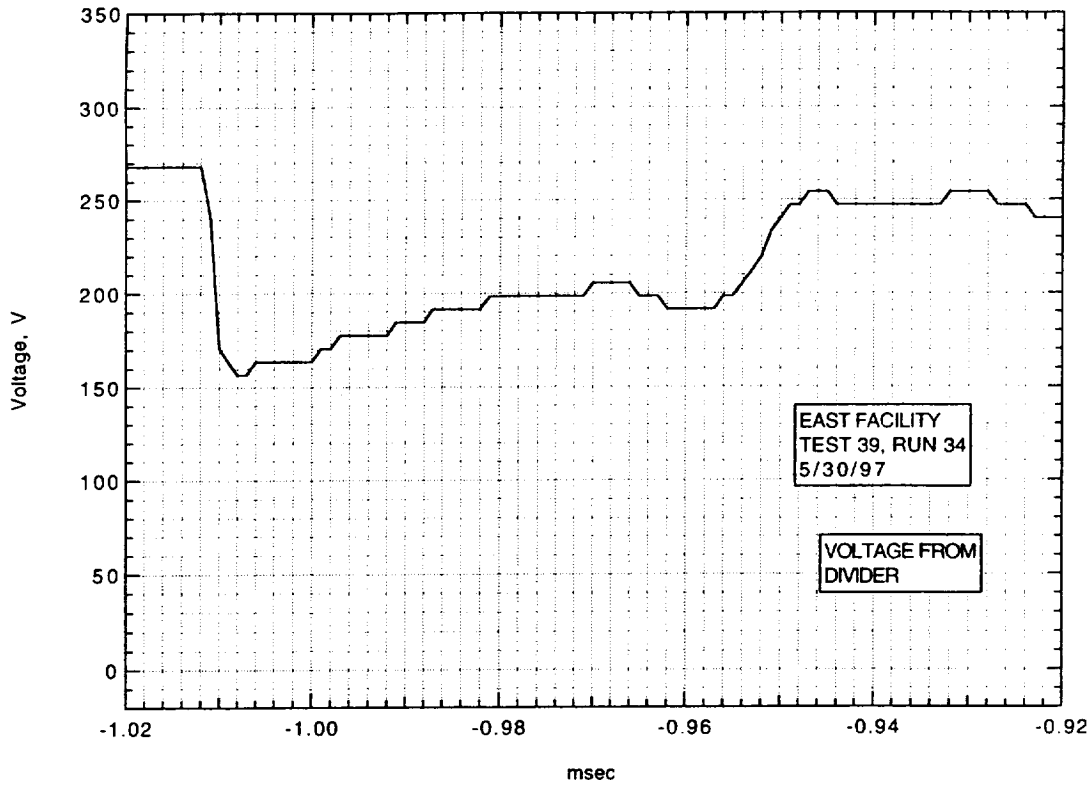

Run 34. Voltage from divider.

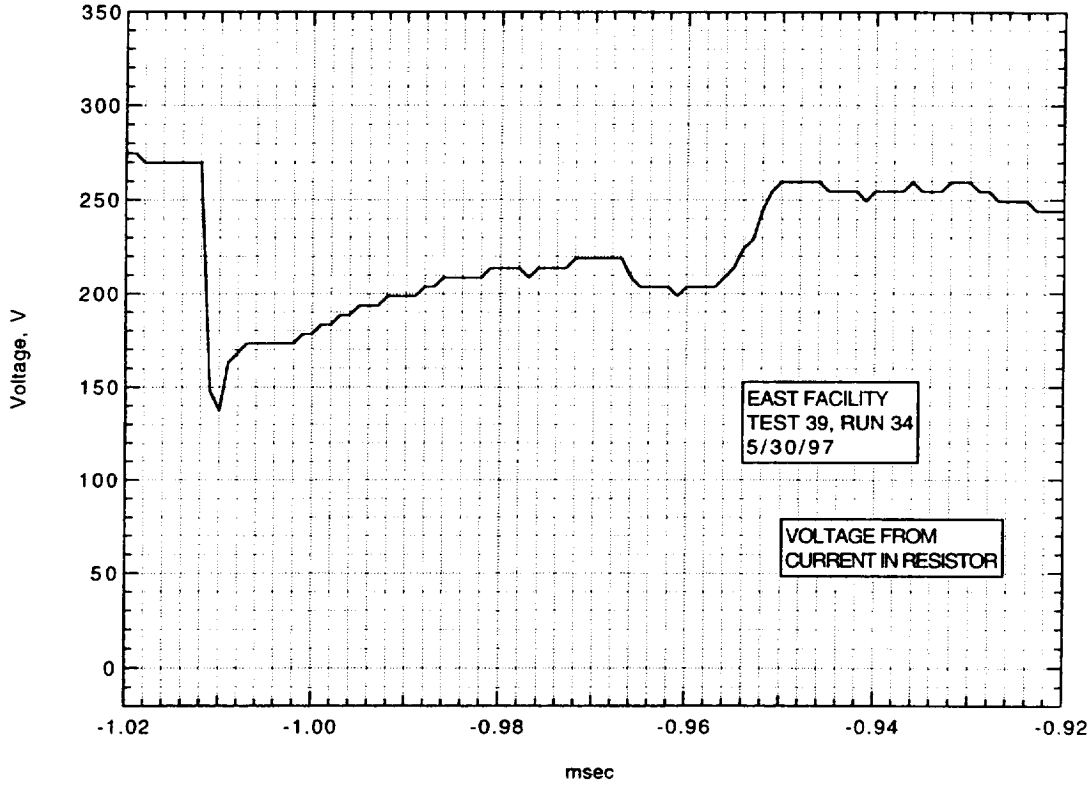

Run 34. Voltage from current in resistor.

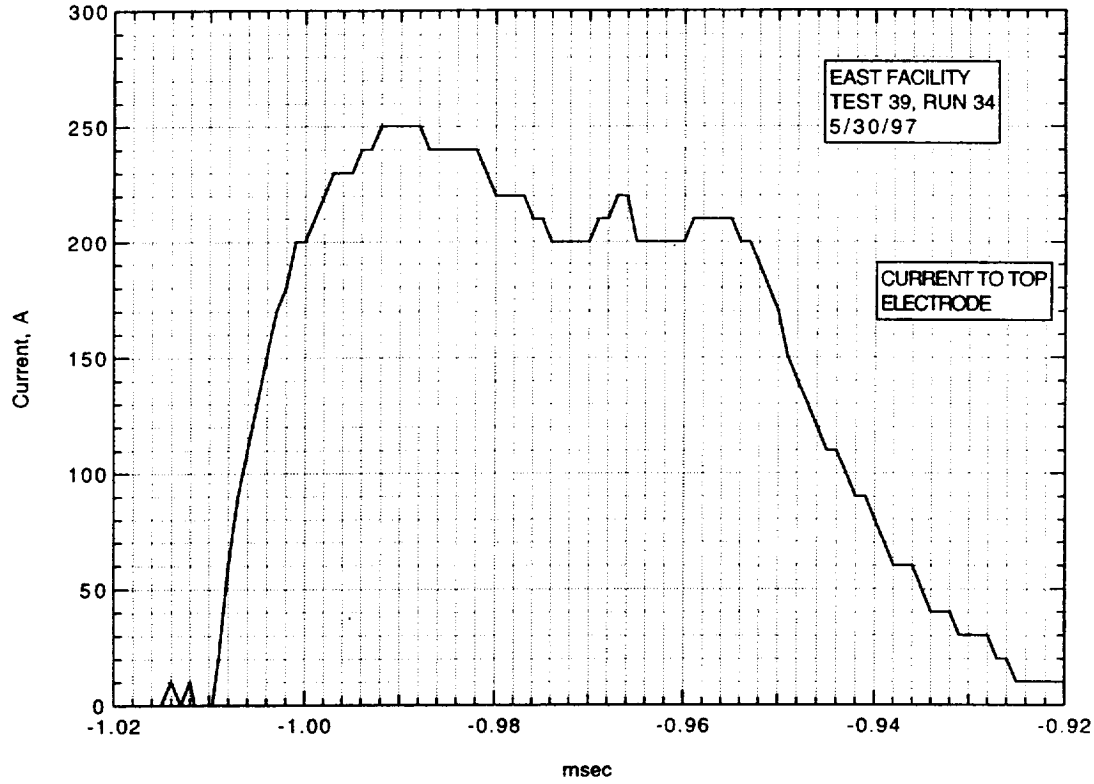

Run 34. Current to top electrode.

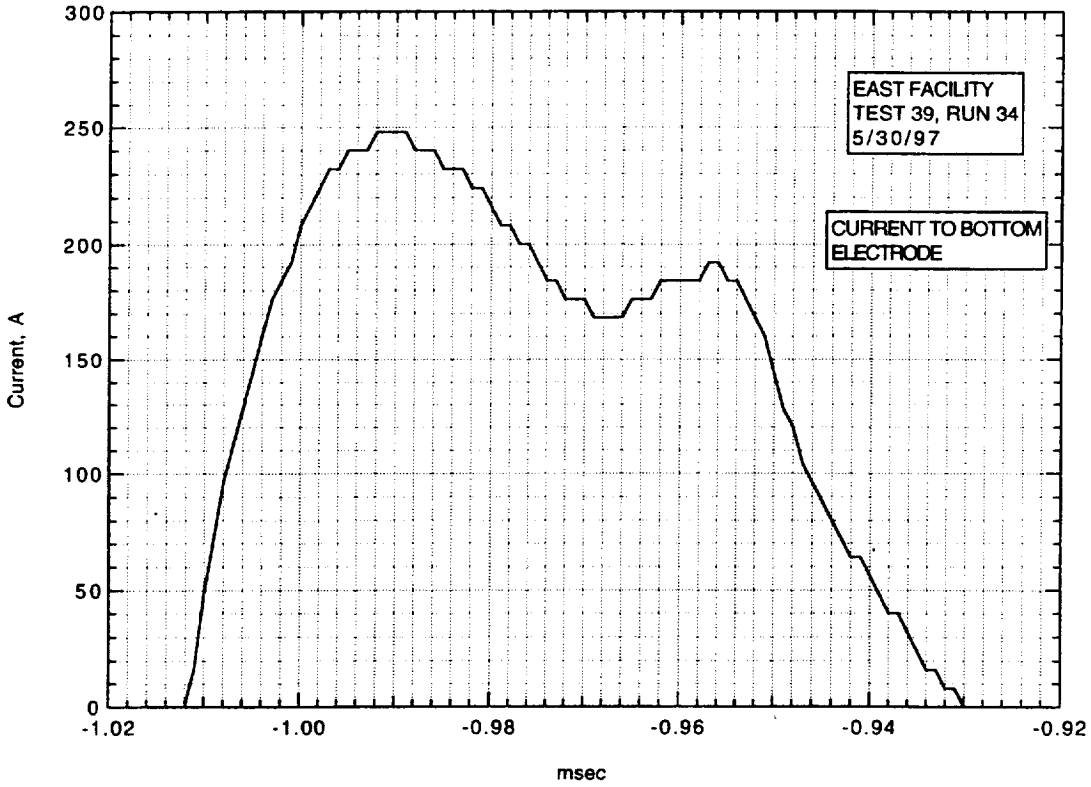

Run 34. Current to bottom electrode.

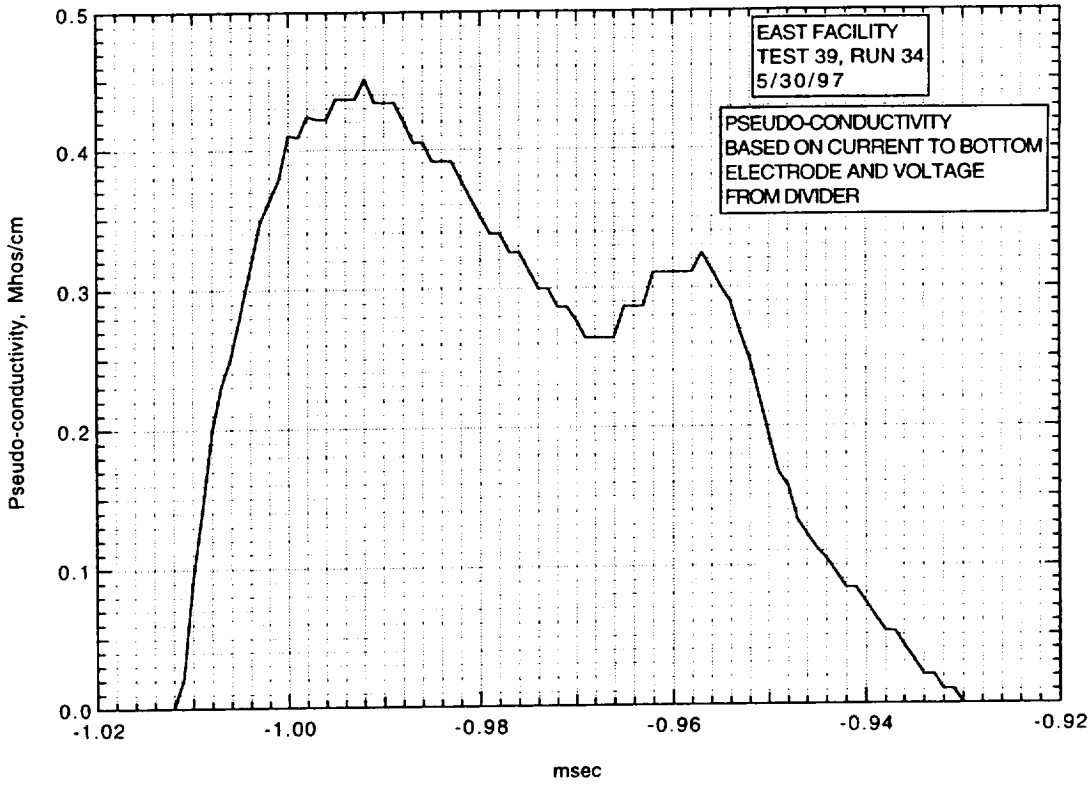

Run 34. Pseudo-conductivity based on current to the bottom electrode and voltage from divider.

AIR CONDUCTIVITY MEASUREMENT IN AMES EAST FACILITY

RUN 39/35, 5/30/97

1. Driven tube conditions:

53.2% N_2O, 46.8% N_2,
Total pressure - 13 Torr
Measured shock velocity between stns D and F - 5.035 km/sec
Estimated shock velocity at electrodes, from Δt(DF) - 4.845 km/sec
Measured shock pressure at stn D - 7.15 atm
Measured shock pressure at stn F - N/A due to large EM noise pickup

2. Electrodes, driven tube dimensions:

Electrode size - 3.10 cm square
Electrode spacing - 3.10 cm
Main diaphragm to electrodes - 454.475 cm
Skimmer nose to electrodes - 39.979 cm
Driven tube diameter - 10.16 cm
Stn D (dn tube) to electrodes (channel) - 77.365 cm
Electrodes (channel) to stn F (channel) - 20.32 cm

3. Nominal test conditions:

Pressure - 5 atm
Voltage across electrodes - 470/310 V

4. Breakdown:

Little or no indication of breakdown.

Run no: 35 **Date:** 5/30/97 **Shock press. at D:** 7.15 atm
Shock vel. at E: 4.91 km/sec **Voltage at start of current flow:** 469 V

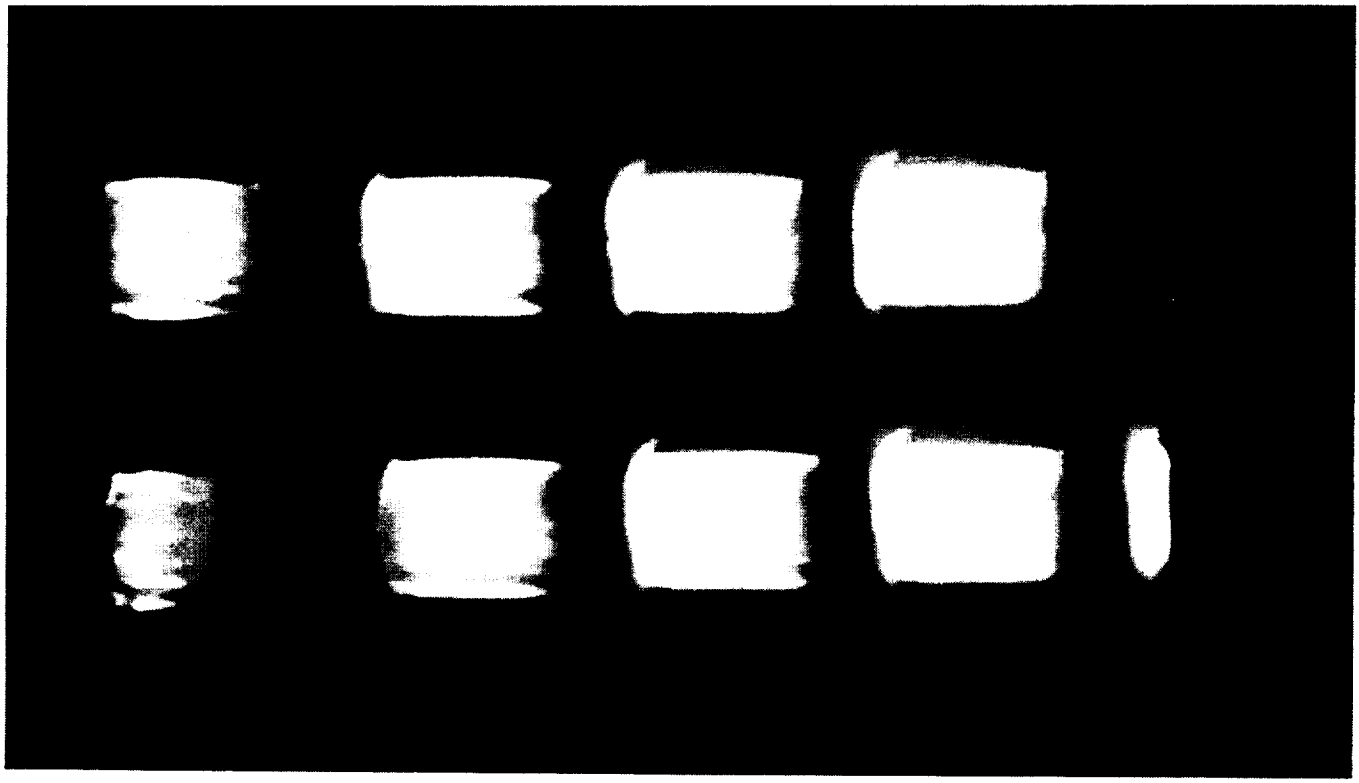

Frame:	**2**	**4**	**6**	**8**
Time:	7.4	15.4	23.4	31.4
Mach no:				
Frame:	**1**	**3**	**5**	**7**
Time:	3.4	11.4	19.4	27.4
Mach no:				

V_I: km/sec V_{CAV}: 5.06 km/sec

IMACON image of the shock-heated test gas flow in the electrode region. The time is measured from the start of the current flow. Mach numbers and velocities are deduced from the image as explained in section A.2.5.3.

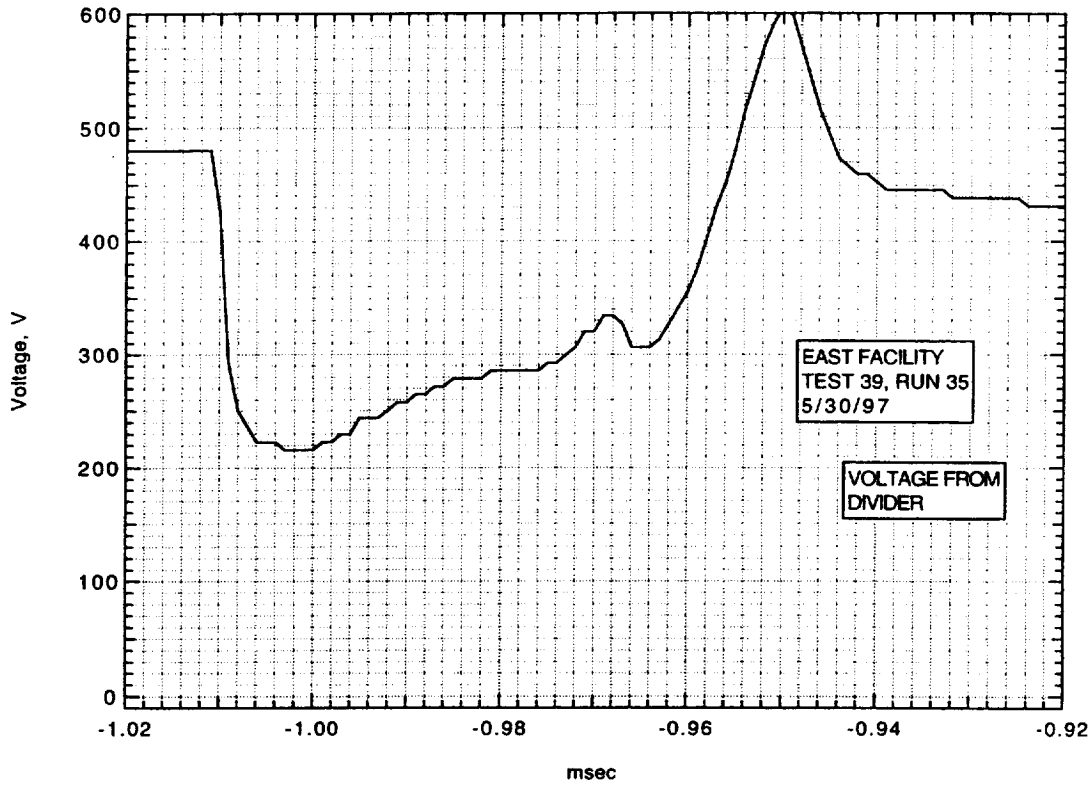

Run 35, voltage from divider.

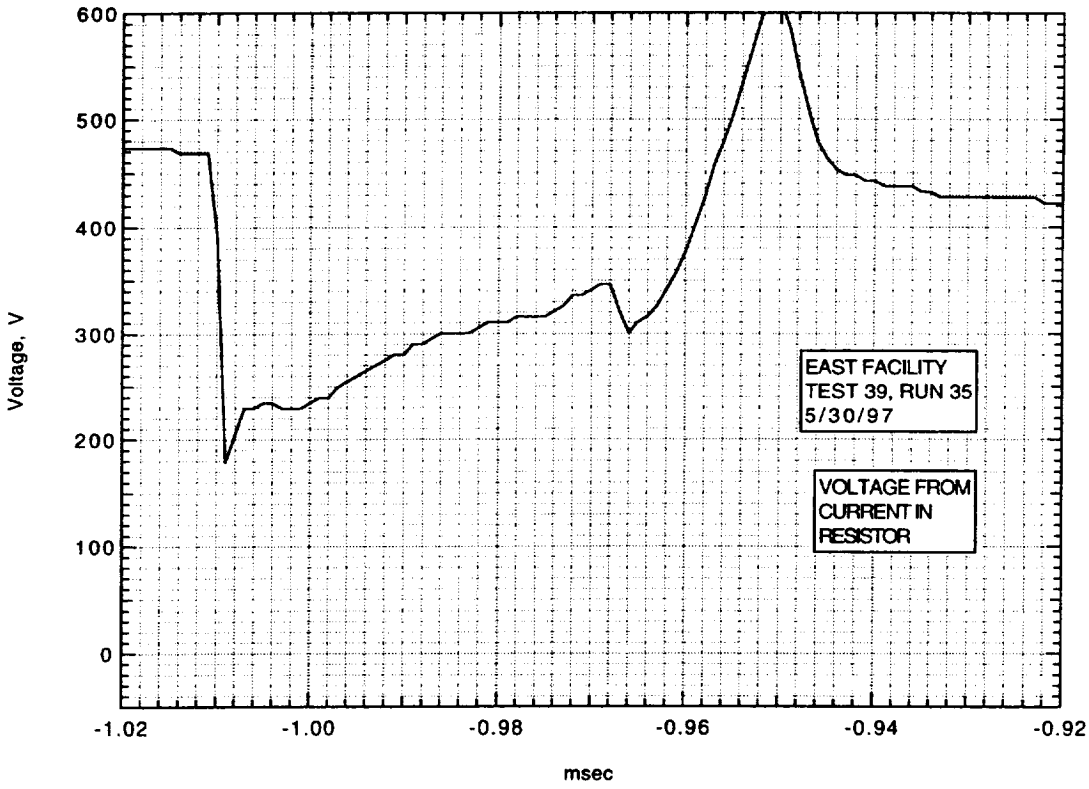

Run 35, voltage from current in resistor.

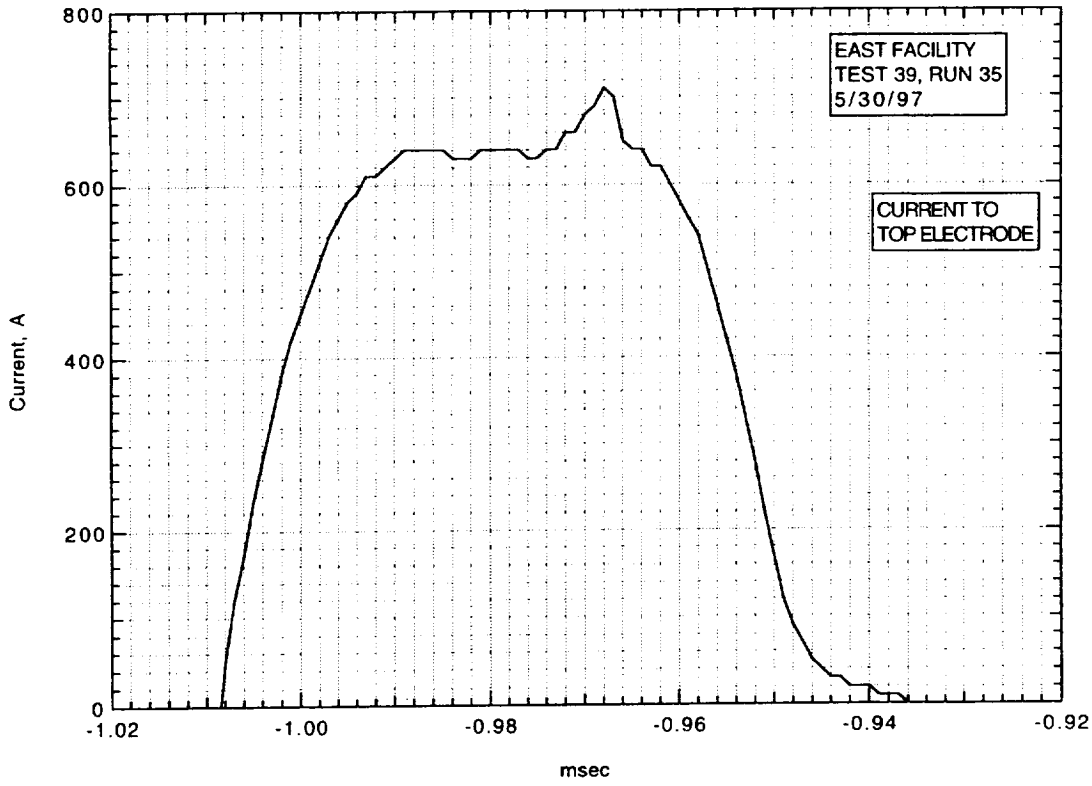

Run 35, current to top electrode.

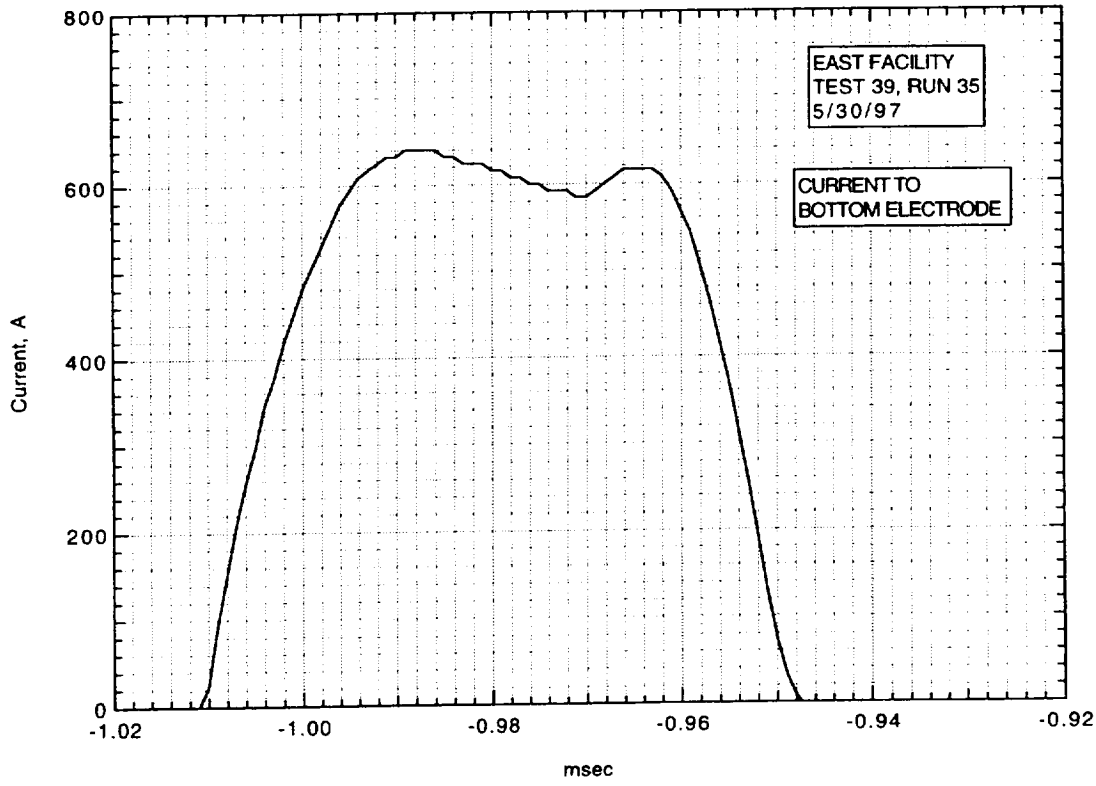

Run 35, current to bottom electrode.

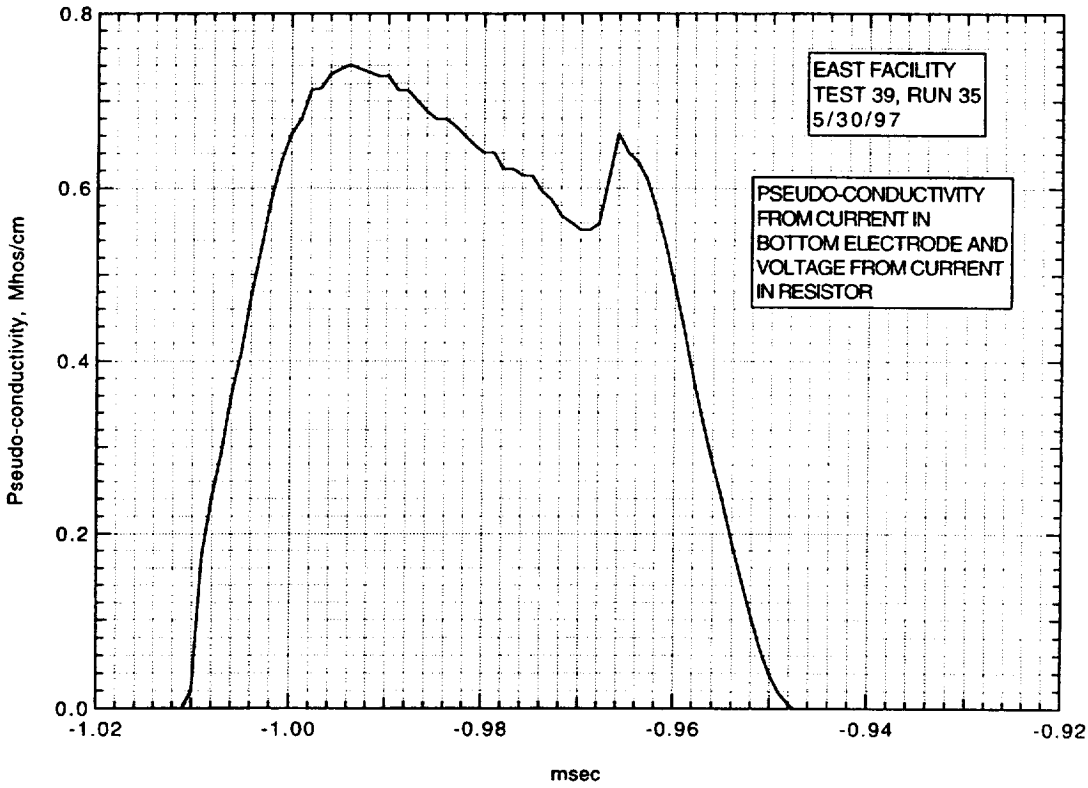

Run 35, pseudo-conductivity from current to bottom electrode and voltage from current in resistor.

AIR CONDUCTIVITY MEASUREMENT IN AMES EAST FACILITY

RUN 39/36, 6/2/97

1. Driven tube conditions:

53.2% N_2O, 46.8% N_2,
Total pressure - 13 Torr
Measured shock velocity between stns D and F - 4.696 km/sec
Estimated shock velocity at electrodes, from $\Delta t(DF)$ - 4.519 km/sec
Measured shock pressure at stn D - 6.17 atm
Measured shock pressure at stn F - N/A due to large EM noise pickup

2. Electrodes, driven tube dimensions:

Electrode size - 3.10 cm square
Electrode spacing - 3.10 cm
Main diaphragm to electrodes - 454.475 cm
Skimmer nose to electrodes - 39.979 cm
Driven tube diameter - 10.16 cm
Stn D (dn tube) to electrodes (channel) - 77.365 cm
Electrodes (channel) to stn F (channel) - 20.32 cm

3. Nominal test conditions:

Pressure - 5 atm
Voltage across electrodes - 706/406 V

4. Breakdown:

Little or no indication of breakdown.

Run no: 36 **Date:** 6/2/97 **Shock press. at D:** 6.17 atm
Shock vel. at E: 4.63 km/sec **Voltage at start of current flow:** 700 V

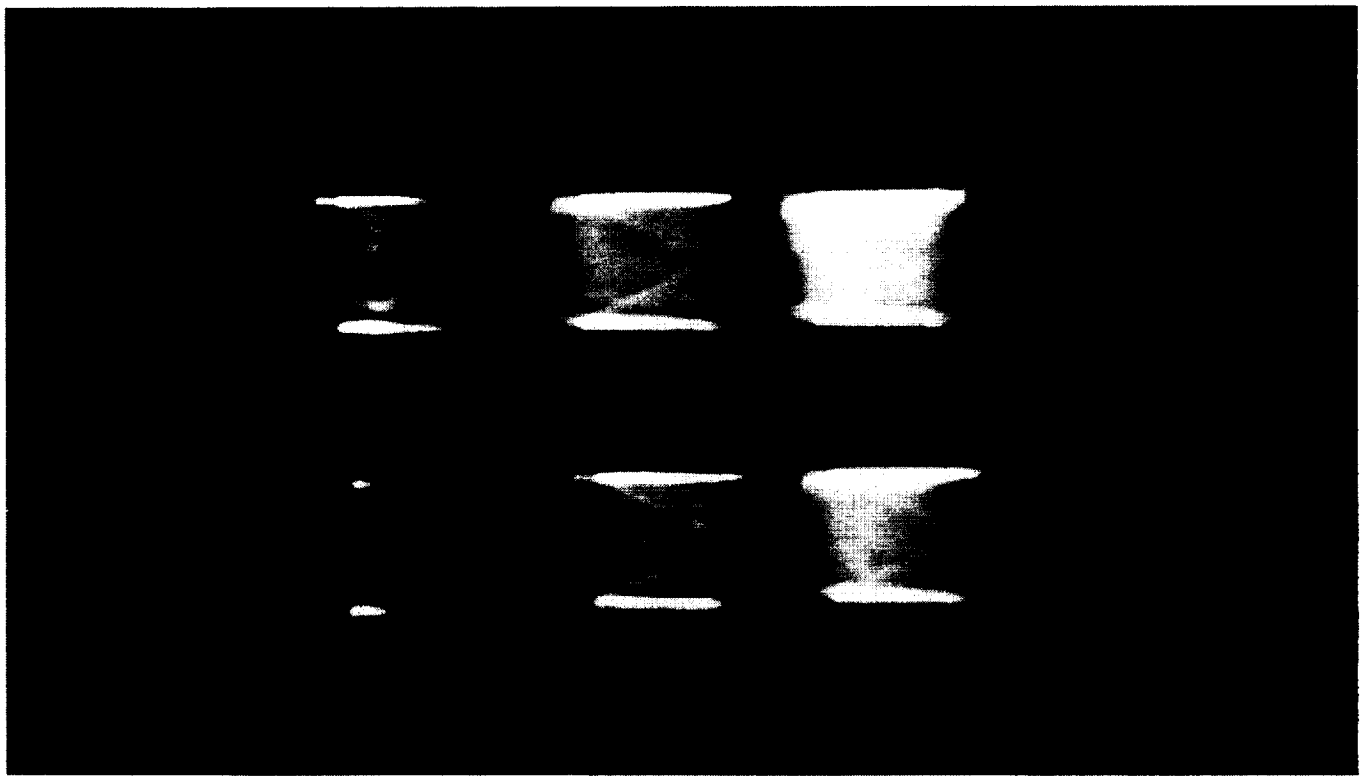

Frame:	**2**	**4**	**6**	**8**
Time:	-1.4	6.6	14.6	22.6
Mach no:			2.14	
Frame:	**1**	**3**	**5**	**7**
Time:	-5.4	2.6	10.6	18.6
Mach no:			2.32	2.14

V_I: km/sec V_{CAV}: 4.80 km/sec

IMACON image of the shock-heated test gas flow in the electrode region. The time is measured from the start of the current flow. Mach numbers and velocities are deduced from the image as explained in section A.2.5.3.

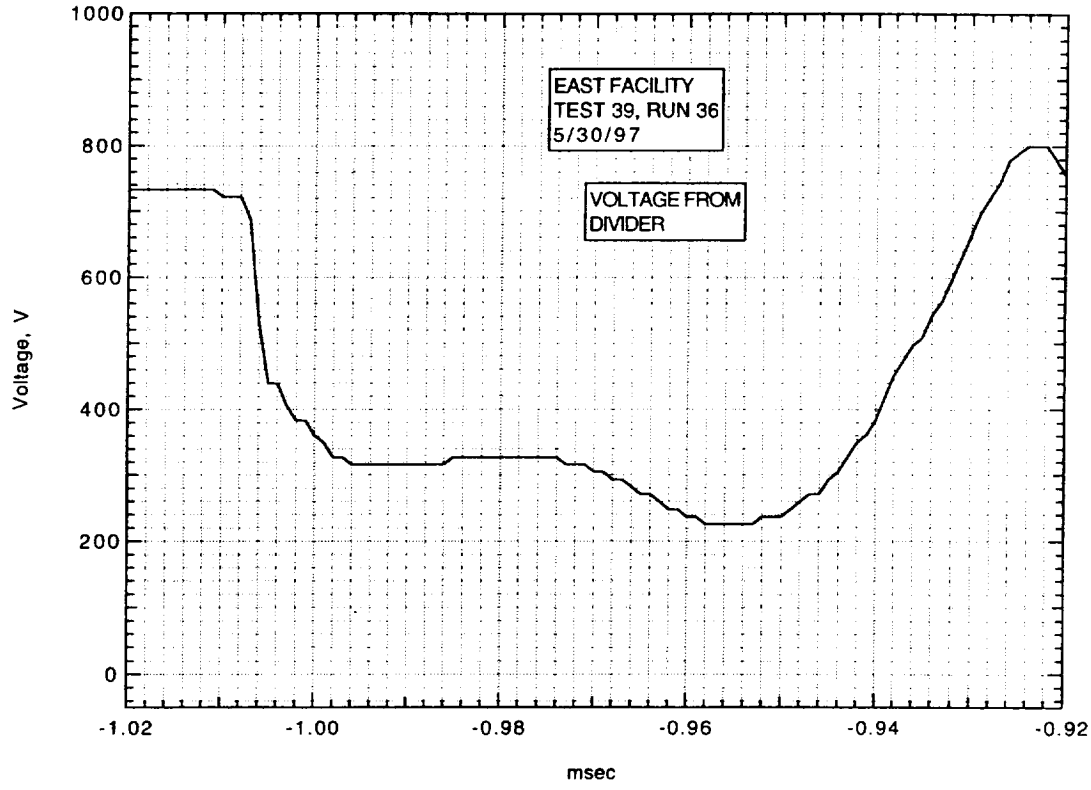

Run 36, voltage across electrodes from divider.

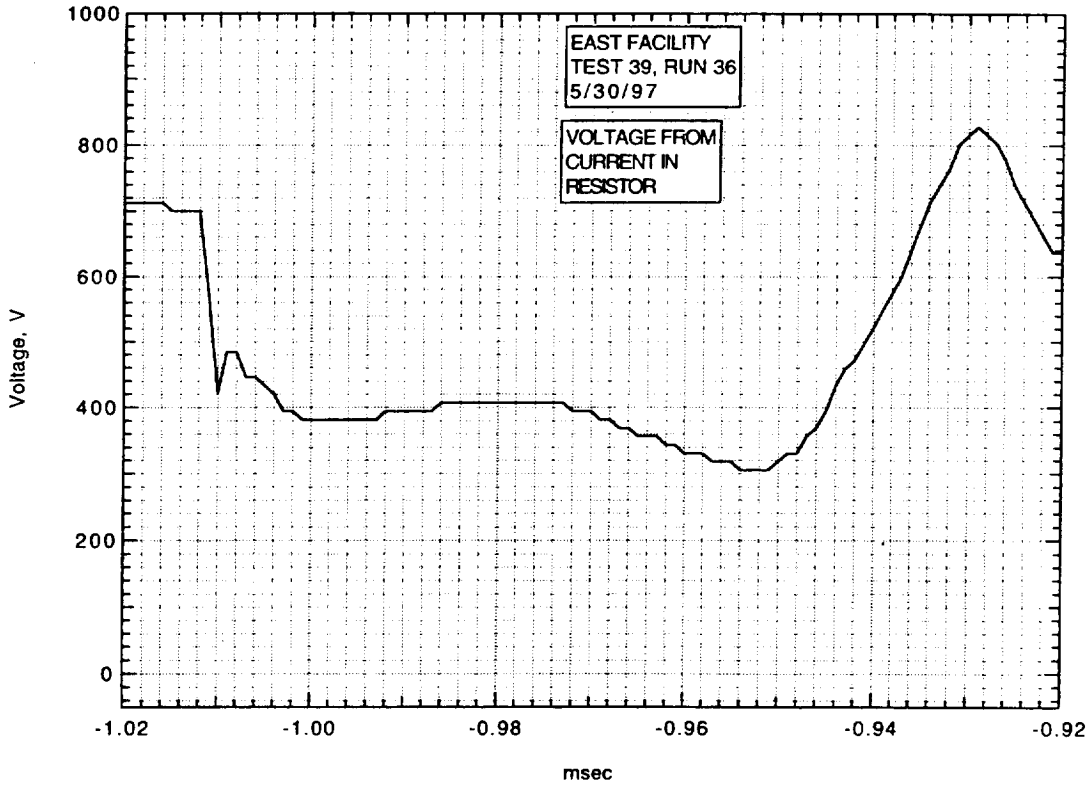

Run 36, voltage across electrodes from current in resistor.

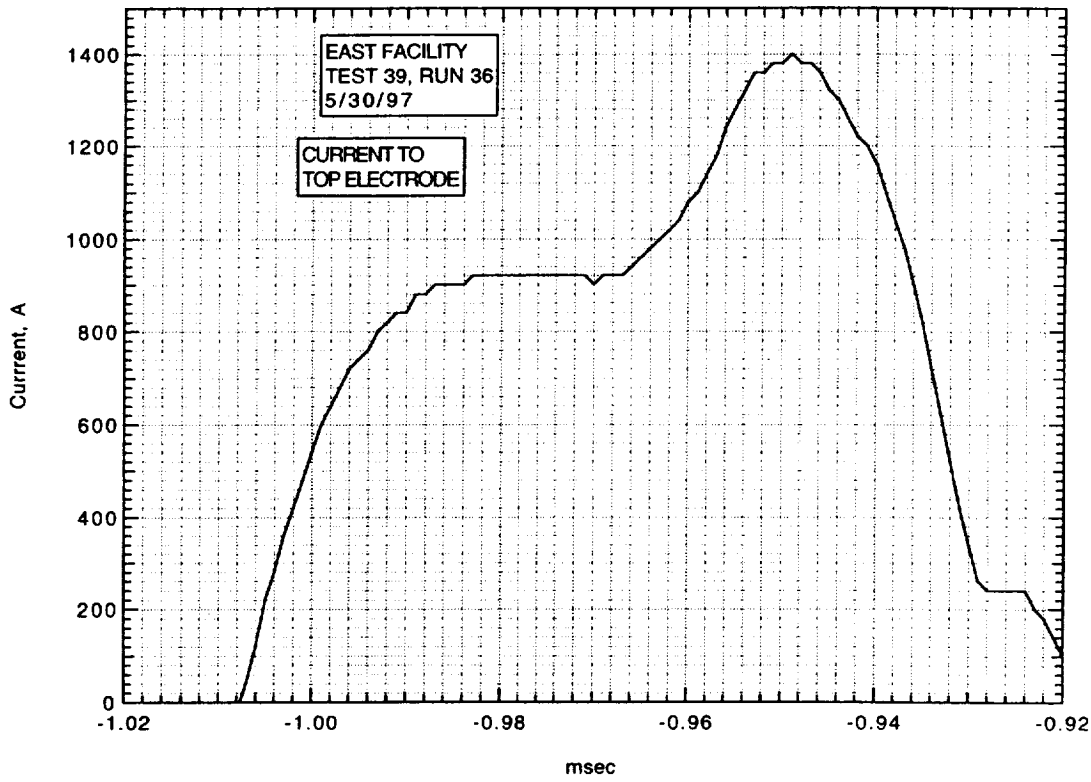

Run 36, current to top electrode.

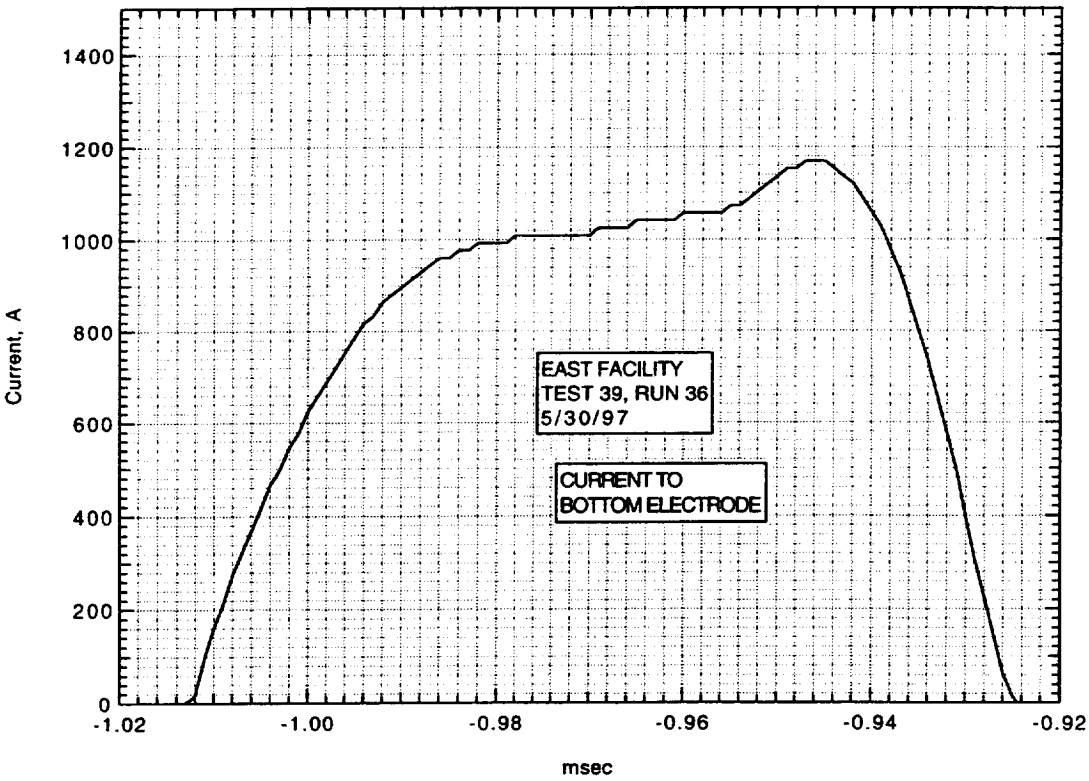

Run 36, current to bottom electrode.

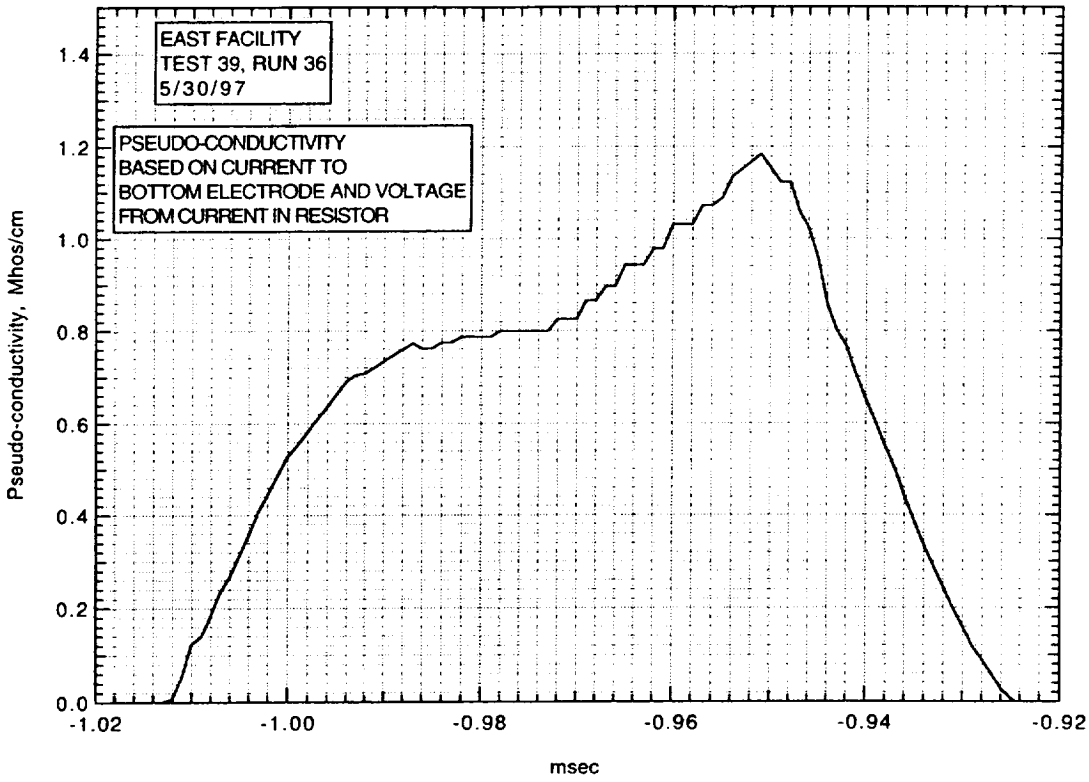

Run 36, pseudo-conductivity from current to bottom electrode and voltage from current in resistor.

AIR CONDUCTIVITY MEASUREMENT IN AMES EAST FACILITY

RUN 39/37, 6/3/97

1. Driven tube conditions:

53.2% N_2O, 46.8% N_2
Total pressure - 13 Torr
Measured shock velocity between stns D and F - N/A
Estimated shock velocity at electrodes - 4.351 km/sec - scaled from times of shock passage past pressure transducer at stn D and start of current flow at electrodes at E
Measured shock pressure at stn D - 6.17 atm
Measured shock pressure at stn F - N/A due to large EM noise pickup

2. Electrodes, driven tube dimensions:

Electrode size - 3.10 cm square
Electrode spacing - 3.10 cm
Main diaphragm to electrodes - 454.475 cm
Skimmer nose to electrodes - 39.979 cm
Driven tube diameter - 10.16 cm
Stn D (dn tube) to electrodes (channel) - 77.365 cm
Electrodes (channel) to stn F (channel) - 20.32 cm

3. Nominal test conditions:

Pressure - 5 atm
Voltage across electrodes - 1024/490 V

4. Breakdown:

Little or no indication of breakdown.

Run no: 37 **Date:** 6/3/97 **Shock press. at D:** 6.17 atm
Shock vel. at E: 4.45 km/sec **Voltage at start of current flow:** 1024 V

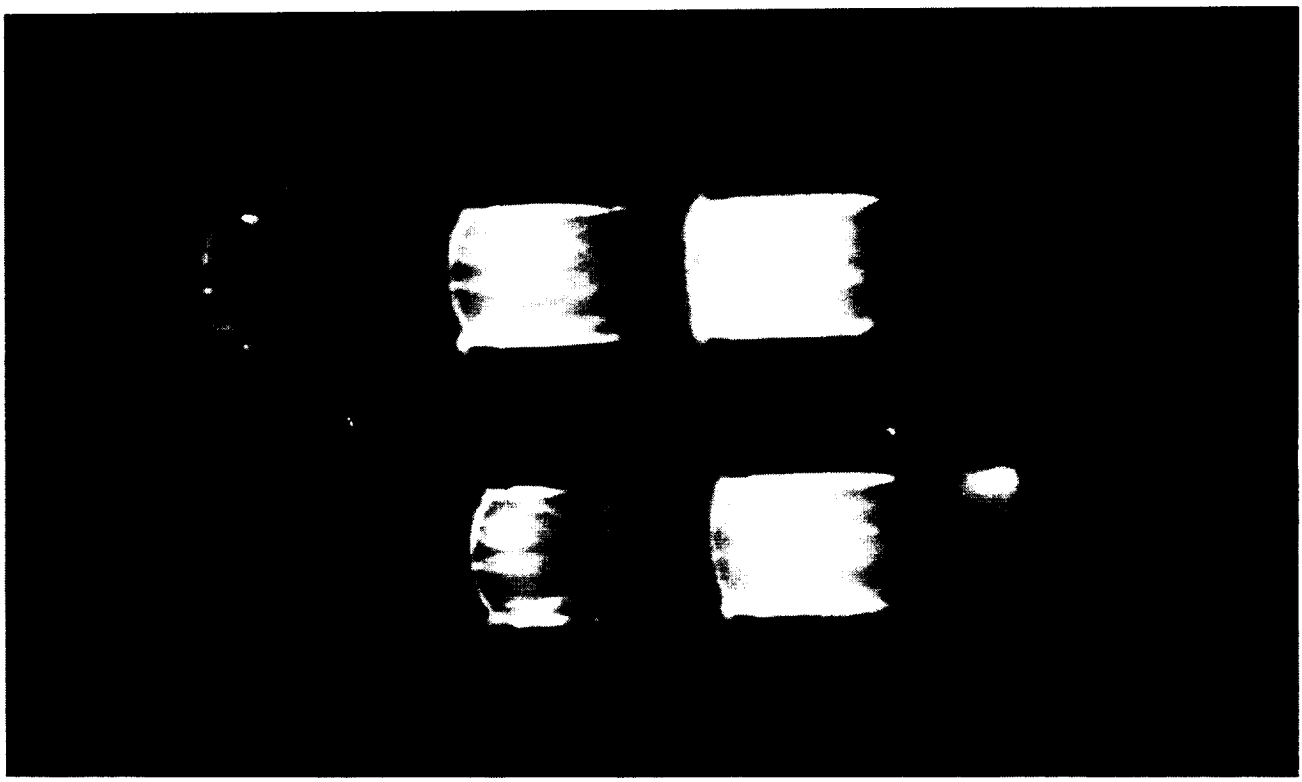

Frame:	**2**	**4**	**6**	**8**
Time:	-7.7	0.3	8.3	16.3
Mach no:				
Frame:	**1**	**3**	**5**	**7**
Time:	-11.7	-3.7	4.3	12.3
Mach no:				

V_I: 4.2 km/sec V_{CAV}: 4.63 km/sec

IMACON image of the shock-heated test gas flow in the electrode region. The time is measured from the start of the current flow. Mach numbers and velocities are deduced from the image as explained in section A.2.5.3.

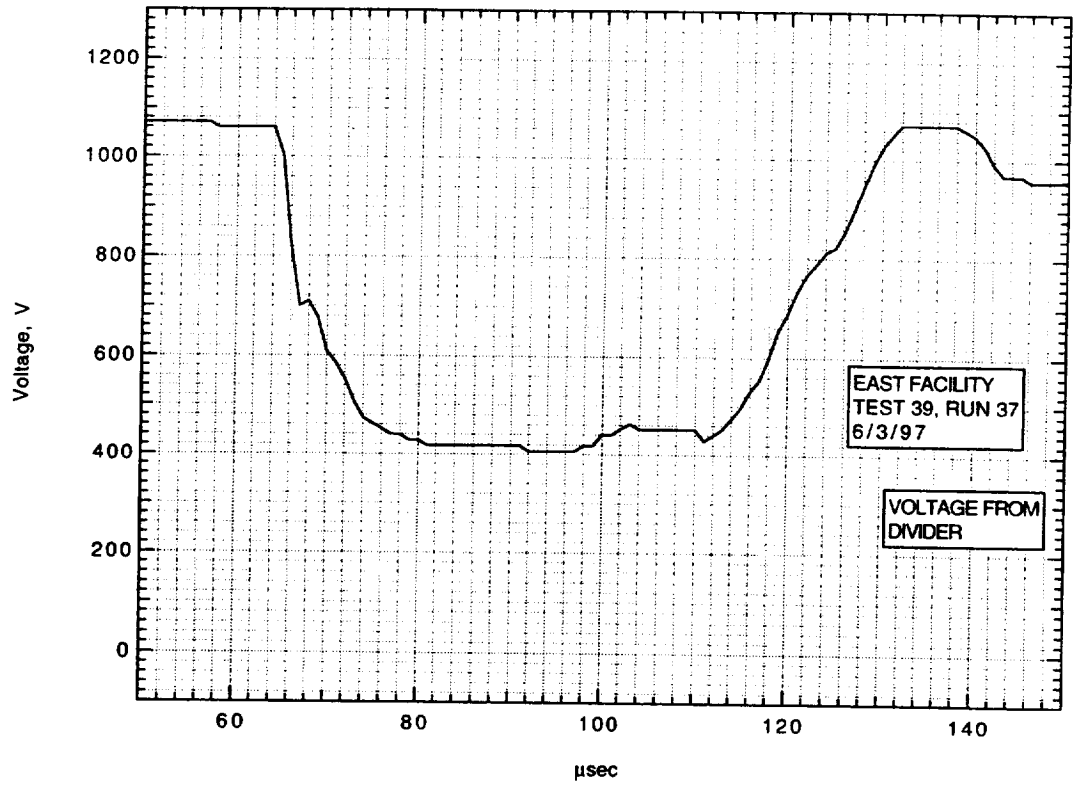

Run 37, voltage across electrodes from divider.

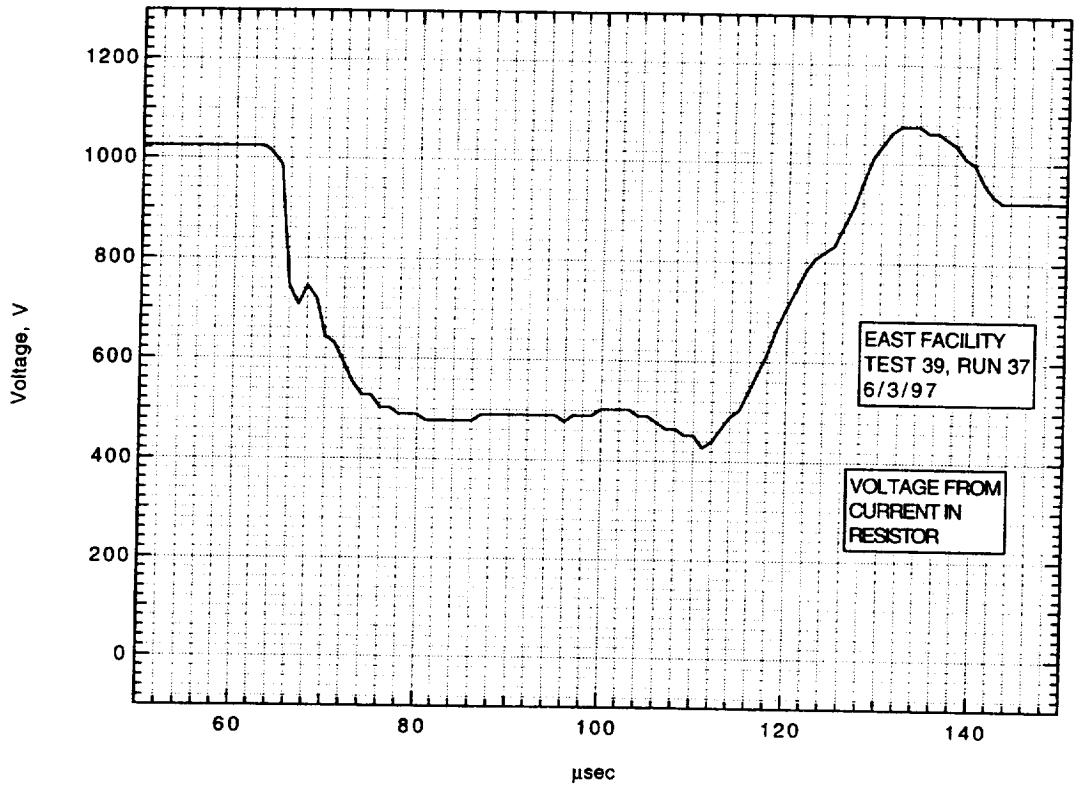

Run 37, voltage across electrodes from current in resistor.

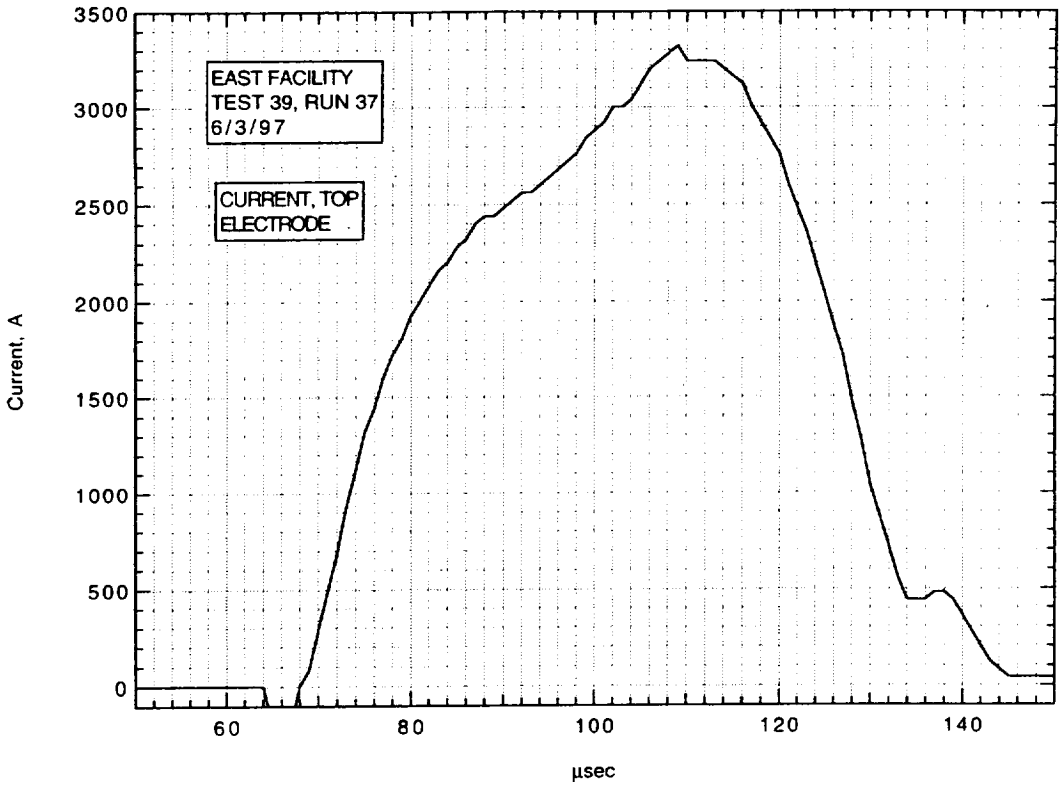

Run 37, current to top electrode.

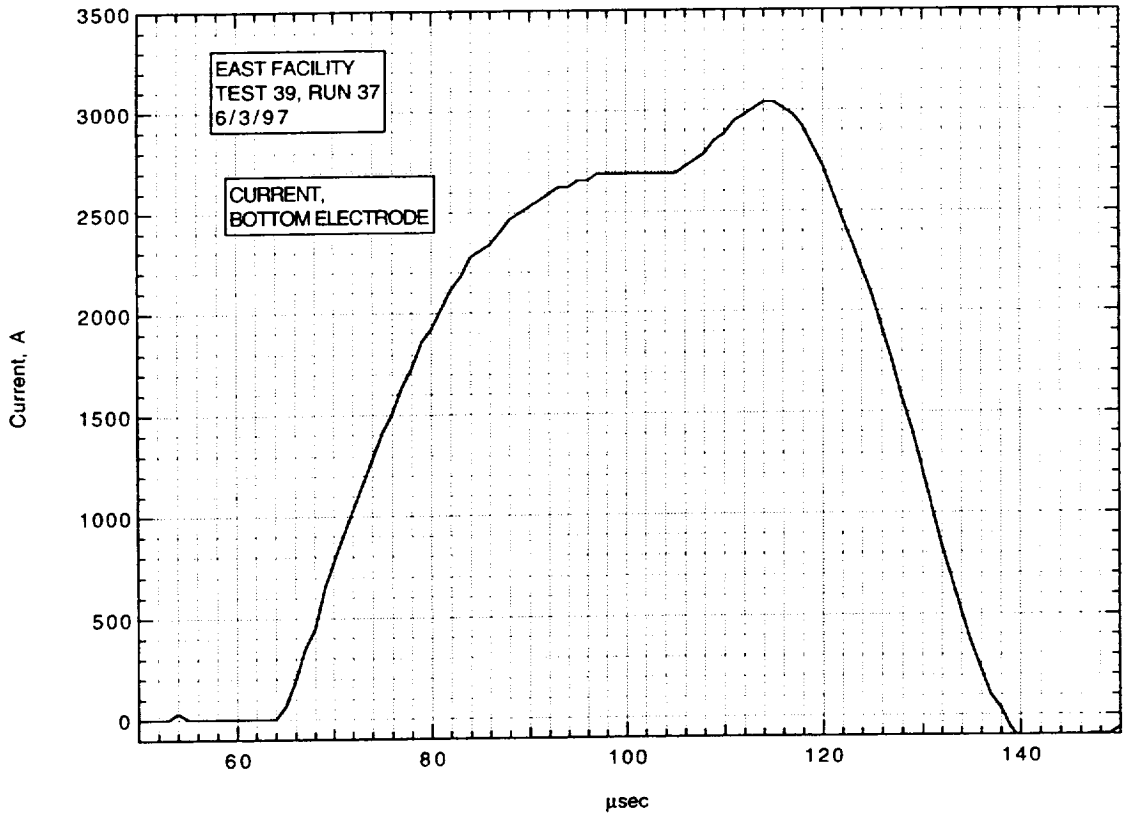

Run 37, current to bottom electrode.

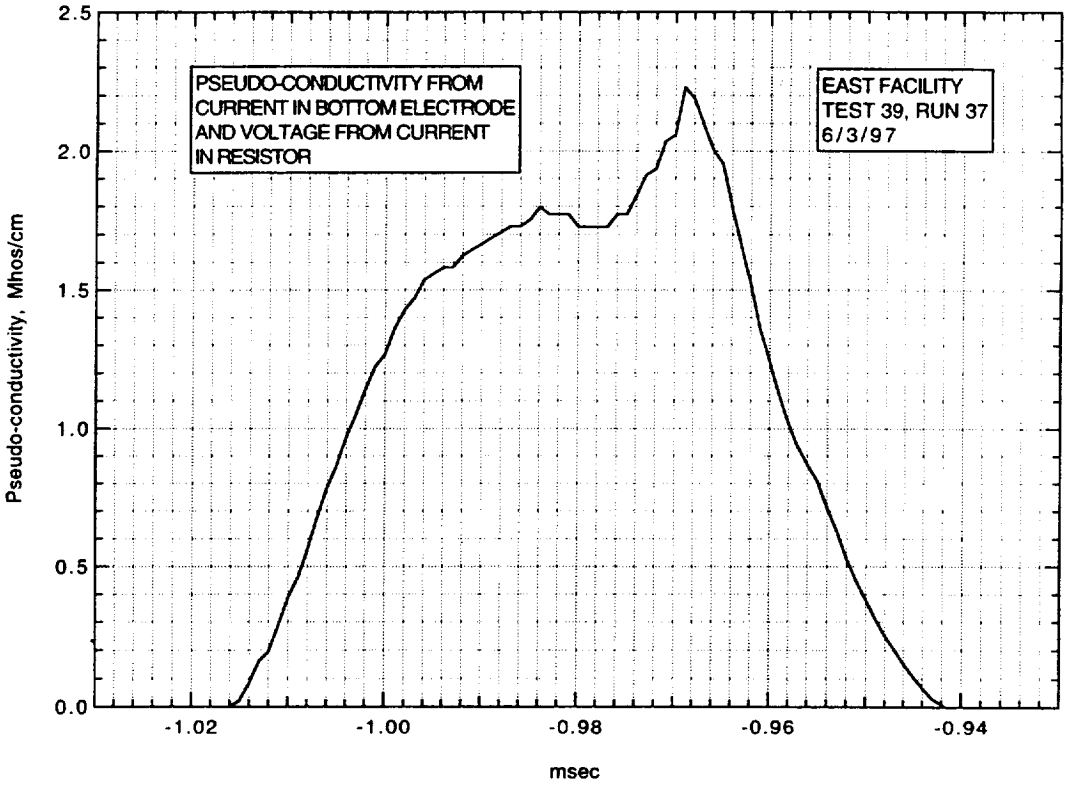

Run 37, pseudo-conductivity from current to bottom electrode and voltage from current in resistor.

AIR CONDUCTIVITY MEASUREMENT IN AMES EAST FACILITY

RUN 39/38, 6/4/97

1. Driven tube conditions:

53.2% N_2O, 46.8% N_2
Total pressure - 13 Torr
Measured shock velocity between stns D and F - N/A
Estimated shock velocity at electrodes - 4.846 km/sec - scaled from times of shock passage past pressure transducer at stn D and start of current flow at electrodes at E
Measured shock pressure at stn D - 7.21 atm
Measured shock pressure at stn F - N/A due to large EM noise pickup

2. Electrodes, driven tube dimensions:

Electrode size - 3.10 cm square
Electrode spacing - 3.10 cm
Main diaphragm to electrodes - 454.475 cm
Skimmer nose to electrodes - 39.979 cm
Driven tube diameter - 10.16 cm
Stn D (dn tube) to electrodes (channel) - 77.365 cm
Electrodes (channel) to stn F (channel) - 20.32 cm

3. Nominal test conditions:

Pressure - 5 atm
Voltage across electrodes - 1020/482 V

4. Breakdown:

Little or no indication of breakdown.

Run no: 38 **Date:** 6/4/97 **Shock press. at D:** 7.21 atm
Shock vel. at E: 4.85 km/sec **Voltage at start of current flow:** 1020 V

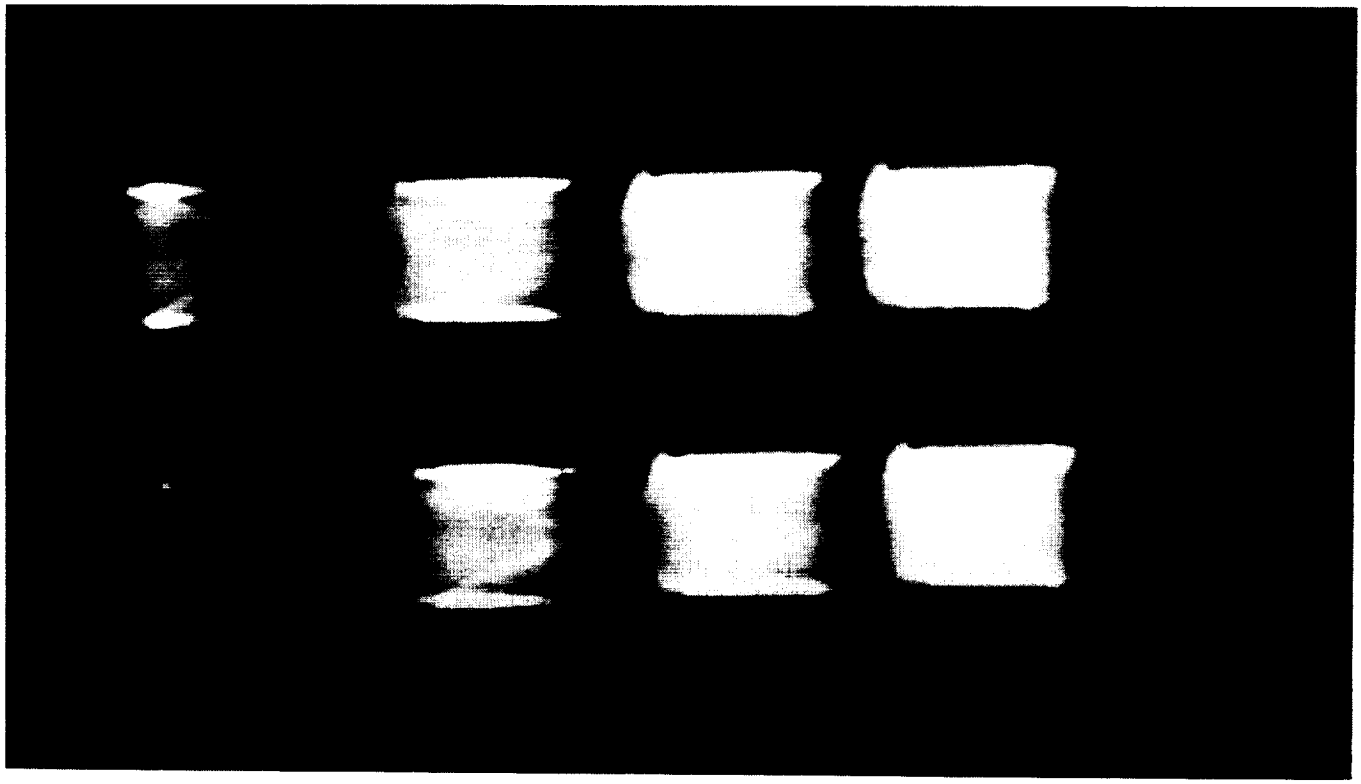

Frame:	**2**	**4**	**6**	**8**
Time:	4.1	12.1	20.1	28.1
Mach no:	2.42	2.31		
Frame:	**1**	**3**	**5**	**7**
Time:	0.1	8.1	16.1	24.1
Mach no:		2.27		

V_I: 4.5 km/sec V_{CAV}: 4.96 km/sec

IMACON image of the shock-heated test gas flow in the electrode region. The time is measured from the start of the current flow. Mach numbers and velocities are deduced from the image as explained in section A.2.5.3.

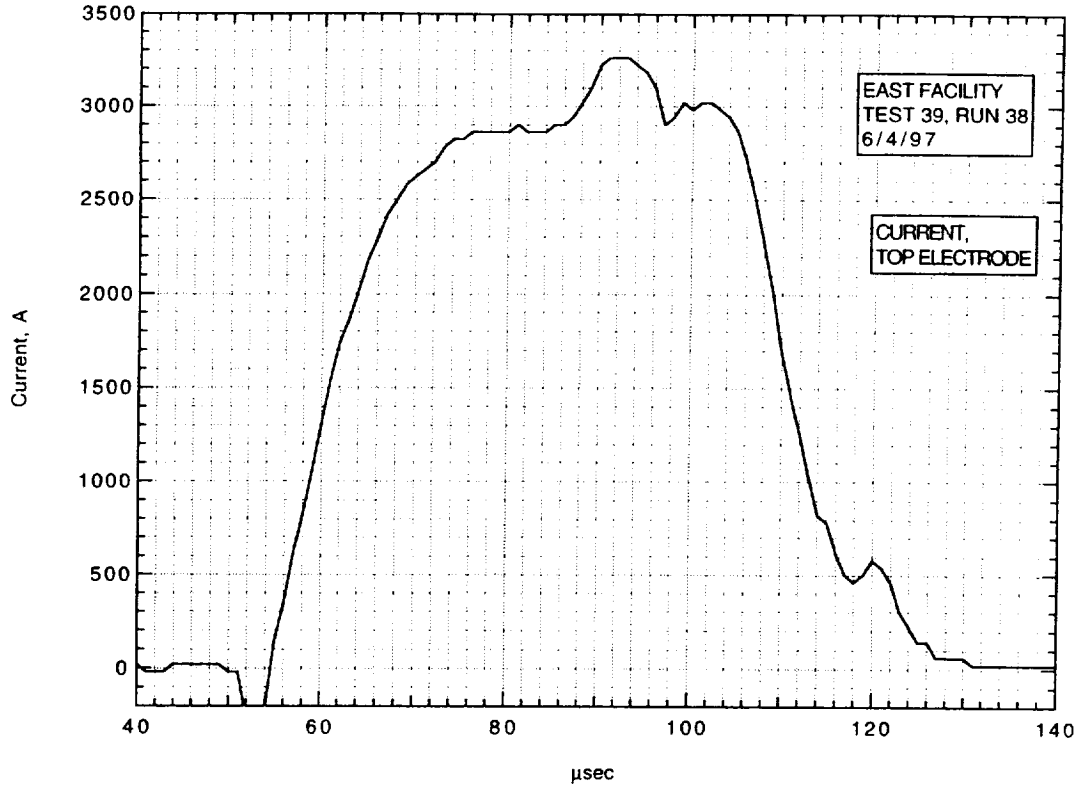

Run 38, current to top electrode.

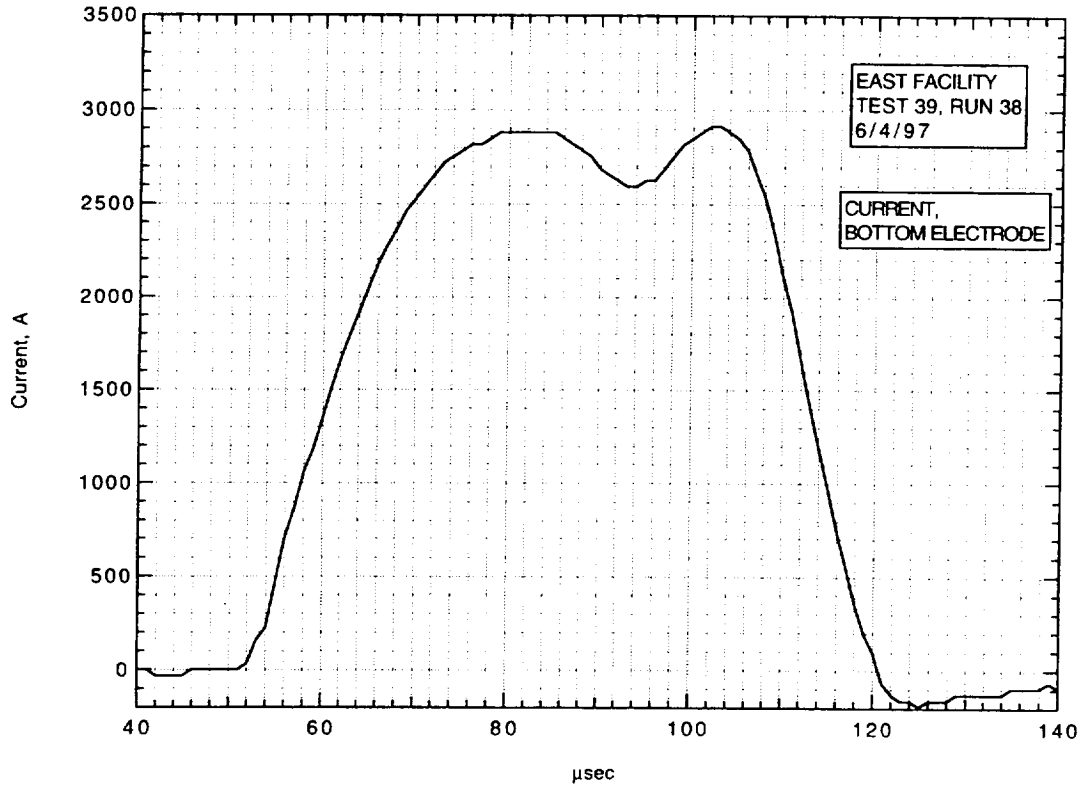

Run 38, current to bottom electrode.

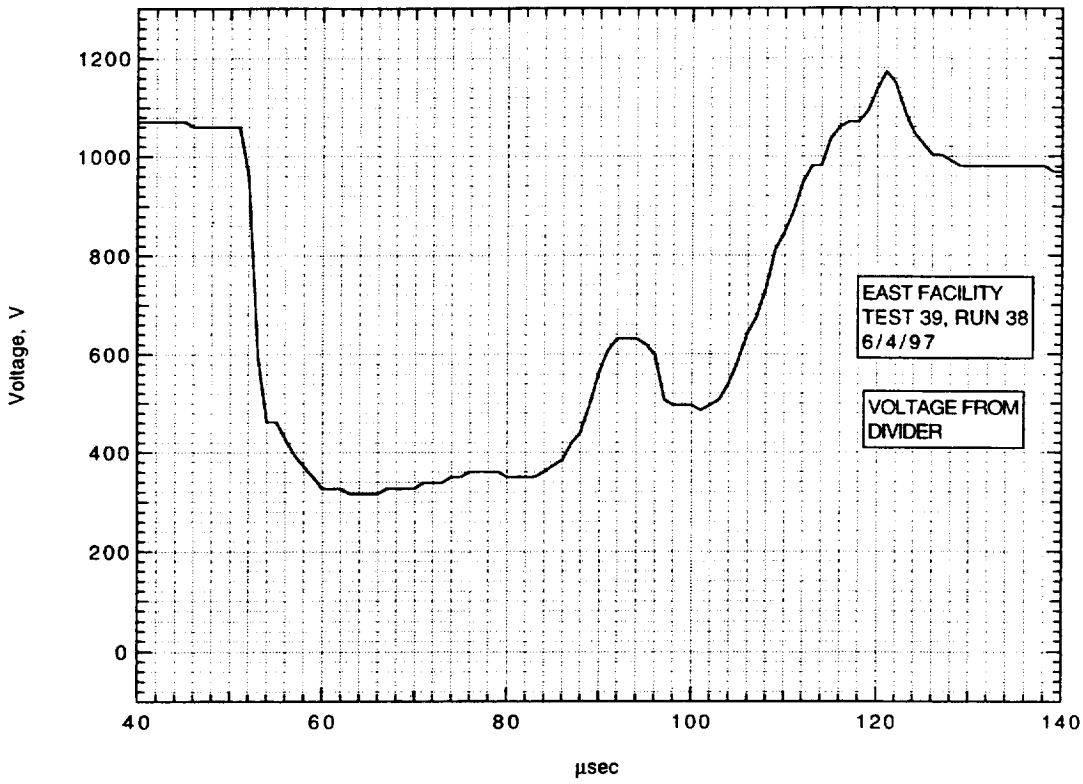

Run 38, voltage across electrodes from divider.

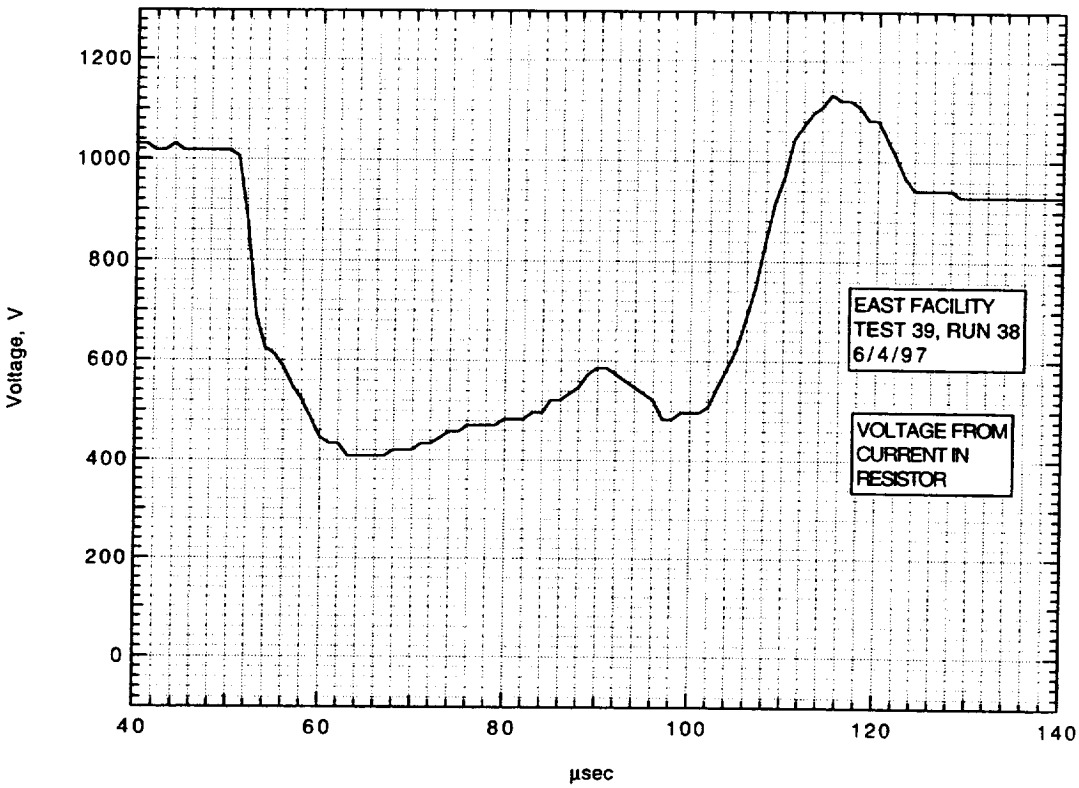

Run 38, voltage across electrodes from current in resistor.

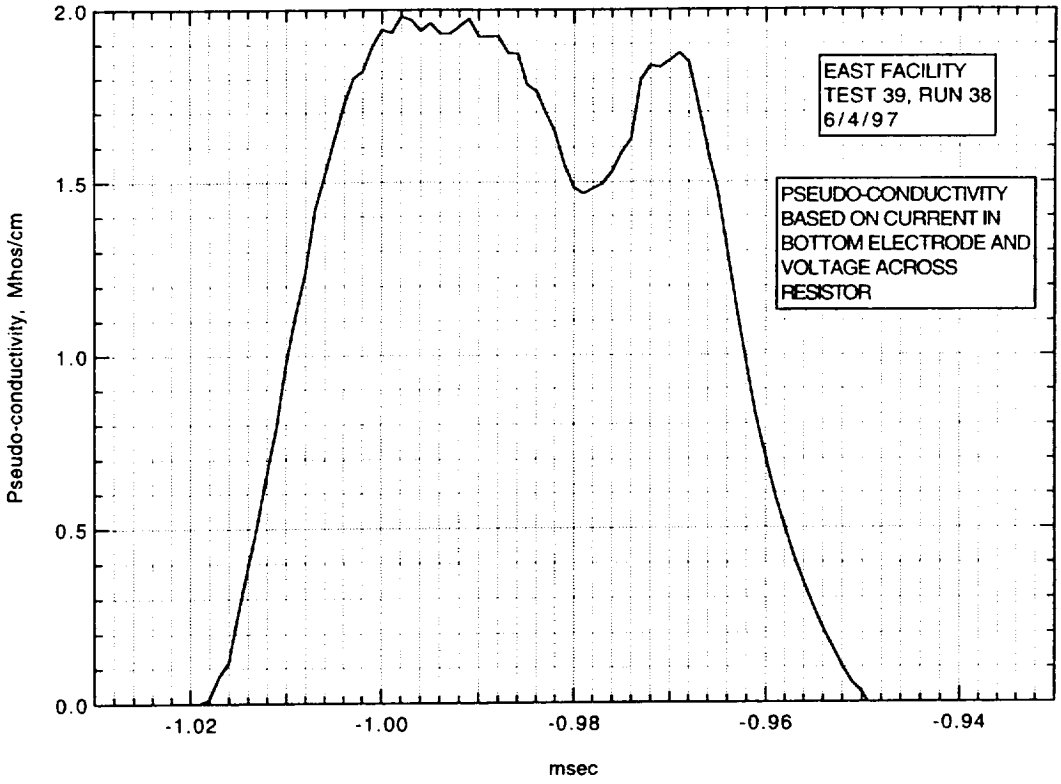

Run 38, pseudo-conductivity from current to bottom electrode and voltage from current in resistor.

AIR CONDUCTIVITY MEASUREMENT IN AMES EAST FACILITY

RUN 39/39, 6/5/97

1. Driven tube conditions:

53.2% N_2O, 46.8% N_2
Total pressure - 13 Torr
Measured shock velocity between stns D and F - N/A
Estimated shock velocity at electrodes - 4.657 km/sec - scaled from times of shock passage past pressure transducer at stn D and start of current flow at electrodes at E
Measured shock pressure at stn D - 6.49 atm
Measured shock pressure at stn F - N/A due to large EM noise pickup

2. Electrodes, driven tube dimensions:

Electrode size - 3.10 cm square
Electrode spacing - 3.10 cm
Main diaphragm to electrodes - 454.475 cm
Skimmer nose to electrodes - 39.979 cm
Driven tube diameter - 10.16 cm
Stn D (dn tube) to electrodes (channel) - 77.365 cm
Electrodes (channel) to stn F (channel) - 20.32 cm

3. Nominal test conditions:

Pressure - 5 atm
Voltage across electrodes - 469/310 V

4. Breakdown:

Little or no indication of breakdown.

Run no: 39 **Date:** 6/5/97 **Shock press. at D:** 6.49 atm
Shock vel. at E: 4.66 km/sec **Voltage at start of current flow:** 469 V

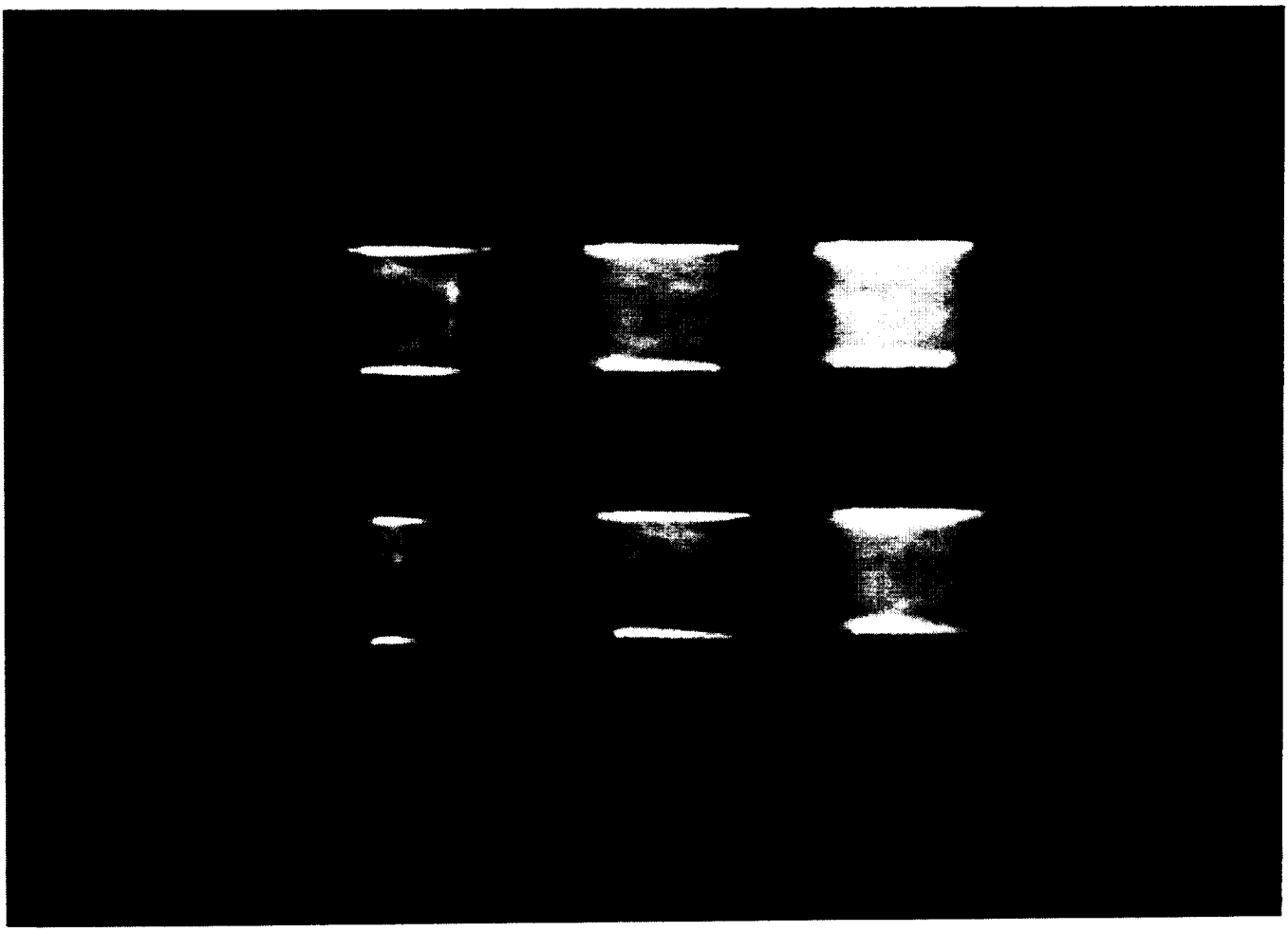

Frame:	**2**	**4**	**6**	**8**
Time:	1.2	9.2	17.2	25.2
Mach no:		2.24	2.42	
Frame:	**1**	**3**	**5**	**7**
Time:	-2.8	5.2	13.2	21.2
Mach no:				

V_I: 4.5 km/sec V_{CAV}: 4.85 km/sec

IMACON image of the shock-heated test gas flow in the electrode region. The time is measured from the start of the current flow. Mach numbers and velocities are deduced from the image as explained in section A.2.5.3.

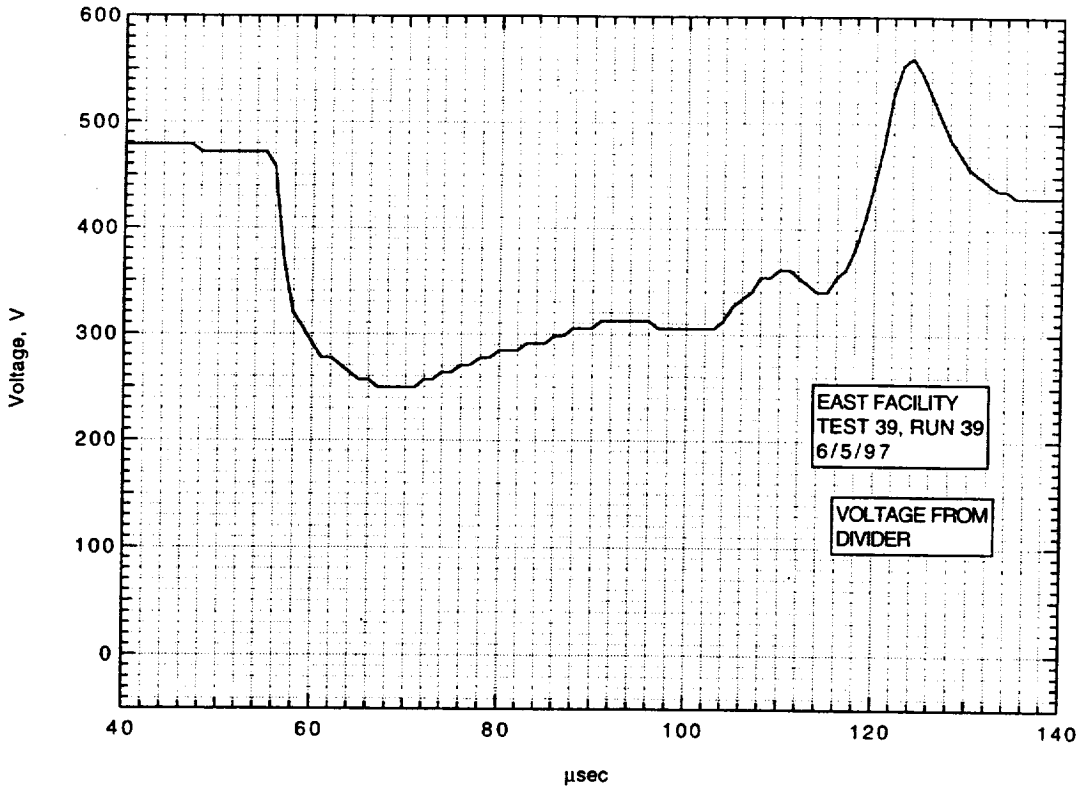

Run 39, voltage across electrodes from divider.

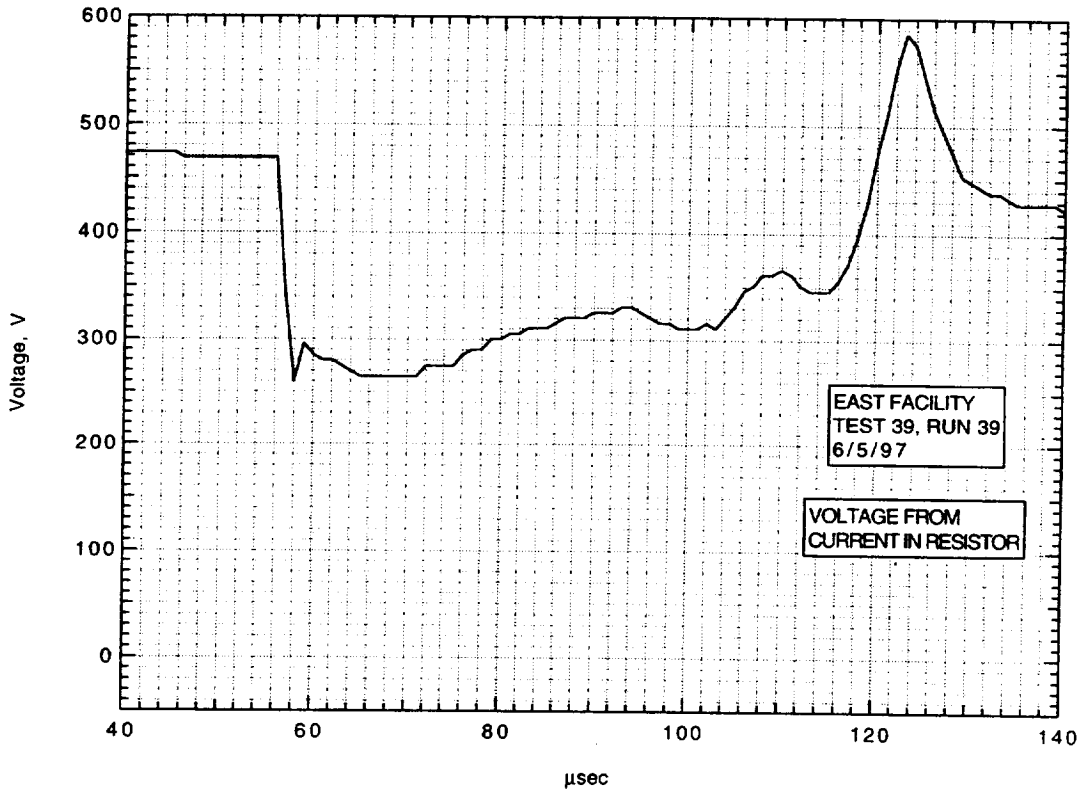

Run 39, voltage across electrodes from current in resistor.

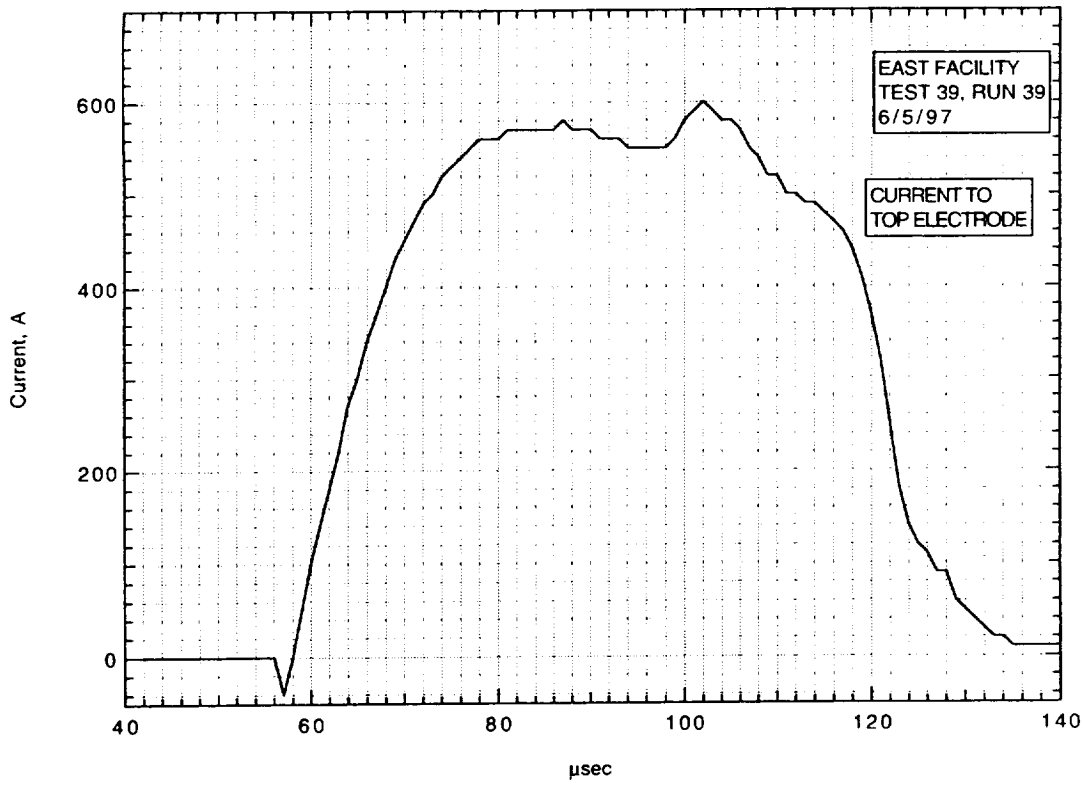

Run 39, current to top electrode.

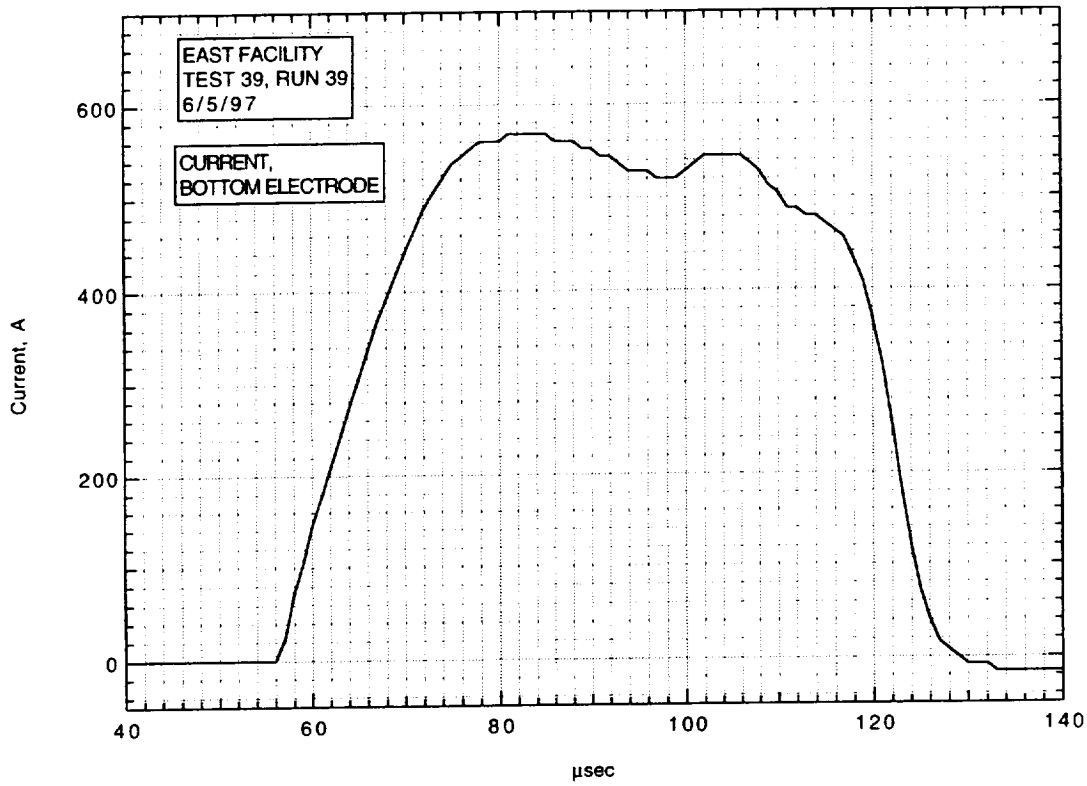

Run 39, current to bottom electrode.

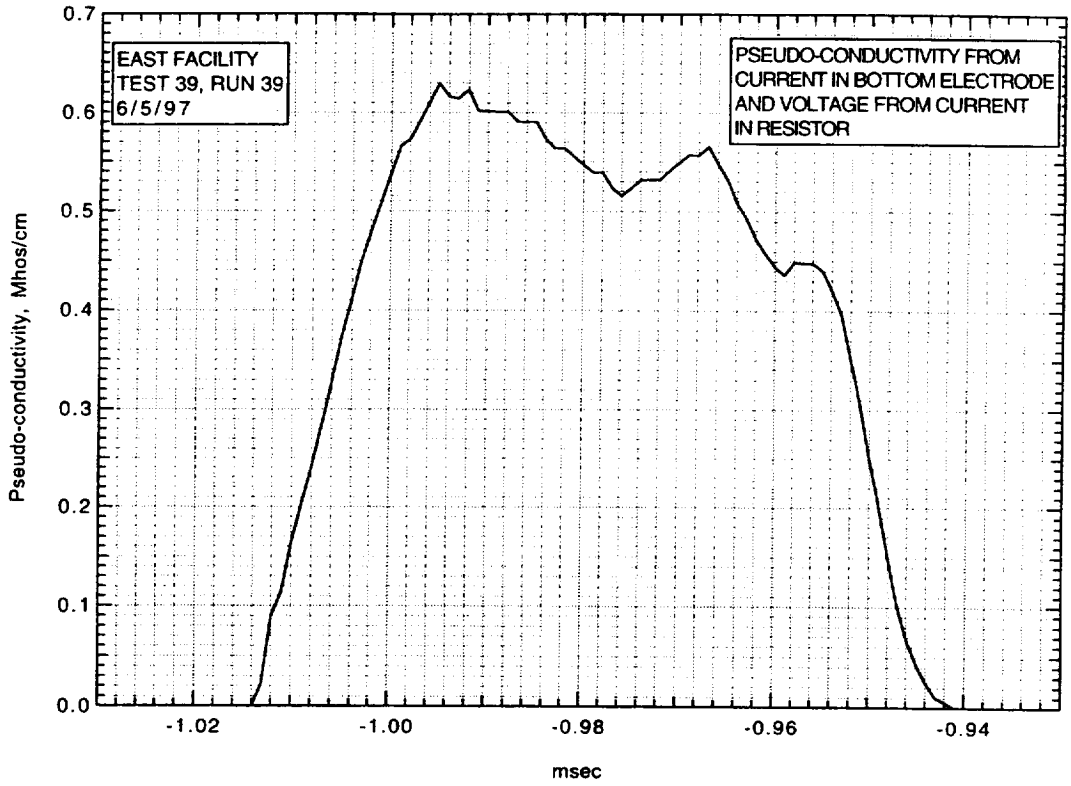

Run 39, pseudo-conductivity from current to bottom electrode and voltage from current in resistor.

AIR CONDUCTIVITY MEASUREMENT IN AMES EAST FACILITY

RUN 39/40, 6/6/97

1. Driven tube conditions:

53.2% N_2O, 46.8% N_2
Total pressure - 13 Torr
Measured shock velocity between stns D and F - N/A
Estimated shock velocity at electrodes - 4.946 km/sec - scaled from times of shock passage past pressure transducer at stn D and start of current flow at electrodes at E
Measured shock pressure at stn D - 8.00 atm
Measured shock pressure at stn F - N/A due to large EM noise pickup

2. Electrodes, driven tube dimensions:

Electrode size - 3.10 cm square
Electrode spacing - 3.10 cm
Main diaphragm to electrodes - 454.475 cm
Skimmer nose to electrodes - 39.979 cm
Driven tube diameter - 10.16 cm
Stn D (dn tube) to electrodes (channel) - 77.365 cm
Electrodes (channel) to stn F (channel) - 20.32 cm

3. Nominal test conditions:

Pressure - 5 atm
Voltage across electrodes - 190/151 V

4. Breakdown:

Little or no indication of breakdown.

Run no: 40 **Date:** 6/6/97 **Shock press. at D:** 8.00 atm
Shock vel. at E: 4.95 km/sec **Voltage at start of current flow:** 190 V

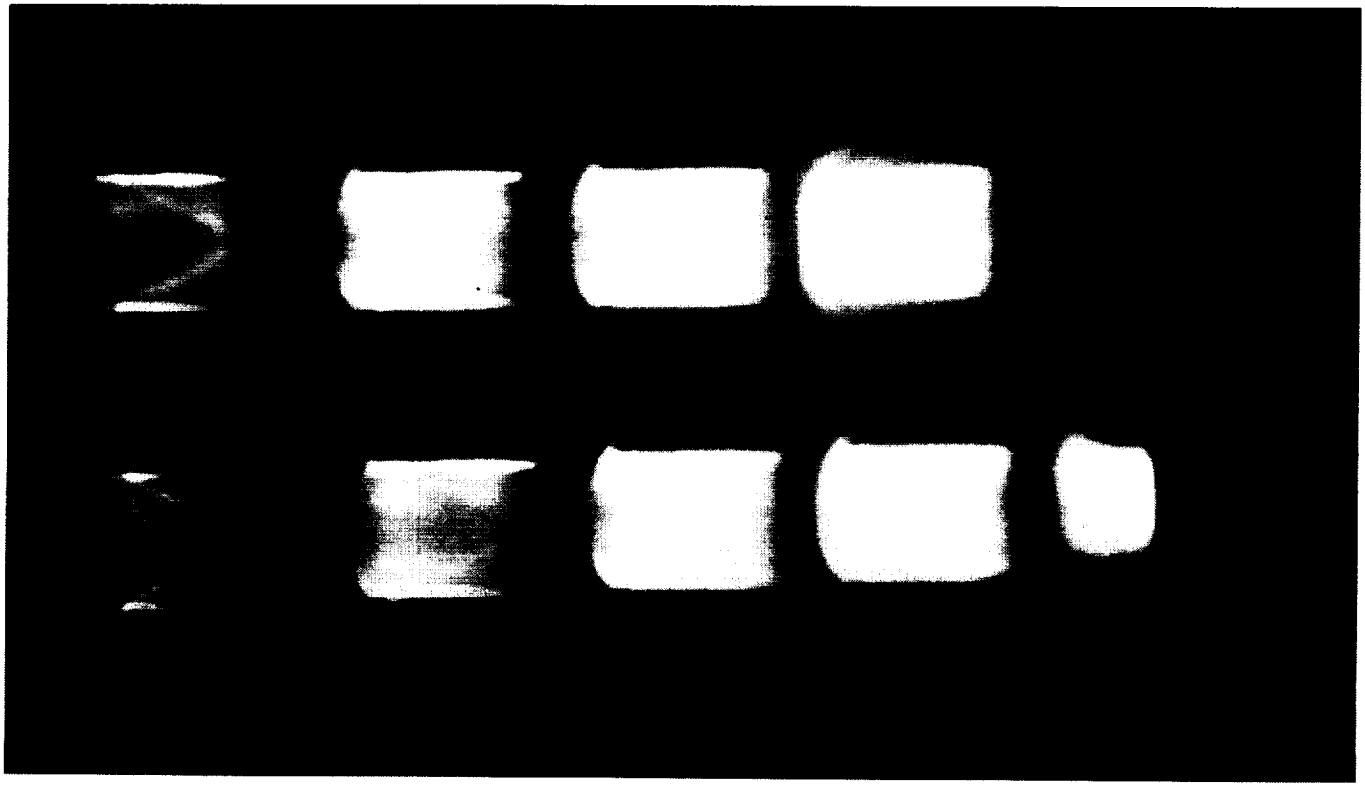

Frame:	**2**	**4**	**6**	**8**
Time:	7.3	15.3	23.3	31.3
Mach no:	2.33			
Frame:	**1**	**3**	**5**	**7**
Time:	3.3	11.3	19.3	27.3
Mach no:		2.40		

V_I: km/sec V_{CAV}: 5.09 km/sec

IMACON image of the shock-heated test gas flow in the electrode region. The time is measured from the start of the current flow. Mach numbers and velocities are deduced from the image as explained in section A.2.5.3.

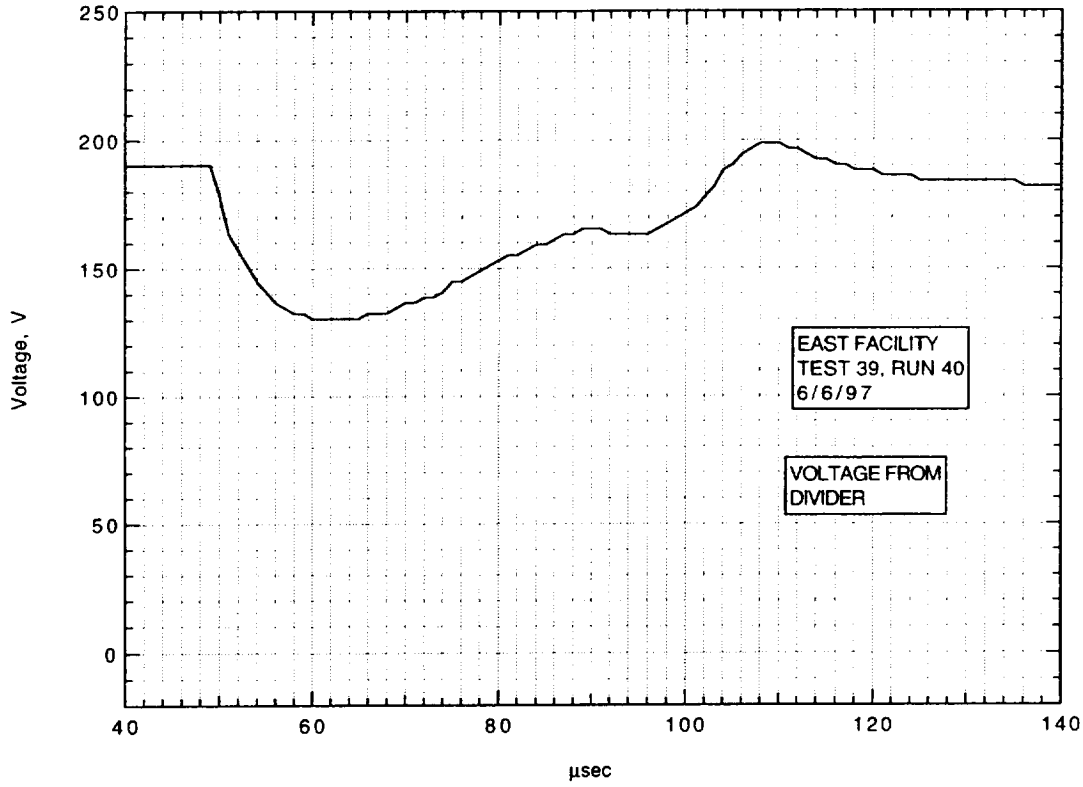

Run 40, voltage across electrodes from divider.

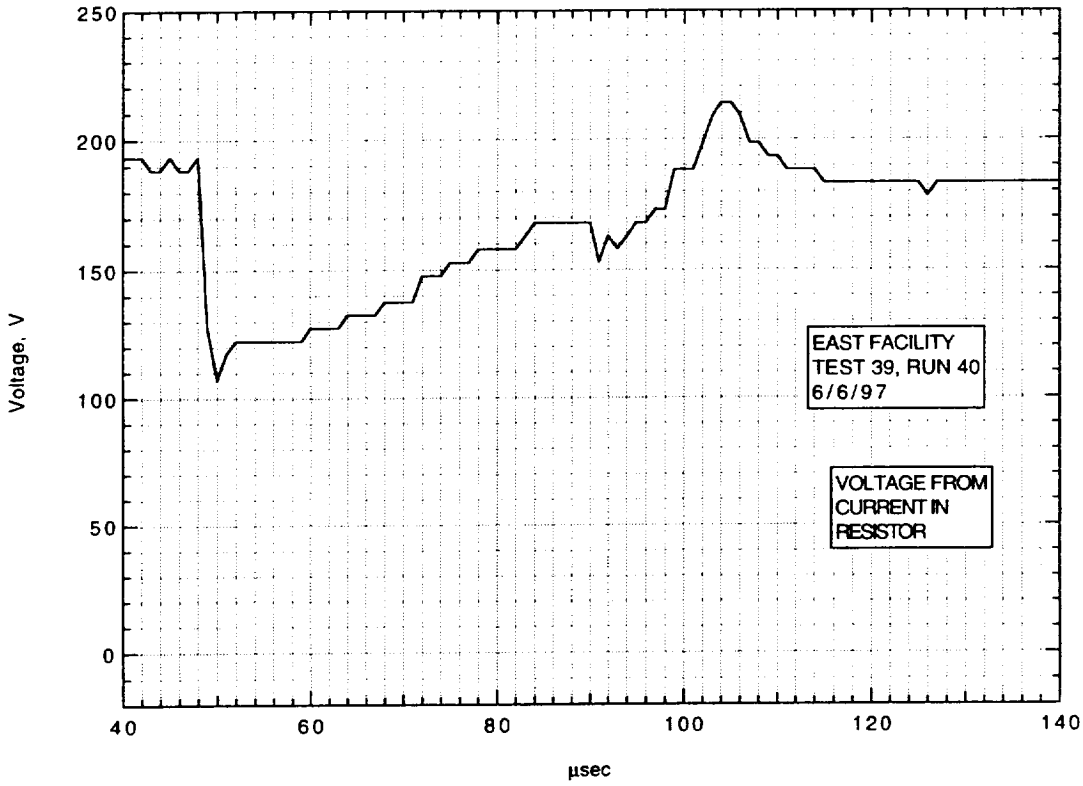

Run 40, voltage across electrodes from current in resistor.

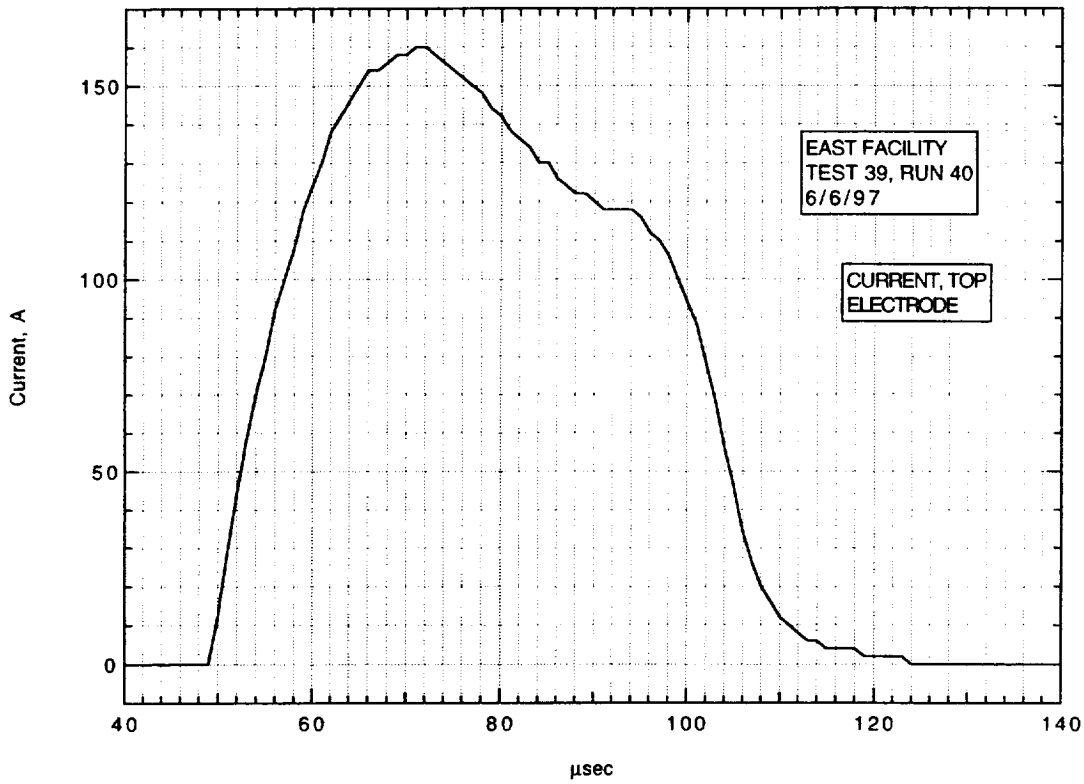

Run 40, current to top electrode.

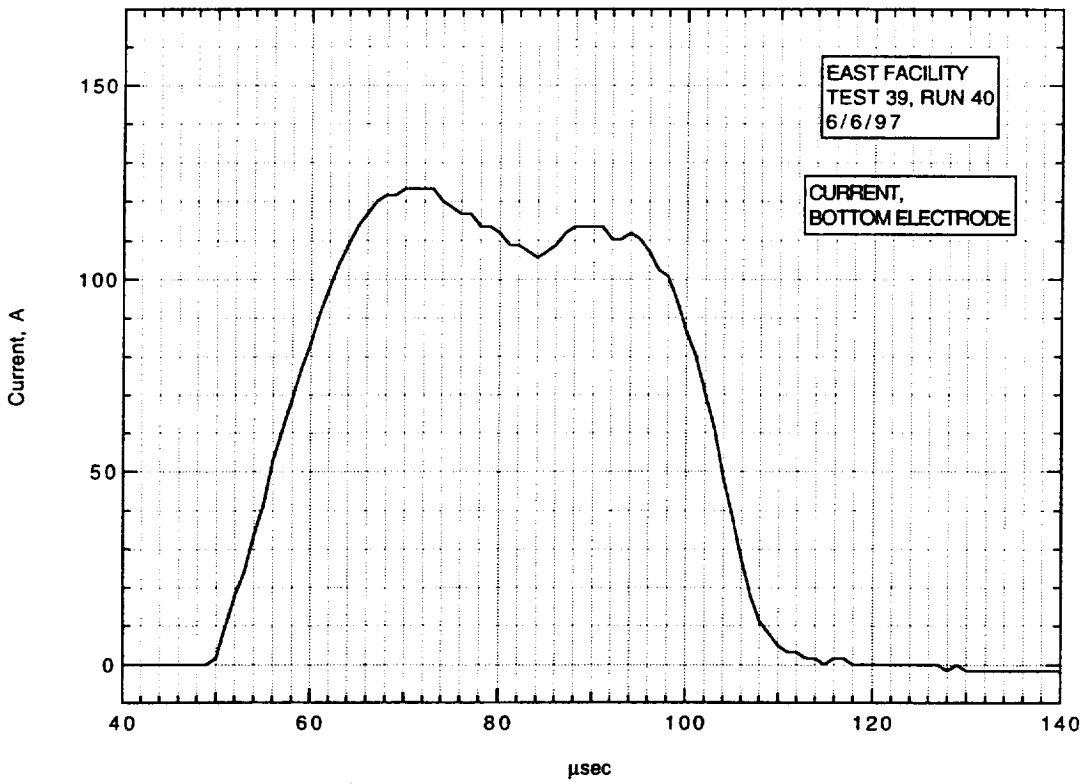

Run 40, current to bottom electrode.

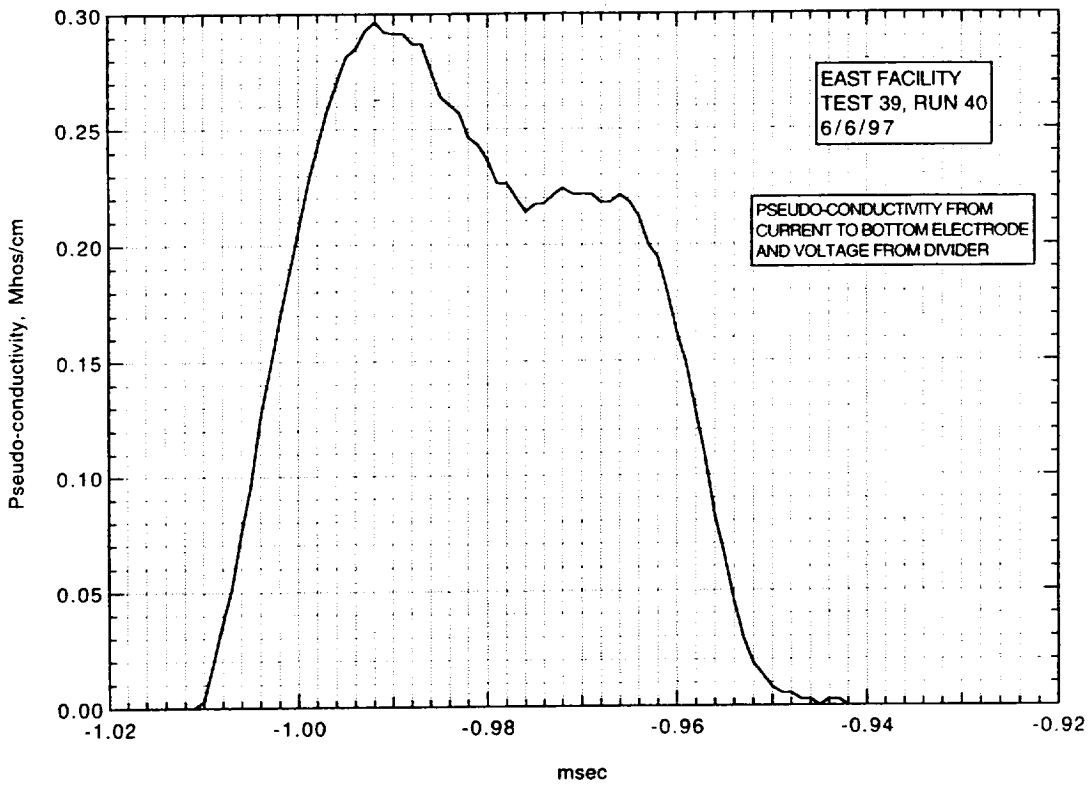

Run 40, pseudo-conductivity from current to bottom electrode and voltage from divider.

AIR CONDUCTIVITY MEASUREMENT IN AMES EAST FACILITY

RUN 39/41, 6/9/97

1. Driven tube conditions:

53.2% N_2O, 46.8% N_2
Total pressure - 13 Torr
Measured shock velocity between stns D and F - 4.909 km/sec
Estimated shock velocity at electrodes - 4.723 km/sec
Measured shock pressure at stn D - 7.28 atm
Measured shock pressure at stn F - N/A due to large EM noise pickup

2. Electrodes, driven tube dimensions:

Electrode size - 3.10 cm square
Electrode spacing - 3.10 cm
Main diaphragm to electrodes - 454.475 cm
Skimmer nose to electrodes - 39.979 cm
Driven tube diameter - 10.16 cm
Stn D (dn tube) to electrodes (channel) - 77.365 cm
Electrodes (channel) to stn F (channel) - 20.32 cm

3. Nominal test conditions:

Pressure - 5 atm
Voltage across electrodes - 45.5/40.3 V

4. Breakdown:

Little or no indication of breakdown.

Run no: 41 **Date:** 6/9/97 **Shock press. at D:** 7.28 atm
Shock vel. at E: 4.72 km/sec **Voltage at start of current flow:** 45.5 V

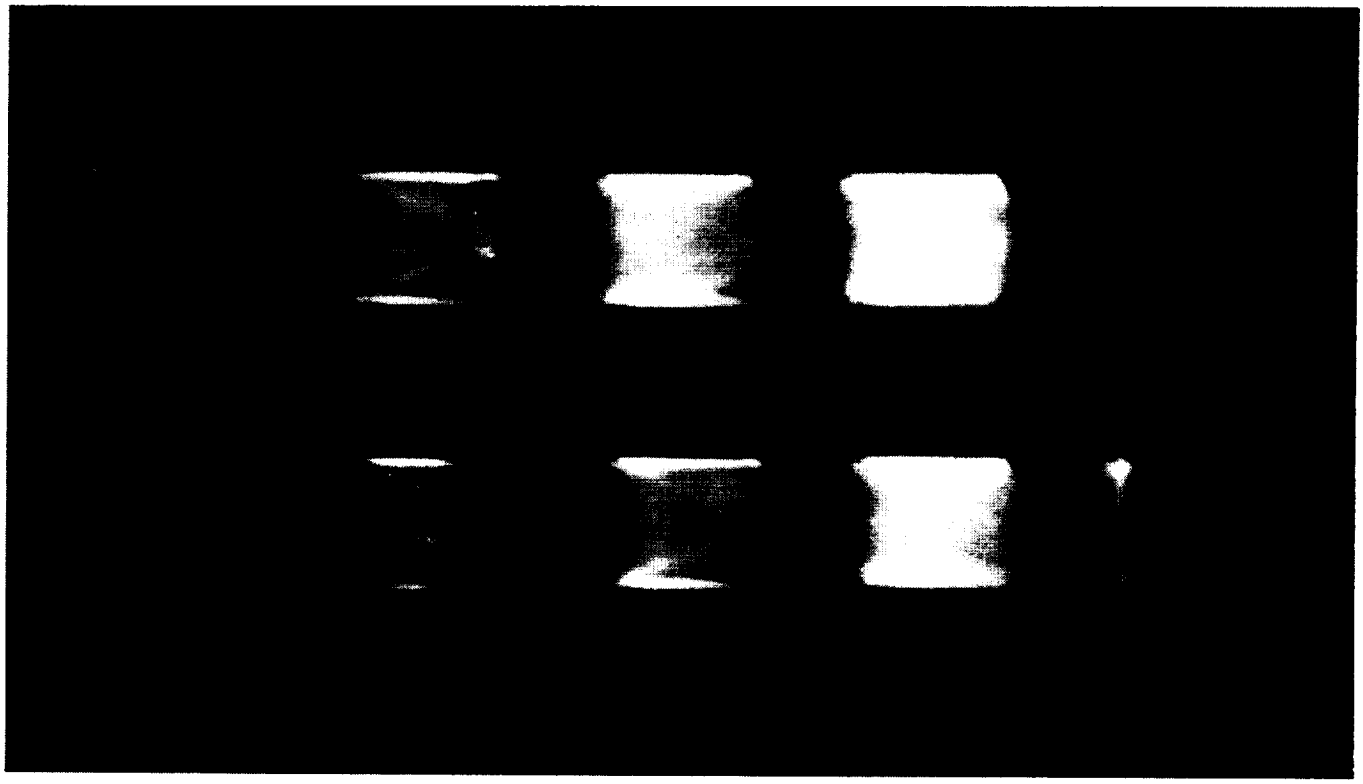

Frame:	**2**	**4**	**6**	**8**
Time:	3.1	11.1	19.1	27.1
Mach no:		2.24		
Frame:	**1**	**3**	**5**	**7**
Time:	-0.9	7.1	15.1	23.1
Mach no:		2.24		

V_I: km/sec V_{CAV}: 4.92 km/sec

IMACON image of the shock-heated test gas flow in the electrode region. The time is measured from the start of the current flow. Mach numbers and velocities are deduced from the image as explained in section A.2.5.3.

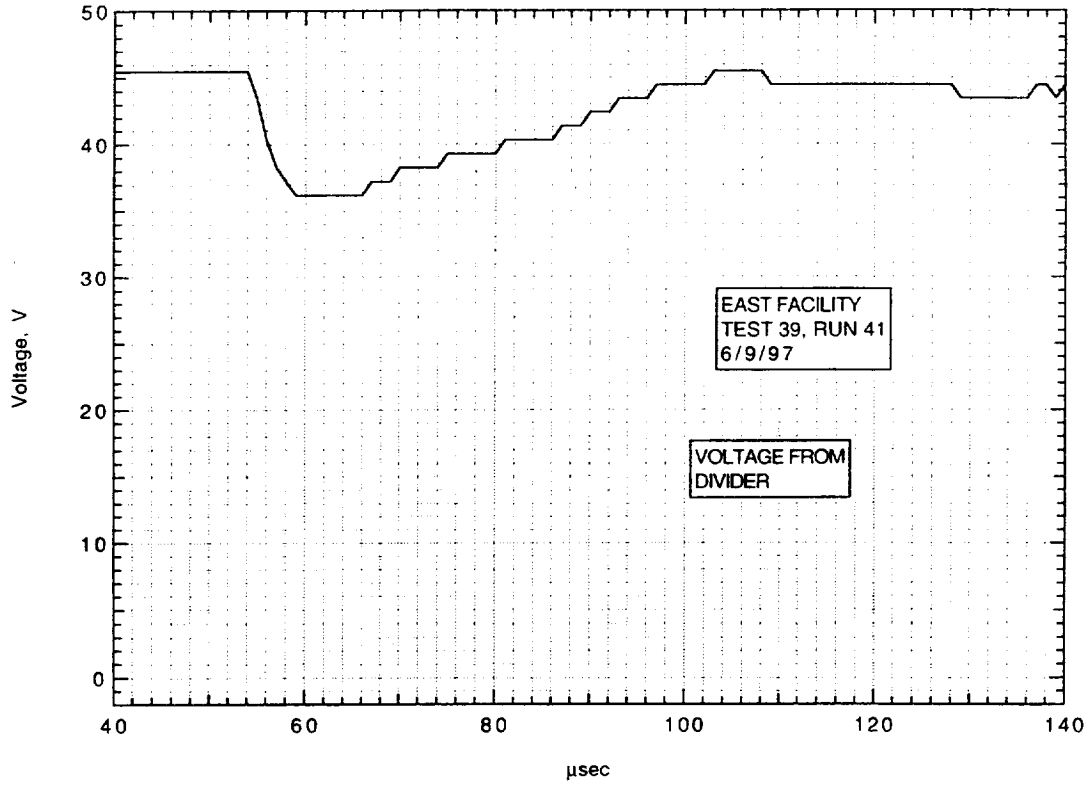

Run 41, voltage across electrodes from divider.

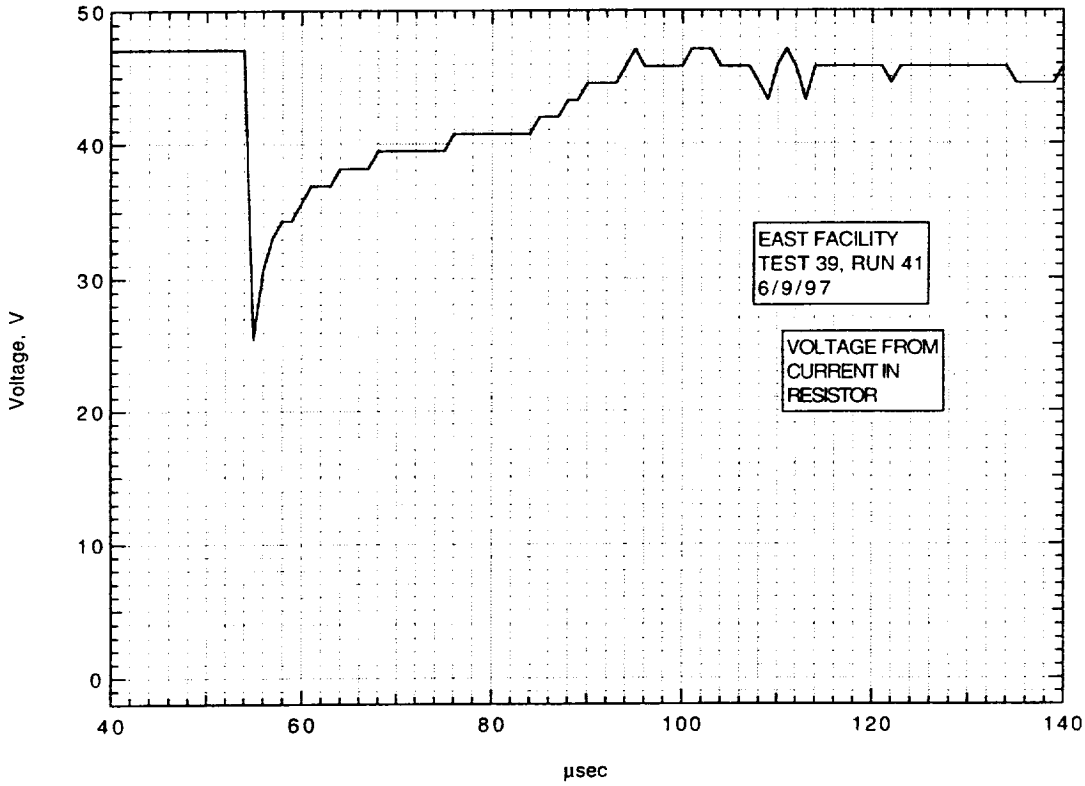

Run 41, voltage across electrodes from current in resistor.

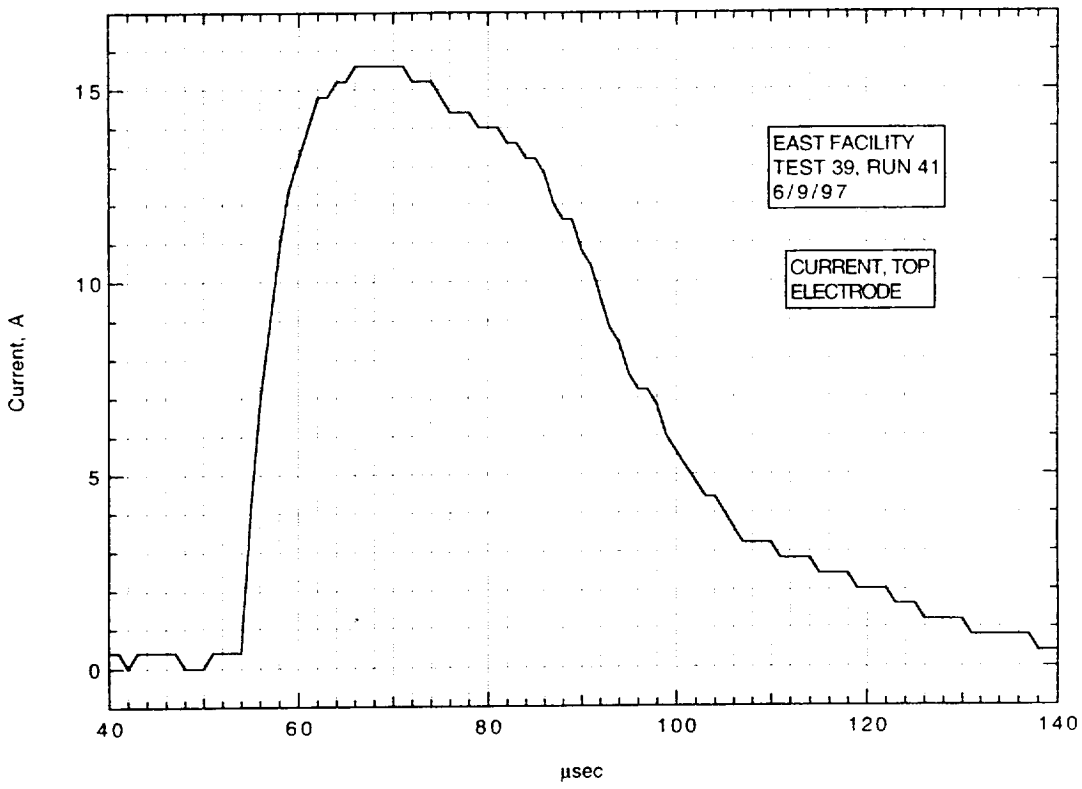

Run 41, current to top electrode.

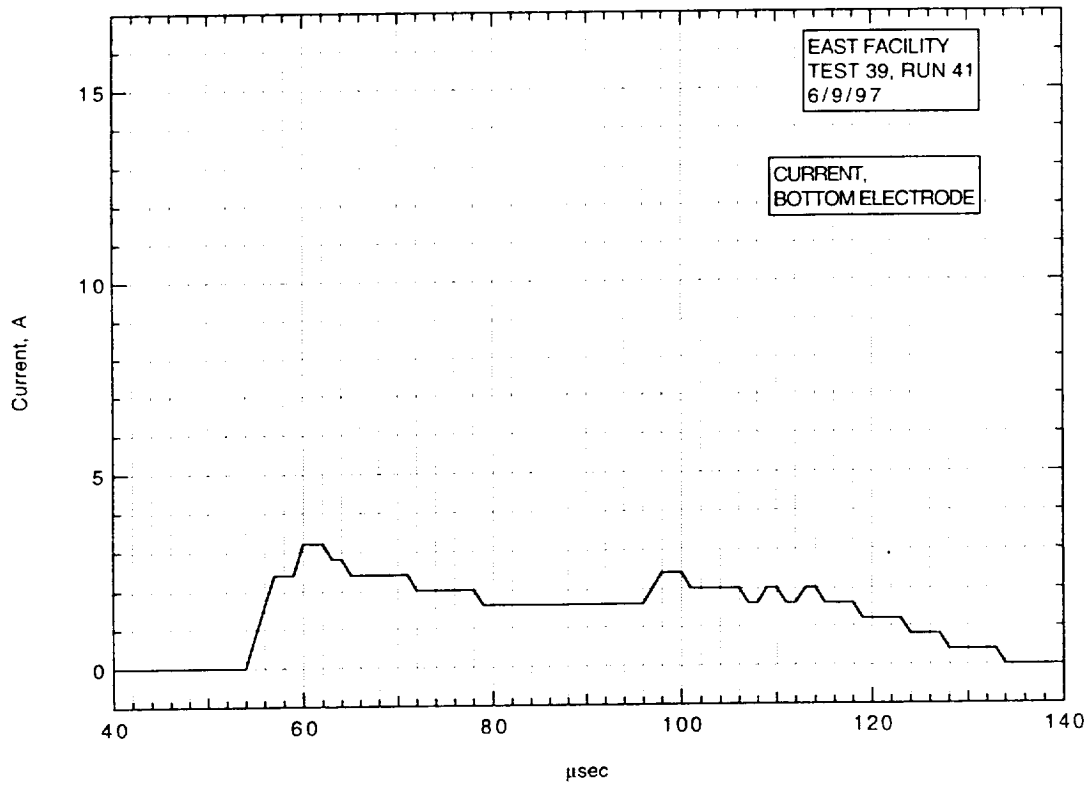

Run 41, current to bottom electrode.

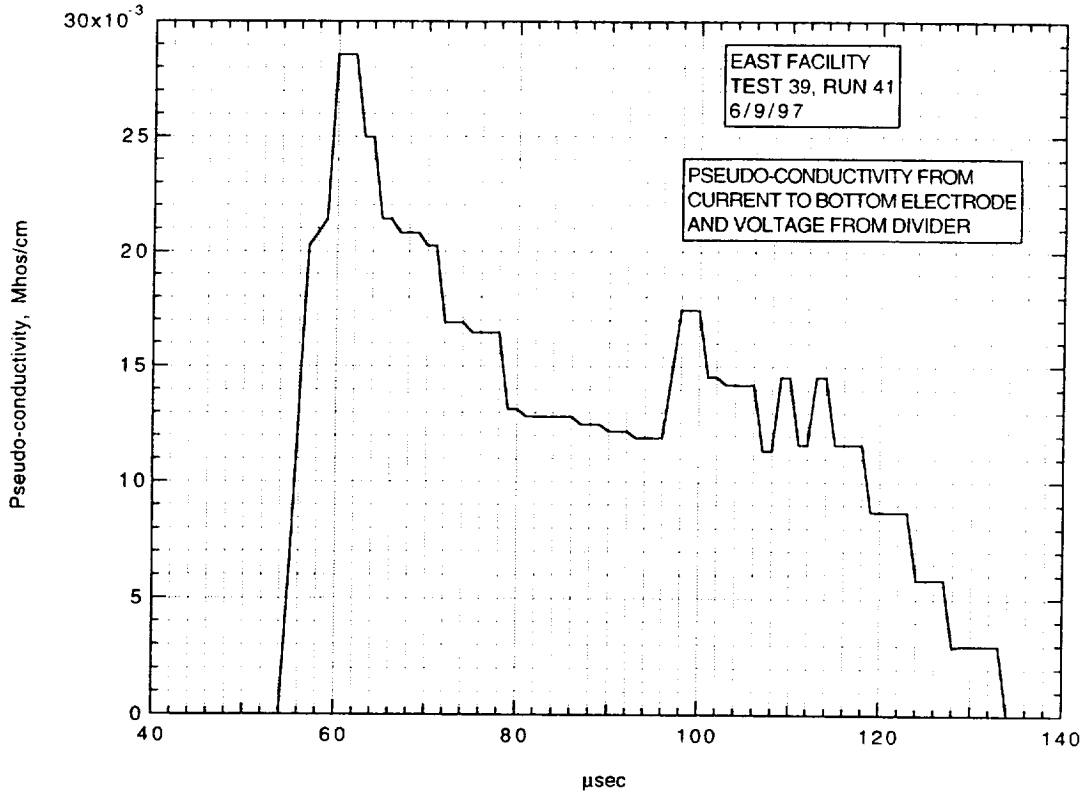

Run 41, pseudo-conductivity from current to bottom electrode and voltage from divider.

AIR CONDUCTIVITY MEASUREMENT IN AMES EAST FACILITY

RUN 39/42, 6/10/97

1. Driven tube conditions:

52.925% N_2O, 46.575% N_2, 0.5%H_2
Total pressure - 5.14 Torr
Measured shock velocity between stns D and F - 6.464 km/sec
Estimated shock velocity at electrodes, from Δt(DF) - 6.224 km/sec
Estimated shock velocity at electrodes, from Δt(DE) - 6.348 km/sec;
(This Δt from pressure transducer at D until start of current flow at electrodes.)
Measured shock pressure at stn D - 4.78 atm
Measured shock pressure at stn F - N/A due to large EM noise pickup

2. Electrodes, driven tube dimensions:

Electrode size - 3.10 cm square
Electrode spacing - 3.10 cm
Main diaphragm to electrodes - 454.475 cm
Skimmer nose to electrodes - 39.979 cm
Driven tube diameter - 10.16 cm
Stn D (dn tube) to electrodes (channel) - 77.365 cm
Electrodes (channel) to stn F (channel) - 20.32 cm

3. Nominal test conditions:

Pressure - 3.2 atm
Voltage across electrodes - 45.5/44.5 V

4. Breakdown:

Little or no indication of breakdown.

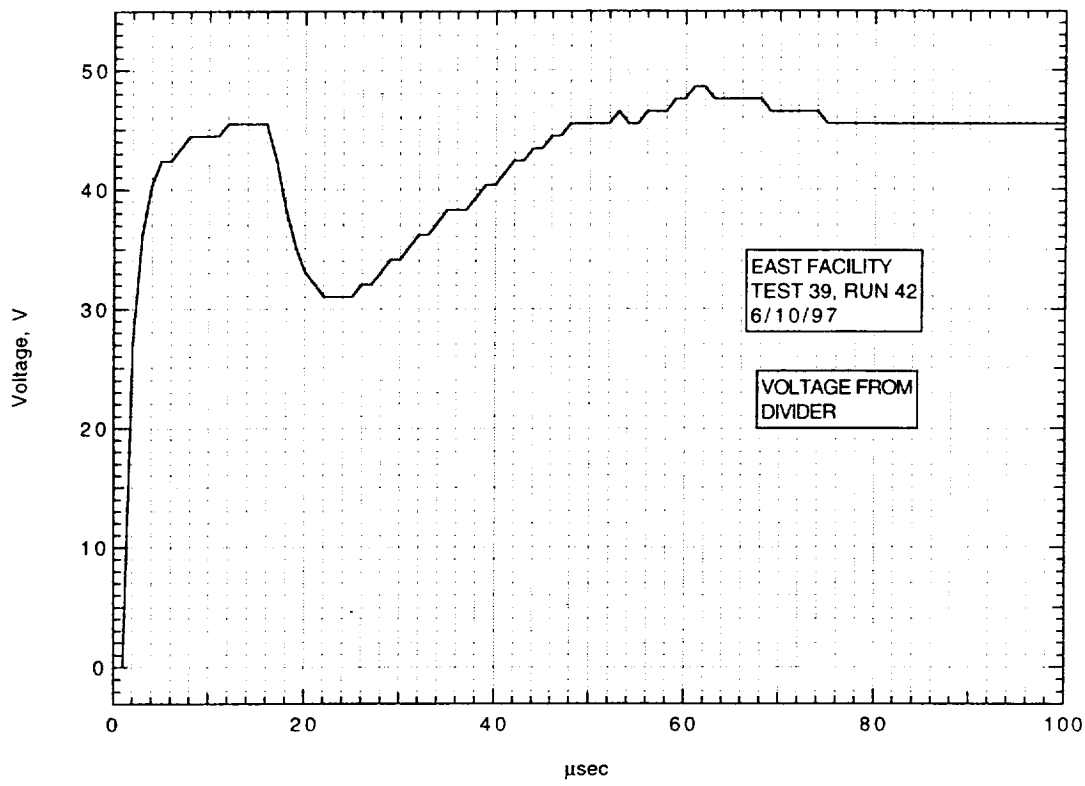

Run 42, voltage across electrodes from divider.

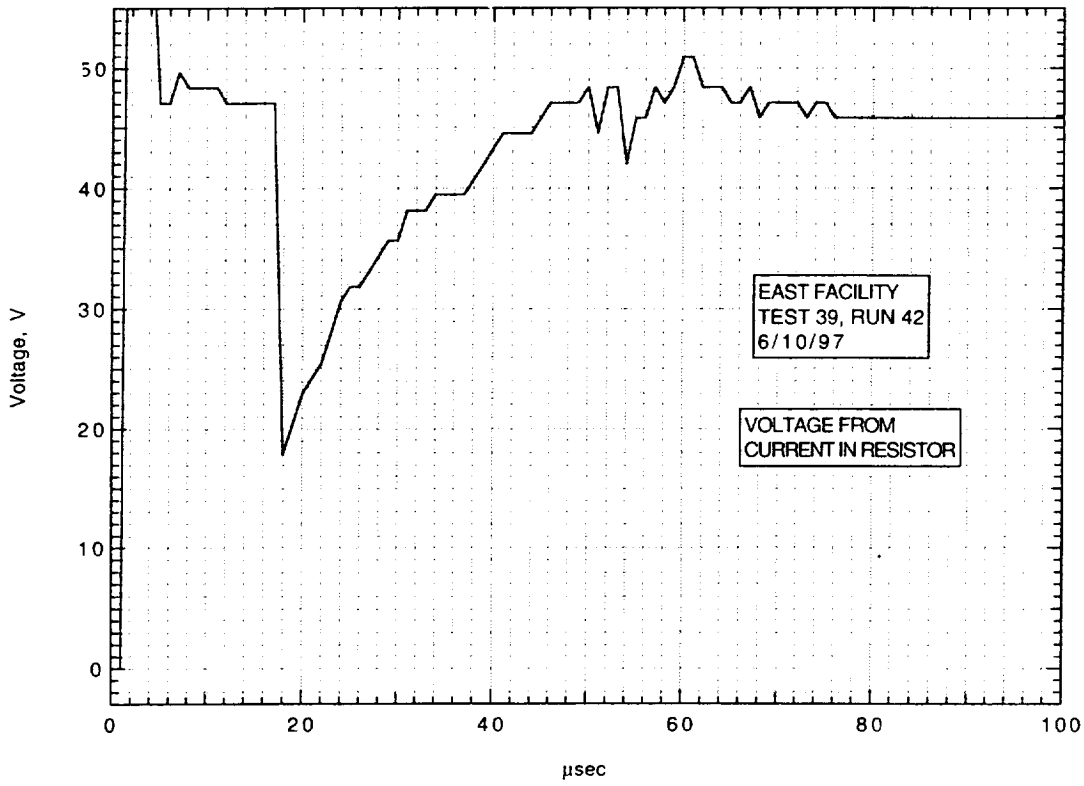

Run 42, voltage across electrodes from current in resistor.

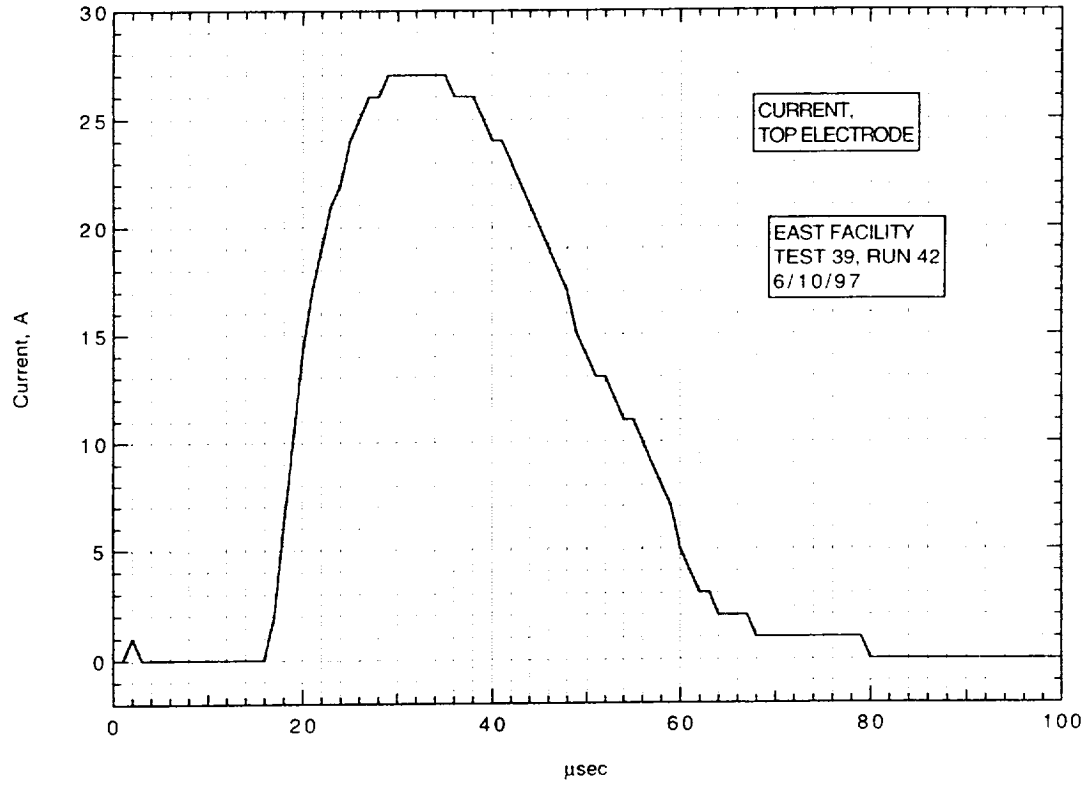

Run 42, current to top electrode.

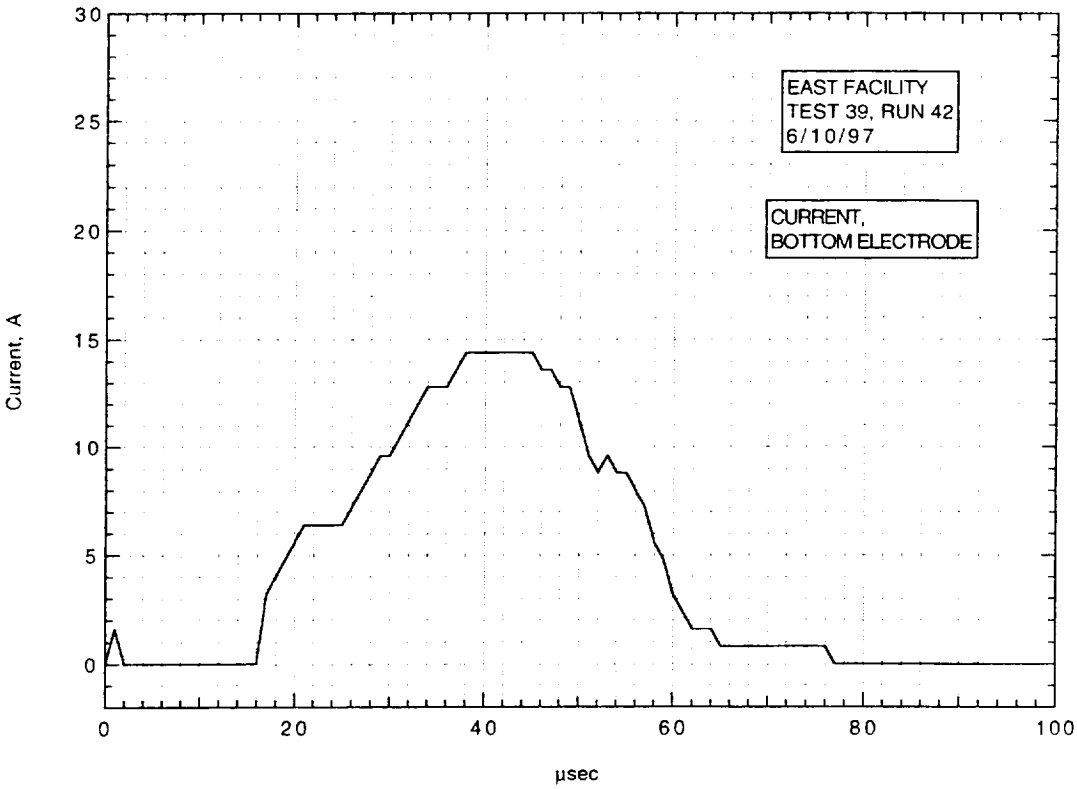

Run 42, current to bottom electrode.

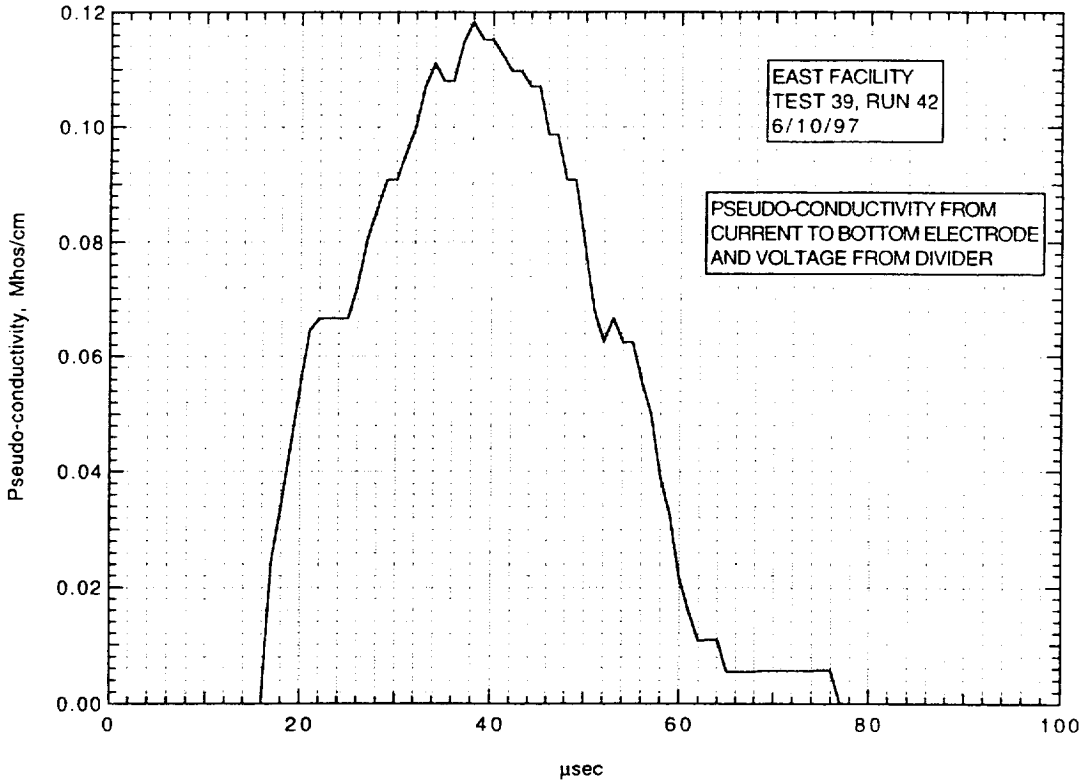

Run 42, pseudo-conductivity from current to bottom electrode and voltage from divider.

AIR CONDUCTIVITY MEASUREMENT IN AMES EAST FACILITY

RUN 39/43, 6/11/97

1. Driven tube conditions:

52.925% N_2O, 46.575% N_2, 0.5%H_2
Total pressure - 6.30 Torr
Measured shock velocity between stns D and F - 5.614 km/sec
Estimated shock velocity at electrodes, from Δt(DF) - 5.401 km/sec
Estimated shock velocity at electrodes, from Δt(DE) - 5.352 km/sec;
(This Δt from pressure transducer at D until start of current flow at electrodes.)
Measured shock pressure at stn D - 3.97 atm
Measured shock pressure at stn F - N/A due to large EM noise pickup

2. Electrodes, driven tube dimensions:

Electrode size - 3.10 cm square
Electrode spacing - 3.10 cm
Main diaphragm to electrodes - 454.475 cm
Skimmer nose to electrodes - 39.979 cm
Driven tube diameter - 10.16 cm
Stn D (dn tube) to electrodes (channel) - 77.365 cm
Electrodes (channel) to stn F (channel) - 20.32 cm

3. Nominal test conditions:

Pressure - 3.2 atm
Voltage across electrodes - 187/115 V

4. Breakdown:

Little or no indication of breakdown.

Run no: 43 **Date:** 6/11/97 **Shock press. at D:** 3.97 atm
Shock vel. at E: 5.38 km/sec **Voltage at start of current flow:** 187 V

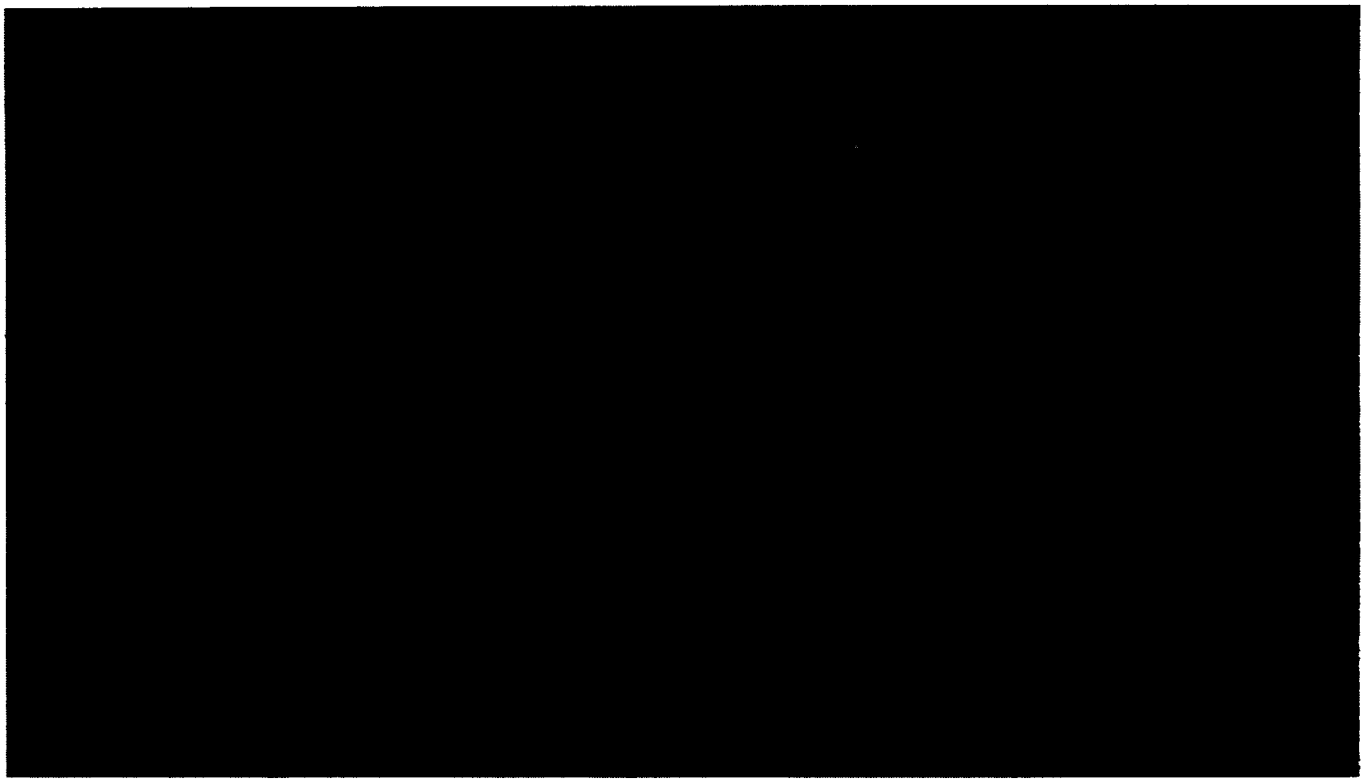

Frame:	**2**	**4**	**6**	**8**
Time:	-8.5	-0.5	7.5	15.5
Mach no:				2.69
Frame:	**1**	**3**	**5**	**7**
Time:	-12.5	-4.5	3.5	11.5
Mach no:				2.69

V_I: km/sec V_{CAV}: 5.77 km/sec

IMACON image of the shock-heated test gas flow in the electrode region. The time is measured from the start of the current flow. Mach numbers and velocities are deduced from the image as explained in section A.2.5.3.

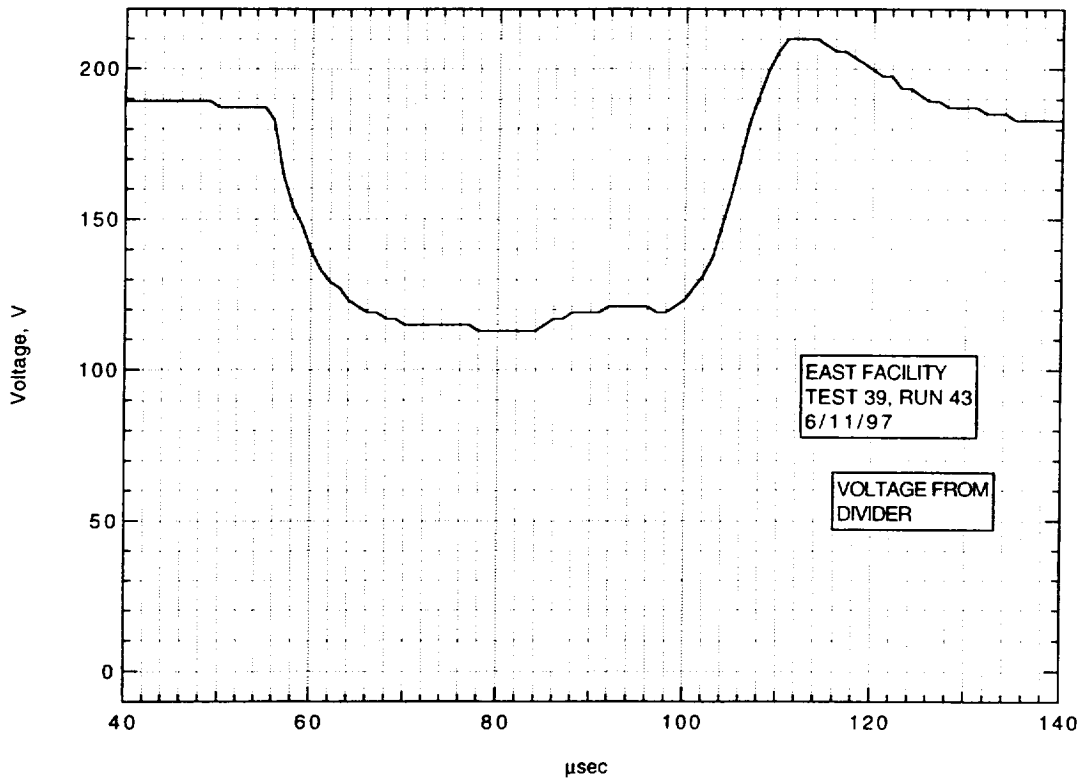

Run 43, voltage across electrodes from divider.

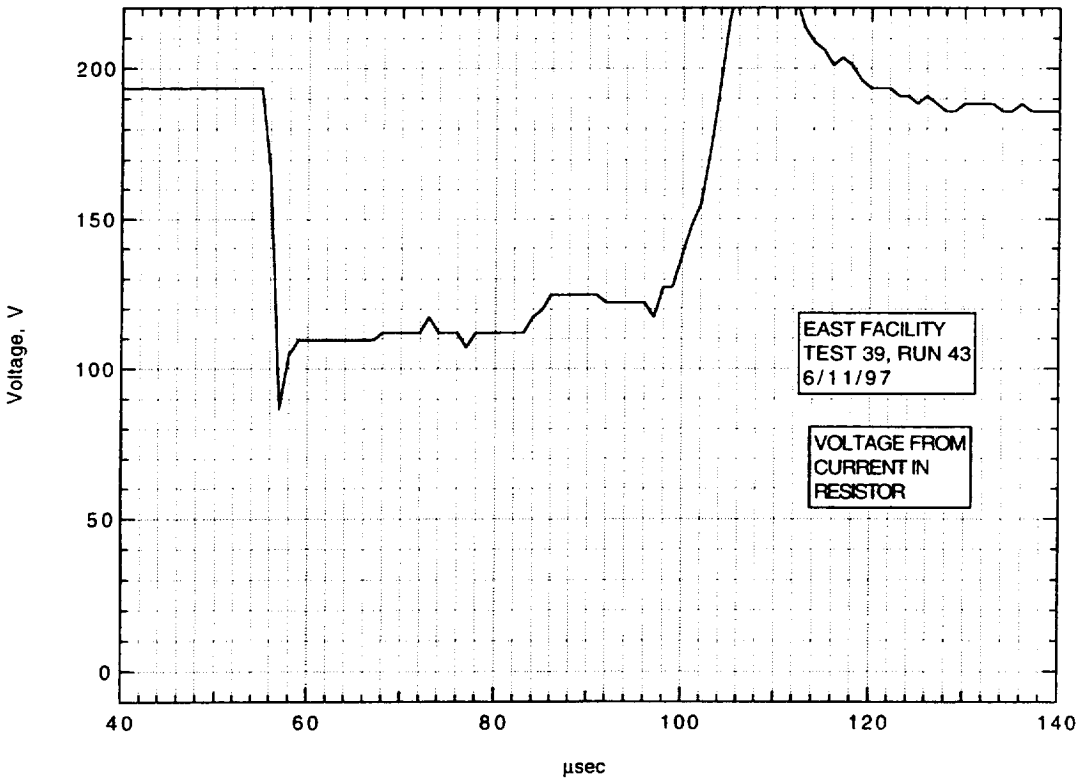

Run 43, voltage across electrodes from current in resistor.

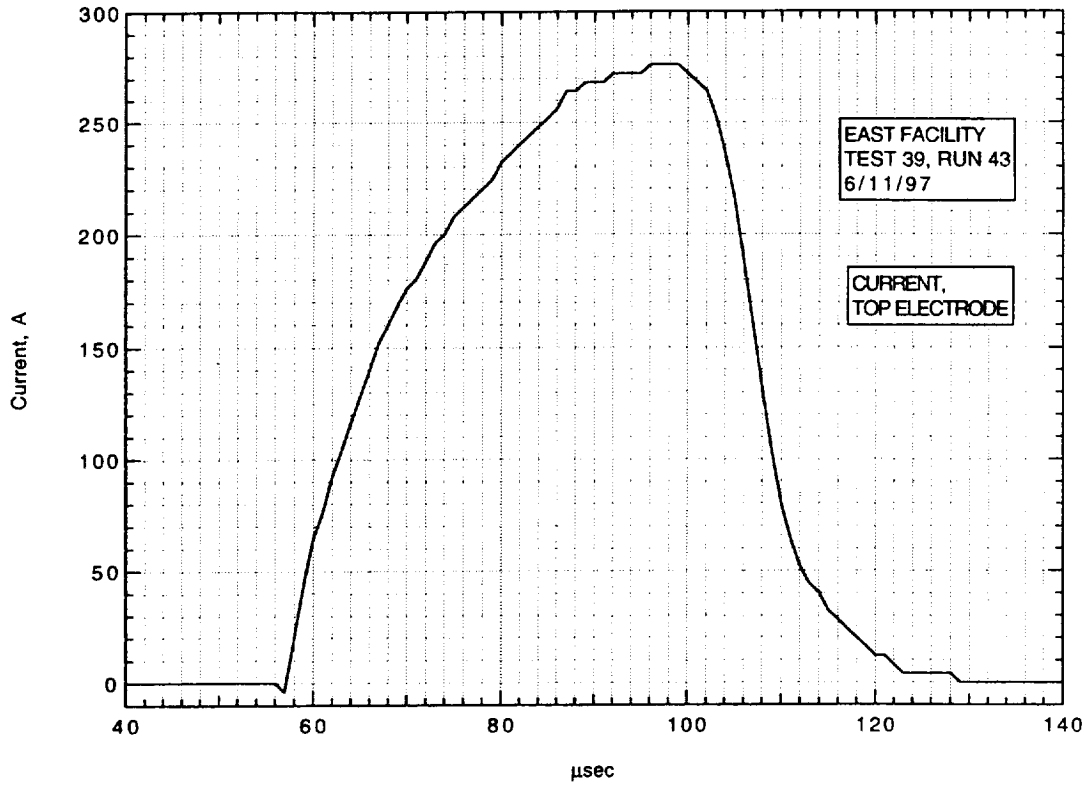

Run 43, current to top electrode.

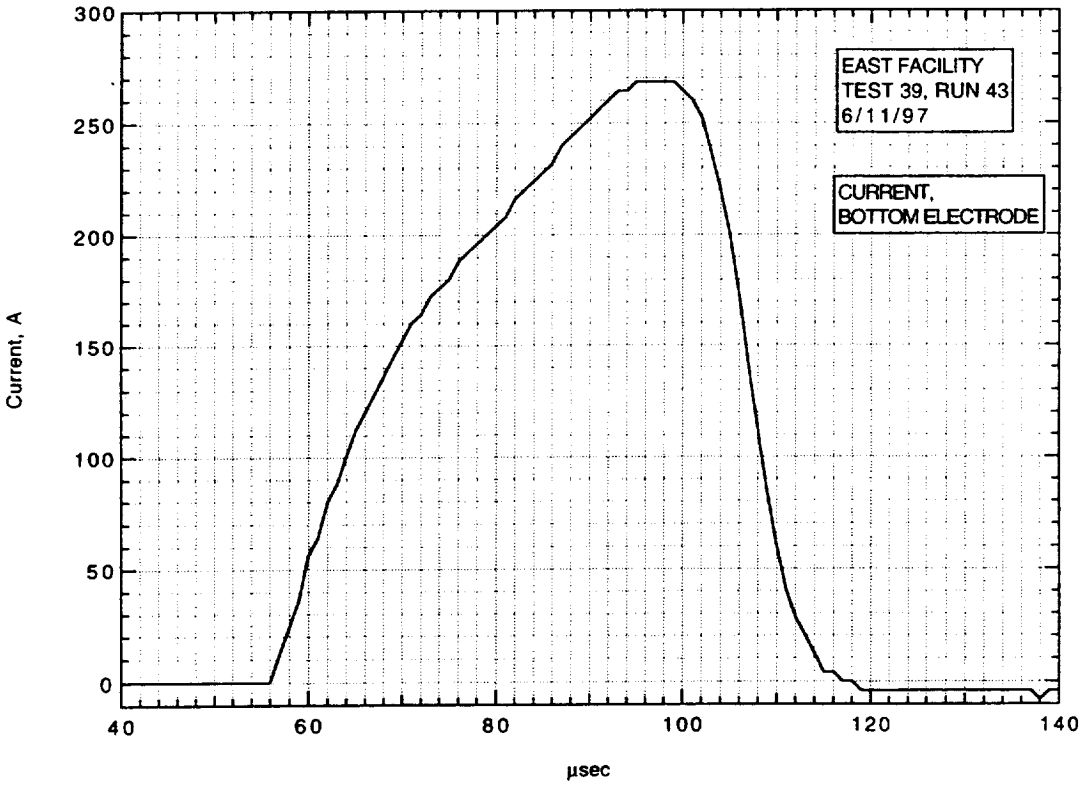

Run 43, current to bottom electrode.

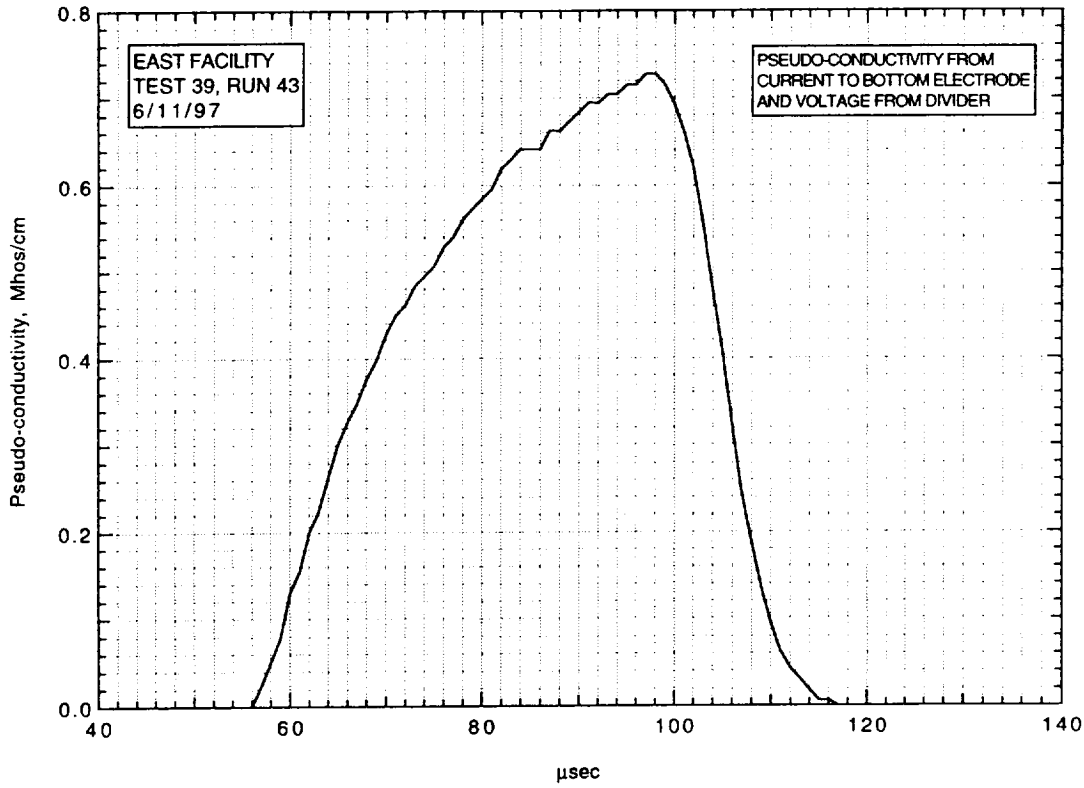

Run 43, pseudo-conductivity from current to bottom electrode and voltage from divider.

AIR CONDUCTIVITY MEASUREMENT IN AMES EAST FACILITY

RUN 39/44, 6/12/97

1. Driven tube conditions:

52.925% N_2O, 46.575% N_2, 0.5%H_2
Total pressure - 31.2 Torr
Measured shock velocity between stns D and F - 5.035 km/sec
Estimated shock velocity at electrodes, from Δt(DF) - 4.844 km/sec
Estimated shock velocity at electrodes, from Δt(DE) - 4.846 km/sec; (This Δt from pressure transducer at D until start of current flow at electrodes.)
Measured shock pressure at stn D - 17.90 atm
Measured shock pressure at stn F - 11.46 atm - rather uncertain due to large EM noise pickup.

2. Electrodes, driven tube dimensions:

Electrode size - 3.10 cm square
Electrode spacing - 3.10 cm
Main diaphragm to electrodes - 454.475 cm
Skimmer nose to electrodes - 39.979 cm
Driven tube diameter - 10.16 cm
Stn D (dn tube) to electrodes (channel) - 77.365 cm
Electrodes (channel) to stn F (channel) - 20.32 cm

3. Nominal test conditions:

Pressure - 13 atm
Voltage across electrodes - 186/145 V

4. Breakdown:

Little or no indication of breakdown.

Run no: 44 **Date:** 6/12/97 **Shock press. at D:** 17.90 atm
Shock vel. at E: 4.85 km/sec **Voltage at start of current flow:** 186 V

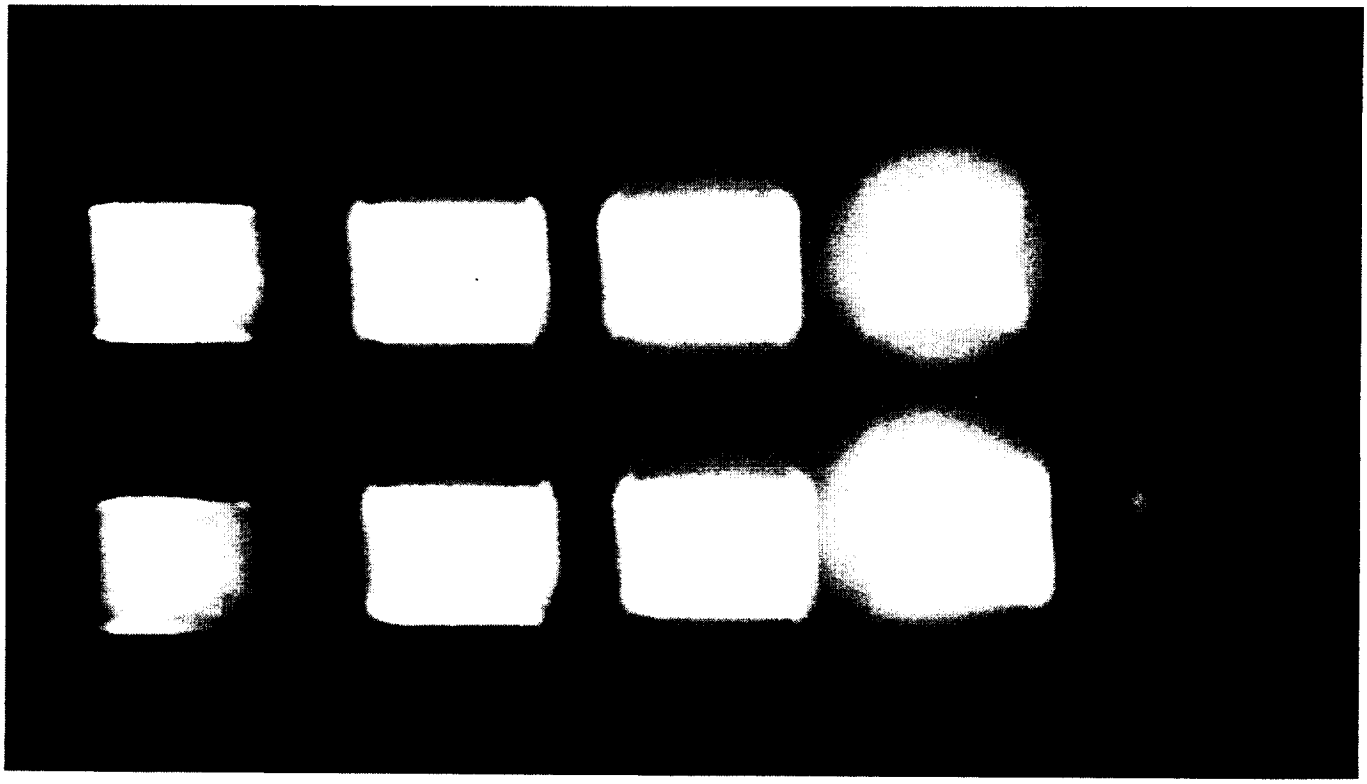

Frame:	**2**	**4**	**6**	**8**
Time:	10.1	18.1	26.1	34.1
Mach no:				
Frame:	**1**	**3**	**5**	**7**
Time:	6.1	14.1	22.1	30.1
Mach no:	2.36			

V_I: km/sec V_{CAV}: 5.03 km/sec

IMACON image of the shock-heated test gas flow in the electrode region. The time is measured from the start of the current flow. Mach numbers and velocities are deduced from the image as explained in section A.2.5.3.

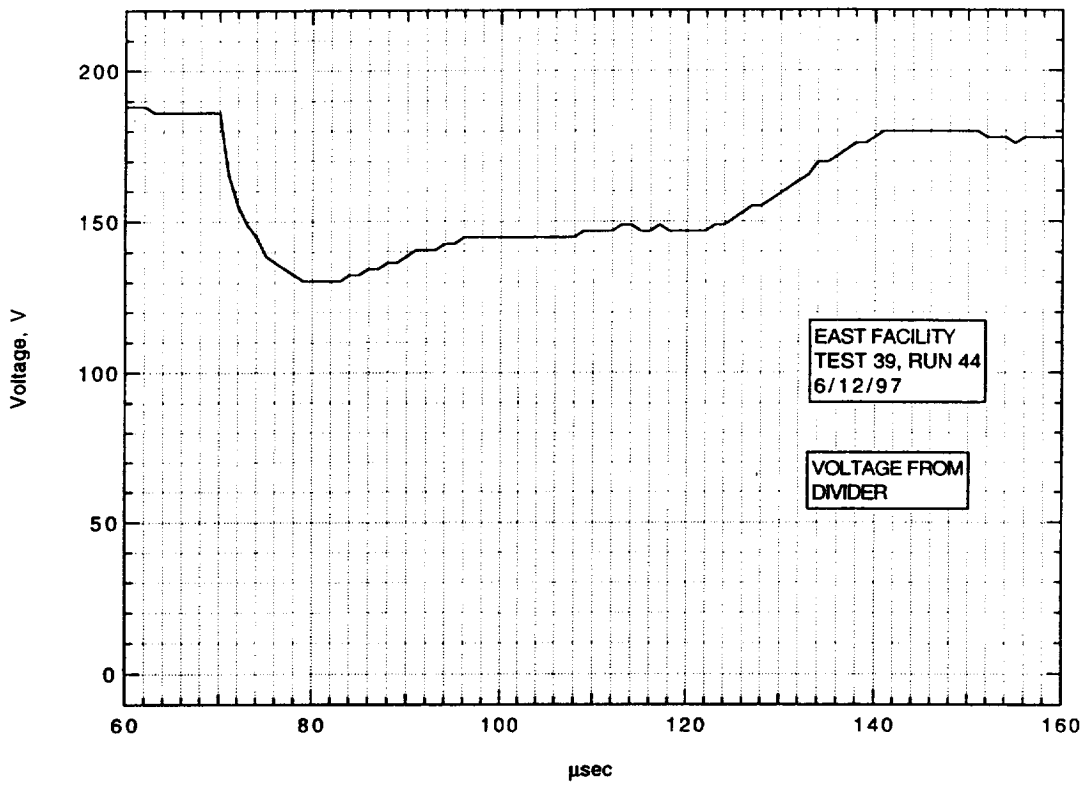

Run 44, voltage across electrodes from divider.

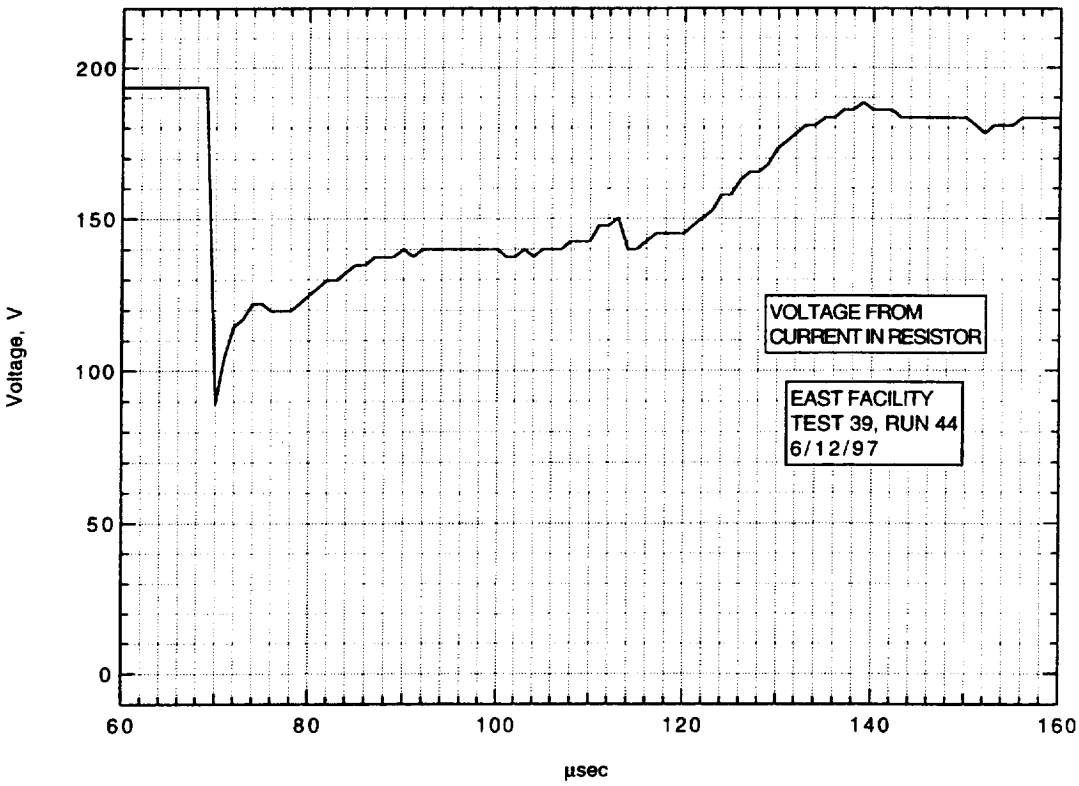

Run 44, voltage across electrodes from current in resistor.

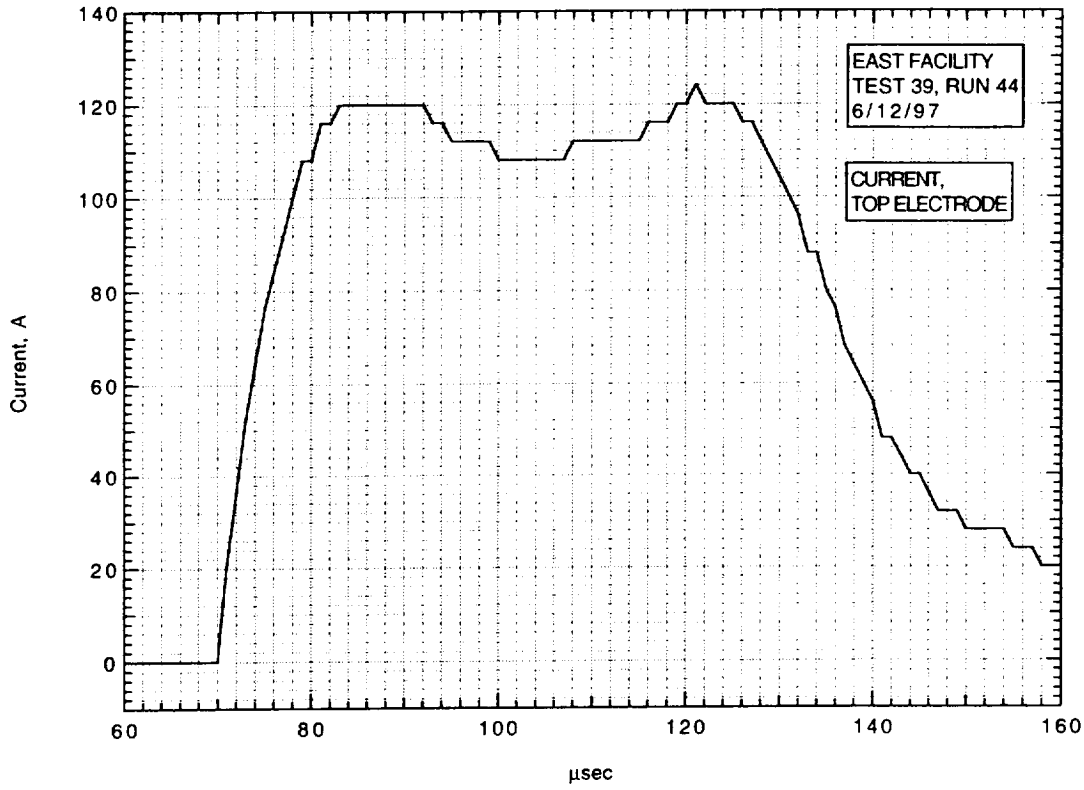

Run 44, current to top electrode.

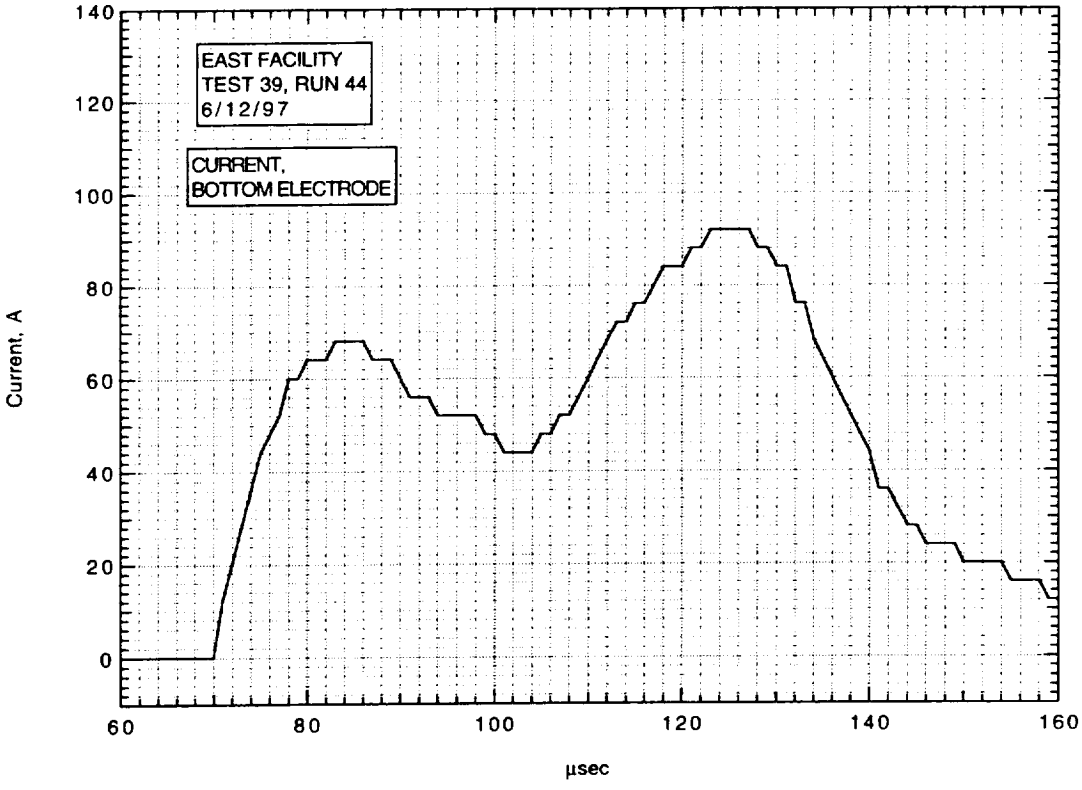

Run 44, current to bottom electrode.

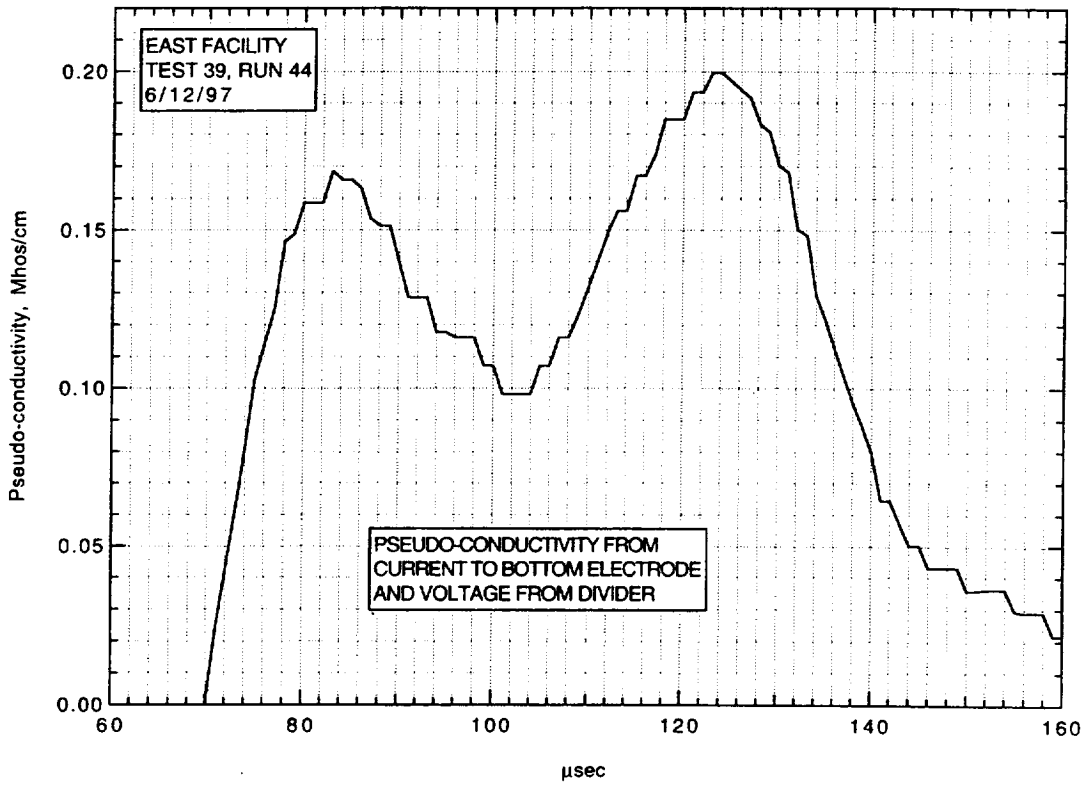

Run 44, pseudo-conductivity from current to bottom electrode and voltage from divider.

AIR CONDUCTIVITY MEASUREMENT IN AMES EAST FACILITY

RUN 39/45, 6/13/97

1. Driven tube conditions:

52.925% N_2O, 46.575% N_2, 0.5%H_2
Total pressure - 35.35 Torr
Measured shock velocity between stns D and F - 4.765 km/sec
Estimated shock velocity at electrodes, from Δt(DF) - 4.585 km/sec
Estimated shock velocity at electrodes, from Δt(DE) - 4.688 km/sec;
(This Δt from pressure transducer at D until start of current flow at electrodes.)
Measured shock pressure at stn D - 19.68 atm
Measured shock pressure at stn F - 14.95 atm - very uncertain due to large EM noise pickup.

2. Electrodes, driven tube dimensions:

Electrode size - 3.10 cm square
Electrode spacing - 3.10 cm
Main diaphragm to electrodes - 454.475 cm
Skimmer nose to electrodes - 39.979 cm
Driven tube diameter - 10.16 cm
Stn D (dn tube) to electrodes (channel) - 77.365 cm
Electrodes (channel) to stn F (channel) - 20.32 cm

3. Nominal test conditions:

Pressure - 13 atm
Voltage across electrodes - 186/115 V

4. Breakdown:

Little or no indication of breakdown.

Run no: 45 **Date:** 6/13/97 **Shock press. at D:** 19.68 atm
Shock vel. at E: 4.64 km/sec **Voltage at start of current flow:** 186 V

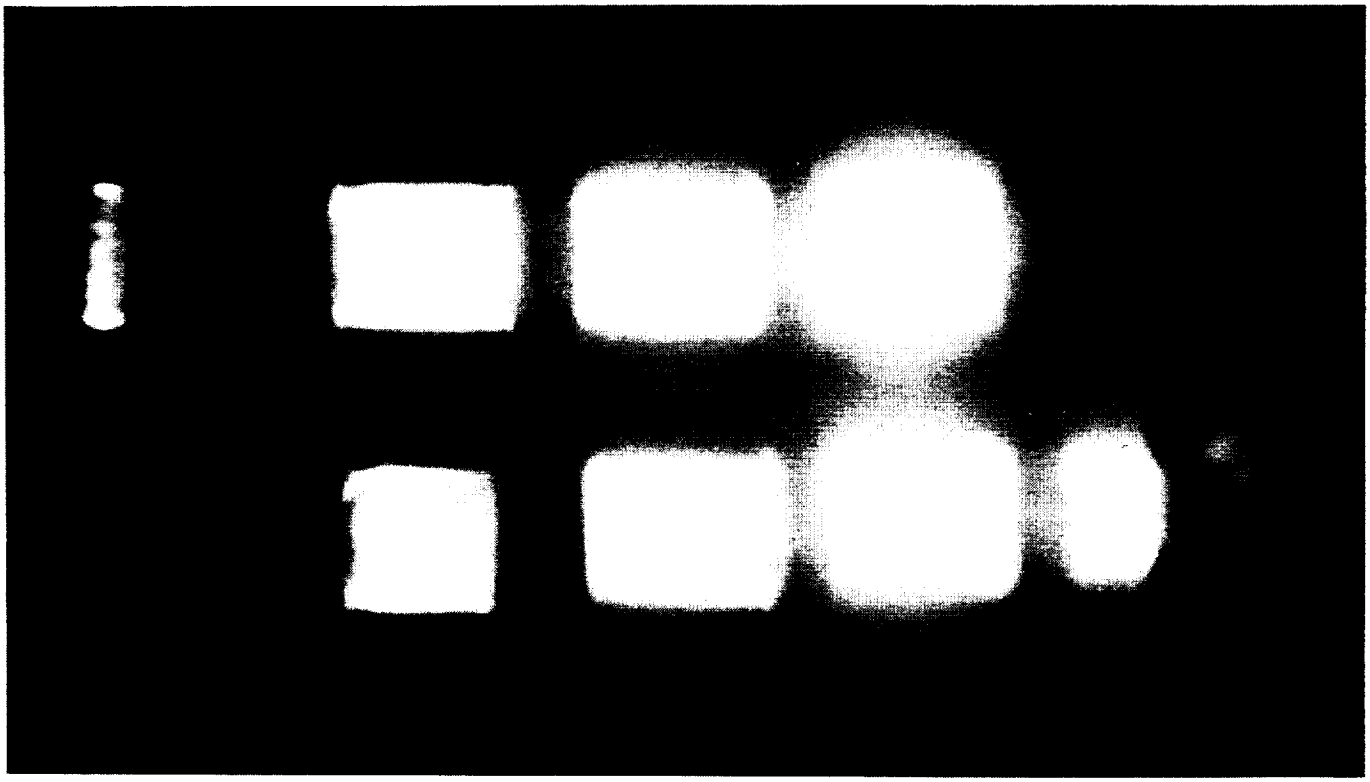

Frame:	**2**	**4**	**6**	**8**
Time:	1.4	9.4	17.4	25.4
Mach no:				
Frame:	**1**	**3**	**5**	**7**
Time:	-2.6	5.4	13.4	21.4
Mach no:				

V_I: 4.8 km/sec V_{CAV}: 4.87 km/sec

IMACON image of the shock-heated test gas flow in the electrode region. The time is measured from the start of the current flow. Mach numbers and velocities are deduced from the image as explained in section A.2.5.3.

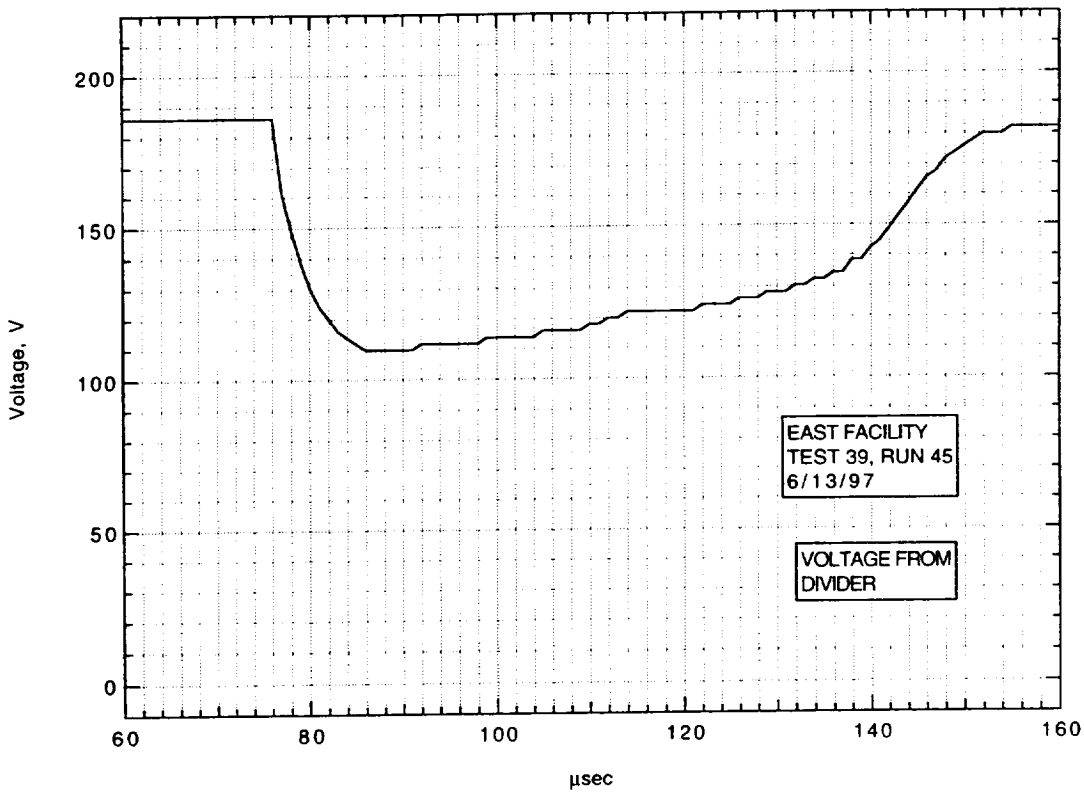

Run 45, voltage across electrodes from divider.

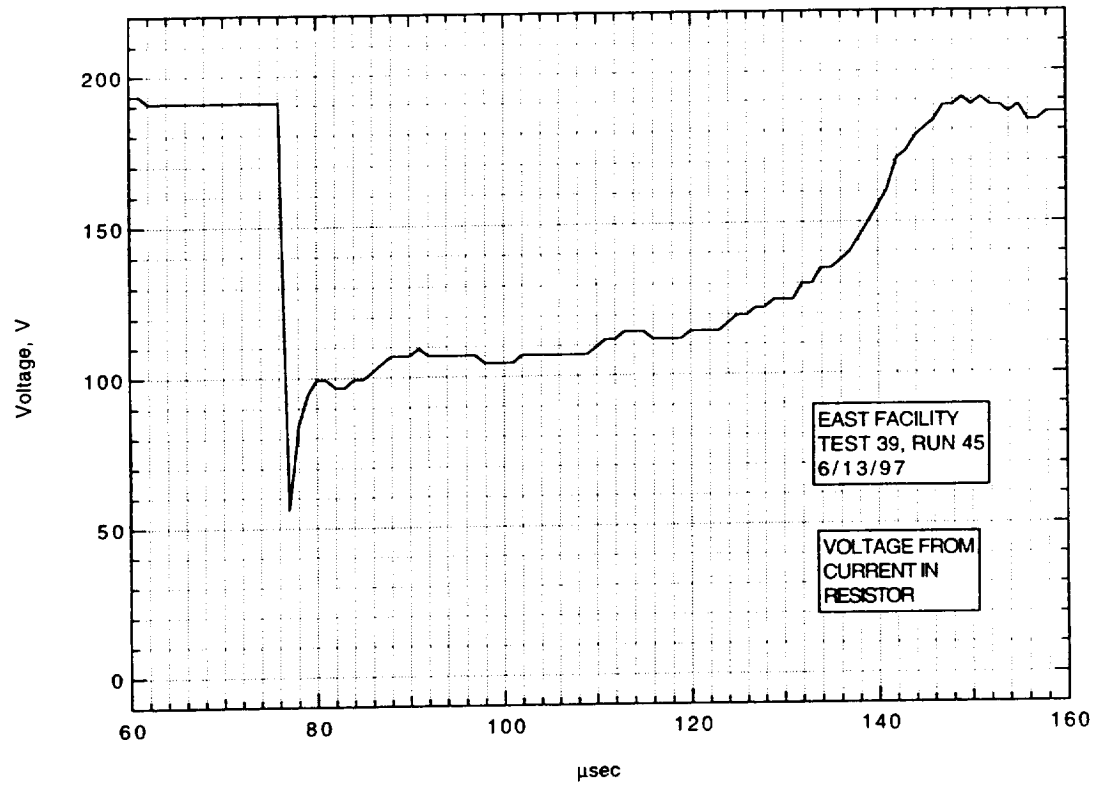

Run 45, voltage across electrodes from current in resistor.

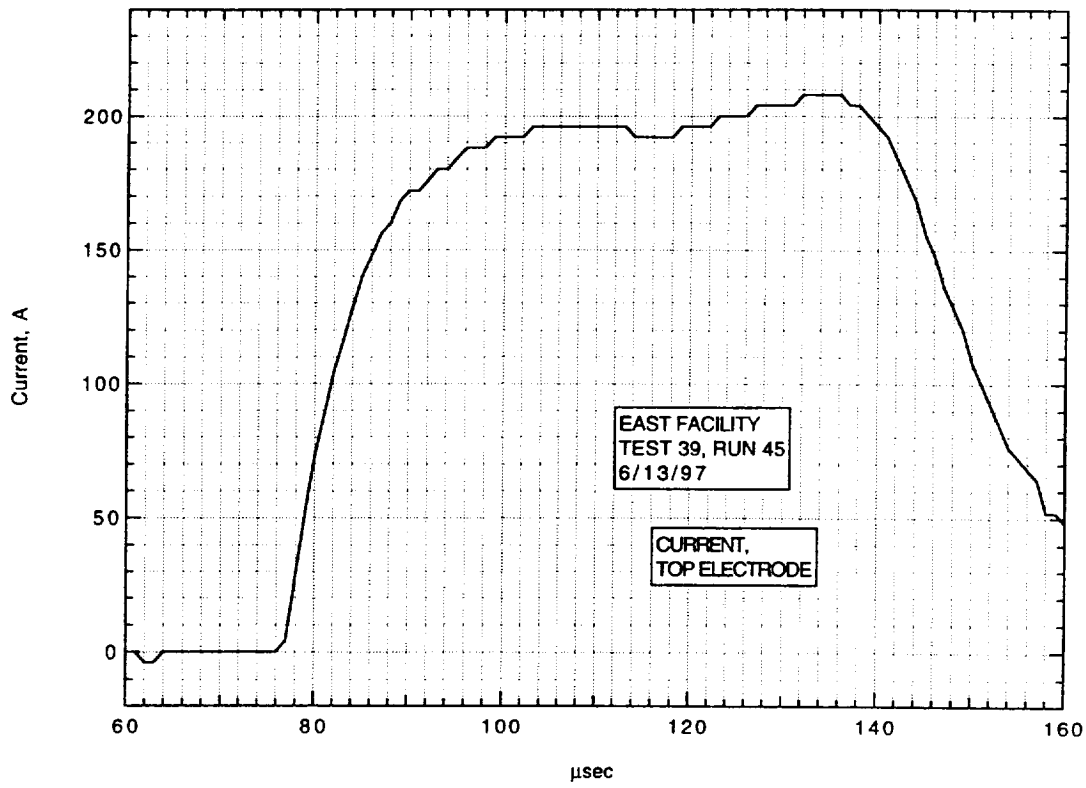

Run 45, current to top electrode.

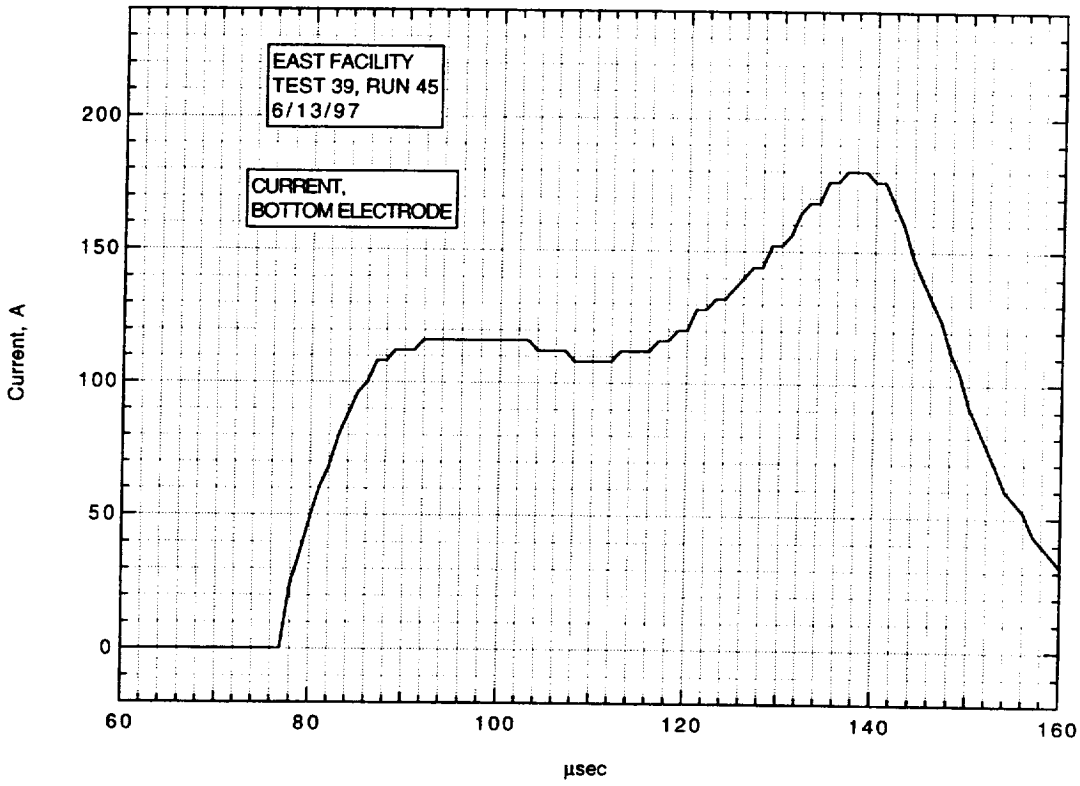

Run 45, current to bottom electrode.

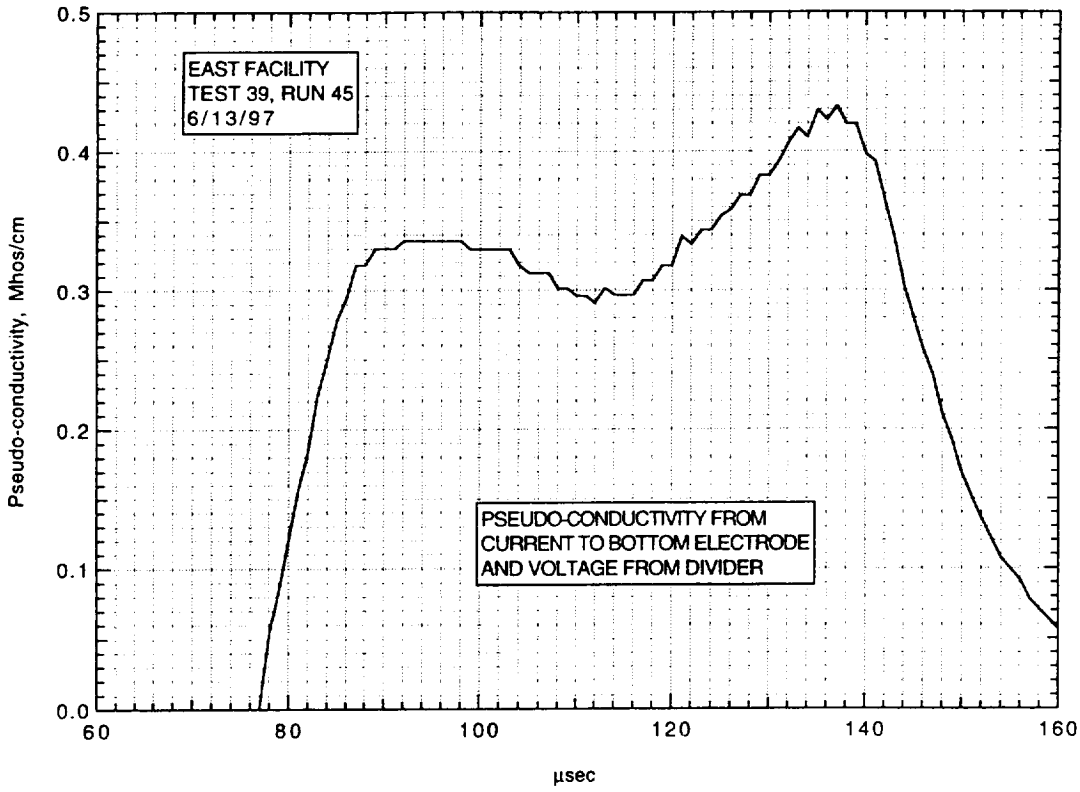

Run 45, pseudo-conductivity from current to bottom electrode and voltage from divider.

AIR CONDUCTIVITY MEASUREMENT IN AMES EAST FACILITY

RUN 39/46, 6/16/97

1. Driven tube conditions:

52.925% N_2O, 46.575% N_2, 0.5%H_2
Total pressure - 35.35 Torr
Measured shock velocity between stns D and F - 4.087 km/sec
Estimated shock velocity at electrodes, from Δt(DF) - 3.933 km/sec
Estimated shock velocity at electrodes, from Δt(DE) - 3.995 km/sec; (This Δt from pressure transducer at D until start of current flow at electrodes.)
Measured shock pressure at stn D - 13.39 atm
Measured shock pressure at stn F - 7.30 atm - very uncertain due to large EM noise pickup.

2. Electrodes, driven tube dimensions:

Electrode size - 3.10 cm square
Electrode spacing - 3.10 cm
Main diaphragm to electrodes - 454.475 cm
Skimmer nose to electrodes - 39.979 cm
Driven tube diameter - 10.16 cm
Stn D (dn tube) to electrodes (channel) - 77.365 cm
Electrodes (channel) to stn F (channel) - 20.32 cm

3. Nominal test conditions:

Pressure - 13 atm
Voltage across electrodes - 312/215 V

4. Breakdown:

Little or no indication of breakdown.

Run no: 46 **Date:** 6/16/97 **Shock press. at D:** 13.39 atm
Shock vel. at E: 3.96 km/sec **Voltage at start of current flow:** 312 V

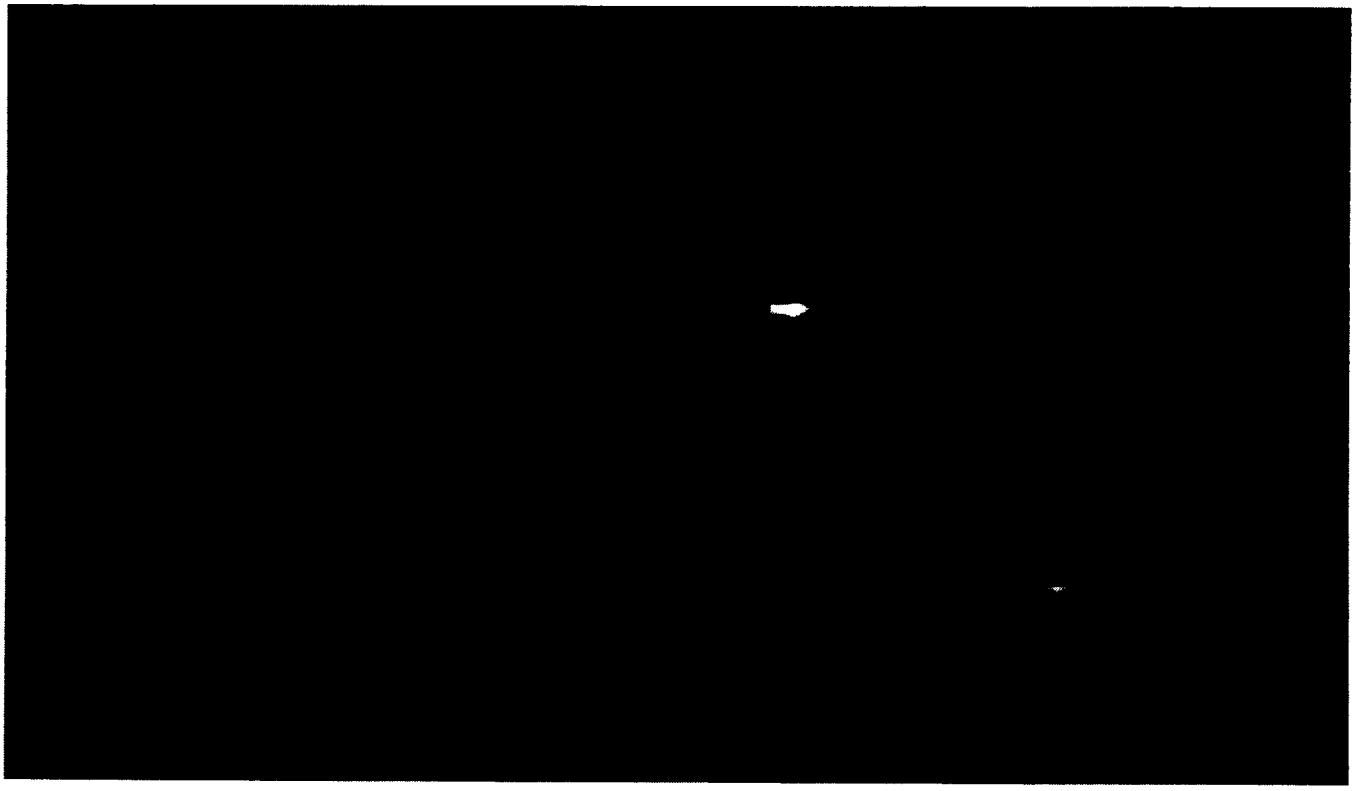

Frame:	**2**	**4**	**6**	**8**
Time:	-22.9	-14.9	-6.9	1.1
Mach no:				
Frame:	**1**	**3**	**5**	**7**
Time:	-26.9	-18.9	-10.9	-2.9
Mach no:				

V_I: km/sec V_{CAV}: 4.24 km/sec

IMACON image of the shock-heated test gas flow in the electrode region. The time is measured from the start of the current flow. Mach numbers and velocities are deduced from the image as explained in section A.2.5.3.

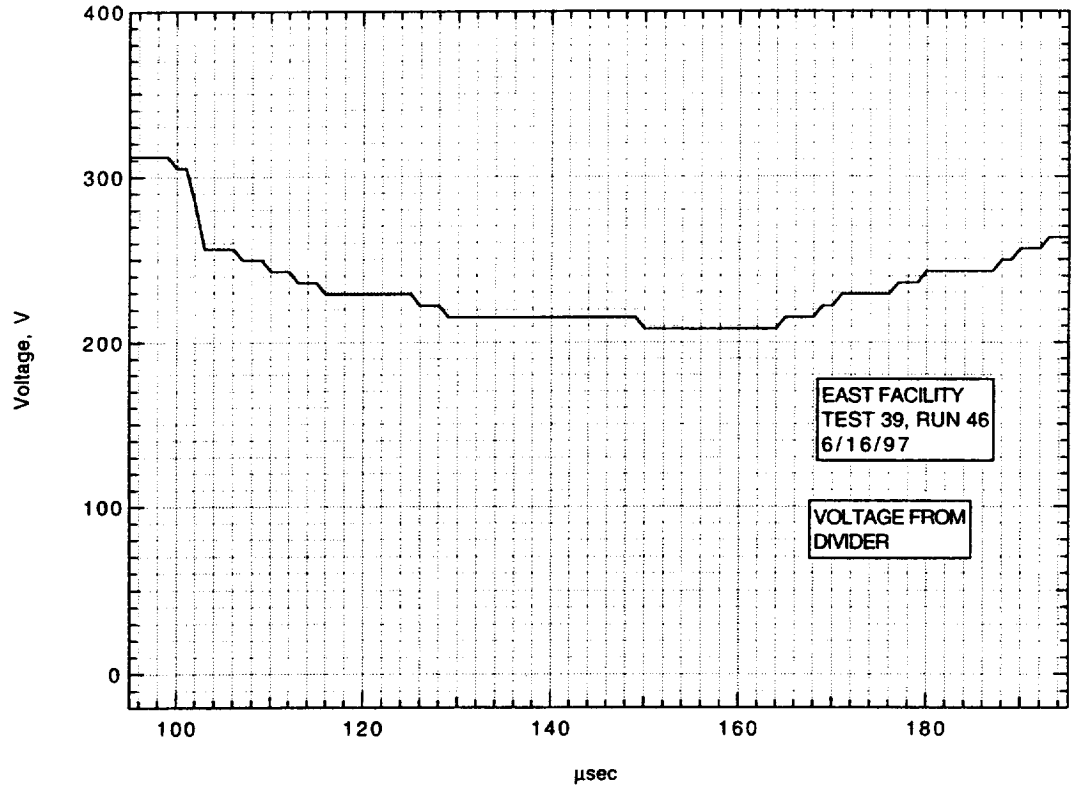

Run 46, voltage across electrodes from divider.

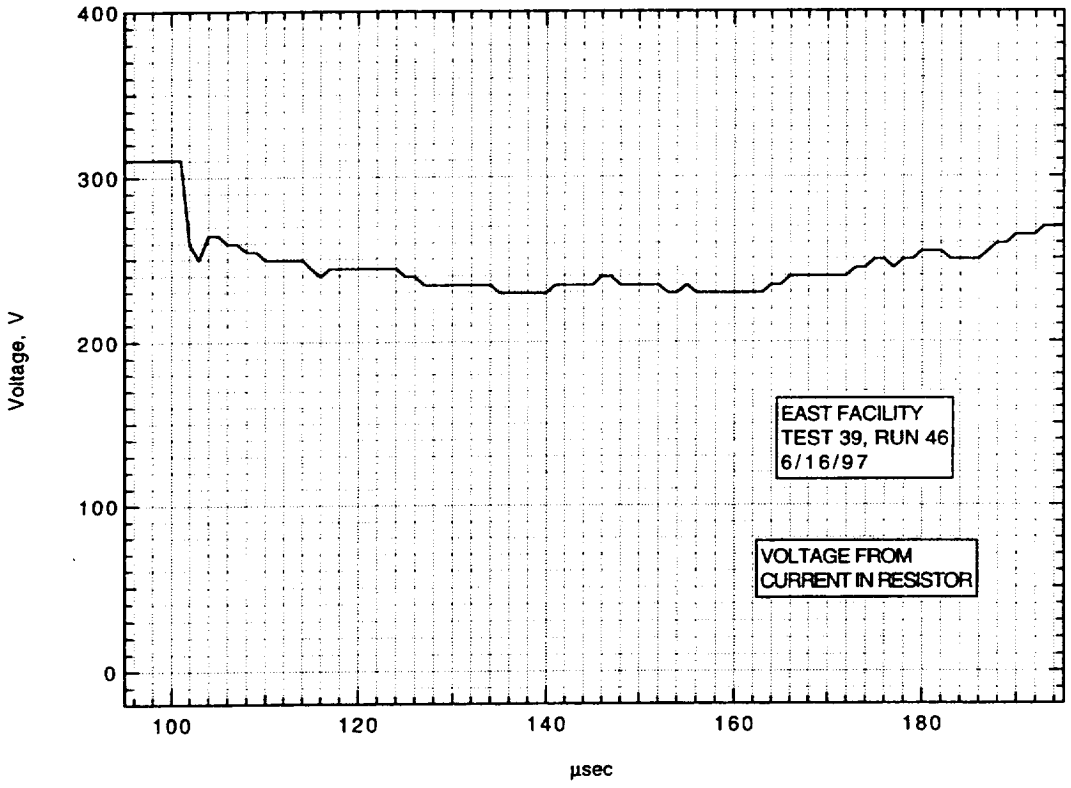

Run 46, voltage across electrodes from current in resistor.

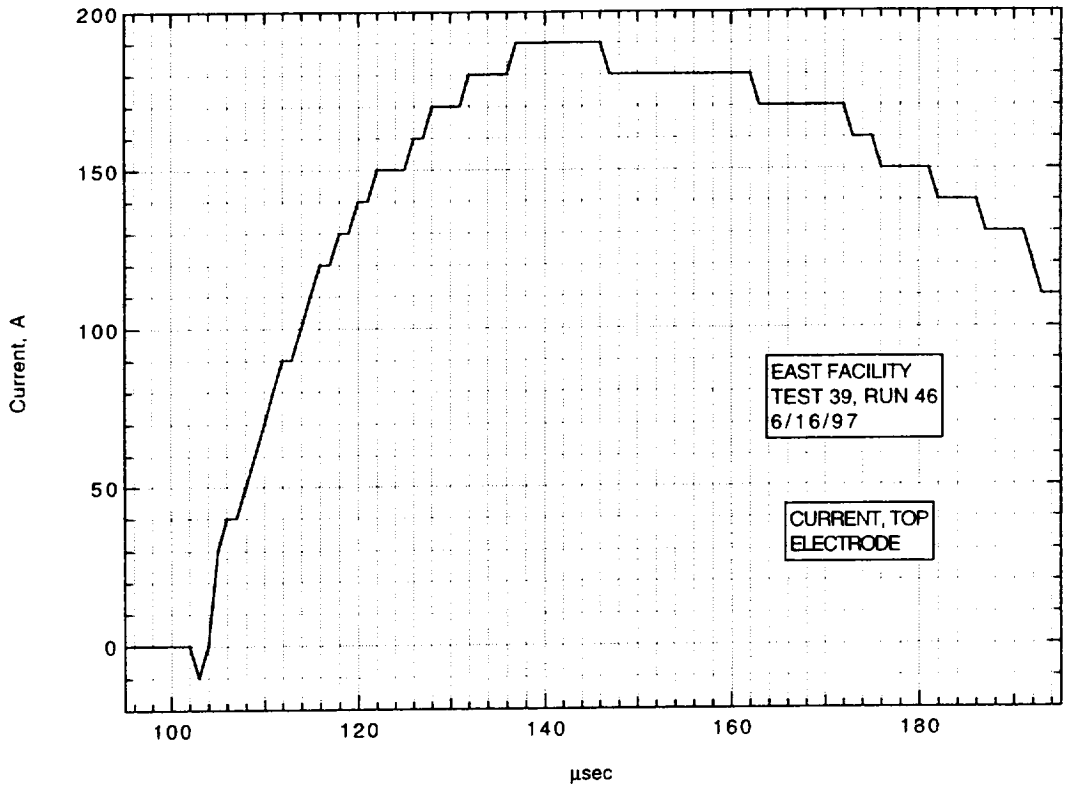

Run 46, current to top electrode.

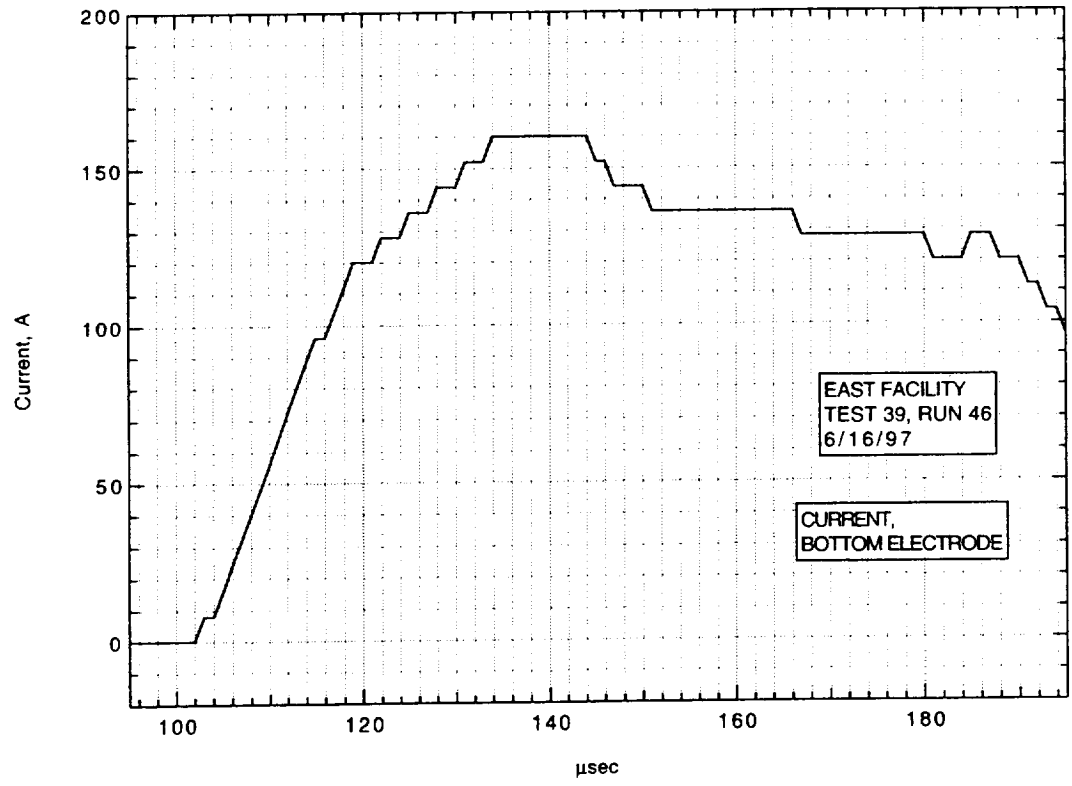

Run 46, current to bottom electrode.

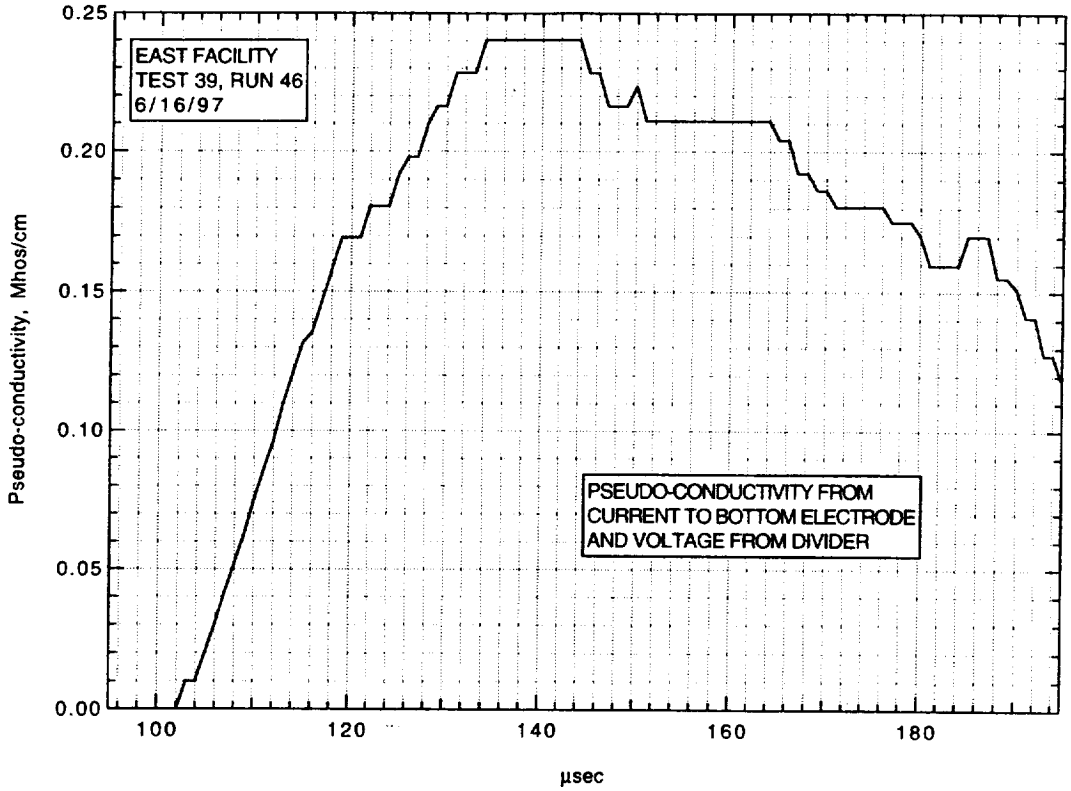

Run 46, pseudo-conductivity from current to bottom electrode and voltage from divider.

AIR CONDUCTIVITY MEASUREMENT IN AMES EAST FACILITY

RUN 39/47, 6/17/97

1. Driven tube conditions:

52.925% N_2O, 46.575% N_2, 0.5%H_2
Total pressure - 35.35 Torr
Measured shock velocity between stns D and F - 5.061 km/sec
Estimated shock velocity at electrodes, from $\Delta t(DF)$ - 4.870 km/sec
Estimated shock velocity at electrodes, from $\Delta t(DE)$ - 4.913 km/sec;
(This Δt from pressure transducer at D until start of current flow at electrodes.)
Measured shock pressure at stn D - 20.65 atm
Measured shock pressure at stn F - 20.71 atm - extremely uncertain due to large EM noise pickup.

2. Electrodes, driven tube dimensions:

Electrode size - 3.10 cm square
Electrode spacing - 3.10 cm
Main diaphragm to electrodes - 454.475 cm
Skimmer nose to electrodes - 39.979 cm
Driven tube diameter - 10.16 cm
Stn D (dn tube) to electrodes (channel) - 77.365 cm
Electrodes (channel) to stn F (channel) - 20.32 cm

3. Nominal test conditions:

Pressure - 13 atm
Voltage across electrodes - 326/229 V

4. Breakdown:

Little or no indication of breakdown.

Run no: 47 **Date:** 6/17/97 **Shock press. at D:** 20.65 atm
Shock vel. at E: 4.89 km/sec **Voltage at start of current flow:** 325 V

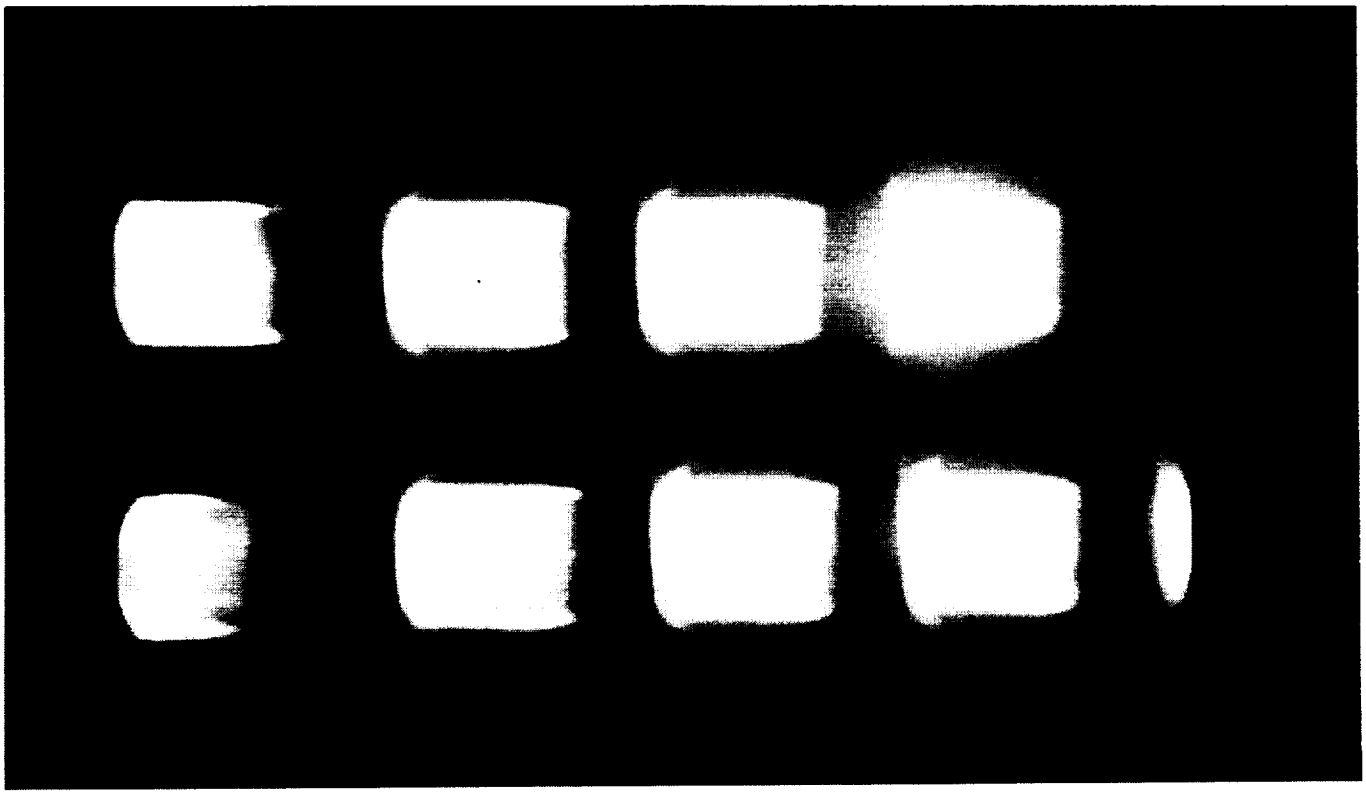

Frame:	**2**	**4**	**6**	**8**
Time:	8.5	16.5	24.5	32.5
Mach no:				
Frame:	**1**	**3**	**5**	**7**
Time:	4.5	12.5	20.5	28.5
Mach no:				

V_I: km/sec V_{CAV}: 5.08 km/sec

IMACON image of the shock-heated test gas flow in the electrode region. The time is measured from the start of the current flow. Mach numbers and velocities are deduced from the image as explained in section A.2.5.3.

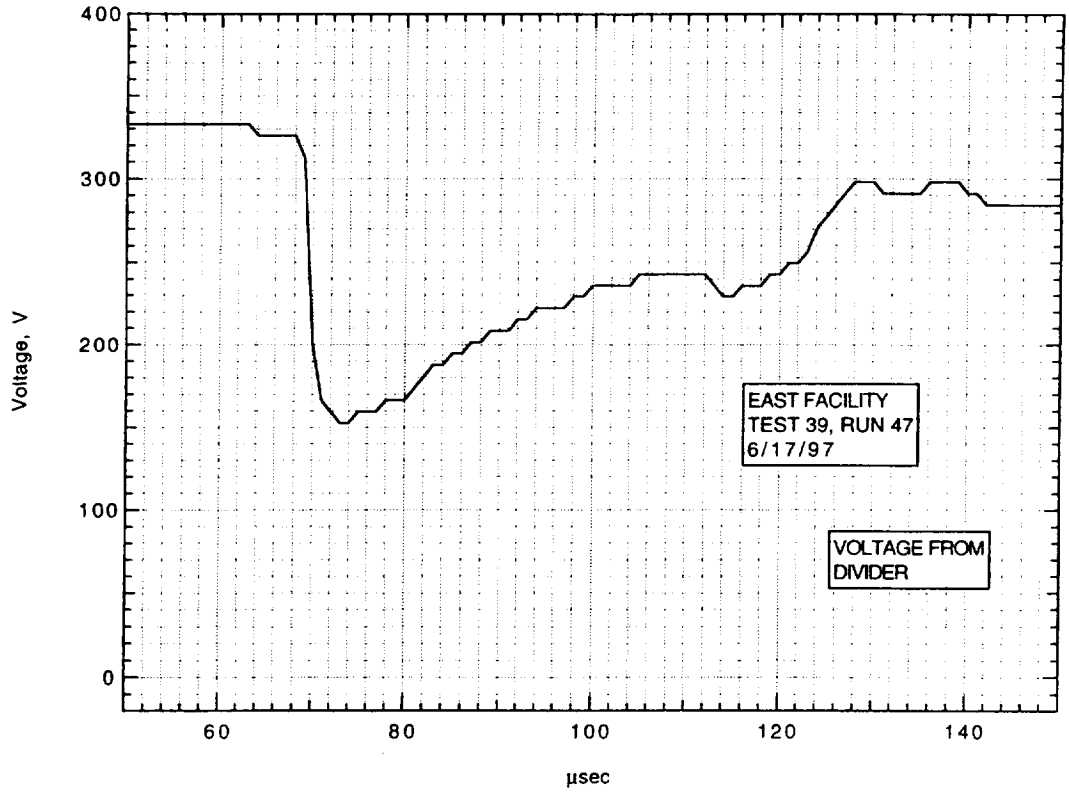

Run 47, voltage across electrodes from divider.

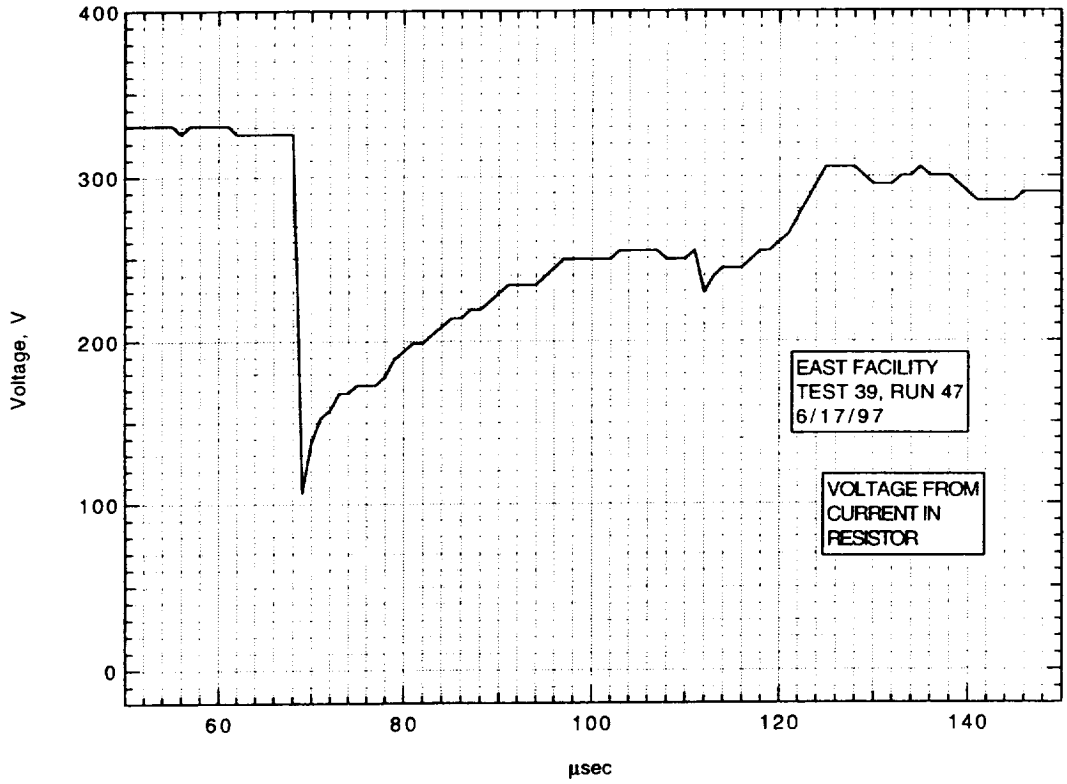

Run 47, voltage across electrodes from current in resistor.

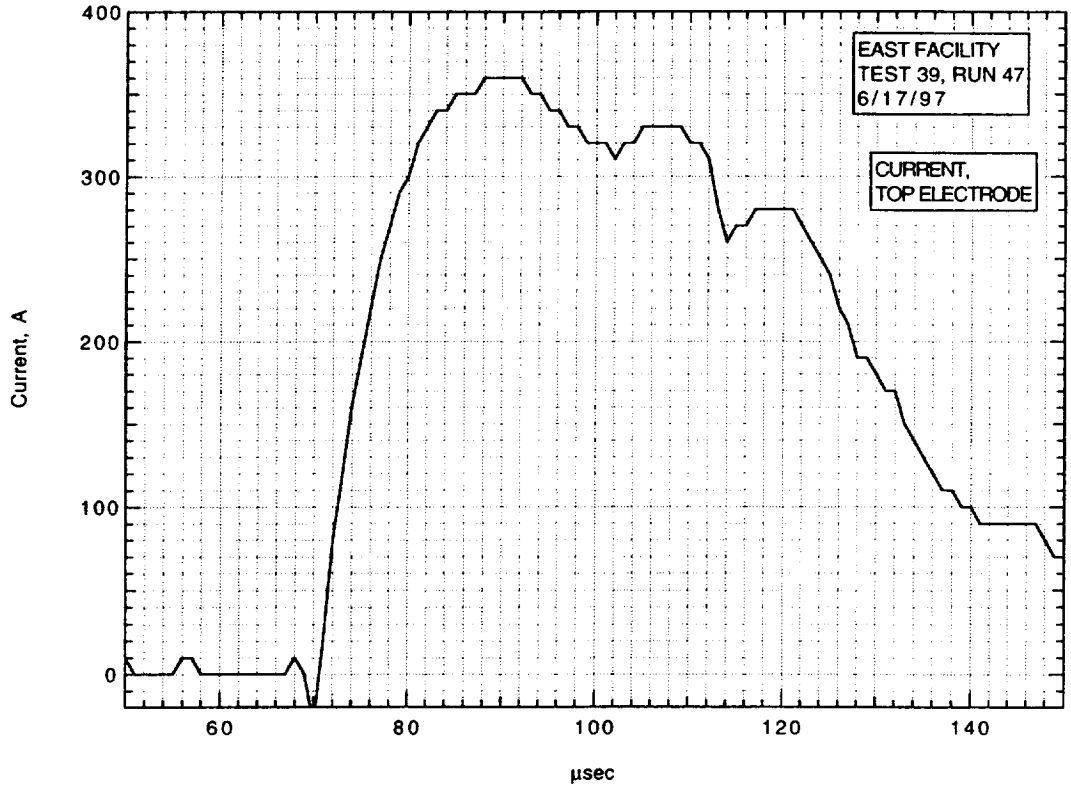

Run 47, current to top electrode.

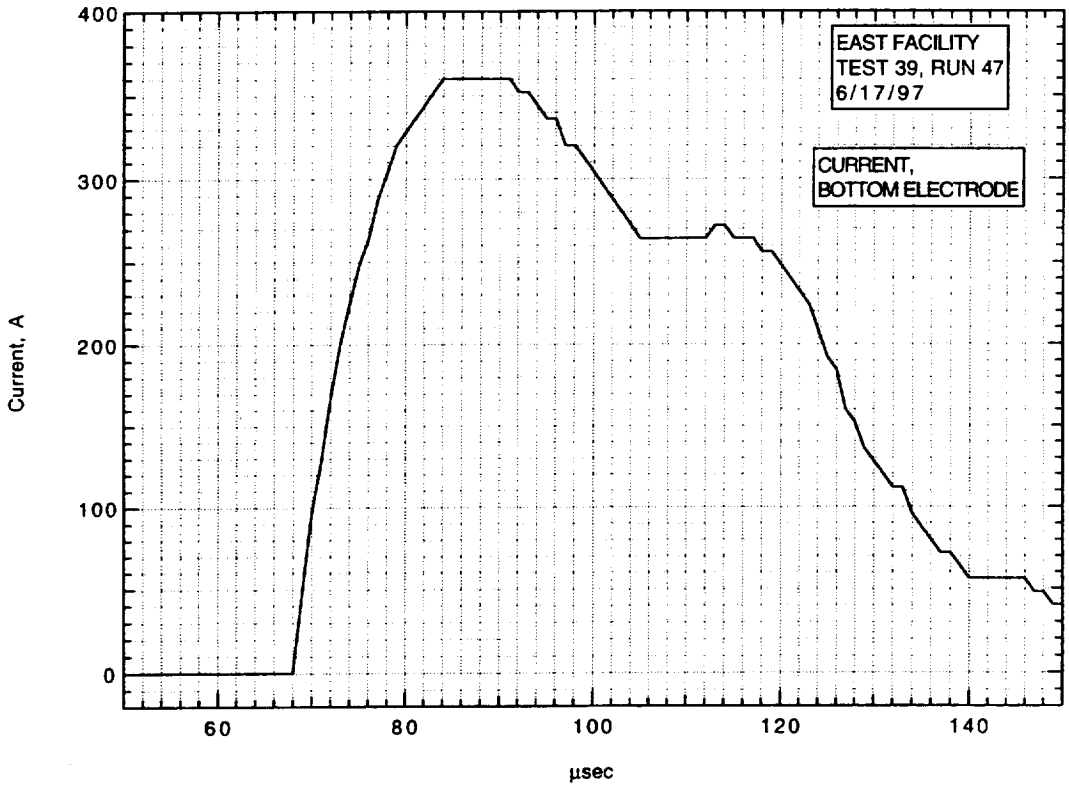

Run 47, current to bottom electrode.

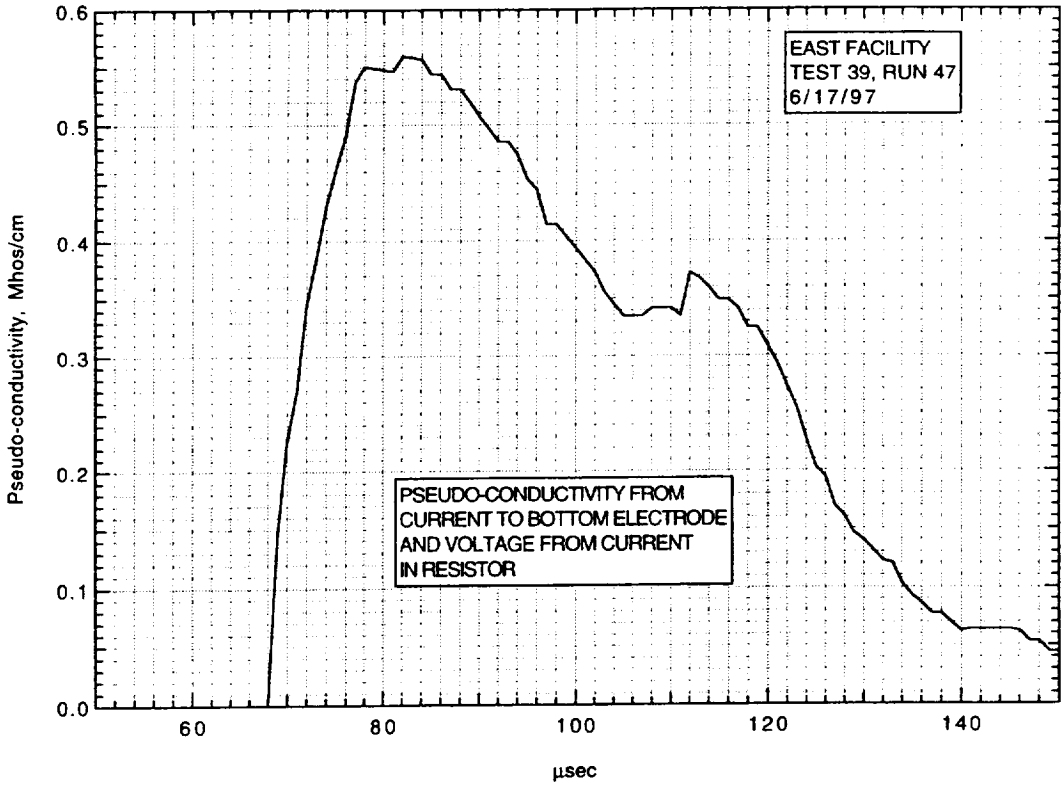

Run 47, pseudo-conductivity from current to bottom electrode and voltage from divider.

AIR CONDUCTIVITY MEASUREMENT IN AMES EAST FACILITY

RUN 39/48, 6/18/97

1. Driven tube conditions:

52.925% N_2O, 46.575% N_2, 0.5%H_2
Total pressure - 35.35 Torr
Measured shock velocity between stns D and F - 4.983 km/sec
Estimated shock velocity at electrodes, from Δt(DF) - 4.795 km/sec
Estimated shock velocity at electrodes, from Δt(DE) - 4.750 km/sec;
(This Δt from pressure transducer at D until start of current flow at electrodes.)
Measured shock pressure at stn D - 18.45 atm
Measured shock pressure at stn F - not available due to large EM noise pickup.

2. Electrodes, driven tube dimensions:

Electrode size - 3.10 cm square
Electrode spacing - 3.10 cm
Main diaphragm to electrodes - 454.475 cm
Skimmer nose to electrodes - 39.979 cm
Driven tube diameter - 10.16 cm
Stn D (dn tube) to electrodes (channel) - 77.365 cm
Electrodes (channel) to stn F (channel) - 20.32 cm

3. Nominal test conditions:

Pressure - 13 atm
Voltage across electrodes - 572/394 V

4. Breakdown:

Little or no indication of breakdown.

Run no: 48 **Date:** 6/18/97 **Shock press. at D:** 18.45 atm
Shock vel. at E: 4.77 km/sec **Voltage at start of current flow:** 572 V

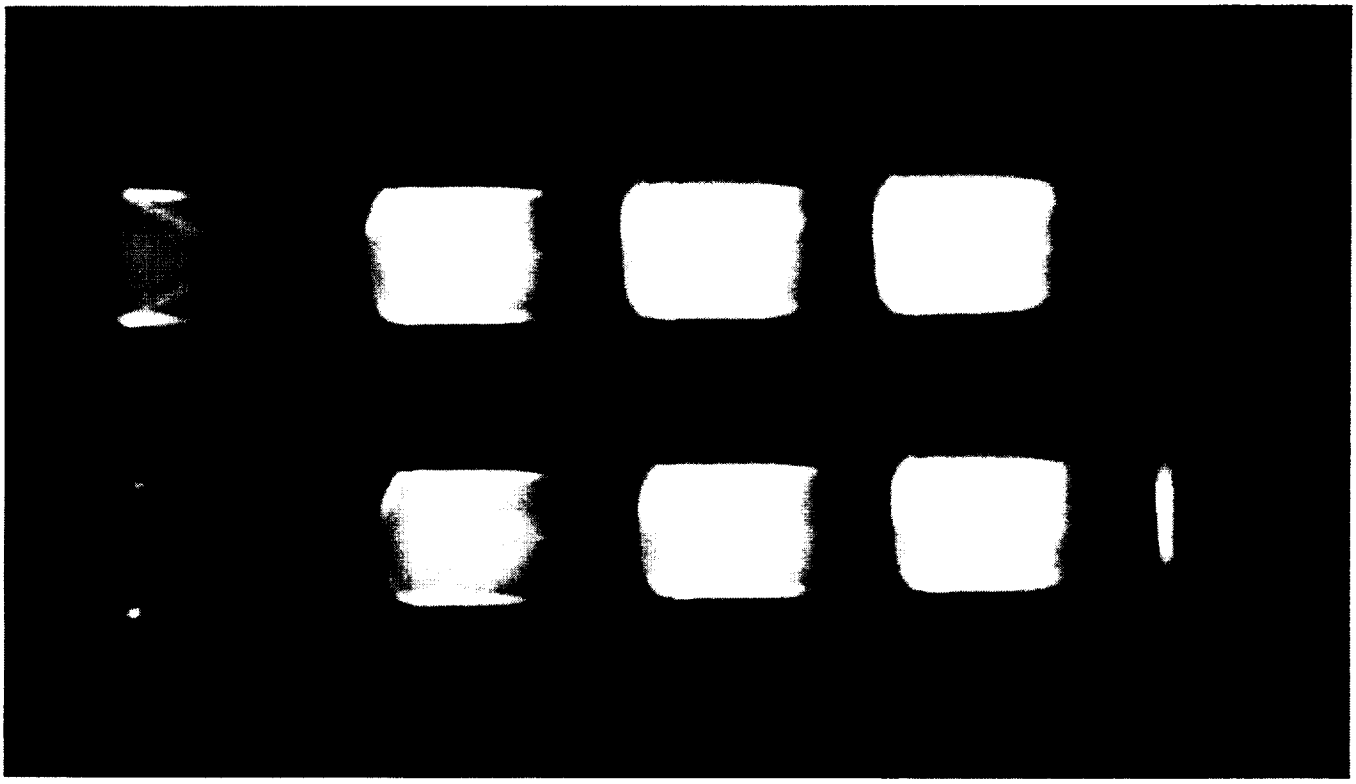

Frame:	**2**	**4**	**6**	**8**
Time:	5.1	13.1	21.1	29.1
Mach no:				
Frame:	**1**	**3**	**5**	**7**
Time:	1.1	9.1	17.1	25.1
Mach no:		2.24		

V_I: 4.2 km/sec V_{CAV}: 4.96 km/sec

IMACON image of the shock-heated test gas flow in the electrode region. The time is measured from the start of the current flow. Mach numbers and velocities are deduced from the image as explained in section A.2.5.3.

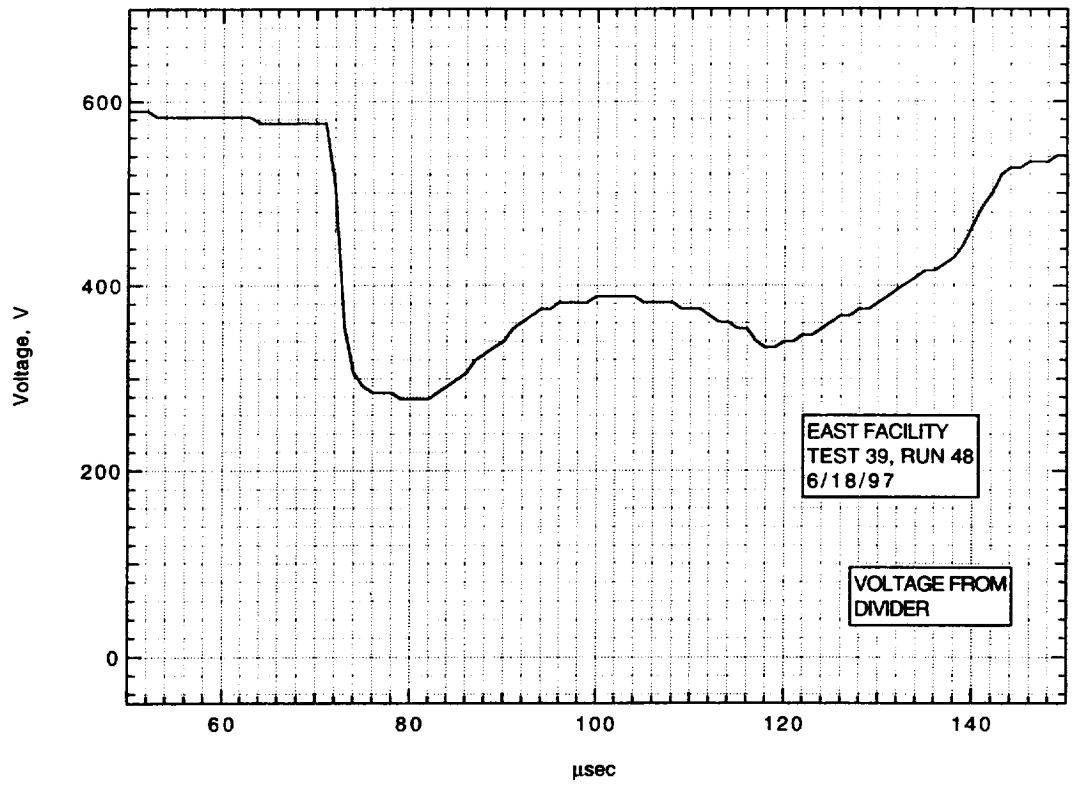

Run 48, voltage across electrodes from divider.

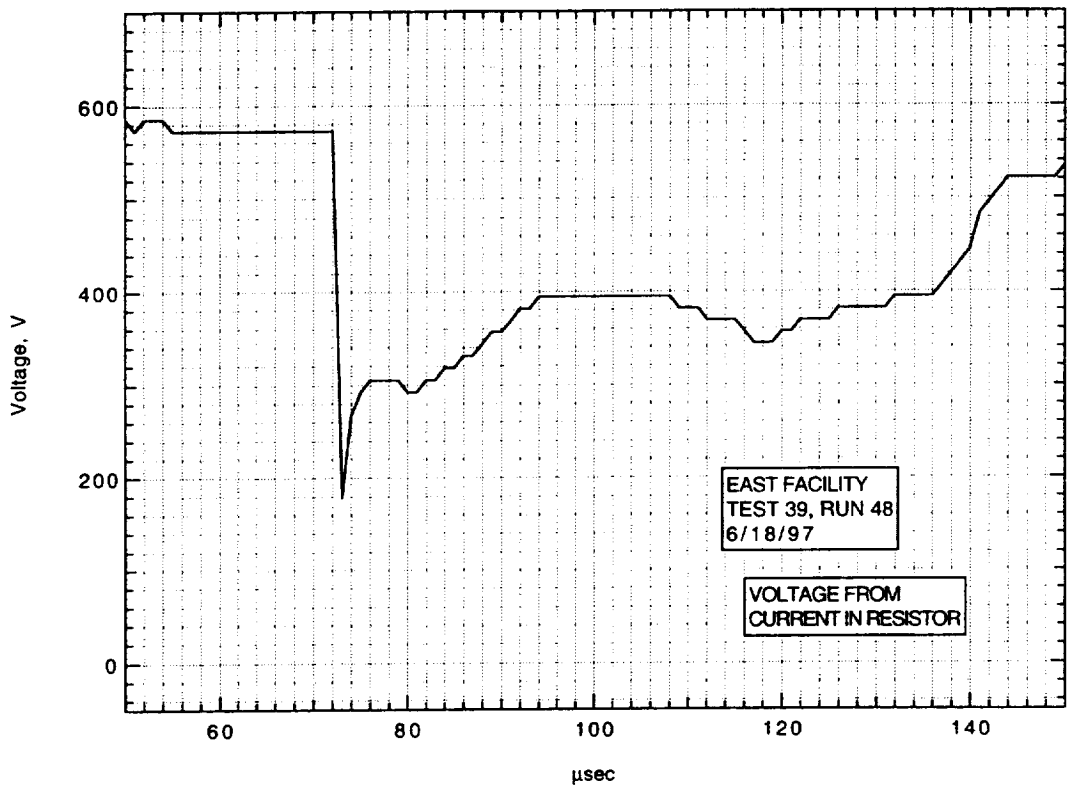

Run 48, voltage across electrodes from current in resistor.

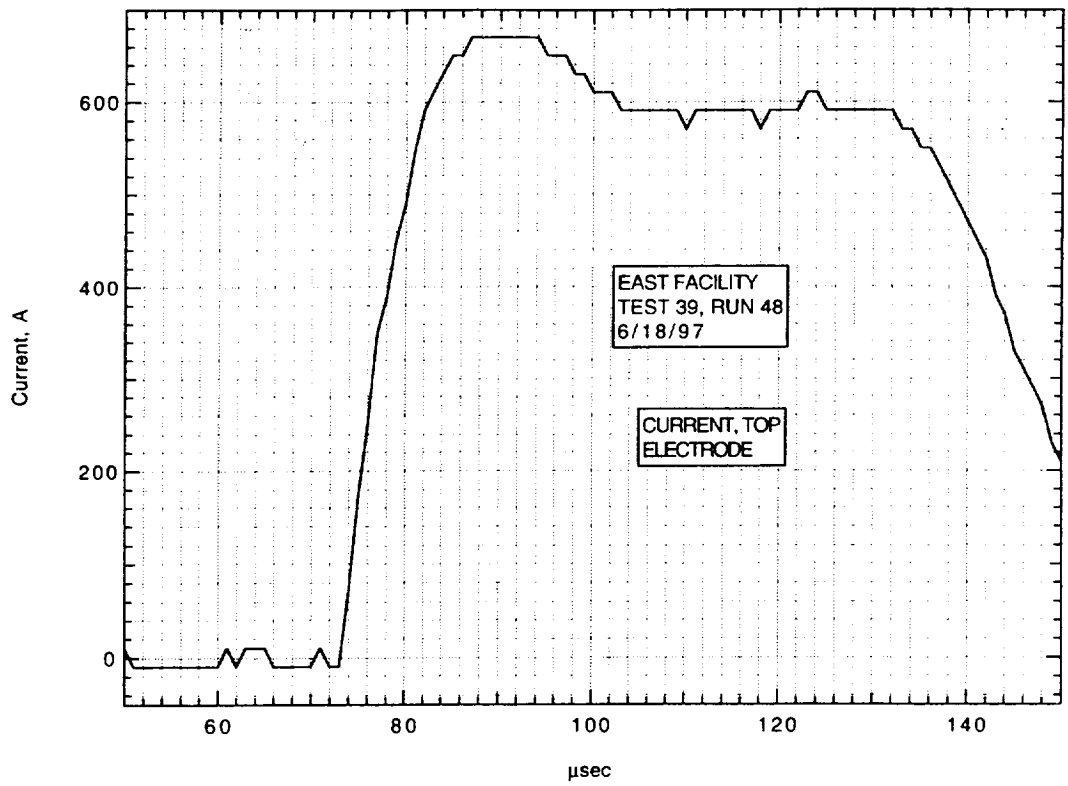

Run 48, current to top electrode.

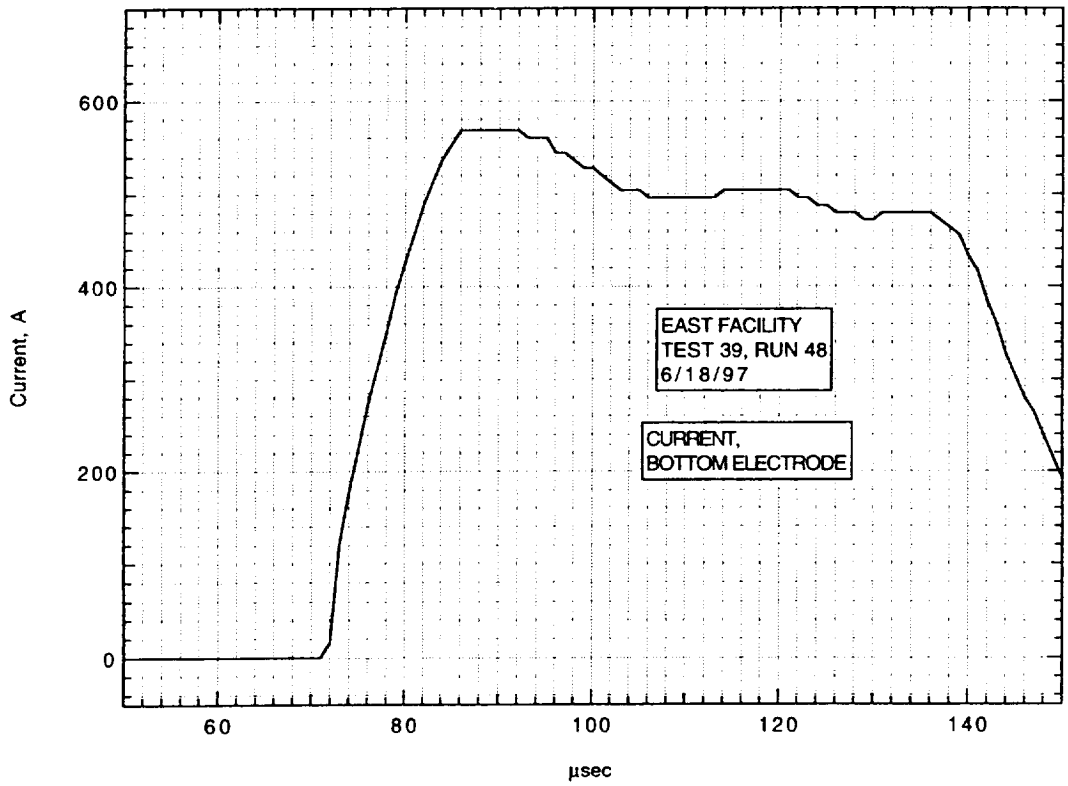

Run 48, current to bottom electrode.

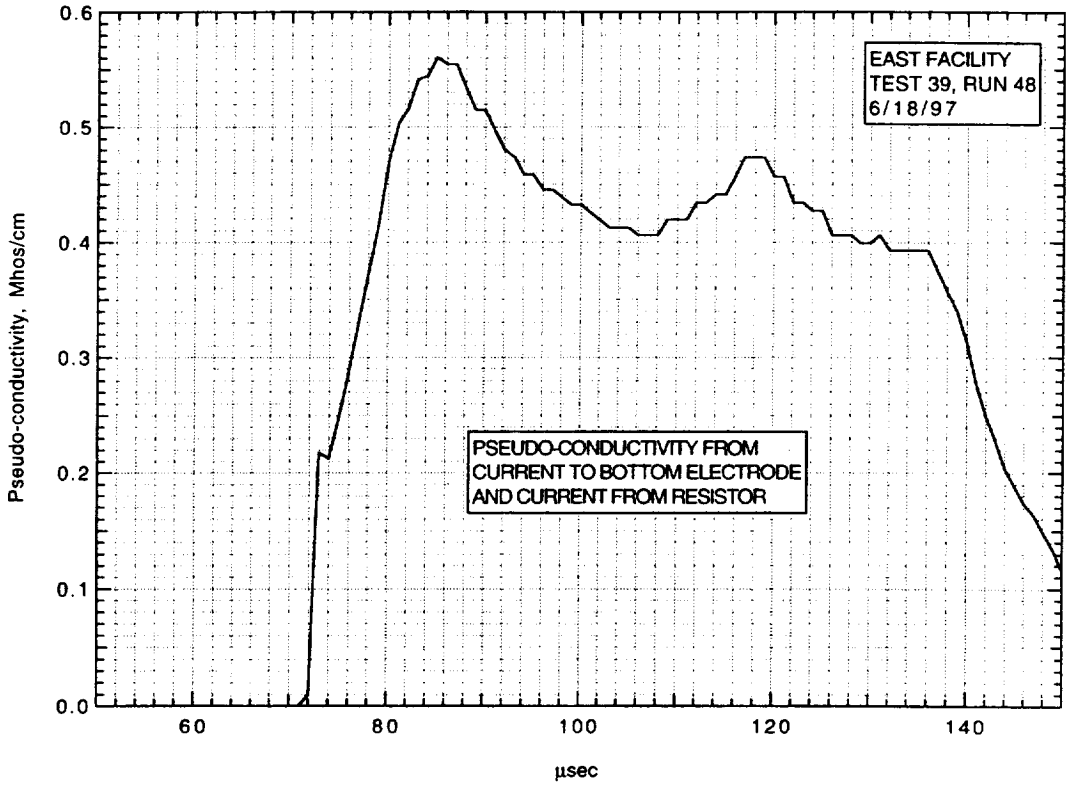

Run 48, pseudo-conductivity from current to bottom electrode and voltage from current in resistor.

AIR CONDUCTIVITY MEASUREMENT IN AMES EAST FACILITY

RUN 39/49, 6/19/97

1. Driven tube conditions:

52.925% N_2O, 46.575% N_2, 0.5%H_2
Total pressure - 35.35 Torr
Measured shock velocity between stns D and F - 4.983 km/sec
Estimated shock velocity at electrodes, from Δt(DF) - 4.795 km/sec
Estimated shock velocity at electrodes, from Δt(DE) - 4.750 km/sec;
(This Δt from pressure transducer at D until start of current flow at electrodes.)
Measured shock pressure at stn D - 14.88 atm
Measured shock pressure at stn F - not available due to large EM noise pickup.

2. Electrodes, driven tube dimensions:

Electrode size - 3.10 cm square
Electrode spacing - 3.10 cm
Main diaphragm to electrodes - 454.475 cm
Skimmer nose to electrodes - 39.979 cm
Driven tube diameter - 10.16 cm
Stn D (dn tube) to electrodes (channel) - 77.365 cm
Electrodes (channel) to stn F (channel) - 20.32 cm

3. Nominal test conditions:

Pressure - 13 atm
Voltage across electrodes -1020/382 V

4. Breakdown:

Little or no indication of breakdown.

Run no: 49 **Date:** 6/19/97 **Shock press. at D:** 14.88 atm
Shock vel. at E: 4.54 km/sec **Voltage at start of current flow:** 1020 V

Frame:	**2**	**4**	**6**	**8**
Time:	-0.2	7.8	15.8	23.8
Mach no:				
Frame:	**1**	**3**	**5**	**7**
Time:	-4.2	3.8	11.8	19.8
Mach no:			2.24	

V_I: 4.2 km/sec V_{CAV}: 4.68 km/sec

IMACON image of the shock-heated test gas flow in the electrode region. The time is measured from the start of the current flow. Mach numbers and velocities are deduced from the image as explained in section A.2.5.3.

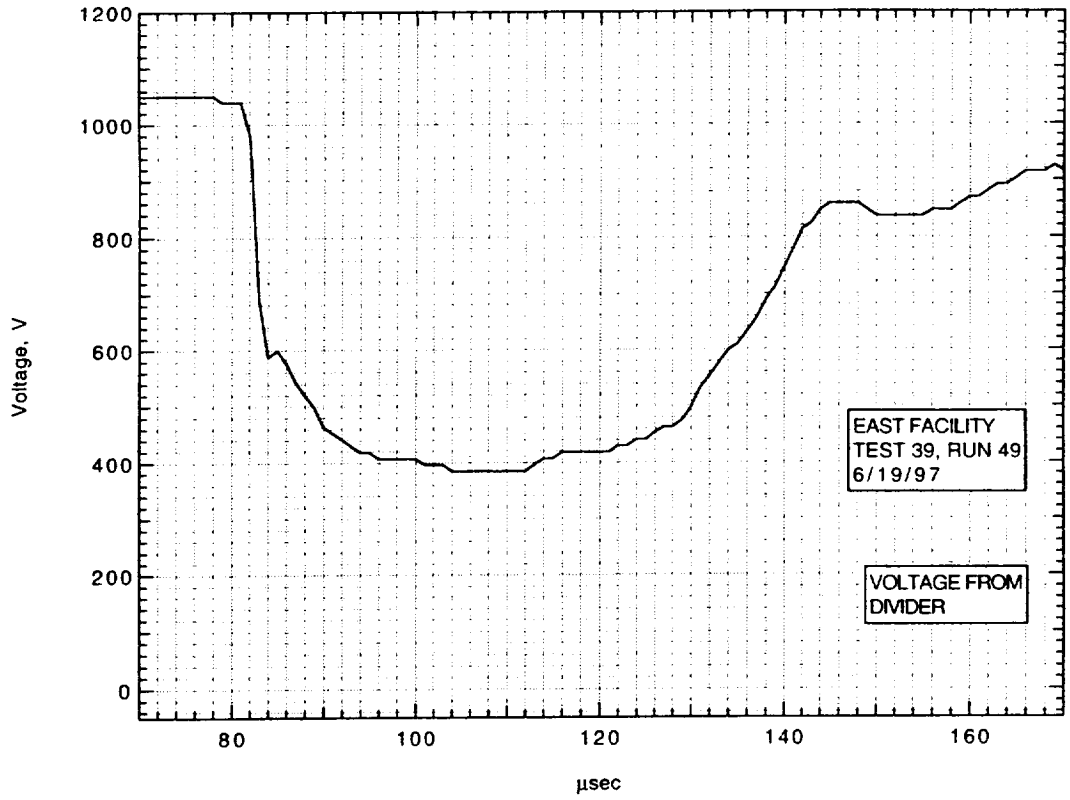

Run 49, voltage across electrodes from divider.

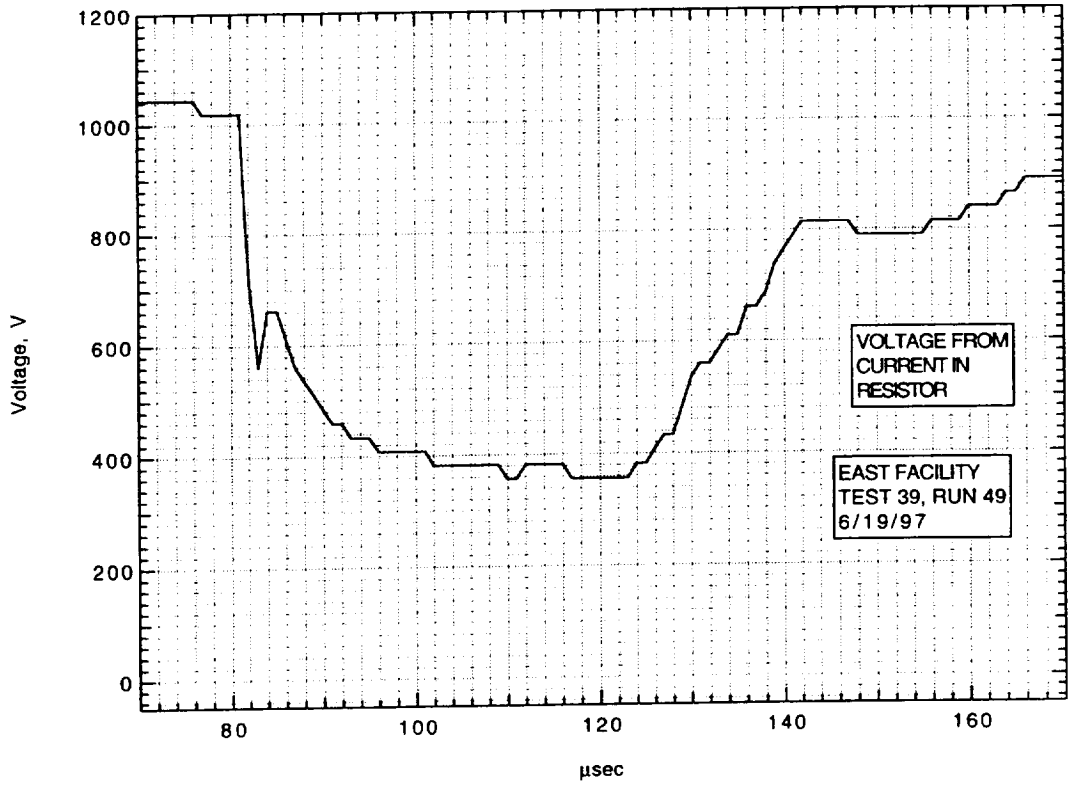

Run 49, voltage across electrodes from current in resistor.

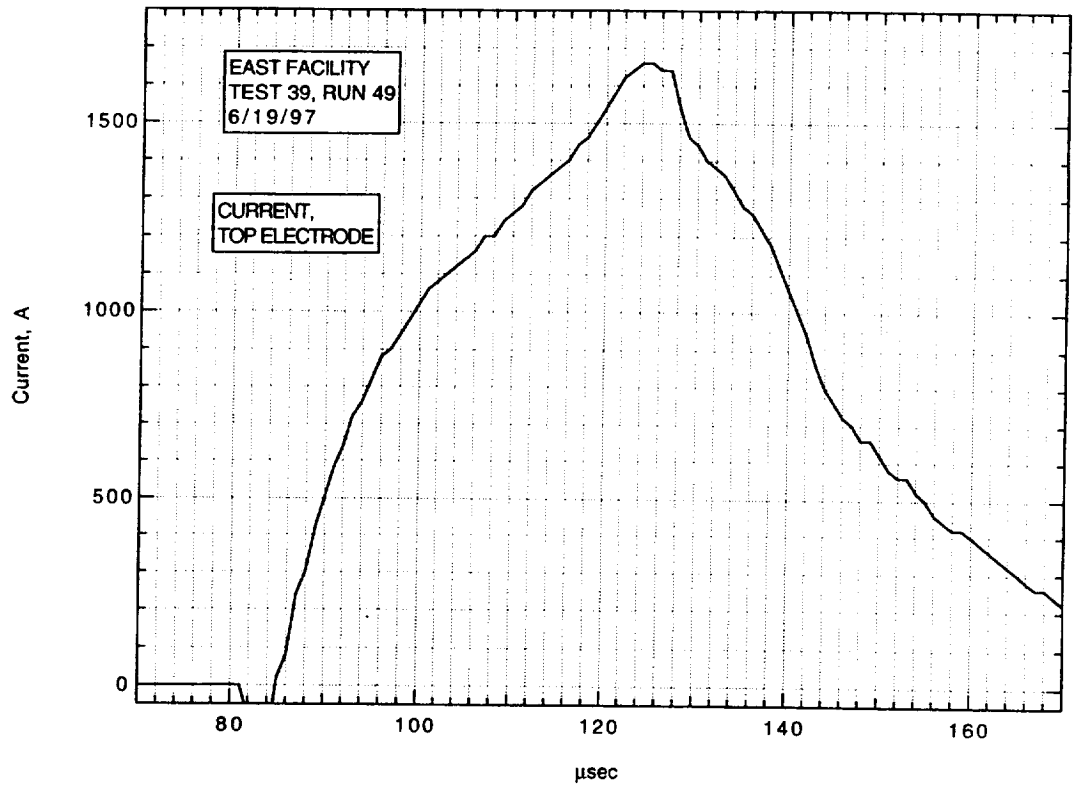

Run 49, current to top electrode.

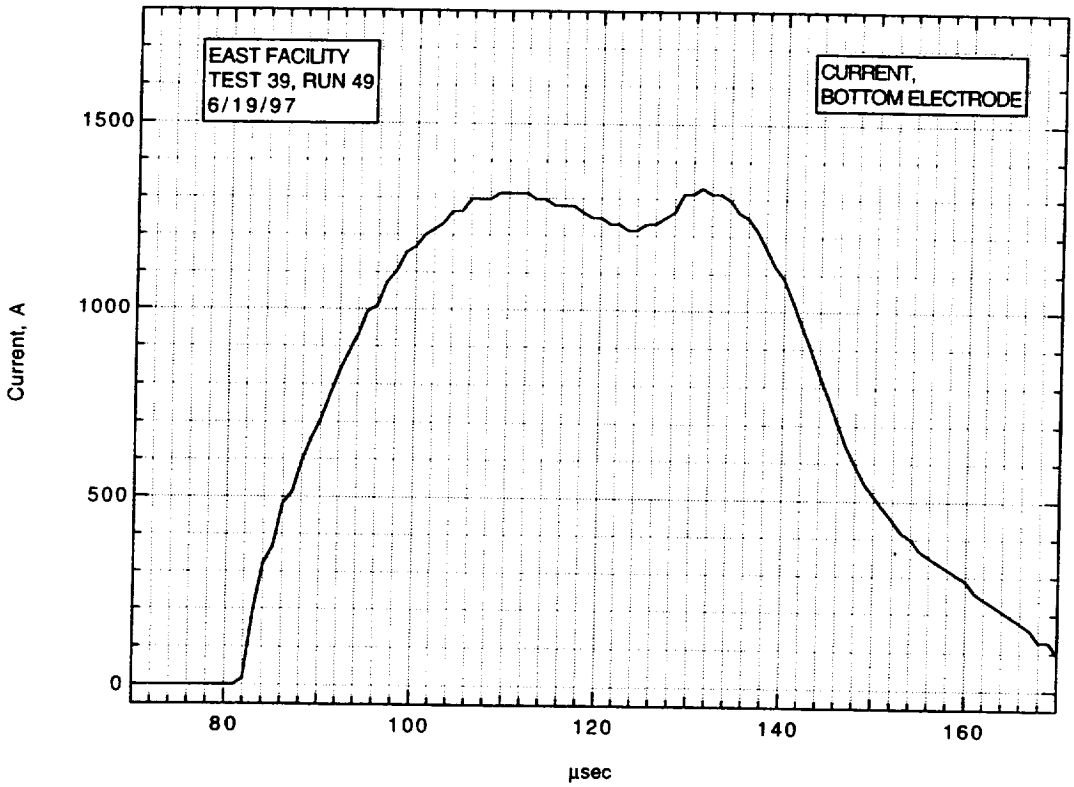

Run 49, current to bottom electrode.

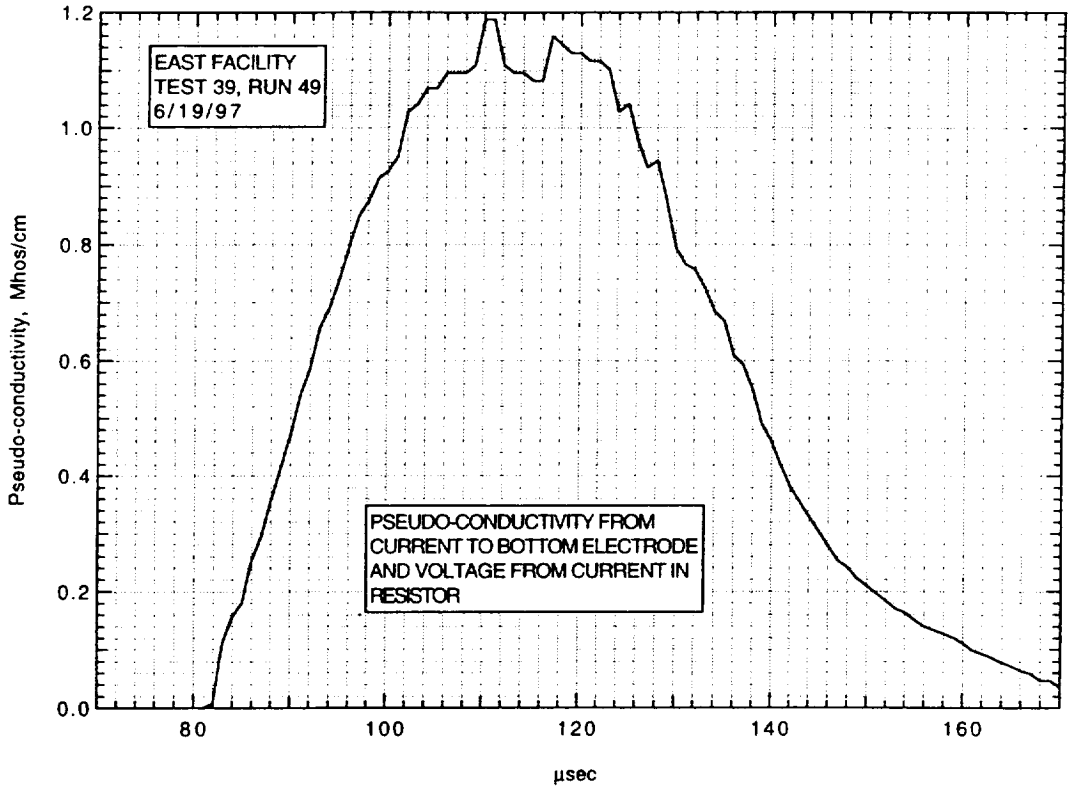

Run 49, pseudo-conductivity from current to bottom electrode and voltage from current in resistor.

AIR CONDUCTIVITY MEASUREMENT IN AMES EAST FACILITY

RUN 39/50, 6/20/97

1. Driven tube conditions:

52.925% N_2O, 46.575% N_2, 0.5%H_2
Total pressure - 35.35 Torr
Measured shock velocity between stns D and F - 5.035 km/sec
Estimated shock velocity at electrodes, from Δt(DF) - 4.845 km/sec
Estimated shock velocity at electrodes, from Δt(DE) - 4.879 km/sec;
(This Δt from pressure transducer at D until start of current flow at electrodes.)
Measured shock pressure at stn D - 19.22 atm
Measured shock pressure at stn F - not available due to large EM noise pickup.

2. Electrodes, driven tube dimensions:

Electrode size - 3.10 cm square
Electrode spacing - 3.10 cm
Main diaphragm to electrodes - 454.475 cm
Skimmer nose to electrodes - 39.979 cm
Driven tube diameter - 10.16 cm
Stn D (dn tube) to electrodes (channel) - 77.365 cm
Electrodes (channel) to stn F (channel) - 20.32 cm

3. Nominal test conditions:

Pressure - 13 atm
Voltage across electrodes - 764/382 V

4. Breakdown:

Little or no indication of breakdown.

Run no: 50 **Date:** 6/20/97 **Shock press. at D:** 19.22 atm
Shock vel. at E: 4.86 km/sec **Voltage at start of current flow:** 764 V

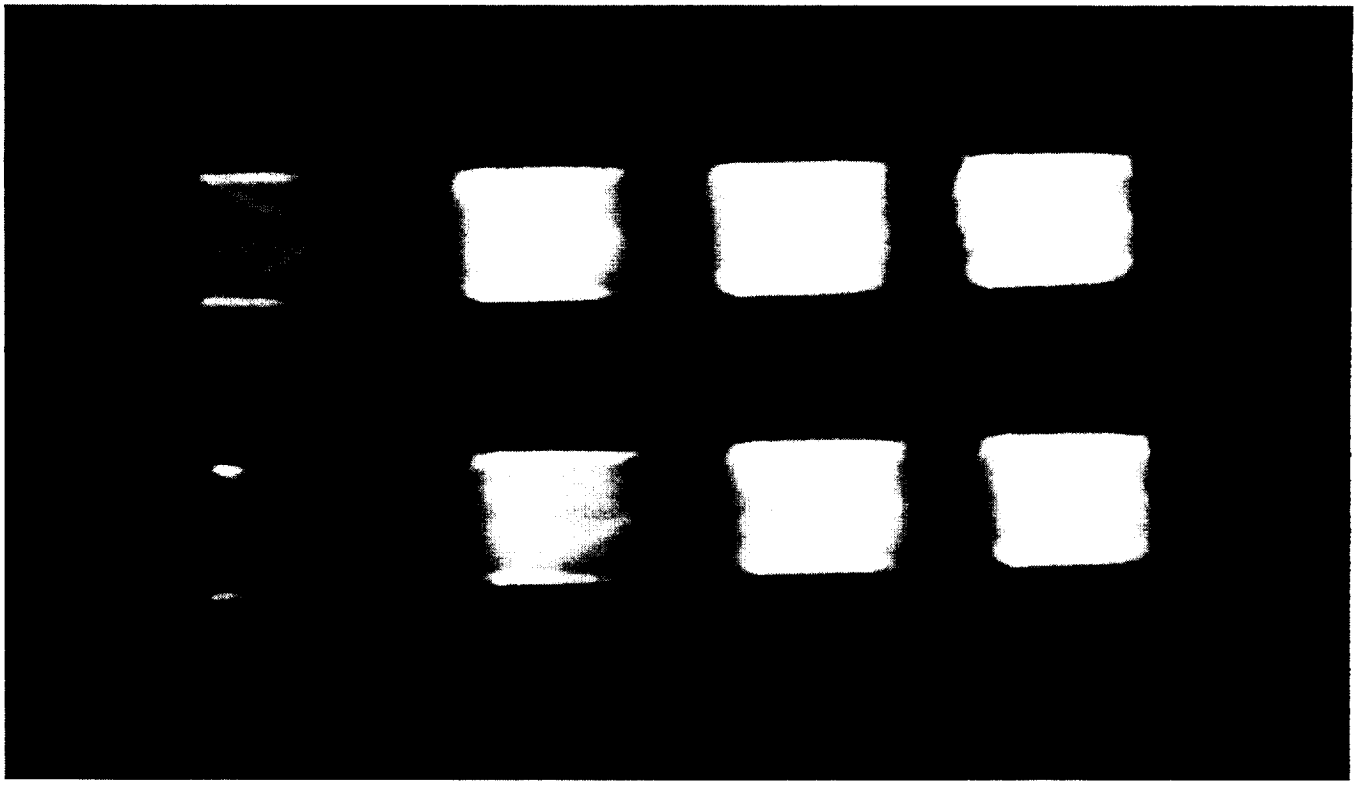

Frame:	**2**	**4**	**6**	**8**
Time:	7.0	15.0	23.0	31.0
Mach no:	2.24			
Frame:	**1**	**3**	**5**	**7**
Time:	3.0	11.0	19.0	27.0
Mach no:		2.40		

V_I: km/sec V_{CAV}: 5.05 km/sec

IMACON image of the shock-heated test gas flow in the electrode region. The time is measured from the start of the current flow. Mach numbers and velocities are deduced from the image as explained in section A.2.5.3.

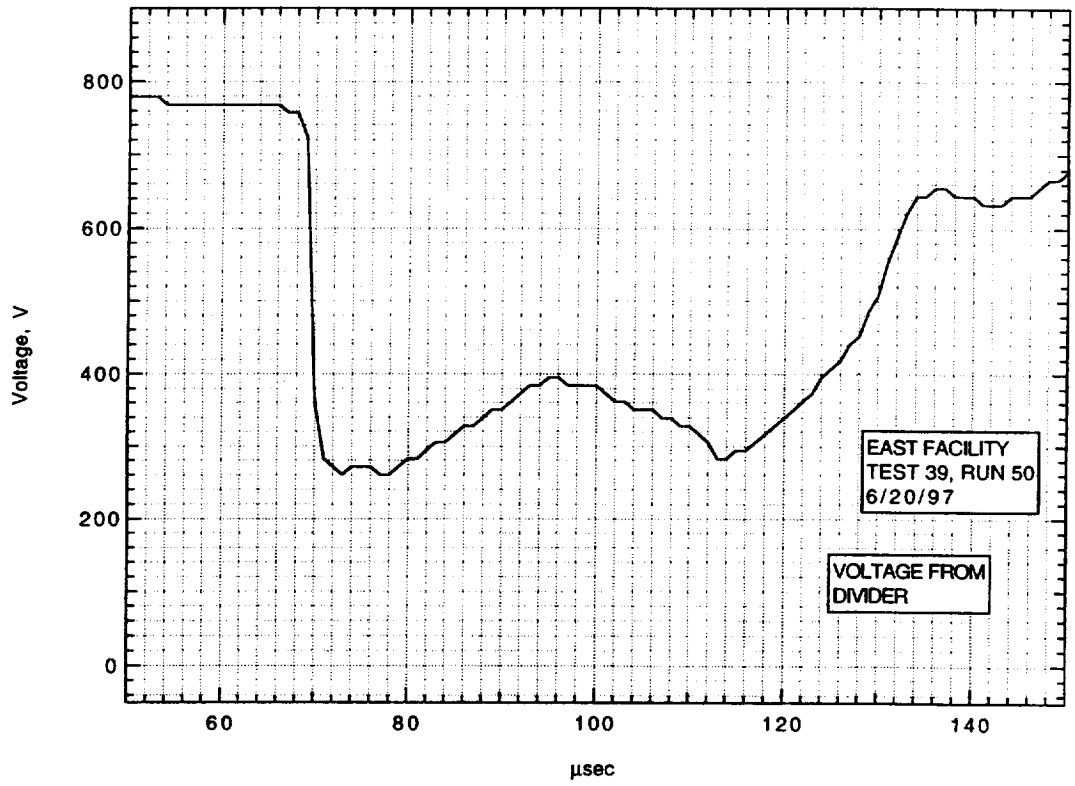

Run 50, voltage across electrodes from divider.

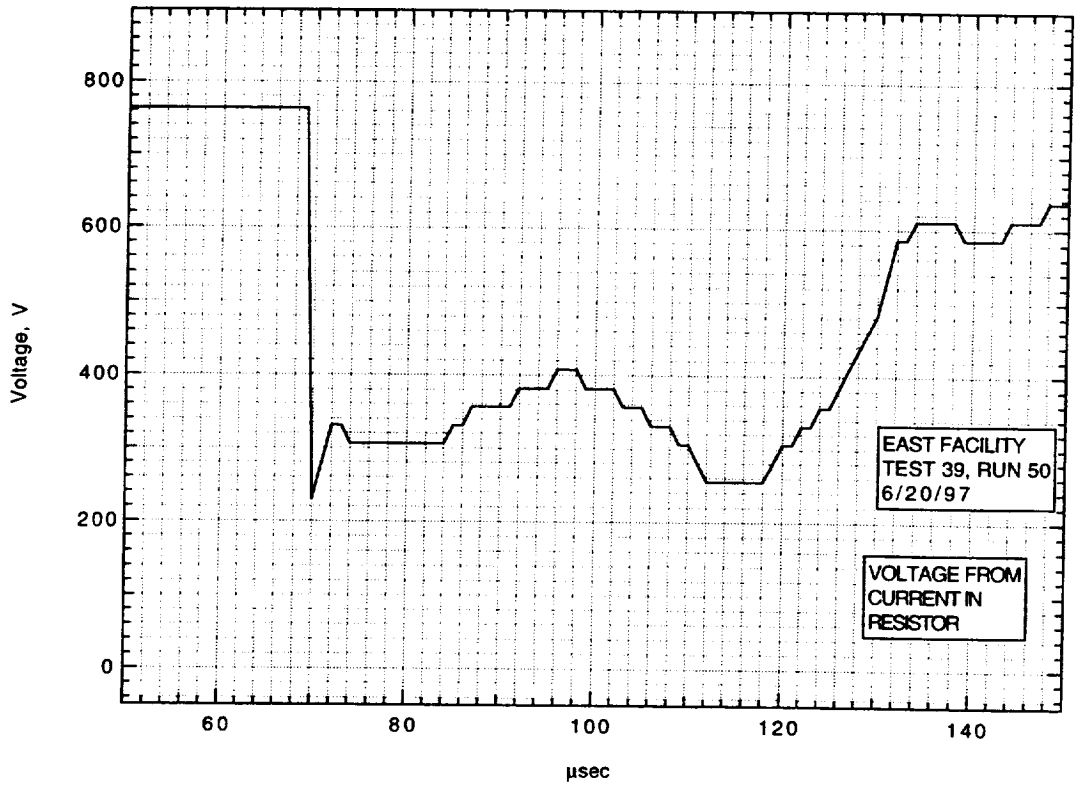

Run 50, voltage across electrodes from current in resistor.

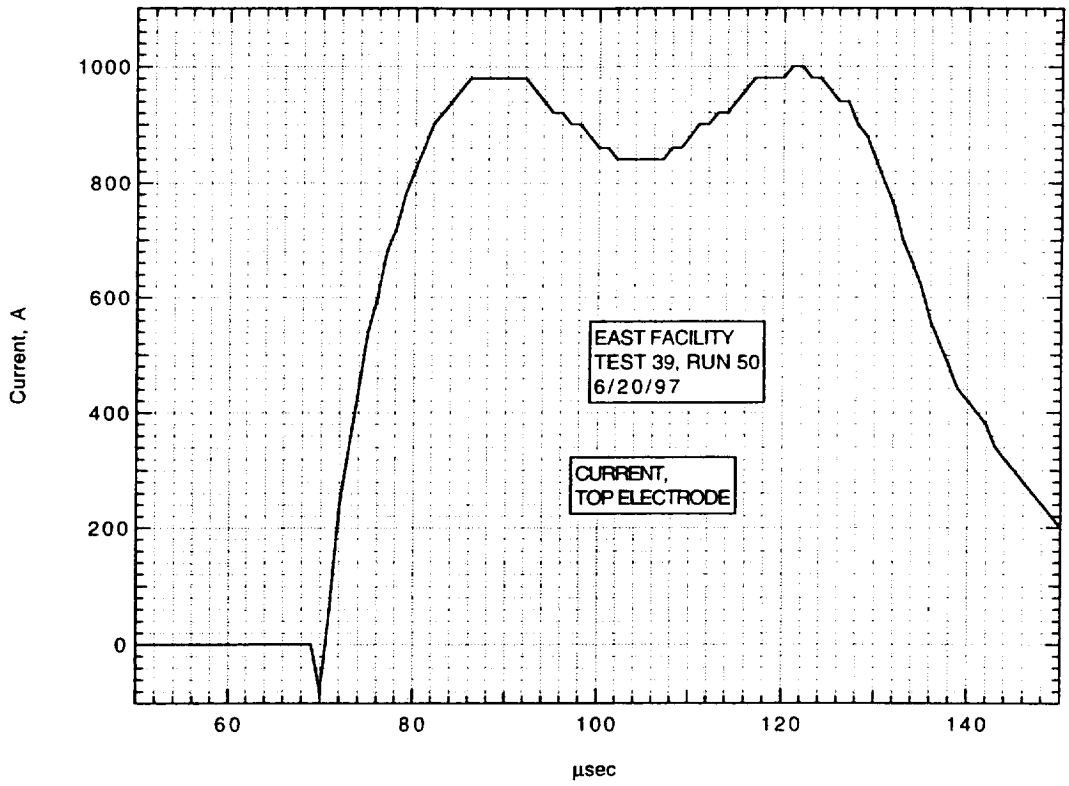

Run 50, current to top electrode.

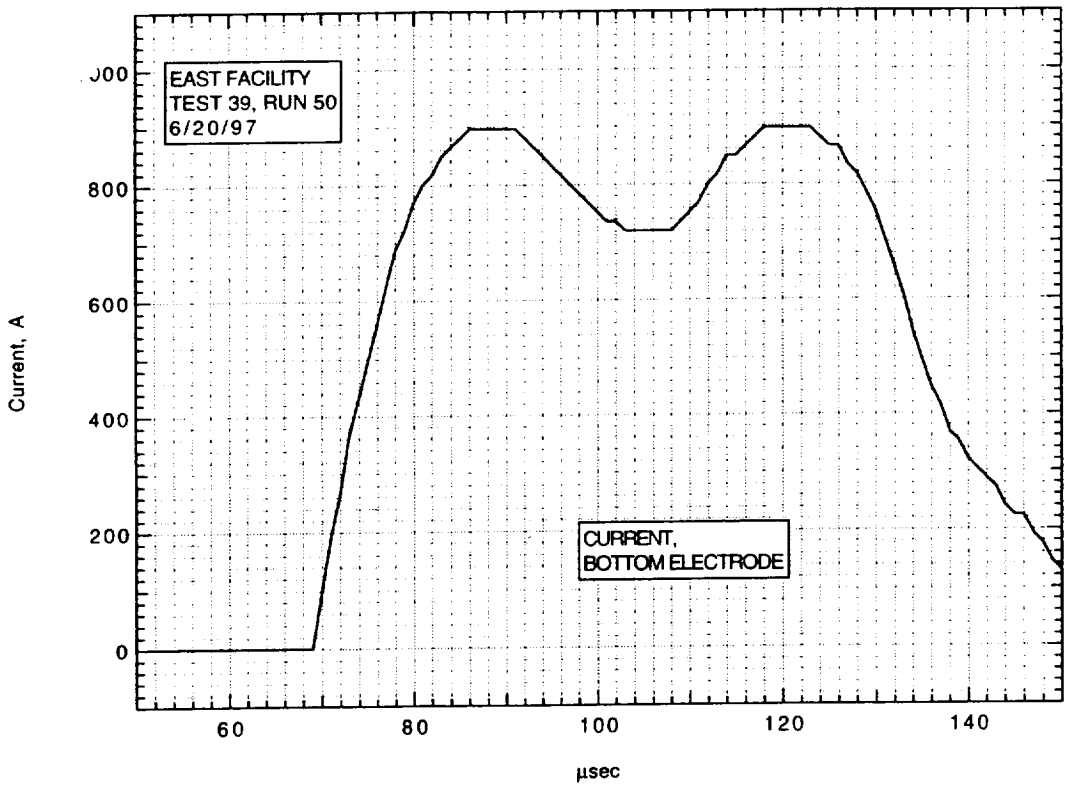

Run 50, current to bottom electrode.

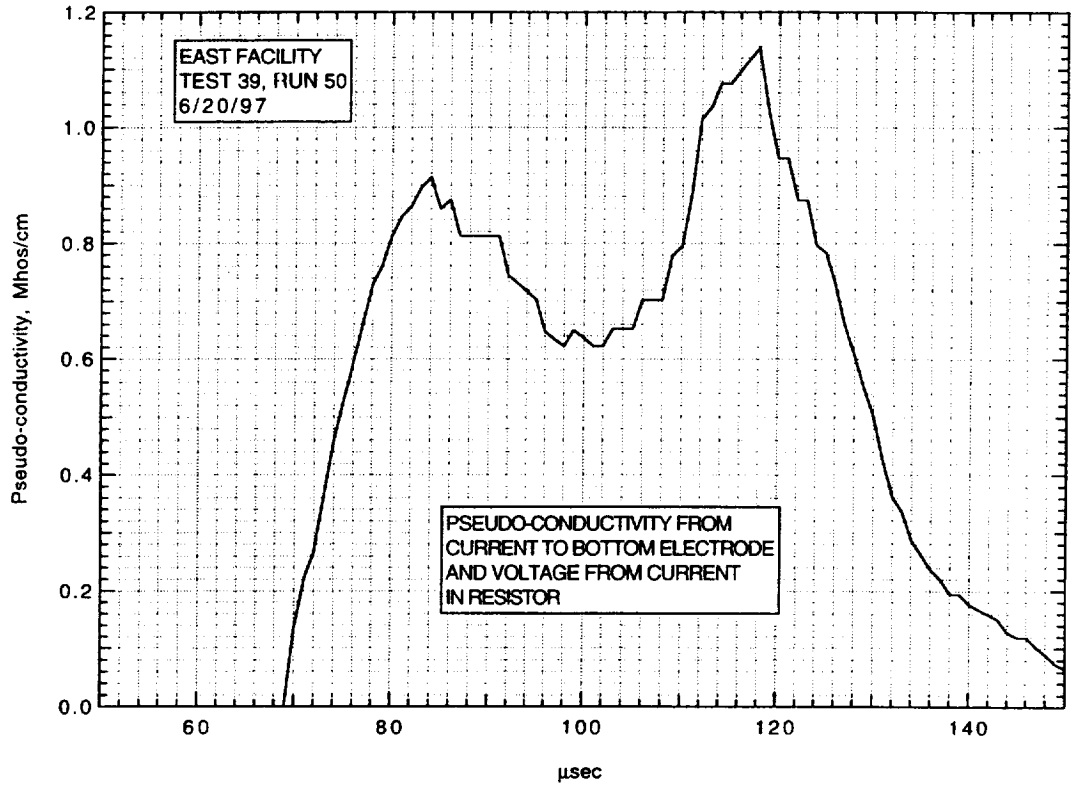

Run 50, pseudo-conductivity from current to bottom electrode and voltage from current in divider.

AIR CONDUCTIVITY MEASUREMENT IN AMES EAST FACILITY

RUN 39/51, 6/20/97

1. Driven tube conditions:

53.2% N_2O, 46.8% N_2,
Total pressure - 35.35 Torr
Measured shock velocity between stns D and F - 4.788 km/sec
Estimated shock velocity at electrodes, from $\Delta t(DF)$ - 4.607 km/sec
Estimated shock velocity at electrodes, from $\Delta t(DE)$ - 4.628 km/sec; (This Δt from pressure transducer at D until start of current flow at electrodes.)
Measured shock pressure at stn D - 18.10 atm
Measured shock pressure at stn F - 9.51 atm - very uncertain due to large EM noise pickup.

2. Electrodes, driven tube dimensions:

Electrode size - 3.10 cm square
Electrode spacing - 3.10 cm
Main diaphragm to electrodes - 454.475 cm
Skimmer nose to electrodes - 39.979 cm
Driven tube diameter - 10.16 cm
Stn D (dn tube) to electrodes (channel) - 77.365 cm
Electrodes (channel) to stn F (channel) - 20.32 cm

3. Nominal test conditions:

Pressure - 13 atm
Voltage across electrodes - 73.2/56.4 V

4. Breakdown:

Little or no indication of breakdown.

Run no: 51 **Date:** 6/20/97 **Shock press. at D:** 18.10 atm
Shock vel. at E: 4.62 km/sec **Voltage at start of current flow:** 73.2 V

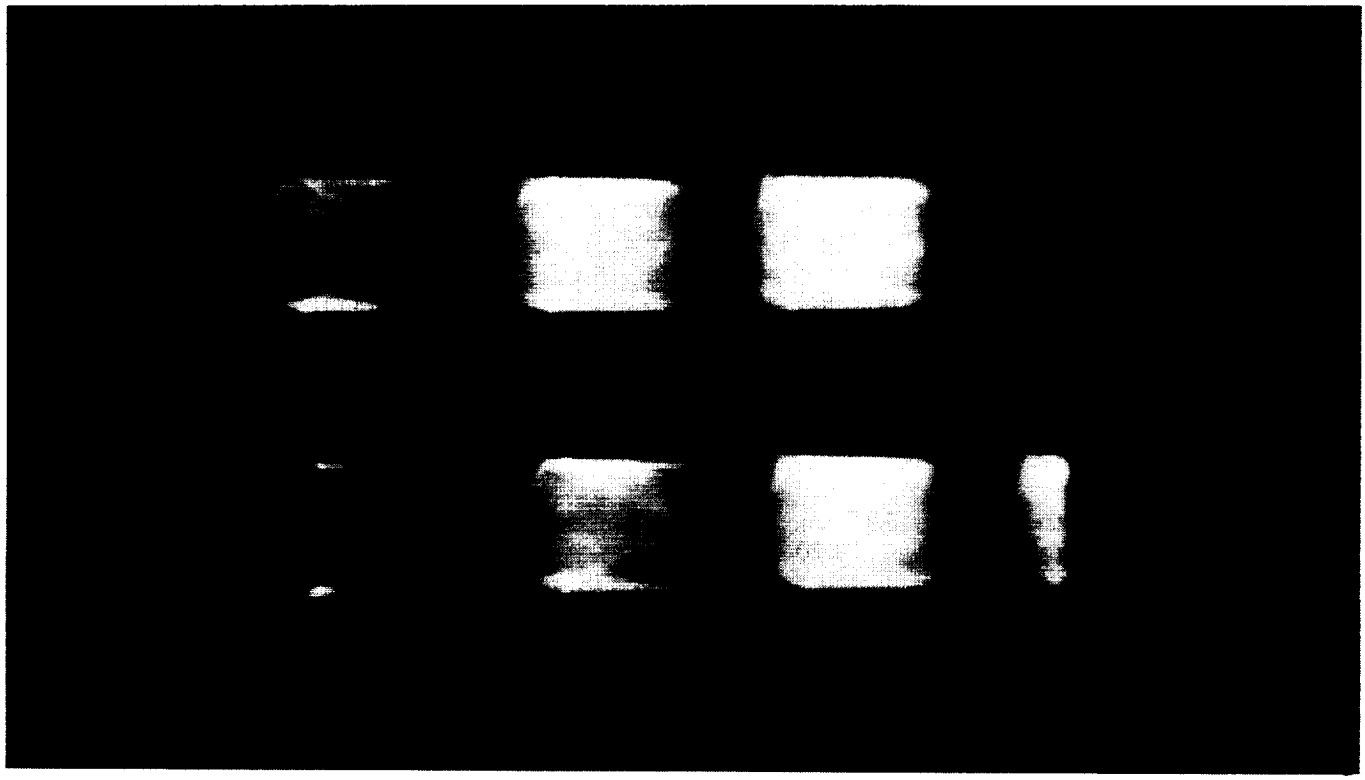

Frame:	**2**	**4**	**6**	**8**
Time:	-1.0	7.0	15.0	23.0
Mach no:				
Frame:	**1**	**3**	**5**	**7**
Time:	-5.0	3.0	11.0	19.0
Mach no:			2.48	

V_I: km/sec **V_{CAV}:** 4.74 km/sec

IMACON image of the shock-heated test gas flow in the electrode region. The time is measured from the start of the current flow. Mach numbers and velocities are deduced from the image as explained in section A.2.5.3.

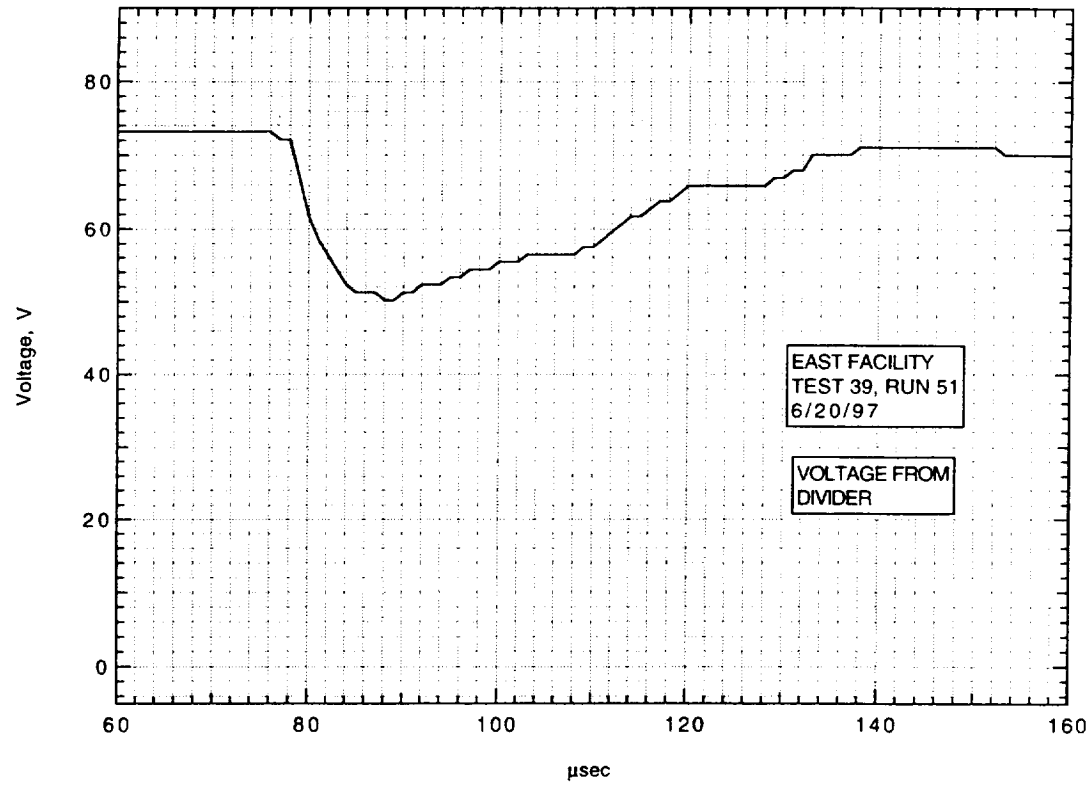

Run 51, voltage across electrodes from divider.

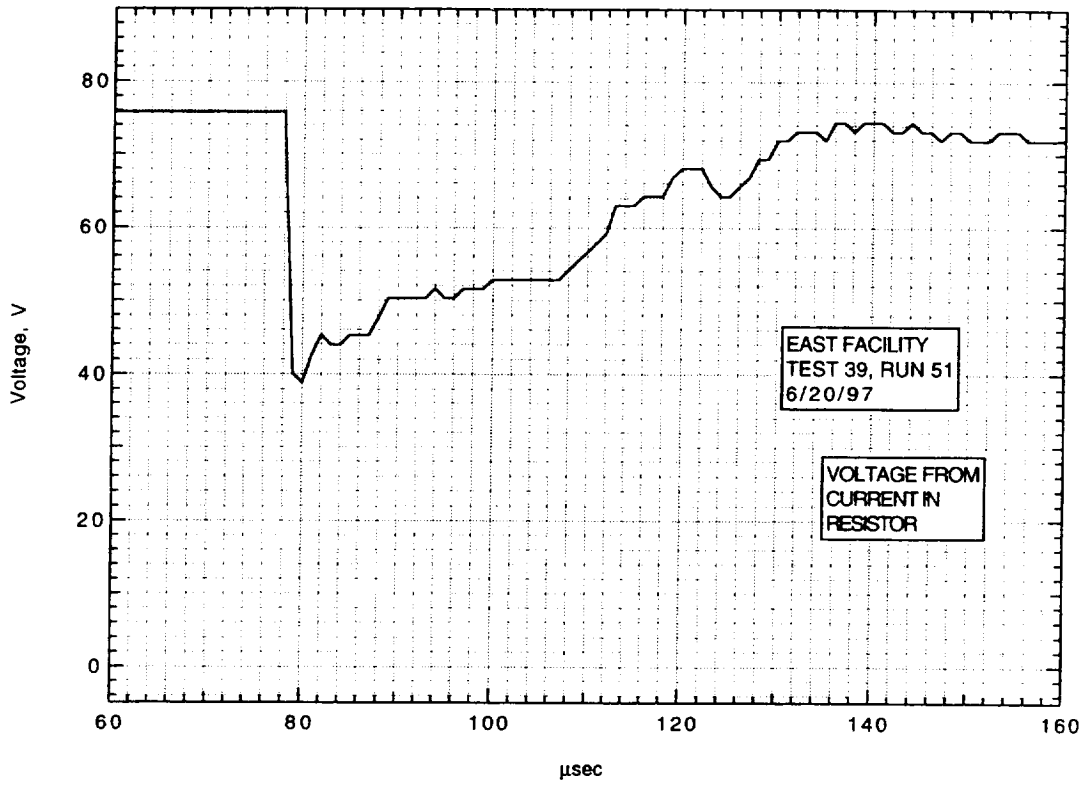

Run 51, voltage across electrodes from current in resistor.

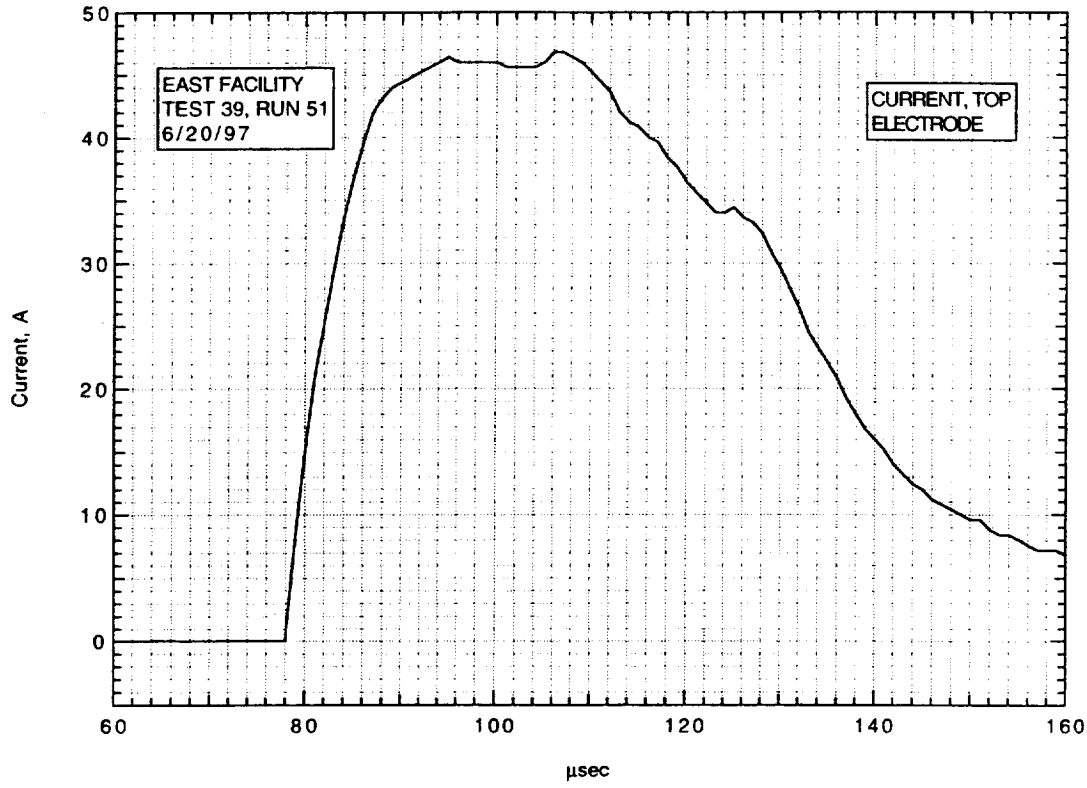

Run 51, current to top electrode.

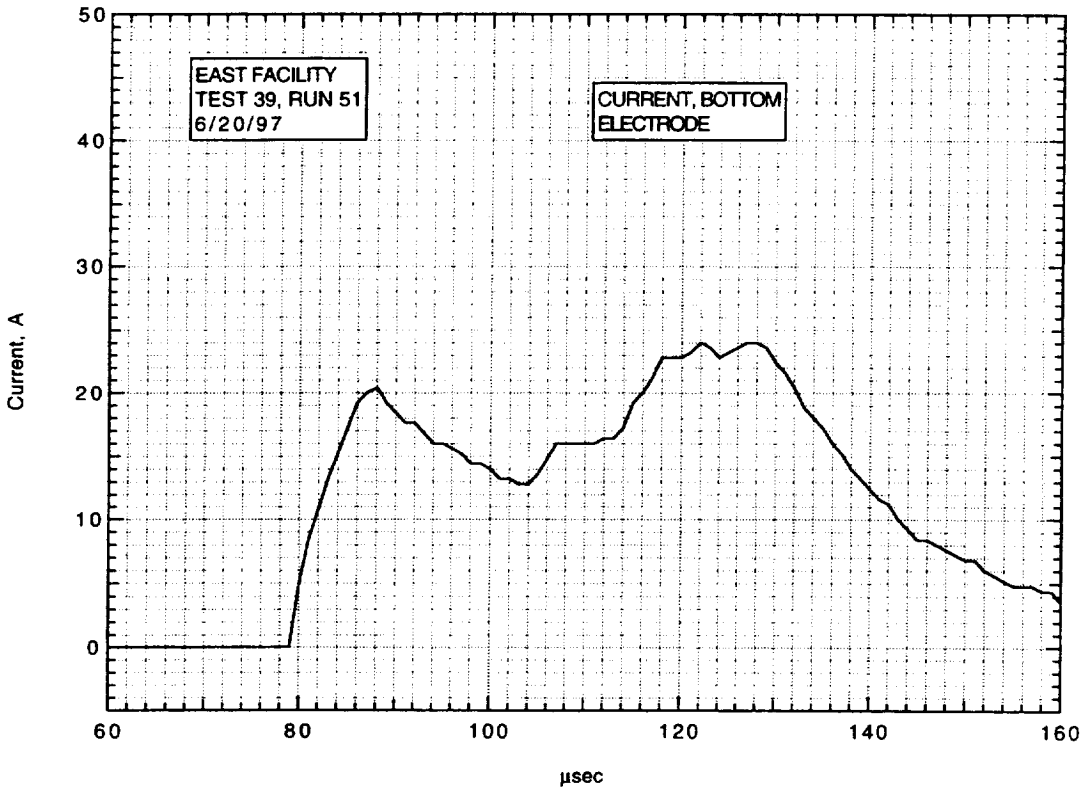

Run 51, current to bottom electrode.

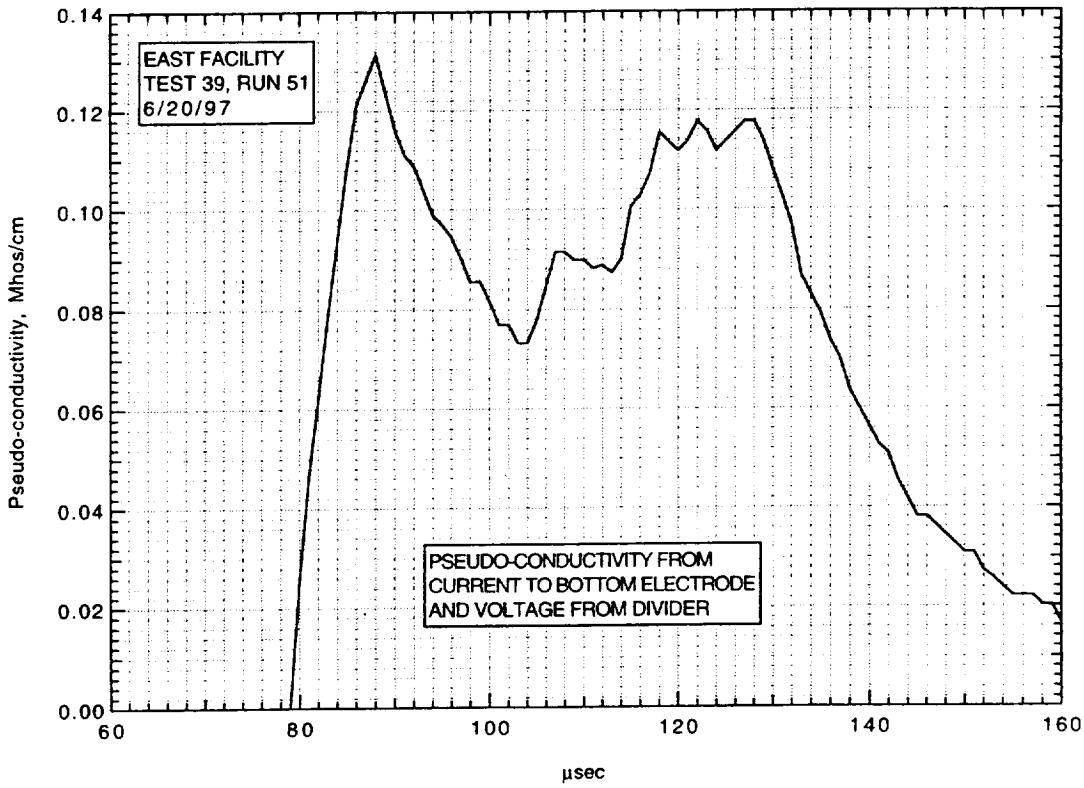

Run 51, pseudo-conductivity from current to bottom electrode and voltage from divider.

REPORT DOCUMENTATION PAGE

Form Approved
OMB No. 07704-0188

1. AGENCY USE ONLY *(Leave blank)*	2. REPORT DATE	3. REPORT TYPE AND DATES COVERED
	October 1997	Contractor Report (April 1995-October 1997)

4. TITLE AND SUBTITLE
Magnetohydrodynamics Accelerator Research Into Advanced Hypersonics (MARIAH) - Final Report

5. FUNDING NUMBERS
PO A45416D

6. AUTHOR(S)
Jack A. Baughman, David A. Micheletti, Gordon L. Nelson, and Gloyd A. Simmons

7. PERFORMING ORGANIZATION NAME(S) AND ADDRESS(ES)
MSE Technology Applications, Inc.
200 Technology Way
P. O. Box 4078
Butte, MT 59702-4078

8. PERFORMING ORGANIZATION REPORT NUMBER
MSE-029

9. SPONSORING/MONITORING AGENCY NAME(S) AND ADDRESS(ES)
U.S. Department of Energy
Federal Energy Technology Center, Pittsburgh, PA and
National Aeronautics and Space Administration
Langley Research Center
Hampton, VA 23681-2199

10. SPONSORING/MONITORING AGENCY REPORT NUMBER
NASA/CR-97-206242/PT1

11. SUPPLEMENTARY NOTES
Technical Monitor: Dennis M. Bushnell, Langley Research Center.
This report was prepared under NASA Ames Research Center Purchase Order A45416D and DOE Contract DE-AC22-96EW96405.

12a. DISTRIBUTION/AVAILABILITY STATEMENT
Unclassified–Unlimited
Subject Category 09 Distribution: Standard
Availability: NASA CASI (301) 621-0390

12b. DISTRIBUTION CODE

13. ABSTRACT ***(Maximum 200 words)***
This report documents the activities, results, conclusions and recommendations of the Magnetohydrodynamics Accelerator Research Into Advanced Hypersonics (MARIAH) Project in which the use of magnetohydrodynamics (MHD) technology is investigated for its applicability to augment hypersonic wind tunnels. The long range objective of this investigation is to advance the development of ground test facilities to support the development of hypervelocity flight vehicles. The MHD accelerator adds kinetic energy directly to the wind tunnel working fluid, thereby increasing its Mach number to hypervelocity levels. Several techniques for MHD augmentation, as well as other physical characteristics of the process are studied to enhance the overall performance of hypersonic wind tunnel design. Specific recommendations are presented to improve the effectiveness of ground test facilities. The work contained herein builds on nearly four decades of research and experimentation by the aeronautics ground test and evaluation community, both foreign and domestic.

14. SUBJECT TERMS
MHD; Accelerator; MARIAH; Hypervelocity; Wind tunnel; Propulsion testing; Ground test facilities; Gas dynamics; Shock tunnel; Computational fluid dynamics; Air chemistry; Seeding; Ionization technologies; Foreign MHD activity

15. NUMBER OF PAGES
640

16. PRICE CODE
A99

17. SECURITY CLASSIFICATION OF REPORT	18. SECURITY CLASSIFICATION OF THIS PAGE	19. SECURITY CLASSIFICATION OF ABSTRACT	20. LIMITATION OF ABSTRACT
Unclassified	Unclassified	Unclassified	